UNIVERSITY OF SOUTHAMPTON

FACULTY OF NATURAL AND ENVIRONMENTAL SCIENCES

School of Chemistry

Stimuli-Responsive Disassembly of the Mechanical Bond: Synthesis and Properties of Ring-Opening 2,2'-Bipyridine Macrocycles

by

Matthew Fitzpatrick

Thesis for the degree of Doctor of Philosophy

July 2022

UNIVERSITY OF SOUTHAMPTON

Abstract

Thesis for the degree of Doctor of Philosophy

Stimuli-Responsive Disassembly of the Mechanical Bond: Synthesis and Properties of Ring-Opening 2,2'-Bipyridine Macrocycles

The development of template-directed methodologies have facilitated the synthesis of structurally-diverse mechanically interlocked molecules (MIMs) and prompted investigations into their unique chemical properties. In doing so, MIMs have been transformed from mere synthetic curiosities to functional materials with applications in a range of fields, such as molecular machines, materials, and catalysis. Although often overlooked among the plethora of application-based MIM literature, the use of MIMs in biological applications is a flourishing field. The introductory chapter provides a scoping review of current literature on synthetic interlocked molecules used for biological applications. By analysing the MIMs with respect to the properties of the mechanical bond, the chemical behaviour underpinning their biological function is elucidated.

Chapter 2 details the synthesis of a ring-opening 2,2'-bipyridine macrocycle, which mediated AT-CuAAC rotaxination with high efficiency. Upon exposure to UVB light, the photolabile diethylaminobenzyl (DEABn) within the macrocycle backbone was cleaved, resulting in the ring-opening and release of the corresponding axle. In lieu of the expected photocleavage pathway, a surprising intramolecular photo-induced rearrangement was instead found to dominate. The photocleavable macrocycle was successfully incorporated into a dinucleotide rotaxane and later into a model oligonucleotide rotaxane structure.

In Chapter 3, the development of a modular platform approach for the generation of ring-opening 2,2'-bipyridine macrocycles is described. A series of macrocycles designed to cleave in response to several different stimuli (pH, chemical, UV, light) were rapidly and conveniently synthesised, and shown to mediate AT-CuAAC rotaxination with high efficiency. Cleavage of the trigger unit in response to the appropriate stimulus generated an intermediate rotaxane species which underwent ring-opening to liberate the axle from the interlocked structure with varying degrees of success. Tailoring the electronic properties of the self-immolative spacer within the macrocycle backbone through judicious structural modification was later shown to significantly improve the ring-opening capability of the macrocycle.

Table of Contents

Declaration of Authorship

I, MATTHEW FITZPATRICK, declare that this thesis and the work presented therein are my own and has been constructed by me as a result of my own original research.

Stimuli-Responsive Disassembly of the Mechanical Bond: Synthesis and Properties of Ring-Opening 2,2'-Bipyridine Macrocycles

I confirm that:

1. This work was done wholly or mainly while in candidature for a research degree at this University.
2. Where any part of this thesis has previously been submitted for a degree or any other qualification at this University or any other institution, this has been clearly stated.
3. Where I have consulted the published work of others, this is always clearly attributed.
4. Where I have quoted from the work of others, the source is always given. With the exception of such quotations, this thesis is entirely my own work.
5. I have acknowledged all main sources of help.
6. Where the thesis is based on work done by myself jointly with others, I have made clear exactly what was done by others and what I have contributed myself.

Acknowledgements

There are numerous people I wish to thank for contributing to this work. For providing me with the opportunity to join the group and pursue my PhD, I would like to express my sincere gratitude to my supervisor, Prof. Steve Goldup. Your continued support and guidance has been invaluable throughout my studies.

To all members of the Goldup group that I've had the fortune to work with — it's been a blast. Without your friendship and encouragement, I never would have made it over the finish line. I hope I didn't complain (too) much. To my flatmate and fam, Arnaud, I thank you for your friendship, excellent cooking, and continued support over an emotionally bumpy few years. P.S. Sorry for abandoning you during a pandemic. To my fellow Celt and climbing buddy, Ellen, thanks for all the craic and for being a sympathetic ear. You're really not as scary as I first thought. David, thank you for the daily torment that inspired me to reach my full potential; and for the four Catalan songs that now play perpetually in my brain. I thank Amanda, with whom the bio-parts of this thesis are in collaboration with, for always having my back, and for igniting my obsession with house plants. For his unique brand of chaos and endless supply of existential memes, I thank my fume hood neighbour, Andrea. To my favourite Frenchman, Noël, I thank you for your wisdom in breaky macrocycle things. Your obsession with butter will forever fuel my soul. To Federica, thank you for joining me on my multiple daily coffee/stress breaks. These chats almost certainly prevented a mental breakdown. Andrew, your bizarre sense humour and never-ending offers of support, both in an out of the lab, made for an excellent desk mate. Jack, thank you for the chats, the runs, and for not including me in your chemical warfare projects. I thank Jorge for his fabulousness, and for being an absolute tornado in the lab. Mike, cheers for always buying the first round at the pub, and for teaching me the ways of a cowboy chemist. To the paradoxical youngest and longest serving member of the Goldup group, Peter, I thank you for your consistently positive vibes. For his puzzling poetry and gentle soul, I thank lecturer Poom. To my captain, Alberto, thank you for cleaning my spatulas. I thank Shu for his infectious carefree attitude and 'nothing'. Peggy for being the kindest and sweetest person I've ever met. Matthieu, for the lycra, and Florian for being the frenchiest of the French. To the newbies of the group — Georgia, Abed and Mandeep — it's been great getting to know you over my last few months in Southampton.

A special thanks goes out to my second supervisor Prof. Ali Tavassoli and all the members of his group for their useful insights into my research, and for putting up with my lack of bio

knowledge during group meetings. To Patrick, I thank you for all your help with crystal-y stuff, and for taking care of Arnaud after I left. Vilma, I thank you for all the coffees, beers and lunches. On a more personal note, I’d like to thank all my friends and family back in Belfast for their support throughout my PhD.

Definitions and Abbreviations

δ	Chemical Shift
λ	Wavelength
A, T/U C, G	Adenine, Thymine/Uracil, Cytosine, Guanine
Ac	Acetyl
AcOH	Acetic Acid
ADC	Antibody-Drug Conjugate
AIE	Aggregation Induced Emission
Alloc	Allyloxycarbonyl
Aq.	Aqueous
Asc	Ascorbate
ASO	Antisense Oligonucleotide
AT-CuAAC	Active Template Cu Catalyzed Azide Alkyne Cycloaddition
ATP	Adenosine Triphosphate
Boc	*tert*-Butyloxycarbonyl
BSA	Bovine Serum Albumin
CB	Cucurbituril
CD	Cyclodextrin
cET	Constrained Ethyl
CM	Coumarin
COSY	Correlation Spectroscopy
CPG	Controlled Pore Glass
CRIPSR	Clustered Regularly Interspaced Short Palindromic Repeats
DEABn	Diethylaminobenzyl
DEAD	Diethyl azidodicarboxylate
DHFR	Dihydrofolate Reductase
DI	Deionised
DIC	Diisopropylcarbodiimide
DIPEA	*N*,*N*'-Diisopropylethylamine
DMAE	Dimethylaminoethyl
DMAP	4-Dimethylaminopyridine
DMF	*N,N'*-Dimethylformamide

DMNB	3,5-dimethoxy-2-nitrobenzene
DMP	Dess-Martine Periodinane
DMSO	Dimethyl Sulfoxide
DMTr	4,4'-Dimethoxytrityl
DNA	Deoxyribonucleic Acid
DNase	Deoxyribonuclease
DO3A	1,4,7,10-Tetraazacyclododecane-1,4,7-triacetic acid
DOTA	1,4,7,10-Tetraazacyclododecane-1,4,7,10-tetrayl tetraacetic acid
DPA	Dipicolyl Amine
DPPA	Diphenylphosphoryl Azide
dr	Diastereomeric Ratio
DTT	Dithiothreitol
EDG	Electron-Donating Group
EDTA	*N,N,N',N'*-Ethylenediaminetetraacetic Acid
EPR	Enhanced Permeability and Retention
Eq.	Equivalent
ER	Endoplasmic Reticulum
ESI	Electrospray Ionisation
Et	Ethyl
EtOAc	Ethyl Acetate
EtOH	Ethanol
ETR	Energy Transfer Relay
EWG	Electron-Withdrawing group
FRET	Förster Resonance Energy Transfer
FT	Fourier Transform
GFP	Green Fluorescent Protein
gRNA	Guide Ribonucleic Acid
GSH	Glutathione
h	Hour
HIV	Human Immunodeficiency Virus
HMBC	Heteronuclear Multiple-Bond Correlation
HOBT	Hydroxybenzotriazole

HPLC	High-Performance Liquid Chromatography
HR-MS	High-Resolution Mass Spectrometry
HSQC	Heteronuclear Single Quantum Correlation
Hv	Light
hyperCEST	Hyperpolarized Xenon Chemical Exchange Saturation Transfer
Hz	Hertz
IPA	Isopropyl Alcohol
^{i}Pr	Isopropyl
IR	Infrared
J	Coupling Constant
JMOD	J-Modulation Spin-Echo
K	Kelvin
LG	Leaving Group
LNA	Locked Nucleic Acid
LR-MS	Low-Resolution Mass Spectrometry
M	Molarity
m.p.	Melting Point
m/z	Mass-to-Charge Ratio
mAB	Monoclonal Antibody
Me	Methyl
MeOH	Methanol
MIM	Mechanically Interlocked Molecule
min	Minute
miRNA	Micro Ribonucleic Acid
MLCT	Metal-To-Ligand Charge Transfer
MMAE	Monomethyl Auristatin E
MMP-2	Matrix Metalloprotease-2
MRI	Magnetic Resonance Imaging
mRNA	Messenger Ribonucleic Acid
MSNP	Mesoporous Silica Nanoparticle
MW	Molecular Weight
NADPH	Nicotinamide Adenine Dinucleotide Phosphate

NBS	N-Bromosuccinimide
NMR	Nuclear Magnetic Resonance
NOE	Nuclear Overhauser Effect
NP	Phosphoramidate
NPOM	6-Nitropiperonyloxymethyl
NQO1	NAD(P)H: Quinone Oxidoreductase 1
OCTN2	Organic Carnitine Transporter Novel type 2
*o*NB	*ortho*-Nitrobenzyl
PCL	Poly(ε-caprolactone)
PCR	Polymerase Chain Reaction
PDI	Perylene Diimide
pDNA	Plasmid Deoxyribonucleic acid
PEG	Polyethylene glycol
PET	Photo-Induced Electron Transfer
PG	Protecting Group
PGA	Penicillin G-Amidase
Ph	Phenyl
pHP	*para*-Hydroxylphenacyl
PMO	Phosphorodiamidate Morpholino Oligomers
PNA	Peptide Nucleic Acid
PPG	Photolabile Protecting Group
ppm	Parts Per Million
PR	Polyrotaxane
PS	Phosphorothioate
quant.	Quantitative
r.t.	Room Temperature
RGD	Arginylglycylaspartic Acid
RNA	Ribonucleic Acid
RNAi	Ribonucleic Acid Interference
ROS	Reactive Oxygen Species
SI	Self-Immolative
siRNA	Small Interfering Ribonucleic Acid

t-LNA	Triazole-linked Locked Nucleic Acid
TAT	Trans-Activator of Transcription
TBA	Tetrabutylammonium
TBAF	Tetrabutylammonium Fluoride
TBDMS-Cl	*tert*-Butyldimethylsilyl chloride
*t*Bu	*tert*-Butyl
TEAB	Tetraethylammonium bicarbonate
TEG	Tetraethylene Glycol
TFA	Trifluoroacetic acid
THF	Tetrahydrofuran
THPTA	tris-Hydroxypropyltriazolylmethylamine
TLC	Thin Layer Chromatography
TMV	Tobacco Mosaic Virus
TPE	Tetraphenylethene
TPP	Triphenylphosphonium
Ts	4-Toluenesulfonyl
UV	Ultraviolet
Vis	Visible
XRD	X-Ray Diffraction

Chapter 1: Introduction

Abstract: Synthetic interlocked molecules have found successful biological application in key areas such as drug discovery and bioimaging, among a host of other diverse uses. However, the chemical behaviour of the mechanical bond which underpins the biological activity of the molecule is often poorly understood or ineffectively articulated and, as a result, this flourishing field is often overlooked amongst the plethora of application-based MIM literature. In this chapter, we present a scoping review of synthetic interlocked molecules used for biological applications and detail the role of interlocking as it relates directly to biological function.

Acknowledgements: This chapter has been prepared as part of a review for *Angew. Chemie* (proposal accepted) in collaboration with Dr. Amanda Acevedo-Jake, who contributed to the literature search and selection of relevant examples. All of the text, graphics, and analyses were prepared independently.

1.1. Introduction

Mechanically interlocked molecules (MIMs) are composed of spatially entangled sub-components held together not through attractive molecular interactions, but by the physical inability of atoms to pass through one another. Rotaxanes, in which a macrocycle encircling an axle is prevented from dissociating by sterically bulky end-groups, and catenanes, where two or more macrocycles are linked in a topological manner, are the quintessential examples of MIMs (Figure **1**).[1,2] The topological entanglement of macrocyclic components in catenanes is clear. However, the distinction between interlocked rotaxanes and supramolecular rotaxanes-like complexes in the literature is often ambiguous.[3,4] For a rotaxane to be considered truly interlocked, the only way to separate mechanical components is through covalent bond cleavage. If the macrocycle is capable of de-threading, even under extreme conditions, then the species is considered a pseudo-rotaxane and is not truly interlocked.

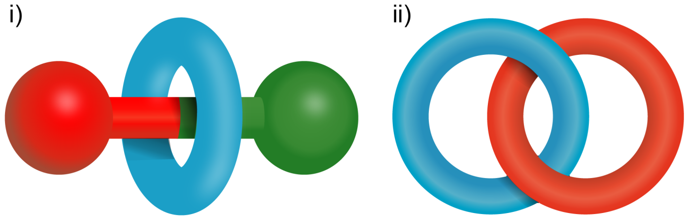

Figure **1**. Schematic representation of a [2]rotaxane (i) and a [2]catenane (ii). The numeral prefix describes the number of sub-components in the interlocked structure.

This robust appeal of the mechanical bond is emphasised by its occurrence in naturally occurring biopolymers, where it can fulfil a variety of functional roles. For instance, extremophilic archaea have been found to use topological linkages to stabilise enzymes against thermal denaturation, allowing them to remain in their functional folded state.[5] The organisation of DNA in catenated or knotted intermediates is also vital to DNA recombination and replication.[6,7] Efforts to synthesise artificial MIMs pre-date the discovery of the first mechanically interlocked biomolecules.[8,9] The introduction of template-directed methodologies by Sauvage and co-workers in the 1980s was transformative to the field of MIMs, facilitating the synthesis of a plethora of structurally-diverse interlocked architectures and prompting investigations into their unique chemical properties.[10–12] In doing so, MIMs have been transformed from mere synthetic curiosities to functional materials with practical applications in a range of fields: artificial molecular machines,[13] smart materials,[14] catalysis,[15] molecular recognition and sensing,[16] among others. Although often overlooked, an ever-increasing number of MIMs have been designed to interact with biological systems.[17,18] The effect of the mechanical bond on the chemistry and bioactivity of the interlocked species varies considerably depending on the application, but can be roughly classified as: (i) acting as structural scaffold to hold multiple functional components together, (ii) stabilising or silencing the biological activity of component parts, (iii) as host complexes to bind biologically-relevant guests, or (iv) those which utilise mechanical motion for biological effect. For the purposes of this overview, only truly interlocked structures will be discussed.

1.2. The Mechanical Bond as a Structural Feature

Combining multiple functionalities within the same molecular scaffold is a common approach to install additional activity or enhance the physiochemical properties of a bioactive substance. For instance, therapeutic drugs can be covalently conjugated to ligands that target biological receptors to improve selectivity, or to imaging functionalities to provide a diagnostic capability.[19] This approach has the disadvantage of requiring a more complex synthetic route to incorporate these covalent linkages. Additionally, the covalent linkages can add a rigidity to the system that limits the ability of the different units to perform their function. Conversely, the mechanical bond is an attractive molecular scaffold that grants sub-components the ability to move and rotate with respect to each other while still retaining their individual molecular and supramolecular character. Depending on the context, there are numerous synthetic and practical benefits of using the mechanical bond over traditional covalent linkage to hold functional components together.

1.2.1. Magnetic Resonance Imaging Contrast Agents

Magnetic resonance imaging (MRI) is a high-resolution, non-invasive, and non-radiative three-dimensional imaging technique that has become an invaluable tool in diagnostic medicine. MRI contrast agents, such as Gd^{3+} chelates, are commonly employed to enhance the contrast and resolution of MRI images by decreasing the spin-lattice (T1) relaxation times of the protons in nearby water molecules. However, the majority of clinically approved Gd^{3+} chelates offer only moderate contrast enhancement, suffer from rapid renal clearance, and extravasate from vascular compartments, which reduces contrast to surrounding tissues.[20] Thompson *et al.* were the first to recognise the PR scaffold as a means to overcome these issues. In their seminal study, the commonly used Gd^{3+} ligand DO3A was conjugated to the mobile β-CD rings of a cholesterol-stoppered PR structure.[21] Relative to the Gd^{3+}-DO3A functionalised β-CD monomer unit, a 3-fold enhancement in ionic relaxivity was observed for the PR structure, as well as significantly longer blood circulatory times which allowed for much greater anatomic detail resolution (Figure **2**). The authors suggest that the enhanced relaxivity was directly correlated to the mechanical bond, which slows the rotation of the CDs units by allowing them to remain in close proximity and form hydrogen bonds. This decreases the molecular rotational correlation time of the appended Gd^{3+}-DO3A chelates — a microscopic parameter that determines the efficiency of a contrast agent — leading to greater relaxivity. A later study found that analogous PR structures with higher numbers of threaded Gd^{3+}-chelate functionalised β-CDs units had much longer blood circulation times, which could be attributed to greater plasma protein binding of the higher molecular weight PRs.[22]

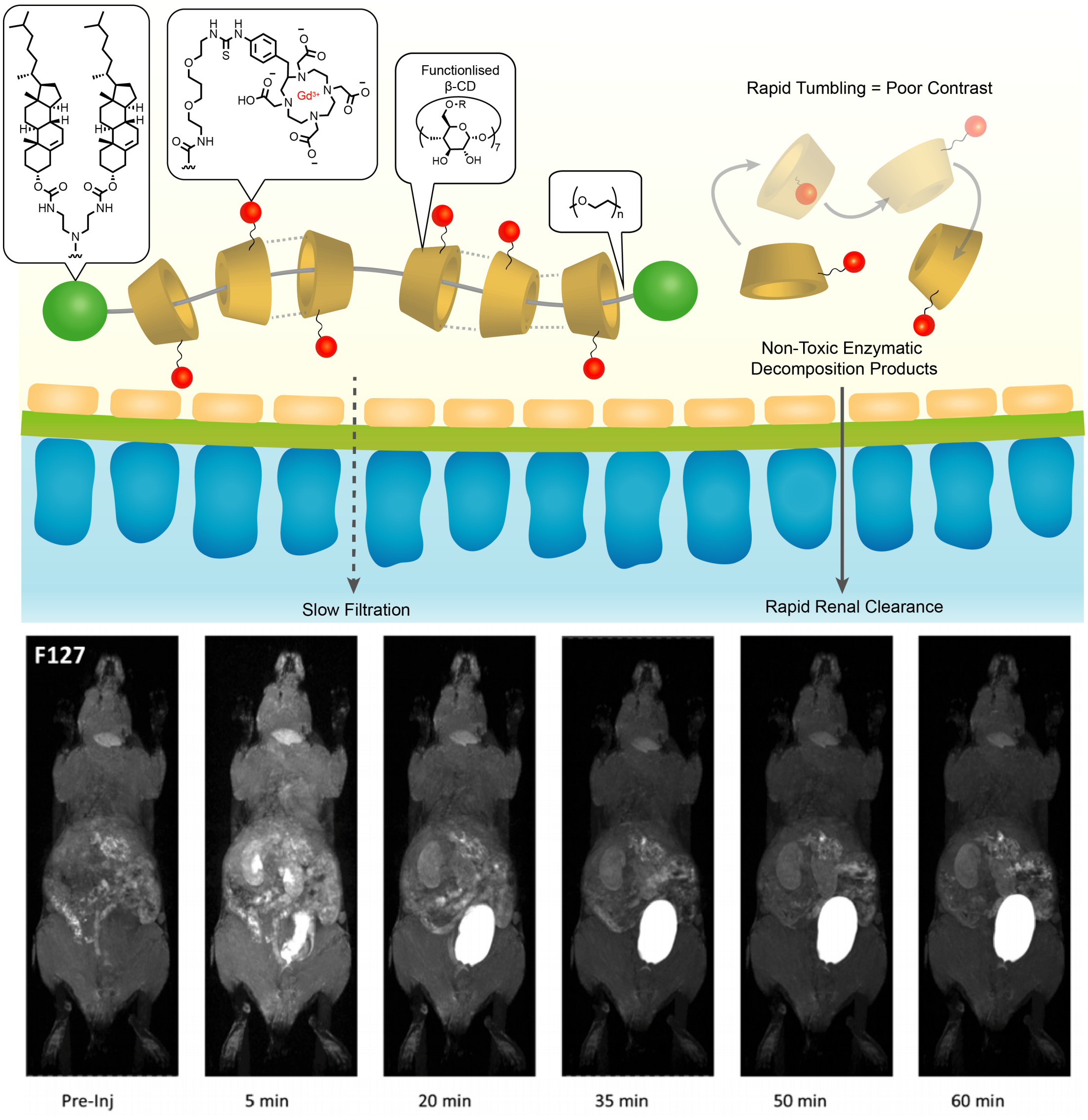

Figure **2**. Structure of the Gd^{3+}-DO3A modified β-CD-based PR contrast agent. MRI images show contrast agent distribution in mice up to 60 minutes after tail vein injection. Images adapted with permission from Thompson *et al.*[22]

1.2.2. Snap-top Nanovalves

Mesoporous silica nanoparticles (MSNPs) have been used extensively in biomedicine for the controlled delivery of diagnostic and therapeutic molecular cargoes.[23] The abundance of examples in the literature arises from the inherent medicinal features of MSNPs, such as their low cytotoxicity, highly tuneable morphology, and ability to passively accumulate in solid tumours *via* the enhanced permeability and retention (EPR) effect.[24] To act as an efficient drug delivery vehicle, the MSNP must be able to protect the encapsulated drug from physiochemical degradation during systemic transport while also preventing its premature release, thus mitigating off-target effects. While comparable to the prodrug approach, using MSNPs to deliver drugs in a tissue-specific manner negates the need for covalent modification and allows many drug molecules to be released in response to a single activation event.

Rotaxane structures bound to the silica matrix are perfectly suited to act as smart gatekeepers to cap the surface apertures of MSNPs.[25] When the bulky macrocyclic component lies close to the pore surface, the valve is "closed" and the molecular cargo cannot escape. Through the incorporation of a stimuli-responsive unit within the rotaxane architecture, most commonly in the axle or stopper component, the macrocycle can de-thread and move away from the surface. This "opens" the valve and releases the cargo in a controlled fashion (Figure **3**). Reversible nano-valves relying on molecular motion to shuttle the macrocycle away from the pore are mechanistically different and will be discussed later.

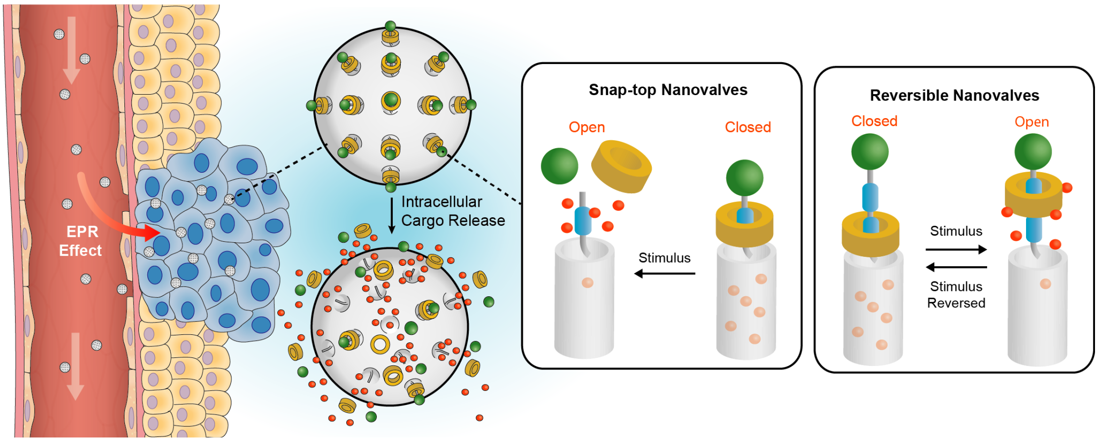

Figure **3**. Stimuli-responsive cargo release from MSNP-functionalised snap-top nanovalves and reversible nanovalves.

Numerous snap-top systems have been employed to selectively release various drugs and dyes in biological systems.[26,27] A common strategy involves designing the stimuli-responsive unit to autonomously cleave upon entering a specific biological environment. Cellular cytosol contains high concentrations of reducing agents, such as glutathione (GSH), that lower its redox potential relative to the extracellular environment. GSH concentrations in cancer cells are even higher still, making it a very attractive activating stimulus to use in combination with the passive tumour targeting ability of MSNPs.[28] Disulfide linkages can undergo selective redox-induced intracellular cleavage and are commonly incorporated within snap-top MSNPs to facilitate controlled-release.[29] Similarly, the expression of many types of enzymes is found to be higher in cancer cells relative to healthy cells. As such, enzyme-responsive moieties are commonplace in snap-top systems.[30] Wu *et al.* have reported an NQO1 enzyme-responsive MSNP for the tumour targeted delivery of anti-cancer drugs *in vivo*.[31] Human NQO1, a quinone reductase enzyme inextricably linked to various cancers, is over-expressed by up to 50-fold in tumour cells relative to healthy tissue, and has found utility as a conditional trigger in numerous responsive drug delivery applications.[32] In this system, a benzoquinone stopper holds mechanically bonded α-CDs close to the surface of the MSNP, preventing cargo release until NQO1 and NADH were both present. The 2-electron reduction of benzoquinone unit and subsequent self-cleavage resulted in the α-CD de-threading, unblocking the pore and releasing the cargo (Figure **4**). Incubation of doxorubicin (**1**) loaded MSNPs in an A549 cancer cell-line known to heavily overexpress NQO1 effectively initiated apoptosis and caused cell death. No significant change in cell viability was observed in an NQO1 negative cell line. Furthermore, *in vivo* studies showed MSNPs loaded with doxorubicin had much greater tumour-suppression ability in live mice relative to free doxorubicin, which was attributed to the inherent tumour-targeting ability of MSNPs.

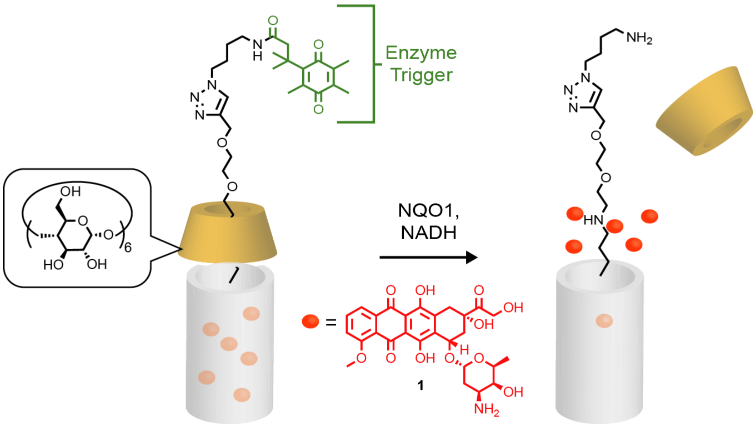

Figure **4**. NQO1 enzyme-responsive release of doxorubicin from a snap-top MSNP.

While the majority of snap-top systems utilise nanovalves solely to control MSNP cargo release, Kros *et al.* have demonstrated dual-functionality by incorporating a membrane targeting peptide within the stopper unit *via* a reducible disulfide linkage.[33] The

12-amino-acid stopper is a fragment of the HIV-1 TAT protein that facilitates translocation of the virus across cell membranes, and is commonly exploited to enhance the cellular uptake of exogenous molecules.[34] While the relatively non-bulky amino-acid sequence may not be a stopper in itself, it has a strong propensity to form a helix structure under aqueous conditions, rendering de-threading kinetically slow. The release of a fluorescein dye was monitored by confocal microscopy upon GSH-activated cleavage of a disulfide linker. Peptide-modified MSNPs showed substantially higher internalisation in HeLa cells (up to 98%) relative to naked MSNPs (13%), which was attributed to the high membrane protein affinity of the TAT peptide sequence. Cai *et al*. have also showed that folate-based stoppers can be used to actively target tumour tissues *in vivo.*[35]

1.2.3. Multivalency For Inhibition

Ligand-immobilized polymers are frequently employed to regulate the multivalent interactions between biological receptors and their partners.[36] However, spatial mismatching between the multiple ligand copies situated along the polymer backbone and the binding sites of receptors is common.[37] Increasing the number of pendant ligands on the polymer chain only increases the likelihood of binding to a certain extent, after which steric crowding becomes thermodynamically unsuitable for multivalent binding.[38] Conjugating ligands to the macrocyclic components in PRs, which possess high molecular mobility due to their ability to freely rotate and slide along the axle, has been reported to overcome these difficulties.[39] In the PR architecture, mobile ligands can move freely and adapt to cells surface to effectively bind multiple biological receptor sites simultaneously, enhancing the cooperative effect of multivalent interactions and resulting in highly potent binding. For instance, the binding of maltose-PR conjugates to lectin Concanavalin A was calculated to be over 3000 times greater than the sum of individual monovalent maltose units.[40]

Yui *et al.* have pioneered research in this area and highlighted the efficacy of modified PR architectures for the sensing and inhibition of numerous therapeutically relevant biological interactions (Figure **5**). An early study by Yui *et al.* reported a Phe-stoppered PR structure with dipeptide (Val-Lys) conjugated α-CDs for the inhibition of hPEPT1 – an intestinal transport protein responsible for the uptake of di- and tripeptides during digestion.[41] *In vitro* studies found that the cellular uptake of a Gly-Sar dipeptide sequence was strongly inhibited in the presence of PR Val-Lys-conjugates, which were not themselves absorbed. The importance of co-operative ligand interactions was highlighted in a series of control experiments which indicated that inhibition did not occur with the analogous unconjugated PRs. Monovalent Val-Lys-modified α-CDs displayed only a slight inhibitory effect, implying that multivalent binding of several hPEPT1 proteins simultaneously was key to successful inhibition.

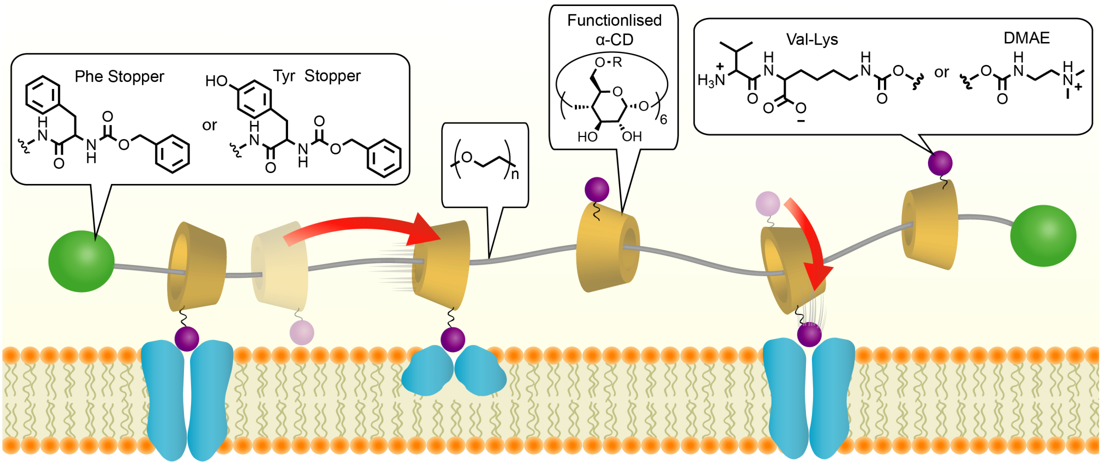

Figure **5**. An overview of the of PR structures developed by Yui *et al*. for the inhibition of membrane transport proteins.[41,42]

Yui *et al.* later expanded the ligand scope and found that cationic dimethylaminoethylcarbamoyl (DMAE)-modified PRs displayed similar efficacy in inhibiting uptake of L-Carnitine by the intestinal organic cationic transporter (OCTN2).[42] Low cytotoxicity was observed at therapeutically relevant doses. Inhibition was more potent with longer polyethylene glycol (PEG) chains, which allowed the PR to interact with multiple copies of the OCTN2 receptor simultaneously. Importantly, the inhibitory effect was also largely independent of the total number of cationic ligands when used in combination with longer PEG chains, which validates the theory that the molecular mobility of ligand-mobilised α-CD rings is key to multivalent binding capability in PR architectures. Through judicious choice of ligand, a variety of other PR structures have been developed and shown to participate in multivalent binding interactions with a variety of proteins, enzymes, and lipid membranes.[43–46] More recently, Yui *et al.* have reported the use of mannose- and carboxyl-modified α-CDs to enhance the cellular uptake of PRs by macrophages through selective binding to scavenger receptor proteins.[47,48]

1.2.4. Polyrotaxane Hydrogels

Hydrogels are three-dimensional hydrophilic polymer networks capable of absorbing large amounts of water while still retaining a well-defined structure. The inherent inhomogeneity of traditional covalently cross-linked hydrogels has been linked to weakened mechanical integrity and toxic side-effects.[49] To overcome these issues, numerous groups have sought to install physical or supramolecular cross-linkages between the mobile macrocyclic units on adjacent PR chains.[50,51] These moveable cross-linkages can slide and deform to relieve internal stress, giving the gels a highly elastic character and extraordinary self-healing ability.[52] Long-chain polymers such as PEG or polypropylene glycol typically make up the thread component, and have been used in combination with various types of macrocycles, such as CDs and crown ethers.[53,54] PRs based on PEG-CD components are by far the most commonly employed for biological applications due to their excellent biodegradability, biocompatibility, and low cytotoxicity of their component parts. The biocompatibility of the PR structures can be further improved through the incorporation of stimuli-responsive units within the stoppers, which initiate mechanical bond disassembly in response to various endogenous chemical or enzymatic triggers once the function of the hydrogel has been served (Figure **6**).[55] Therapeutic drugs have been formulated within the hydrogel matrix to prevent premature physiochemical degradation and to enhance aqueous solubility and transport properties. For instance, Cooper-White *et al*. have reported a hydrolytically degradable PEG-α-CD-based PR hydrogel for the encapsulation and controlled intracellular delivery of poorly water-soluble compounds.[56] By altering the number α-CD units and degree of cross-linking, the rate of hydrogel degradation through hydrolytic ester cleavage could also be controlled to slowly release 6-aminofluoroscein *in vitro* over 2-8 days.

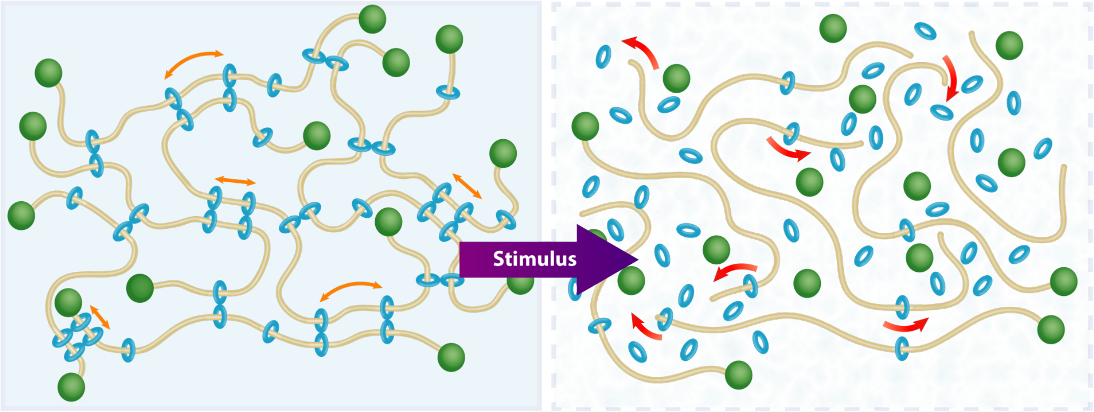

Figure **6**. Biodegradation of PR-based hydrogels upon stimuli-responsive stopper cleavage.

Due to their excellent biocompatibility and highly-tuneable three-dimensional aqueous networks, CD-based PR hydrogels have also been used extensively as implantable biomaterial scaffolds for soft tissue engineering and regenerative medicine applications.[57] The erosion time of these materials can be tailored to the specific application by varying the PEG/CD ratio, which essentially equates to the cross-linking density, or by altering the stimuli-responsive component that initiates endogenous mechanical bond disassembly.[58,59] Such load-bearing scaffolds have the benefit of degrading naturally when they are no longer needed, avoiding the need to remove implants through surgery. The porous micro-environment of swollen PR hydrogels can mimic the extracellular matrix to facilitate the metabolism of tissue fluid and allow rapid exchange of gases, supporting cellular adhesion and proliferation — processes that are fundamental to tissue and cartilage regeneration.[60–65]

More recently, PR hydrogels have been reported as highly efficient and biocompatible crosslinkers for collagen, a naturally abundant triple-helix forming structural protein used extensively in tissue regeneration applications.[66] To facilitate its use in living systems, artificial collagen must be cross-linked to improve its mechanical and physiochemical properties.[67] Linking the amino-functionalities of collagen side chains with the mobile CD units in PR hydrogels has been reported to negate the problems associated with traditional crosslinking approaches, such as insufficient crosslinking efficiency or cytotoxicity caused by residual coupling agents. Ren *et al*. have reported aldehyde functionalized β-CD-polypropylene glycol PR hydrogels capable of covalently crosslinking collagen chains *via* imine formation, with a maximum efficiency of 87.1%, which is considerably higher than analogous covalent crosslinking approaches.[68] PR-crosslinked collagen showed a marked improvement in tensile strength and enhanced thermal and enzymatic stability, which was attributed to covalent crosslinks combined with additional stabilisation from supramolecular hydrogen bonding interactions. These highly biocompatible PR-linked collagens displayed negligible cytotoxicity at relevant concentrations and were later used as materials for artificial cornea repair.[69] The study found that the PR-linked collagens possessed similar water content, permeability and optical properties relative to the human cornea and also displayed excellent *in vitro* healing capability. Similar efficacy was observed when applied to *in vivo* corneal repairs, with complete epithelization observed within 16 days with no adverse effects, showing a significant improvement over traditionally cross-linked collagen materials.

1.2.5. Polyrotaxanes to Transport Biomolecules

The intracellular delivery of biomacromolecules is essential to an array of therapeutic treatments and research applications.[70] However, the size and hydrophilic nature of these species make transport through the semi-permeable cell membrane a challenge, meaning they often require formulation. Biodegradable PRs can be employed to mask the negative charge of biomacromolecules through electrostatic interaction with cationic ligand-conjugated macrocycles.[71] These spontaneously-formed polyelectrolyte complexes are typically stable during transport and interact strongly with the plasma membrane to facilitate cellular internalisation. Stimuli-responsive linkers in the stoppers facilitate autonomous intracellular PR dissociation at the desired location, releasing the biomacromolecule and restoring bioactivity. Mobilising the ligands in the flexible PR structure serves a dual function. By allowing the positive charges to move and adapt to the surface of the biomacromolecule, electrostatic polyplex association is enhanced and the need to incorporate copious numbers of ligands is negated. Furthermore, macrocycle de-threading and PR dissociation occur rapidly in response to the stimuli-responsive cleavage event of only one cleavable linker. This negates the need to incorporate numerous cleavable linkers – a property that has been found to overly stabilise the polyplex and inhibit the release of the biomacromolecule.[72]

Spurred by the success in regulating multivalent biological interactions with PRs, Yui *et al.* later turned their attention to the non-viral intracellular delivery of plasmid DNA (pDNA).[73,74] PRs comprised of cationic DMAE-conjugated α-CDs threaded along a PEG chain were shown to form polyplexes with pDNA through electrostatic interaction with the negatively charged phosphodiester backbone. The ratio of positively-charged amino groups to negatively-charged phosphate groups (N/P ratio) required to form stable polyplexes was analysed *via* gel electrophoresis and found to be significantly less in PRs (0.25-0.5) compared to linear polyethyleneimine (≈2.0), or free DMAE-α-CDs, which showed negligible pDNA complexation. The highly efficient pDNA condensation at low charge ratios highlights the importance of macrocycle mobility in avoiding spatial mismatches and facilitating tight polyplex packing. DNA polyplexes with positive surface charge adsorb strongly to the cell membrane and become internalised *via* endocytosis. Confocal laser scanning microscopy showed that complete escape of the polyplex from endosome/lysosome occurred within 90 minutes, and that approximately 30% was localised within the nucleus. Once released, high intracellular concentrations of the reducing agent dithiothreitol (DTT) cause cleavage of the disulfide link and de-threading of the α-CDs, which are then free to interexchange with other polyanions to decondense the polyplex and release pDNA (Figure **7**). As expected, control experiments showed that pDNA decondensation was not observed when using PRs with no terminal disulfide linkages. In a later study, the efficacy of transfection was found to be highly dependent on the number of threaded α-CDs and total number of DMAE groups.[75,76] Greater numbers of α-CDs and amino groups were found to form more stable, tightly packed polyplexes. However, the over-stabilisation resulted in decreased pDNA release under reductive conditions, and the higher number of free cations was also believed to inhibit post-transcription mechanisms, lowering the overall transfection activity. In contrast, lower numbers of α-CDs and amino groups formed weaker polyplexes that were less stable to exchange with polyanions and suffered from premature cytosolic release. PRs with intermediate numbers of α-CDs and amino groups possessed the best transfection ability, highlighting the importance of optimizing DNA release timing for the greatest transcription efficiency.

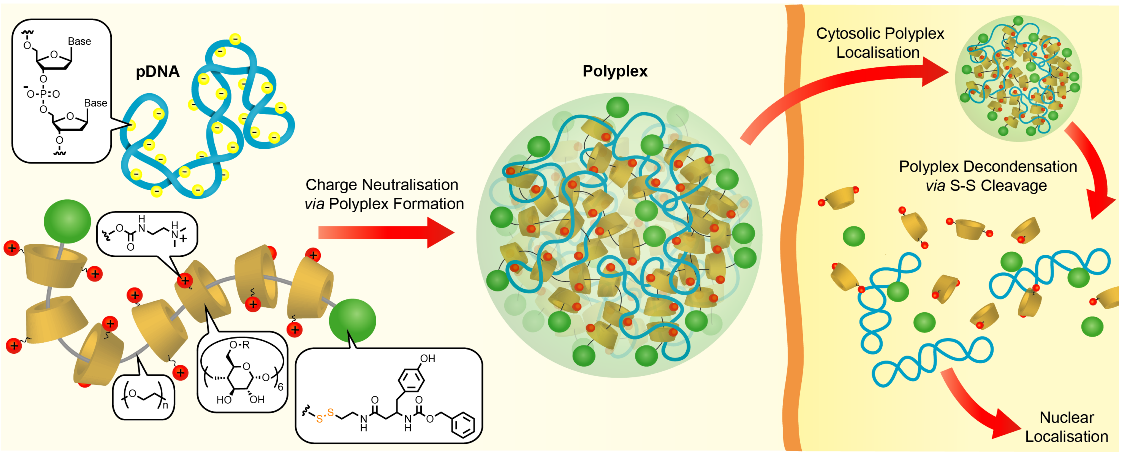

Figure **7**. Cationic DMAE-PRs developed by Yui *et al.* for the intracellular transport of pDNA.[77]

Biodegradable cationic PRs have also been successfully used for the intracellular delivery of small interfering RNA (siRNA), which is considerably more difficult due to the short base-pair lengths and rigid secondary structure of siRNA which weakens electrostatic interactions and destabilizes the polyplex.[78,79] The intracellular uptake and gene silencing activity was enhanced by carefully tailoring the number of threaded α-CDs and cationic groups. Relatively high numbers of α-CD threading were found to stabilise siRNA polyplexes and enhance intracellular uptake up to 27-fold relative to linear poly(ethyleneimine). Endosomal escape capability of the polyplex was initially quite poor due the low endosomal concentration of GSH, which limits disulfide cleavage. This was later addressed by replacing the disulfide unit with 3-sulfanylpropionyl ester linkages, which are labile to the low pH environment of the endosome. Linker cleavage triggers the dissociation of the polyplex and destabilization of the endosome *via* the removal of phospholipids and cholesterol from the membrane, facilitating the escape of siRNA.[80] Anionic enzymes such as β-galactosidase have also been successfully delivered and re-activated in living cells using cationic PRs.[81–83]

1.2.6. Multifunctional Theranostic Rotaxanes

Theranostic platforms that simultaneously tackle disease and output diagnostic information from the same molecular scaffold are a relatively new concept in personalized medicine.[84] Given the wealth of literature showcasing rotaxane architectures as effective molecular scaffolds, it is unsurprising that they have found use in theranostic applications. Huang *et al.* have used the mechanical bond to integrate therapeutic, targeting and diagnostic functionality within a single [2]rotaxane scaffold.[85] The resulting mitochondria-targeting theranostic device was capable of releasing an anticancer drug in cells while simultaneously reporting the intracellular location of its release *via* fluorescence signalling. Triphenylphosphonium (TPP), a lipophilic cation that targets mitochondrial membranes due to their negative potential gradient, and tetraphenylethene (TPE), an aggregation induced emission (AIE)-active fluorogenic probe, act as stoppers to prevent dissociation of an encircling pillar[5]arene macrocycle. Two molecules of the fluorescent anti-cancer drug doxorubicin (**1**) were conjugated to the modified macrocyclic component through pH-responsive imine bonds. The AIE effect in rotaxane **2** was significantly enhanced relative to the non-interlocked axle due to the restricted intramolecular rotation of benzene rings in the TPE moiety, which reduces non-radiative decay pathways. The optimal proximity of the doxorubicin and TPE units in the interlocked structure also establishes a dual-fluorescence-quenched system which inactivates the fluorescence of both units in a HeLa cancer cell line by up to 81% *via* the energy transfer relay (ETR) effect, facilitated by Förster resonance energy transfer (FRET). The low pH of the endo/lysosomes results in the hydrolysis of imine bonds, releasing both doxorubicin units and interrupting the ETR process to restore the fluorescence of rotaxane **3** in a time-dependant manner (Figure **8**). Doxorubicin, when administered alone, was primarily found to co-localise within the nucleus, whereas rotaxane **3** was found strictly in the mitochondria due to active targeting by the TPP unit. Furthermore, the cytotoxicity of rotaxane **2** was significantly greater in cancer cells relative to healthy cells due to their more negative membrane potential which is actively targeted by TPP.

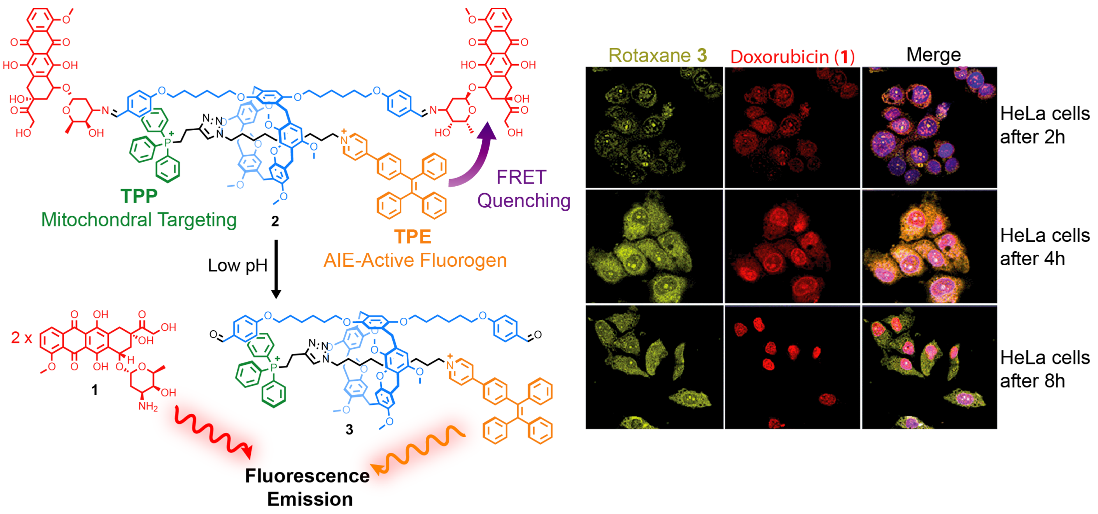

Figure **8**. Mitochondria-targeting theranostic rotaxane **2** and its dual pH-responsive drug release and fluorescence activation. Confocal microscopy images alongside show the subcellular localization in a HeLa cancer cell line administered with rotaxane **2**, doxorubicin (**1**) and a merge**.** Images adapted with permission from Huang *et al*.[85]

Chen and co-workers have similarly employed the PR scaffold as a theranostic platform.[86] Structurally, the PR consists of amino-modified β-CDs threaded onto a poly(ε-caprolactone) (PCL) axle, stoppered by perylene diimide (PDI) and a cyclic RGD peptide sequence. Driven by π–π stacking interactions between PDI stoppers and hydrophobic interactions between PCL axles, the PR self-assembled into a core-shell structured nanoparticle and was used to encapsulate hydrophobic anticancer drugs, such as camptothecin and paclitaxel. β-CD-NH_2 macrocycles lying between the hydrophobic core and hydrophilic outer shell on the ambiphilic axle hinder drug release but do not prevent it, with 61.6% of encapsulated released after 24h. Introduction of mobile disulfide cross-linkages between β-CD-NH_2 units act as an additional barrier, significantly reducing leakage to 6.3% after 24h in the absence of GSH. Intracellular GSH-responsive release of encapsulated drugs was enhanced by the PDI stopper unit, which absorbs strongly in the near-IR region and can act a photothermal agent to increase solution temperature upon laser irradiation (up to 61.9 °C). The thermo-chemotherapeutic drug delivery mechanism combined with the cyclic RGD ligand was used to selectively induce cell death in a HeLa cancer cell line over-expressing $\alpha_v\beta_3$ membrane integrin receptors. Almost all cells (97.7%) treated in combination with laser irradiation displayed significant apoptosis/necrosis, which was significantly greater than those treated without using the photothermal function (51.6%). Core-shell structured nano-particles displayed excellent blood transport properties and were also found to be of optimal size to benefit from the passive-tumour targeting EPR effect. The nanoparticles displayed high antimetastatic activity *in vivo* and were highly effective in suppressing primary tumour growth in mice. Moreover, the NIR-absorption and photothermal effect of the PDI stoppers allowed these materials to be used as contrast agents for photo-acoustic imaging of tumours. The mobile β-CD-NH_2 units could also be conjugated to DOTA complexes and used to transport radionuclide ^{64}Cu, effectively acting as a contrast agent for positron emission topography imaging.

1.3. Using the Mechanical Bond to Stabilise

Precise control over a substance's biological stability is a pre-requisite for biomedical application. To date, numerous approaches based on direct covalent modification have been successful in achieving this. The non-covalent incorporation of subunits within MIMs presents an innovative opportunity to alter the chemical and biological stability of the substance without the need for chemical modification, which often has distinct advantages.

1.3.1. Stabilisation of Squaraine Dyes

Fluorescent probes have emerged as powerful tools to non-invasively image biological processes in living organisms.[87] However, the chemical dyes used for these applications are typically comprised of small organic molecules that suffer numerous difficulties *in vivo*, such as cytotoxicity and poor stability. Squaraines are a class of such dyes that exhibit intense fluorescent absorption and emission bands in the deep-red and near-IR region, with relatively high quantum yields and excellent photostability. By virtue of their electron-deficient cyclobutene ring, they are hydrolytically unstable and susceptible to attack from biological nucleophiles, making them unsuitable for biological imaging applications in their native form.[88,89] Additionally, squaraine dyes have a propensity to self-aggregate in aqueous conditions, which leads to substantial broadening of their absorption bands and quenching of fluorescent output.[90] Smith *et al.* have reported irreversible encapsulation of the squaraine motif within the sterically-shielded cavity of the mechanical bond as a means to improve both the physiological and photochemical properties of squaraine dyes under biological conditions.[91] In their foundational study, a squaraine fluorophore was conjugated to bulky stopper units on both ends, preventing the encircling tetralactam macrocycle from de-threading from the rotaxane structure (Figure **9**).[92] Relative to the corresponding non-interlocked axle (**4**), squaraine rotaxane **5** displayed remarkable stability toward cysteine under aqueous conditions. This was attributed to the xylene units of the tightly encircled macrocycle blocking both faces of the electrophilic cyclobutene core from nucleophilic attack. Additionally, the squaraine rotaxane displayed enhanced quantum yields and only minor spectral broadening, which was again attributed to the interlocked structure preventing aggregation under aqueous conditions.

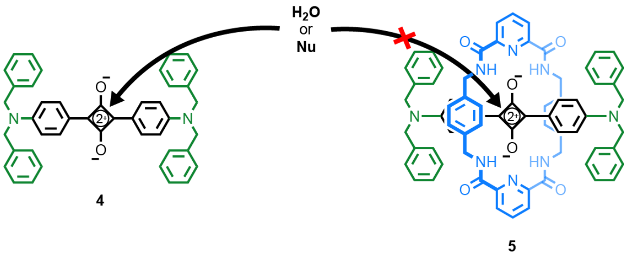

Figure **9**. The mechanical bond prevents nucleophilic attack on the squaraine moiety.

The structure of rotaxane **5** was later modified to incorporate zinc(II)-dipicolyl-amine (Zn-DPA) as the stoppers motifs, which are popular targeting ligands for the anionic surfaces of bacterial cells.[93] Relative to a commonly used Zn-DPA-conjugated cyanine dye (Cy-5),[94] the biostability of the squaraine rotaxane was far superior and facilitated the real-time fluorescence imaging of cell-division in bacterial cells. Moreover, the excellent photostability and low phototoxicity of the interlocked dye prompted its use for *in vivo* NIR imaging in mice. By taking advantage of the squaraine motifs ability to act as a photosensitizer for molecular oxygen,[95] Smith *et al.* were later able to expand the fluorescent molecular imaging platform to incorporate a dual-chemiluminescence functionality.[96] Irradiation of squaraine rotaxane **6** with deep-red light in the presence of air generates singlet oxygen which then reacts with the anthracene component of the macrocycle to form a thermally unstable 9,10-endoperoxide. Endoperoxide formation occurred only on the inner face of the anthracene unit, as evidenced by multi-dimensional NMR. The authors used this observation to rationalise the exclusive mono-selectivity of endoperoxide formation, as the additional steric bulk projecting into the tight mechanical cavity prevents attack by singlet oxygen on the second anthracene unit. Additionally, endoperoxide formation had negligible impacts on the photophysical properties of the encapsulated squaraine motif, meaning that the native fluorescence of rotaxane **6** remained intact in endoperoxide **7**. Furthermore, the endoperoxide species (**7**) was indefinitely stable at -20 °C and could be stored until needed. Unimolecular cycloreversion of the endoperoxide unit occurred spontaneously at body temperature to regenerate squaraine rotaxane **6**, release singlet oxygen, and emit a near-IR chemiluminescent signal capable of passing through living tissue (Figure **10**).

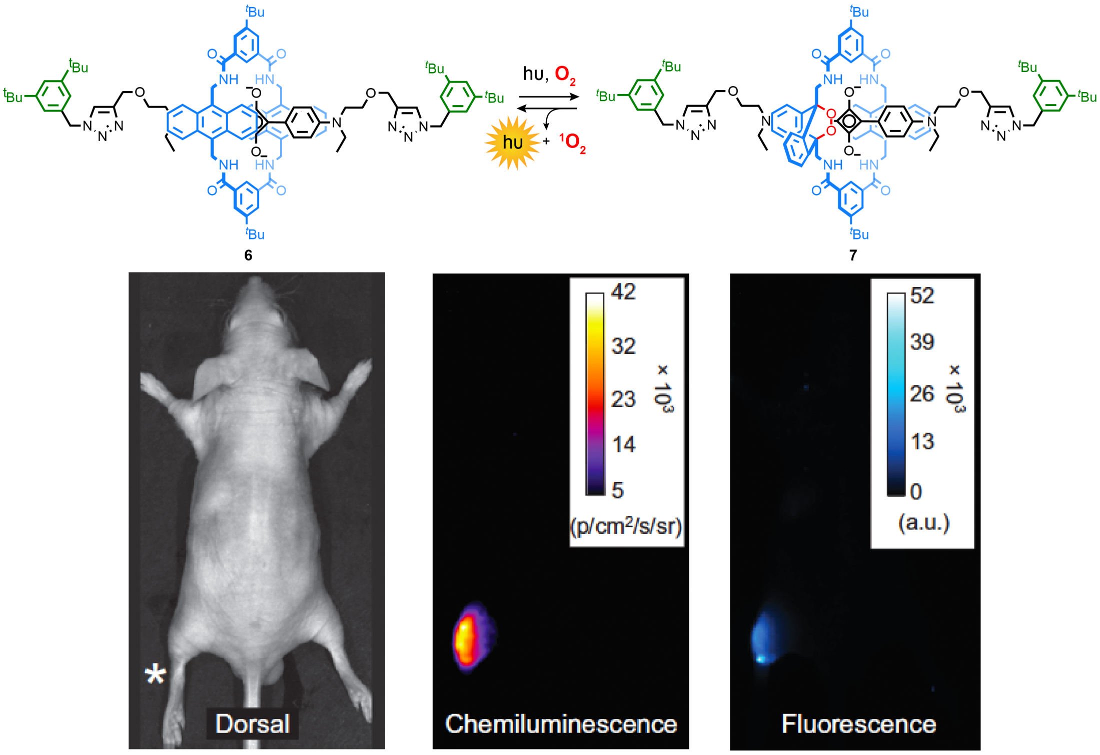

Figure **10**. Photoreaction of **6** with oxygen to generate endoperoxide rotaxane **7.** Thermal cycloreversion of **7** occurs spontaneously at r.t. to release $^1O_2$ and emit a near-IR signal. Chemiluminescence imaged alongside the native fluorescence of the squaraine unit when **7** was injected into the rear leg of a mouse. Images adapted with permission from Smith *et al.*[96]

To evaluate *in vivo* imaging capability, rotaxane **6** was loaded into polystyrene nanoparticles, irradiated to generate the endoperoxide species (**7**), and then injected subcutaneously into the leg of a mouse. The cycloreversion-induced near-IR chemiluminescence displayed excellent tissue penetration and was imaged through up to ~7 mm of skin and leg tissue. As the chemiluminescent probe requires no excitation beam, background autofluorescence by endogenous biomolecules was negligible and signal contrast was far superior to the fluorescent function. Conversely, the fluorescent signal intensity of the squaraine motif was excellent at shallow depths (1 mm) but decreased markedly in deeper tissue (7 mm). The combination of imaging modalities granted the squaraine endoperoxide dyes the ability to locate relatively deep anatomical structures by chemiluminescence while also imaging surface microscopic targets *via* fluorescence. The modular design of the rotaxane imaging platform places the distinct imaging modalities on separate components of the mechanically bonded structure, which suggests the approach holds promise for the creation of next-generation multi-functional dyes.

1.3.2. Enhanced Stability in Catenated Proteins

The topological links uncovered in naturally occurring proteins grant additional structural diversity and are associated with enhanced stability toward chemical, heat and proteolytic degradation.[97–99] The most striking example of this unconventional protein topology is in the outer chainmail-like structure of the HK-97 bacteriophage capsid.[100] The sophisticated network comprised of 420 interlocked protein macrocycles grants the capsid extraordinary thermal and mechanical stability, allowing it to protect its densely packed genetic material even under extremely harsh conditions. Furthermore, cells have been found to employ interlocking as a means to modulate the association of proteins and peptides with their biological partners, and so regulate their bioactivity.[101–103] It is, therefore, unsurprising that numerous research groups have sought to incorporate artificial topological links within proteins to enhance their physiochemical properties and modulate bioactivity.[104]

The first examples of synthetic topologically-linked proteins were pioneered by Dawson *et al*. using solid-state chemistry to generate peptidic sequences containing self-assembling p53 domains, followed by chemical ligation to form the mechanical bond.[105,106] The resulting catenated proteins displayed enhanced thermal stability relative to the non-interlocked analogues. Recently, Zhang *et al.* have reported the first direct cellular synthesis of functionally folded, fully programmable protein homocatenanes based on the genetically encoded SpyTag-SpyCatcher motif.[107] In their methodology, the genetic sequence for a protein of interest was inserted between a p53 dimerization (p53dim) domain and the SpyCatcher domain in a plasmid construct. Upon cellular expression of the plasmid, the peptide chains of p53dim domains self-assemble to become intertwined and pre-organize the two identical polypeptide chains into catenane precursor. Construction of the mechanical bond proceeds spontaneously under cellular conditions *via* intramolecular isopeptide formation between the C-terminal SpyCatcher domain and the complementary N-terminal SpyTag sequence. Due to the close proximity of their N- and C-termini, green fluorescent protein variant GFPrm and dihydrofolate reductase (DHFR) were chosen as model proteins for the study and their catenated analogues were successfully expressed *in vivo* (Figure **11**).

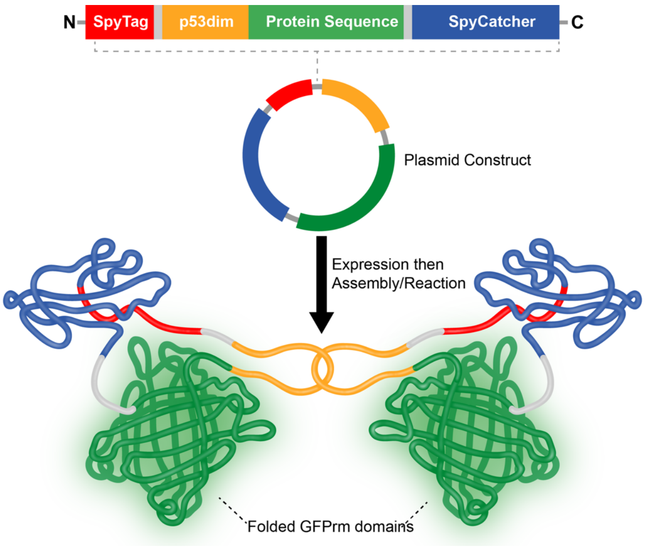

Figure **11.** Cellular synthesis of protein homocatenanes with folded GFPrm structural domains.

The introduction of the mechanical bond was found to significantly enhance stability without compromising the intrinsic properties or activity of folded protein sub-units. As GFP fluoresces only when correctly folded, its fluorescence is a convenient indication of whether the structure was correctly folded. Catenated dimers of GFPrm exhibited the same characteristic strong green florescence with identical excitation and fluorescent emission spectra relative to the non-interlocked native protein, while also showing enhanced stability toward chemical denaturation. Interestingly, interlocked GFPrm was also more resistant to photobleaching and possessed excellent anti-aggregation properties. DHFR was also found to retain its functional folded state once catenated and displayed similar anti-aggregation properties alongside enhanced resistance to proteolytic degradation and a +4 °C increase in melting temperature. A 27% increase in catalytic activity was also observed for catenated DHFR, which was attributed to the improved structural stability of the protein and synergistic effects between adjacent catalytic sub-units afforded by the mechanical bond. Zhang *et al.* later expanded the methodology to include the cellular synthesis to heterocatenanes using the analogous SpyStapler technology.[108] Using this approach, the aforementioned GFPrm and DHFR protein were later incorporated within the same mechanically interlocked architecture. Favourable physiochemical properties, such as enhanced resistance to extreme temperatures or proteolytic degradation, were again bestowed upon the proteins while allowing them to retain their individual fluorescence or catalytic activity respectively. The study highlights the utility of the mechanical bond as a platform to improve the physiochemical properties of functionally folded proteins while retaining or improving their functionality.

1.4. Using the Mechanical Bond to Control Bioactivity

In addition to stabilising key functionalities from attack by endogenous species, the mechanical bond can act as a steric barrier to silence the activity of one or more sub-components without the need for covalent modification.

1.4.1. Transient Silencing of Macrocycle Activity

Numerous literature examples have shown the ability of the mechanical bond to modulate the physiochemical properties and bioactivity of functionalities within the axle component of MIMs.[109–112] However, the encircling macrocyclic components can themselves exhibit potent biological activity that becomes altered when threaded with an axle component. For instance, β-CDs possess hydrophobic interiors that are capable of binding plasma-bound cholesterol molecules, which can destabilize organelle membranes and induce autophagy — a catabolic mechanism of self-digestion in which intracellular proteins and organelles, including mitochondria and endoplasmic reticulum (ER), are degraded and the resulting nutrients re-used by the cell.[113] Dysregulation of autophagic pathways has been linked to numerous pathological diseases and is an important therapeutic target.[114] Tamura *et al*. have recently utilized the PR scaffold to control the cholesterol-binding and, therefore, autophagic induction capability of methylated β-CDs.[115] In the interlocked structure, the threading of a Pluronic axle through multiple Me-β-CDs, an average of 12.8 per PR, blocks the hydrophobic cavity and prevents guest binding. Upon cellular internalization, exposure to the low pH of lysosomes and endosomes cleaves an acid-labile unit within the trityl stoppers and initiates de-threading of Me-β-CDs, unblocking the hydrophobic cavity and restoring their ability to sequester cholesterol.

Solution-phase studies showed that Me-β-CD PRs possessed excellent stability under physiological conditions (pH 7.4, 37 °C), with no degradation observed up to 48 h. At pH 5.0, which is representative of lysosomal pH levels, complete consumption of Me-β-CDs PR was observed within 12 hours, alongside the release of de-threaded Me-β-CDs. A control PR lacking the acid-labile stopper motif showed no such degradation, indicating that the controlled release of Me-β-CDs was a direct result of the acid-catalysed disassembly of the mechanical bond. Additionally, Me-β-CDs PRs were unable to solubilise cholesterol at neutral pH, whereas at pH 5.0 the cholesterol solubility increased in a concentration dependant manner due to encapsulation within released Me-β-CDs. Non-labile control PR showed no ability to solubilise cholesterol at either of the tested pH levels. To assess applicability for *in vitro* cholesterol sequestration, Me-β-CDs PRs were introduced to a mammalian cell line. The accumulation of Me-β-CDs PRs and Me-β-CDs in lysosomes suggested that they became internalized *via* endocytic pathways. After mechanical bond disassembly triggered by the low pH environment, and subsequent escape from the lysosome, Me-β-CDs were found to localise primarily in the ER (Figure **12**). Encapsulation of membrane-bound cholesterol molecules by Me-β-CDs disrupts homeostatic pathways and damages the ER, as evidenced by the morphological changes to the organelle. This resulted in ER stress and ultimately led to autophagic cell death, even in apoptosis-resistant cells.

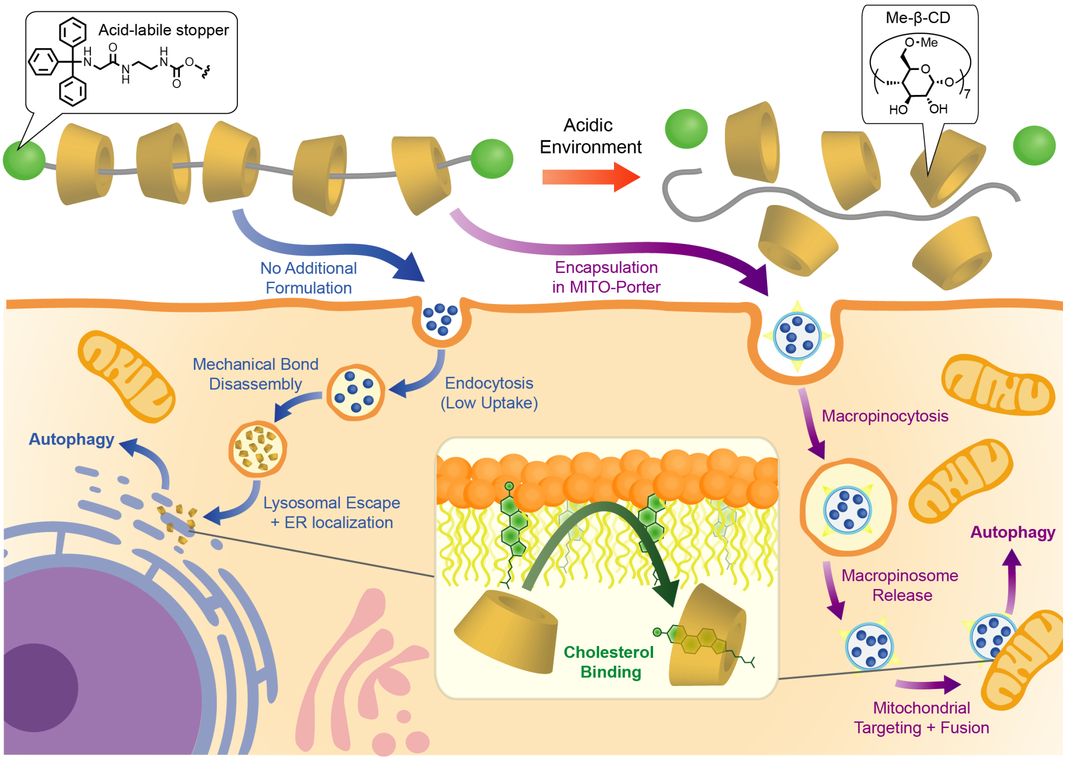

Figure **12**. The PR scaffold developed by Tamura *et al.* as a delivery vehicle for therapeutic Me-β-CDs, which bind cholesterol and lead to cell death *via* autophagic pathways.[115,116]

However, the poor cellular uptake and lack of mitochondrial localisation of Me-β-CD PRs limited their capacity to induce autophagy at therapeutically desirable concentrations and was improved upon in a later study through encapsulation within a S2-MITO-porter — a liposome-type nanodevice that selectively targets and fuses with mitochondrial membranes.[116] Mechanistically, the S2-MITO-porter (Me-β-CD PR) is efficiently internalized through macropinocytosis and binds to the mitochondria *via* electrostatic interactions after release from the macropinosome (Figure **12**). Upon fusion with the membrane, Me-β-CD PRs are delivered to the mitochondrial intermembrane space where the weakly acidic conditions trigger mechanical bond disassembly and release of Me-β-CDs. S2-MITO-Porter (Me-β-CD

PR) showed extensive mitochondrial co-localization and also induced autophagy at significantly lower concentrations than Me-β-CD PR or Me-β-CD administered alone.

Francis *et al.* have similarly employed the [2]rotaxane scaffold to modulate the ^{129}Xe binding capability of a cucurbit[6]uril (CB6) macrocycle for the selective detection of a protease enzyme *via* hyperpolarized xenon chemical exchange saturation transfer (hyperCEST) NMR.[117] ^{129}Xe — a nontoxic and non-reactive noble gas — has a high solubility in blood, tissue, and lipophilic membranes and can be delivered to living organisms *via* injection or inhalation.[118] Hyperpolarization of ^{129}Xe by spin-exchange optical pumping can be used to enhance signal strength by several orders of magnitude and facilitate ultra-sensitive detection.[119] Additionally, ^{129}Xe is highly sensitive to its local chemical environment and has chemical shift values that can range over several hundred ppm in biological samples, enabling the imaging of local spin environments that are often indistinguishable *via* traditional MRI (^{1}H nuclei). Numerous researchers have employed CB6 as contrast agents for hyperCEST NMR as ^{129}Xe undergoes rapid exchange into and out of the macrocycle cavity (K_a = 490 M^{-1}) on a faster timescale than T1 relaxation, creating a distinct ^{129}Xe chemical shift and reducing the observed signal of bulk ^{129}Xe dissolved in solution.[120]

The interlocked imaging platform developed by Francis *et al.* silences the ^{129}Xe-binding ability of the macrocycle and suppresses the characteristic CB6 hyperCEST change in the ^{129}Xe NMR signal. Once the region of interest has been reached, a biological trigger cleaves a chemical bond in the axle motif and initiates mechanical bond disassembly that restores CB6-binding ability and ^{129}Xe NMR signal attenuation. By designing the cleavable unit to degrade in response to certain biological markers, such as those involved in disease, indirect detection of these species and their associated diseases can be achieved *via* ^{129}Xe hyperCEST NMR. The authors first targeted the detection of matrix metalloprotease-2 (MMP-2), a protease enzyme overexpressed in a range of metastatic tumours. The CB6-rotaxane (**8**) contained pyrene and (5,6)-carboxytetramethylrhodamine stoppers which locked the macrocycle on the axle and effectively prevented background release in the absence of MMP-2 (Figure **13**). When incubated with MMP-2 at 37 °C, cleavage of a PLG-LAG recognition sequence within the peptidic axle allowed the CB6 macrocycle to de-thread, with approximately 60% cleavage observed within 24 h. Upon de-threading, CB6 was able to interact strongly with ^{129}Xe, producing a significant increase in hyperCEST response (15% CEST effect) which allowed MMP-2 to be successfully detected *via* ^{129}Xe hyperCEST NMR. By altering to peptidic recognition sequence, the platform could in theory be used to detect a wide variety of proteases.

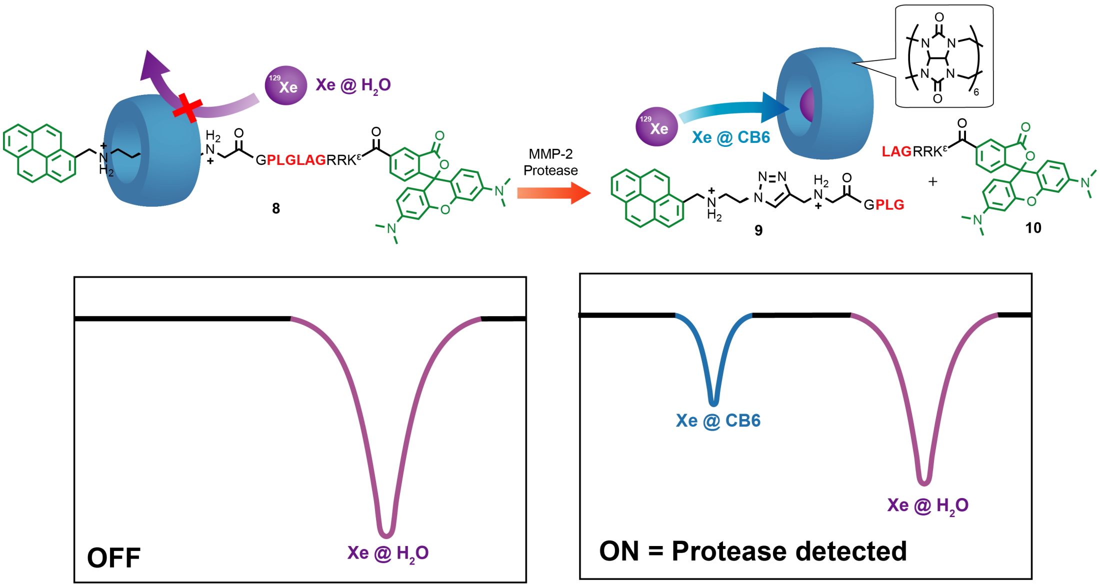

Figure **13**. The interlocked hyperCEST NMR imaging platform developed by Francis *et al.* for the detection of the protease enzyme MMP-2.[117]

The authors later expanded the triggering stimuli to facilitate the selective detection of H_2O_2, the upregulation of which is implicated in oxidative stress mechanisms that are linked to numerous diseases, such as cancer and cardiovascular disease.[121] In this case, the axle featured a phenylboronic acid unit that underwent selective oxidation to the corresponding phenol in the presence of H_2O_2. This initiated a self-immolative 1,6-elimination reaction that cleaved the axle and allowed the CB6 macrocycle to de-thread and bind ^{129}Xe. Two CB6 rotaxanes were used in this study. The first contained a fluorescein stopper, and the second contained a maleimide stopper. Oxidation of the boronic acid occurred rapidly in both rotaxanes, with full conversion to the phenol observed within 1 h, however the subsequent 1,6-elimination was slow, with <50% cleavage observed after 16 h even in the presence of excess H_2O_2. Although a hyperCEST response was again observed, this effect became saturated at around 25-28%, which was likely due to complexation of CB6 with the cleaved half-axle, which was detected *via* LC-MS. The maleimide cap on the second rotaxane also enabled conjugation to cysteine residues on the surface of tobacco mosaic virus (TMV) protein-based nanoparticle, which are being investigated for drug delivery applications. When administered to a HEK 293T tumour cell line known for heavily overexpressing cellular H_2O_2, rotaxane-functionalised TMV nanoparticles produced a ^{129}Xe hyperCEST NMR response that was successfully monitored for up to 24 h. The results demonstrated that CB6 rotaxanes enabled the selective detection of endogenously produced H_2O_2 at biologically relevant concentrations by ^{129}Xe hyperCEST NMR.

1.5. Using the Mechanical Bond to Bind

The various templating strategies used to synthesise interlocked molecules often lend themselves to very well-defined three-dimensional mechanical bond cavities adorned with multidentate ligands that can strongly bind guests.[16] The molecular recognition ability of MIMs often surpasses that of their non-interlocked counterparts, with the mechanical binding cavity capable of discriminating between guests of marginally different size and shape, and even between stereoisomers.[122]

1.5.1. Rotaxane Sensors

By including a reporting moiety in close proximity to the binding unit that can release an output in response to a guest binding event, such as fluorescence, biologically-relevant guests can be sensed and their concentration quantified. To be useful in a biological context, the sensor must be able to operate under aqueous conditions, a feat that is intrinsically difficult due the highly polar nature of water and its ability to form hydrogen bonds with both host and guest species.[123] As a consequence, relatively few interlocked receptors have been reported to operate in competitive aqueous mixtures, whereas numerous MIMs have been designed to recognise guests in organic solvents.[124] However, significant progress has been made in recent years to overcome these challenges, with numerous groups reporting interlocked structures capable of binding charged guests with high affinity and selectivity in aqueous mixtures. Such molecular probes have great potential for use in diagnostic medicine for the sensing of biologically relevant analytes and bioimaging of living systems. For this purpose, only those systems where the measurable output is directly modulated by the binding event are considered, and not those interlocked systems which rely on molecular motion (shuttling, pirouetting) to elicit a response.

The cellular concentration of metal ions is kept within a narrow range by various homeostatic mechanisms, allowing fundamental processes such as signal transduction and metabolism to occur. Diseases such as cancer disrupt metal homeostasis, causing diseased cells to display abnormal concentrations of metals.[125] Consequently, the detection and quantification of the metal ions associated with disease is of great therapeutic interest. Goldup *et al*. have recently reported a structurally simple [2]rotaxane scaffold as a Zn^{2+} selective fluorescent sensor in CH_3CN/H_2O (98:2 *v/v*).[126] Solid state studies suggested that a reorientation of macrocyclic component relative to the fluorophore was responsible for enhancing the optical output upon guest binding. Lin *et al*. have reported a [2]rotaxane sensor for the selective detection of Fe^{3+} in aqueous co-solvent mixtures and used it to monitor the reduction of Hemin to Heme in solution.[127]

Leung *et al*. have recently reported a water-compatible fluorescent [2]rotaxane (**11**) for the selective recognition of Au^{3+}.[128] When interlocked, the highly fluorescent output of BODIPY-stoppered axle component becomes quenched, resulting in rotaxane **11** showing only weak fluorescence. The authors suggest that the close proximity of the macrocycle to the fluorophore in the unbound state could facilitate photo-induced electron transfer (PET), which quenches the fluorescent signal. Upon Au^{3+} binding, the macrocycle in rotaxane **12** adopts a conformation in which the aromatic units are unable to participate in PET, inhibiting the quenching process and restoring the fluorescence activity. NMR titration experiments indicated that the dialkylammonium unit in the axle was protonated upon Au^{3+} binding and shifted considerably along with the pyridyl and phenyl protons of the macrocyclic ring, which suggests that Au^{3+} was indeed bound within the cavity. The interference from a range of other metal analytes was found to be negligible and, due to linear relationship between fluorescent output and concentration of Au^{3+}, the amounts of Au^{3+} could be roughly quantified. The quick recognition times, low detection limits (0.35 µM) and wide working fluorescence pH range (pH 4-10) suggested that rotaxane **11** had potential for *in vitro* imaging applicability. A cell viability study showed that **11** was well-tolerated and could be used to image HeLa cells treated with Au^{3+} (Figure **14**). Rotaxane **11**, which displays a weak green fluorescence (λ_{em} = 518 nm) in the unbound state, was only able to lightly stain cells prior to Au^{3+} treatment. The green fluorescent output increased in a concentration-dependant manner with Au^{3+} and was found to localise primarily within membrane-bound vacuole organelles.

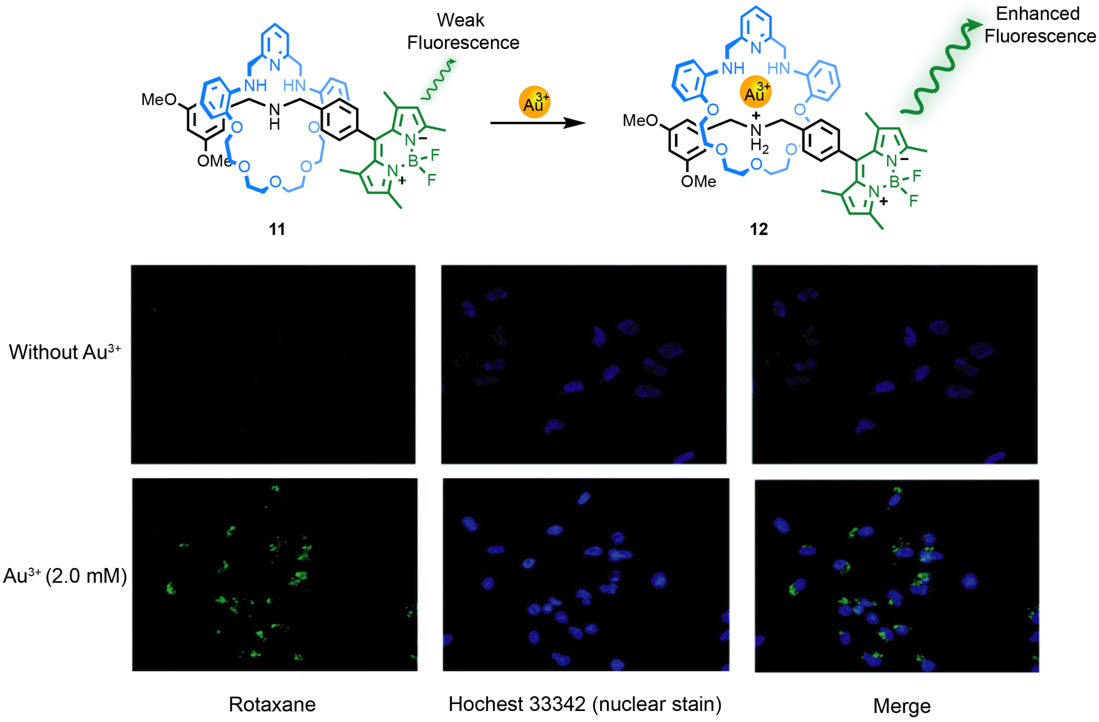

Figure **14**. A [2]rotaxane which shows enhanced fluorescence output upon Au^{3+} binding in HeLa cells.[128] Images adapted with permission from Leung *et al.*[128]

Interlocked structures have similarly been employed to sense anionic species under aqueous conditions. To overcome the high degrees of solvation experienced by biologically-relevant anions, Beer *et al.* have proposed the use of interlocked halogen-bonding receptors for the selective recognition of guests in aqueous mixtures.[129] Integration of four distinct halogen-bonding motifs within a [2]rotaxane architecture created a spherical anion binding cavity that displayed extraordinary binding affinity and a high selectivity for halide ions (I^-, Br^-, Cl^-) over a host of other non-uniform oxoanions in up to 50% H_2O/CH_3CN mixtures.[130] Monitoring the intensity of the metal-to-ligand charge transfer (MLCT) emission band from a luminescent $Rh^{(I)}$-bipyridine moiety bound within the macrocyclic component enabled optical sensing capabilities. While analogous to hydrogen-bonding in directionality and strength, a later study confirmed that halogen-bonding was far superior for binding anions in pure water.[131] Interlocked halogen-bonding motifs bound relevant guests up to two times stronger than their hydrogen-bonding counterparts. Building on previous work, Beer *et al.* introduced permethylated β-CDs as stoppers in a $Rh^{(II)}$ functionalised [2]rotaxane scaffold, leading to enhanced water solubility.[132] Convergent halogen- and hydrogen-bonding interactions within the binding cavity were found to strongly bind I^- with high selectivity over smaller halides and SO_4^{2-} in pure water, and could be sensed by luminescence spectroscopy.

Despite these promising results, the utility of interlocked halogen-bonding receptors for *in vitro* sensing/imaging of anionic species is yet to be demonstrated.

1.6. Mechanical Motion for Biological Activity

The mechanical bond can hold discreet sub-components together and prevent dissociation while still permitting them sufficient co-conformational freedom to move and rotate with respect to one another. The translational (shuttling) movement of the macrocycle along the axle in rotaxane structures or the rotational movement (pirouetting) of rings in a catenane are primary examples of this. Through rational chemical modification of the interlocked structure, these co-conformational movements can be induced by various external stimuli. This is known as mechanical motion and is a critical feature of MIMs used in molecular machines — several of which have been designed to mimic the mechanical motion of natural biological processes.[133] Although these systems are of little biological relevance, numerous interlocked structures have been designed to exploit controlled mechanical motion achieve a desired biological effect.

1.6.1. Rotaxanes as Cellular Transport Agents

Synthetic scaffolds have been designed to mimic the function of protein binding sites by carefully positioning amino acids or peptides around a hydrophobic pocket, allowing them to bind and transport biologically relevant molecules throughout the cell.[134] However, achieving guest recognition through a traditional covalent approach is synthetically challenging due to the precise spatial arrangement of convergent functional groups needed to resemble the three-dimensionally folded binding domains. Rotaxane-based cellular transport agents build on many of the properties found in rotaxane sensors to overcome these limitations. As hosts, rotaxanes can organise functional groups within their semi-flexible scaffold to effectively recognise and bind guests while shielding them from the external aqueous environment. The unique translational motion afforded by the mechanical bond is also critical to allow the passage of bound cargo through otherwise impermeable cell membranes.

In their seminal study, Smithrud *et al.* reported a [2]rotaxane scaffold capable of mimicking the complex cellular functions of biological transport proteins for the intracellular delivery of various amino acids, peptides and fluorophores.[135] The [2]rotaxane delivery systems possessed two key components: a cationic diarginine-functionalised crown ether macrocycle which promotes cellular internalisation *via* cell surface binding, and a host-binding moiety incorporated within the stopper that mimics the hydrophobic binding pocket. The synthetic binding epitopes consisted of flexible cyclophane-pockets (**13**) or acyclic aromatic clefts (**14**) that could strongly bind guests through dispersion forces, π–π stacking interactions and the hydrophobic effect. Despite the hydrophobic pocket, host [2]rotaxanes displayed reasonable aqueous solubility (up to 98% v/v H_2O/DMSO) and also formed stable complexes in a range of solvents, indicating their suitability to transport membrane impermeable guests through the varying polarity of environments experienced during cellular internalisation. The ability of [2]rotaxanes to successfully transport fluorescein through the cell membrane and even into the nucleus of COS-7 cells was confirmed *via* fluorescence microscopy. In the absence of a [2]rotaxane transport agent, negatively charged fluorescein could not permeate the membrane and no uptake in cellular fluorescence was observed. A concentration dependant increase in cellular fluorescence intensity was only observed when fluorescein was co-administered with [2]rotaxanes **13** or **14** (Figure **15**).

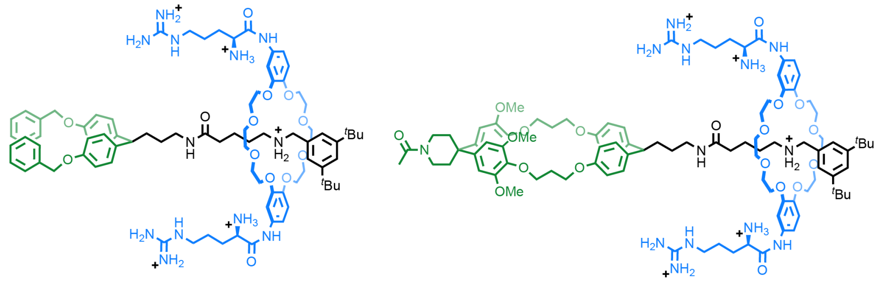

13 **14**

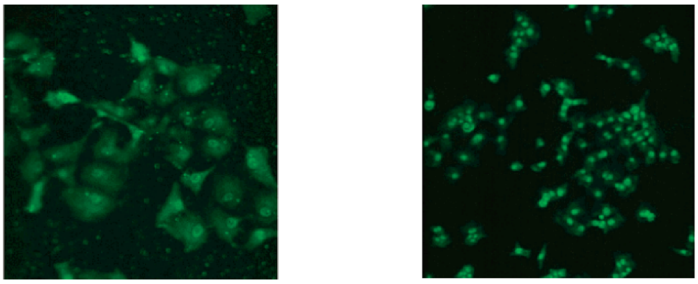

Fluorescein + **13** Fluorescein + **14**

Figure **15**. [2]Rotaxane cellular transport agents possessing aromatic cleft (**13**) and cyclophane (**14**) binding pockets effectively deliver fluorescein to the intracellular environment. [135]

Despite showing similar binding affinities with relevant guests, cyclophane [2]rotaxane **14** was substantially better at transporting fluorescein through the cell membrane, which prompted an investigation into the intracellular transport mechanism. The study found that the molecular mobility of the macrocycle in **14** enhanced guest binding and played a vital role in the permeabilization process.[136] Multi-dimensional NMR analysis indicated that when a guest was bound within the hydrophobic cavity, rotaxane **14** had a strong propensity to adopt one of two possible co-conformations depending on solvent choice. In $CDCl_3$, which represents the apolar environment of the lipid bilayer, strong association between electron-rich oxygen atoms in the macrocycle and the charged ammonium unit in the axle maintain the rotaxane in an "open" conformation with the macrocycle positioned away from the cleft. Competitive hydrogen bonding with water molecules in aqueous solutions — representative of the extracellular environment — weakens the association and shifts the macrocycle closer to the cleft where aromatic and aliphatic residues associate *via* the hydrophobic effect (Figure **16**). In the "closed" conformation the hydrophobic binding site is ideal for complexation. Upon binding, the macrocycle adjusts its conformation and moves slightly further away from the cleft unit to permit guest sequestration, which is evident from the loss of NOE signals between macrocycle and cleft. It is also suggested that non-covalent interactions (salt-bridges, cation-π interactions) with arginine residues give the complexed guest additional stabilisation in both "open" and "closed" conformations, and also help to mask negative charge to facilitate permeabilization. In a control experiment, acetylation of the thread's amine unit removed favourable interactions with the macrocycle and provided an additional steric barrier to lock the rotaxane in the "closed" conformation. Being unable to slide into the thermodynamically favoured "open" conformation when traversing the apolar bilayer significantly diminishes the transport capability of rotaxanes as tight guest binding could not be maintained.

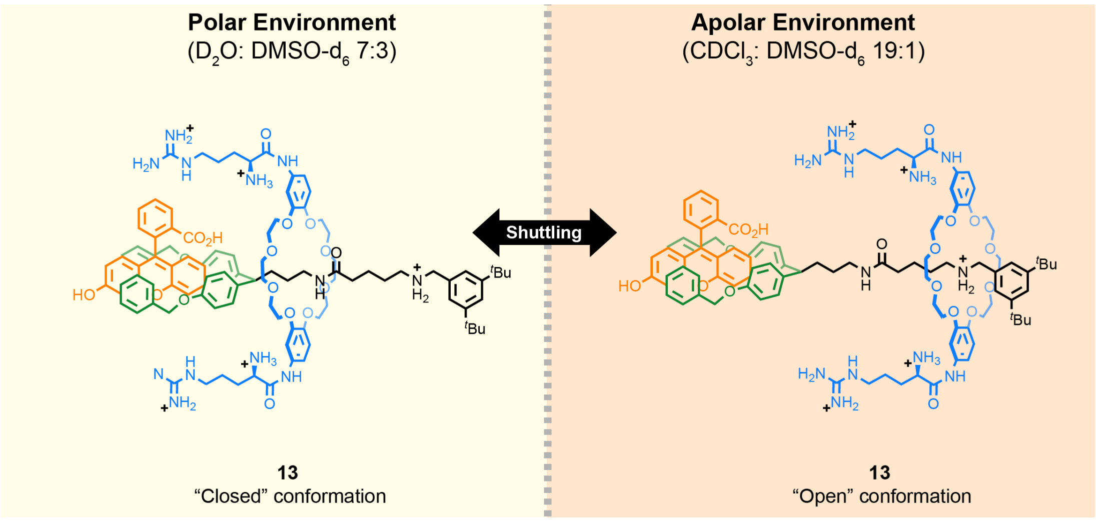
Polar Environment
(D_2O: DMSO-d_6 7:3)

Apolar Environment
($CDCl_3$: DMSO-d_6 19:1)

13
"Closed" conformation

13
"Open" conformation

Figure **16**. [2]Rotaxane **13** uses a mechanical shuttling motion to adopt a co-conformation that maintains strong guest binding depending on the polarity of its environment.

The uptake of a fluorescent peptide was then analysed by flow cytometry and showed that [2]rotaxane **13** transported Fl-AVWAL into a higher percentage of COS-7 cells (90%) compared to the conformationally locked counterpart (23%), indicating that mechanical motion is vital to the cellular internalisation process. Cellular immobilisation using low temperature (4 °C) or ATP depletion was found to have minimal impact on the internalisation efficiency of Fl-AVWAL, suggesting that rotaxane **13** utilizes a passive pathway to enter the cell as opposed to an active cell-mediated process such as endocytosis. A later study used cyclophane [2]rotaxane **14** to successfully deliver and release a host of peptides with varying degrees of side-chain polarity into cells.[136] The activity of **14** was also shown to be largely temperature and ATP independent. Moreover, as a greater than stoichiometric amount of peptide transportation was observed, with respect to **14** as the limiting reagent, this may suggest that upon guest release, the rotaxane returns to the extracellular environment to bind and transport more guests.

The transport of biologically relevant metal cations across the lipid bilayer can alter the intracellular pH and electrochemical membrane potential to cause cell death, and is of equal therapeutic interest.[137] Smithrud *et al.* have incorporated a crown ether as a metal-cation-binding stopper component within a [2]rotaxane scaffold.[138] The bacterial ionophore mimic was highly selective for Ca^{2+} binding and capable of efficiently transporting it to the intracellular environment of a prostate cancer cell line, where the high concentrations of Ca^{2+} triggered apoptotic mechanisms and resulted in cell death.[139] Bao *et al*. have recently utilised the [2]rotaxane architecture and its inherent mechanical motion in a different manner to achieve selective bilayer cation transport (Figure **17**).[140] Guest recognition motifs in the aforementioned examples were incorporated within the stopper components, whereas this work tethered a selective K^+ binding crown ether directly to the mobile macrocyclic component of a [2]rotaxane. Two positively-charged ammonium stations at either end of the pseudo-symmetric axle act as strong binding stations for the interlocked electron-rich macrocycle. A third, weaker, binding station comprised of an *N*-methyltriazolium moiety, acts as a central relay to accelerate shuttling between the two more favourable terminal stations. NMR analysis in the absence of K^+ revealed that the macrocycle had a strong propensity to remain on one of the two ammonium stations and that the rate of shuttling in organic solvent mixtures was relatively slow (k = 0.082 Hz).

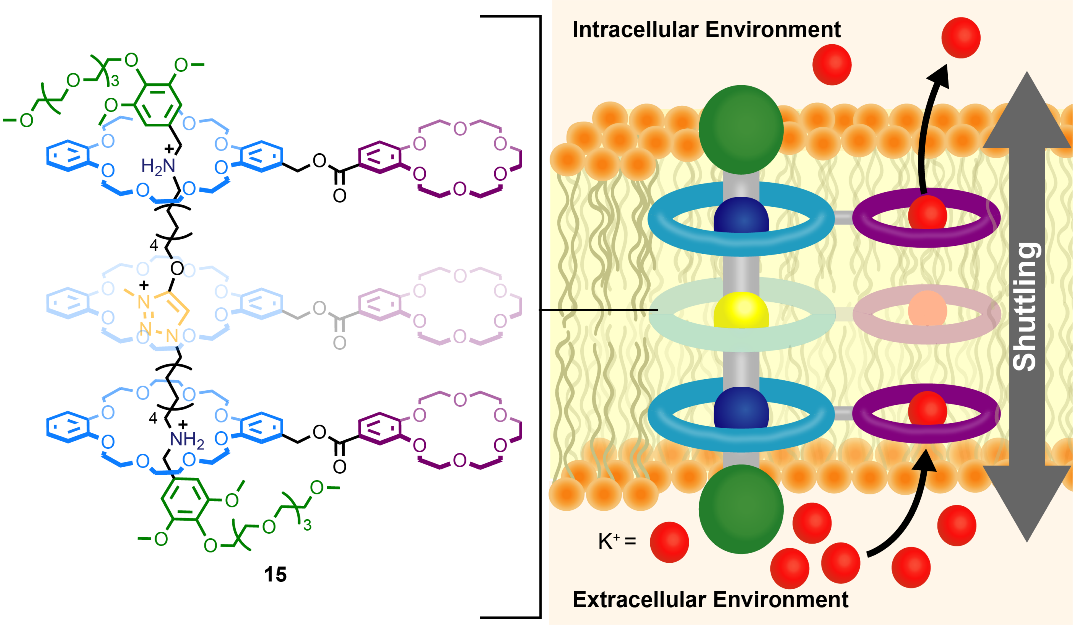

Figure **17**. Structure of the selective K⁺ membrane transport [2]rotaxane developed by Bao *et al.* and the shuttling mechanism it employs to facilitate cellular internalisation.[140]

Functionalisation of the stoppers with tetraethylene glycol units enhanced the hydrophilicity of the [2]rotaxane and granted it the ambiphilic character necessary to embed itself within lipid bilayers without significantly disrupting the membrane integrity. A fluorescence assay showed that when incorporated within liposomal membranes, [2]rotaxane **15** and the corresponding axle displayed <10% leakage of the encapsulated dye. Voltage clamp measurements also confirmed the formation of stable channels/pores across the membrane from unimolecular insertion of the ambiphilic species. The cellular transport activity of [2]rotaxane **15** followed a similar trend to the metal ion binding behaviour of the crown ether, and decreased in the order $K^+ >> Rb^+ \geq Cs^+ > Na^+ > Li^+$, highlighting its role in the selective permeabilization process. The axle component, lacking an appropriate metal cation-binding motif, displayed no such distinction. The importance of shuttling on the transport activity was by investigated by varying pH: deprotonation of charged ammonium stations at higher pH conditions caused the macrocycle to favour the central *N*-methyltriazolium and remains static, which prevented shuttling and blocked the exchange of ions across lipid layers.

1.6.2. Reversible Nanovalves

Rotaxane architectures are well suited to block the surface apertures of MSNPs, preventing the release of encapsulated cargo until the target site is reached. Snap-top MSNPs undergo stimuli-responsive bond cleavage to break the mechanical and irreversibly unblock the surface pores. While complete drug release is desirable in some cases, various applications would benefit from the nanocarrier being able to release its cargo in a more controlled manner. Reversible rotaxane nanovalves have been designed to use discreet mechanical motion to shuttle the macrocycle away from the surface, opening the pores and allowing the payload to be released. In response to a second stimulus, or upon removal of the initial stimulus, the macrocycle returns to its initial position to again block the pore and prevent cargo release. Reversible systems have the added advantage of not releasing the cleaved pore-blocking units, which can often produce toxic side-effects.[25,141]

Numerous reversible MSNPs have been designed to shuttle ring positions from one recognition site to the other, “opening” and “closing” the pores, in response to redox and pH changes.[142,143] However, these are yet to be applied to controlled drug release applications in biological systems. Due to the excellent biocompatibility and high degree of spatiotemporal control that can be achieved over responsive drug delivery systems with light, nanovalves based on photo-switchable rotaxane structures are held in high regard. These systems utilize light-activated *cis*/*trans* photoisomerization of axle-bound chromophores to induce structural changes which either favour or disfavour a given station, resulting in shuttling of the macrocyclic component and “opening/closing” of the surface pores. Berná *et al.* have reported reversible nanovalve-functionalised MSNPs based on photo-switching of the fumaramide motif.[144] The azobenzene motif is among the most well-studied photoswitchable units and has found excellent utility in reversible nanovalves.[145] Zhao *et. al.* reported azobenzene-functionalised nanovalves in MSNPs for the photothermally controlled release of drugs *in vivo*.[146] The interlocked gatekeepers are composed of an α-CD threaded along a linear azobenzene-containing axle. A bulky napthalene unit functionalised with two sulfonate groups prevents the α-CD from de-threading and enhances the water solubility of the nanoparticles. Exposure to heat (37 °C) or visible light induces a *cis*-to-*trans* isomerization of the azobenzene unit, resulting in a large change in dipole moment that makes the unit less hydrophilic. The α-CD unit possesses a hydrophobic interior and favourably binds to the *trans*-azobenzene unit, moving away from the nanoparticle surface and “opening” the pore to allow cargo release. Irradiation with 365 nm light results in *cis* isomerisation, which reduces the hydrophobicity of the azobenzene unit and adds additional steric hindrance, causing the α-CD to return to its original pore-blocking position over the triazole/ethylene glycol units and preventing cargo release (Figure **18**). In the *cis* conformation, negligible amounts of encapsulated drugs/dyes leaked from “closed” nanovalves.

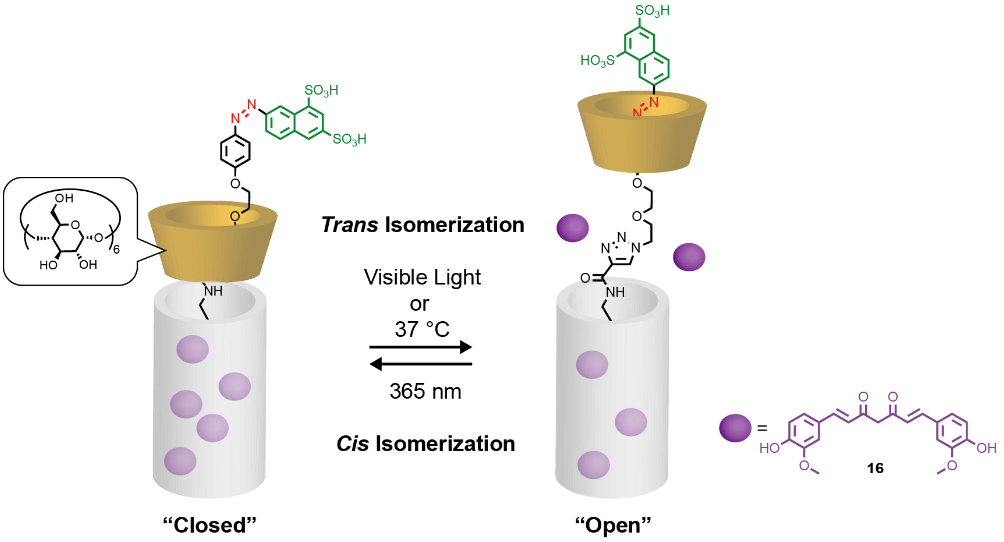

Figure **18.** Azobenzene-functionalised rotaxanes as reversible gatekeeper in MSNPs.[146]

The *in vivo* photothermal drug release capability was evaluated by injecting MSNPs loaded with the fluorophore curcumin (**16**) into zebrafish larvae. When incubated for 1 h at 24 °C in the dark, a reduction of 11.5% in the overall curcumin fluorescence intensity was observed, which was attributed to the *in vivo* metabolism of released curcumin. Conversely, in the presence of visible light at 24 °C, a 34.9% reduction in fluorescence intensity was observed after 1 h. After incubation in the dark at an elevated temperature (37 °C), a 45.9% reduction was observed after 1 h. Curcumin displays excellent antioxidant properties making it suitable for the treatment of heart failure. However, its poor aqueous solubility limits its application.[147] This study found that curcumin-loaded MSNPs displayed excellent therapeutic properties when used to treat heart failure, successfully restoring cardiac function in zebrafish embryos. The utility of reversible nanovalves is not limited to MSNPs. Zhao *et al.* later reconfigured the same azobenzene functionalized [2]rotaxanes to act as near-IR-responsive gatekeepers on the surface of Au-nanorod-mesoporous silica core-shell hybrid particles and successfully showed the release of doxorubicin *in vivo.*[148]

1.7. Conclusions

The mechanical bond is a remarkably versatile platform for designing and developing synthetic molecules for applications in biology and medicine. Despite the successful application of MIMs to problem areas such as drug delivery and bioimaging, their potential is often overlooked among the plethora of MIM literature, which focuses primarily on aspects of synthesis,[149] the history,[150] chirality or more conventual applications, such as catalysis,[151] materials,[152] or as components in molecular machines.[153] Even among comprehensive review articles, coverage of MIMs in a biological context is drastically under-represented and often omitted entirely.[154] In part, the lack of recognition is due to the interdisciplinary nature of the research, which often features in journals focused on biological/ medical properties and, as a result, the chemistry underpinning the system is either: a) not the primary focus, b) poorly articulated, or c) inadequately understood/ investigated. The few reviews that discuss the biological applications of MIMs do so as minor sub-sections of a larger narrative,[155] for specific applications,[23] or in an incomplete fashion that neglects the underlying structure-activity relationship of the MIM.[17, 18]

In this chapter, we attempted to address these issues by conducting an in-depth literature review of synthetic MIMs designed to function in, or interact with, biological systems. By drawing together and analysing the relevant literature in a coherent and uniform manner, the unique properties of the mechanical bond that endow the MIM with their biological function were elucidated. Firstly, the mechanical bond can be used as a structural scaffold to hold multiple components together to achieve biological function — an approach used to generate interlocked PR-based contrast agents for MRI and snap-top MSNPs for drug delivery, along with numerous other functional platforms. Using the macrocyclic component as a molecular shield to enhance the stability of labile units within MIMs has facilitated the use of otherwise incompatible substances, such as squaraine dyes, under biological conditions. Similarly, the mechanical bond can be used to block the bioactivity of the macrocycle component while interlocked — restoring function in response to a desired biological stimulus for both diagnostic and therapeutic applications. Mechanical bonds often possess well-defined three-dimensional cavities that are ideal for guest binding. The change in fluorescence output of such MIMs upon guest binding has been used to generate sensors for biologically relevant species. Lastly, the use of mechanical motion to achieve biological function has been highlighted in several applications, including rotaxane cellular transport agents, reversible MSNPs, and membrane ion shuttles. In many interlocked systems, the mechanical bond can fulfil several of these roles simultaneously, emphasising the highly versatile nature of the platform. Although numerous advances remain to be accomplished (i.e., *in vivo* studies or evaluation in clinical trials), the use of synthetic MIMs for biological is becoming a well-established field, with an ever-increasing range of molecules used for biological applications being reported to benefit from mechanical interlocking.

.

1.8. Bibliography

[1] C. J. Bruns, J. F. Stoddart in *The Nature of the Mechanical Bond*, John Wiley & Sons, Inc., Hoboken, NJ, USA, **2016**.

[2] D. Sluysmans, J. F. Stoddart, *Trends Chem.* **2019**, 1, 185–197.

[3] P. R. Ashton, I. Baxter, M. C. T. Fyfe, F. M. Raymo, N. Spencer, J. F. Stoddart, A. J. P. White, D. J. Williams, *J. Am. Chem. Soc.* **1998**, 120, 2297–2307.

[4] H. L. Sun, H. Y. Zhang, Z. Dai, X. Han, Y. Liu, *Chem. Asian J.* **2017**, 12, 265–270.

[5] D. R. Boutz, D. Cascio, J. Whitelegge, L. J. Perry, T. O. Yeates, *J. Mol. Biol.* **2007**, 368, 1332–1344.

[6] M. A. Krasnow, A. Stasiak, S. J. Spengler, F. Dean, T. Koller, N. R. Cozzarelli, *Nature* **1983**, 304, 559–560.

[7] B. Hudson, J. Vinograd, *Nature* **1967**, 216, 647–652.

[8] E. Wasserman, *J. Am. Chem. Soc.* **1960**, 82, 4433–4434.

[9] G. Schill, A. Lüttringhaus, *Angew. Chemie Int. Ed.* **1964**, 3, 546–547.

[10] C. O. Dietrich-Buchecker, J. P. Sauvage, J. P. Kintzinger, *Tetrahedron Lett.* **1983**, 24, 5095–5098.

[11] B. Taghavi Shahraki, S. Maghsoudi, Y. Fatahi, N. Rabiee, S. Bahadorikhalili, R. Dinarvand, M. Bagherzadeh, F. Verpoort, *Coord. Chem. Rev.* **2020**, 423, 213484.

[12] J. E. M. Lewis, P. D. Beer, S. J. Loeb, S. M. Goldup, *Chem. Soc. Rev.* **2017**, 46, 2577–2591.

[13] J. F. Stoddart, *Angew. Chemie Int. Ed.* **2017**, 56, 11094–11125.

[14] S. Mena-Hernando, E. M. Pérez, *Chem. Soc. Rev.* **2019**, 48, 5016-5032.

[15] A. Martinez-Cuezva, A. Saura-Sanmartin, M. Alajarin, J. Berna, *ACS Catal.* **2020**, 10, 7719–7733.

[16] K. M. Bąk, K. Porfyrakis, J. J. Davis, P. D. Beer, *Mater. Chem. Front.* **2020**, 4, 1052–1073.

[17] N. Pairault, R. Barat, I. Tranoy-Opalinski, B. Renoux, M. Thomas, S. Papot, *Comptes Rendus Chim.* **2016**, 19, 103–112.

[18] J. Riebe, J. Niemeyer, *Eur. J. Org. Chem.* **2021**, 2021, 5106–5116.

[19] S. Hapuarachchige, D. Artemov, *Front. Oncol.* **2020**, 10, 1131.

[20] J. Wahsner, E. M. Gale, A. Rodríguez-Rodríguez, P. Caravan, *Chem. Rev.* **2019**, 119, 957–1057.

[21] Z. Zhou, Y. Mondjinou, S. H. Hyun, A. Kulkarni, Z. R. Lu, D. H. Thompson, *ACS Appl. Mater. Interfaces* **2015**, 7, 22272–22276.

[22] Y. A. Mondjinou, B. P. Loren, C. J. Collins, S.-H. Hyun, A. Demoret, J. Skulsky, C. Chaplain, V. Badwaik, D. H. Thompson, *Bioconjug. Chem.* **2018**, 29, 3550–3560.

[23] Z. Li, J. C. Barnes, A. Bosoy, J. F. Stoddart, J. I. Zink, *Chem. Soc. Rev.* **2012**, 41, 2590–2605.

[24] Y. Matsumura, H. Maeda, *Cancer Res.* **1986**, 46, 6387–6392.

[25] M. W. Ambrogio, C. R. Thomas, Y. L. Zhao, J. I. Zink, J. F. Stoddart, *Acc. Chem. Res.* **2011**, 44, 903–913.

[26] W. Chen, C. A. Glackin, M. A. Horwitz, J. I. Zink, *Acc. Chem. Res.* **2019**, 52, 1531–1542.

[27] N. Kumar, W. Chen, C. A. Cheng, T. Deng, R. Wang, J. I. Zink, *Enzymes* **2018**, 43, 31–65.

[28] A. Bansal, M. Celeste Simon, *J. Cell Biol.* **2018**, 217, 2291–2298.

[29] M. W. Ambrogio, T. A. Pecorelli, K. Patel, N. M. Khashab, A. Trabolsi, H. A. Khatib, Y. Y. Botros, J. I. Zink, J. F. Stoddart, *Org. Lett.* **2010**, 12, 3304–3307.

[30] K. Patel, S. Angelos, W. R. Dichtel, A. Coskun, Y. W. Yang, J. I. Zink, J. F. Stoddart, *J. Am. Chem. Soc.* **2008**, 130, 2382–2383.

[31] S. R. Gayam, P. Venkatesan, Y. M. Sung, S. Y. Sung, S. H. Hu, H. Y. Hsu, S. P. Wu, *Nanoscale* **2016**, 8, 12307–12317.

[32] X. Yang, J. Duan, L. Wu, *Future Med. Chem.* **2022**, 14, 363–383.

[33] F. Porta, G. E. M. Lamers, J. I. Zink, A. Kros, *Phys. Chem. Chem. Phys.* **2011**, 13, 9982–9985.

[34] M. Rizzuti, M. Nizzardo, C. Zanetta, A. Ramirez, S. Corti, *Drug Discov. Today* **2015**, 20, 76–85.

[35] Z. Luo, X. Ding, Y. Hu, S. Wu, Y. Xiang, Y. Zeng, B. Zhang, H. Yan, H. Zhang, L. Zhu, J. Liu, J. Li, K. Cai, Y. Zhao, *ACS Nano* **2013**, 7, 10271–10284.

[36] M. Mammen, S. K. Choi, G. M. Whitesides, *Angew. Chemie Int. Ed.* **1998**, 37, 2754–2794.

[37] M. A. Van Dongen, C. A. Dougherty, M. M. Banaszak Holl, *Biomacromolecules* **2014**, 15, 3215–3234.

[38] W. S. Hlavacek, R. G. Posner, A. S. Perelson, *Biophys. J.* **1999**, 76, 3031–3043.

[39] N. Yui, T. Ooya, *Chem. Eur. J.* **2006**, 12, 6730–6737.

[40] T. Ooya, M. Eguchi, N. Yui, *J. Am. Chem. Soc.* **2003**, 125, 13016–13017.

[41] N. Yui, T. Ooya, T. Kawashima, Y. Saito, I. Tamai, Y. Sai, A. Tsuji, *Bioconjug. Chem.* **2002**, 13, 582–587.

[42] H. Utsunomiya, R. Katoono, N. Yui, T. Sugiura, Y. Kubo, Y. Kato, A. Tsuji, *Macromol. Biosci.* **2008**, 8, 665–669.

[43] T. Ooya, N. Yui, *J. Control. Release* **2002**, 80, 219–228.

[44] N. Yui, T. Ooya, T. Kumeno, *Bioconjug. Chem.* **1998**, 9, 118–125.

[45] M. Eguchi, T. Ooya, N. Yui, *J. Control. Release* **2004**, 96, 301–307.

[46] T. Ooya, N. Yui, H. Sugawara, *Drug Deliv. Syst.* **1997**, 12, 89–94.

[47] K. Shibaguchi, A. Tamura, M. Terauchi, M. Matsumura, H. Miura, N. Yui, *Molecules* **2019**, 24, 439.

[48] H. Matsui, A. Tamura, M. Osawa, A. Tonegawa, Y. Arisaka, M. Matsumura, H. Miura, N. Yui, *Macromol. Biosci.* **2018**, 18, 1800059.

[49] S. Bashir, M. Hina, J. Iqbal, A. H. Rajpar, M. A. Mujtaba, N. A. Alghamdi, S. Wageh, K. Ramesh, S. Ramesh, *Polymers* **2020**, 12, 1–60.

[50] Y. Okumura, K. Ito, *Adv. Mater.* **2001**, 13, 485–487.

[51] K. Ito, *Polym. J.* **2007**, 39, 489–499.

[52] Y. Noda, Y. Hayashi, K. Ito, *J. Appl. Polym. Sci.* **2014**, 131, 40509.

[53] A. Harada, J. Li, M. Kamachi, *J. Am. Chem. Soc.* **1994**, 116, 3192–3196.

[54] J. Sawada, D. Aoki, H. Sogawa, K. Nakajima, T. Takata, *Macromol. Symp.* **2019**, 385, 1800186.

[55] T. Ooya, N. Yui, *J. Biomater. Sci. Polym. Ed.* **1997**, 8, 437–455.

[56] C. Pradal, L. Grøndahl, J. J. Cooper-White, *Biomacromolecules* **2015**, 16, 389–403.

[57] A. K. Rajendan, Y. Arisaka, N. Yui, S. Iseki, *Inflamm. Regen.* **2020**, 40, 1–8.

[58] T. Ichi, J. Watanabe, T. Ooya, N. Yui, *Biomacromolecules* **2001**, 2, 204–210.

[59] T. Ichi, K. Nitta, W. K. Lee, T. Ooya, N. Yui, *J. Biomater. Sci. Polym. Ed.* **2003**, 14, 567–579.

[60] N. Q. Tran, Y. K. Joung, E. Lih, K. M. Park, K. D. Park, *Macromol. Res.* **2011**, 19, 300–306.

[61] K. Hyodo, Y. Arisaka, S. Yamaguchi, T. Yoda, N. Yui, *Macromol. Biosci.* **2019**, 19, 1800346.

[62] W. K. Lee, T. Ichi, T. Ooya, T. Yamamoto, M. Katoh, N. Yui, *J. Biomed. Mater. Res.* **2003**, 67A, 1087–1092.

[63] T. Ooya, T. Ichi, T. Furubayashi, M. Katoh, N. Yui, *React. Funct. Polym.* **2007**, 67, 1408–1417.

[64] W. Tachaboonyakiat, T. Furubayashi, M. Katoh, T. Ooya, N. Yui, *J. Biomater. Sci. Polym. Ed.* **2004**, 15, 1389–1404.

[65] Y. Arisaka, A. Tonegawa, A. Tamura, N. Yui*, J. Appl. Polym. Sci.* **2021**, 138, 49706.

[66] C. Dong, Y. Lv, *Polymers* **2016**, 8, 42.

[67] S. O. Sarrigiannidis, J. M. Rey, O. Dobre, C. González-García, M. J. Dalby, M. Salmeron-Sanchez, *Mater. Today Bio* **2021**, 10, 100098.

[68] X. Zhao, W. Song, W. Li, S. Liu, L. Wang, L. Ren, *RSC Adv.* **2017**, 7, 28865–28875.

[69] X. Lei, Y. G. Jia, W. Song, D. Qi, J. Jin, J. Liu, L. Ren, *ACS Appl. Bio Mater.* **2019**, 2, 3861–3869.

[70] D. Morshedi Rad, M. Alsadat Rad, S. Razavi Bazaz, N. Kashaninejad, D. Jin, M. Ebrahimi Warkiani, *Adv. Mater.* **2021**, 33, 2005363.

[71] J. J. Li, F. Zhao, J. Li, *Appl. Microbiol. Biotechnol.* **2011**, 90, 427–443.

[72] D. Oupický, R. C. Carlisle, L. W. Seymour, *Gene Ther.* **2001**, 8, 713–724.

[73] T. Ooya, H. S. Choi, A. Yamashita, N. Yui, Y. Sugaya, A. Kano, A. Maruyama, H. Akita, R. Ito, K. Kogure, H. Harashima, *J. Am. Chem. Soc.* **2006**, 128, 3852–3853.

[74] A. Yamashita, N. Yui, T. Ooya, A. Kano, A. Maruyama, H. Akita, K. Kogure, H. Harashima, *Nat. Protoc.* **2007**, 1, 2861–2869.

[75] A. Yamashita, D. Kanda, R. Katoono, N. Yui, T. Ooya, A. Maruyama, H. Akita, K. Kogure, H. Harashima, *J. Control. Release* **2008**, 131, 137–144.

[76] Y. Yamada, T. Nomura, H. Harashima, A. Yamashita, N. Yui, *Biomaterials* **2012**, 33, 3952–3958.

[77] T. Ooya, H. S. Choi, A. Yamashita, N. Yui, Y. Sugaya, A. Kano, A. Maruyama, H. Akita, R. Ito, K. Kogure, H. Harashima, *J. Am. Chem. Soc.* **2006**, 128, 3852–3853.

[78] Y. Yamada, M. Hashida, T. Nomura, H. Harashima, Y. Yamasaki, K. Kataoka, A. Yamashita, R. Katoono, N. Yui, *ChemPhysChem* **2012**, 13, 1161–1165.

[79] A. Tamura, N. Yui, *Biomaterials* **2013**, 34, 2480–2491.

[80] A. Tamura, N. Yui, *J. Mater. Chem. B* **2013**, 1, 3535–3544.

[81] A. Tamura, G. Ikeda, J. H. Seo, K. Tsuchiya, H. Yajima, Y. Sasaki, K. Akiyoshi, N. Yui, *Sci. Rep.* **2013**, 3, 2252.

[82] A. Tamura, G. Ikeda, K. Nishida, N. Yui, *Macromol. Biosci.* **2015**, 15, 1134–1145.

[83] K. Nishida, A. Tamura, N. Yui, *Biomacromolecules* **2018**, 19, 2238–2247.

[84] J. Kost, E. Mathiowitz, A. Azagury, *Adv. Funct. Mater.* **2021**, 31, 2108838.

[85] G. Yu, D. Wu, Y. Li, Z. Zhang, L. Shao, J. Zhou, Q. Hu, G. Tang, F. Huang, *Chem. Sci.* **2016**, 7, 3017–3024.

[86] G. Yu, Z. Yang, X. Fu, B. C. Yung, J. Yang, Z. Mao, L. Shao, B. Hua, Y. Liu, F. Zhang, Q. Fan, S. Wang, O. Jacobson, A. Jin, C. Gao, X. Tang, F. Huang, X. Chen, *Nat. Commun.* **2018**, 9, 766.

[87] D. Kong, K. Zhang, J. Tian, L. Yin, X. Sheng, *Adv. Mater. Technol.* **2022**, 7, 2100006.

[88] K. Ilina, W. M. MacCuaig, M. Laramie, J. N. Jeouty, L. R. McNally, M. Henary, *Bioconjug. Chem.* **2020**, 31, 194–213.

[89] J. He, Y. J. Jo, X. Sun, W. Qiao, J. Ok, T. il Kim, Z. Li, *Adv. Funct. Mater.* **2021**, 31, 2008201.

[90] H. Chen, M. S. Farahat, K. Y. Law, D. G. Whitten, *J. Am. Chem. Soc.* **1996**, 118, 2584–2594.

[91] J. J. Gassensmith, J. M. Baumes, B. D. Smith, *Chem. Commun.* **2009**, 6329–6338.

[92] E. Arunkumar, C. C. Forbes, B. C. Noll, B. D. Smith, *J. Am. Chem. Soc.* **2005**, 127, 3288–3289.

[93] J. R. Johnson, N. Fu, E. Arunkumar, W. M. Leevy, S. T. Gammon, D. Piwnica-Worms, B. D. Smith, *Angew. Chemie Int. Ed.* **2007**, 46, 5528–5531.

[94] W. M. Leevy, S. T. Gammon, H. Jiang, J. R. Johnson, D. J. Maxwell, E. N. Jackson, M. Marquez, D. Piwnica-Worms, B. D. Smith, *J. Am. Chem. Soc.* **2006**, 128, 16476–16477.

[95] E. Arunkumar, P. K. Sudeep, P. V. Kamat, B. C. Noll, B. D. Smith, *New J. Chem.* **2007**, 31, 677–683.

[96] J. M. Baumes, J. J. Gassensmith, J. Giblin, J.-J. Lee, A. G. White, W. J. Culligan, W. M. Leevy, M. Kuno, B. D. Smith, *Nat. Chem.* **2010**, 2, 1025–1030.

[97] D. R. Boutz, D. Cascio, J. Whitelegge, L. J. Perry, T. O. Yeates, *J. Mol. Biol.* **2007**, 368, 1332–1344.

[98] H. X. Zhou, *J. Am. Chem. Soc.* **2003**, 125, 9280–9281.

[99] J. D. Hegemann, M. Zimmermann, X. Xie, M. A. Marahiel, *Acc. Chem. Res.* **2015**, 48, 1909–1919.

[100] W. R. Wikoff, L. Liljas, R. L. Duda, H. Tsuruta, R. W. Hendrix, J. E. Johnson, *Science* **2000**, 289, 2129–2133.

[101] X. W. Wang, W. Bin Zhang, *Trends Biochem. Sci.* **2018**, 43, 806–817.

[102] C. M. Zimanyi, N. Ando, E. J. Brignole, F. J. Asturias, J. Stubbe, C. L. Drennan, *Structure* **2012**, 20, 1374–1383.

[103] B. Lee, K. H. Kim, S. J. Park, S. H. Eom, H. K. Song, S. W. Suh, *EMBO J.* **2004**, 23, 2029–2038.

[104] D. Liu, W. H. Wu, Y. J. Liu, X. L. Wu, Y. Cao, B. Song, X. Li, W. Bin Zhang, *ACS Cent. Sci.* **2017**, 3, 473–481.

[105] L. Z. Yan, P. E. Dawson, *Angew. Chemie Int. Ed.* **2001**, 40, 3625–3627.

[106] J. W. Blankenship, P. E. Dawson, *J. Mol. Biol.* **2003**, 327, 537–548.

[107] X.-W. Wang, W.-B. Zhang, *Angew. Chemie Int. Ed.* **2017**, 129, 14173–14177.

[108] X. Da, W. Zhang, *Angew. Chemie Int. Ed.* **2019**, 131, 11214–11221.

[109] A. Acevedo-Jake, A. T. Ball, M. Galli, M. Kukwikila, M. Denis, D. G. Singleton, A. Tavassoli, S. M. Goldup*, J. Am. Chem. Soc.* **2020**, 142, 5985–5990.

[110] T. Kench, P. A. Summers, M. K. Kuimova, J. E. M. Lewis, R. Vilar, *Angew. Chemie Int. Ed.* **2021**, 133, 11023–11029.

[111] R. Barat, T. Legigan, I. Tranoy-Opalinski, B. Renoux, E. Péraudeau, J. Clarhaut, P. Poinot, A. E. Fernandes, V. Aucagne, D. A. Leigh, S. Papot, *Chem. Sci.* **2015**, 6, 2608–2613.

[112] M. Liu, Q. Zhang, Z. Li, J. Gu, J. D. Brennan, Y. Li, *Nat. Commun.* **2016**, 7, 12074.

[113] R. Zidovetzki, I. Levitan, *Biochim. Biophys. Acta Biomembr.* **2007**, 1768, 1311–1324.

[114] B. Levine, G. Kroemer, *Cell* **2008**, 132, 27–42.

[115] K. Nishida, A. Tamura, N. Yui, *J. Control. Release* **2018**, 275, 20–31.

[116] Y. Yamada, S. Daikuhara, A. Tamura, K. Nishida, N. Yui, H. Harashima, *Chem. Commun.* **2019**, 55, 7203–7206.

[117] C. C. Slack, J. A. Finbloom, K. Jeong, C. J. Bruns, D. E. Wemmer, A. Pines, M. B. Francis, *Chem. Commun.* **2017**, 53, 1076–1079.

[118] H. Marshall, N. J. Stewart, H. F. Chan, M. Rao, G. Norquay, J. M. Wild, *Prog. Nucl. Magn. Reson. Spectrosc.* **2021**, 122, 42–62.

[119] M. S. Albert, G. D. Cates, B. Driehuys, W. Happer, B. Saam, C. S. Springer, A. Wishnia, *Nature* **1994**, 370, 199–201.

[120] Y. Wang, I. J. Dmochowski, *Chem. Commun.* **2015**, 51, 8982–8985.

[121] S. H. Klass, A. E. Truxal, T. A. Fiala, J. Kelly, D. Nguyen, J. A. Finbloom, D. E. Wemmer, A. Pines, M. B. Francis, *Angew. Chemie Int. Ed.* **2019**, 58, 9948–9953.

[122] K. M. Bąk, K. Porfyrakis, J. J. Davis, P. D. Beer, *Mater. Chem. Front.* **2020**, 4, 1052–1073.

[123] M. J. Langton, C. J. Serpell, P. D. Beer, *Angew. Chemie Int. Ed.* **2016**, 55, 1974–1987.

[124] M. J. Langton, P. D. Beer, *Acc. Chem. Res.* **2014**, 47, 1935–1949.

[125] K. P. Carter, A. M. Young, A. E. Palmer, *Chem. Rev.* **2014**, 114, 4564–4601.

[126] M. Denis, J. Pancholi, K. Jobe, M. Watkinson, S. M. Goldup, *Angew. Chemie Int. Ed.* **2018**, 57, 5310–5314.

[127] T. Shukla, A. K. Dwivedi, R. Arumugaperumal, C. M. Lin, S. Y. Chen, H. C. Lin, *Dye. Pigment.* **2016**, 131, 49–59.

[128] S. M. Chan, F. K. Tang, C.-S. Kwan, C. Y. Lam, S. C. K. Hau, K. C. F. Leung, *Mater. Chem. Front.* **2019**, 3, 2388–2396.

[129] N. L. Kilah, M. D. Wise, C. J. Serpell, A. L. Thompson, N. G. White, K. E. Christensen, P. D. Beer, *J. Am. Chem. Soc.* **2010**, 132, 11893–11895.

[130] B. R. Mullaney, A. L. Thompson, P. D. Beer, *Angew. Chemie Int. Ed.* **2014**, 53, 11458–11462.

[131] M. J. Langton, S. W. Robinson, I. Marques, V. Félix, P. D. Beer, *Nat. Chem.* **2014**, 6, 1039–1043.

[132] M. J. Langton, I. Marques, S. W. Robinson, V. Félix, P. D. Beer, *Chem. Eur. J.* **2016**, 22, 185–192.

[133] L. Zhang, V. Marcos, D. A. Leigh, *Proc. Natl. Acad. Sci*. **2018**, 115, 9397–9404.

[134] B. A. McNally, W. M. Leevy, B. D. Smith, *Supramol. Chem.* **2007**, 19, 29–37.

[135] V. Dvornikovs, B. E. House, M. Kaetzel, J. R. Dedman, D. B. Smithrud, *J. Am. Chem. Soc.* **2003**, 125, 8290–8301.

[136] X. Wang, X. Bao, M. McFarland-Mancini, I. Isaacsohn, A. F. Drew, D. B. Smithrud, *J. Am. Chem. Soc.* **2007**, 129, 7284–7293.

[137] D. A. Kevin, D. A. F. Meujo, M. T. Hamann, *Expert Opin. Drug Discov.* **2009**, 4, 109–146.

[138] D. B. Smithrud, X. Wang, P. Tarapore, S. M. Ho, *ACS Med. Chem. Lett.* **2013**, 4, 27-31.

[139] D. B. Smithrud, L. Powers, J. Lunn, S. Abernathy, M. Peschka, S. mei Ho, P. Tarapore, *ACS Med. Chem. Lett.* **2017**, 8, 163–167.

[140] S. Chen, Y. Wang, T. Nie, C. Bao, C. Wang, T. Xu, Q. Lin, D. H. Qu, X. Gong, Y. Yang, L. Zhu, H. Tian, *J. Am. Chem. Soc.* **2018**, 140, 17992–17998.

[141] K. K. Cotí, M. E. Belowich, M. Liong, M. W. Ambrogio, Y. A. Lau, H. A. Khatib, J. I. Zink, N. M. Khashab, J. F. Stoddart, *Nanoscale* **2009**, 1, 16–39.

[142] T. D. Nguyen, H. R. Tseng, P. C. Celestre, A. H. Flood, Y. Liu, J. F. Stoddart, J. I. Zink, *Proc. Natl. Acad. Sci.* **2005**, 102, 10029–10034.

[143] T. D. Nguyen, Y. Liu, S. Saha, K. C. F. Leung, J. F. Stoddart, J. I. Zink, *J. Am. Chem. Soc.* **2007**, 129, 626–634.

[144] A. Martinez-Cuezva, S. Valero-Moya, M. Alajarin, J. Berna, *Chem. Commun.* **2015**, 51, 14501–14504.

[145] D. Tarn, D. P. Ferris, J. C. Barnes, M. W. Ambrogio, J. F. Stoddart, J. I. Zink, *Nanoscale* **2014**, 6, 3335–3343.

[146] H. Yan, C. Teh, S. Sreejith, L. Zhu, A. Kwok, W. Fang, X. Ma, K. T. Nguyen, V. Korzh, Y. Zhao, *Angew. Chemie Int. Ed.* **2012**, 51, 8373–8377.

[147] M. Sökmen, M. Akram Khan, *Inflammopharmacology* **2016**, 24, 81–86.

[148] M. Li, H. Yan, C. Teh, V. Korzh, Y. Zhao, *Chem. Commun.* **2014**, 50, 9745–9748.

[149] J. E. Beves, B. A. Blight, C. J. Campbell, D. A. Leigh, R. T. McBurney, *Angew. Chemie Int. Ed.* **2011**, 50, 9260–9327.

[150] J. F. Stoddart, *Chem. Soc. Rev.* **2009**, 38, 1802–1820.

[151] D. A. Leigh, V. Marcos, M. R. Wilson, *ACS Catal.* **2014**, 4, 4490–4497.

[152] S. Mena-Hernando, E. M. Pérez, *Chem. Soc. Rev.* **2019**, 48, 5016-5032.

[153] A. W. Heard, S. M. Goldup, *ACS Cent. Sci.* **2020**, 6, 2, 117–128.

[154] M. Xue, Y. Yang, X. Chi, X. Yan, F. Huang, *Chem. Rev.* **2015**, 115, 7398–7501.

[155] S. F. van Dongen, S. Cantekin, J. A. Elemans, A. E. Rowans, R. J. Nolte *Chem. Soc. Rev.*, **2014**, 43, 99-122.

Chapter 2: A Photolabile 2,2'-Bipyridine Macrocycle for Light-Triggered Mechanical Bond Cleavage

Abstract: A photocleavable 2,2'-bipyridine macrocycle was conveniently synthesized and found to mediate AT-CuAAC rotaxane formation with high efficiency. Exposure to UVB light cleaved the photolabile diethylaminobenzyl (DEABn) unit and resulted in the macrocycle opening to release the corresponding axle. The rate of photolytic axle release was investigated in rotaxanes possessing mechanical bonds with differing degrees of steric hindrance. The photocleavable macrocycle was then successfully incorporated into a dinucleotide rotaxane and later into a model oligonucleotide rotaxane structure.

Prior publication: None of this work has been previously published.

2.1. Introduction

Investigating the complex interactions between biological molecules is key to understanding cellular function and disease. Using conditional chemical probes to perturb and manipulate these dynamic events is often difficult, however, due to the high spatiotemporal control required to mimic the precision of natural biological processes.[1] Light is an ideal tool in this regard, as it is a non-invasive and tuneable external stimulus that offers precise control over the release of photocaged molecules. Provided the activating wavelength is not too short (>400 nm), light is also orthogonal to most cellular processes and has been used extensively as a conditional trigger to study complex physiological events.[2,3] Achieving photochemical control over a bioactive species generally involves the installation of photosensitive trigger motifs at key structural sites, which inhibit biological function by either: i) blocking supramolecular interactions between biological partners, or ii) preventing key functional group transformations from taking place. Upon exposure to a particular wavelength of light, the photocage is cleaved and the biological activity of the molecule is restored. Modern lasers and confocal microscopes allow the location and timing of activation to be precisely controlled, meaning decaging occurs only in the tissues, cells, or subcellular compartments of interest.[4,5]

The use of photocages to modulate the activity of biologically active molecules was first introduced by Kaplan *et al.* using adenosine triphosphate (ATP) caged with the *ortho*-nitrobenzyl (*o*NB) group — a motif already being used as a photolabile protecting group (PPG) for synthetic purposes.[6] The study found that Na^+/K^+-ATPase pumps could not use caged ATP **1** as an energy source to facilitate active transport. Photolytic cleavage of the *o*NB group released free ATP molecules (**2**), which were subsequently hydrolysed to activate ATPase pumps, as evidenced by Na^+ efflux. (Figure **19**).[7] *o*NB and related analogues featured heavily in early biological photoactivation studies and are still widely used today. Advances in synthetic chemistry have since led to the development of a plethora of PPGs that have been used to achieve optochemical control over virtually every kind of biologically-relevant molecule, ranging from macromolecules such as proteins and DNA to small-molecule neurotransmitters and cell-signalling agents, among others.[8–11]

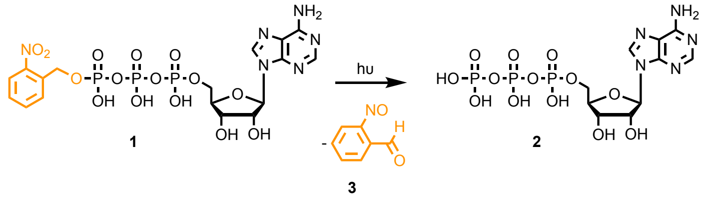

Figure **19**. The principle of photocages showing the first example of UV-activation with *o*-nitrobenzyl (*o*NB)-caged adenosine triphosphate **1** to liberate free ATP **2**.[7]

2.1.1. Photocleavable Protecting Groups

The optimal choice of PPG is dependent on the structure of the biological candidate and the process under study. However, there are a few general criteria that should be fulfilled. The PPG-caged species should be highly soluble and stable in biological media prior to and during photolysis. Complete shutdown of bioactivity is also ideal, although not always attainable. In such cases, the background activity should fall below the threshold required for induction of the biological effect to be deemed successful. The photoreaction should also be clean and occur with a high quantum yield at non-damaging wavelengths, preferably producing only low-absorbing nontoxic by-products. Additionally, when studying the kinetics of light-induced biological events, it is imperative that uncaging occurs faster than the molecular process under investigation.

Over the years, numerous classes of PPGs relying on photochemically distinct mechanisms to liberate caged guests have been developed.[12,13] *o*NB derivatives are by far the most commonly used PPGs and have been successfully employed to cage a range of biological functional groups, the nature of which influence the rate and quantum yields of photocleavage.[14] The cleavage of an unmodified *o*NB group (**I**) is typically slow and occurs at low absorption wavelengths that are unsuitable for applications in living biological systems.[15,16] Fortunately, the relatively simple structure of *o*NB lends itself to facile modification, with numerous analogues reported to overcome these limitations (Figure **20**). Altering aromatic substituents can shift the absorbance of the chromophore to longer, more biologically-friendly wavelengths (**II**, **V**, **VI**).[15,17,18] For instance, the inclusion of methoxy groups in 3,5-dimethoxynitrobenzene (DMNB) (**II** and **V**) results in a bathochromic shift that moves λ_{max} to a more suitable, lower energy wavelength. Modification at the benzylic position (**IV**) has similarly led to enhanced rates of substrate release with greater quantum yields and at friendlier wavelengths.20

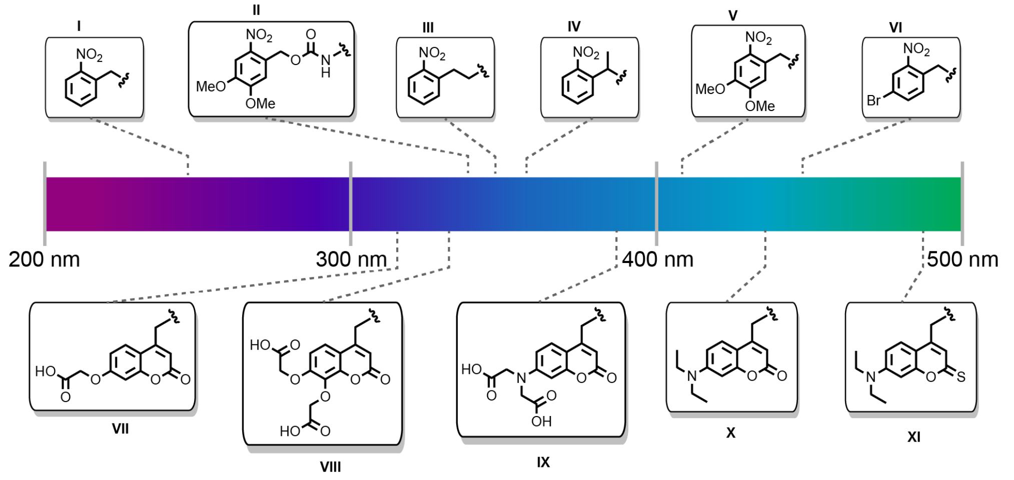

Figure **20**. Structure and approximate deprotection wavelength of *o*NB (**I**,[6] **II**,[15] **III**,[19] **IV**,[20] **V**,[17] and **VI**[18])- and coumarin (**VII**,[21] **VIII**,[22] **IX**,[23] **X**,[24] and **XI**[25])-based PPGs.

However, photolytic cleavage of the *o*NB group is known to proceed *via* Norrish type II pathways (Scheme **1**), generating strongly-absorbing cytotoxic nitrosoaldehyde (**3**) by-products that are harmful to the biological system and can also interfere with the photolytic release of remaining caged species.[26] Despite significant efforts being made to negate the formation of interfering photo-decomposition products through further derivatisation of the *o*NB scaffold, such as with 2-nitrophenylethyl (**III**),[19] many groups have switched their attention towards other classes of PPGs which do not suffer the same limitations.

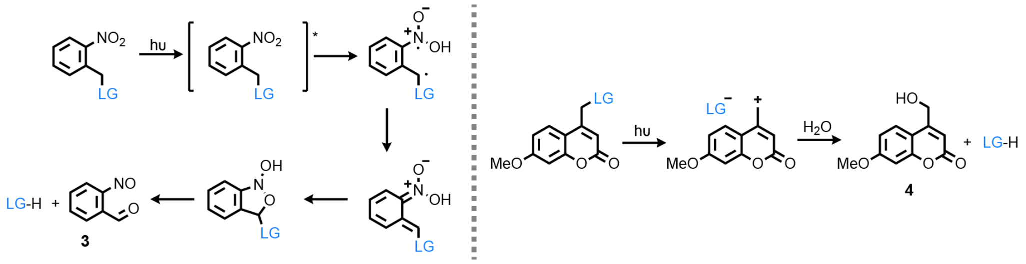

Scheme **1**. Photocleavage of an unmodified *o*NB molecule proceeding *via* a Norrish type II pathway (left), alongside the photo heterolytic cleavage of a coumarin motif (right).

Coumarin-based photocages are becoming increasingly popular due to their synthetic accessibility, biocompatibility and favourable release wavelengths.[27] Photolysis proceeds through direct heterolytic cleavage of the C-O bond upon excitation, releasing the caged substrate (LG^-) and generating a positively charged coumarin intermediate (CM^+) that is subsequently quenched by water (Scheme **1**).[28] The need to stabilise the photolytically generated ion pair usually requires the caged substrates possess low pK_a leaving groups, such as carbamates, carbonates, phosphates or carboxy groups. Although, several modifications have been reported to allow the release of poorer leaving groups.[28] Similar to *o*NB derivatives, relatively minor alterations to the coumarin scaffold can lead to substantial changes in the deprotection wavelength that extend far into the visible region (Figure **20**). The introduction of carboxylic acid-containing electron-donating groups (EDGs) at the 7-position results in higher intensity red-shifted absorptions while simultaneously enhancing the hydrophilicity of the caged species (**VII**, **VII**, **IX**).[21–23] Increasing the electron-donating ability using alkylated amino substituents results in more pronounced red shifts and greater quantum yields upon photolysis (**X**).[24] This can be improved even further through the replacement of the carbonyl oxygen with sulfur.[25] The main drawback of coumarin-based PPGs is that they have limited aqueous solubility, even once possessing multiple polar modifications. This can lead to difficulty releasing non-hydrophilic species from coumarin photocages under biological conditions.

A host of other PPGs have been reported for use in biological contexts, such as nitroindoline, benzoin, perylene diimides and various ruthenium complexes.[29–32] The *p*-hydroxyphenacyl (pHP) group is a promising alternative to the aforementioned *o*NB and coumarin-based photocages that exhibits excellent aqueous solubility, biological stability, high quantum yields, and a rapid/clean release profile.[33,34] The photo-Favorskii pathway tends to dominate in aqueous conditions, proceeding *via* an intriguing skeletal rearrangement to liberate the caged species and generate a spirodienedione intermediate (**5**) that is subsequently hydrolysed (Scheme **2**).[35] The main photolytic by-product, *p*-hydroxyphenylacetic acid (**6**), is nontoxic and blue-shifted relative to the caged chromophore and therefore does not interfere with photocleavage. Although absorption of the pHP chromophore is weak above 300 nm, this can be easily amended by incorporating EDGs such as methoxy or carboxyl at the *meta* position or through the extension of the conjugated ring system.[36]

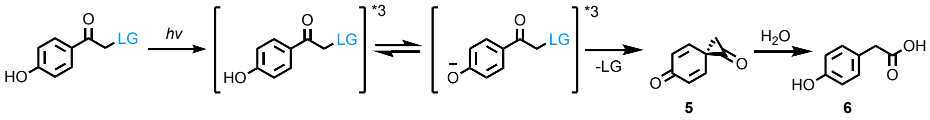

Scheme **2**. The Photo-Favorskii photocleavage pathway of caged pHP substrates in aqueous solvents.

2.1.2. Oligonucleotides in Biology and Medicine

Inhibiting the cellular pathways associated with dysfunctional proteins can mitigate their toxic effect and is a common strategy to investigate and treat disease. However, the functional interfaces of many proteins are large hydrophobic surfaces which lack small-molecule binding sites, meaning only a minority are targetable through a traditional approach.[37] In such cases, it can be highly advantageous to instead target RNA, the genetic precursor to the disease-causing protein. The regulation of RNA through gene silencing methods essentially expands the number of targetable proteins to any sequenced gene of interest in a modular fashion.[38] Targeted gene silencing approaches utilize naturally occurring cellular pathways to selectively target and destroy mRNA, blocking the expression of the corresponding protein. RNA interference (RNAi) is a process that occurs in eukaryotic cells, whereby sequence-specific post-transcriptional gene silencing is triggered by naturally produced double-stranded RNA species, such as small interfering RNA (siRNA) or micro RNA (miRNA).[39] Among other cellular functions, these short double-stranded RNA species have evolved to defend the genome from the invasive nucleic acids of pathogenic species such as viruses, bacteria, and transposons.[40]

Antisense oligonucleotides (ASOs) are synthetic single-stranded oligonucleotides that sequence-specifically bind to complementary mRNA sequences *via* Watson-Crick base pairing to modulate function and control protein expression.[41] Upon cellular internalization, ASOs locate and hybridize target mRNA with extraordinarily high sequence fidelity capable of differentiating between even a singly mismatched nucleotide sequence.[42,43] The post-binding mechanism differs considerably depending on the structure of the ASO and the subcellular location of the RNA target, but can be broadly classified as either: i) ASOs which cause interference without inducing degradation, such as those that inhibit ribosomal activity *via* steric blocking; or ii) ASOs that recruit endogenous enzymes, such as RNAse H, to degrade the target mRNA sequence (RNA knockdown).[44] The RNAse H-mediated degradation pathway is the most commonly employed and proceeds *via* recognition and binding of RNAse H1 to the RNA-ASO heteroduplex through an N-terminal RNA binding domain. Cleavage typically occurs 8-12 nucleotides from the 5'-RNA end, releasing mRNA as short sequences while leaving the ASO (DNA) strand intact, allowing it to act catalytically.[45,46] The presence of RNAse enzymes in both the nucleus and the cytoplasm has led to success in silencing untranslated regions of RNA (pre-mRNA), as well as cytoplasmic intron RNA (mRNA).[47]

2.1.3. Oligonucleotide Modifications

Unmodified oligonucleotides suffer from several drawbacks that prevent their use under physiological conditions.[48,49] Firstly, as relatively large, polyanionic species, they experience poor cellular uptake and generally require formulation to become internalized. They are rapidly digested by endogenous phosphodiester-cleaving DNase enzymes, both intracellularly and in serum. They lack the necessary binding affinity to overcome the highly ordered intramolecular stem and loop structures adopted by intracellular RNA targets.[50]

The weak binding of unmodified oligonucleotides to plasma proteins also results in rapid renal clearance, leading to unfavourable pharmacokinetic profiles.[51] To be useful in a biological context, oligonucleotides must be structurally modified to grant resistance to nucleolytic degradation and improve pharmacokinetic properties while still retaining, or enhancing, affinity to target sequences so that they can compete with endogenous RNA secondary structures.

Using chemical modifications to overcome the therapeutically limiting features of unmodified oligonucleotides has facilitated their use in gene-silencing applications. Improvements can be achieved by introducing chemical modifications at one or several nucleotide sites simultaneously (Figure **21**). The phosphorothioate (PS) modification was among the first reported backbone alterations and is still widely used today.[52] By replacing the non-bridging phosphodiester oxygen with a sulfur atom, PS modified ASOs showed enhanced resistance toward nucleolytic degradation — up to 45 times slower degradation *in vitro* — leading to much longer circulation times.[53] Significant pharmacokinetic improvements, including stronger plasma protein binding and enhanced tissue uptake, were also observed without the need for formulation. Importantly, the RNAse H degradation pathway was retained with the PS modification.[54] However, the PS modification has been linked to cellular toxicity through strong off-target interactions with various intracellular proteins.[55] PS modified oligonucleotides also showed a reduced affinity for complementary RNA sequences, destabilizing RNA-ASO heteroduplexes and limiting their utility when used alone.[56]

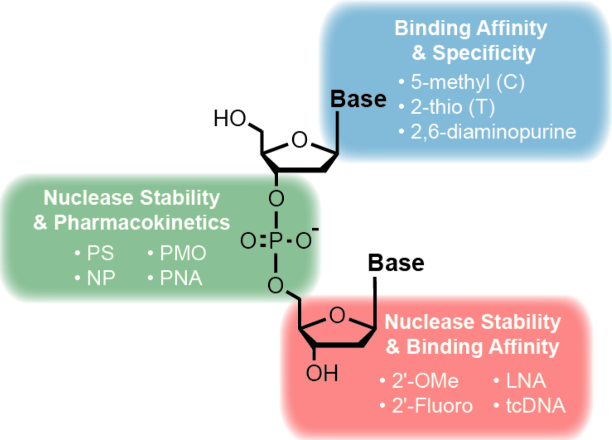

Figure **21**. Representation of the three common sites of oligonucleotide modification and examples of each: i) the nucleobase (5-methyl (C),[57] 2-thio (T),[58], 2,6-diaminopurine[59]), ii) the phosphodiester backbone (PS,[53] PMO,[60] NP,[61] PNA[62]), and iii) the pentose ring (2'-OMe,[63] 2'-Fluoro,[64] LNA,[65] tcDNA[66]).

Numerous other backbone modifications, such as phosphoramidate (NP),[61] peptide nucleic acids (PNAs),[62] and phosphorodiamidate morpholino oligomers (PMOs)[60] have attempted to tackle this problem. While successful in improving target affinity, these modifications are unable to support the RNAse H dependent cleavage mechanisms, an inherent characteristic needed for most ASO agents to function. Nucleobase modifications have similarly been reported to enhance binding affinity toward complementary nucleic acids.[67] For instance, 2,6-diaminopurines, or alteration of the C5' substitution in pyrimidine nucleobases, has been shown to increase target affinity by forming more stable duplexes without interrupting the potential for RNAse H degradation.[63,68] Although potent antisense activity was observed, severe cytotoxicity has prevented their application in a therapeutic context.

The furanose ring of native nucleic acids is in dynamic equilibrium between two possible conformations: 2'-*endo* (B-form), the ring conformation favoured in the native DNA double helix, and 3'-*endo* (A-form), the predominant conformation in DNA-RNA heteroduplexes (Figure **22**).[69] Chemical modifications that force the sugar ring into a preorganized RNA-like 3'-*endo* puckered conformation have been investigated to enhance binding affinity and resistance to nucleolytic degradation.[70] Electronegative substituents in the 2'-OMe and 2'-Fluoro modifications improve nucleolytic stability and shift the conformational equilibrium toward a 3'-*endo* sugar pucker, increasing RNA binding affinity.[63,64] The locked nucleic acid (LNA) modification tethers the 2'-hydroxyl group to the 4'-carbon atom, generating a 2,4-methylene bridged bicyclic nucleic acid that is conformationally locked in the 3'-*endo* conformation.[65,71] The resulting ASOs displayed remarkable RNA binding affinity and duplex stability, up to an additional $T_m \approx 5.6$ °C per modification, as well as enhanced resistance toward nuclease enzymes.[72] Although purely LNA modified ASOs are unable to support RNase H degradation mechanisms, when used in co-polymeric LNA/DNA gapmer constructs, they have shown to be non-toxic and highly potent ASO agents.[73]

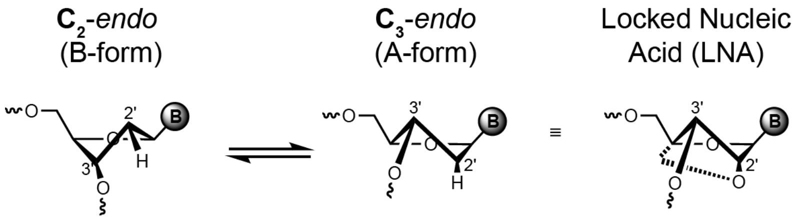

Figure **22**. The dynamic equilibrium of natural DNA ribose rings between C_2-*endo* and C_3-*endo* conformations alongside a locked nucleic acid.

2.1.4. Triazole-Linked Oligonucleotides

Triazole mimics of the phosphodiester backbone have attracted considerable attention in recent years.[74] The most successful of these modifications is the six-atom triazole linkage developed by Brown *et al.* (Figure **23**).[75] As well as significantly enhancing the stability of the oligonucleotide toward nuclease enzymes, the triazole motif is fully biocompatible and acts as a bioisostere that can be read through by DNA and RNA polymerases with high fidelity in bacterial and human cells.[76,77] Reduction in the overall anionic character of the modified oligonucleotide is also likely to have a positive impact on the cellular uptake of triazole-linked oligonucleotides. The approach has proven to be an excellent biological tool for synthesizing long oligonucleotide fragments, and even whole genes, which have been shown to remain transcriptionally active *in vitro*.[76,77] However, minor structural disturbances around the triazole linkage destabilize duplex formation with complementary RNA/DNA targets, suggesting that when used alone, the modification is unsuitable for applications where a high binding affinity is required.[78]

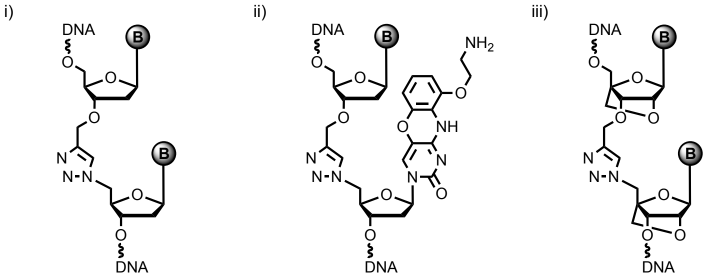

Figure **23**. Structure of oligonucleotides containing biocompatible six-atom triazole link (i)[75] in combination with a nucleobase G-clamp (ii)[79] and LNA modifications (iii).[80]

Attempts have been made to address this issue by combining the triazole linkage with additional modifications (Figure **23**). The presence of an aminoethylphenoxazine nucleobase (G-clamp) on the 3'-side of the linkage was found to enhance π-π stacking and H-bonding interactions, preventing base-pair fraying adjacent to the triazole linkage and stabilising hybrid oligonucleotide-RNA duplex formation to levels comparable to canonical DNA.[79] However, its use is limited to cytidine nucleobase combinations and was also found to be mildly mutagenic.[81] Oligonucleotides combining internal triazole-linkages with flanking LNA moieties, dubbed triazole-linked locked nucleic acids (t-LNAs), have recently been developed. The introduction of the LNA modification to the 3'-triazole side has been found to significantly increase specificity for target RNA and enhance the stability of the resulting heteroduplexes.[80] Substituting the native phosphodiester linkage with 3-LNA modified triazole moieties at four separate sites in the sequence also resulted in a striking resistance toward nucleolytic degradation relative to unmodified oligonucleotides. Thus, t-LNA modified oligonucleotides have the potential for use as biological tools or therapeutic agents.

2.1.5. Photocaged Oligonucleotides

Optochemical control of oligonucleotide function is most commonly achieved by blocking hybridisation to complementary sequences through the installation of photoresponsive units at the nucleobase — an effect that is enhanced when multiple sites are caged simultaneously.[9] Deiters *et al.* have shown that the hybridisation of a PS-modified ASO to its complementary mRNA target was disrupted through the inclusion of 6-nitropiperonyloxymethyl (NPOM)-caged thymidine bases.[82] ASOs incorporating three or four NPOM-modified nucleobases within the sequence showed no observable hybridisation to target mRNA.[83] Photo-irradiation at 365 nm rapidly cleaved the NPOM groups and restored hybridisation to the level of the uncaged ASO, leading to *in vitro* degradation of the target mRNA *via* the RNAse H-dependent pathway (Figure **24**). NPOM-thymine photocages were later introduced to morpholino ASOs known to block translation through mechanisms independent of RNAse H1 and showed similar efficacy as antisense agents.[84]

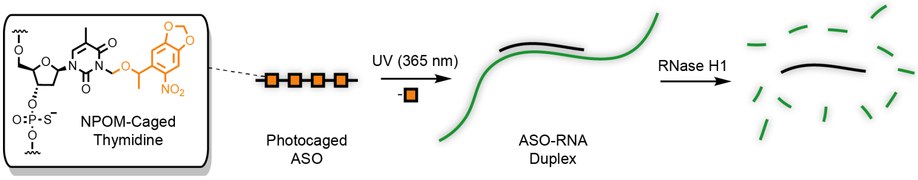

Figure **24**. NPOM-caged thymidine nucleobases inhibit complementary hybridisation until activation through brief exposure to UV irradiation (365nm).[83]

Photocleavable groups incorporated within the polymeric backbone have also been reported to inhibit oligonucleotide hybridisation. However, oligonucleotides caged in this manner generally require significantly more positions to be modified relative to the nucleobase caging approach to achieve similar levels of inhibition.[85,86] Numerous groups have instead sought to immobilize the oligonucleotide within an inactive structure using a single photocleavable linker. Dmochowski *et al.* have designed a DNA hairpin structure in which an ASO (20mer) is covalently bound to a short complementary blocking oligonucleotide (12mer) through a 2-nitrophenylethyl-containing covalent linker, forming a very stable duplex (T_m = 80 °C).[87] Upon irradiation, the covalent linker is cleaved, and the duplex is greatly de-stabilized (T_m = 51 °C), allowing the ASO to hybridize to the target mRNA sequence and catalyse its degradation *via* an RNAse H mediated mechanism (Figure **25**). The strategy was later applied to the inhibition of proto-oncogene mRNA, with PS-modified hairpin ASOs showing significant knockdown (52%) of the corresponding c-MYB transcription factor upon photoactivation in human leukaemia cells.[88] Joining the terminal ends of oligonucleotide sequences through a single photocleavable has similarly been employed to generate photocaged circular ASOs that are incapable of hybridizing with complementary mRNA sequences prior to photoactivation.[89–91]

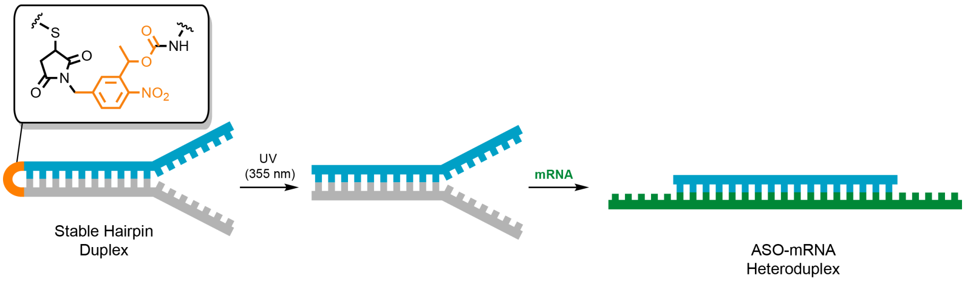

Figure **25.** DNA hairpin structure prevents hybridisation of an ASO sequence to a complementary mRNA target. UV irradiation (355 nm) cleaves the 2-nitrophenylethyl linker, destabilizing the duplex and facilitating mRNA hybridisation.[87]

The photo-modulation of oligonucleotide activity is not limited to antisense applications and has recently been used to achieve spatiotemporal control over the CRISPR-Cas9 gene-editing system using photocaged guide RNA (gRNA).[92] These gRNA sequences are complexed to Cas9 and are responsible for directing the protein to its desired genomic target *via* complementary base pairing and thus are critical to function. Stevens *et al*. have recently shown that the incorporation of just two NPOM-caged thymidine nucleobases within the targeting gRNA region was sufficient to completely block hybridisation.[93] Irradiation with low-intensity UV light (365 nm) resulted in rapid and complete cleavage of NPOM groups, allowing gRNA to guide Cas9 proteins to their targets and induce double-stranded DNA breaks in a variety of genes — facilitating gene regulation and transcriptional activation *in vitro*. The system was then applied to spatiotemporally control gene editing *in vivo*. Photoactivation at particular stages in the development cycle of zebrafish embryos resulted in the highly selective mutation of genes in one eye (Figure **26**). An independent study published shortly after by Deiters *et al.* also showed similar efficacy in controlling the Cas9 gene-editing system with NPOM-caged gRNA, highlighting the utility of photo-modulation for gene-editing applications.[94]

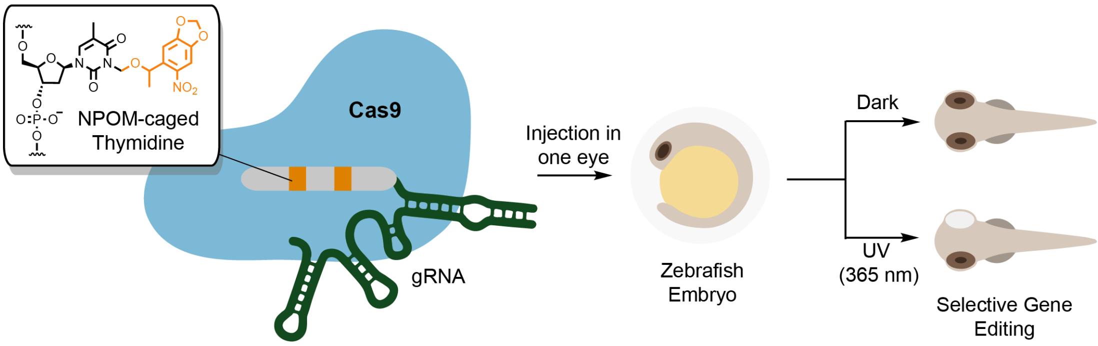

Figure **26**. Photo-modulation of the CRISPR-Cas9 gene-editing system *in vivo* using NPOM-caged gRNA sequences. [93]

2.1.6. Mechanically Interlocked DNA

The use of the mechanical bond to modify the properties of the sub-components in molecularly interlocked architectures is long-standing and occurs frequently throughout nature.[95] Topological links between cellular proteins in extremophilic bacteria/archaea, for instance, have been found to enhance catalytic activity and grant additional stability, allowing the folded structures to remain functional in the high-temperature and low pH conditions of their native environments.[96–98] Lasso peptides — a class of ribosomally assembled and post-translationally modified natural products synthesised by various bacteria — adopt a rigid 3D structure in which the C-terminal chain is threaded through a macrolactam ring.[99] Constraining the peptidic sequence in a lariot knot-like structure grants extraordinary resistance to thermal, chemical, and proteolytic degradation that allows lasso peptides to service a broad range of therapeutically relevant functions.[100,101] Topoisomerase enzymes have been found to utilize catenated and knotted DNA as key intermediates in cellular processes such as DNA replication and recombination.[102–104] The formation of rotaxane architectures between double-stranded DNA and *pseudo*-macrocyclic λ-exonucleases has also been observed during DNA replication and repair (Figure **27**).[105,106]

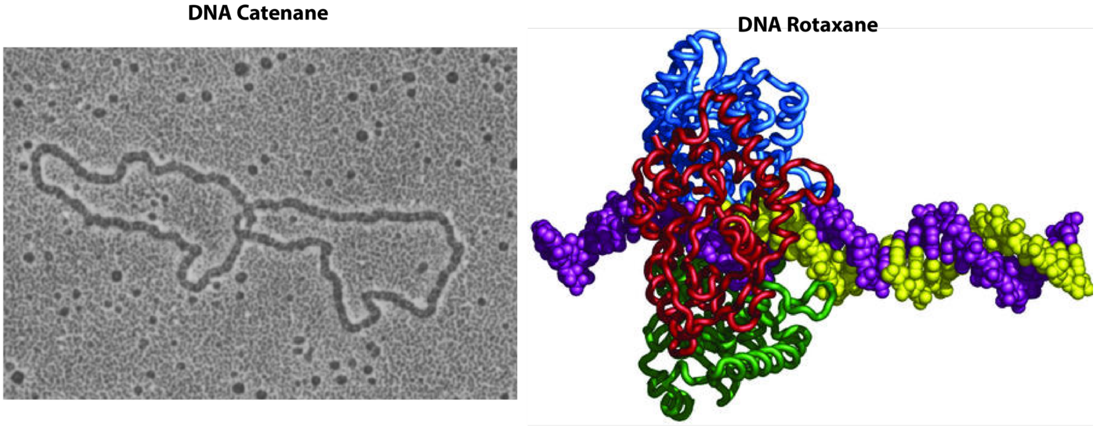

Figure **27**. Electron micrograph of catenated DNA by alongside an illustrative model of a DNA-λ-exonuclease rotaxane. Images adapted with permission from Kreuzer *et al.*,[103] and Myers *et al.*[105]

Numerous synthetic interlocked structures have been designed to interact with DNA in a stimuli-responsive manner. For instance, biodegradable polyrotaxane gels have been used as formulation agents to facilitate the cellular internalization of DNA.[107] Lewis *et al.* have recently demonstrated the controlled release of DNA-targeting metallodrugs from a photocleavable rotaxane (Figure **28**).[108] When incorporated within rotaxane structure **7**, the steric bulk of the macrocyclic component prevented π-π stacking interactions between the Pt^{II}-salphen complex and DNA nucleobases, leading to a complete shutdown in DNA-binding ability. Although the cellular uptake of the G4 ligand (**9**) was negligible, rotaxane **7** displayed excellent permeability and was also found to be highly stable and non-cytotoxic. Exposure to UV light (365 nm) resulted in cleavage of the photolabile DMNB moieties that acted as blocking groups, allowing the macrocycle to de-thread. Lacking the steric bulk to deter enzymatic activity, the aryl ester unit in the axle (**9**) was rapidly hydrolysed and the active ligand (**10**) was released — restoring G4 DNA-binding capability and *in vitro* cytotoxicity. This study highlights the potential of the mechanical bond as a platform to enhance the physiochemical properties of a biologically active compound whilst maintaining precise control over its activation.

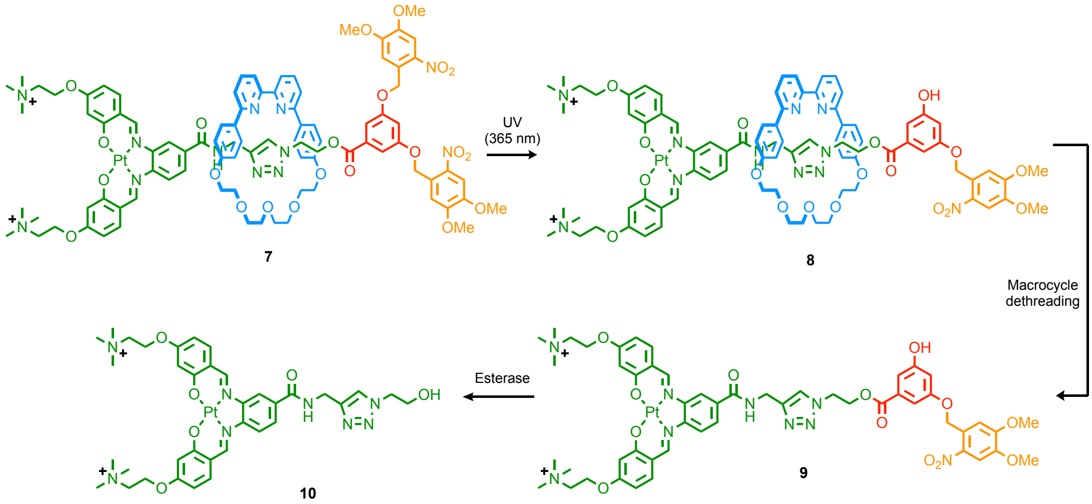

Figure **28**. Release of a G4 Ligand (**10**) from rotaxane **7** upon UV irradiation.[108]

Sophisticated interlocked DNA-based materials have been created using self-assembly approaches, such as DNA-origami. However, the programmed sequences that drive self-assembly in these approaches are extremely large and of limited biological or therapeutic utility.[109,110] The synthesis and investigation of interlocked oligonucleotide structures where one component is purely synthetic (i.e., not DNA-based), remains relatively unexplored. This is in part due to the structure of the native sugar-phosphate backbone in DNA which is not amenable to traditional mechanical bond-forming methodologies, such as hydrophobic threading, which rely on passive templation to pre-organize the individual mechanical components prior to covalent bond formation. Applying such an approach to the phosphorylation process would not be possible without making significant changes to DNA structure that would undoubtedly result in a loss of biological function.

Numerous backbone modifications have been reported to enhance the nucleolytic stability and pharmacokinetic profiles of oligonucleotides while retaining bioactivity. Many of these could also lend themselves to templation strategies. Click DNA-ligation (Figure **23**) is one such opportunity, as the active template Cu-mediated alkyne/azide cycloaddition (AT-CuAAC) methodology developed by Leigh *et al.* allows the formation of the 1,2,3-triazole and the mechanical bond simultaneously.[111] Recently, Goldup *et al.* have developed the first generation of oligonucleotide-rotaxanes based on the biologically relevant T7 promoter sequence (Scheme **3**).[112] By combining Goldups small macrocycle variation of the AT-CuAAC reaction with the DNA click-ligation approach,[113] azide and alkyne modified nucleotides were “clicked” together inside the cavity of a 2,2'-bipyridine macrocycle — facilitating the installation of the triazole and mechanical bond simultaneously. To evaluate the impact of the mechanical bond on biological activity, the duplex-forming ability of two T7 oligonucleotide-rotaxanes with differing click sites, **14a** and **14b**, was investigated.

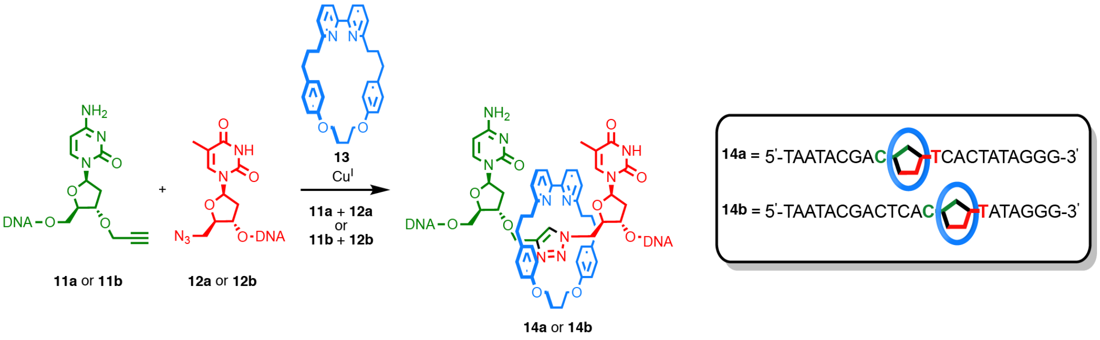

Scheme **3**. Synthesis of oligonucleotide-rotaxanes using the small macrocycle modification of the AT-CuAAC approach with modified oligonucleotide alkyne and azides.[112]

The results found that the corresponding non-interlocked axles could form duplexes with complementary T7 reverse sequences and serve as primers for PCR replication. The duplex-forming ability of oligonucleotide-rotaxanes **14a** and **14b** was suppressed and PCR completely shut down, indicating that the mechanical bond acts as a cage to silence oligonucleotide activity (Figure **29**). It is also inferred that the presence of the bulky macrocyclic component will help stabilise the oligonucleotide from enzymatic degradation through steric-blocking, in a similar manner to previously reported peptide rotaxanes,[114] however this is yet to be confirmed. Cleaving the macrocycle and breaking the mechanical bond is expected to restore the bioactivity of the triazole-linked oligonucleotide sequences and could therefore be used to generate novel stimuli-responsive therapeutic ASO agents or DNA-based tools for studying gene regulation.

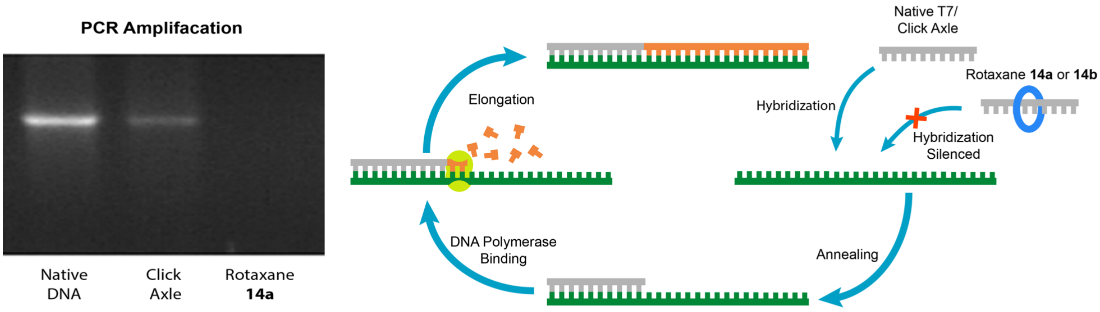

Figure **29**. Suppression of PCR amplification with the mechanical bond.[112]

2.2. Results and Discussion

Previous work has shown that the mechanical bond acts as a cage to silence the activity of biological oligonucleotide rotaxanes.[112] Incorporating stimuli-responsive units within the macrocyclic component that can be selectively cleaved would allow the oligonucleotide axle to be released in a controlled manner, restoring hybridisation capability and biological activity (Scheme **4**). Such responsive DNA-based materials have potential applications as ASO tools for studying cellular functions or treating disease.

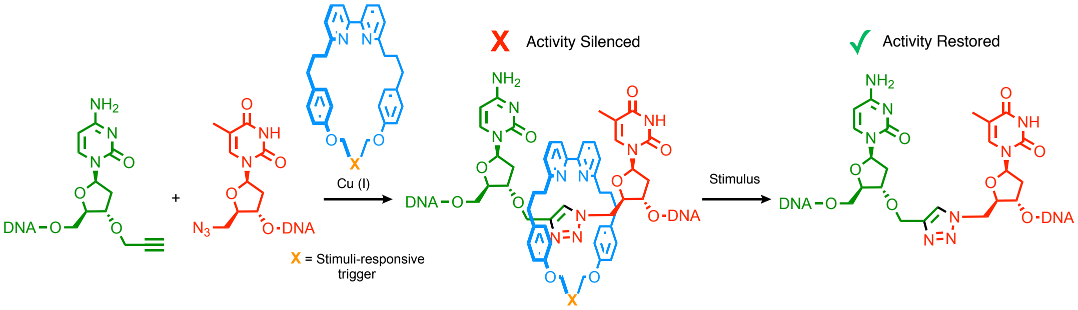

Scheme **4**. Principle aims of the project: i) development of a stimuli-responsive ring-opening 2,2'-bipyridine macrocycle, ii) incorporation of the cleavable macrocycle within an oligonucleotide rotaxane structure, and iii) proof-of-concept restoration of oligonucleotide activity upon mechanical bond cleavage.

Incorporating the caging group within the macrocyclic component of the oligonucleotide rotaxane is a conceptually different approach than previously reported methods of generating responsive DNA-based materials, which rely on direct covalent modification or formulation within biodegradable polymeric gels.[115] Light is the most common conditional trigger to control caged nucleic acid function and has numerous advantages over endogenous activating stimuli. The ever-increasing range of structurally diverse PPGs also provides greater flexibility in designing the responsive interlocked DNA platform. As such, light was initially targeted as the activating stimulus to cleave the macrocyclic component and restore oligonucleotide function. The photolytic release capability of the cleavable macrocycles was initially investigated in simple interlocked substrates to determine their efficacy and, if successful, were then incorporated into oligonucleotide sequences *via* AT-CuAAC coupling.

2.2.1. Synthesis of Photocleavable Macrocycle **25**

To demonstrate the photolytic release of axle from rotaxane, a macrocycle containing a photolabile unit was first needed. Goldup *et al.* have shown that 2,2'-bipyridine macrocycles mediate the AT-CuAAC reaction more efficiently than pyridine groups.[116] 2,2'-bipyridine macrocycles can be readily synthesised *via* the Ni-catalysed intramolecular homocoupling of 2-bromopyridyl groups, negating the poor yields observed when attempting to cyclise

2,2'-bipyridine containing macrocycle precursors.[117] To be incorporated within the macrocyclic backbone, the PPG must possess appropriate structural connectivity and be chemically tolerant to the numerous synthetic steps required to attain the final product. Furthermore, as the ability of 2,2'-bipyridine macrocycles to mediate rotaxane formation is critical to their function, the projection of sterically bulky groups into the cavity of the macrocycle should be avoided, as this would interfere with the AT-CuAAC process. Among the plethora of PPGs reported to operate under aqueous conditions, *m*-aniline and *o*NB derivatives were deemed among the most compatible.[6,118]

Although *o*NB derivatives were favoured initially due to their frequent occurrence in photo-caged biological systems, a robustness screen completed by fellow group members indicated that the nitro-group did not survive Ni-mediated macrocyclization conditions.[119] Reduction of the nitro-group by elemental Mn, a reducing agent used in the macrocyclization, is the suspected cause of this incompatibility.[120] Conversely, aniline and related *N*-alkylated variants were well tolerated and displayed no adverse effects on the efficacy of the macrocyclization procedure. The structurally analogous diethylaminobenzyl (DEABn) protecting group has recently been reported by Wang *et al.* to directly release poor leaving groups, such as alcohols and carboxylic acids, under aqueous conditions.[118,121,122] Macrocycle **25** was designed to position the photolabile DEABn unit as far from the catalytic 2,2'-bipyridine site as possible to minimise interference during mechanical bond formation.

Synthesis of DEABn linker **18** and its incorporation into macrocycle precursor **24** was straightforward and performed according to literature procedure (Scheme **5**).[118] Alkylation of commercially available **15** and subsequent $LiAlH_4$ reduction afforded **17**, which then underwent chlorination with $SOCl_2$ to afford linker **18** in 80% yield. Preparation of phenol **23** also proceeded according to literature procedure.[117,123] Hydrobromination of **19** *via* the anti-Markovnikov pathway afforded linear product **20** as the predominant regioisomer (97:3 linear: branched) in 95% yield. The crude material from this reaction was carried through a Negishi coupling with **21**, followed by deprotection in HBr to provide **23** in 83% yield. The base-catalysed alkylation of **23** with DEABn linker **18** gave macrocycle precursor **24** in 89% yield.

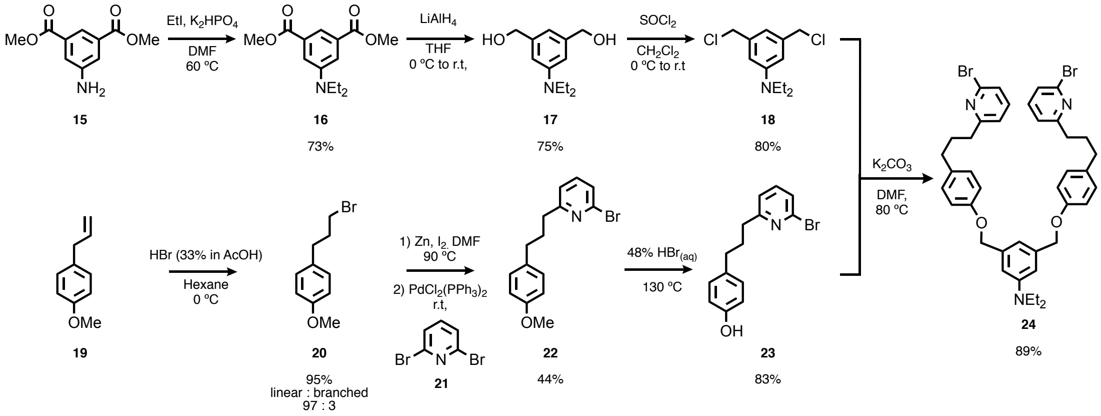

Scheme **5**. Synthesis of macrocycle precursor **24** containing the photocleavable DEABn group.

Macrocycle precursor **24** successfully underwent Ni-catalysed macrocyclization to afford **25** in 58% yield (Scheme **6**). Analysis of the crude reaction mixture indicated that **24** was fully consumed, and that and that the photolabile DEABn unit was well tolerated.

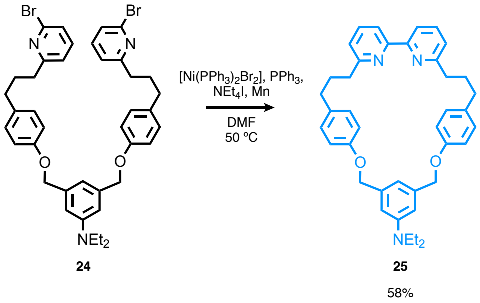

Scheme **6**. Ni-mediated macrocyclization of precursor **24**.

Single crystals suitable for XRD were obtained from the vapour diffusion of Et_2O into a saturated solution of **25** in CH_2Cl_2. Upon solving the crystal structure, $NiCl_2$ was found to be coordinated within the bipyridine unit (Figure **30**).[1] Given that only one macrocycle species was observed *via* ^{1}H NMR, this was surprising. LC-MS analysis similarly gave no indication of a Ni-complex. The Ni-bound macrocycle is likely a minor impurity, which happened to crystallise preferentially due to the presence of the metal, and thus is not representative of the entire sample.

---

[1] Crystal structure of **25-NiCl$_2$** complex was solved by Therapoom Boonprab.

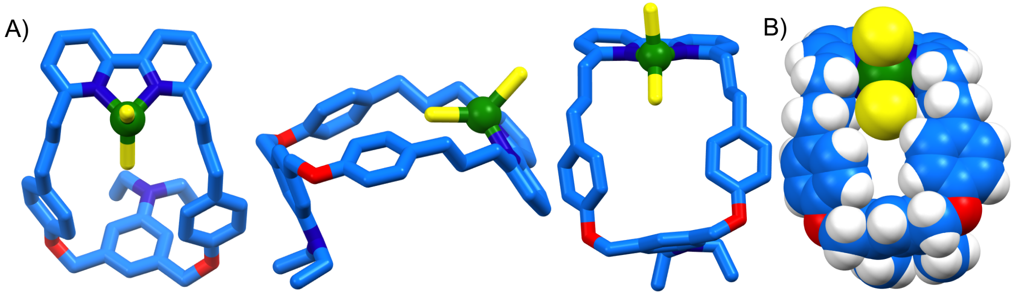

Figure **30.** A) Solid-state structure of macrocycle **25**-$NiCl_2$ complex displayed in partial sticks (macrocycle framework)/ ball-and-stick (Ni^{II}) representations. Hydrogen atoms omitted for clarity. B) Space-filling representation. Colours: H = white, C = blue, N = dark blue, O = red, Ni = green, Cl = yellow. Thermal ellipsoids drawn at 50% probability.

The tetrahedrally coordinated Ni^{II}-bipyridine complex provided insight into how macrocycle **25** would mediate rotaxane formation *via* AT-CuAAC catalysed by tetrahedral Cu^{I}. The solid-state structure shows that the macrocycle adopts a bowl-like conformation in which the DEABn group lies almost perpendicular to the plane of the macrocycle. The outlying position of the DEABn unit and projection of the steric bulk away from the active catalytic site suggests that it should not interrupt the mechanical bond forming step. However, both Cl ligands in the Ni-complex are however shown to project from the same face of the macrocycle, whereas incoming azide and alkyne half-axles must approach from either side of the cavity to form the mechanical bond. While this could result in the formation of non-interlocked axle *via* failed AT-coupling,[124] it should be noted that the size of bulky half-axle components will be significantly greater than the Cl atoms in the above structure. The additional steric bulk upon Cu-acetylide formation is expected to lock the macrocycle in a conformation where the incoming azide half-axle must approach from the opposite face, facilitating rotaxination.

2.2.2. Synthesis of Functionalisable Macrocycle **32**

Installing additional functionality within the 2,2'-bipyridine macrocycles while still retaining photocleavability could be highly beneficial for a host of biological applications. Provided the inductive effects at the chromophore remain relatively constant, *N*-alkylation should provide a facile handle to add additional functionality to the macrocycle. Bearing substrate tolerance in mind, a synthetic route to macrocycle **32** containing a free aniline unit was devised (Scheme **7**).

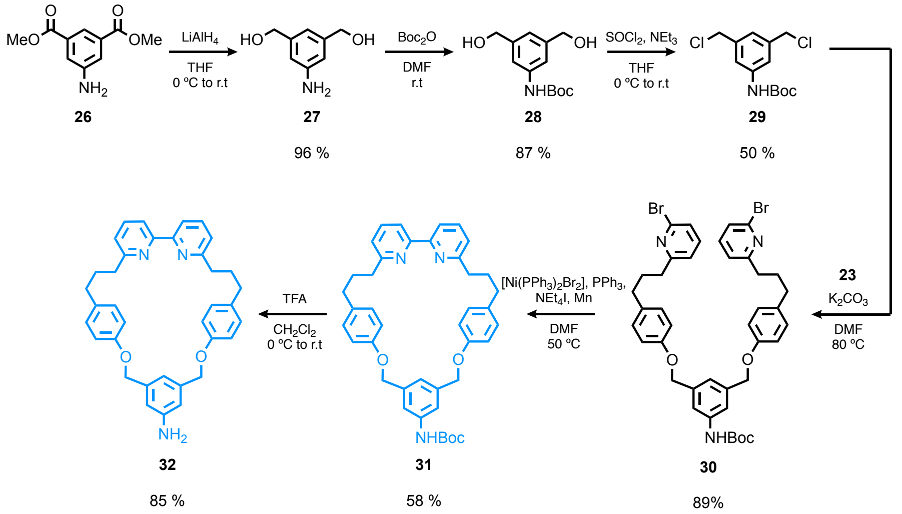

Scheme **7**. Synthesis of functionalisable macrocycle **32**.

The synthesis of **32** is analogous to that of **25**. $LiAlH_4$ reduction of commercially available **26** followed by *N*-Boc protection gave **28** in excellent yield. Chlorination of **28** with $SOCl_2$ afforded linker **29** in 50% yield. The alkylation of with **23** with **29** gave precursor **30**, which then underwent macrocyclization to provide **31** in 58% yield. Acidic *N*-Boc deprotection yielded readily functionalisable macrocycle **32** in 85% yield.

Solubility under aqueous conditions is a prerequisite for most biological applications. Wang *et al.* recently demonstrated that a DEABn analogue containing carboxylate chains in place of *N*-ethyl units retained its photocleavability and facilitated its use in aqueous solutions.[122] To demonstrate the utility of our functionalisable platform, water-solubilising carboxylic acid moieties were added to macrocycle **32** (Scheme **8**). Conversion of macrocycle **32** to the mono-alkylated product occurred rapidly when reacted with **33**, with a full conversion of **32** observed within 2 hours. However, transformation to dialkylated product **34** was much slower. The reaction was stopped after 3 days to afford **34** in 47% yield. Basic hydrolysis of **34** yielded dicarboxylic macrocycle **35** in 97% yield.

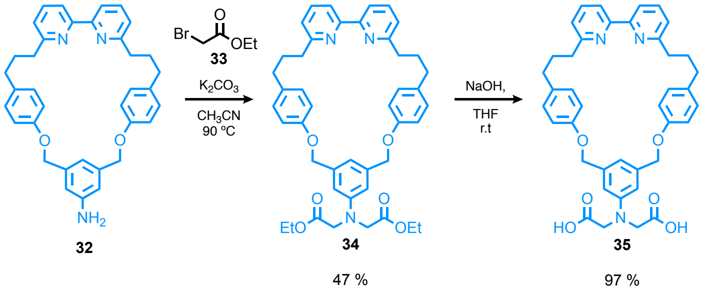

Scheme **8**. Synthesis of carboxylic acid-functionalised macrocycle **35**.

2.2.3. Photolysis Experiments

We next sought to determine whether macrocycles **25** and **35** would cleave upon exposure to the appropriate wavelength of UV light. The UV-Vis absorption spectra of selected macrocycles are shown below (Figure **31**). Due to the insolubility of **35** in organic solvents, the UV-Vis spectra of ester-protected macrocycle **34** was recorded instead. The structurally analogous macrocycle **13**, containing no photolabile unit, was used as a positive control in the photolysis experiments, and its absorption spectrum is also shown below.

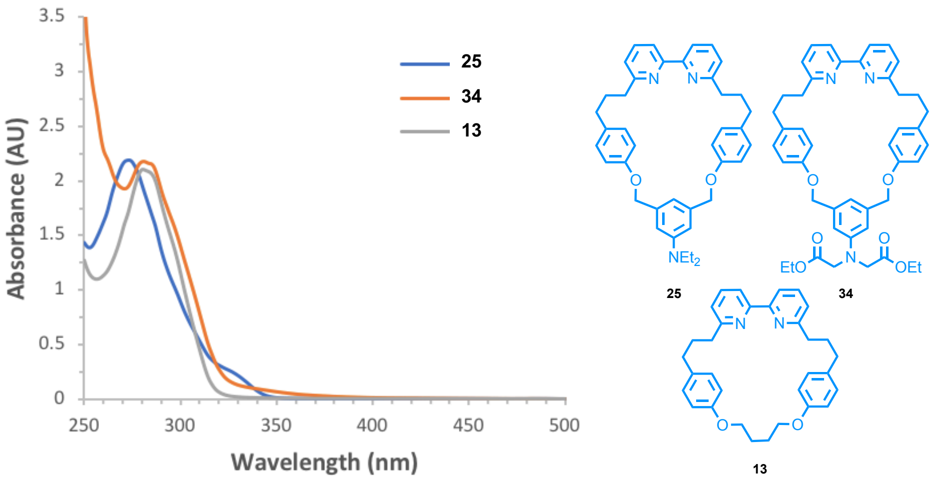

Figure **31**. UV-Vis absorption spectra (5 x 10^{-5} M in $CHCl_3$) of photocleavable macrocycles **25** and **34** alongside macrocycle **13** containing no photocleavable group.

DEABn groups are reported to have absorption bands in the upper UVB region (λ_{max}~310 nm), which agrees with the data obtained from the UV-Vis spectra of macrocycle **25** and **34**, showing broad absorptions at ~320 nm, which are of low intensity relative to bipyridine absorptions at ~280 nm.[118] Lacking the photoactive unit, macrocycle **13** shows no such absorbance at ~320 nm.

2.2.4. Photolysis of Macrocycle 25

The photolytic degradation pathway of the DEABn group is based on the excited state *meta* effect.[125] π-π* excitation increases electron density at *meta* benzylic positions to facilitate heterolytic C-O bond cleavage, releasing the alcohol and generating a benzylic carbocation intermediate which is rapidly quenched *via* reaction with the nucleophilic solvent.[126] As the chromophore of the DEABn group remains intact after the first cleavage, macrocycle **25** should theoretically cleave sequentially at both *meta* benzylic positions. If so, a mixture of products is possible upon quenching the carbocation intermediate with the nucleophilic solvent, which in this case is H_2O or CH_3CN. An attack by H_2O should afford the corresponding alcohol product, whereas an attack by CH_3CN should generate an isocyanate intermediate that will become rapidly hydrolysed to form the acetamide (Scheme **9**).

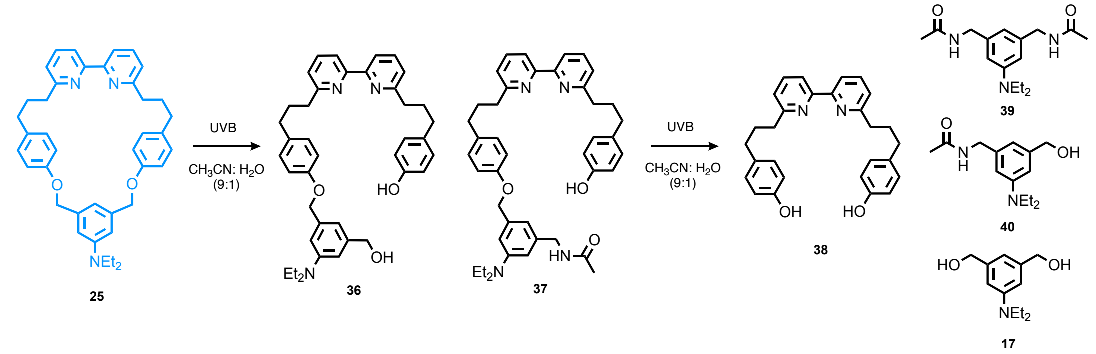

Scheme **9.** Photolysis of macrocycle **25** showing expected decomposition products.

The photolysis of macrocycle **25** was performed in deuterated solvents so that the outcome could be immediately analysed *via* ^{1}H NMR, avoiding the need to concentrate samples *in vacuo*, which could potentially obscure the outcome of photodecomposition. Samples of macrocycle **25** (5.0 mM in CD_3CN: D_2O 9:1) were irradiated for differing amounts of time with a narrowband UVB lamp (2 x 9W, λ_{em} = 305-315 nm) without deaeration, then analysed *via* ^{1}H NMR (Figure **32**).

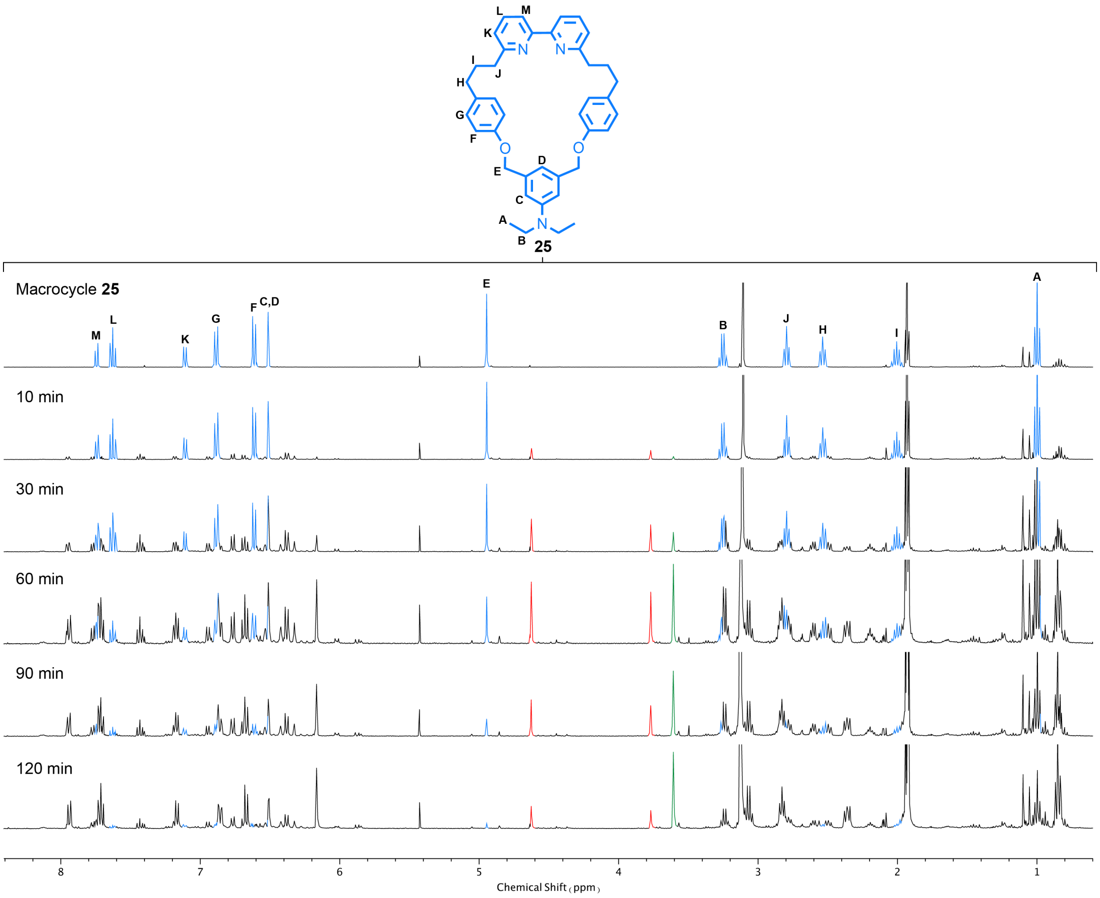

Figure **32**. ^{1}H NMR ($CD_3CN:D_2O$ (9:1), 400 MHz) stack plot (δ range = 8.4-0.6 ppm) showing the photodecomposition of macrocycle **25** over time. Assigned macrocycle **25** signals are shown in blue. Benzylic positions of photodecomposition intermediate (red, δ_H = 4.63 & 3.77 ppm) and final photodecomposition product (green, δ_H = 3.61 ppm) are shown.

^{1}H NMR analysis shows that macrocycle **25** cleaves efficiently in response to UVB light, with only trace amounts remaining after 120 min of irradiation. Performing the reaction in deuterated versus non-deuterated solvents had no apparent influence on the efficiency of the photolysis reaction or composition of the resulting mixtures. Multi-dimensional NMR analysis was used to identify the corresponding benzylic signals in the photodecomposition products. By tracking the change in the benzylic proton signals (4.95-3.61 ppm), it can be inferred that photolysis of **25** generates an intermediate species where the symmetry of the macrocycle is broken (red), and one of the resulting benzylic signals is significantly shielded (δ_H = 3.77 ppm), which is indicative of cleaving one of the benzylic C-O bonds. Extended photolysis results in consumption of this intermediate and formation of a second species (green) where the symmetry of the macrocycle is restored, with the benzylic signal again shifting further upfield (δ_H = 3.61 ppm). While the observed benzylic signals could account for the selective formation of expected intermediates **36** or **37**, followed by a symmetrical final decomposition product **17** or **39**, the chemical shift values are much lower than would be expected for a benzylic alcohol (~4.6 ppm) or acetamide (~4.3 ppm), bringing ambiguity to the actual structure of the decomposition products.

In an attempt to confirm whether the expected bis-phenol product was produced after extended photolysis, **38** was synthesised in two steps from **22** (Scheme **10**) and its ^{1}H NMR spectrum was compared with data obtained from the photolysis experiments. Surprisingly, **38** was not observed at any point during the photolysis experiment.

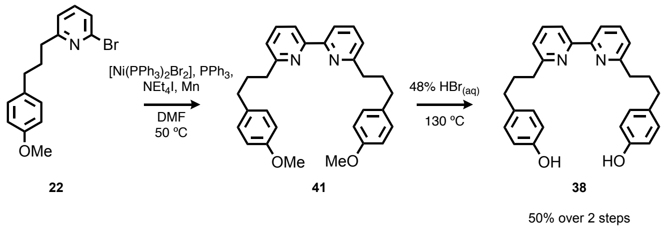

Scheme **10**. Synthesis of the expected bis-phenol decomposition product **38**.

Compound **17**, a symmetrical building block used in the synthesis of macrocycle **25**, which could have been a potential by-product of the bottom fragment, was also not observed. LC-MS analysis of crude photolysis mixtures revealed that both unknown species identified in the ^{1}H NMR had $[M+H]^+$ = 598.5 m/z, possessing the same mass and isotopic pattern as macrocycle **25**, suggesting that an intramolecular rearrangement was favoured over the expected cleavage pathway. Rearranged macrocycles **42** and **43** were later isolated from the combined photolysis mixtures *via* silica-gel chromatography (Figure **33**).

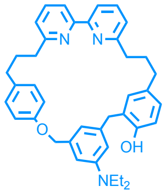

42

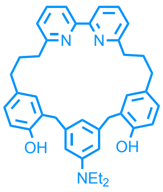

43

Figure **33.** Structure of photolysis products **42** and **43**.

The ^{1}H NMR spectra of **42** is shown below, overlaid with that of macrocycle **25** (Figure **34**). The spectrum of intermediate **42** clearly shows that the mirror symmetry of the macrocycle has been broken, with all previously equivalent proton environments within the macrocyclic backbone now splitting into chemically distinct signals. The three aromatic protons of the DEABn motif, which previously overlapped at 6.50 ppm, have now split into three distinct signals, suggesting that de-symmetrisation occurred close to this unit. The integration of the characteristic doublet of doublets from the *para*-disubstituted phenyl ring has also decreased by half, with three new signals observed in lieu (*). The splitting pattern and coupling constants of the new signals are congruent with a 1,2,4-substituted phenyl ring. The combined NMR and HR-MS data are consistent with structure **42**.

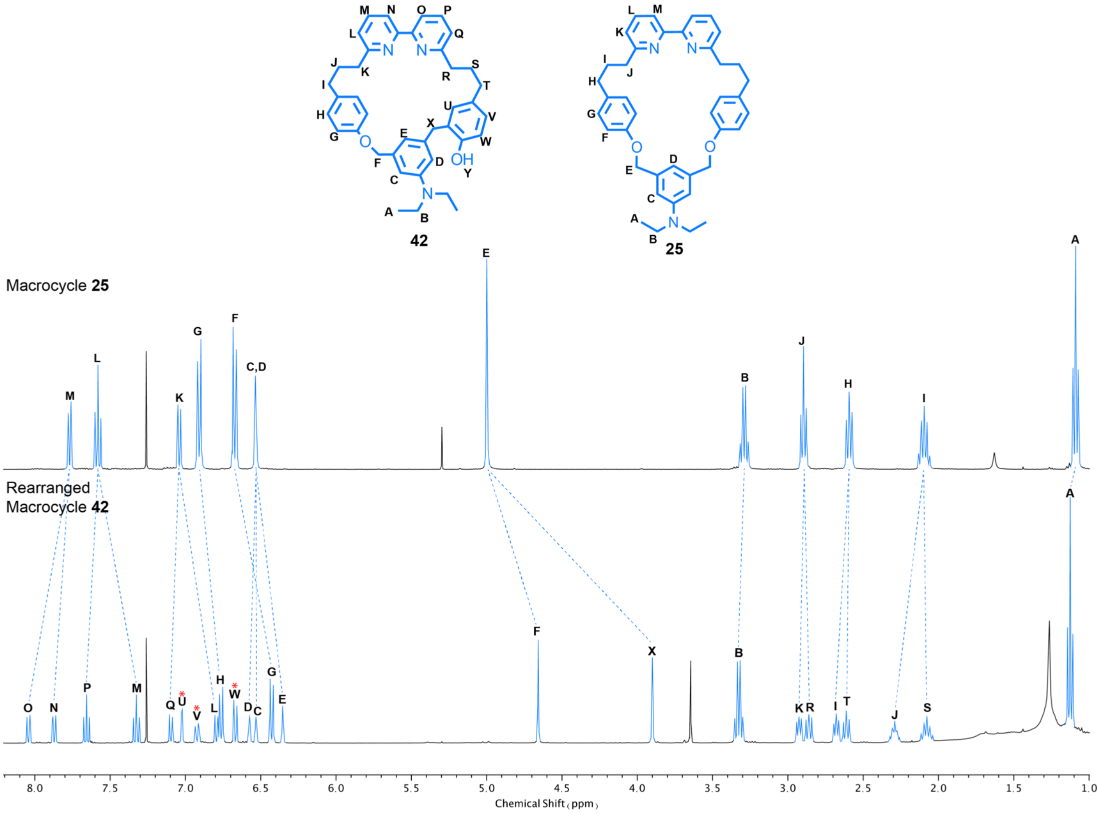

Figure **34**. Assigned ^{1}H NMR ($CDCl_3$, 400 MHz) of macrocycle **25** overlaid with rearranged macrocycle **42** (δ range = 8.2-1.0 ppm). Dashed lines = de-symmetrised signals, asterisk (*) = new signals with different multiplicity.

A more polar product that displayed poor solubility in $CDCl_3$ and CD_3OD was also isolated. ^{1}H NMR data in DMSO-d_6 shows that the mirror symmetry of the macrocycle has been restored. The characteristic *para*-disubstituted phenyl ring signals in the ^{1}H NMR spectrum of **25** and **42** are also absent here (Figure **35**). Combined with HR-MS, the data is consistent with structure **43**.

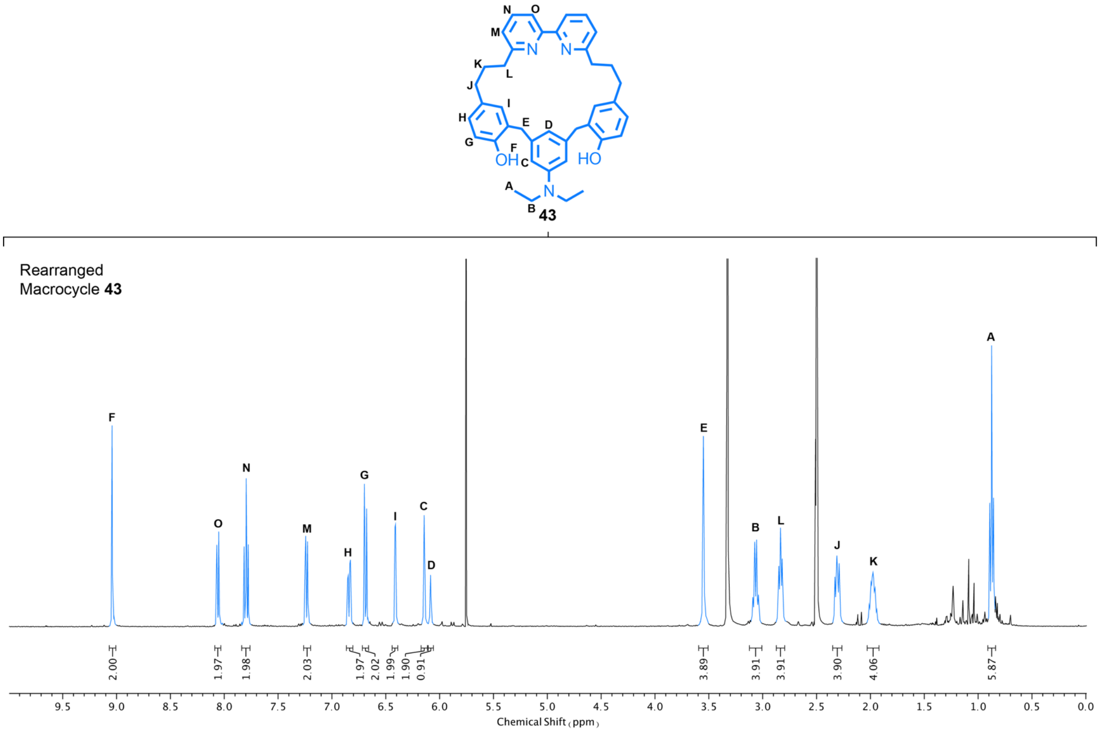

Figure **35.** Assigned ^{1}H NMR (DMSO-d_6, 400 MHz) of rearranged macrocycle **43** (δ range = 10.0-0.0 ppm).

Single crystals obtained from the slow evaporation of a saturated solution of **43** in MeOD were analysed *via* XRD and confirmed the structure (Figure **36**).[2] Two consecutive photo-induced ring contractions have reduced the number of atoms in the macrocyclic backbone from 27 (**25**) to 23 (**43**), which has significant implications for the solid-state behaviour of the macrocycle. The reduced ring size combined with the change from *para* to *meta* substation at the site of rearrangement results in **43** adopting a conformation in which the DEABn unit lies nearly parallel to the plane of the macrocycle, blocking one of its faces. The folded conformation is much more pronounced relative to the metal-bound structure of **25** (Figure **30**) and likely arises from the need to minimise angle strain at the benzylic positions.

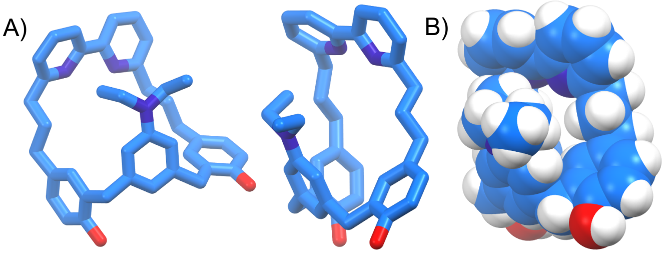

Figure **36**. A) Solid-state structure of rearranged macrocycle **43** displayed in partial stick representations. Hydrogen atoms omitted for clarity. B) Space-filling representation. Colours: H = white, C = blue, N = dark b, O = red. Thermal ellipsoids drawn at 50% probability.

---

[2] Crystal structure of **43** was solved by Therapoom Boonprab.

Analysis of the solid-state structure of **43** brings into question the mechanism of its formation. If the mechanism proceeds *via* heterolytic cleavage of the C-O bond, as has been reported in the literature, then a zwitterionic pair will be created that does not become quenched *via* reaction with the nucleophilic solvent (Scheme **11**).

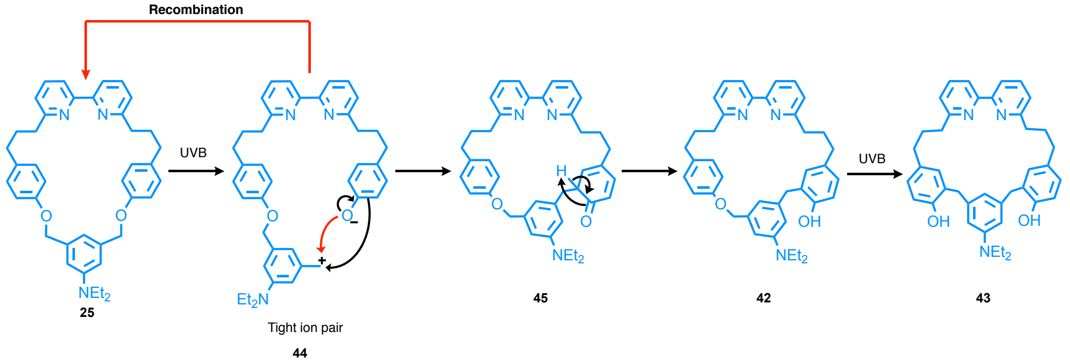

Scheme **11**. A plausible mechanism for the formation of rearranged macrocycles **42** and **43**.

The formation of a tight ion pair has previously been proposed to rationalise the recombination of photolytically-released guests from coumarin-based PPGs. Although this has not yet been reported with DEABn PPGs, it could account for the lack of expected solvolysis products in this case.[27,127] In the absence of adventitious solvent molecules, two plausible mechanisms are proposed. The most obvious is direct intramolecular recombination of the charge-separated species (**44**), resulting in the re-formation of the photolabile benzylic C-O bond, which can then undergo photocleavage again. The other is an intramolecular electrophilic aromatic substitution between the phenolate and benzyl carbocation. This pathway would result in the formation of a photochemically stable C-C bond (**45**), which then undergoes tautomerization to restore aromaticity. Wang *et al*. have observed a similar intermolecular photochemical C-C bond formation with DEABn-caged tyrosine, albeit to a lesser extent (Scheme **12**).[122]

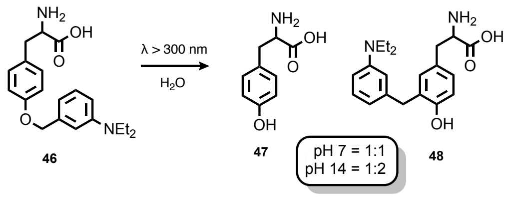

Scheme **12**. The photochemical C-C bond formation of DEABn-caged Tyrosine observed by Wang *et al*.[122]

Given the highly selective formation of rearranged macrocycles **42** and **43**, diffusion of charged intermediate **44** out of the solvent cage is likely much slower than either of the suggested mechanisms. However, if our proposed mechanism is correct, then acyclic intermediate **44** must re-cyclise, a process that would be highly unfavourable due to the strong propensity of the 2,2'-bipyridine motif to adopt a *trans*-conformation.[128] This is especially problematic when considering the small ring-size and folded conformation adopted to minimise angle strain in the solid-state structure of **43** (Figure **36**), assuming that the first and second rearrangements proceed *via* the same pathway. As sequential ring-opening and closing should be highly unfavourable, another suggestion could be that the mechanism is concerted, albeit by an unidentified pathway, and that the macrocycle does not open at all — meaning it would be incapable of releasing mechanically bonded sub-components.

Performing the photolysis experiments in solvent mixtures with a larger aqueous component was expected to enhance the rate of photocleavage and perhaps even lead to the formation of expected solvolytic decomposition products by introducing more H_2O nucleophiles to compete with the intramolecular rearrangement pathway. However, due to the poor aqueous solubility of **25**, photocleavage experiments in >10% D_2O/ CD_3CN could not be performed. Going to the other extreme, the rate of photolysis was significantly slower in CD_3CN relative to CD_3CN: D_2O (9:1) (Figure **37**). After irradiation for 120 min in CD_3CN, 23% of macrocycle **25** remained relative to rearranged macrocycles **42** (55%) and **43** (22%). Whereas in CD_3CN: D_2O (9:1), less than 3% of **25** remained relative to **42** (32%) and **43** (64%). The introduction of an internal ^{1}H NMR standard (1,1,2,2-tetrachloroethane) to the crude photolytic mixtures indicated that signals from **25**, **42** and **43** accounted for 95% and 93% of total expected macrocyclic signals in CD_3CN or CD_3CN: D_2O (9:1) respectively, indicating that the rearrangement pathway was highly favoured in both solvent systems.

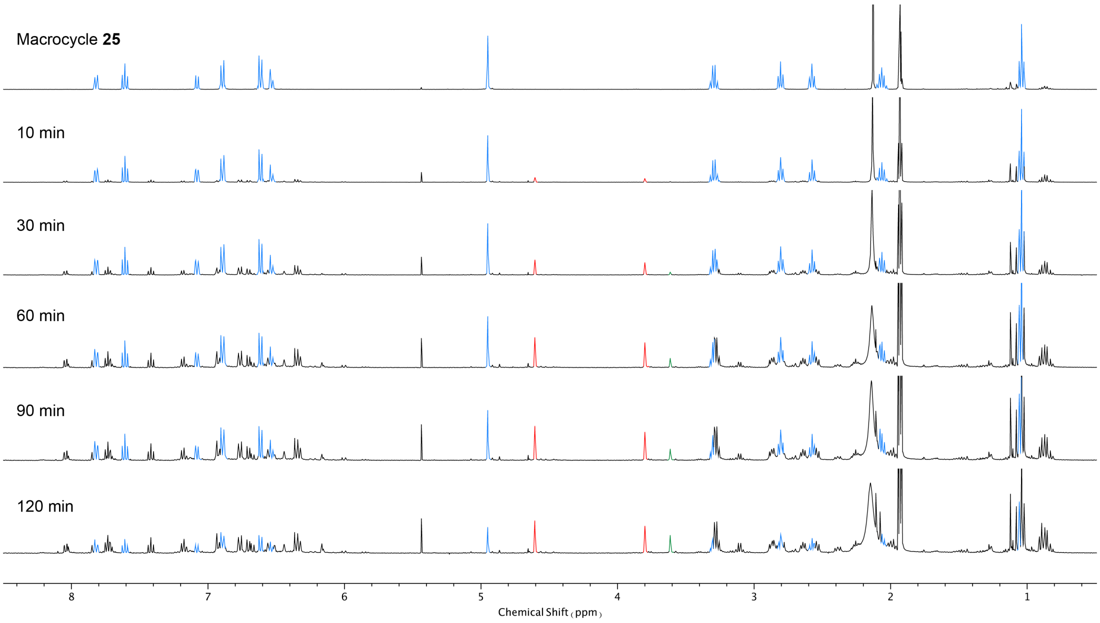

Figure **37**. ^{1}H NMR (CD_3CN, 400 MHz) stack plot showing the photodecomposition of macrocycle **25** over time (δ range = 8.5-0.5 ppm). Macrocycle **25** signals are shown in blue. Benzylic positions of photodecomposition intermediate **42** (red, δ_H = 4.61 & 3.80 ppm) and final photodecomposition product **43** (green, δ_H = 3.61 ppm) are highlighted.

2.2.5. Photolysis of Macrocycle 35

Dicarboxylic acid macrocycle **35** displayed similar behaviour when irradiated with UVB light in CD_3CN: D_2O (9:1) (Scheme **13**). However, due to the poor solubility of decomposition products in the deuterated medium, the photolysis mixtures had to be concentrated *in vacuo* and then re-dissolved in DMSO-d$_6$ to be analysed *via* ^{1}H NMR. As **35** displayed reasonable aqueous solubility, photolysis experiments could also be performed in pure water.

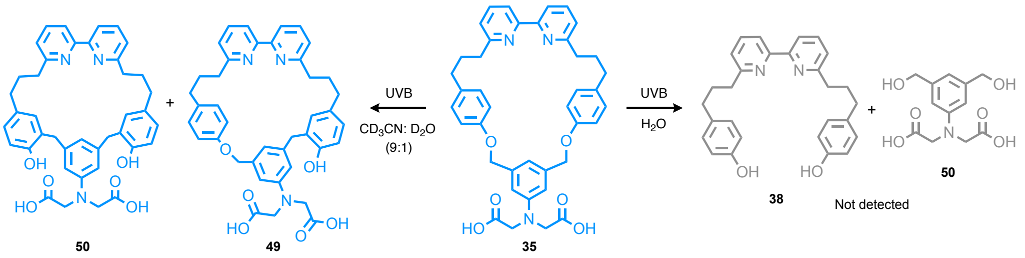

Scheme **13**. Photolysis of macrocycle **35** in CH_3CN: H_2O (9:1) or H_2O.

After 60 minutes of UVB irradiation, the composition of the two mixtures differed considerably, which suggests contrasting photocleavage/ solvolytic pathways (Figure **38**). Significant amounts of **35** were present in both mixtures, alongside the formation of a sharp peak at ~7.75 ppm, which may be indicative of phenol formation. However, this species did not correspond to the expected bis-phenol decomposition product (**38**) in either case. Due to the poor solubility of the decomposition products in organic solvents, attempts to isolate the by-products *via* silica-gel chromatography were unsuccessful.

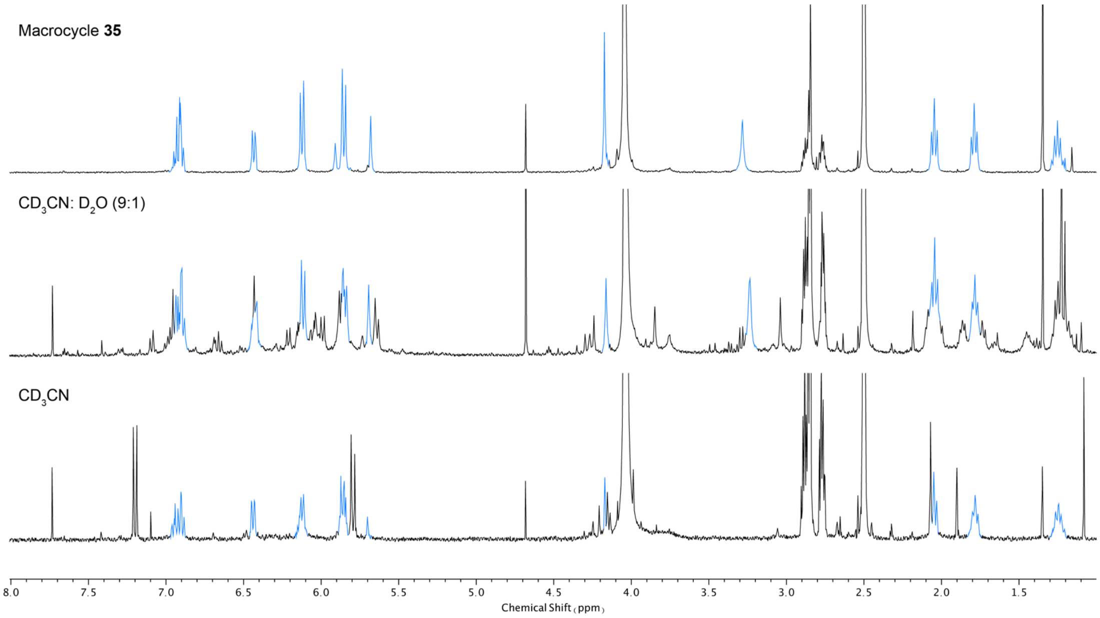

Figure **38**. ^{1}H NMR (DMSO-d$_6$, 400 MHz) spectra of macrocycle **35** and product mixtures after photolysis for 60 min in CD_3CN:D_2O (9:1) and D_2O (δ range = 8.0-1.0 ppm).

LC-MS analysis of the photolysis experiment in CD_3CN: D_2O (9:1) showed the formation of two species with the same m/z value and isotopic pattern as macrocycle **35** but with greater polarity, suggesting that sequential photoinduced rearrangement is also favoured by macrocycle **35** (Figure **39**). The assumed rearrangement products, **49** and **50**, were not isolated. No other species with the same m/z value as **35** were observed when the experiment was performed in D_2O. Numerous other species with longer retention times than were observed, suggesting the decomposition products are less polar. However, the m/z values for these species could not be correlated to any of the expected decomposition products, such as **38** or **50**. This suggests that, although macrocycle **35** is being consumed, it is uncertain whether a ring-opening mechanism occurs in pure D_2O.

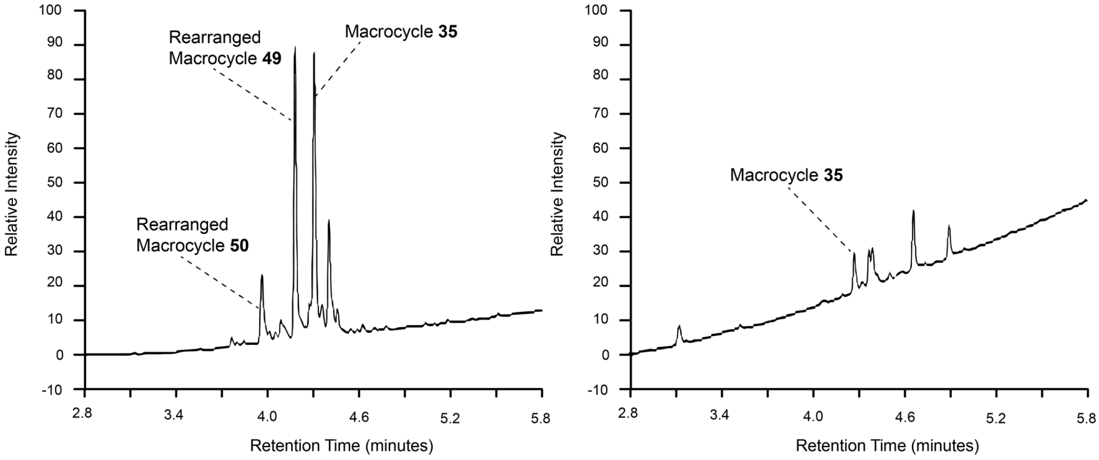

Figure **39**. LC-MS UV trace of photolysis reactions in CD_3CN:D_2O (9:1) (left) and D_2O (right).

2.2.6. Synthesis of Rotaxanes **53** and **54**

The ambiguity in rationalising the photolytic cleavage mechanisms from macrocycles **25** and **35** raised the question of whether they will be able to release mechanically bonded sub-components. To determine this, photocleavable rotaxane **53** was synthesised in 75% from the AT-CuAAC reaction of macrocycle **25**, azide **52** and alkyne **51** (Scheme **14**). ^{1}H NMR analysis of the crude reaction mixture indicated that **25** mediated the AT-CuAAC reaction with high efficiency, with <10% axle (**55**) formation when used with equimolar amounts of half-axles **51** and **52**. Rotaxane **54** was similarly synthesised in 73% yield from the structurally analogous macrocycle **13**, which possessed a non-photolabile butyl chain in place of the DEABn group, and was used as a negative control in the photolysis experiments.

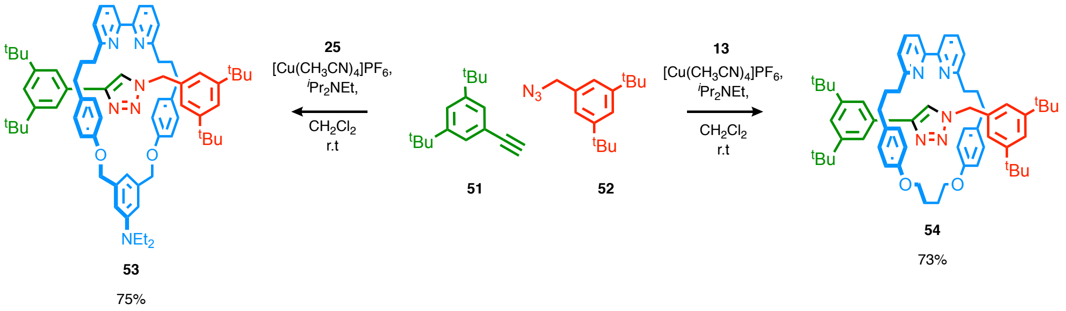

Scheme **14**. AT-CuAAC synthesis of rotaxanes **53** and **54**.

Several signals in the ^{1}H NMR spectrum of rotaxane **53** are shifted relative to their non-interlocked counterparts **25** and **55**, giving insight into the chemical environment of the mechanical bond (Figure **40**). The significant downfield shift of the triazole signal (*), from 7.69 to 9.48 ppm, indicates strong hydrogen bonding interaction to the bipyridine unit and is characteristic of a tight mechanical bond cavity. Significant shielding of the benzylic axle protons (*) would suggest they are orientated toward the steric bulk of the macrocycle. The facial symmetry of the macrocyclic component has also been broken, as shown by the splitting of previously equivalent aliphatic signals (*). Overall, these observations signify a rigid, well-defined mechanical bond.

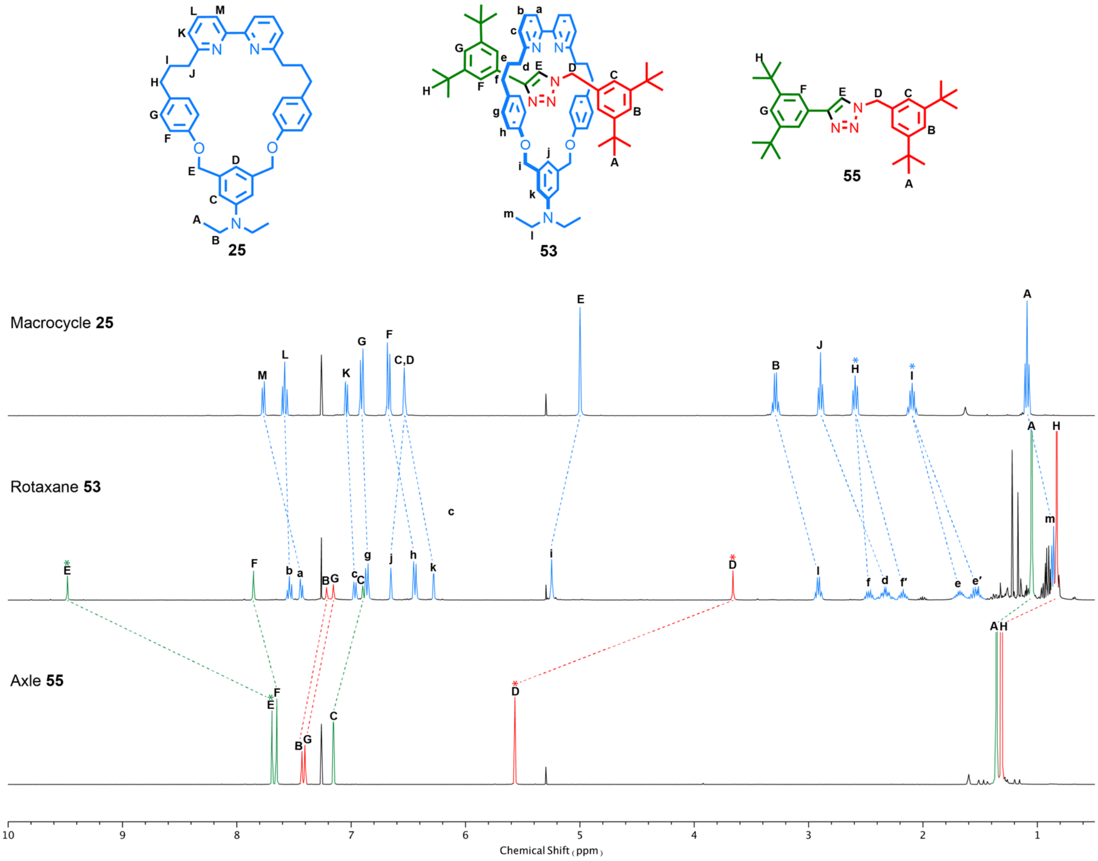

Figure **40**. Assigned ^{1}H NMR stack plot ($CDCl_3$, 400 MHz) of macrocycle **25**, rotaxane **53** and axle **55**. Proton signals of each sub-component have been colour-coded and chemical shift changes upon interlocking are shown.

2.2.7. Photolysis of Rotaxanes 53 and 54

Samples of rotaxane **53** (5.0 mM in CD_3CN: H_2O (9:1)) were irradiated with a narrowband UVB lamp for a given time, concentrated *in vacuo,* re-dissolved in $CDCl_3$ and then analysed *via* ^{1}H NMR (Scheme **15**).

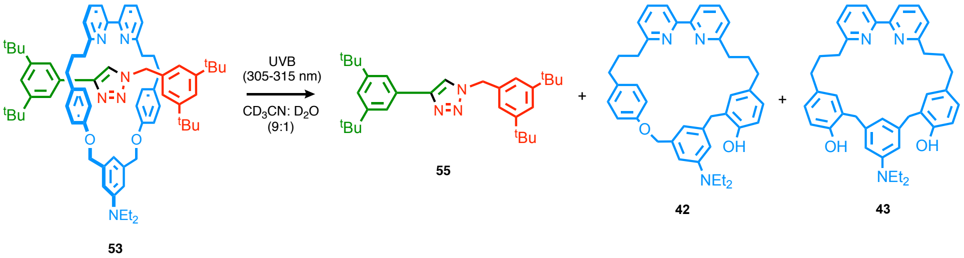

Scheme **15**. Release of axle **55** from rotaxane **53** upon UVB photolysis.

^{1}H NMR analysis indicated that axle **55** was successfully liberated from rotaxane **53** upon irradiation with UVB light (Figure **41**). Moreover, photolysis of the DEABn group appeared to be accelerated in the presence of the mechanical bond, as >95% of axle **55** had been released within 30 minutes, relative to only 52% consumption of non-interlocked macrocycle **25** under the same conditions. Assuming quantitative release from rotaxane **53**, axle **55** can be used as an internal ^{1}H standard to calculate the relative conversion to the photolysis products. The photolysis of rotaxane **55** appears to follow the same highly selective rearrangement pathway as macrocycle **25**, with near-full conversion to macrocycles **42** (55%) and **43** (42%) observed.

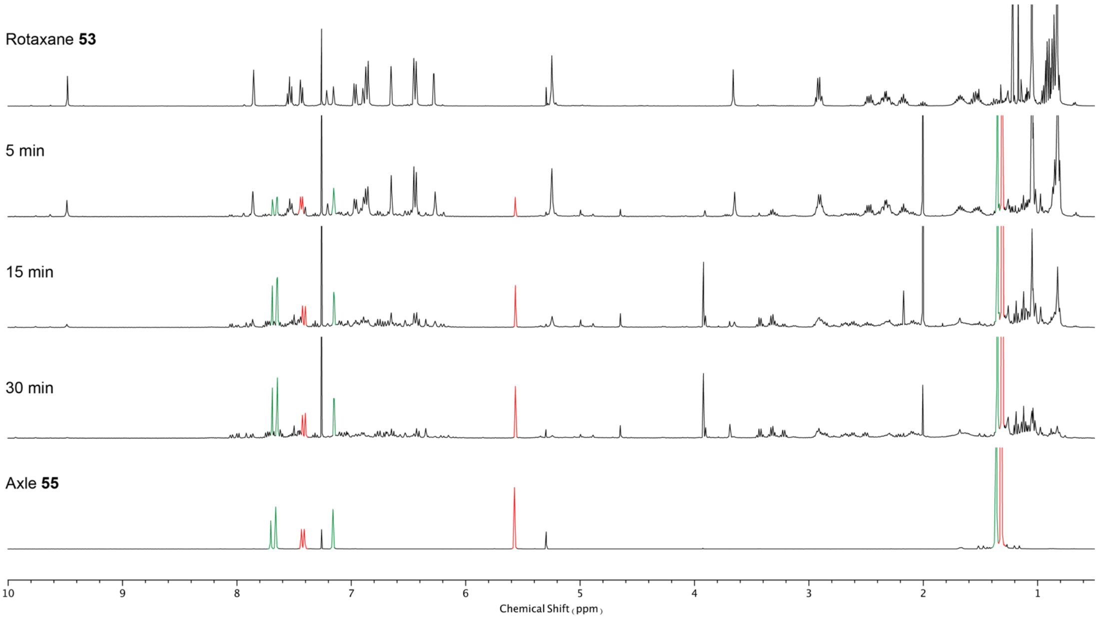

Figure **41**. ^{1}H NMR ($CDCl_3$, 400 MHz) stack plot showing release of axle **55** from rotaxane **53** upon UVB photolysis (δ range = 10.0-0.5 ppm).

To confirm that axle **55** was released due to cleavage of the DEABn unit and not some other process, such as ring slippage, a control experiment was set up under identical conditions with non-photolabile rotaxane **54** (Scheme **16**). Even after extended periods of photolysis (180 min), the release of axle **55** was not detected.

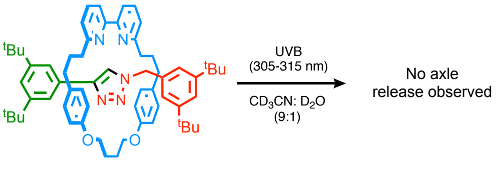

54

Scheme **16**. Photolysis of non-photolabile rotaxane **54**.

The formation of rearranged macrocycle **42** from the photolysis of rotaxane **53** provides evidence that the photo-rearrangement mechanism is not concerted (assuming an identical mechanism in interlocked vs non-interlocked substrates), as this pathway could not account for the release of axle **55**. The high degree of selectivity for re-cyclisation over polymerisation combined with the further absence of expected decomposition products would also suggest that the intramolecular rearrangement occurs after the release of axle **55**, most likely in a solvent-caged manner where adventitious nucleophiles are excluded. It would also suggest that intramolecular electrostatic interactions in the acyclic solvent-caged intermediate override the propensity of the bipyridine unit to adopt the *trans* conformation, pre-organising the molecule into a conformation where re-cyclisation is favourable.

The accelerated photocleavage of the DEABn group in the presence of the mechanical bond is an interesting observation. Förster Resonance Energy Transfer (FRET) between adjacent mechanical components in rotaxane architectures has previously been used to generate fluorescent probes for a variety of sensing/ imaging applications.[129,130] Provided there is sufficient overlap between the emission spectrum of the donor (axle) and the absorption spectrum of the acceptor (PPG), it is plausible that such an energy transfer process could also lead to enhanced excitation of DEABn and result in faster photocleavage. However, given the poor expected overlap between the DEABn chromophore (λ_{abs} ~315 nm) and di-*tert*-butyl-based axle ($\lambda_{em} < 270$ nm), no such process would be expected in this case.

The enhancement may instead be due to the reduced conformational freedom of the macrocyclic component when interlocked, as evidenced in the ^{1}H NMR spectrum of rotaxane **53** (Figure **40**). The rigid mechanical bond could either force the macrocycle (specifically the DEABn unit) into a conformation where heterolytic C-O cleavage is more favourable upon excitation or by preventing the adoption of unfavourable conformations that would hinder photolysis. In such a case, increasing the length of the linker within the stoppers would likely allow the macrocyclic component to be more dynamic and move around the axle, essentially expanding the conformational space. In contrast, the need to minimise steric repulsion between the macrocycle and bulky stopper units would be exacerbated when using shorter stoppers, severely limiting conformation mobility.

2.2.8. Synthesis of Rotaxanes **60**, **61** and **62**

To investigate the effect of conformational rigidity on the rate of photocleavage, a series of photocleavable rotaxanes were synthesised *via* AT-CuAAC coupling of macrocycle **25** with various di-*tert*-butyl-based stoppers in yields of 52-67% (Figure **42**).

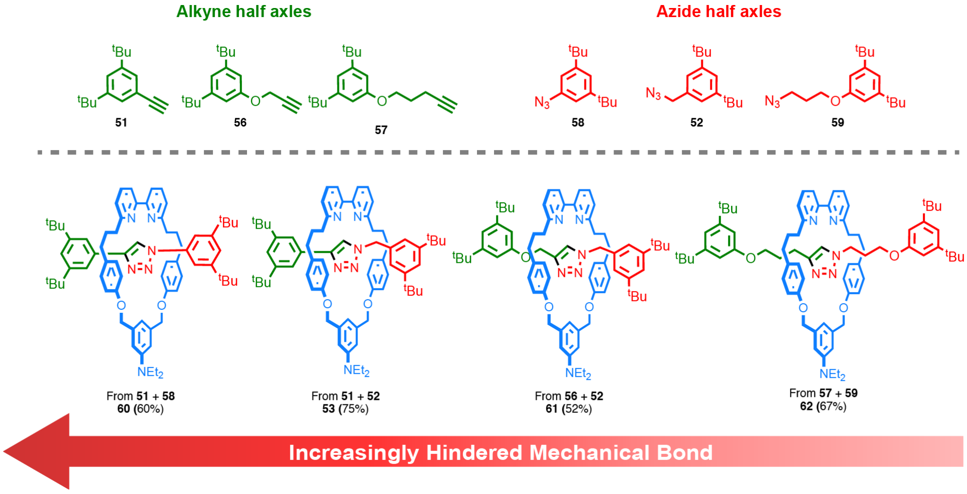

Figure **42**. Synthesis of rotaxanes **60, 61 and 62** with varying degrees of steric hindrance around the mechanical bond.

^{1}H NMR analysis suggests that the shortest stoppers (**51** + **58**) produce the rotaxane (**60**) with the tightest mechanical bond, highlighted by the inequivalence at key benzylic positions and a greatly deshielded C-triazole (10.35 ppm) chemical shift relative to rotaxane **53** (9.48 ppm (Figure **43**). The shift of corresponding triazole signals decreases in a linear fashion moving to less hindered rotaxanes **61** (7.75 ppm) and **62** (6.90 ppm), indicating that hydrogen bonding to the bipyridine unit of macrocycle **25** is weaker as a result of greater conformational flexibility. Weakening hydrogen bonding interactions between *ortho* DEABn proton and the N-triazole motif are also indicative of a less rigid mechanical bond.

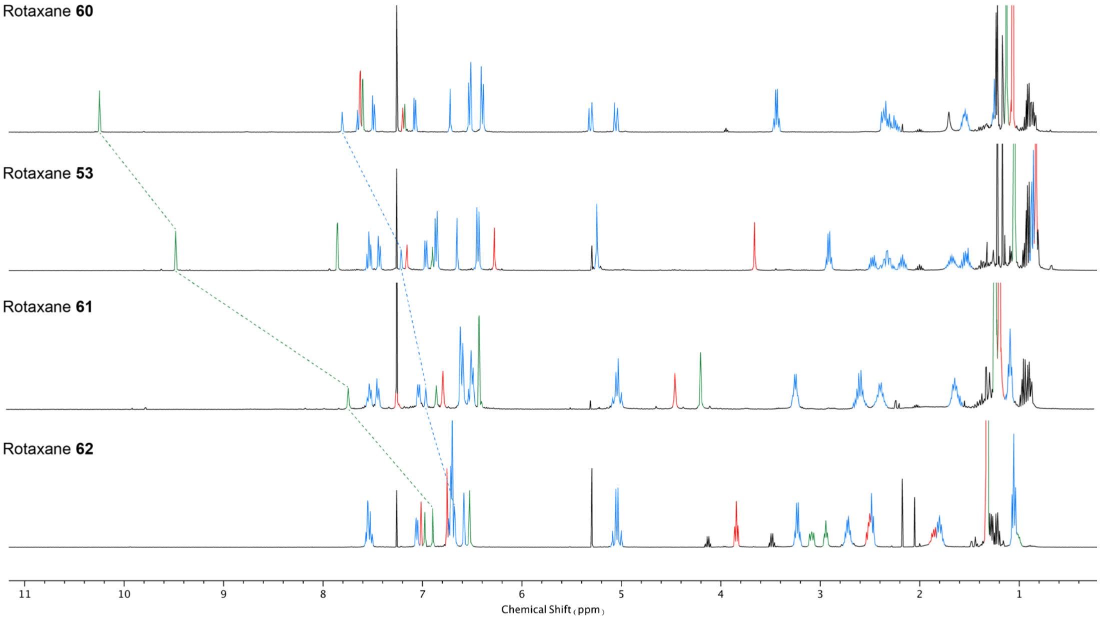

Figure **43**. ^{1}H NMR ($CDCl_3$, 400 MHz) stack plot of rotaxanes **60, 53**, **61** and **62** (δ range = 11.1-0.2 ppm).

2.2.9. Photolysis of Rotaxanes **60**, **61** and **62**

Rotaxanes **60**, **61** and **62** were irradiated under the same conditions as rotaxane **53** using a narrowband UVB lamp. The extent of photocleavage after 30 min was determined by the amount of starting rotaxane remaining relative to the corresponding axle released (or rearranged products with macrocycle **25**) *via* ^{1}H NMR (Figure **44**).

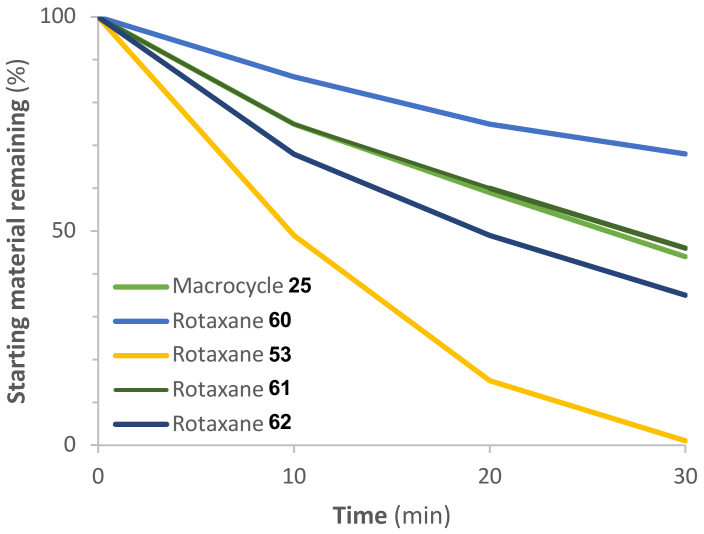

Figure **44**. Consumption of rotaxane/macrocycle when irradiated with UVB light over 30 min. Determined *via* ^{1}H NMR analysis.

Although highly selective conversion (>90%) to rearranged macrocycles **42** and **43** was observed in all cases, the rate of axle release from the corresponding rotaxanes structures (**53**, **60**, **61** and **62**) differed considerably and had no direct causal relationship with the conformational flexibility of the mechanical bond. The most conformationally flexible rotaxane (**62**) showed only marginal improvements in photocleavability relative to non-interlocked macrocycle **25**. However, release from rotaxane slightly more hindered rotaxane **61** gave no such improvement. Surprisingly, the rate of release from the most the rigid rotaxane (**60**) was considerably slower than all others, including non-interlocked macrocycle **25**, with 68% remaining after 30 min. In contrast, previously studied rotaxane **53**, which differs from **60** by only a single methylene unit (-CH_2-), possessed the fastest axle release ability by far, with <3% remaining after 30 minutes.

Given the drastic variability observed in the rate of photocleavage using several different *tert*-butyl-based stoppers, it is reasonable to assume that FRET processes do not account for the observed trends. However, it is also clear that the relationship between the rate of photocleavage and conformational rigidity of the rotaxane structure is not linear. Seemingly small changes in the environment of the mechanical bond appear to have a significant effect, meaning that the rate of photocleavage will be highly dependent on the precise structure of the rotaxane.

2.2.10. Synthesis of Dinucleotide Rotaxanes 70 and 71

To determine if macrocycle **25** was suitable for the synthesis of oligonucleotide rotaxanes, it was first incorporated into a simplified model of the chain termini used in the click DNA-ligation process. 5'-azido-modified thymidine **66** was synthesized in three steps from thymidine **63** according to literature procedure (Scheme **17**).[112]

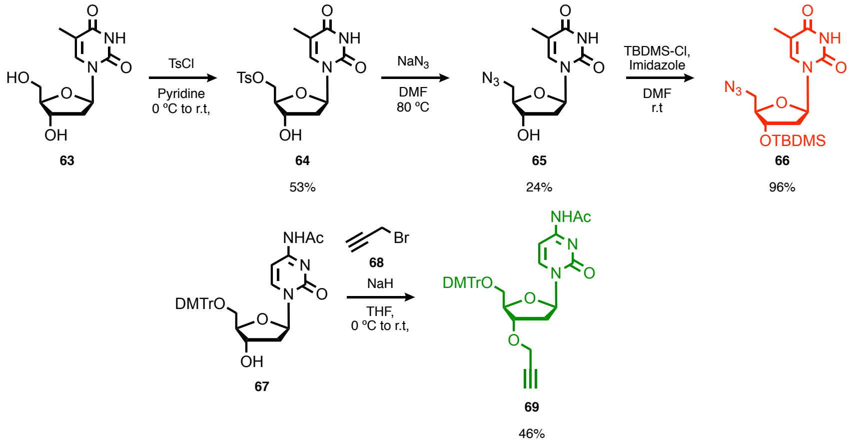

Scheme **17**. Synthesis of 5'-azido-modified thymidine **66** and 3'-propargyl-modified cytidine **69**.

Tosylation of **63** proceeded with reasonable regioselectivity for the 5'-position to afford **64**, which then underwent nucleophilic substitution with NaN_3 to yield **65** in 24% yield. Silylation of **66** with TBDMS-Cl afforded **66** in 96% yield. 3'-propargyl-modified cytidine **69** was prepared in reasonable yield from the alkylation of commercially available **67** with **68**. Dinucleotide rotaxane **70** was synthesized in 59% yield *via* the AT-CuAAC coupling of propargyl-modified cytidine **69** and azide-modified thymidine **66** in the presence of macrocycle **25** (Scheme **18**).

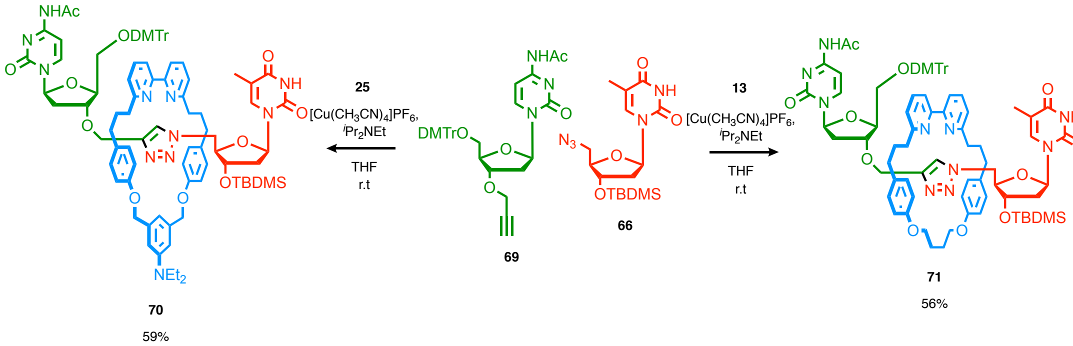

Scheme **18**. AT-CuAAC synthesis of dinucleotide rotaxanes **70** and **71**.

^{1}H NMR analysis of the crude reaction mixture indicated that macrocycle **25** mediated dinucleotide rotaxination with reasonable efficiency. Full consumption of **69** and **66** was observed, alongside the formation of rotaxane **70** (73%) and the corresponding axle (**72**) (27%). A similar ratio of rotaxane (75%) to axle (25%) was observed in the synthesis of non-photolabile dinucleotide rotaxane **71**, which was successfully isolated in a 56% yield. Alongside the characteristic shift of the triazole signal in the ^{1}H NMR of **70** (Figure **45**), HR-MS analysis also confirmed the formation of the expected interlocked product.

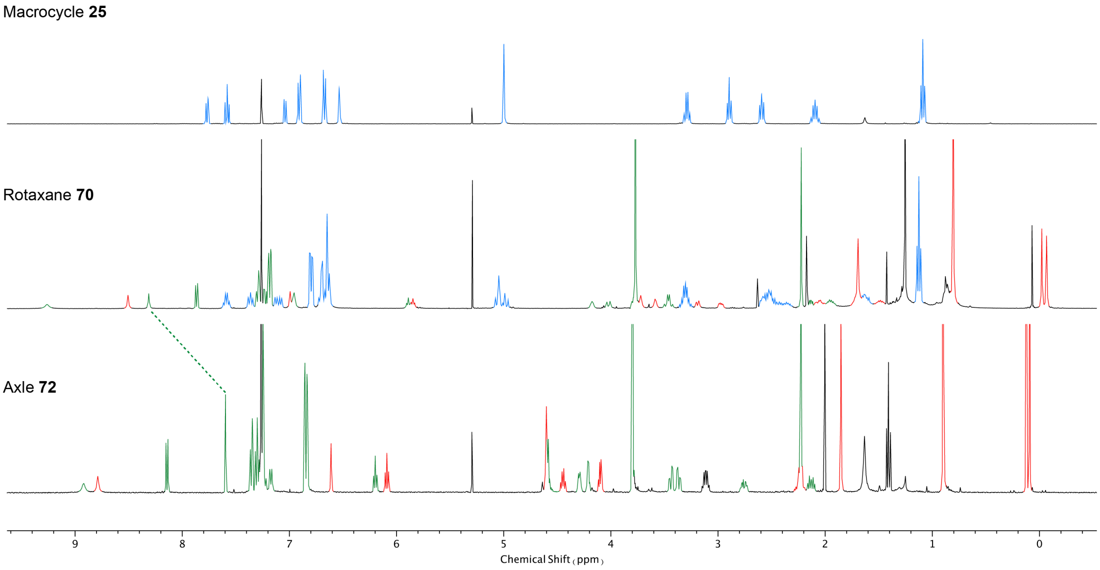

Figure **45**. ^{1}H NMR stack plot ($CDCl_3$, 400 MHz) of macrocycle **25**, rotaxane **70** and axle **72** (δ range = 9.6- -0.5 ppm). Proton signals of each sub component have been colour-coded and chemical shift changes upon interlocking are shown.

2.2.11. Photolysis of Dinucleotide Rotaxanes 70 and 71

The release of axle **72** was observed from dinucleotide rotaxane **70** when subjected to UVB irradiation under the same conditions as previous experiments (5.0 mM, CD_3CN: H_2O (9:1)) (Scheme **19**).

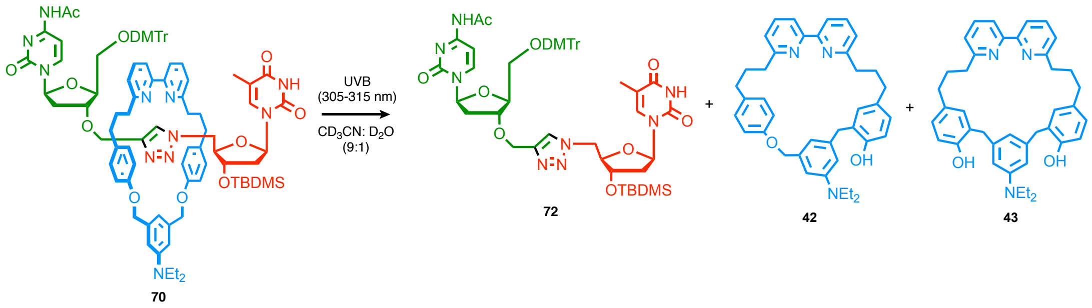

Scheme **19**. Photolysis of dinucleotide rotaxane **70**.

A high selectivity for the formation of rearranged macrocycles **42** and **43** was again observed. However, the rate of axle release was slow from dinucleotide rotaxane **70**. Only 43% of axle had been released after 1 h, and 70% after 3 h (Figure **46**). While this is roughly in line with what would be expected for the poorest photocleavable rotaxane (**60**), which released 32% after 30 min, the presence of other functional units (DMTr) that absorb strongly in the UVB region may elicit a quenching effect that slows photolysis.

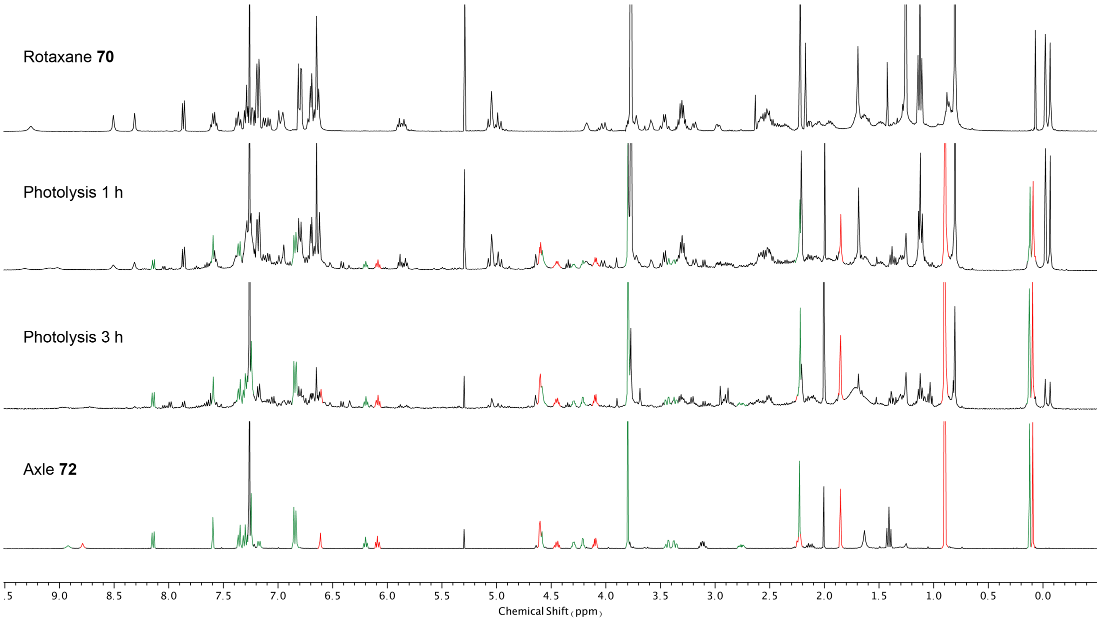

Figure **46**. ^{1}H NMR ($CDCl_3$, 400 MHz) stack plot showing release of axle **72** from rotaxane **70** upon photolysis (δ range = 9.5- -0.5 ppm).

To confirm that axle **72** was released due to cleavage of the macrocyclic component, a control experiment was performed under identical conditions with non-photolabile dinucleotide rotaxane **71** (Figure **47**). No release of axle **72** was detected after 3 h, indicating that no ring-opening was observed in the absence of the DEABn group. Dinucleotide axle **72** was also subjected to the same conditions to confirm that it did not degrade in the presence of UVB light. No decomposition was observed after 3 h, suggesting that the axle release values obtained *via* ^{1}H NMR analysis of the photolysis experiment are valid.

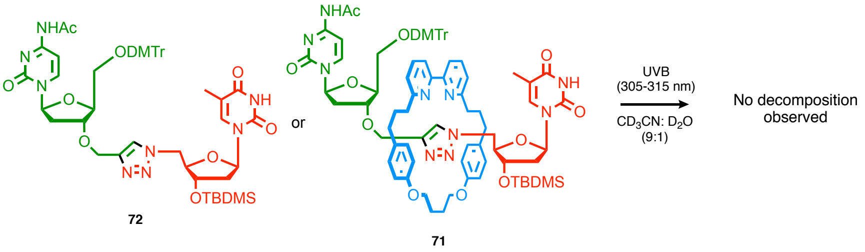

Figure **47**. Photolysis control experiments with dinucleotide rotaxane **71** and axle **72.**

2.2.12. Oligonucleotide Rotaxanes

Overexposure to UV radiation can give rise to mutagenic mechanisms that result in DNA damage. For instance, the cyclodimerization of adjacent pyrimidine bases causes structural deformation and base-pair mismatching, which can result in sequence misreading and inhibition of polymerases.[131] However, studies have shown that short periods of narrowband UVB (305-315 nm) irradiation at low dosages are safe, with the risk of DNA damage being negligible.[132] Having successfully demonstrated the principle of photo-controlled axle release with simple rotaxane models, attention was then focused on oligonucleotide sequences. The 20 base T7 promoter sequence that was previously shown to be silenced by the presence of the mechanical bond was chosen for this proof-of-concept study.

2.2.13. Synthesis of Oligonucleotide T7 Half-Axles **78** and **79**

Thymidine monomer **75** was prepared in two steps according to literature procedure (Scheme **20**).[75] Regioselective iodination of **63** was achieved *via* reaction with methyltriphenoxyphosphonium iodide to afford **73** in 52% yield, which subsequently underwent phosphitylation under standard conditions to give thymidine monomer **75** in 82% yield.

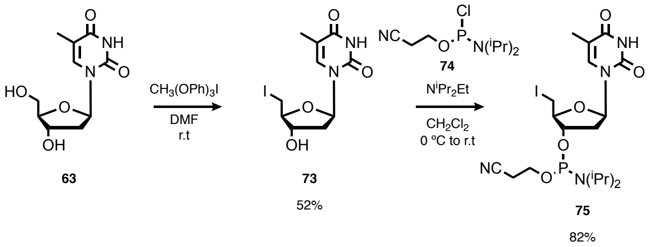

Scheme **20**. Synthesis of iodo-phosphoramidite monomer **75**.

Propargyl modified cytidine **76** was attained in 55% yield from the reaction of **66** with **68**, followed by quenching and simultaneous acetyl group deprotection with MeOH (Scheme **21**).[77] **76** was then loaded onto an amino controlled pore glass (CPG) resin, pre-activated with succinic anhydride, *via* coupling with *N*,*N*'-diisopropylcarbodiimide (DIC) and hydroxybenzotriazole (HOBT). The coupling efficiency was determined to be 33% and was calculated by measuring the absorbance of the cleaved DMTr cation at 495 nm.

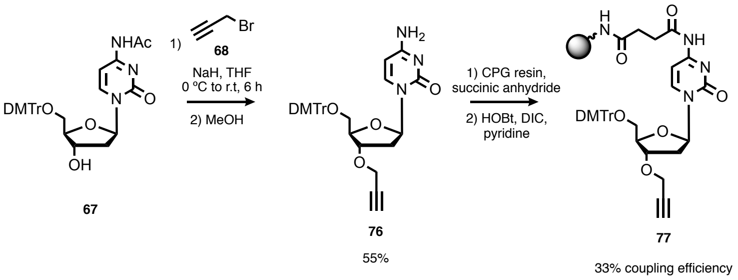

Scheme **21**. Synthesis of **76** and its loading onto CPG resin.

Modified oligonucleotide sequences were synthesized using standard phosphoramidite cycles consisting of acid-catalyzed detritylation, coupling, capping and iodine oxidation (Figure **48**). Oligonucleotides possessing a terminal azide were synthesized up to the penultimate monomer, at which point **75** was incorporated as the final monomer. Conversion of 5'-iodo to the 5'-azide functional group was achieved by treating the resin-bound oligonucleotide with NaN_3. The oligonucleotide was cleaved from the solid support and simultaneously deprotected through exposure to aqueous NH_3 to afford 5'-azido-modified oligonucleotide **79**. 3'-propargyl modified oligonucleotide **78** was assembled from functionalized resin **77**. Once synthesis was complete, deprotection and simultaneous cleavage from the solid support was achieved as described above. Modified T7 half-sequences **78** and **79** were then purified *via* HPLC and characterized *via* LC-MS.

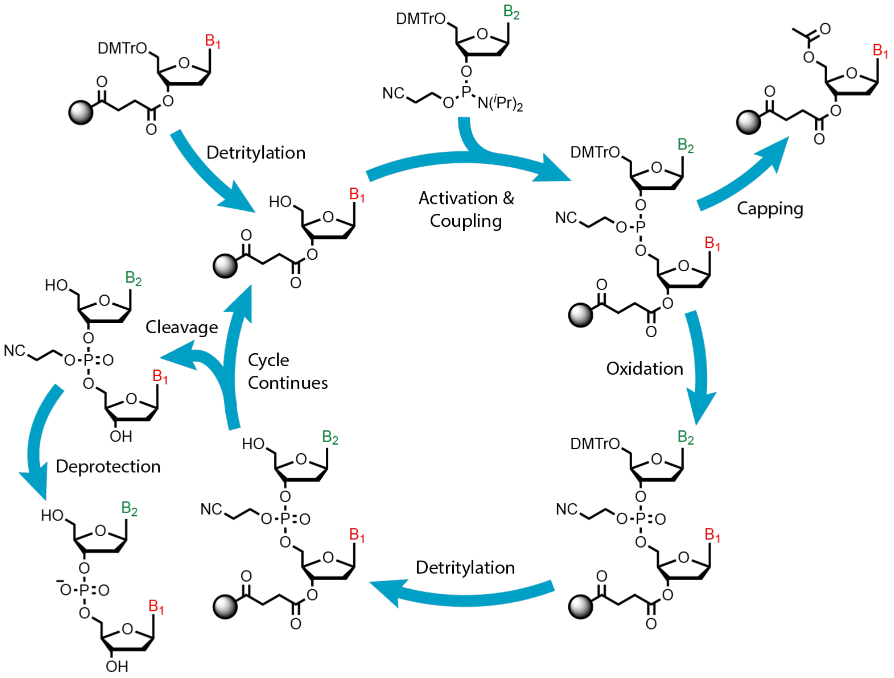

Figure **48**. The standard solid-phase phosphoramidite cycle.

2.2.14. Synthesis of Non-Interlocked T7 Axles

Non-interlocked T7 click axle **80** was first synthesised *via* CuAAC of **78** and **79** using $CuSO_4$ and NaAsc as the water-soluble source of the catalytic Cu^I, along with tris-hydroxypropyltriazolylmethylamine (THPTA) to stabilize Cu^I under aqueous conditions (Scheme **22**). Axle **80** was purified by semi-preparative HPLC, and its purity/identity was confirmed *via* LC-MS analysis (Figure **49**).

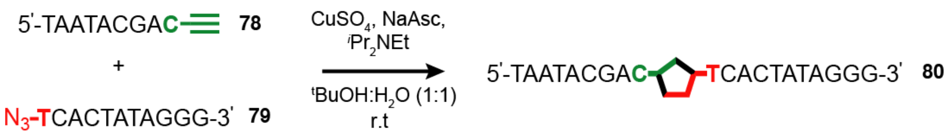

Scheme **22**. Synthesis of T7-click axle **80**. Axle conditions: **78** (1.0 eq.), **79** (1.0 eq.), $CuSO_4.5H_2O$ (39 eq.), NaAsc (250 eq.), THPTA (175 eq.).

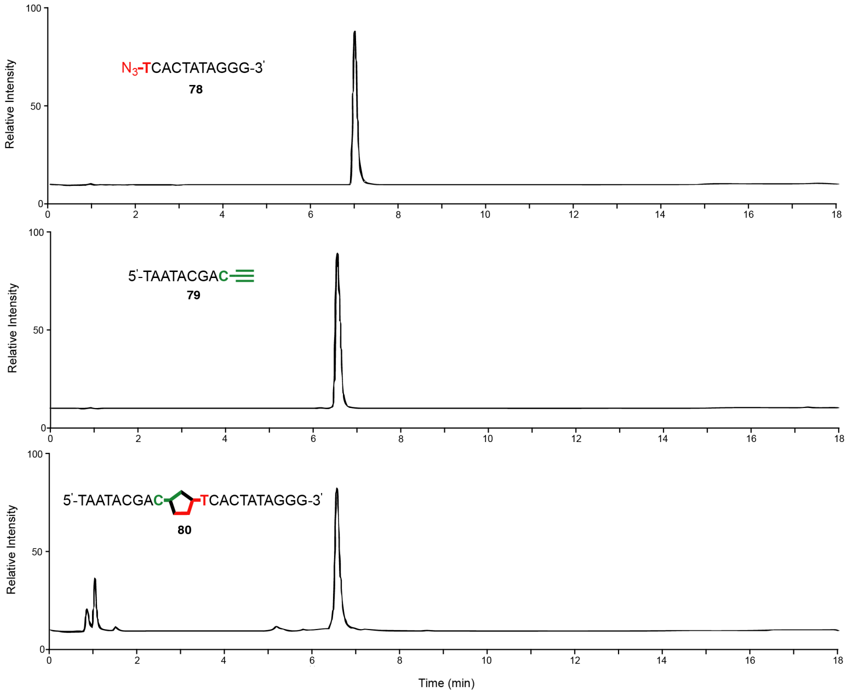

Figure **49**. UV trace from LC-MS analysis of T7 half azide **78**, T7 half alkyne **79**, non-interlocked T7 click axle **80**.

2.2.15. Synthesis of Oligonucleotide Rotaxanes

T7 oligonucleotide rotaxanes were synthesised *via* AT-CuAAC of modified half-axles **78** and **79** with the appropriate macrocycle (**13** or **25**) using the same Cu^I source with *i*-Pr_2NEt as the base catalyst (Figure **50**). Rotaxination reactions were performed using a slight excess (1.1 eq.) of azide half axle **78** to ensure full consumption of alkyne half axle **79**.

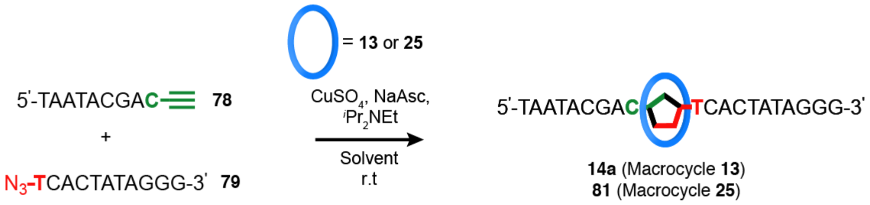

Figure **50**. Synthesis of T7 oligonucleotide rotaxanes **14a** and **81**. Rotaxane conditions: **78** (1.0 eq.), **79** (1.1 eq.), macrocycle **13** or **25** (21 eq.), $CuSO_4.5H_2O$ (10 eq.), NaAsc (50 eq.), DIPEA (1000 eq.). Solvent choice dependant on macrocycle: **13** (THF: H_2O 1:1), **25** (CH_3CN: H_2O 3:7).

Oligonucleotide rotaxane **14a** was synthesised according to literature procedure to be used as a positive control in photolysis experiments.[112] Aliquots were taken and analysed *via* LC-MS to monitor reaction progress (Figure **51**). After 24 h, no remaining alkyne half axle **78** could be detected, indicating that the reaction had gone to completion. The AT-CuAAC reaction also appears to be highly selective for rotaxane formation, as non-interlocked axle **80** could not be detected in the mixture. This could be due to the susceptibility of Cu^I to oxidation to catalytically inactive Cu^{II} in the absence of any stabilizing ligand (THPTA). Cu^I bound to the macrocyclic bipyridine unit is, however, stabilized and can facilitate triazole formation. The large peak at 8.5 min corresponds to free oligonucleotide rotaxane **14a**. Residual Cu-rotaxane complex accounts for the smaller peak at 8.0 min. Treating the mixture with EDTA sequesters remaining metal cations and releases remaining oligonucleotide rotaxane **14a**, which was subsequently purified *via* semi-preparative HPLC.

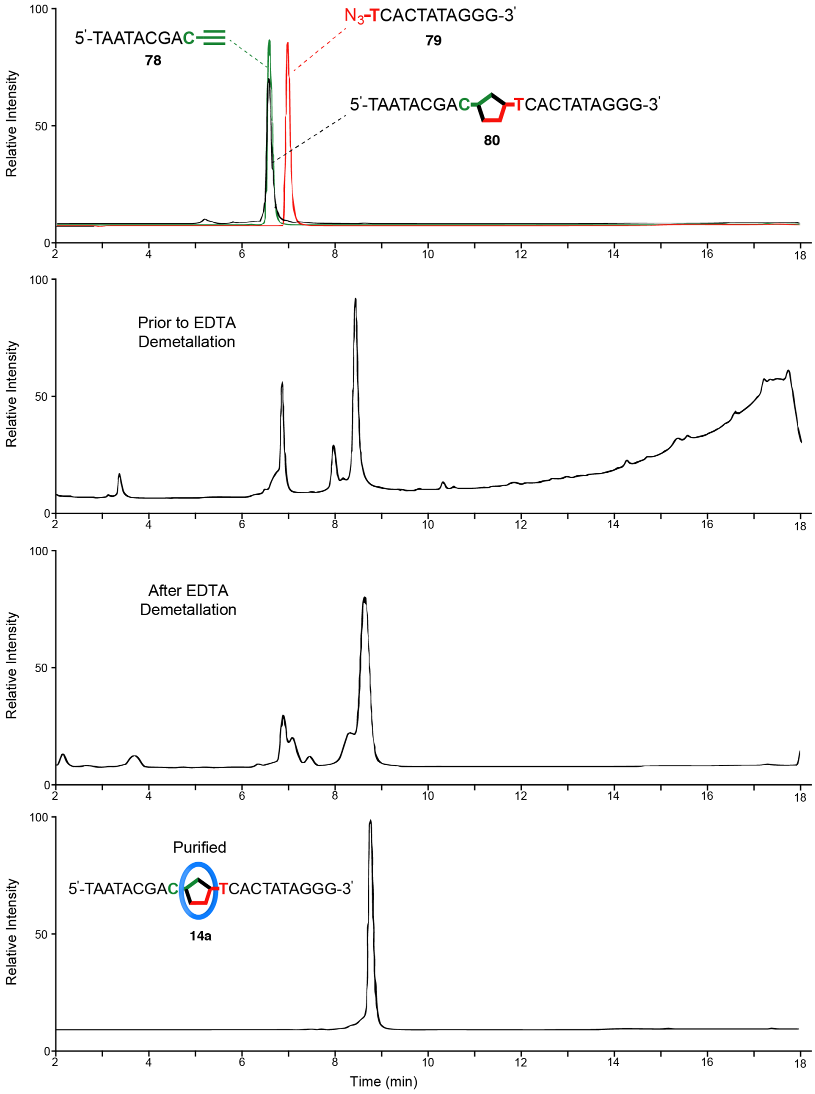

Figure 51. UV trace from LC-MS analysis showing an overlay of azide **79**, alkyne **78** and axle **80** (top) with the crude mixture before and after demetallation with EDTA and **14a** after HPLC purification.

We next attempted to incorporate photocleavable macrocycle **25** into the model T7 sequence. Poor conversion to oligonucleotide rotaxane **81** was observed using the previously employed conditions due to the low solubility of macrocycle **25** in aqueous-THF mixtures, meaning alternative co-solvents mixtures had to be explored. CH_3CN: H_2O (3:7) proved the most suitable, with full consumption of alkyne half-axle **78** observed. A mixture of oligonucleotide rotaxane **81** (8.6 min) and corresponding Cu-rotaxane (8.0 min) was again obtained and treated with EDTA (Figure 52). The lack of non-interlocked axle **80** again suggests a high selectivity for rotaxination under the employed conditions. However, due to instrumentation issues (HPLC, LC-MS) and time constraints, oligonucleotide rotaxane **81** could not be isolated, and therefore photolysis experiments could not be performed.

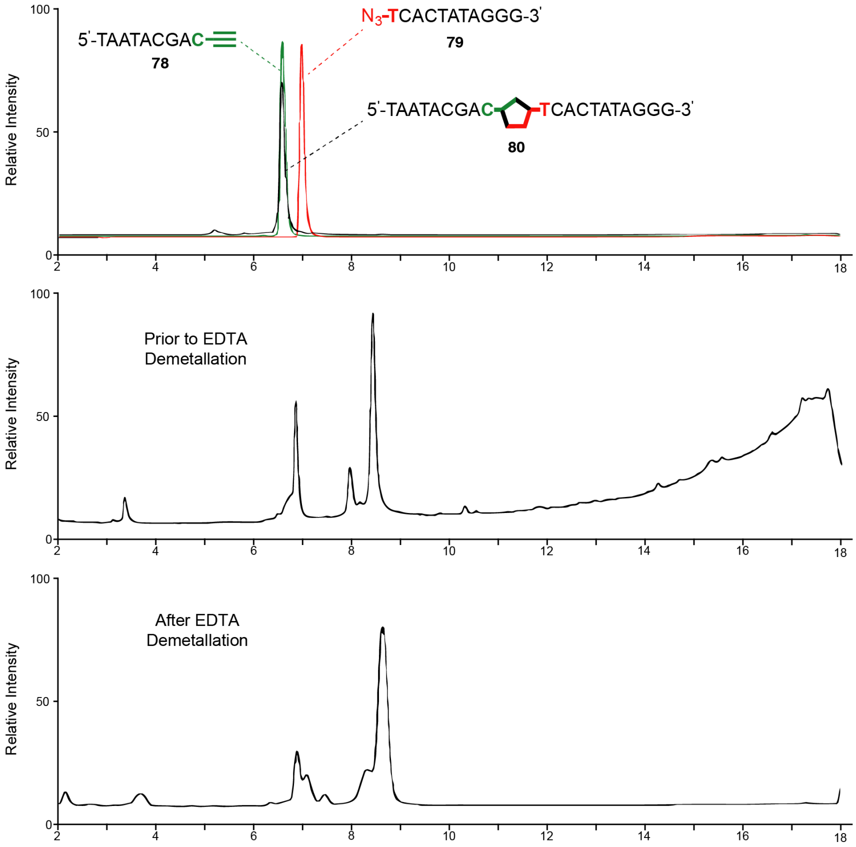

Figure **52**. UV trace from LC-MS analysis showing an overlay of azide **79**, alkyne **78** and axle **80** (top) with the crude mixture with photocleavable macrocycle **25** before and after demetallation with EDTA.

2.3. Conclusion and Future Work

Photocleavable 2,2'-bipyridine macrocycle **25** containing a DEABn-linked backbone was conveniently synthesized and shown to mediate AT-CuAAC rotaxane formation with high efficiency. Modifiable macrocycle **32** was similarly synthesized and could be readily derivatized through *N*-alkylation to install additional functionality, such as enhanced water solubility (**35**), while still retaining photocleavability. Exposure to UVB light successfully cleaved the photolabile unit, resulting in the macrocycle opening to release the corresponding axle in clean and prompt manner in aqueous-organic co-solvent mixtures.

In lieu of expected solvolytic decomposition products, an intramolecular rearrangement pathway instead dominated and was found to be highly favoured in organic (CD_3CN) and mixed organic-aqueous (CD_3CN: D_2O (9:1)) mixtures with both rotaxane and non-interlocked macrocycle models. While the rearrangement mechanism is still under investigation, the evidence suggests that it is not concerted and likely proceeds through heterolytic C-O cleavage followed by a Fries-type rearrangement. An initial observation of accelerated photocleavage in rotaxane model **53** led us to investigate the effect of conformational rigidity by synthesizing a series of varyingly hindered ^{t}Bu-based rotaxanes. No causal relationship was uncovered between rate of photocleavage and the hindrance of the mechanical bond. The variability of cleavage suggesting that it is highly dependent on the precise environment of each individual mechanical bond.

Having successfully demonstrated photolytic release from simple rotaxane models, we next turned our attention toward oligonucleotide-based rotaxanes. Macrocycle **25** successfully mediated the formation of model dinucleotide rotaxane **70** and also released the corresponding axle in response to UVB irradiation, suggesting its suitability for longer interlocked oligonucleotides. Incorporation of photocleavable macrocycles **25** into a model T7 oligonucleotide appears to have been successful. However, due to instrument problems and time constraints, oligonucleotide rotaxane **81** could not be isolated.

Initial efforts should be directed toward isolating photocaged oligonucleotide rotaxane **81** and characterizing its activity, which is expected to silenced. UVB-responsive removal of the macrocyclic component is expected to restore hybridisation capability to complementary sequences and biological function (Scheme **23**). Proof-of-concept light-responsive reactivation could be validated using numerous methods: circular dichroism, duplex melting temperatures (T_m), polymerase chain reaction (PCR) or most simply *via* LC-MS given the large difference in retention time between interlocked and non-interlocked triazole-linked oligonucleotides. If successful, these single-stranded DNA-based materials have a host of potential biological applications, ranging from use as optochemical tools to study gene function to therapeutic ASO agents.

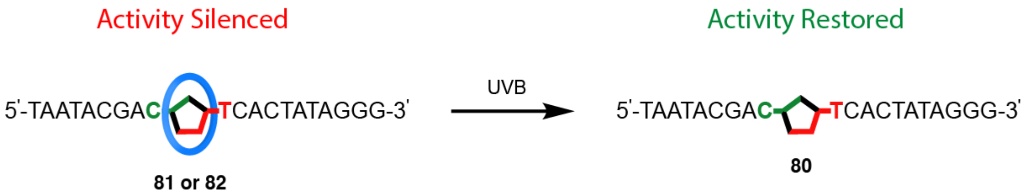

Scheme **23.** Release of axle **80** from oligonucleotide rotaxanes **81** upon UVB irradiation.

2.4. Experimental

2.4.1. General Experimental

Unless otherwise stated, all reagents, including anhydrous solvents, were purchased from commercial sources and used without further purification. Reagents for oligonucleotide synthesis were purchased from Applied Biosystem. All reactions were carried out under an inert an atmosphere of N_2 using anhydrous solvents unless otherwise stated. Flash column chromatography was performed using Biotage Isolera-4 or a Biotage Isolera-1 automated chromatography system, employing Biotage SNAP or ZIP cartridges (50 µm, irregular silica, default flow rates). Analytical TLC was performed on precoated silica gel plates (0.25 mm thick, 60F254, Merck, Darmstadt, Germany) and observed under UV light or with potassium permanganate solution. NAP 10 gel-filtration columns were purchased from GE Healthcare and used according to the manufacturer's instructions. Petrol refers to the fraction of petroleum ether boiling in the range 40-60 °C. IPA refers to isopropyl alcohol. EDTA-NH_3 solution refers to an aqueous solution of NH_3 (17% w/w) saturated with sodium-ethylenediaminetetraacetate. $[Cu(CH_3CN)_4]PF_6$ was prepared as described by Pigorsch and Köckerling.[133]

NMR spectra were recorded on Bruker AV400, AV3-400 and AV500 FT-NMR spectrometers in the indicated deuterated solvent at a constant temperature of 300 K. Chemical shifts for ^1H and ^{13}C spectra are reported on the delta (δ) scale in parts per million (ppm) from low to high field and referenced to residual solvent. Coupling constants (*J*) are reported in Hertz (Hz). Standard abbreviations indicating multiplicity were used as follows: m = multiplet, q = quartet, t = triplet, d = doublet, s = singlet, app. = apparent, br = broad. Diastereomeric proton signals are differentiated as H_x or H_x' where appropriate. Signal assignment was carried out using 2D NMR methods (HSQC, HMBC, COSY) where necessary. For clarity, all proton signals in rotaxane structures corresponding to the axle component are in upper case (H_X), and all proton signals corresponding to the macrocycle components are in lower case case (H_x).

UV-vis absorption spectra were measured on a Biotek Instruments XS spectrometer using quartz cuvettes of 1 cm path length. All melting points were determined using a Griffin apparatus. Low resolution mass spectrometry (LR-MS) was carried out by the mass spectrometry services at the University of Southampton (Waters TQD mass spectrometer equipped with a triple quadrupole analyser with UHPLC injection [BEH C_{18} column; CH_3CN-hexane gradient {0.2% formic acid}]). High resolution mass spectrometry (HR-MS) was carried out by the mass spectrometry services at the University of Southampton (MaXis, Bruker Daltonics, with a Time of Flight (TOF) analyser; samples were introduced to the mass spectrometer *via* an Acquity H-Class quaternary solvent manager (with TUV detector at 254 nm, sample and column manager) and UHPLC pump in a gradient of 20% CH_3CN in hexane (0.2% formic acid) to 100% CH_3CN (0.2% formic acid) over 10 min at a flow rate of 0.6 mL/min (column: Acquity UPLC BEH C_{18} (Waters) 1.7 µm 50 mm × 2.1 mm). As accurate mass measurements are of limited value for compounds with MW >1000 Da, in these cases a graphical comparison of the observed isotope pattern and the predicted isotopic distribution is provided.

2.4.2. Experimental Procedures

General Procedure (1): Rotaxination

A solution of macrocycle (1.0 eq.), azide stopper (1.0 eq.), alkyne stopper (1.0 eq.) and $Cu(MeCN)_4PF_6$ (0.95 eq.) in CH_2Cl_2 (0.1 M) was degassed under N_2. DIPEA (2.0 eq.) was added and stirred at room temperature overnight. The mixture was then diluted with CH_2Cl_2 (0.05 M) and sat. EDTA.NH_3 (1:1 with volume of CH_2Cl_2) was added and stirred vigorously to sequester $Cu^{I/II}$ ions. Demetallation of the Cu-rotaxane was monitored *via* LC-MS, taking between 10 min – 3 days depending on the structure. The organic phase was separated and washed with H_2O then brine. Combined aqueous phases were extracted with CH_2Cl_2 (x2). The combined organic extracts were dried over anhydrous $MgSO_4$, filtered and concentrated *in vacuo*. The crude product was purified *via* silica-gel chromatography using a Biotage Isolute SPE column.

Compound **16**

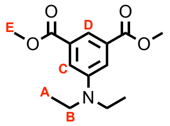

To a mixture of **15** (5.0 g, 23.90 mmol, 1.0 eq.) and K_2HPO_4 (24.98 g, 143.40 mmol, 6.0 eq.) in anhydrous DMF (75 mL) was added iodoethane (14.90 g, 95.60 mmol, 4.0 eq.). The mixture was heated to 60 °C and stirred for 16 h. The mixture was then cooled to room temperature, diluted with H_2O (100 mL) and extracted with EtOAc (3 x 50 mL). The organic extracts were washed with brine (100 mL), dried over anhydrous $MgSO_4$, filtered, and concentrated *in vacuo*. The crude product was purified *via* silica-gel chromatography using a Biotage Isolute SPE column (eluent 19:1 → 8:2 petrol: EtOAc) to afford **16** as a pale yellow oil (4.60 g, 17.35 mmol, 73%).^{1}H NMR (400 MHz, $CDCl_3$, 298 K) δ_H 7.91 (1H, t, *J* = 1.4 Hz, H_D), 7.49 (2H, d, *J* = 1.4 Hz, H_C), 3.91 (6H, s, H_E), 3.42 (4H, q, *J* = 7.1 Hz, H_B), 1.18 (6H, t, *J* = 7.1 Hz, H_A).^{13}C NMR (101 MHz, $CDCl_3$, 298 K) δ_C 167.3, 148.0, 131.4, 117.4, 116.6, 52.3, 44.6, 12.5. HR-ESI-MS (CH_3CN): *m/z* = 266.1391 [M+H]$^+$ calc. 266.1387.

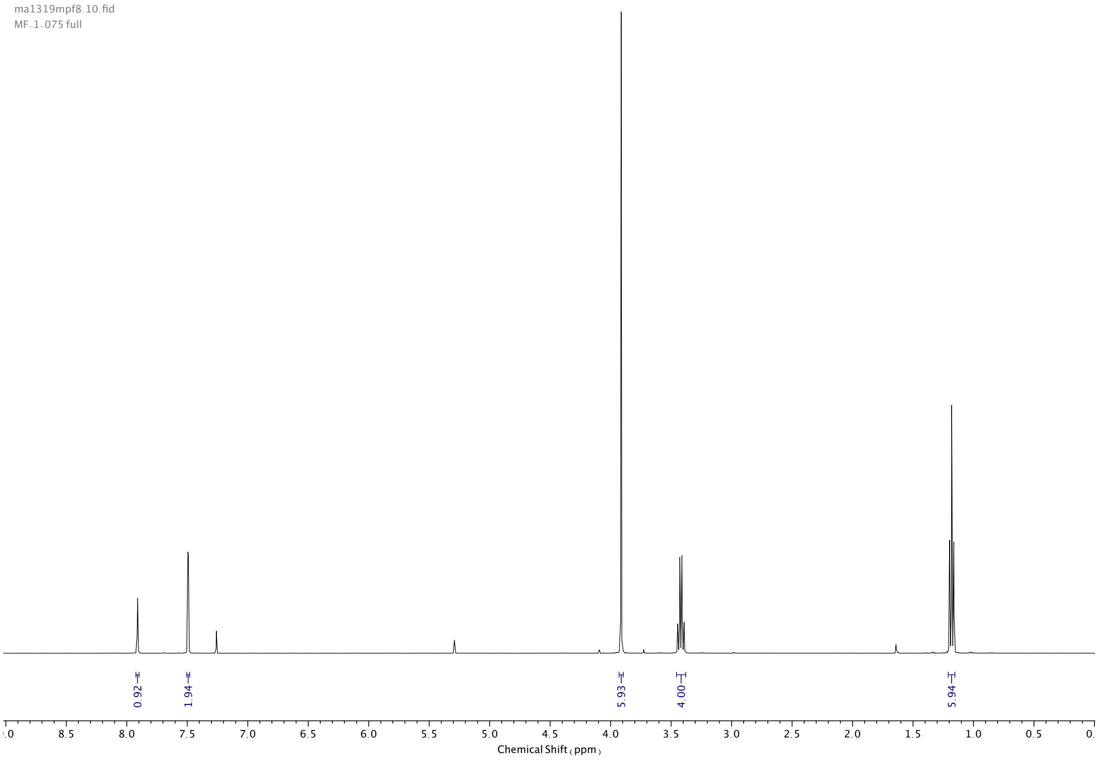

Figure **53**. ^{1}H NMR ($CDCl_3$, 400 MHz) of **16**.

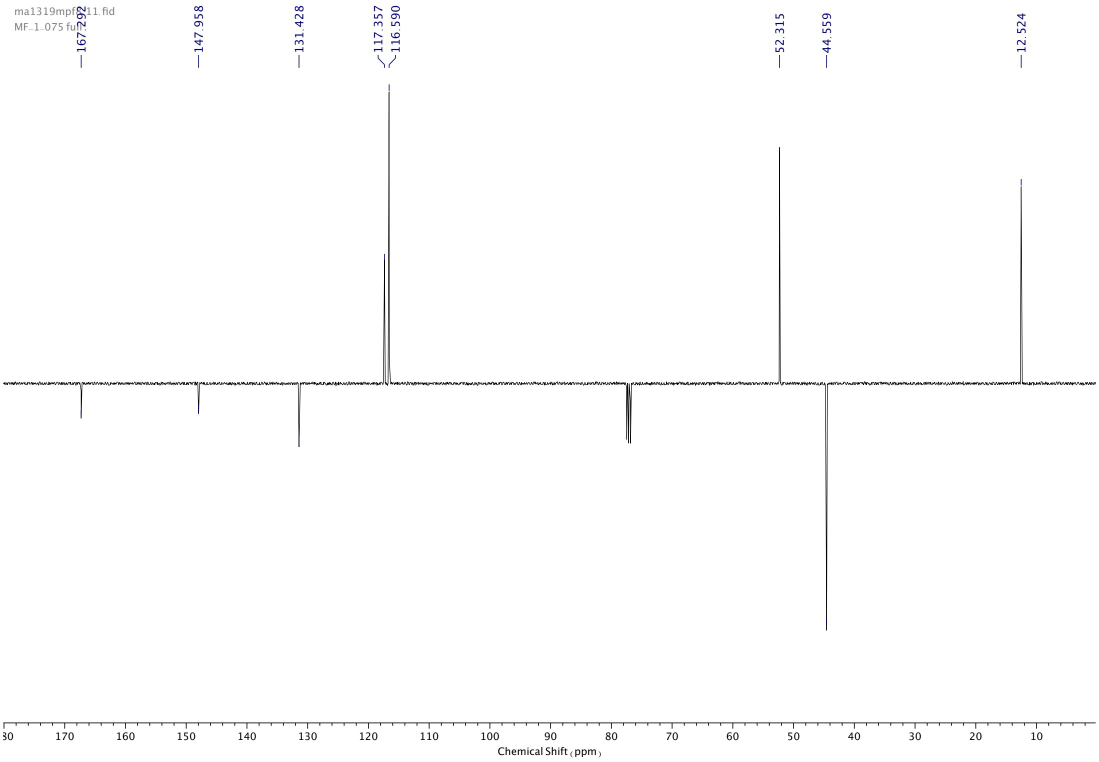

Figure **54**. ^{13}C NMR (CDCl$_3$, 101 MHz) of **16**.

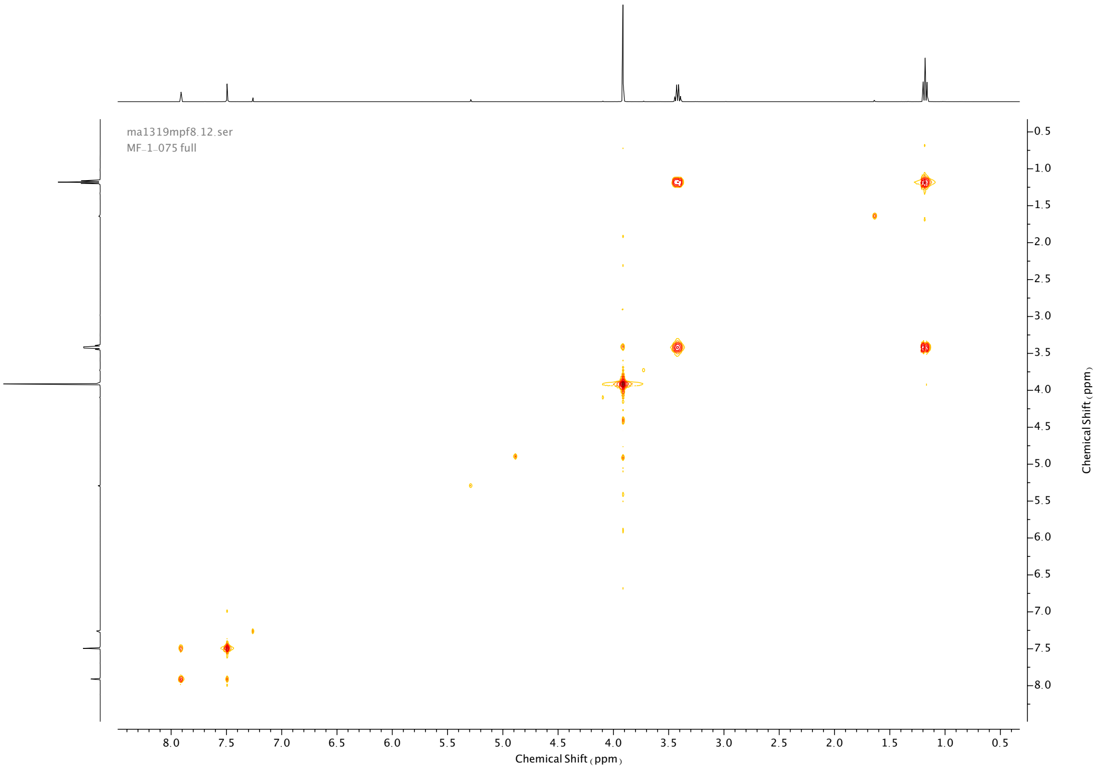

Figure **55**. COSY NMR (CDCl$_3$) of **16**.

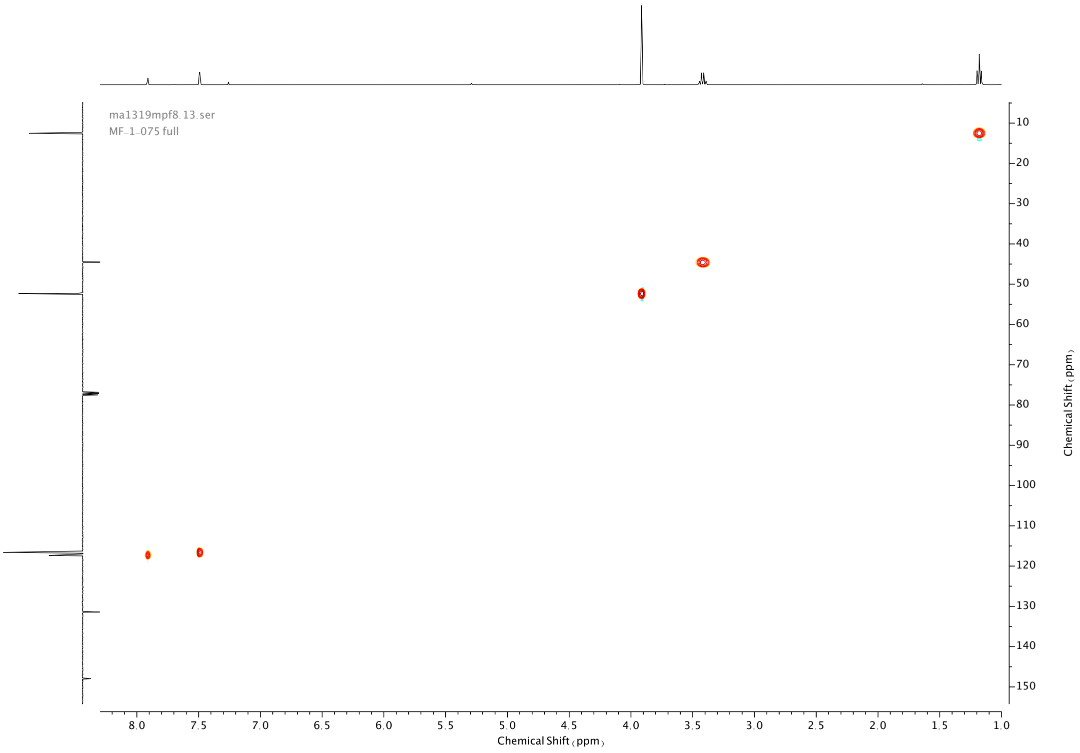

Figure **56**. HSQC NMR (CDCl$_3$) of **16**.

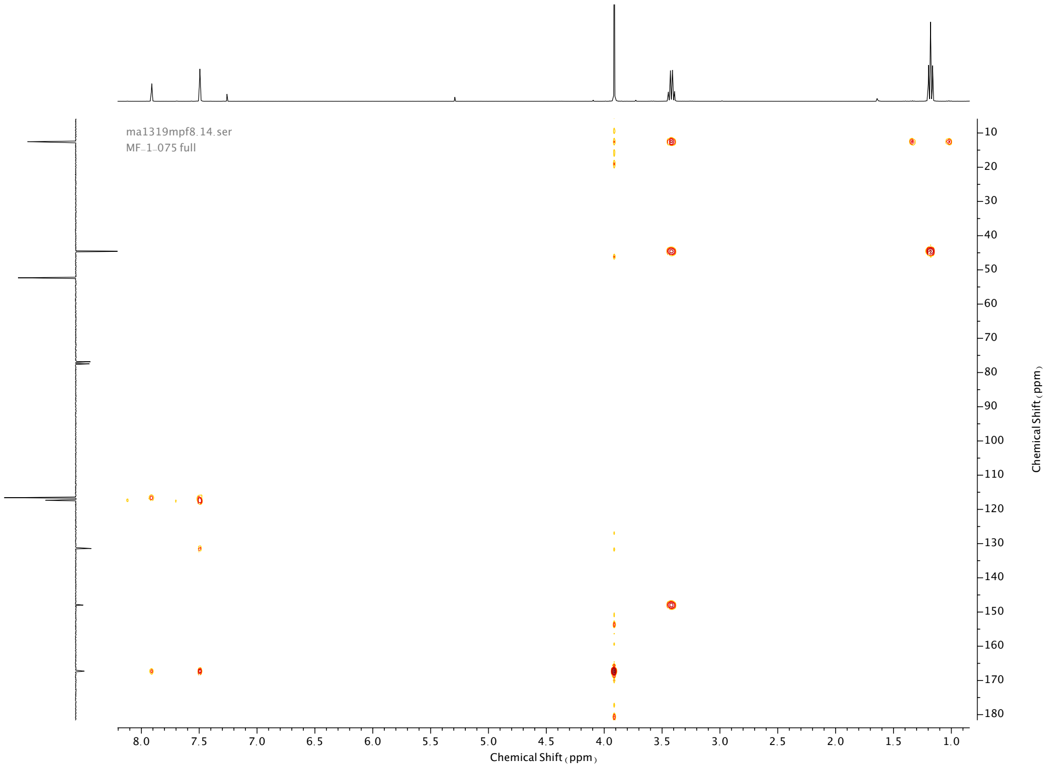

Figure **57**. HMBC NMR (CDCl$_3$) of **16**.

Compound **17**

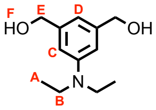

To a pre-dried flask containing $LiAlH_4$ (1.15 g, 30.18 mmol, 2.0 eq.) was added a solution of **16** (4.0 g, 15.09 mmol, 1.0 eq.) in anhydrous THF (60 mL) at 0 °C over 1 h, which was then slowly allowed to reach room temperature and stirred overnight. The mixture was quenched at -10 °C through the sequential addition of EtOAc (10 mL), H_2O (1.2 mL), 10M NaOH (1.2 mL), then H_2O (4 mL) again. The resulting mixture stirred at room temperature for 2 h, then diluted with THF (50 mL), dried over anhydrous $MgSO_4$, filtered, and concentrated *in vacuo.* The crude product which was purified *via* silica-gel chromatography using a Biotage Isolute SPE column (eluent 1:0 → 19:1 CH_2Cl_2: MeOH) to afford **17** as a yellow oil (2.35 g, 11.24 mmol, 75%).^{1}H NMR (400 MHz, $CDCl_3$, 298 K) δ_H 6.60 (3H, d, *J* = 2.8 Hz, H_C & H_D), 4.59 (4H, s, H_E), 3.36 (4H, q, *J* = 6.8 Hz, H_B), 2.06 (2H, br. s, O-H_F), 1.16 (6H, t, *J* = 6.8 Hz, H_A). ^{13}C NMR (101 MHz, $CDCl_3$, 298 K) δ_C 148.5, 142.6, 112.7, 109.7, 66.0, 44.6, 12.7. HR-ESI-MS (CH_3CN): *m/z* = 210.1489 $[M+H]^+$ calc. 210.1489.

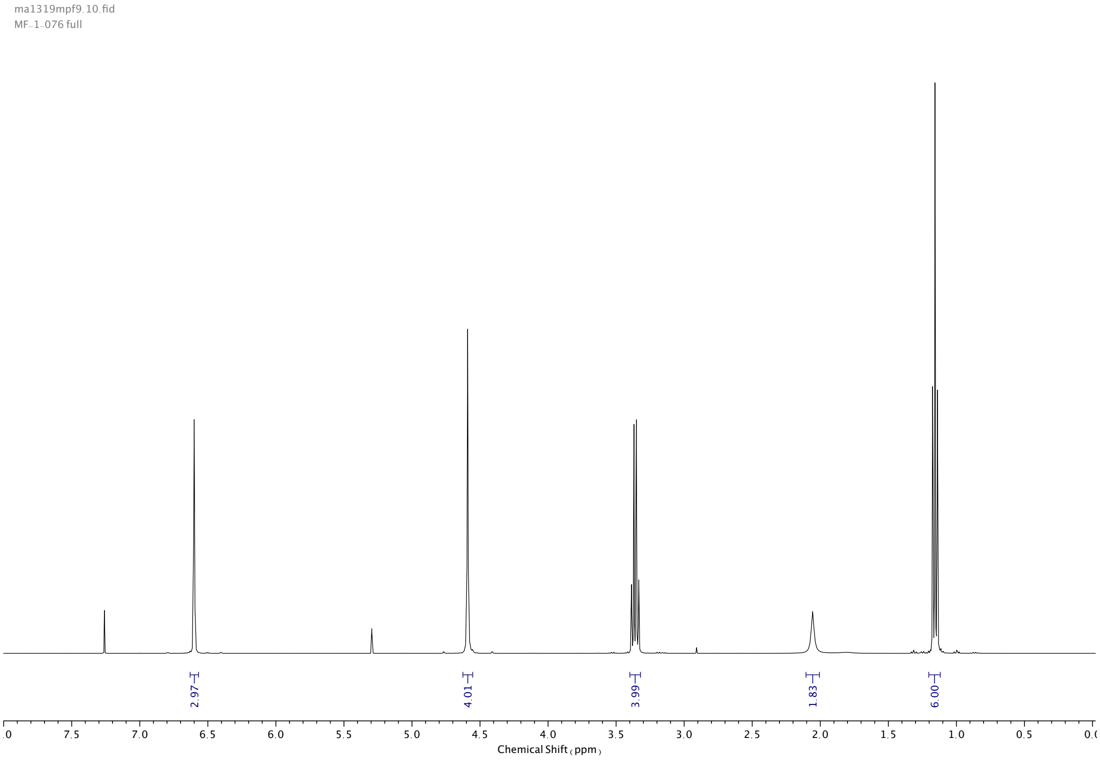

Figure **58**. ^{1}H NMR ($CDCl_3$, 400 MHz) of **17**.

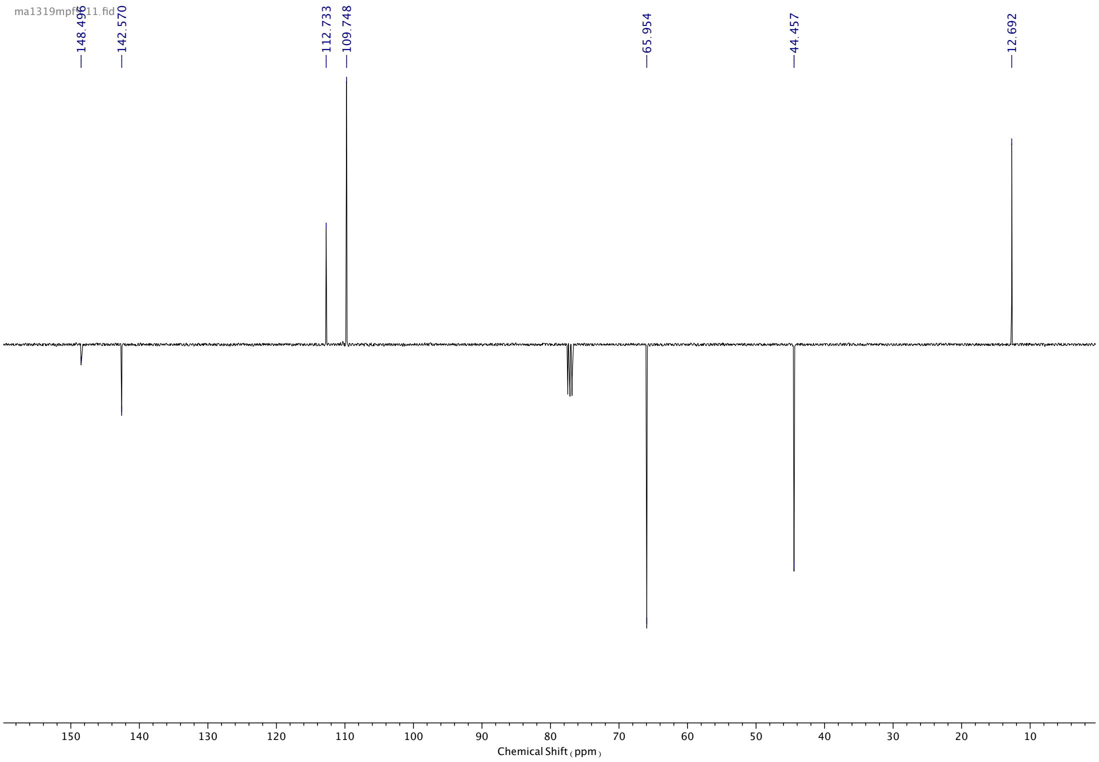

Figure **59**. ^{13}C NMR (CDCl$_3$, 101 MHz) of **17**.

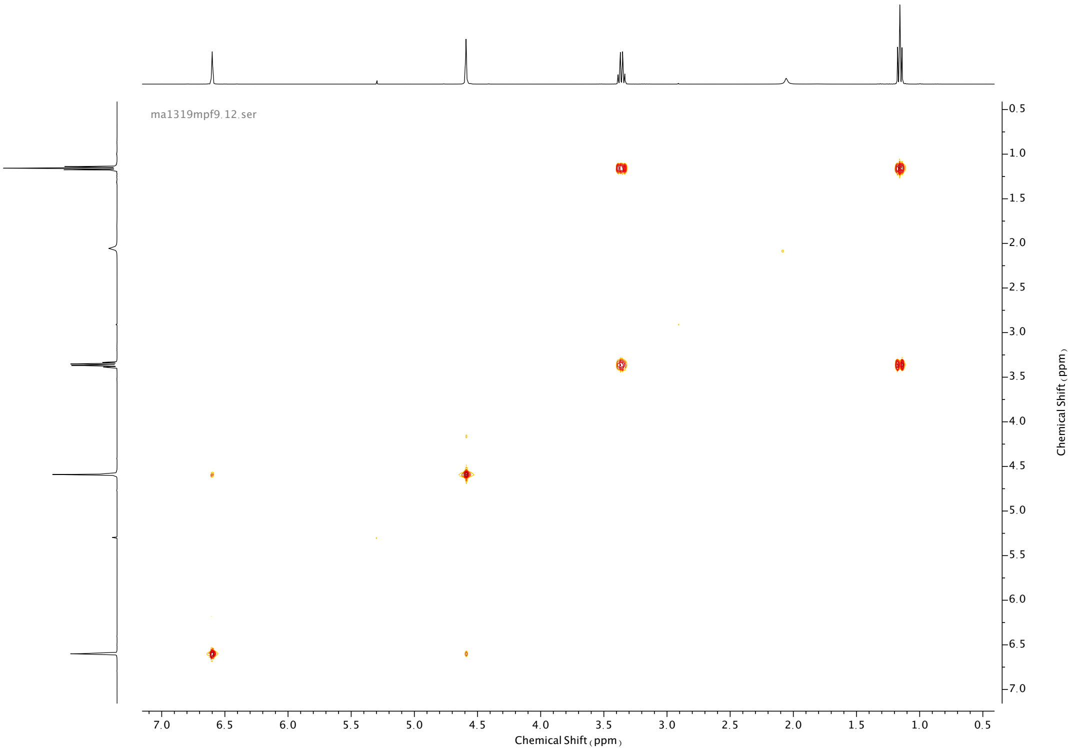

Figure **60**. COSY NMR (CDCl$_3$) of **17**.

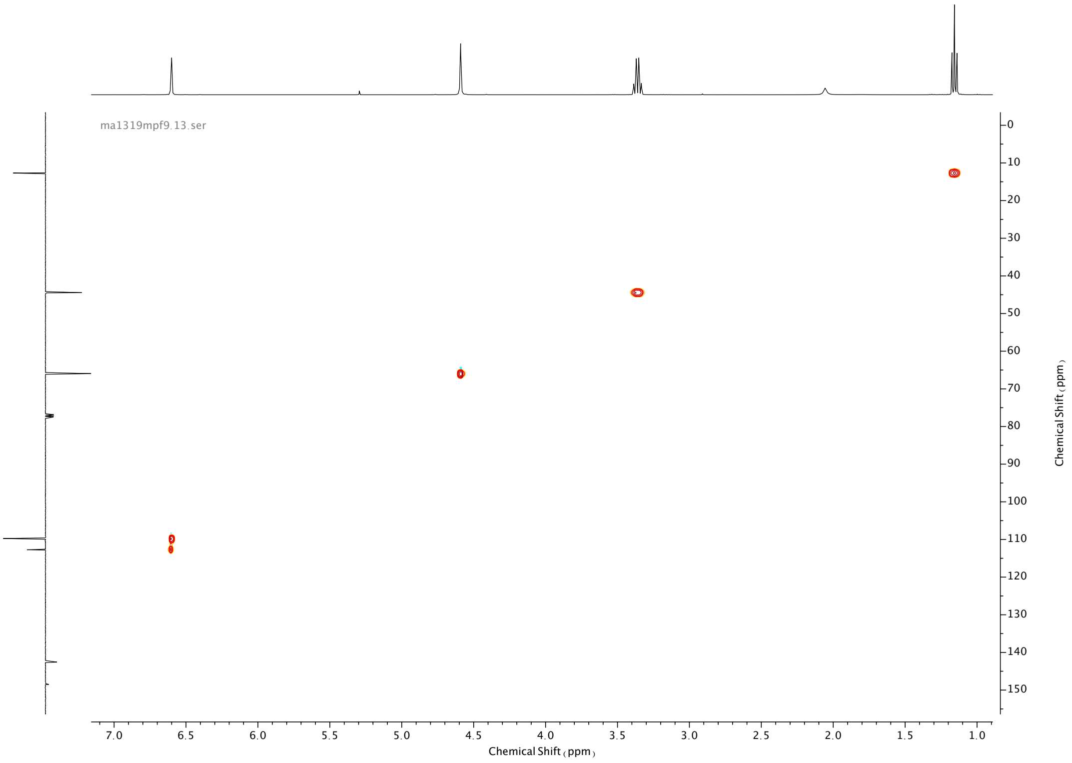

Figure **61**. HSQC NMR ($CDCl_3$) of **17**.

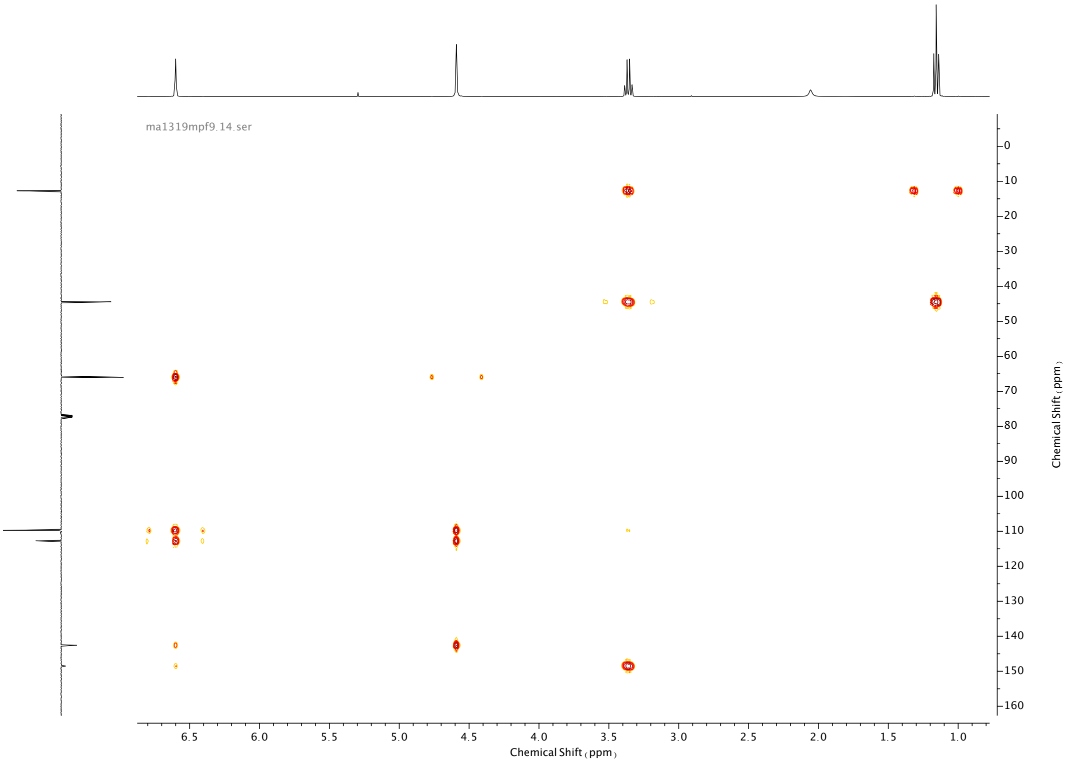

Figure **62**. HMBC NMR ($CDCl_3$) of **17**.

Compound **18**

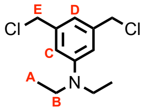

To a solution of **17** (3.0 g, 14.34 mmol, 1.0 eq.) in anhydrous CH_2Cl_2 (100 mL) at 0 °C was added $SOCl_2$ (3.12 mL, 43.0 mmol, 3.0 eq.) over 10 min. The resulting solution was stirred at 0 °C for 30 min, then at room temperature for a further 5 h. The mixture was then quenched with H_2O (75 mL), neutralized with $NaHCO_3$ (50mL), and extracted with CH_2Cl_2 (3 x 75 mL). Combined organic extracts were dried over anhydrous $MgSO_4$, filtered, and concentrated *in vacuo*. The crude product was purified *via* silica-gel chromatography using a Biotage Isolute SPE column (eluent 9:1 → 7:3 petrol: CH_2Cl_2, silica deactivated) to afford **18** as a yellow oil (2.62 g, 10.69 mmol, 75%). ^1H NMR (400 MHz, $CDCl_3$, 298 K) δ_H 6.67 (1H, s, H_D), 6.62 (2H, d, *J* = 1.2 Hz, H_C), 4.53 (4H, s, H_E), 3.37 (4H, q, *J* = 7.2, H_B), 1.18 (6H, t, *J* = 7.2 Hz, H_A). ^{13}C NMR (101 MHz, $CDCl_3$, 298 K) δ_C 148.5, 139.1, 115.6, 111.8, 46.9, 44.5, 12.65. HR-ESI-MS (CH_3CN): *m/z* = 246.0813 $[M+H]^+$ calc. 246.0811.

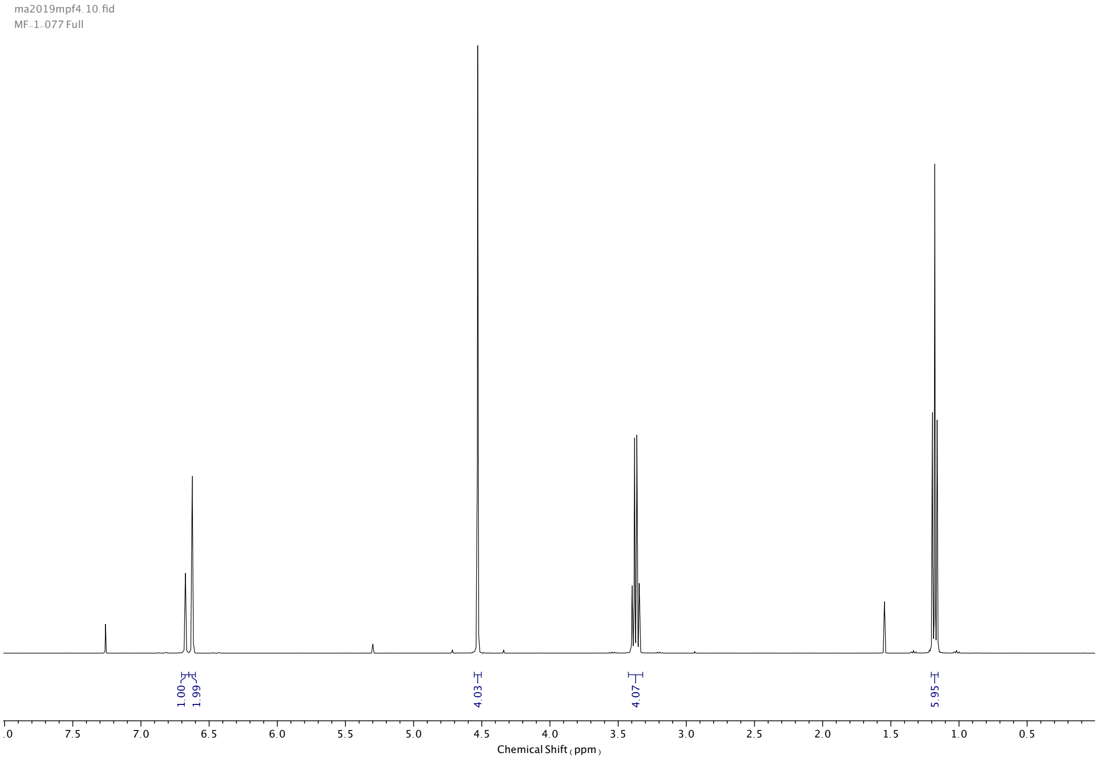

Figure **63**. ^1H NMR ($CDCl_3$, 400 MHz) of **18**.

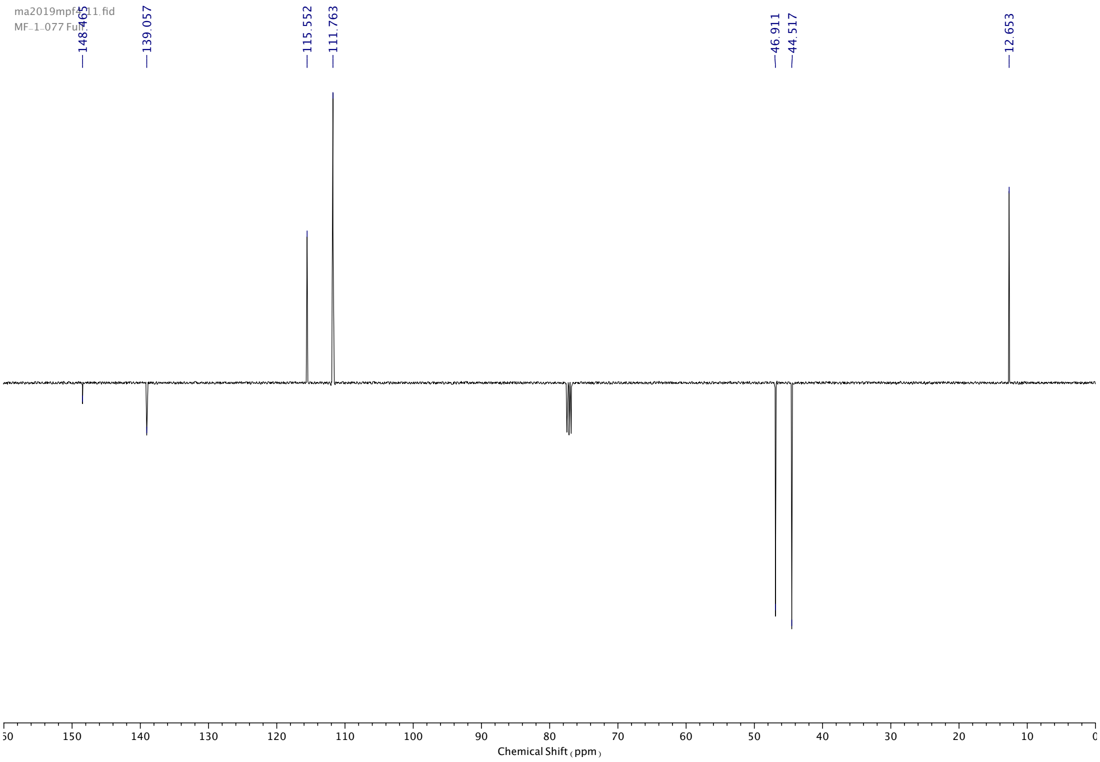

Figure **64**. ^{13}C NMR (CDCl$_3$, 101 MHz) of **18**

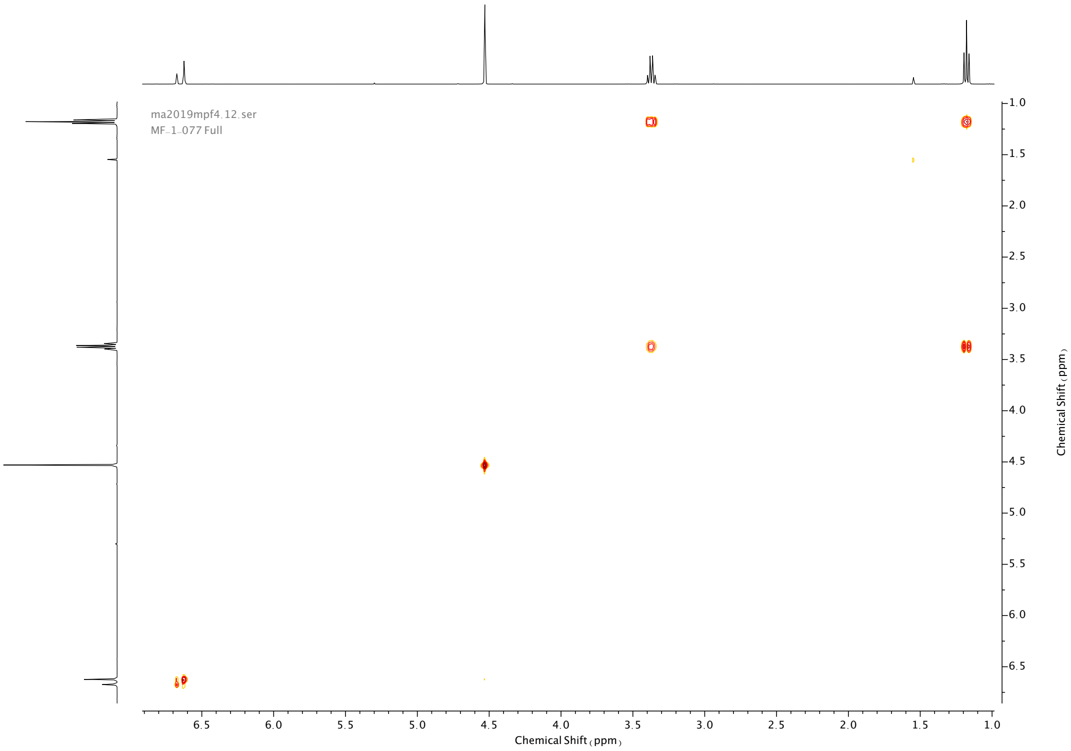

Figure **65**. COSY NMR (CDCl$_3$) of **18**.

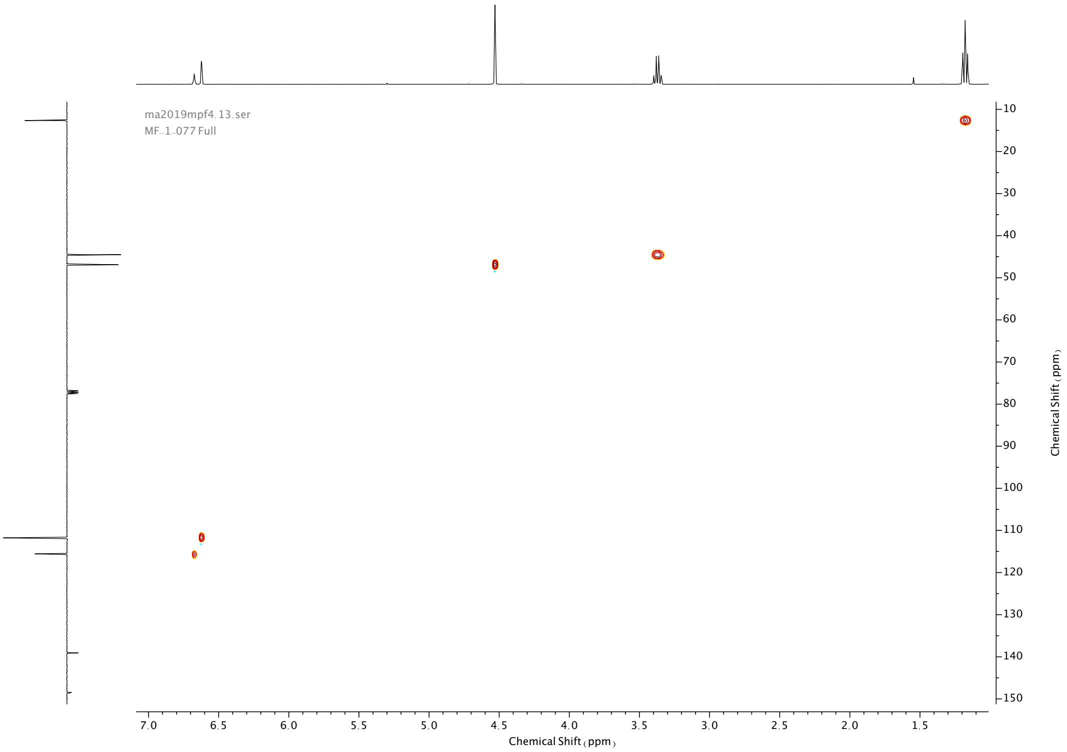

Figure **66**. HSQC NMR ($CDCl_3$) of **18**.

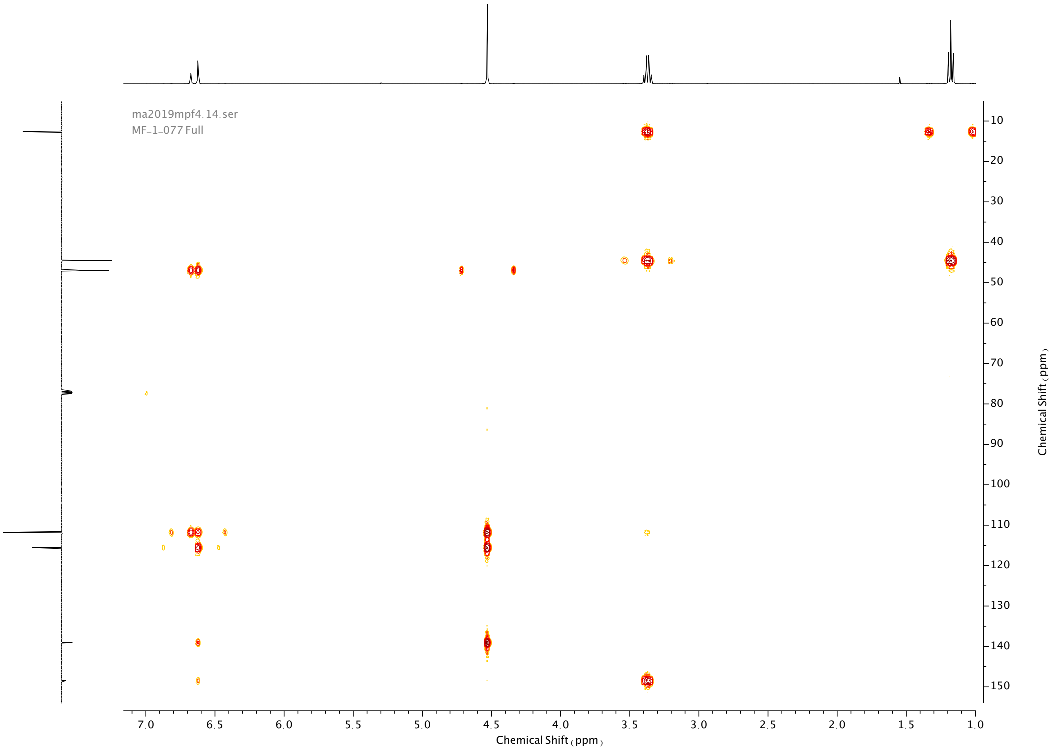

Figure **67**. HMBC NMR ($CDCl_3$) of **18**.

Compound **20**

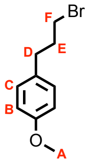

Dry air was bubbled through a solution of freshly distilled **19** (17 mL, 108.5 mmol, 1.0 eq.) in hexane (570 mL) for 2 h at 0 °C, after which a 33% w/v solution of HBr in acetic acid (50 mL) was added in one portion. The resulting mixture was sealed with an unpierced septum and stirred vigorously at 0 °C for 2 h. The mixture was then allowed to settle and the hexane layer was decanted and neutralized with $NaHCO_3$ (600 mL), washed with brine (200 mL), dried over anhydrous $MgSO_4$, filtered and concentrated *in vacuo* to afford **20** as a pale green oil (23.5 g, 102.8 mmol, 95%, linear: branched 97:3). ^{1}H NMR (400 MHz, $CDCl_3$, 298 K) δ_H 7.12 (2H, app. d, *J* = 8.7 Hz, H_C), 6.85 (2H, app. d, *J* = 8.7 Hz, H_B), 3.80 (3H, s, H_A), 3.41 (2H, t, 6.6 Hz, H_F), 2.73 (2H, t, *J* = 7.3 Hz, H_D), 2.14 (2H, app. q, *J* = 6.7 Hz, H_E). ^{13}C NMR (101 MHz, $CDCl_3$, 298 K) δ_C 158.2, 132.7, 129.6, 114.0, 55.4, 34.5, 33.3, 33.2.

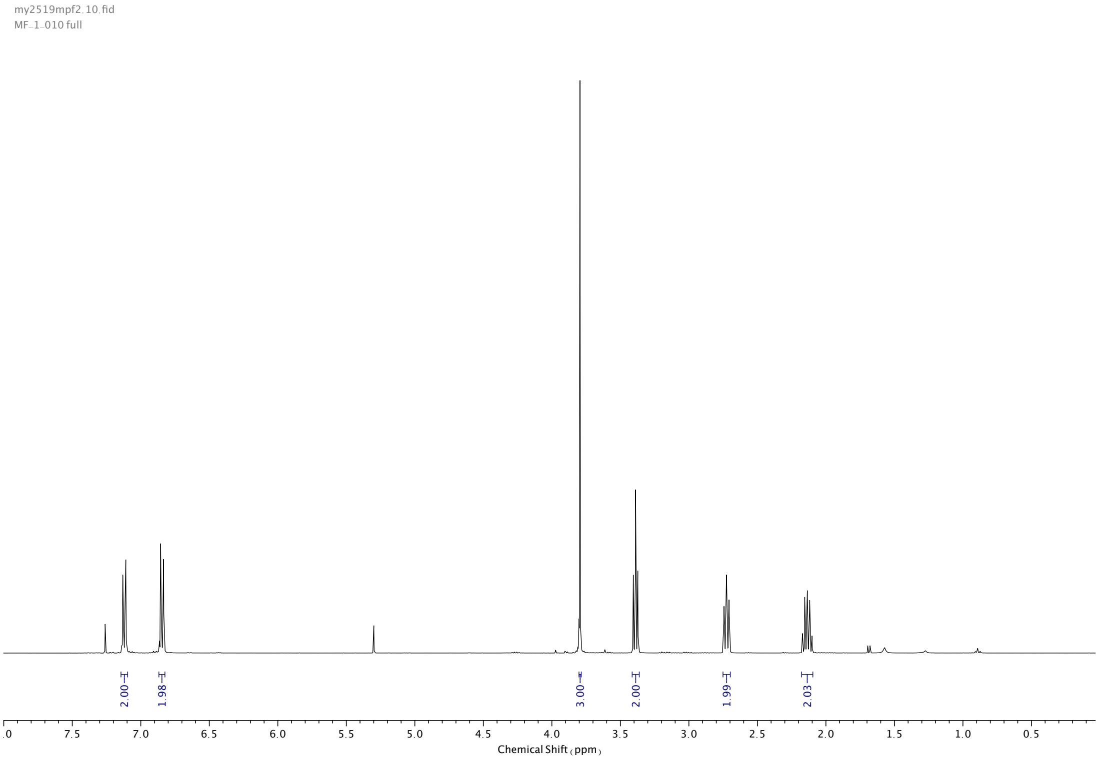

Figure **68**. ^{1}H NMR ($CDCl_3$, 400 MHz) of **20**.

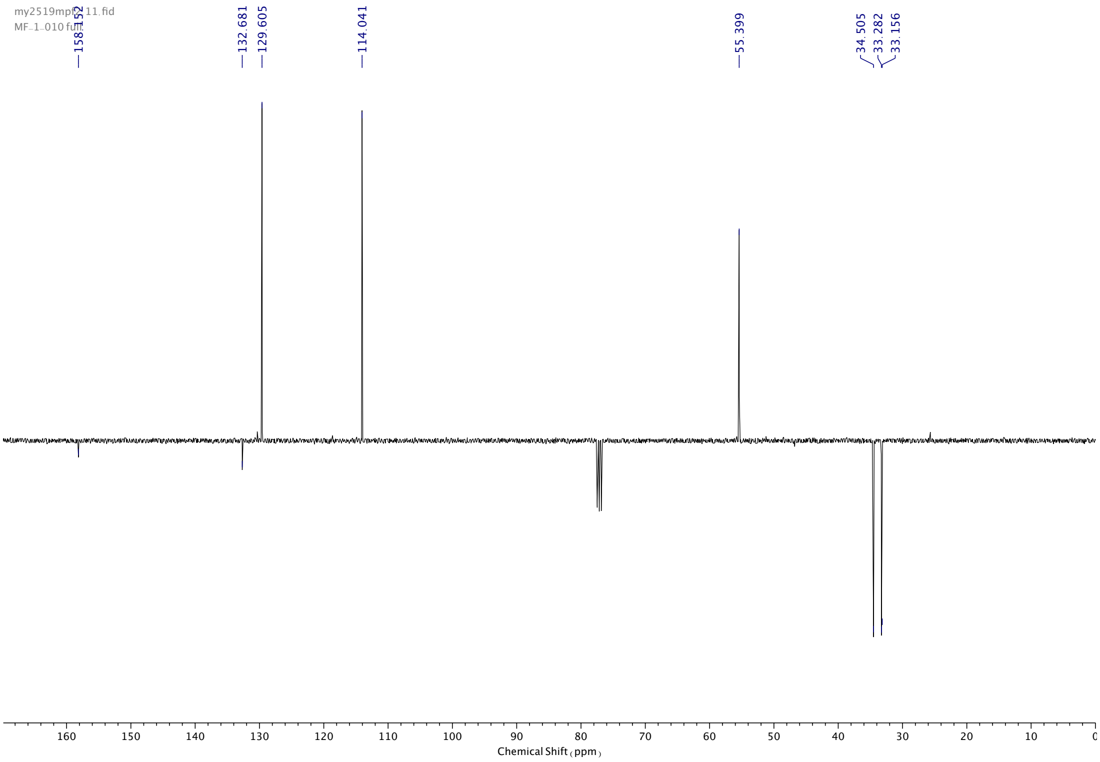

Figure **69**. ^{13}C NMR (CDCl$_3$, 101 MHz) of **20**.

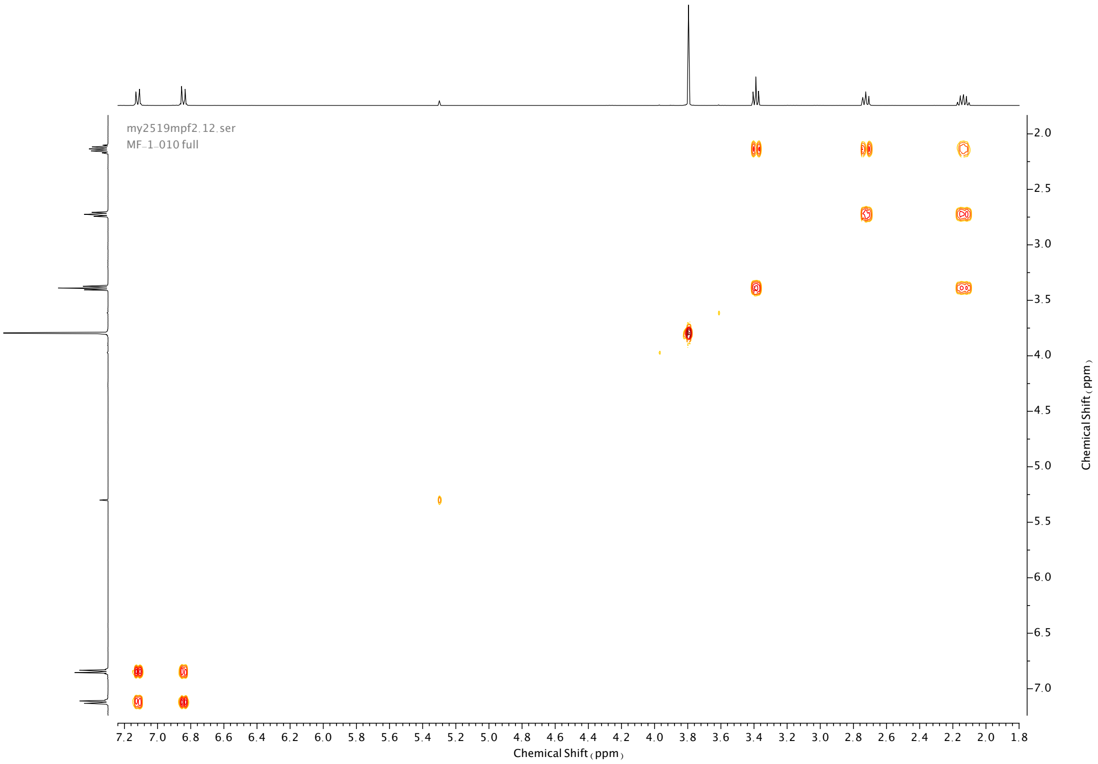

Figure **70**. COSY NMR (CDCl$_3$) of **20**.

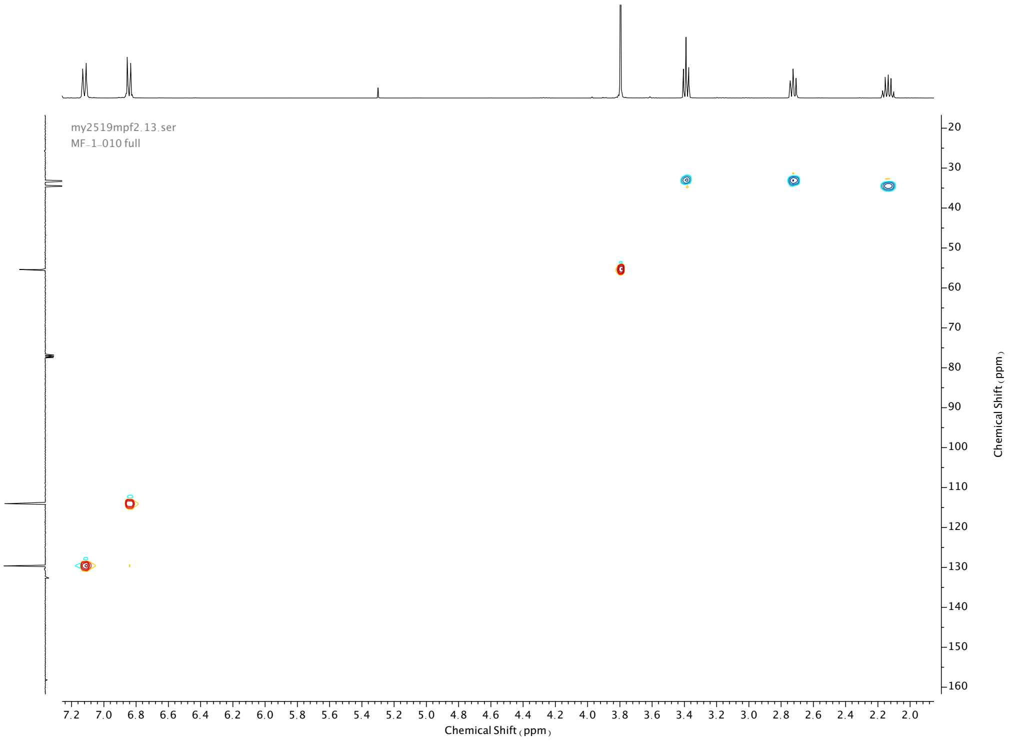

Figure **71**. HSQC NMR ($CDCl_3$) of **20**.

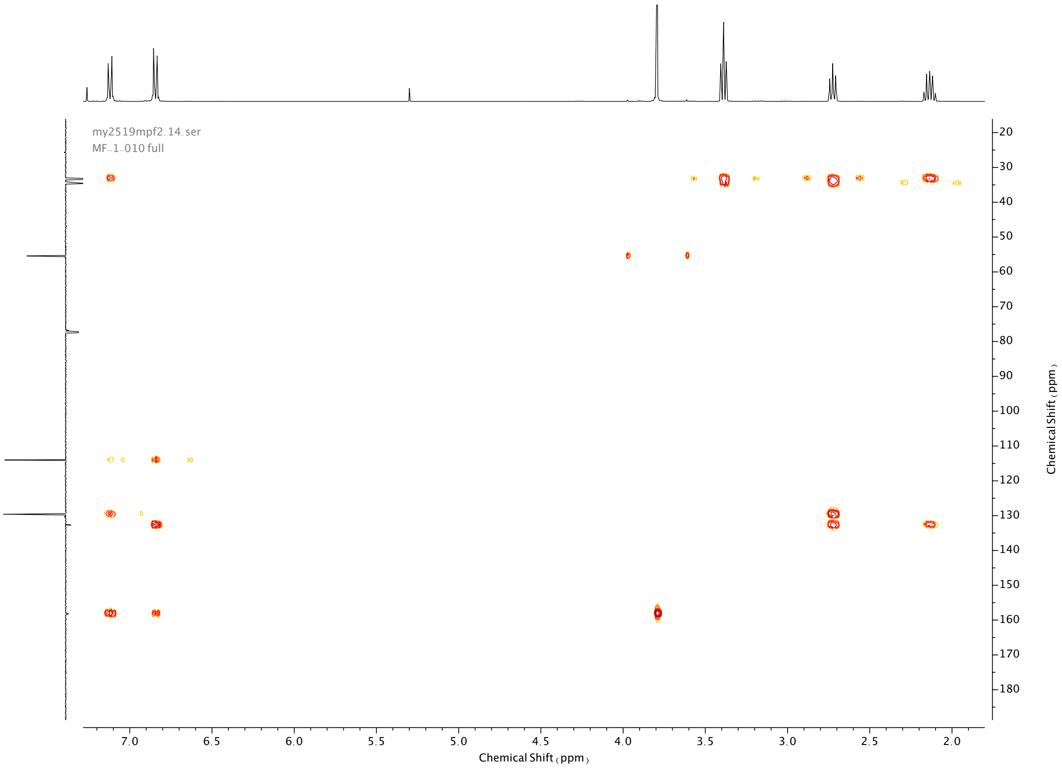

Figure **72**. HMBC NMR ($CDCl_3$) of **20**.

Compound **22**

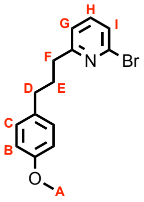

To a mixture of activated Zn dust (9.81 g, 150.0 mmol, 1.5 eq.) and I_2 (1.27 g, 50.0 mmol, 0.5 eq.) in anhydrous DMF (60 mL), degassed under N_2, was added **20** (22.91 g, 100 mmol, 1.0 eq.) in anhydrous DMF (20 mL). The mixture was stirred rigorously at 90 °C for 2 h then allowed to cool to room temperature before being transferred under N_2 *via* cannula to a flask containing **21** (18.95 g, 80.00 mmol, 0.8 mmol) and $PdCl_2(PPh_3)_2$ (0.70 g, 1.00 mmol, 0.01 eq.), then stirred at room temperature for a further 3 h. The mixture was quenched with saturated NH_4Cl (250 mL), then washed with 5% w/v aqueous LiCl (100 mL). Aqueous washings were extracted with Et_2O (2 x 100 mL), combined and dried over anhydrous $MgSO_4$, filtered, then concentrated *in vacuo*. The crude product was purified *via* silica-gel chromatography (eluent 95:5 petrol: Et_2O) to afford **22** as a colourless oil (13.51 g, 44.28 mmol, 44%). ^1H NMR (400 MHz, $CDCl_3$, 298 K) δ_H 7.43 (1H, t, *J* = 7.7 Hz, H_H), 7.29 (1H, d, *J* = 7.8 Hz, H_I), 7.10 (2H, d, *J* = 8.6, H_C), 7.07 (1H, d, *J* = 8.0 Hz, H_G), 6.79 (2H, d, *J* = 8.7 Hz, H_B), 3.78 (s, 6H, H_A), 2.78 (2H, t, *J* = 7.6 Hz, H_F), 2.62 (2H, t, *J* = 7.7 Hz, H_D), 2.01 (2H, q, *J* = 7.6 Hz, H_E). ^{13}C NMR (101 MHz, $CDCl_3$, 298 K) δ_C 163.9, 157.9, 141.7, 138.7, 134.0, 129.4, 125.4, 121.6, 113.9, 55.4, 37.5, 34.6, 31.6.

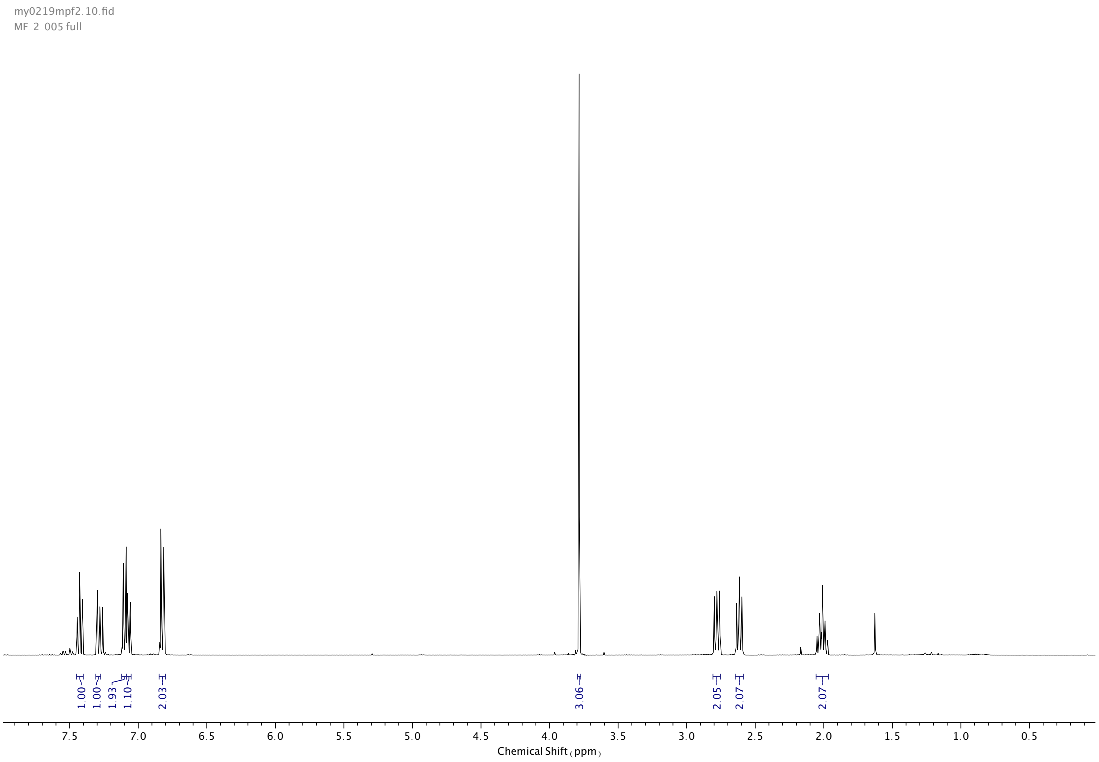

Figure **73**. ^{1}H NMR (CDCl$_3$, 400 MHz) of **22**.

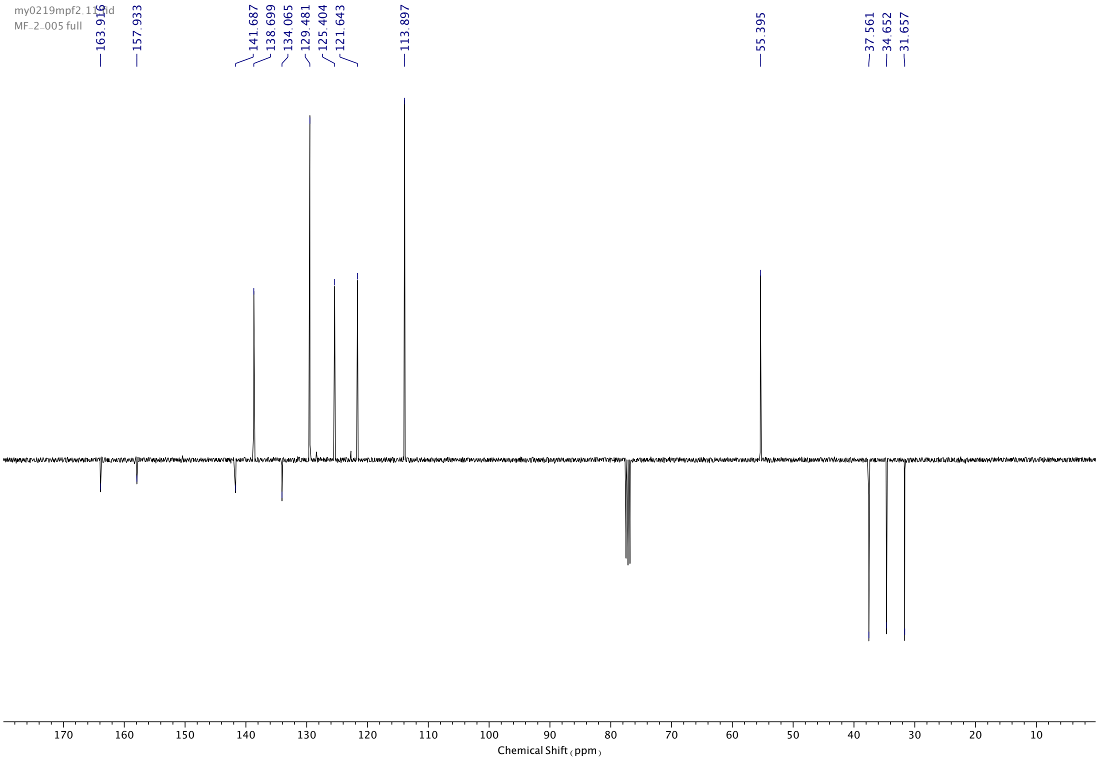

Figure **74**. ^{13}C NMR (CDCl$_3$, 101 MHz) of **22.**

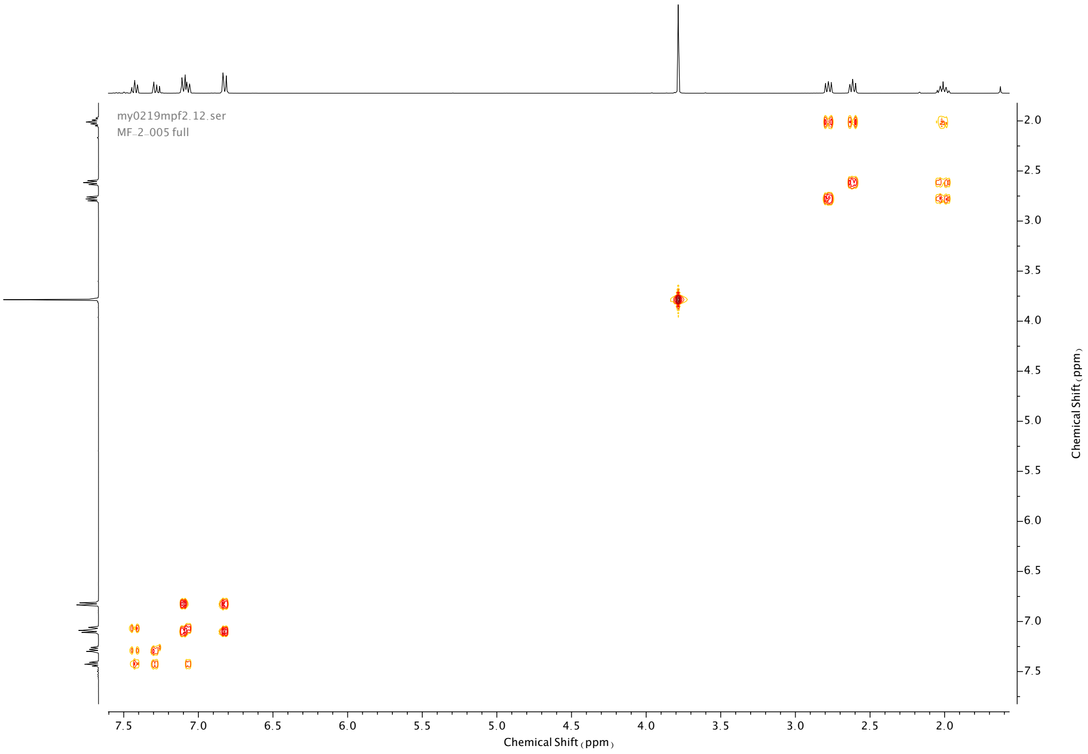

Figure **75**. COSY NMR ($CDCl_3$) of **22**.

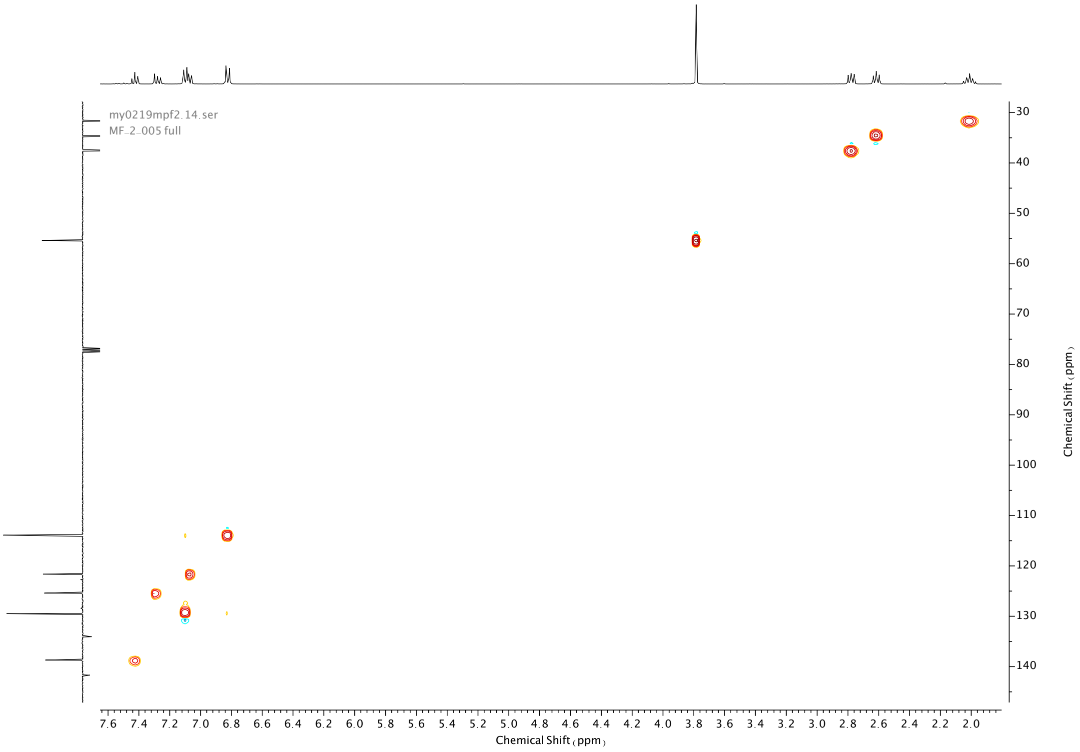

Figure **76**. HSQC NMR ($CDCl_3$) of **22**.

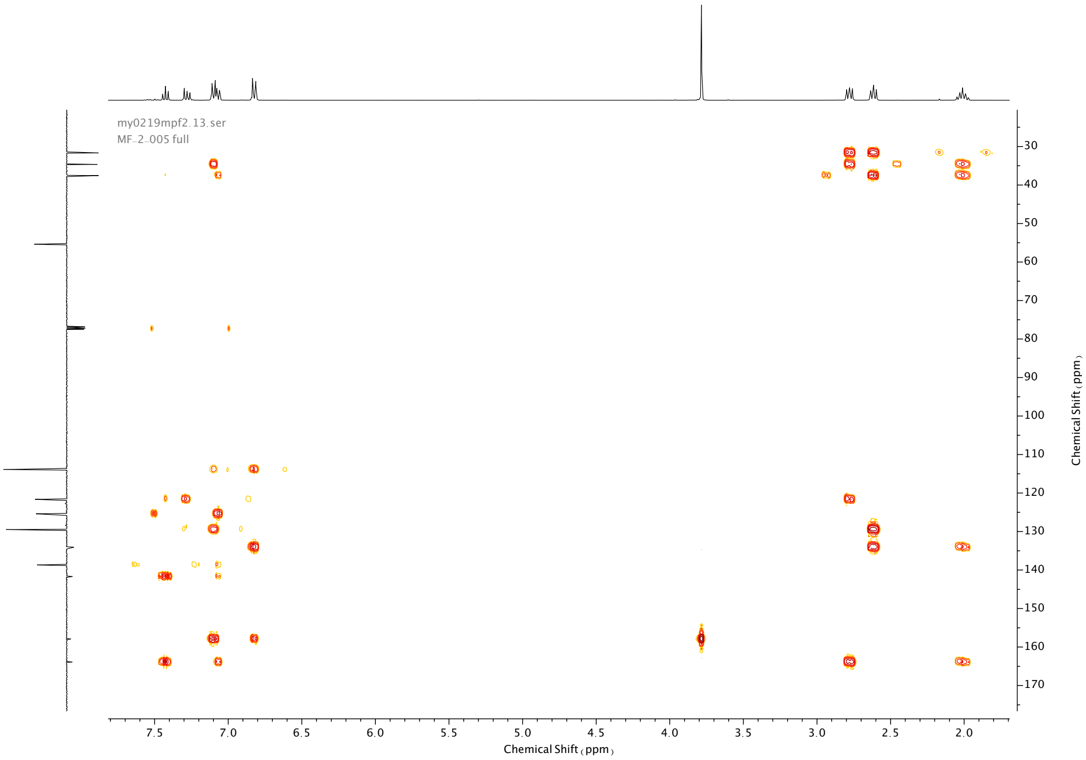

Figure **77**. HMBC NMR ($CDCl_3$) of **22**.

Compound **23**

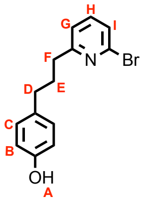

A solution of **22** (13.30 g, 43.59 mmol) in HBr (48% w/v in H_2O, 44 mL) was stirred vigorously at 130 °C overnight. The mixture was cooled to room temperature then diluted with H_2O (50 mL) and neutralized with 10M NaOH. The product was extracted from the aqueous phase with CH_2Cl_2 (3 x 100 mL), dried over anhydrous $MgSO_4$, filtered, then concentrated *in vacuo*. The crude product was purified by silica-gel chromatography (eluent 1:0 → 9:1 CH_2Cl_2 : Et_2O) to afford **23** as a white solid (10.50 g, 36.08 mmol, 83%).^{1}H NMR (400 MHz, $CDCl_3$, 298 K) δ_H 7.44 (1H, t, *J* = 7.7 Hz, H_H), 7.30 (1H, dd, *J* = 7.9, 0.9 Hz, H_I), 7.08 (1H, dd, *J* = 7.5, 0.9 Hz, H_G), 7.02 (2H, d, *J* = 8.7 Hz, H_C), 6.75 (2H, d, *J* = 8.5 Hz, H_B), 5.50 (1H, s, O-H_A), 2.80-2.75 (2H, m, H_F), 2.58 (2H, t, *J* = 7.7 Hz, H_D), 2.03-1.94 (2H, m, H_E).^{13}C NMR (101 MHz, $CDCl_3$, 298 K) δ_C 164.0, 154.0, 141.6, 138.9, 133.9, 129.6, 125.5, 121.8, 115.4, 37.5, 34.7, 31.7.

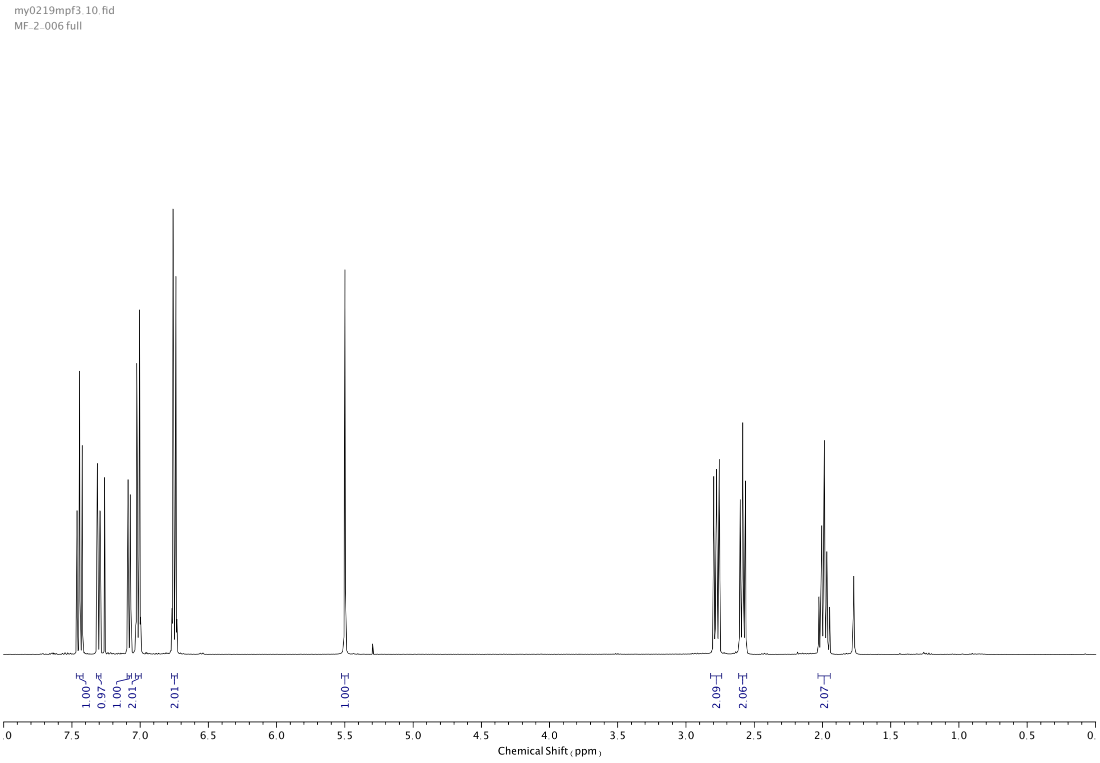

Figure **78**. ^{1}H NMR ($CDCl_3$, 400 MHz) of **23**.

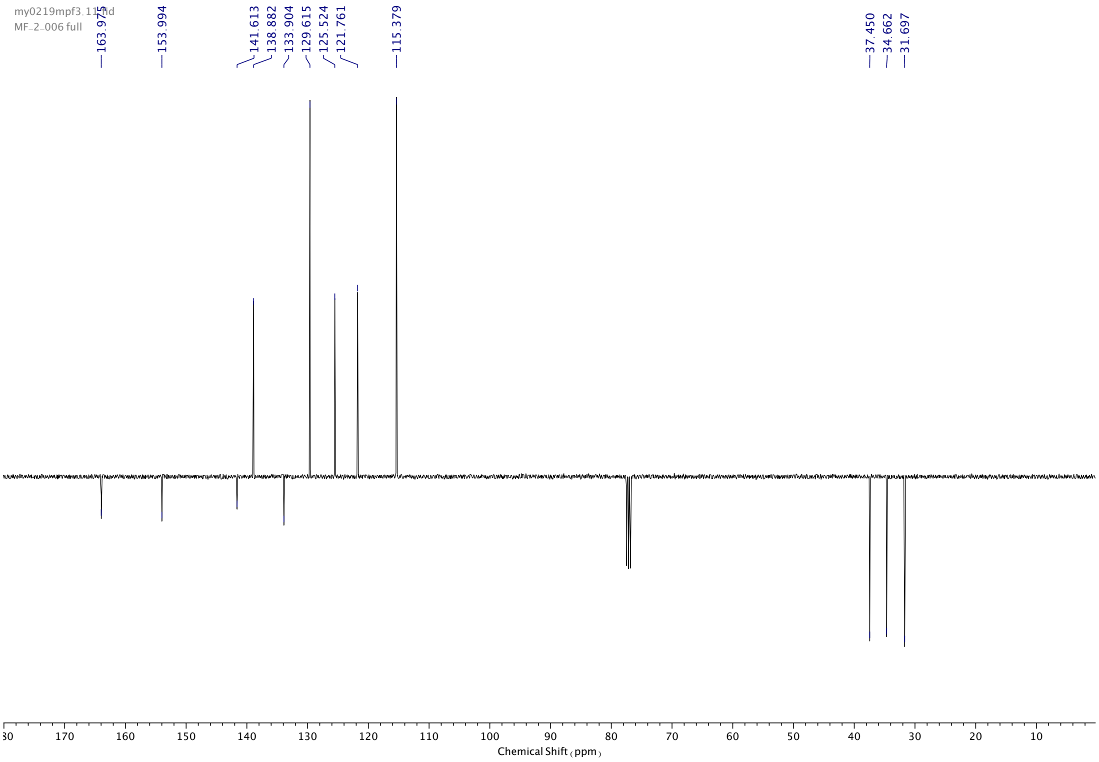

Figure **79**. ^{13}C NMR (CDCl$_3$, 101 MHz) of **23.**

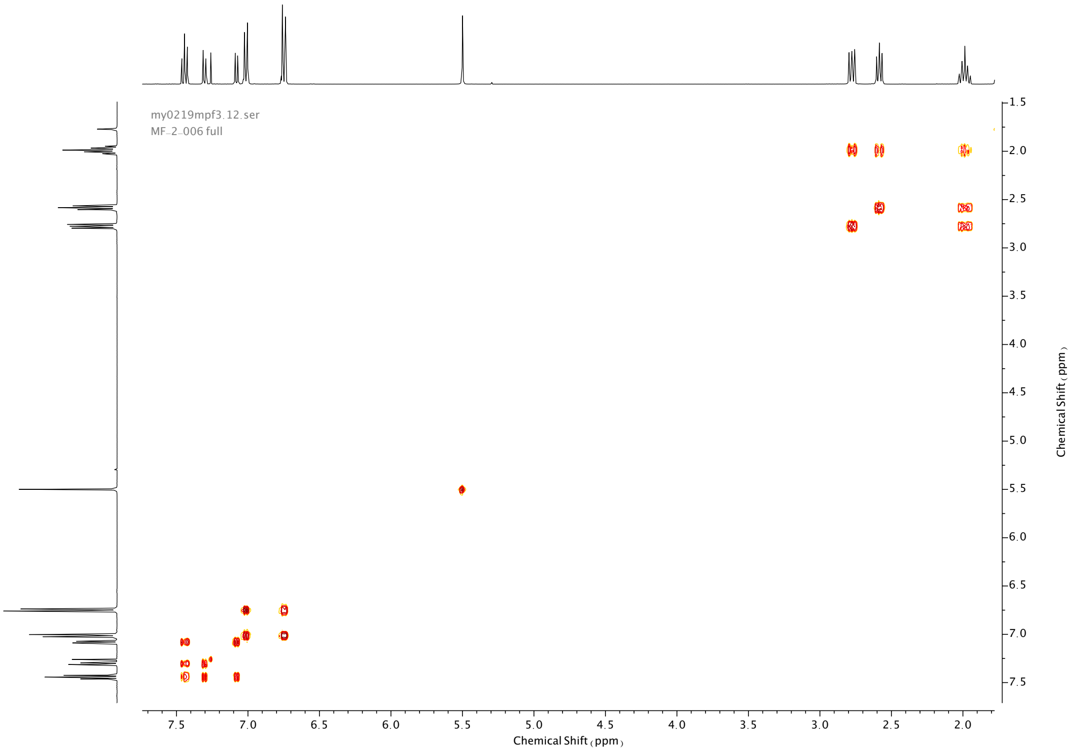

Figure **80**. COSY NMR (CDCl$_3$) of **23**.

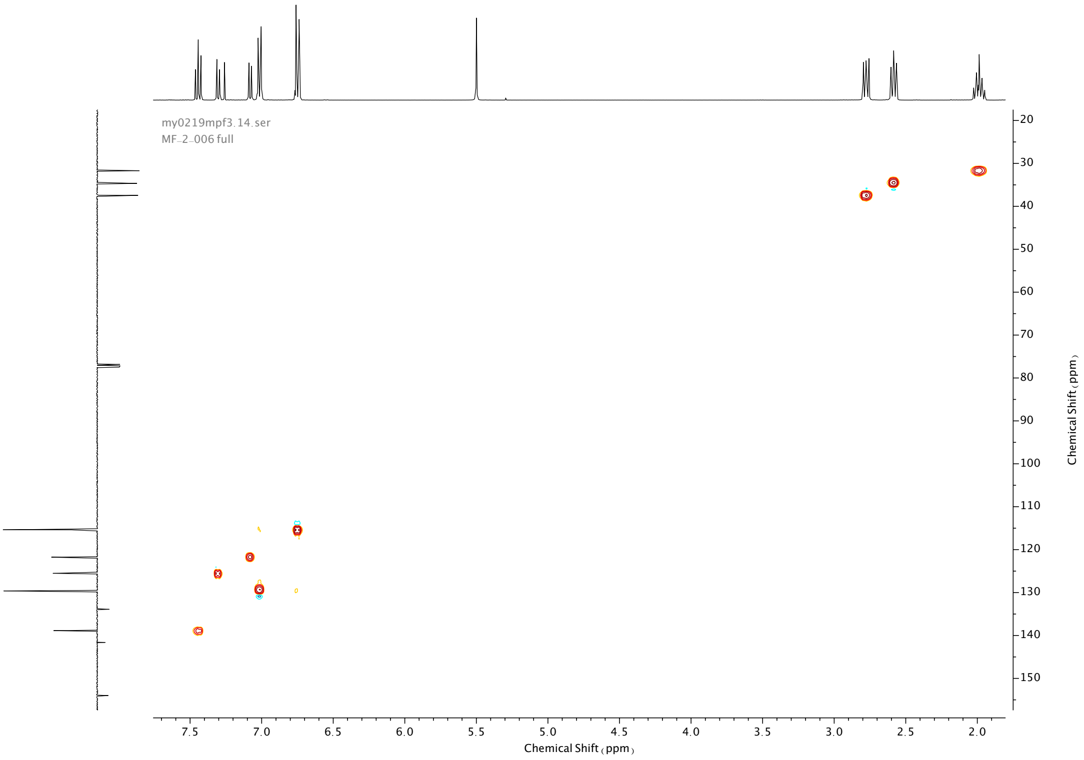

Figure **81**. HSQC NMR ($CDCl_3$) of **23**.

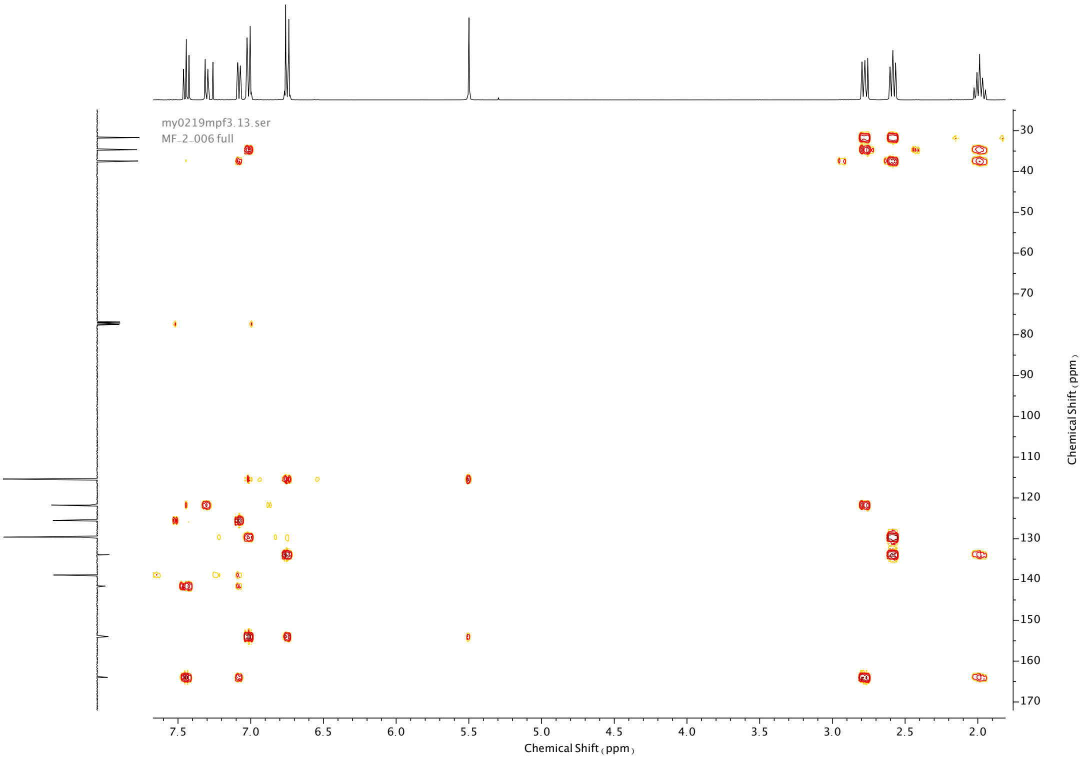

Figure **82**. HMBC NMR ($CDCl_3$) of **23**.

Compound **24**

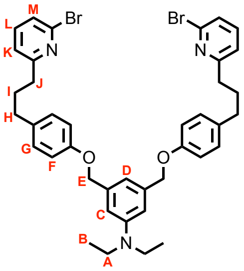

A solution of linker **18** (0.44 g, 1.81 mmol, 1.0 eq.), **23** (1.05 g, 3.61 mmol, 2.0 eq.) and K_2CO_3 (3.55 g, 14.48 mmol, 8.0 eq.) in DMF (50 mL) was stirred at 80 °C overnight. The mixture was then cooled to room temperature, diluted with CH_2Cl_2 (100 mL), washed with water (75 mL) and brine (75 mL), then dried over anhydrous $MgSO_4$, filtered, and concentrated *in vacuo.* The crude product was purified *via* silica-gel chromatography using a Biotage Isolute SPE column (eluent 1:0 → 9:1 Petrol: EtOAc) to afford **24** as a yellow-orange oil (1.10 g, 1.46 mmol, 96%). ^{1}H NMR (400 MHz, $CDCl_3$, 298 K) δ_H 7.42 (2H, t, *J* = 7.7 Hz, H_L), 7.29 (2H, dd, *J* = 7.9, 0.9 Hz, H_M), 7.11-7.05 (6H, m, H_K & H_G), 6.91 (4H, d, *J* = 8.7 Hz, H_F), 6.77-6.74 (1H, m, H_D), 6.67 (2H, d, *J* = 1.4 Hz, H_C), 4.99 (4H, s, H_E), 3.35 (4H, q, *J* = 7.1 Hz, H_B), 2.80-2.75 (4H, m, H_J), 2.61 (4H, t, *J* = 7.6 Hz, H_H), 2.06-1.96 (4H, m, H_I), 1.13 (6H, t, *J* = 7.0 Hz, H_A). ^{13}C NMR (101 MHz, $CDCl_3$, 298 K) δ_C 163.9, 157.4, 148.4, 141.7, 138.7, 138.6, 134.2, 129.5, 125.4, 121.7, 114.9, 113.8, 110.5, 70.8, 44.5, 37.6, 34.7, 31.6, 12.7. HR-ESI-MS (CH_3CN): *m/z* = 758.1775 $[M+H]^+$ calc. 756.1795.

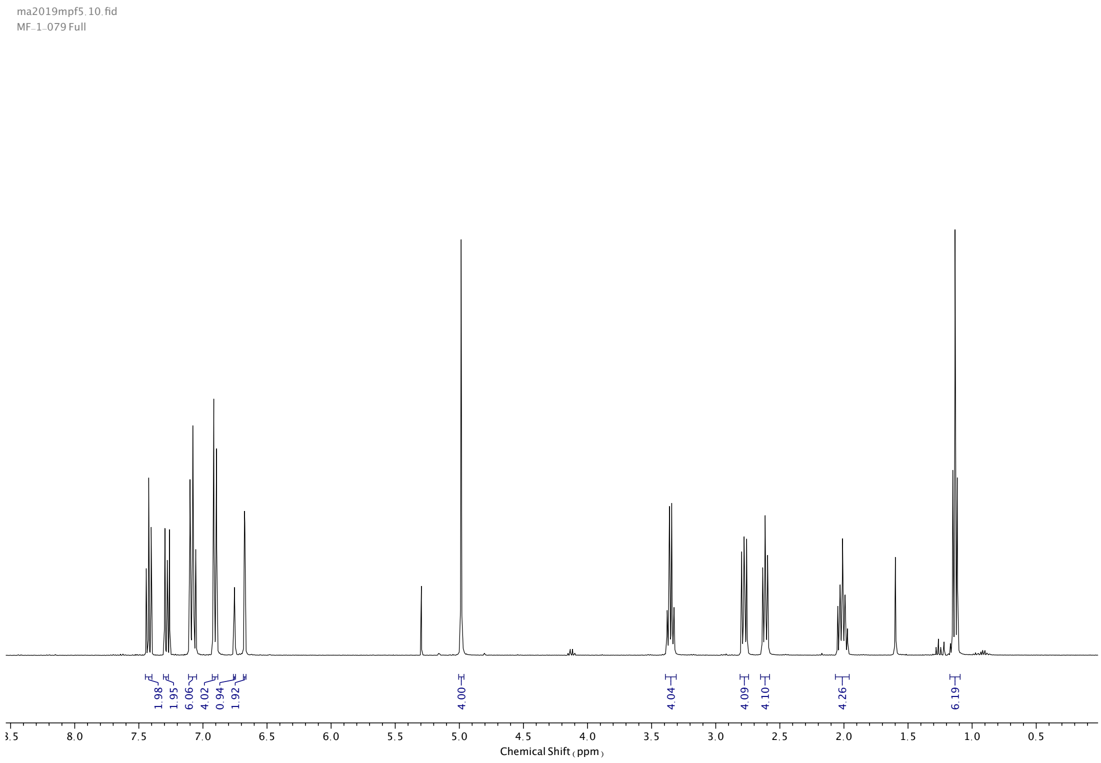

Figure **83**. ^{1}H NMR (CDCl$_3$, 400 MHz) of **24**.

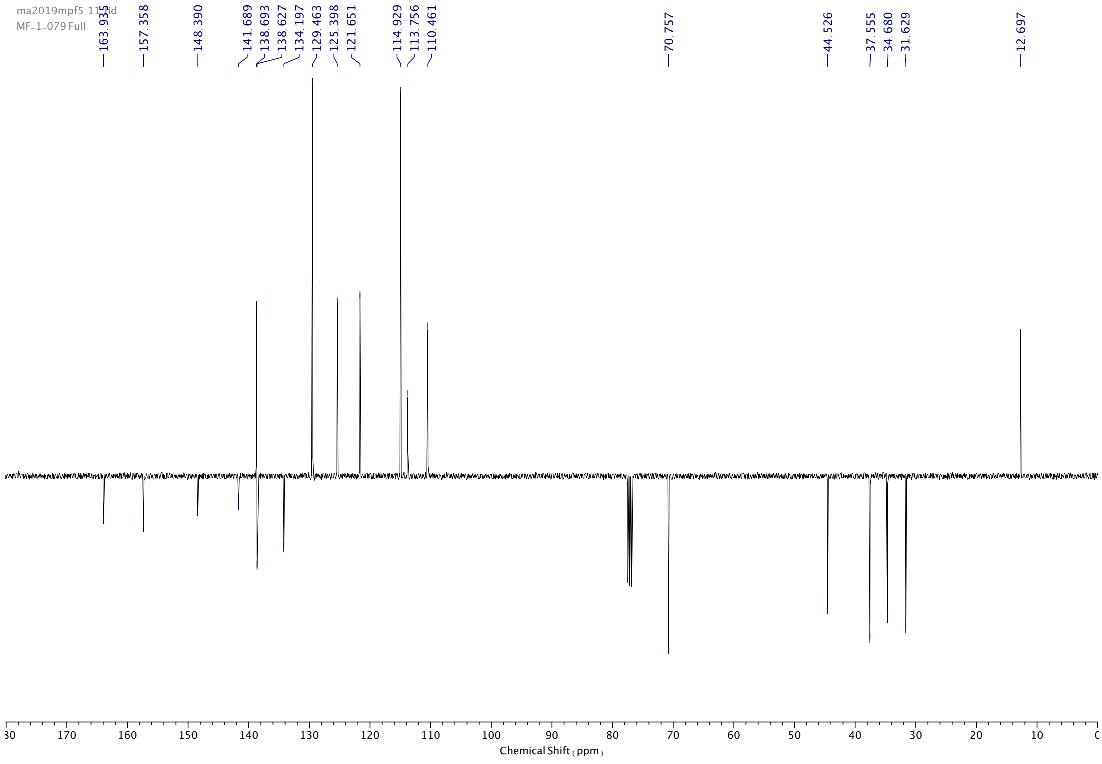

Figure **84**. ^{13}C NMR (CDCl$_3$, 101 MHz) of **24.**

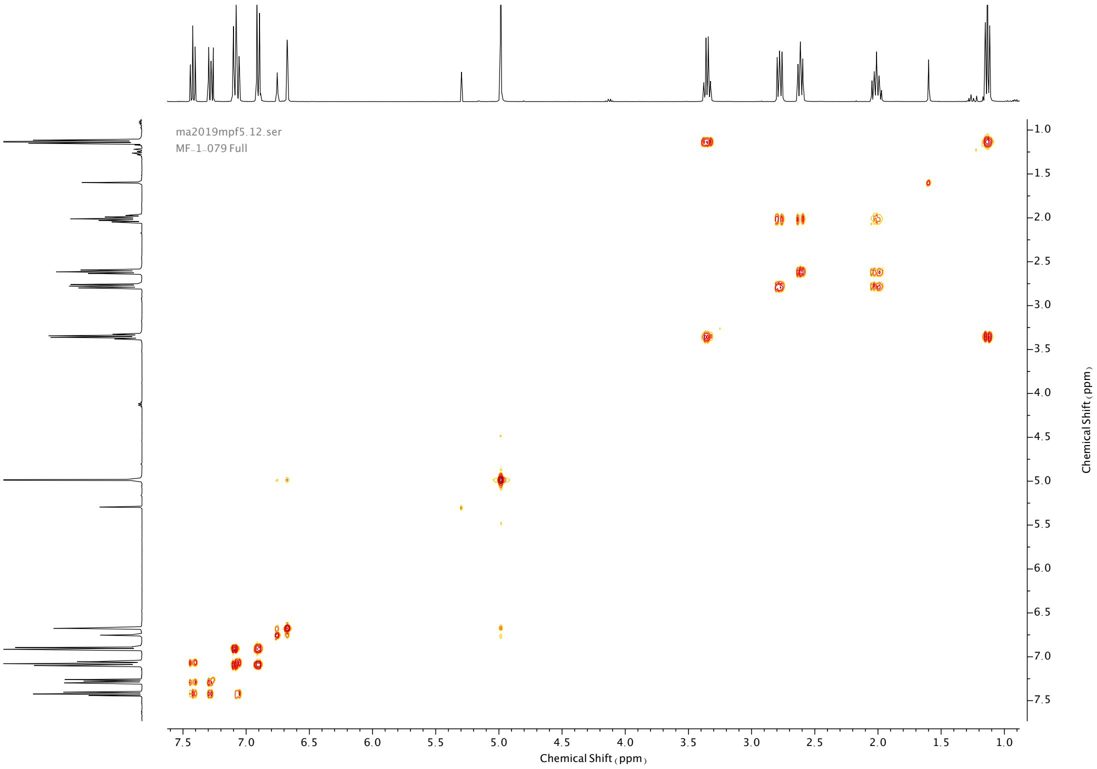

Figure **85**. COSY NMR ($CDCl_3$) of **24**.

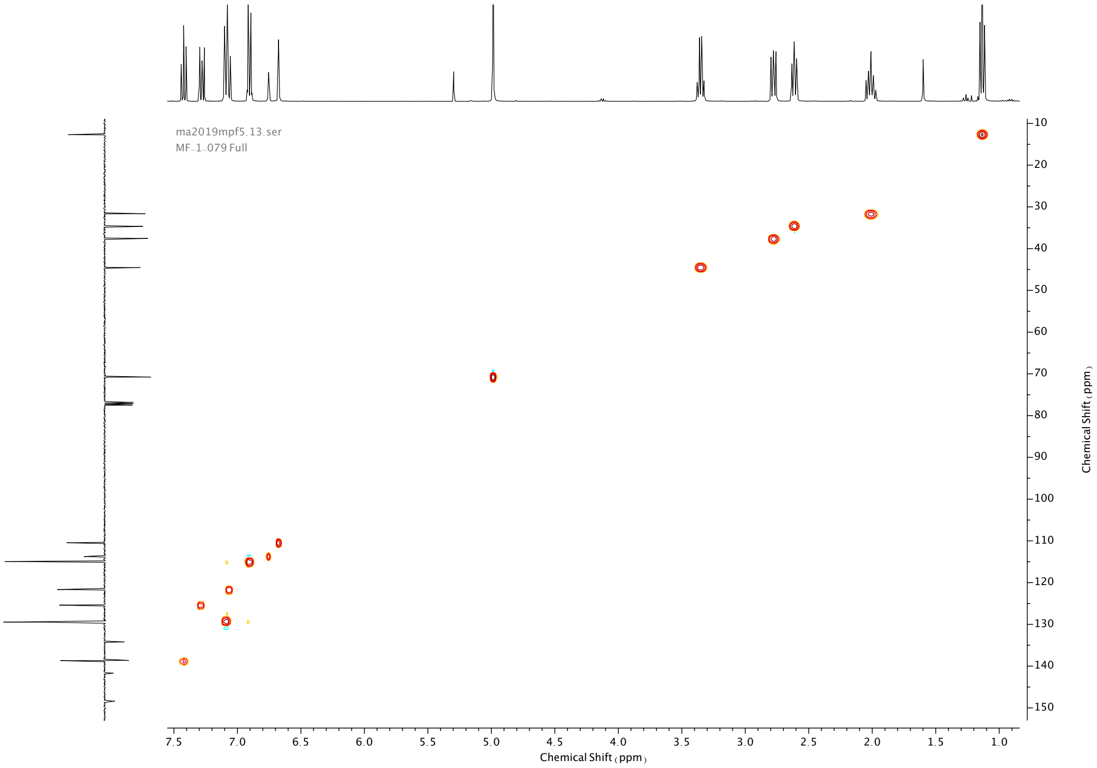

Figure **86**. HSQC NMR ($CDCl_3$) of **24**.

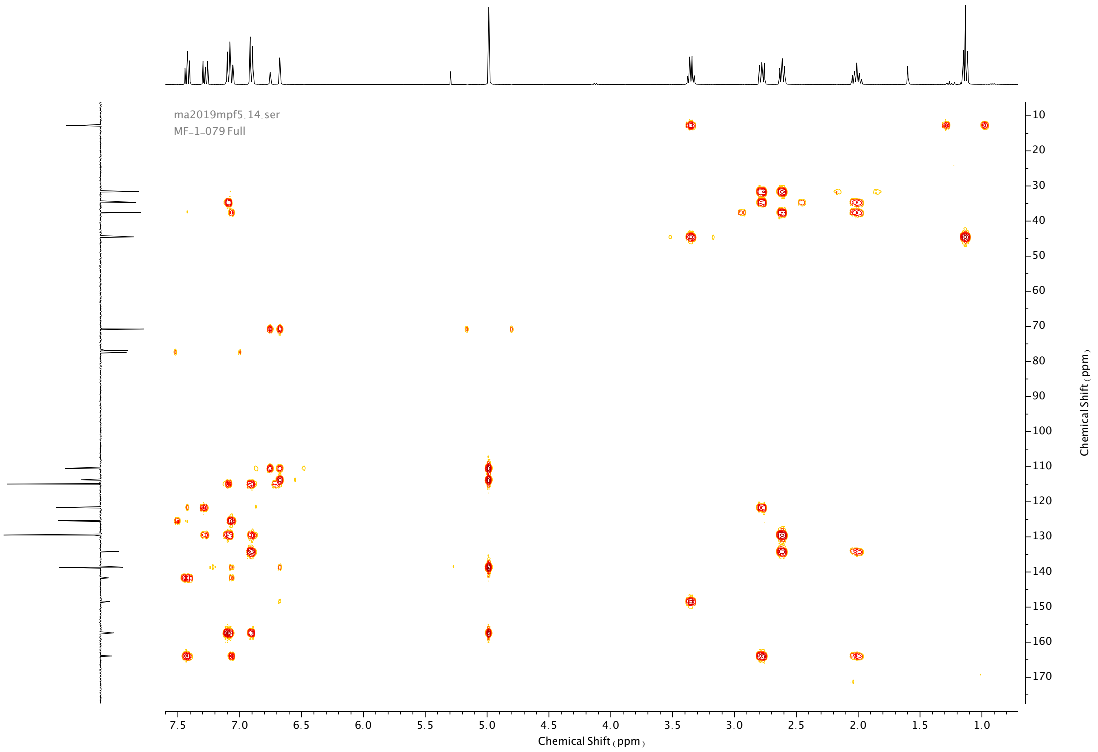

Figure **87**. HMBC NMR (CDCl$_3$) of **24**.

Compound **25**

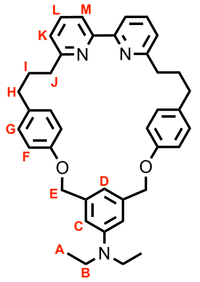

$[Ni(PPh_3)_2Br_2]$ (251 mg, 0.40 mmol, 1.0 eq.), PPh_3 (178 mg, 0.68 mmol, 2.0 eq.), NEt_4I (87 mg, 0.40 mmol, 1.0 eq.) and Mn (186 mg, 3.39 mmol, 10.0 eq.) were added to an oven-dried CEM microwave vial and degassed under N_2. Anhydrous DMF (3.4 mL) was added and the mixture sonicated for 15 min, followed by stirring at 50 °C for a further 15 min. To the activated catalyst mixture was added macrocycle precursor **24** (256 mg, 0.40 mmol, 1.0 eq.) in anhydrous DMF (3.4 mL) *via* syringe pump over 4 h at 50 °C, followed by additional stirring for 30 min. The mixture was then cooled to room temperature, diluted with CH_2Cl_2 (20 mL) and washed with EDTA-NH_3 (15 mL) then brine (15mL). Combined aqueous washings were extracted with CH_2Cl_2 (2 x 15 mL). The combined organic extracts were dried over anhydrous $MgSO_4$, filtered and concentrated *in vacuo*. The crude product was purified via silica-gel chromatography using a Biotage Isolute SPE column (eluent 1:0 → 9:1 (petrol : CH_2Cl_2 1:1) : EtOAc) to afford **25** as an off-white foam (139 mg, 0.23 mmol, 58%). ^{1}H NMR (400 MHz, $CDCl_3$, 298 K) δ_H 7.77 (2H, dd, *J* = 7.8, 1.0 Hz, H_M), 7.58 (2H, t, *J* = 7.7 Hz, H_L), 7.07 (2H, dd, *J* = 7.6, 1.0 Hz, H_K) 6.91 (4H, app. d, *J* = 8.8 Hz, H_G), 6.67 (4H, app. d, 8.9 Hz, H_F), 6.55-6.52 (3H, m, H_C, H_D), 5.00 (4H, s, H_E), 3.29 (4H, q, *J* = 7.1 Hz, H_B), 2.90 (4H, t, *J* = 7.1 Hz, H_J), 2.59 (4H, t, *J* = 7.8 Hz, H_H), 2.09 (4H, quint, *J* = 7.3 Hz, H_I), 1.09 (6H, t, *J* = 7.0 Hz, H_A). ^{13}C NMR (101 MHz, $CDCl_3$, 298 K) δ_C 161.9, 157.0, 156.7, 148.4, 139.2, 136.7, 134.7, 129.4, 122.6, 119.1, 115.4, 112.6, 109.1, 70.7, 44.4, 37.9, 34.4, 31.4, 12.7. HR-ESI-MS (CH_3CN): *m/z* = 598.343 $[M+H]^+$ calc. 598.3428.

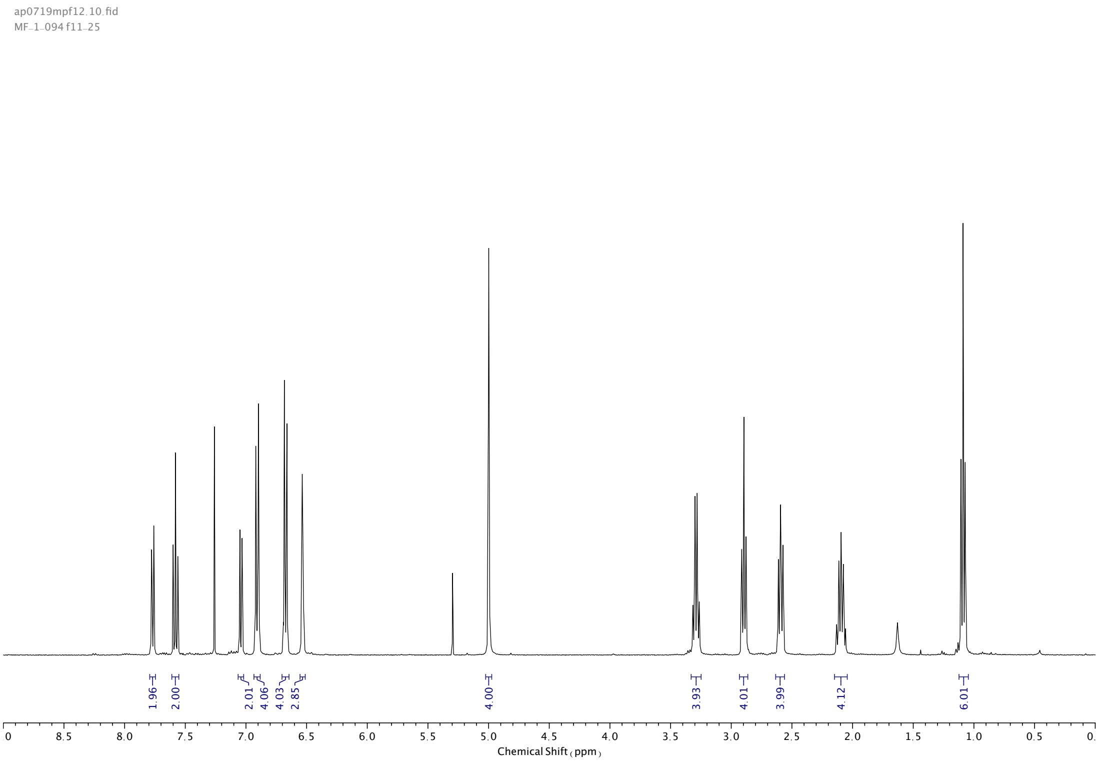

Figure **88**. ^{1}H NMR (CDCl$_3$, 400 MHz) of **25**.

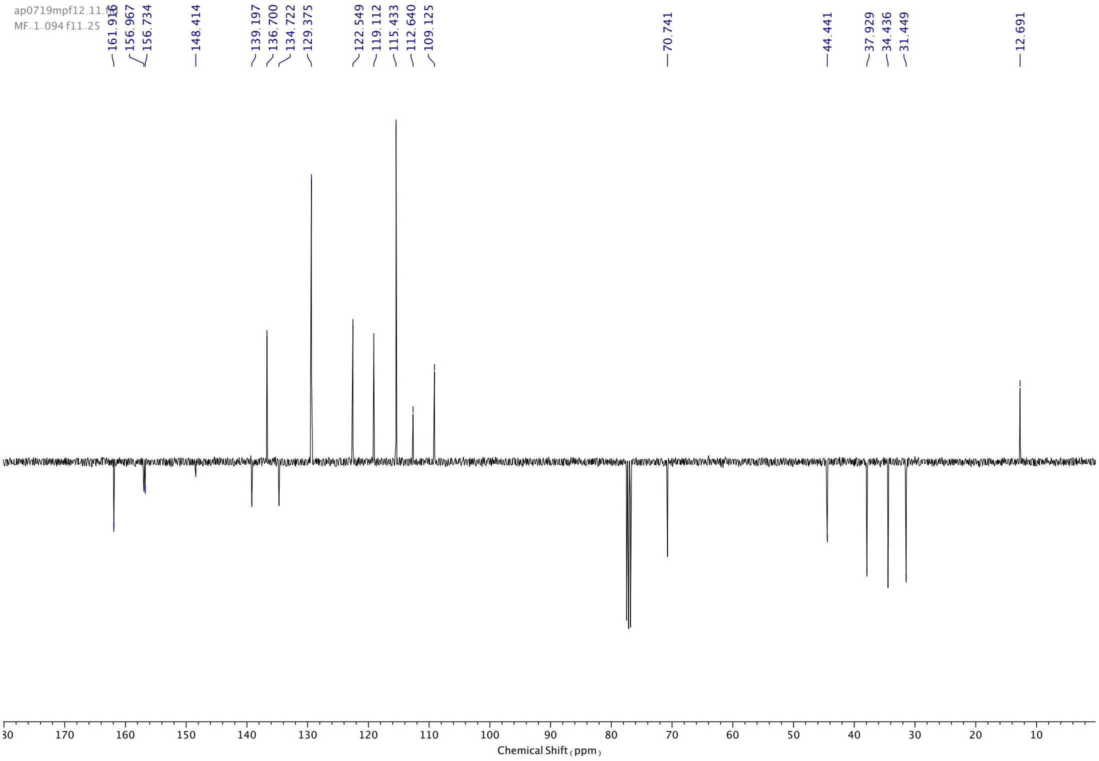

Figure **89**. ^{13}C NMR (CDCl$_3$, 101 MHz) of **25.**

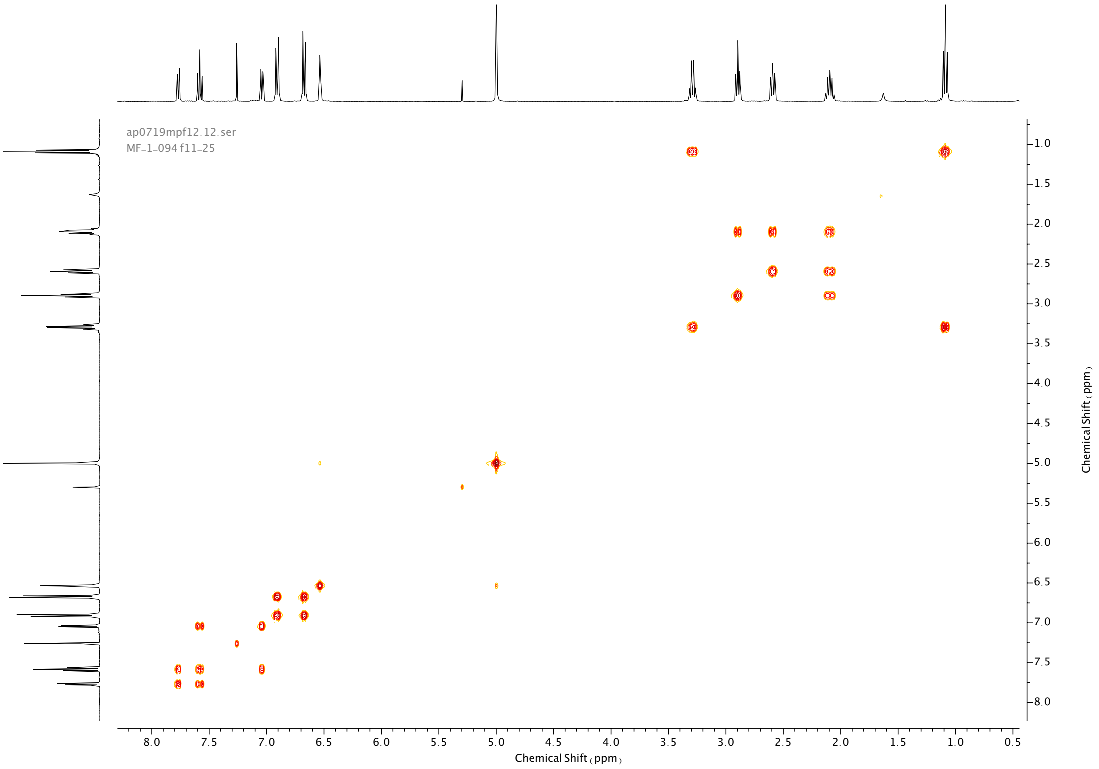

Figure **90**. COSY NMR ($CDCl_3$) of **25**.

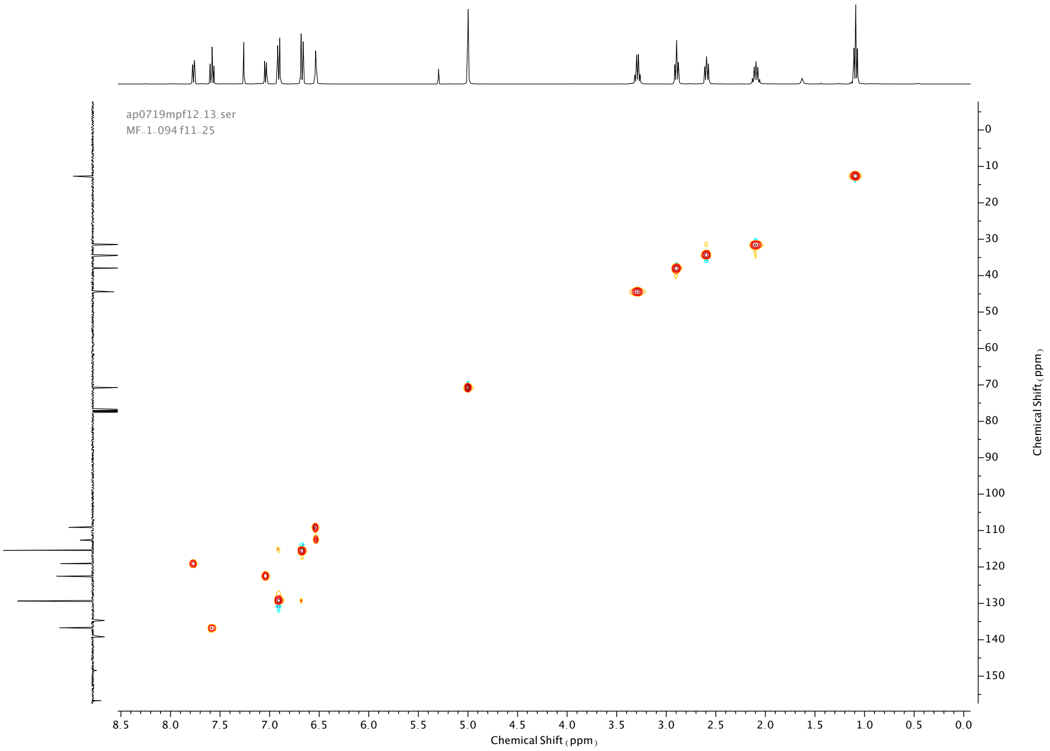

Figure **91**. HSQC NMR ($CDCl_3$) of **25**.

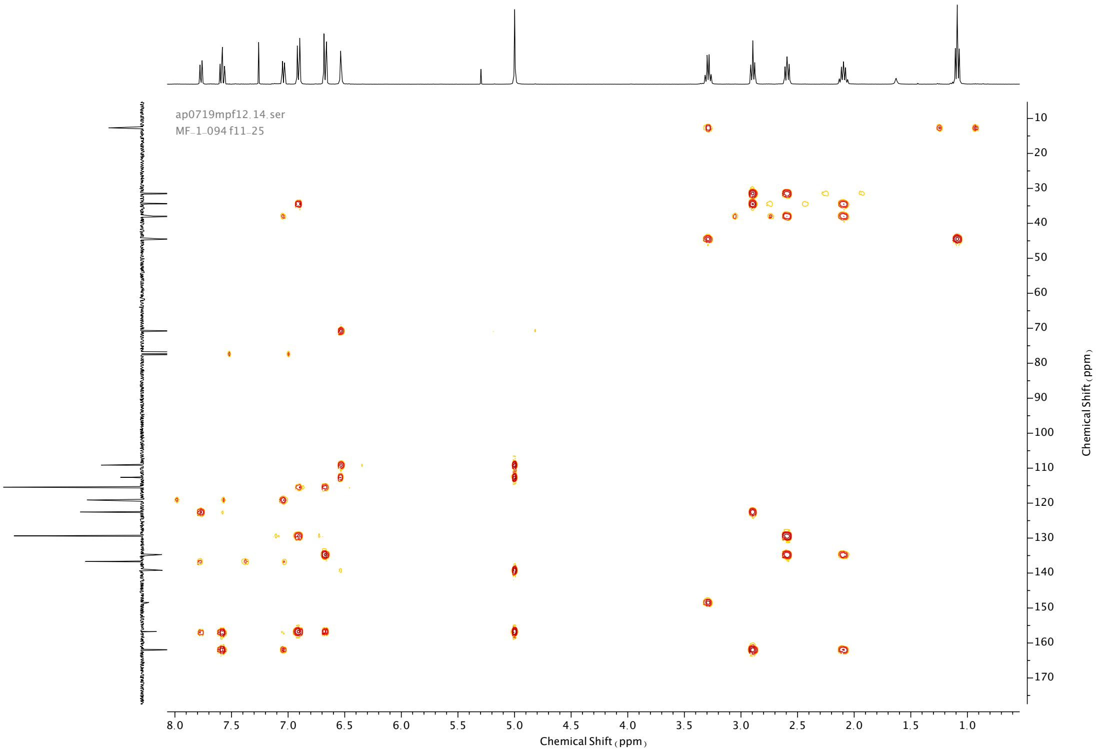

Figure **92**. HMBC NMR ($CDCl_3$) of **25**.

Compound **27**

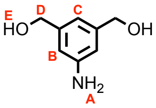

To a pre-dried flask containing $LiAlH_4$ (1.82 g, 47.83 mmol, 2.0 eq.) was added a solution of **26** (5.0 g, 47.83 mmol, 1.0 eq.) in anhydrous THF (100 mL) at 0 °C over 1 h, then allowed to reach room temperature and stirred overnight. The mixture was quenched at -10 °C through the sequential addition of EtOAc (10 mL), H_2O (1.8 mL), 10M NaOH (1.8 mL), then H_2O (4 mL) again. The resulting mixture was stirred at room temperature for a further 2 h, diluted in THF (50 mL), dried over anhydrous $MgSO_4$, filtered, and concentrated *in vacuo.* The crude product was purified *via* silica-gel chromatography using a Biotage Isolute SPE column (eluent 19:1→ 9:1 CH_2Cl_2: MeOH) to afford **27** as an off-white solid (3.51 g, 22.92 mmol, 96%). ^{1}H NMR (400 MHz, DMSO-d_6, 298 K) δ_H 6.42 (1H, s, H_C), 6.41 (2H, s, H_C), 5.01 (2H, t, *J* = 5.8 Hz, O-H_E), 4.91 (2H, br. s, N-H_A) 4.33 (4H, d, *J* = 5.7 Hz, H_D).^{13}C NMR (101 MHz, DMSO-d_6, 298 K) δ_C 148.3, 142.9, 112.7, 110.6, 63.4.

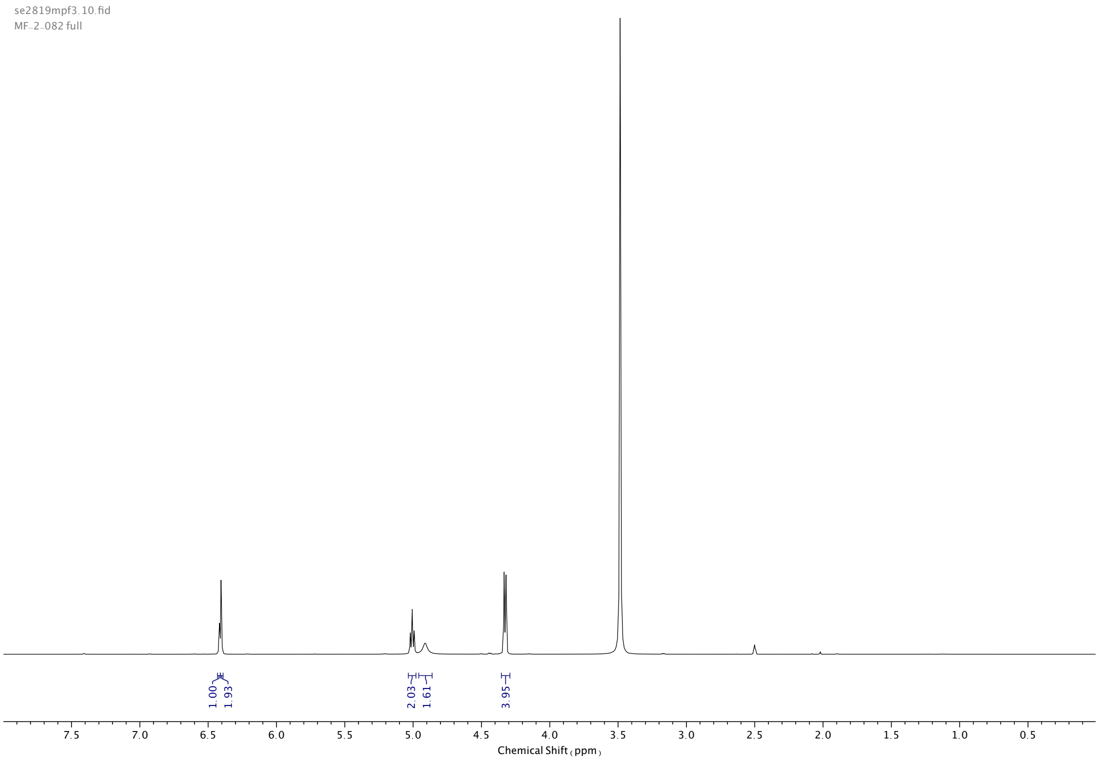

Figure **93**. ^{1}H NMR (DMSO-d_6, 400 MHz) of **27**.

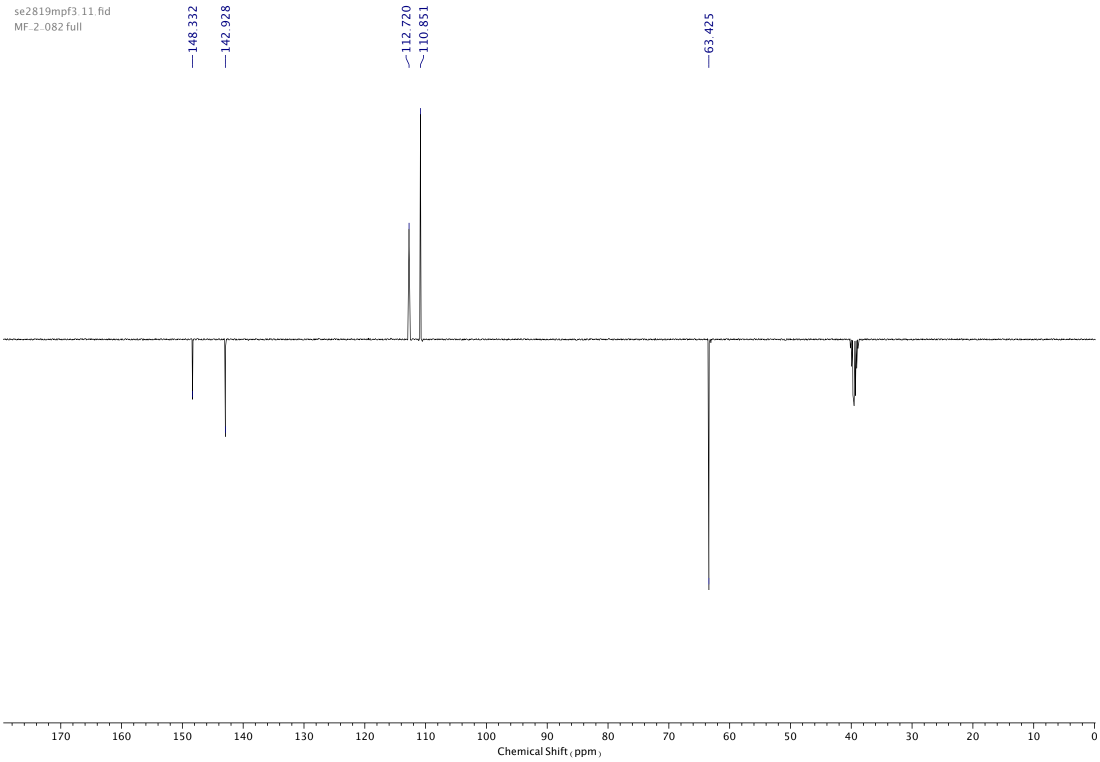

Figure **94**. ^{13}C NMR (DMSO-d_6, 101 MHz) of **27.**

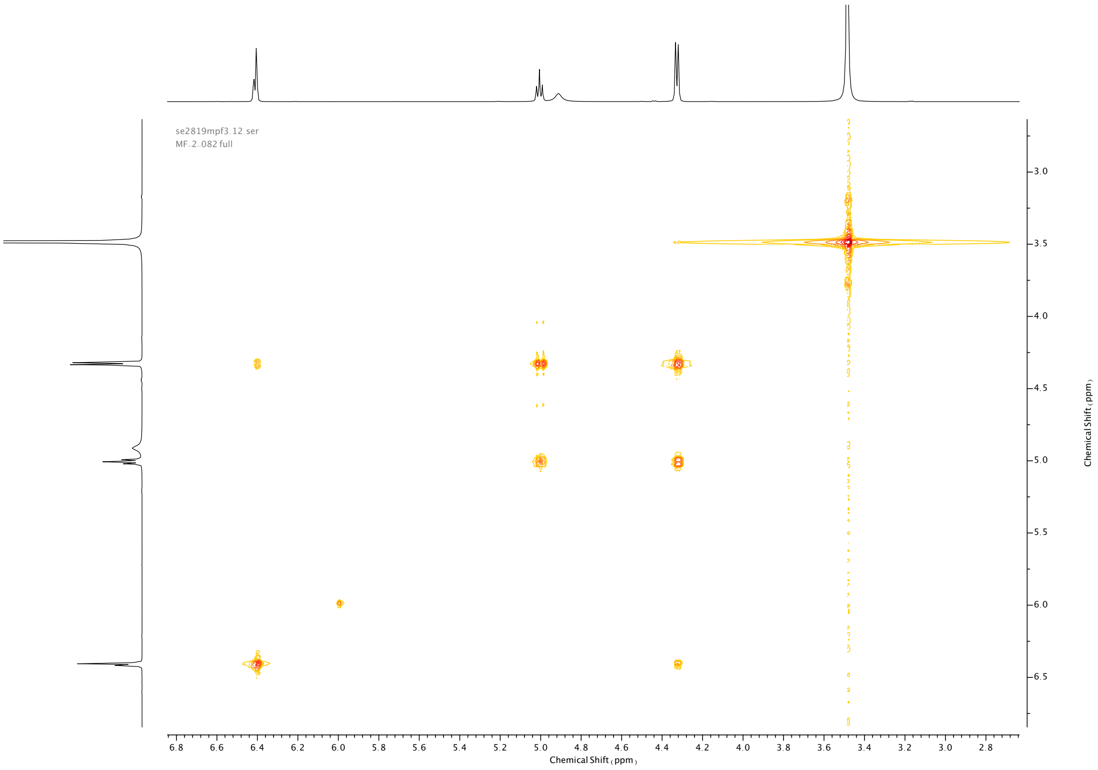

Figure **95**. COSY NMR (DMSO-d_6) of **27**.

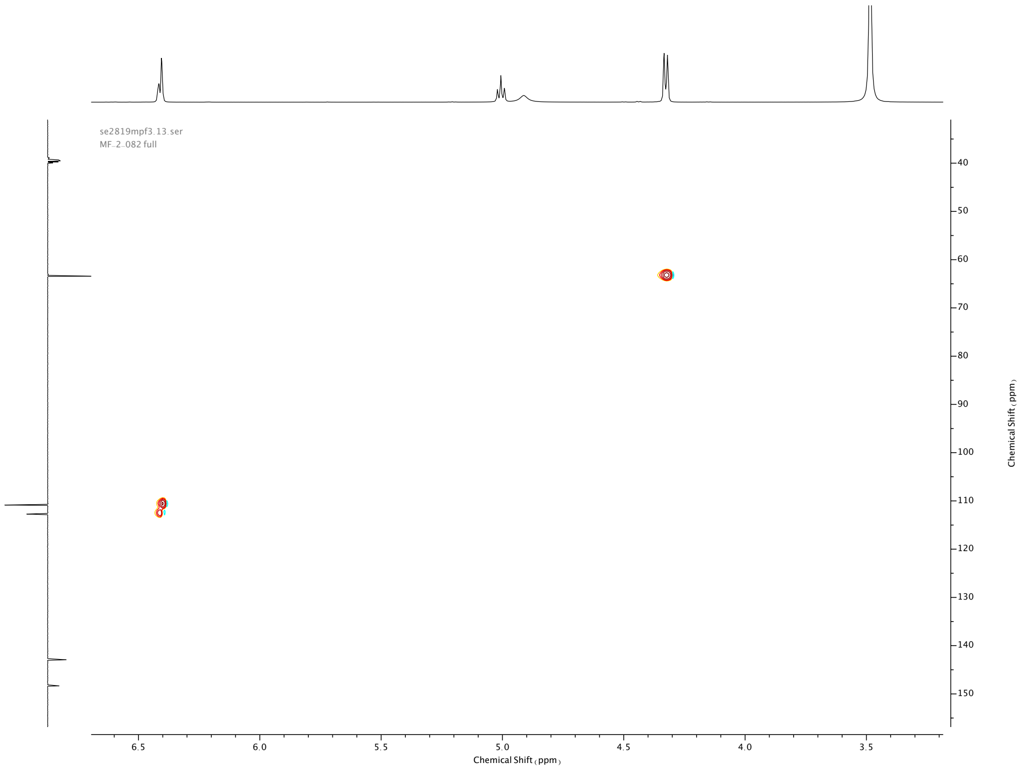

Figure **96**. HSQC NMR (DMSO-d_6) of **27**.

Figure **97**. HMBC NMR (DMSO-d_6) of **27**.

Compound **28**

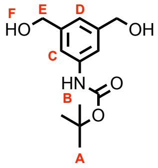

To a mixture of **27** (866 mg, 5.66 mmol, 1.0 eq.) and DIPEA (1.97 mL, 11.31 mmol, 2.0 eq.) in anhydrous DMF (50 mL) was added Boc$_2$O (1.36 g, 6.22 mmol, 1.1 eq.) in anhydrous DMF (5 mL) over 10 min. The resulting mixture was stirred overnight at room temperature then diluted with EtOAc (50 mL) and washed with H_2O (30 mL) then brine (30 mL). The combined aqueous phases were extracted with EtOAc (3 x 20 mL). Combined organic extracts were dried over anhydrous $MgSO_4$, filtered, then concentrated *in vacuo*. The crude product which was purified *via* silica-gel chromatography using a Biotage Isolute SPE column (eluent 19:1 CH_2Cl_2: MeOH) to afford **28** as a white solid (1.25 g, 4.94 mmol, 87%). ^{1}H NMR (400 MHz, MeOD, 298 K) δ_H 7.32 (2H, s, H$_D$), 7.01 (1H, m, H$_C$), 4.86, (4H, s, H$_E$), 1.52 (9H, s, H$_A$). ^{13}C NMR (101 MHz, MeOD, 298 K) δ_C 155.3, 143.5, 140.7, 120.8, 117.3, 80.8, 65.2, 28.7.

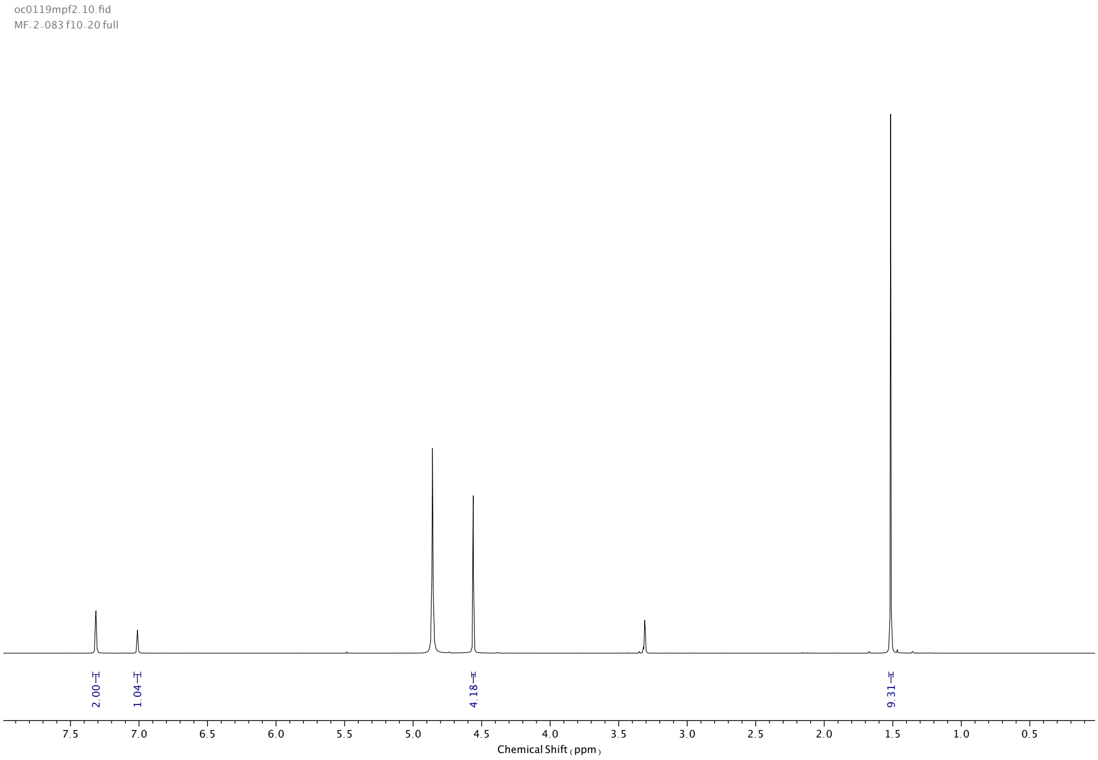

Figure **98**. ^{1}H NMR (MeOD, 400 MHz) of **28**.

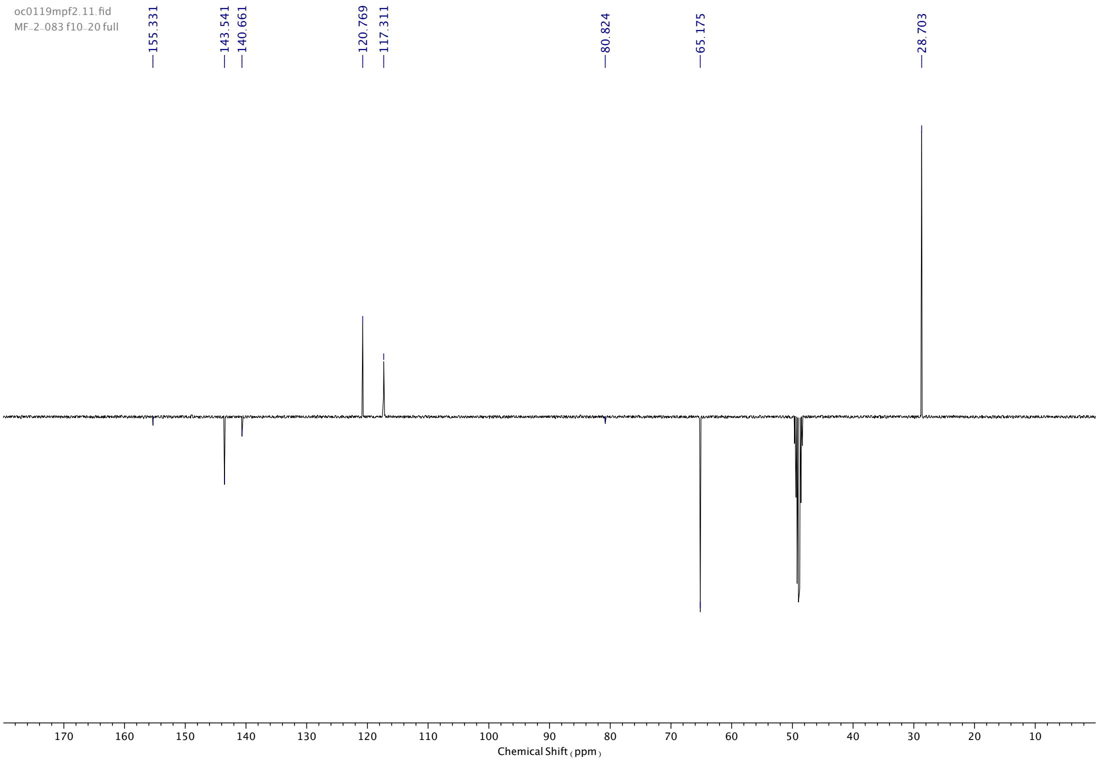

Figure **99**. ^{13}C NMR (MeOD, 101 MHz) of **28.**

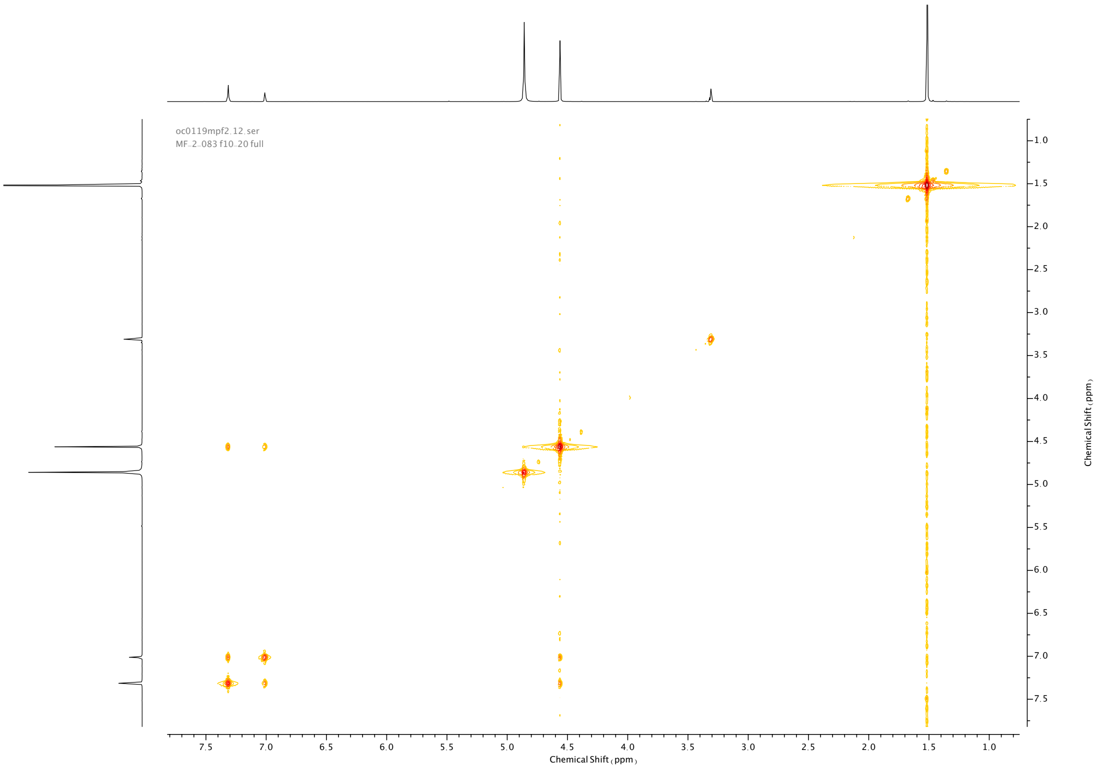

Figure **100**. COSY NMR (MeOD) of **28**.

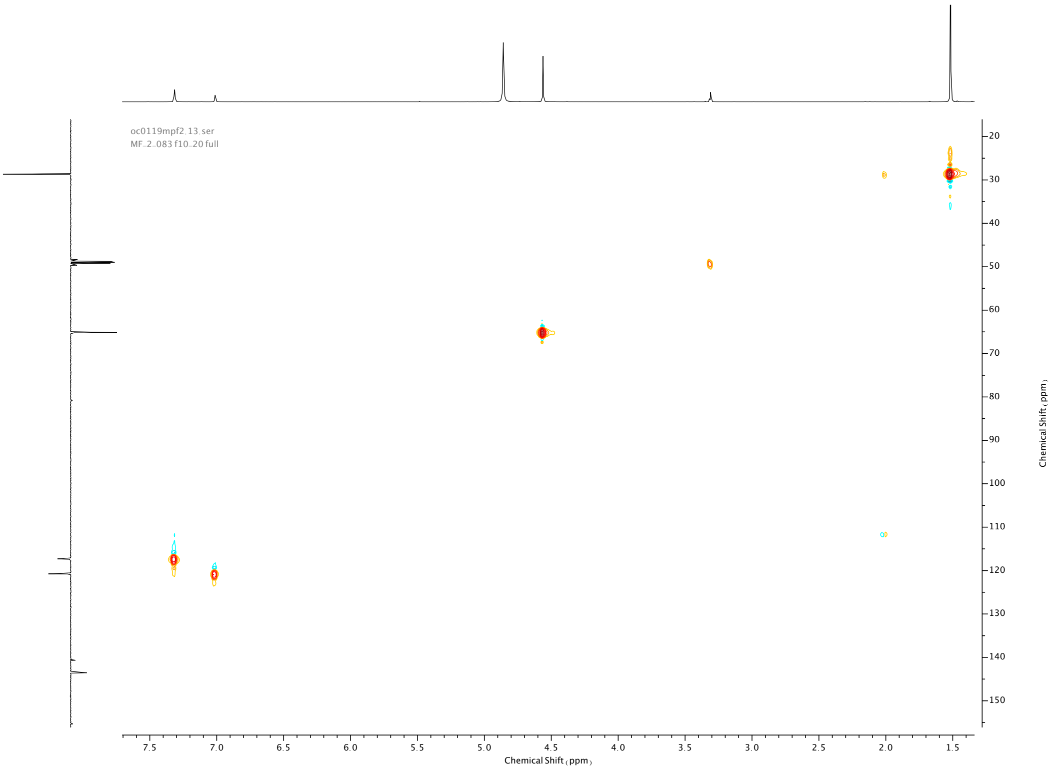

Figure **101**. HSQC NMR (MeOD) of **28**.

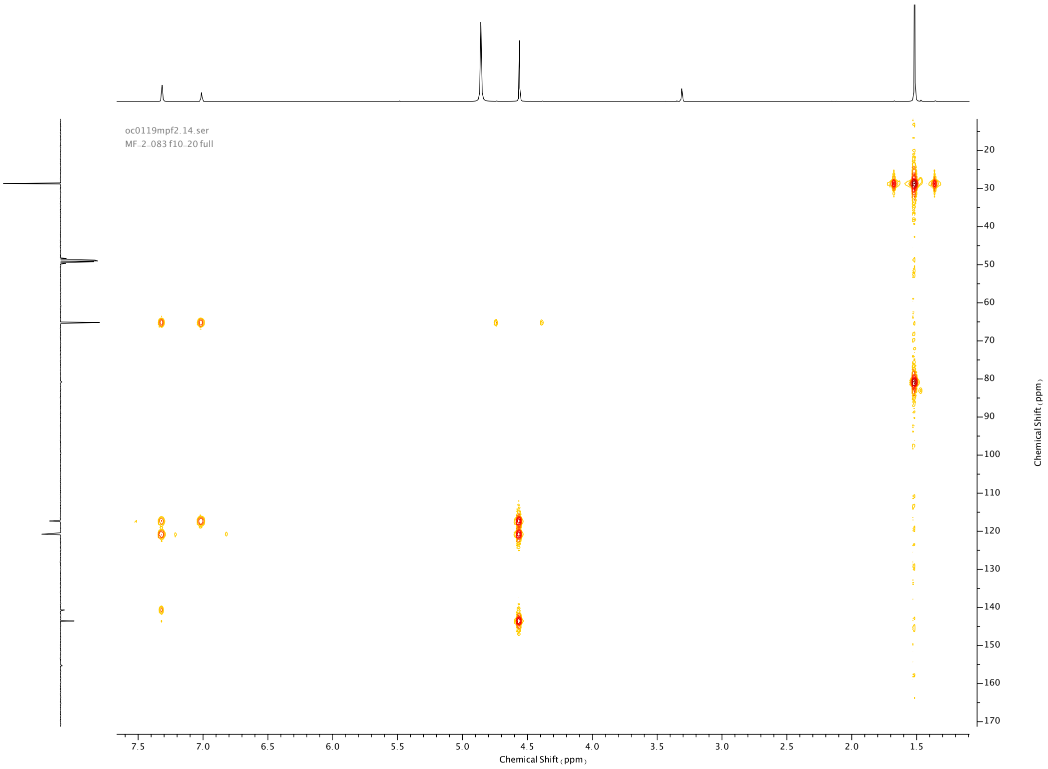

Figure **102**. HMBC NMR (MeOD) of **28**.

Compound **29**

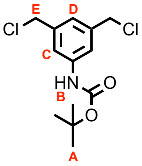

To a solution of **28** (1.25 g, 4.95 mmol, 1.0 eq.) and NEt_3 (1.3 mL, 9.87 mmol, 2.0 eq.) in anhydrous THF (40 mL) at 0 °C was added $SOCl_2$ (3.12 mL, 43.0 mmol, 3.0 eq.) over 10 min. The resulting solution was stirred at 0 °C for 30 min then at room temperature overnight. The mixture was diluted with CH_2Cl_2 (50 mL), quenched with H_2O (25 mL), neutralized with $NaHCO_3$ (20mL), and extracted with CH_2Cl_2 (3 x 75 mL). Combined organic extracts were dried over anhydrous $MgSO_4$, filtered, and concentrated *in vacuo*. The crude product was purified *via* silica-gel chromatography using a Biotage Isolute SPE column (eluent 4:1 → 2:3 petrol: Et_2O, silica deactivated) to afford **29** as a pale-yellow oil (707 mg, 2.47 mmol, 50%). ^1H NMR (400 MHz, $CDCl_3$, 298 K) δ_H 7.38 (2H, d, *J* = 1.4 Hz, H_C), 7.09 (1H, t, *J* = 1.6 Hz), 6.54 (1H, br. s, N-H_B), 4.54 (4H, s, H_E), 1.52 (9H, s, H_A).^{13}C NMR (101 MHz, $CDCl_3$, 298 K) δ_C 152.7, 139.3, 139.0, 123.2, 118.5, 81.2 (HMBC) 45.8, 28.4.

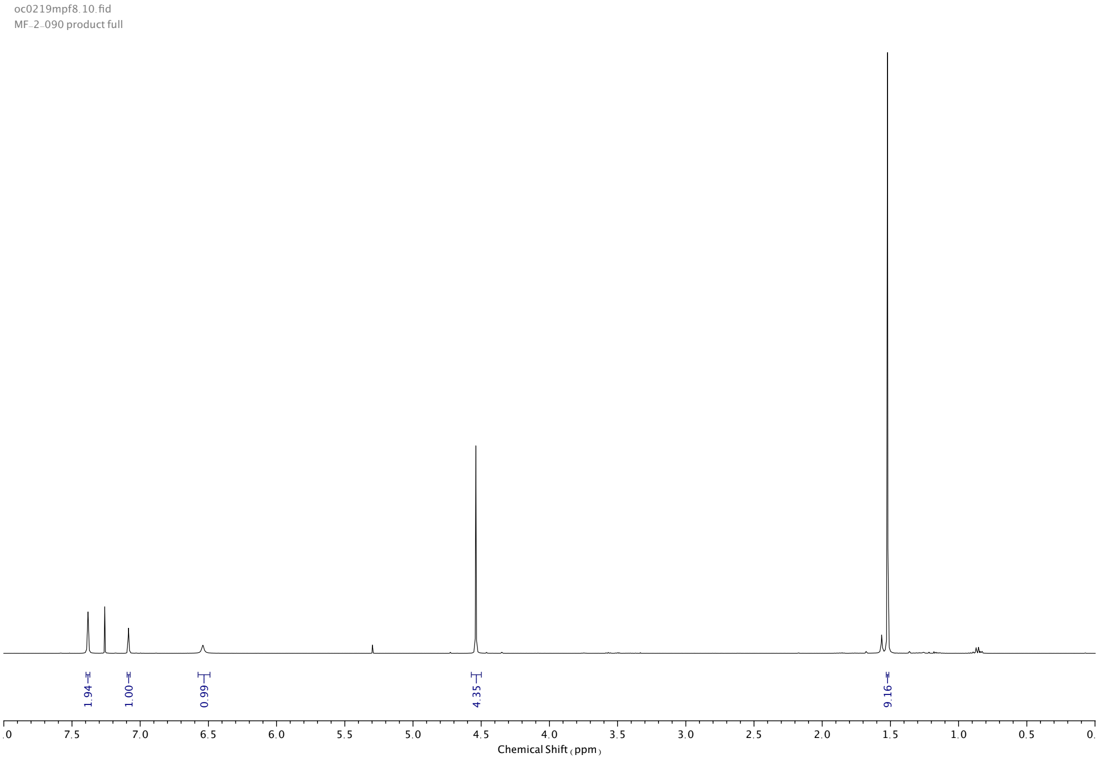

Figure **103**. ^1H NMR ($CDCl_3$, 400 MHz) of **29**.

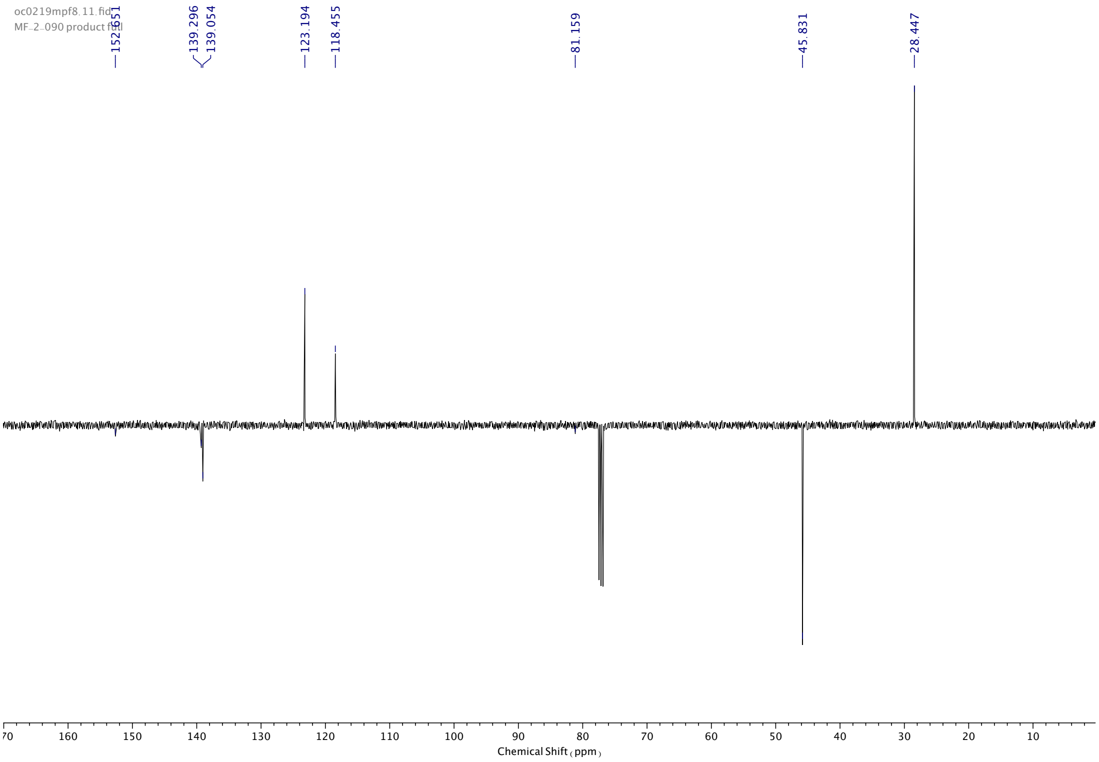

Figure **104**. ^{13}C NMR (CDCl$_3$, 101 MHz) of **29.**

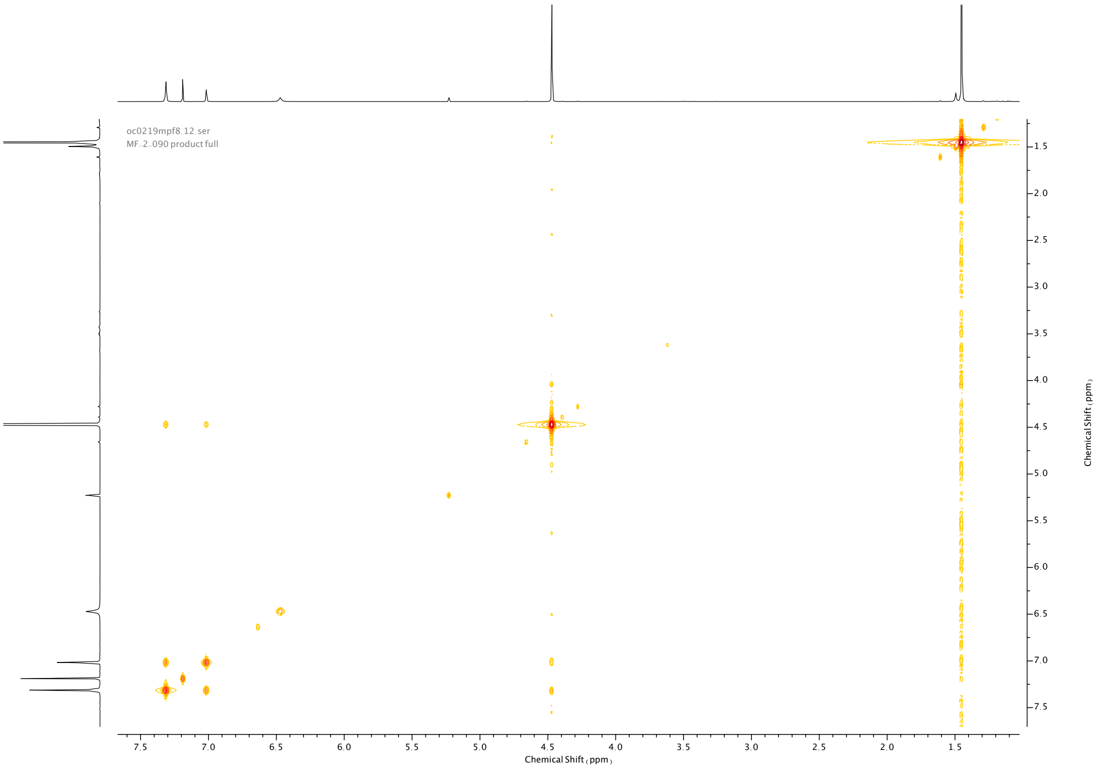

Figure **105**. COSY NMR (CDCl$_3$) of **29**.

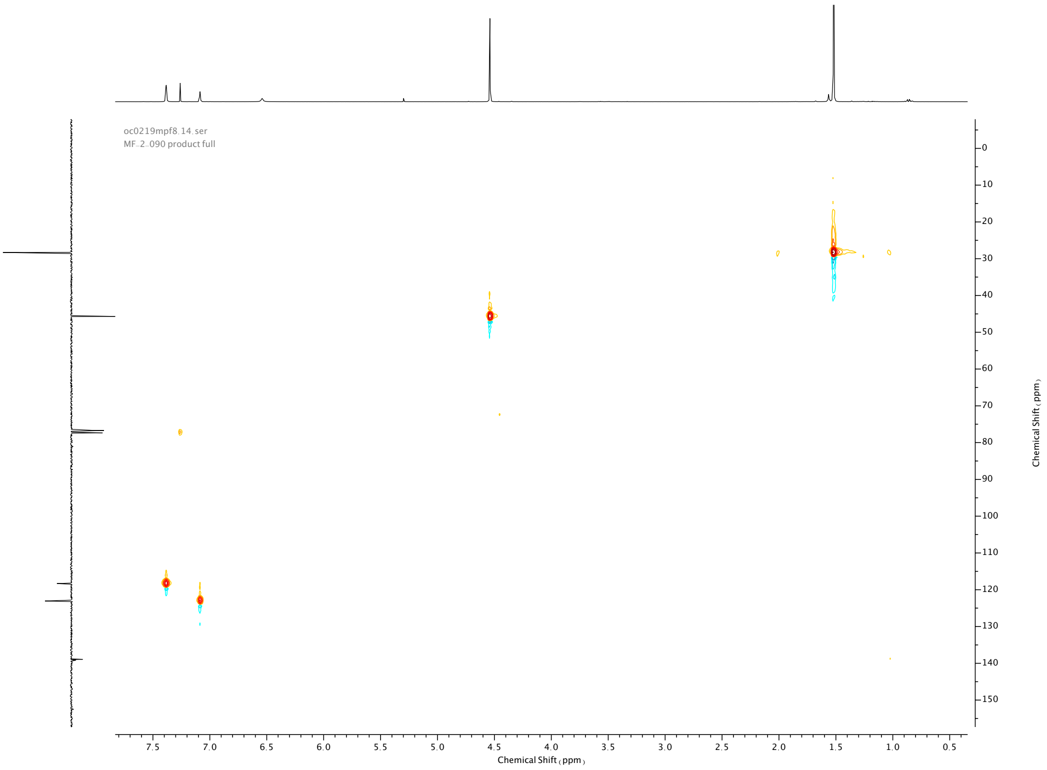

Figure **106**. HSQC NMR ($CDCl_3$) of **29**.

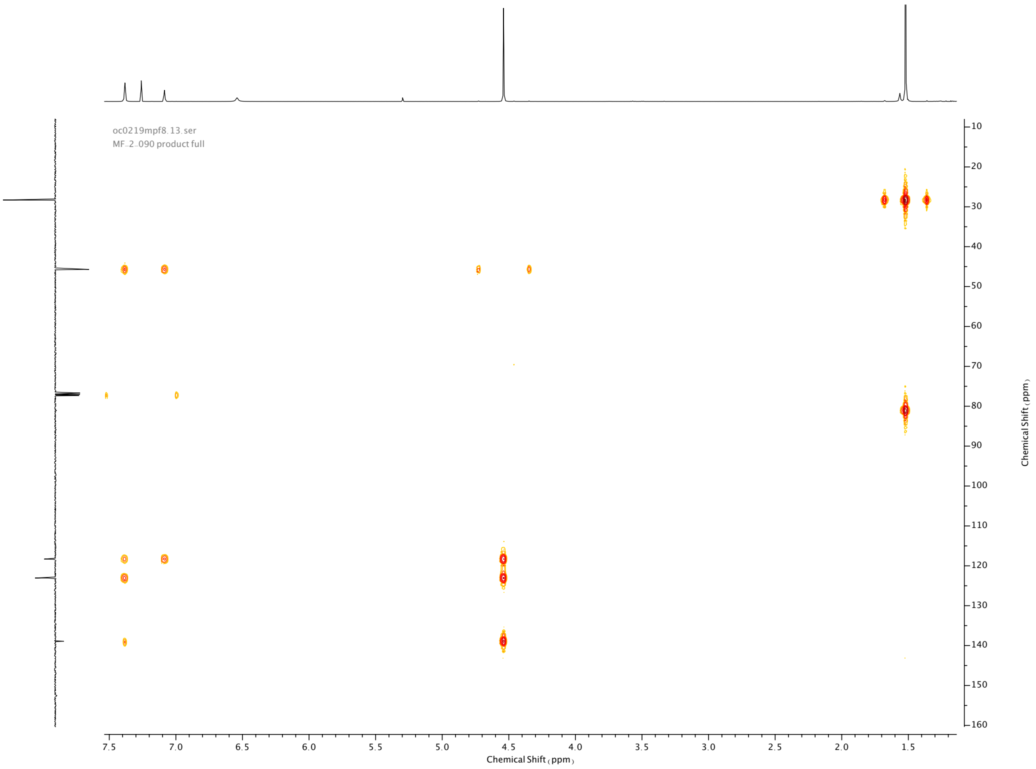

Figure **107**. HMBC NMR ($CDCl_3$) of **29**.

Compound **30**

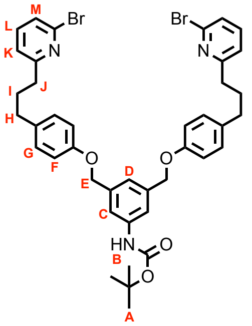

A mixture of linker **29** (1.88 g, 6.50 mmol, 1.0 eq.), **23** (3.78 g, 13.0 mmol, 2.0 eq.) and K_2CO_3 (7.19 g, 52.03 mmol, 8.0 eq.) in DMF (100 mL) were stirred at 80 °C overnight. The mixture was then cooled to room temperature, diluted with CH_2Cl_2 (100 mL), washed with water (100 mL), brine (100 mL), dried over anhydrous $MgSO_4$, filtered, and concentrated *in vacuo.* The crude product was purified *via* silica-gel chromatography using a Biotage Isolute SPE column (eluent 1:0 → 4:1 Petrol: EtOAc) to afford **30** as a yellow oil (4.62 g, 5.79 mmol, 89%). ^{1}H NMR (400 MHz, $CDCl_3$, 298 K) δ_H 7.42 (2H, t, *J* = 7.7 Hz, H_L), 7.40 (2H, s, H_C), 7.23 (2H, d, *J* = 7.9 Hz, H_M), 7.10-7.05 (1H, m, H_D), 7.08 (6H, m, H_K & H_G), 6.87 (4H, d, *J* = 8.8 Hz, H_F), 6.55 (1H, br. s, N-H_B), 5.02 (4H, s, H_E), 2.77 (4H, app. t, *J* = 7.8 Hz, H_H), 2.61 (4H, app. t, *J* = 7.8 Hz, H_J), 2.05-1.96 (4H, m, H_I), 1.51 (9H, s, H_A). ^{13}C NMR (101 MHz, $CDCl_3$, 298 K) δ_C 163.9, 157.1, 152.8, 141.7, 139.1, 138.8, 138.7, 134.4, 129.5, 125.4, 121.7, 120.7, 116.7, 114.9, 80.8 (HMBC), 69.9, 37.6, 34.7, 31.6, 28.5. RP-HRMS-ESI (CH_3CN): *m/z* = 800.1700 [M+H$^+$] calc. 800.1699.

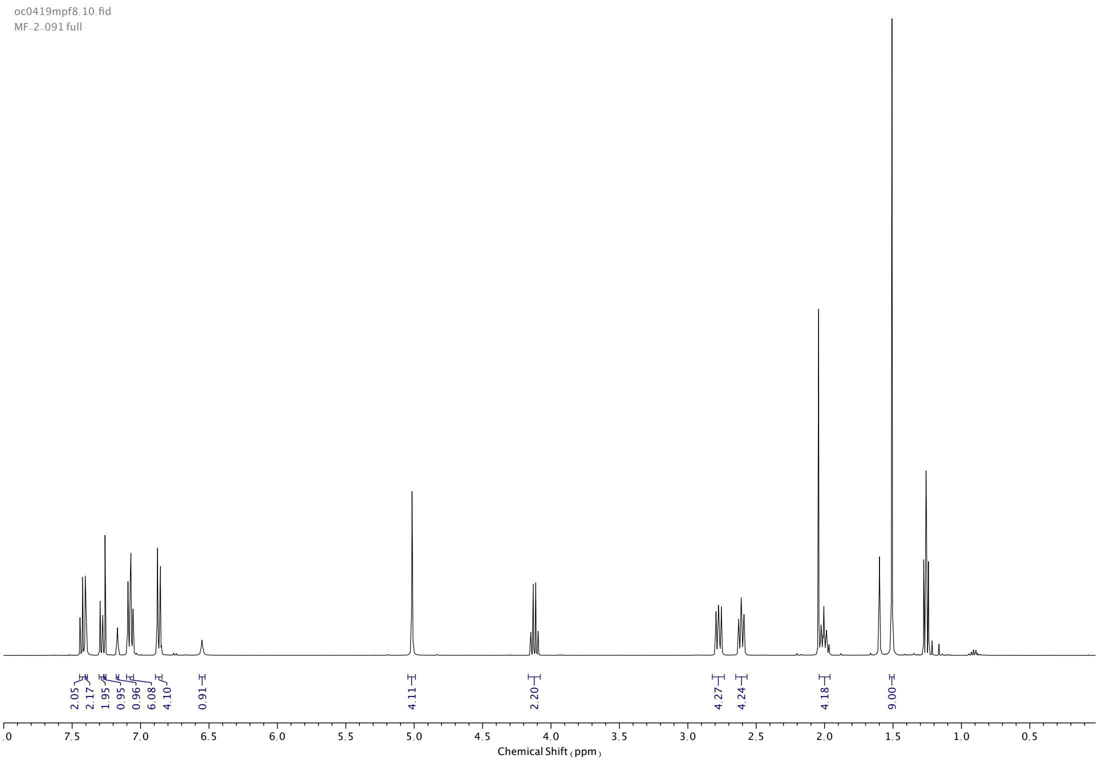

Figure **108**. ^{1}H NMR ($CDCl_3$, 400 MHz) of **30**.

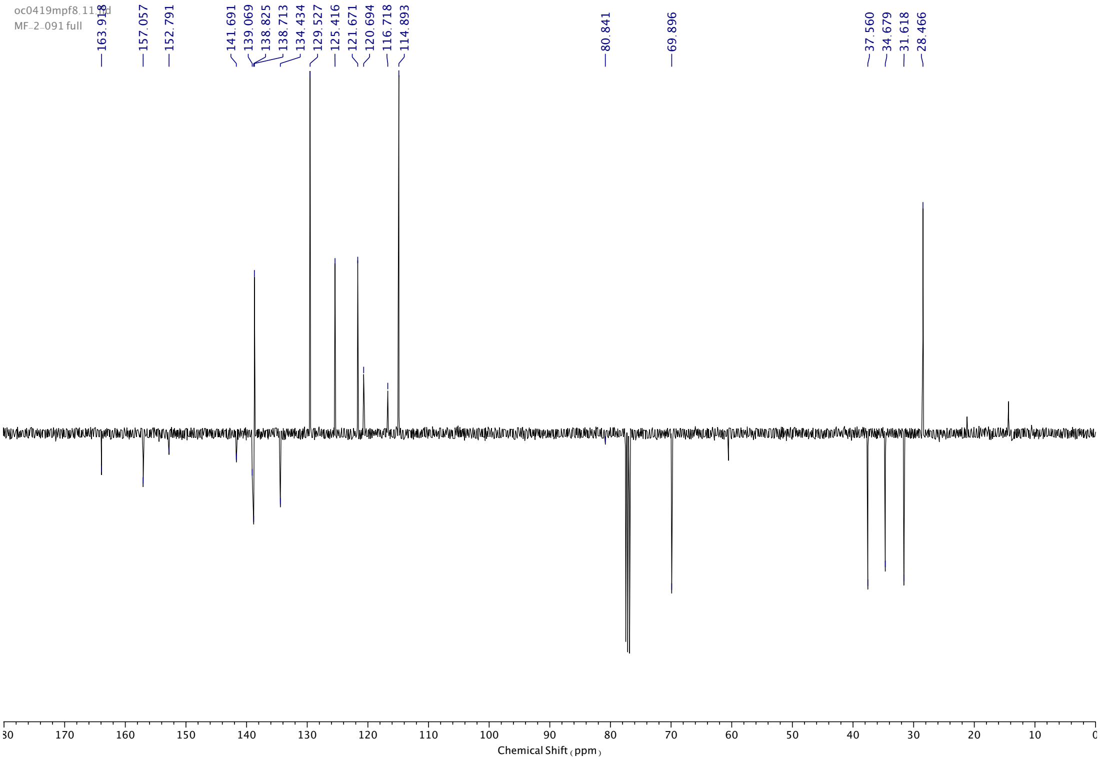

Figure **109**. ^{13}C NMR ($CDCl_3$, 101 MHz) of **30.**

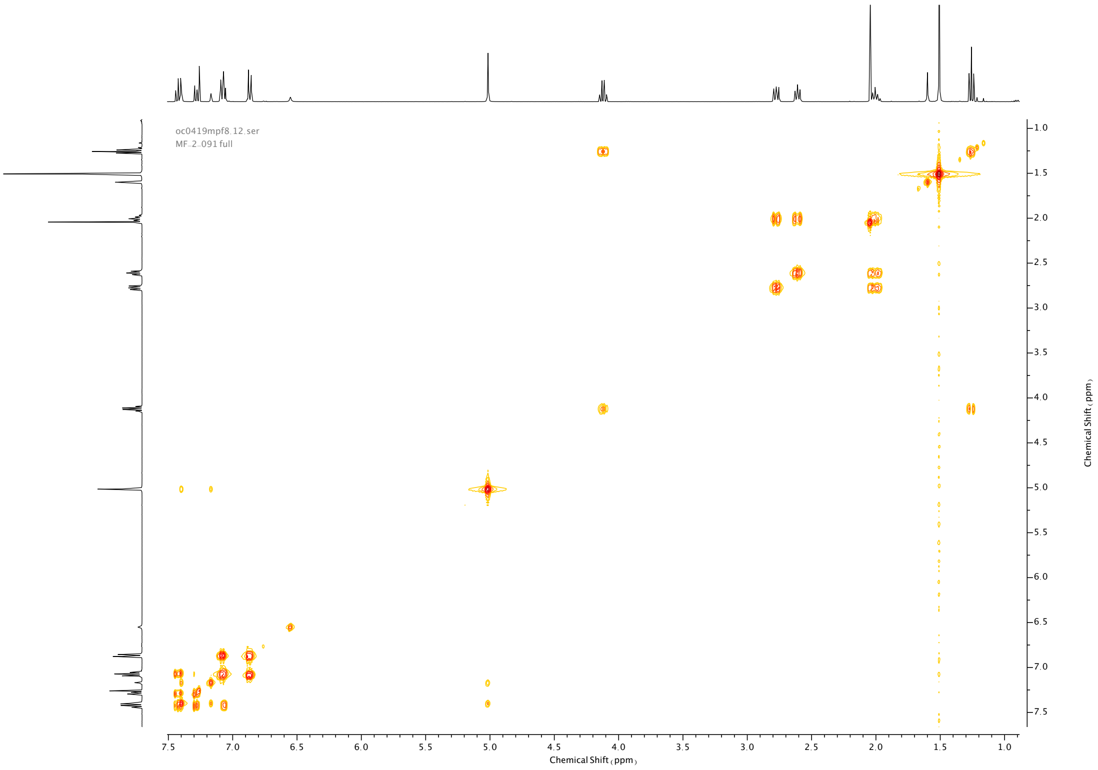

Figure **110**. COSY NMR ($CDCl_3$) of **30**.

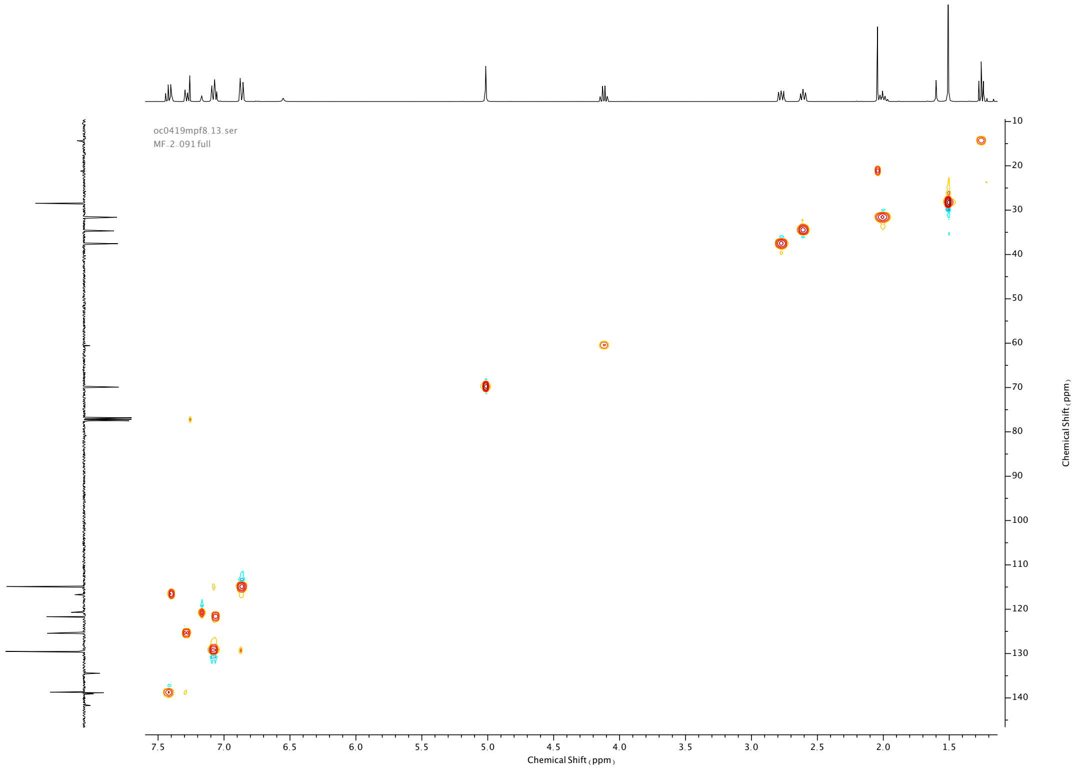

Figure **111**. HSQC NMR ($CDCl_3$) of **30**.

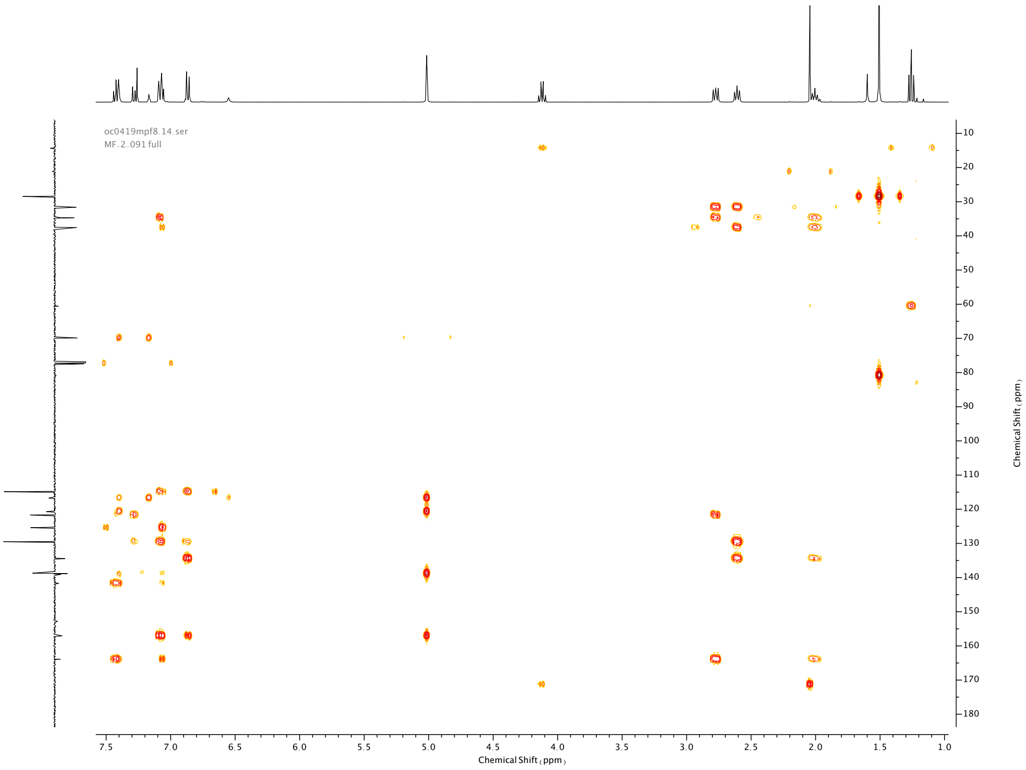

Figure **112**. HMBC NMR (CDCl$_3$) of **30**.

Compound **31**

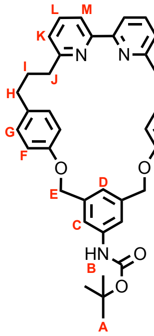

$[Ni(PPh_3)_2Br_2]$ (344 mg, 0.46 mmol, 1.0 eq.), PPh_3 (243 mg, 0.93 mmol, 2.0 eq.), NEt_4I (119 mg, 0.46 mmol, 1.0 eq.) and Mn (254 mg, 4.63 mmol, 10.0 eq.) were added to an oven-dried CEM microwave vial and degassed under $N_{2.}$ Anhydrous DMF (5 mL) was added and the mixture sonicated for 15 min, followed by stirring at 50 °C for a further 15 min. To the activated catalyst mixture was added macrocycle precursor **30** (370 mg, 0.46 mmol, 1.0 eq.) in anhydrous DMF (5 mL) *via* syringe pump over 4 h at 50 °C, followed by additional stirring for 30 min. The reaction was then cooled to room temperature, diluted with CH_2Cl_2 (30 mL) and washed with EDTA-NH_3 (20 mL) and brine (20 mL). Combined aqueous washings were extracted with CH_2Cl_2 (2 x 20 mL). The combined organic extracts were dried over anhydrous $MgSO_4$, filtered and concentrated *in vacuo*. The crude product was purified *via* silica-gel chromatography using a Biotage Isolute SPE column (eluent 1:0 → 9:1 (CH_2Cl_2: petrol 1:1): EtOAc) to afford **31** as yellow oil (171 mg, 0.27 mmol, 58%). ^{1}H NMR (400 MHz, $CDCl_3$, 298 K) δ_H ^{1}H NMR (400 MHz, $CDCl_3$) 7.75 (2H, dd, J = 7.7, 0.8 Hz, H_M), 7.58 (2H, t, J = 7.8 Hz, H_L), 7.27-7.25 (2H, m, H_C), 7.04 (2H, dd, J = 7.6 Hz, 0.9 Hz, H_K) 6.94-6.92 (1H, m, H_D), 6.90 (4H, app. d, J = 8.6 Hz, H_G), 6.62 (4H, app. d, J = 8.6 Hz, H_F), 6.45 (1H, br. s, N-H_B), 5.02 (4H, s, H_E), 2.89 (4H, t, J = 7.2 Hz, H_J) 2.60 (4H, app. t, J = 7.2 Hz, H_H), 2.09 (4H, quin, J = 7.3 Hz, H_I), 1.49 (9H, s, H_A). ^{13}C NMR (101 MHz, $CDCl_{3,}$ 298 K) δ_C 161.9, 156.4, 152.8, 139.3, 139.0, 136.8, 134.9, 129.5, 122.6, 119.7, 119.2, 115.7, 80.8 (HMBC), 69.9, 37.9, 34.5, 31.4, 28.4, 24.0, 20.9. RP-HRMS-ESI (CH_3CN): m/z = 642.3339 $[M+H^+]$ calc. 642.3326.

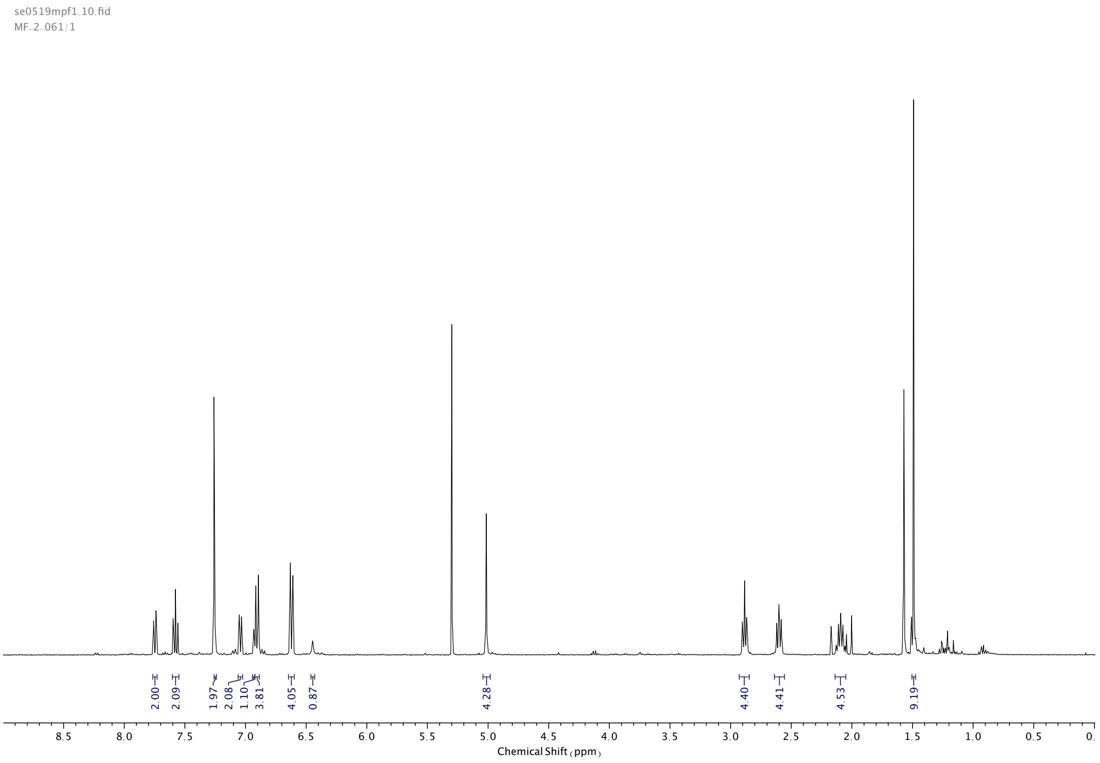

Figure **113**. ^{1}H NMR (CDCl$_3$, 400 MHz) of **31**.

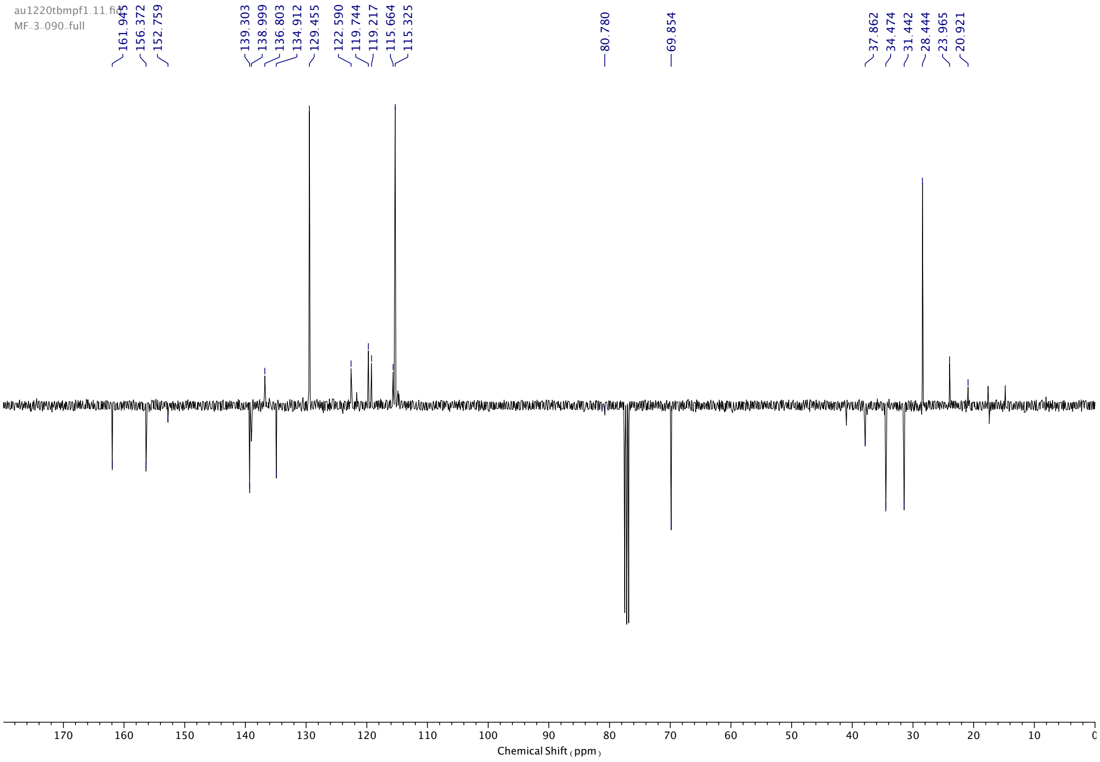

Figure **114**. ^{13}C NMR (CDCl$_3$, 101 MHz) of **31.**

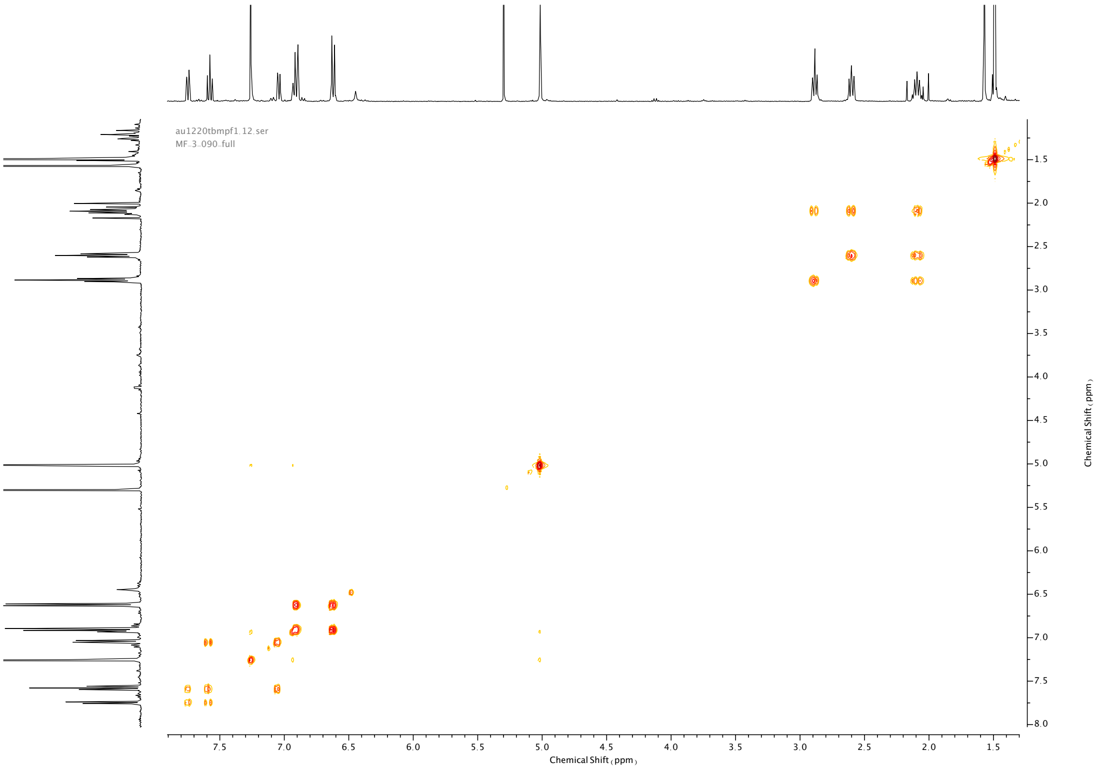

Figure **115**. COSY NMR (CDCl$_3$) of **31**.

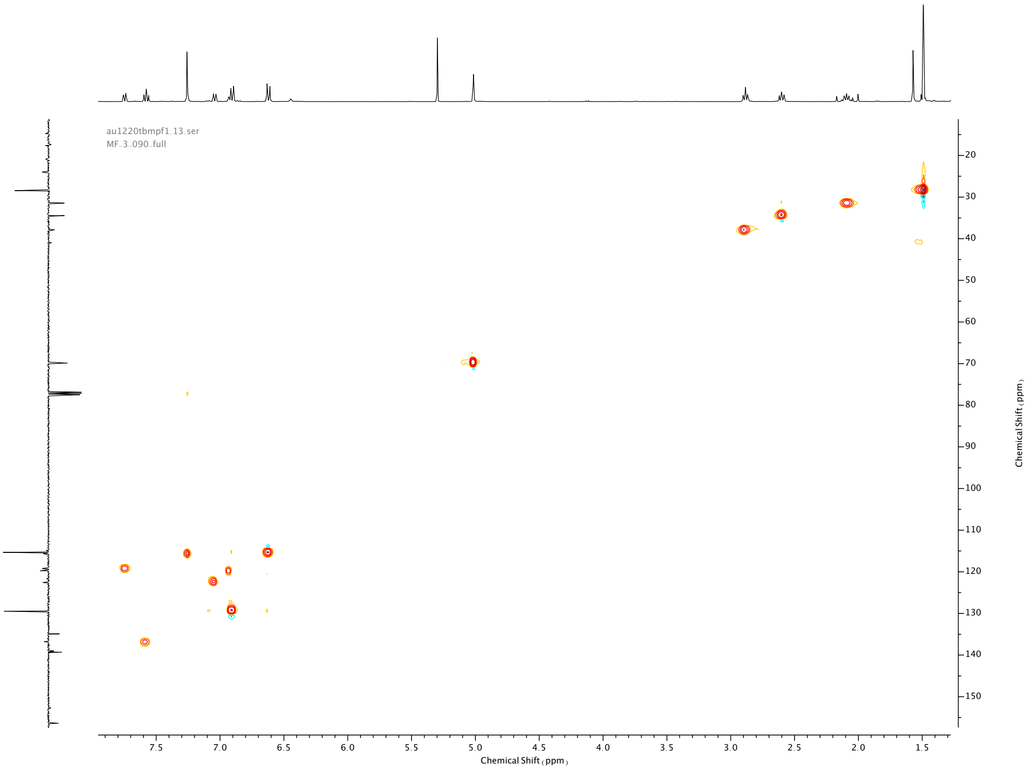

Figure **116**. HSQC NMR (CDCl$_3$) of **31**.

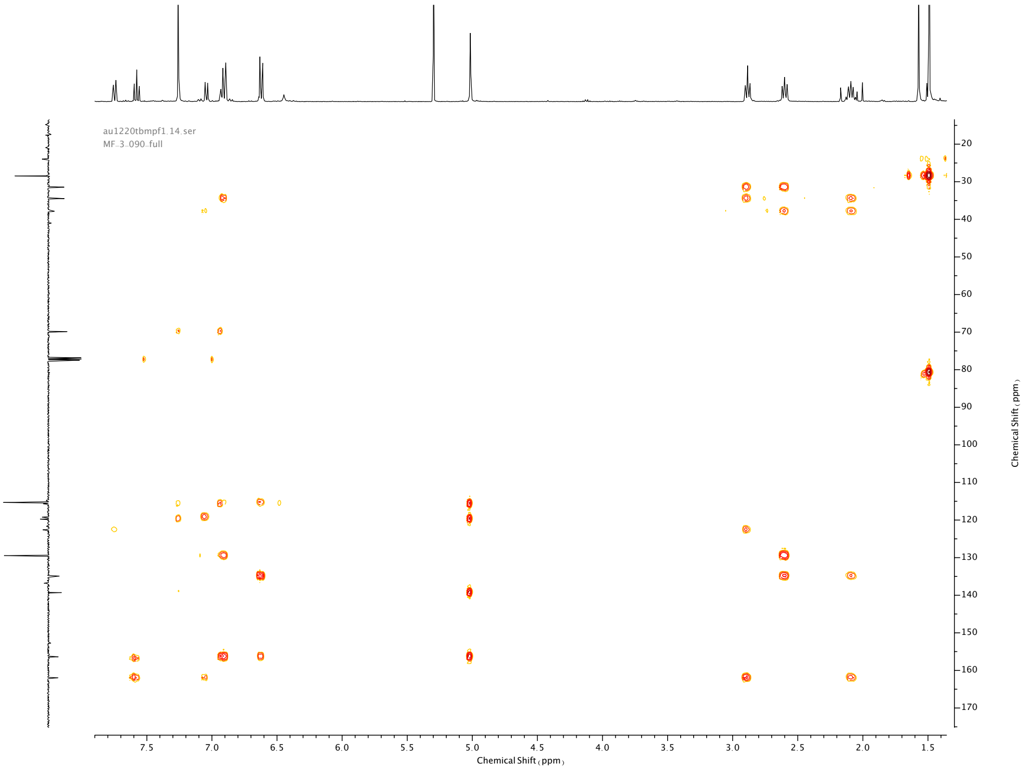

Figure **117**. HMBC NMR ($CDCl_3$) of **31**.

Compound **32**

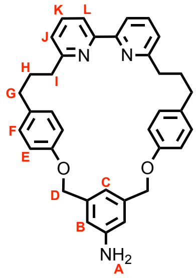

To a solution of **31** (210 mg, 0.33 mmol, 1.0 eq.) in CH_2Cl_2 (10 mL) was added TFA (0.15 mL, 1.96 mmol, 6.0 eq.) at 0 °C. The resulting suspension was allowed to reach room temperature and stirred overnight. The mixture was then diluted with CH_2Cl_2 (20 mL), washed with $NaHCO_3$ (20 mL) and brine (20 mL) then dried over anhydrous $MgSO_4$, filtered, and concentrated *in vacuo* to afford **32** yellow oil (152 mg, 0.29 mmol, 85%.). ^{1}H NMR (400 MHz, $CDCl_3$) δ_H 7.76 (2H, dd, *J* = 7.8, 0.9 Hz, H_L), 7.59 (2H, t, *J* = 7.7 Hz, H_K), 7.04 (2H, dd, *J* = 7.6 Hz, 0.9 Hz, H_J) 6.90 (4H, app. d, *J* = 8.7 Hz, H_F), 6.66-6.63 (5H, m, H_E & H_C), 6.55 (2H, m, H_B), 4.97 (4H, s, H_D), 2.89 (4H, t, *J* = 7.1 Hz, H_I) 2.59 (4H, app. t, *J* = 7.2 Hz, H_G), 2.08 (4H, quin, *J* = 7.7 Hz, H_H). ^{13}C NMR (101 MHz, $CDCl_3$, 298 K) δ_C 161.9, 156.8 (HMBC), 156.5, 147.1, 139.5, 136.8, 134.8, 129.4, 122.6, 119.2, 115.5, 115.4, 112.5, 70.1, 37.9, 34.5, 31.5. HR-ESI-MS (CH_3CN): *m/z* = 542.2808 $[M+H]^+$ calc. 542.2808.

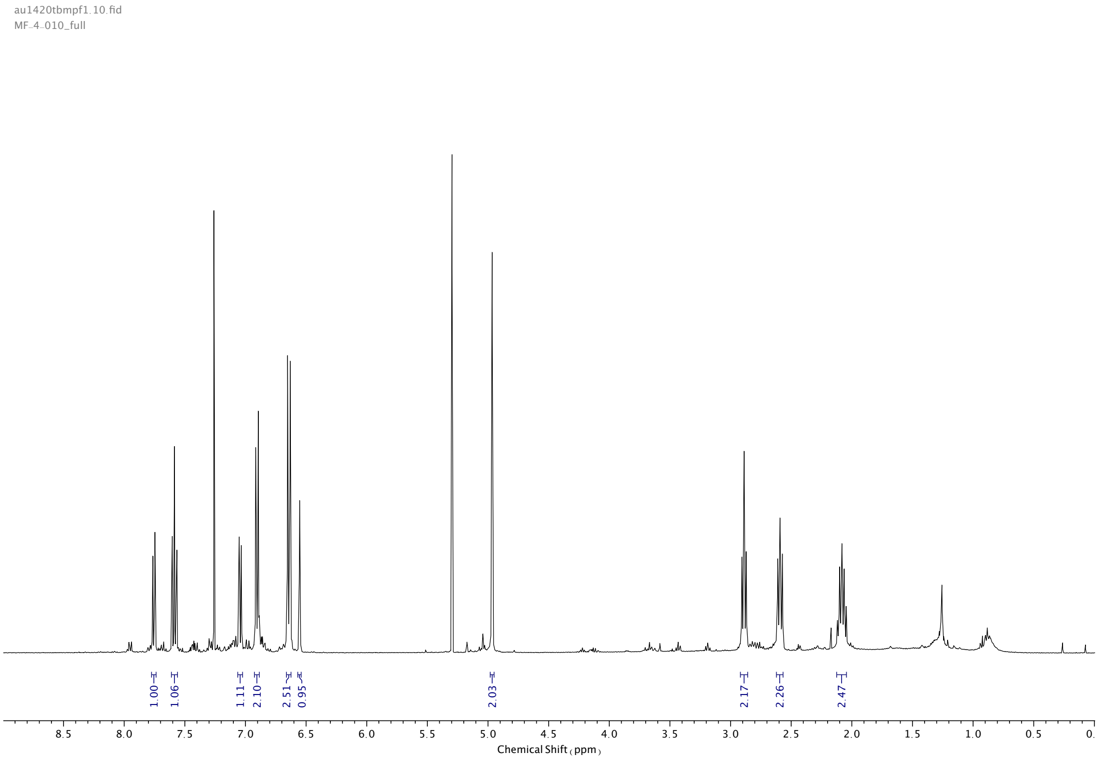

Figure **118**. ^{1}H NMR ($CDCl_3$, 400 MHz) of **32**.

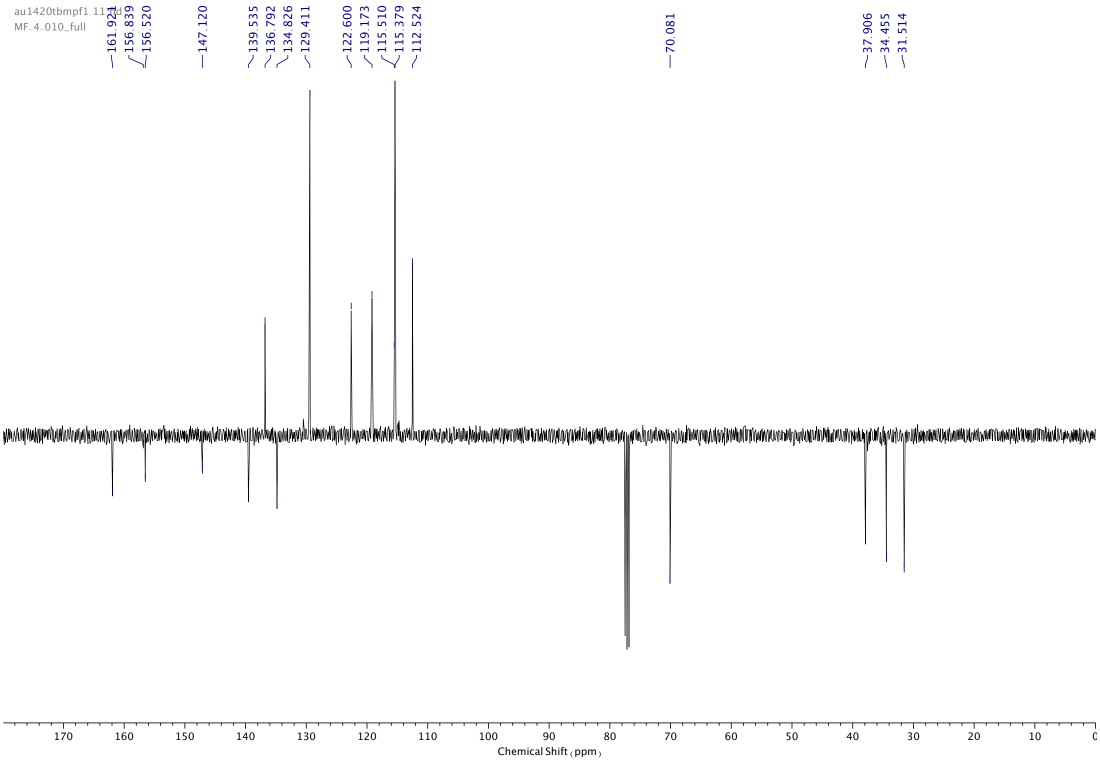

Figure **119**. ^{13}C NMR (CDCl$_3$, 101 MHz) of **32.**

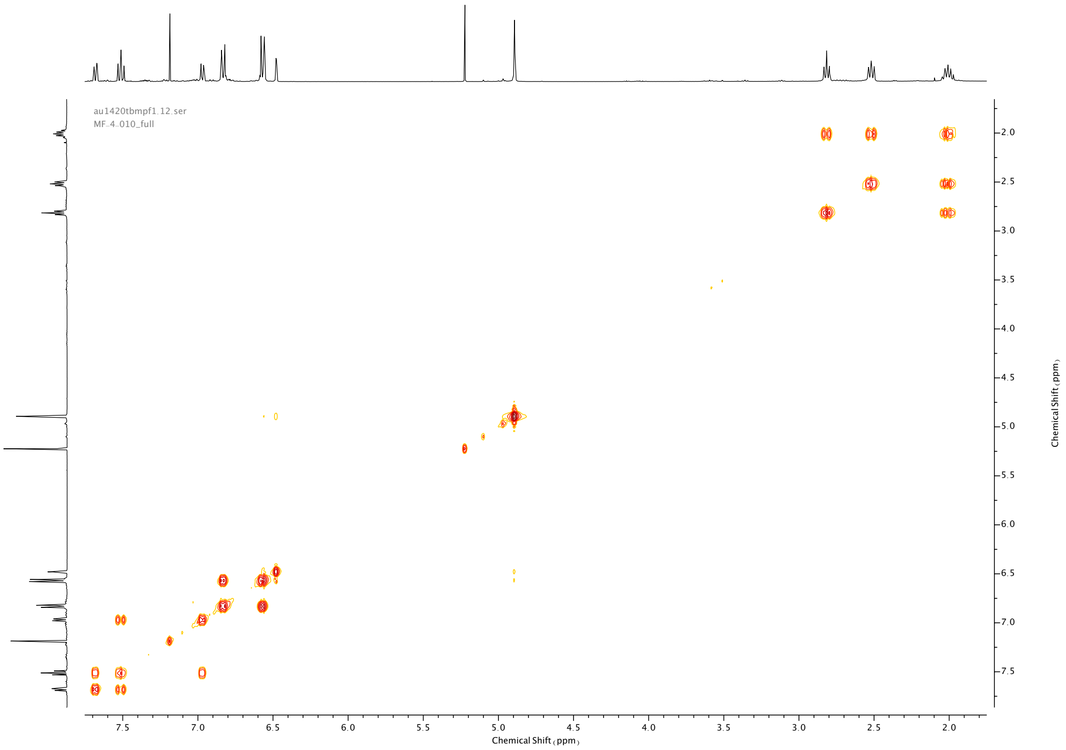

Figure **120**. COSY NMR (CDCl$_3$) of **32**.

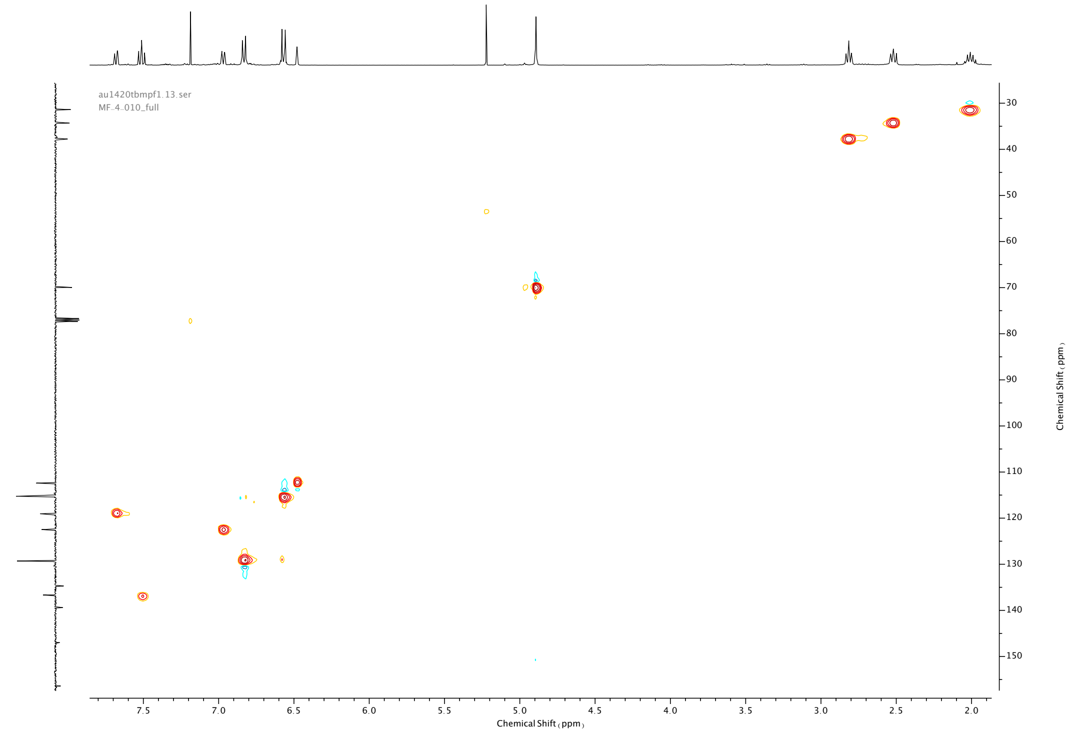

Figure **121**. HSQC NMR ($CDCl_3$) of **32**.

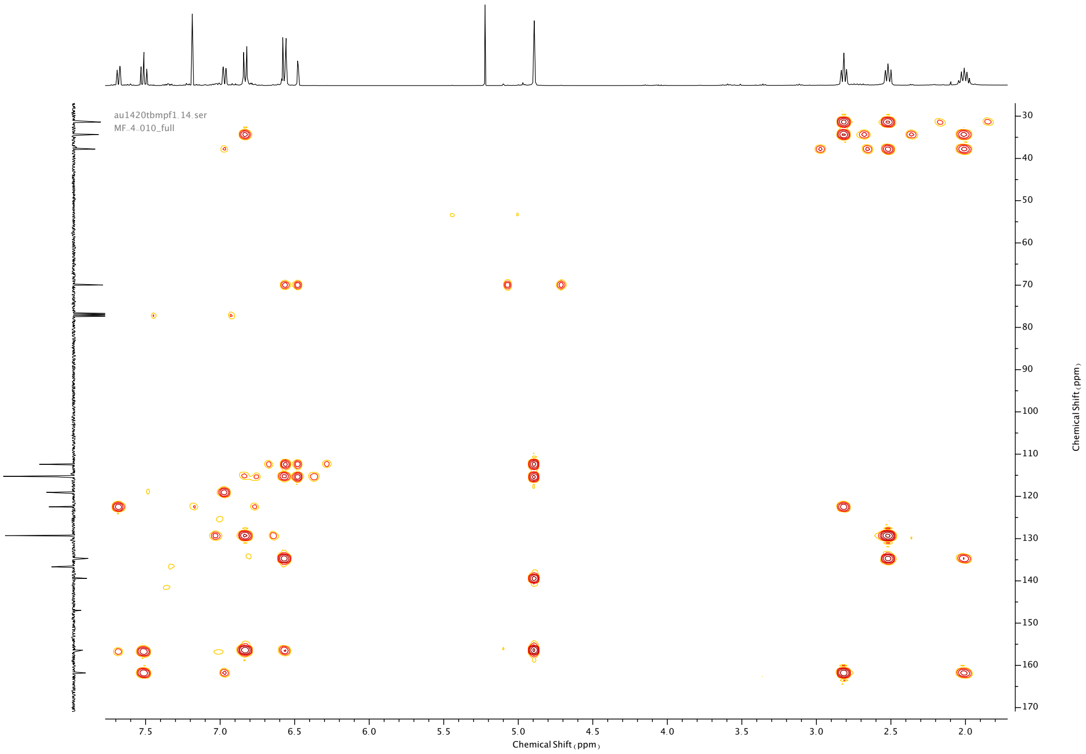

Figure **122**. HMBC NMR ($CDCl_3$) of **32**.

Compound **34**

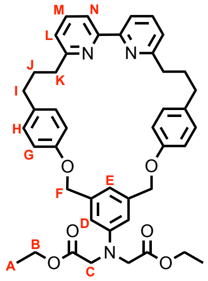

A mixture of **32** (690 mg, 1.27 mmol, 1.0 eq.), **33** (1.12 mL, 10.2 mmol, 8.0 eq.), K_2CO_3 (1.06 g, 7.65 mmol, 6.0 eq.) and NaI (1.53 g, 10.2 mmol, 8.0 eq.) in CH_3CN (100 mL) was stirred for 4 days at 80 °C. The mixture was allowed to reach room temperature, diluted with CH_2Cl_2 (100 mL) then washed with H_2O (100 mL) and brine (100 mL). Combined aqueous phases were extracted with CH_2Cl_2 (2 x 50 mL). Combined organic extracts were dried over anhydrous $MgSO_4$, filtered and concentrated *in vacuo*. The crude product was purified *via* silica-gel chromatography using a Biotage Isolute SPE column (9:1 (CH_2Cl_2: petrol 1:1): EtOAc) to afford **34** as an orange oil (430 mg, 0.59 mmol, 47%). ^{1}H NMR (400 MHz, $CDCl_3$, 298 K) δ_H 7.76 (2H, d, *J* = 7.6 Hz, H_N), 7.58 (2H, t, *J* = 7.7 Hz, H_M), 7.04 (2H, dd, *J* = 7.7, 0.9 Hz, H_L), 6.90 (4H, app. d, *J* = 8.6 Hz, H_H), 6.67 (1H, m, H_E), 6.62 (4H, app. d, *J* = 8.7 Hz, H_G), 6.48 (2H, s, H_D), 4.97 (4H, s, H_F), 4.13 (4H, q, *J* = 7.1 Hz, H_B), 4.08 (4H, s, H_C), 2.89 (4H, t, *J* = 7.0 Hz, H_J), 2.59 (4H, app. t, *J* = 7.2 Hz, H_I), 2.13-2.05 (4H, m, H_J), 1.20 (6H, t, *J* = 7.1 Hz, H_A). ^{13}C NMR (101 MHz, $CDCl_3$, 298 K) δ_C 170.9, 161.9, 157.0, 156.6, 148.6, 139.4, 136.7, 134.9, 129.4, 122.6, 119.1, 115.5, 115.4, 110.0, 70.4, 61.3, 41.0, 38.0, 34.5, 31.5, 14.3. HR-ESI-MS (CH_3CN): *m/z* = 714.3548 $[M+H]^+$ calc. 714.3538.

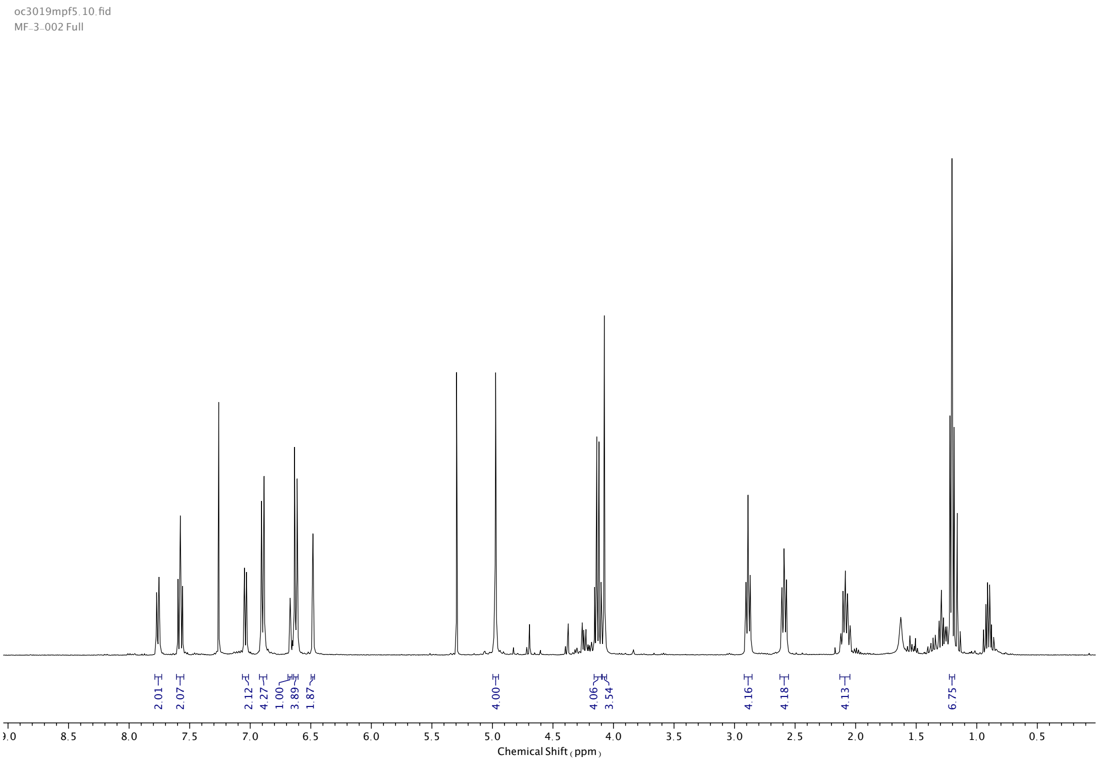

Figure **123**. ^{1}H NMR ($CDCl_3$, 400 MHz) of **34**.

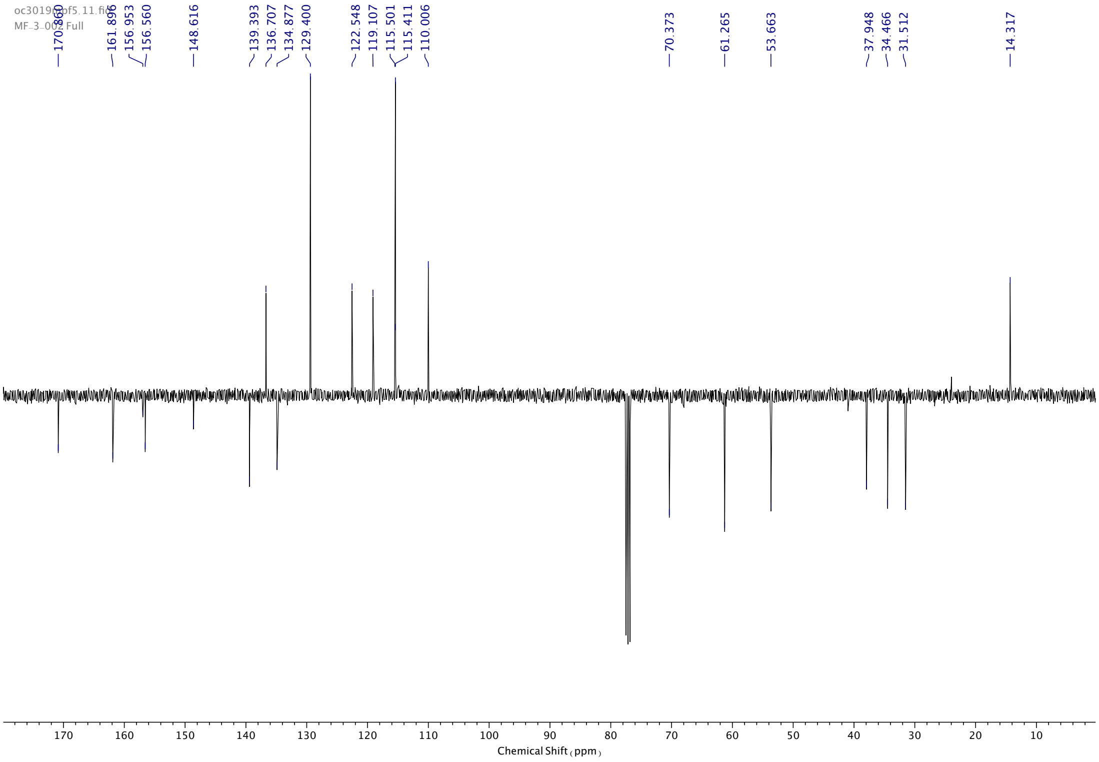

Figure **124**. ^{13}C NMR ($CDCl_3$, 101 MHz) of **34.**

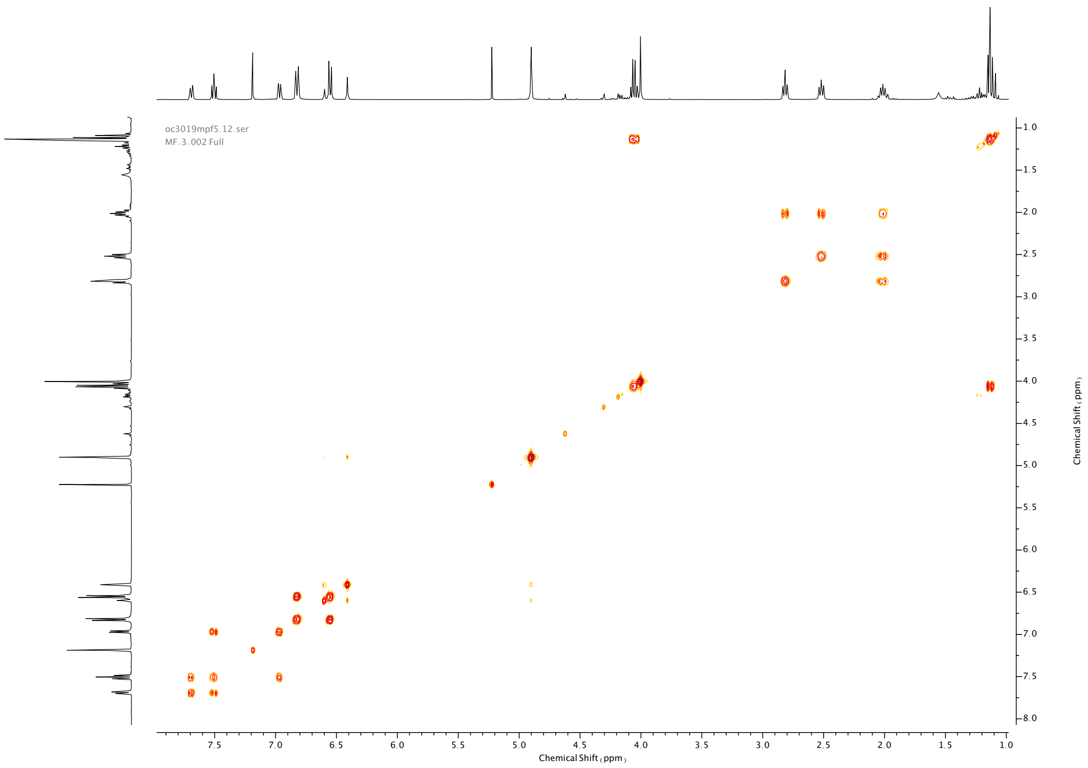

Figure **125**. COSY NMR ($CDCl_3$) of **34**.

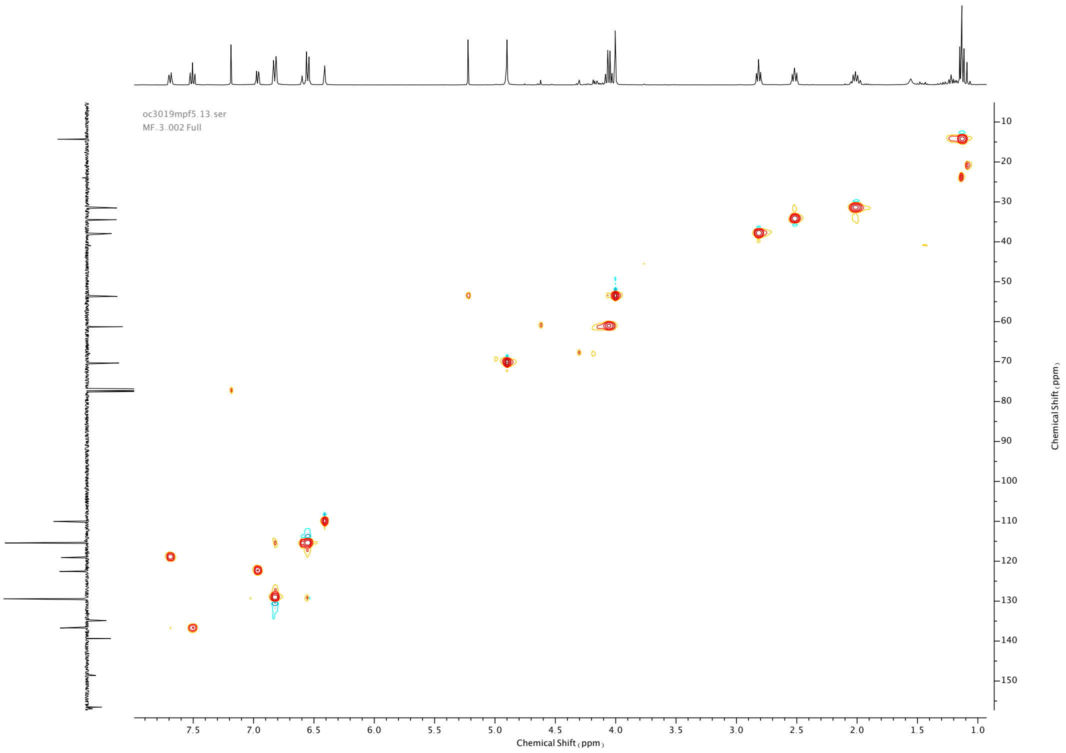

Figure **126**. HSQC NMR ($CDCl_3$) of **34**.

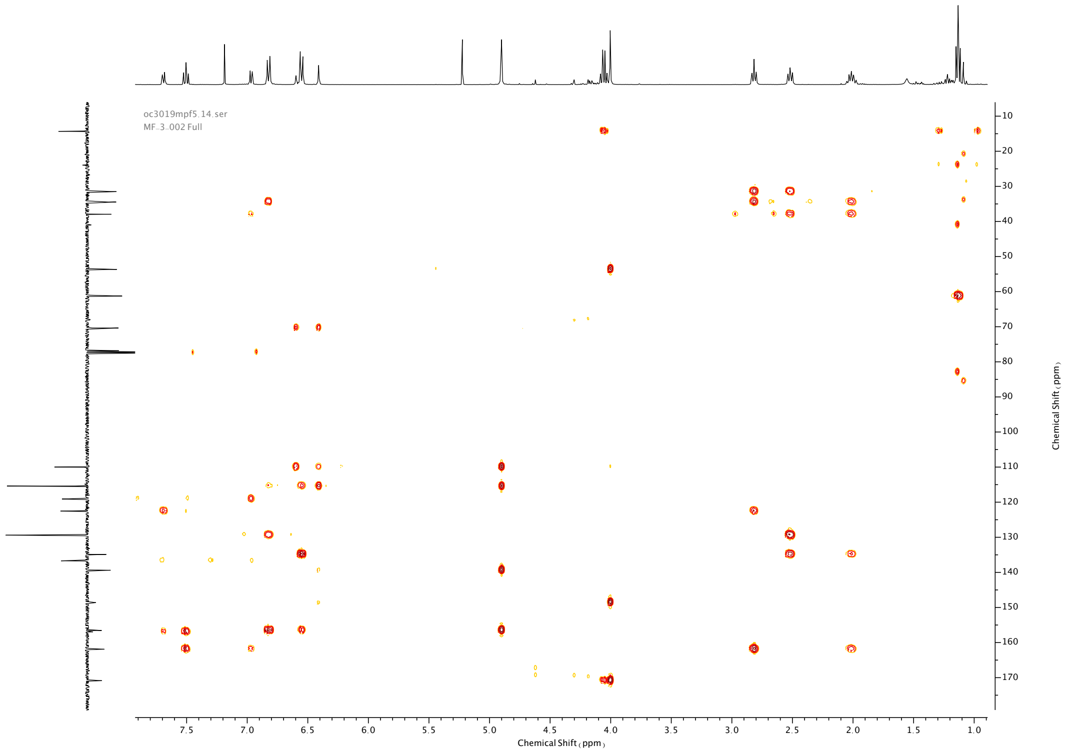

Figure **127**. HMBC NMR ($CDCl_3$) of **34**.

Compound **35**

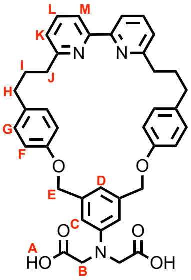

To a solution of **34** (145mg, 0.20 mmol, 1.0 eq.) in THF (4 mL) was added NaOH (1 M, 0.20 mmol, 10.0 eq.). The resulting mixture was stirred at room temperature overnight then acidified *via* dropwise with HCl (1M) until pH 3, diluted with H_2O (50 mL), extracted with EtOAc (3 x 30 mL) then washed with brine (20 mL) and concentrated *in vacuo* to afford **35** as a yellow solid (130 mg, 0.19 mmol, 97%). Thermal decomposition before melt at 220 °C. ^{1}H NMR (400 MHz, DMSO-d_6, 298 K) δ_H 7.82 (2H, dd, *J* = 7.8 Hz, 1.0 Hz, H_M), 7.69 (2H, t, *J* = 7.7 Hz, H_L), 7.16 (2H, dd, *J* = 7.7, 0.9 Hz, H_K), 6.87 (4H, app. d, *J* = 8.7 Hz, H_G), 6.69 (4H, app. d, *J* = 8.7 Hz, H_F), 6.61-6.60 (1H, m, H_D), 6.35 (2H, m, H_C), 4.92 (4H, s, H_E), 3.96 (4H, br. s, H_B) 2.79 (4H, t, *J* = 6.9 Hz, H_J) 2.52 (4H, t, *J* = 7.3 Hz, H_H), 2.00 (4H, quint, *J* = 7.1 Hz, H_I). ^{13}C NMR (101 MHz, DMSO-$d_{6,}$ 298 K) δ_C 161.09, 156.09, 155.76, 138.48, 138.17, 136.95, 133.96, 129.10, 122.71, 118.49, 114.88, 114.28 (HMBC), 108.80 (HMBC), 69.43, 36.82, 33.48, 30.62.[3] HR-ESI-MS (CH_3CN): *m/z* = 658.2924 $[M+H]^+$ calc. 658.2912.

---

[3] ^{13}C signals for the carboxylate chain (-$\underline{C}H_2\underline{C}OOH$) of **35** could not be detected.

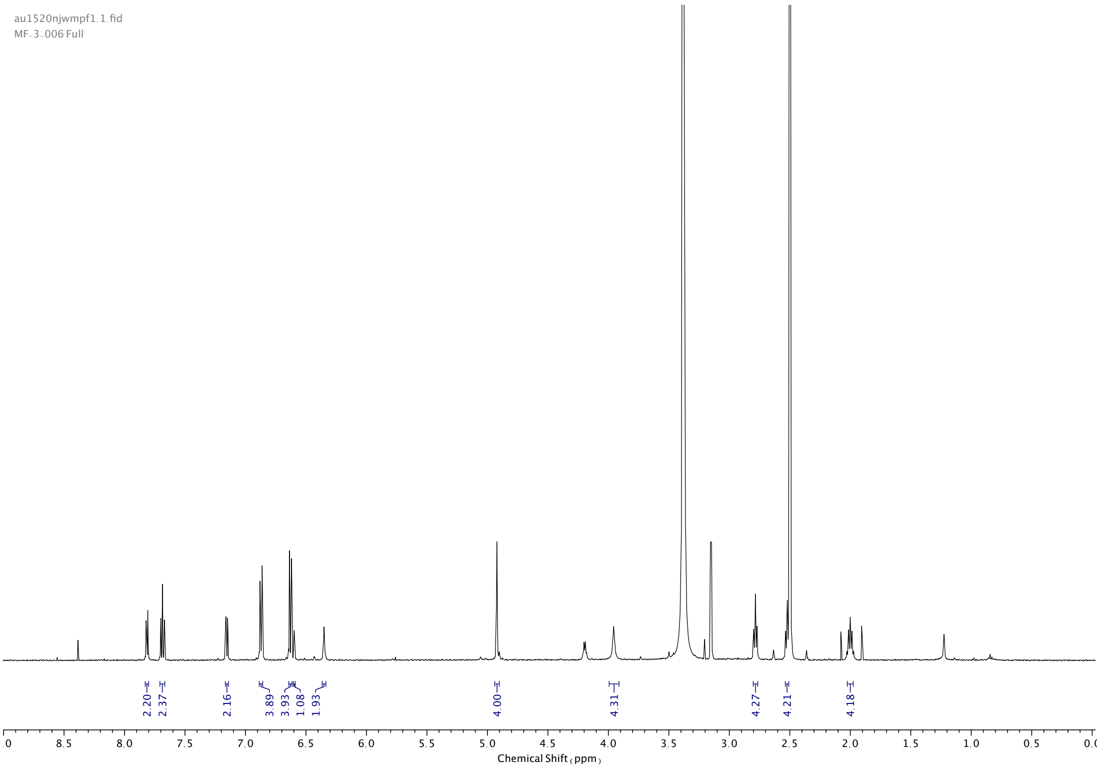

Figure **128**. ^{1}H NMR (DMSO-d$_6$, 400 MHz) of **35**.

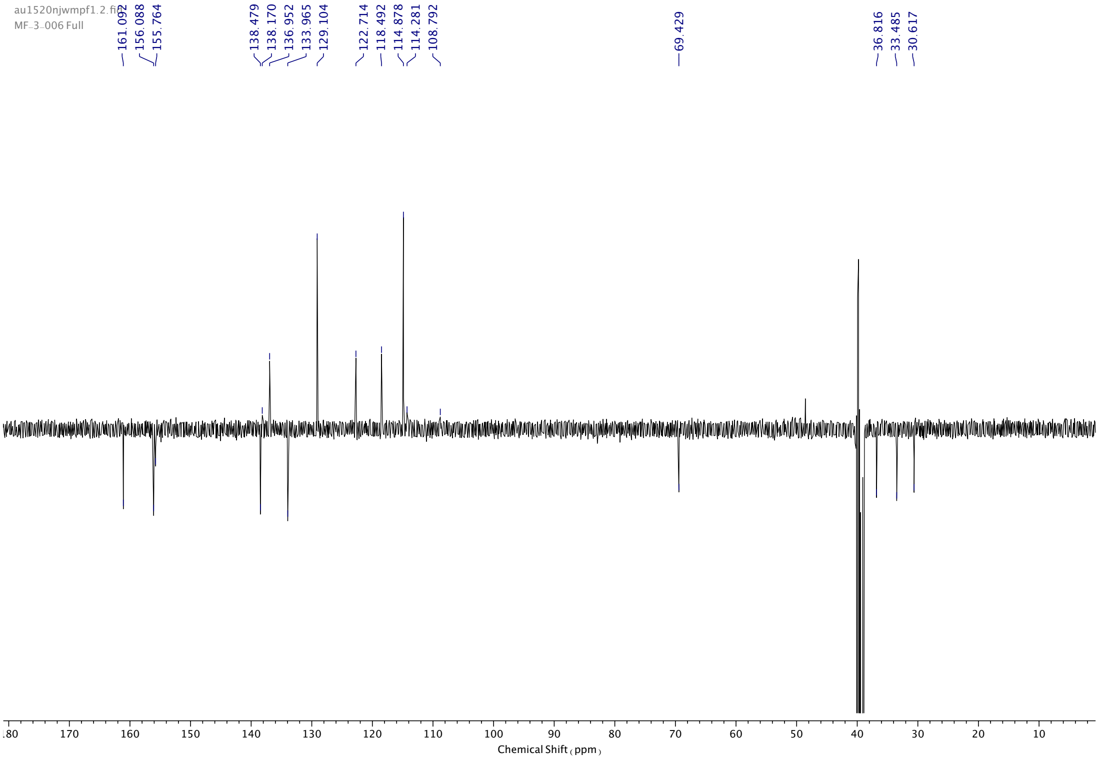

Figure **129**. ^{13}C NMR (DMSO-d$_6$, 101 MHz) of **35.**

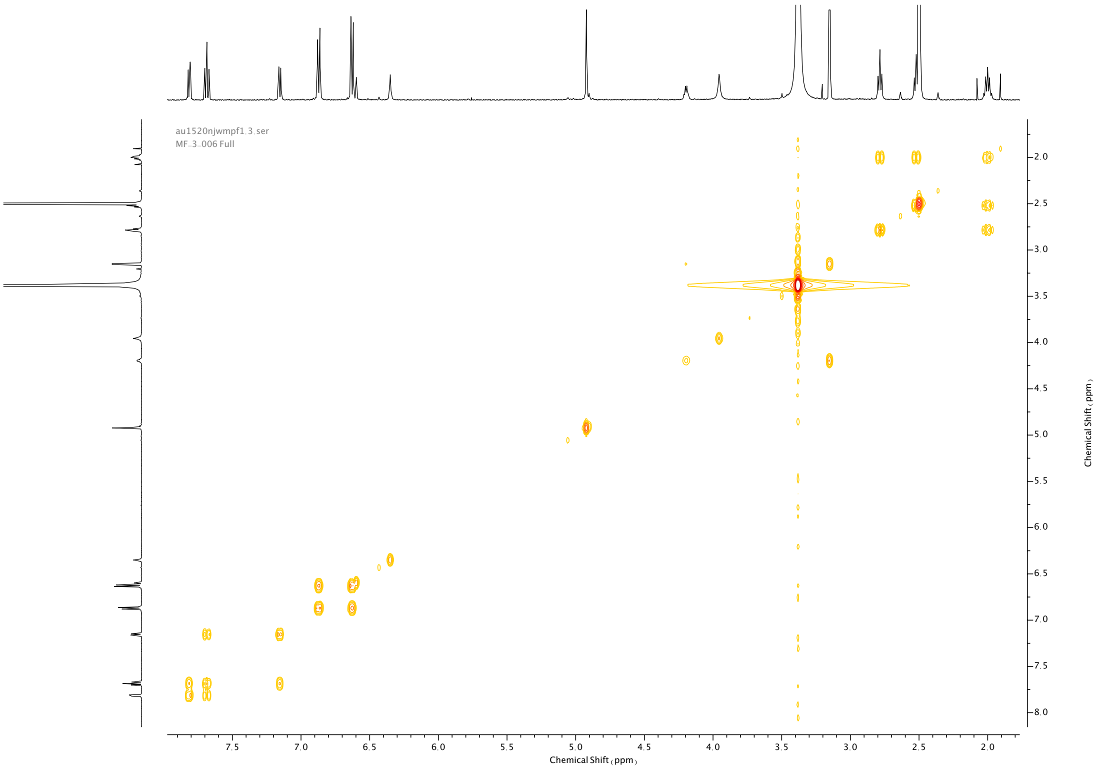

Figure **130**. COSY NMR (DMSO-d$_6$) of **35**.

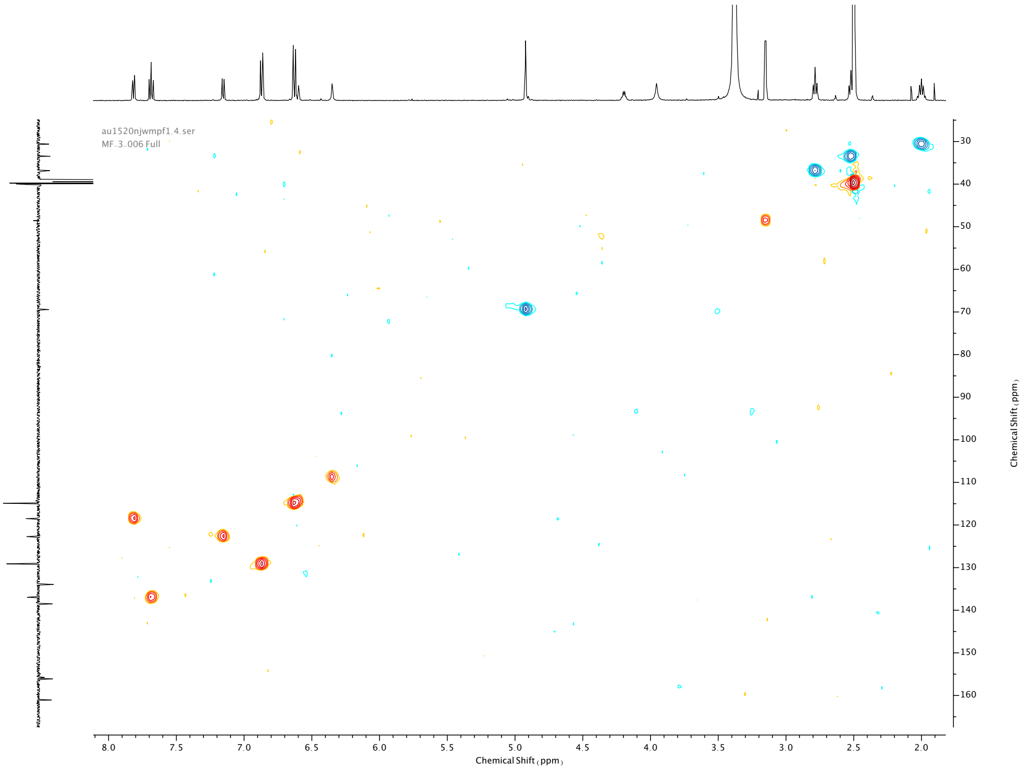

Figure **131**. HSQC NMR (DMSO-d$_6$) of **35**.

Figure **132**. HMBC NMR (DMSO-d$_6$) of **35**.

Compound **35**

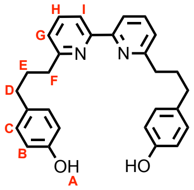

[$Ni(PPh_3)_2Br_2$] (1.21 g, 1.63 mmol, 0.5 eq.), PPh_3 (857 mg, 3.27 mmol, 1.0 eq.), NEt_4I (419 mg, 0.46 mmol, 0.5 eq.) and Mn (895 mg, 16.3 mmol, 5.0 eq.) were added to an oven-dried CEM microwave vial and degassed under N_2. Anhydrous DMF (20 mL) was added and the mixture sonicated for 15 min, followed by stirring at 50 °C for a further 15 min. To the activated his catalyst mixture was added **22** (1.0 g, 3.27 mmol, 1.0 eq.) in anhydrous DMF (15 mL) in one portion and the resulting mixture stirred at 50 °C for 3h. The reaction was cooled to room temperature, diluted with CH_2Cl_2 (50 mL) then washed with EDTA-NH_3 (30 mL) and brine (30 mL). Combined aqueous washings were extracted with CH_2Cl_2 (2 x 20 mL). The combined organic extracts were dried over anhydrous $MgSO_4$, filtered and concentrated *in vacuo*. The crude product was loaded onto a pad of silica and eluted with 1:1 petrol: CH_2Cl_2 (150 mL) to remove PPh_3, then with 1:1 CH_2Cl_2: EtOAc (300 mL) to afford **41** as an orange oil that was then dissolved in HBr (48% w/v in H_2O, 10 mL) and stirred vigorously at 130 °C for 6 h. The mixture was cooled to room temperature then diluted with H_2O (20 mL) and neutralized with NaOH (10 M). The product was extracted from the aqueous phase with CH_2Cl_2 (3 x 50 mL), dried over anhydrous $MgSO_4$, filtered, then concentrated *in vacuo*. The crude product was purified *via* silica-gel chromatography using a Biotage Isolute SPE column (eluent 9:1 CH_2Cl_2: MeOH) to afford **38** as a colourless oil (674 mg, 1.60 mmol, 50% over two steps). ^{1}H NMR (400 MHz, MeOD, 298 K) δ_H 8.09 (2H, dd, *J* = 7.8, 0.9 Hz, H_I), 7.76 (2H, t, *J* = 7.8 Hz, H_H), 7.21 (2H, dd, *J* = 7.7 Hz, 0.9 Hz, H_G), 7.01 (4H, app. d, *J* = 8.6 Hz, H_C), 6.70 (4H, app. d, *J* = 8.6 Hz, H_B), 2.84 (4H, app. t, *J* = 7.5 Hz, H_F), 2.59 (4H, app. t, *J* = 7.5 Hz, H_D), 2.08-2.01 (4H, m, H_E). ^{13}C NMR (101 MHz, MeOD) δ_C 163.0, 157.2, 156.4, 138.5, 134.3, 130.4, 124.1, 120.0, 116.1, 38.4, 35.6, 33.1. HR-ESI-MS (CH_3CN): *m/z* = 425.2234 $[M+H]^+$ calc. 425.2229.

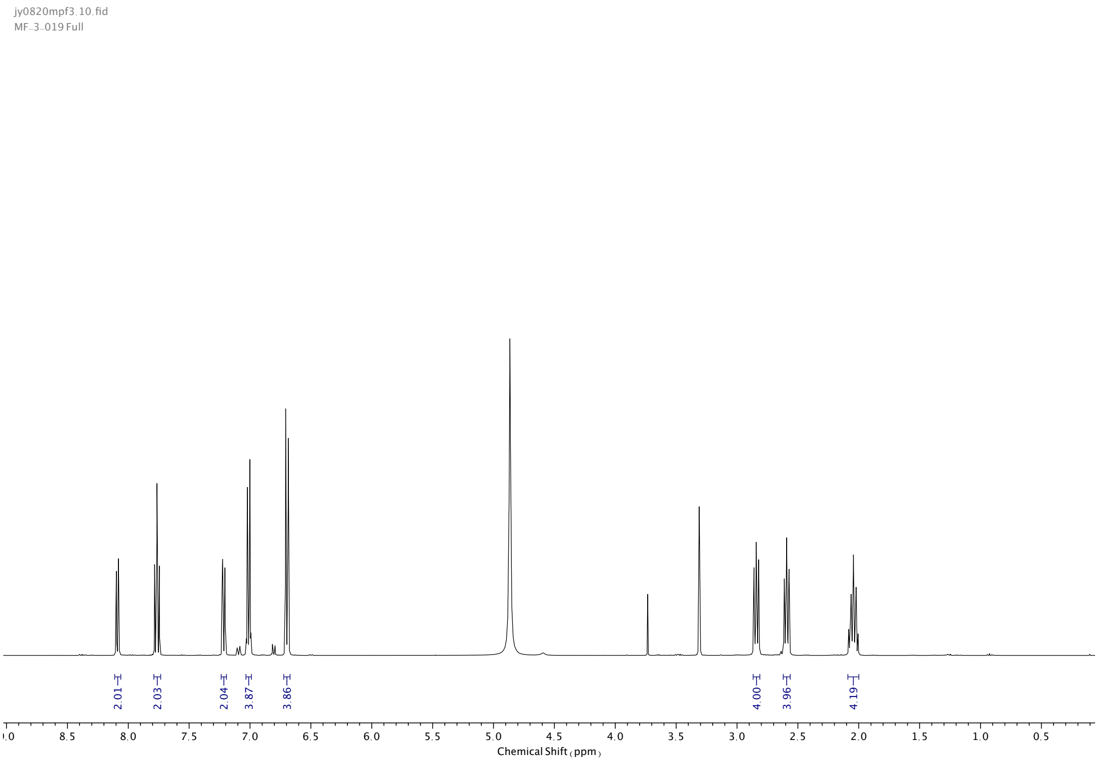

Figure **133**. ^{1}H NMR (MeOD, 400 MHz) of **38**.

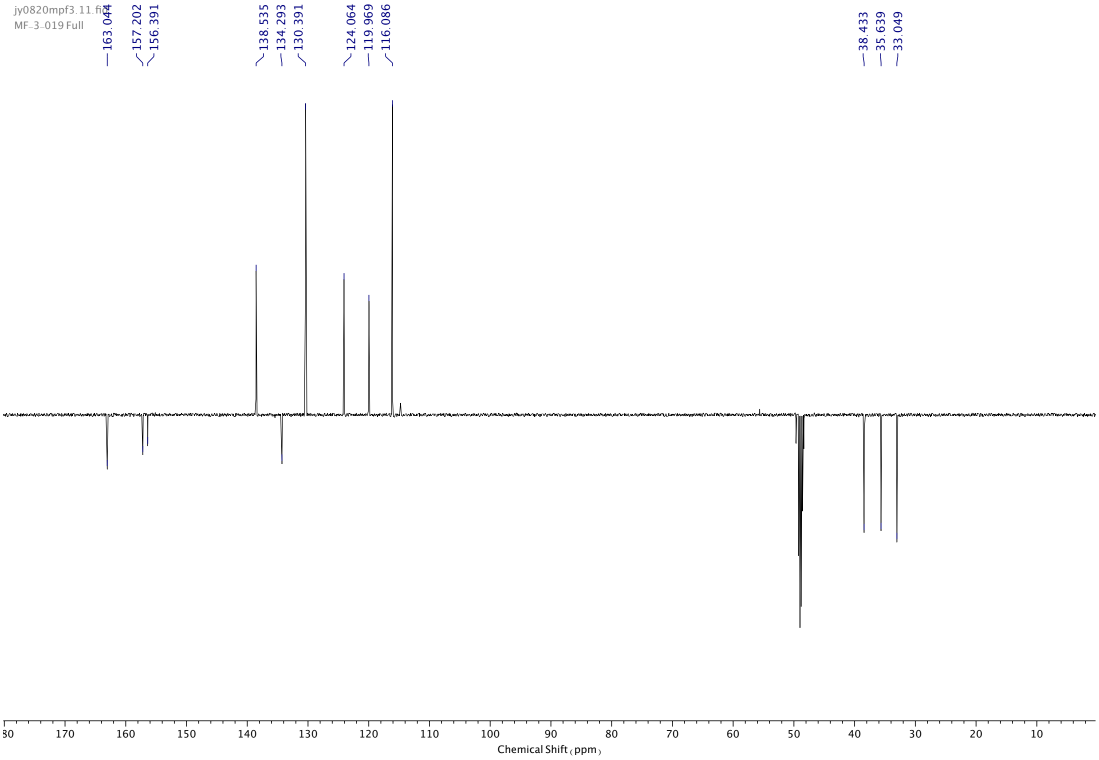

Figure **134**. ^{13}C NMR (MeOD, 101 MHz) of **38.**

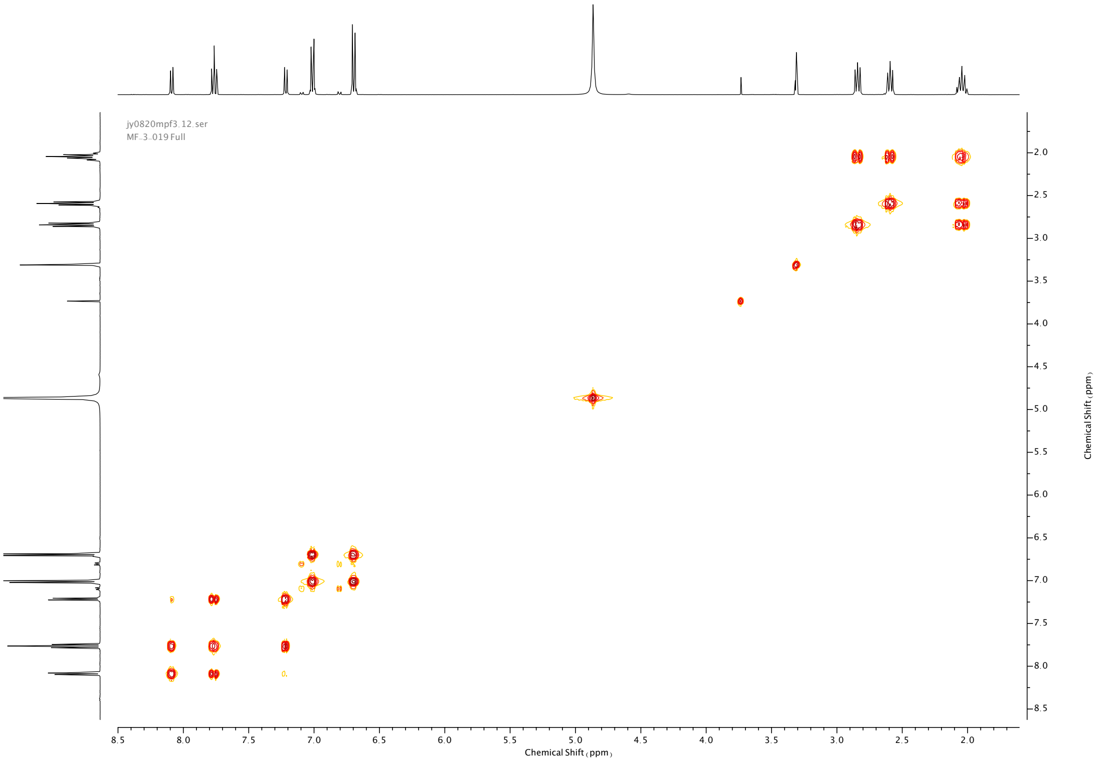

Figure **135**. COSY NMR (MeOD) of **38**.

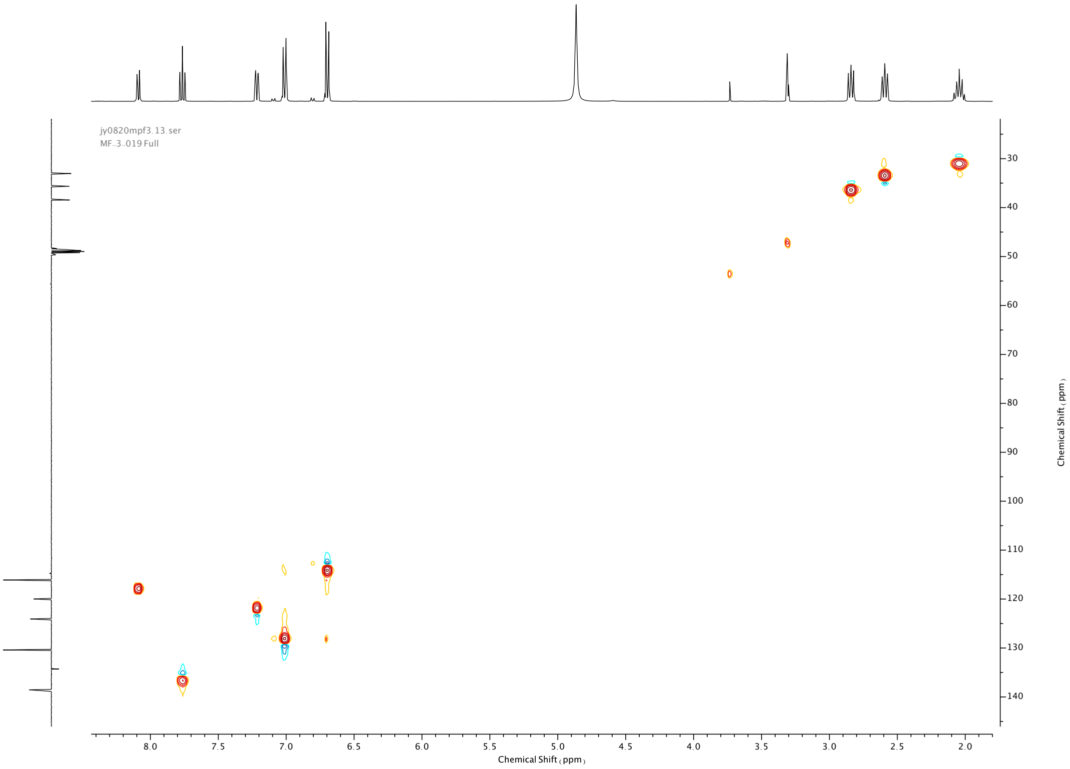

Figure **136**. HSQC NMR (MeOD) of **38**.

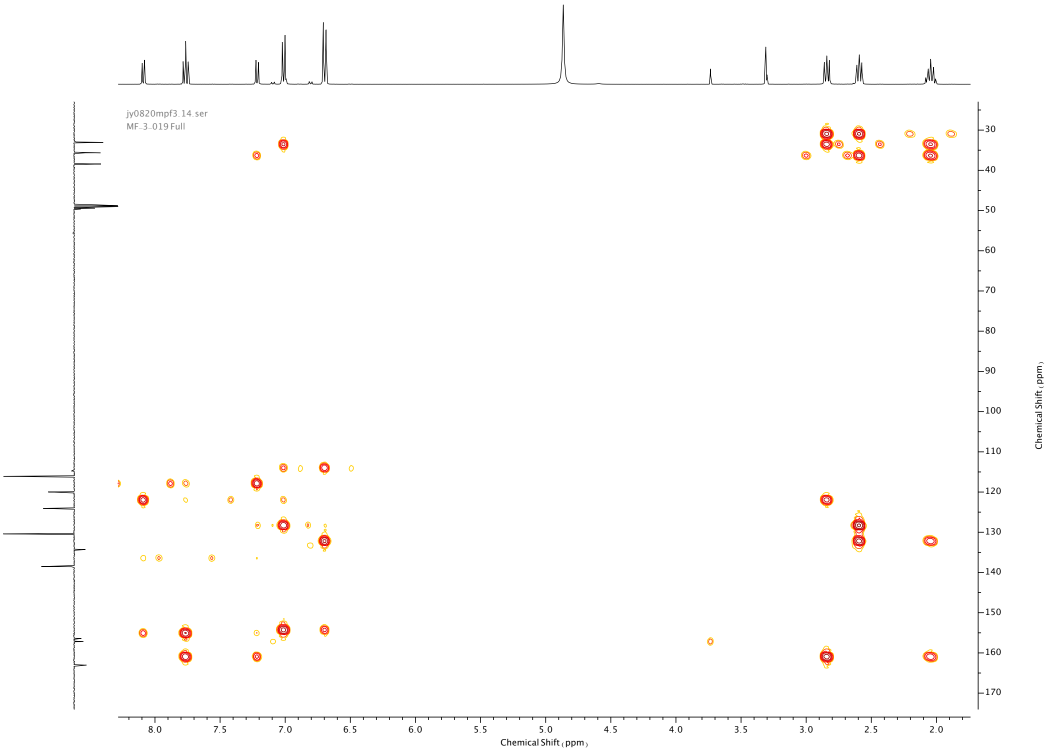

Figure **137**. HMBC NMR (MeOD) of **38**.

Compound **42**

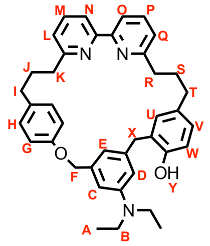

42 was a by-product in the photolysis of macrocycle **25** and was isolated *via* silica-gel chromatography using a Biotage Isolute SPE column (eluent 9:1 → 4:1 petrol: acetone), affording **42** as a white foam. ^{1}H NMR (400 MHz, $CDCl_3$, 298 K) δ_H 8.04 (1H, dd, *J* = 7.8, 0.9 Hz, H_O), 7.87 (1H, dd, *J* = 7.7, 0.9 Hz, H_N), 7.66 (1H, t, *J* = 7.7 Hz, H_P), 7.33 (1H, t, *J* = 7.7 Hz, H_M), 7.10 (1H, dd, *J* = 7.6, 0.9 Hz, H_Q), 7.02 (1H, d, *J* = 2.1 Hz, H_U), 6.92 (1H, dd, *J* = 8.1, 2.2 Hz, H_V), 6.80 (1H, dd, *J* = 7.7, 0.9 Hz, H_L), 6.76 (2H, app. d, *J* = 8.8 Hz, H_H), 6.67 (2H, d, *J* = 8.1 Hz, H_W), 6.59-6.56 (1H, m, H_D), 6.54-6.52 (1H, m, H_C), 6.42 (2H, app. d, *J* = 8.6 Hz, H_G), 6.36-6.34 (1H, m, H_E), 4.65 (2H, s, H_F), 3.90 (2H, s, H_X), 3.33 (4H, q, *J* = 7.1 Hz, H_B), 2.94-2.90 (2H, m, H_K), 2.86 (2H, app. t, *J* = 8.0 Hz, H_R), 2.68 (2H, app. t, *J* = 6.2 Hz, H_I), 2.62 (2H, app. t, *J* = 7.8 Hz, H_T), 2.33-2.25 (2H, m, H_J), 2.11-2.03 (2H, m, H_S), 1.12 (6H, t, *J* = 7.1 Hz, H_A). ^{13}C NMR (101 MHz, $CDCl_{3,}$ 298 K) δ_C 161.6, 161.1, 156.6, 156.3, 155.6, 152.0, 148.4, 141.3, 138.8, 136.8, 136.3, 134.7, 134.1, 131.1, 129.7, 127.6, 127.1, 123.1, 122.4, 118.5, 118.2, 115.6, 114.5 (x2), 112.0, 108.6, 70.9, 70.7, 44.5, 38.3, 37.8, 35.1, 34.8, 32.0, 29.4, 12.8. HR-ESI-MS (CH_3CN): *m/z* = 598.3434 $[M+H]^+$ calc. 598.3434.

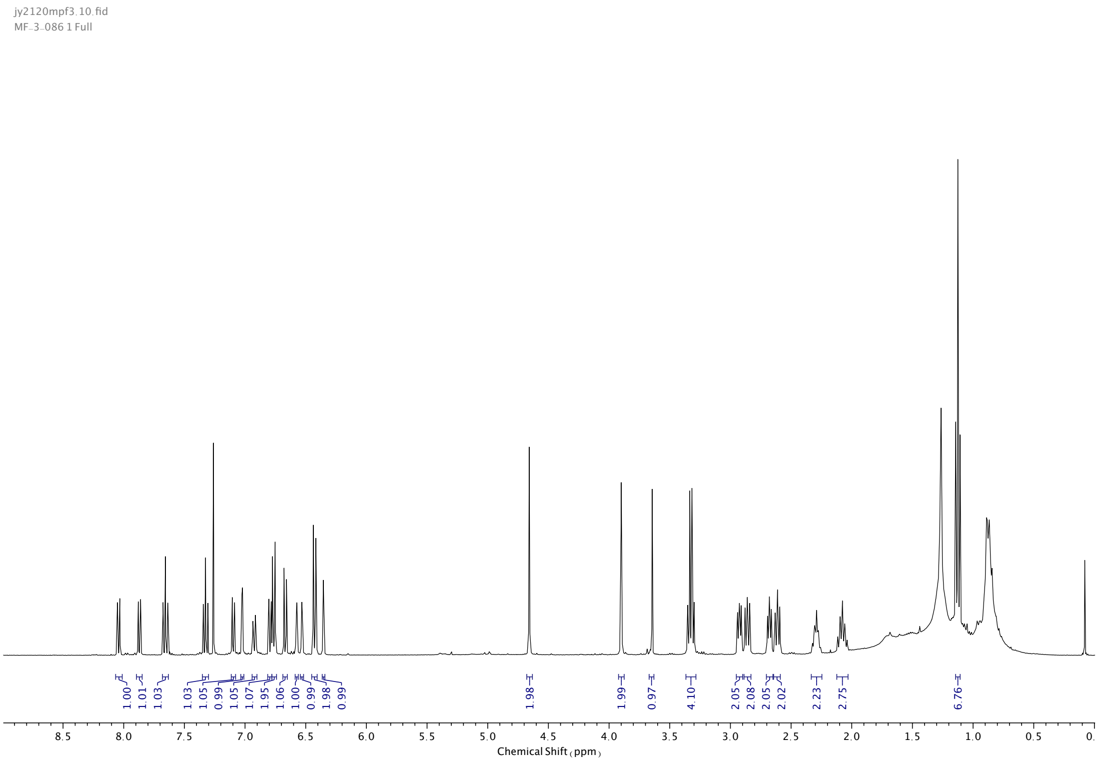

Figure **138**. ^{1}H NMR (CDCl$_3$, 400 MHz) of **42**.

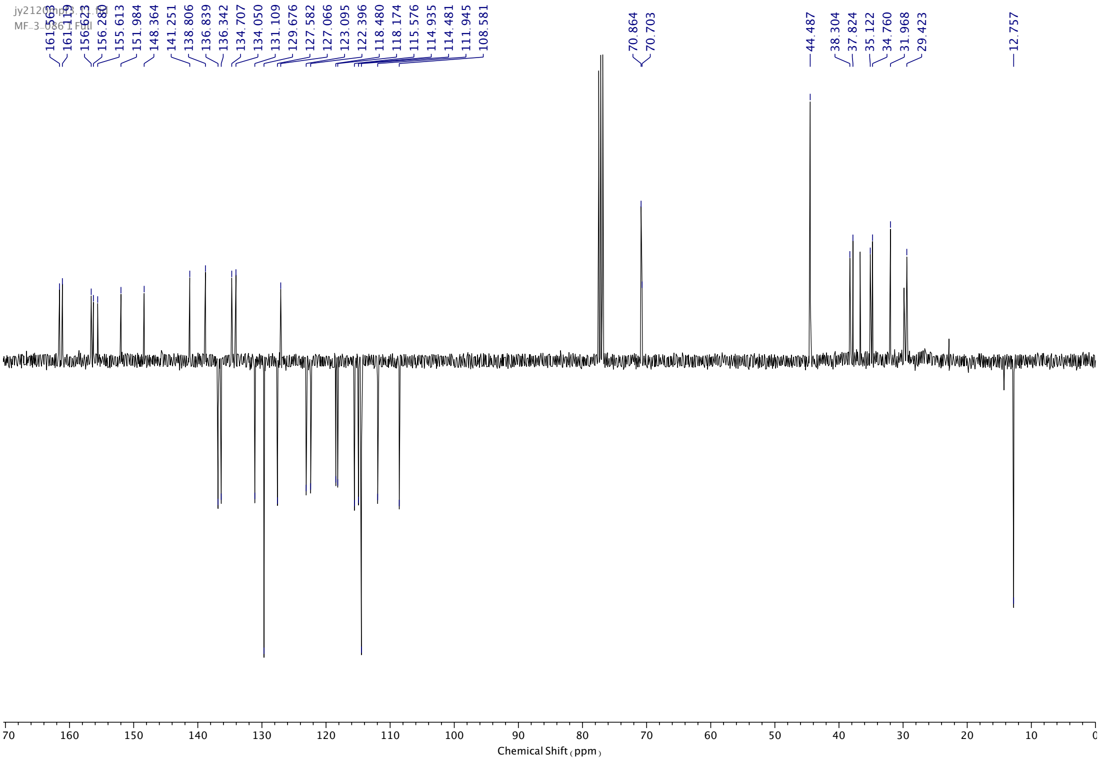

Figure **139**. ^{13}C NMR (CDCl$_3$, 101 MHz) of **42.**

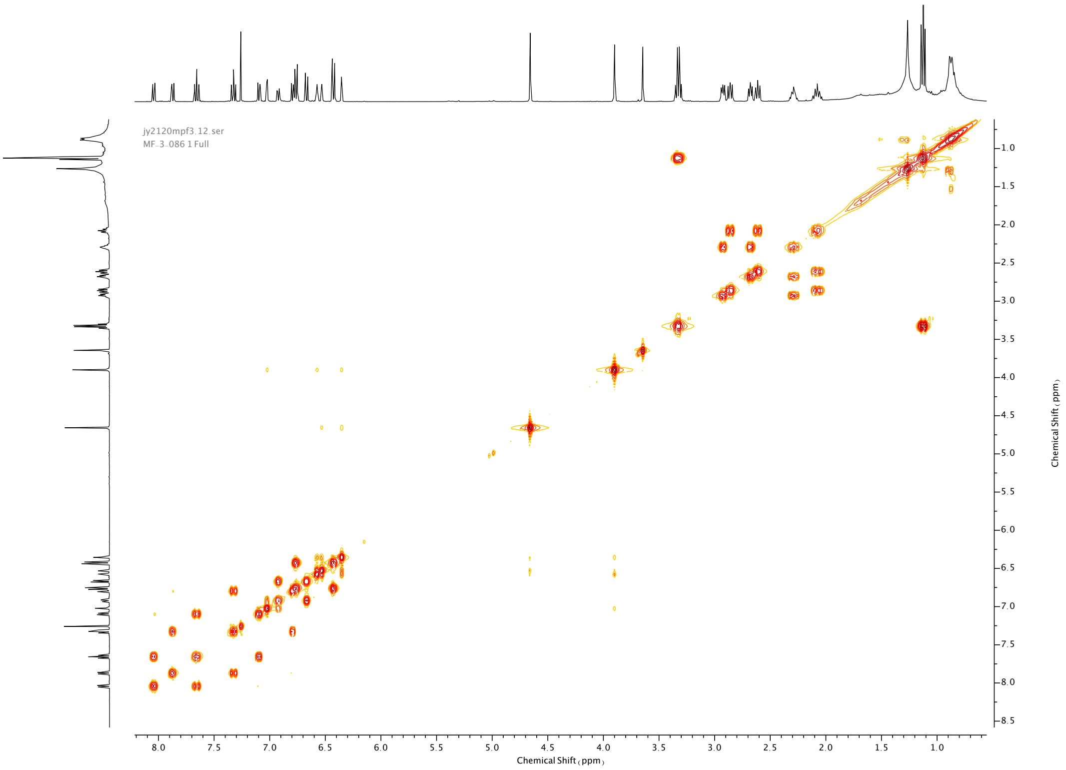

Figure **140**. COSY NMR ($CDCl_3$) of **42**.

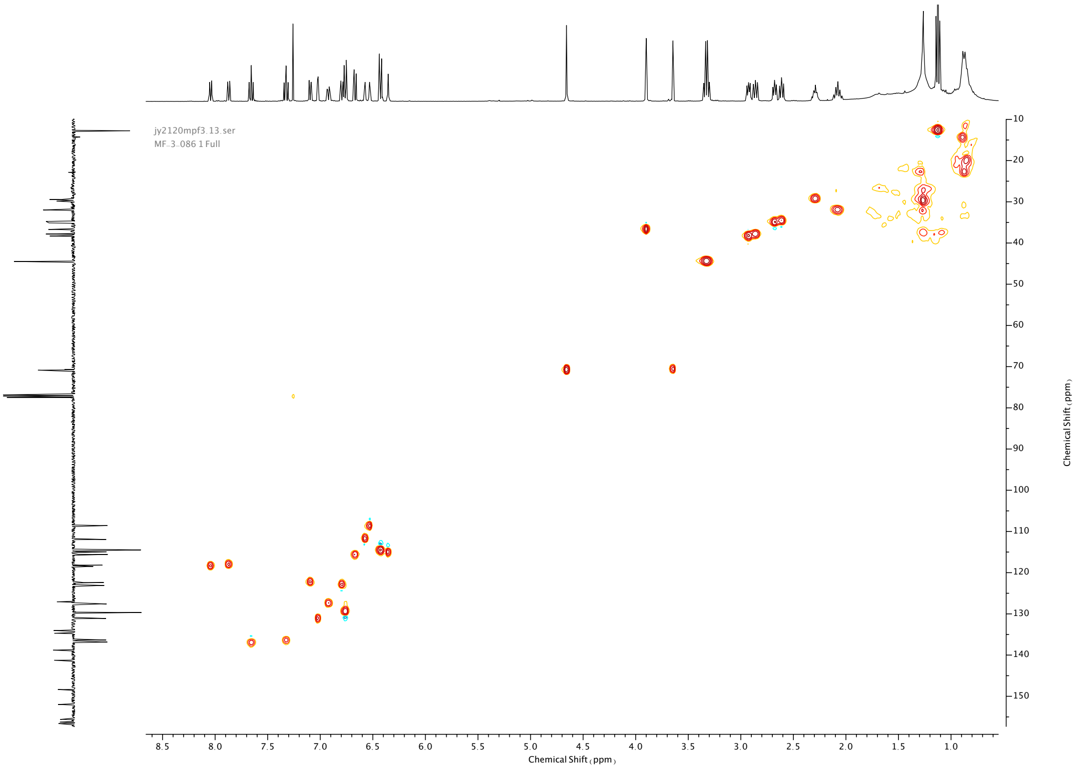

Figure **141**. HSQC NMR ($CDCl_3$) of **42**.

Figure **142**. HMBC NMR ($CDCl_3$) of **42**.

Compound **43**

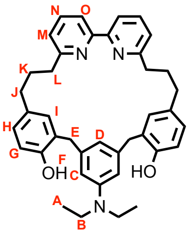

43 was a by-product in the photolysis of macrocycle **25** and was isolated *via* silica-gel chromatography using a Biotage Isolute SPE column (eluent 4:1 → 1:1 petrol: acetone), affording **43** as a white solid. M.p. 158-160 °C. ^{1}H NMR (400 MHz, DMSO-d$_6$, 298 K) δ_H 9.04 (2H, s, O-H$_F$), 8.06 (2H, dd, *J* = 7.8, 0.8 Hz, H$_O$), 7.79 (2H, t, *J* = 7.7 Hz, H$_N$), 7.23 (2H, dd, *J* = 7.8, 0.8 Hz, H$_M$), 6.84 (2H, dd, *J* = 8.2, 2.1 Hz, H$_H$), 6.69 (2H, d, *J* = 8.2 Hz, H$_G$), 6.41 (2H, d, *J* = 2.1 Hz, H$_I$), 6.14 (2H, s, H$_C$), 6.09 (1H, s, H$_D$), 3.55 (4H, s, H$_E$), 3.07 (4H, q, *J* = 7.2 Hz, H$_B$), 2.84 (4H, t, *J* = 6.4 Hz, H$_L$), 2.34-2.28 (4H, m, H$_J$), 2.03-1.93 (4H, m, H$_K$), 0.88 (6H, t, *J* = 7.0 Hz, H$_A$). ^{13}C NMR (101 MHz, DMSO-d$_6$, 298 K) δ_C 160.8, 155.6, 152.9, 147.3, 141.4, 137.2, 131.9, 130.12 126.9, 126.3, 123.3, 118.2, 116.3, 114.7, 109.8, 43.7, 36.3, 35.1, 32.8, 30.7, 12.4. HR-ESI-MS (CH$_3$CN): *m/z* = 598.3432 [M+H]$^+$ calc. 598.3434.

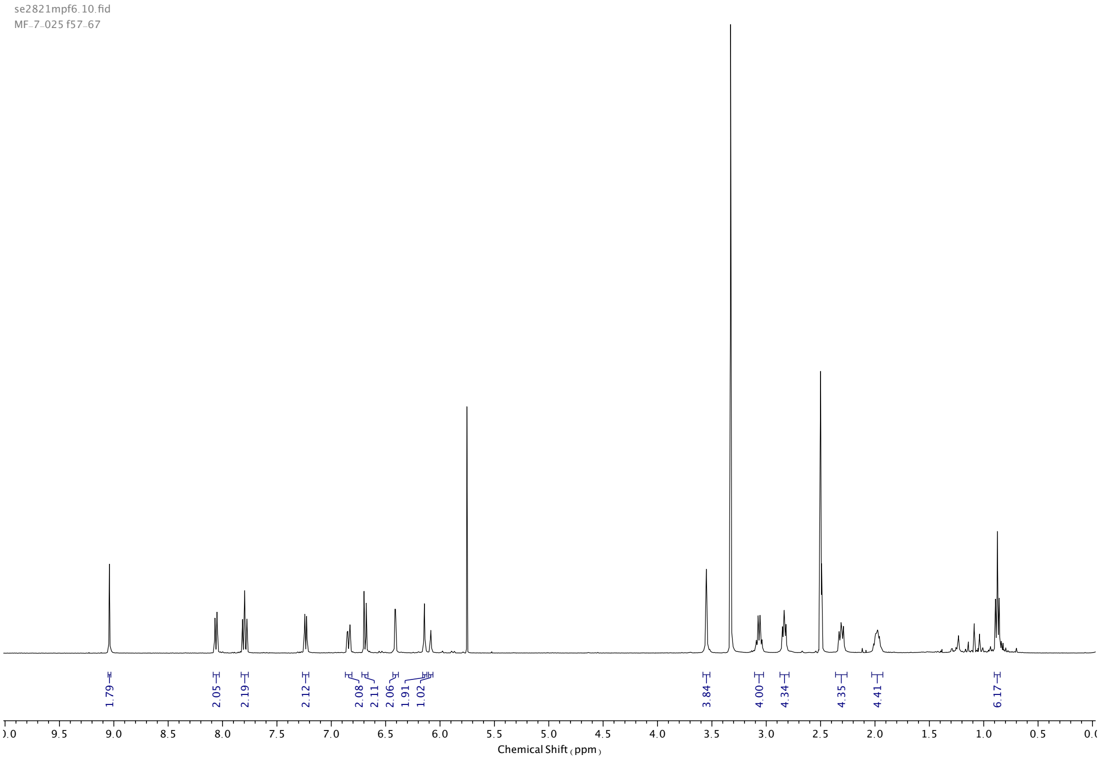

Figure **143**. ^{1}H NMR (DMSO-d$_6$, 400 MHz) of **43**.

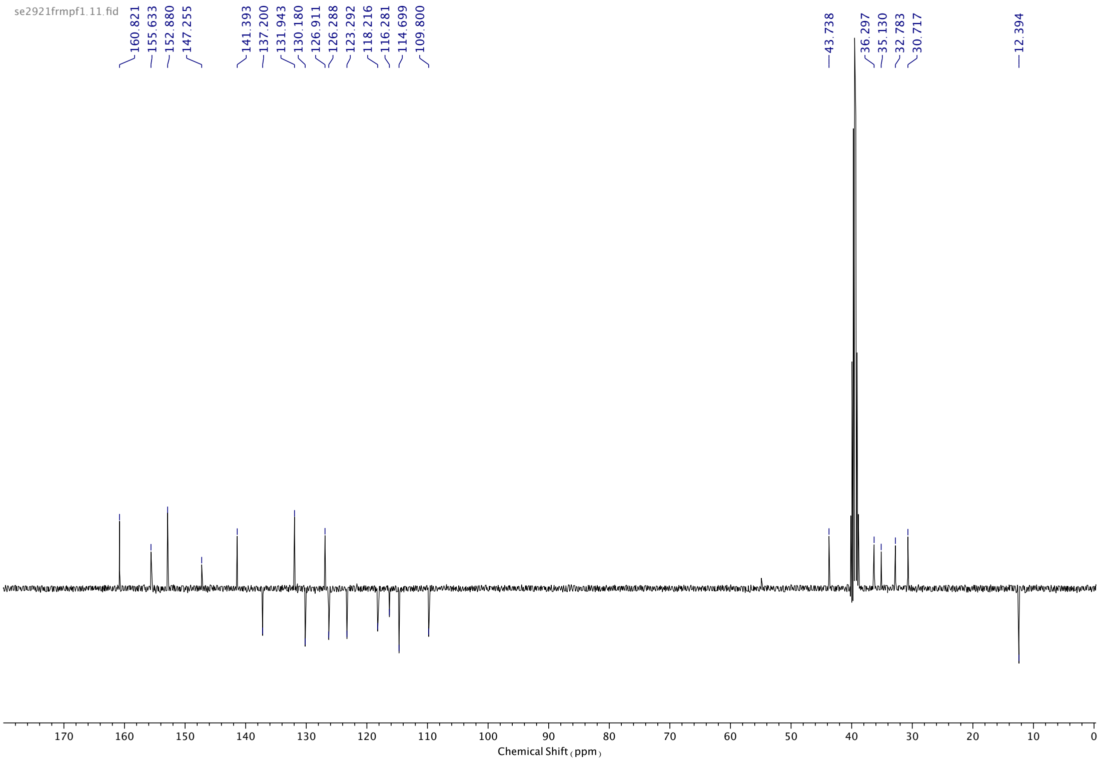

Figure **144**. ^{13}C NMR (DMSO-d$_6$, 101 MHz) of **43.**

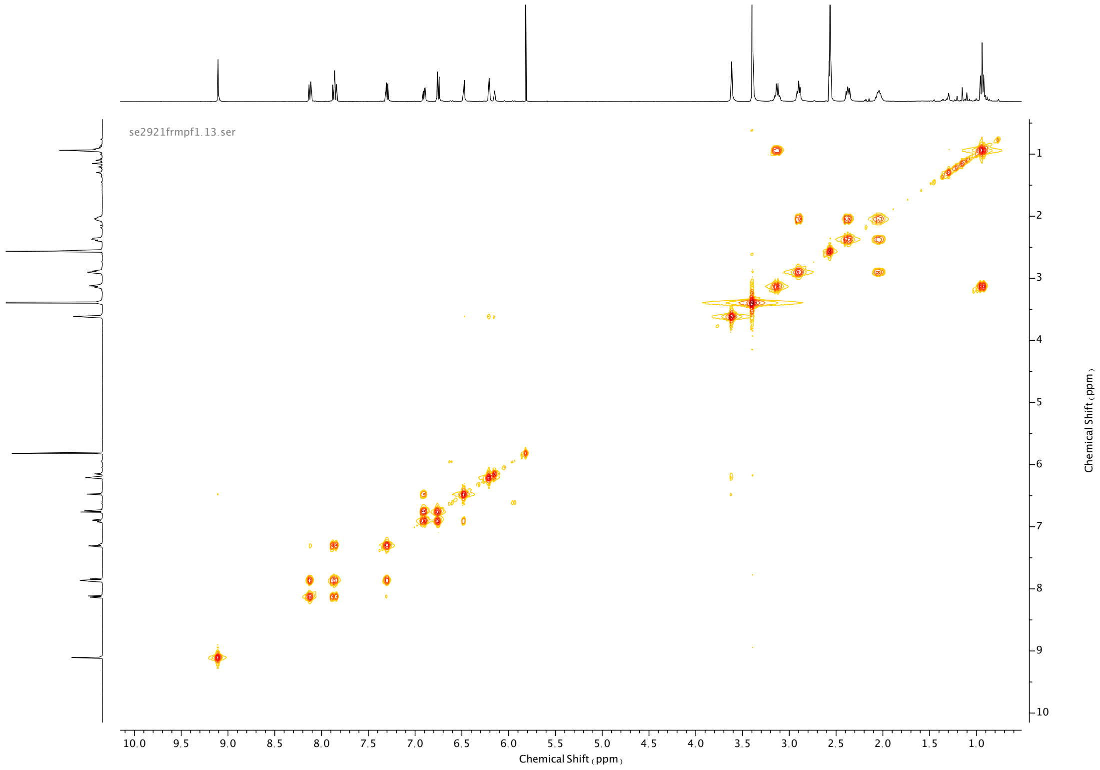

Figure **145**. COSY NMR (DMSO-d$_6$) of **43**.

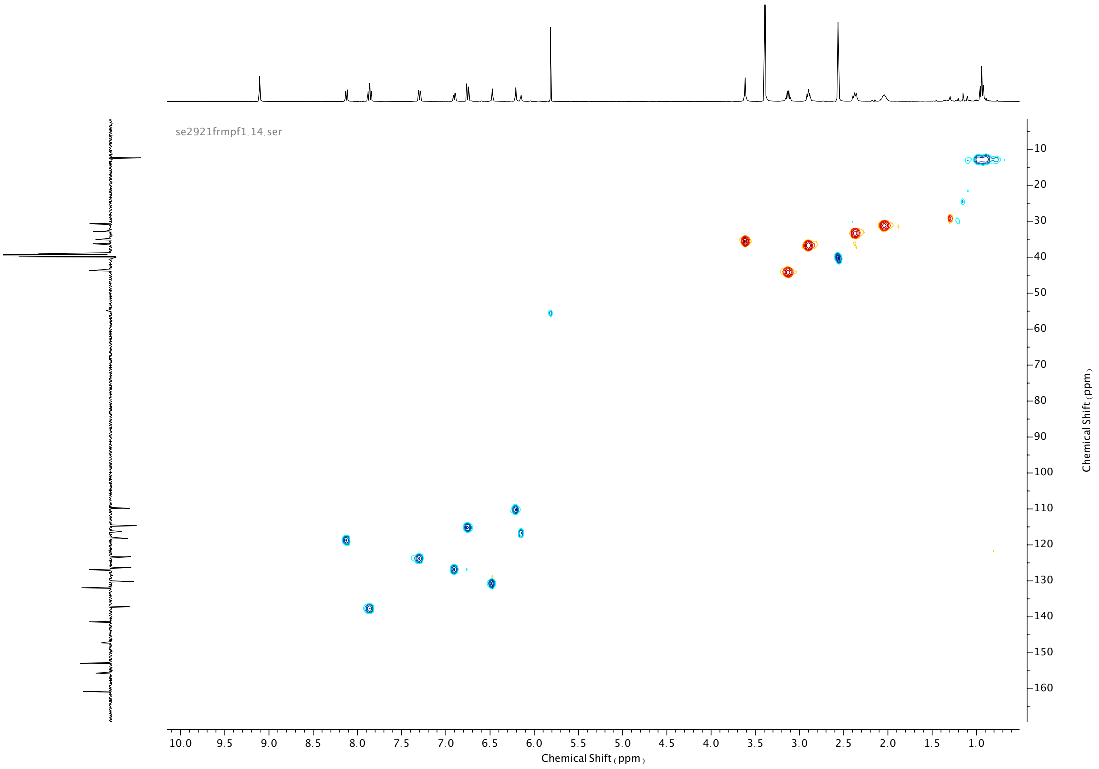

Figure **146**. HSQC NMR (DMSO-d$_6$) of **43**.

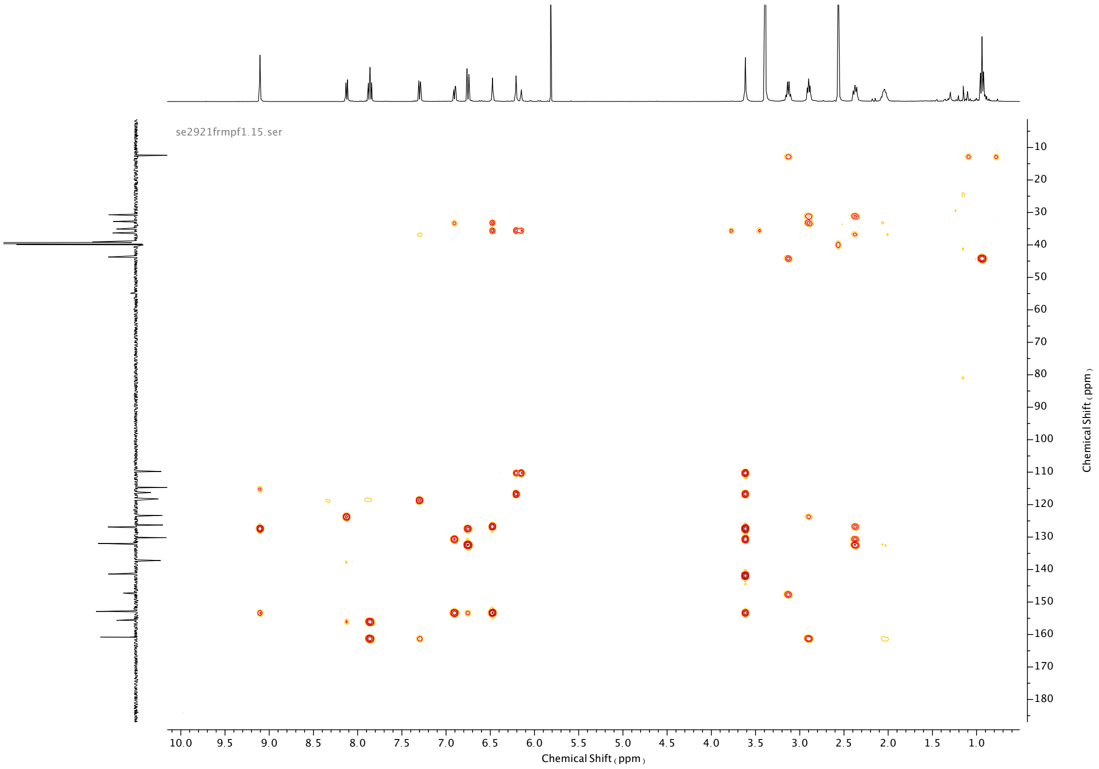

Figure **147**. HMBC NMR (DMSO-d$_6$) of **43**.

Compound **53**

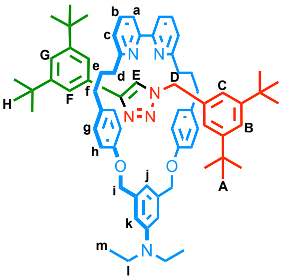

53 was synthesised according to general procedure **(1)** from macrocycle **25** (150 mg, 0.25 mmol, 1.0 eq.), azide stopper **52** (91 mg, 0.37 mmol, 1.5 eq.), and alkyne stopper **51** (78 mg, 0.37 mmol, 1.5 eq.). Purification by column chromatography (eluent 1:0 → 4:1 CH_2Cl_2: Et_2O) afforded **53** as a white foam (201 mg, 0.19 mmol, 75%). ^{1}H NMR (400 MHz, $CDCl_3$, 298 K) δ_H 9.48 (1H, s, H_E), 7.86 (2H, d, *J* = 1.8 Hz, H_F), 7.54 (2H, t, *J* = 7.8 Hz, H_b), 7.43 (2H, d, *J* = 7.7 Hz, H_a), 7.22-7.20 (1H, m H_j), 7.16 (1H, t, *J* = 1.9 Hz, H_G), 6.97 (2H, d, *J* = 7.6 Hz, H_c), 6.89 (1H, t, *J* = 1.9 Hz, H_B), 6.65 (2H, d, *J* = 1.3 Hz, H_k), 6.27 (2H, d, *J* = 1.8 Hz, H_C), 5.25 (4H, s, H_i), 3.65 (2H, s, H_D), 2.91 (4H, q, *J* = 7.0 Hz, H_l), 2.48 (2H, app. dt, *J* = 13.5, 6.6 Hz, H_f & $H_{f'}$), 2.33 (4H, td, *J* = 11.7, 5.4 Hz, H_d), 2.21-2.15 (2H, m, H_f & $H_{f'}$), 1.74-1.62 (2H, m, H_e & $H_{e'}$), 1.58-1.47 (2H, m, H_e & $H_{e'}$), 1.04 (18H, s, H_H), 0.85 (6H, t, *J* = 7.1 Hz, H_m), 0.83 (18H, s, H_A). ^{13}C NMR (101 MHz, $CDCl_3$, 298 K) δ_C 162.8, 156.7, 156.5, 150.2, 150.0, 148.5, 147.4, 144.0, 140.0, 136.5, 133.3, 132.5, 131.8, 129.4, 124.0, 122.8, 121.1, 120.5, 119.2, 115.2, 113.8, 109.0, 69.7, 53.8, 44.2, 37.2, 35.2, 34.8, 34.3, 31.4, 31.3, 31.1, 12.6. HR-ESI-MS (CH_3CN): *m/z* =1057.7030 $[M+H]^+$ calc. 1057.7047.

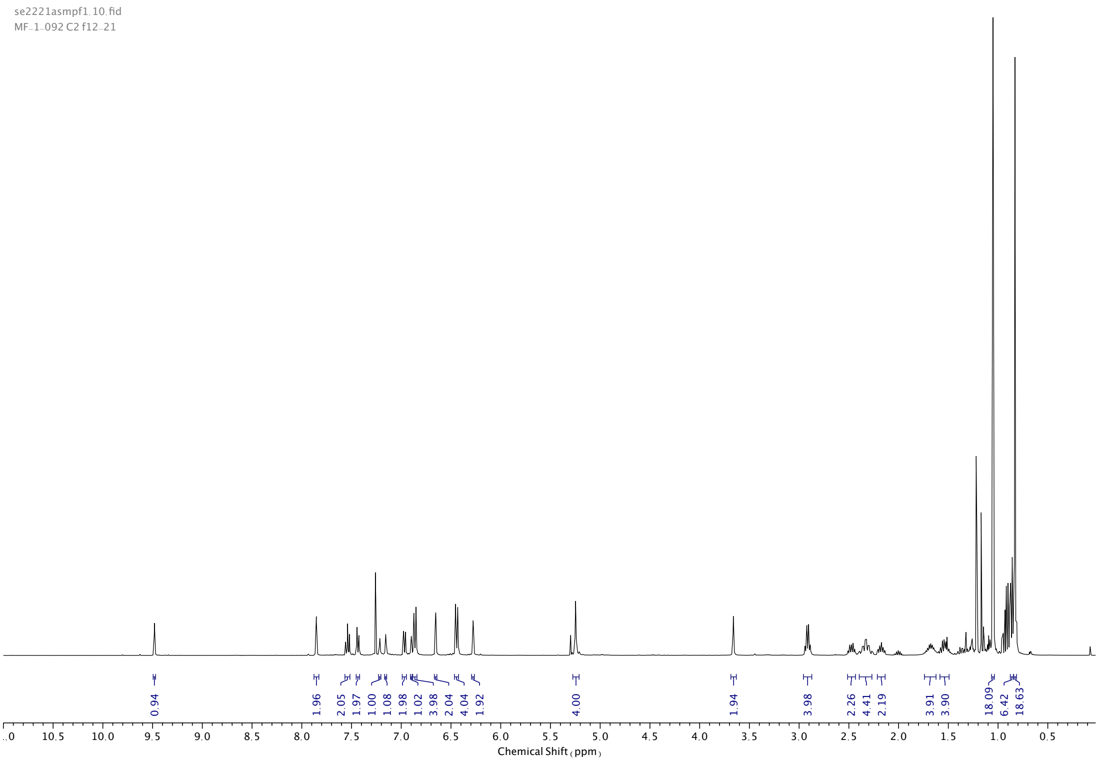

Figure **148**. ^{1}H NMR (CDCl$_3$, 400 MHz) of **53**.

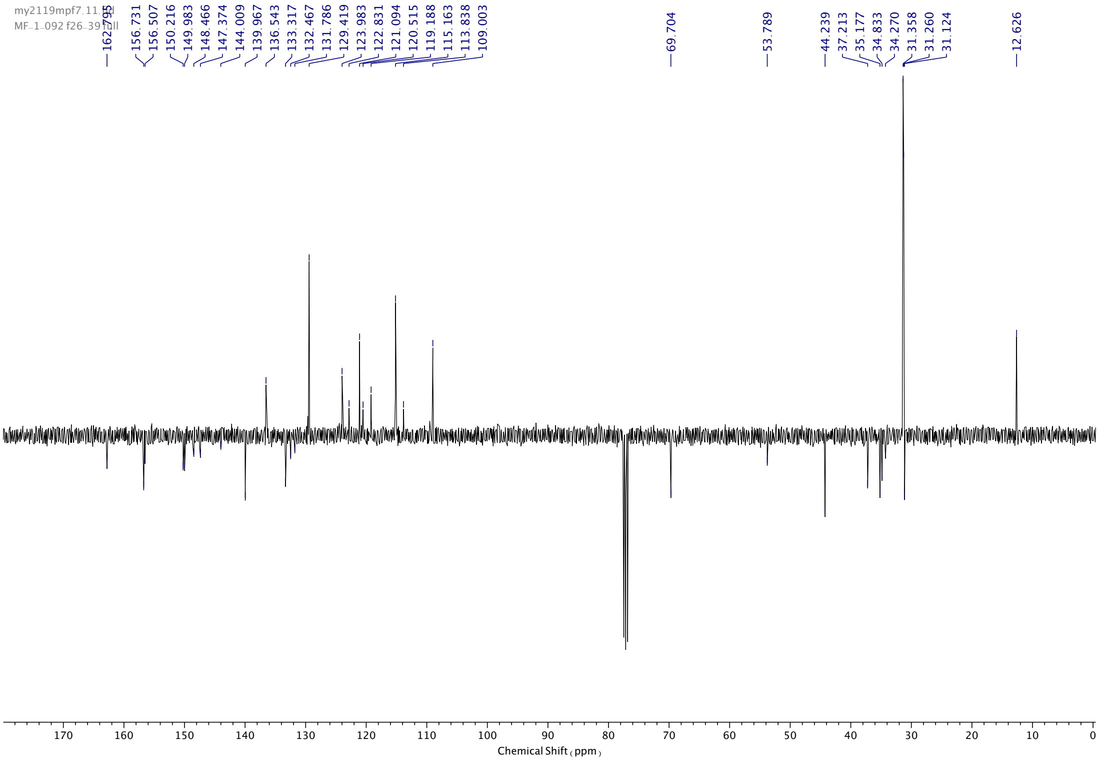

Figure **149**. ^{13}C NMR (CDCl$_3$, 101 MHz) of **53.**

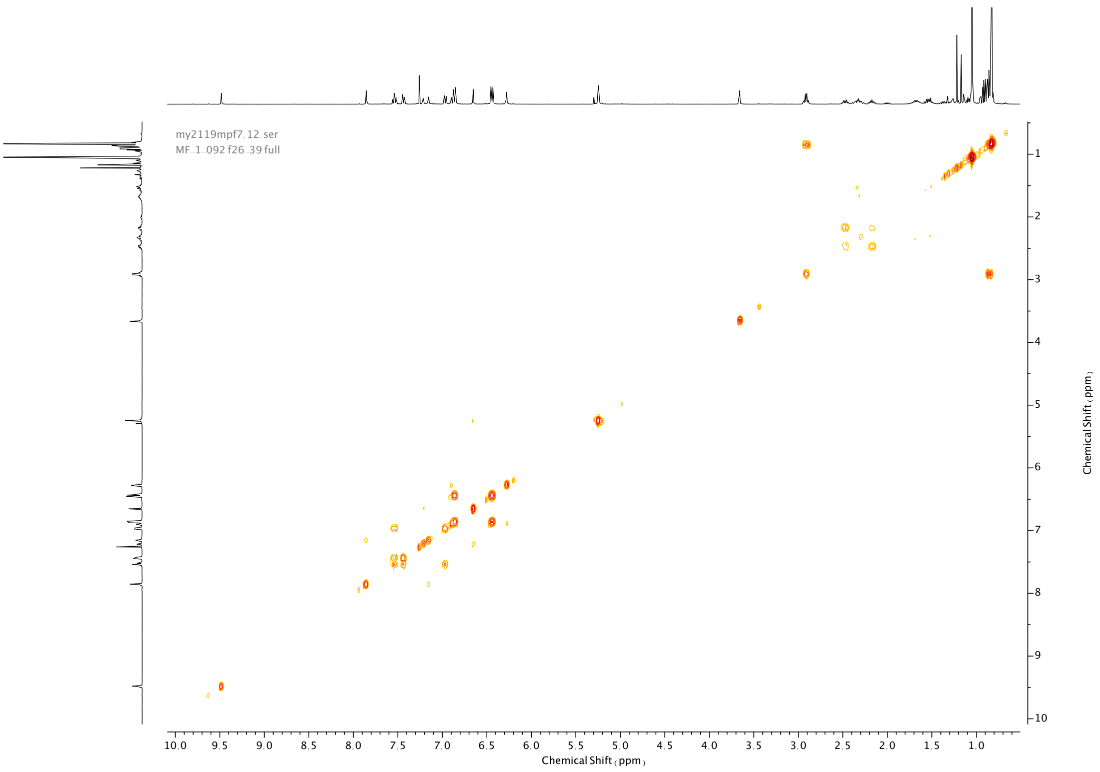

Figure **150**. COSY NMR ($CDCl_3$) of **53**.

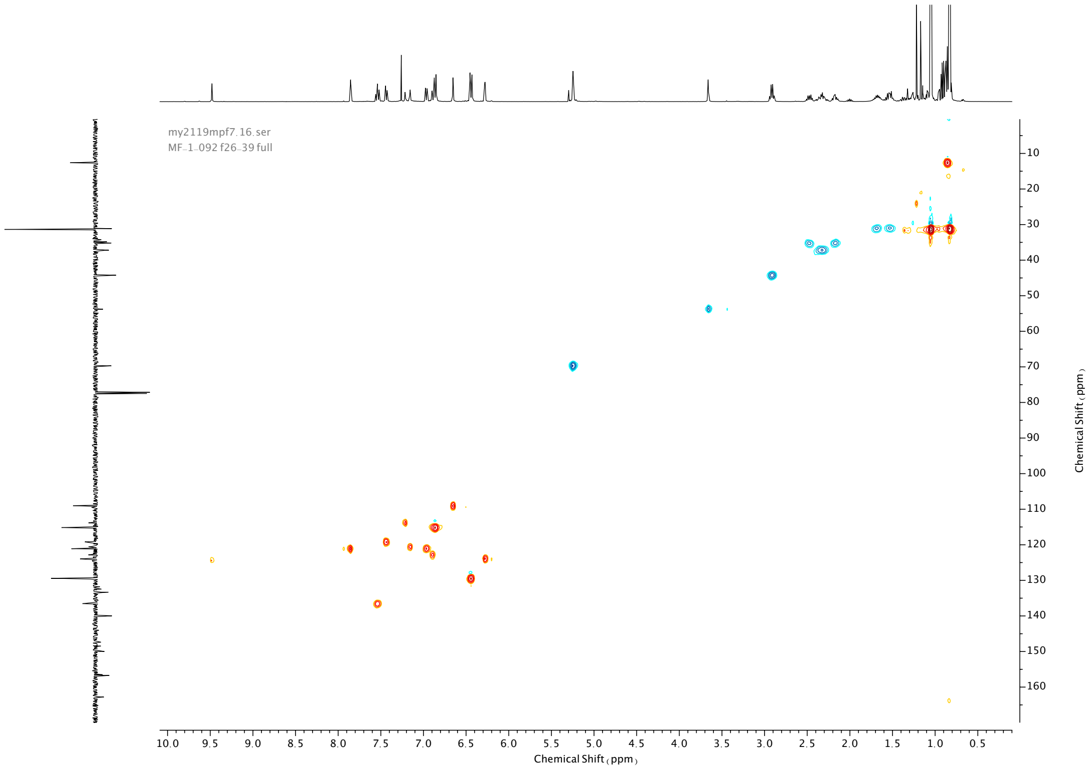

Figure **151**. HSQC NMR ($CDCl_3$) of **53**.

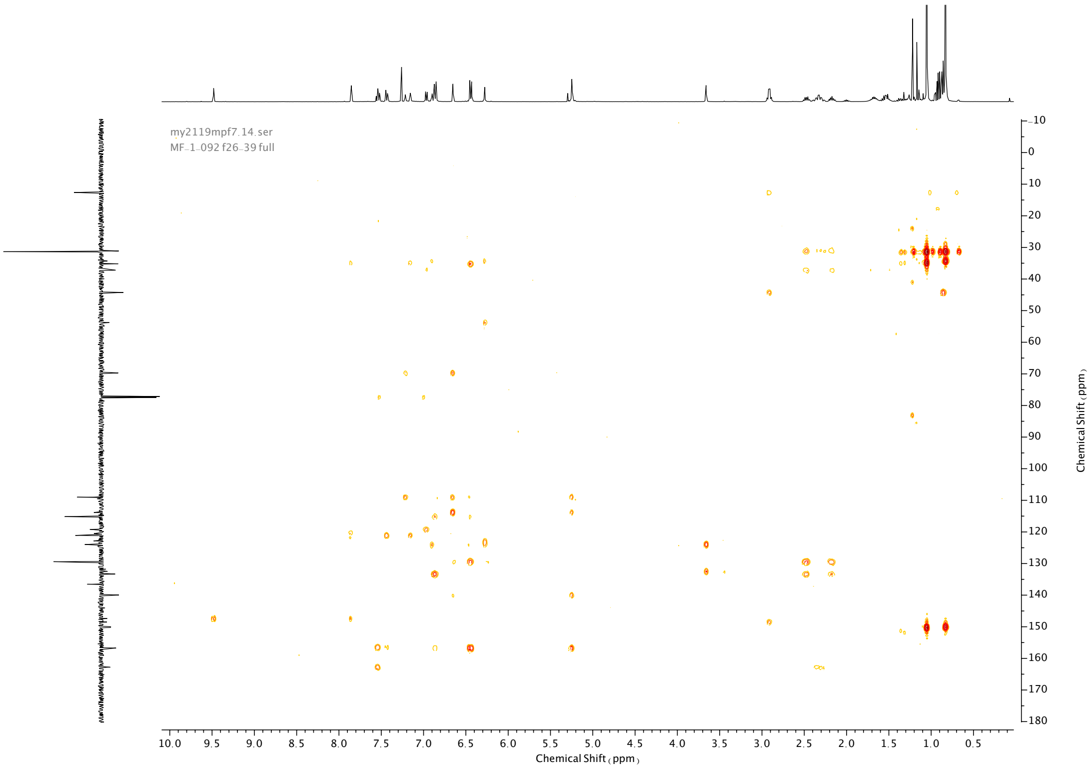

Figure **152**. HMBC NMR ($CDCl_3$) of **53**.

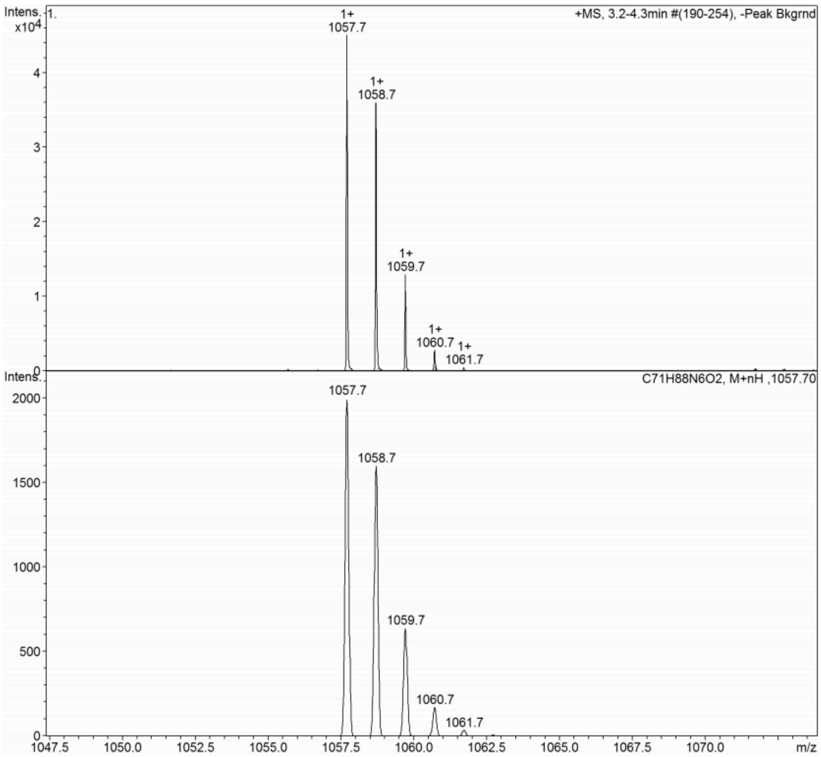

Figure **153**. Rotaxane **53** isotope pattern.

Compound **54**

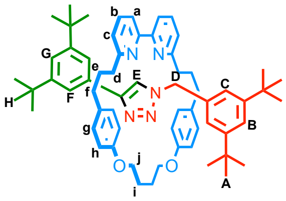

54 was synthesised according to general procedure **(1)** from macrocycle **13** (77 mg, 0.16 mmol, 1.0 eq.), azide stopper **52** (58 mg, 0.24 mmol, 1.5 eq.) and alkyne stopper **51** (50 mg, 0.24 mmol, 1.5 eq.). Purification by column chromatography (eluent 1:0 → 4:1 petrol: Et_2O) afforded **54** as a white foam (110 mg, 0.12 mmol, 73%). ^{1}H NMR (400 MHz, $CDCl_3$, 298 K) δ_H 9.93 (1H, s, H_E), 7.67 (2H ,t, J = 7.7 Hz, H_b), 7.53 (2H, d, J = 7.7 Hz, H_a), 7.46 (2H, d, J = 1.9 Hz, H_F), 7.33 (1H, t, J = 1.8 Hz, H_B), 7.13 (1H, t, J = 1.9 Hz, H_G), 7.12-7.07 (4H, m, H_C & H_c), 6.48 (4H, d, J = 8.5 Hz, H_h), 6.30 (4H, d, J = 8.5 Hz, H_g), 4.62 (2H, s, H_D), 4.50 (4H, t, J = 6.4 Hz, H_i), 2.40-2.15 (12H, m, H_f, H_d, H_j), 1.65-1.45 (4H, m, H_e), 1.18 (18H, s, H_A), 1.17 (18H, s, H_H). ^{13}C NMR (101 MHz, $CDCl_3$, 298 K) δ_C 163.4, 157.6, 157.4, 150.8, 149.6, 146.6, 136.8, 134.6, 131.9, 131.6, 128.3, 124.2, 123.1, 121.8, 121.3 (HMBC), 120.7, 120.1, 119.7, 115.2, 66.9, 53.8, 36.9, 35.1, 34.8, 31.6, 31.5, 31.4 (x2), 25.1. RP-HRMS-ESI (CH_3CN): m/z = 938.6320 $[M+H]^+$ calc. 938.6312.

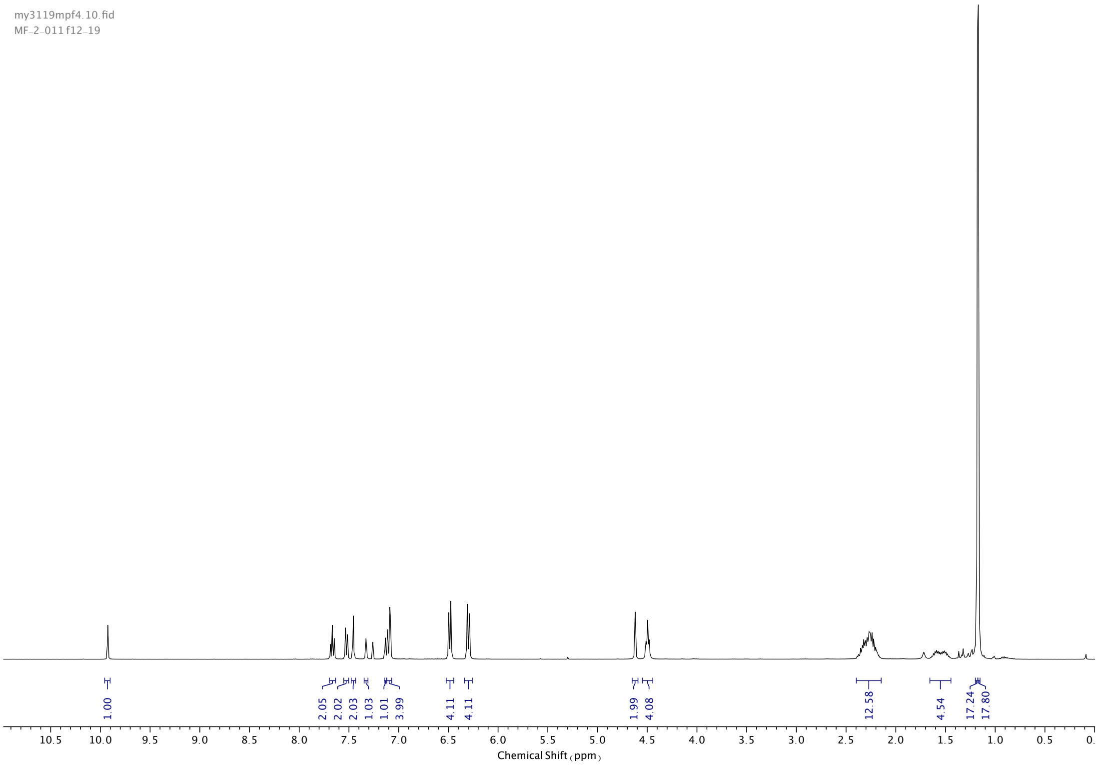

Figure **154**. ^{1}H NMR ($CDCl_3$, 400 MHz) of **54**.

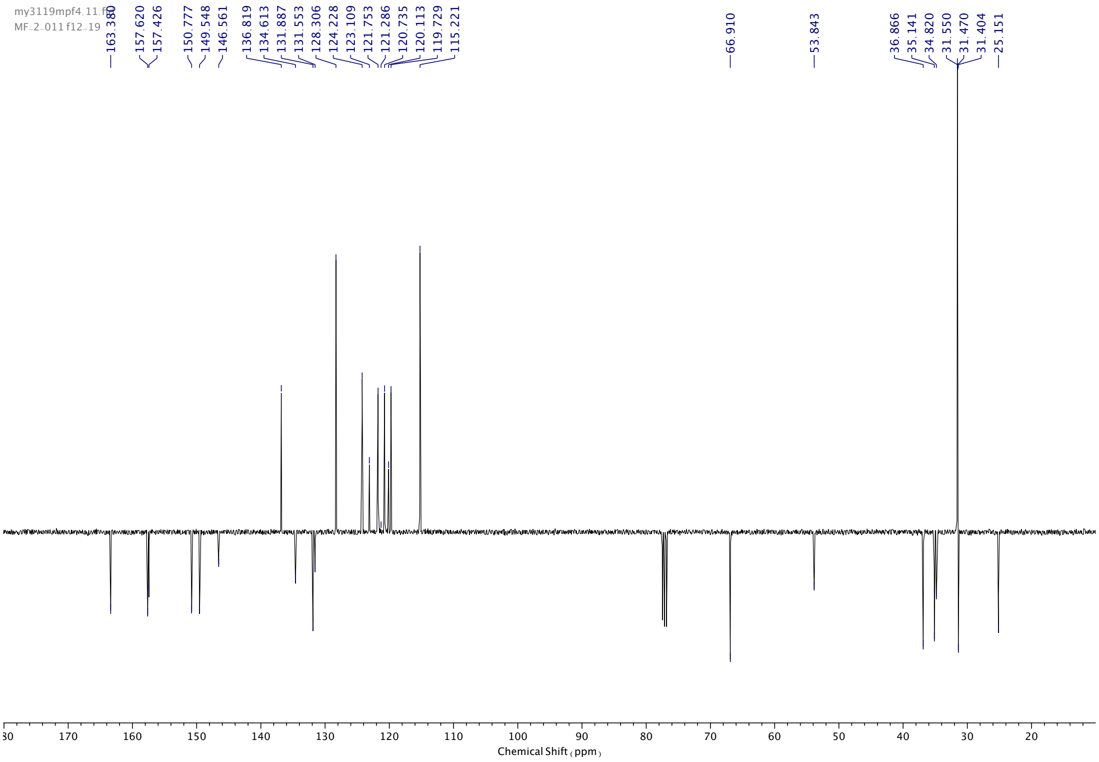

Figure **155**. ^{13}C NMR (CDCl$_3$, 101 MHz) of **54.**

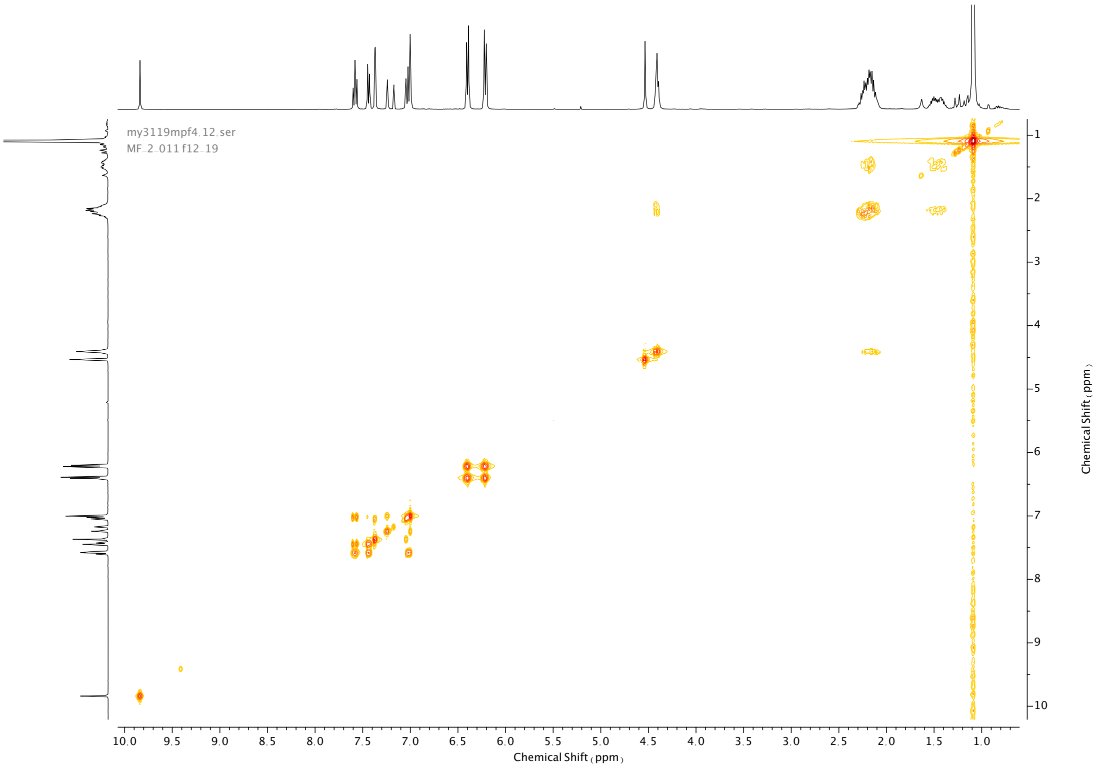

Figure **156**. COSY NMR (CDCl$_3$) of **54**.

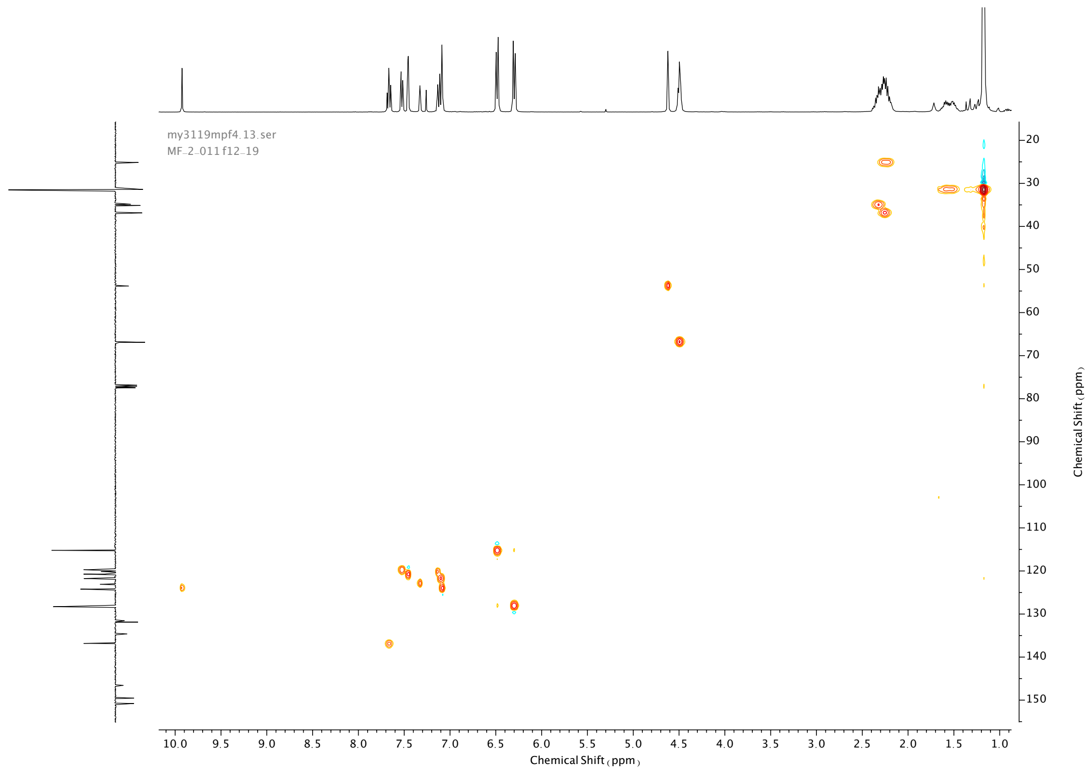

Figure **157**. HSQC NMR ($CDCl_3$) of **54**.

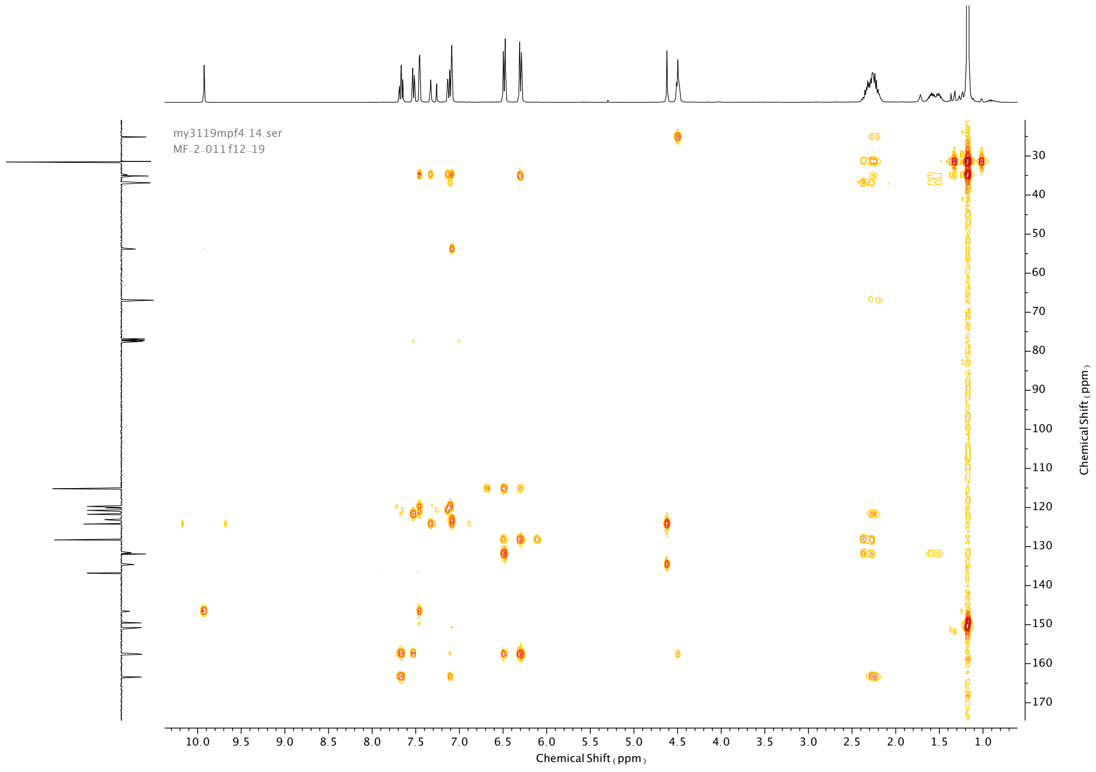

Figure **158**. HMBC NMR ($CDCl_3$) of **54**.

Compound **55**

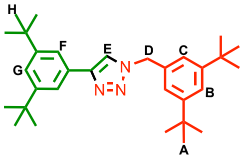

Compound **55** was isolated as a by-product in the synthesis of rotaxane **53**. ^{1}H NMR (400 MHz, $CDCl_3$, 298 K) δ_H 7.69 (1H, br. s, H_E), 7.65 (2H, d, *J* = 1.8 Hz, H_F), 7.43 (1H, t, *J* = 1.8 Hz, H_B), 7.40 (1H, t, *J* = 1.9 Hz, H_G), 7.15 (2H, d, *J* = 1.8 Hz, H_C), 5.57 (2H, s, H_D), 1.36 (18H, s, H_A), 1.31 (18H, s, H_H). ^{13}C NMR (101 MHz, $CDCl_3$, 298 K) δ_C 151.9, 151.4, 149.2, 134.2, 130.1, 122.9, 122.5, 122.4, 120.3, 119.6, 54.9, 35.1 (x2), 31.6, 31.5.

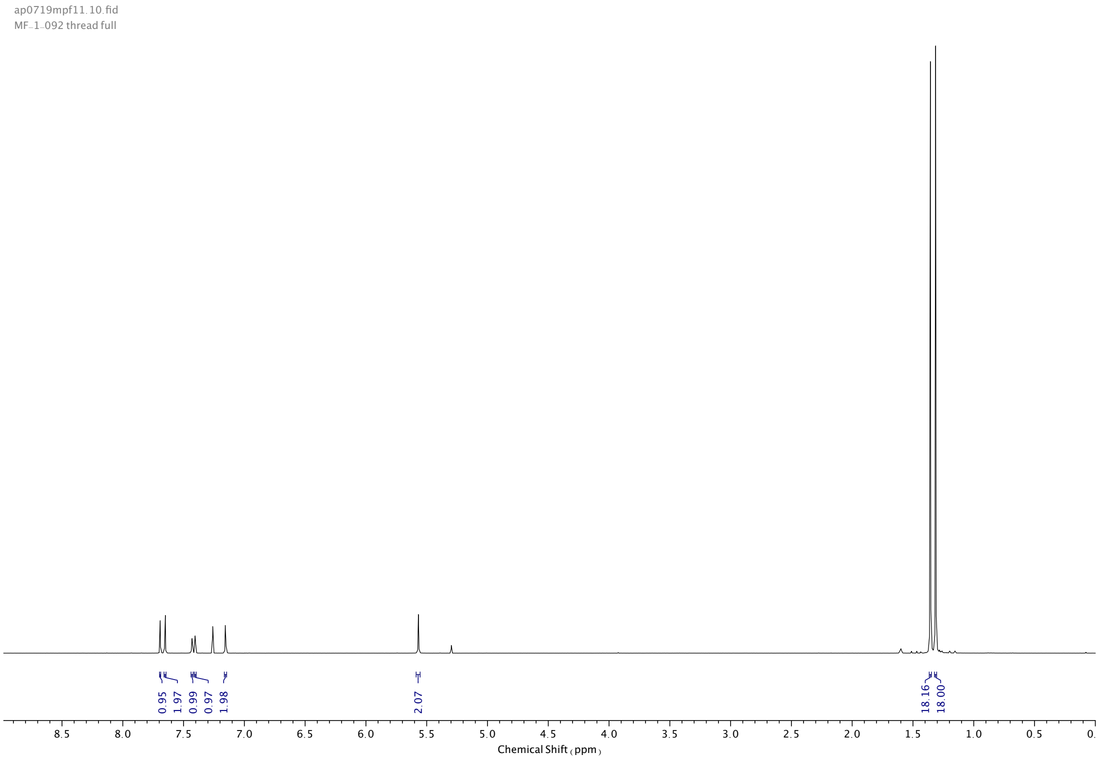

Figure **159**. ^{1}H NMR ($CDCl_3$, 400 MHz) of **55**.

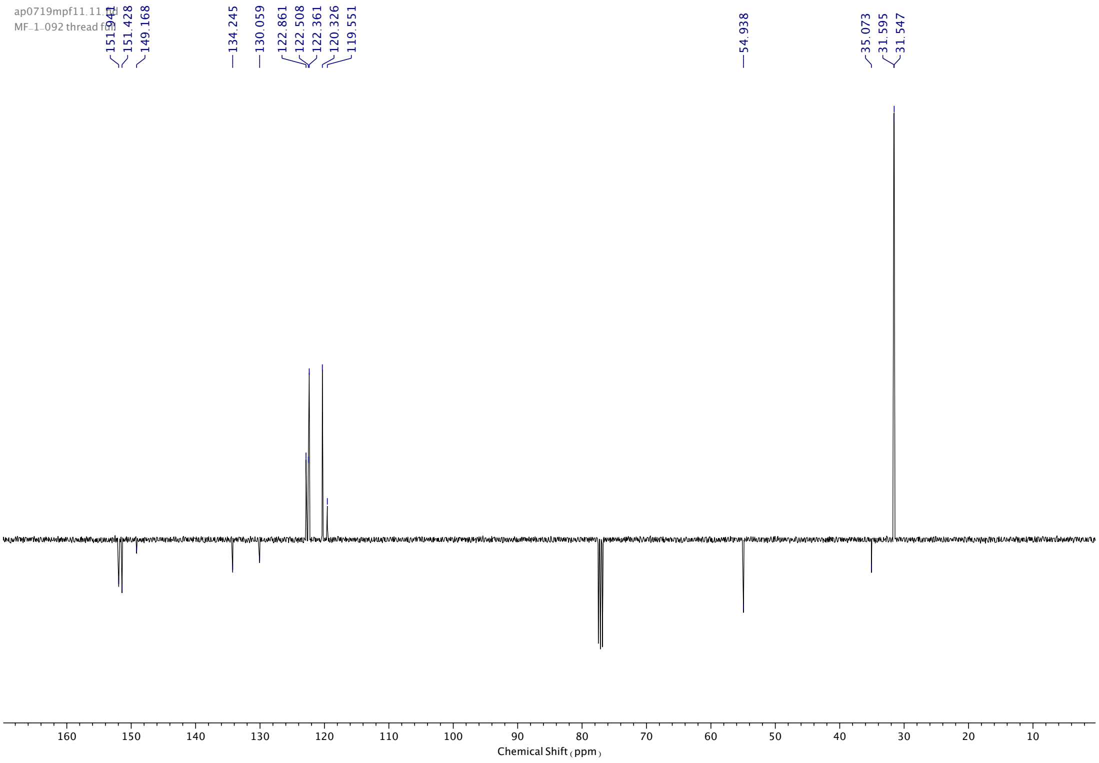

Figure **160**. ^{13}C NMR (CDCl$_3$, 101 MHz) of **55.**

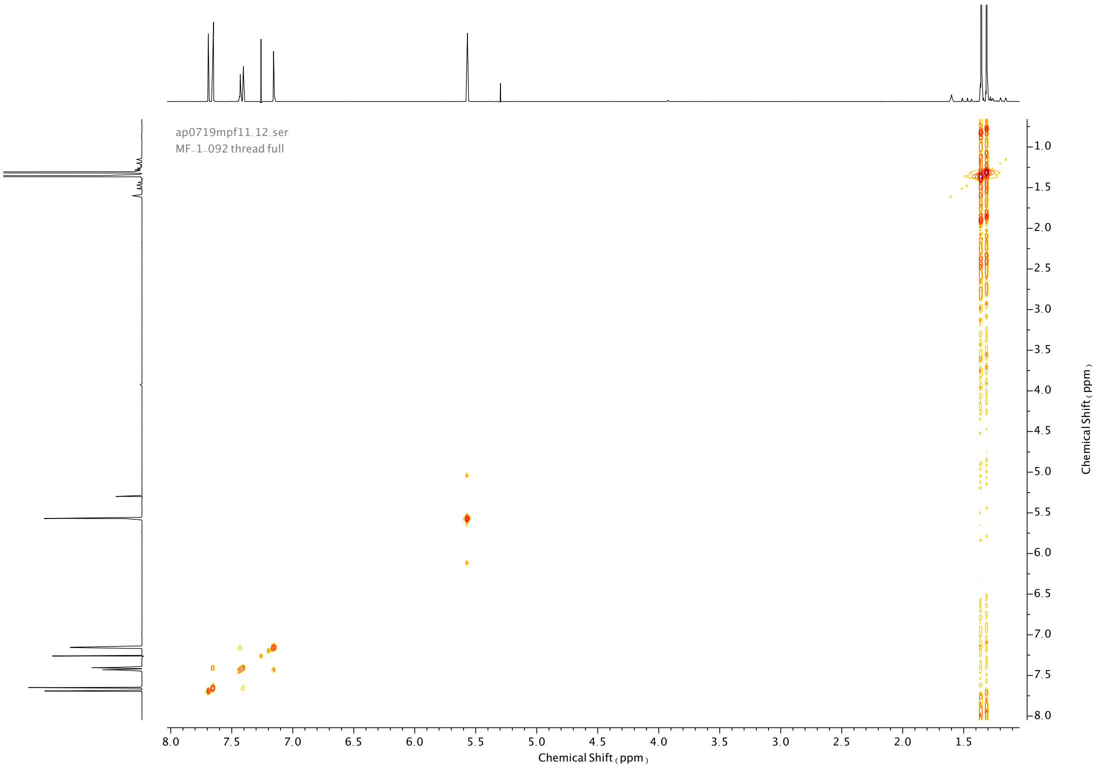

Figure **161**. COSY NMR (CDCl$_3$) of **55**.

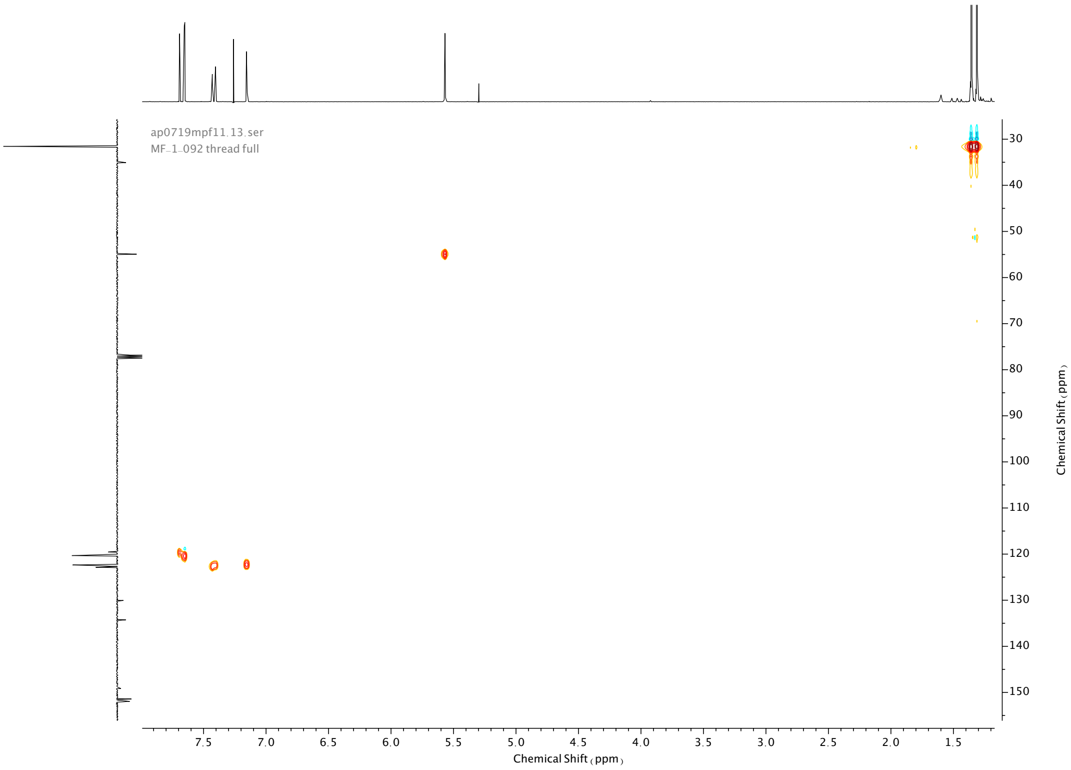

Figure **162**. HSQC NMR (CDCl$_3$) of **55**.

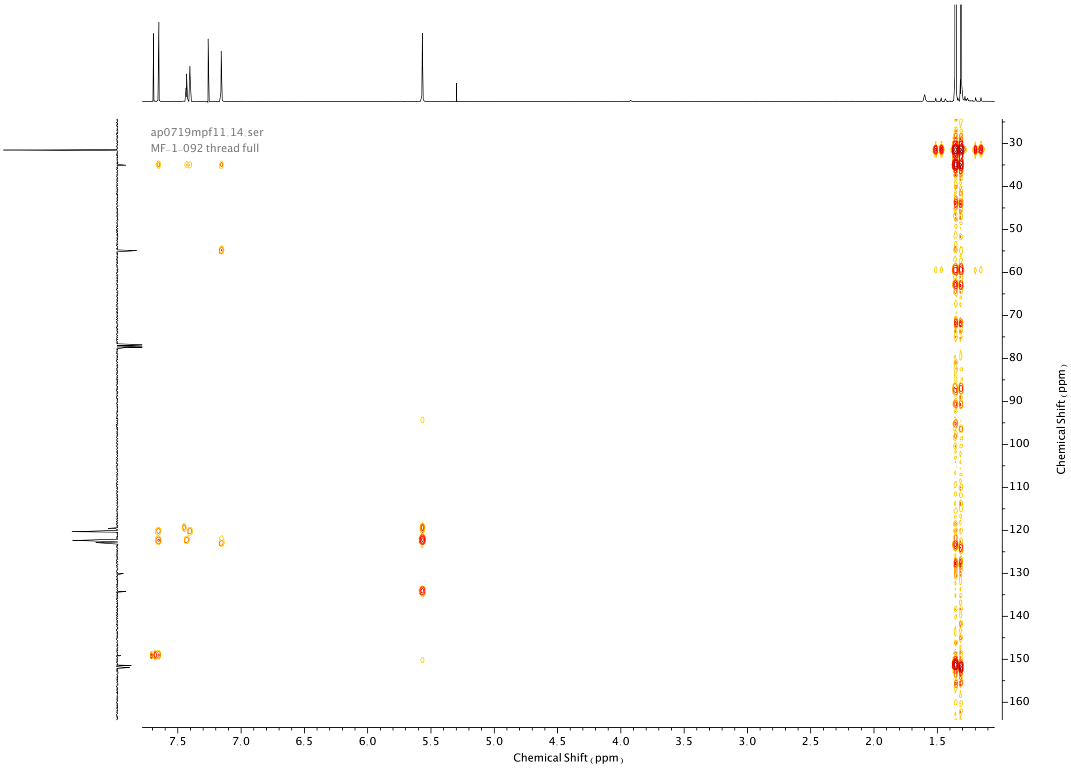

Figure **163**. HMBC NMR (CDCl$_3$) of **55**.

Compound **60**

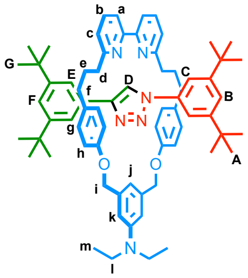

60 was synthesised according to general procedure **(1)** from macrocycle **25** (105 mg, 0.18 mmol, 1.0 eq.), azide stopper **58** (62 mg, 0.27 mmol, 1.5 eq.) and alkyne stopper **51** (58 mg, 0.27 mmol, 1.5 eq.). Purification by column chromatography (eluent 19:1 → 9:1 petrol: acetone) afforded **60** as a white foam (115 mg, 0.11 mmol, 60%). ^{1}H NMR (400 MHz, $CDCl_3$, 298 K) δ_H 10.35 (1H, s, H_D), 7.82 (1H, s, H_j), 7.66-7.61 (4H, m, H_b & H_C), 7.60 (2H, d, *J* = 1.8 Hz, H_E), 7.49 (2H, dd, *J* = 7.8, 0.7 Hz, H_a), 7.20 (1H, t, *J* = 1.7 Hz, H_B), 7.18 (1H, t, *J* = 1.8 Hz, H_F), 7.09 (2H, dd, *J* = 7.8, 0.7 Hz, H_c), 6.62 (2H, s, H_k), 6.52 (4H, d, *J* = 8.7 Hz, H_h), 6.40 (4H, d, *J* = 8.6 Hz, H_g), 5.31 (2H, d, *J* = 12.0 Hz, H_i or H_i'), 5.06 (2H, d, *J* = 11.8 Hz, H_i or H_i'), 3.44 (4H, q, *J* = 7.0 Hz, H_l), 2.40-2.20 (8H, m, H_d & H_f), 1.59-1.50 (4H, m, H_e), 1.23 (6H, t, *J* = 7.1 Hz, H_m), 1.13 (18H, s, H_G), 1.07 (18H, s, H_A). ^{13}C NMR (101 MHz, $CDCl_3$, 298 K) δ_C 163.6, 157.7, 157.1, 151.2, 150.3, 148.1, 147.1, 139.3, 137.5, 136.8, 132.1, 131.7, 128.7, 128.6, 122.1, 120.7, 120.5, 120.4, 120.0, 117.8, 115.0, 114.6, 111.3, 70.7, 44.6, 37.6, 35.2, 35.0, 34.9, 31.5 (x2), 31.3, 12.9. RP-HRMS-ESI (CH_3CN): *m/z =* 1043.6889 M+H]$^+$ calc. 1043.6891

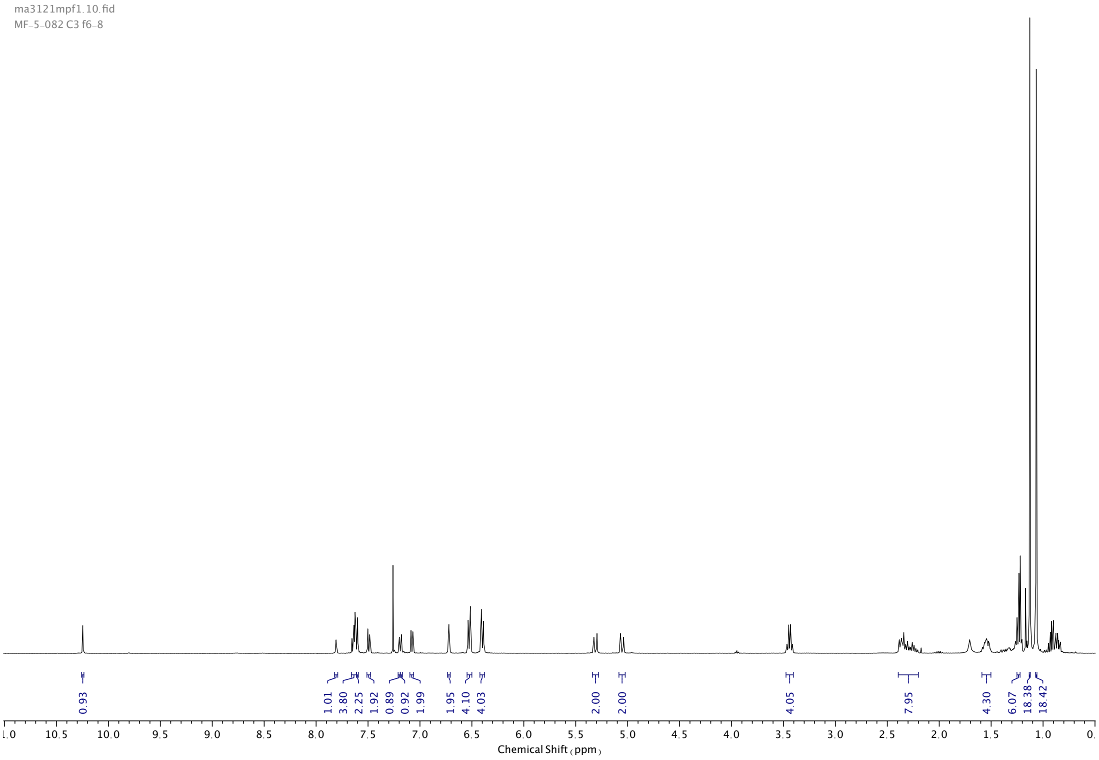

Figure **164**. ^{1}H NMR ($CDCl_3$, 400 MHz) of **60**.

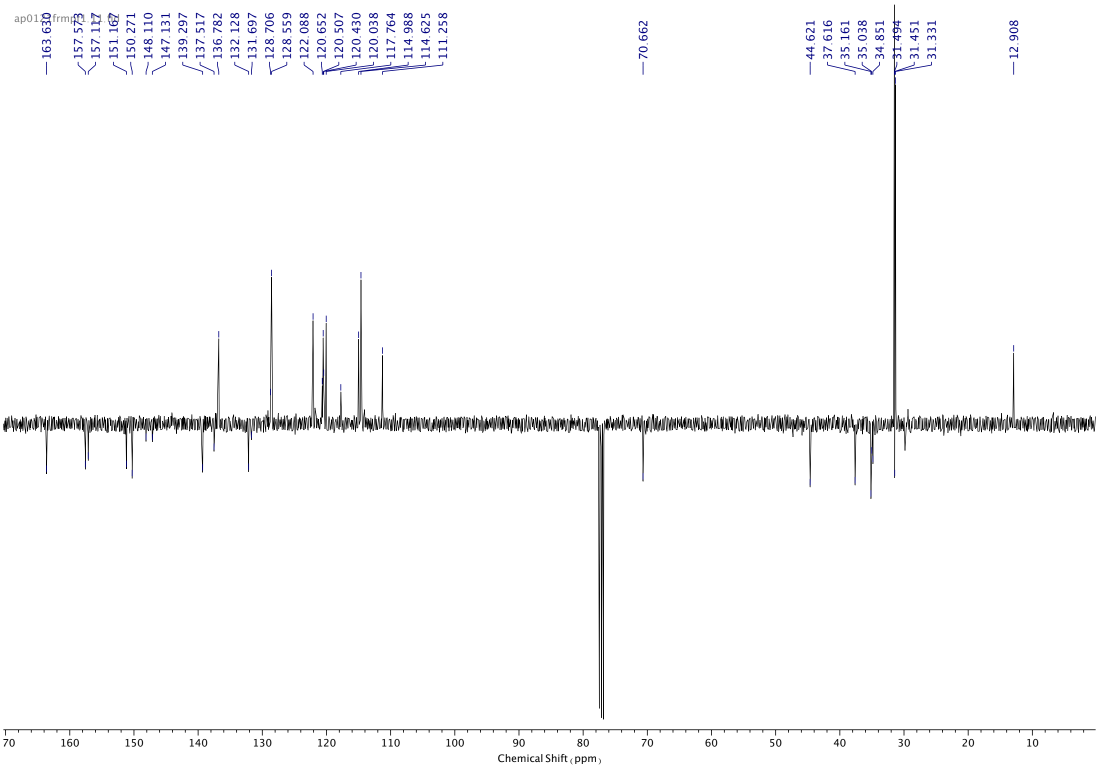

Figure **165**. ^{13}C NMR ($CDCl_3$, 101 MHz) of **60**.

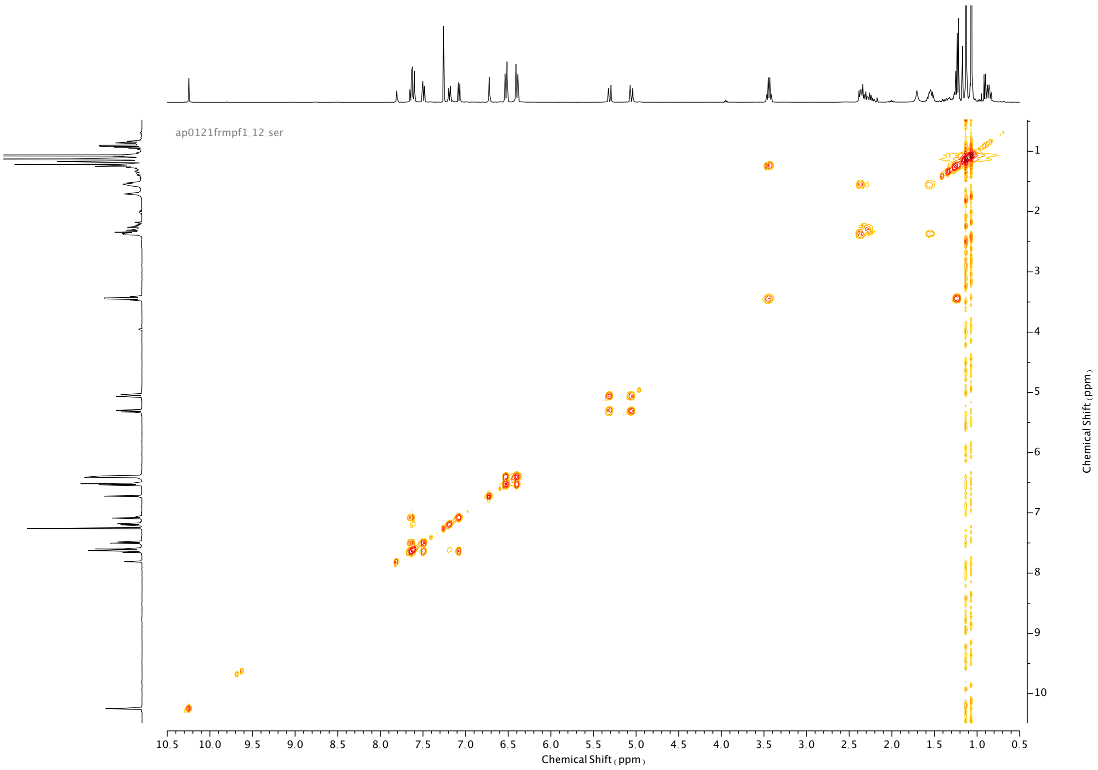

Figure **166**. COSY NMR ($CDCl_3$) of **60**.

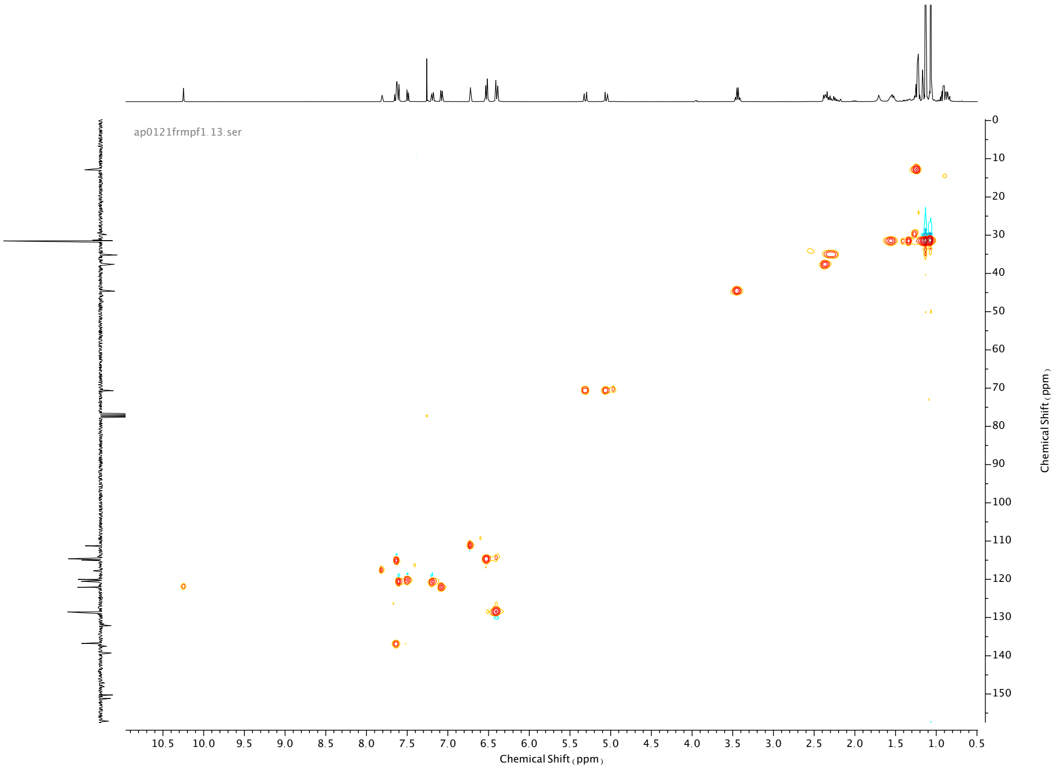

Figure **167**. HSQC NMR ($CDCl_3$) of **60**.

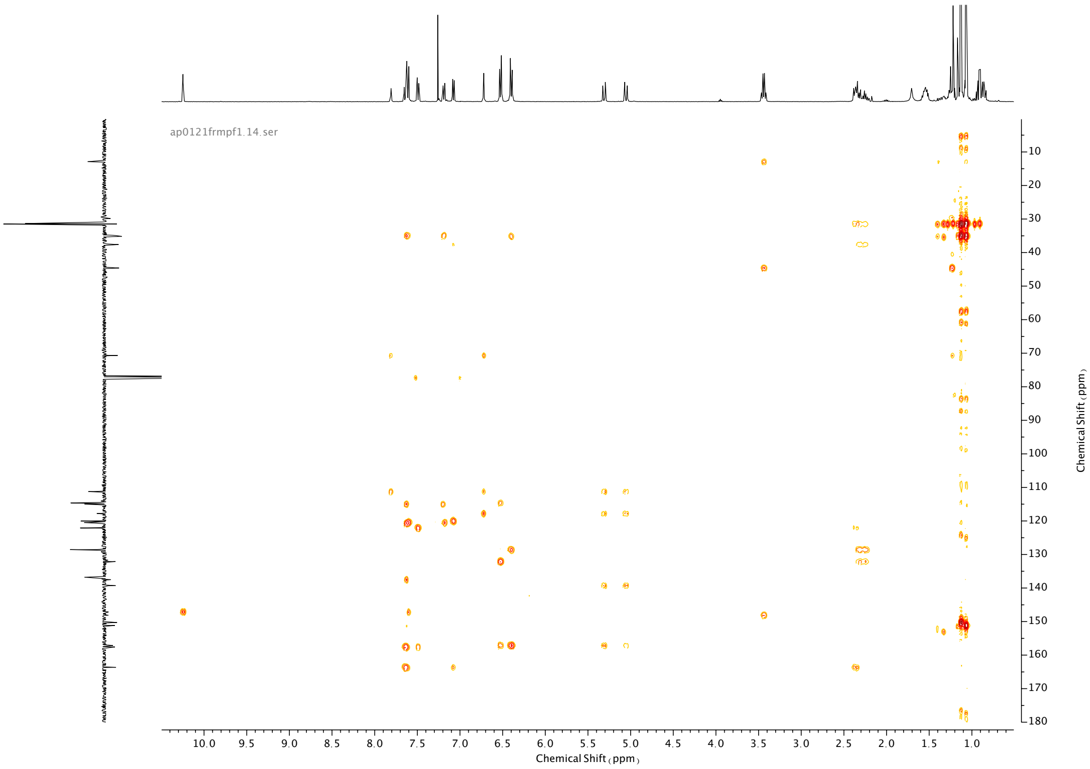

Figure **168**. HMBC NMR ($CDCl_3$) of **60**.

Compound **61**

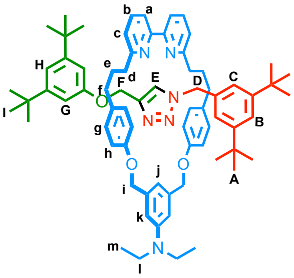

61 was synthesised according to general procedure **(1)** from macrocycle **25** (75 mg, 0.13 mmol, 1.0 eq.), azide stopper **52** (49 mg, 0.20 mmol, 1.5 eq.) and alkyne stopper **56** (49 mg, 0.20 mmol, 1.5 eq.). Purification by column chromatography (eluent 19:1 → 9:1 petrol: acetone) afforded **61** as a white foam (73 mg, 0.068 mmol, 52%). ^{1}H NMR (400 MHz, $CDCl_3$, 298 K) δ_H 7.75 (1H, s, H_E), 7.54 (2H, t, *J* = 7.7 Hz, H_b), 7.45 (2H, d, *J* = 7.8 Hz, H_a), 7.27-7.25 (1H, m, H_B), 7.04 (2H, d, *J* = 7.8 Hz, H_c), 6.96 (1H, s, H_j), 6.86 (1H, t, *J* = 1.6 Hz, H_H), 6.79 (2H, d, *J* = 1.8 Hz, H_C), 6.64-6.56 (6H, m, H_k & H_h), 6.54-6.46 (4H, m, H_g), 6.43 (2H, d, *J* = 1.6 Hz, H_G), 5.08-4.97 (4H, m, H_i), 4.44 (2H, s, H_D), 4.19 (2H, s, H_F), 3.22 (4H, q, *J* = 7.0 Hz, H_l), 2.64-2.50 (4H, m, H_d), 2.44-2.29 (4H, m, H_f), 1.68-1.55 (4H, m, H_e), 1.20 (18H, s, H_I), 1.16 (18H, s, H_A), 1.05 (6H, t, *J* = 7.0 Hz, H_m). ^{13}C NMR (101 MHz, $CDCl_3$, 298 K) δ_C 162.7, 158.5, 157.9, 156.9, 151.3, 150.9, 148.3, 144.0, 139.6, 139.5, 136.6, 134.1, 133.7, 129.2, 123.1, 122.7, 121.8, 119.9, 115.0, 114.0 (x2), 109.7, 109.5, 70.2, 61.6, 53.4, 44.4, 37.9, 35.0, 34.9, 34.8, 31.8, 31.6, 31.5, 12.7. HR-ESI-MS (CH_3CN): *m/z* = 1087.7 $[M+H]^+$ calc. 1087.7153

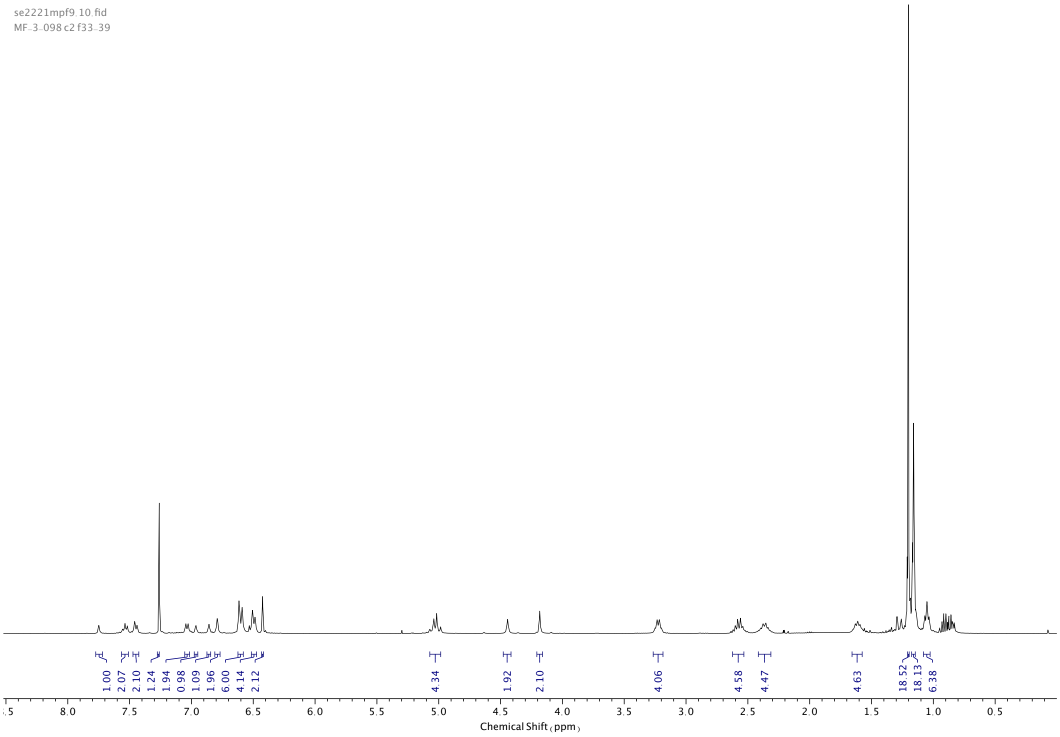

Figure **169**. ^{1}H NMR (CDCl$_3$, 400 MHz) of **61**.

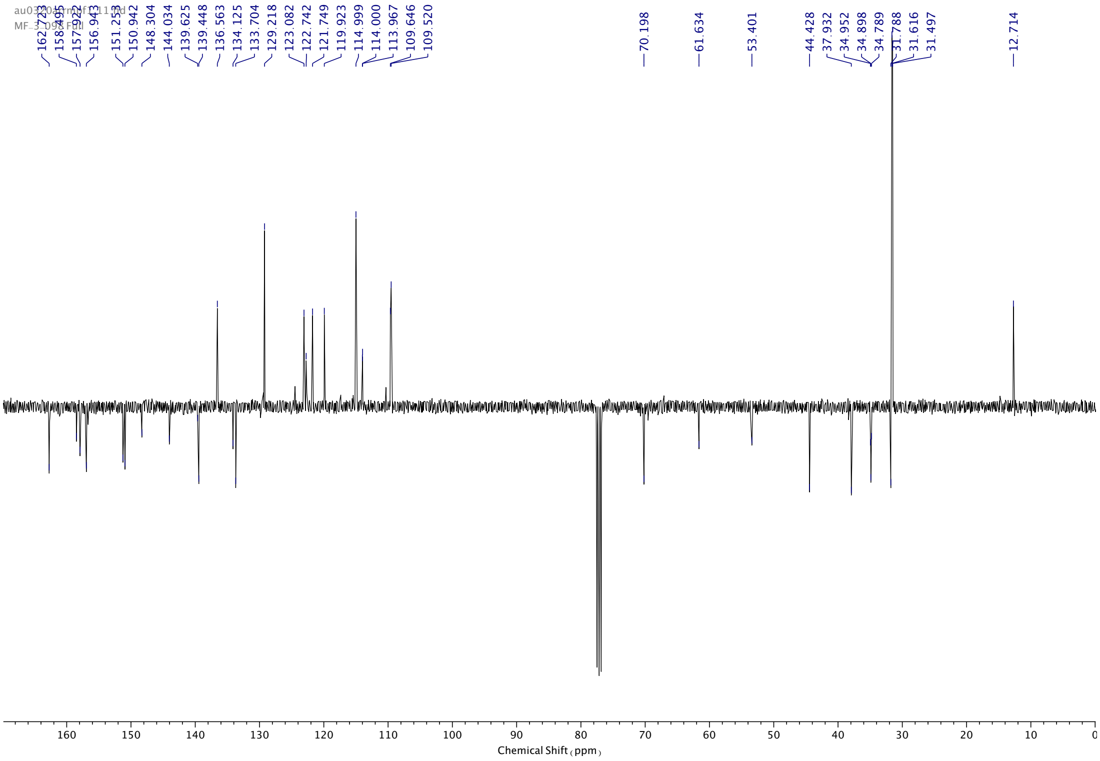

Figure **170**. ^{13}C NMR (CDCl$_3$, 101 MHz) of **61.**

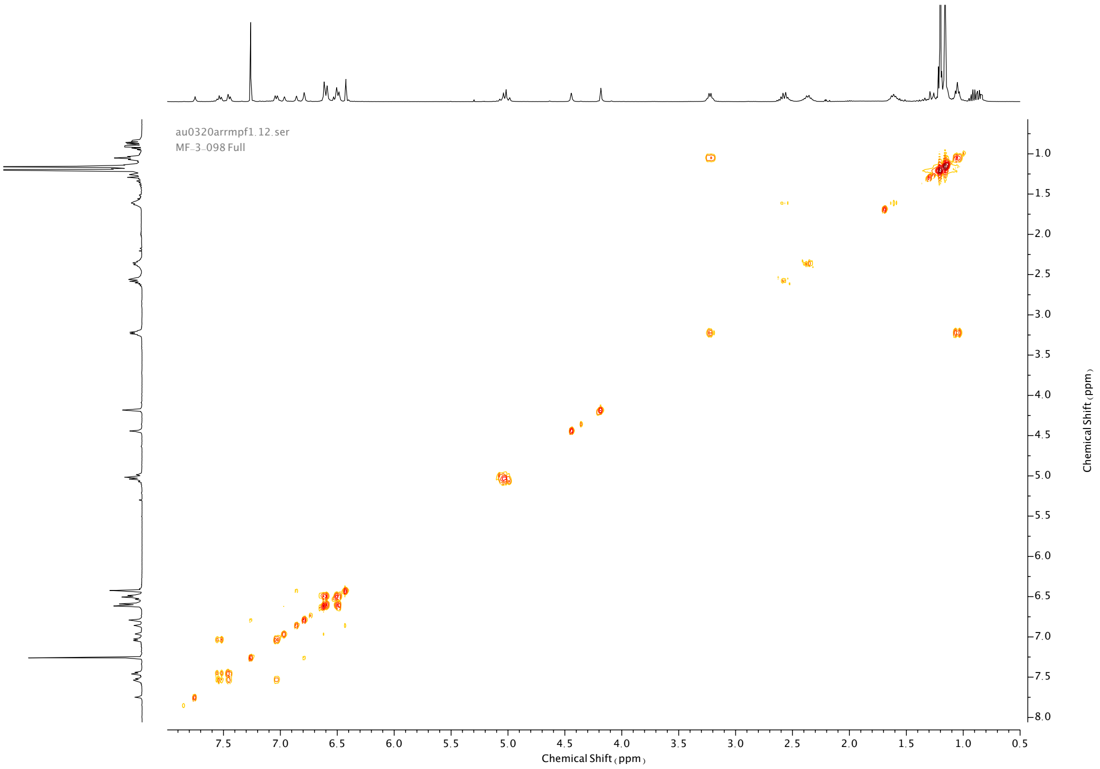

Figure **171**. COSY NMR ($CDCl_3$) of **61**.

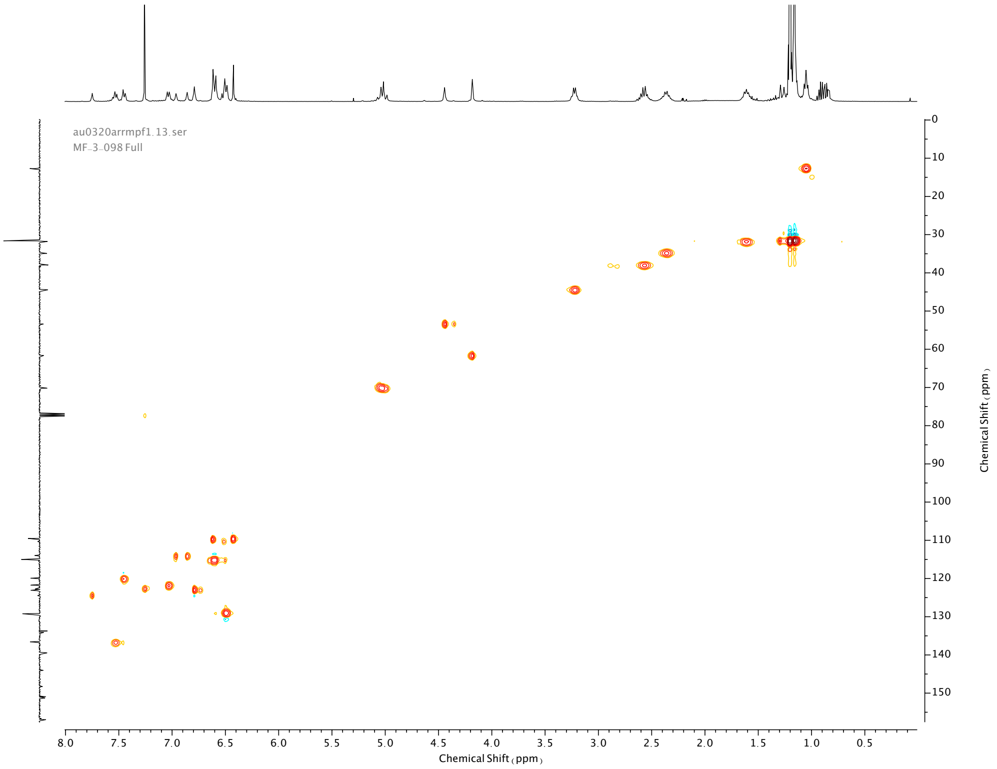

Figure **172**. HSQC NMR ($CDCl_3$) of **61**.

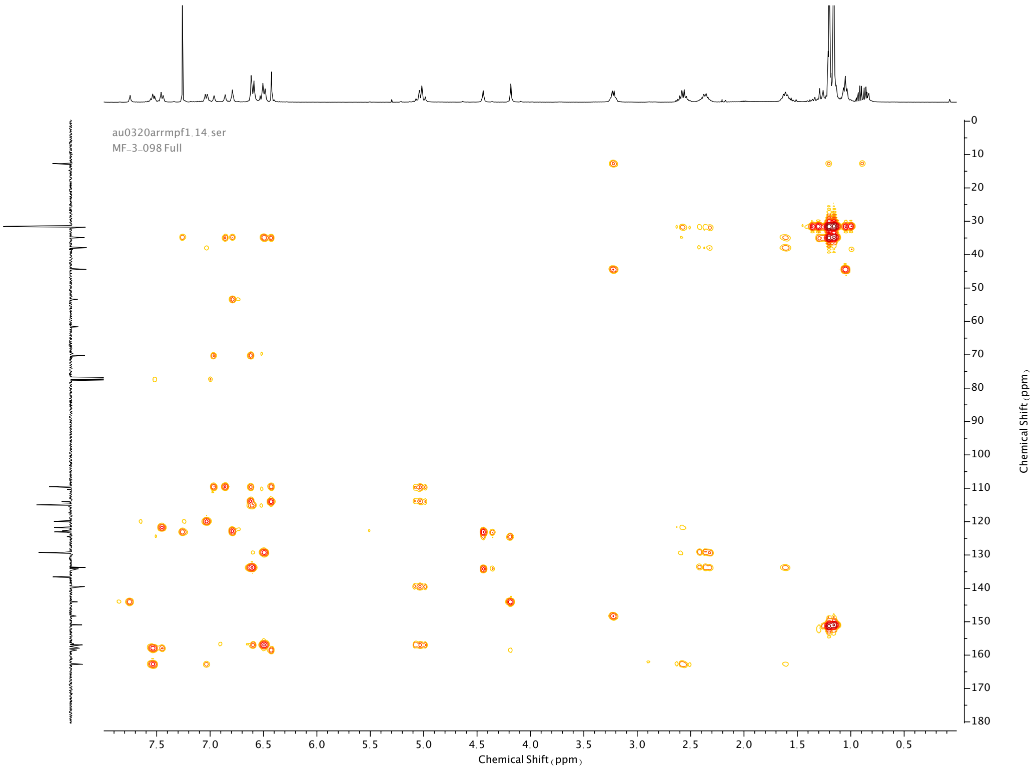

Figure **173**. HMBC NMR ($CDCl_3$) of **61**.

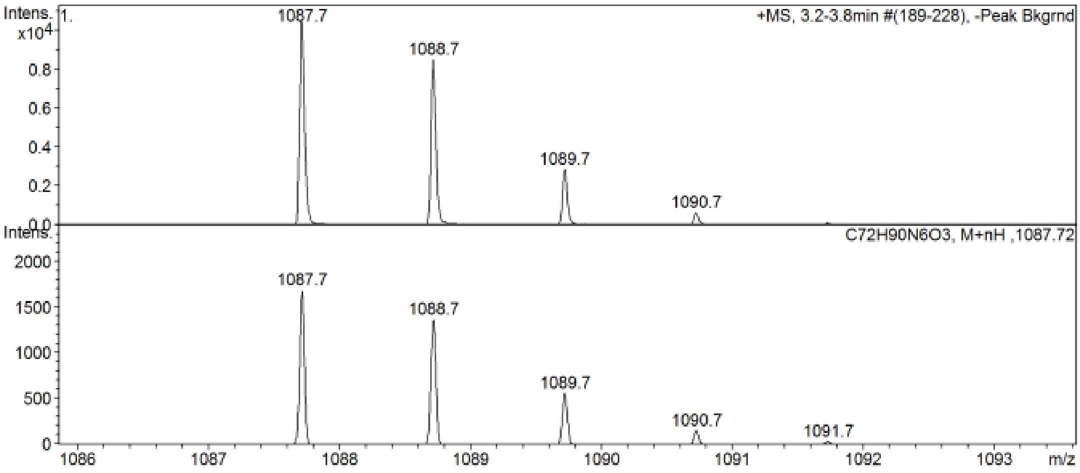

Figure **174**. Rotaxane **62** isotope pattern.

Compound **62**

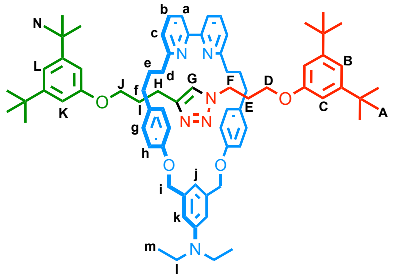

62 was synthesised according to general procedure **(1)** from macrocycle **25** (72 mg, 0.12 mmol, 1.0 eq.), azide stopper **59** (52 mg, 0.18 mmol, 1.5 eq.) and alkyne stopper **57** (49 mg, 0.18 mmol, 1.5 eq.). Purification by column chromatography (eluent 19:1 → 9:1 petrol: acetone) afforded **62** as an off-white foam (93 mg, 0.08 mmol, 67%). ^{1}H NMR (400 MHz, $CDCl_3$, 298 K) δ_H 7.58-7.50 (4H, m, H_a & H_b), 7.06 (2H, d, *J* = 7.1 Hz, H_c), 7.02 (1H, t, *J* = 1.7 Hz, H_B), 6.98 (1H, t, *J* = 1.6 Hz, Hz, H_L), 6.90 (1H, s, H_G), 6.75 (2H, d, *J* = 1.6 Hz, H_C), 6.74-6.66 (9H, m, H_j, H_g & H_h), 6.58 (2H, s, H_k), 6.52 (2H, s, H_K), 5.10-5.00 (4H, m, H_i), 3.84 (2H, t, *J* = 6.3 Hz, H_F), 3.23 (4H, q, *J* = 7.0 Hz, H_l), 3.12-3.06 (2H, m, H_H), 2.94 (2H, t, *J* = 6.0 Hz, H_J), 2.80-2.66 (4H, m, H_d), 2.54-2.45 (6H, m, H_D & H_f), 1.90-1.76 (6H, m, H_E & H_e), 1.33 (18H, s, H_A or H_N), 1.32 (18H, s, H_A or H_N), 1.08-0.98 (6H, t, *J* = 7.0 Hz, H_m & H_l). ^{13}C NMR (101 MHz, $CDCl_3$, 298 K) δ_C 162.1, 158.8, 158.6, 158.0, 157.0, 152.2, 151.8, 146.3, 139.3, 138.3, 136.7, 134.3, 129.3, 122.0, 121.4, 120.1, 115.4, 114.9, 114.5, 109.2, 109.0, 108.9, 76.8, 70.2, 66.9, 64.0, 46.5, 44.4, 37.8, 35.1, 34.3, 32.3 (x2), 31.7, 31.6, 29.0, 22.2, 12.7. HR-ESI-MS (CH_3CN): *m/z* = 1159.8 [M+H]$^+$ calc. 1159.7728

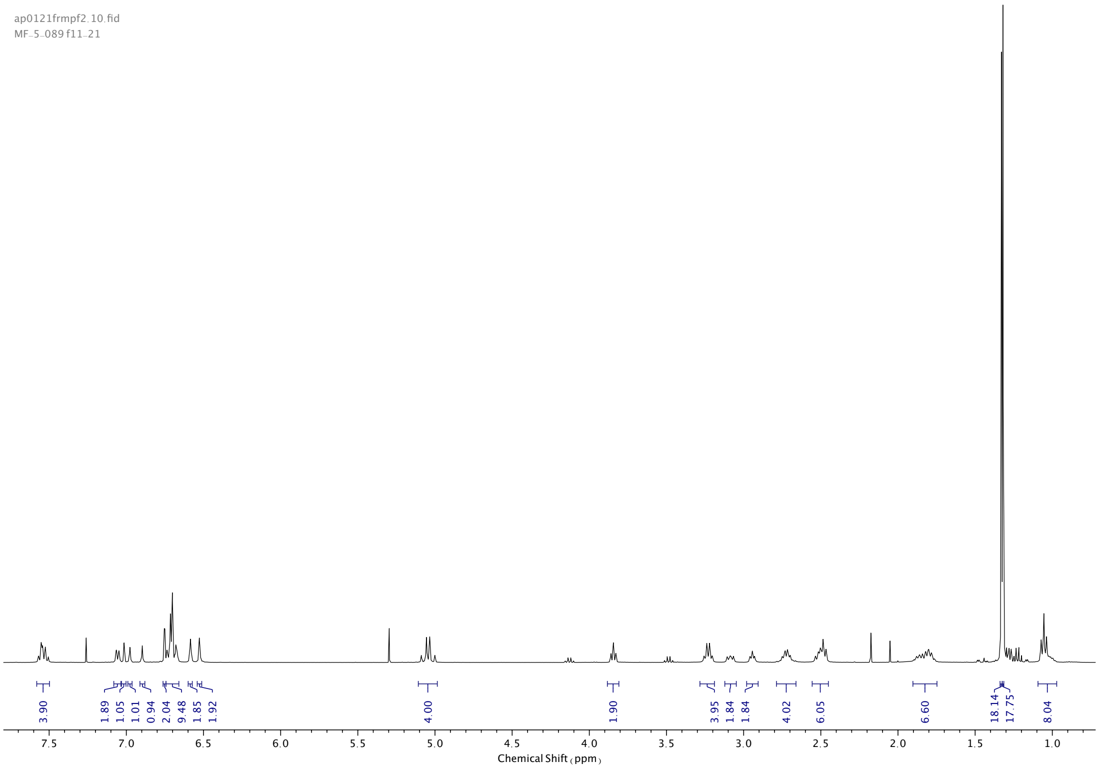

Figure **175**. ^{1}H NMR ($CDCl_3$, 400 MHz) of **62**.

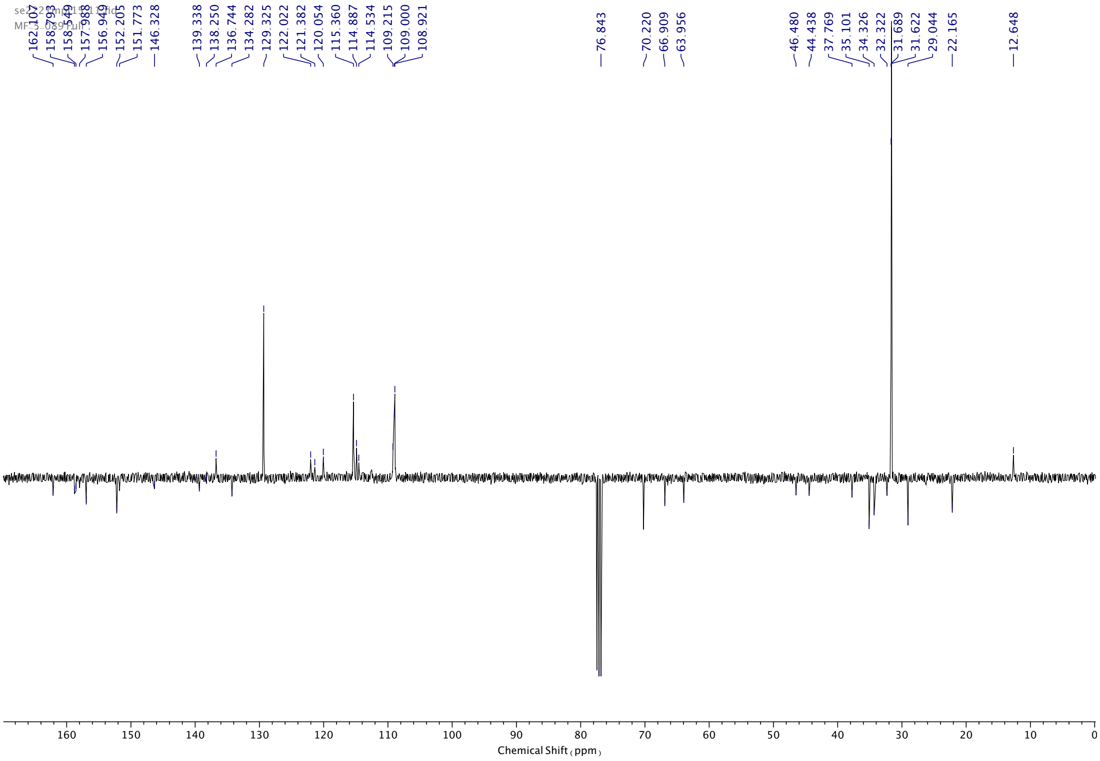

Figure **176**. ^{13}C NMR ($CDCl_3$, 101 MHz) of **62.**

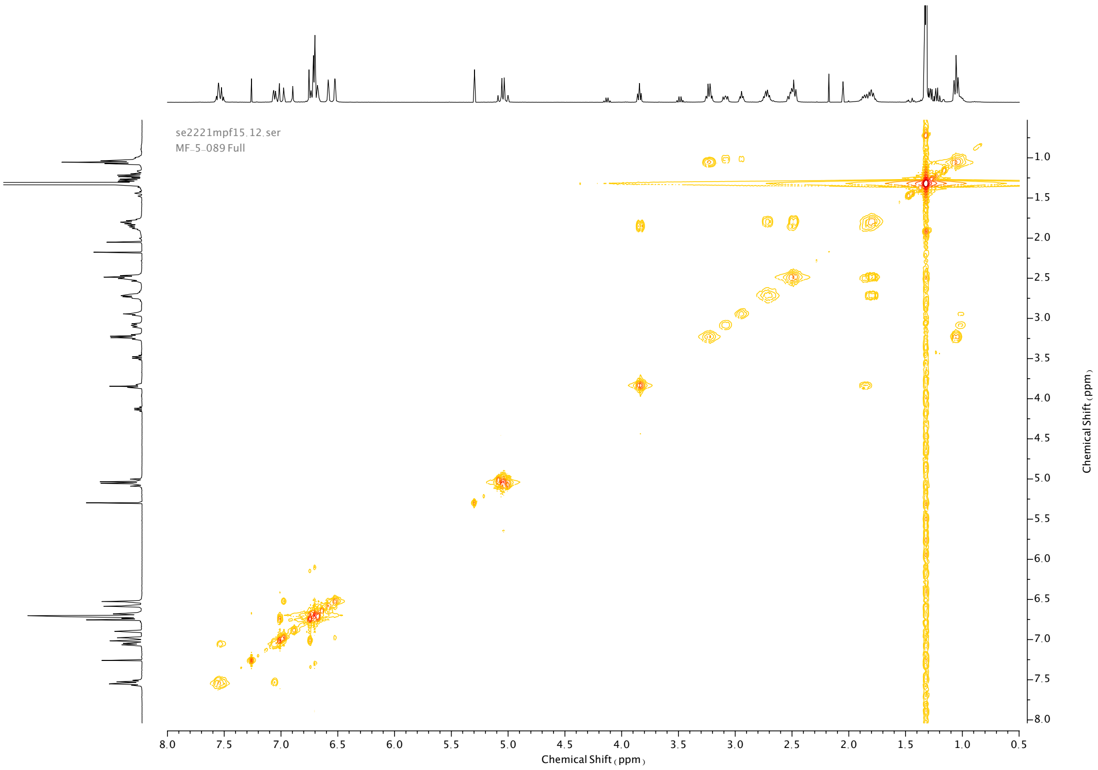

Figure **177**. COSY NMR ($CDCl_3$) of **62**.

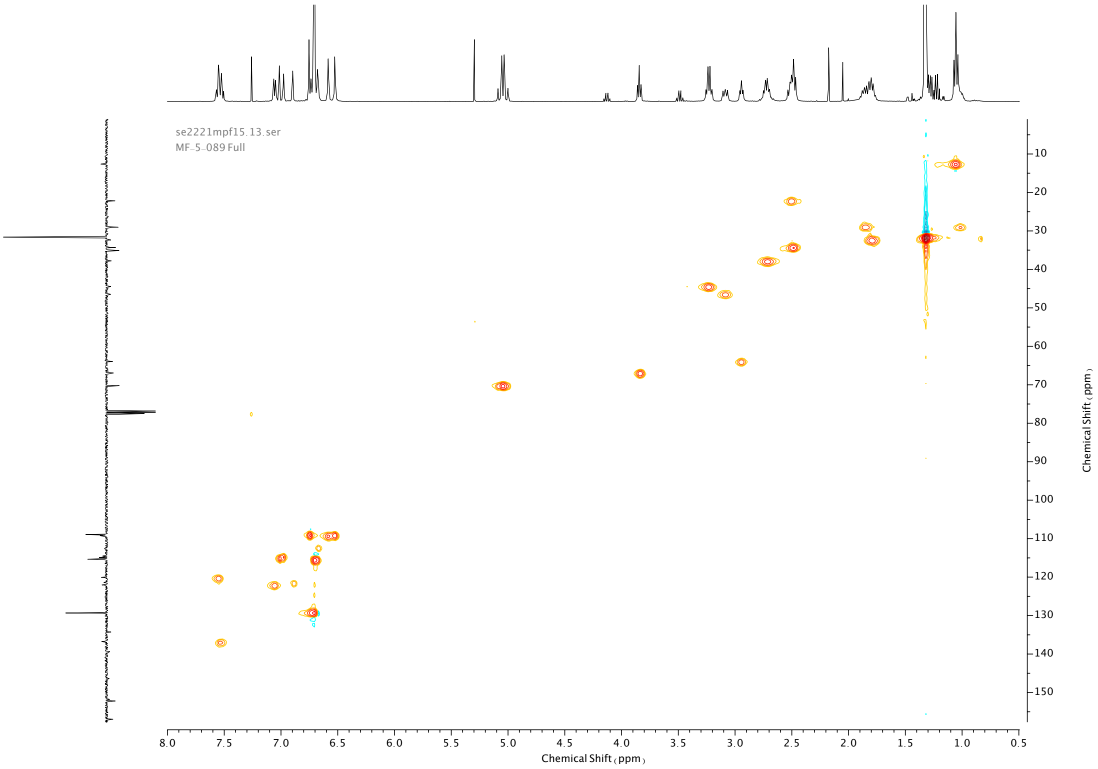

Figure **178**. HSQC NMR ($CDCl_3$) of **62**.

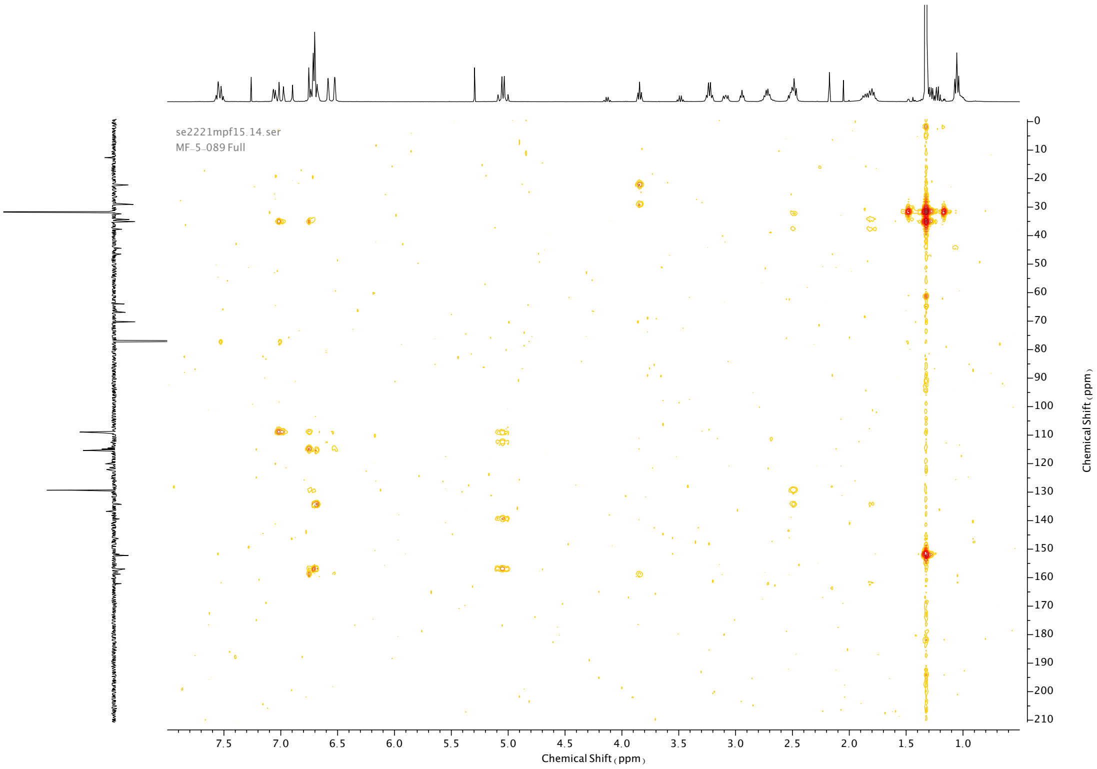

Figure **179**. HMBC NMR ($CDCl_3$) of **62**.

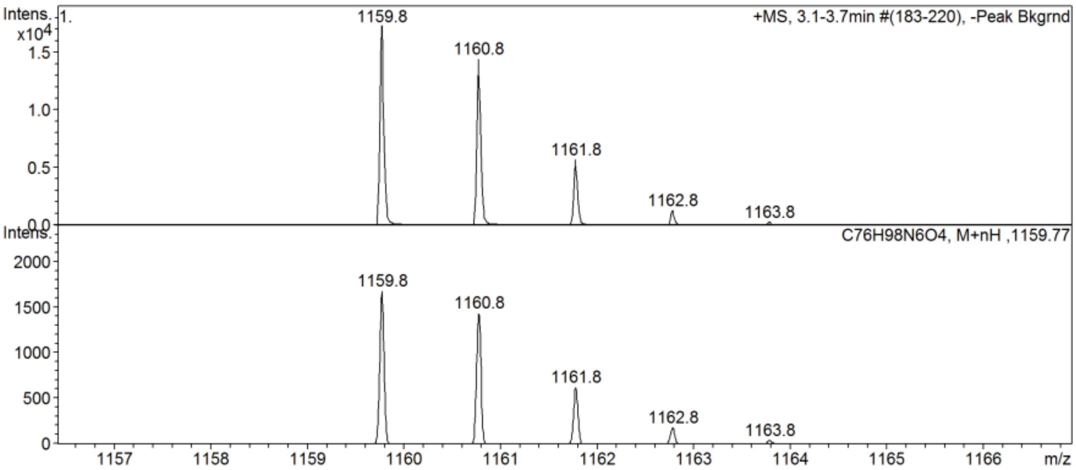

Figure **180**. Rotaxane **62** isotope pattern.

Compound **64**

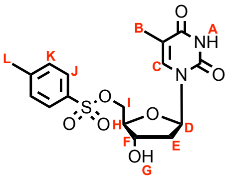

p-TsCl (4.33 g, 22.70 mmol, 1.1 eq.) in anhydrous pyridine (10 mL) was slowly added to a solution of **63** (5.0 g, 20.64 mmol, 1.0 eq.) in anhydrous pyridine (20 mL) over 2 h at 0 °C. The mixture was then allowed to reach room temperature and stirred overnight. The reaction was quenched *via* addition of MeOH (10 mL), stirred for a further 15 min at room temperature then concentrated *in vacuo.* The crude residue underwent several azeotropes (5 x 15 mL) to remove residual pyridine and was then taken up in EtOAc (500 mL) and washed with H_2O (250 mL), $NaHCO_3$ (100 mL) and brine (100 mL). Combined aqueous washings were extracted with EtOAc (3 x 100 mL). The combined organic extracts were dried over anhydrous $MgSO_4$, filtered, and concentrated *in vacuo.* The crude product was purified *via* silica-gel chromatography using a Biotage Isolute SPE column (eluent 19:1 → 9:1 CH_2Cl_2: MeOH) to afford **64** as a white solid (4.30 g, 10.86 mmol, 53%). ^{1}H NMR (400 MHz, DMSO-d$_6$, 298 K) δ_H 11.31 (1H, s, N-H$_A$), 7.79 (2H, d, *J* = 7.9 Hz, H$_J$), 7.47 (2H, d, *J* = 8.0 Hz, H$_K$), 7.38 (1H, s, H$_C$), 6.14 (1H, t, *J* = 6.9 Hz, H$_D$), 5.43 (1H, d, *J* = 4.4 Hz, O-H$_G$), 4.26 (1H, dd, *J* = 10.9, 3.4 Hz, H$_F$), 4.19-4.14 (2H, m, H$_I$), 3.87 (1H, dt, *J* = 5.7, 3.5 Hz, H$_H$), 2.41 (3H, s, H$_L$), 2.15 (1H, dt, *J* = 13.7, 6.9 Hz, H$_E$ or H$_{E'}$), 2.06 (1H, ddd, *J* = 13.6, 6.6, 4.0 Hz, H$_E$ or H$_{E'}$), 1.76 (3H, d, *J* = 1.2 Hz, H$_B$). ^{13}C NMR (101 MHz, DMSO-d$_6$, 298 K) δ_C 163.7, 150.4, 145.2, 135.9, 132.1, 130.2, 127.6, 109.8, 84.0, 83.2, 70.2, 70.0, 38.4, 21.1, 12.1.

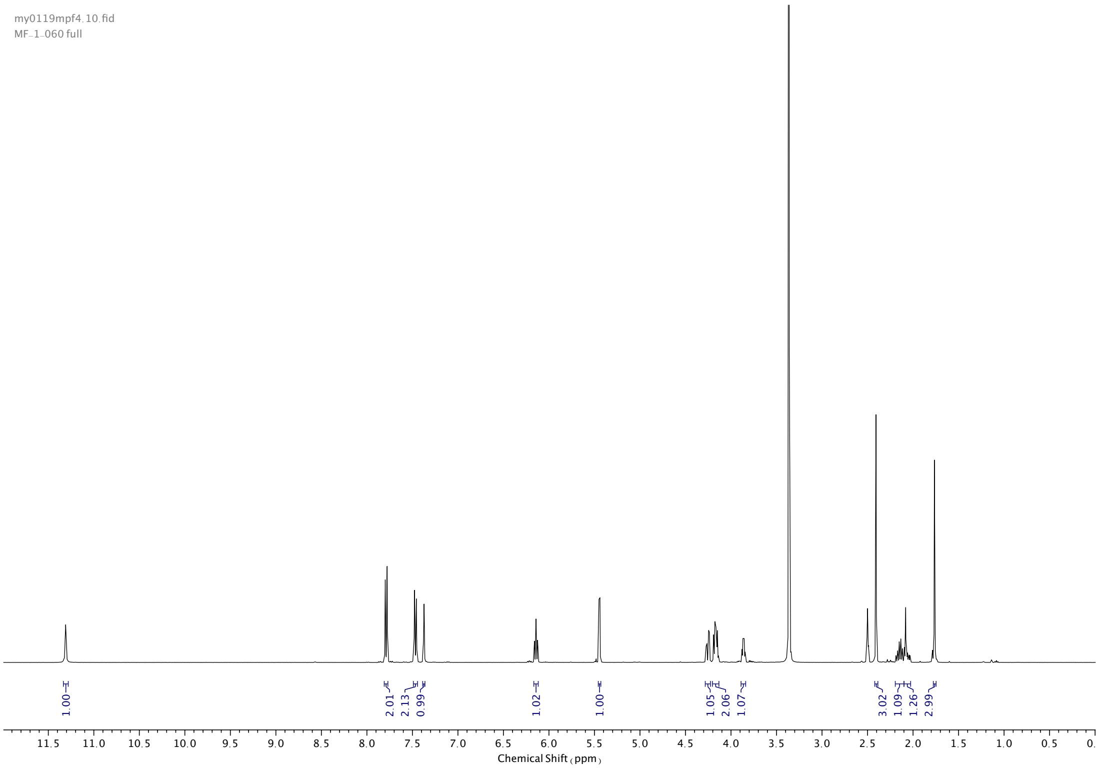

Figure **181**. ^{1}H NMR (DMSO-d$_6$, 400 MHz) of **64**.

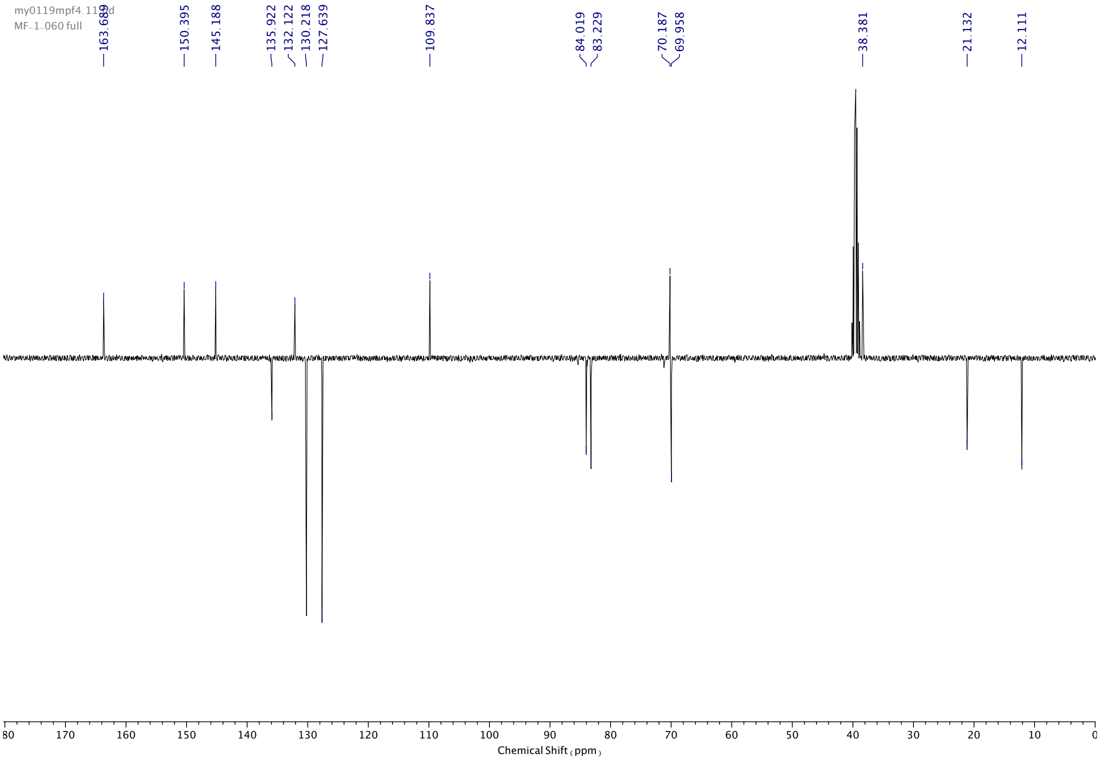

Figure **182**. ^{13}C NMR (DMSO-d$_6$, 101 MHz) of **64.**

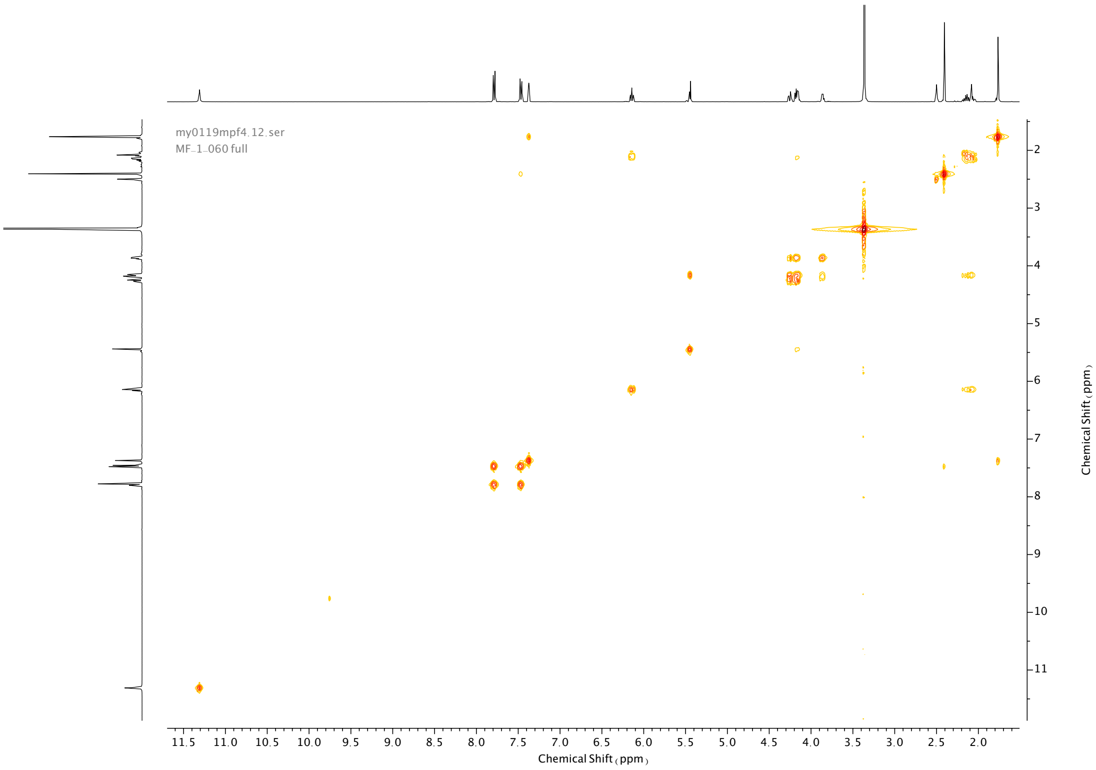

Figure **183**. COSY NMR (DMSO-d$_6$) of **64**.

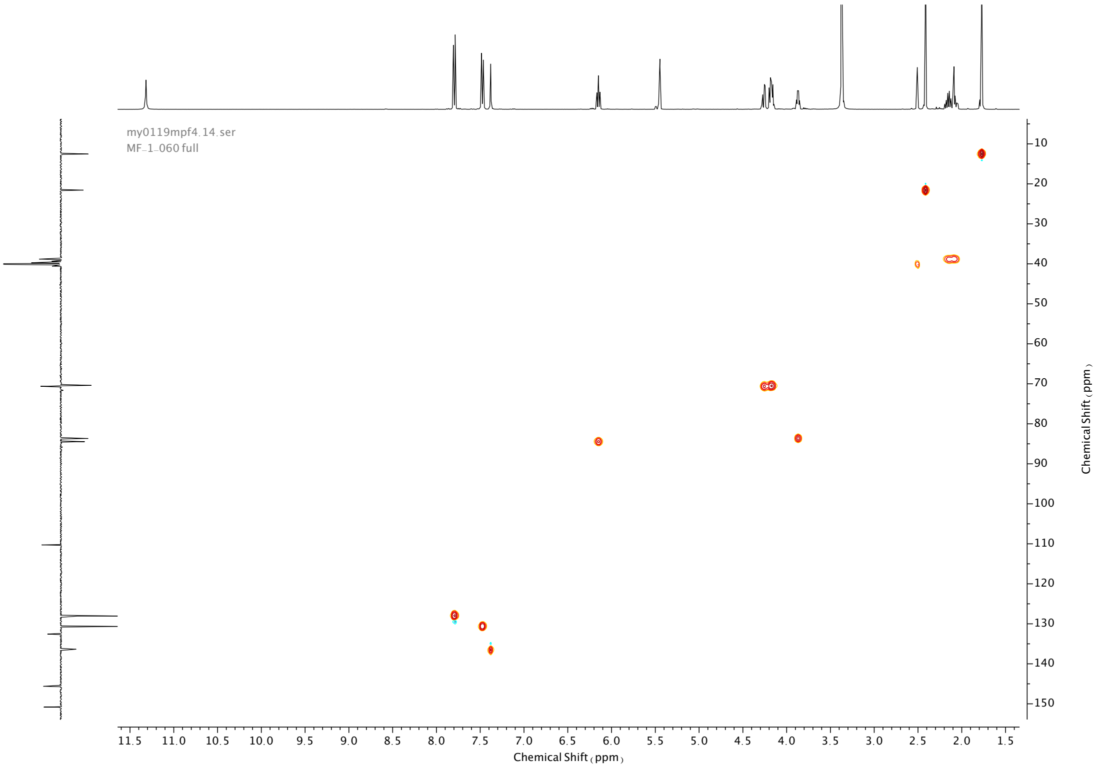

Figure **184**. HSQC NMR (DMSO-d$_6$) of **64**.

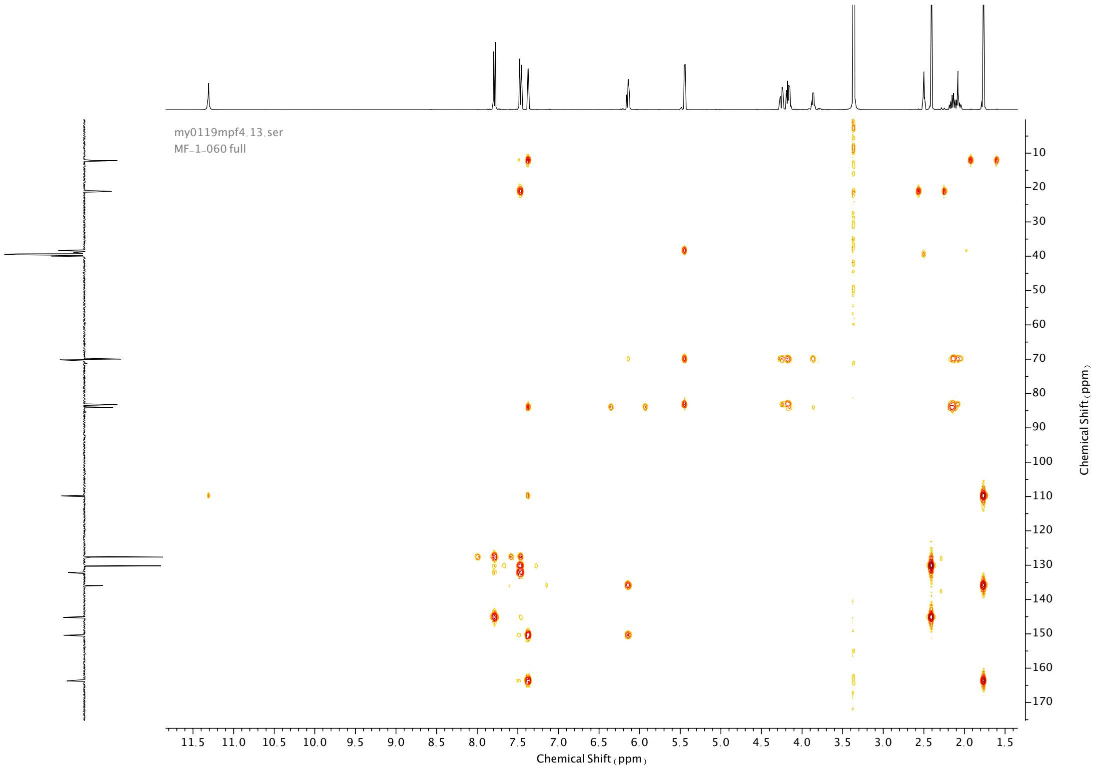

Figure **185**. HMBC NMR (DMSO-d$_6$) of **64**.

Compound **65**

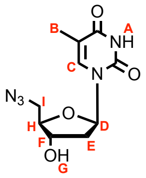

A mixture of **64** (50 mg, 1.26 mmol, 1.0 eq.) and NaN_3 (124 mg, 1.90 mmol, 1.5 eq.) in DMF (5 mL) were added to a round-bottom flask and stirred overnight at 80 °C. The mixture was then concentrated *in vacuo* and the crude residue taken up in CH_2Cl_2 (20 mL) and washed with H_2O (20 mL). Aqueous washings were extracted with CH_2Cl_2 (2 x 20 mL) and the combined organic extracts dried over anhydrous Na_2SO_4, filtered and concentrated *in vacuo.* The crude product was purified *via* silica-gel chromatography using a Biotage Isolute SPE column (eluent 19:1 CH_2Cl_2: MeOH), to afford **65** as a white solid (78 mg, 0.29 mmol, 24%).^{1}H NMR (400 MHz, DMSO-d_6, 298 K) δ_H 11.37-11.28 (1H, br. s, N-H_A), 7.48 (1H, s, H_C), 6.20 (1H, t, *J* = 7.0 Hz, H_D), 5.42 (1H, d, *J* = 4.2 Hz, O-H_G), 4.21-4.16 (1H, m, H_F), 3.84 (1H, td, *J* = 5.2, 3.5 Hz, H_H), 3.55 (2H, d, *J* = 5.2 Hz, H_I), 2.25 (1H, dt, *J* = 13.6, 7.0, H_E & $H_{E'}$), 2.12-2.05 (1H, m, H_E & $H_{E'}$), 1.79 (3H, d, *J* = 1.2 Hz, H_B).^{13}C NMR (101 MHz, DMSO-d_6, 298 K) δ_C 163.7, 150.5, 136.1, 109.9, 84.6, 83.9, 70.8, 51.7, 38.1, 12.1.

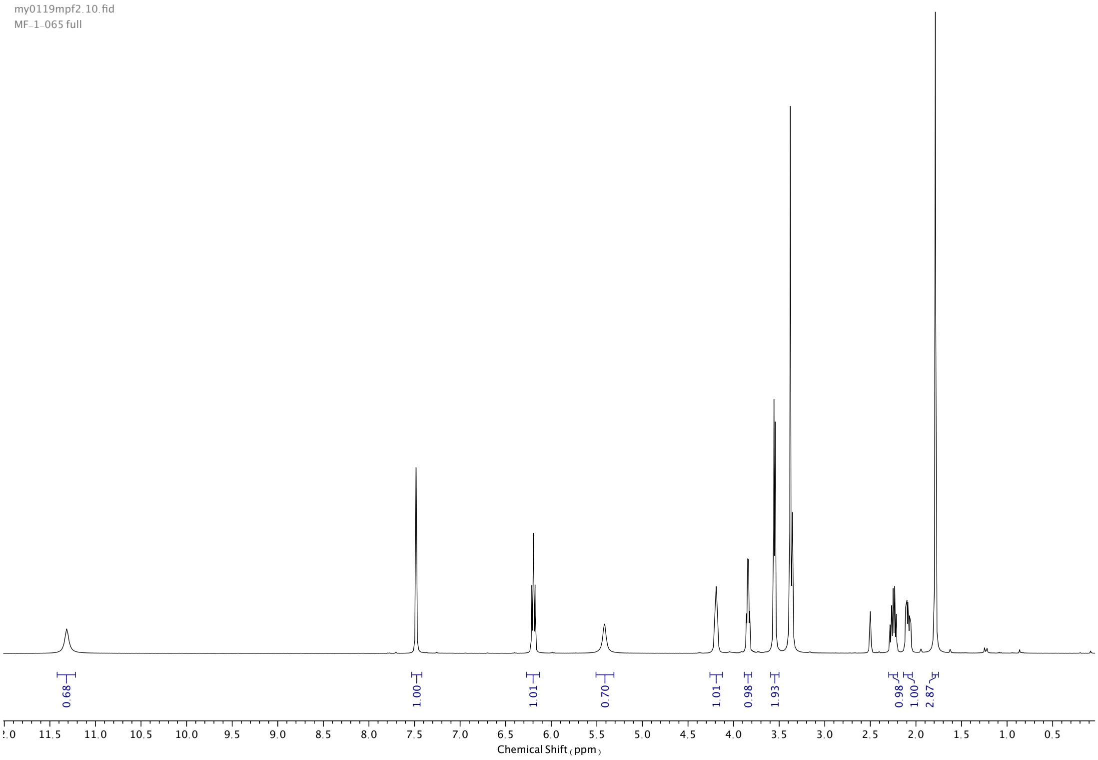

Figure **186**. ^{1}H NMR (DMSO-d_6, 400 MHz) of **65**.

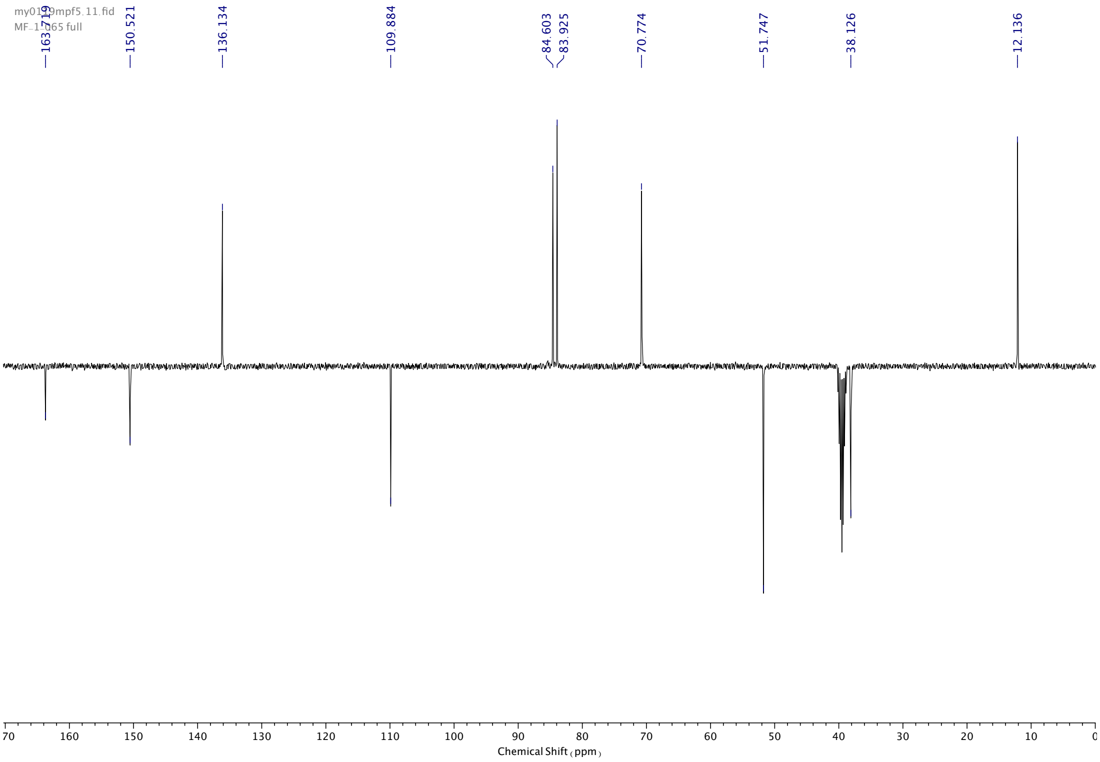

Figure **187**. ^{13}C NMR (DMSO-d_6, 101 MHz) of **65.**

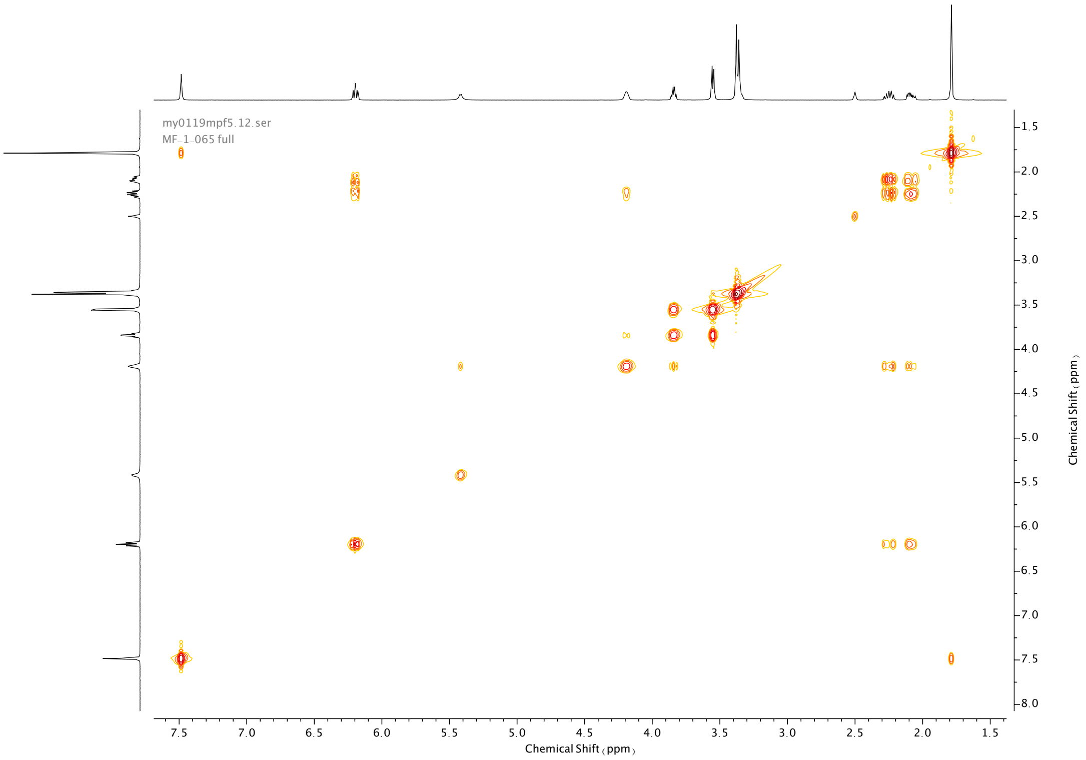

Figure **188**. COSY NMR (DMSO-d_6) of **65**.

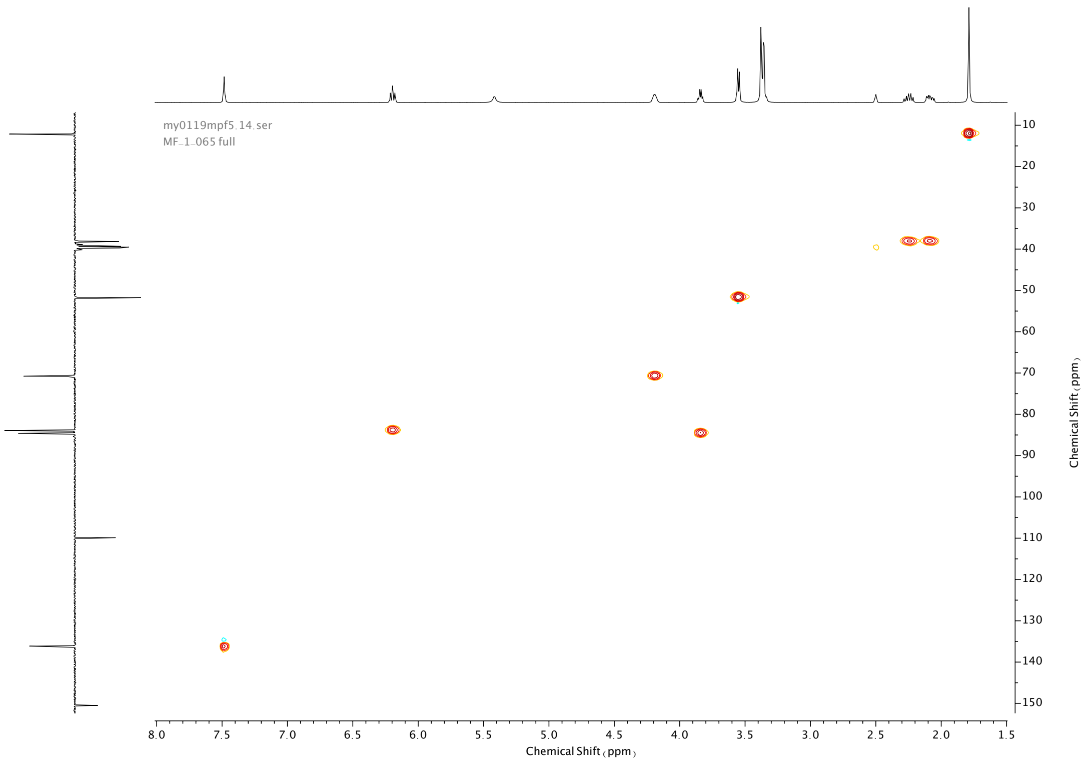

Figure **189**. HSQC NMR (DMSO-d$_6$) of **65**.

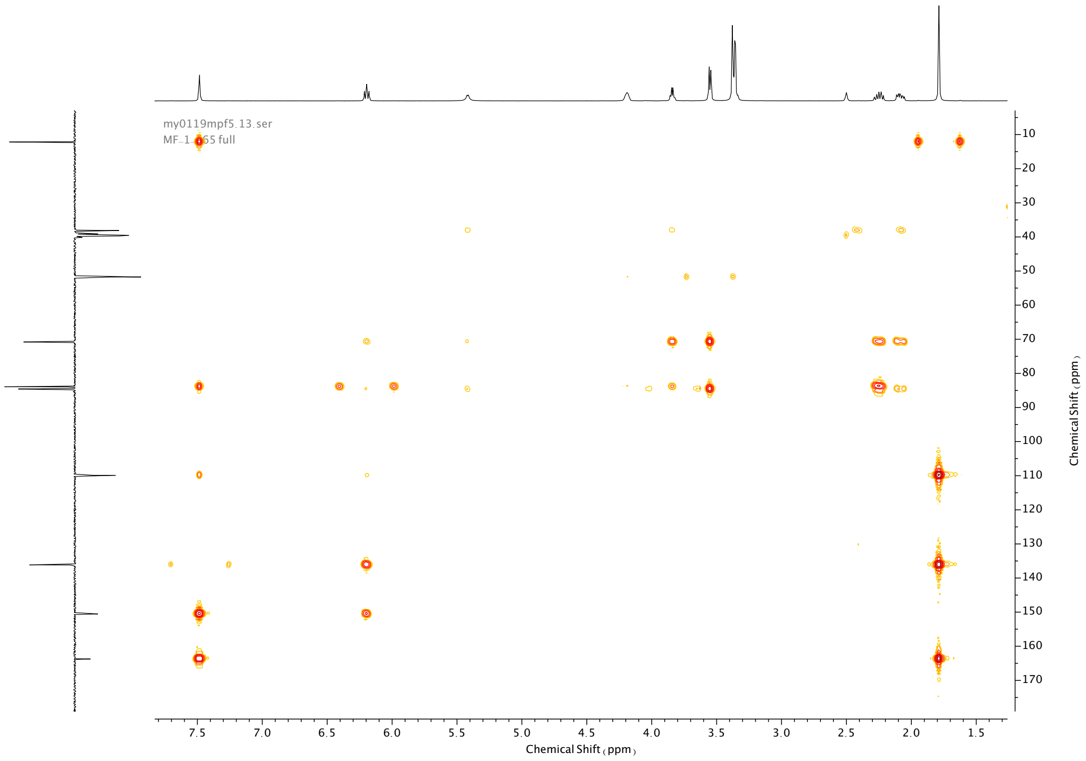

Figure **190**. HMBC NMR (DMSO-d$_6$) of **65**.

Compound **66**

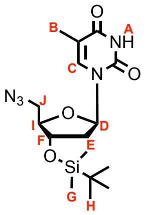

65 (50 mg, 0.19 mmol, 1.0 eq.) and imidazole (32 mg, 0.47 mmol, 2.5 eq.) were charged to a dry CEM vial with anhydrous DMF (1 mL). TBDMS-Cl (38 mg, 0.25 mmol, 1.33 eq.) was then added to the mixture over 10 min which was stirred at room temperature overnight. The mixture was then concentrated *in vacuo* and the crude residue taken up in EtOAc (10 mL), washed with $NaHCO_3$ (5 mL) and brine (10 mL). Aqueous washings were extracted with EtOAc (3 x 15 mL). The combined organic extracts were dried over anhydrous Na_2SO_4, filtered, and concentrated *in vacuo* to afford **66** as a colourless oil (69 mg, 0.18 mmol, 96%).^{1}H NMR (400 MHz, $CDCl_3$, 298 K) δ_H 8.92 (1H, s, N-H_A), 7.31 (1H, q, *J* = 1.2 Hz, H_C), 6.24 (1H, t, *J* = 6.6 Hz, H_D), 4.34 (1H, dt, *J* = 7.0, 4.4 Hz, H_F), 3.93 (1H, q, *J* = 4.4 Hz, H_I), 3.70 (1H, dd, *J* = 13.3, 3.4 Hz, H_J or $H_{J'}$), 3.49 (1H, dd, *J* = 13.3, 3.6 Hz, H_J or $H_{J'}$), 2.28 (1H, ddd, *J* = 13.6 Hz, 6.6 Hz, 4.3 Hz, $H_{E,}$ $H_{E'}$) 2.16 (1H, ddd, *J* = 13.6, 6.7 Hz, 6.7 Hz, $H_{E,}$ $H_{E'}$), 1.94 (3H, d, *J* = 1.3 Hz, H_B), 0.88 (9H, s, H_H), 0.08 (6H, s, H_G). ^{13}C NMR (101 MHz, $CDCl_{3,}$ 298 K) δ_C 163.8, 150.4, 135.5, 111.5, 84.9, 71.8, 51.8, 40.8, 25.8, 18.0, 12.8, -4.5, -4.8.

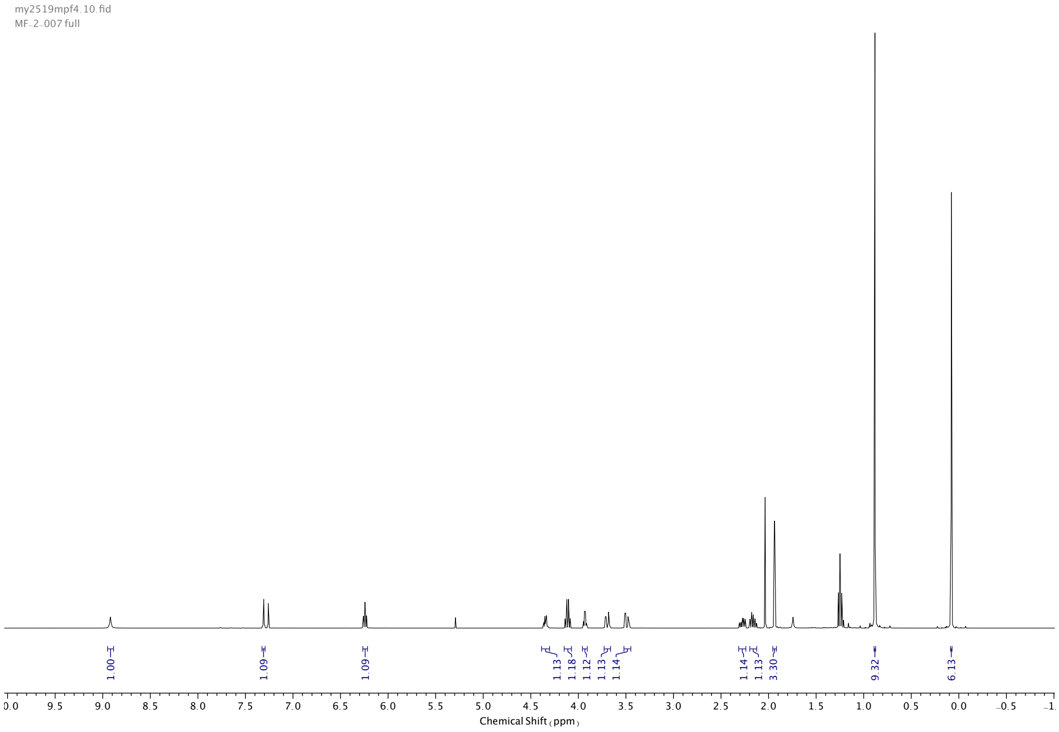

Figure **191**. ^{1}H NMR ($CDCl_3$, 400 MHz) of **66**.

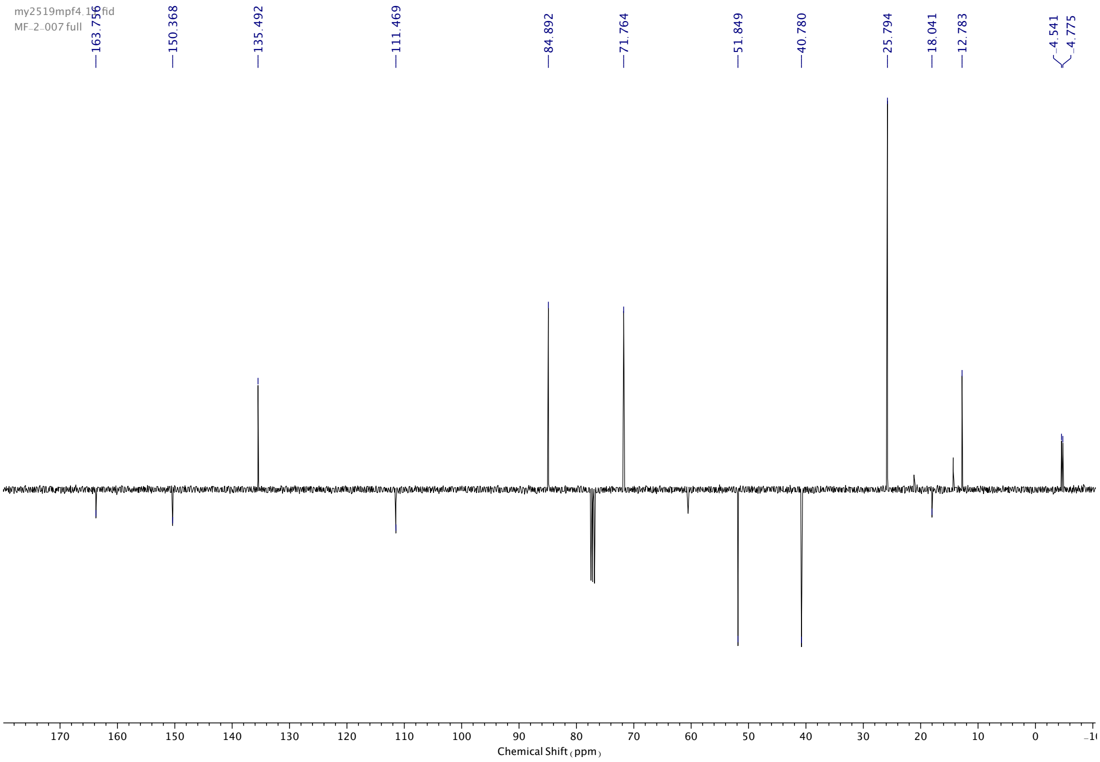

Figure **192**. ^{13}C NMR (CDCl$_3$, 101 MHz) of **66.**

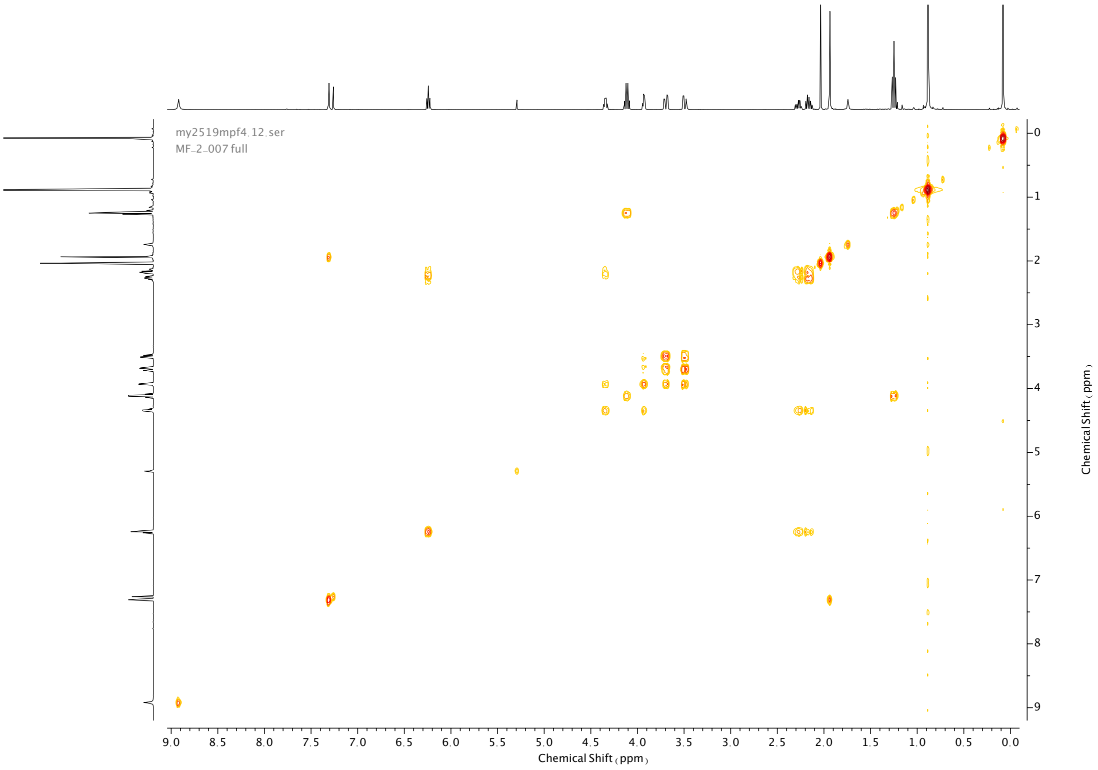

Figure **193**. COSY NMR (CDCl$_3$) of **66**.

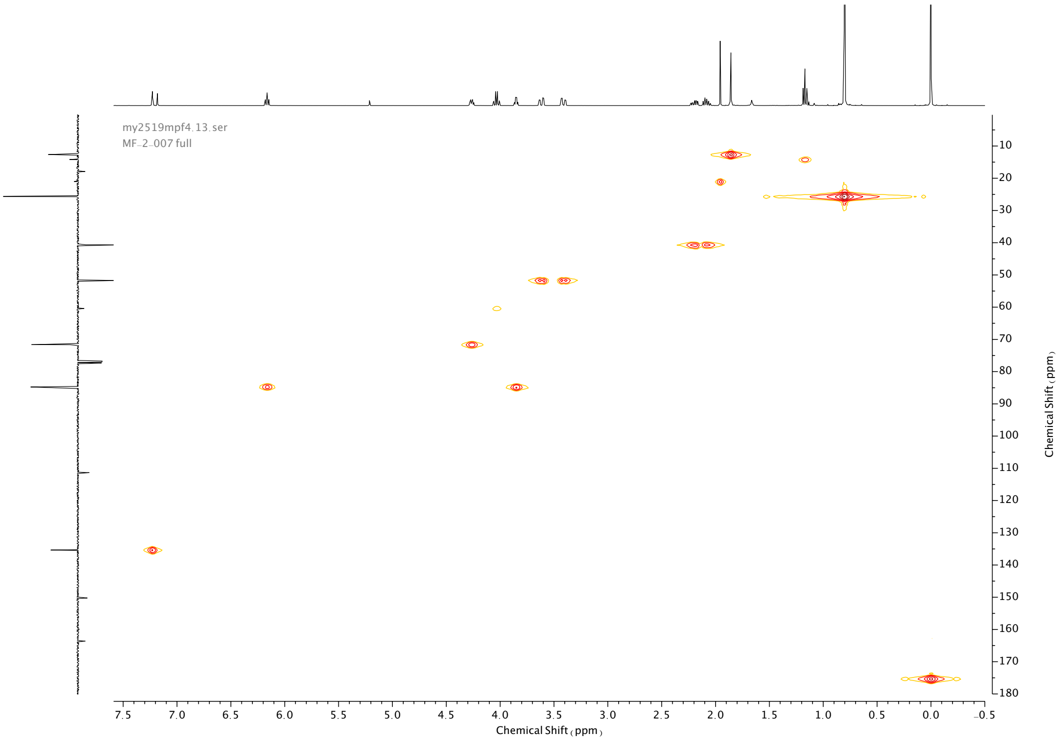

Figure **194**. HSQC NMR ($CDCl_3$) of **66**.

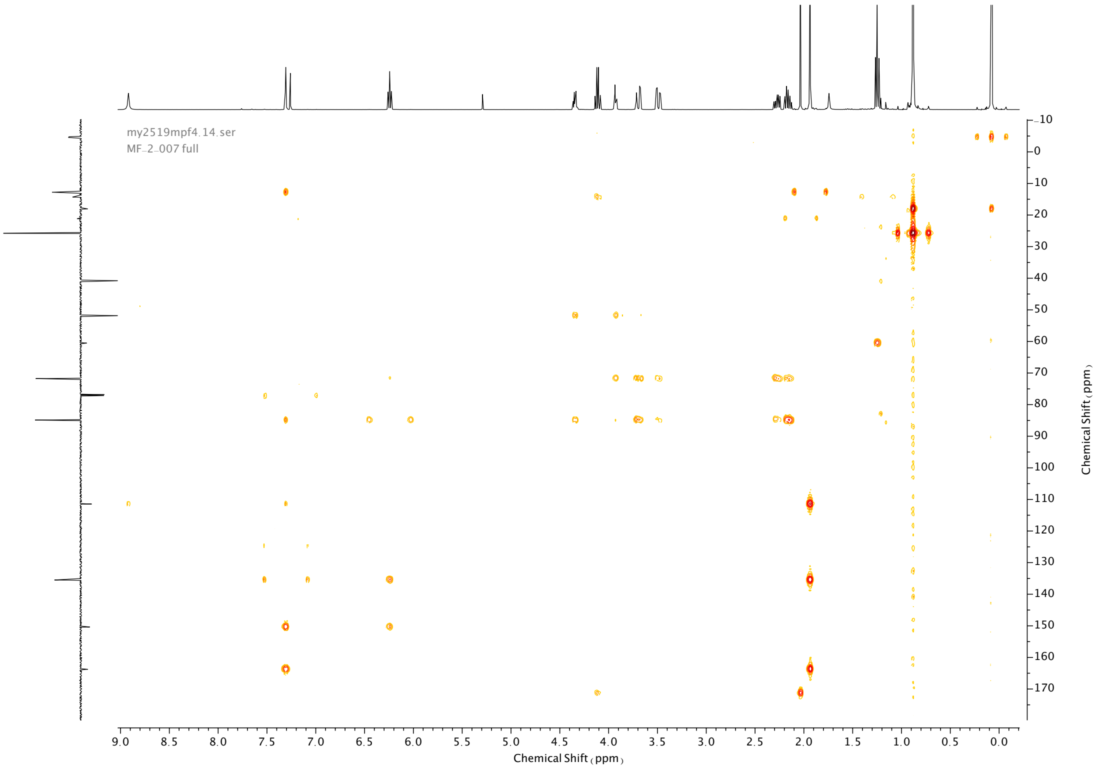

Figure **195**. HMBC NMR ($CDCl_3$) of **66**.

Compound **69**

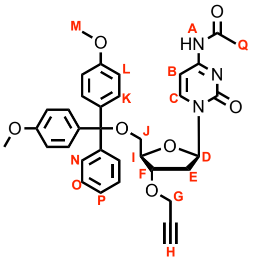

67 (1.0 g, 1.75 mmol, 1.0 eq.) was charged to a pre-dried round-bottom flask and degassed under N_2. Sodium hydride (60% dispersion in mineral oil, 0.2 g, 8.1 mmol, 4.6 eq.) was then added followed by anhydrous THF (10 mL). The mixture was stirred at -10 °C and **68** (0.5 mL, 4.38 mmol, 2.5 eq.) was added over 10 min. The mixture was allowed to reach room temperature and stirred for a further 6 h. The mixture was quenched *via* dropwise addition onto ice-water (30 mL) then extracted with CH_2Cl_2 (3 x 20 mL). The combined organic extracts were washed with brine (30 mL), dried over anhydrous $MgSO_4$, filtered, and concentrated *in vacuo*. The crude product was purified *via* silica-gel chromatography using a Biotage Isolute SPE column (eluent 19:1 CH_2Cl_2: MeOH, silica deactivated), to afford **69** as a white foam (490 mg, 0.8 mmol, 46 %). ^{1}H NMR (400 MHz, $CDCl_3$, 298 K) δ_H 9.45-9.41 (1H, br. s, N-H_A), 8.24 (1H, d, *J* = 7.5 Hz, H_C), 7.42-7.37 (2H, m, $H_{N,}$ H_O), 7.33-7.26 (6H, m, $H_{L,}$ $H_{K,}$ $H_{N,}$ H_O), 7.24 (1H, tt, *J* = 7.2, 1.3 Hz, H_P), 7.16 (1H, d, *J* = 7.5 Hz, H_B), 6.85 (4H, app. d, *J* = 8.9 Hz, $H_{K,}$ H_L), 6.20 (1H, t, *J* = 5.9 Hz, H_D), 4.46 (1H, dt, *J* = 6.2, 4.5 Hz, H_F), 4.22-4.18 (1H, m, H_I), 4.15 (2H, ddd, *J* = 17.5,16.0, 2.4 Hz, H_G), 3.80 (6H, s, H_M), 3.44 (2H, ddd, *J* = 11.0, 10.7, 3.0, H_J), 2.72 (1H, ddd, *J* = 13.9, 6.3, 4.7 Hz, $H_{E,}$ $H_{E'}$), 2.42 (1H, t, *J* = 2.3 Hz, H_H), 2.25 (3H, s, H_Q), 2.20 (1H, dt, *J* = 13.8, 6.0 Hz, $H_{E,}$ $H_{E'}$). ^{13}C NMR (101 MHz, $CDCl_{3,}$ 298 K) δ_C 162.6, 158.8, 155.1, 144.6, 144.4, 135.5, 130.2, 130.1, 128.2, 128.1, 127.3, 113.5, 96.5, 87.2, 87.1, 84.5, 79.2, 77.0, 75.3, 62.5, 57.0, 55.4, 38.9, 25.1.

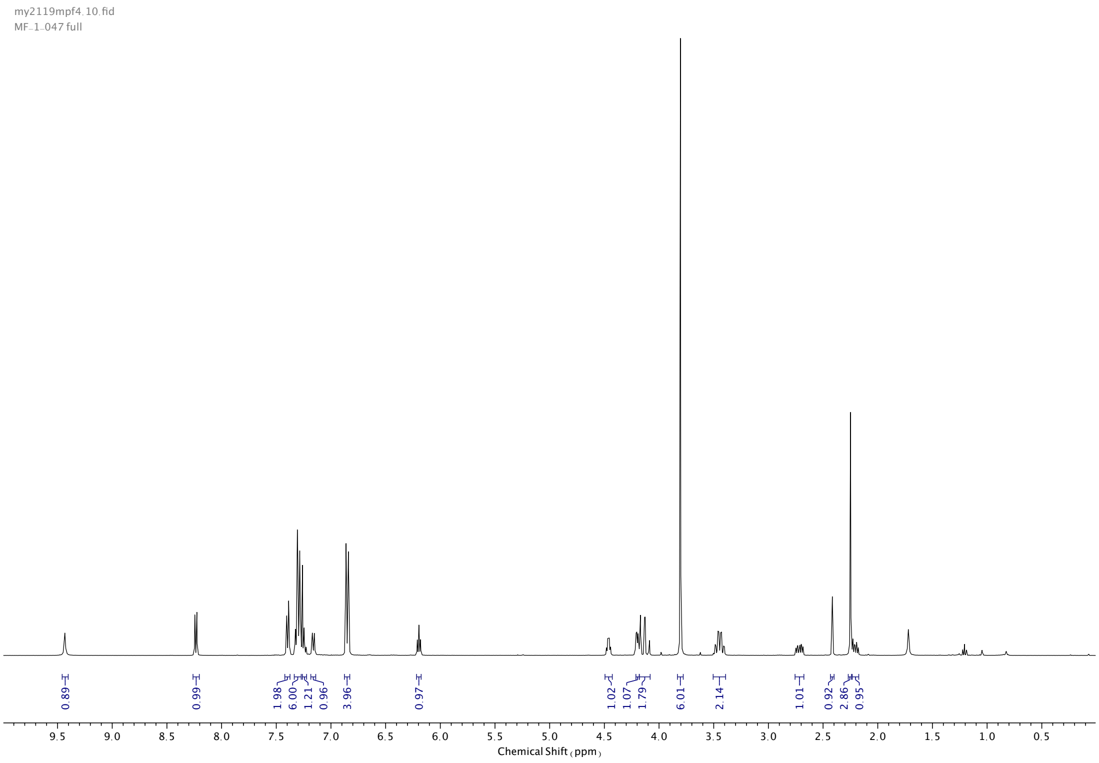

Figure **196**. ^{1}H NMR (CDCl$_3$, 400 MHz) of **69**.

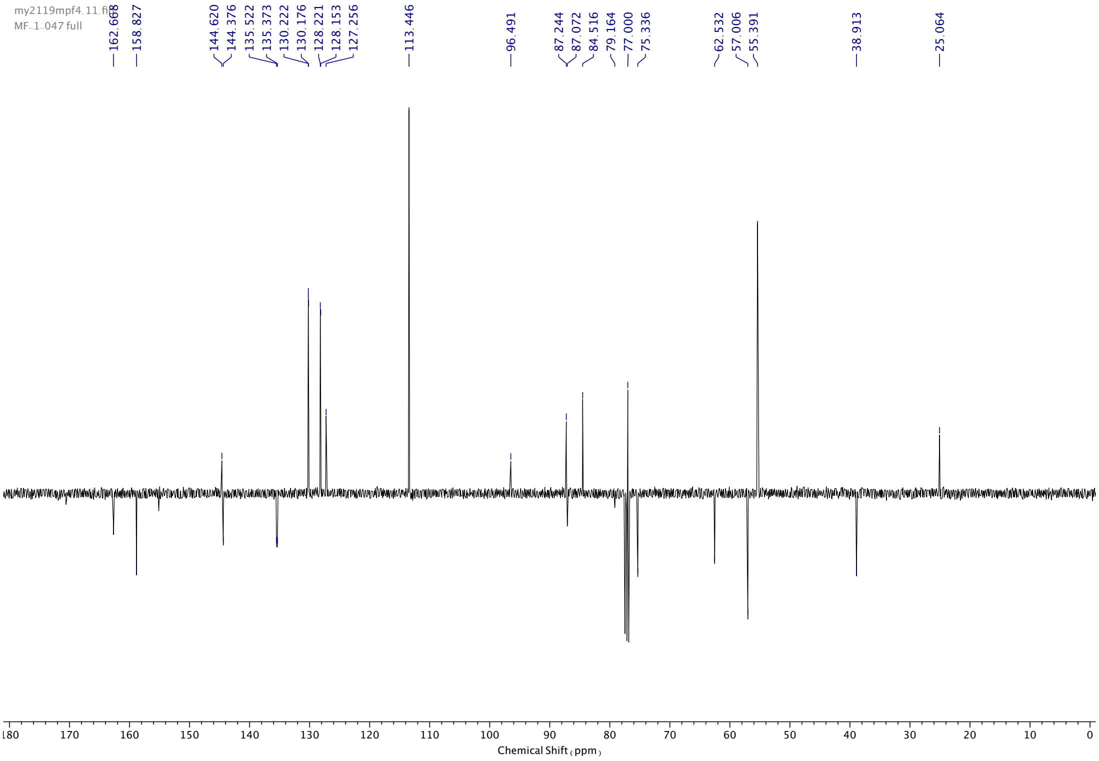

Figure **197**. ^{13}C NMR (CDCl$_3$, 101 MHz) of **69.**

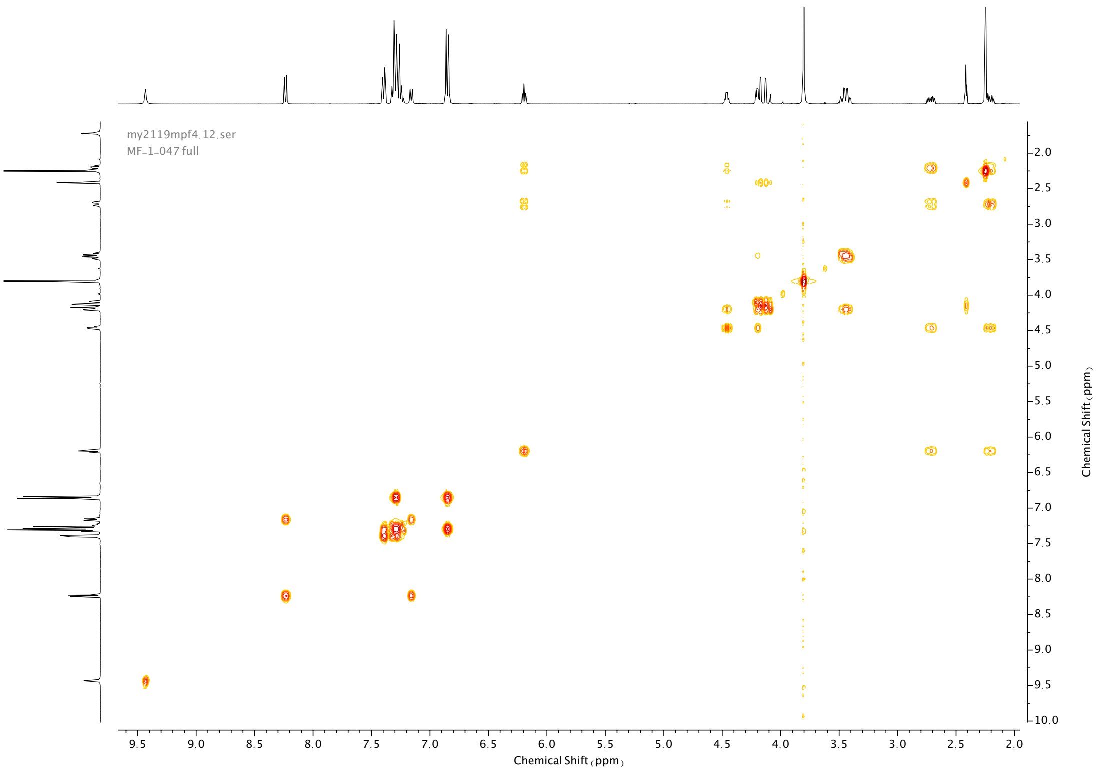

Figure **198**. COSY NMR (CDCl$_3$) of **69**.

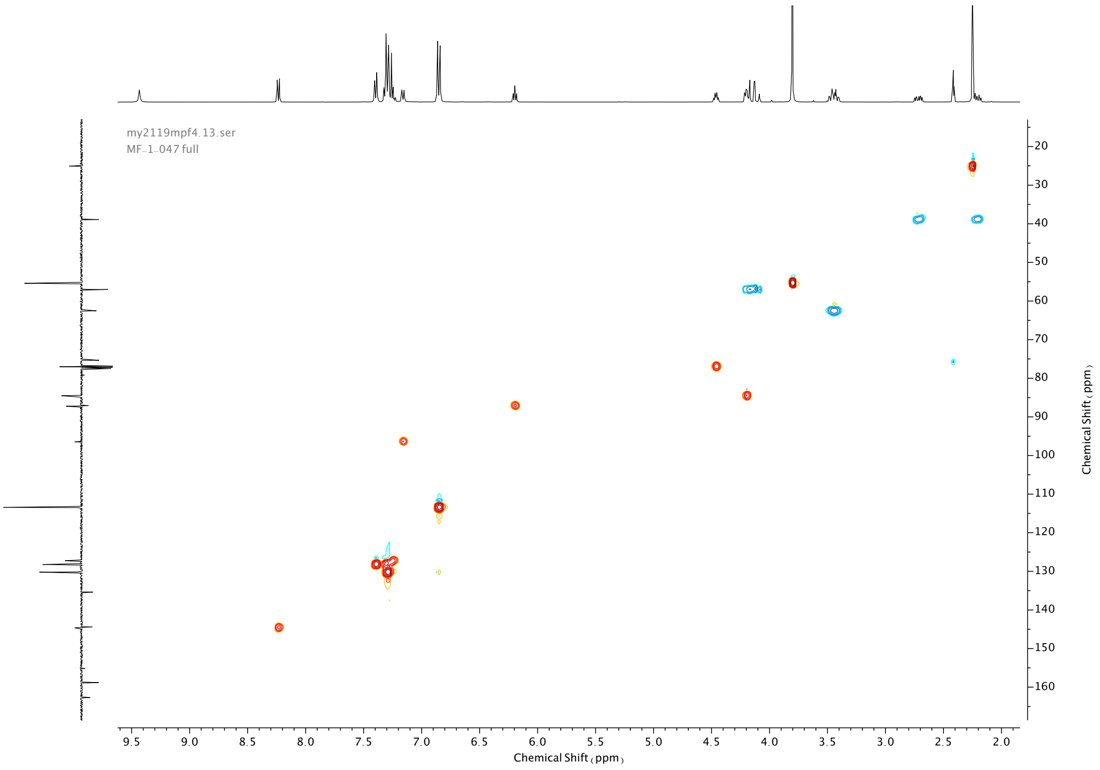

Figure **199**. HSQC NMR (CDCl$_3$) of **69**.

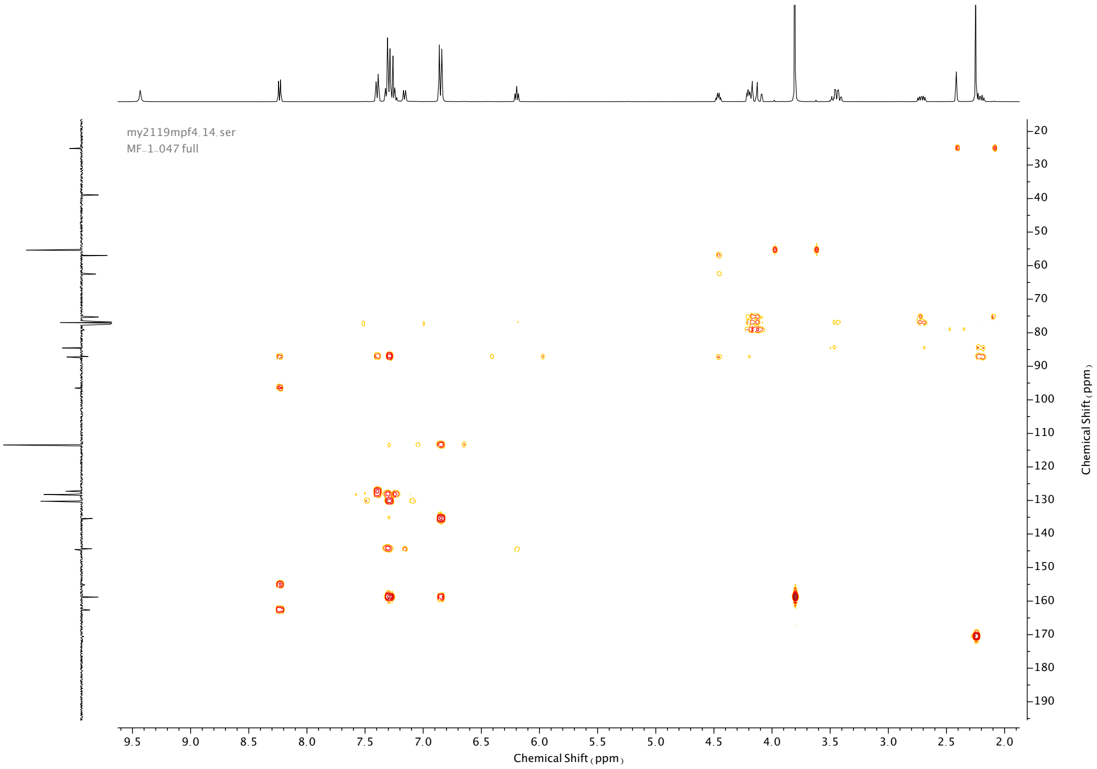

Figure **200**. HMBC NMR ($CDCl_3$) of **69**.

Compound **70**

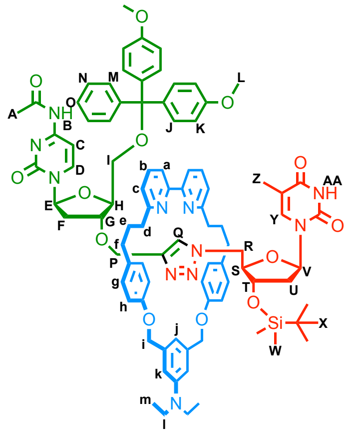

To a dry CEM vial was added macrocycle **25** (122 mg, 0.20 mmol, 1.0 eq.), azide **66** (78 mg, 0.20 mmol, 1.0 eq.), alkyne **69** (124 mg, 0.20 mmol, 1.0 eq.) and $[Cu(MeCN)_4]PF_6$ (48 mg, 0.19 mmol, 0.96 eq.). The vial was flushed with N_2 then anhydrous THF (12 mL) was added followed by DIPEA (71μL, 0.73 mmol, 2.0 eq.). The resulting mixture was stirred at room temperature overnight, then diluted with CH_2Cl_2 (22 mL), washed with EDTA-NH_3 (10 mL) then brine (20 mL), dried over anhydrous $MgSO_4$, filtered, then concentrated *in vacuo*. The crude product was purified *via* silica-gel chromatography using a Biotage Isolute SPE column (eluent 9:1 → 4:1 petrol: acetone) to afford **70** as a white foam (190 mg, 0.12 mmol, 59%). ^{1}H NMR (400 MHz, $CDCl_3$, 298 K) δ_H 9.37 (1H, br. s, N-H_B), 8.30 (1H, s, H_Q), 7.86 (1H, d, J = 7.5 Hz, H_D), 7.58 (2H, app. q, J = 7.8 Hz, H_b), 7.36 (2H, app. t, J = 8.6 Hz, H_c), 7.31-7.22 (5H, m, H_M, H_N & H_O), 7.18 (4H, dd, J = 8.8, 1.5 Hz, H_J or H_K), 7.12 (1H, d, J = 7.7 Hz, H_a or $H_{a'}$), 7.08 (1H, d, J = 7.5 Hz, H_a or $H_{a'}$), 7.00-6.93 (4H, m, H_h & $H_{h'}$), 6.99 (1H, d, J = 1.0 Hz, H_Y), 6.96 (1H, d, J = 7.6 Hz, H_C), 6.96-6.94 (1H, m, H_j), 6.78 (4H, dd, J = 9.1, 3.5 Hz, H_J or H_K), 6.71-6.64 (4H, m, H_g & $H_{g'}$), 6.62 (2H, m, H_k), 5.89 (1H, t, J = 6.7 Hz, H_E), 5.85 (1H, t, J = 6.6 Hz, H_V), 5.09-4.95 (4H, m, H_i & $H_{i'}$), 4.64-4.54 (1H, m, H_I or $H_{I'}$), 4.19-4.17 (1H, m, H_G), 4.02 (1H, d, J = 11.2 Hz, H_I or $H_{I'}$), 3.80-3.78 (1H, m, H_H), 3.77 (6H, s, H_L), 3.73-3.70 (1H, m, H_S), 3.59-3.55 (1H, m, H_T), 3.50-3.41 (2H, m, H_P), 3.35-3.24 (4H, m, H_l), 3.19 (1H, dd, J = 10.2, 2.5 Hz, H_R or $H_{R'}$), 2.97 (1H, dd, J = 10.3, 4.9 Hz, H_R or $H_{R'}$), 2.60-2.30 (8H, m, H_d & H_f), 2.22 (3H, s, H_A), 2.18-2.11 (1H, m, H_F or $H_{F'}$), 2.10-2.03 (1H, m, H_U or $H_{U'}$), 1.99-1.91 (1H, m, H_F or $H_{F'}$), 1.69 (3H, d, J = 0.9 Hz, H_Z), 1.66-1.60 (4H, m, H_e), 1.52-1.45 (1H, m, H_U or $H_{U'}$), 1.12 (6H, t, J = 7.1 Hz, H_m), 0.80 (9H, s, H_X), -0.02 (3H, s, H_W or $H_{W'}$), -0.07 (3H, s, H_W or $H_{W'}$). ^{13}C NMR (101 MHz, $CDCl_3$, 298 K) δ_C 163.7, 162.7, 162.6, 162.3, 158.8, 158.7, 158.0, 157.8, 157.2, 149.9, 148.2, 144.9, 144.4, 139.4, 139.3, 136.8, 136.7, 136.0, 135.6, 135.4, 133.8, 133.6, 130.3, 130.2, 129.3, 129.2, 128.4, 128.0, 127.2, 121.9, 121.6, 120.2, 120.1, 115.1, 115.0, 114.8, 113.3, 110.9, 110.3, 110.2, 96.0

(HMBC), 87.3, 86.7, 85.5, 84.7, 83.9, 79.3, 72.9, 70.6, 63.9, 62.8, 55.3, 51.1, 44.4, 40.4, 38.6, 37.9, 37.4, 35.0, 34.8, 31.9, 32.0, 27.0, 25.8, 25.1, 17.9, 12.4, -4.7, -4.8.[4] HR-ESI-MS (CH_3CN): *m/z* = 1588.9 $[M+H]^+$ calc. 1588.7741.

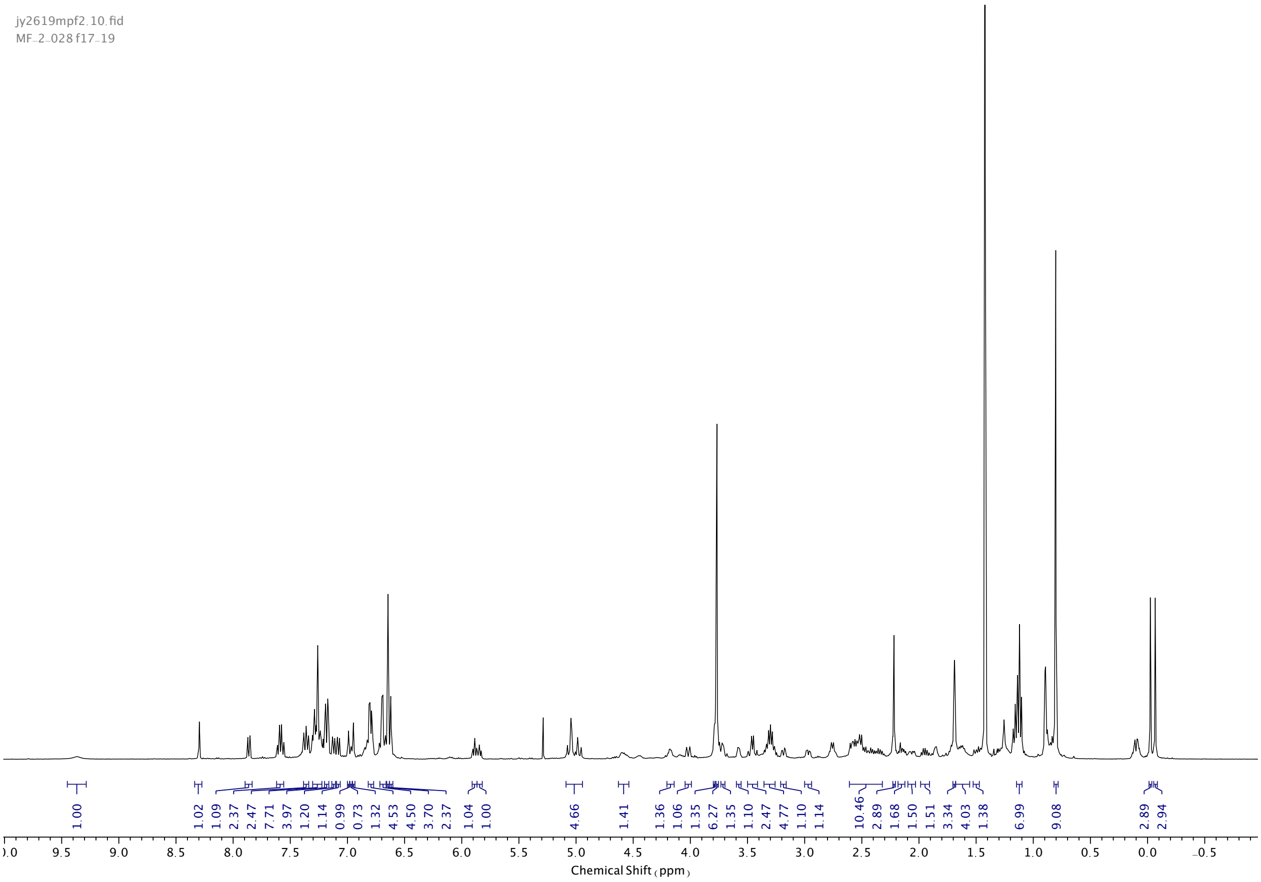

Figure **201**. ^1H NMR ($CDCl_3$, 400 MHz) of **70**.

---

[4] Several macrocyclic carbon signals are magnetically inequivalent. Signals at δ_C = 35.0 & 34.8, 32.0 & 31.9, 110.3 & 110.2, 115.1 & 115.0, 136.8 & 136.7, 120.2 & 120.1, 130.31 & 130.2, 136.0 & 135.6, 149.9 & 148.2 correspond to the same carbon atom in the above macrocycle structure. Determined using HSQC and HMBC.

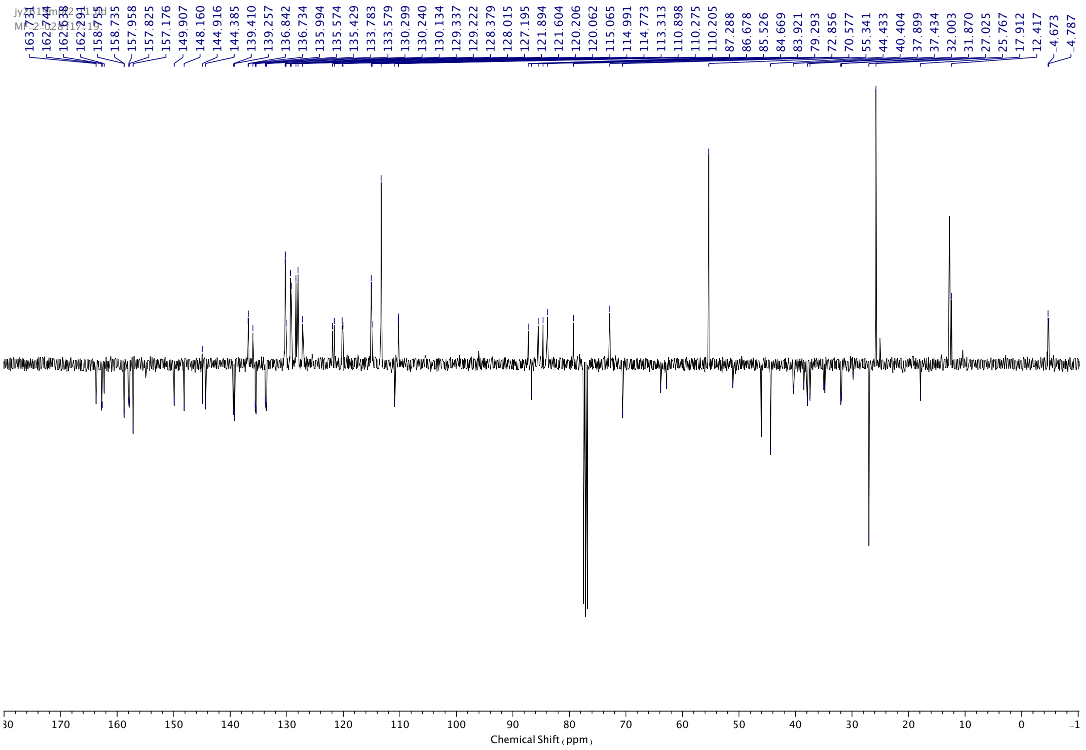

Figure **202**. ^{13}C NMR (CDCl$_3$, 101 MHz) of **70**.

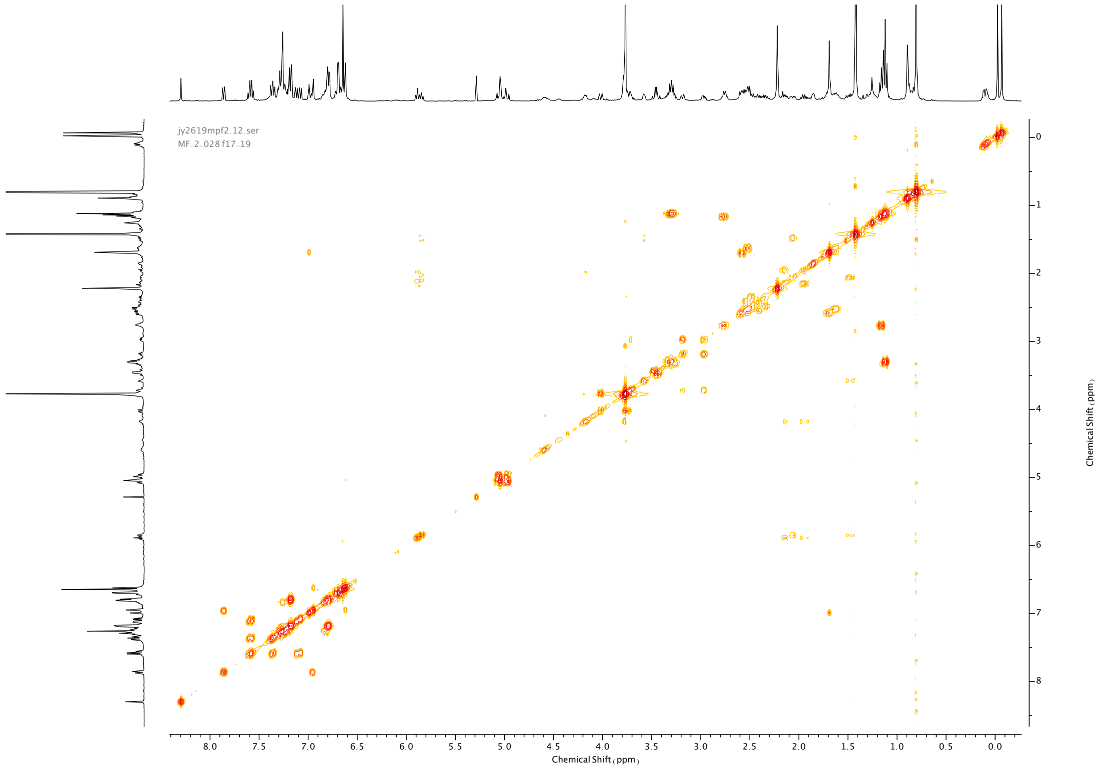

Figure **203**. COSY NMR (CDCl$_3$) of **70**.

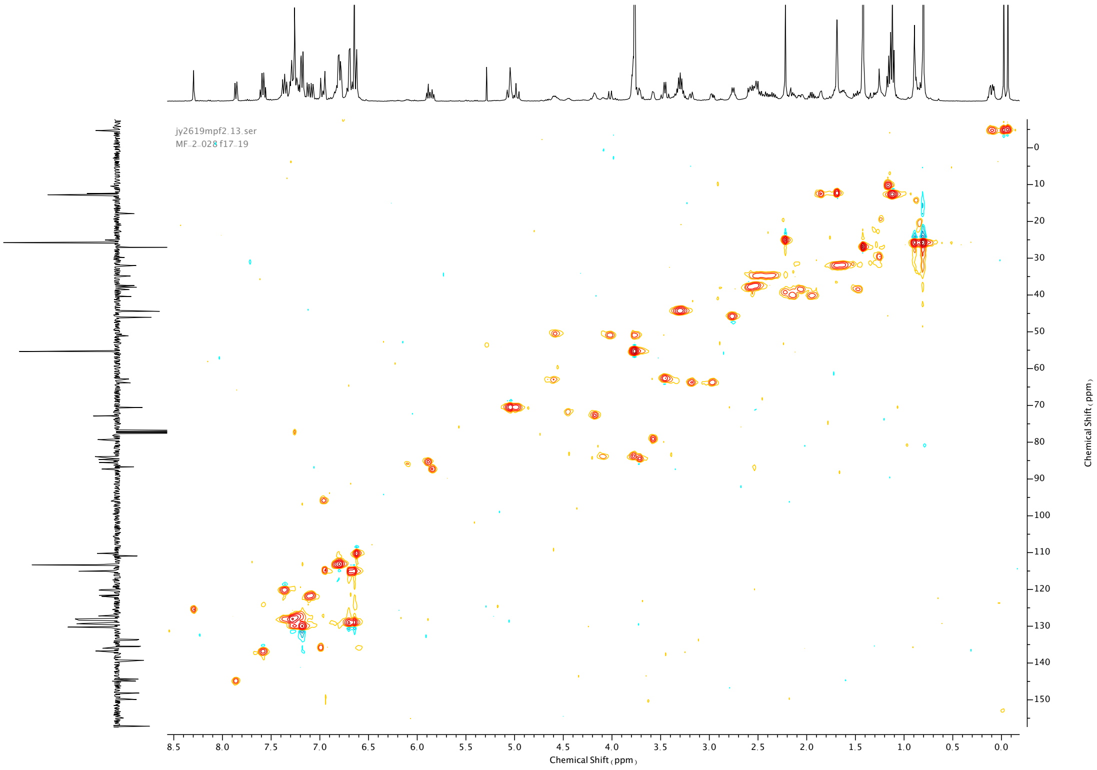

Figure **204**. HSQC NMR ($CDCl_3$) of **70**.

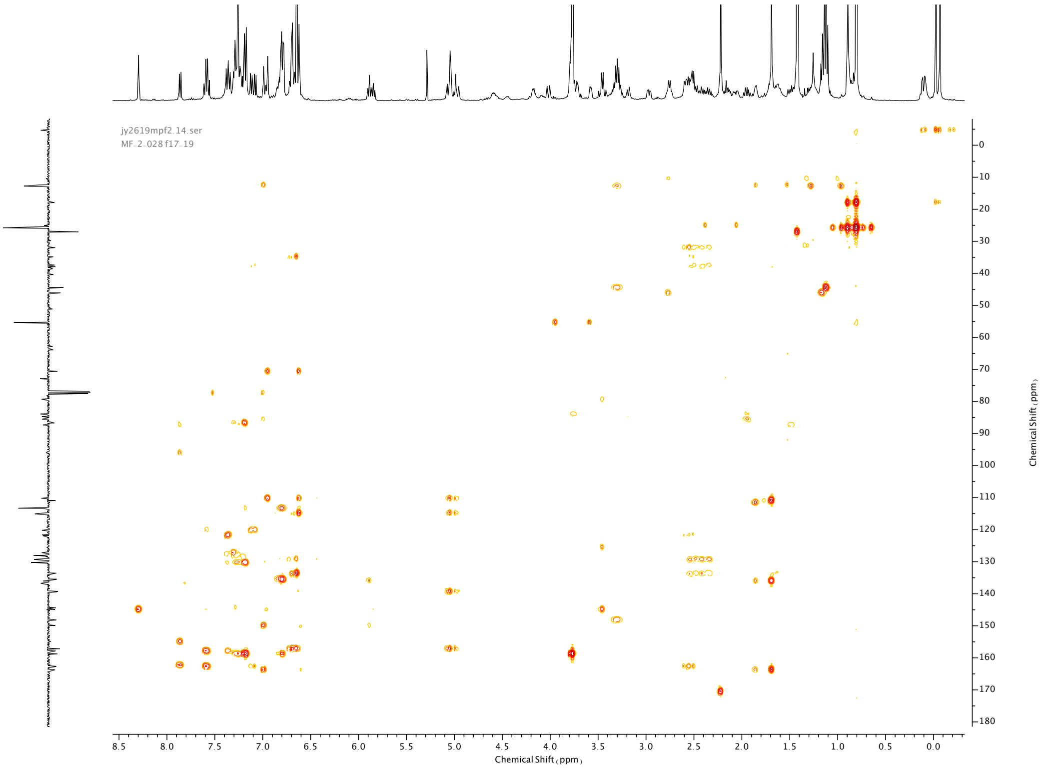

Figure **205**. HMBC NMR ($CDCl_3$) of **70**.

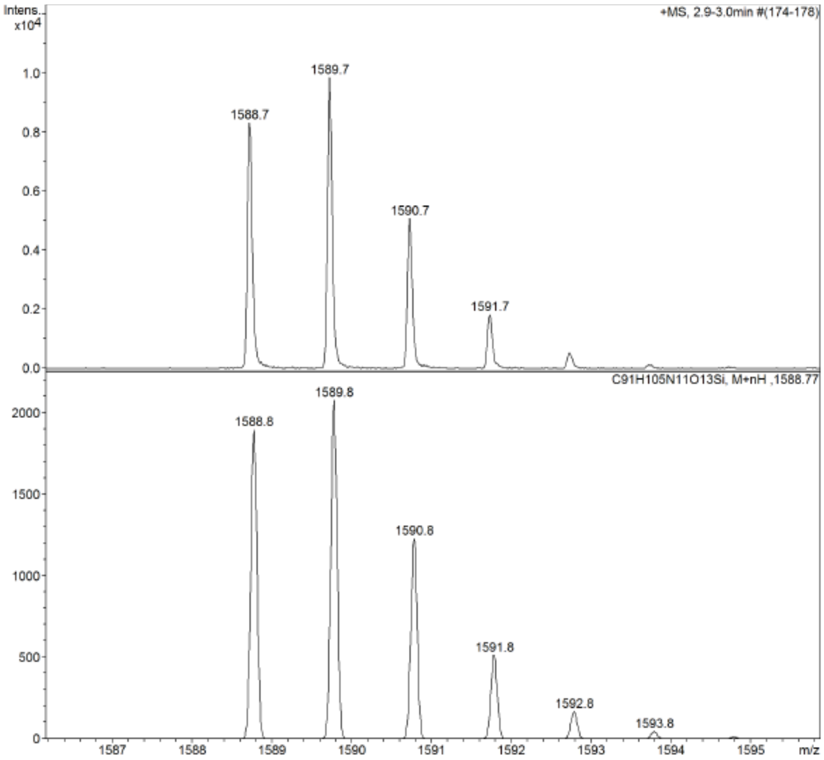

Figure **206**. Rotaxane **70** isotope pattern.

Compound **71**

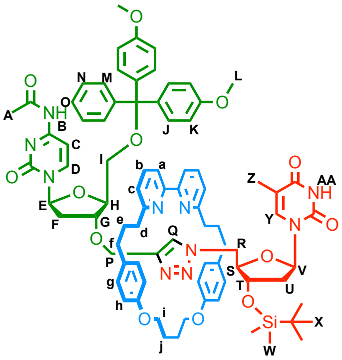

To a dry CEM vial was added macrocycle **13** (35 mg, 0.07 mmol, 1.0 eq.), azide **66** (27 mg, 0.07 mmol, 1.0 eq.), alkyne **69** (43 mg, 0.07 mmol, 1.0 eq.) and [Cu(MeCN)$_4$]PF$_6$ (26 mg, 0.07 mmol, 0.96 eq.). The vial was flushed with N_2 then anhydrous THF (12 mL) was added followed by DIPEA (71µL, 0.73 mmol, 2.0 eq.). The resulting mixture was stirred at room temperature overnight, then diluted with CH_2Cl_2 (22 mL), washed with EDTA-NH_3 (10 mL) then brine (20 mL), dried over anhydrous $MgSO_4$, filtered, then concentrated *in vacuo*. The crude product was purified *via* silica-gel chromatography using a Biotage Isolute SPE column (eluent 1:0 → 19:1 (1:1 CH_2Cl_2: PE): MeOH, silica deactivated) to afford **71** as a white foam (58 mg, 0.04 mmol, 56%). ^{1}H NMR (400 MHz, $CDCl_3$, 298 K) δ_H 9.40 (1H, s, H_Q), 8.96-8.90 (1H, br. s, N-H_{AA}), 8.29-8.26 (1H, br. s, N-H_B) 7.92 (1H, d, *J* = 7.5 Hz, H_D), 7.59 (1H, t, *J* = 7.8 Hz, H_b or H_{b}'), 7.55 (1H, t, *J* = 7.8 Hz, H_b or H_{b}'), 7.34-7.28 (3H, m, H_M & H_a or H_{a}'), 7.26-7.21 (3H, m, $H_{O,}$ H_N & H_a or H_{a}'), 7.19 (4H, dd, *J* = 8.9, 2.3 Hz, H_J), 7.16 (1H, d, *J* = 7.8, H_c or H_{c}'), 7.07 (1H, d, *J* = 7.8, H_c or H_{c}'), 6.97 (1H, d, *J* = 7.3 Hz, H_C), 6.87 (1H, s, H_Y), 6.83-6.77 (4H, m, H_K), 6.75-6.71 (2H, m, H_g or H_{g}'), 6.70-6.66 (2H, m, H_h or H_{h}'), 6.66-6.63 (2H, m, H_g or H_{g}'), 6.63-6.58 (2H, m, H_h or H_{h}'), 5.87 (1H, t, *J* = 6.4 Hz, H_E), 5.67 (1H, t, *J* = 6.3 Hz, H_V), 4.44-4.32 (2H, m, H_i or H_{i}'), 4.24-4.10 (2H, m, H_i or H_{i}'), 4.07 (1H, d, *J* = 13.1 Hz. H_R or H_{R}'), 3.96 (1H, q, *J* = 5.1 Hz, H_T), 3.85-3.80 (2H, m, H_G & H_H), 3.78 (3H, s, H_L or H_{L}'), 3.77 (3H, s, H_L or H_{L}'), 3.75 (2H, br. s, H_P), 3.57-3.48 (1H, m, H_R or H_{R}') 3.49-3.45 (1H, m, H_S), 3.25 (1H, d, *J* = 10.1 Hz, H_I or H_{I}'), 3.05 (1H, dd, *J* = 10.2, 4.5 Hz, H_I or H_{I}'), 2.64 (1H, dt, *J* = 13.8, 6.0 Hz, H_f or H_{f}'), 2.55-2.45 (1H, m, H_f or H_{f}'), 2.43-2.32 (4H, m, H_d or H_{d}'), 2.26 (1H, dd, *J* = 13.9, 5.9 Hz, H_F or H_{F}'), 2.20 (3H, s, H_A), 2.15-1.95 (5H, m, H_U or $H_{U}'_{,}$ H_j or H_{j}'), 1.90-1.83 (1H, m, H_U & H_{U}'), 1.78-1.71 (4H, m, H_e & H_{e}'),1.66-1.59 (1H, m, H_F or H_{F}'), 1.47 (3H, s, H_Z), 0.90 (9H, s, H_X), 0.09 (3H, s, H_W or H_{W}'), 0.05 (3H, s, H_W or H_{W}'). ^{13}C NMR (101 MHz, $CDCl_{3,}$ 298 K) δ_C 170.4 (HMBC), 163.4, 162.9 (x2), 162.3, 158.8 (x2), 157.5 (x2), 157.4, 157.3, 154.8 (HMBC), 149.5, 144.9, 144.4, 144.2, 136.9, 136.8, 135.6, 135.5, 135.4, 132.9, 132.8, 130.3, 130.2, 129.2, 129.1 128.3, 128.1, 127.5, 127.2, 121.6, 121.0, 120.1, 119.8, 115.0, 114.9, 113.4, 113.4, 110.5, 96.0 (HMBC), 87.4, 86.7, 85.0, 84.7 83.5, 79.0, 72.7, 66.4, 66.3, 63.7, 62.6, 55.4, 51.4, 41.0, 38.9, 37.3 (x2), 36.4, 35.4, 35.1, 31.9, 31.3, 25.9, 25.1 (x2), 25.0, 18.0, 12.2, -4.4, -4.5.[5] HR-ESI-MS (CH_3CN): *m/z* = 1469.6964 $[M+H]^+$ calc. 1469.7006.

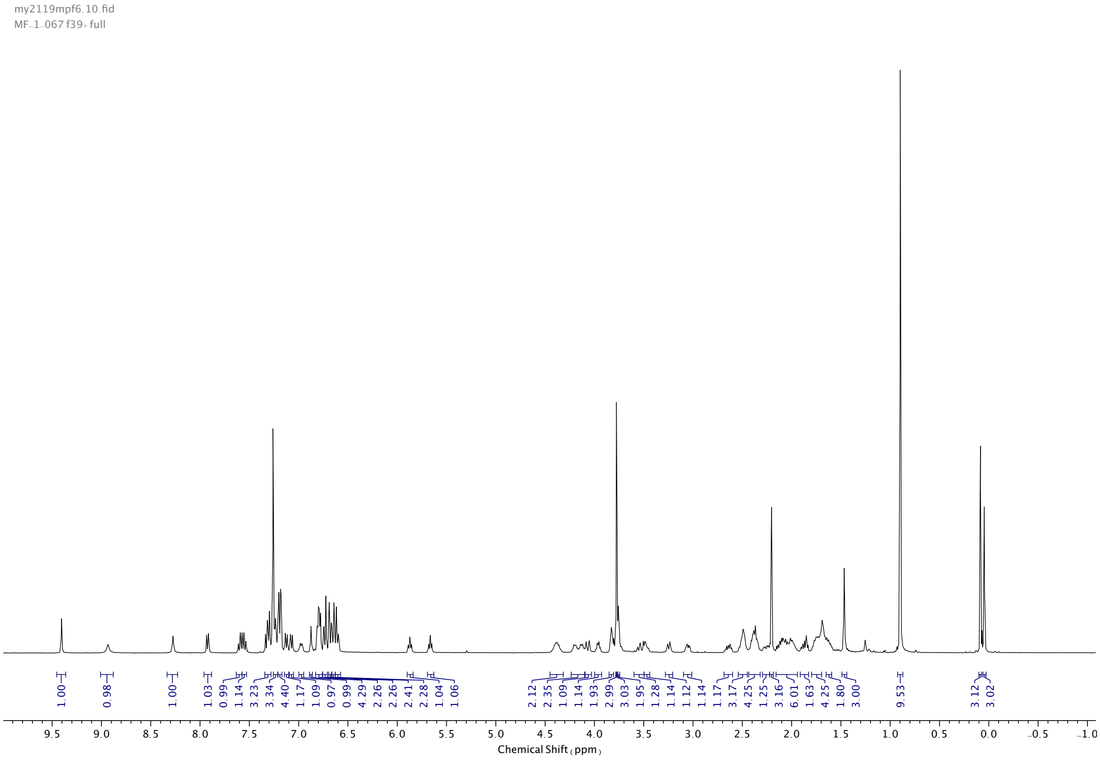

Figure **207**. ^1H NMR ($CDCl_3$, 400 MHz) of **71**.

---

[5] Several Macrocyclic carbon signals are magnetically inequivalent. Signals at δ_C = 162.9 (x2), 157.5 (x2), 157.4 & 157.3, 136.9 & 136.7, 132.9 & 132.8, 129.1 & 129.0, 121.6 & 121.0, 120.1 & 119.8, 115.0 & 114.9, 37.3 (x2), 35.4 & 35.1, 31.7 & 31.3, 25.1 & 25.0 correspond to the same carbon atom in the above macrocycle structure. Determined using HSQC and HMBC.

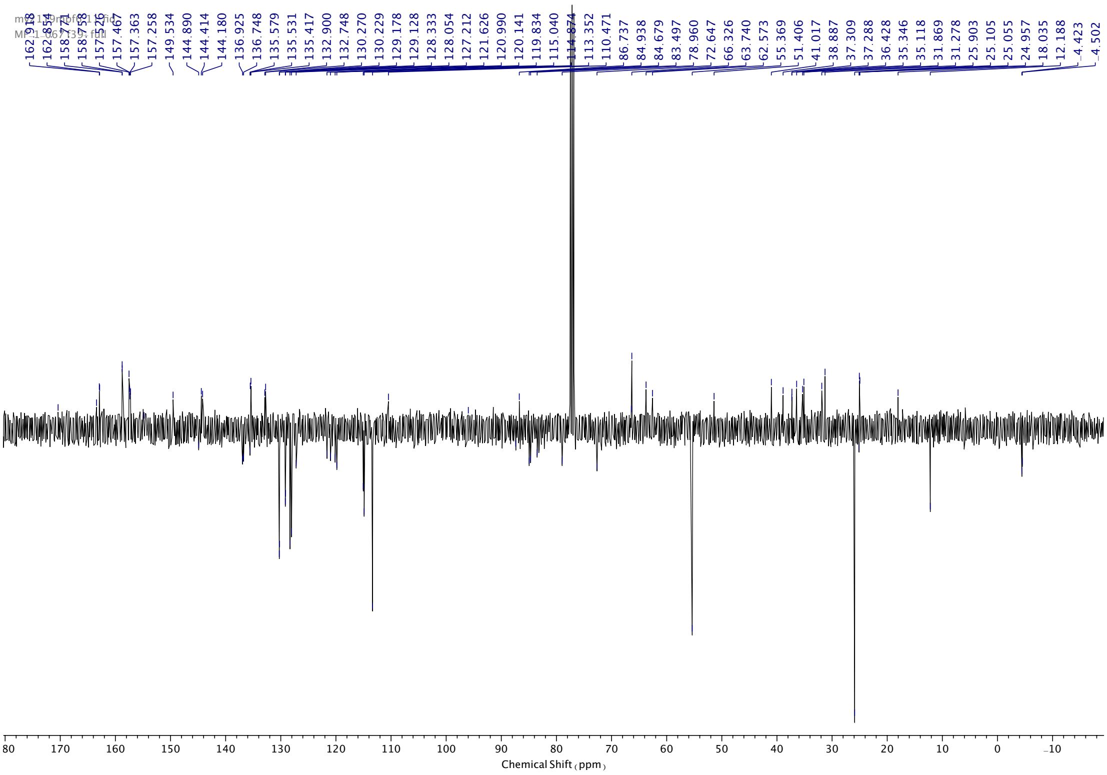

Figure **208**. ^{13}C NMR (CDCl$_3$, 101 MHz) of **71**

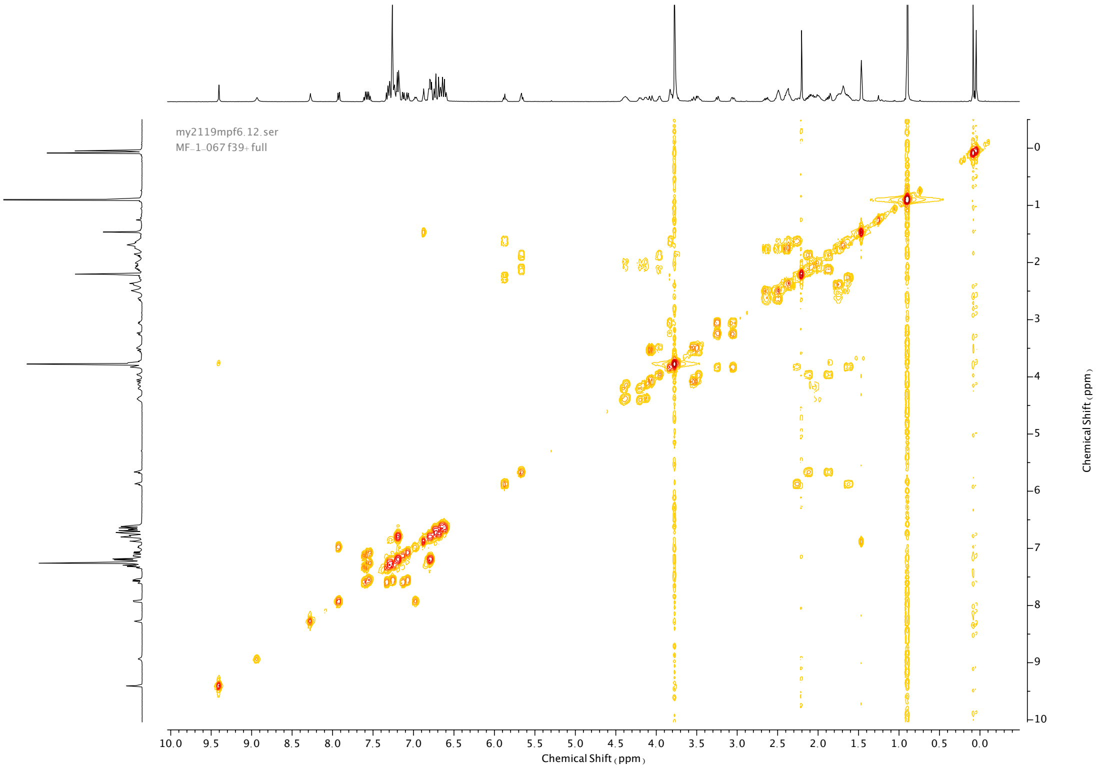

Figure **209**. COSY NMR (CDCl$_3$) of **71**.

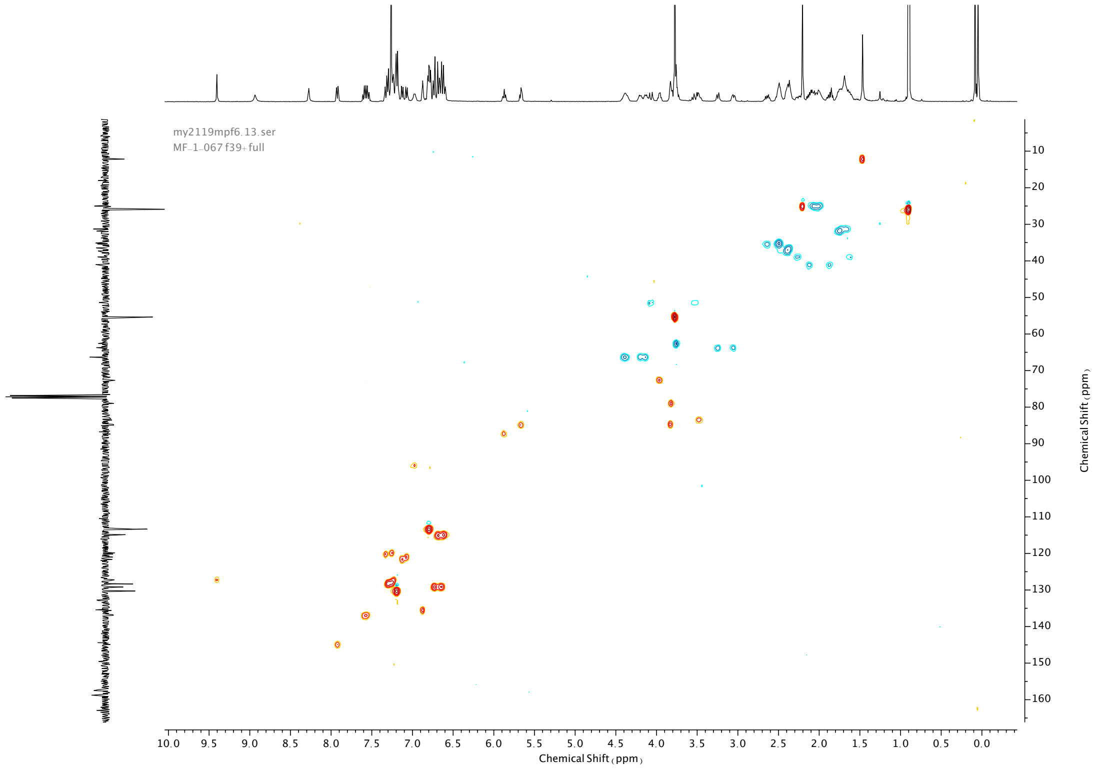

Figure **210**. HSQC NMR ($CDCl_3$) of **71**.

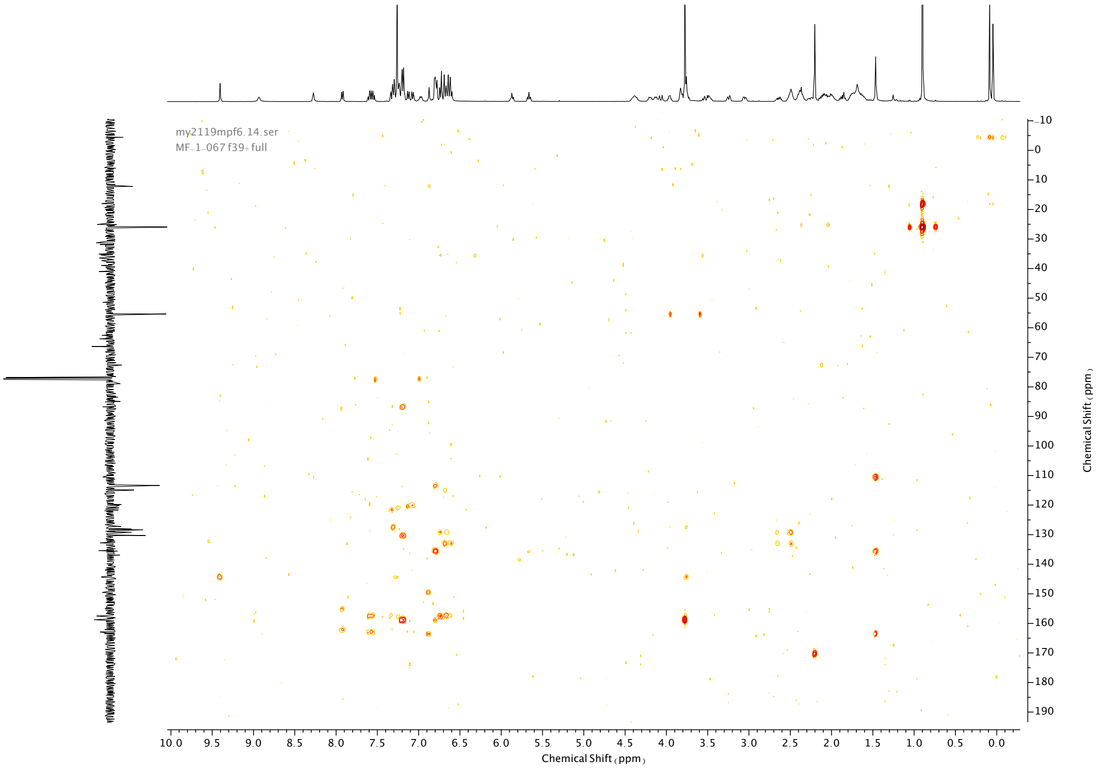

Figure **211**. HMBC NMR ($CDCl_3$) of **71**.

Compound **72**

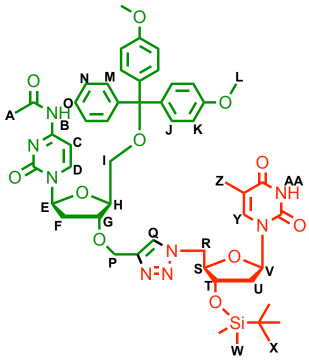

To a dry CEM vial was added azide **66** (25 mg, 0.066 mmol, 1.0 eq.), alkyne **69** (40 mg, 0.066 mmol, 1.0 eq.) and [Cu(CH$_3$CN)$_4$]PF$_6$ (23 mg, 0.063 mmol, 0.96 eq.). The vial was flushed with N$_2$ then anhydrous THF (2 mL) was added followed by DIPEA (114 μL, 0.66 mmol, 10 eq.). The resulting mixture was stirred at room temperature overnight, then diluted with CH$_2$Cl$_2$ (20 mL), washed with EDTA-NH$_3$ (20 mL) then brine (20 mL), dried over anhydrous MgSO$_4$, filtered and concentrated *in vacuo*. The crude product was purified *via* silica-gel chromatography using a Biotage Isolute SPE column (eluent 1:0 → 9:1 CH$_2$Cl$_2$: MeOH) to afford **72** as a white foam (31 mg, 0.031 mmol, 48 %). ^{1}H NMR (400 MHz, CDCl$_3$, 298 K) δ_H 8.14 (1H, d, *J* = 7.5 Hz, H$_D$), 7.59 (1H, s, H$_Q$), 7.37-7.34 (2H, m, H$_M$), 7.32-7.22 (7H, m, H$_J$, H$_O$ & H$_N$), 7.16 (1H, d, *J* = 7.4 Hz, H$_C$), 6.84 (4H, dd, *J* = 9.0, 1.4 Hz, H$_K$), 6.61 (1H, d, *J* = 1.3 Hz, H$_Y$), 6.20 (1H, t, *J* = 6.1 Hz, H$_E$), 6.10 (1H, t, *J* = 6.5 Hz, H$_V$), 4.62-4.56 (4H, m, H$_P$ & H$_R$), 4.44 (1H, q, *J* = 5.5 Hz, H$_S$), 4.29 (1H, dt, *J* = 5.8, 3.7 Hz, H$_G$), 4.21 (1H, q, *J* = 3.4 Hz, H$_H$), 4.10 (1H, q, *J* = 4.7 Hz, H$_T$), 3.80 (6H, s, H$_L$), 3.44 (1H, dd, *J* = 10.7, 3.4 Hz, H$_i$ or H$_i$'), 3.37 (1H, dd, *J* = 10.6, 3.4 Hz, H$_i$ or H$_i$'), 2.79-2.72 (1H, m, H$_F$ or H$_F$'), 2.25-2.20 (5H, m, H$_A$ & H$_U$ or H$_U$'), 2.15-2.09 (1H, m, H$_F$ or H$_F$'), 1.85 (3H, d, *J* = 1.2 Hz, H$_Z$), 0.90 (9H, s, H$_x$), 0.12 (3H, s, H$_W$ or H$_W$'), 0.09 (3H, s, H$_W$ or H$_W$'). ^{13}C NMR (101 MHz, CDCl$_3$, 298 K) δ_C 170.4 (HMBC), 164.1 (HMBC), 162.5 (HMBC), 158.8, 155.0 (HMBC), 150.1, 144.9, 144.5, 144.4, 136.0, 135.4 (x2), 130.2 (x2), 128.2 (x2), 127.3, 124.5 (HMBC), 113.5, 111.5, 87.3, 87.1, 86.1, 84.1, 79.0, 71.9, 63.3, 55.4, 50.7, 39.4, 39.1, 29.8, 25.8, 25.1, 18.0 (HMBC), 12.1, -4.5, -4.6.

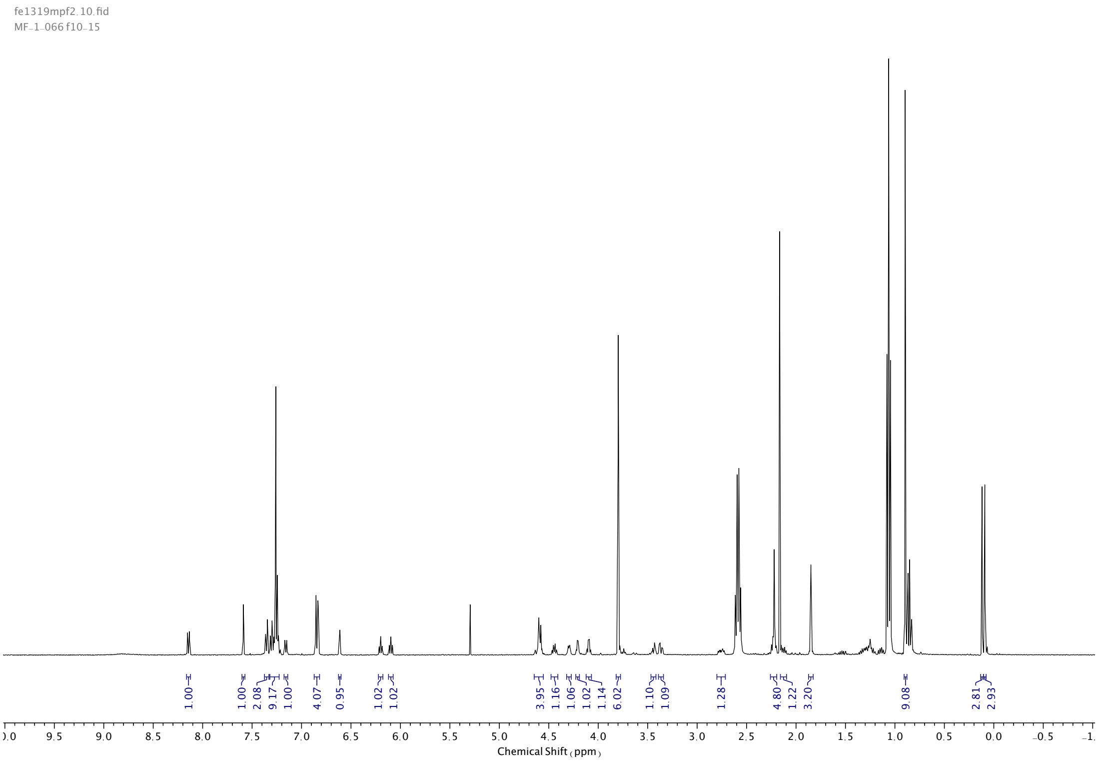

Figure **212**. ^{1}H NMR (CDCl$_3$, 400 MHz) of **72**.

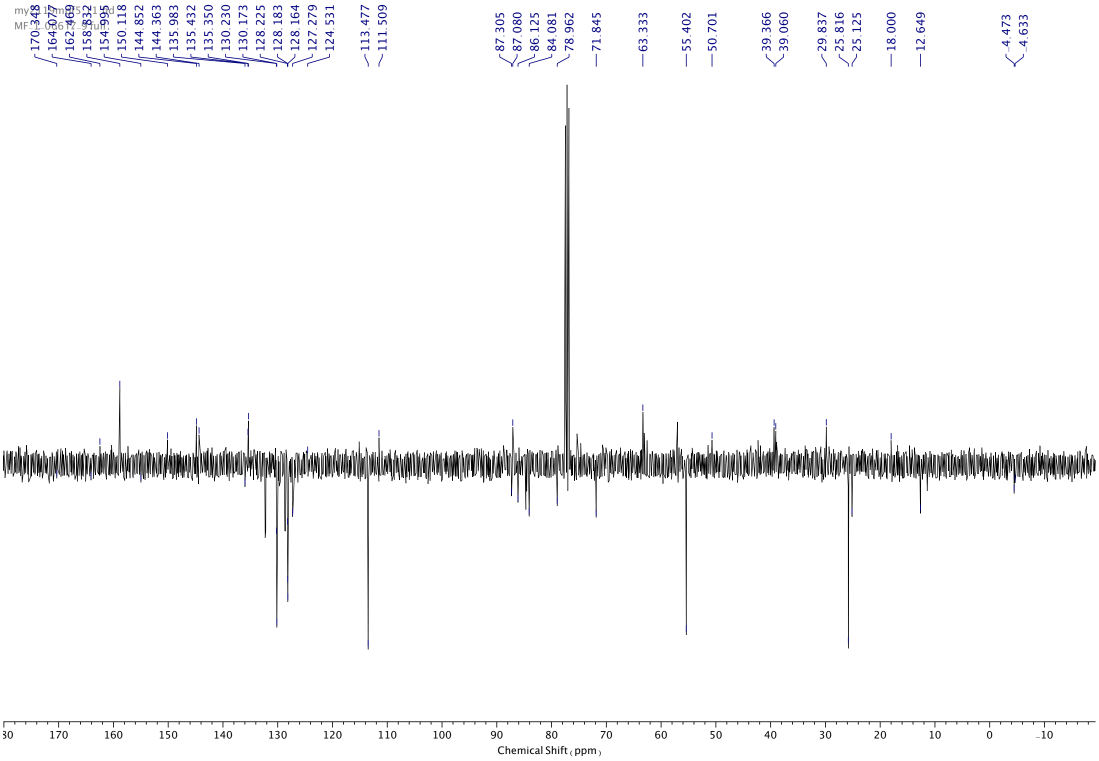

Figure **213**. ^{13}C NMR (CDCl$_3$, 101 MHz) of **72.**

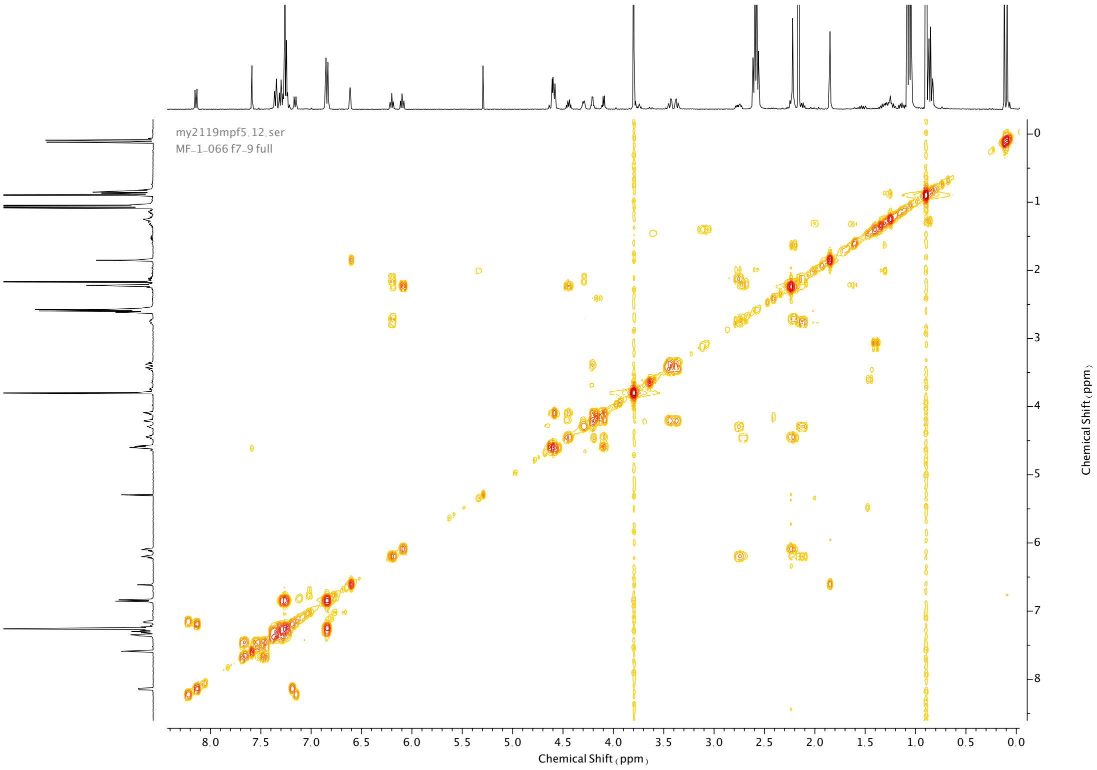

Figure **214**. COSY NMR ($CDCl_3$) of **72**.

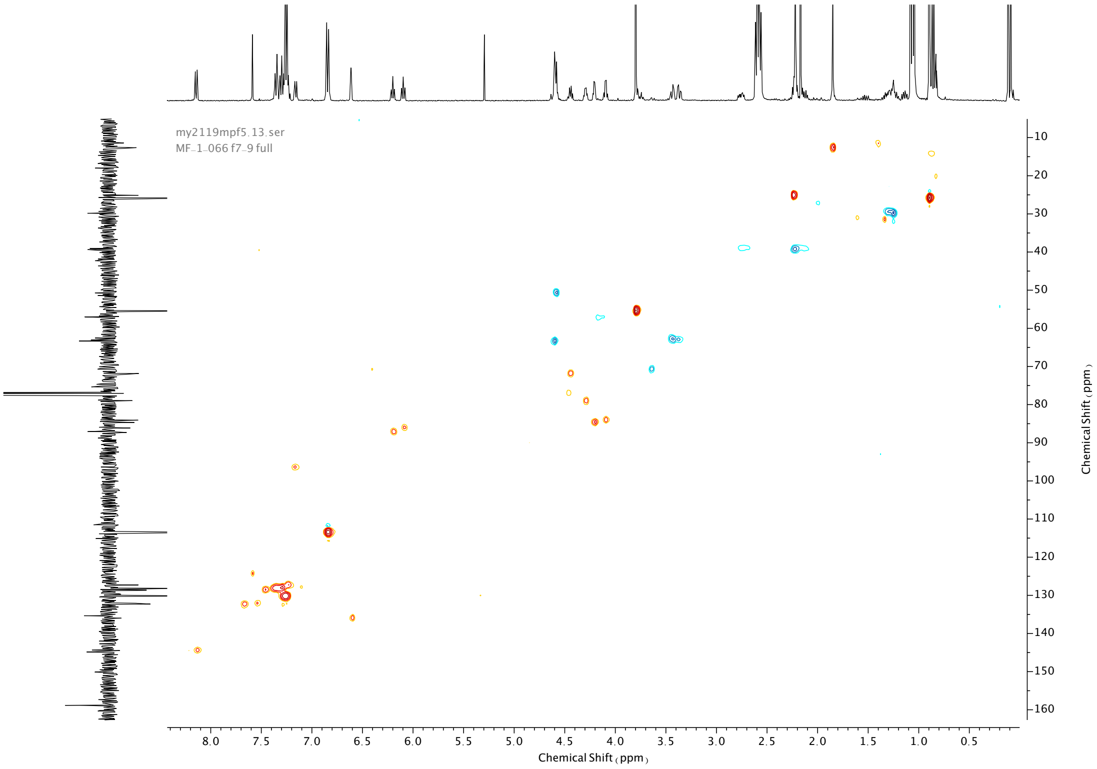

Figure **215**. HSQC NMR ($CDCl_3$) of **72**.

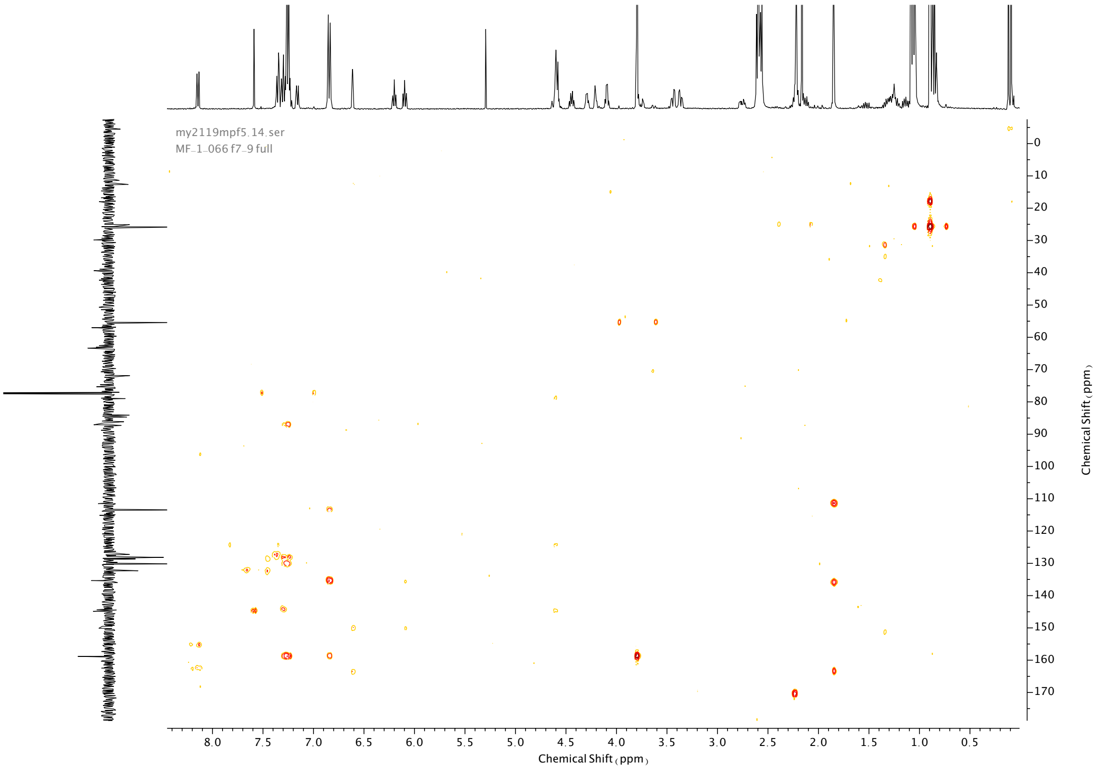

Figure **216**. HMBC NMR ($CDCl_3$) of **72**.

Compound **73**

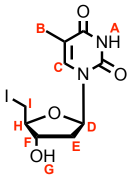

63 (1.50 g, 6.19 mmol, 1.0 eq.), $CH_3P(OPh)_3I$ (3.36 g, 7.43 mmol, 1.2 eq.) and anhydrous DMF (8 mL) were added to a pre-dried flask and stirred at room temperature overnight. MeOH (8 mL) was then added and the mixture stirred for a further 15 min. The mixture was then concentrated *in vacuo* and crude residue taken up in EtOAc (100 mL), washed with $Na_2S_2O_3$ (50 mL) and brine (50 mL), then dried over anhydrous $MgSO_4$, filtered and concentrated *in vacuo*. The crude product was purified *via* silica-gel chromatography using a Biotage Isolute SPE column (eluent 1:0 → 9:1 CH_2Cl_2: MeOH) to afford **73** as a white solid (1.13 g, 3.16 mmol, 52%).^{1}H NMR (400 MHz, DMSO-d_6, 298 K) δ_H 11.34-11.31 (1H, br. s, N-H_A), 7.52 (1H, d, *J* = 1.2 Hz, H_C), 6.22 (1H, dd, *J* = 8.1, 6.2 Hz, H_D), 5.48 (1H, d, *J* = 4.3 Hz, O-H_G), 4.20-4.15 (1H, m, H_F), 3.80 (1H, td, *J* = 6.2, 2.9 Hz, H_H), 3.52 (1H, dd, *J* = 10.4, 6.2 Hz, H_I or H_I'), 3.39 (1H, dd, *J* = 10.4, 6.3 Hz, H_I or H_I'), 2.33-2.24 (1H, m, H_E or H_E'), 2.08 (1H, ddd, *J* = 13.6, 6.3, 3.1, H_E or H_E'), 1.80 (3H, d, *J* = 1.2 Hz, H_B).^{13}C NMR (101 MHz, DMSO-d_6, 298 K) δ_C 163.7, 150.5, 136.2, 109.9, 85.4, 84.0, 73.1, 38.0, 12.2, 8.0.

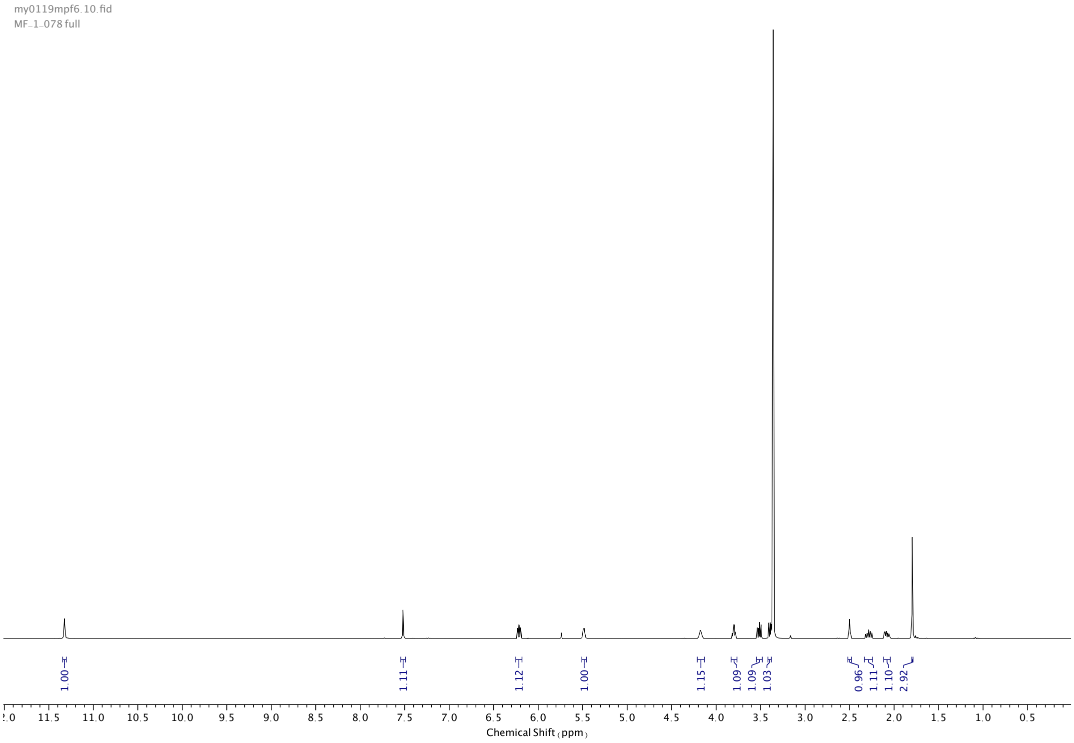

Figure **217**. ^{1}H NMR (DMSO-d_6, 400 MHz) of **73**.

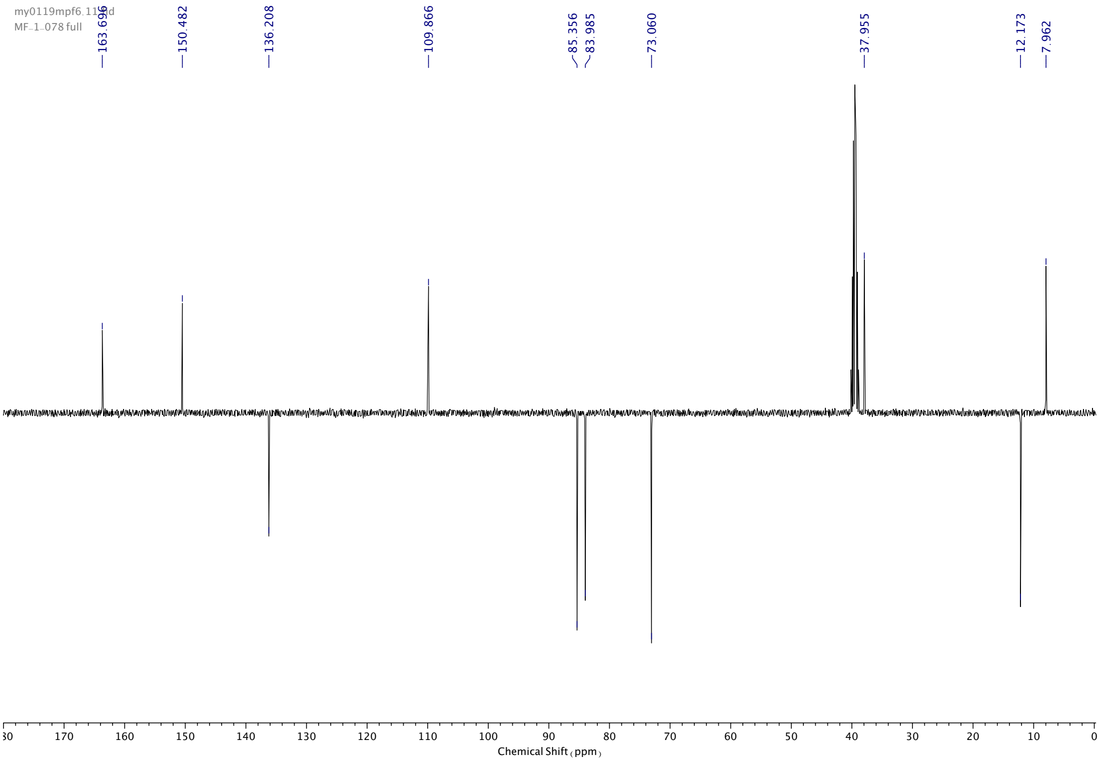

Figure **218**. ^{13}C NMR (DMSO-d_6, 101 MHz) of **73.**

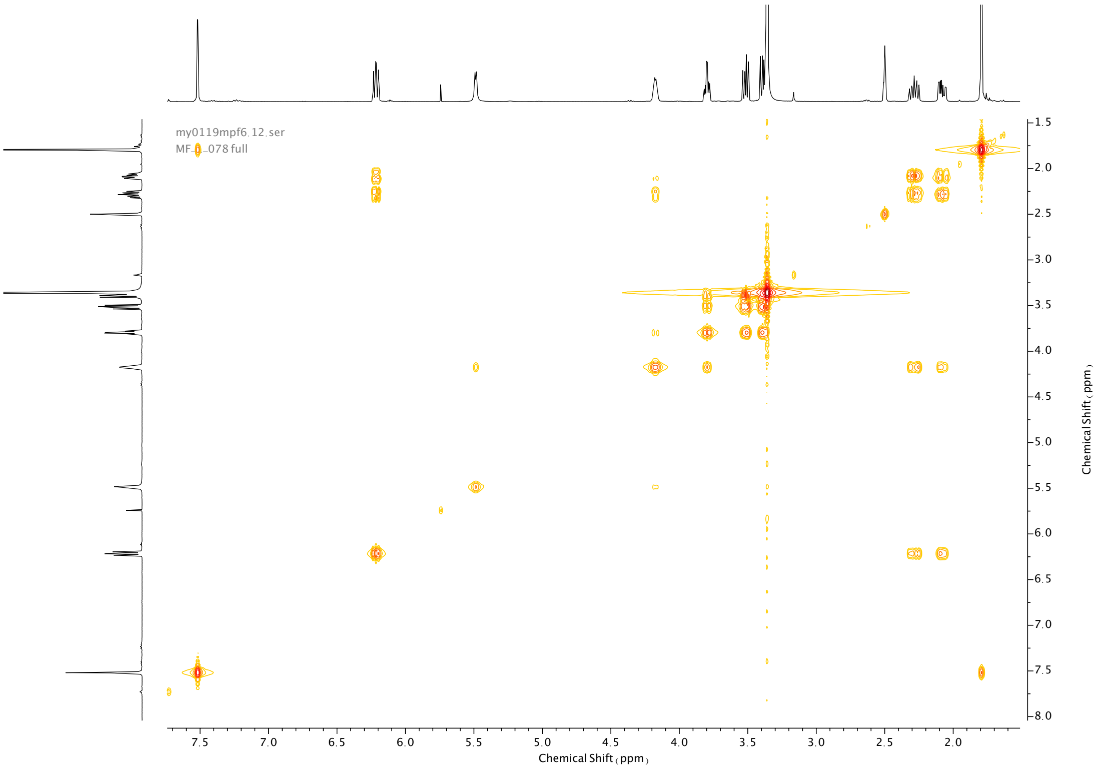

Figure **219**. COSY NMR (DMSO-d_6) of **73**.

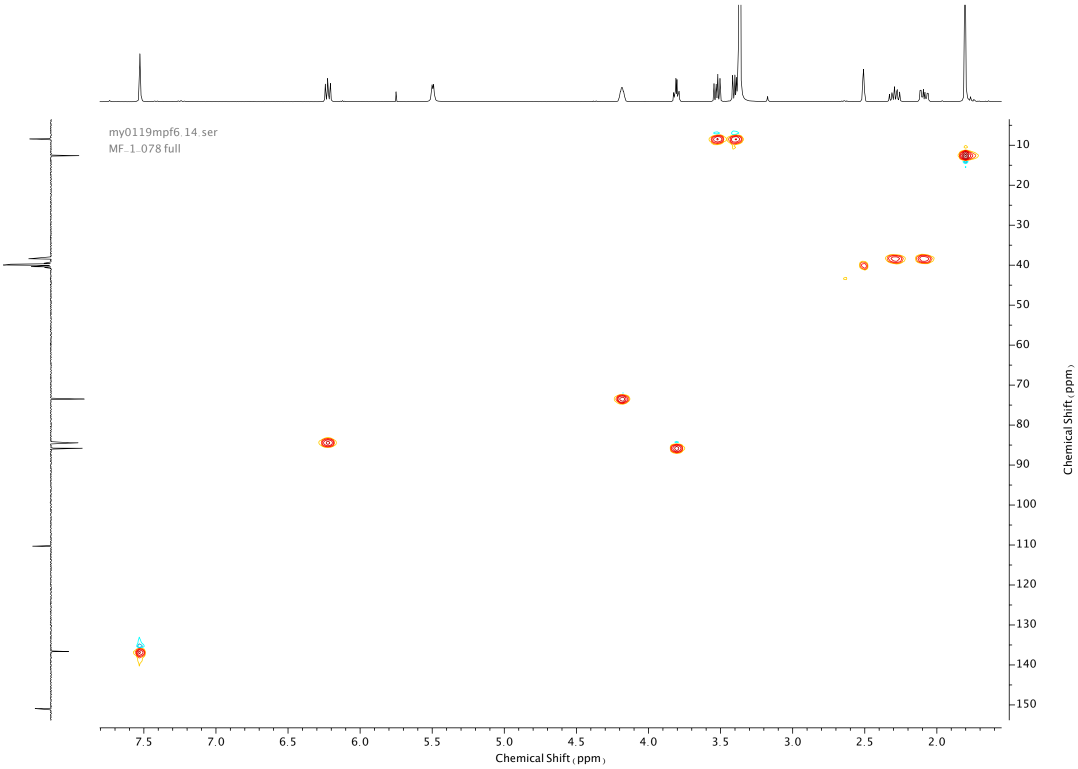

Figure **220**. HSQC NMR (DMSO-d$_6$) of **73**.

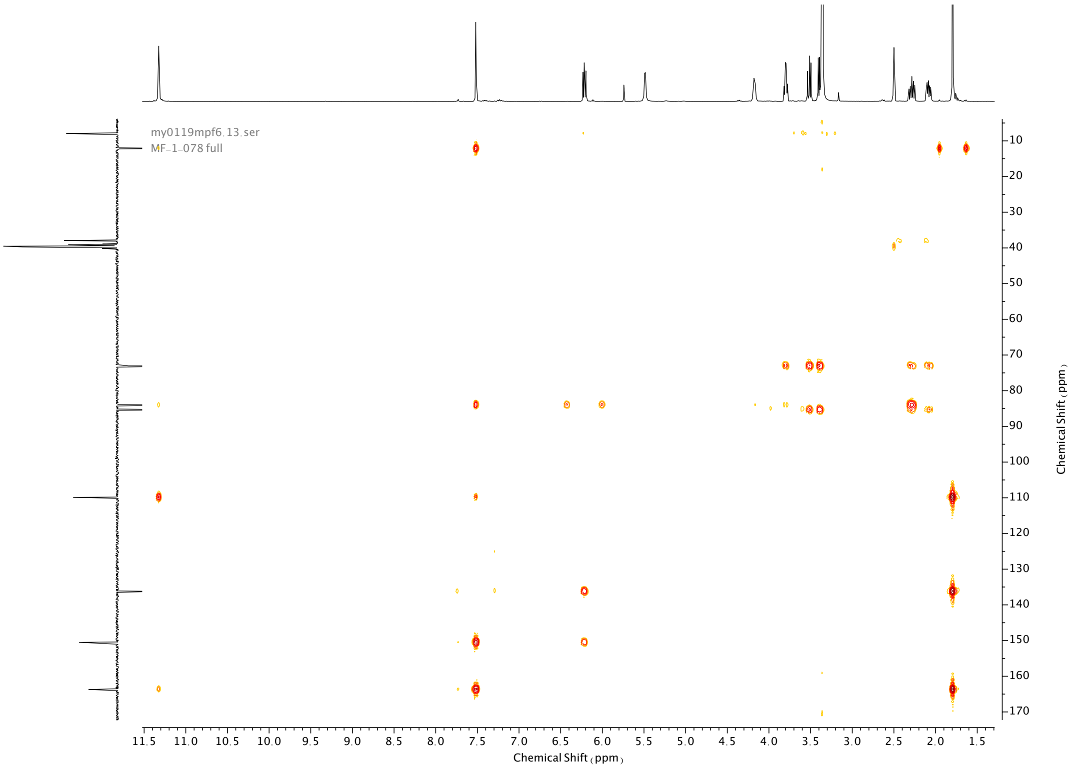

Figure **221**. HMBC NMR (DMSO-d$_6$) of **73**.

Compound **75**

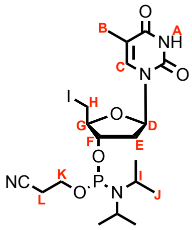

73 (201 mg, 0.57 mmol, 1.0 eq.) was charged to a pre-dried round-bottom flask, flushed with N_2, then anhydrous CH_2Cl_2 (7 mL) and DIPEA (0.4 mL, 2.27 mmol, 4.0 eq.) were added. 2-Cyanoethyl N,N-diisopropylchlorophosphoramidite (0.15 mL, 0.68 mmol, 1.2 eq.) was added over 10 min at 0 °C then allowed to reach room temperature and stirred for a further 2.5 h. The mixture was diluted with CH_2Cl_2 (25 mL) then washed with $NaHCO_3$ (20 mL) and brine (20 mL). The combined aqueous washings were extracted with CH_2Cl_2 (3 x 20 mL). Combined organic extracts were dried over anhydrous Na_2SO_4, filtered, and concentrated *in vacuo*. The crude product was purified *via* silica-gel chromatography using a Biotage Isolute SPE column (eluent 4:1 → 5:2 petrol: EtOAc, silica deactivated) to afford **75**, a mixture of diastereoisomers (d.r 7:3), as a white foam (188 mg, 0.34 mmol, 60 %). ^{1}H NMR (400 MHz, $CDCl_3$, 298 K) δ_H 9.52 (1H, br. s, N-H_A), 7.43 (1H, s, H_C), 7.38 (1H, s, H_c), 6.29-6.21 (2H, m, H_D & H_d), 4.39-4.30 (2H, m, H_F & H_f), 3.87-3.77 (5H, m, H_G, H_g, H_H, H_I & H_i), 3.75-3.64 (2H, m, H_I’, H_i’), 3.60-3.50 (4H, m, H_L, H_l), 3.46 (1H, dd, *J* = 4.1, 1.8 Hz, H_H’), 3.45-3.31 (2H, m, H_h & H_h’), 2.64-2.52 (4H, m, H_J & H_j’), 2.45 (1H, ddd, *J* = 14.1, 6.3, 3.4 Hz, H_e), 2.37 (1H, ddd, *J* = 14.0, 6.3, 3.4 Hz, H_E), 2.31-2.15 (2H, m, H_E’ & H_e’), 1.87 (3H, s, H_B, H_b), 1.16-1.10 (24H, m, H_K & H_k’).[6] ^{13}C NMR (101 MHz, $CDCl_3$, 298 K) δ_C 164.0 (x2), 150.5, 150.4, 136.0, 135.9, 135.7, 135.6, 117.7, 117.7, 111.5, 111.4, 84.6, 84.5 (d, *J* = 3.4 Hz), 83.3 (d, *J* = 3.4 Hz), 76.4 (d, *J* = 16.4 Hz), 76.2 (d, *J* = 16.5 Hz), 58.3 (d, *J* = 18.9 Hz), 58.1 (d, *J* = 19.5 Hz), 43.4 (d, *J* = 12.4 Hz), 43.4 (d, *J* = 12.3 Hz), 39.2 (d, *J* = 4.5 Hz), 39.1 (d, *J* = 3.0 Hz), 24.6 (d, *J* = 7.1 Hz), 24.5 (d, *J* = 7.5 Hz), 20.5 (x2), 12.6 (x2). ^{31}P NMR (162 MHz, $CDCl_3$, 298 K) δ_P 149.1, 149.0.

---

[6] The ^{1}H NMR spectra shows the diastereoisomers in approximately a 7:3 mixture. The ^{1}H characterization figures above denote each diastereoisomer (**X** and **x**) in a 1:1 ratio for simplicity.

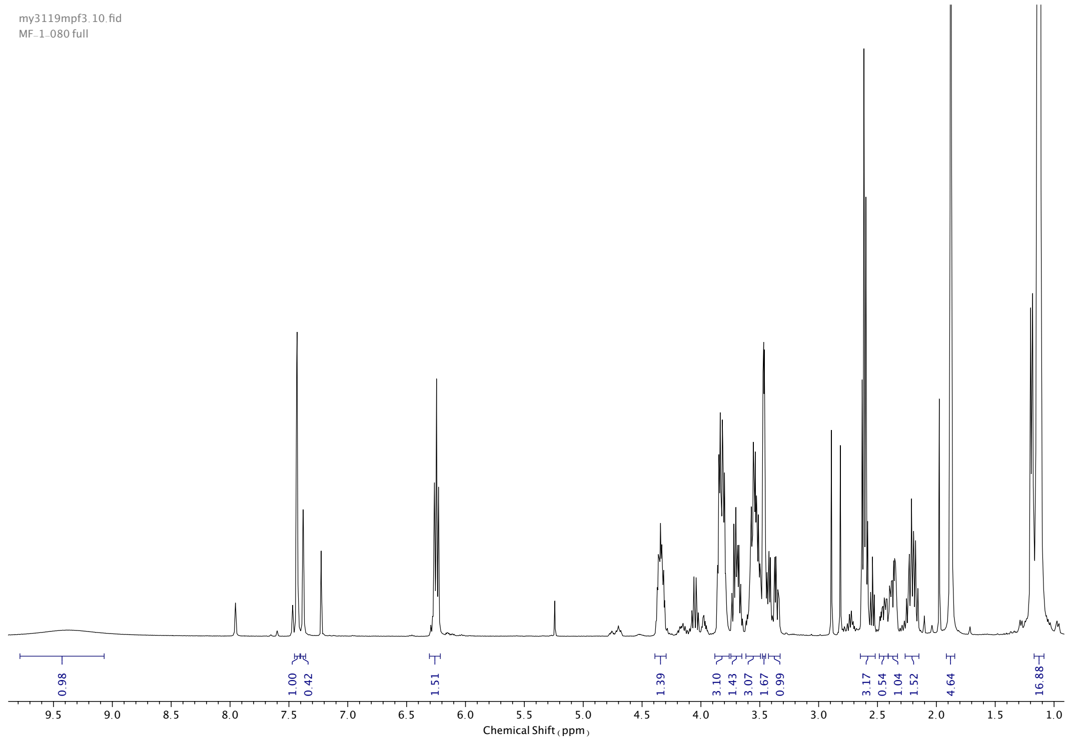

Figure **222**. ^{1}H NMR (CDCl$_3$, 400 MHz) of **75**.

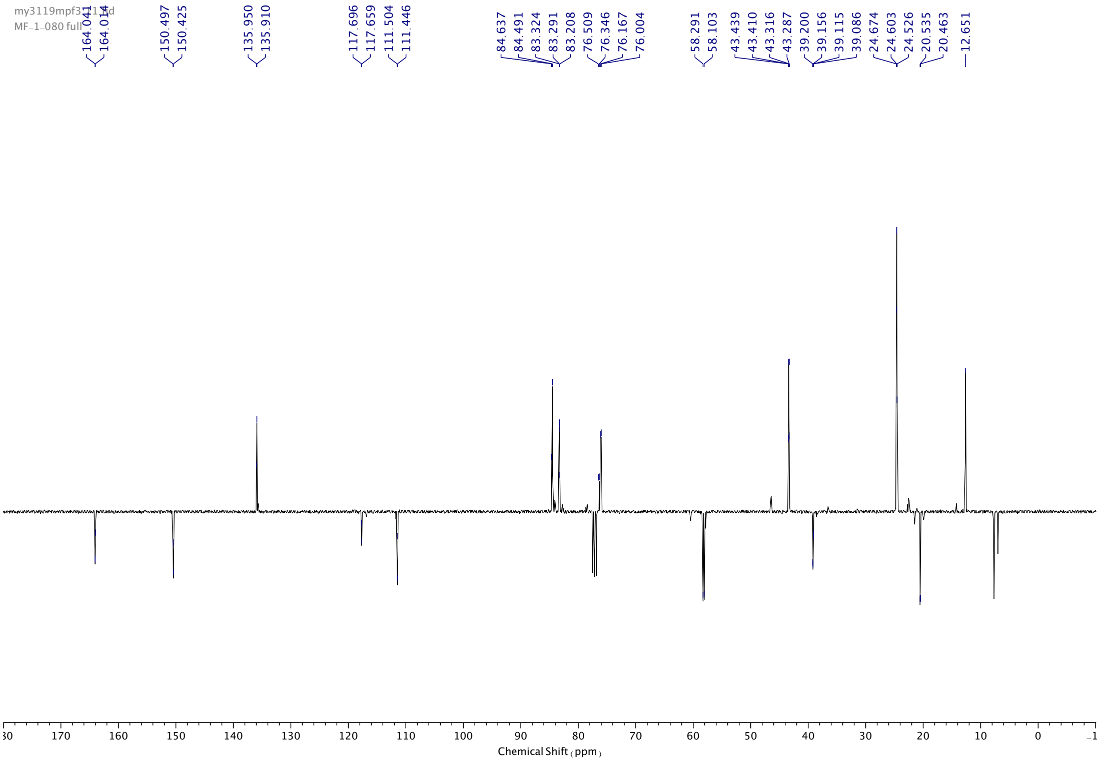

Figure **223**. ^{13}C NMR (CDCl$_3$, 101 MHz) of **75**.

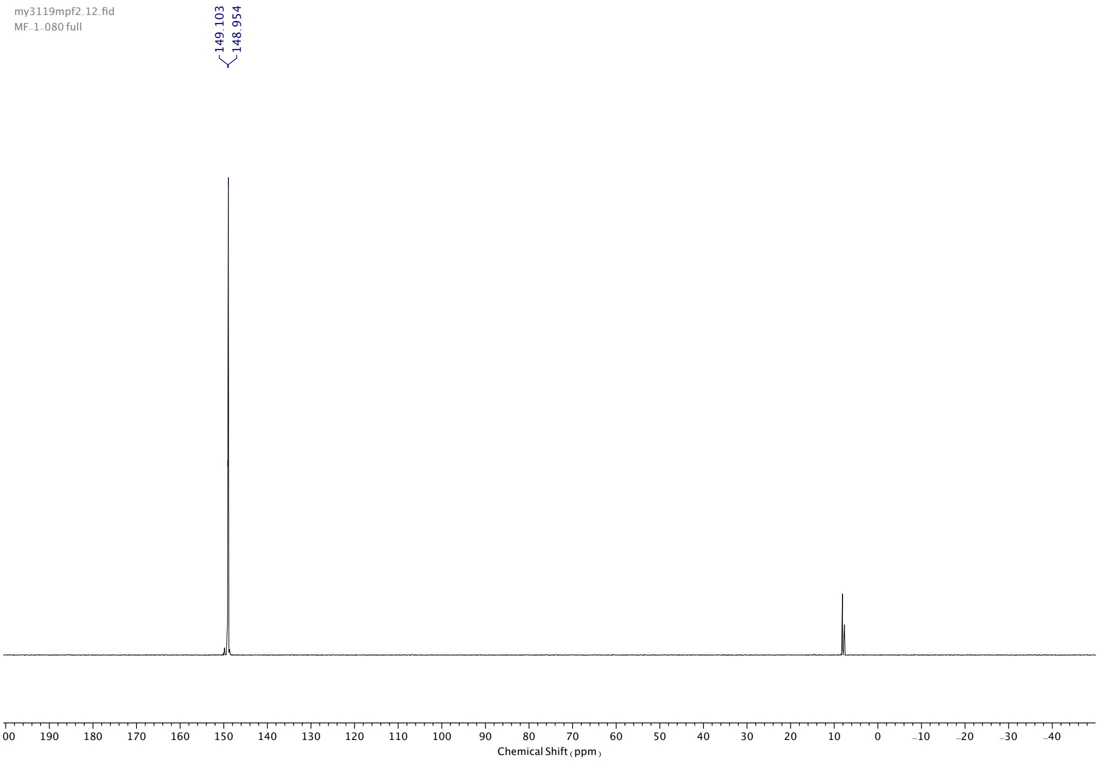

Figure **224**. ^{31}P NMR (162 MHz, $CDCl_3$, 298 K) of **75**.

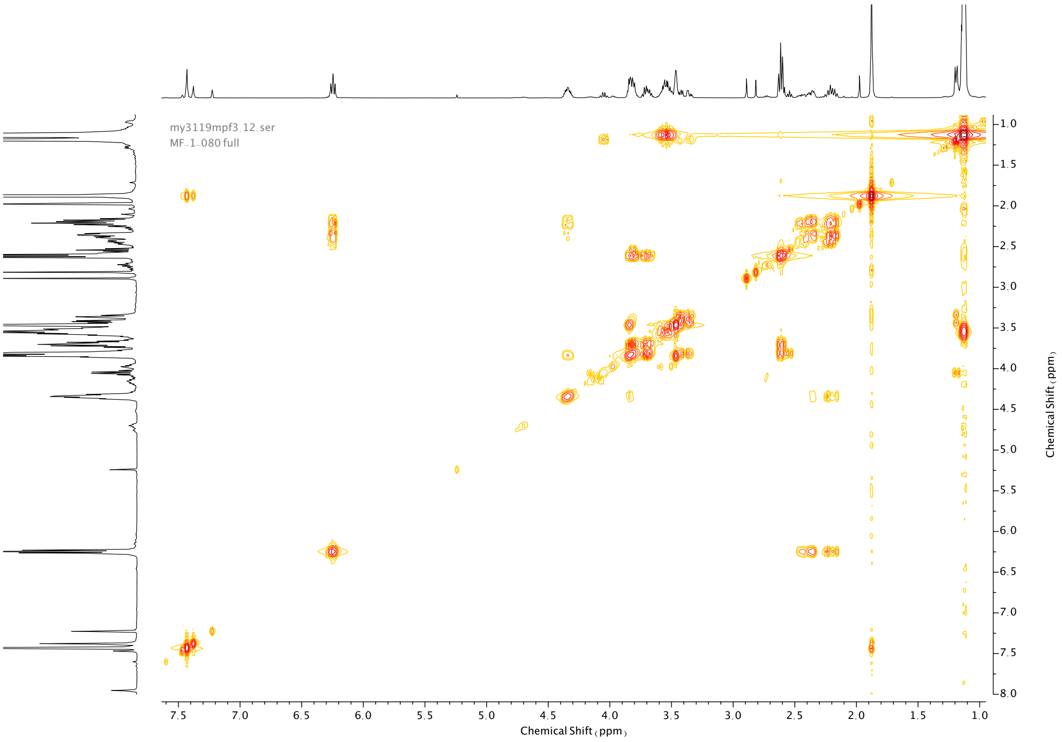

Figure **225**. COSY NMR ($CDCl_3$) of **75**.

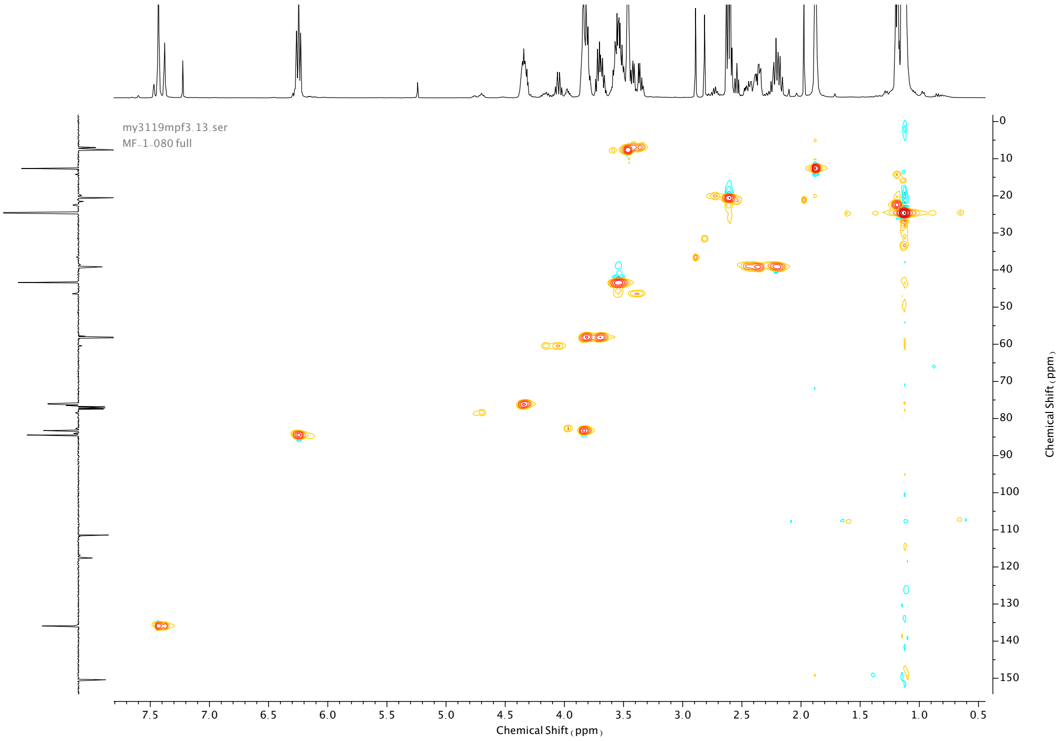

Figure **226**. HSQC NMR (CDCl$_3$) of **75**.

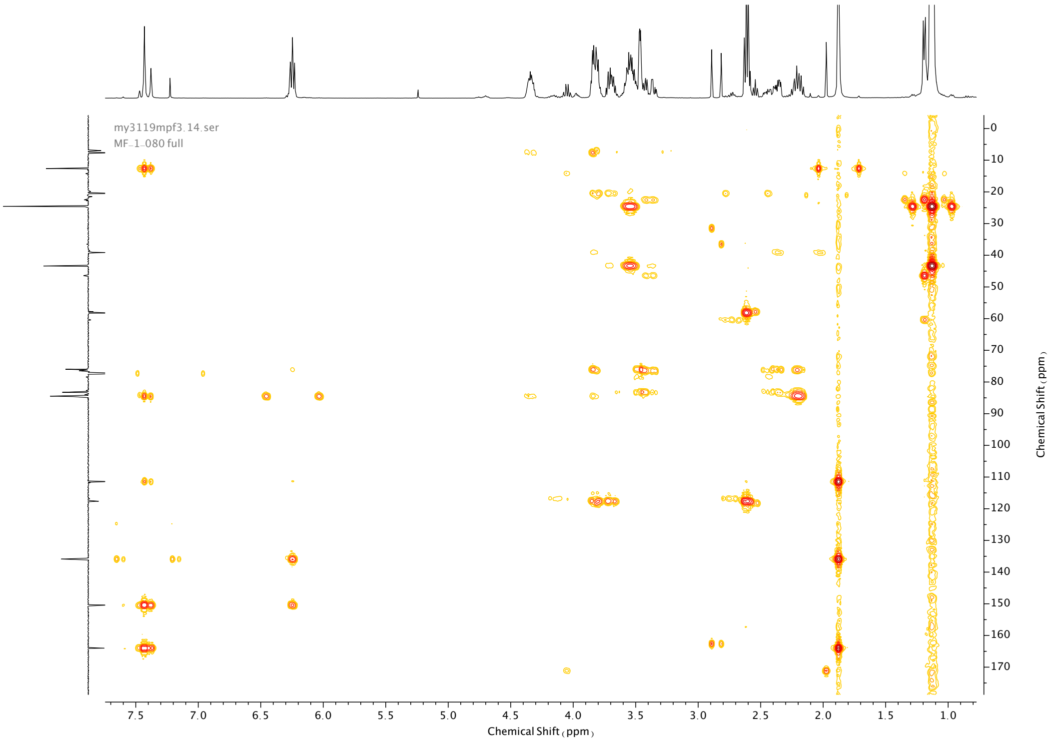

Figure **227**. HMBC NMR (CDCl$_3$) of **75**.

Compound **76**

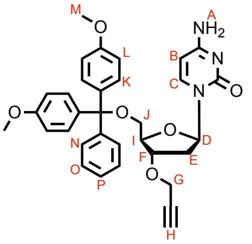

67 (1.0 g, 1.75 mmol, 1.0 eq.) was charged to a pre-dried round-bottom flask and degassed under N_2. Sodium hydride (0.19 g, 8.05 mmol, 4.6 eq.) was added followed by anhydrous THF (10 mL). **68** (0.5 mL, 4.38 mmol, 2.5 eq.) was added to the mixture over 10 min at -10 °C. The mixture was then allowed to reach room temperature and stirred for 30 min. MeOH (40 mL) was added and the mixture stirred at room temperature for a further 30 min. The mixture was then concentrated *in vacuo* and the crude residue taken up in CH_2Cl_2 (100 mL), washed with H_2O (100 mL) and brine (100 mL), then dried over anhydrous $MgSO_4$, filtered, and concentrated *in vacuo*. The crude product was purified *via* silica-gel chromatography using a Biotage Isolute SPE column (eluent 49:1 → 19:1 CH_2Cl_2: MeOH, silica deactivated), to afford **76** as an off-white foam (560 mg, 0.98 mmol, 55%). ^{1}H NMR (400 MHz, $CDCl_3$, 298 K) δ_H 7.90 (1H, d, *J* = 7.5 Hz, H_C), 7.42-7.39 (2H, m, $H_{N,}$ H_O), 7.32-7.27 (6H, m, $H_{L,}$ $H_{K,}$ H_N & H_O), 7.25-7.20 (1H, m, H_P), 6.84 (4H, d, *J* = 9.0 Hz, $H_{L,}$ H_K), 6.22 (1H, t, *J* = 6.0 Hz, H_D), 5.49 (1H, d, *J* = 7.4 Hz, H_B), 4.45 (1H, dt, *J* = 6.4, 4.4 Hz, H_F), 4.20-4.06 (3H, m, H_I & $H_{G,}$ or H_G’), 4.09 (1H, dd, *J* = 16.0, 2.5 Hz, H_G or H_G’), 3.79 (6H, s, H_M), 3.45 (1H, dd, *J* = 10.7, 3.3 Hz, H_J or H_J’), 3.38 (1H, dd, *J* = 10.7, 3.3 Hz, H_J or H_J’), 2.61 (1H, ddd, *J* = 13.8, 6.2, 4.4 Hz, H_E or H_E’), 2.39 (1H, t, *J* = 2.4 Hz, H_H), 2.18 (dt, 1H, *J* = 13.6, 6.4 Hz, H_E or H_E’). ^{13}C NMR (101 MHz, $CDCl_3$, 298 K) δ_C 165.4, 158.8, 155.7, 144.6, 141.5, 135.7, 135.6, 130.2, 128.3, 128.1, 127.2, 113.4, 94.1, 86.7, 86.4, 84.0, 77.3, 75.2, 62.7, 56.9, 55.4, 38.7.

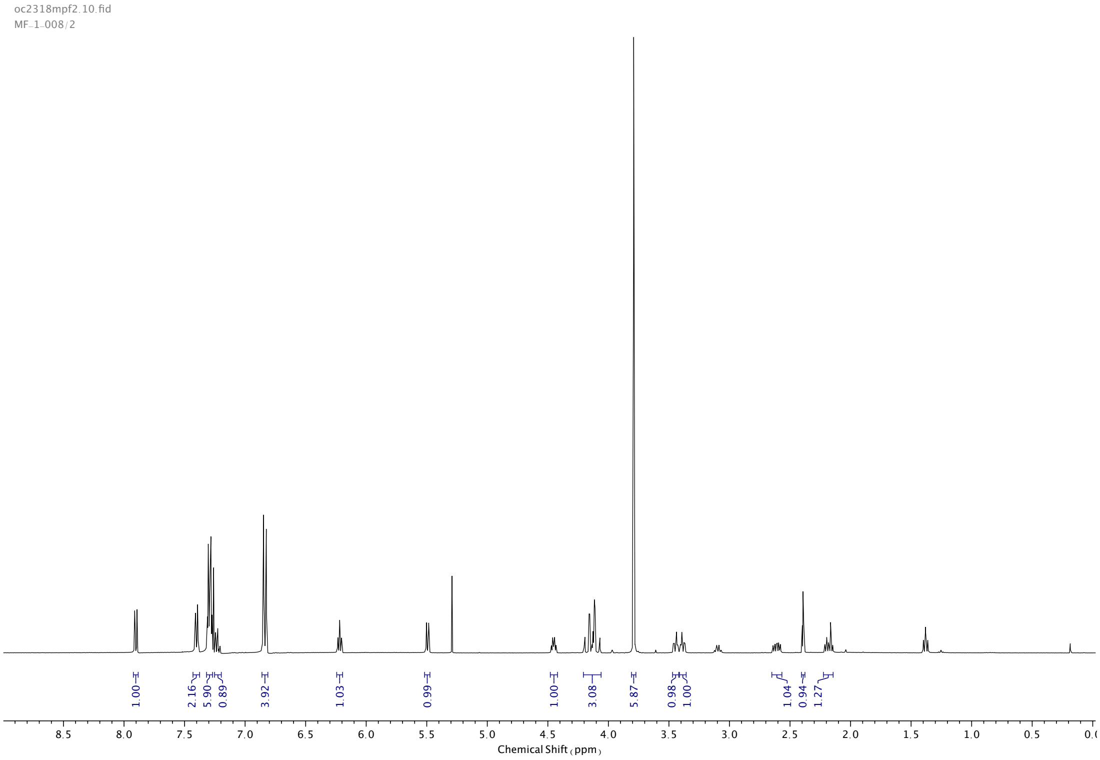

Figure **228**. ^{1}H NMR (CDCl$_3$, 400 MHz) of **76**.

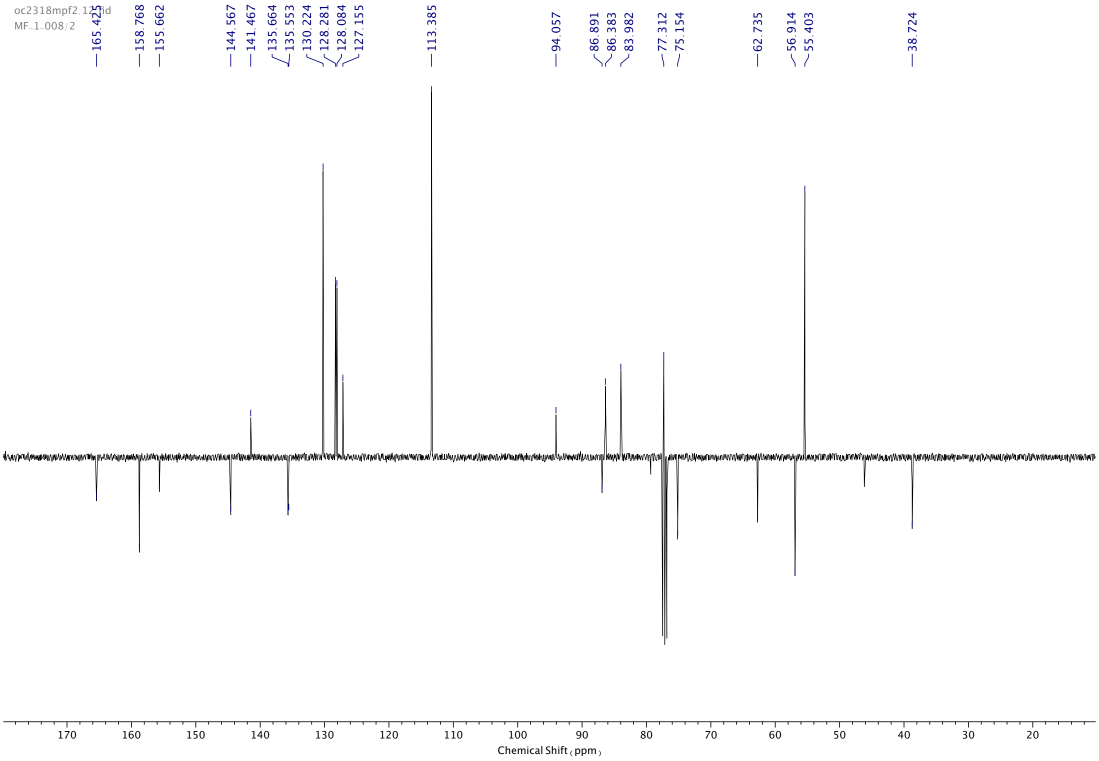

Figure **229**. ^{13}C NMR (CDCl$_3$, 101 MHz) of **76.**

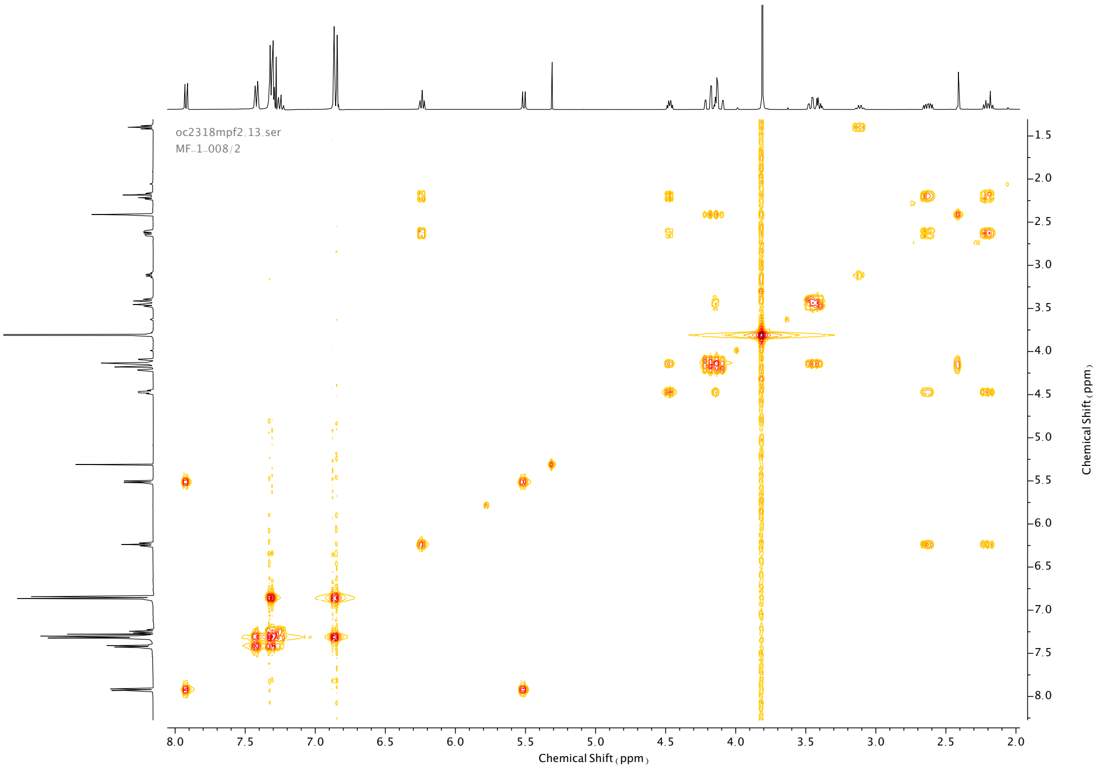

Figure **230**. COSY NMR ($CDCl_3$) of **76**.

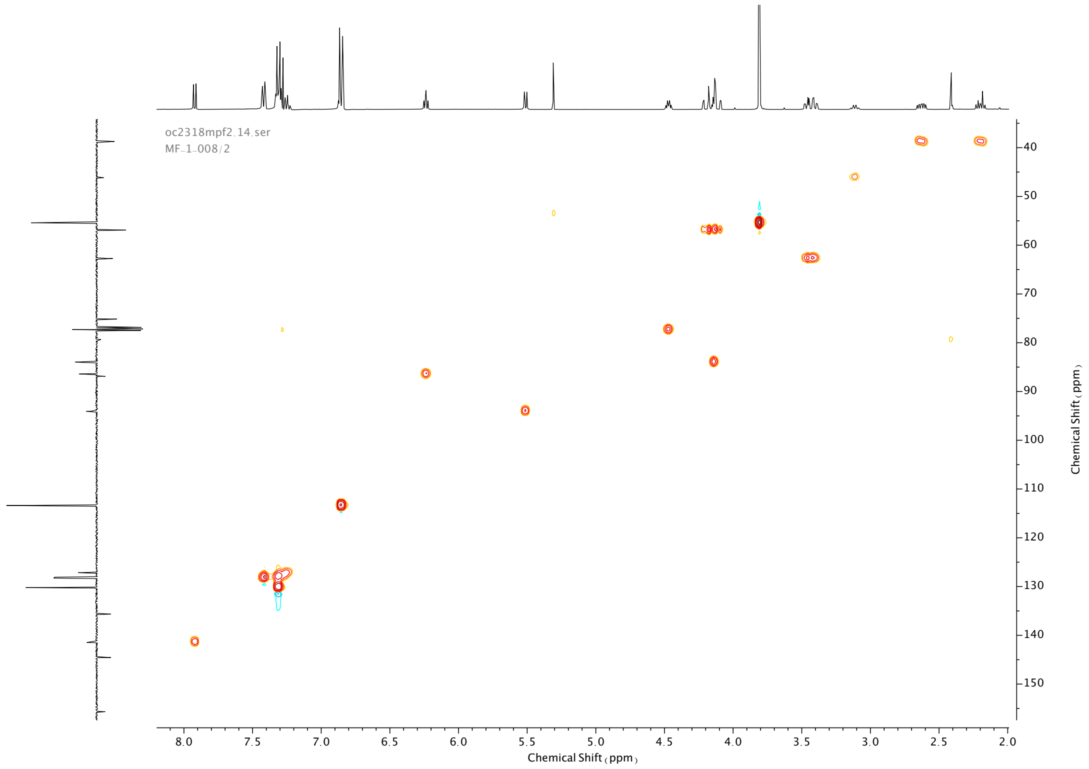

Figure **231**. HSQC NMR ($CDCl_3$) of **76**.

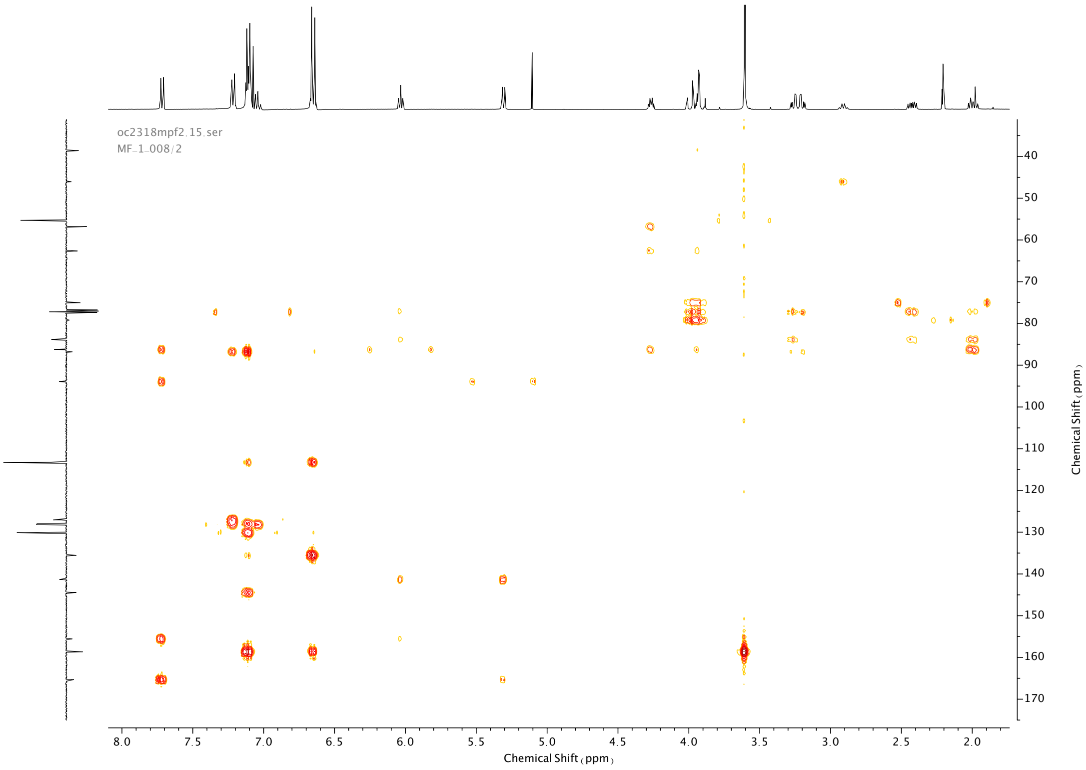

Figure **232**. HMBC NMR ($CDCl_3$) of **76**.

Compound **77**

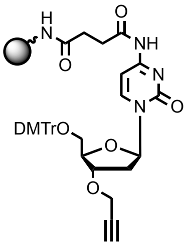

Using a previously published protocol,[134] amino-SynBase™ CPG resin (2 g, 69 µmol/g free amine) was activated with 3% trichloroacetic acid (TCA) in CH_2Cl_2 for 3 h. The solvents were then removed by filtration and the support washed with NEt_3: DIPEA (9:1), CH_2Cl_2 and Et_2O. The solid support was then dried under vacuum for 1 h then soaked in anhydrous pyridine for 5 min. A solution of succinic anhydride (400 mg, 4.0 mmol) and 4-DMAP (80 mg, 0.64 mmol) in anhydrous pyridine (12 mL) was added and the mixture rocked on an orbital shaker overnight at room temperature. The support was then washed with pyridine, CH_2Cl_2 and Et_2O, then dried and soaked in pyridine for 10 min. Diisopropyl carbodiimide (DIC) (280 µL, 1.80 mmol), HOBT (280 mg, 2.08 mmol) and propargyl cytidine **76** (272 mg, 0.48 mmol) were dissolved in anhydrous pyridine (4 mL) and added to the solid support which was rocked overnight on an orbital shaker at room temperature. Pentachlorophenol (136 mg, 0.52 mmol) was added and mixed for a further 2 h. The solvents were removed by filtration and the support was washed with CH_2Cl_2 and Et_2O. Piperidine (10% in DMF, 12 mL) was then added and mixed for 5 min, then the solid support was washed with CH_2Cl_2 and Et_2O. Capping reagent (oligonucleotide synthesis grade, acetic anhydride/pyridine/tetrahydrofuran: N-methyl imidazole in THF, 1:1, 12 mL) was added and the vessel was rotated for 1 h. The support was then washed with pyridine, CH_2Cl_2 and Et_2O then left to dry under vacuum overnight. Loading of the resulting resin **77** was determined to be 22.7 µmol/g (33% coupling efficiency) by measuring the absorbance of the cleaved DMT cation at 495 nm.

2.4.3. Oligonucleotide Synthesis Procedures

Synthesis of oligonucleotides was carried out by ATDBio. An Applied Biosystems 394 automated DNA/RNA synthesizer was used, adopting a standard phosphoramidite cycle (1.0 µmole) of acid-catalyzed detritylation, coupling, capping, and iodine oxidation. Coupling efficiencies and yields were determined by automated trityl cation conductivity measurement (>98.0%). β-cyanoethyl phosphoramidite monomers were dissolved in dry CH_3CN (0.1 M). The coupling time for standard DNA monomers and modified monomers was 40 s and 10 min respectively.

Oligonucleotide alkyne synthesis

For the synthesis of the 3'-alkyne modified oligonucleotide (**78**), functionalized resin **77** (35 mg) was packed onto a twist column (Glen Research). Once solid-phase synthesis was complete, deprotection and simultaneous cleavage of the oligonucleotide from the solid-support was achieved by exposure to aqueous ammonia in a sealed tube for 1 h at room temperature, then 5 h at 55 °C. For oligonucleotides that possessed a 5'-phosphate group, Chemical Phosphorylation Reagent (Link Technologies) was coupled to them on the solid-support prior to deprotection and cleavage. Product was then purified *via* HPLC. Combined product fractions were frozen at -80 °C and lyophilized overnight. The lyophilized solid was made up to 1 mL in DI H_2O (typically 180-220 µM) and analysed *via* LC-MS (Figure **233**).

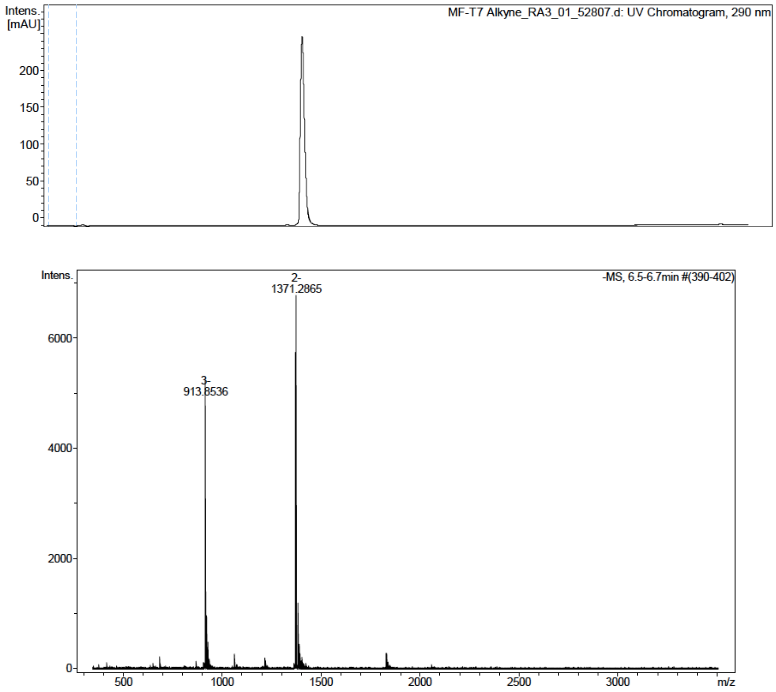

Figure **233**. LC-MS data for oligonucleotide alkyne **78**. UV (top) and MS (bottom). Calculated m/z = 2743.53, found = 2742.57.

Oligonucleotide azide synthesis

Oligonucleotides that possessed a terminal azide were synthesized up to the penultimate monomer at which point 5'-iodo-2'-deoxthymidine-3'-phosphoramidite **75** was coupled as the last monomer. To convert the 5'-iodo group to the azide, sodium azide (50 mg) was suspended in DMF (1 mL) then heated at 70 °C for 20 min. The supernatant was passed back and forth through the twist column using two 1 mL syringes. The column was heated at 55 ºC for 5 h then DMF (2 x 5 mL) and CH_3CN (3 x 10 mL) were passed through the column to wash away excess sodium azide. The solid-support was dried by passing argon gas through the column and the oligonucleotide was deprotected, cleaved from the solid-support as described above and purified *via* HPLC. Combined product fractions were frozen at -80 °C and lyophilized overnight. The lyophilized solid was made up to 1 mL in DI H_2O (typically 180-220 µM) and analysed *via* LC-MS (Figure **234**).

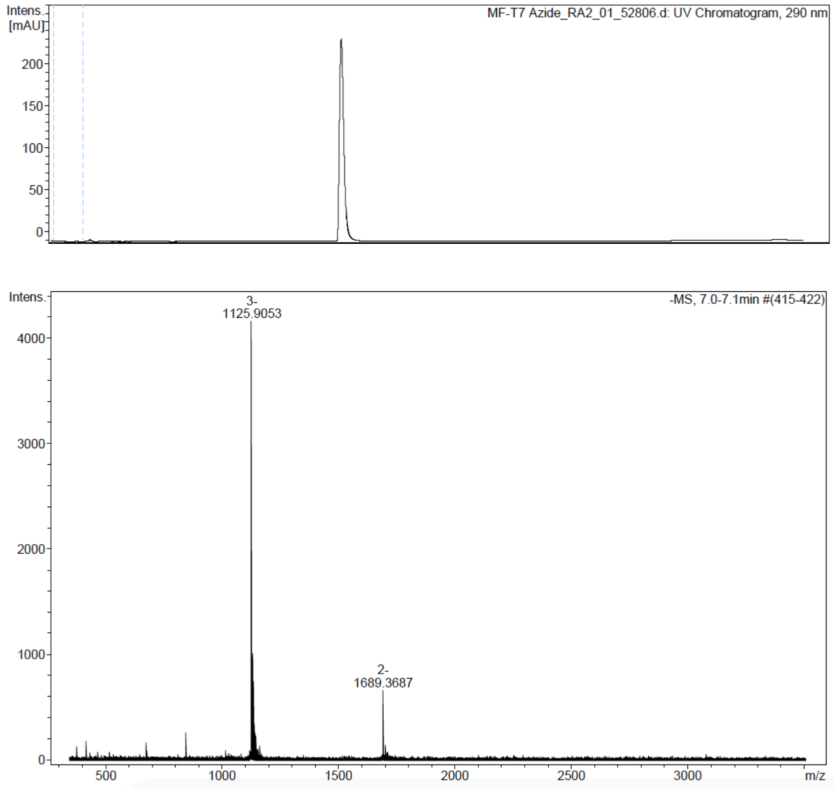

Figure **234**. LC-MS data for oligonucleotide azide **79**. UV (top) and MS (bottom). Calculated m/z = 3379.61, found = 3378.73.

Synthesis of Oligonucleotide Axle

Oligonucleotide alkyne **78** (20 nmol, stock solution in 0.1 M TEAB) and oligonucleotide azide **79** (20 nmol, stock solution in 0.1 M TEAB) were added to a 1 mL screw cap vial. Accounting for the addition of NaAsc, $CuSO_4$ and THPTA, the final reaction volume was 480 μL. ^{t}BuOH (240 μL) and the required volume DI H_2O (typically between 40-80 μL) were then added to the oligonucleotide mixture. In a separate vial, $CuSO_4$ (39 μL of 20 mM stock solution, 780 nmol, 39 eq.), NaAsc (50 μL of 100 mM stock solution, 5000 nmol, 250 eq.) and THPTA (35 μL of 100 mM stock solution, 3500 nmol, 175 eq.) were combined and then transferred to the oligonucleotide solution. The combined mixture was shaken overnight at room temperature on an orbital shaker. An aliquot (10 μL) was taken from the crude reaction mixture, diluted with DI H_2O (10 μL) and analysed *via* LC-MS to confirm the success of the reaction. The reaction mixture was then diluted to a total volume of 1 mL with DI H_2O (530 μL) and passed through a NAP-10 to remove excess salts. The eluent was frozen at -80 °C and lyophilized overnight. The lyophilized solid was resuspended in DI H_2O (120 μL) and purified *via* HPLC. The product fractions were combined, frozen at -80 °C and lyophilized overnight. The purified sample was made up to an appropriate concentration in DI H_2O (≈ 10 mM) and analysed *via* LC-MS (Figure **235**).

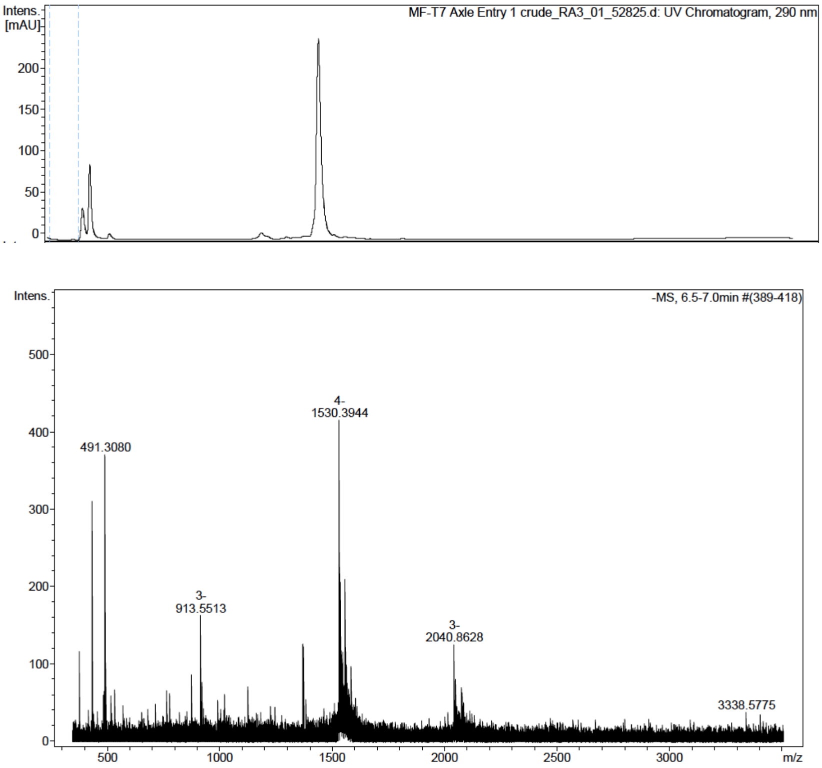

Figure **235**. LC-MS data for oligonucleotide axle **80**. UV (top) and MS (bottom). Calculated m/z = 6125.15, found = 6122.59.

Synthesis of Oligonucleotide Rotaxanes

Three separate solutions were prepared in 1 mL plastic screw cap vials. In vial 1, oligonucleotide azide **79** (20 nmol from stock solution, 1.0 eq.) and oligonucleotide alkyne **78** (22 nmol from stock solution, 1.1 eq.) were combined. In vial 2, macrocycle **13** or **25** (420 nmol, 42 μL from 10 mM solution, 21 eq.) and the remaining amount of organic co-solvent required were added. In vial 3, $CuSO_4$ (200 nmol, 10 μL from 20 mM solution, 10 eq.), NaAsc (1000 nmol, 10 μL from 100 mM solution, 50 eq.) and the remaining quantity of DI H_2O was added. The solution in vial 2 was added to vial 3, followed by the solution in 1 to vial 3. DIPEA (3.4 μL neat, 975 eq.) was then added and the mixture was shaken overnight at room temperature on an orbital shaker. Organic solvent (THF or CH_3CN) was removed under a stream of N_2 gas. An aliquot (10 μL) was then taken from the reaction mixture, diluted with DI H_2O (10 μL) and the success of the reaction was judged *via* LC-MS. EDTA (120 μL of 0.1 M) was added to the crude mixture to sequester metal cations. An aliquot (10 μL) was taken from the demetallated mixture, diluted with DI H_2O (10 μL) analysed *via* LC-MS. The sample was frozen at -80 °C and lyophilized overnight. The lyophilized solid was resuspended in DI H_2O (120 μL) and purified *via* HPLC (rotaxane **14a**). The product fractions were combined, frozen at -80 °C and lyophilized overnight. The purified sample was made up to an appropriate concentration in DI H_2O (≈ 10 mM) and analysed *via* LC-MS.

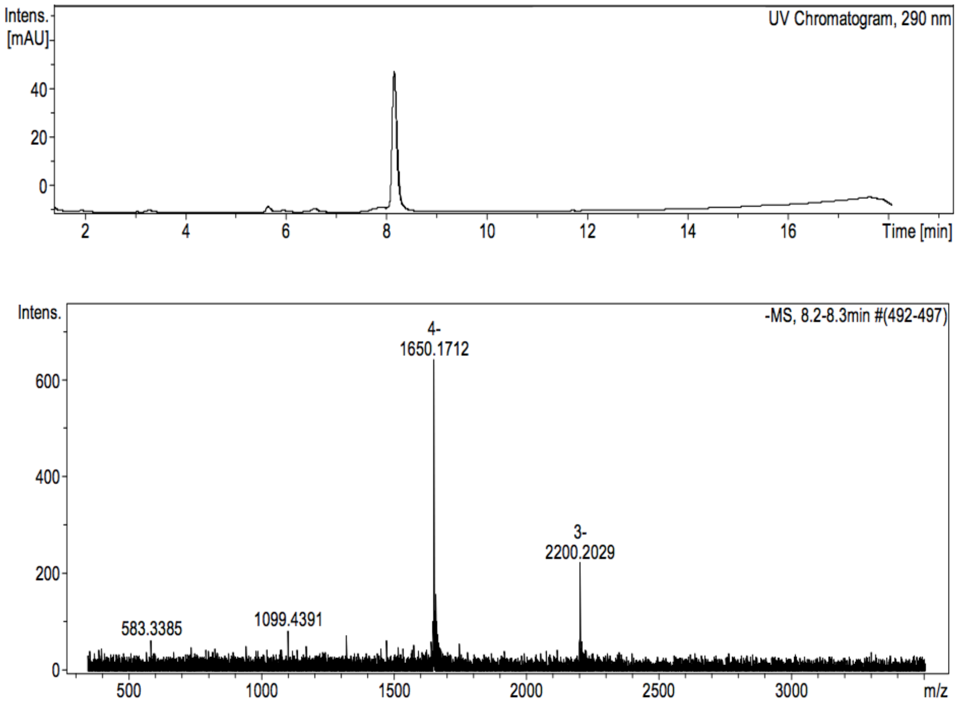

Figure **236**. LC-MS data for oligonucleotide rotaxane **14a**. UV (top) and MS (bottom). Calculated m/z = 6604.3, found = 6600.6.

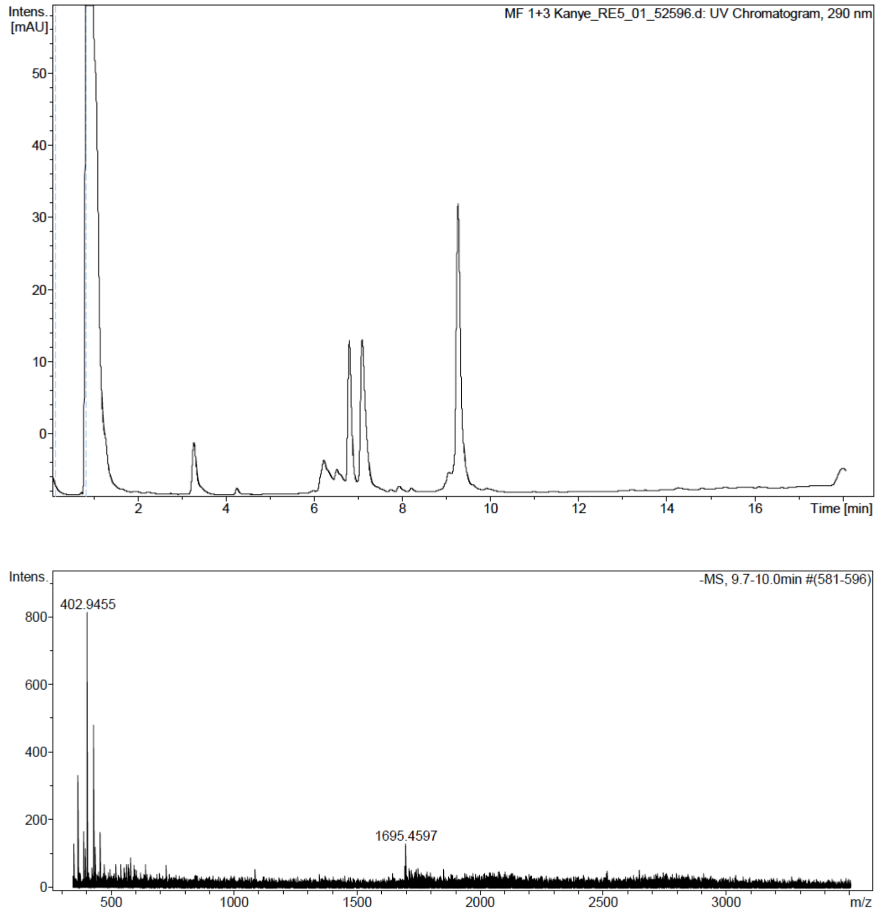

Figure **237**. LC-MS data for oligonucleotide rotaxane **81** (not isolated). UV (top) and MS (bottom). Calculated m/z = 6723.1, found = 6781.8.

2.4.4. Single Crystal X-Ray Data

Single crystals of the **25**-$NiCl_2$ complex were grown *via* vapour diffusion of Et_2O into a saturated solution of the compound in CH_2Cl_2 at room temperature. Data for **25**-$NiCl_2$ was collected on a Rigaku 007 HF diffractometer equipped with a Saturn 944+ enhanced sensitivity detector. The crystal was kept at 100 K during data collection. Using Olex2,[135] the structure of **25**-$NiCl_2$ was solved with the ShelXT[136] structure solution program using intrinsic phasing and refined with the ShelXL[137] refinement package using Least Squares minimisation.

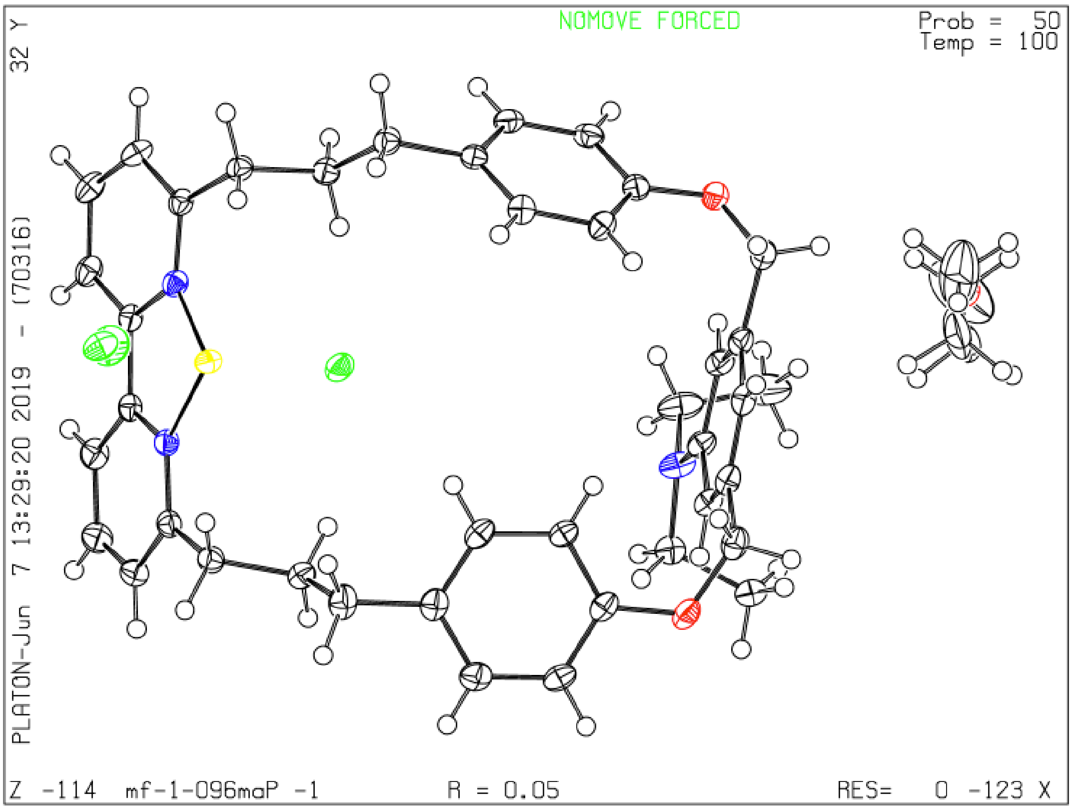

Figure **238**. Ellipsoid plot of **25**-$NiCl_2$ (ellipsoids shown at 50% probability).

Table **1**. Crystal data and structure refinement for **25**-$NiCl_2$.

Compound	**25**-$NiCl_2$
Empirical formula	$C_6H_6Br_{0.12}Cl_{0.12}Cu_{0.12}NNiO_6$
Formula weight	727.40
Temperature/K	100.01(11)
Crystal system	triclinic
Space group	P-1
a/Å	12.7297(4)
b/Å	12.9025(3)
c/Å	13.8853(5)
α/°	69.353(3)
β/°	78.331(3)
γ/°	75.689(2)
Volume/$Å^3$	2051.16(12)
Z	8
$\rho_{calc}g/cm^3$	1.743
μ/mm^{-1}	2.668
F(000)	1081.0
Crystal size/mm^3	0.15 × 0.1 × 0.06
Radiation	MoKα (λ = 0.71073)
2Θ range for data collection/°	5.748 to 62.658
Index ranges	$-17 \leq h \leq 17, -18 \leq k \leq 18, -19 \leq l \leq 19$
Reflections collected	55822
Independent reflections	12319 [R_{int} = 0.0447, R_{sigma} = 0.0428]
Data/restraints/parameters	12319/0/494
Goodness-of-fit on F^2	0.799
Final R indexes [$I>=2\sigma(I)$]	$R_1 = 0.0530$, $wR_2 = 0.1310$
Final R indexes [all data]	$R_1 = 0.0666$, $wR_2 = 0.1416$
Largest diff. peak/hole / e $Å^{-3}$	0.65/-0.48

Single crystals of **43** were grown *via* the slow evaporation of an MeOD solution of the compound. Data for **43** was collected on a Kat diffractometer. The crystal was kept at 100 K during data collection. Using Olex2, the structure of **43**. Using Olex2,[135] the structure of **25**-$NiCl_2$ was solved with the ShelXT[136] structure solution program using intrinsic phasing and refined with the ShelXL[137] refinement package using Least Squares minimisation.

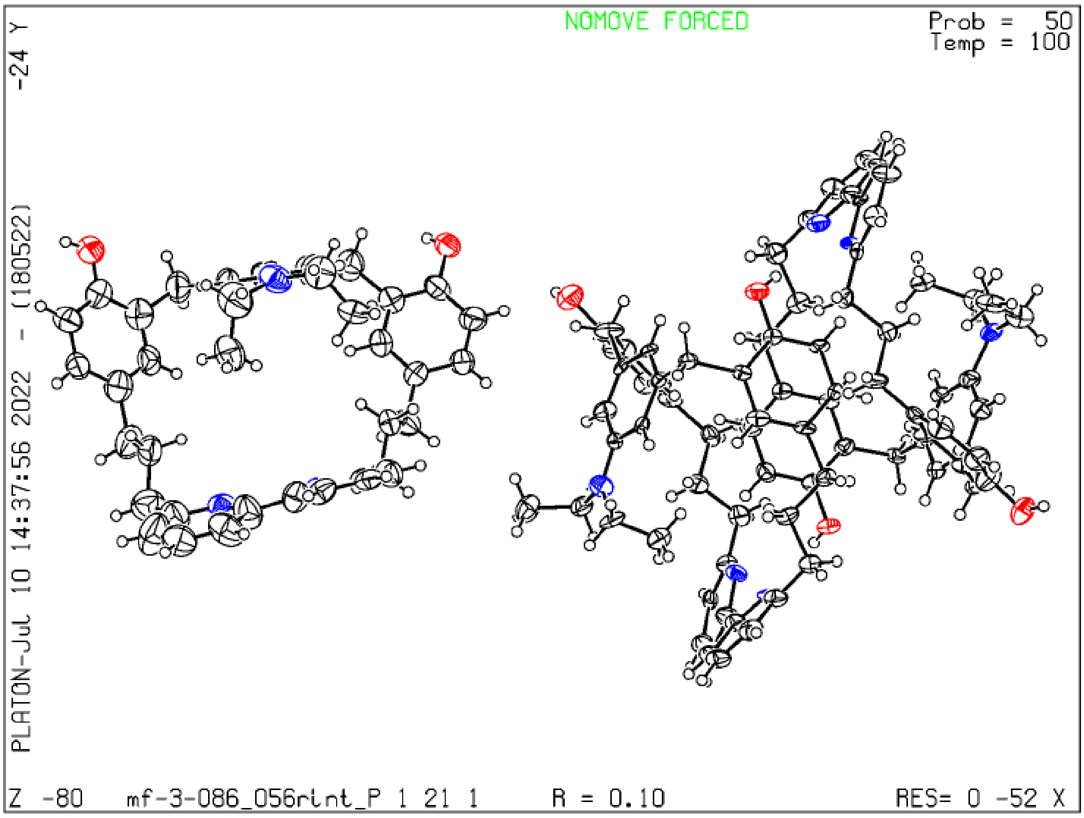

Figure **239**. Ellipsoid plot of **43** (ellipsoids shown at 50% probability).

Table **2**. Crystal data and structure refinement for **43**.

Compound	**43**
Empirical formula	$C_{40}H_{43}N_3O_2$
Formula weight	597.77
Temperature/K	100.01
Crystal system	monoclinic
Space group	$P2_1$
a/Å	21.3984(13)
b/Å	10.0496(5)
c/Å	30.098(3)
α/°	90
β/°	101.384(8)
γ/°	90
Volume/Å^3	6345.1(8)
Z	6
ρ_{calc} g/cm^3	0.939
μ/mm^{-1}	0.058
F(000)	1920.0
Crystal size/mm^3	0.1 × 0.1 × 0.05
Radiation	MoKα (λ = 0.71073)
2Θ range for data collection/°	5.716 to 46.51
Reflections collected	48445
Independent reflections	15882 [R_{int} = 0.2269, R_{sigma} = 0.3020]
Data/restraints/parameters	15882/1072/1048
Goodness-of-fit on F^2	0.936
Final R indexes [I>=2σ (I)]	R_1 = 0.1010
Final R indexes [all data]	wR_2 = 0.2417
Largest diff. peak/hole / e Å^{-3}	0.296/-0.268

2.5. Bibliography

[1] G. Mayer, A. Heckel, *Angew. Chemie Int. Ed.* **2006**, 45, 4900–4921.

[2] H. Yu, J. Li, D. Wu, Z. Qiu, Y. Zhang, *Chem. Soc. Rev*. **2010**, 39, 464-473.

[3] C. Brieke, F. Rohrbach, A. Gottschalk, G. Mayer, A. Heckel, *Angew. Chemie Int. Ed.* **2012**, 51, 8446–8476.

[4] S. T. Hess, T. P. K. Girirajan, M. D. Mason, *Biophys. J.* **2006**, 91, 4258–4272.

[5] H. Shroff, C. G. Galbraith, J. A. Galbraith, E. Betzig, *Nat. Methods* **2008**, 5, 417–423.

[6] J. A. Barltrop, P. J. Plant, P. Schofield, *Chem. Commun.* **1966**, 822–823.

[7] J. H. Kaplan, B. Forbush, J.F. Hoffman, *Biochemistry* **1978**, 17, 1920–1935.

[8] T. Courtney, A. Deiters, *Curr. Opin. Chem. Biol.* **2018**, 46, 99–107.

[9] Q. Liu, A. Deiters, Acc. *Chem. Res.* **2014**, 47, 45–55.

[10] A. Bardhan, A. Deiters, *Curr. Opin. Struct. Biol.* **2019**, 57, 164–175.

[11] J. M. Silva, E. Silva, R. L. Reis, *J. Control. Release* **2019**, 298, 154–176.

[12] P. Klán, T. Šolomek, C. G. Bochet, A. Blanc, R. Givens, M. Rubina, V. Popik, A. Kostikov, J. Wirz, *Chem. Rev.* **2013**, 113, 119–191.

[13] A. P. Pelliccioli, J. Wirz, *Photochem. Photobiol. Sci.* **2002**, 1, 441–458.

[14] T. Šolomek, S. Mercier, T. Bally, C. G. Bochet, *Photochem. Photobiol. Sci.* **2012**, 11, 548–555.

[15] C. G. Bochet, *Tetrahedron Lett.* **2000**, 41, 6341–6346.

[16] A. M. Piloto, S. P. G. Costa, M. S. T. Gonçalves, *Tetrahedron* **2014**, 70, 650–657.

[17] C. G. Bochet, *Angew. Chem. Int. Ed.* **2001**, 40, 2071-2073.

[18] V. San Miguel, C. G. Bochet, A. Del Campo, *J. Am. Chem. Soc.* **2011**, 133, 5380–5388.

[19] S. Bühler, I. Lagoja, H. Giegrich, K. P. Stengele, W. Pfleiderer, *Helv. Chim. Acta* **2004**, 87, 620–659.

[20] A. Hasan, K. P. Stengele, H. Giegrich, P. Cornwell, K. R. Isham, R. A. Sachleben, W. Pfleiderer, R. S. Foote, *Tetrahedron* **1997**, 53, 4247–4264.

[21] W. A. Velema, J. P. Van Der Berg, W. Szymanski, A. J. M. Driessen, B. L. Feringa, *ACS Chem. Biol.* **2014**, 9, 1969–1974.

[22] N. Kotzur, B. Briand, M. Beyermann, V. Hagen, *J. Am. Chem. Soc.* **2009**, 131, 16927–16931.

[23] M. A. Priestman, L. Sun, D. S. Lawrence, *ACS Chem. Biol.* **2011**, 6, 377–384.

[24] J. P. Olson, M. R. Banghart, B. L. Sabatini, G. C. R. Ellis-Davies, *J. Am. Chem. Soc.* **2013**, 135, 15948–15954.

[25] L. Fournier, C. Gauron, L. Xu, I. Aujard, T. Le Saux, N. Gagey-Eilstein, S. Maurin, S. Dubruille, J. B. Baudin, D. Bensimon, M. Volovitch, S. Vriz, L. Jullien, *ACS Chem. Biol.* **2013**, 8, 1528–1536.

[26] C. H. Bamford, R. G. W. Norrish, *J. Chem. Soc.* **1935**, 1504–1511.

[27] R. Weinstain, T. Slanina, D. Kand, P. Klán, *Chem. Rev.* **2020**, 120, 13135–13272.

[28] A. Z. Suzuki, T. Watanabe, M. Kawamoto, K. Nishiyama, H. Yamashita, M. Ishii, M. Iwamura, T. Furuta, *Org. Lett.* **2003**, 5, 4867–4870.

[29] G. Papageorgiou, D. C. Ogden, A. Barth, J. E. T. Corrie, *J. Am. Chem. Soc.* **1999**, 121, 6503–6504.

[30] R. S. Rock, K. C. Hansen, R. W. Larsen, S. I. Chan, *Chem. Phys.* **2004**, 307, 201–208.

[31] A. Jana, K. T. Nguyen, X. Li, P. Zhu, N. S. Tan, H. Ågren, Y. Zhao, *ACS Nano* **2014**, 8, 5939–5952.

[32] T. Joshi, V. Pierroz, C. Mari, L. Gemperle, S. Ferrari, G. Gasser, *Angew. Chemie Int. Ed.* **2014**, 126, 3004–3007.

[33] R. S. Givens, K. Stensrud, P. G. Conrad, A. L. Yousef, C. Perera, S. N. Senadheera, D. Heger, J. Wirz, *Can. J. Chem.* **2011**, 89, 364–384.

[34] R. S. Givens, M. Rubina, J. Wirz, *Photochem. Photobiol. Sci.* **2012**, 11, 472–488.

[35] T. Field, J. Peterson, C. Ma, P. Jagadesan, J. P. Da Silva, M. Rubina, V. Ramamurthy, R. S. Givens, *Photochem. Photobiol. Sci.* **2020**, 19, 1364–1372.

[36] P. G. Conrad, R. S. Givens, J. F. W. Weber, K. Kandler, *Org. Lett.* **2000**, 2, 1545–1547.

[37] H. Lu, Q. Zhou, J. He, Z. Jiang, C. Peng, R. Tong, J. Shi, *Signal Transduct. Target. Ther.* **2020**, 5, 1–23.

[38] J. C. Kaczmarek, P. S. Kowalski, D. G. Anderson, *Genome Med.* **2017**, 9, 60.

[39] C. Chakraborty, A. R. Sharma, G. Sharma, C. G. P. Doss, S. S. Lee, *Mol. Ther. Nucleic Acids* **2017**, 8, 132–143.

[40] K. B. Spurgers, C. M. Sharkey, K. L. Warfield, S. Bavari, *Antiviral Res.* **2008**, 78, 26–36.

[41] S. T. Crooke, X. H. Liang, B. F. Baker, R. M. Crooke, *J. Biol. Chem.* **2021**, 296, 100416–100417.

[42] T. A. Vickers, S. Koo, C. F. Bennett, S. T. Crooke, N. M. Dean, B. F. Baker, *J. Biol. Chem.* **2003**, 278, 7108–7118.

[43] B. P. Monia, J. F. Johnston, D. J. Ecker, M. A. Zounes, W. F. Lima, S. M. Freier, *J. Biol. Chem.* **1992**, 267, 19954–62.

[44] C. F. Bennett, E. E. Swayze, *Annu. Rev. Pharmacol. Toxicol.* **2010**, 50, 259–293.

[45] S. J. Schultz, J. J. Champoux, *Virus Res.* **2008**, 134, 86–103.

[46] M. Nowotny, S. A. Gaidamakov, R. Ghirlando, S. M. Cerritelli, R. J. Crouch, W. Yang, *Mol. Cell* **2007**, 28, 264–276.

[47] X.-H. Liang, H. Sun, J. G. Nichols, S. T. Crooke, *Mol. Ther.* **2017**, 25, 2075–2092.

[48] C. F. Bennett, B. F. Baker, N. Pham, E. Swayze, R. S. Geary, *Annu. Rev. Pharmacol. Toxicol.* **2017**, 57, 81–105.

[49] R. S. Geary, D. Norris, R. Yu, C. F. Bennett, *Adv. Drug Deliv. Rev.* **2015**, 87, 46–51.

[50] T. A. Vickers, J. R. Wyatt, S. M. Freier, *Nucleic Acids Res.* **2000**, 28, 1340–1347.

[51] H. J. Gaus, R. Gupta, A. E. Chappell, M. E. Østergaard, E. E. Swayze, P. P. Seth, *Nucleic Acids Res.* **2019**, 47, 1110–1122.

[52] F. Eckstein, *Nucleic Acid Ther.* **2014**, 24, 374–387.

[53] J. Temsamani, J. Y. Tang, A. Padmapriya, M. Kubert, S. Agrawal, *Antisense Res. Dev.* **1993**, 3, 277–284.

[54] P. J. Furdon, Z. Dominski, R. Kole, *Nucleic Acids Res.* **1989**, 17, 9193–9204.

[55] S. T. Crooke, P. P. Seth, T. A. Vickers, X. H. Liang, *J. Am. Chem. Soc.* **2020**, 142, 14754–14771.

[56] S. M. Freier, K. H. Altmann, *Nucleic Acids Res.* **1997**, 25, 4429–43.

[57] S. Wang, E. T. Kool, *Biochemistry* **1995**, 34, 4125–4132.

[58] S. M. Testa, M. D. Disney, D. H. Turner, R. Kierzek, *Biochemistry* **1999**, 38, 16655–16662.

[59] C. Cheong, I. Tinoco, A. Chollet, *Nucleic Acids Res.* **1988**, 16, 5115–5122.

[60] J. Summerton, *Biochim. Biophys. Acta - Gene Struct. Expr.* **1999**, 1489, 141–158.

[61] S. Gryaznov, *Nucleic Acids Res.* **1996**, 24, 1508–1514.

[62] F. Pellestor, P. Paulasova, *Eur. J. Hum. Genet.* **2004**, 12, 694–700.

[63] B. P. Monia, E. A. Lesnik, C. Gonzalez, W. F. Lima, D. McGee, C. J. Guinosso, A. M. Kawasaki, P. D. Cook, S. M. Freier, *J. Biol. Chem.* **1993**, 268, 14514–14522.

[64] P. S. Pallan, E. M. Greene, P. A. Jicman, R. K. Pandey, M. Manoharan, E. Rozners, M. Egli, *Nucleic Acids Res.* **2011**, 39, 3482–3495.

[65] S. Obika, D. Nanbu, Y. Hari, K. Morio, Y. In, T. Ishida, T. Imanishi, *Tetrahedron Lett.* **1997**, 38, 8735–8738.

[66] S. Murray, D. Ittig, E. Koller, A. Berdeja, A. Chappell, T. P. Prakash, M. Norrbom, E. E. Swayze, C. J. Leumann, P. P. Seth, *Nucleic Acids Res.* **2012**, 40, 6135–6143.

[67] S. Ochoa, V. T. Milam, *Molecules* **2020**, 25, 4659.

[68] L. Shen, A. Siwkowski, E. V. Wancewicz, E. Lesnik, M. Butler, D. Witchell, G. Vasquez, B. Ross, O. Acevedo, G. Inamati, H. Sasmor, M. Manoharan, B. P. Monia, *Antisense Nucleic Acid Drug Dev.* **2003**, 13, 129–142.

[69] A. Rich, *Nat. Struct. Biol.* **2003**, 10, 247–249.

[70] T. P. Prakash, *Chem. Biodivers.* **2011**, 8, 1616–1641.

[71] J. Wengel, *Acc. Chem. Res.* **1999**, 32, 301–310.

[72] A. A. Koshkin, S. K. Singh, P. Nielsen, V. K. Rajwanshi, R. Kumar, M. Meldgaard, C. E. Olsen, J. Wengel, *Tetrahedron* **1998**, 54, 3607–3630.

[73] C. Wahlestedt, P. Salmi, L. Good, J. Kela, T. Johnsson, T. Hokfelt, C. Broberger, F. Porreca, J. Lai, K. Ren, M. Ossipov, A. Koshkin, N. Jakobsen, J. Skouv, H. Oerum, M. H. Jacobsen, J. Wengel, *Proc. Natl. Acad. Sci.* **2000**, 97, 5633–5638.

[74] D. Baraniak, J. Boryski, *Biomedicines* **2021**, 9, 628.

[75] A. H. El-Sagheer, A. P. Sanzone, R. Gao, A. Tavassoli, T. Brown, *Proc. Natl. Acad. Sci.* **2011**, 108, 11338–11343.

[76] C. N. Birts, A. P. Sanzone, A. H. El-Sagheer, J. P. Blaydes, T. Brown, A. Tavassoli, *Angew. Chemie Int. Ed.* **2014**, 126, 2394–2397.

[77] M. Kukwikila, N. Gale, A. H. El-Sagheer, T. Brown, A. Tavassoli, *Nat. Chem.* **2017**, 9, 1089–1098.

[78] A. Dallmann, A. H. El-Sagheer, L. Dehmel, C. Mügge, C. Griesinger, N. P. Ernsting, T. Brown, *Chem. Eur. J.* **2011**, 17, 14714–14717.

[79] A. H. El-Sagheer, T. Brown, *Chem. Sci.* **2014**, 5, 253–259.

[80] P. Kumar, A. H. El-Sagheer, L. Truong, T. Brown, *Chem. Commun.* **2017**, 53, 8910–8913.

[81] A. Shivalingam, A. E. S. Tyburn, A. H. El-Sagheer, T. Brown, *J. Am. Chem. Soc.* **2017**, 139, 1575–1583.

[82] H. Lusic, D. D. Young, M. O. Lively, A. Deiters, *Org. Lett.* **2007**, 9, 1903–1906.

[83] D. D. Young, H. Lusic, M. O. Lively, J. A. Yoder, A. Deiters, *ChemBioChem* **2008**, 9, 2937–2940.

[84] A. Deiters, R. A. Garner, H. Lusic, J. M. Govan, M. Dush, N. M. Nascone-Yoder, J. A. Yoder, *J. Am. Chem. Soc.* **2010**, 132, 15644–15650.

[85] D. Matsunaga, H. Asanuma, M. Komiyama, *J. Am. Chem. Soc.* **2004**, 126, 11452–11453.

[86] B. Ghosn, F. R. Haselton, K. R. Gee, W. T. Monroe, *Photochem. Photobiol.* **2005**, 81, 953-959.

[87] X. Tang, I. J. Dmochowski, *Angew. Chemie Int. Ed.* **2006**, 45, 3523–3526.

[88] X. Tang, J. Swaminathan, A. M. Gewirtz, I. J. Dmochowski, *Nucleic Acids Res.* **2007**, 36, 559–569.

[89] X. Tang, M. Su, L. Yu, C. Lv, J. Wang, Z. Li, *Nucleic Acids Res.* **2010**, 38, 3848–3855.

[90] L. Wu, Y. Wang, J. Wu, C. Lv, J. Wang, X. Tang, *Nucleic Acids Res.* **2013**, 41, 677–686.

[91] L. Yang, H. B. Kim, J.-Y. Sul, S. B. Yeldell, J. H. Eberwine, I. J. Dmochowski, *ChemBioChem* **2018**, 19, 1250–1254.

[92] P. K. Jain, V. Ramanan, A. G. Schepers, N. S. Dalvie, A. Panda, H. E. Fleming, S. N. Bhatia, *Angew. Chemie Int. Ed.* **2016**, 55, 12440–12444.

[93] E. V. Moroz-Omori, D. Satyapertiwi, M. C. Ramel, H. Høgset, I. K. Sunyovszki, Z. Liu, J. P. Wojciechowski, Y. Zhang, C. L. Grigsby, L. Brito, L. Bugeon, M. J. Dallman, M. M. Stevens, *ACS Cent. Sci.* **2020**, 6, 695–703.

[94] W. Zhou, W. Brown, A. Bardhan, M. Delaney, A. S. Ilk, R. R. Rauen, S. I. Kahn, M. Tsang, A. Deiters, *Angew. Chemie Int. Ed.* **2020**, 59, 8998–9003.

[95] C. J. Bruns, J. F. Stoddart in *The Nature of the Mechanical Bond*, John Wiley & Sons, Inc., Hoboken, NJ, USA, **2016**.

[96] M. J. Smeulders, T. R. M. Barends, A. Pol, A. Scherer, M. H. Zandvoort, A. Udvarhelyi, A. F. Khadem, A. Menzel, J. Hermans, R. L. Shoeman, H. J. C. T. Wessels, L. P. Van Den Heuvel, L. Russ, I. Schlichting, M. S. M. Jetten, H. J. M. Op Den Camp, *Nature* **2011**, 478, 412–416.

[97] M. B. Van Eldijk, B. J. Pieters, V. A. Mikhailov, C. V. Robinson, J. C. M. Van Hest, J. Mecinović, *Chem. Sci.* **2014**, 5, 2879–2884.

[98] D. R. Boutz, D. Cascio, J. Whitelegge, L. J. Perry, T. O. Yeates, *J. Mol. Biol.* **2007**, 368, 1332–1344.

[99] J. D. Hegemann, M. Zimmermann, X. Xie, M. A. Marahiel, *Acc. Chem. Res.* **2015**, 48, 1909–1919.

[100] M. Tsunakawa, S. L. Hu, Y. Hoshino, D. J. Detlefson, S. E. Hill, T. Furumai, R. J. White, M. Nishio, K. Kawano, S. Yamamoto, Y. Fukagawa, T. Oki, *J. Antibiot.* **1995**, 48, 433–434.

[101] M. A. Delgado, M. R. Rintoul, R. N. Farías, R. A. Salomón, *J Bacteriol*. **2001**, 183, 4543-4550.

[102] B. Hudson, J. Vinograd, *Nature* **1967**, 216, 647–652.

[103] K. N. Kreuzer, N. R. Cozzarelli, *Cell* **1980**, 20, 245–254.

[104] M. A. Krasnow, A. Stasiak, S. J. Spengler, F. Dean, T. Koller, N. R. Cozzarelli, *Nature* **1983**, 304, 559–560.

[105] K. Subramanian, W. Rutvisuttinunt, W. Scott, R. S. Myers, *Nucleic Acids Res.* **2003**, 31, 1585–1596.

[106] R. Kovall, B. W. Matthews, *Science*, **1997**, 277, 1824–1827.

[107] T. Ooya, H. S. Choi, A. Yamashita, N. Yui, Y. Sugaya, A. Kano, A. Maruyama, H. Akita, R. Ito, K. Kogure, H. Harashima, *J. Am. Chem. Soc.* **2006**, 128, 3852–3853.

[108] T. Kench, P. A. Summers, M. K. Kuimova, J. E. M. Lewis, R. Vilar, *Angew. Chemie Int. Ed.* **2021**, 133, 11023–11029.

[109] J. List, E. Falgenhauer, E. Kopperger, G. Pardatscher, F. C. Simmel, *Nat. Commun.* **2016**, 7, 12414.

[110] J. T. Powell, B. O. Akhuetie-Oni, Z. Zhang, C. Lin, *Angew. Chemie Int. Ed.* **2016**, 55, 11412–11416.

[111] V. Aucagne, K. D. Hänni, D. A. Leigh, P. J. Lusby, D. B. Walker, *J. Am. Chem. Soc.* **2006**, 128, 2186–2187.

[112] A. Acevedo-Jake, A. T. Ball, M. Galli, M. Kukwikila, M. Denis, D. G. Singleton, A. Tavassoli, S. M. Goldup, *J. Am. Chem. Soc.* **2020**, 142, 5985–5990.

[113] H. Lahlali, K. Jobe, M. Watkinson, S. M. Goldup, *Angew. Chemie Int. Ed.* **2011**, 50, 4151–4155.

[114] A. Fernandes, A. Viterisi, F. Coutrot, S. Potok, D. A. Leigh, V. Aucagne, S. Papot, *Angew. Chemie Int. Ed.* **2009**, 48, 6443–6447.

[115] T. Ooya, H. S. Choi, A. Yamashita, N. Yui, Y. Sugaya, A. Kano, A. Maruyama, H. Akita, R. Ito, K. Kogure, H. Harashima, *J. Am. Chem. Soc.* **2006**, 128, 3852–3853.

[116] H. Lahlali, K. Jobe, M. Watkinson, S. M. Goldup, *Angew. Chemie Int. Ed.* **2011**, 50, 4151–4155.

[117] J. E. M. Lewis, R. J. Bordoli, M. Denis, C. J. Fletcher, M. Galli, E. A. Neal, E. M. Rochette, S. M. Goldup, *Chem. Sci.* **2016**, 7, 3154–3161.

[118] P. Wang, W. Lu, D. A. Devalankar, Z. Ding, *Org. Lett.* **2015**, 17, 2114–2117.

[119] J. Maynard, PhD Thesis, University of Southampton (UK), **2019**.

[120] P. Sarmah, D. K. Dutta, *J. Chem. Res.* **2003**, 236–237.

[121] X. Ding, P. Wang, *J. Org. Chem.* **2017**, 82, 7309–7316.

[122] X. Ding, P. Wang, *J. Org. Chem.* **2018**, 83, 7459–7466.

[123] M. Galli, C. J. Fletcher, M. del Pozo, S. M. Goldup, *Org. Biomol. Chem.* **2016**, 14, 5622–5626.

[124] M. Denis, S. M. Goldup, *Nat. Rev. Chem.* **2017**, 1, 0061.

[125] J. W. Chamberlin, *J. Org. Chem.* **1966**, 31, 1658–1660.

[126] Đ. Škalamera, V. Blažek Bregović, I. Antol, C. Bohne, N. Basarić, *J. Org. Chem.* **2017**, 82, 12554–12568.

[127] T. Eckardt, V. Hagen, B. Schade, R. Schmidt, C. Schweitzer, J. Bendig, *J. Org. Chem.* **2002**, 67, 703–710.

[128] E. C. Constable, C. E. Housecroft, *Molecules* **2019**, 24, 3951.

[129] H. Onagi, J. Rebek, *Chem. Commun.* **2005**, 4604–4606.

[130] G. Yu, D. Wu, Y. Li, Z. Zhang, L. Shao, J. Zhou, Q. Hu, G. Tang, F. Huang, *Chem. Sci.* **2016**, 7, 3017–3024.

[131] R. P. Sinha, D. P. Häder, *Photochem. Photobiol. Sci.* **2002**, 1, 225–236.

[132] E. Lee, J. Koo, T. Berger, *Int. J. Dermatol.* **2005**, 44, 355–360.

[133] A. Pigorsch, M. Köckerling, *Cryst. Growth Des.* **2016**, 16, 4240–4246.

[134] A. H. El-Sagheer, T. Brown, *Proc. Natl. Acad. Sci.* **2010**, 107, 15329–15334.

[135] O. V. Dolomanov, L. J. Bourhis, R. J. Gildea, J. A. K. Howard, H. Puschmann, *J. Appl. Crystallogr.* **2009**, 42, 339–341.

[136] G. M. Sheldrick, *Acta Crystallogr. Sect. A Found. Adv.* **2015**, 71, 3–8.

[137] G. M. Sheldrick, *Acta Crystallogr. Sect. C Struct. Chem.* **2015**, 71, 3–8.

Chapter 3: A Platform Approach for the Synthesis of Cleavable 2,2'-Bipyridine Macrocycles

Abstract: A platform methodology for the synthesis of cleavable 2,2'-bipyridine macrocycles was developed. Installation of the trigger motif post-macrocyclisation granted rapid and convenient access to a small library of cleavable macrocycles, which were shown to mediate AT-CuAAC rotaxination with high efficiency. Cleavage of the trigger unit in response to the appropriate stimulus (pH, chemical, UV light) generated an intermediate rotaxane species which, depending on the employed conditions, underwent ring-opening to liberate the axle from the interlocked structure with varying success. Tailoring the electronic properties of the self-immolative spacer within the platform macrocycle backbone through judicious structural modification was later shown to significantly improve the ring-opening capability of the macrocycle.

Acknowledgements: Synthesis and route optimisation of fluorinated phenol **108** was performed by Dr. Noël Pairault.

Prior Publication: None of this work has been previously published.

3.1. Introduction

The use of protecting groups to modulate the physiological properties of chemical substances is common in biology and medicine. These protected substrates, known as prodrugs, mask biological function during systemic transport and restore bioactivity only once the desired pathological site has been reached. Transient modifications can also confer favourable *in vivo* properties upon the prodrug, such as enhanced stability, water solubility and improved pharmacokinetic profiles. However, in many cases, the proximity of the protecting group to the caged compound can impair cleavage, hindering its release. For instance, enzymatic cleavage of protecting groups is highly sensitive to steric effects and becomes ineffective when the caged species is too bulky.[1] An alternative strategy is to incorporate an additional linker between the protecting group and the active compound. Self-immolative (SI) linkers are stable covalent constructs capable of undergoing spontaneous disassembly upon the stimuli-responsive removal of a protecting group, liberating the active compound (Figure **240**).[2]

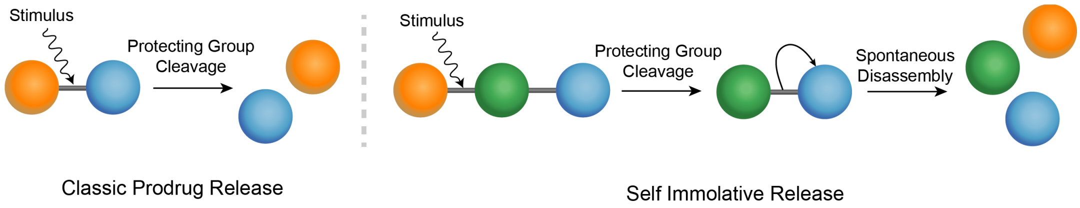

Figure **240**. Differences between the classic prodrug and self-immolative linker approaches.

SI linkers are frequently used in conjugate systems for controlled drug delivery,[3] as well as for the generation of molecular amplifiers and stimuli-responsive materials.[4,5] As such, a variety of structurally diverse molecules have been caged through conjugation with protected SI linkers, ranging from fluorophores and molecular probes to anticancer drugs.6-8 In each case, the compound to be caged must contain a functional group that can be readily converted into an efficient leaving group — amines, thiols and alcohols are all commonly used in this regard.[9] Alcohols can be converted to carbonates during SI linker installation, significantly enhancing their leaving group ability. However, due to their susceptibility to background hydrolysis under physiological conditions, the utility of carbonate linkages is limited in a biological context.[10,11] Conversely, carbamates are among the most frequently used linkages to connect hydroxyl- or amino-functionalities to the spacer due to their biocompatibility and systemic hydrolytic stability, which prevents premature non-specific cargo release.[12]

3.1.1. Self-Immolative Linker Design

Removal of the protecting group reveals a nucleophilic functionality that can initiate SI linker disassembly *via* an intramolecular elimination or cyclisation mechanism. SI linkers which rely on quinone-methide elimination and related mechanisms are by far the most commonly employed.[2,13,14] For such linkers, the disassembly proceeds through a cascade of sequential electronic eliminations that are driven by a positive change in entropy coupled with the irreversible formation of thermodynamically stable products such as CO_2 (Scheme **24**).

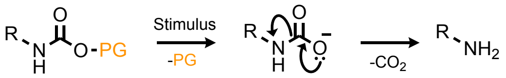

Scheme **24**. Spontaneous decarboxylation of the carbamate linkage upon protection group removal.

Such linkers generally consist of polysubstituted electron-rich aromatic systems with protected highly electron-donating groups (-OH, -SH, NH_2) conjugated to benzylic leaving groups at *ortho* and/or *para* positions. 2- and 4-amino-, hydroxy- and mercapto-functionalised benzylic alcohols, which undergo 1,4- or 1,6- elimination respectively upon activation, have been thoroughly investigated as SI linkers (Figure **241**).2,13,15-17 The extended π-systems in *para*-amino/hydroxy cinnamyl alcohols and coumarinyl alcohols have also proven suitable for disassembly *via* 1,8-eliminations and have found utility as SI spacers.[18–20] When performed under aqueous conditions, the methide quinone elimination by-product is expected to be quenched by water to form the corresponding alcohol. However, alkylation of biological nucleophiles (proteins, DNA) *via* reaction with these reactive intermediates can also occur, leading to significant cytotoxic effects *in vivo*.[21] Irreversible suicide-based inhibition is particularly problematic when using enzymes to initiate linker disassembly.[22,23]

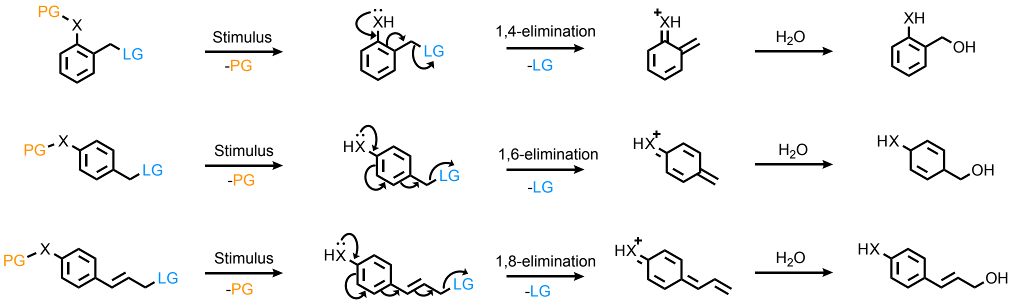

Figure **241**. Self-immolative mechanisms of disassembly for linkers relying on elimination. **PG** = protecting group, **LG** = Leaving group, **X** = -O, -S or -NH.

Aminobenzyl alcohols, which disassemble *via* charged azaquinone methide intermediates, typically have superior self-immolative ability relative to their oxygen-containing counterparts due to the greater availability of the nitrogen lone-pair to the conjugated system and are more commonly used.[3] Further improvements to linker properties have been achieved through judicious structural modification. Hay *et al.* showed that the rate of self-immolative elimination in 4-aminobenzyl carbamates could be enhanced by incorporating electron-donating groups at the 2-position, which stabilizes the formation of the azaquinone methide intermediate.[24,25] α-Methyl substitution of benzylic positions was similarly found to have a strong stabilising effect and led to further improvements to the rate of elimination. Phillips *et al.* have reported a tuneable aminobenzyl-based SI linker for the controlled release of phenols under neutral conditions (Figure **242**).[26] The unmodified linker (R_1 = H, R_2 = H) was useful for the release of only highly acidic phenols (pK_a < 9.2) under the employed mixed organic-aqueous conditions. Modification with electron-donating methoxy groups at *ortho* positions led to substantial improvement in the rate of self-immolative elimination, generating a spacer capable of releasing virtually all types of phenols, regardless of their pK_a. The study also found that the methoxy modifications had a similar effect on hydroxybenzyl-based SI linkers.

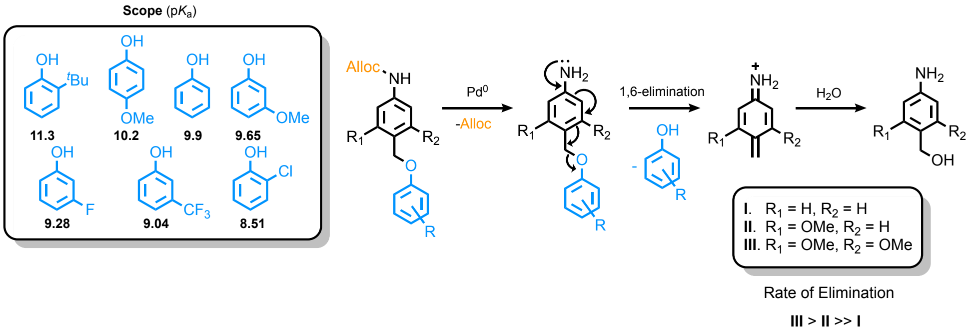

Figure **242**. A tuneable aminobenzyl-based linker for the controlled release of various phenols.[26]

Although less common, numerous linkers which rely on a cyclization event to liberate the caged species have also been developed. Removal of the protecting group unveils a nucleophilic heteroatom (-OH, -SH, -NH_2), which then performs an intramolecular attack on an electrophilic carbonyl centre in the alkyl chain (Figure **243**). This approach is also driven by a positive change in entropy and the formation of thermodynamically stable products — usually 5- or 6-membered cyclic esters, amides, ureas, carbamates or thiocarbonates.[27–31] Self-immolative cyclization rates are usually considerably slower than the cascade elimination approach. However, this can be beneficial for applications where sustained release is preferred. From a toxicological perspective, the stable cyclic decomposition products are generally less of a problem compared to the highly reactive quinone methide species generated in cascade eliminations.

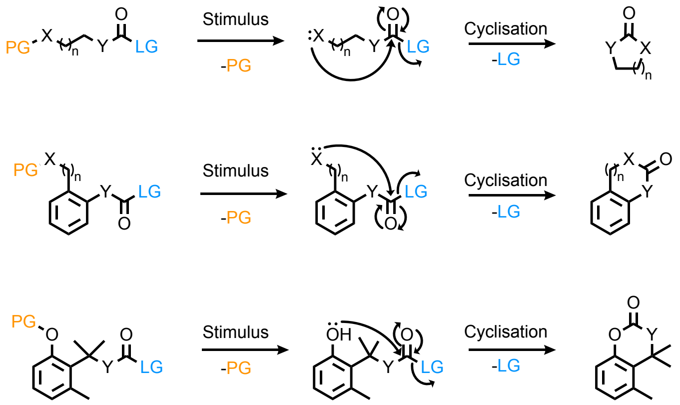

Figure **243**. Self-immolative mechanisms of disassembly for linkers relying on cyclization. **PG** = protecting group, **LG** = Leaving group, **X** = -NH, -S or -O, **Y** = CH_2, NH or O.

Combinations of elimination and cyclization-based SI linkers have been employed to improve stability or facilitate enzymatic activation by further lowering the steric hindrance, although when limited by slow rates of self-immolative cyclization, they have extended half-lives, which limits their utility.[32,33] The practicality of SI cyclization linkers can be improved by altering electronic and steric substituent effects or by fine-tuning the nucleophilicity and electrophilicity of the sites involved in cyclisation. For instance, Gillies *et al*. found that replacing carbamate linkages to *N*-methylaminoethanol cyclization-based spacers with more electrophilic carbonate units resulted in a 500-fold increase in the self-immolative rate of cyclisation.[34] A nucleophilic enhancement was also achieved by substituting the amino functionality for a thiol, which led to further improvements to the rate of linker disassembly.

3.1.2. Protecting Groups/ Triggers

For the disassembly to begin, the protecting group must first be removed. The choice of protecting group — and the stimulus required to cleave it — is therefore paramount and must be selected carefully, bearing in mind the function of the caged compound and the desired location of its reactivation. SI drug conjugates have been capped with an assortment of structurally diverse protecting groups designed to cleave quickly and efficiently in response to internal (chemical, enzyme, pH, ROS) or external stimuli (light). Photolabile protecting groups (PPGs), discussed extensively in Chapter 2, provide unparalleled spatiotemporal control over the release of photocaged substrates and are often used in conjugation with SI linkers. The main advantage of including SI linkers is that the caged substrate can be released after light-activation in a time-dependent manner that is consistent with the linker structure, which can improve treatment efficacy and safety.[35] SI linker-containing dendrimers can also facilitate the release of multiple compounds from the same molecule after a single photocleavage event, something that is not possible with the traditional light-activated prodrug approach. Such materials have found utility in cellular imaging and drug delivery applications.[36]

3.1.3. Chemical Triggers

Chemical cleavage is often used to unmask the nucleophilic functionalities that initiate disassembly due to the ease at which reagents can be introduced and the outcomes analysed. Allyloxy and allylamino protecting groups have been readily cleaved with Pd^0 under reductive conditions.[26,37–39] The reduction of nitro groups with Zn/AcOH has also been used to generate electron-rich amines that initiate cascade eliminations.[18,40] Activation of self-immolation *via* nucleophilic attack is quite common: fluoride sources have been used to cleave silyl ethers;[41,42] ester hydrolysis has also been shown to afford slow activation under aqueous conditions.[33] While these chemical triggers have proven useful for studying the kinetic disassembly of their systems in abiotic media, they are of little relevance biologically.[9]

Numerous conjugate SI drug-delivery systems have been designed to exploit the subtle pH differences between healthy cells and therapeutic targets. The extracellular environment of tumour sites, for instance, is slightly acidic (pH ≈ 6.5) due to the high concentrations of carbonic and lactic acid, which arise from abnormal metabolic pathways.[43] Drugs entering cells *via* endocytic pathways are similarly subjected to the low pH environment of endosomes (≈ pH 5-6) and lysosomes (≈ pH 4-5) and can be exploited for selective intracellular drug delivery.[44] Numerous SI prodrug carriers bearing acid-labile carbamate and azobenzene functionalities have been designed to selectively release drugs in these acidic environments.[45–48]

Biological reductants such as glutathione (GSH) are present at significantly higher concentrations in the cytoplasm relative to the extracellular matrix and have been targeted for selective intracellular drug delivery.[31] GSH is also heavily overexpressed in solid tumours and has been used as an activating stimulus to discriminately target cancer cells over healthy cells. SI linkers with redox-sensitive disulfide bonds have proven particularly useful for selective drug activation[49,50] and the delivery of activatable cellular imaging agents.[51,52] Polymeric micellar nanoparticles employing disulfide-cross-linkages have been reported to encapsulate and selectively release drugs and diagnostic probes.[53,54] Formulation of macromolecules within disulfide-linked gels has also been reported as a method for the site-selective delivery of biological therapeutics.[55,56] In these examples, the disulfide bonds themselves are stable in the extracellular environment and, being weakly nucleophilic, they are incapable of activating the self-immolative decomposition pathways. High intracellular levels of GSH, or other biological reductants, facilitate bioreductive disulfide cleavage, generating a highly nucleophilic thiolate which initiates disassembly *via* cascade elimination or cyclisation pathways, selectively liberating the caged drug. Norbeck *et al.* demonstrated the first instance of redox-activated drug release in their seminal publication (Figure **244**).[57] Caging of antibacterial agent AADO (**4**) through a redox-sensitive SI linker afforded conjugate **1**, with greatly enhanced membrane permeability toward gram-negative bacteria. Upon reaching the cytosolic target the disulfide was rapidly cleaved, initiating a self-immolative cyclization pathway that resulted in the formation of a cyclic thioether by-product (**3**) along with the liberation of active antibacterial agent **4** — restoring cytotoxicity to bacterial cells.

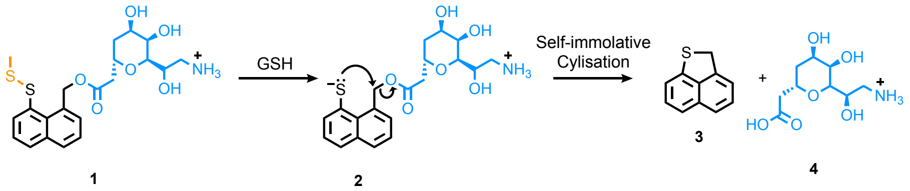

Figure **244**. Intracellular GSH-mediated disulfide cleavage initiates a self-immolative cyclisation mechanism that results in the release of active antibiotic **4**.[57]

Conjugate drug-delivery systems have also been devised to exploit the high levels of small reactive oxygen species (ROS) present in cells under oxidative stress — a characteristic feature of several diseases.[58] Boronate esters are among the most frequently used protecting groups for ROS-sensitive SI linkers due to the ease at which they undergo physiological oxidation by H_2O_2, and have found application as structural components in various H_2O_2-sensitive cellular imaging agents and drug delivery vehicles.[59–62] Nucleophilic attack of H_2O_2 on the boron atom is followed by a 1,2-rearrangement, generating an intermediate that is rapidly hydrolysed to liberate the corresponding phenolate.[63,64] Huimin *et al.* have recently reported a H_2O_2-triggered arylboronate-caged naphthalimide capable of monitoring the intracellular release of H_2S *via* fluorescence imaging in real-time.[65] The SI thiocarbamate linker serves an important dual function in this system: releasing the caged fluorophore *via* cascade elimination and simultaneously generating carbonyl sulfide, which is subsequently converted to H_2S by endogenous carbonic anhydrase. Fluorophore conjugate **5** showed excellent biocompatibility and a high degree of selectivity for activation by H_2O_2 over other interfering intracellular species. A pronounced fluorescence activation upon linker disassembly allowed the live release of pathological H_2S to be imaged in RAW264.7 cells, an inflammatory cell under induced oxidative stress (Figure **245**). Healthy cells showed no such uptake in fluorescence, indicating that elimination was not initiated. Most importantly, the study found that cells incubated with fluorescent conjugate **5** were protected against cellular inflammation, which is known to promote apoptosis. The anti-inflammatory behaviour was attributed to the ROS-scavenging ability of linker-derived H_2S, hinting toward its viability in future therapeutic applications.

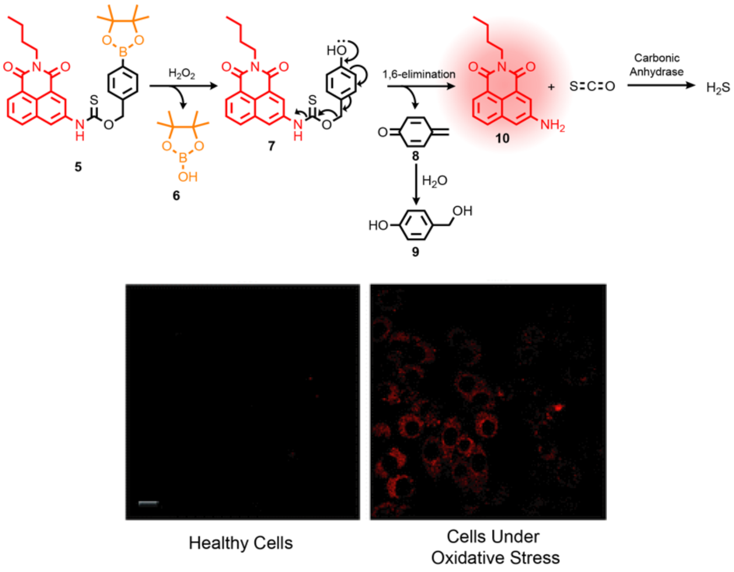

Healthy Cells

Cells Under Oxidative Stress

Figure **245**. The H_2O_2-triggered arylboronate-caged naphthalimide for monitoring the release of H_2S *via* fluorescence imaging. Images have been reproduced with permission from Huimin *et al.*[65]

The ever-growing range of ROS-sensitive protecting groups allows activation to be tailored to the precise biological application.[66] For instance, Höcherl *et al.* have recently reported the use of oxalate functionalities in SI polyprodrug nanoparticles, which disassembled in H_2O_2-rich tumour microenvironments to release a chemotherapeutic hormone analogue.[67] The polyprodrug was found to be more active *in vitro* than the native drug and also displayed significantly lower cytotoxicity against healthy cells due to ROS-selective activation.

3.1.4. Enzymatic Triggers

Enzymatic activation has become increasingly popular in clinical scenarios — exploiting the overexpression of certain enzymes/proteins in pathological targets to selectively activate the drug. Penicillin-G-Amidase (PGA)[29] and Bovine Serum Albumin (BSA)[68] readily cleave phenylacetamide moieties and are frequently used as model triggers to study the disassembly of SI prodrug conjugates under physiological conditions. However, these triggers are of little use therapeutically. Site-selective delivery is particularly important with the administration of chemotherapeutic agents, which typically possess a narrow therapeutic window and cause severe off-target effects if active in healthy cells. Several anticancer prodrug conjugates bearing enzyme-labile SI linkers have been reported for site-selective delivery to tumour cells.[35,69] Cathepsin B, a cysteine protease overexpressed in metastatic tumours, has observed clinical success as a stimulus for the site-selective activation of anticancer drugs when incorporated within antibody-drug conjugates (ADCs) — a strategy used to minimise the off-target toxicity associated with highly potent cytotoxic agents.[70] The structure of these ADCs generally consist of a cathepsin B-labile peptidic sequence, such as the valine-citrulline dipeptide,[71] attached on one end to the drug through a SI linker, and to a monoclonal antibody-binding moiety on the other. The structure of brentuximab vedotin, a clinically-approved cathepsin B-activated ADC of the highly potent antimitotic agent monomethyl auristatin E (MMAE), is shown below (Figure **246**).[72,73]

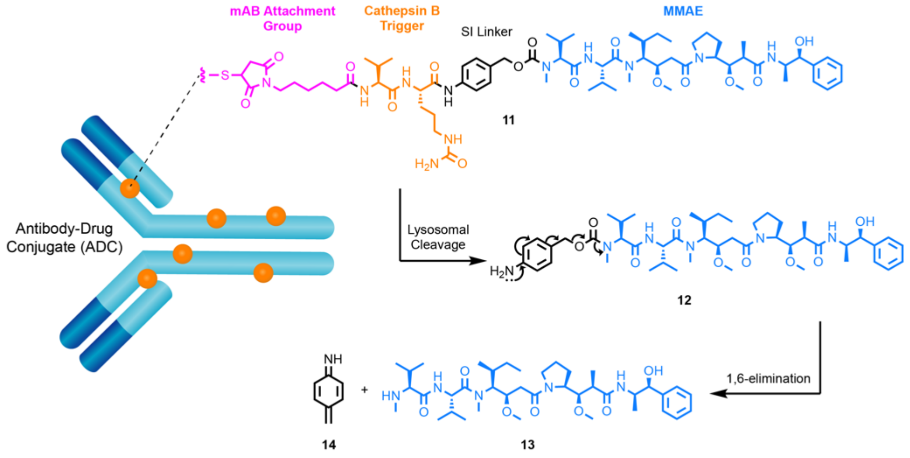

Figure **246**. Structure of the clinically approved ADC brentuximab vedotin and its mechanism of intracellular activation.

The lack of cathepsin B in extracellular media means that the conjugate exhibits excellent serum stability and, due to the active tumour-targeting ability of the bio-conjugated monoclonal antibody, is delivered to cancerous cells with high selectivity. Lysosomal cathepsin B hydrolyses the peptidic trigger sequence and initiates a spontaneous 1,6-elimination to release MMAE (**13**) — which exerts a highly cytotoxic effect on cells in the tumour microenvironment.

β-glucuronidase is another popular cancer target due to its overexpression in numerous malignant tumours.[74,75] Papot *et al.* have developed several β-glucuronidase-responsive anticancer drug-delivery systems.[76–79] Enzymatic cleavage of the glucuronide group releases an NO_2-modified phenolic linker which undergoes a 1,6-elimination to release the active anticancer drug, which in this case is cyclopamine (**18**) (Figure **247**).[80] *Para* quinone methide **19** then reacts with water to form the corresponding alcohol (**20**).[81] Protected cyclopamine (**15**) was non-toxic at therapeutically relevant concentrations, with cytotoxicity to glioblastoma cells fully restored upon cleavage of the glucuronide moiety. The inclusion of a hydrophilic side chain within the linker later led to an enhanced drug release profile and better aqueous solubility.[79]

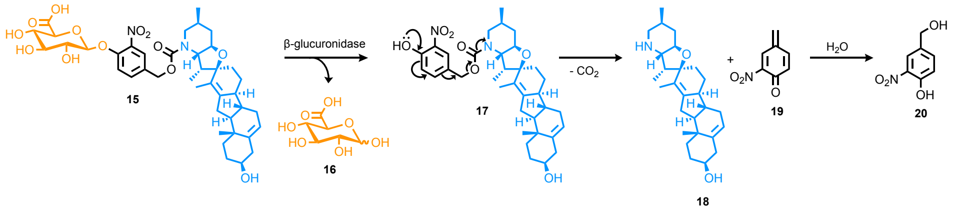

Figure **247**. β-glucuronidase-triggered release of cyclopamine (**18**) from SI-linked drug conjugate **15**.[80]

The selectivity of these anticancer drug delivery systems could be further improved through the addition of folate ligands, which actively target overexpressed folate receptors on the surface of tumour cells.[76] Based on this approach, the group were able to develop a new generation of tumour-targeting galactoside-triggered MMAE prodrugs, without the need for antibody bioconjugation (Figure **248**).[82] *In vitro* cytotoxicity was found to be significantly greater in cancer lines with higher levels of folate receptor expression, which was confirmed to be due to the intracellular β-glucuronidase-initiated release of MMAE (**13**). The prodrug conjugates were also highly effective for the *in vivo* treatment of folate-overexpressing solid tumours without any detectable toxicity in healthy tissue.

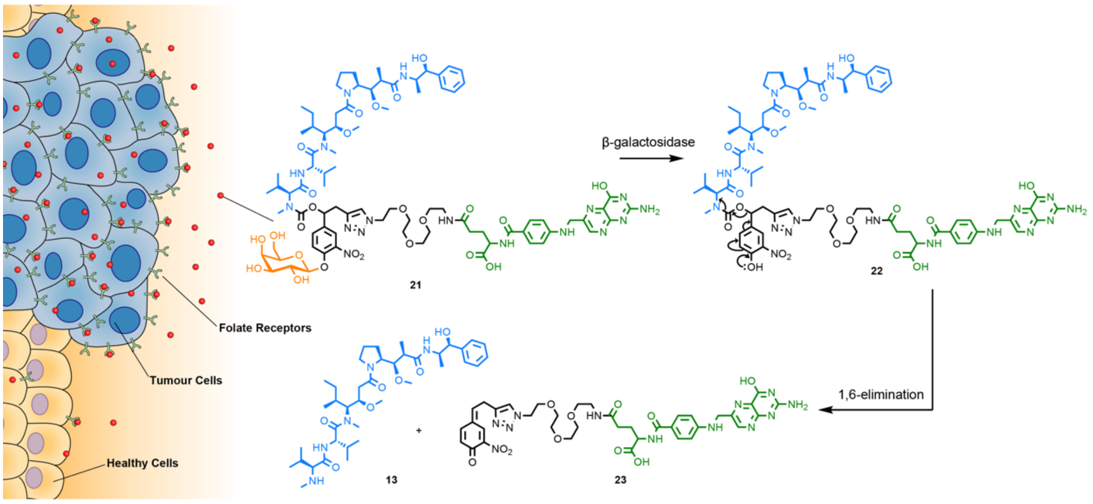

Figure **248**. A folate-targeting galactoside-triggered MMAE prodrug (**21**).[82]

3.1.5. Stimuli-Cleavable Mechanical Bonds

Many stimuli-responsive interlocked architectures have proven useful for biological applications.[83,84] In these systems, the mechanical bond acts as a means to stabilise or control the activity of biologically relevant substances. Rotaxanes have been used as gatekeepers to cap the surface apertures of mesoporous silica nanoparticles, controlling the intracellular release of diagnostic and therapeutic molecular cargoes in response to various internal (redox, pH, enzymes) and external stimuli (light).[85–88] Biodegradable polyrotaxanes have similarly found utility as drug delivery vehicles or as formulation agents for the transport of biological macromolecules.[89,90]

Papot *et al*. have developed an enzyme-responsive prodrug in which a benzylic amide-based macrocycle encircles the pentapeptide Met-enkephalin — an anticancer drug which suffers from poor *in vivo* stability as a result of its rapid degradation by proteolytic enzymes.[91] In this dynamic system, the macrocycle can to occupy several binding sites along the length of the peptide, effectively acting as a steric barrier to prevent enzymatic binding. Peptide rotaxane **24** displayed remarkable stability toward a range of exonuclease and endonuclease enzymes over several days. In contrast, non-mechanically bonded peptide axle **28** was rapidly hydrolyzed. In the presence of β-galactosidase, the protecting group is selectively cleaved, initiating a self-immolative mechanism that results in de-threading of the macrocycle and release of the bioactive peptide (**25**) (Figure **249**). Although the approach holds promise for the delivery of peptide-based therapeutics, the utility of these peptide-rotaxanes was hampered by their poor aqueous solubility. A later study showed that solubility could be increased by up to 50,000-fold through the derivatization of the macrocyclic component with hydrophilic side chains.[92]

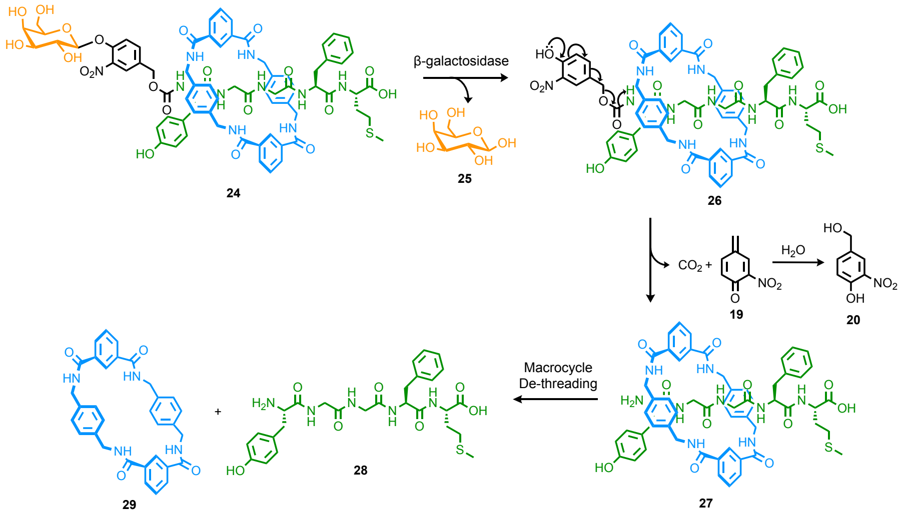

Figure **249**. Enzyme responsive peptide-sheaths developed by Papot *et al*.[91]

The concept was later applied to develop biocompatible [2]rotaxane **30** for the controlled intracellular delivery of an anticancer drug (Figure **250**).[93] In this system, the potent antimitotic agent paclitaxel is linked through an esterase-labile unit to water-solubilising Gly-TEG moieties. Encircling the axle is a self-opening macrocycle conjugated through a SI linker to a glycosidase protecting group. The mechanical bond was again found to protect the axle component from premature degradation by extracellular esterase enzymes during transport, with no detected release of paclitaxel observed after 48 h in blood plasma. Upon entry to the intracellular environment, the high concentration of β-galactosidase, which is overexpressed in tumour cells, resulted in the cleavage of the galactoside protecting group. This initiated a cascade disassembly process which cleaved the carbamate moieties within the macrocyclic framework, opening the macrocycle and releasing axle **34**. Full release of axle **34** was observed within 28 h. Lacking the steric barrier afforded by the macrocycle, the ester linkage is rapidly hydrolyzed and paclitaxel (**35**) released. The cytotoxicity of the rotaxane was found to be dependent on the intracellular concentration of β-galactosidase and, although less potent than paclitaxel, was selectively activated in cancer cells. The functional aspect of these systems is conceptually similar to the previously discussed prodrug conjugates. The stimuli-responsive removal of a protecting group results in the cleavage of another bond — in this case, it's the mechanical bond.

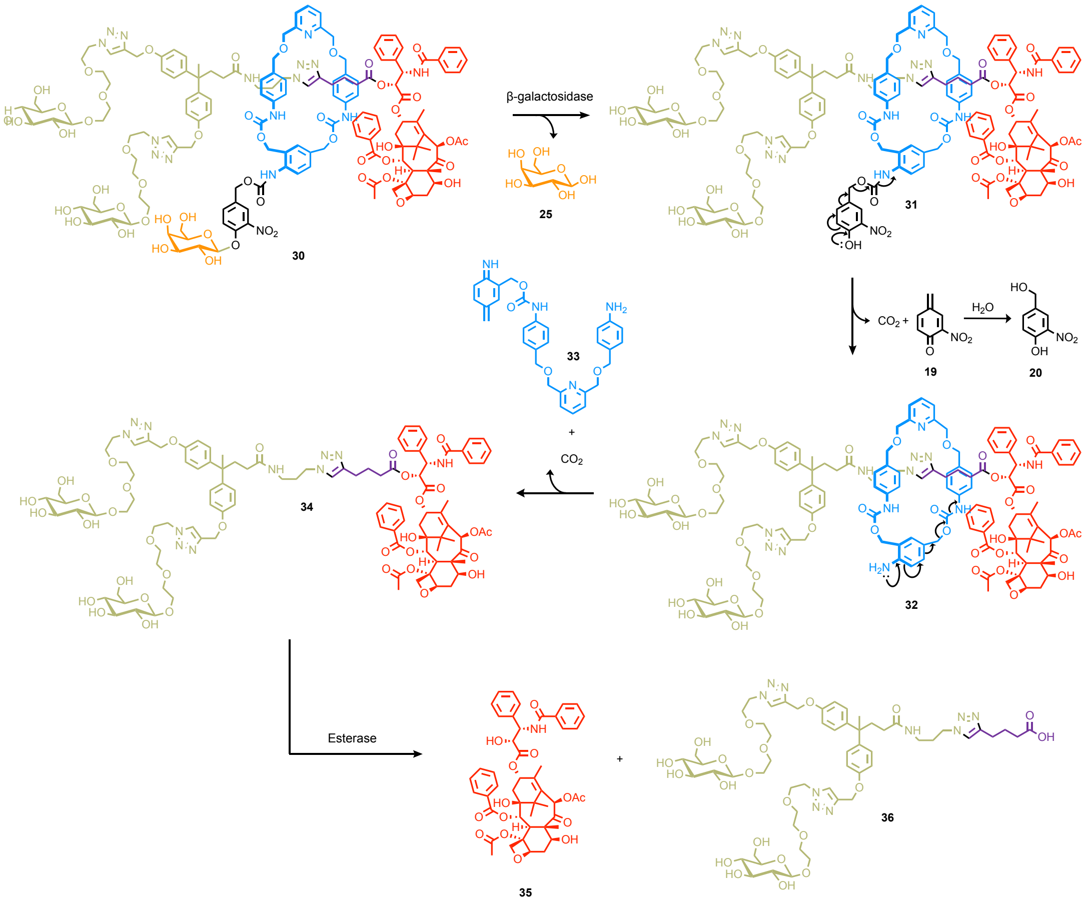

Figure **250.** Autonomous delivery of paclitaxel from a biocompatible [2]rotaxane **30**.[93]

3.2. Results and Discussion

In the previous chapter, we showed how the direct incorporation of a photocleavable protecting group within the macrocyclic framework could be used to achieve optochemical control over the release of axles from rotaxane structures. While this approach proved successful, it lacks generality when attempting to broaden the scope to other protecting groups, limiting the choice of stimuli available to initiate mechanical bond disassembly. Many protecting groups lack appropriate structure and/or connectivity to be successfully incorporated within the macrocyclic backbone. Others are chemically incompatible with the synthetic route to the final product — harsh Ni-mediated macrocyclisation conditions are particularly problematic.[94] Even if successfully incorporated, the conformational behaviour of the macrocycle will vary considerably depending on the structure of the protecting group, which could potentially influence the efficiency of the AT-CuAAC process.

Developing a platform approach in which the trigger motif is installed as the final synthetic step at a peripheral site would overcome chemical instability issues and grant rapid access to a library of cleavable macrocycles. To ring-open and liberate mechanically bonded sub-components, covalent bond(s) must be broken within the backbone of the macrocycle. Rather than placing the stimuli-responsive unit directly within the macrocyclic framework, a self-immolative spacer could instead be used and conjugated through a carbamate linkage to the trigger moiety on the periphery of the macrocycle, where steric effects are less likely to interrupt the AT-CuAAC reaction. Spontaneous decarboxylation following stimuli-responsive protecting group cleavage would unmask an electron-rich aniline that initiates the cascade disassembly process, resulting in covalent bond cleavage within the self-immolative spacer and ring-opening of the macrocycle (Scheme **25**).

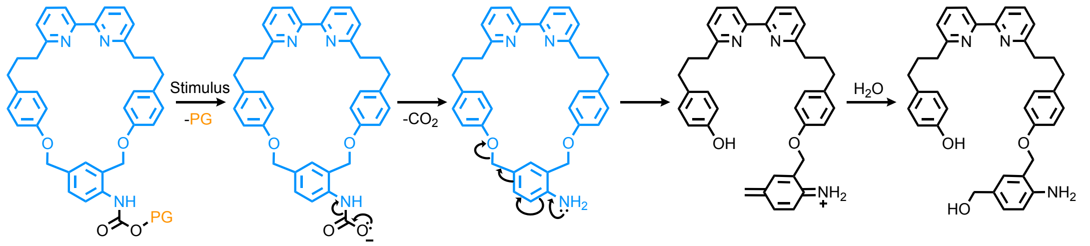

37 **38** **39** **40**

Scheme **25**. Design principle of the cleavable macrocycle showing the expected ring-opening mechanism upon removal of protecting group under aqueous conditions.

1,4- and 1,2-aminobenzyl-based spacers that disassemble through azaquinone methide intermediates are well-established in polymeric drug delivery systems and, given their structural similarity to the macrocycles synthesized in the previous chapter, should possess the correct geometry to be successfully incorporated within the macrocycle structure. Phenolic ethers are prevalent structural features in the 2,2'-bipyidine macrocycles reported by Goldup *et al.*[95] They have also been reported as effective leaving groups for azaquinone-based spacers and were used here due to their ease of incorporation and stability to background hydrolysis.[26]

To achieve post-macrocyclisation installation of the trigger motif, the functional handle must be carried through the synthesis as a stable protecting group that does not initiate spacer disassembly. Conversion of the inert group to the protected active moiety could be achieved simultaneously with the installation of the trigger motif *via* carbamate bond formation. Carbamate formation is most commonly achieved *via* the reaction of an amine with an electrophilic carbonyl source. However, this approach is unsuitable for our purposes, as the amino functionality is also expected to initiate spacer disassembly.[96] Alternatively, isocyanates can be readily synthesised through the 1,2-rearrangement of acyl azides or carboxamides and subsequently trapped as the carbamate *via* reaction with an appropriate trigger alcohol (Scheme **26**).

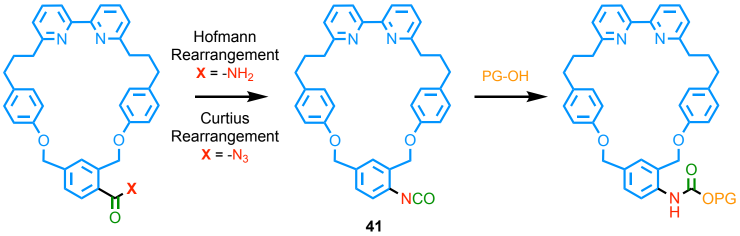

Scheme **26**. Proposed installation of the trigger moiety post-macrocyclisation through either Hofmann or Curtius rearrangement.

3.2.1. Macrocycle Synthesis (1st Generation)

Methyl esters are expected to be stable toward the chemical transformations employed in the synthesis of 2,2'-bipyridine macrocycles and can be readily converted to the corresponding acyl azide or carboxamide post-macrocyclisation. A synthetic route to carboxamide-containing macrocycle **50** was devised (Scheme **27**). Fischer esterification of **42** gave **43** in 92% yield. Bromination of **43** with NBS afforded **44** as a mixture of the di- and tri-brominated species (94:6) that was carried forward to an alkylation with **45** to give macrocycle precursor **46** in 84% yield over the two steps. Ni-mediated macrocyclisation of **46** afforded **47** in 62% yield, which was subsequently hydrolysed under basic conditions to give carboxylic acid macrocycle **48** in 88% yield. Acid chloride **49** was generated *in situ* by treating macrocycle **48** with $SOCl_2$ and quenched with aqueous NH_3 to give carboxamide **50** in 87% yield over two steps.

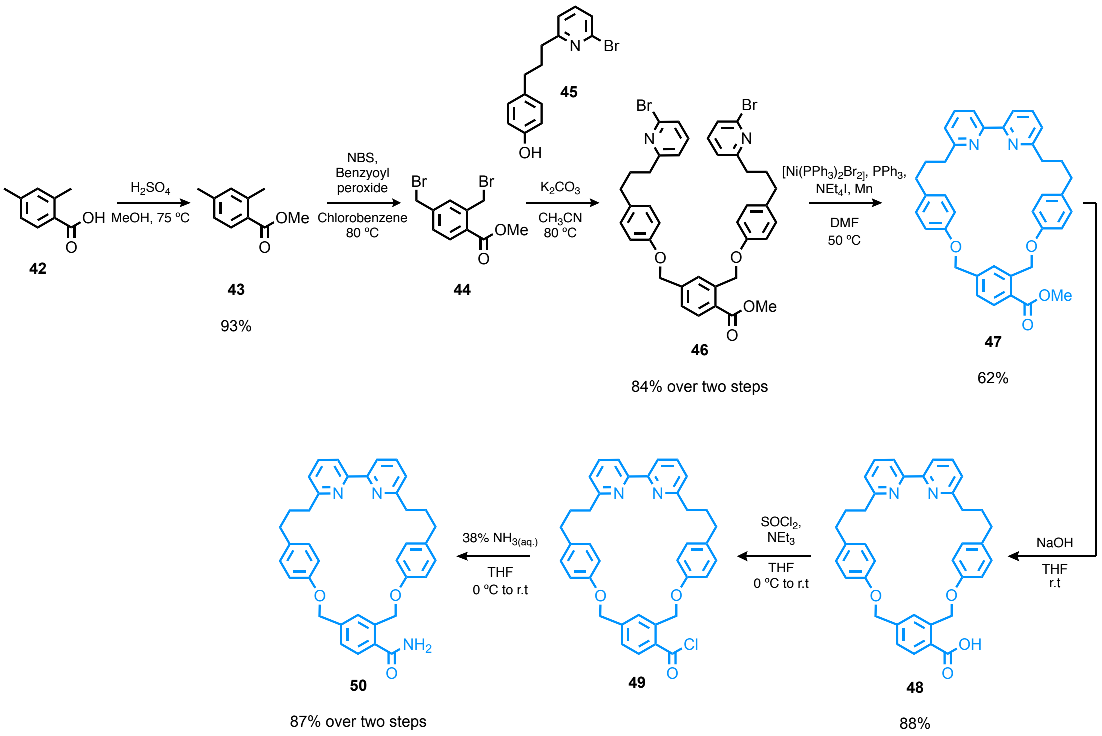

Scheme **27**. Synthesis of carboxamide macrocycle **50**.

Carboxamides can be converted to isocyanates *via* Hofmann rearrangement.[97] While traditionally requiring harsh oxidative conditions (i.e., treatment of the primary amide with alkaline hypohalites or a combination of halogens and strong bases under aqueous conditions), hypervalent iodine reagents have recently been reported to affect this change under much milder conditions (neutral pH, r.t.).[98–100] Hu *et al.* have recently reported a convenient synthesis of isocyanates *via* Hofmann rearrangement of carboxamides, induced by iodosylbenzene (PhIO) at room temperature in a range of organic solvents.[101] The mild and operationally simple conditions for isocyanate formation combined with the ease at which PhIO could be prepared led us to explore this approach initially. Once formed, the isocyanate could be trapped as the carbamate by reaction with the appropriate alcohol.

Treatment of carboxamide **50** with PhIO (2.0 eq.) at room temperature led to the successful formation of isocyanate intermediate **41**, which was trapped as carbamate **52** or **55** in the one-pot mixture *via* reaction with fluoride-sensitive trigger **51** or PGA trigger **54** in isolated yields of 15% and 17% respectively (Scheme **27**).

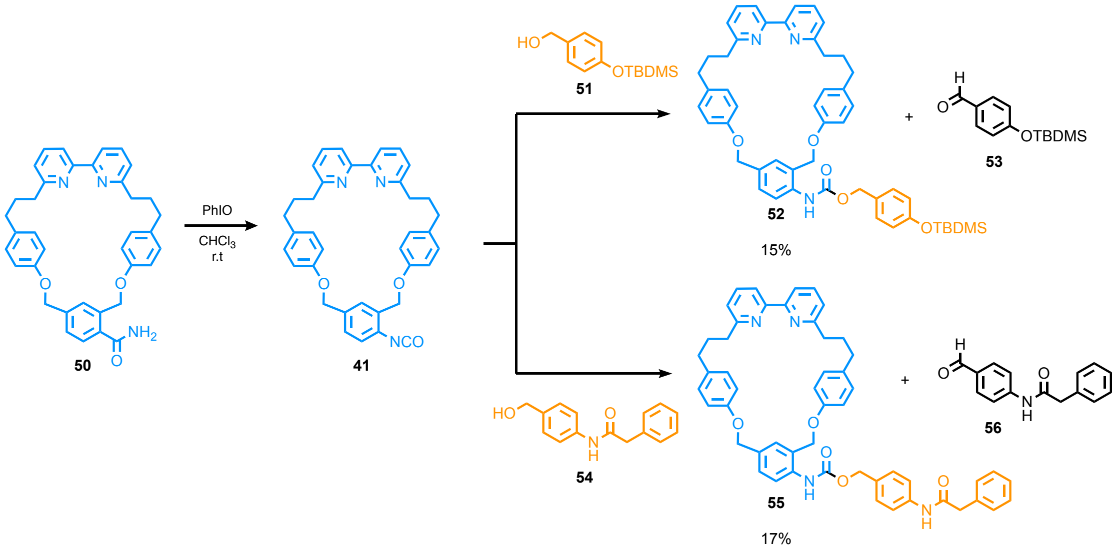

Scheme **28**. Synthesis of carbamate macrocycles **52** and **55** *via* direct reaction of triggers **51** and **54** with isocyanate intermediate **41**. One-pot reaction conditions: Carboxamide **50** (1.0 eq.), trigger **51** or **54** (2.0 eq.), PhIO (2.0 eq.) in $CHCl_3$, 2 h at r.t.

A screening of reaction solvents found that the formation of isocyanate **41** was observed only in chlorinated solvents ($CHCl_3$, CH_2Cl_2). Although the transformation has been reported in various non-chlorinated solvents, negligible conversion of carboxamide **50** was observed when attempted in THF, CH_3CN and acetone. Qualitative assessment suggests this is due to the insolubility of PhIO in these non-chlorinated solvents. The oxidation of benzylic alcohols **51** and **54** to the corresponding aldehydes was found to be a significant side-reaction, which is unsurprising given the utility of hypervalent iodine reagents as oxidants for alcohols.[102] The poor conversion of **50** observed in the crude ^1H NMR spectra is likely due to this undesired consumption of PhIO. Increasing the eq. of PhIO (4.0 eq.) led to full consumption of **50**. However, significantly more aldehyde formation was observed and isolated product yields remained <17%.

To overcome this incompatibility, benzylic alcohols and other readily oxidizable functionalities should be avoided when using PhIO. Instead of installing the desired trigger alcohol *via* direct reaction with isocyanate intermediate **41**, an activated carbamate macrocycle could be synthesised. Ideally, this activated species should be stable enough to purify and store but will also readily undergo substitution with the trigger alcohols to afford the desired macrocycle. Activated phenyl carbamates are versatile intermediates in the formation of carbonates and carbamates and should be ideal in this regard.[103] The attempted formation of phenyl carbamates **59** or **60** *via* one-pot reaction with phenols **57** or **58** was unsuccessful (Scheme **29**). Negligible consumption of starting material **50** was observed in both cases, even after extending the reaction time to 4 h. The reaction with *p*NO_2-phenol (**61**) was successful. ^{1}H NMR analysis of aliquots taken from the crude reaction mixture indicate that full consumption of **50** was observed within 1 h at room temperature using 3.5 eq. of PhIO and phenol **61** respectively (Figure **251**). LC-MS also confirmed that *p*NO_2-phenyl carbamate macrocycle **62** was the major species in the mixture. However, attempts to isolate macrocycle **62** were unsuccessful due to its apparent instability toward silica gel (including deactivated silica).

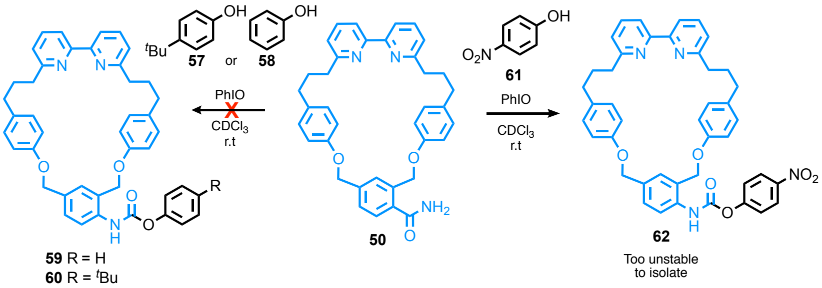

Scheme **29**. Attempted synthesis of activated phenyl carbamate macrocycles **59**, **60** and **62**. Reaction conditions: **50** (1.0 eq.), PhIO (3.5 eq.), Phenol (3.5 eq.), $CDCl_3$, r.t.

In the first instance, it is possible that more nucleophilic phenols **57** and **58** are reacting with PhIO to form adduct species, inhibiting the formation of isocyanate **41**. Interestingly, a control experiment performed under identical conditions in the absence of any alcohol also showed poor consumption of **50**, which may suggest that the presence of the nucleophilic phenol is not the sole problem. One major difference between the entries is the rate at which the initially heterogeneous reaction mixture becomes homogenous. Assessed qualitatively, poorly converting entries **1**, **2** and **4** remained heterogeneous even after stirring for several hours, whereas entry **3**, which went to full conversion, became homogenous after stirring for several minutes. This may suggest that *p*NO_2-phenol **61** plays a role in solubilising the heterogeneous reaction mixture through hydrogen-bonding interactions with PhIO. The quenching of isocyanate **41** with phenol **61** is also likely to drive the reaction toward complete consumption of starting material **50**.

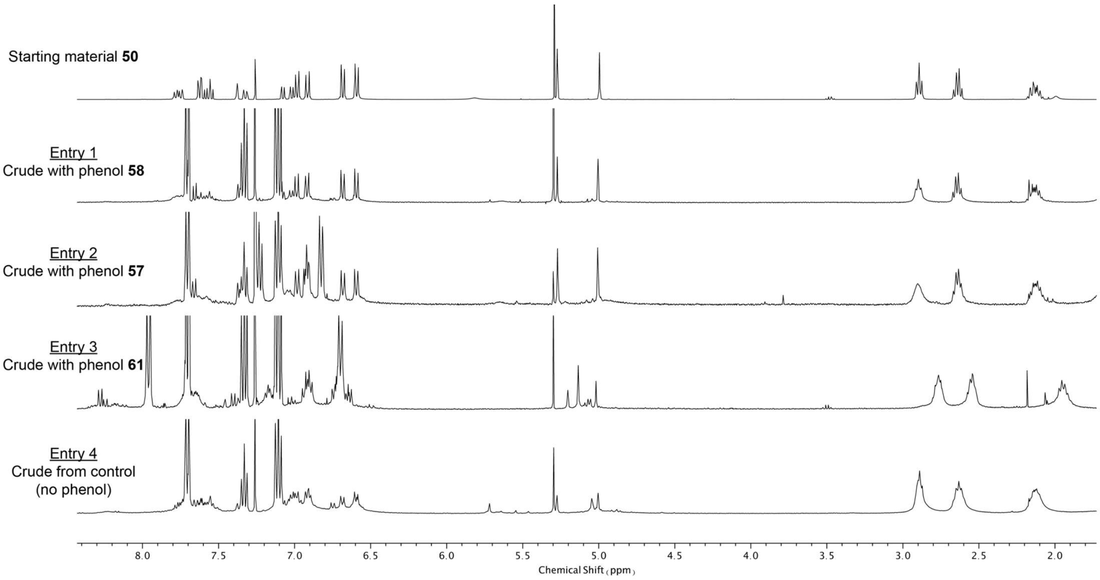

Figure **251**. ^{1}H NMR stack plot in $CDCl_3$ (δ range = 8.5-1.5 ppm) showing starting material **50** overlaid with the crude mixtures from reactions with phenol **57**, **58** or **61** and control reaction with no phenol.

In situ displacement of *p*NO_2-phenyl carbamate **62** could be achieved through the addition of phenol **58** and DIPEA to the crude reaction mixture, facilitating the formation of phenyl carbamate **59**, which could not be synthesised directly (Scheme **30**). Phenyl carbamate **59** was stable enough to be isolated *via* silica-gel chromatography and, after reaction optimisation, was isolated in a 64% yield. When stored under N_2 in the absence of moisture, phenyl carbamate **59** did not show any sign of degradation.

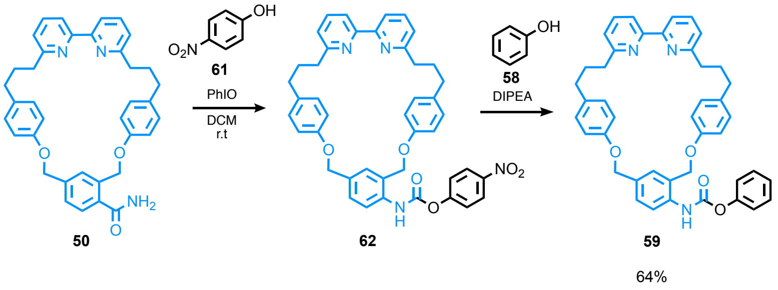

Scheme **30**. Optimised synthesis of phenyl carbamate macrocycle **59**. Optimised conditions: PhIO (2.0 eq.), **61** (3.5 eq.), CH_2Cl_2, r.t. for 2h, then add **58** (5.0 eq.) and DIPEA (3.0 eq.), r.t. for 2h.

The Curtius rearrangement can similarly be employed to generate isocyanates *via* the thermal rearrangement of acyl azides and was later investigated as a more convenient method to generate phenyl carbamate macrocycle **59**.[104] Using diphenylphosphoryl azide (DPPA) to convert the carboxylic acid directly into the acyl azide is a common approach.[105] Treatment of carboxylic acid macrocycle **48** with DPPA and phenol **58** in a one-pot method successfully led to the formation of isocyanate **41**, which was subsequently quenched *in situ* by phenol **58** (Scheme **31**). After reaction optimisation, macrocycle **53** was isolated in a 90% yield.

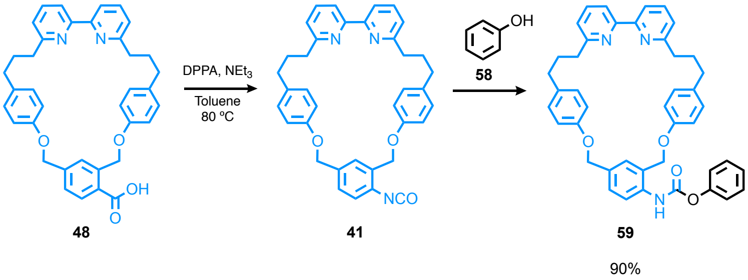

Scheme **31**. Curtius rearrangement of macrocycle **48** to generate **59**. Optimised conditions: one-pot mixture of DPPA (1.3 eq.), NEt$_3$ (1.3 eq.) and phenol **58** (3.0 eq.) in toluene at 80 °C 2 h.

Phenyl carbamate **59** readily underwent displacement *via* reaction with the appropriate trigger alcohol to afford the desired cleavable macrocycle. To demonstrate the utility of this platform approach, a small library of cleavable macrocycles bearing different stimuli-responsive units (UV, chemical, pH, enzyme) was synthesised in 63-77% yield (Figure **252**). Prior to protecting group cleavage, all macrocycles could be isolated *via* silica-gel chromatography and were stable when stored under N$_2$ at room temperature.

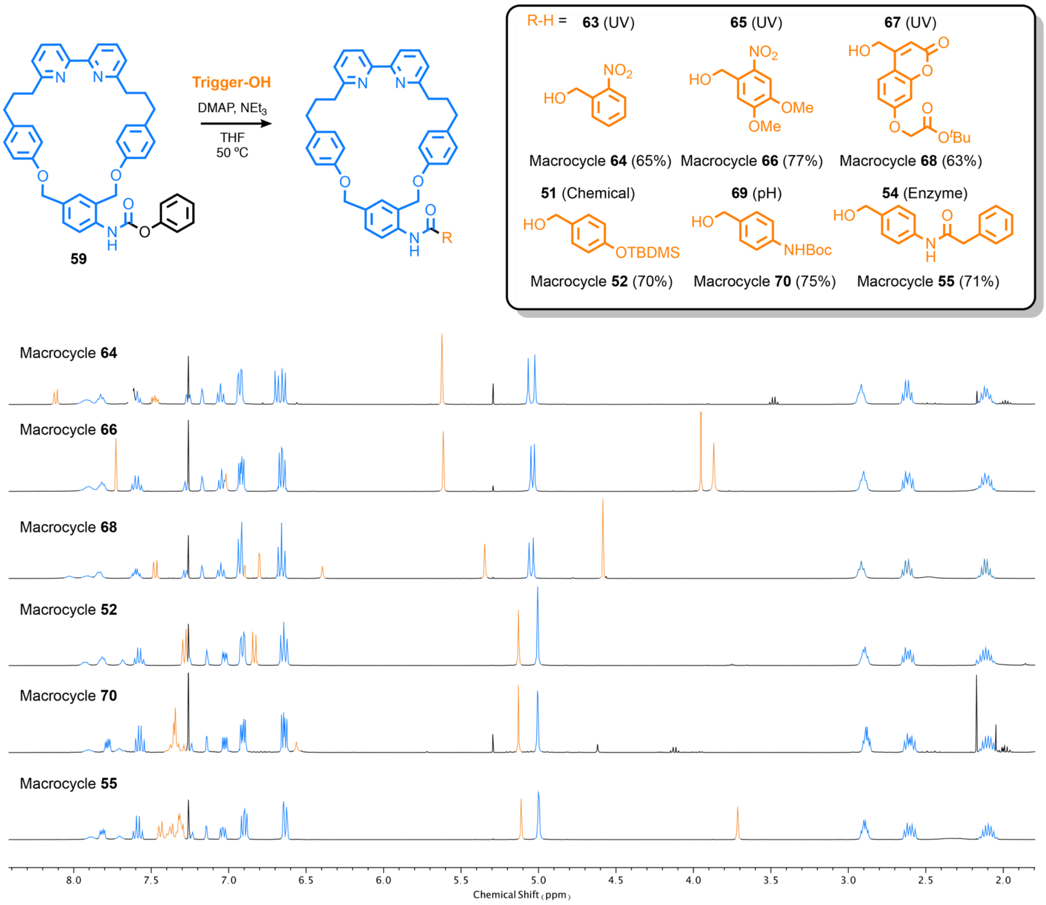

Figure **252**. Synthesis of a small library of cleavable macrocycles *via* displacement of phenyl carbamate macrocycle **59** with the appropriate trigger alcohol. Stacked ^{1}H NMR spectra (δ range = 8.5-1.8 ppm) of cleavable macrocycles is shown. Signals in blue = macrocyclic backbone, orange = trigger motif.

3.2.2. Rotaxane Synthesis (1st Generation)

The ability of macrocycles **52, 66**, **68** and **70** to mediate the AT-CuAAC rotaxination of model half-stoppers **71** and **72** was then investigated using $[Cu(CH_3CN)_4]PF_6$ as the source of Cu^I. The reaction was found to proceed efficiently, with full conversion observed for all macrocycles when used with 1.5 eq. of stoppers **71** and **72**. The corresponding rotaxanes (**73**-**76**) were isolated in a 45-65% yield (Figure **253**). Rotaxane **76** required several iterative attempts at silica-gel purification to completely remove non-interlocked macrocycle **70**, resulting in a lower yield of 45%. Overall, the results suggest that the peripheral site of functionalisation is far enough from the bipyridine unit so that it does not greatly interfere with the AT-CuAAC process, even in the presence of sterically bulky groups, such as in macrocycle **68**.

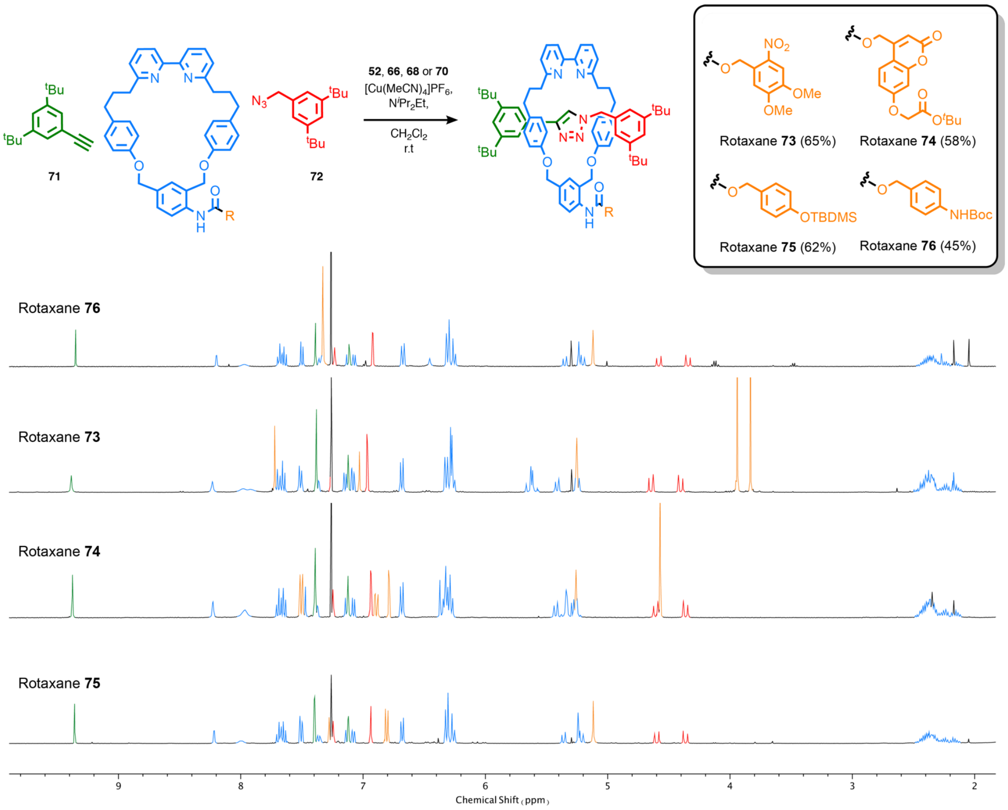

Figure **253**. Synthesis of cleavable rotaxanes *via* AT-CuAAC reaction of half-stoppers **71** and **72** with the appropriate macrocycle. ^{1}H NMR stack plot of rotaxanes **73**, **74, 75** and **76** in $CDCl_3$ is shown (δ range = 9.8-1.8 ppm). Signals are colour-coded to represent the different components of the interlocked structures. Blue = macrocycle backbone, orange = trigger motif, green/red = axle.

The ^{1}H NMR stack above suggests that the chemical environment of the mechanical bond in the four interlocked structures is quite similar. In each structure, the chemical shift of the triazole proton (δ ≈ 9.35 ppm) remains within ± 0.01 ppm of each other. With the exception of rotaxane **73**, the chemical shift of the remaining protons within the axle and the macrocyclic backbone also remain quite constant. Some signals in rotaxane **73** are deshielded relative to the other structures. Most notably the macrocyclic benzylic ether positions and the benzylic position in the axle, which may be due to interaction with the proximal -NO_2 group. All other signals are consistent with the other interlocked structures. Overall, the solution-phase conformity between interlocked structures suggests that the four macrocycles (**73-76**) adopt analogous conformations when interlocked, which appears to be largely independent of the peripheral trigger motif.

3.2.3. Rotaxane Cleavage Experiments (1st Generation)

Upon trigger cleavage, the ring-opening behaviour of aniline macrocycle **38** may differ considerably when interlocked, as was highlighted in the chapter 2. As such, the ring-opening capability was studied in rotaxanes **73**-**76**, where success could be quantified by the amount of axle released upon exposure to a given stimulus: **76** in response to acidic pH; **75** in response to a fluoride source; **73** and **74** in response to the appropriate wavelength of UV light. Due to its poor solubility under aqueous conditions, enzymatic cleavage experiments with macrocycle **55**, or the corresponding rotaxane, could not be attempted.

3.2.4. Acidic Cleavage of Rotaxane 76

The trigger group of rotaxane **76** consists of a self-immolative 4-aminobenzyl spacer protected with an acid-sensitive *tert*-butyloxycarbonyl (Boc) group. Cleavage of the NH-Boc group in acidic media should initiate a cascade elimination that results in the formation of aniline rotaxane **77**, which subsequently decomposes *via* an azaquinone methide pathway to release axle **78**. A solution of rotaxane **76** in $CDCl_3$ was treated with TFA (3.0 eq.) at room temperature. Its decomposition was monitored was *via* ^{1}H NMR and LC-MS (Figure **254**). When no further changes in sample composition were observed *via* ^{1}H NMR, the mixture was neutralized *via* filtration over K_2CO_3.

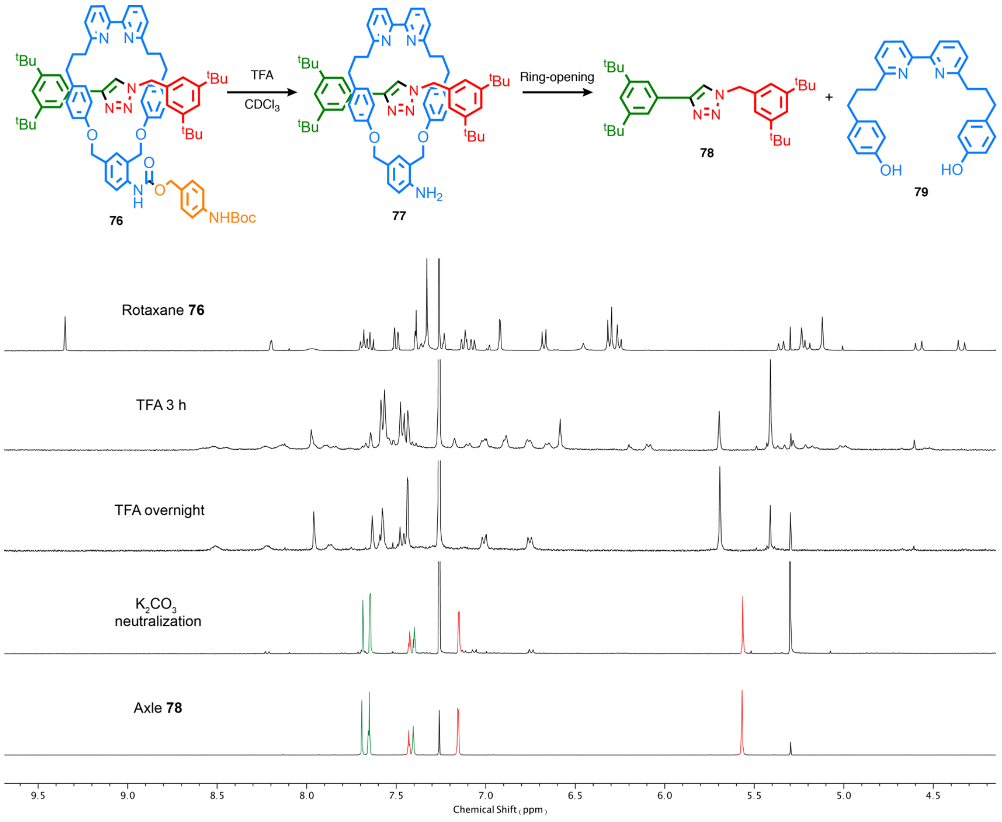

Figure **254**. Acid-triggered ring-opening of rotaxane **76**. ^{1}H NMR stack (δ range = 9.7-4.2 ppm) showing the decomposition of rotaxane **76** to release axle **78** upon treatment with TFA (3.0 eq.) in $CDCl_3$.

LC-MS analysis confirmed the absence of rotaxane **76** after 3 h and found aniline rotaxane **77** and axle **78** as the major species in the mixture. After leaving to stand overnight, only axle **78** and bis-phenol decomposition product **79** were detectable *via* LC-MS. No further changes to the ^{1}H NMR spectra were observed after this point, which also suggested that full release of axle **78** had occurred. The ^{1}H signals of axle **78** were significantly shifted in the acidic media — filtration of the crude mixture over K_2CO_3 neutralised the mixture and restored signals to their expected shifts. Due to its poor solubility in neutral $CDCl_3$, bis-phenol **79** precipitated and was removed upon filtration over K_2CO_3. Overall, the results indicate that free-aniline rotaxane **77** does undergo ring-opening to liberate the axle component. However, under acidic conditions this process is slow. This could be due to protonation of the aniline motif, reducing the electron-donating ability of the SI linker and impeding the ring-opening elimination pathway, resulting in the slow liberation of axle **78**.

3.2.5. Photocleavage of Rotaxanes **73** and **74**

Macrocycles **64**, **66** and **68** are joined through a carbamate linkage to the well-established photocleavable triggers *ortho*-nitrobenzene (*o*NB), 4,5-dimethoxy-2-nitrobenzyl (DMNB) and 7-alkoxycoumarin respectively.[106–108] The UV-Vis absorption spectra of macrocycles **64**, **66** and **68** in $CHCl_3$ are shown below (Figure **255**).

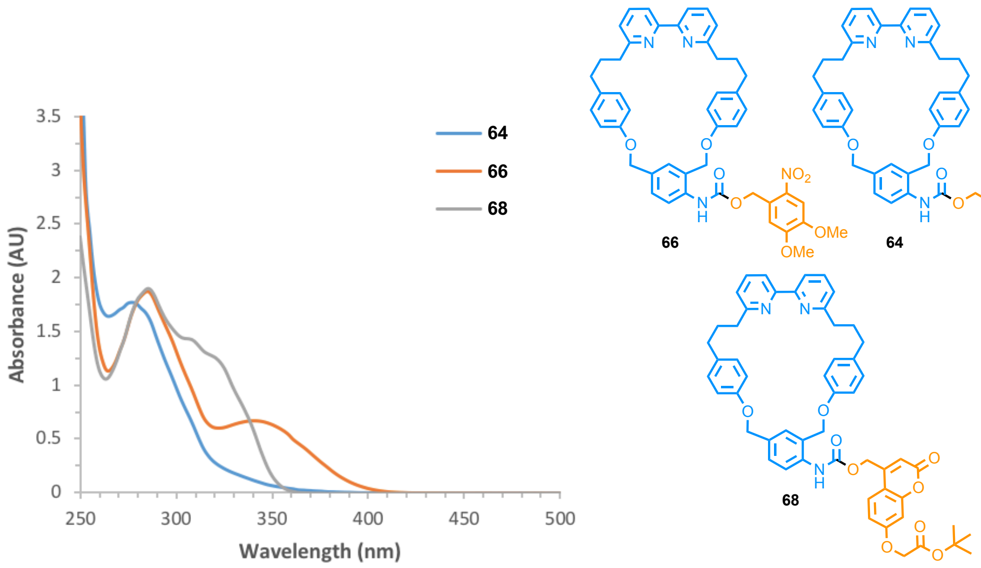

Figure **255**. UV-Vis absorption spectra of macrocycles **64**, **66** and **68** in $CHCl_3$.

The deprotection of the unmodified *o*NB PPG is associated with poor quantum yields.[109] The optimal deprotection wavelength is also highly dependent on the leaving group of the caged species, with *o*NB-caged carbamates reported to cleave most effectively under high-energy UVC irradiation ($\lambda_{max} \approx 254$ nm).[110] Due to a lack of appropriate photolysis equipment, this experiment was not attempted, nor was the corresponding rotaxane of macrocycle **64** synthesised. Macrocycle **66** contains the DMNB group, a derivative of *o*NB that has been reported as an effective PPG to release carbamates, with absorption bands that show a λ_{max}

of ≈ 350 nm, which is concurrent with the absorption spectra above.[111] Macrocycle **68** contains a 7-alkoxycoumarin derivative that has also been reported as an efficient PPG for carbamates. The reported absorption bands with λ_{max} of ≈ 315 nm also agree with the above spectra.[107] Photolysis experiments were performed on the corresponding rotaxanes, **73** and **74**, using an appropriate UV source.

Samples of **73** in MeOD or CD_3CN: D_2O (9:1) were irradiated with a UVA lamp (2 x 9W, λ_{max} = 365 nm) for 3 h, and the release of axle **78** was monitored *via* ^1H NMR and LC-MS (Figure **256**). Significant peak broadening of rotaxane **73** and aniline **77** signals was observed in the ^1H NMR spectra of the crude photolytic mixtures, meaning that accurate values for the relative amount of each species in the crude mixture could not be obtained. However, qualitative ^1H NMR assessment does suggest that axle **78** is the major species in both crude photolytic mixtures and that more axle was released in MeOD than in CD_3CN: D_2O (9:1). More polar solvent mixtures are expected to enhance the rate of self-immolative elimination from aniline rotaxane **77** by stabilising partial charges in the transition states, which would account for the greater amounts of axle **78** released. Although the removal of DMNB appears to be slow, it is roughly in line with previously reported DMNB-caged carbamates.[111] It should be noted that only trace amounts of bis-phenol decomposition product (**79**) could be detected in the crude mixtures. This may indicate that the non-interlocked decomposition product does not undergo sequential eliminative cleavage to release the second phenol. Alternatively, once formed bis-phenol **79** may undergo another unknown transformation.

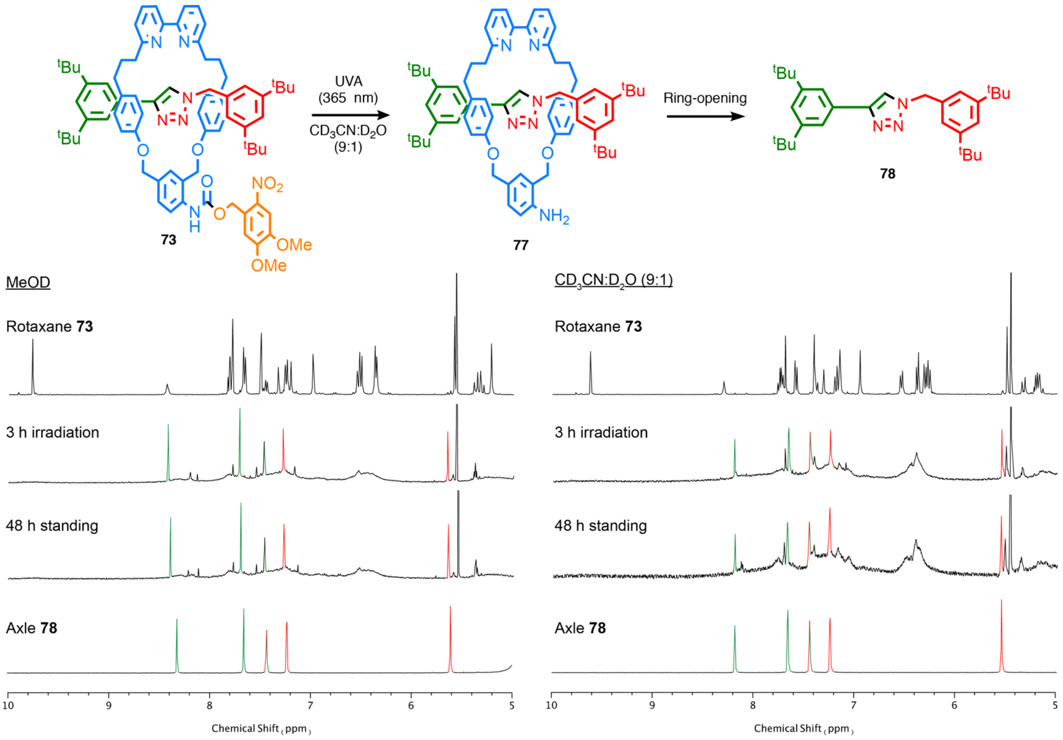

Figure **256**. Release of axle **78** upon photo-irradiation (365 nm) of rotaxane **73**. ^{1}H NMR stack plots (δ range = 10.0-5.0 ppm) in MeOD (left) and CD_3CN: D_2O (9:1) (right).

LC-MS analysis confirmed axle **78** as a major species in both mixtures and also indicated that aniline rotaxane **77** was present alongside rotaxane **73** (Figure **257**). Several other species with m/z values within a ± 100 m/z range of rotaxane **73** ($[M+H]^+$ m/z = 1139.7) and free-aniline rotaxane **77** ($[M+H]^+$ m/z = 1000.6) were also detected. However, these signals could not be correlated with any structures and are assumed to be photo-decomposition products from unknown pathways. Leaving to stand at room temperature for 48 h resulted in no change in the composition of either mixture. LC-MS analysis confirmed that significant amounts of aniline rotaxane **77** remained, which is surprising given it is expected to decompose to release axle **78**. Protonation of the aniline functionality of **77**, which may be indicated by the broadening of rotaxane signals in the ^{1}H NMR spectra, could inhibit the self-immolative ring-opening mechanism, preventing the release of axle **78**. Another plausible explanation is that aniline rotaxane **77** is simply too stable under the employed conditions.

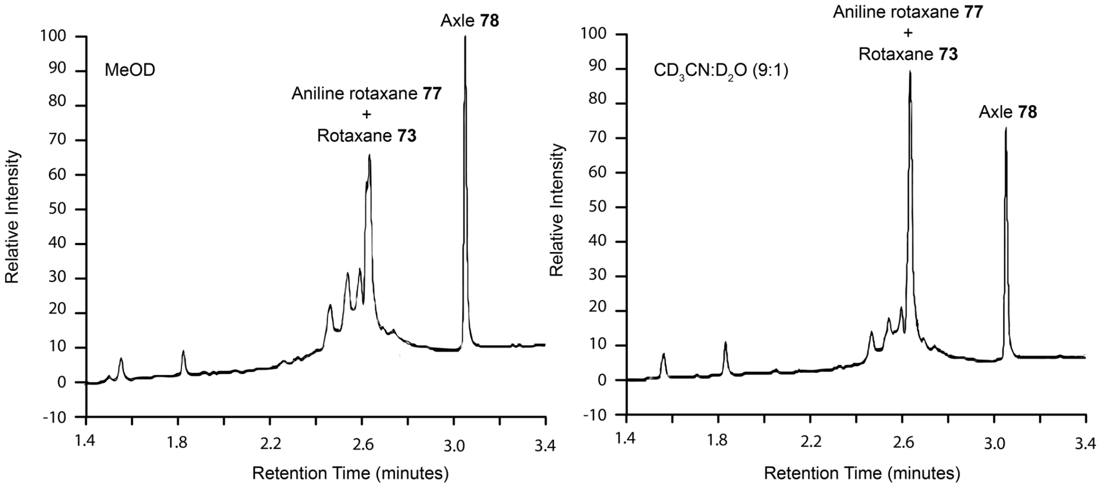

Figure **257**. UV trace from LC-MS analysis of crude photolytic mixtures after UVA irradiation of rotaxane **73** for 3 h. Relevant peaks have been annotated.

Given that significant axle release was observed only during photolysis, it is likely that the azaquinone-methide elimination of free-aniline **77** is accelerated under UV irradiation, which has been previously reported in the literature.[112] To confirm this, the crude photolytic mixture in MeOD was irradiated for an additional 1 h and re-analysed *via* LC-MS (Figure **258**). After additional irradiation, significantly more axle **78** was present in the mixture relative to rotaxane **73** and aniline **77**, which are present in relatively small amounts. When left to stand for a further 1 week, the relative amount of aniline rotaxane **77** remained constant, further indicating its stability in the absence of UVA light.

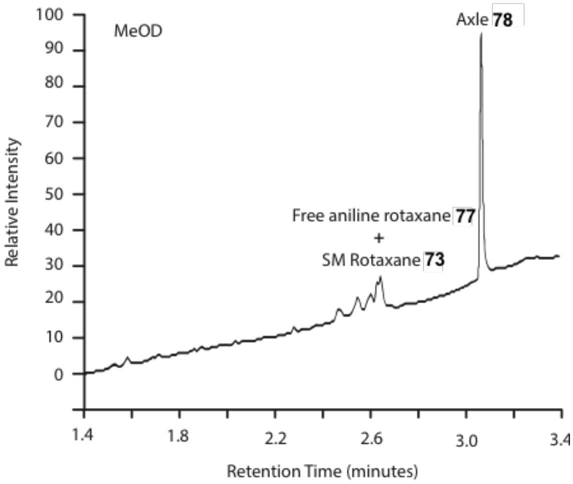

Figure **258**. UV trace from LC-MS analysis of crude photolytic mixture (**73**) in MeOD after additional UVA irradiation for 1 h. Relevant peaks have been annotated.

Samples of rotaxane **74** in MeOD or CD$_3$CN: D$_2$O (9:1) were irradiated with a narrowband UVB lamp (λ_{max}= 315 nm) for 3 h, and the release of axle **78** was monitored *via* ^{1}H NMR and

LC-MS (Figure **259**). Similar to the previous photolysis experiment, peak broadening in the ^1H NMR spectra of crude photolytic mixtures made it difficult to quantitatively assess the composition of the mixture. Qualitative assessment suggests that the release of axle **78** is slower than in the previous experiment, particularly in CD_3CN: D_2O (9:1), where rotaxane **74** is the predominant species. This is expected given the poorer quantum yields associated with photocleavage of the coumarin PPG.[107] The greater amount of axle **78** released in MeOD relative to CD_3CN: D_2O (9:1) again suggests that the rate of PPG cleavage and/or ring-opening is faster in the more polar solvent. In contrast to the previous photolysis experiment, compositional changes to the ^1H NMR spectra of both solvent mixtures were observed when left to stand at room temperature. The ring-opening pathway corresponds to a minor amount of this change, as the relative amount of axle **78** appears to remain fairly constant.

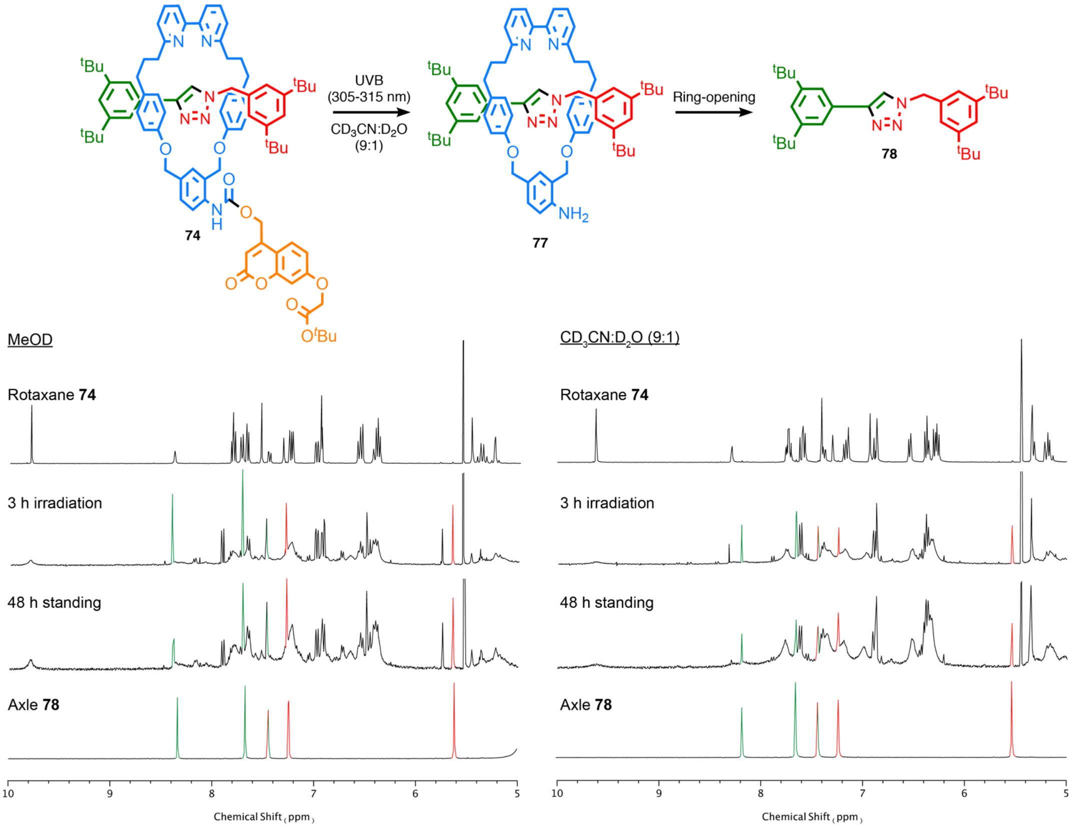

Figure **259**. Release of axle **78** upon photo-irradiation (315 nm) of rotaxane **74**. ^1H NMR stack plots (δ range = 10.0-5.0 ppm) in MeOD (left) and CD_3CN: D_2O (9:1) (right).

LC-MS analysis of the MeOD mixture denoted only minor compositional changes when left to stand for one week (Figure **260**). A slight decrease in the amount of aniline **77** and an increase in the amount of axle **78** was observed relative to rotaxane **74** — indicative of a minor amount of the ring-opening pathway occurring. Aniline **77** remained the predominant species after one week, further indicating its stability under the employed conditions. LC-MS also detected the formation of a new major species ($[M+H]^+$ m/z = 1288.7), corresponding to recombined rotaxane **82**.

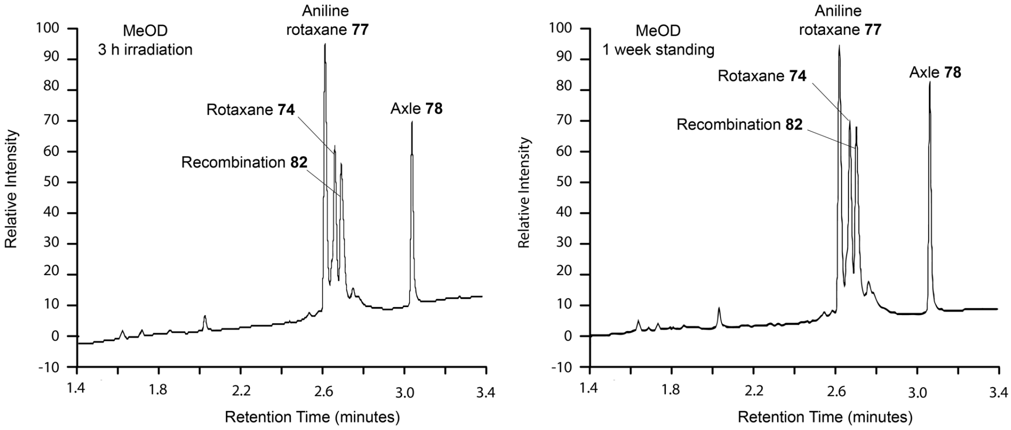

Figure **260**. UV trace from LC-MS analysis of crude photolytic mixture in MeOD after irradiation for 3 h (left) and when left to stand for one week (right). Relevant peaks have been annotated.

This species was likely produced *via* nucleophilic attack of aniline **77** on the carbocation generated through photolytic cleavage of the coumarin PPG (Scheme **32**). Under the conditions, it is expected that carbocation intermediate **81** would react rapidly with nucleophilic solvent molecules to form the corresponding product, making the formation of **82** highly surprising. Recombined rotaxane **82** was stable in solution. Lacking an appropriate leaving group, the new chromophore was also found to be non-photolabile and prevented the release of axle **78** from **82** upon additional UVB irradiation.

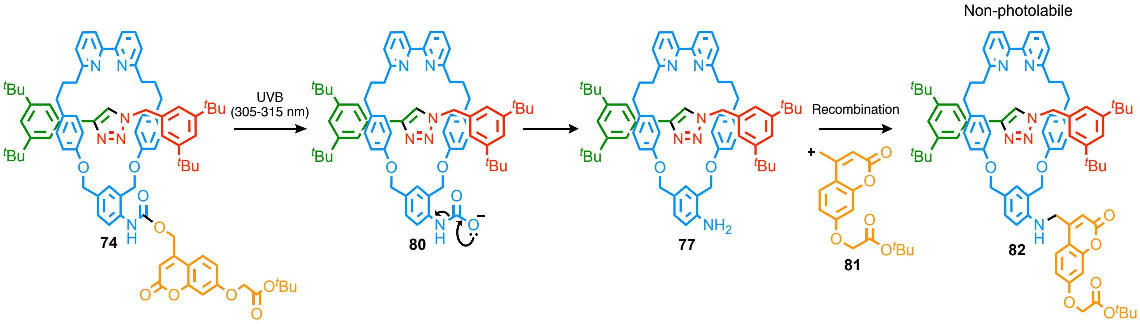

Scheme **32**. Plausible pathway for the formation of recombined rotaxane **82**.

No such recombination products were detected in the photolysis of rotaxane **73**, which is likely due to the different photocleavage mechanisms. Photocleavage of the coumarin moiety in **77** proceeds *via* an excited state *meta* pathway,[113] resulting in heterolytic C-O bond cleavage and generating reactive carbocation species **81** and carbamic acid **80**, which undergoes spontaneous decarboxylation to produce aniline **77** (Scheme **32**). The majority of recombination between **77** and **81** occurs under UVB irradiation, with the relative amount of **82** in the mixture increasing only marginally after one week. In contrast, the photocleavage of the DMNB group is known to proceed *via* a Norrish type II pathway, generating a nitroso aldehyde by-product (**83**).[111] While the recombination of aniline **77** and aldehyde **83** to generate imine **84** is possible, it is a reversible process, whereas the formation of stable secondary amine **82** is irreversible (Scheme **33**).

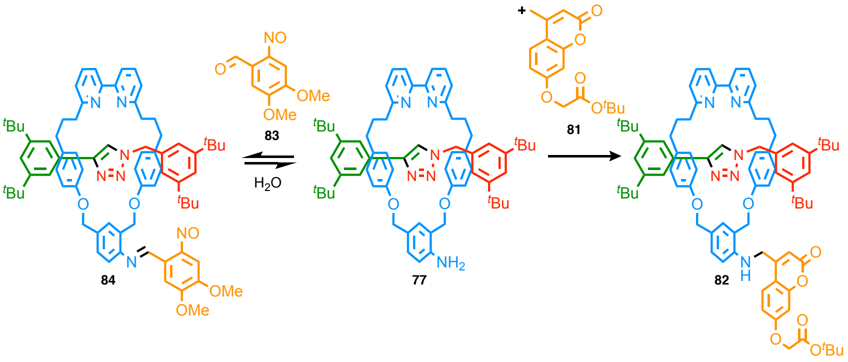

Scheme **33**. Differences in the photodecomposition by-products of rotaxanes **73** and **74**. Rational to justify the formation of recombined rotaxane **82**.

In summary, the PPGs in rotaxanes **73** and **74** were both shown to cleave effectively in response to the appropriate wavelength of UV light to afford aniline rotaxane **77**. The ring-opening mechanism to release axle **77** occurred primarily only when the mixture was actively being irradiated — suggesting that aniline rotaxane **77** is stable under the employed conditions in the absence of UV light. In the case of rotaxane **74**, the recombination of aniline **77** with photocleavage by-product **81** was found to be a significant side reaction that rendered the rotaxane architecture photolytically inert, trapping the axle.

3.2.6. Chemical Cleavage of Rotaxane 75

Analysing the decomposition of aniline **77** proved difficult with photocleavable rotaxanes **73** and **74** due to the slow rate of photolytic deprotection combined with the competing mechanistic pathways that inhibited axle release. Rotaxane **75**, containing the *tert*-butyldimethylsilyl (TBDMS) ether trigger group, is a promising alternative to study the ring-opening process as fluoride-mediated deprotection of silyl groups is clean and typically occurs within minutes.[114] Furthermore, silyl deprotection has been reported to proceed smoothly under aqueous buffer conditions, allowing decomposition to be monitored at neutral pH.[115] Rotaxane **75** in THF-d_8: D_2O (3:1) was treated with TBAF and stirred at 37 °C

(Scheme **34**). Aliquots were taken at given time intervals and analysed *via* ^{1}H NMR and LC-MS.

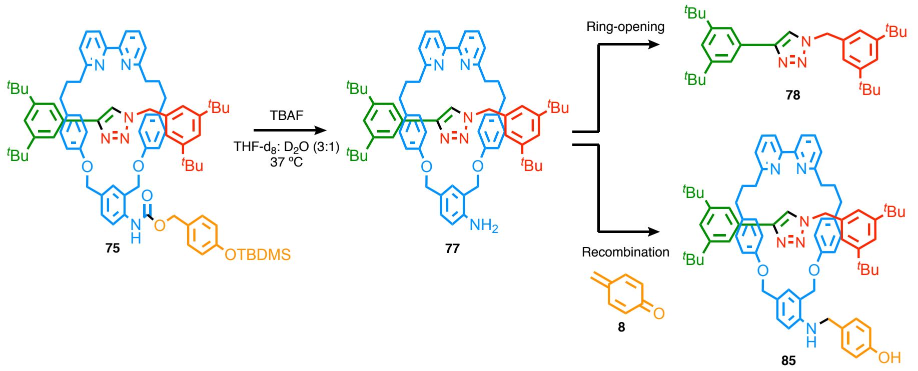

Scheme **34**. Fluoride-triggered deprotection of rotaxane **75** with TBAF (3.0 eq.) in THF-d_8: D_2O (3:1). The competing mechanistic pathways of aniline rotaxane **77** are shown.

Aliquots were taken at given time intervals and analysed *via* ^{1}H NMR and LC-MS. Full cleavage of the TBDMS group was observed within 1 h, resulting in the formation of aniline **77** as the sole interlocked species (Figure **261**). When left to stir for 24 h, ^{1}H NMR analysis showed the formation of a second triazole signal (δ ≈ 9.46 ppm), indicating the formation of a second interlocked species (**85**) which was indefinitely stable in solution. The relative amount of this species further increased after 48 h. No release of axle **78** could be observed *via* ^{1}H NMR, with significant amounts of aniline **77** remained after stirring for several days.

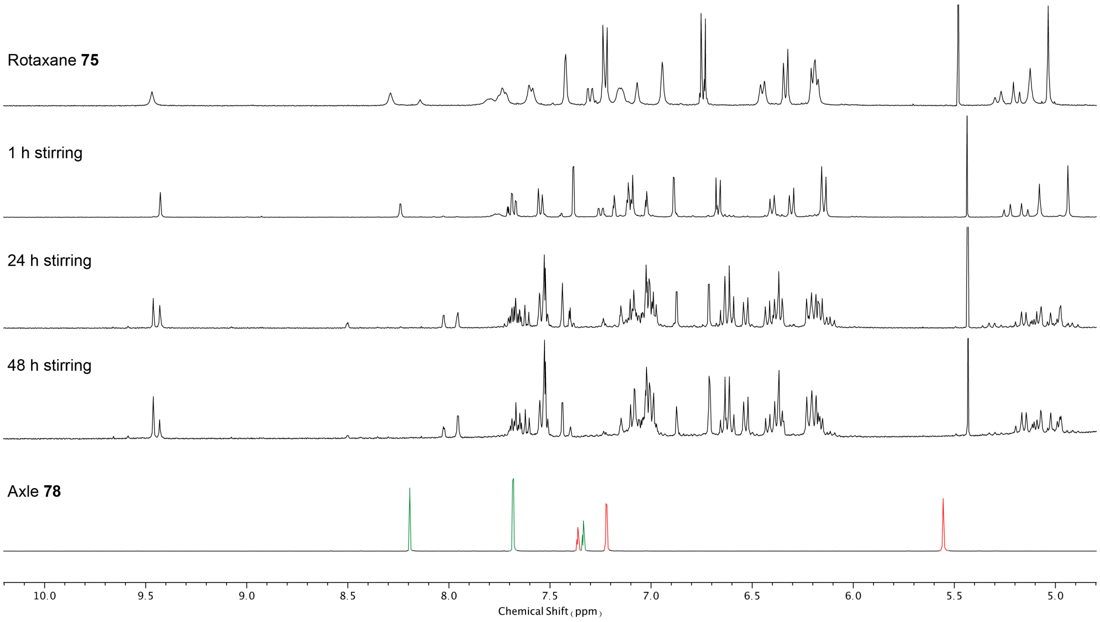

Figure **261**. ^{1}H NMR stack plot (δ range = 10.2-4.8 ppm) of rotaxane **75** when treated with TBAF (3.0 eq.) in THF-d_8: D_2O (3:1), overlaid with axle **78**.

LC-MS analysis identified the second interlocked species as rotaxane **85** ($[M+H]^+$ m/z = 1108.1), formed through the recombination of aniline **77** with reactive quinone methide intermediate **8**. In contrast to photolytically generated recombination product **82**, the formation of **85** occurred much slower. The fate of quinone-methide **8** is highly dependent on the aqueous composition and pH of the media, as well as the presence of other nucleophilic species.[116] The reaction with bulk H_2O (or D_2O) to form the corresponding benzylic alcohol (**9**) is known to be reversible, which would explain the gradual formation of recombined rotaxane **85** (Figure **262**).[117] Substituents on the *para*-quinone methide and the structure of the reacting amine dictate whether the formation of the alkylated adduct is reversible or essentially irreversible.[118] In the case of aniline **77**, it appears to be the latter. Performing the release experiments with D_2O or buffered D_2O (pD = 7.2) had no apparent impact on the amount of axle **78** released or the composition of species in the mixture.

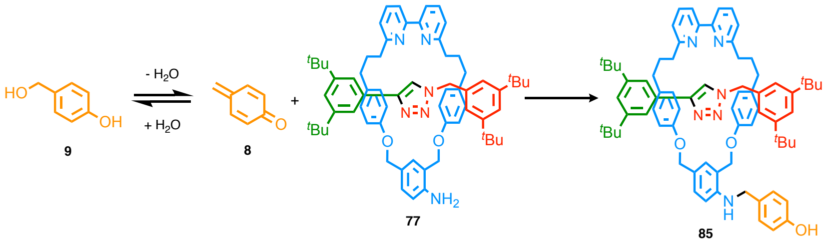

Figure **262**. Formation of recombined rotaxane **85** from aniline **77** and quinone methide **8**.

3.2.7. 2nd Generation Macrocycles

Upon cleavage of trigger motif, aniline rotaxane **77** was capable of releasing axle **78** only under certain conditions (low pH, UV light). At neutral pH in the absence of UV light, the ring-opening pathway was negligible and also found to be competing with the formation of a recombined species, which prevented the macrocyclic component from opening. To facilitate release under these conditions, the electronic properties of the macrocycle must be modified to enhance the rate of ring-opening (Figure **263**). The addition of electron-donating groups (EDGs) *ortho* and *para* to the benzylic ethers (e.g., OMe groups) will increase electron density in these positions, stabilising the formation of the corresponding azaquinone methide intermediate. Positioning electron-withdrawing groups (EWGs) *ortho* to the phenolic ether should also increase the acidity of the phenolate, enhancing the nucleofugality of the leaving group.

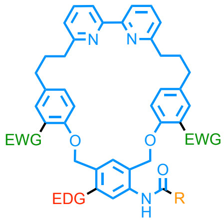

Figure **263**. Sites of possible modification to enhance rate of ring-opening.

3.2.8. Macrocycle Synthesis (2nd Generation)

A route to methoxy-modified linker **96** was devised (Scheme **35**). Stoichiometric nitration of **87** with NH_4NO_3 and H_2SO_4 gave an inseparable regioisomeric mixture of **88** and **89** (2.5:7.5) in 96% yield. Fischer esterification of the mixture afforded the regioisomers **90** and **91** (2.5:7.5) in 95% yield, which subsequently underwent transfer hydrogenation over Pd/C. **92** could be separated from the unwanted regioisomer *via* silica-gel chromatography and was isolated in 54%. Treatment of **92** with $NaNO_2$ and H_2SO_4 generated a diazonium salt, which was then heated in aqueous sulfuric acid to afford a mixture of **93** and **94** (3:2). Alkylation of the crude mixture with MeI afforded **95** in 94% yield over the two steps. Bromination of **95** with NBS afforded linker **96** in 68% yield.

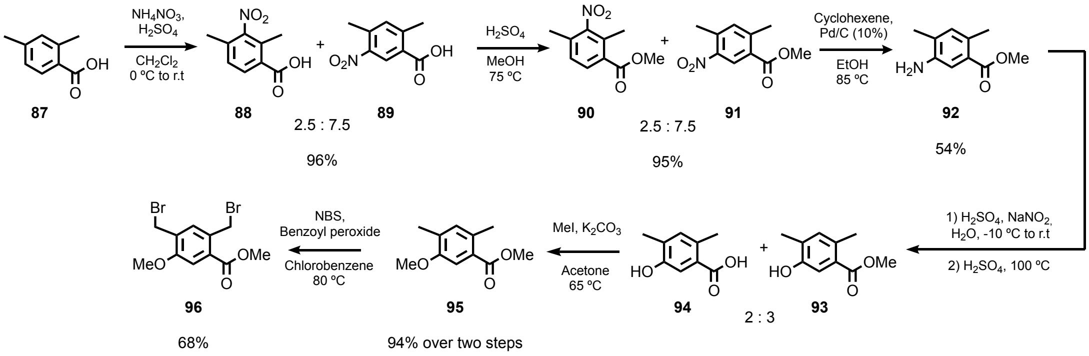

Scheme **35**. Synthesis of methoxy-modified linker **96**.

The incorporation of linker **87** into the macrocycle structure was analogous to that of linker **44** (Scheme **36**). Alkylation of **45** with **96** proceeded in 55% yield to give precursor **97**, which then underwent Ni-mediated macrocyclisation to afford **98** in 48% yield. Ester hydrolysis under basic conditions afforded carboxylic acid **99** in 95% yield, which subsequently underwent Curtius rearrangement in presence of phenol **58** under optimised conditions to generate methoxy-modified macrocycle **100** in 62% yield.

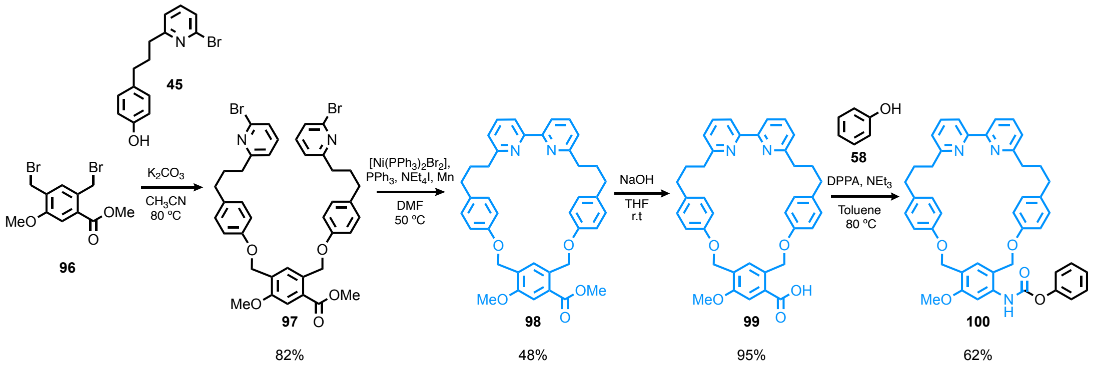

Scheme **36**. Synthesis of methoxy-modified macrocycle **100**.

A route to fluorinated phenol fragment **108** was also devised (Scheme **37**).[7] Reduction of commercially available **103** with $LiAlH_4$ gave alcohol **104** in 65% yield. Oxidation of **104** to aldehyde **105** was achieved in 72% yield using DMP. Phosphonium ylide **102** was prepared by stirring **101** with PPh_3 overnight, followed by the addition of potassium *tert*-butoxide. Addition of **105** to the crude mixture of **102** afforded **106** in 62% yield. Reduction of **106** with $TsNHNH_2$ gave **107** in 88% yield, which then underwent deprotection with BBr_3 to afford phenol **108** in 92% yield.

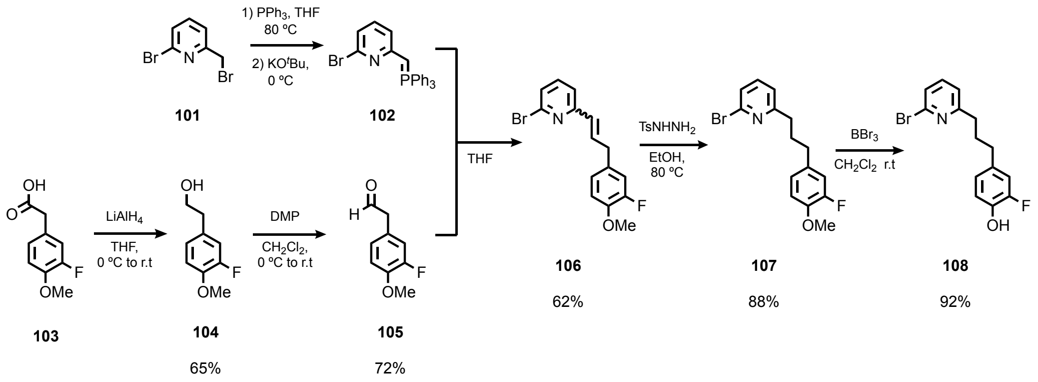

Scheme **37**. Synthesis of fluorinated phenol fragment **108**.

Synthesis of fluorinated macrocycle **112** proceeded as before (Scheme **38**). Alkylation of **108** with **44** proceeded in 84% yield to afford precursor **109**, which then underwent macrocyclisation to give **110**. Difficulty in separating **110** from PPh_3O led to a lower isolated yield of 34%. Basic ester hydrolysis afforded carboxylic acid **111** in 92% yield, which then underwent Curtius rearrangement in presence of phenol **58** under optimised conditions to generate macrocycle **112** in 42% yield.

---

[7] Synthesis and route optimisation of fluorinated phenol **108** was performed by Dr. Noël Pairault.

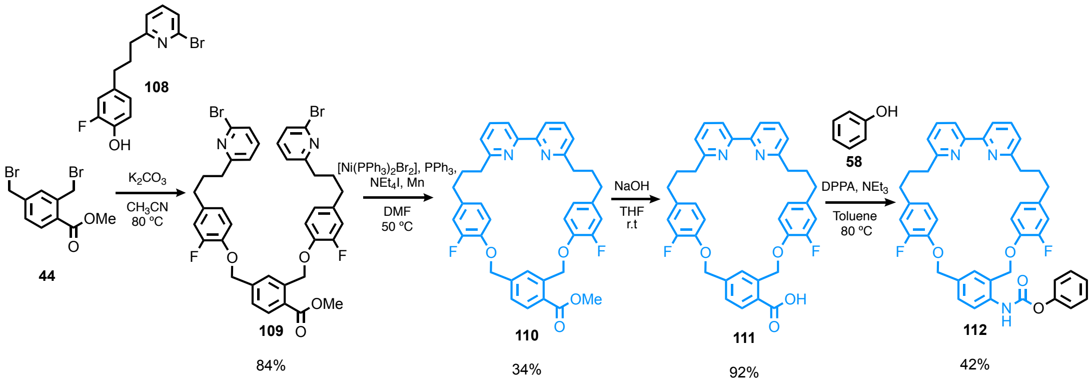

Scheme **38**. Synthesis of fluorinated macrocycle **112**.

Macrocycle **116**, possessing methoxy and fluorine modifications, was similarly synthesised (Scheme **39**). Alkylation of **108** with **96** proceeded in 97% to give precursor **113**, which underwent macrocyclisation to afford **114** in 63% yield. Quantitative conversion of carboxylic acid **115** was achieved *via* basic hydrolysis of **114**. Curtius rearrangement of **115** in presence of phenol **58** under optimised conditions afforded dual-modified macrocycle **116** in 58% yield.

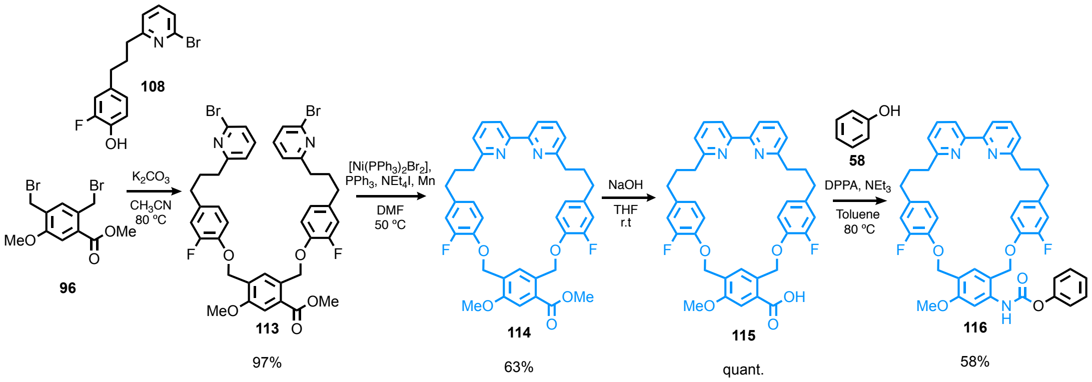

Scheme **39**. Synthesis of methoxy and fluorine dual-modified macrocycle **116**.

The fluoride-triggered generation of aniline **77** from rotaxane **75** previously provided the most convenient method to study the self-immolative ring-opening process under neutral conditions. As such, modified platform macrocycles **100**, **112** and **116** were reacted with trigger **51** to generate the various TBDMS-ether protected macrocycles in 69-85% yield (Scheme **40**), which is comparable to that of previously synthesised unmodified macrocycle **52** (70%).

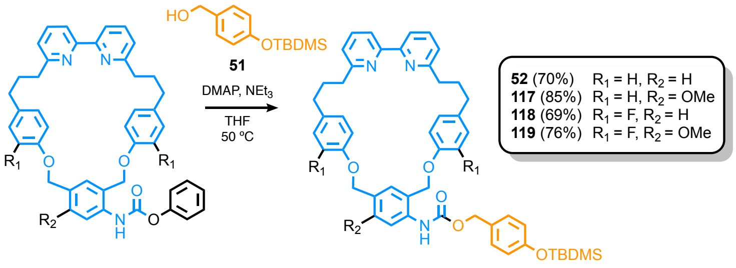

Scheme **40**. Synthesis of TBDMS protected macrocycles **52**, **117**, **118** and **119**.

3.2.9. Rotaxane Synthesis (2nd Generation)

The incorporation of macrocycles **117**, **118** and **119** into the model rotaxane architecture proceeded successfully *via* the AT-CuAAC reaction with **71** and **72** under standard rotaxination conditions (Figure **264**).

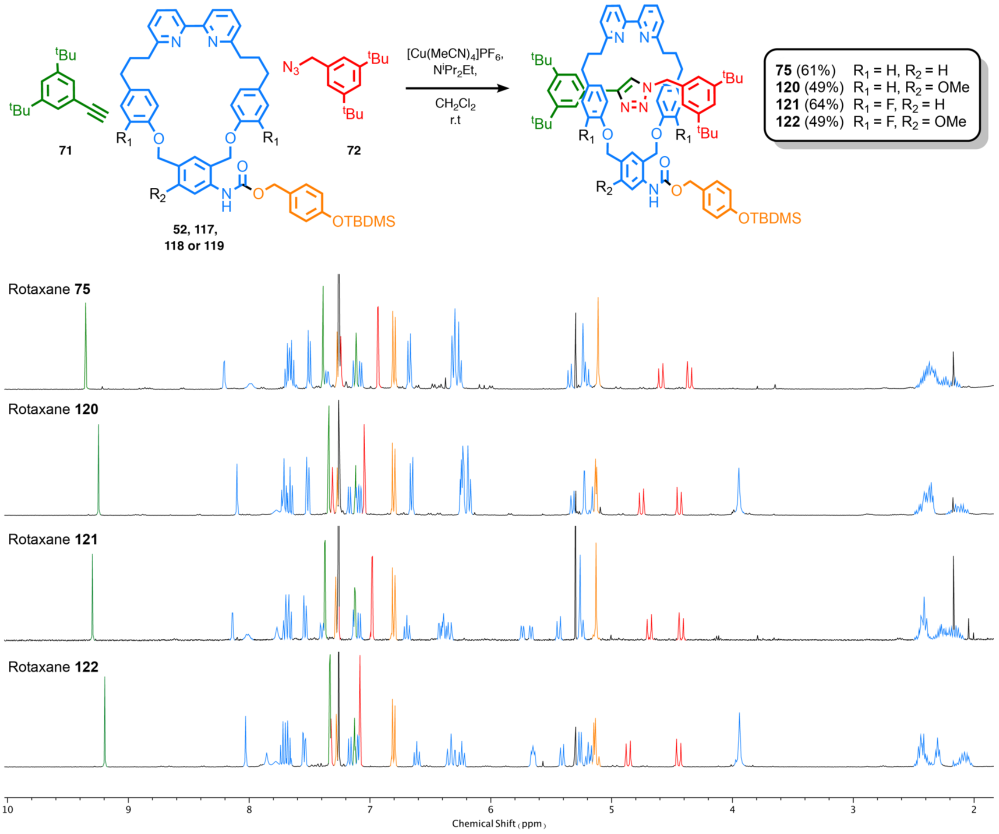

Figure **264**. Synthesis of TBDMS-ether protected rotaxanes **75**, **120**, **121** and **122**. ^{1}H NMR stackplot (δ range = 10-1.8 ppm) of rotaxanes in $CDCl_3$ is shown. Signals are colour-coded to represent the different components of the interlocked structures. Blue = macrocycle backbone, orange = trigger motif, green/red = axle.

Rotaxination reactions with macrocycles **120** and **122**, possessing the methoxy modification, were lower yielding (49%) than with unmodified macrocycle **121** (62%), which can possibly be attributed to additional steric bulk of the methoxy group. Fluorine modifications alone had no impact on efficiency of AT-CuAAC coupling, with rotaxane **121** achieved in comparable yield (64%) to unmodified rotaxane **75** (62%).

3.2.10. Chemical Cleavage of Rotaxanes **120**, **121** and **122**

Fluoride-triggered protecting group cleavage was performed under identical conditions to the previous experiment with unmodified rotaxane **75** (Scheme **34**). The ring-opening ability of rotaxanes **120** and **121,** possessing the singular methoxy or fluoro modification, respectively, was first examined by dissolving in THF-d_8: D_2O (3:1) and treating with TBAF (3.0 eq.) at 37 °C (Figure **265**). Aliquots were taken at given time intervals and analysed *via* ^1H NMR and LC-MS.

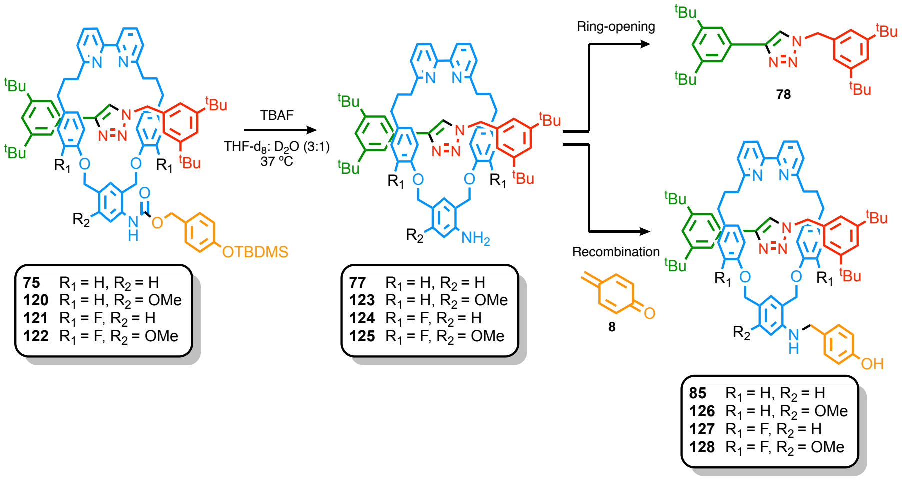

Figure **265**. Fluoride-triggered deprotection of TBDMS-ether rotaxanes **75**, **120**, **121** and **122** with TBAF (3.0 eq.) in THF-d_8: D_2O (3:1). The competing mechanistic pathways of the corresponding aniline rotaxane are shown.

Full TBDMS-ether deprotection was observed within 1 h for both rotaxanes (Figure **266**). After 1 h, the corresponding aniline (**123** or **124**) was the predominant species in both mixtures, with minor amounts of recombined rotaxanes **126** and **127** also observed. The formation of another major triazole signal (δ ≈ 9.40 ppm) was also observed after 1 h in the case of rotaxane **120**. Although this species could not be identified, when left to stir, it was consumed. Similar to the experiment with unmodified rotaxane **75**, the relative amount of recombined rotaxanes **126** and **127** increased over time. After 48 h, no release of axle **78** could be detected *via* ^1H NMR in either mixture.

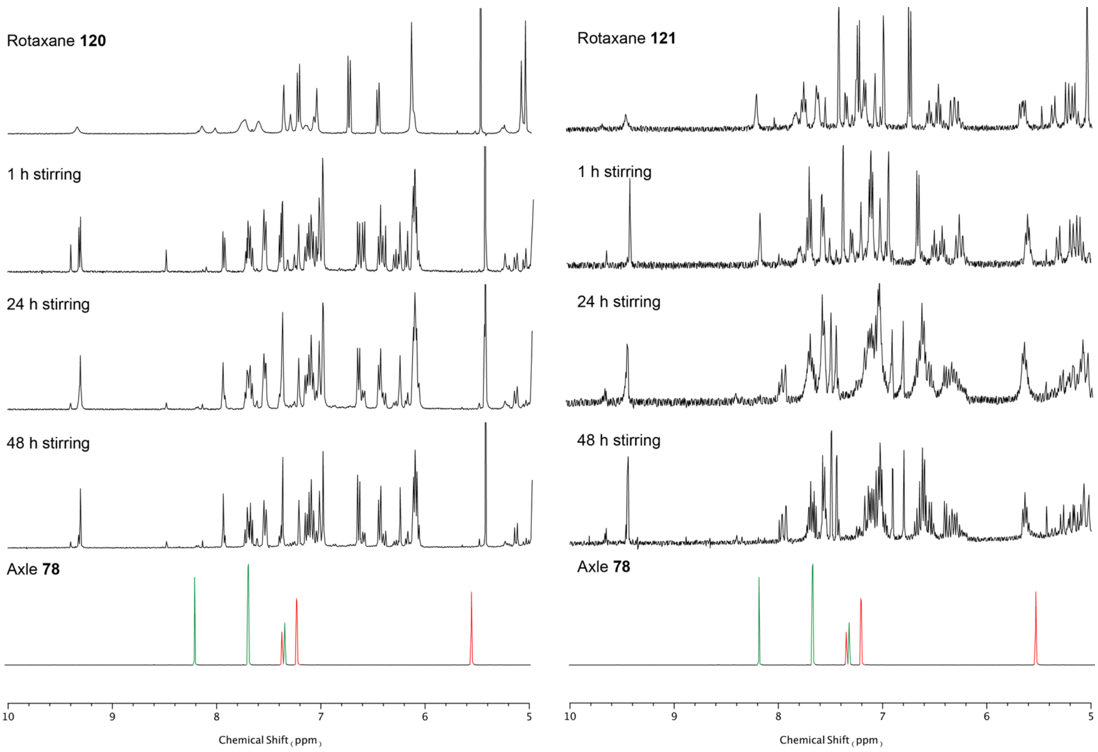

Figure **266**. ^{1}H NMR stackplot (δ range = 10.0-5.0 ppm) of TBDMS-ether rotaxanes **120** and **121** upon treatment with TBAF (3.0 eq.) in THF-d_8: D_2O (3:1).

LC-MS analysis confirmed that substantial amounts of the corresponding aniline rotaxane (**123** or **124**) and recombined rotaxane (**126** or **127**) were present in both mixtures after stirring for 48 h (Figure **267**). Trace amounts of axle **78** could be detected *via* LC-MS, with slightly more released from methoxy-modified aniline **124** relative to fluorinated aniline **123**. Combined, the findings indicate that the presence of the methoxy- or fluoro-modifications alone led to only minor improvements in ring-opening ability relative to unmodified aniline rotaxane **77**.

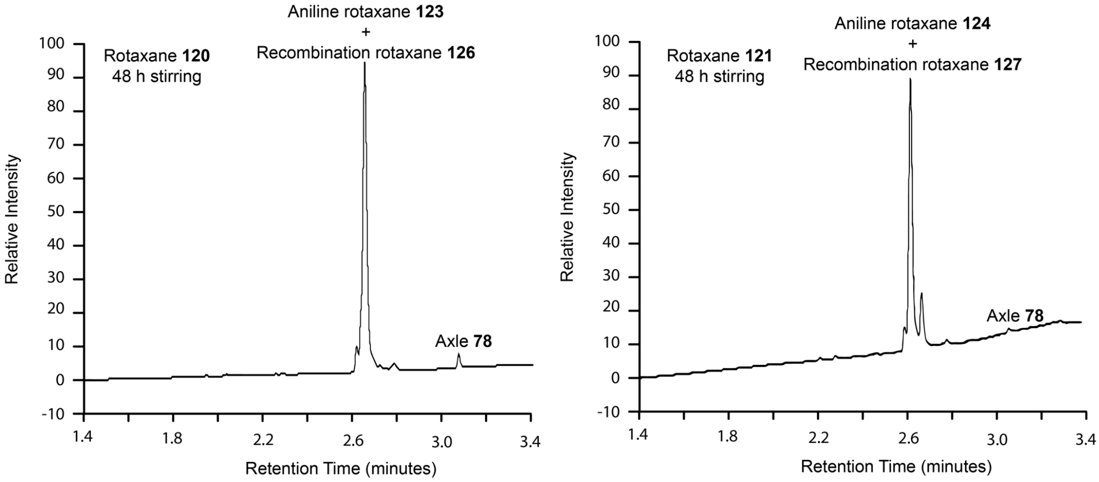

Figure **267**. LC-MS of rotaxane **120** and **121** fluoride-triggered cleavage after 48 h.

Although insufficient to enhance the ring-opening ability when employed separately, it was hoped that the synergistic effect of both modifications would sufficiently destabilise the aniline rotaxane and facilitate the release of axle **78**. Rotaxane **122**, possessing both modifications, in THF-d_8: D_2O (3:1) was treated with TBAF (3.0 eq.) at 37 °C, and the release of axle **78** was monitored *via* ^{1}H NMR and LC-MS (Figure **268**).

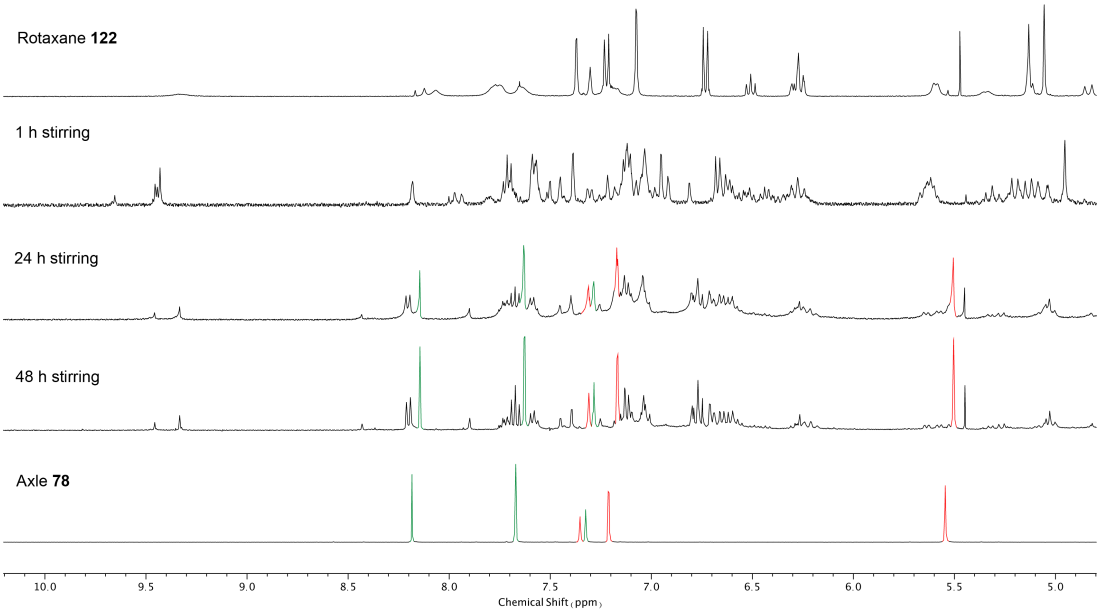

Figure **268**. ^{1}H NMR stack of TBDMS-ether rotaxane **122** after fluoride-triggered cleavage.

The deprotection of the TBDMS-ether group was again found to be complete within 1 h, giving the corresponding aniline (**125**) as the major species. No release of axle **78** was detected after 1 h (Figure **268**). However, when left to stir for 24 h, significant amounts of axle **78** were observed in the mixture alongside recombined rotaxane **128** and minor amounts of aniline **125**. After 48 h, only trace amounts of aniline **125** remained, with the relative amounts of axle **78** and recombined rotaxane **128** increasing accordingly. LC-MS analysis confirmed that only trace amounts of aniline rotaxane **125** remained after 48 h and that axle **78** was the major species in the mixture, alongside recombined rotaxane **128** and bis-phenol decomposition product **79** (Figure **269**). Overall, the results indicate that the incorporation of both modifications is sufficient to destabilise aniline rotaxane **125** and facilitate the release of axle **78** under neutral conditions, albeit slowly.

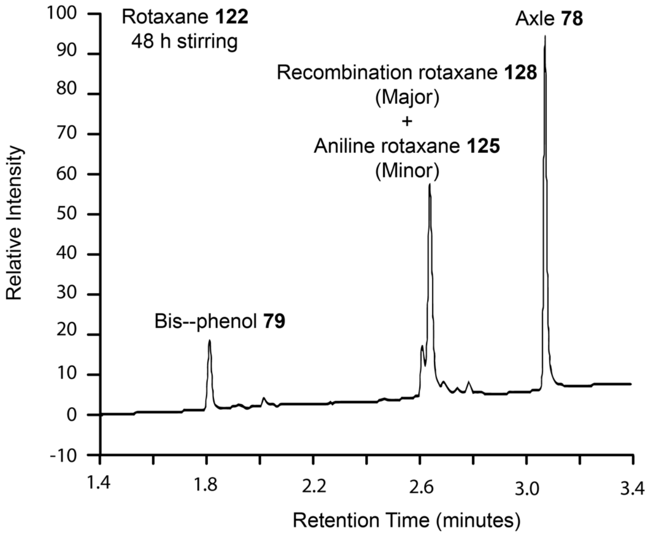

Figure **269**. LC-MS of rotaxane **122** fluoride-triggered cleavage after 48 h.

3.3. Conclusions and Future Work

A platform approach was developed for the synthesis of stimuli-responsive ring-opening 2,2'-bipyridine macrocycles. The conversion of a functionally inert macrocycle to a stable activated intermediate was readily achieved *via* Hofmann or Curtius rearrangement — the latter proving a milder approach with superior functional group tolerance. Subsequent carbamate displacement with an appropriate trigger alcohol granted rapid access to a library of stimuli-cleavable macrocycles in good yield. Incorporation of these macrocycles into a model rotaxane architectures proceeded efficiently *via* AT-CuAAC coupling in comparable yields. In combination with ^{1}H NMR analysis, this would suggest that the peripheral site of the trigger motif does not significantly interfere with the rotaxination process, or the conformational behaviour of the interlocked products.

The ring-opening behaviour was studied in the simple rotaxane models, where success was judged by the amount of axle (**78**) released in response to a given stimulus. Successful removal of the corresponding trigger moiety was observed in response to pH, UV light and chemical activation. However, ring-opening of the resulting aniline rotaxane (**77**) was observed only under highly acidic conditions or while being actively irradiated with UV light. Under neutral conditions, as demonstrated with the fluoride-responsive cleavage of rotaxane **75**, aniline rotaxane **77** was stable over several days. The recombination of aniline **77** with electrophilic decomposition products was also found to be a significant side-reaction, trapping the rotaxane and preventing the release of axle **78**, even under UV irradiation.

A push-pull system was envisioned to alter the electronic effects of the SI spacer within the macrocyclic backbone and enhance the ring-opening ability. Building blocks bearing electron-donating methoxy or electron-withdrawing fluoride groups at appropriate positions were synthesised and incorporated into fluoride-cleavable macrocycles **117, 118** and **119**. Macrocycle **118**, possessing only fluoride modifications, mediated the model AT-CuAAC with similar efficiency to unmodified macrocycle **75**, whereas the methoxy group in macrocycles **117** and **119** was found to hinder rotaxination slightly. When subjected to fluoride sources, rotaxanes **117** and **118** bearing only the electron-donating OR the electron-withdrawing modification, respectively, showed only marginal axle releasing capability relative to the unmodified version. Rotaxane **119**, possessing both modifications, showed significant release of axle **78** over several days — indicating that the design may be suitable for releasing interlocked components under neutral conditions (Figure **270**). Efforts to study and improve the release capability of these systems are ongoing.

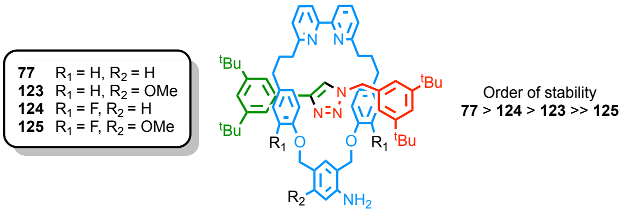

Figure **270**. Order of stability of aniline rotaxanes.

Several issues must be addressed for the platform to be applicable for the release of mechanically caged interlocked molecules in biological applications. The first is that the rate of ring-opening post trigger-cleavage is slow. While this may be advantageous for sustained drug delivery, rapid reactivation of the caged biomolecule is favourable in most applications. As stated previously, the rate of ring-opening in the aniline rotaxane will be highly dependent on the polarity of solvent mixture. For instance, Phillips *et al.* noted a ≈12-fold decrease in the half-life of an analogous phenol-releasing amino-benzyl spacer when moving from 30% to 70% H_2O in CH_3CN.[119] Due to the poor solubility of the synthesised rotaxanes in mixed aqueous-organic solvent mixtures (typically ≤ 25% v/v H_2O in THF or CH_3CN), this relationship could not be investigated. Efforts should initially be directed toward studying the release process in solvent mixtures with a higher aqueous component, which is likely to lead an enhanced rate of ring-opening, possibly even with mono- or unmodified macrocycles. This could be achieved by using hydrophilic protecting groups as the trigger motif, of which there are many (Figure **271**). Another possibility is to incorporate the water-solubilising moieties within the axle component, which has been shown as an effective approach by other groups.[92,93]

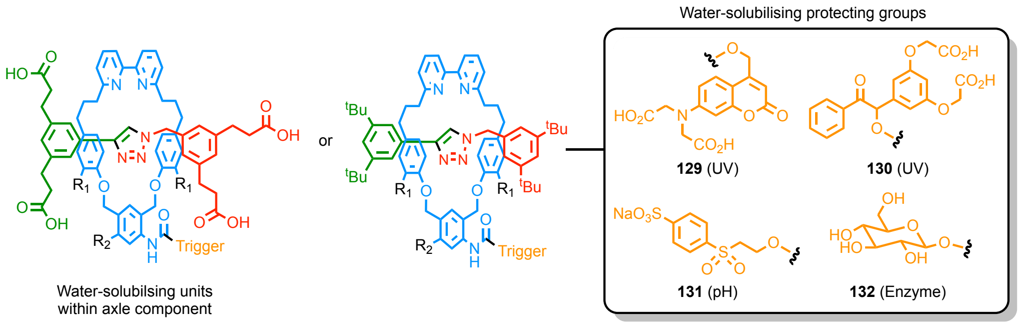

Figure **271**. Approaches to enhance the solubility of rotaxanes under aqueous conditions.

If, under aqueous conditions, the release of axle remains slow, then the electronic properties of the macrocycle could be further improved through additional structural modification. The addition of a second methoxy group *ortho* to the benzylic ethers is likely to further destabilise the C-O bond and lead to faster cleavage. However, projection of the methoxy group into the macrocyclic cavity may hinder AT-CuAAC capability. Increasing the acidity of the phenolate leaving group may prove less problematic and could be achieved simply by adding a second *ortho* fluorine atom. The effect of such modifications on aqueous solubility should also be investigated.

The formation of reactive quinone methide intermediates also proved problematic due to reaction with the nucleophilic aniline rotaxane, trapping it as the recombined species and preventing axle release. Although switching to more aqueous solvent mixtures should discourage the recombination pathway by introducing more quenching nucleophilic species, the reaction of *para* quinone-methide with H_2O is reversible and may still prove problematic. As such, alternative self-immolative linker designs should also be explored. Modifying the typical *para* hydroxy/aminobenzyl alcohol linkers with an *ortho*-NO_2 group not only accelerates the rate of 1,6-elimination, but the corresponding quinone methide is also much less cytotoxic owing to its inability to irreversibly inhibit the amino groups at enzymatic active sites — an indication that recombination with the aniline may also be less favorable (Figure **272**).[80,120]

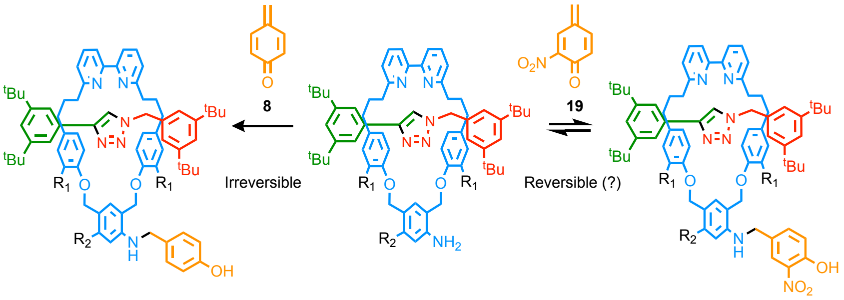

Figure **272**. Using a different linker to prevent recombination with the quinone-methide species

3.4. Experimental

3.4.1. General Experimental

Unless otherwise stated, all reagents, including anhydrous solvents, were purchased from commercial sources and used without further purification. Reagents for oligonucleotide synthesis were purchased from Applied Biosystem. All reactions were carried out under an inert an atmosphere of N_2 using anhydrous solvents unless otherwise stated. Flash column chromatography was performed using Biotage Isolera-4 or a Biotage Isolera-1 automated chromatography system, employing Biotage SNAP or ZIP cartridges (50 µm, irregular silica, default flow rates). Analytical TLC was performed on precoated silica gel plates (0.25 mm thick, 60F254, Merck, Darmstadt, Germany) and observed under UV light or with potassium permanganate solution. NAP 10 gel-filtration columns were purchased from GE Healthcare and used according to the manufacturer's instructions. Petrol refers to the fraction of petroleum ether boiling in the range 40-60 °C. IPA refers to isopropyl alcohol. EDTA-NH_3 solution refers to an aqueous solution of NH_3 (17% w/w) saturated with sodium-ethylenediaminetetraacetate. $[Cu(CH_3CN)_4][PF_6]$ was prepared as described by Pigorsch and Köckerling.[121]

NMR spectra were recorded on Bruker AV400, AV3-400 and AV500 FT-NMR spectrometers in the indicated deuterated solvent at a constant temperature of 300 K. Chemical shifts for ^1H and ^{13}C spectra are reported on the delta (δ) scale in parts per million (ppm) from low to high field and referenced to residual solvent. Coupling constants (*J*) are reported in Hertz (Hz). Standard abbreviations indicating multiplicity were used as follows: m = multiplet, q = quartet, t = triplet, d = doublet, s = singlet, app. = apparent, br = broad. Diastereomeric proton signals are differentiated as H_x or H_x' where appropriate. Signal assignment was carried out using 2D NMR methods (HSQC, HMBC, COSY) where necessary. For clarity, all proton signals in rotaxane structures corresponding to the axle component are in upper case (H_X), and all proton signals corresponding to the macrocycle components are in lower case case (H_x).

UV-vis absorption spectra were measured on a Biotek Instruments XS spectrometer using quartz cuvettes of 1 cm path length. All melting points were determined using a Griffin apparatus. Low resolution mass spectrometry (LR-MS) was carried out by the mass spectrometry services at the University of Southampton (Waters TQD mass spectrometer equipped with a triple quadrupole analyser with UHPLC injection [BEH C_{18} column; CH_3CN-hexane gradient {0.2% formic acid}]). High resolution mass spectrometry (HR-MS) was carried out by the mass spectrometry services at the University of Southampton (MaXis, Bruker Daltonics, with a Time of Flight (TOF) analyser; samples were introduced to the mass spectrometer *via* an Acquity H-Class quaternary solvent manager (with TUV detector at 254 nm, sample and column manager) and UHPLC pump in a gradient of 20% CH_3CN in hexane (0.2% formic acid) to 100% CH_3CN (0.2% formic acid) over 10 min at a flow rate of 0.6 mL/min (column: Acquity UPLC BEH C_{18} (Waters) 1.7 µm 50 mm × 2.1 mm). As accurate mass measurements are of limited value for compounds with MW >1000 Da, in these cases a graphical comparison of the observed isotope pattern and the predicted isotopic distribution is provided.

3.4.2. Experimental Procedures

Compounds **45**,[95] **51**,[122] **54**,[123] **67**,[107] **69**,[124] **71**,[125] **72**,[126] **101**[95] and PhIO[127] were synthesised according to literature procedure. Spectra for these compounds were consistent with previous literature reports.

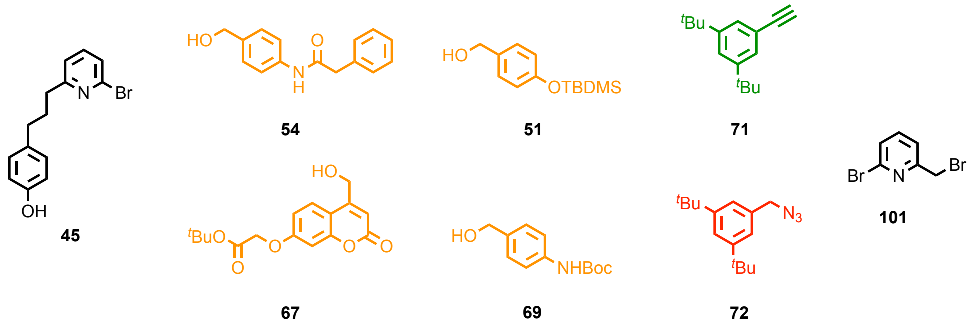

Figure **273**. Compounds synthesised according to literature procedure.

General Procedure (1): Macrocycle Precursor Synthesis

A mixture of phenol (2 eq.), linker (1 eq.) and K_2CO_3 (6 eq.) in DMF (0.1 M) was stirred at 80 °C for 16 h. The suspension was then cooled to room temperature, diluted with CH_2Cl_2 and washed with water then brine. Combined aqueous phases were extracted with CH_2Cl_2 (x3). The combined organic extracts were dried over anhydrous $MgSO_4$, filtered and concentrated *in vacuo*. The crude product was purified *via* silica-gel chromatography using a Biotage Isolute SPE column.

General Procedure (2): Macrocyclisation

[Ni(PPh_3)$_2$$Br_2$] (1 eq.), PPh_3 (2 eq.), NEt_4I (1 eq.) and Mn (10 eq.) were charged to an oven-dried CEM microwave vial and degassed under N_2. Anhydrous DMF (0.1 M) was added and the mixture sonicated for 15 min, followed by stirring at 50 °C for a further 15 min. To this catalyst mixture was added macrocycle precursor (1 eq.) in anhydrous DMF (0.1 M) *via* syringe pump over 4 h at 50 °C, followed by an additional stirring for 30 min. The reaction was cooled to room temperature, diluted with CH_2Cl_2 and washed with EDTA-NH_3, water then brine. Combined aqueous phases were extracted with CH_2Cl_2 (x3). The combined organic extracts were dried over anhydrous $MgSO_4$, filtered and concentrated *in vacuo*. The crude product was purified *via* silica-gel chromatography using a Biotage Isolute SPE column.

General Procedure (3): Macrocycle Ester Hydrolysis

A mixture of macrocycle (1 eq.) and NaOH (10 eq.) in THF (0.1 M) was stirred at room temperature for 16 h. The mixture was diluted with water, neutralized with aqueous HCl (1 M) and extracted with Et_2O (x3). Combined organic extracts were then washed with water, dried over anhydrous $MgSO_4$, filtered and concentrated *in vacuo* to afford the pure product.

General Procedure (4): Hofmann Rearrangement

A mixture of carboxamide (1 eq.), PhIO (2 eq.) and *p*NO_2-phenol **61** (3.5 eq.) in anhydrous CH_2Cl_2 (0.1 M) was stirred at room temperature for 2 h, then phenol **58** (5 eq.) and DIPEA (3 eq.) was added and stirred for a further 2 h. The mixture was diluted with CH_2Cl_2, washed with citric acid, water and brine. Combined aqueous phases were extracted with CH_2Cl_2 (x3). The combined organic extracts were dried over anhydrous $MgSO_4$, filtered and concentrated *in vacuo*. The crude product was purified *via* silica-gel chromatography using a Biotage Isolute SPE column.

General Procedure (5): Curtius Rearrangement

A mixture of carboxylic acid macrocycle (1 eq.) and NEt_3 (1.2 eq.) in anhydrous toluene (0.1 M) was degassed under N_2. DPPA (1.2 eq.) was added and heated at 80 °C for 2 h, then cooled to room temperature and stirred for a further 30 min. The mixture was diluted with CH_2Cl_2, washed with citric acid, water and brine. Combined aqueous phases were extracted with CH_2Cl_2 (x3). The combined organic extracts were dried over anhydrous $MgSO_4$, filtered and concentrated *in vacuo*. The crude product was purified *via* silica-gel chromatography using a Biotage Isolute SPE column.

General Procedure (6): Carbamate Displacement

A degassed mixture of phenyl carbamate macrocycle (1 eq.), trigger alcohol (3 eq.), DMAP (1 eq.) and NEt_3 (1.5 eq.) in anhydrous THF (0.1 M) was heated at 50 °C for 3 h. Once cooled to room temperature the mixture was diluted with CH_2Cl_2 then washed with water and brine. Combined aqueous phases were extracted with CH_2Cl_2 (x2). The combined organic extracts were dried over anhydrous $MgSO_4$, filtered and concentrated *in vacuo*. The crude product was purified *via* silica-gel chromatography using a Biotage Isolute SPE column.

General Procedure (7): Rotaxination

A solution of macrocycle (1.0 eq.), azide stopper **72** (1.5 eq.), alkyne stopper **71** (1.5 eq.) and $Cu(CH_3CN)_4PF_6$ (0.95 eq.) in CH_2Cl_2 (0.1 M) was degassed under N_2. DIPEA (2.0 eq.) was added and stirred at room temperature overnight. The mixture was then diluted with CH_2Cl_2 (0.05 M) and EDTA-NH_3 (1:1 with volume of CH_2Cl_2) was added and stirred vigorously to sequester Cu ions. Demetallation of the Cu-rotaxane was monitored *via* LC-MS, taking between 10 min to 3 days depending on the structure. The organic phase was separated and washed with water then brine. Combined aqueous phases were extracted with CH_2Cl_2 (x2). The combined organic extracts were dried over anhydrous $MgSO_4$, filtered and concentrated *in vacuo*. The crude product was purified *via* silica-gel chromatography using a Biotage Isolute SPE column.

Compound **43**

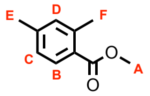

A mixture of **42** (5.9 g, 39.3 mmol, 1.0 eq.) and H_2SO_4 (0.2 mL, 3.9 mmol, 0.1 eq.) in MeOH (30 mL) was refluxed at 75 °C overnight. Once cooled to room temperature, the mixture was diluted with CH_2Cl_2 (100 mL), washed with water (100 mL), $NaHCO_3$ (100 mL) and brine (100 mL). Combined aqueous phases were extracted with CH_2Cl_2 (2 x 50 mL). The combined organic extracts were then dried over anhydrous $MgSO_4$, filtered and concentrated *in vacuo* to afford **43** as a colourless liquid (5.9 g, 36.5 mmol, 93%). ^{1}H NMR (400 MHz, $CDCl_3$, 298 K) δ_H 7.83 (1H, d, J = 7.8 Hz, H_B), 7.06-7.02 (2H, m, H_C & H_D), 3.87 (3H, s, H_A), 2.57 (3H, s, H_F), 2.35 (3H, s, H_E). ^{13}C NMR (101 MHz, $CDCl_3$, 298 K) δ_C 168.1, 142.6, 140.5, 132.6, 130.9, 126.7, 126.6, 51.8, 21.9, 21.5.

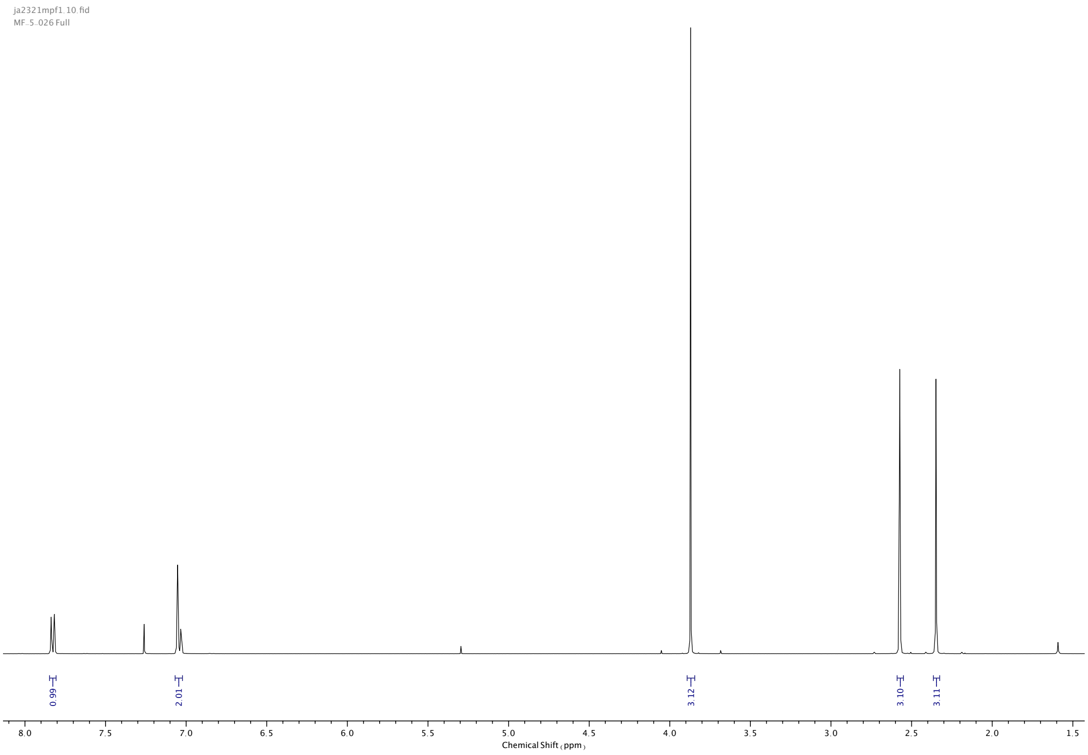

Figure **274**. ^{1}H NMR ($CDCl_3$, 400 MHz) of **43**.

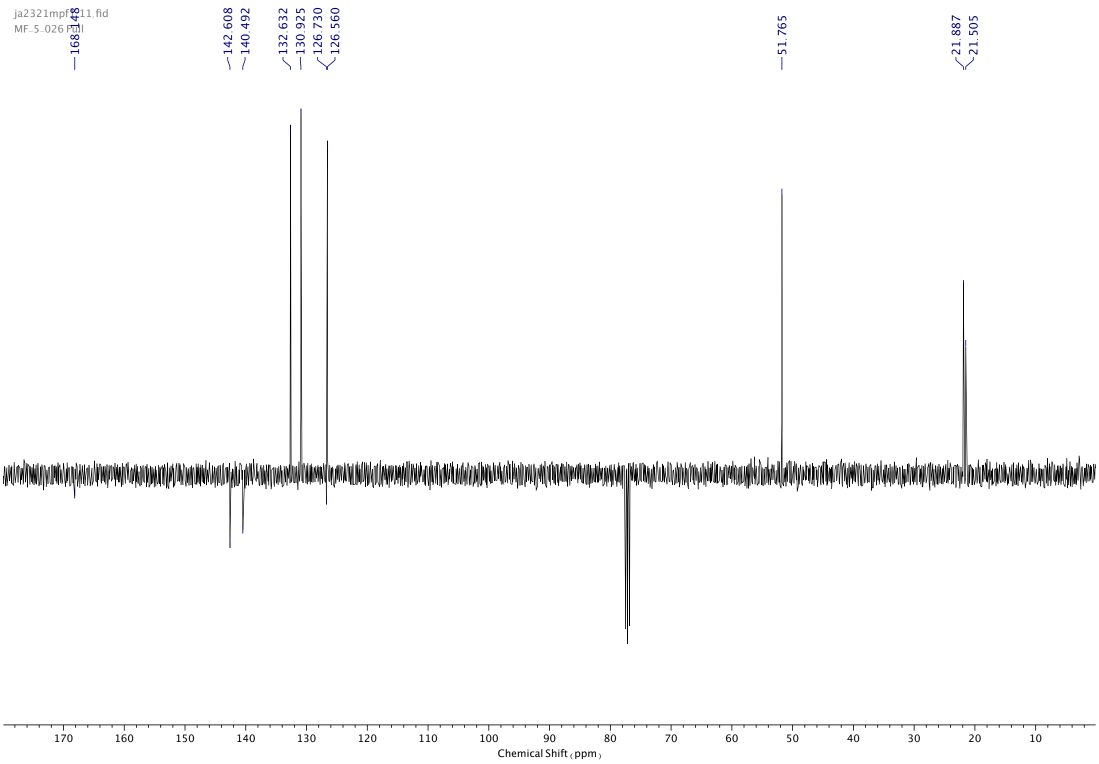

Figure **275**. ^{13}C NMR ($CDCl_3$, 101 MHz) of **43**.

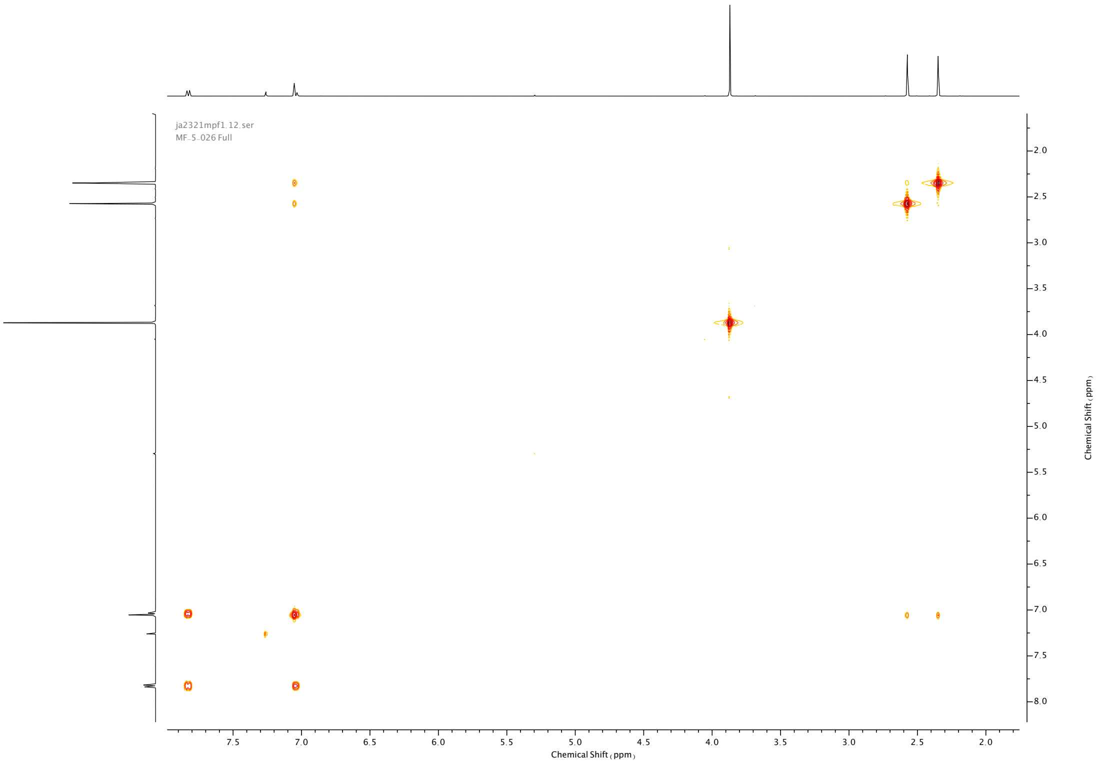

Figure **276**. COSY NMR ($CDCl_3$) of **43**.

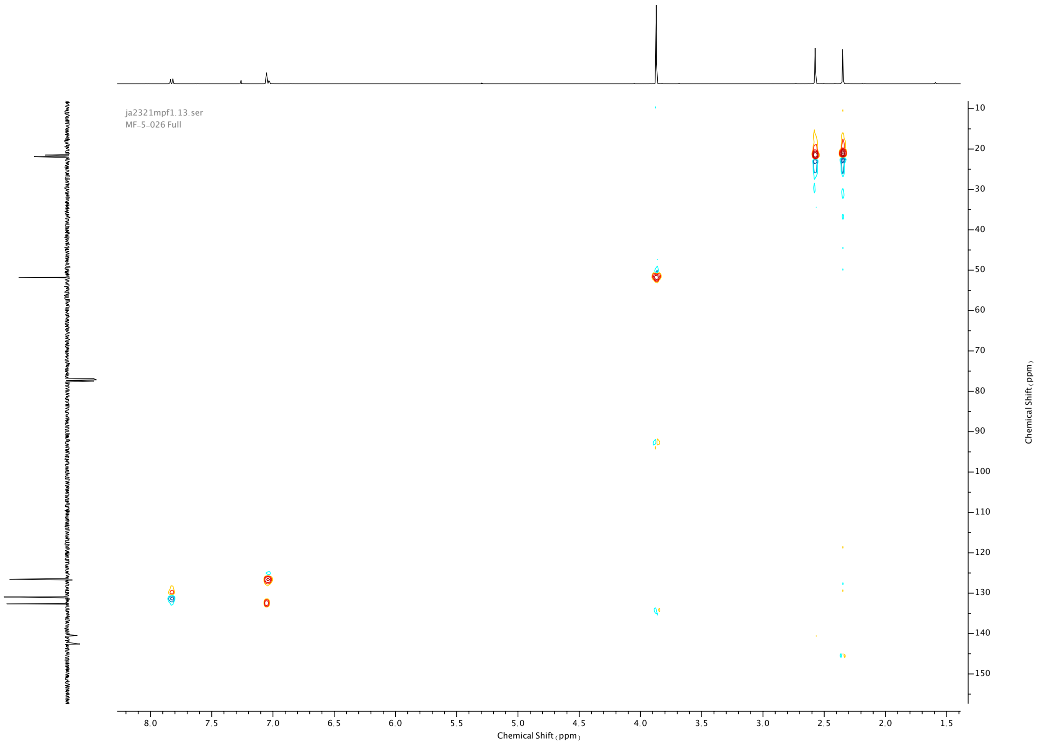

Figure **277**. HSQC NMR ($CDCl_3$) of **43**.

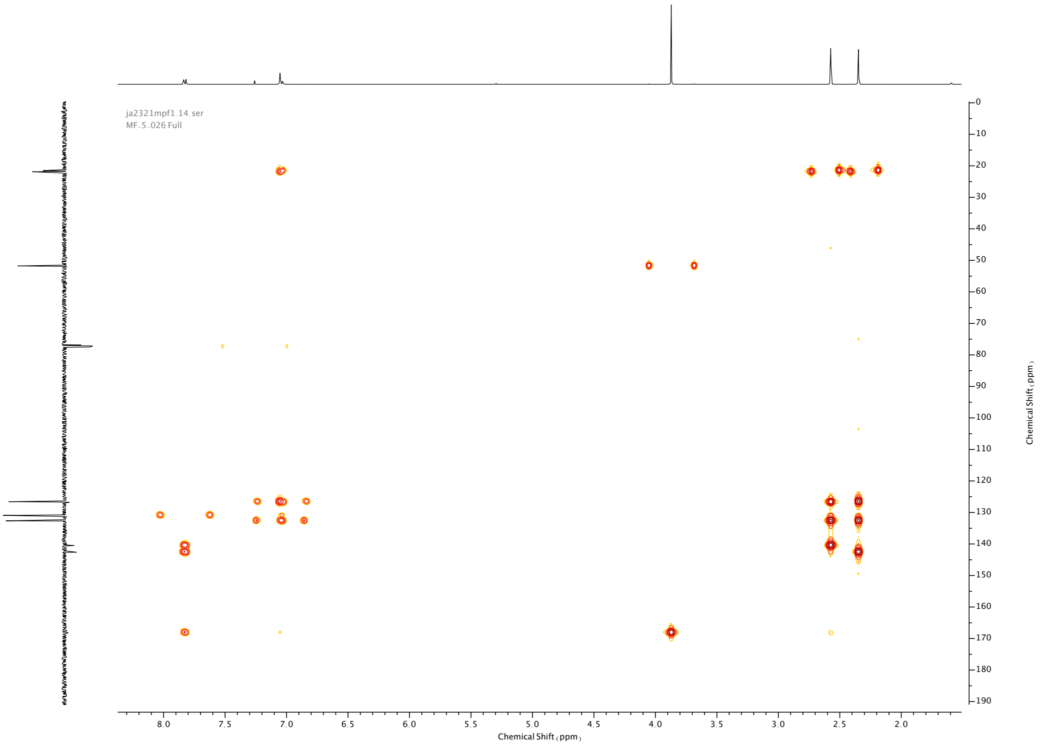

Figure **278**. HMBC NMR ($CDCl_3$) of **43**.

Compound **44**

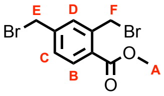

A mixture of **43** (2.24 g, 13.7 mmol, 1.0 eq.), NBS (5.35 g, 30.1 mmol, 2.2 eq.) and benzoyl peroxide (198 mg, 0.82 mmol, 0.05 eq.) in chlorobenzene (20 mL) was heated at 80 °C for 2 h. Once cooled to room temperature, the mixture was diluted with EtOAc (100 mL), washed with water (100 mL), $NaHCO_3$ (100 mL) and brine (100 mL). Combined aqueous phases were extracted with EtOAc (2 x 50 mL). The combined organic extracts were then dried over anhydrous $MgSO_4$, filtered and concentrated *in vacuo*. The crude product was purified *via* silica-gel chromatography using a Biotage Isolute SPE column (eluent 1:0 → 19.1 PE: Et_2O) to afford a mixture of di-brominated product **44**: tri-brominated by-product (94:6) as a white solid (4.33 g) that was carried forward to the next step. ^1H NMR (400 MHz, $CDCl_3$, 298 K) δ_H 7.95 (1H, d, J = 8.1 Hz, H_B), 7.49 (1H, d, J =1.9 Hz, H_D), 7.39 (1H, dd, J = 8.1, 1.9 Hz, H_C), 4.94 (2H, s, H_F), 4.47 (2H, s, H_E), 3.94 (3H, s, H_A). ^{13}C NMR (101 MHz, $CDCl_3$, 298 K) δ_C 166.8 (HMBC), 142.4, 140.1, 140.0, 132.3, 132.1, 129.1, 52.5, 31.7, 31.2.

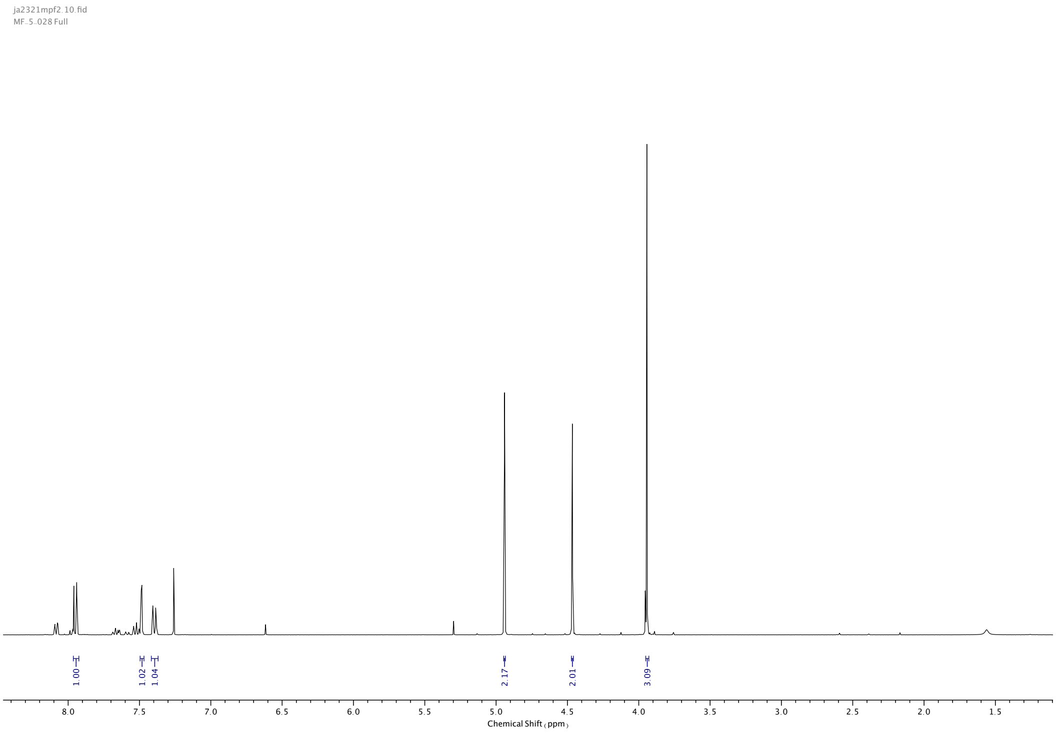

Figure **279**. ^1H NMR ($CDCl_3$, 400 MHz) of **44**.

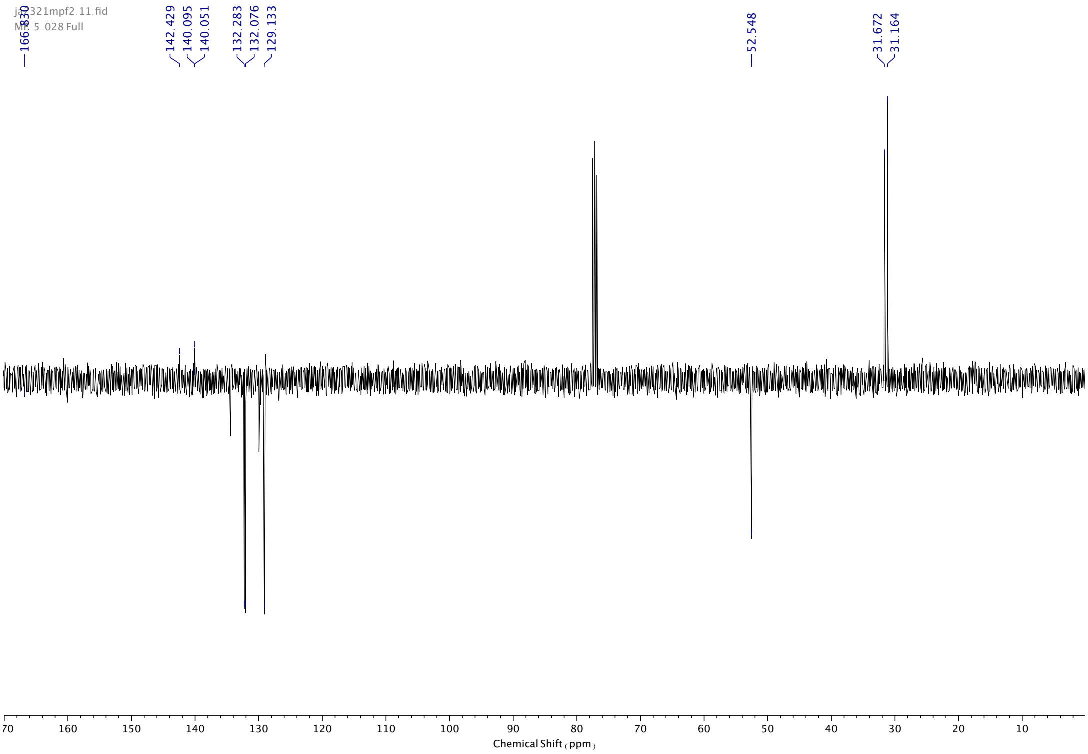

Figure **280**. ^{13}C NMR (CDCl$_3$, 101 MHz) of **44**.

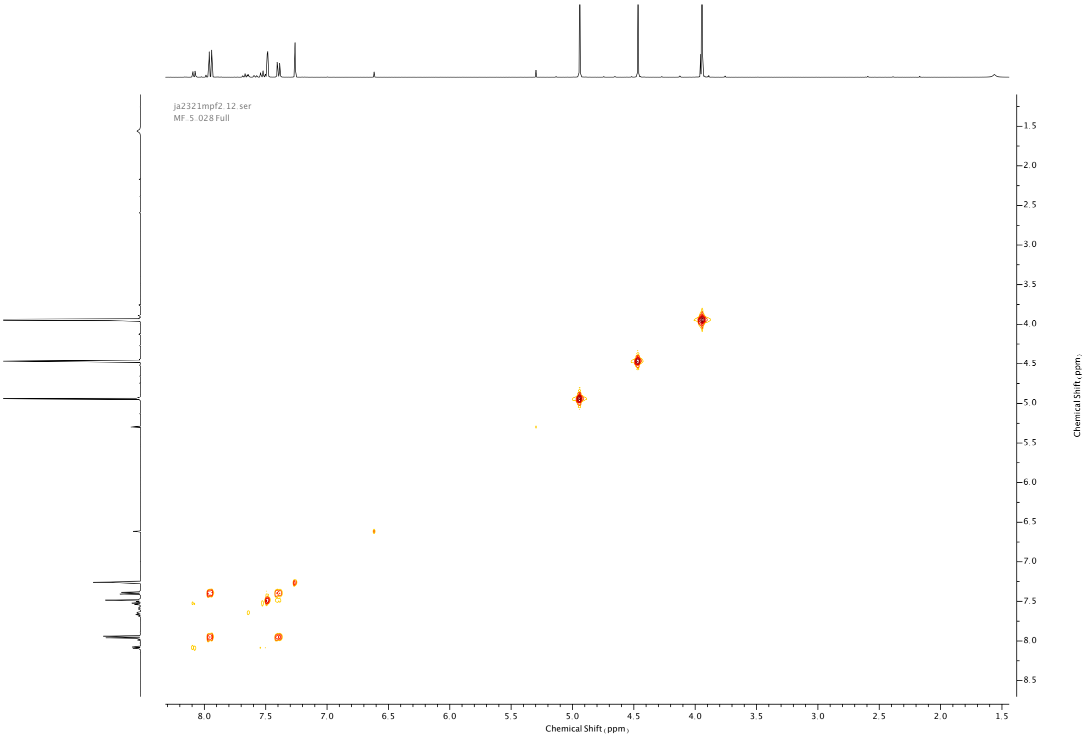

Figure **281**. COSY NMR (CDCl$_3$) of **44**.

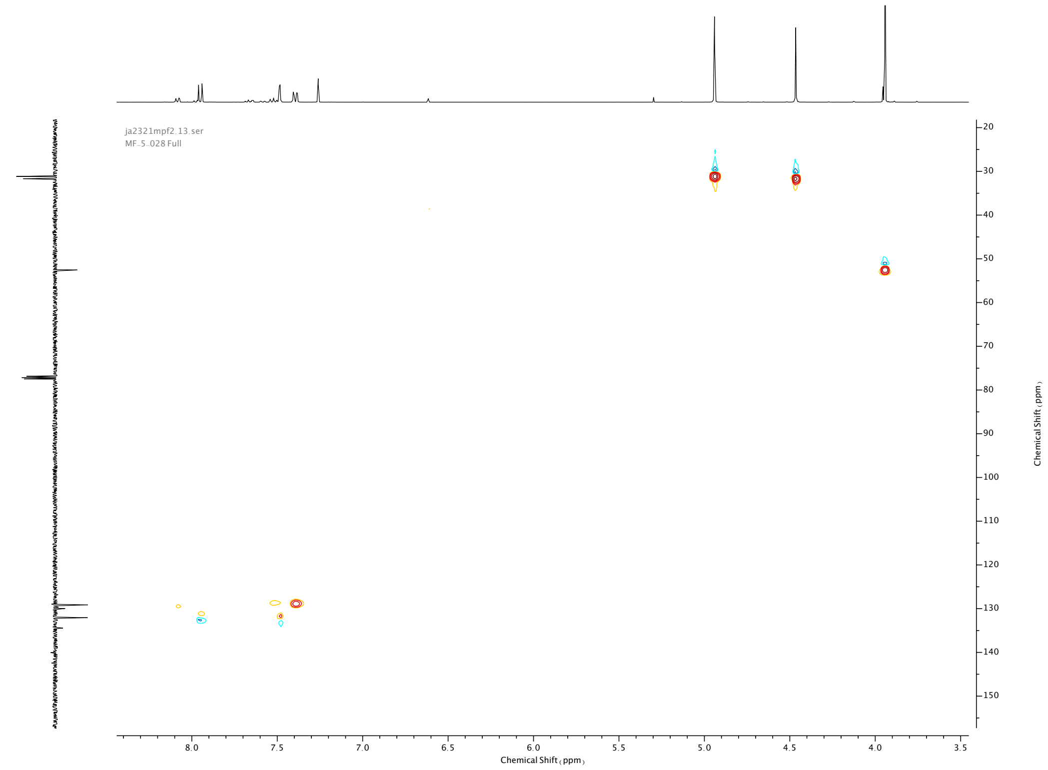

Figure **282**. HSQC NMR (CDCl$_3$) of **44**.

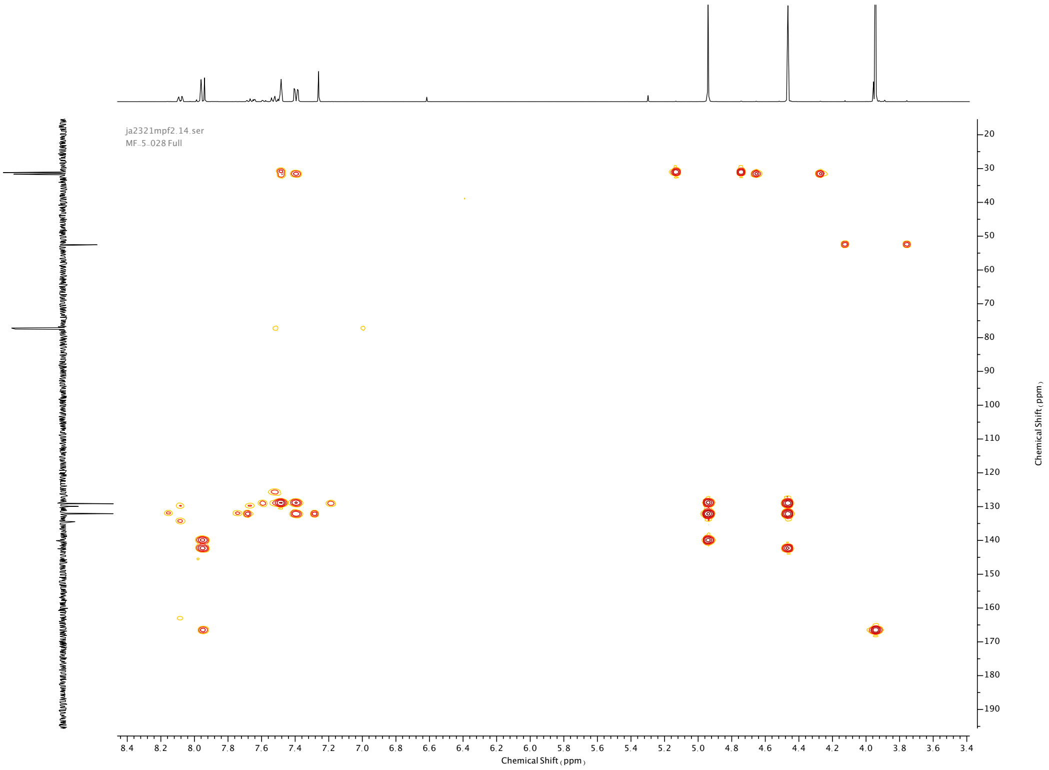

Figure **283**. HMBC NMR (CDCl$_3$) of **44**.

Compound **46**

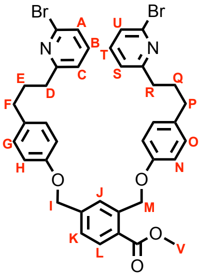

46 was prepared according to general procedure **(1)** from phenol **45** (7.8 g, 26.8 mmol, 2.0 eq.) and linker **44** (4.3 g, 13.4 mmol, 1.0 eq.). Purification by column chromatography (eluent 49:1 → 19:1 (petrol: CH_2Cl_2 1:1): EtOAc) afforded **46** as a yellow oil (8.5 g, 11.5 mmol, 84% over two steps). ^1H NMR (400 MHz, $CDCl_3$, 298 K) δ_H 8.04 (1H, d, J = 8.1 Hz H_L), 7.82 (1H, s, H_J), 7.47-7.40 (3H, m, H_K, H_B & H_T), 7.29 (2H, d, J = 7.9 Hz, H_A & H_U), 7.12-7.04 (6H, m, H_G, H_O, H_C & H_S), 6.92 (2H, d, J = 8.7 Hz, H_H or H_N), 6.86 (2H, d, J = 8.7 Hz, H_H or H_N), 5.48 (2H, s, H_M), 5.10 (2H, s, H_I), 3.89 (3H, s, H_V), 2.82-2.74 (4H, m, H_D & H_R), 2.65-2.58 (4H, m, H_F & H_P), 2.06-1.96 (4H, m, H_E & H_Q). ^{13}C NMR (101 MHz, $CDCl_3$, 298 K) δ_C 167.3, 163.9 (x2), 157.1, 156.9, 142.4, 141.7 (x2), 140.5, 138.7 (x2), 134.7, 134.5, 131.3, 129.6 (x2), 127.1, 126.1, 125.9, 125.4 (x2), 121.7, 121.7, 115.0, 114.9, 69.6, 68.3, 52.2, 37.6 (x2), 34.7 (x2), 31.6 (x2). HR-ESI-MS (CH_3CN): m/z = 743.1112 $[M+H]^+$ calc. 743.1115.

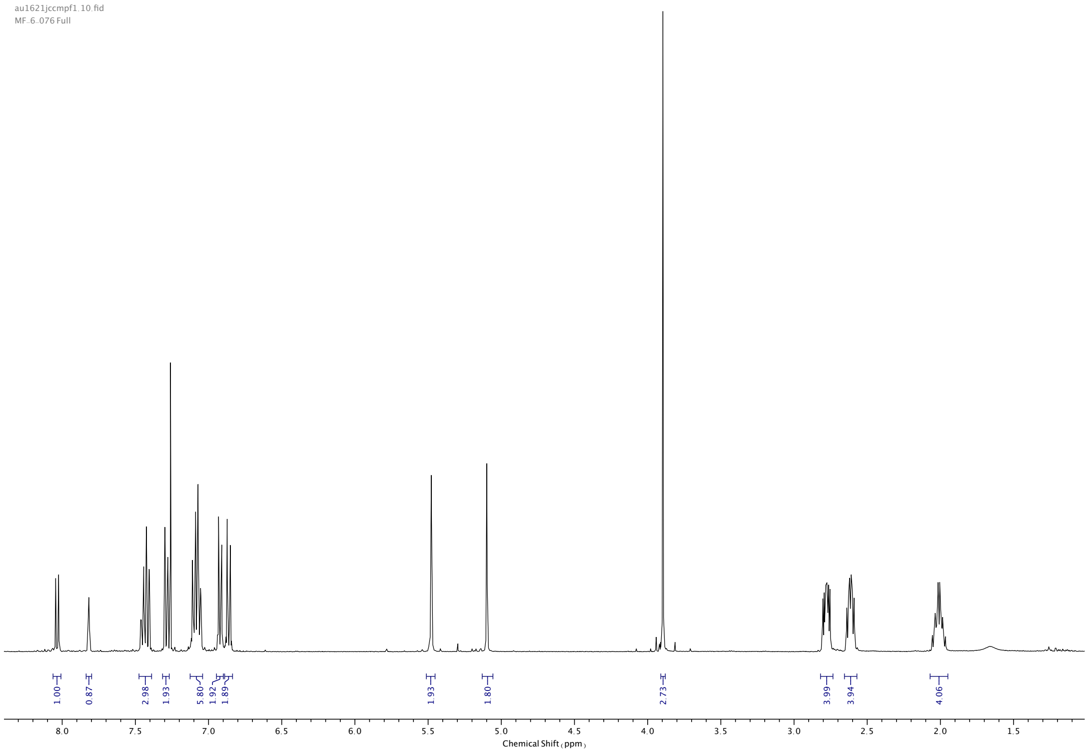

Figure **284**. ^1H NMR ($CDCl_3$, 400 MHz) of **46**.

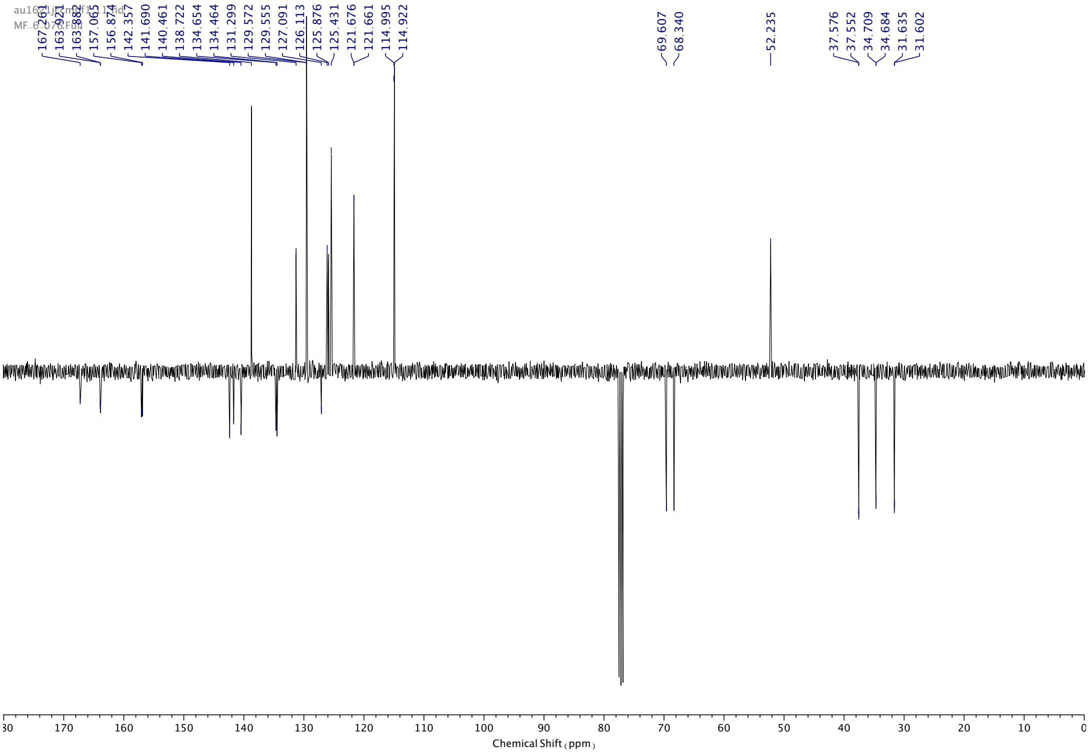

Figure **285**. ^{13}C NMR (CDCl$_3$, 101 MHz) of **46**.

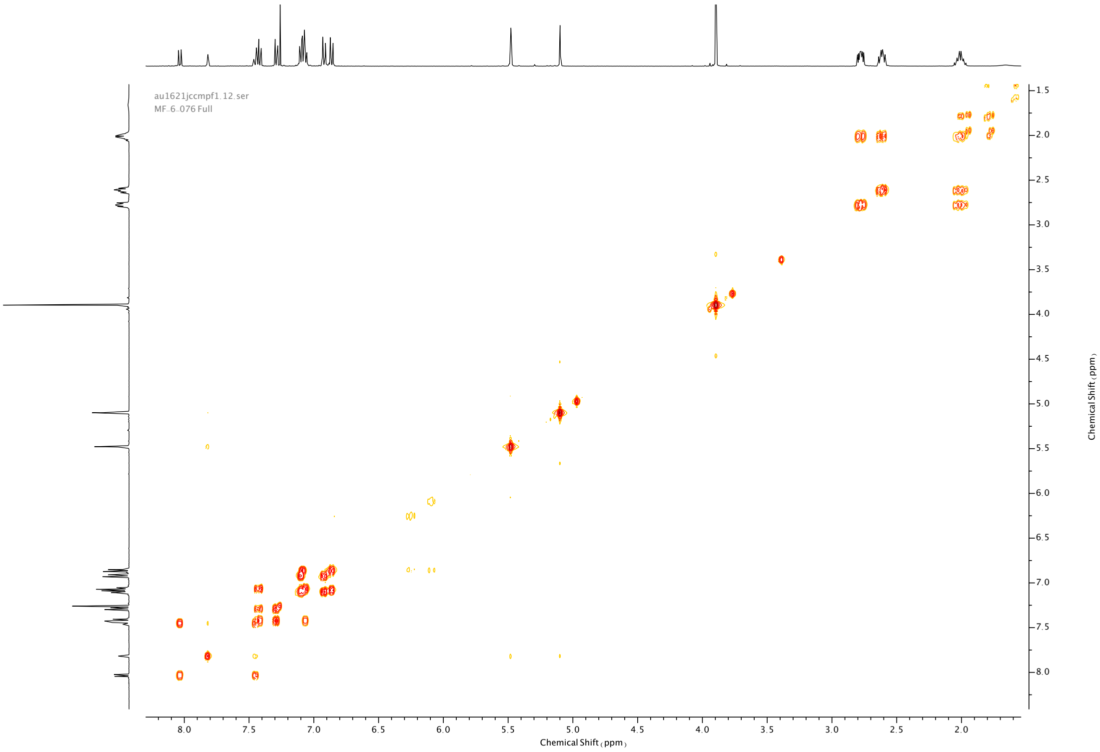

Figure **286**. COSY NMR (CDCl$_3$) of **46**.

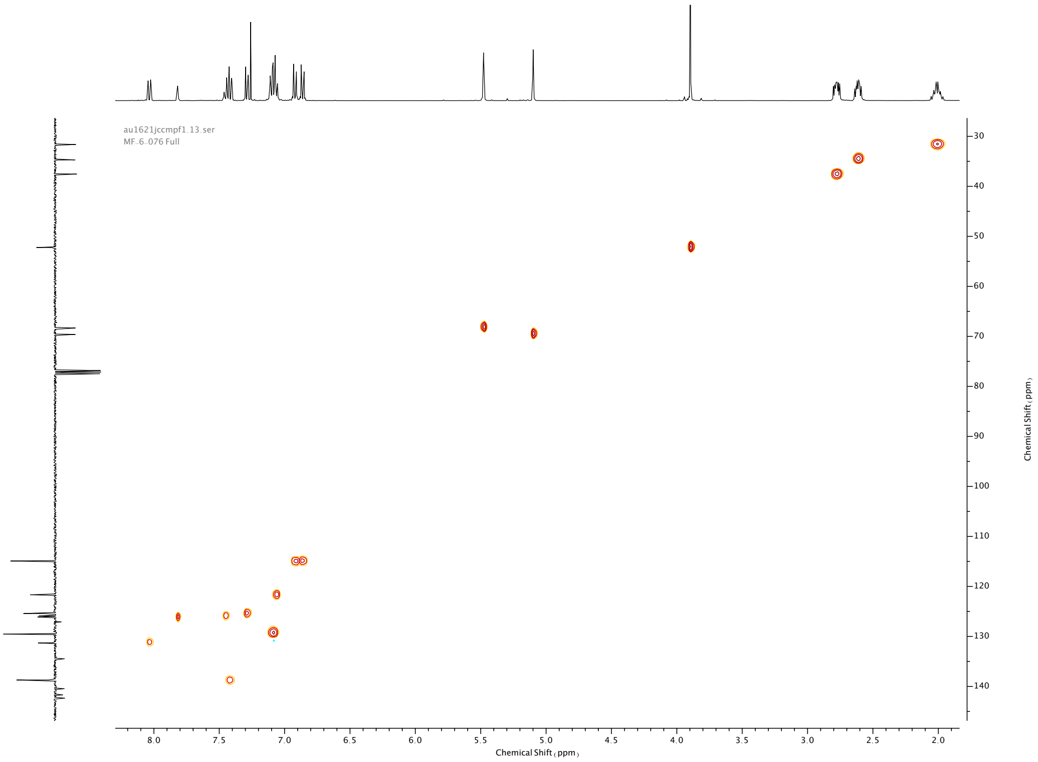

Figure **287**. HSQC NMR ($CDCl_3$) of **46**.

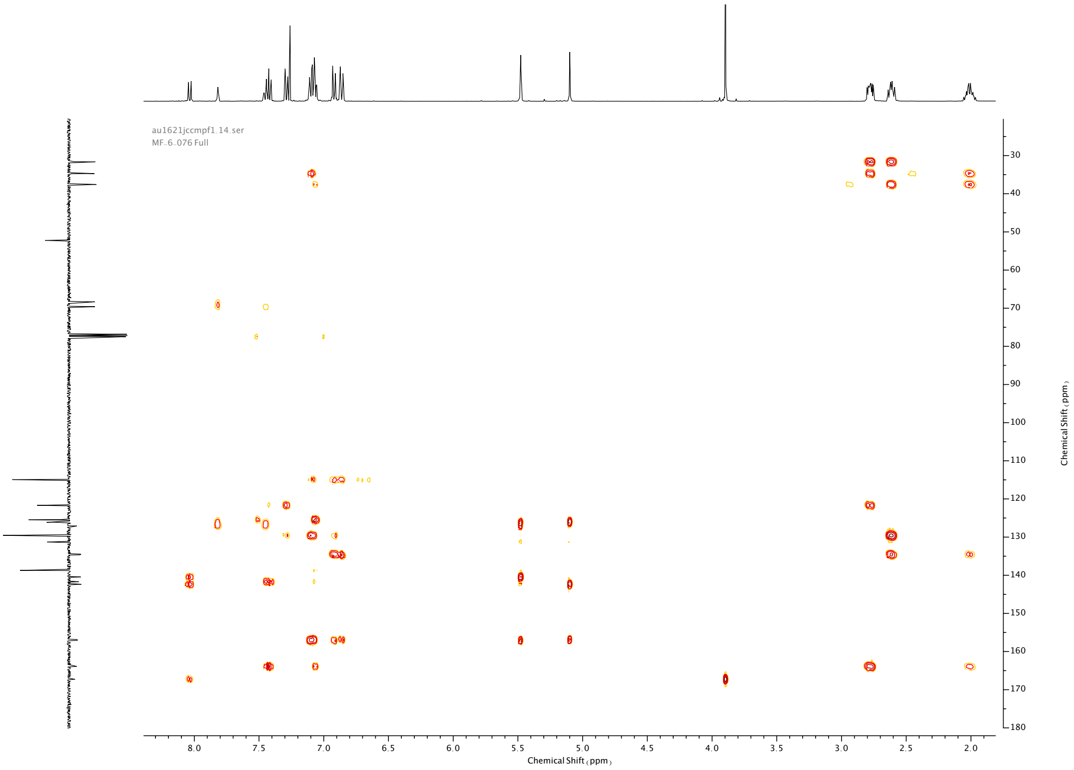

Figure **288**. HMBC NMR ($CDCl_3$) of **46**.

Compound **47**

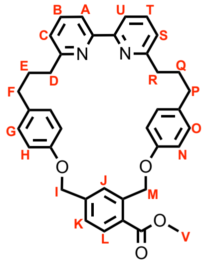

47 was prepared according to general procedure **(2)** from macrocycle precursor **46** (6.6 g, 8.9 mmol). Purification by column chromatography (eluent 1:0 → 9:1 (petrol: CH_2Cl_2 1:1): EtOAc) afforded **47** as an off-white foam (3.2 g, 5.5 mmol, 62%). ^{1}H NMR (400 MHz, $CDCl_3$, 298 K) δ_H 8.01 (1H, d, *J* = 8.1 Hz, H$_L$), 7.73 (1H, d, *J* = 7.9 Hz, H$_A$ or H$_U$), 7.68 (1H, d, *J* = 7.8 Hz, H$_A$ or H$_U$), 7.63 (1H, t, *J* = 7.7 Hz, H$_B$ or H$_T$), 7.58 (1H, s, H$_J$), 7.55 (1H, t, *J* = 7.7 Hz, H$_B$ or H$_T$), 7.33 (1H, dd, *J* = 8.1, 1.7 Hz, H$_K$), 7.12 (1H, dd, *J* = 7.6, 1.0 Hz, H$_C$ or H$_S$), 7.04-6.99 (3H, m, H$_O$ & H$_C$ or H$_S$), 6.89 (2H, d, *J* = 8.7 Hz, H$_G$), 6.69 (2H, d, *J* = 8.7 Hz, H$_N$), 6.56 (2H, d, *J* = 8.7 Hz, H$_H$), 5.55 (2H, s, H$_M$), 5.00 (2H, s, H$_I$), 3.91 (3H, s, H$_V$), 2.90 (4H, t, *J* = 7.2 Hz, H$_D$ & H$_R$), 2.65 (2H, t, *J* = 7.4 Hz, H$_F$ or H$_P$), 2.61 (2H, t, *J* = 7.4 Hz, H$_F$ or H$_P$), 2.18-2.07 (4H, m, H$_E$ & H$_Q$). ^{13}C NMR (101 MHz, $CDCl_3$, 298 K) δ_C 167.2, 162.1, 162.0, 156.6 (x2), 156.3 (x2), 142.8, 141.2, 136.8, 136.7, 135.1, 135.0, 131.4, 129.6 (x2), 126.4, 125.6, 125.2, 122.6, 122.4, 119.3, 119.2, 115.1, 115.0, 69.6, 68.5, 52.2, 37.9, 37.8, 34.6, 34.4, 31.6, 30.9. HR-ESI-MS (CH_3CN): *m/z* = 585.2744 $[M+H]^+$ calc. 585.2748.

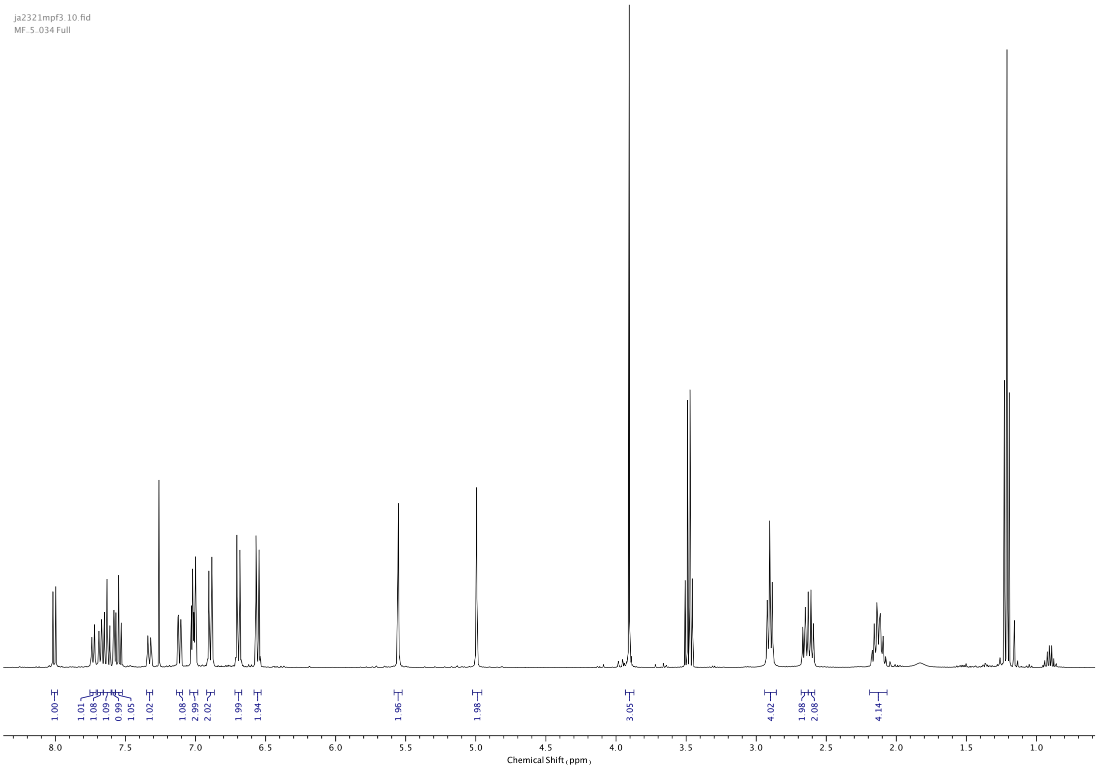

Figure **289**. ^{1}H NMR ($CDCl_3$, 400 MHz) of **47**.

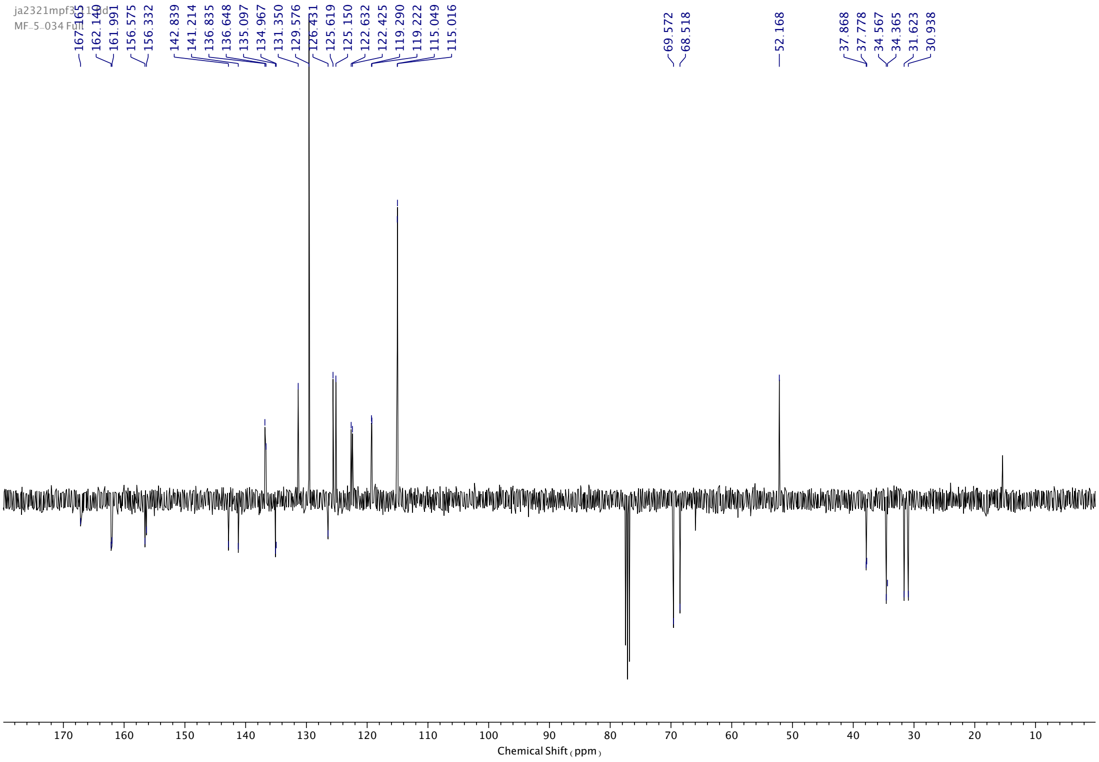

Figure **290**. ^{13}C NMR ($CDCl_3$, 101 MHz) of **47**.

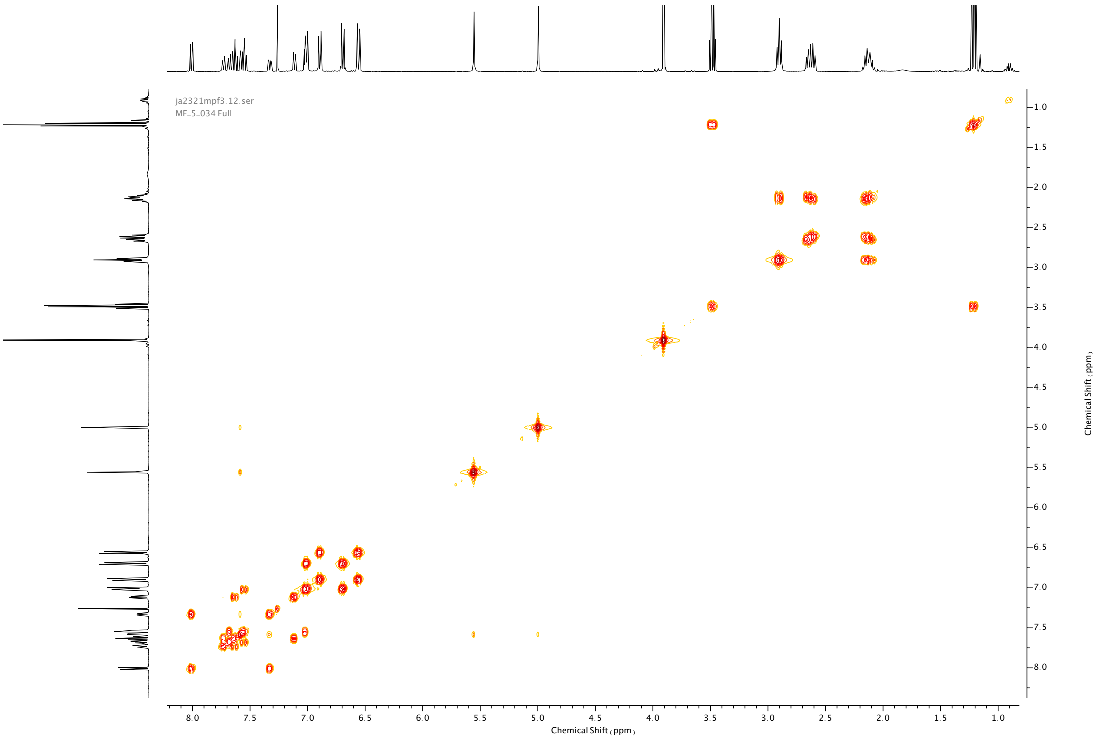

Figure **291**. COSY NMR ($CDCl_3$) of **47**.

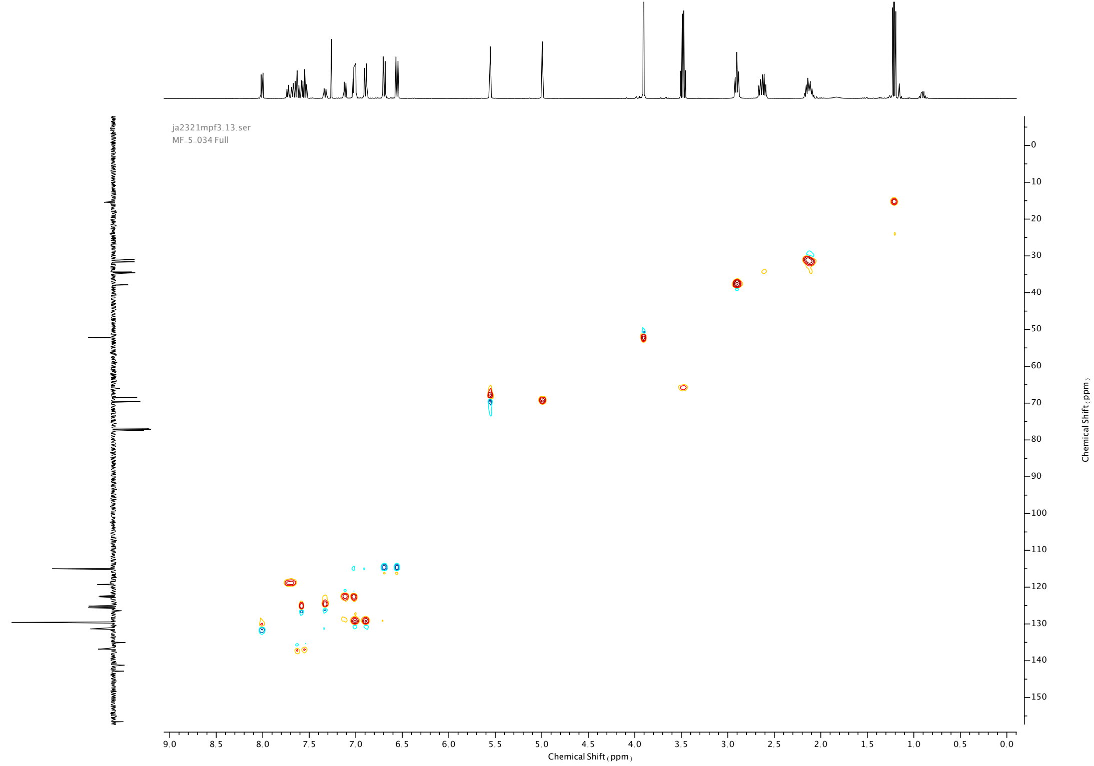

Figure **292**. HSQC NMR ($CDCl_3$) of **47**.

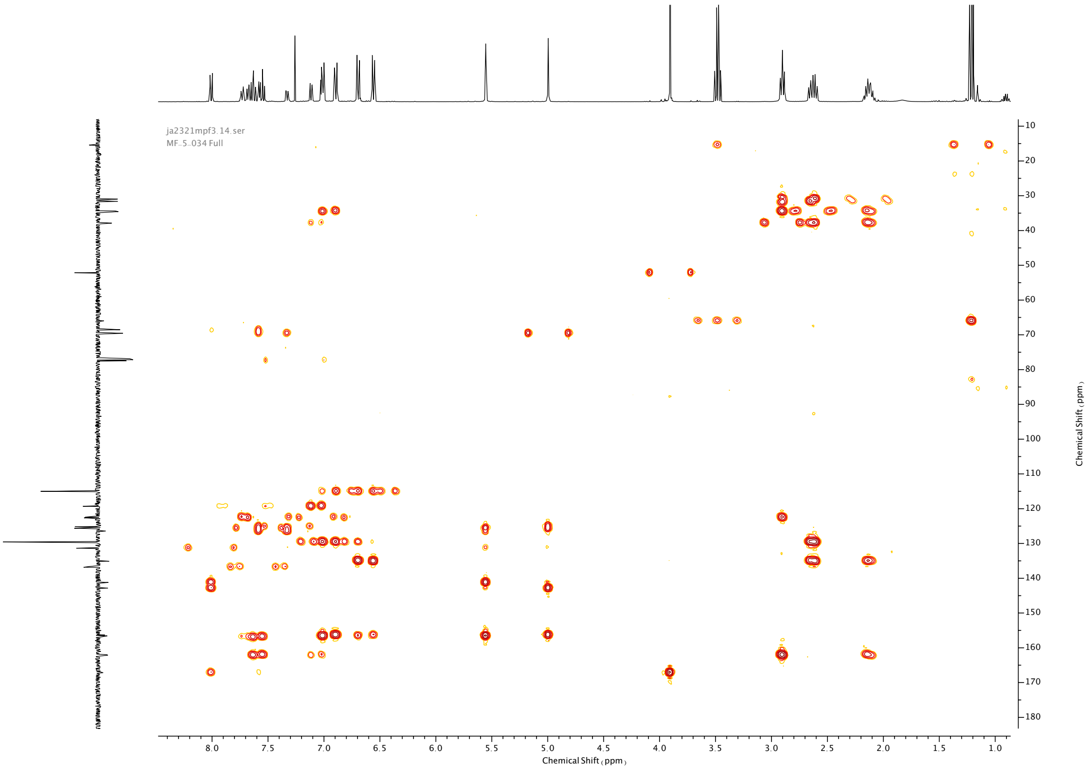

Figure **293**. HMBC NMR ($CDCl_3$) of **47**.

Compound **48**

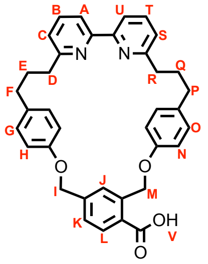

48 was prepared according to general procedure **(3)** from macrocycle **47** (1.3 g, 2.2 mmol). **48** was achieved as an off-white solid (1.12 g, 1.95 mmol, 88%) and used in the next step without further purification. M.p. 212-215 °C. ^{1}H NMR (400 MHz, DMSO-d_6, 298 K) δ_H 7.91 (1H, d, *J* = 7.9 Hz, H_L), 7.82-7.75 (2H, m, H_A & H_U), 7.73 (1H, t, *J* = 7.7 Hz, H_B or H_T), 7.67 (1H, t, *J* = 7.7 Hz, H_B or H_T), 7.49 (1H, s, H_J), 7.34 (1H, d, *J* = 7.9 Hz, H_K), 7.22 (1H, dd, *J* = 7.5, 0.9 Hz, H_C or H_S), 7.16 (1H, dd, *J* = 7.6, 0.9 Hz, H_C or H_S), 6.98 (2H, d, *J* = 8.6 Hz, H_G or H_O), 6.88 (2H, d, *J* = 8.6 Hz, H_G or H_O), 6.66 (2H, d, *J* = 8.6 Hz, H_H or H_N), 6.58 (2H, d, *J* = 8.7 Hz, H_H or H_N), 5.49 (2H, s, H_M), 5.03 (2H, s, H_I), 2.79 (4H, t, *J* = 7.0 Hz, H_D & H_R), 2.59-2.50 (4H, m, H_F & H_P), 2.07-1.96 (4H, m, H_E & H_Q).^{13}C NMR (101 MHz, DMSO-$d_{6,}$ 298 K) δ_C 168.6 (HMBC), 161.2, 161.1, 156.0 (x2) 155.9, 155.8, 141.3, 139.4, 137.0, 136.8, 134.3, 134.2, 130.7 (x2), 129.6, 129.2, 128.9 (HMBC), 128.8 (HMBC), 125.6, 125.3, 118.7 (x2), 114.6 (x2), 68.4, 67.5, 36.7 (x2), 33.5, 33.3, 30.8, 30.4. HR-ESI-MS (CH$_3$CN): *m/z* = 571.2599 [M+H]$^+$ calc. 571.2605.

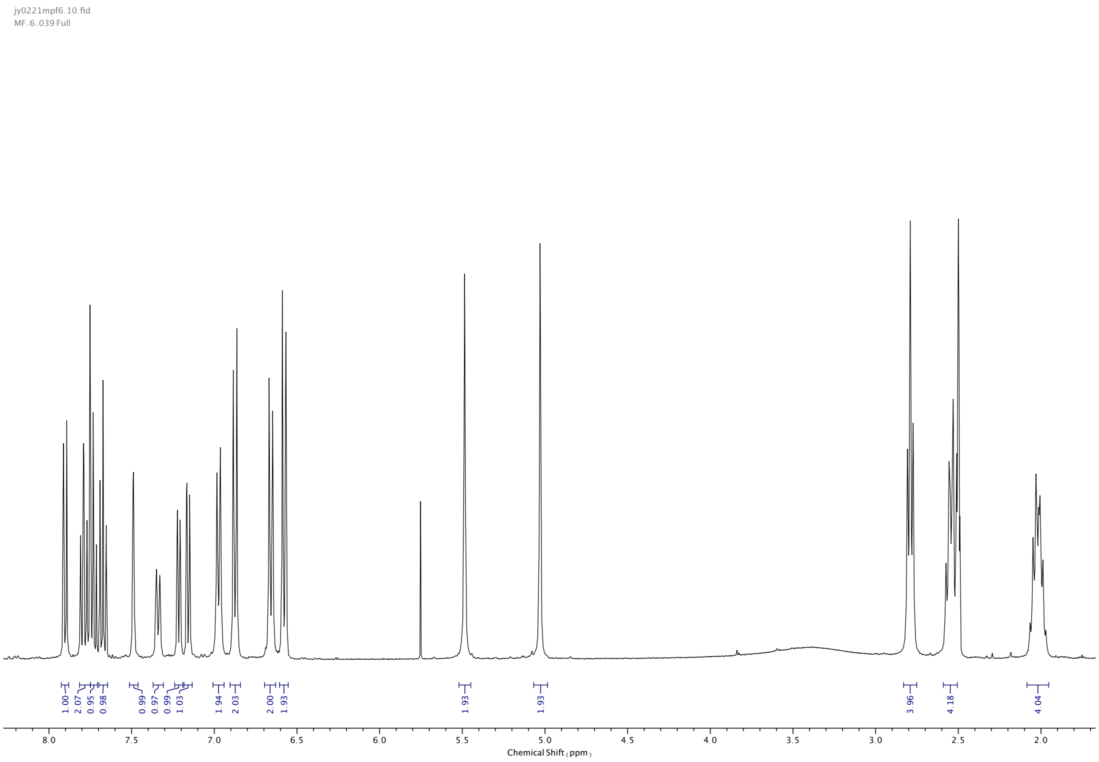

Figure **294**. ^{1}H NMR (DMSO-d$_6$, 400 MHz) of **48**.

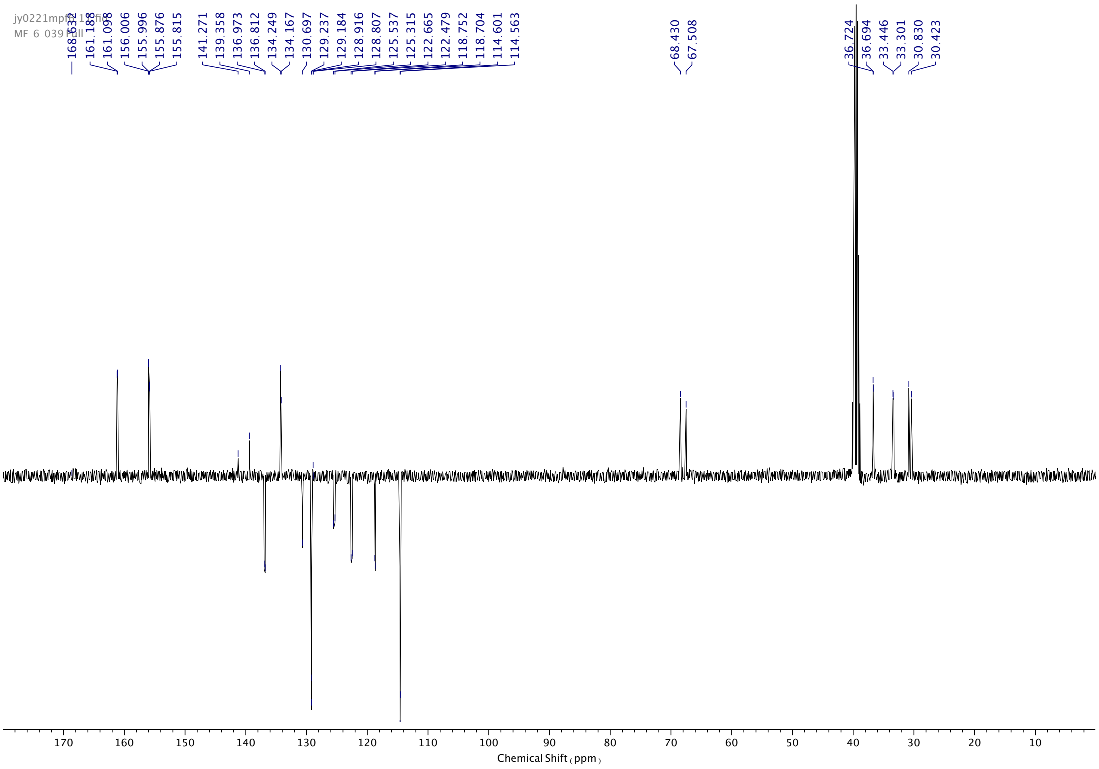

Figure **295**. ^{13}C NMR (DMSO-d$_6$, 101 MHz) of **48**.

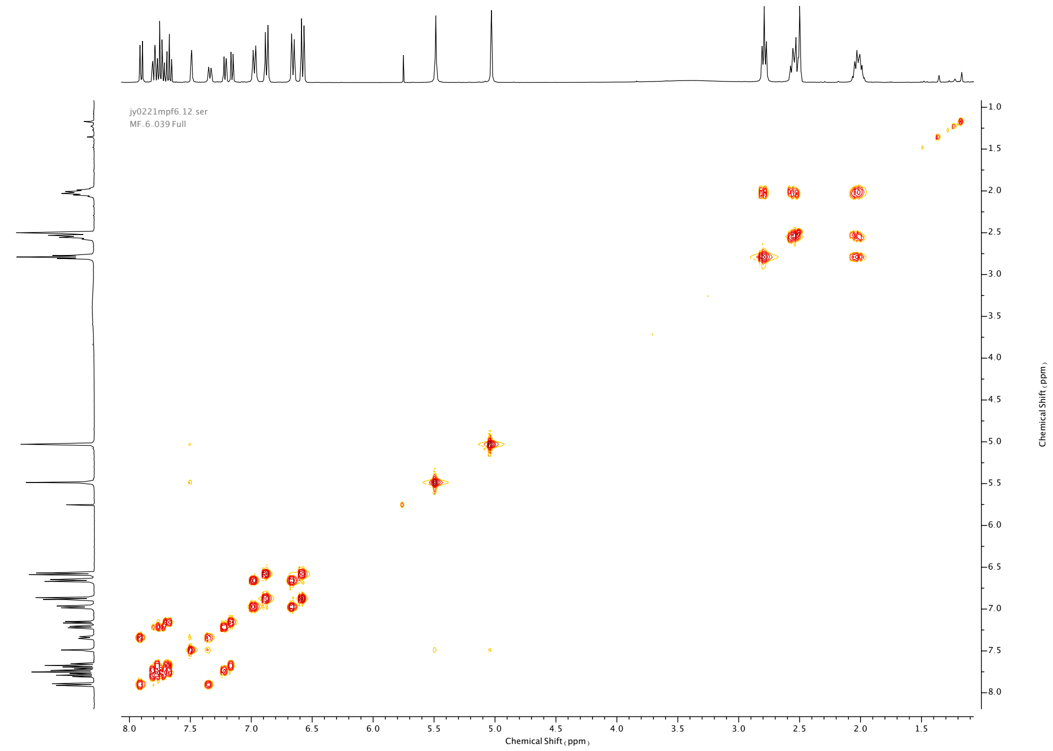

Figure **296**. COSY NMR (DMSO-d$_6$) of **48**.

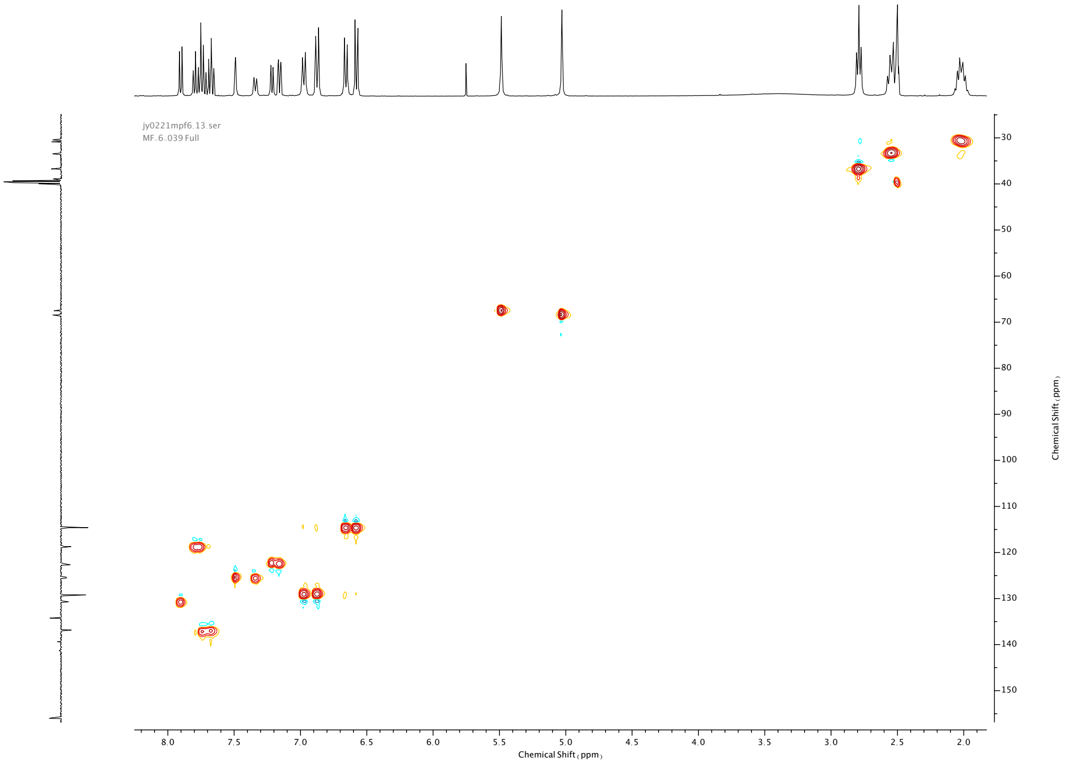

Figure **297**. HSQC NMR (DMSO-d$_6$) of **48**.

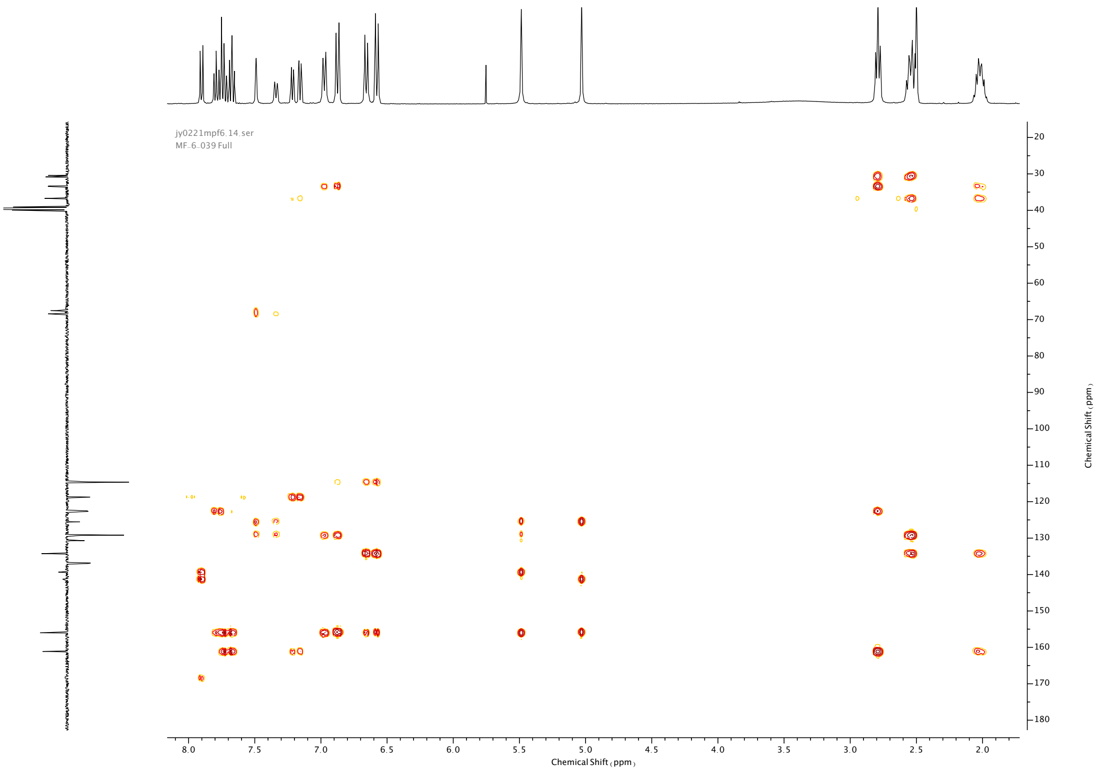

Figure **298**. HMBC NMR (DMSO-d$_6$) of **48**.

Compound **50**

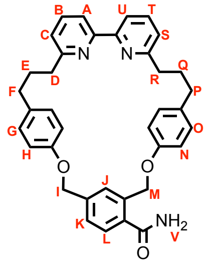

To a degassed solution of **48** (1.50 g, 2.63 mmol, 1.0 eq.) and NEt_3 (0.73 mL, 2.0 eq.) in anhydrous THF (25 mL) was added $SOCl_2$ (0.38 mL, 2.0 eq.) dropwise at 0 °C. The mixture was stirred 0 °C for 30 min then at room temperature for a further 2 h. NH_3 (38% in H_2O) (10 mL) was then added at 0 °C and then stirred at room temperature for 2 h. The mixture was then diluted with EtOAc (100 mL), washed with water (100 mL) and brine (100 mL), then dried over anhydrous $MgSO_4$, filtered and concentrated *in vacuo*. The crude product was purified *via* silica-gel chromatography using a Biotage Isolute SPE column (eluent 1:0 → 4.1 CH_2Cl_2: Et_2O) to afford **50** as a white foam (1.30 g, 2.28 mmol, 87%).^1H NMR (400 MHz, $CDCl_3$, 298 K) δ_H 7.78 (1H, d, *J* = 7.7 Hz, H_A & H_U), 7.75 (1H, d, *J* = 7.7, H_A & H_U), 7.64-7.59 (2H, m, H_L & H_B or H_T), 7.56 (1H, t, *J* = 7.7 Hz, H_B or H_T), 7.38 (1H, s, H_J), 7.32 (1H, dd, *J* = 7.9, 1.7 Hz, H_K), 7.08 (1H, dd, *J* = 7.7, 0.9 Hz, H_C or H_S), 7.02 (1H, dd, *J* = 7.7, 0.8 Hz, H_C or H_S), 6.98 (2H, d, *J* = 8.7 Hz, H_O), 6.92 (2H, d, *J* = 8.7 Hz, H_G), 6.68 (2H, d, *J* = 8.7 Hz, H_N), 6.59 (2H, d, *J* = 8.7 Hz, H_H), 5.82 (1H, br. s, N-H_V), 5.27 (2H, s, H_M), 4.99 (2H, s, H_I), 2.89 (4H, t, *J* = 7.2 Hz, H_D & H_R), 2.64 (4H, app. q, *J* = 7.3 Hz, H_F & H_P), 2.19-2.07 (4H, m, H_E & H_Q). ^{13}C NMR (101 MHz, $CDCl_3$, 298 K) δ_C 170.4, 161.9 (x2), 156.3 (x2), 156.0, 140.9, 136.8, 136.7, 136.3, 135.7, 135.1, 133.4 (x2), 129.6 (x2), 128.9, 128.3, 126.4, 122.7, 122.5, 119.2, 119.1, 116.0, 115.1, 69.5, 69.3, 37.8, 37.8, 34.6, 34.5, 31.3, 30.9. HR-ESI-MS (CH_3CN): *m/z* = 570.2765 $[M+H]^+$ calc. 570.2751.

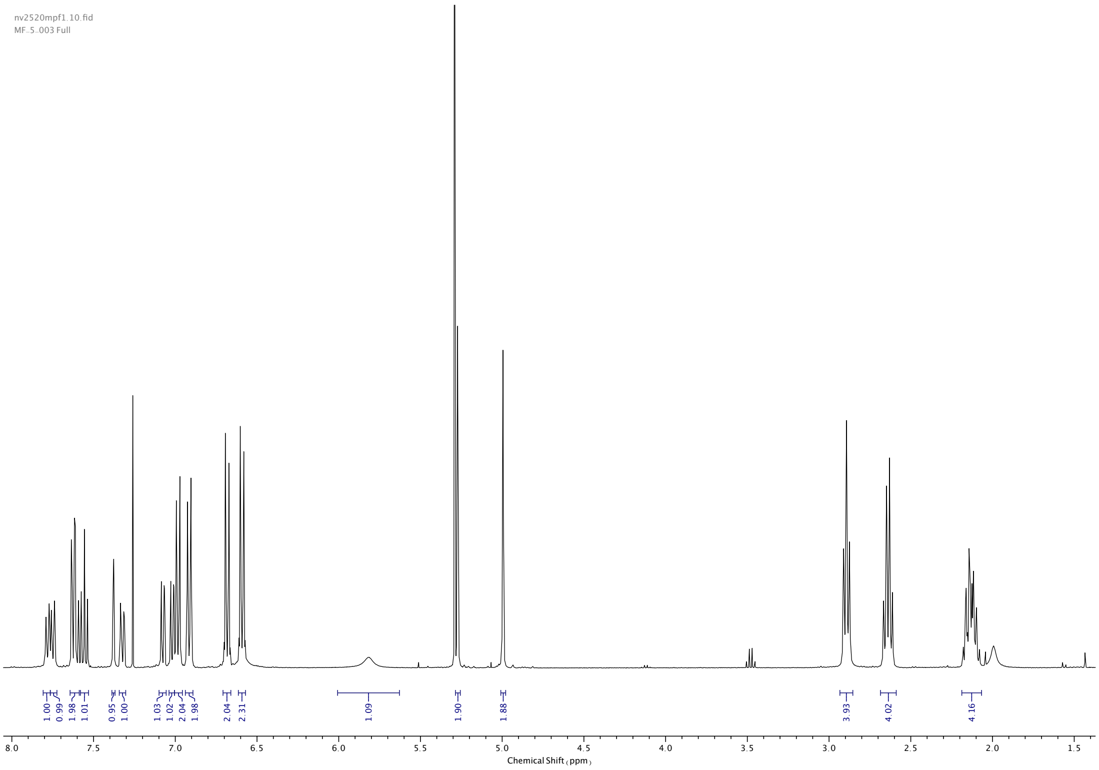

Figure **299**. ^{1}H NMR (CDCl$_3$, 400 MHz) of **50**.

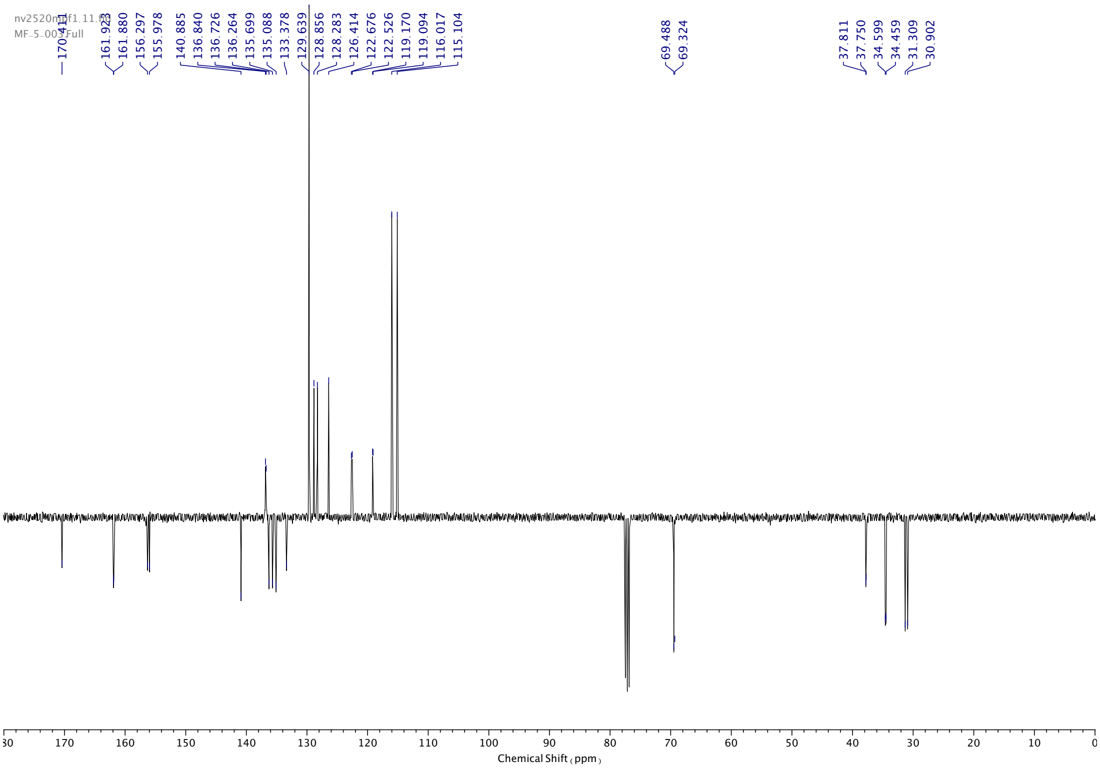

Figure **300**. ^{13}C NMR (CDCl$_3$, 101 MHz) of **50**.

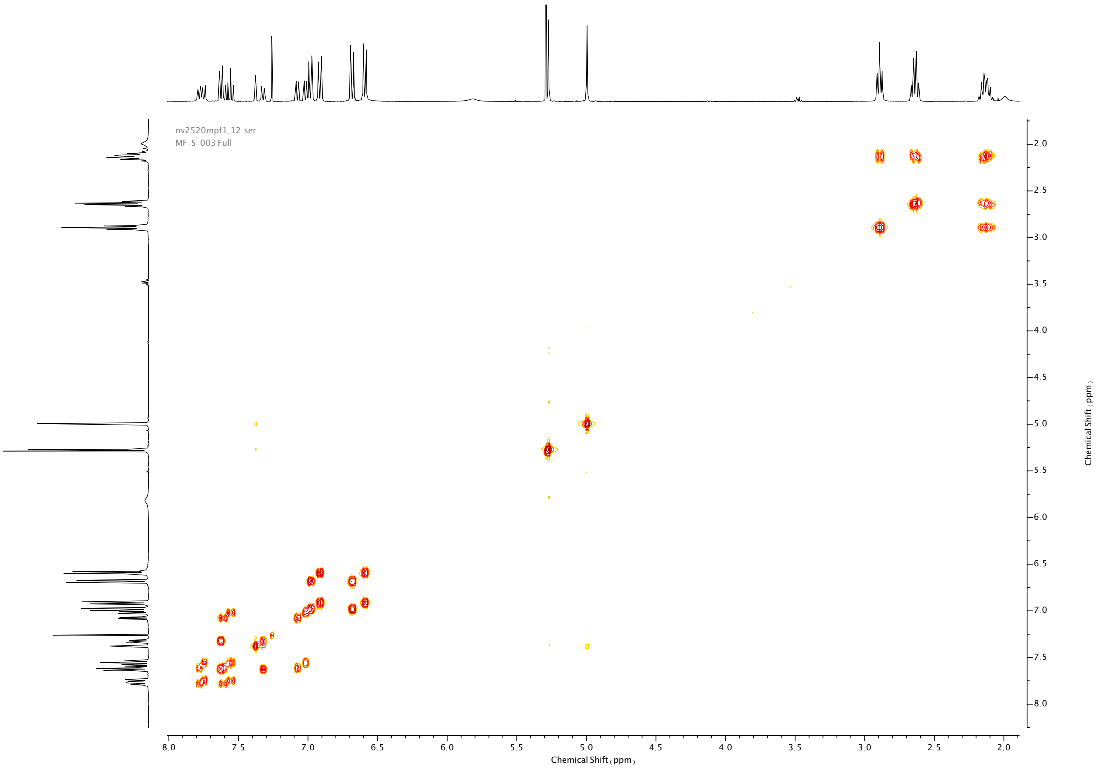

Figure **301**. COSY NMR ($CDCl_3$) of **50**.

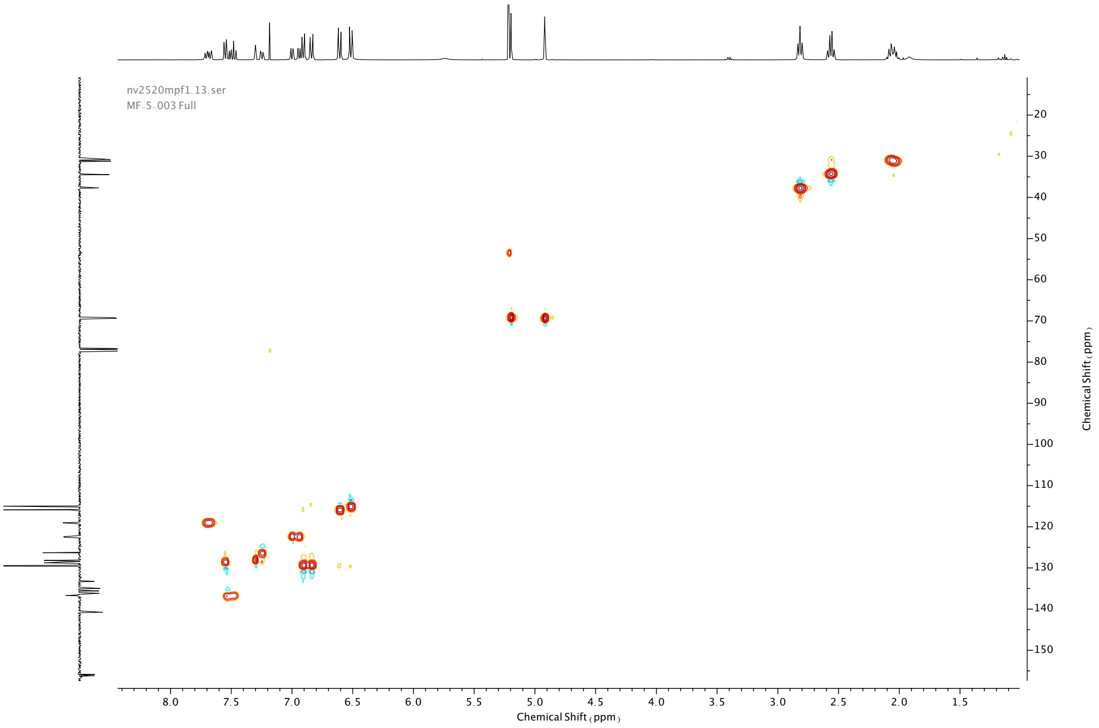

Figure **302**. HSQC NMR ($CDCl_3$) of **50**.

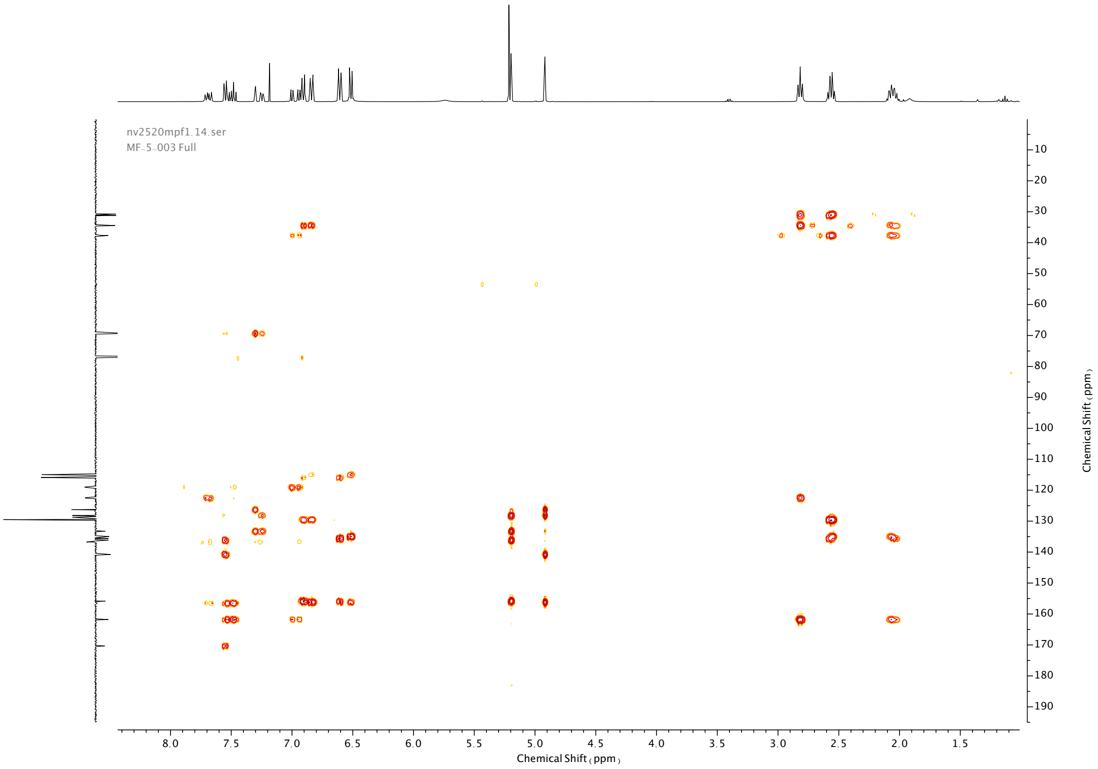

Figure **303**. HMBC NMR ($CDCl_3$) of **50**.

Compound **59**

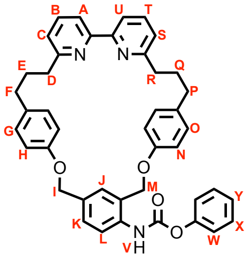

59 was prepared according to general procedure **(4)** from macrocycle **50** (345 mg, 0.61 mmol). Purification by column chromatography (eluent 1:0 → 19:1 CH_2Cl_2: Et_2O) afforded **59** as an off-white foam (258 mg, 0.39 mmol, 64%).

or

Prepared according to general procedure **(5)** from macrocycle **48** (297 mg, 0.53 mmol). Purification by column chromatography (eluent 1:0 → 19:1 CH_2Cl_2: Et_2O) afforded **59** as an off-white foam (315 mg, 0.48 mmol, 90%). ^{1}H NMR (400 MHz, $CDCl_3$, 298 K) δ_H 8.11 (1H, br. s, H_v), 7.98 (1H, d, *J* = 7.9 Hz, H_L), 7.82 (2H, app. t, *J* = 6.9 Hz, H_A & H_U), 7.62 (1H, t, *J* = 7.7 Hz, H_B or H_T), 7.58 (1H, t, *J* = 7.7 Hz, H_B or H_T), 7.39 (2H, t, *J* = 8.0 Hz, H_W), 7.28 (1H, d, *J* = 8.2, 1.9 Hz, H_K), 7.26-7.18 (4H, m, H_J, H_X & H_Y), 7.05 (2H, t, *J* = 7.9 Hz, H_S & H_C), 6.94 (2H, d, *J* = 8.6 Hz, H_O), 6.93 (2H, d, *J* = 8.6 Hz, H_G), 6.72 (2H, d, *J* = 8.7 Hz, H_H), 6.66 (2H, d, *J* = 8.6 Hz, H_N), 5.11 (2H, s, H_M), 5.04 (2H, s, H_I), 2.90 (4H, app. t, *J* = 7.2 Hz, H_D & H_R), 2.64 (2H, t, *J* = 7.9 Hz, H_F or H_P), 2.62 (2H, t, *J* = 7.9 Hz, H_F or H_P), 2.18-2.06 (4H, m, H_E & H_Q). ^{13}C NMR (101 MHz, $CDCl_3$, 298 K) δ_C 161.8 (x2), 156.6 (x2), 156.5 (x2), 155.5, 152.0, 150.8, 136.8, 136.7 (X2), 136.1, 135.2, 129.6, 129.5 (x2), 128.34, 128.0 (x2), 125.8, 122.7, 122.6 (x2), 121.8, 119.0 (x2), 115.9, 115.6, 70.2, 69.9, 37.9 (x2), 34.5 (x2), 31.2 (x2). HR-ESI-MS (CH_3CN): *m/z* = 662.3023 $[M+H]^+$ calc. 662.3013

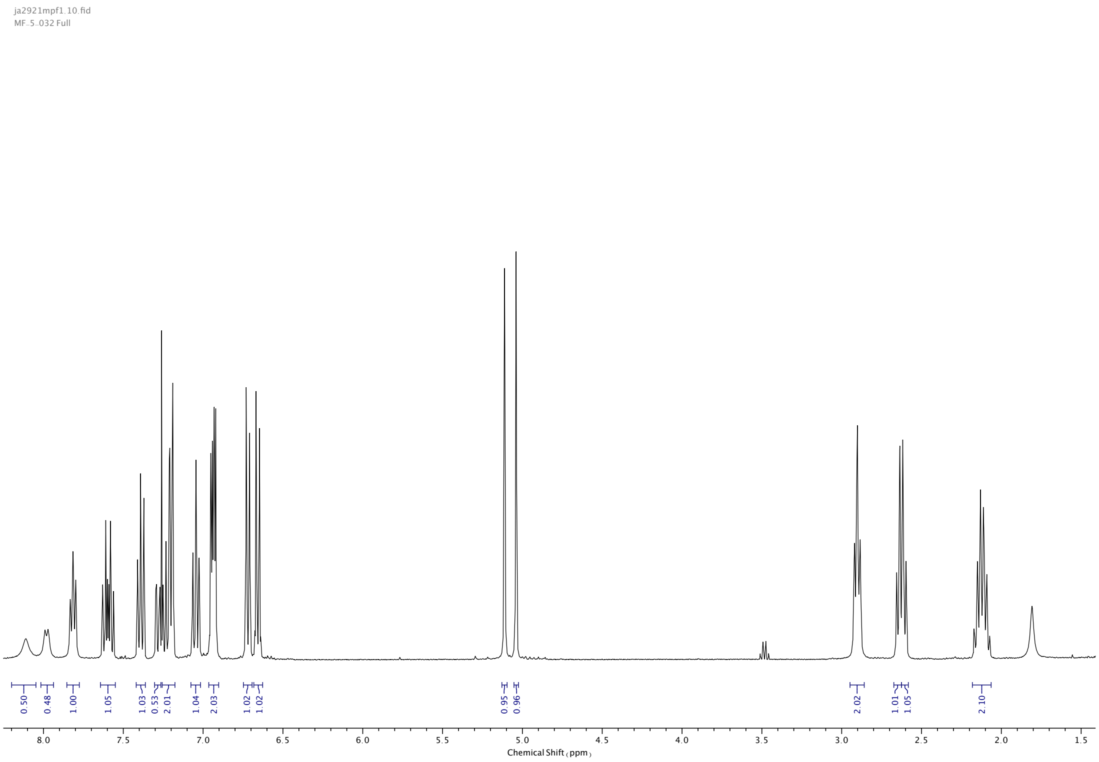

Figure **304**. ^{1}H NMR (CDCl$_3$, 400 MHz) of **59**.

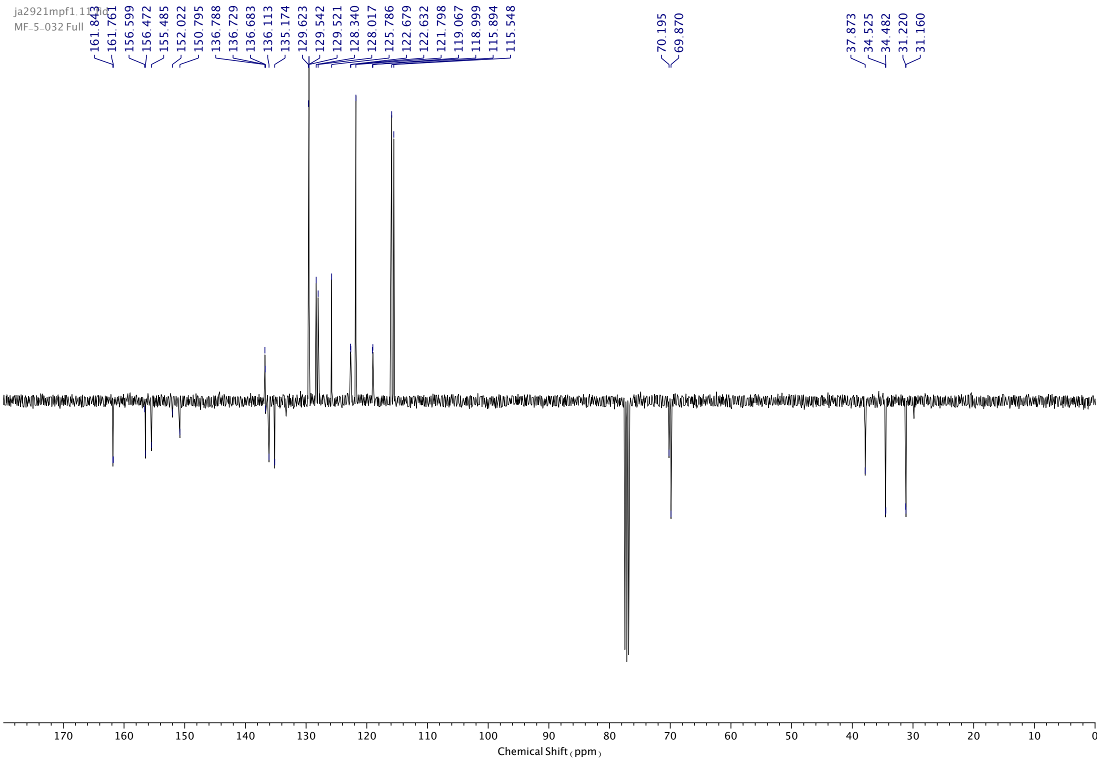

Figure **305**. ^{13}C NMR (CDCl$_3$, 101 MHz) of **59**.

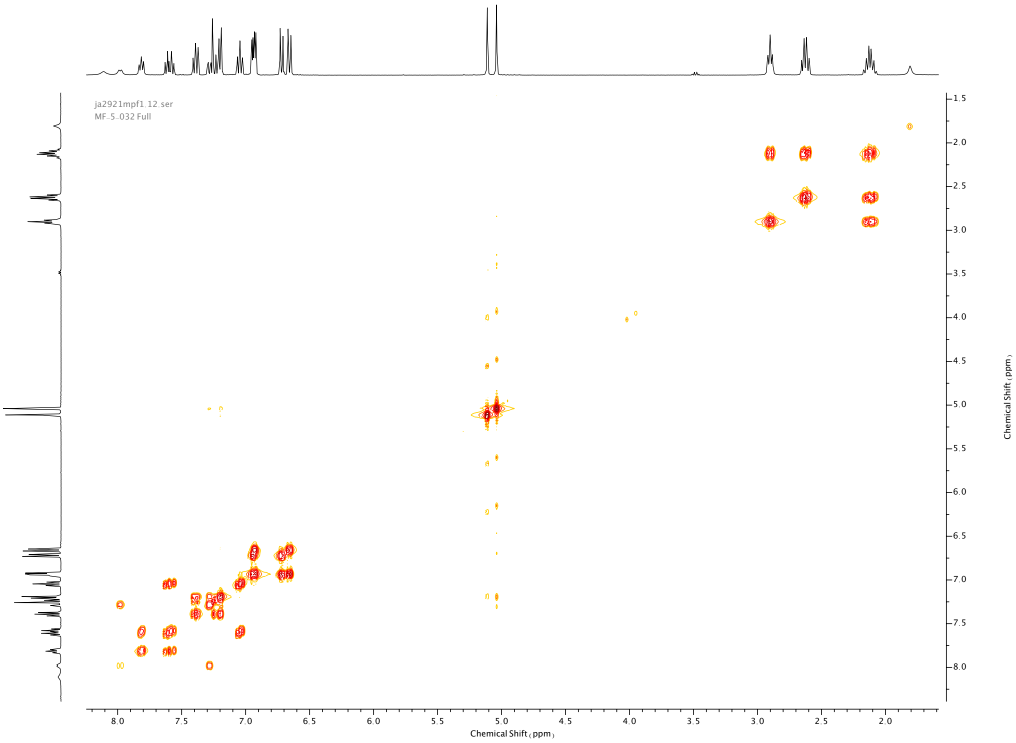

Figure **306**. COSY NMR (CDCl$_3$) of **59**.

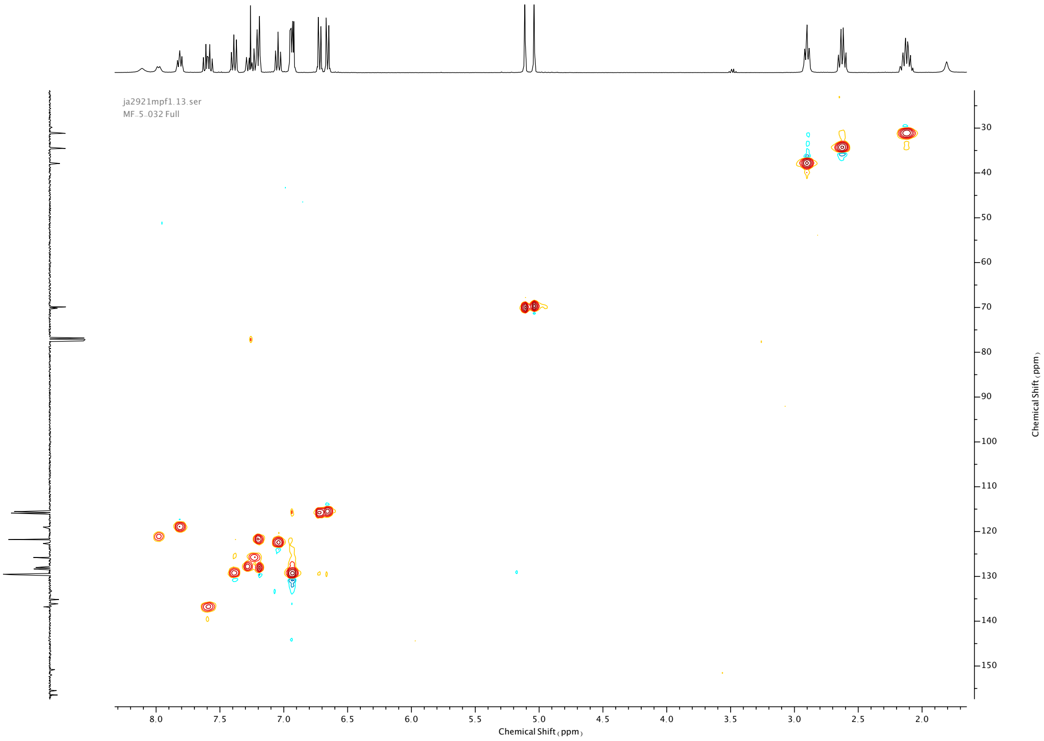

Figure **307**. HSQC NMR (CDCl$_3$) of **59**.

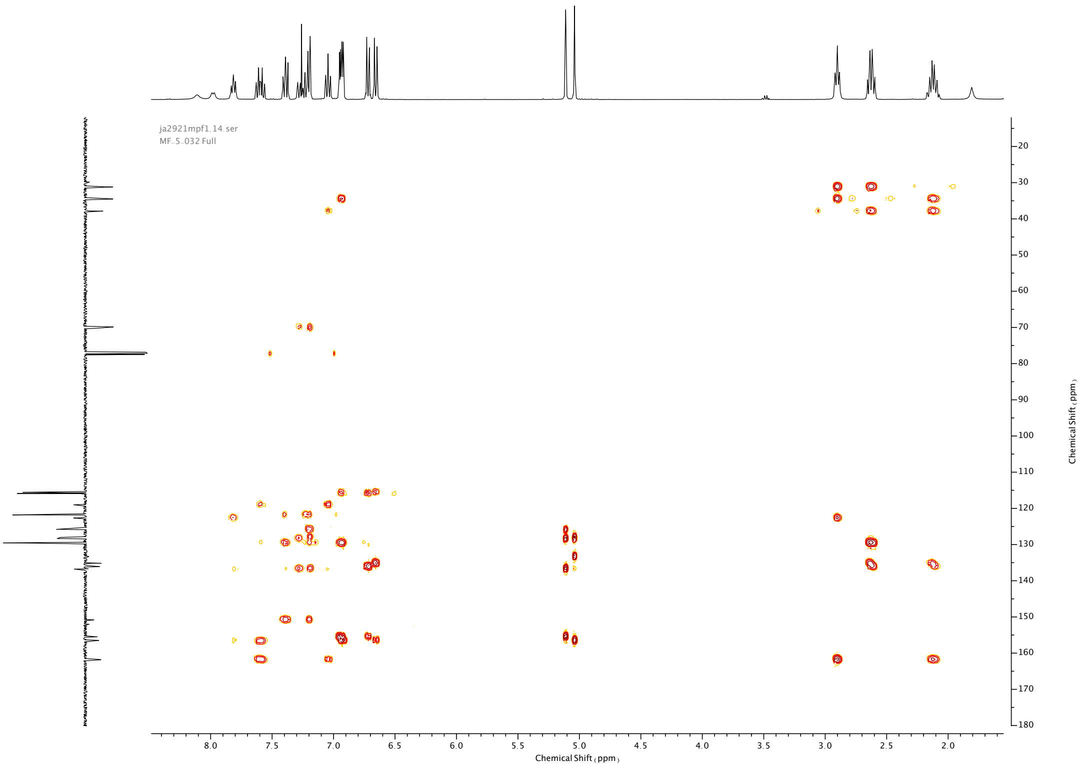

Figure **308**. HMBC NMR ($CDCl_3$) of **59**.

Compound **64**

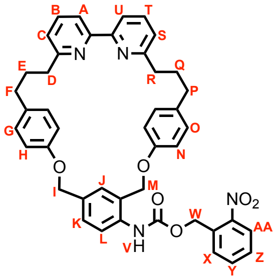

64 was synthesised according to general procedure **(6)** from macrocycle **59** (25 mg, 0.038 mmol) and trigger alcohol **63** (17 mg, 0.114 mmol). Purification by column chromatography (eluent 1:0 → 9:1 CH_2Cl_2: Et_2O) afforded **64** as an orange foam (18 mg, 0.025 mmol, 65%).^{1}H NMR (400 MHz, $CDCl_3$, 298 K) δ_H 8.12 (1H, d, *J* = 7.9 Hz, H_{AA}), 7.98-7.79 (3H, m, H_L, H_A & H_U), 7.65-7.56 (4H, m, H_B, H_T, H_X & H_Y), 7.50-7.45 (1H, m, H_Z), 7.26 (1H, dd, *J* = 8.4, 1.9 Hz, H_K), 7.17 (1H, d, *J* = 1.8 Hz, H_J), 7.05 (2H, app. t, *J* = 7.6 Hz, H_C & H_S), 6.95 (4H, m, H_G & H_O), 6.69 (2H, d, *J* = 8.7 Hz, H_H or H_N), 6.64 (2H, d, *J* = 8.7 Hz, H_H or H_N), 5.62 (2H, s, H_W), 5.07 (2H, s, H_M), 5.02 (2H, s, H_I), 2.92 (4H, m, H_D & H_R), 2.66-2.58 (4H, m, H_F & H_P), 2.17-2.06 (4H, m, H_E & H_Q).^{13}C NMR (101 MHz, $CDCl_3$, 298 K) δ_C 161.8, 161.7, 156.4 (x2), 155.4 (x2), 153.2, 147.5, 137.0 (x2), 136.7 (x2), 136.1, 135.1, 133.9, 133.2, 132.9, 129.6, 129.5, 128.8 (x2), 128.3, 128.0, 125.2, 122.8 (x2), 121.2 (HSQC), 119.2 (x2), 115.9, 115.5, 70.1, 69.8, 63.7, 37.7 (x2), 34.5 (x2), 31.3, 31.2. HR-ESI-MS (CH_3CN): *m/z* = 721.3022 $[M+H]^+$ calc. 721.3021.

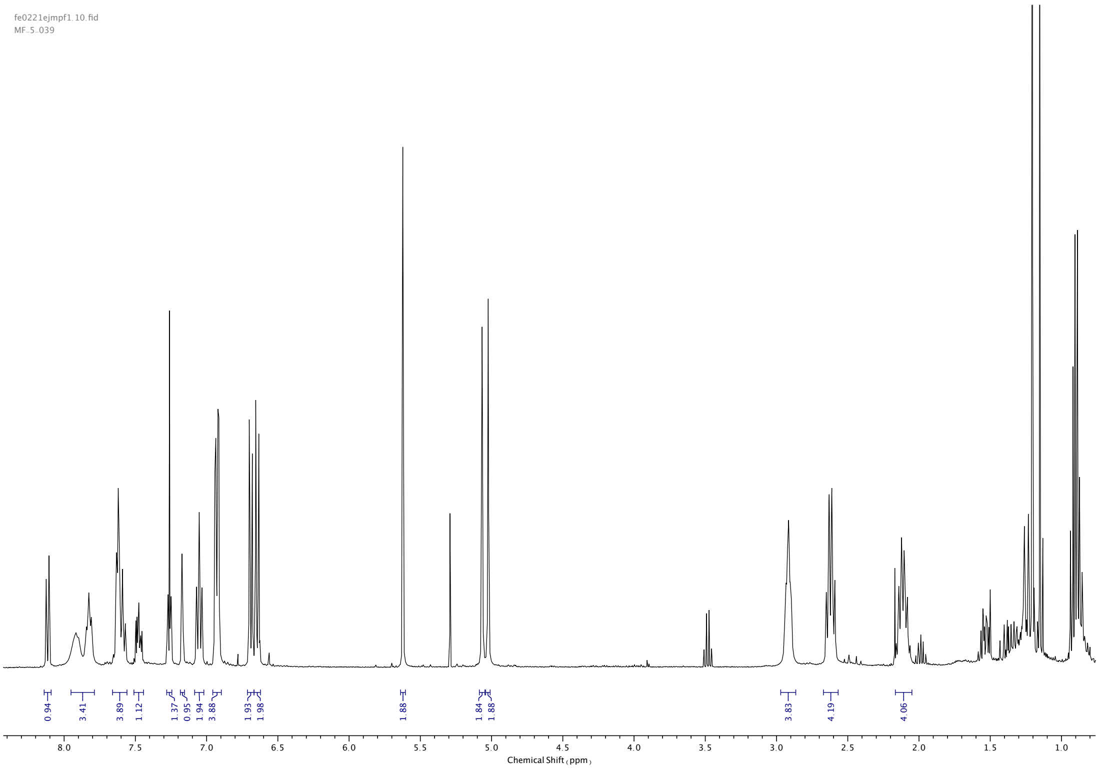

Figure **309**. ^{1}H NMR (CDCl$_3$, 400 MHz) of **64**.

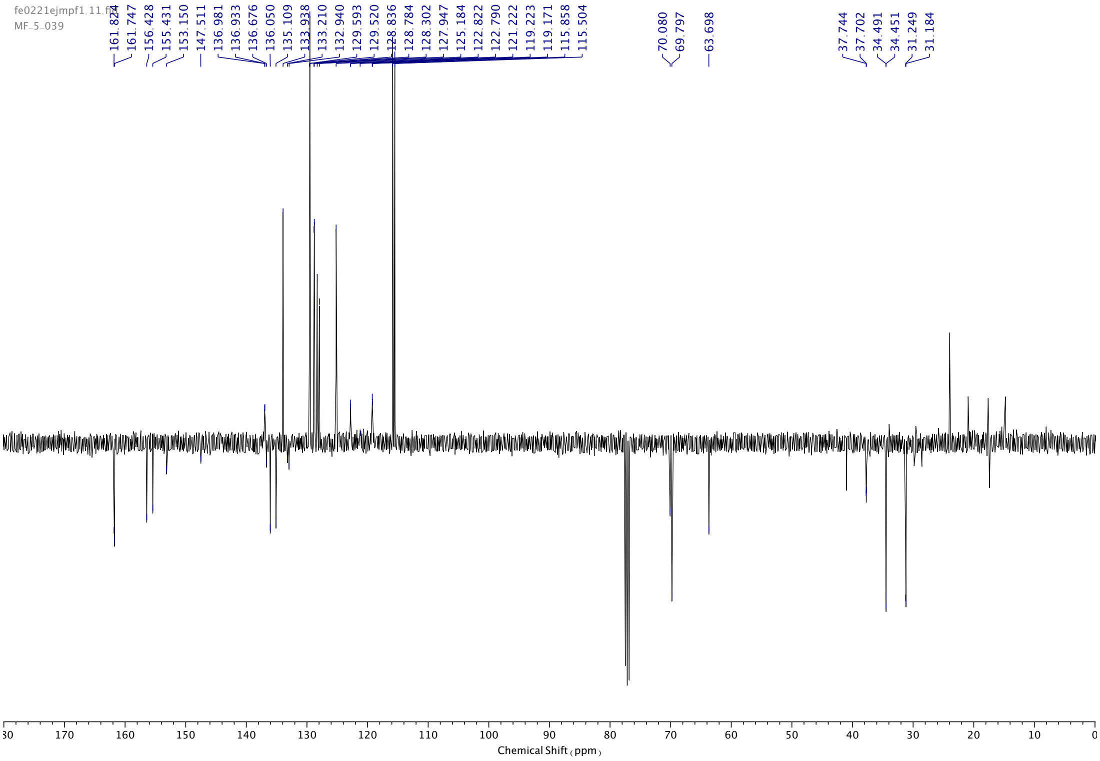

Figure **310**. ^{13}C NMR (CDCl$_3$, 101 MHz) of **64**.

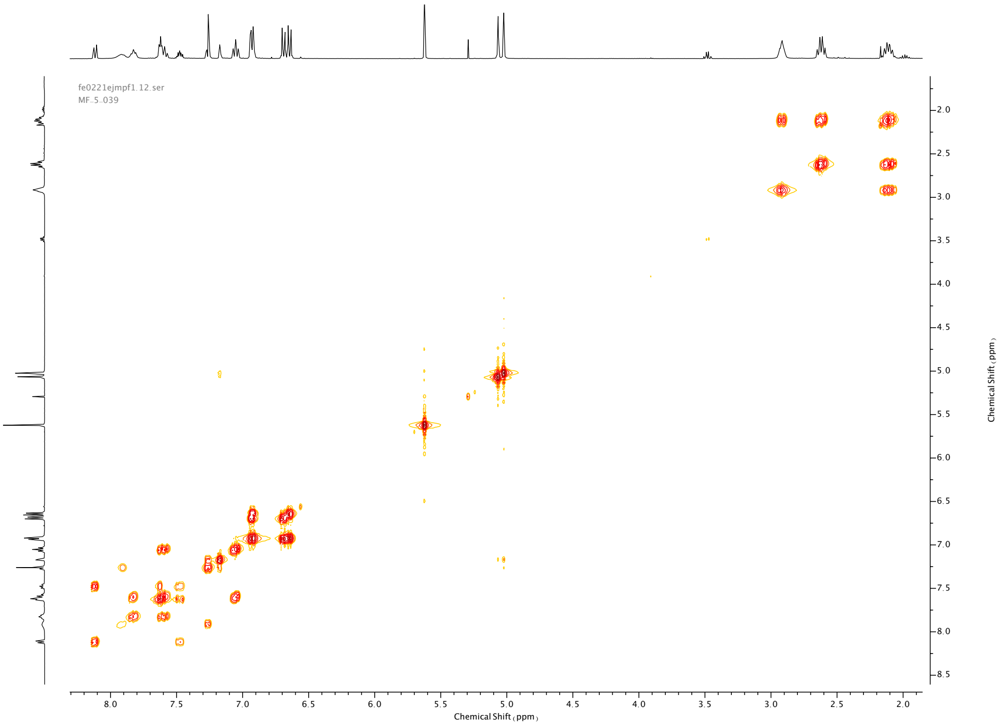

Figure **311**. COSY NMR (CDCl$_3$) of **64**.

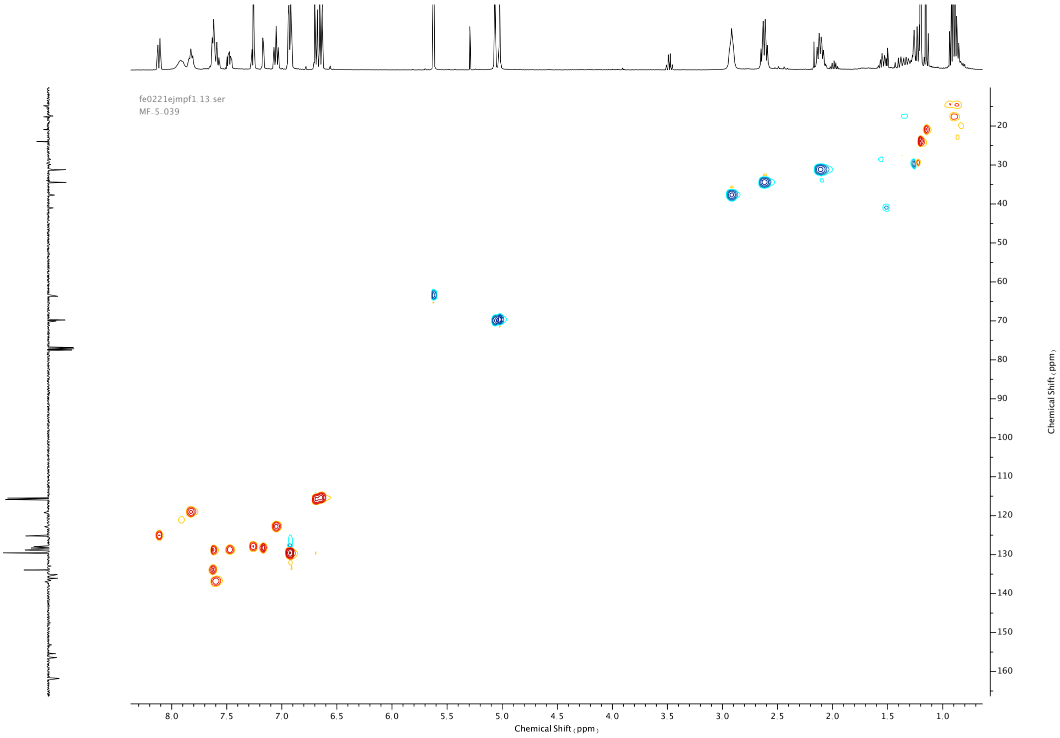

Figure **312**. HSQC NMR (CDCl$_3$) of **64**.

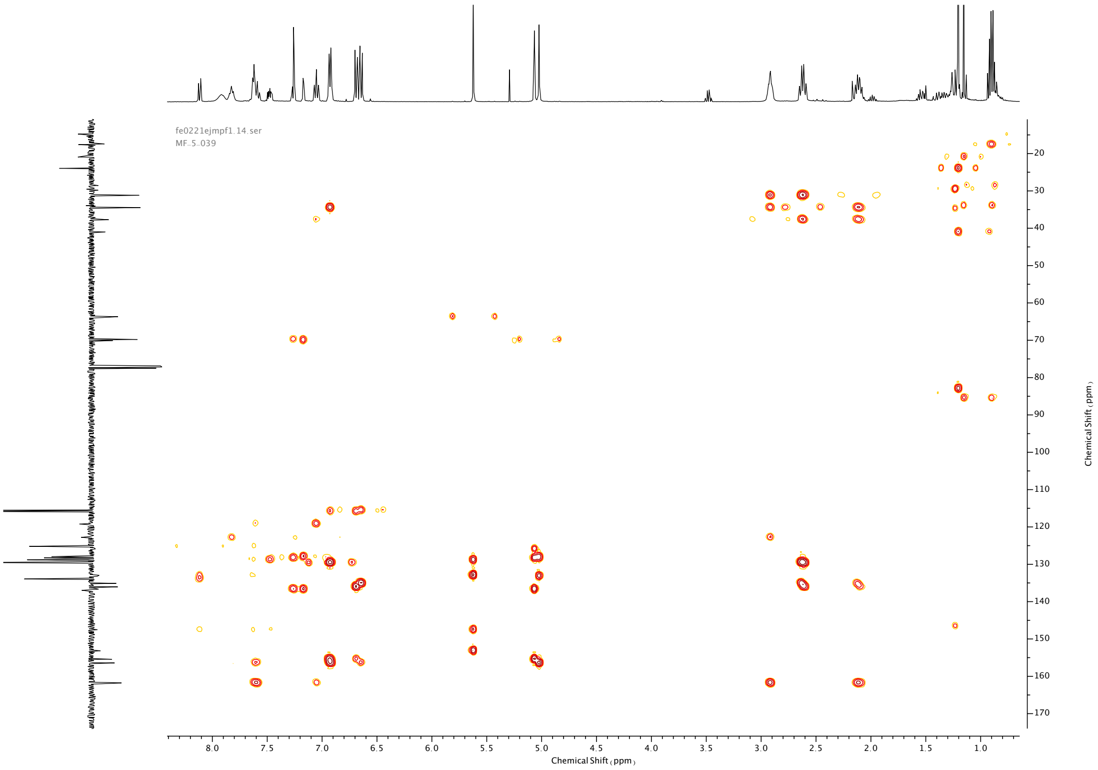

Figure **313**. HMBC NMR ($CDCl_3$) of **64**.

Compound **66**

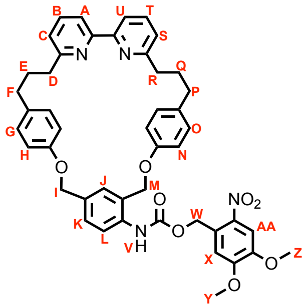

66 was synthesised according to general procedure **(6)** from macrocycle **59** (207 mg, 0.31 mmol) and trigger alcohol **65** (200 mg, 0.94 mmol). Purification by column chromatography (eluent 9:1 → 4:1 Hexane: Acetone) afforded **66** as a yellow foam (187 mg, 0.24 mmol, 77%). ^{1}H NMR (400 MHz, $CDCl_3$, 298 K) δ_H 7.95-7.86 (1H, m, H$_L$), 7.85-7.82 (2H, m, H$_A$ & H$_U$), 7.72 (1H, s, H$_{AA}$), 7.59 (2H, app. q, *J* = 8.0 Hz, H$_B$ & H$_T$), 7.27 (1H, dd, *J* = 8.6, 2.0 Hz, H$_K$), 7.17 (1H, d, *J* = 1.8 Hz, H$_J$), 7.07-7.01 (3H, m, H$_X$, H$_C$ & H$_S$), 6.93 (2H, d, *J* = 8.7 Hz, H$_G$ or H$_O$), 6.91 (2H, d, *J* = 8.7 Hz, H$_G$ or H$_O$), 6.66 (2H, d, *J* = 8.7 Hz, H$_H$ or H$_N$), 6.65 (2H, d, *J* = 8.7 Hz, H$_H$ or H$_N$), 5.62 (2H, s, H$_W$), 5.05 (2H, s, H$_I$ or H$_M$), 5.03 (2H, s, H$_I$ or H$_M$), 3.95 (3H, s, H$_Z$), 3.87 (3H, s, H$_Y$), 2.94-2.87 (4H, m, H$_D$ & H$_R$), 2.63 (2H, t, *J* = 7.6 Hz, H$_F$ or H$_P$), 2.60 (2H, t, *J* = 7.6 Hz, H$_F$ or H$_P$), 2.17-2.05 (4H, m, H$_E$ & H$_Q$). ^{13}C NMR (101 MHz, $CDCl_3$, 298 K) δ_C 161.8, 161.7, 156.5 (x2), 155.5, 153.7, 153.2, 148.3, 140.0, 136.9 (x2), 136.7 (x2), 136.1, 135.1, 133.3, 129.6, 129.6, 128.3, 128.0, 127.9, 126.5 (HMBC), 122.7 (x2), 121.3 (HSQC), 119.1 (x2), 115.8, 115.5, 110.2, 108.4, 70.1, 69.8, 64.0, 56.6, 56.5, 37.8 (x2), 34.50 (x2), 31.2, 31.1. HR-ESI-MS (CH_3CN): *m/z* = 781.3244 [M+H]$^+$ calc. 781.3232.

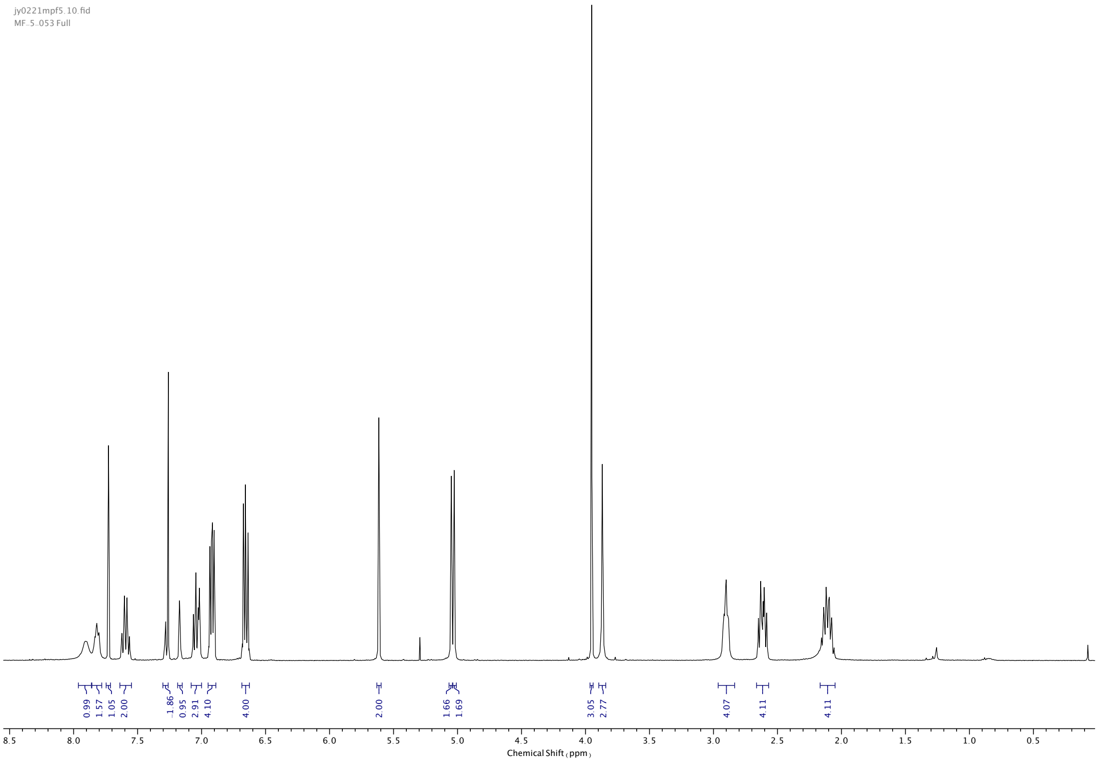

Figure **314**. ^{1}H NMR ($CDCl_3$, 400 MHz) of **66**.

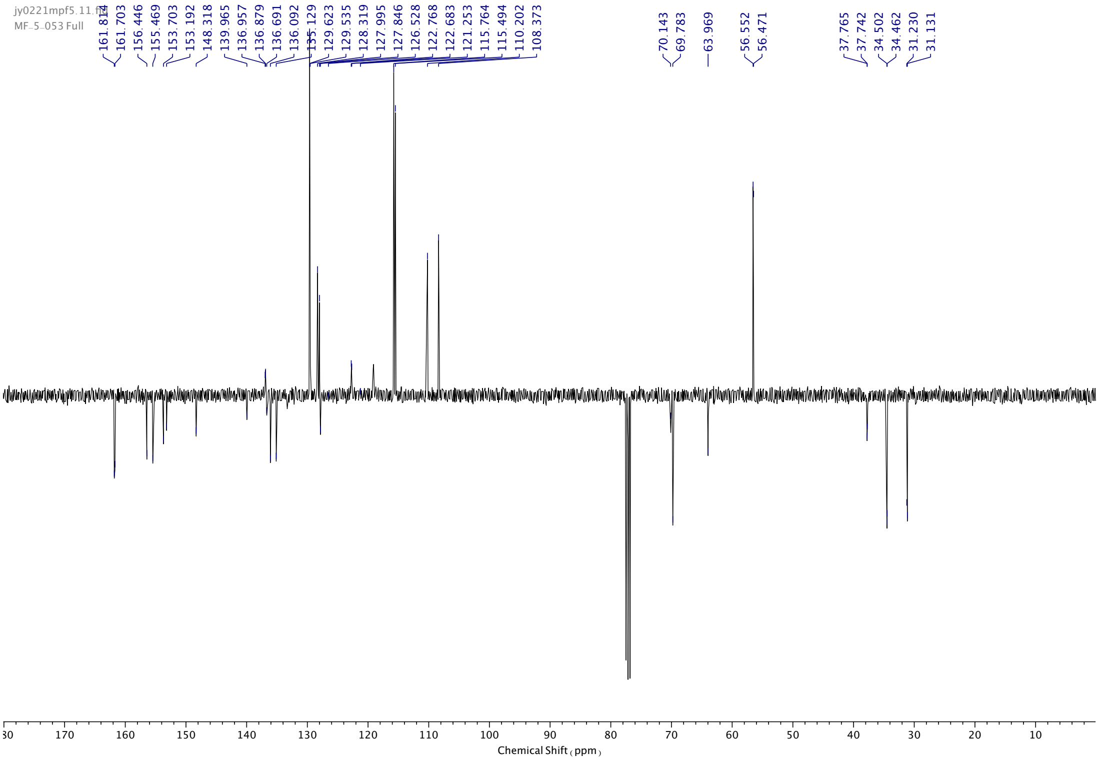

Figure **315**. ^{13}C NMR ($CDCl_3$, 101 MHz) of **66**.

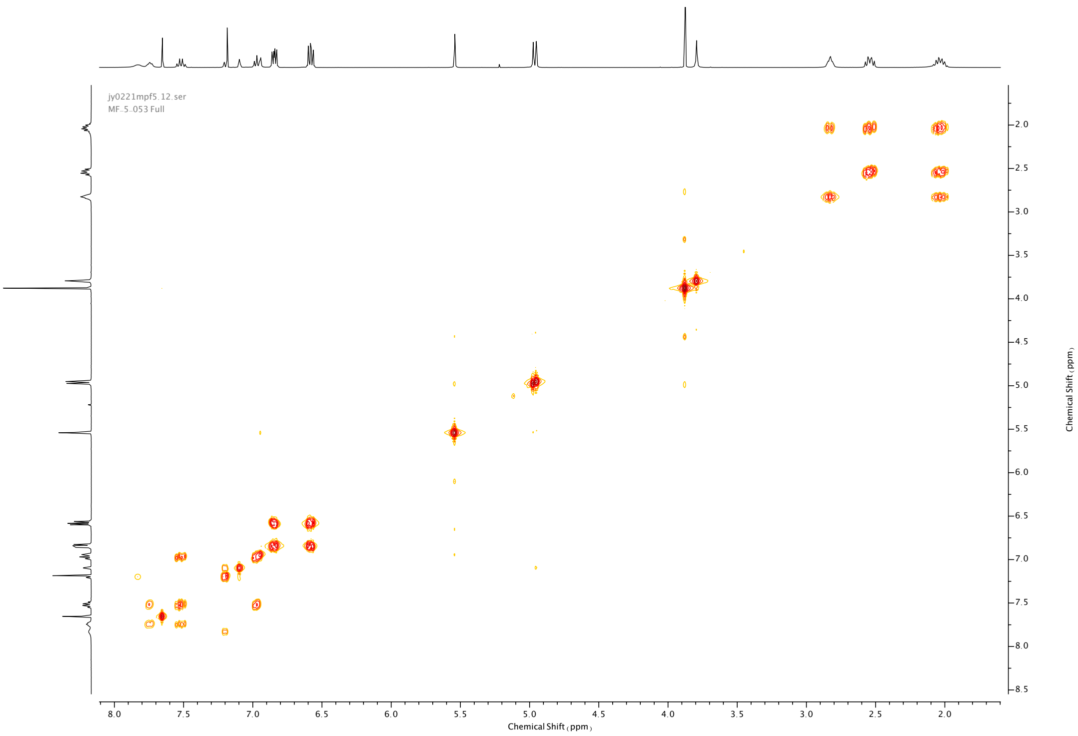

Figure **316**. COSY NMR (CDCl$_3$) of **66**.

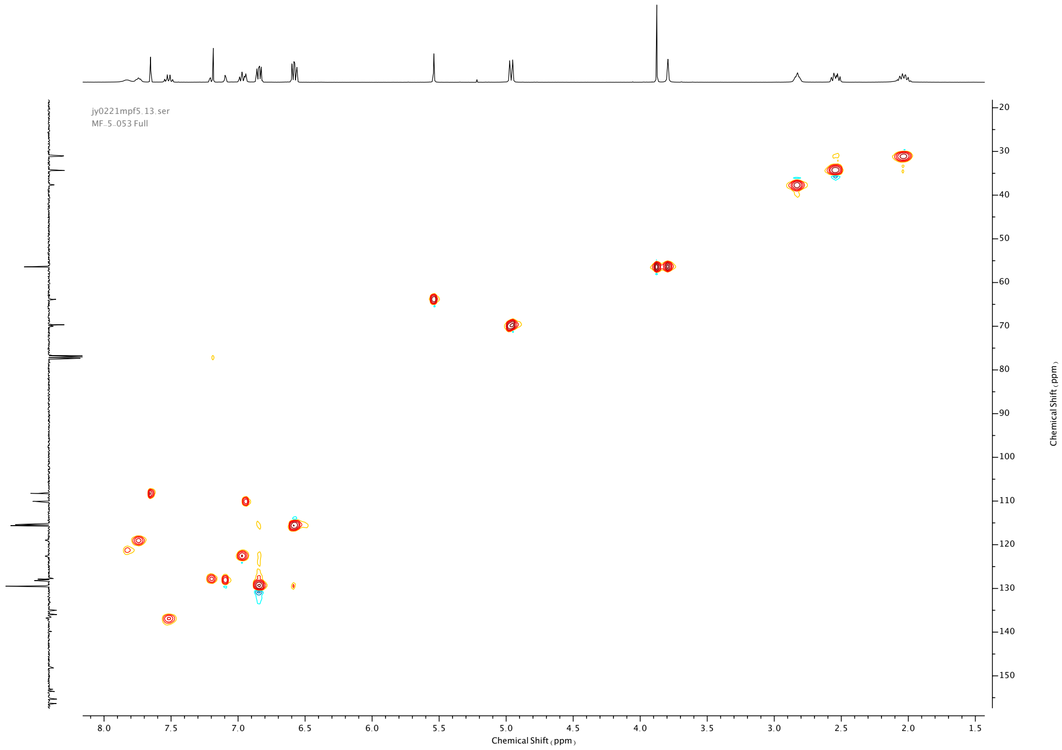

Figure **317**. HSQC NMR (CDCl$_3$) of **66**.

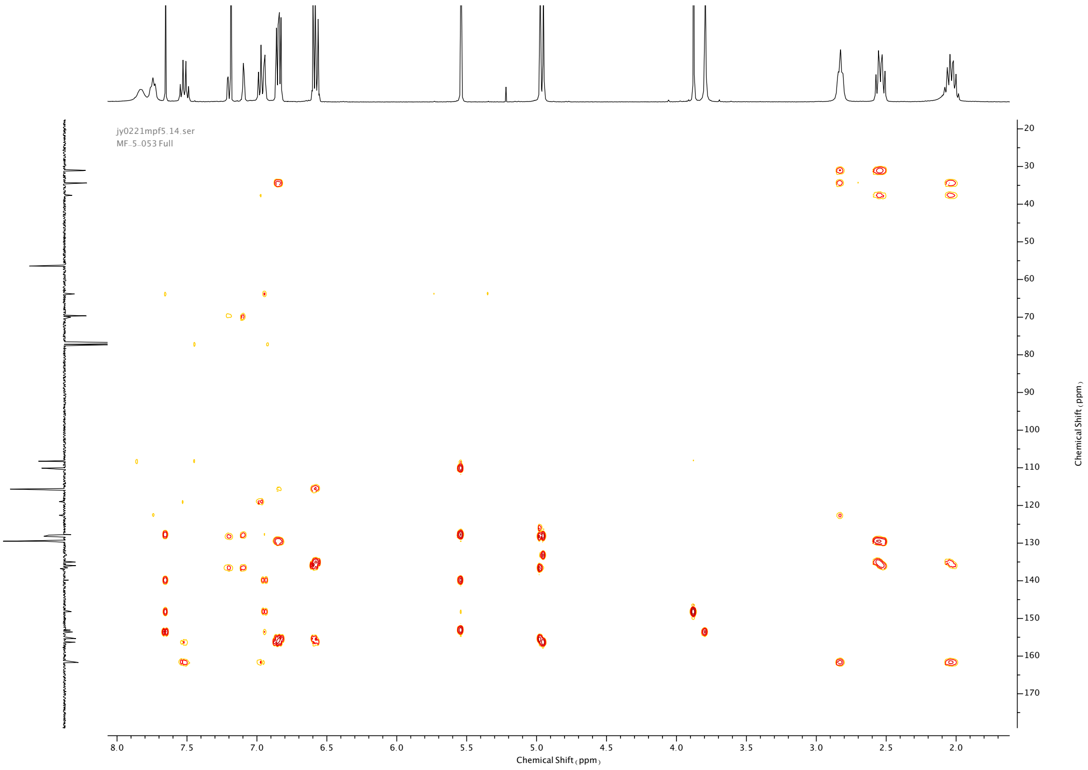

Figure **318**. HMBC NMR ($CDCl_3$) of **66**.

Compound **68**

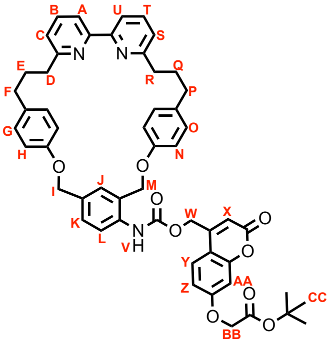

68 was synthesised according to general procedure **(6)** from macrocycle **59** (50 mg, 0.076 mmol) and trigger alcohol **67** (69 mg, 0.23 mmol). Purification by column chromatography (eluent 9:1 → 4:1 CH_2Cl_2: Et_2O) afforded **68** as a white foam (42 mg, 0.048 mmol, 63%). ^1H NMR (400 MHz, $CDCl_3$, 298 K) δ_H 8.03 (1H, br. s, N-H_V), 7.95-7.88 (1H, m, H_L), 7.84 (2H, d, *J* = 7.7 Hz, H_A & H_U), 7.60 (1H, t, *J* = 7.7 Hz, H_B or H_T), 7.59 (1H, t, *J* = 7.7 Hz, H_B or H_T), 7.47 (1H, d, *J* = 8.9 Hz, H_Y), 7.28 (1H, dd, *J* = 8.4, 1.9 Hz, H_K), 7.17 (1H, d, *J* = 1.8 Hz, H_J), 7.05 (2H, app. t, *J* = 7.6 Hz, H_C & H_S), 6.95-6.89 (5H, m ,H_G, H_O & H_Z), 6.80 (1H, d, *J* = 2.6 Hz, H_{AA}), 6.60 (4H, app. t, *J* = 8.8 Hz, H_H & H_N), 6.39 (1H, br. s, H_X), 5.34 (2H, d, *J* = 1.4 Hz, H_W), 5.06 (2H, s, H_M), 5.03 (2H, s, H_I), 4.58 (2H, s, H_{BB}), 2.92 (4H, t, *J* = 6.7 Hz, H_D & H_R), 2.66-2.58 (4H, m, H_F & H_P), 2.17-2.05 (4H, m, H_E & H_Q), 1.50 (9H, s, H_{CC}). ^{13}C NMR (101 MHz, $CDCl_3$, 298 K) δ_C 167.1, 161.8 (x2) 161.2, 160.8, 156.4 (x2), 155.5, 155.4, 152.7, 149.6, 143.9 (HMBC), 136.9 (x2), 136.4, 136.1, 135.1, 133.5, 129.7, 129.5, 128.3, 128.0, 126.2 (HMBC), 124.8, 122.9 (x2), 121.1 (HSQC), 119.1 (x2), 115.8, 115.6, 113.1, 111.5, 110.6, 102.1, 83.2, 70.1, 69.8, 65.8, 62.0, 37.7 (x2), 34.5, 34.4, 31.2, 31.1, 28.2. HR-ESI-MS (CH_3CN): *m/z* = 874.3710 $[M+H]^+$ calc. 874.3698.

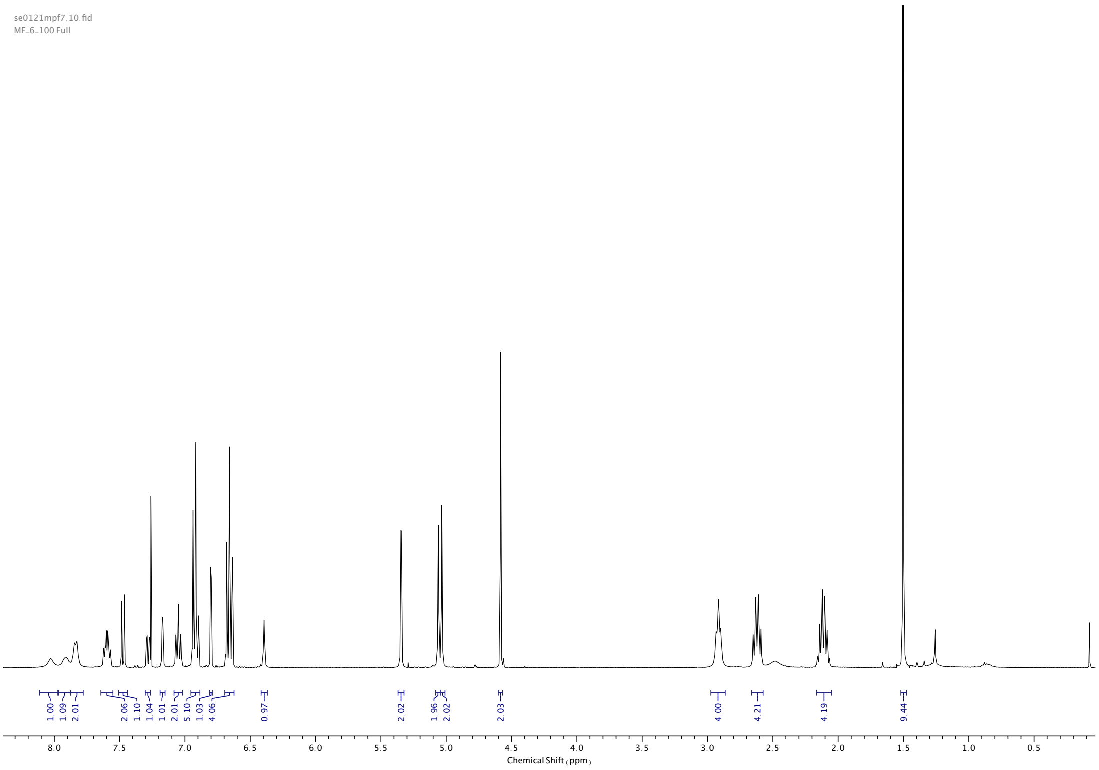

Figure **319**. ^{1}H NMR (CDCl$_3$, 400 MHz) of **68**.

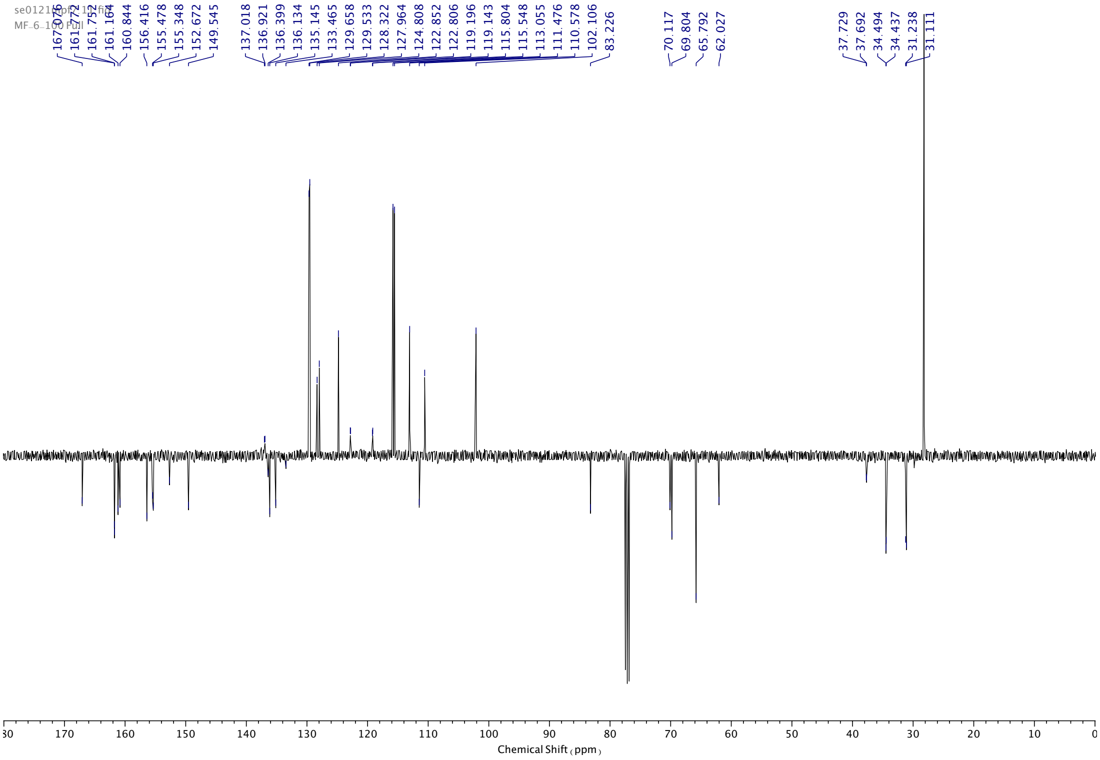

Figure **320**. ^{13}C NMR (CDCl$_3$, 101 MHz) of **68**.

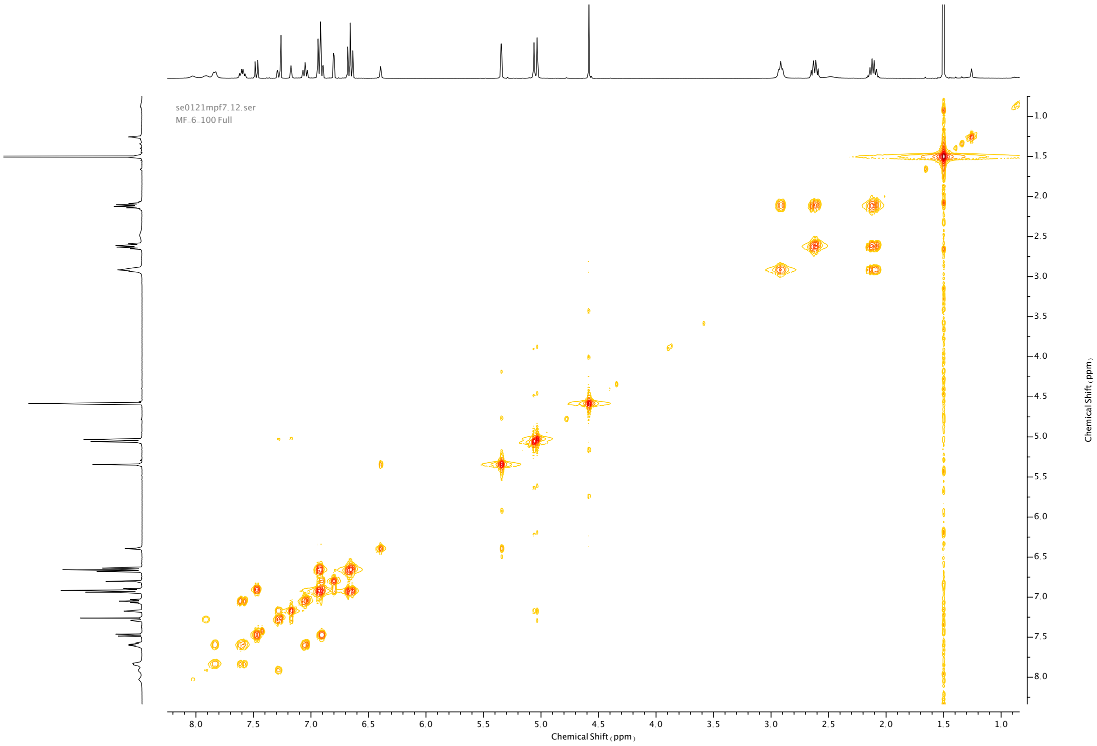

Figure **321**. COSY NMR ($CDCl_3$) of **68**.

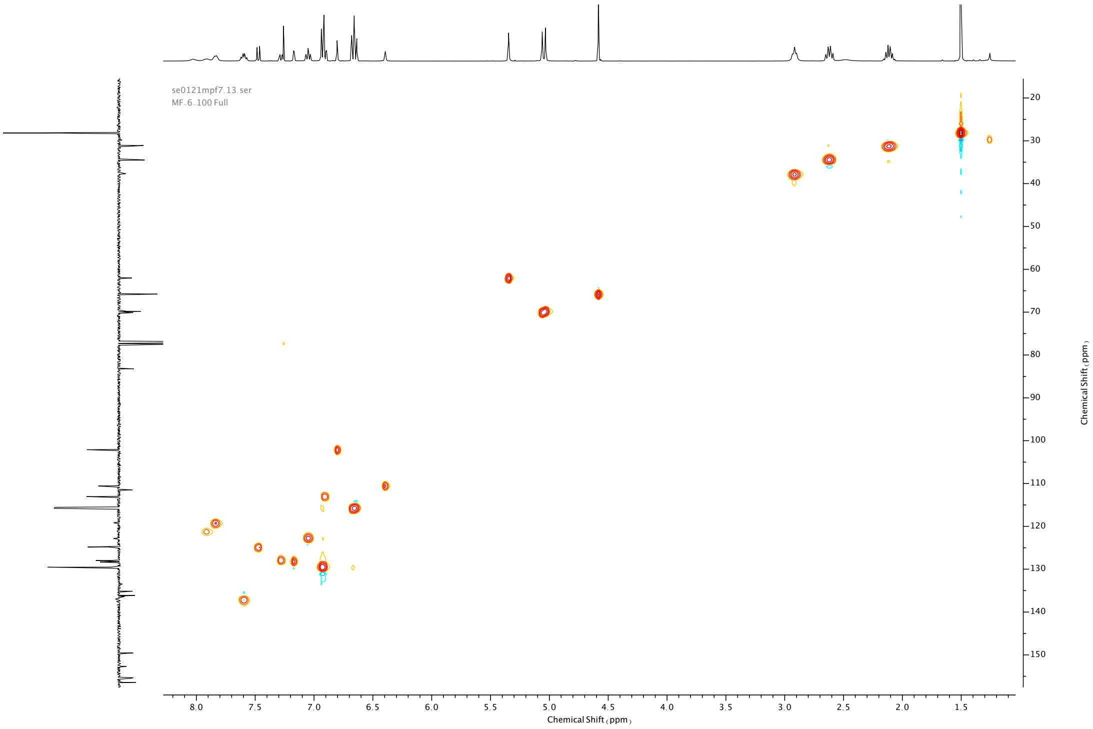

Figure **322**. HSQC NMR ($CDCl_3$) of **68**.

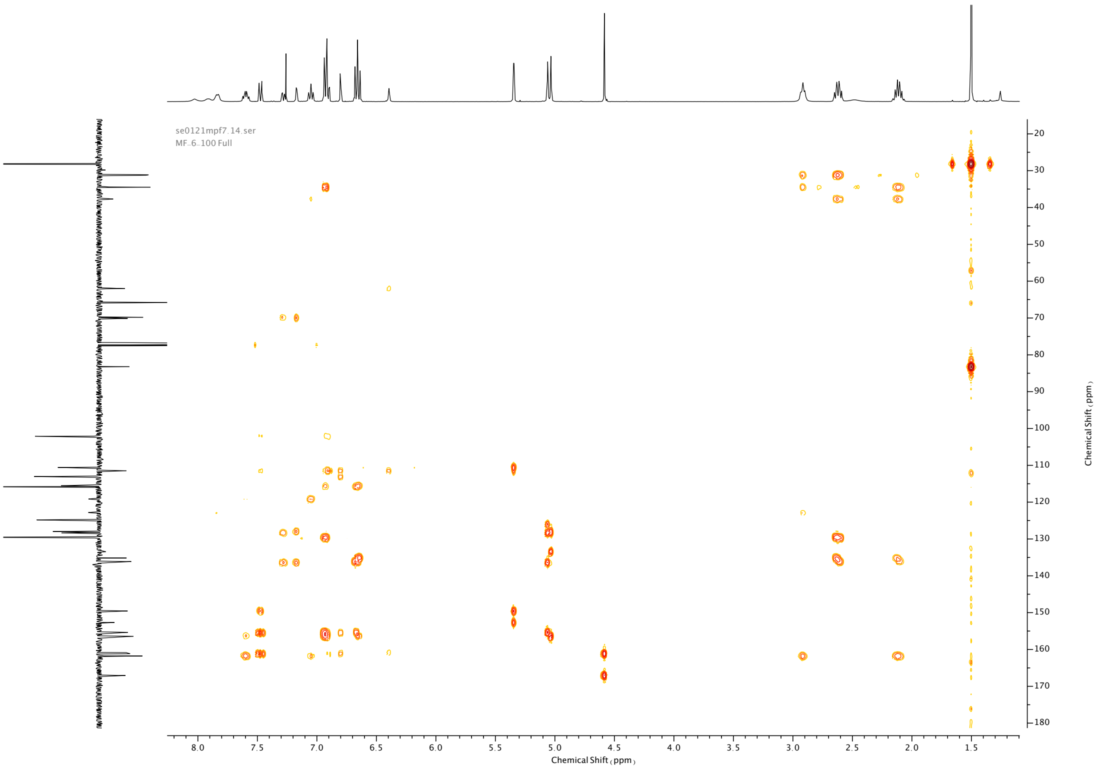

Figure **323**. HMBC NMR ($CDCl_3$) of **68**.

Compound **52**

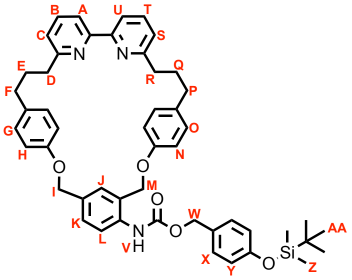

52 was synthesised according to general procedure **(6)** from macrocycle **59** (94 mg, 0.14 mmol) and trigger alcohol **51** (101 mg, 0.42 mmol). Purification by column chromatography (eluent 49:1 → 9:1 PE: Acetone) afforded **52** as a white foam (80 mg, 0.099 mmol, 70%). ^{1}H NMR (400 MHz, $CDCl_3$, 298 K) δ_H 7.93 (1H, d, *J* = 7.7 Hz, H_L), 7.86-7.78 (2H, m, H_A & H_U), 7.68 (1H, br. s, N-H_V), 7.59 (1H, t, *J* = 7.7 Hz, H_B or H_T), 7.57 (1H, t, *J* = 7.7 Hz, H_B or H_T), 7.31-7.25 (3H, m, H_K & H_X), 7.14 (1H, d, *J* = 1.8 Hz, H_J), 7.03 (1H, d, *J* = 7.6 Hz, H_C or H_S), 7.02 (1H, d, *J* = 7.6 Hz, H_C or H_S), 6.94-6.89 (4H, m, H_G & H_O), 6.84 (2H, d, *J* = 8.5 Hz, H_Y), 6.68-6.61 (4H, m, H_H & H_N), 5.13 (2H, s, H_W), 5.00 (4H, br. s, H_I & H_M), 2.94-2.86 (4H, m, H_D & H_R), 2.63 (2H, t, *J* = 7.4 Hz, H_F or H_P), 2.60 (2H, t, *J* = 7.4 Hz, H_F or H_P), 2.18-2.05 (4H, m, H_E & H_Q), 0.99 (9H, s, H_{AA}), 0.20 (6H, s, H_Z). ^{13}C NMR (101 MHz, $CDCl_3$, 298 K) δ_C 161.8, 161.7, 156.5 (x2), 156.0, 155.5, 153.9, 149.2, 137.0, 136.8 (x2), 135.9, 135.1, 132.8, 130.2, 129.5 (x2), 129.0, 128.4, 127.9, 125.8, 122.7 (x2), 121.3 (HSQC), 120.2, 119.1 (x2), 116.0, 115.5, 70.0 (x2), 67.0 37.8 (x2), 34.5 (x2), 31.1 (x2), 25.8, 18.3 (HMBC), -4.3. HR-ESI-MS (CH_3CN): *m/z* = 806.3995 $[M+H]^+$ calc. 806.3984.

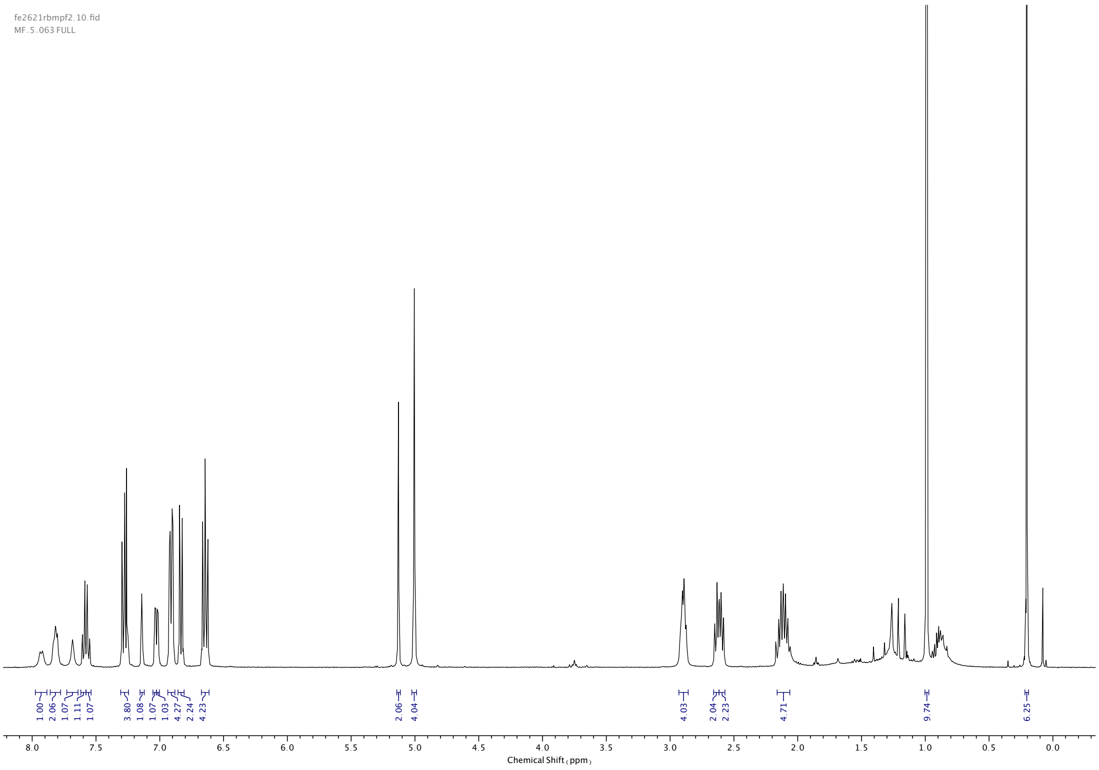

Figure **324**. ^{1}H NMR (CDCl$_3$, 400 MHz) of **52**.

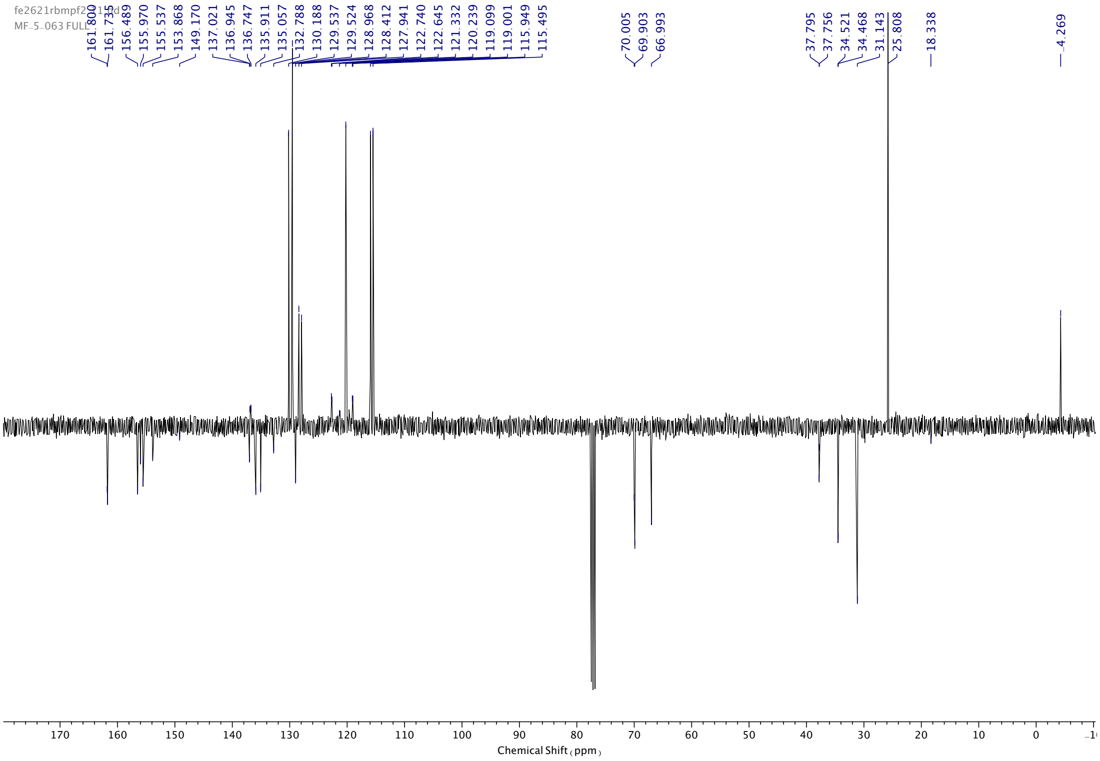

Figure **325**. ^{13}C NMR (CDCl$_3$, 101 MHz) of **52**.

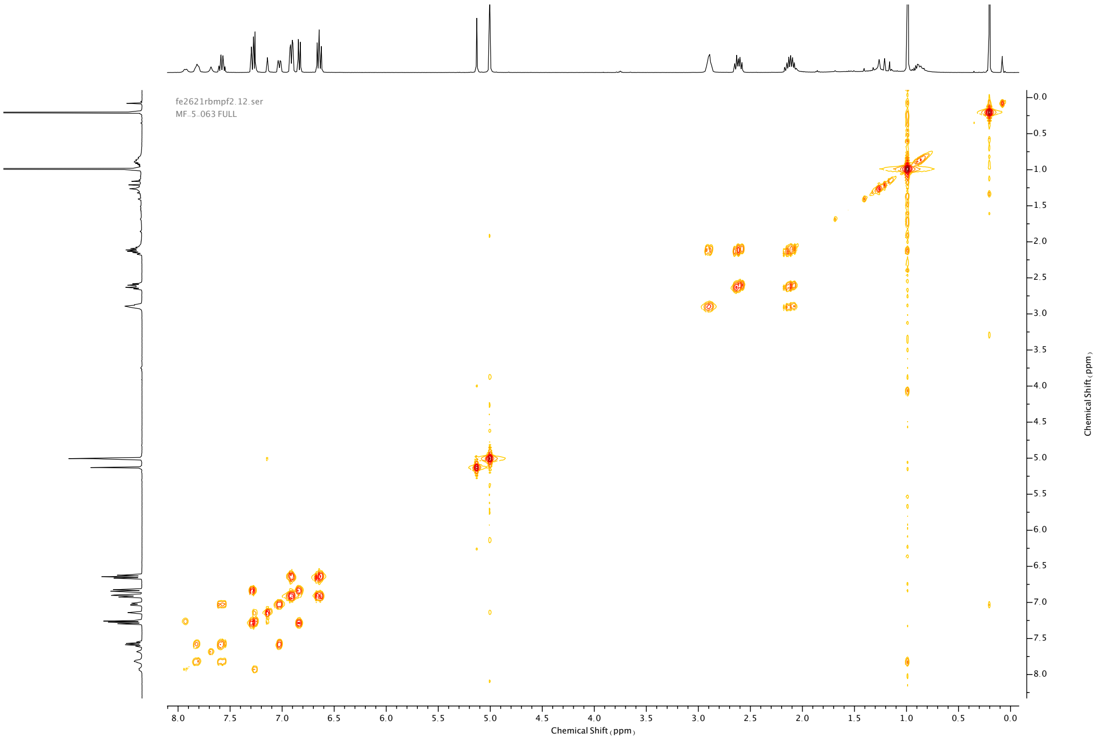

Figure **326**. COSY NMR ($CDCl_3$) of **52**.

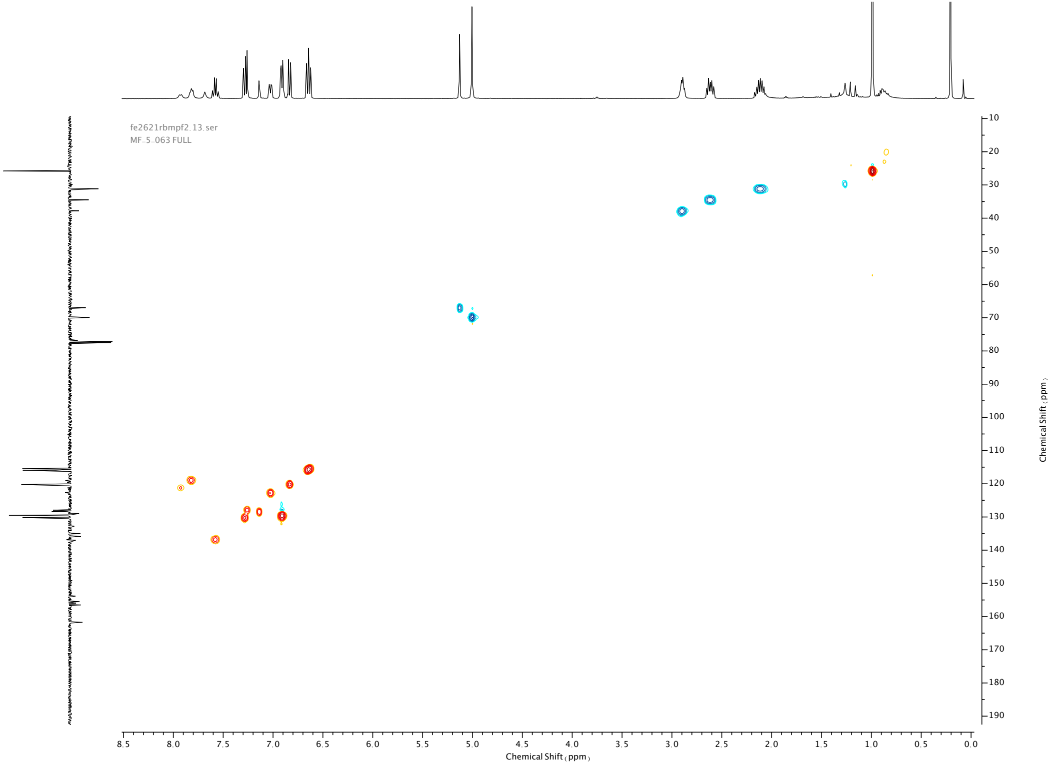

Figure **327**. HSQC NMR ($CDCl_3$) of **52**.

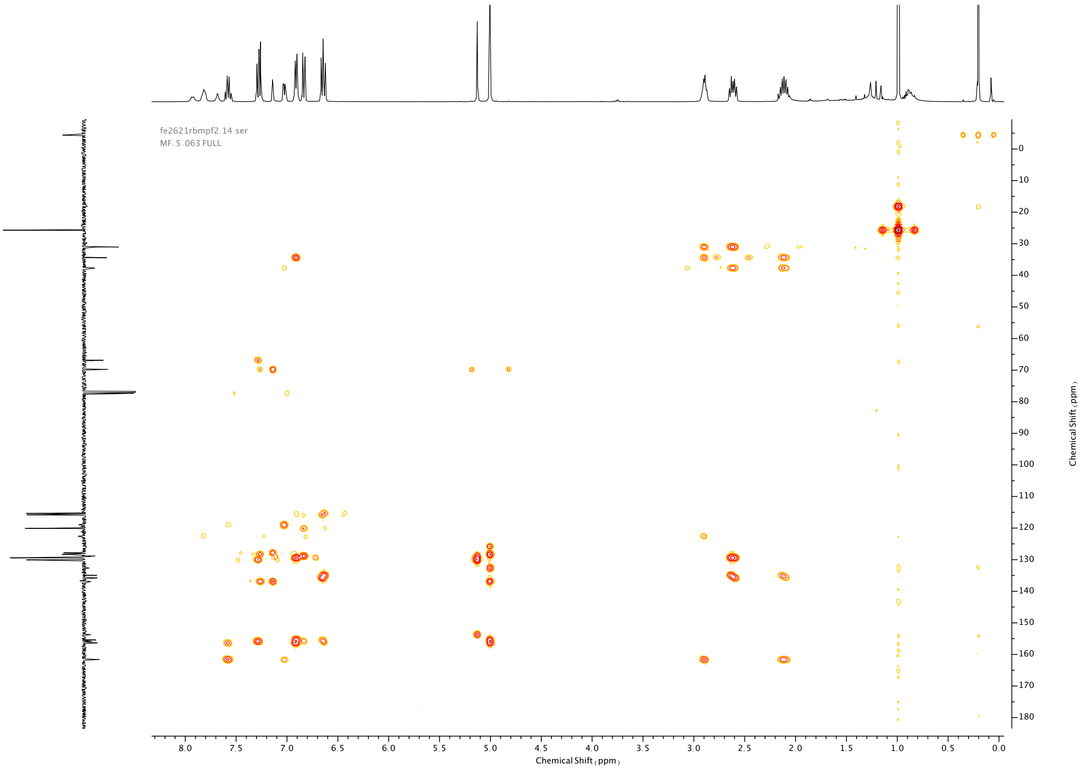

Figure **328**. HMBC NMR ($CDCl_3$) of **52**.

Compound **70**

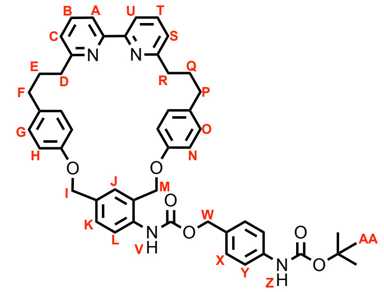

70 was synthesised according to general procedure **(6)** from macrocycle **59** (50 mg, 0.076 mmol) and trigger alcohol **69** (51 mg, 0.23 mmol). Purification by column chromatography (eluent 1:0 → 9:1 CH_2Cl_2: Et_2O) afforded **70** as a white foam (45 mg, 0.056 mmol, 75%). ^{1}H NMR (400 MHz, $CDCl_3$, 298 K) δ_H 7.95-7.85 (1H, m, H_L), 7.79 (1H, d, J = 7.7 Hz, H_A or H_U), 7.78 (1H, d, J = 7.7 Hz, H_A or H_U), 7.71 (1H, br. s, N-H_v), 7.58 (1H, t, J = 7.7 Hz, H_B or H_T), 7.57 (1H, t, J = 7.7 Hz, H_B or H_T), 7.40-7.31 (4H, m, H_X & H_Y), 7.25 (1H, dd, J = 8.6, 1.9 Hz, H_K), 7.14 (1H, d, J = 1.9 Hz, H_J), 7.03 (1H, dd, J = 7.7, 0.9 Hz, H_C or H_S), 7.02 (1H, dd, J = 7.7, 0.9 Hz, H_C or H_S), 6.93 (4H, m, H_G & H_O), 6.67-6.61 (4H, m, H_H & H_N), 6.56 (1H, br. s, N-H_Z), 5.13 (2H, s, H_W), 5.01 (4H, s, H_I & H_M), 2.92-2.85 (4H, m, H_D & H_R), 2.62 (2H, t, J = 7.2 Hz, H_F or H_P), 2.59 (2H, t, J = 7.2 Hz, H_F or H_P), 2.16-2.06 (4H, m, H_E & H_Q), 1.52 (9H, s, H_{AA}). ^{13}C NMR (101 MHz, $CDCl_3$, 298 K) δ_C 161.7 (x2), 156.4, 155.4, 153.7, 152.7, 138.5, 136.8 (x2), 136.7, 136.6, 135.8, 135.0, 132.7, 130.6, 129.5, 129.4 (x2), 128.2, 127.8, 122.5 (x2), 121.4 (HSQC), 118.9, 118.9, 118.5, 115.8, 115.4, 80.7 (HMBC), 69.8 (x2), 66.8, 65.0, 40.9, 37.8 (x2), 34.4 (x2), 31.1 (x2), 28.3. HR-ESI-MS (CH_3CN): m/z = 791.3803 [M+H]$^+$ calc. 791.3803.

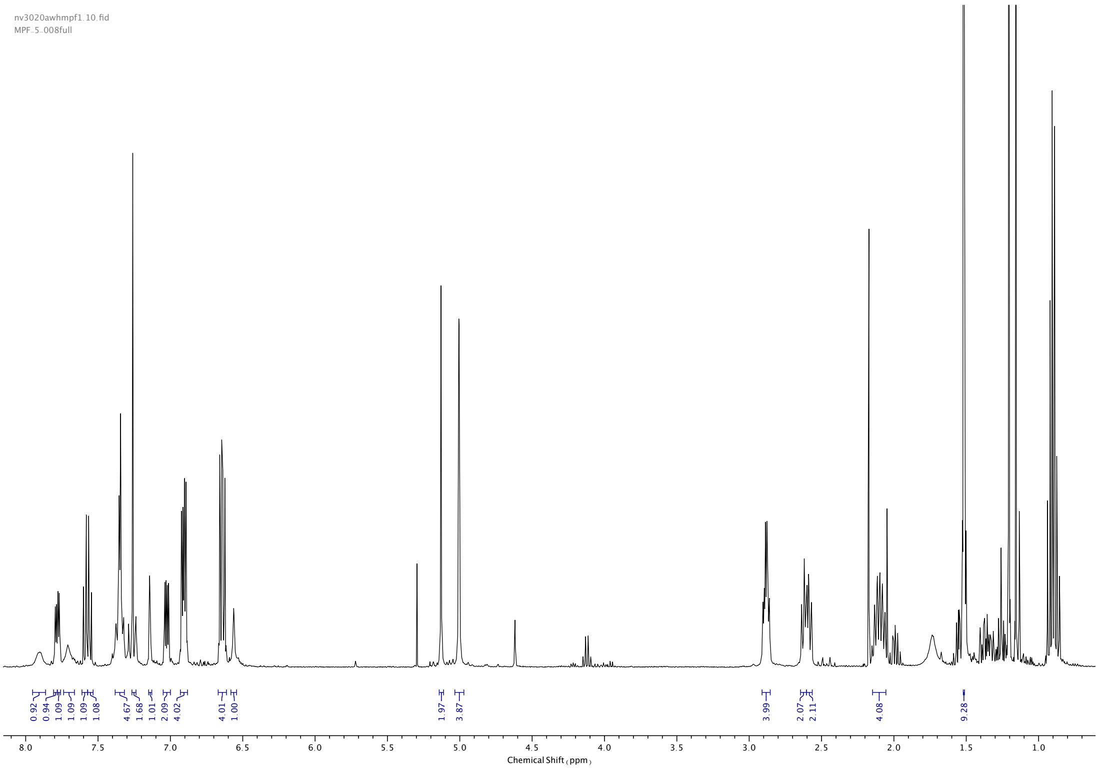

Figure **329**. ^{1}H NMR (CDCl$_3$, 400 MHz) of **70**.

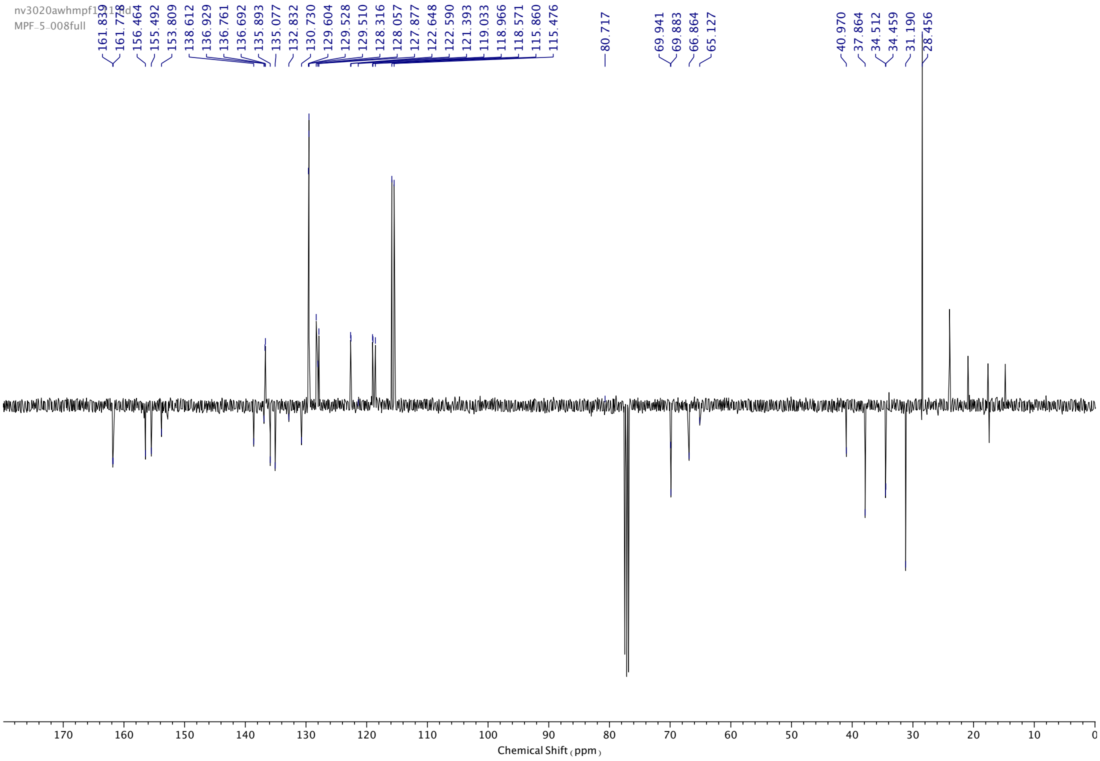

Figure **330**. ^{13}C NMR (CDCl$_3$, 101 MHz) of **70**.

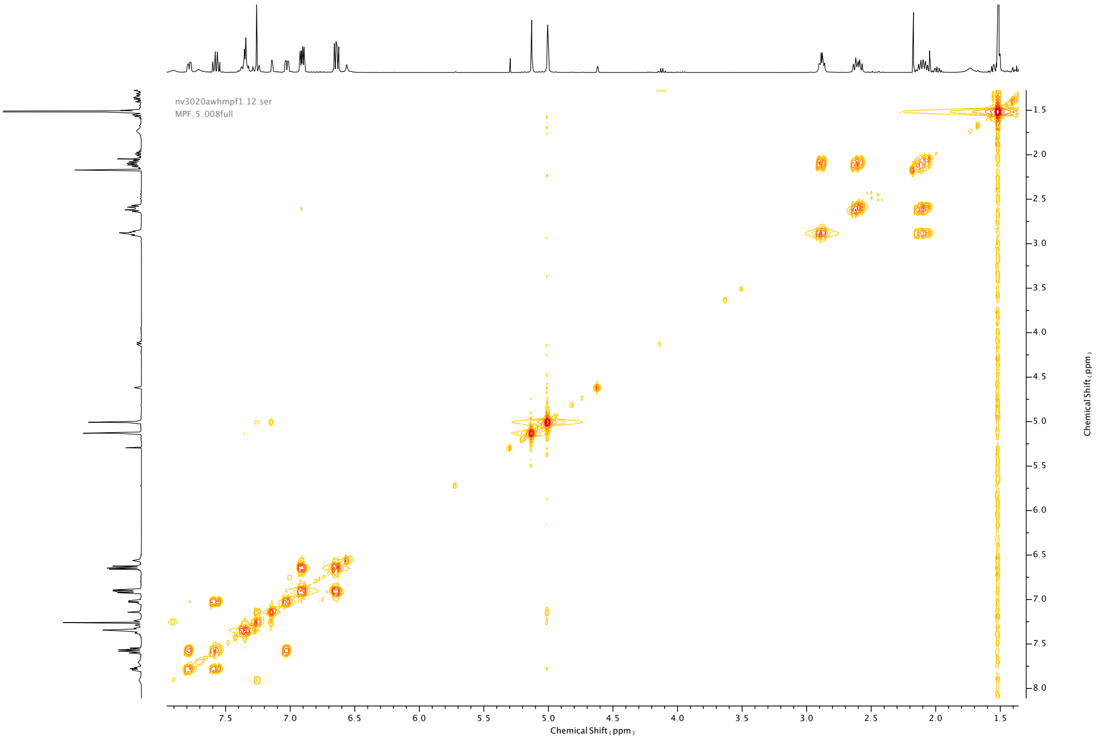

Figure **331**. COSY NMR ($CDCl_3$) of **70**.

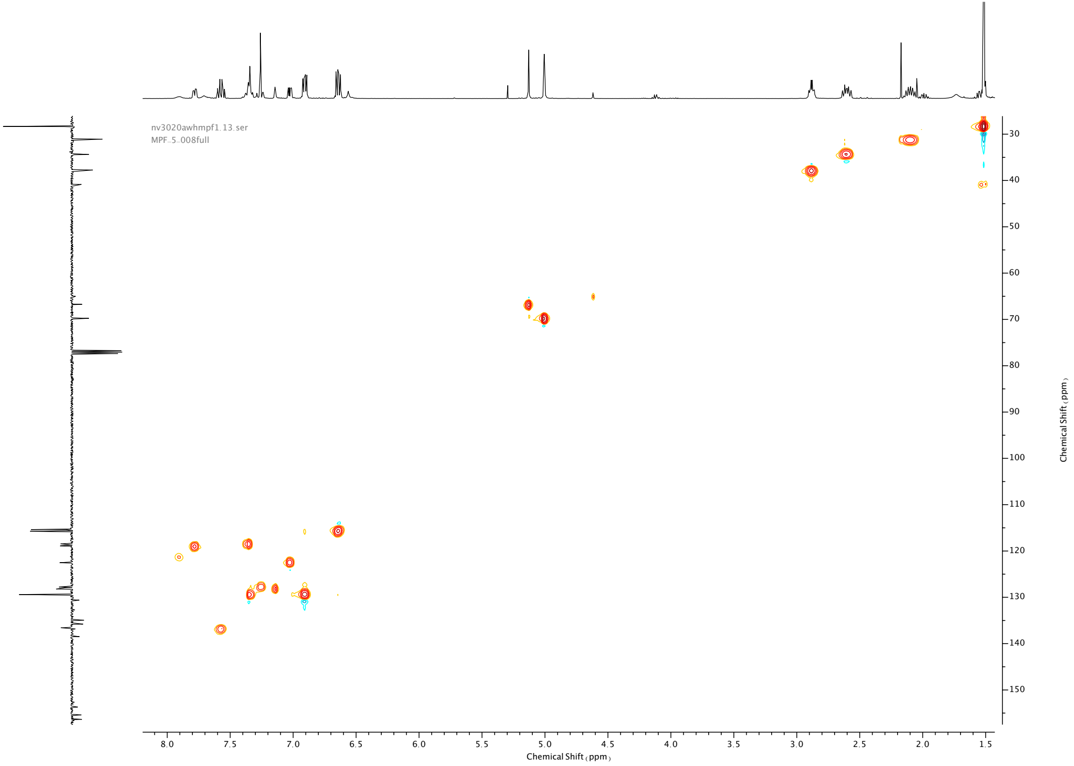

Figure **332**. HSQC NMR ($CDCl_3$) of **70**.

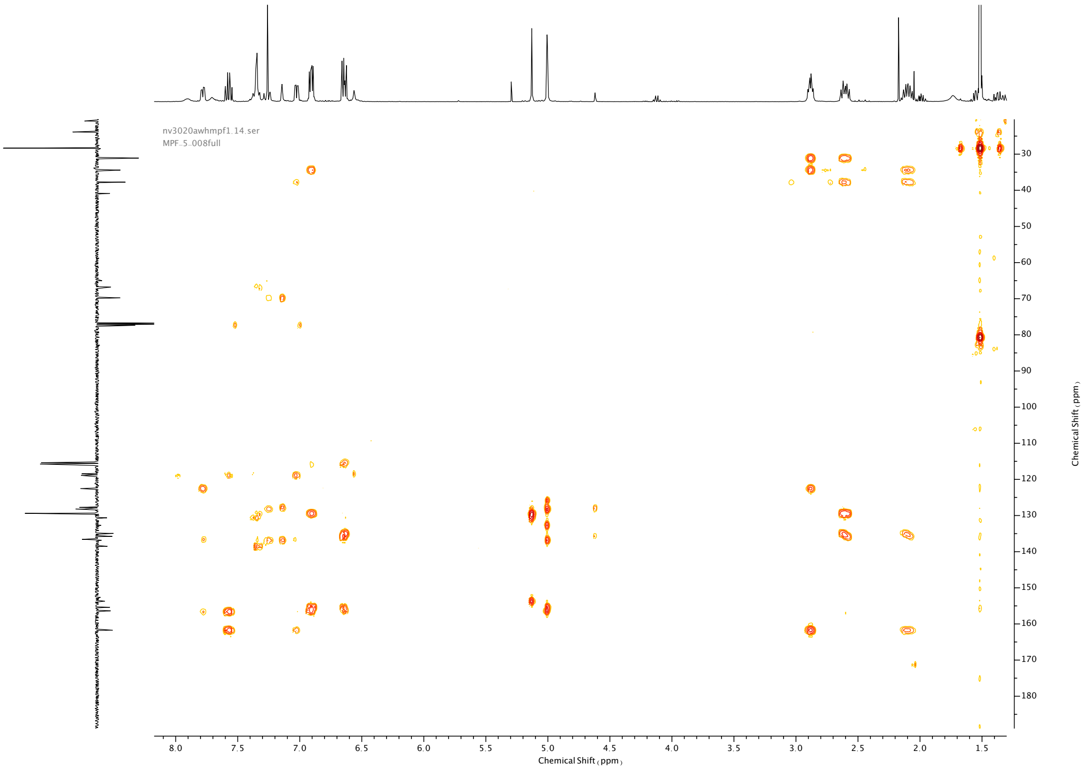

Figure **333**. HMBC NMR ($CDCl_3$) of **70**.

Compound **55**

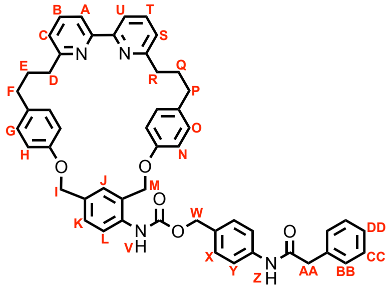

55 was synthesised according to general procedure **(6)** from macrocycle **59** (40 mg, 0.061 mmol) and trigger alcohol **54** (44 mg, 0.18 mmol). Purification by column chromatography (eluent 9:1 → 4:1 PE: Acetone) afforded **55** as a white foam (35 mg, 0.043 mmol, 71%). ^{1}H NMR (400 MHz, $CDCl_3$, 298 K) δ_H 7.93-7.86 (1H, m, H_L), 7.82 (1H, d, *J* = 7.7 Hz, H_A or H_U), 7.81 (1H, d, *J* = 7.7 Hz, H_A or H_U), 7.71 (1H, br. s, N-H_V), 7.60 (1H, t, *J* = 7.7 Hz, H_B or H_T), 7.58 (1H, t, *J* = 7.6 Hz, H_B or H_T), 7.44 (2H, d, *J* = 8.4 Hz, H_Y), 7.41-7.35 (3H, m, H_{BB}, N-H_Z), 7.34-7.28 (5H, m, H_X, H_{CC} & H_{DD}), 7.25 (1H, dd, *J* = 8.4, 1.9 Hz, H_K), 7.14 (1H, d, *J* = 1.8 Hz, H_J), 7.04 (1H, d, *J* = 7.6 Hz, H_C or H_S), 7.03 (1H, d, *J* = 7.6 Hz, H_C or H_S), 6.91 (2H, d, *J* = 8.7 Hz, H_G or H_O), 6.89 (2H, d, *J* = 8.6 Hz, H_G or H_O), 6.66-6.62 (4H, m, H_H & H_N), 5.11 (2H, s, H_W), 5.00 (2H, s, $H_{I\ or}$ H_M), 4.99 (2H, s, $H_{I\ or}$ H_M), 3.71 (2H, s, H_{AA}), 2.93-2.86 (4H, m, H_D & H_R), 2.62 (2H, t, *J* = 7.3 Hz, H_F or H_P), 2.59 (2H, t, *J* = 7.6 Hz, H_F or H_P), 2.16-2.04 (4H, m, H_E & H_Q). ^{13}C NMR (101 MHz, $CDCl_3$, 298 K) δ_C 169.2, 161.8, 161.7, 156.5, 155.5, 153.7, 144.6 (HMBC), 137.9, 136.9 (x2), 136.8, 135.8, 135.0, 134.5, 132.9, 132.2, 129.6, 129.5 (x2), 129.3 (x2), 128.3, 127.9, 127.8, 126.1, 122.8 (x2), 121.3 (x2), 119.9, 119.2, 119.1, 115.9, 115.5, 69.9 (x2), 66.7, 44.9, 37.7 (x2), 34.5, 34.4, 31.1 (x2). HR-ESI-MS (CH_3CN): *m/z* = 809.3704 $[M+H]^+$ calc. 809.3697.

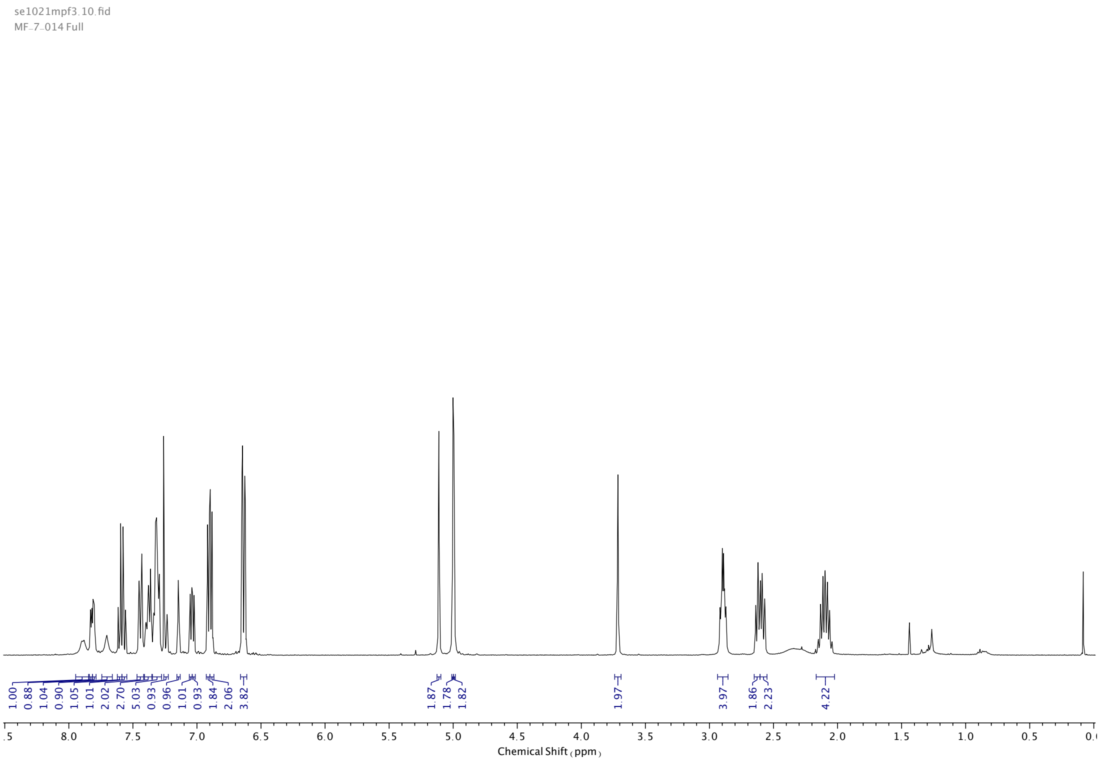

Figure **334**. ^{1}H NMR (CDCl$_3$, 400 MHz) of **55**.

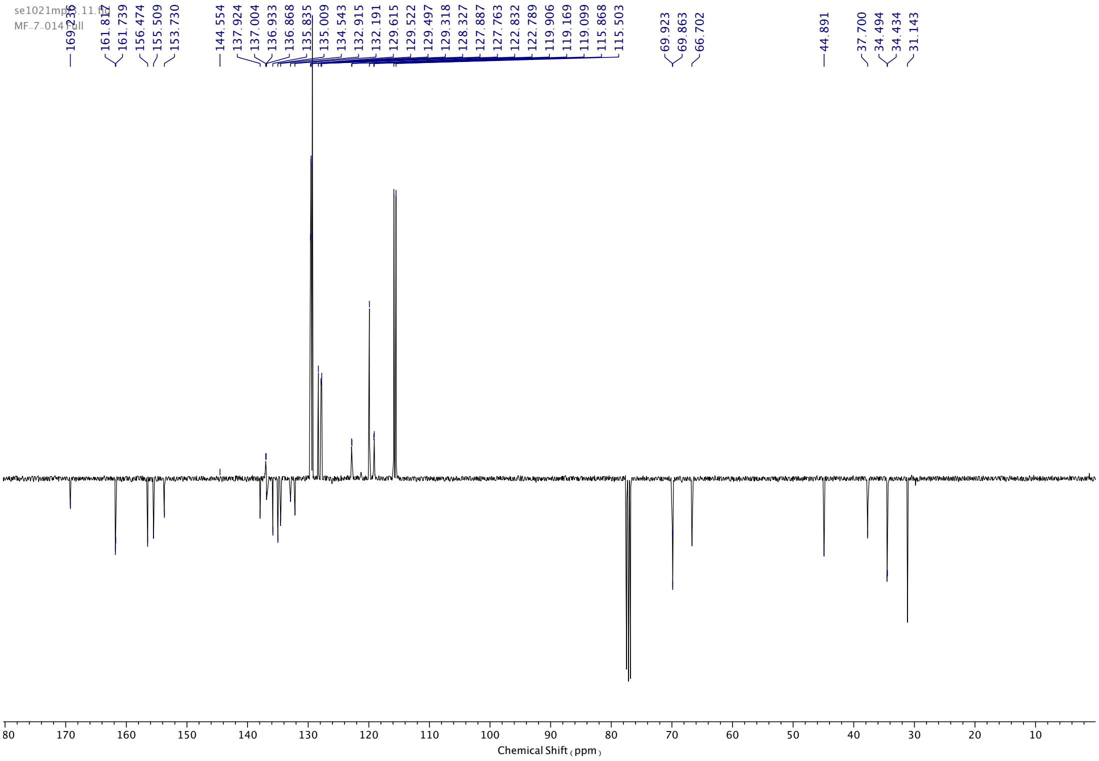

Figure **335**. ^{13}C NMR (CDCl$_3$, 101 MHz) of **55**.

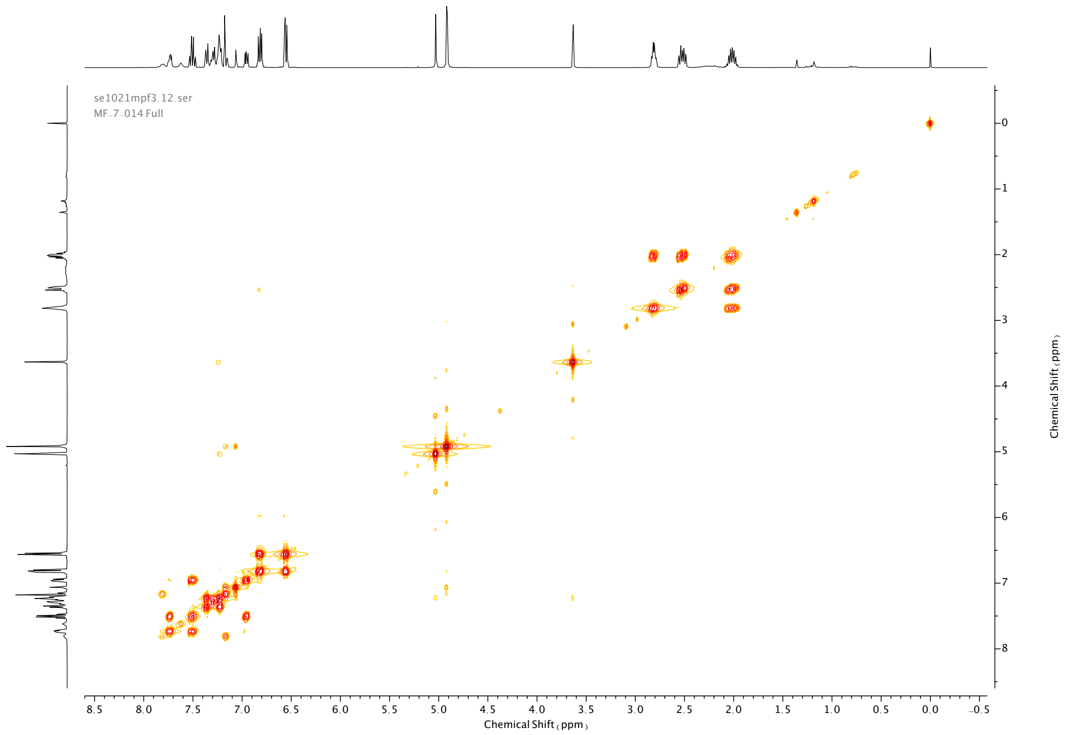

Figure **336**. COSY NMR ($CDCl_3$) of **55**.

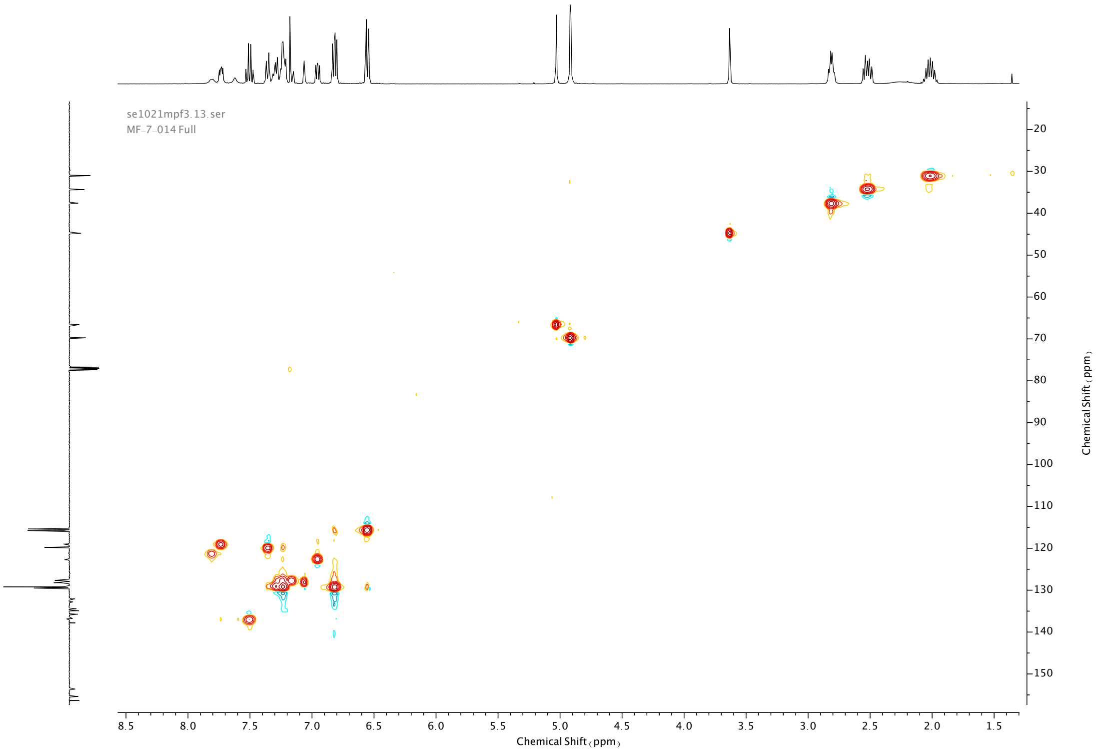

Figure **337**. HSQC NMR ($CDCl_3$) of **55**.

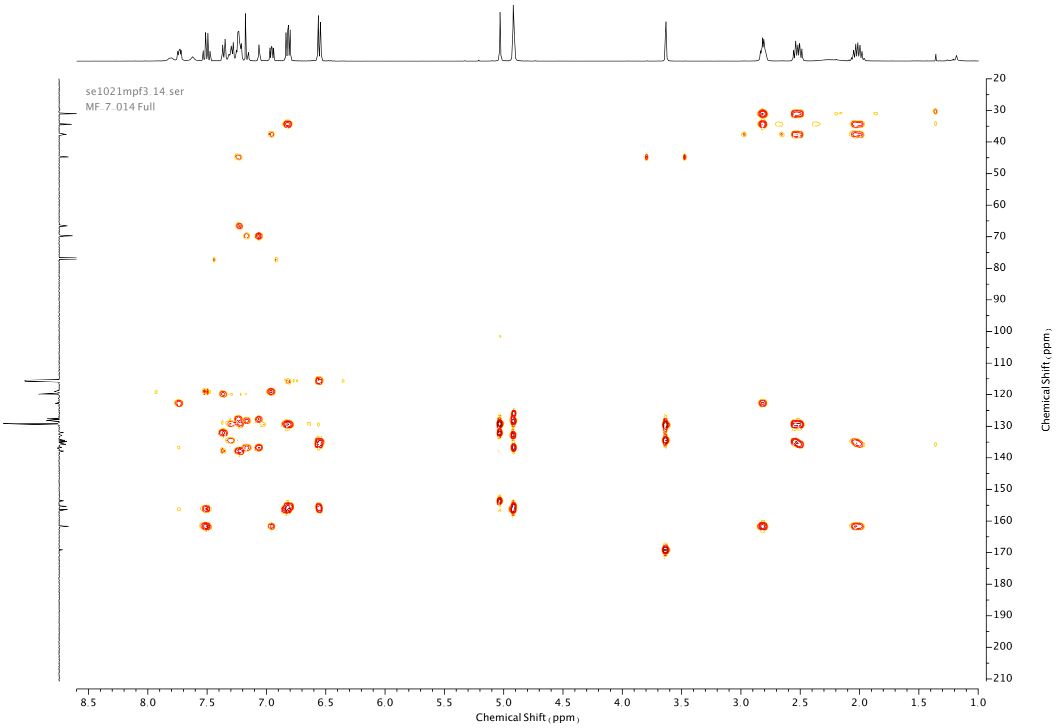

Figure **338**. HMBC NMR (CDCl$_3$) of **55**.

Compound **76**

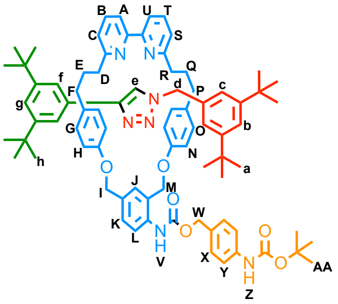

76 was synthesised according to general procedure **(7)** from macrocycle **70** (35 mg, 0.044 mmol), azide stopper **72** (16 mg, 0.066 mmol) and alkyne stopper **71** (14 mg, 0.066 mmol). Purification by column chromatography (eluent 19:1 → 9:1 PE: Acetone) afforded **76** as a white foam (25 mg, 0.02 mmol, 45%). ^{1}H NMR (400 MHz, CDCl$_3$, 298 K) δ_H 9.35 (1H, s, H_e), 8.20 (1H, d, *J* = 1.9 Hz, H_J), 8.02-7.92 (1H, m, H_L), 7.71-7.62 (3H, m, H_B, H_T & N-H_V), 7.50 (2H, dd, *J* = 7.7, 0.8 Hz, H_A & H_U), 7.39 (2H, d, *J* = 1.9 Hz, H_f), 7.37-7.28 (5H, m, H_K, H_X & H_Y), 7.23 (1H, t, *J* = 1.8 Hz, H_b), 7.14-7.10 (2H, m, H_g & H_C or H_S), 7.07 (1H, dd, *J* = 7.7, 0.9 Hz, H_C or H_S), 6.92 (2H, d, *J* = 1.8 Hz, H_c), 6.67 (2H, d, *J* = 8.7 Hz, H, H_H or H_N), 6.45 (1H, br. s, N-H_Z), 6.33-6.29 (4H, m, H_H or H_N & H_G or H_O), 6.23 (2H, d, *J* = 8.7 Hz, H_G or H_O), 5.35 (1H, d, *J* = 10.9 Hz, H_M or $H_{M'}$), 5.24 (2H, s, H_I), 5.20 (1H, d, *J* = 10.9 Hz, H_M or $H_{M'}$), 5.12 (2H, s, H_W), 4.58 (1H, d, *J* = 14.1 Hz, H_d or $H_{d'}$), 4.34 (1H, d, *J* = 14.1 Hz, H_d or $H_{d'}$), 2.48-2.10 (8H, m, H_D, H_R, H_F & H_P), 1.70-1.54 (4H, m, H_E & H_Q), 1.51 (9H, s, H_{AA}), 1.06 (18H, s, H_a or H_h), 1.05 (18H, s, H_a or H_h). ^{13}C NMR (101 MHz, CDCl$_3$, 298 K) δ_C 163.23 (x2), 157.9, 157.8, 157.1, 156.2, 150.8, 149.9, 147.5, 137.3, 136.9, 136.8, 134.4, 133.1, 132.9, 131.0 (x2), 130.4, 129.7, 129.6, 129.3, 129.1, 129.0, 128.9, 128.7, 128.1, 127.6, 122.9 (x2), 122.0, 121.8, 120.7, 120.5, 120.3, 120.0 (x2),118.6, 115.1, 114.6, 113.8, 69.7, 68.7, 66.9, 53.8, 38.0, 37.0, 35.0, 34.8, 34.7 (x2), 31.8, 31.5, 31.4 (x2), 30.7, 28.5. HR-ESI-MS (CH$_3$CN): *m/z* = 1250.7 $[M+H]^+$ calc. 1250.7422.

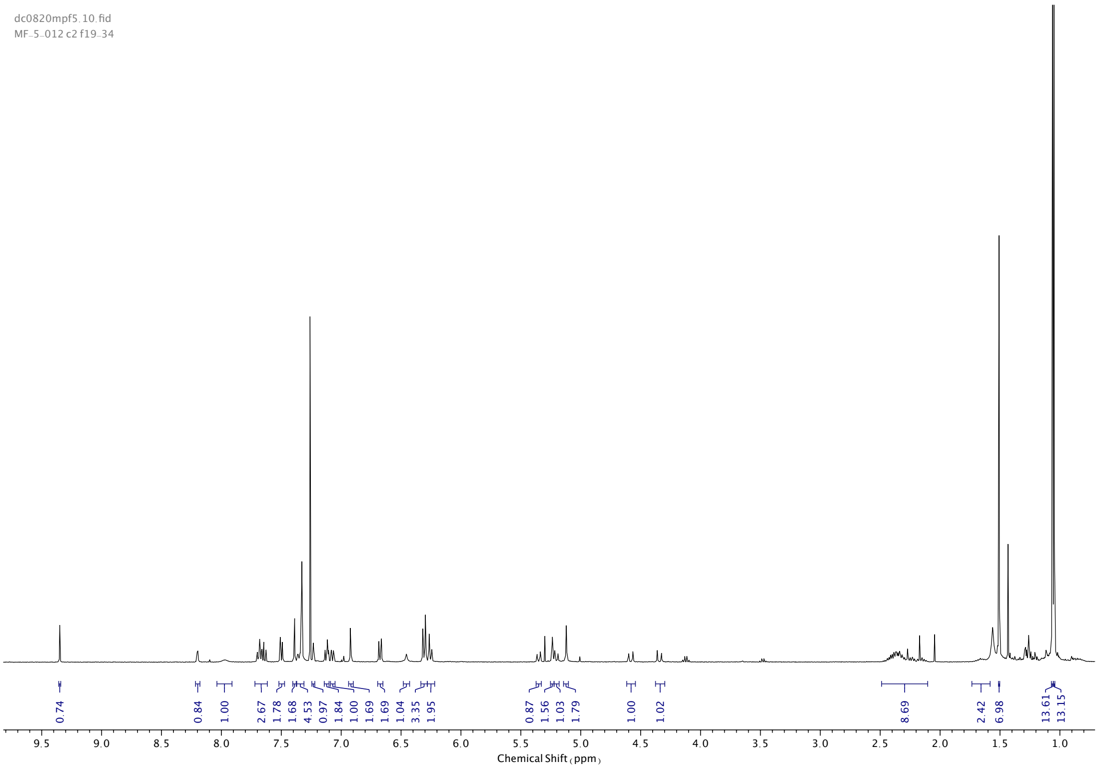

Figure **339**. ^{1}H NMR (CDCl$_3$, 400 MHz) of **76**.

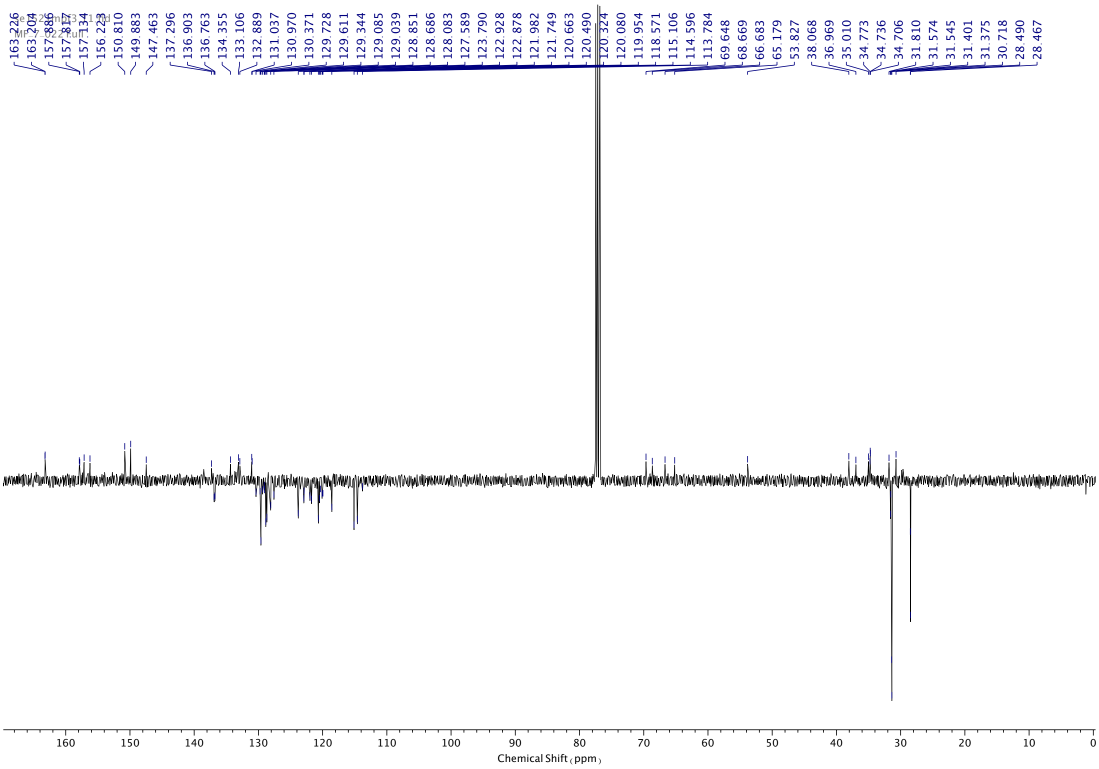

Figure **340**. ^{13}C NMR (CDCl$_3$, 101 MHz) of **76**.

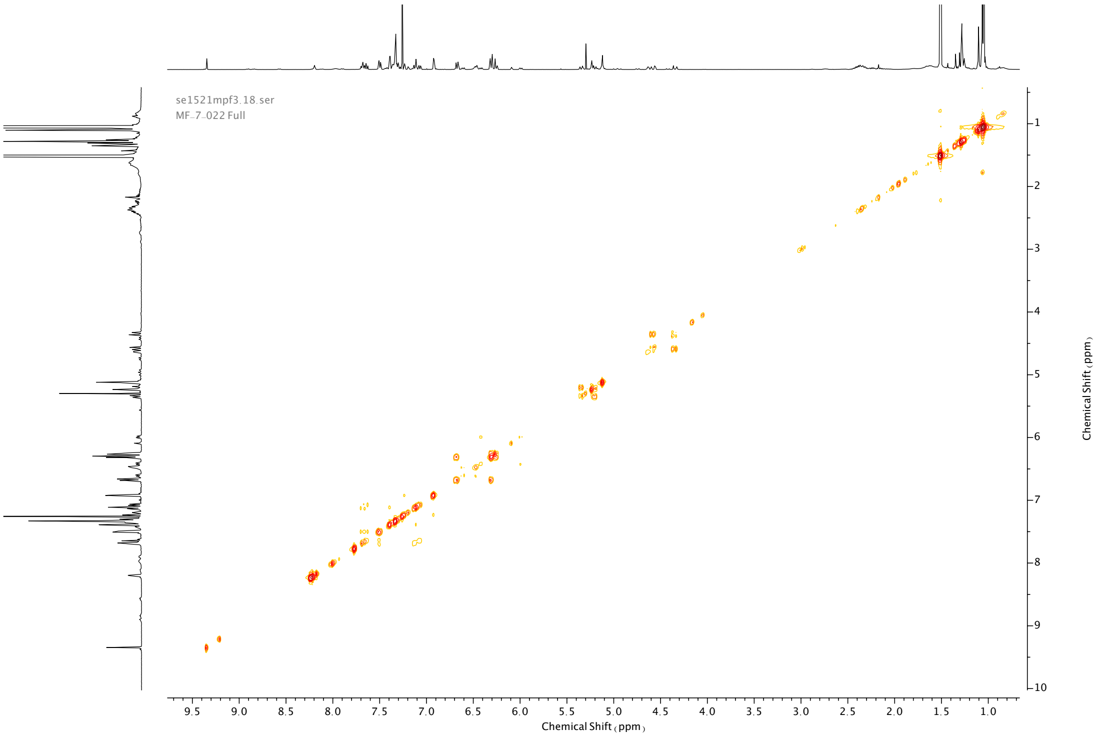

Figure **341**. COSY NMR ($CDCl_3$) of **76**.

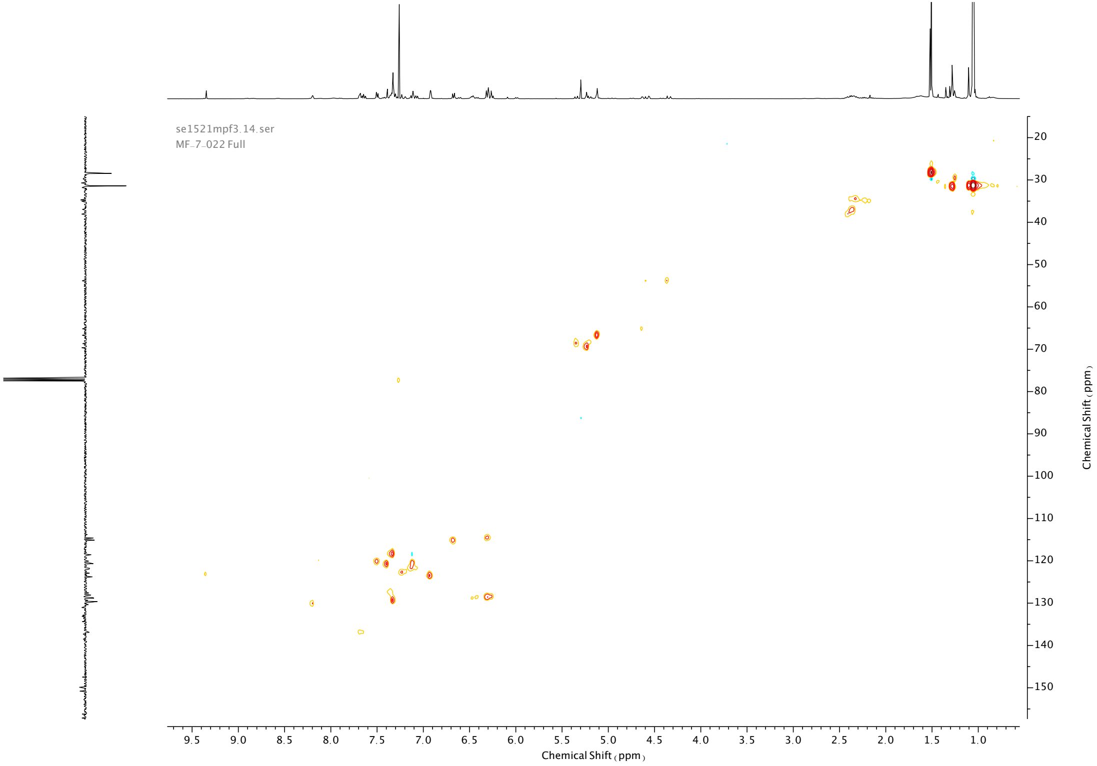

Figure **342**. HSQC NMR ($CDCl_3$) of **76**.

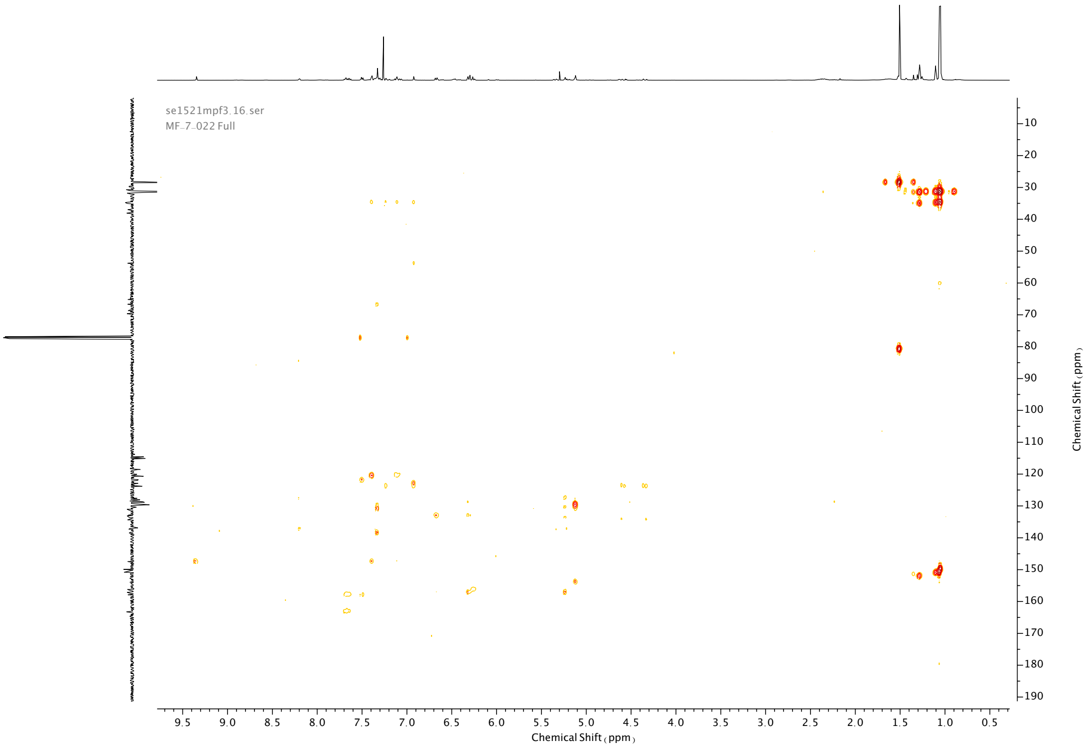

Figure **343**. HMBC NMR ($CDCl_3$) of **76**.

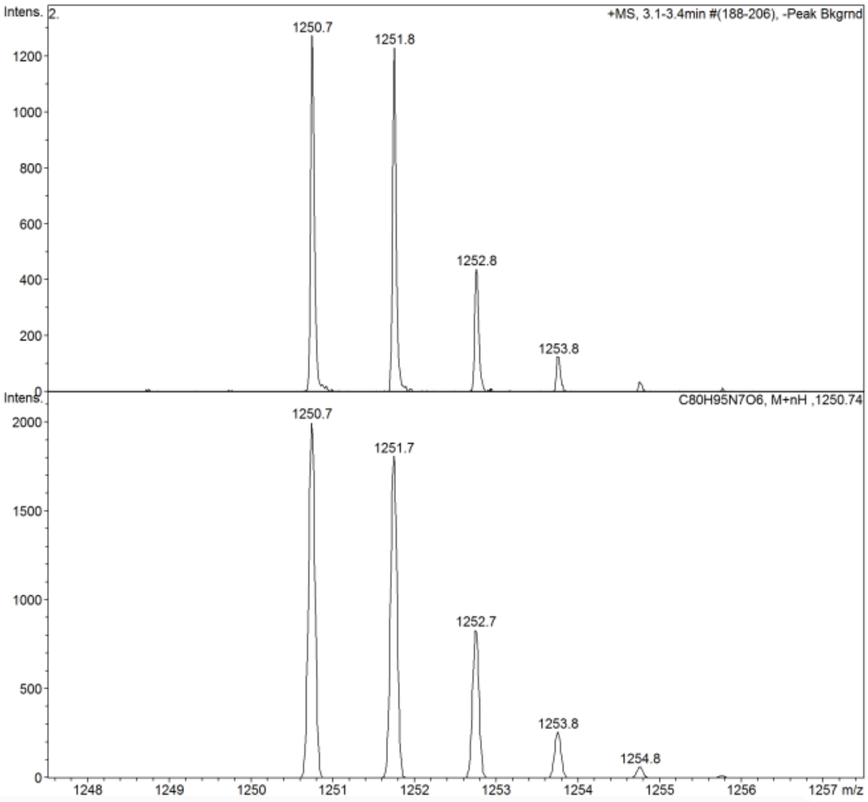

Figure **344**. Isotope pattern of **76**.

Compound **73**

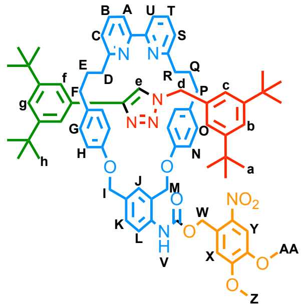

73 was synthesised according to general procedure **(7)** from macrocycle **66** (54 mg, 0.069 mmol), azide stopper **72** (24 mg, 0.10 mmol) and alkyne stopper **71** (21 mg, 0.10 mmol). Purification by column chromatography (eluent 1:0 → 4:1 CH_2Cl_2: Et_2O) afforded **73** as a yellow foam (56 mg, 0.045 mmol, 65%). ^{1}H NMR (400 MHz, $CDCl_3$, 298 K) δ_H 9.36 (1H, s, H_e), 8.23 (1H, s, H_J), 8.06-7.86 (2H, m, H_L & N-H_V), 7.73-7.68 (2H, m, H_Y & H_B or H_T), 7.66 (1H, t, J = 7.7 Hz, H_B or H_T), 7.53-7.49 (2H, m, H_A & H_U), 7.40-7.35 (3H, m, H_K & H_f), 7.26 (1H, t, J = 1.8 Hz, H_b), 7.15 (1H, dd, J = 7.8, 0.6 Hz, H_C or H_S), 7.12 (1H, t, J = 1.8 Hz, H_g), 7.08 (1H, dd, J = 7.7, 0.8 Hz, H_C or H_S), 7.03 (1H, s, H_X), 6.97 (2H, d, J = 1.9 Hz, H_c), 6.68 (2H, d, J = 8.6 Hz, H_H or H_N), 6.32 (2H, d, J = 8.7 Hz, H_G or H_O), 6.29-6.24 (4H, m, H_G or H_O, H_H or H_N), 5.67-5.55 (2H, m, H_M & $H_{M'}$), 5.41 (1H, d, J = 10.9 Hz, H_I or $H_{I'}$), 5.27-5.23 (3H, m, H_W & H_I or $H_{I'}$), 4.65 (1H, d, J = 14.2 Hz, H_d or $H_{d'}$), 4.41 (1H, d, J = 14.2 Hz, H_d or $H_{d'}$), 3.94 (3H, s, H_{AA}), 3.83 (3H, s, H_Z), 2.50-2.10 (8H, m, H_D, H_R, H_F & H_P), 1.74-1.42 (4H, m, H_E & H_Q), 1.09 (18H, s, H_h or H_a), 1.06 (18H, s, H_h or H_a). ^{13}C NMR (101 MHz, $CDCl_3$, 298 K) δ_C 163.2 (x2), 157.9, 157.8, 157.5, 157.0, 156.1, 153.7, 153.2, 150.9, 149.9, 148.2, 147.5, 139.8, 137.0 (x2), 136.8, 134.4, 134.1, 133.2, 133.1, 131.0, 130.4, 128.9, 128.7, 128.3, 127.6, 123.8, 123.5, 123.0, 122.0, 121.8, 120.6 (x2), 120.5, 120.2, 120.0, 115.1, 114.4, 109.9, 108.3, 69.5, 68.8, 63.7, 56.5, 56.4, 53.9, 38.1, 36.9, 35.0, 34.7 (x2), 31.9 (x2), 31.4 (x2) 30.7. HR-ESI-MS (CH_3CN): m/z = 1240.7 $[M+H]^+$ calc. 1240.6851.

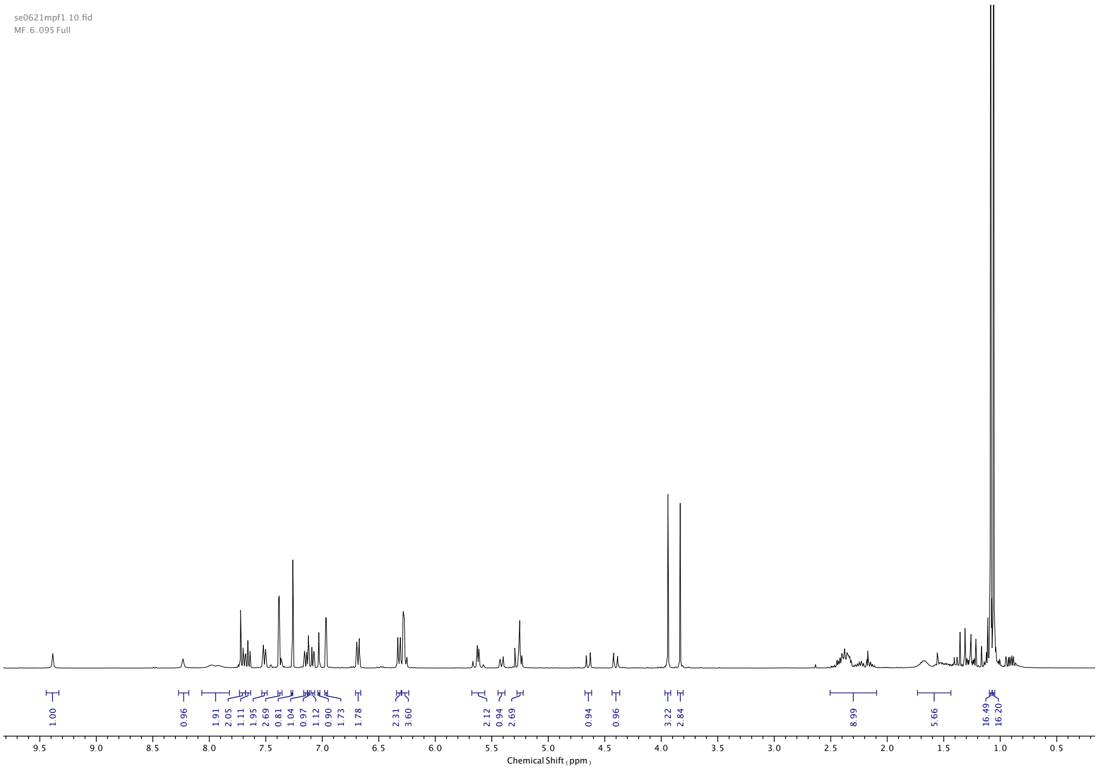

Figure **345**. ^{1}H NMR ($CDCl_3$, 400 MHz) of **73**.

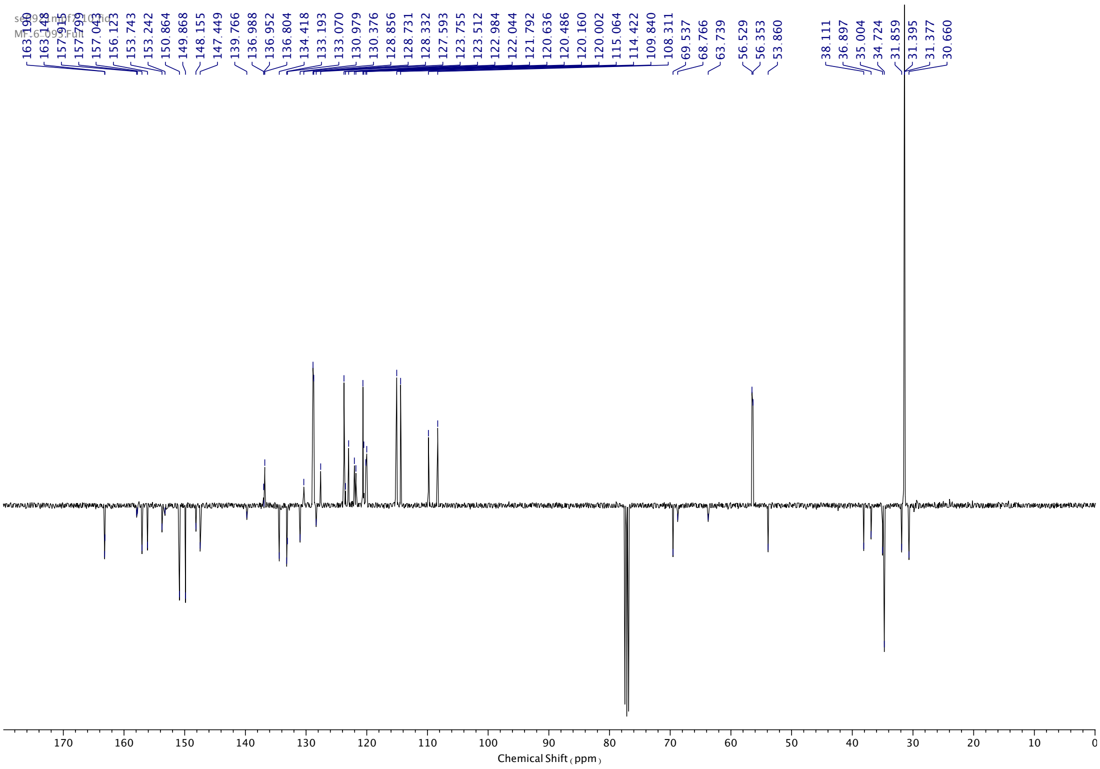

Figure **346**. ^{13}C NMR ($CDCl_3$, 101 MHz) of **73**.

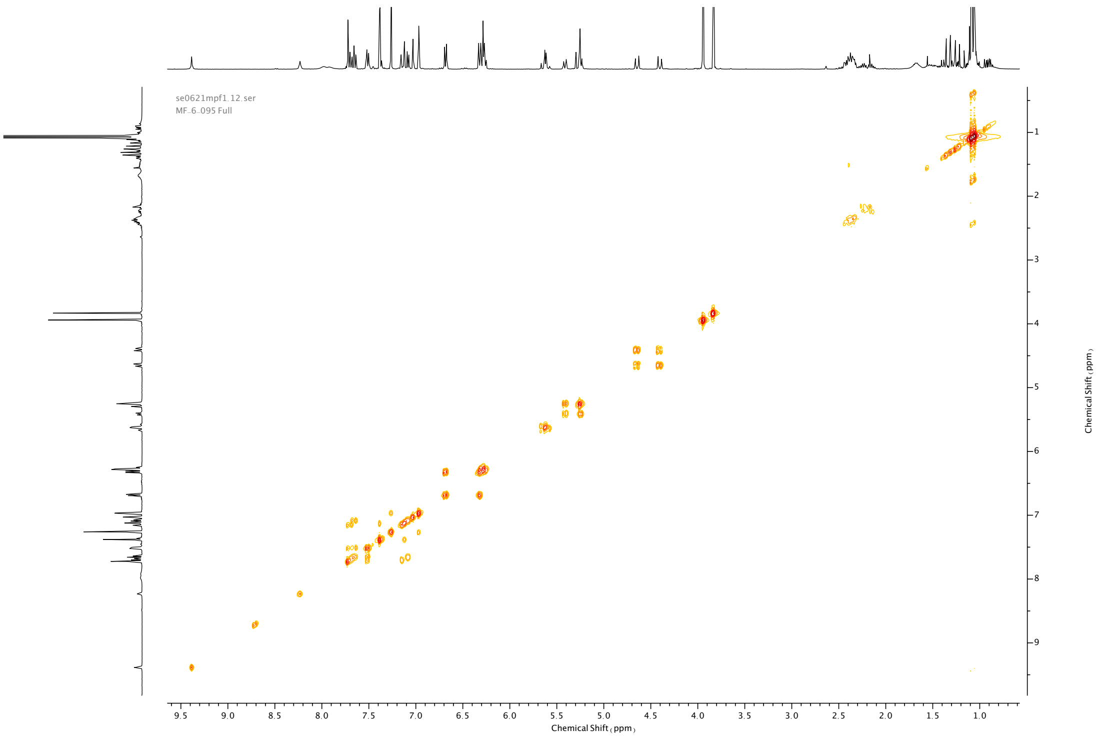

Figure **347**. COSY NMR ($CDCl_3$) of **73**.

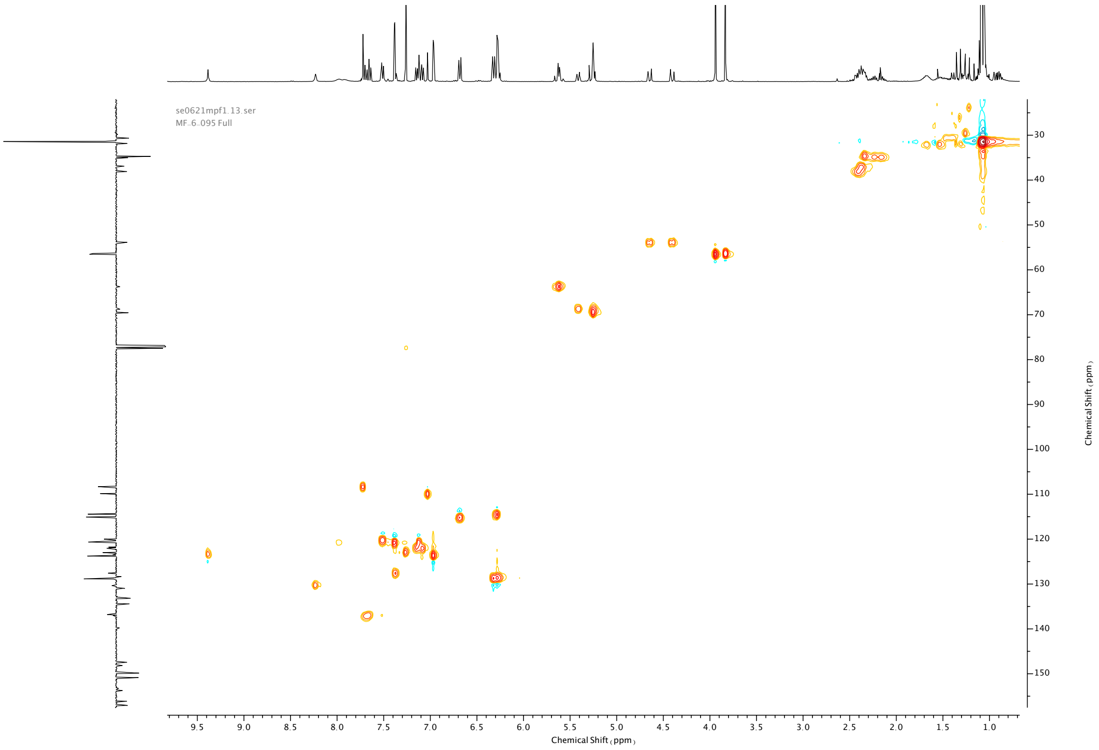

Figure **348**. HSQC NMR ($CDCl_3$) of **73**.

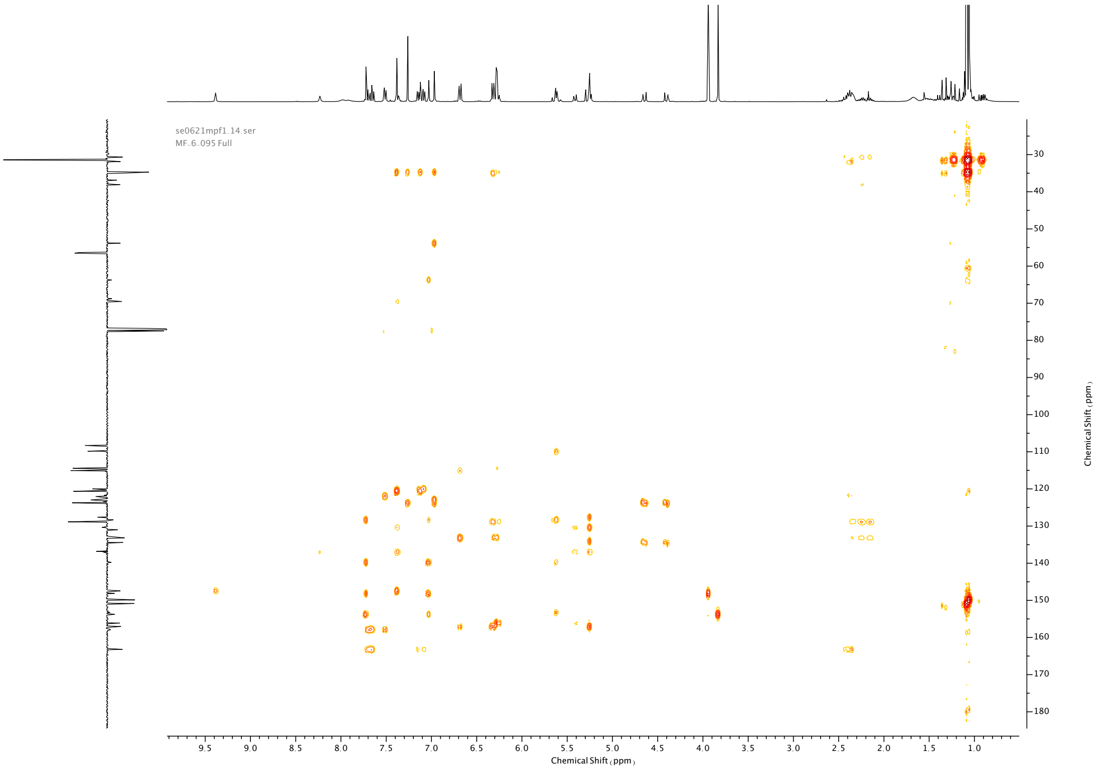

Figure **349**. HMBC NMR ($CDCl_3$) of **73**.

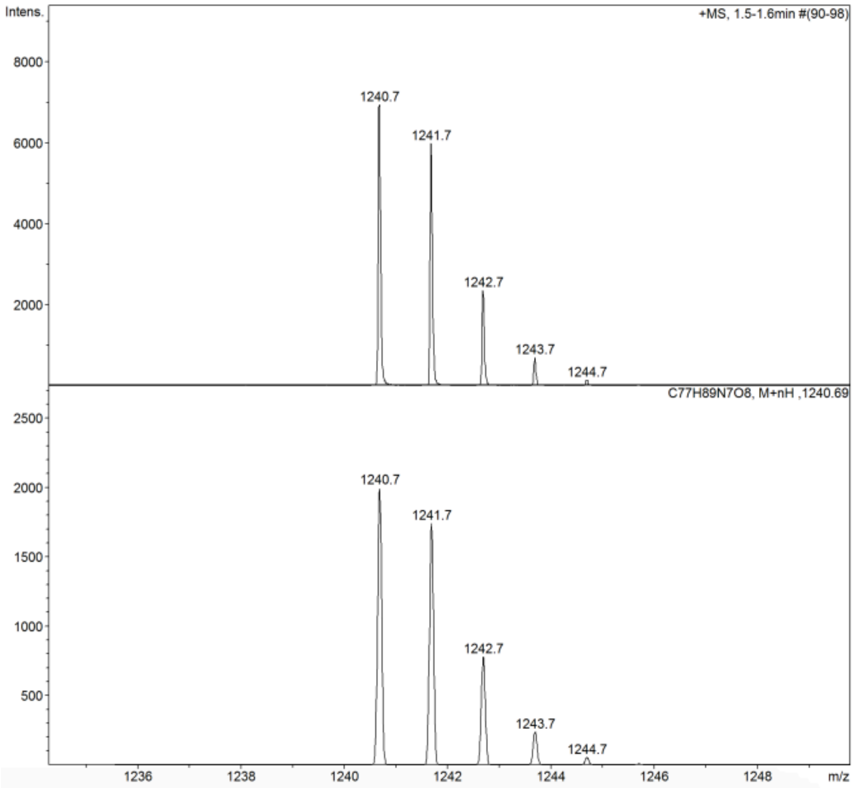

Figure **350**. Isotope pattern of **73**.

Compound 74

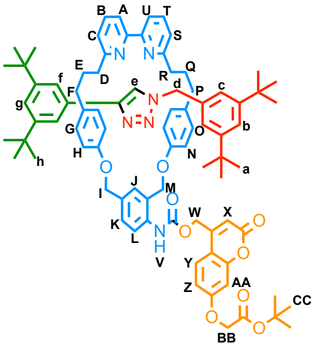

74 was synthesised according to general procedure **(7)** from macrocycle **68** (35 mg, 0.04 mmol), azide stopper **72** (10 mg, 0.06 mmol) and alkyne stopper **71** (9 mg, 0.06 mmol). Purification by column chromatography (eluent 19:1 → 4:1 PE: Acetone) afforded **74** as a white foam (31 mg, 0.023 mmol, 58%). ^{1}H NMR (400 MHz, CDCl$_3$, 298 K) δ_H 9.38 (1H, s, H_e), 8.23 (1H, s, H_J), 8.05-7.88 (2H, m, H_L, N-H_v), 7.69 (1H, t, *J* = 7.7 Hz, H_B or H_T), 7.65 (1H, t, *J* = 7.7 Hz, H_B or H_T), 7.53-7.46 (3H, m, H_A, H_U & H_Y), 7.41-7.36 (3H, m, H_f & H_K), 7.25 (1H, t, *J* = 1.8 Hz, H_b), 7.15-7.11 (2H, m, H_g & H_C or H_S), 7.08 (1H, d, *J* = 7.7 Hz, H_C or H_S), 6.94 (2H, d, *J* = 1.7 Hz, H_c), 6.89 (1H, dd, *J* = 8.9, 2.6 Hz, H_Z), 6.79 (1H, d, *J* = 2.6 Hz, H_{AA}), 6.68 (2H, d, *J* = 8.7 Hz, H_H or H_N), 6.37 (1H, *J* = 1.2 Hz, H_X), 6.35-6.26 (6H, m, H_H or H_N, H_G & H_O), 5.45-5.23 (6H, m, H_I, H_M & H_W), 4.61 (1H, d, *J* = 14.3 Hz, H_d or $H_{d'}$), 4.57 (2H, s, H_{BB}), 4.36 (1H, d, *J* = 14.1 Hz, H_d or $H_{d'}$), 2.50-2.10 (8H, m, H_D, H_R, H_F & H_P), 1.75-1.54 (4H, m, H_E & H_Q), 1.50 (9H, s, H_{CC}), 1.07 (18H, s, H_h or H_a), 1.06 (18H, s, H_h or H_a). ^{13}C NMR (101 MHz, CDCl$_3$, 298 K) δ_C 167.1, 163.2 (x2), 161.1, 160.9, 157.9 (x2), 157.1, 156.1, 155.5, 152.9, 150.8, 149.9, 149.6, 147.5, 136.9, 136.8, 136.7 (x2), 134.4, 133.2, 133.1, 131.0, 130.4, 128.9, 128.8, 127.5, 124.9, 123.8, 123.0, 122.0, 121.8, 120.6, 120.5, 120.1, 120.0, 115.1, 114.6, 113.0, 111.6, 110.8, 102.1, 83.2, 69.6, 68.8, 65.8, 62.0, 53.9, 38.1, 36.9, 35.0, 34.7, 34.7, 31.8 (x2), 31.4, 31.4, 30.7, 28.2. HR-ESI-MS (CH$_3$CN): *m/z* = 1333.7 [M+H]$^+$ calc. 1333.7317.

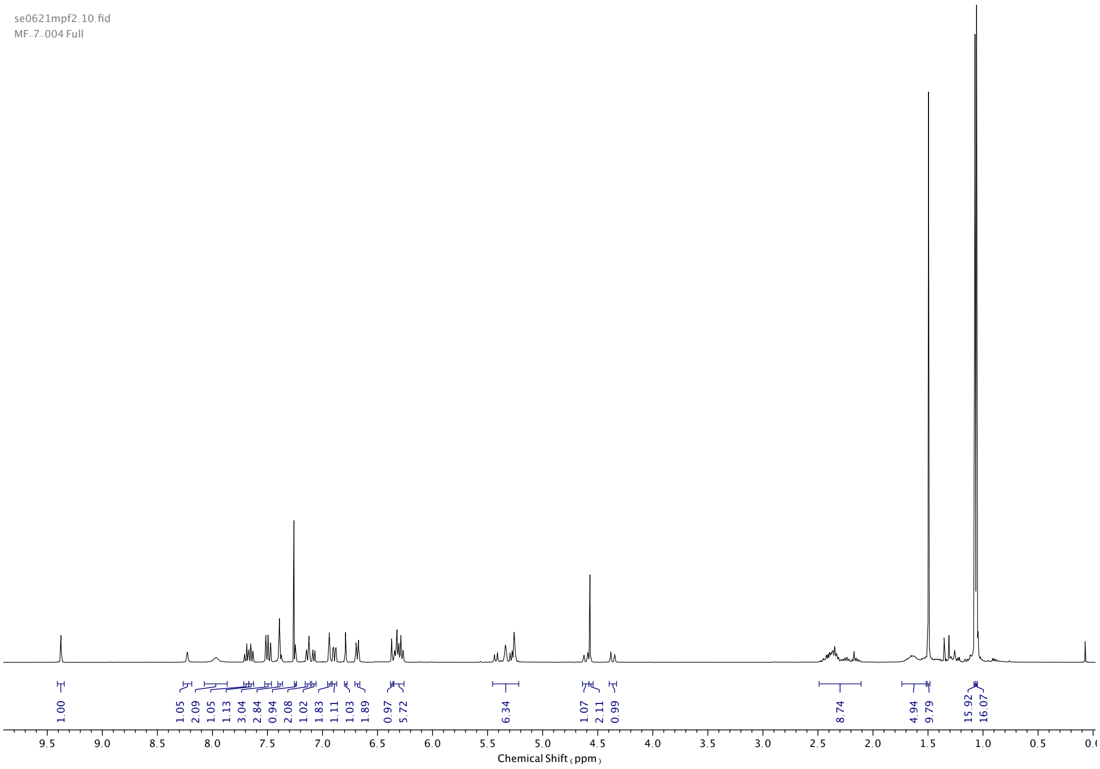

Figure **351**. ^{1}H NMR ($CDCl_3$, 400 MHz) of **74**.

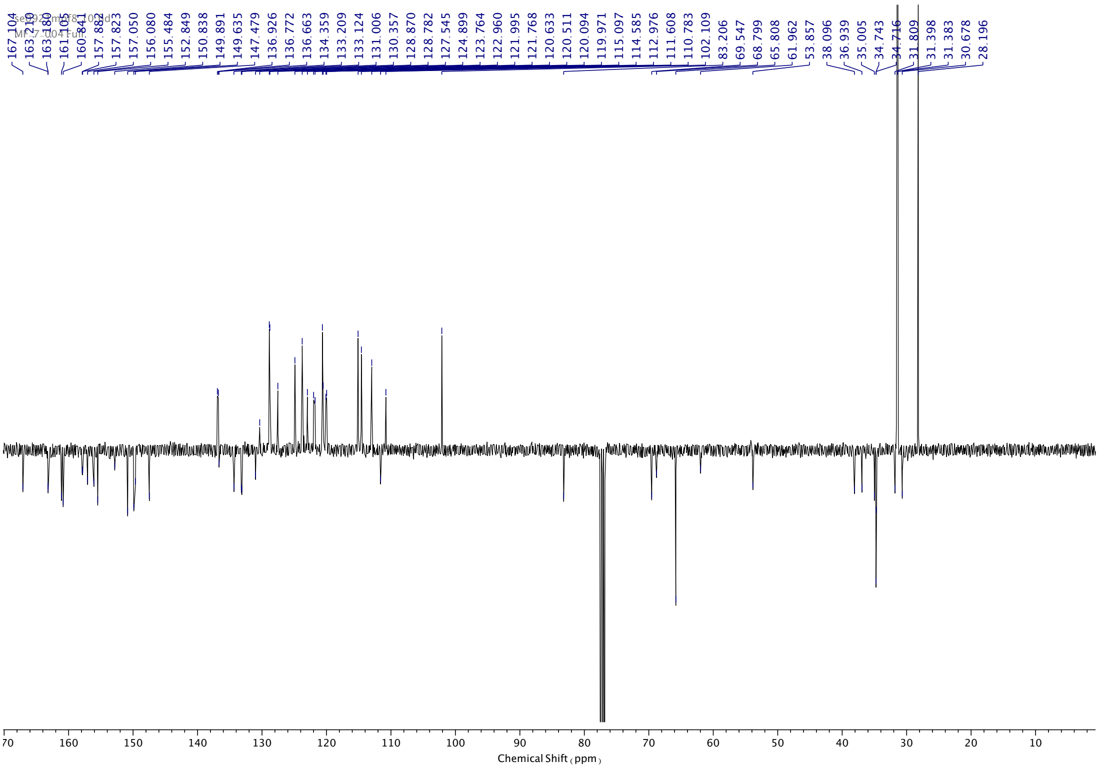

Figure **352**. ^{13}C NMR ($CDCl_3$, 101 MHz) of **74**.

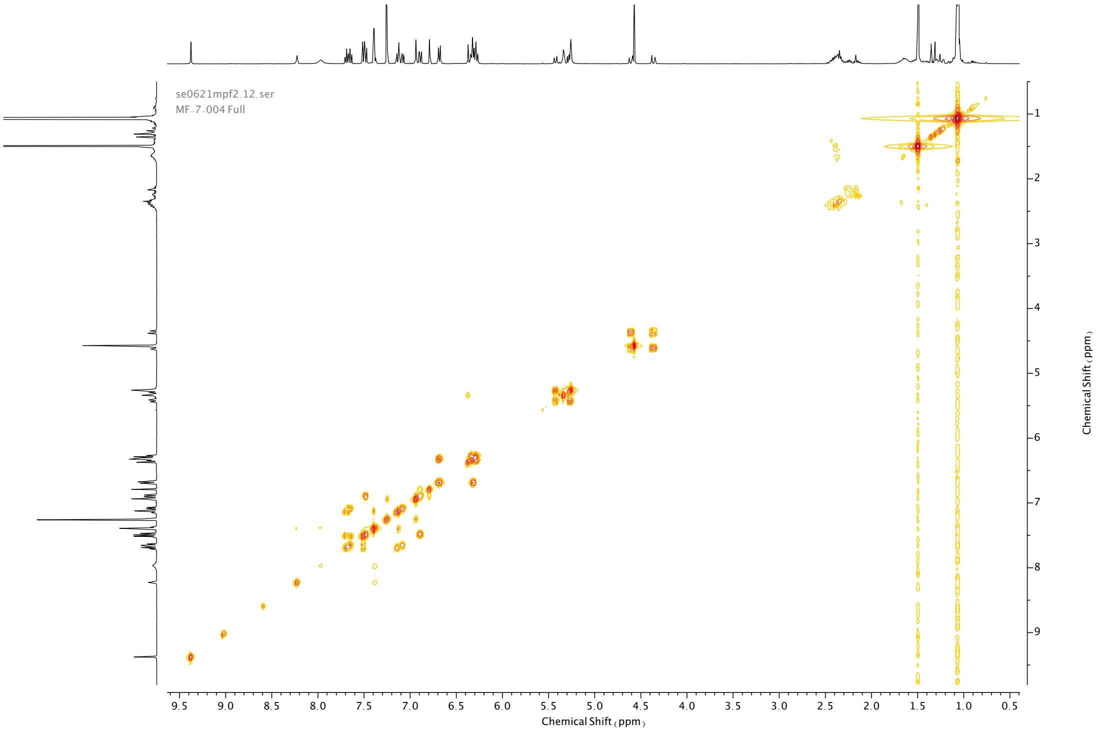

Figure **353**. COSY NMR ($CDCl_3$) of **74**.

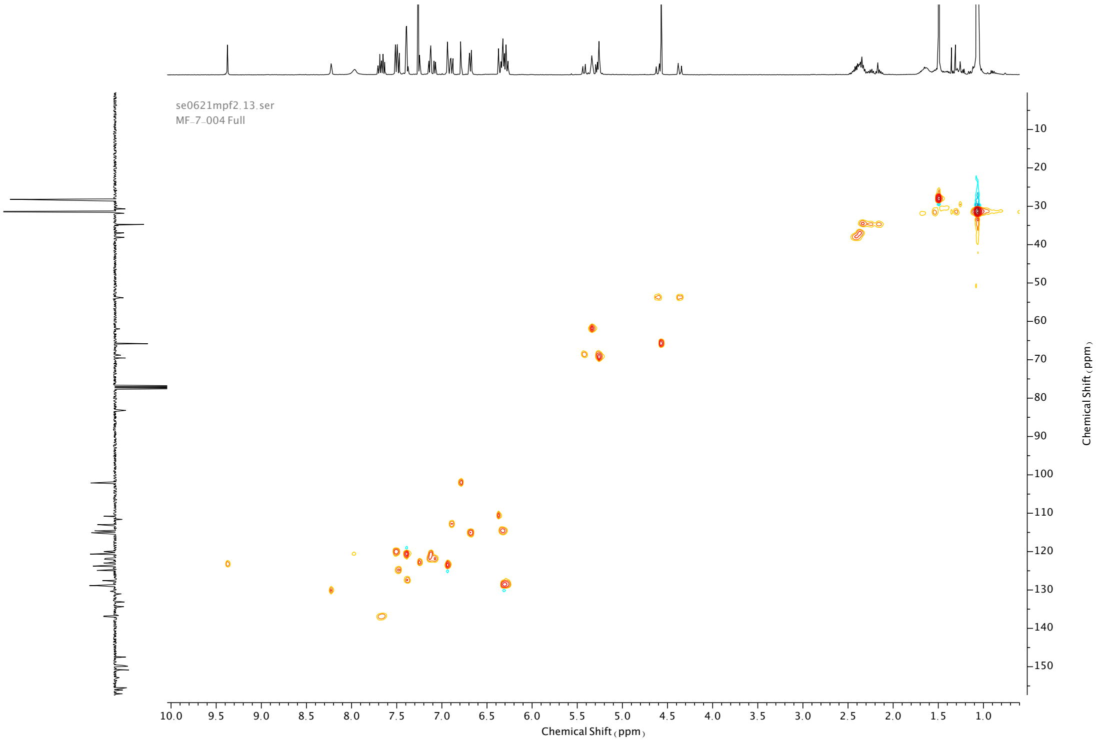

Figure **354**. HSQC NMR ($CDCl_3$) of **74**.

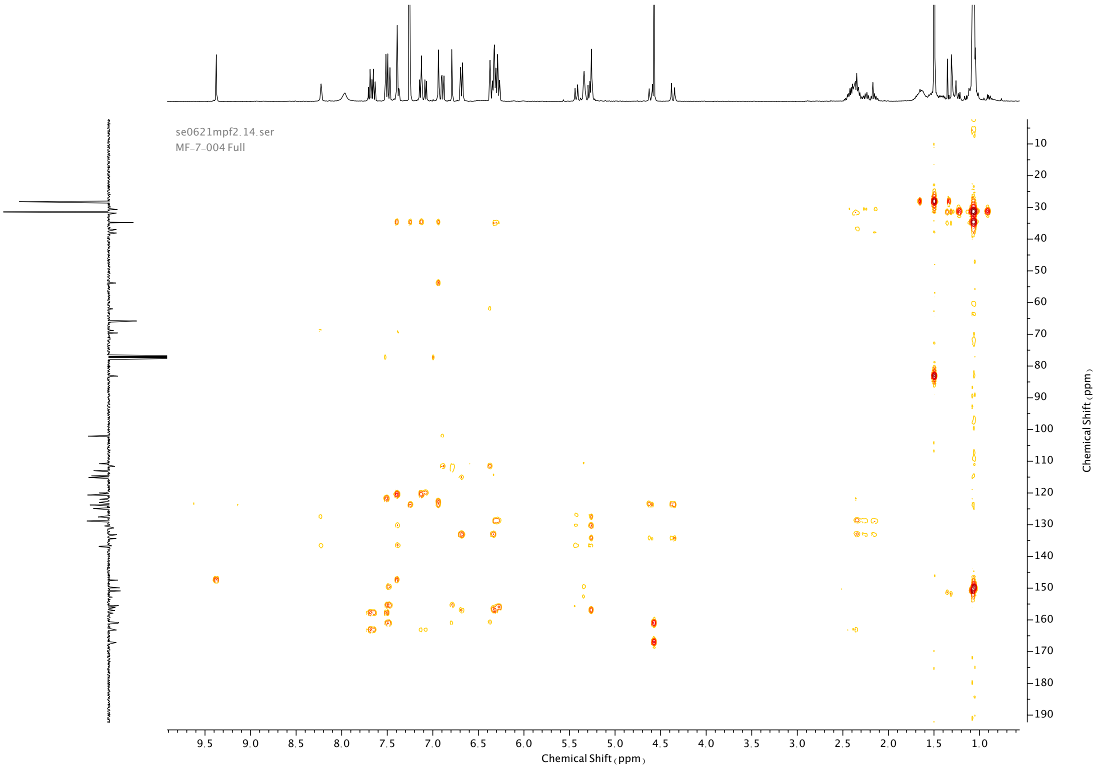

Figure **355**. HMBC NMR ($CDCl_3$) of **74**.

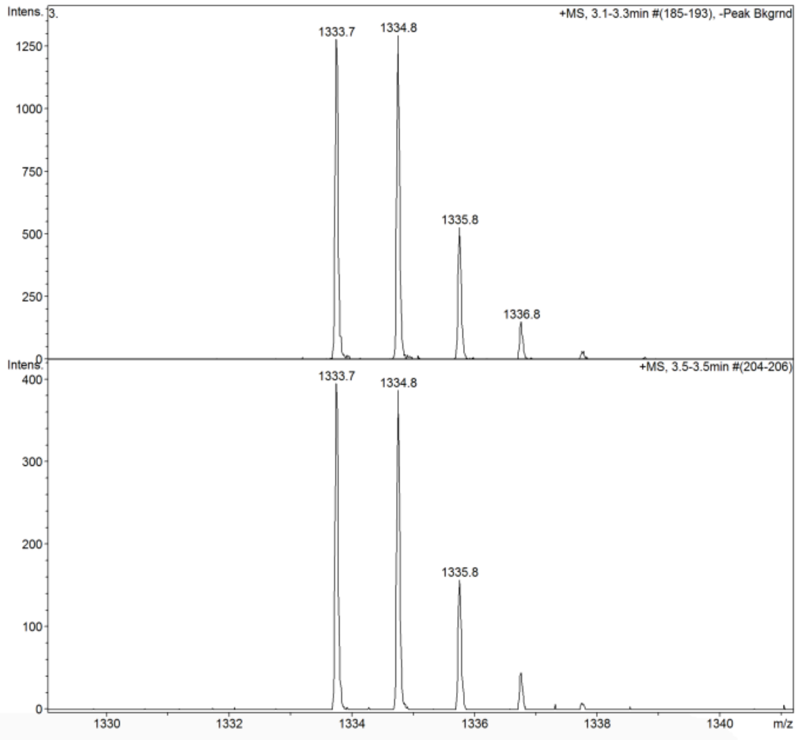

Figure **356**. Isotope pattern of **74**.

Compound **75**

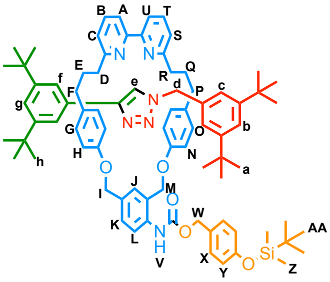

75 was synthesised according to general procedure **(7)** from macrocycle **52** (51 mg, 0.063 mmol), azide stopper **72** (23 mg, 0.095 mmol) and alkyne stopper **71** (20 mg, 0.095 mmol). Purification by column chromatography (eluent 49:1 → 9:1 PE: Acetone) afforded **75** as a yellow foam (49 mg, 0.039 mmol, 62%).^{1}H NMR (400 MHz, $CDCl_3$, 298 K) δ_H 9.36 (1H, s, H_e), 8.22 (1H, d, J = 1.9 Hz, H_J), 8.05-7.95 (1H, m, H_L), 7.71-7.63 (3H, m, H_B & H_T, N-H_V), 7.51 (2H, dd, J = 7.6, 0.6 Hz, H_A & H_U), 7.40 (2H, d, J = 1.8 Hz, H_f), 7.36 (1H, dd, J = 8.4, 2.0 Hz, H_K), 7.27 (2H, d, J = 8.6 Hz, H_X), 7.25 (1H, t, J = 1.8 Hz, H_b), 7.15-7.11 (2H, m, H_g & H_C or H_S), 7.08 (1H, dd, J = 7.8, 0.8 Hz, H_C or H_S), 6.94 (2H, d, J = 1.8 Hz, H_c), 6.81 (2H, d, J = 8.6 Hz, H_Y), 6.68 (2H, d, J = 8.7 Hz, H_H or H_N), 6.34-6.30 (4H, m, H_H or H_N, H_G or H_O), 6.26 (2H, d, J = 8.7 Hz, H_G or H_O), 5.36 (1H, d, J = 10.9 Hz, H_M or $H_{M'}$), 5.24 (2H, s, H_I), 5.22 (1H, d, J = 10.9 Hz, H_M or $H_{M'}$), 5.12 (2H, s, H_W), 4.60 (1H, d, J = 14.2 Hz, Hz, H_d or $H_{d'}$), 4.37 (1H, d, J = 14.2 Hz, Hz, H_d or $H_{d'}$), 2.50-2.12 (8H, m, H_D, H_R, H_F & H_P), 1.75-1.40 (4H, m, H_E & H_Q), 1.07 (18H, s, H_a), 1.06 (18H, s, H_h), 0.98 (9H, s, H_{AA}), 1.89 (6H, s, H_Z). ^{13}C NMR (101 MHz, $CDCl_3$, 298 K) δ_C 163.2 (x2), 157.9, 157.8, 157.1, 156.3, 155.9, 154.0, 150.8, 149.9, 147.5, 137.3, 136.9, 136.8, 134.4, 133.7, 130.3, 133.1, 132.9, 131.0, 130.4, 130.2, 129.1, 128.8, 128.7, 127.6, 123.8, 123.5, 122.9, 122.0, 121.8, 120.7, 120.5 (x2), 120.2, 120.1, 120.0, 115.1, 114.6, 69.7, 68.7, 66.8, 53.8, 38.1, 37.0, 34.8, 34.7 (x2), 31.8, 31.6, 31.5, 31.4, 30.7, 29.8, 25.8, -4.3. HR-ESI-MS (CH_3CN): *m/z* = 1265.8 $[M+H]^+$ calc. 1265.7603.

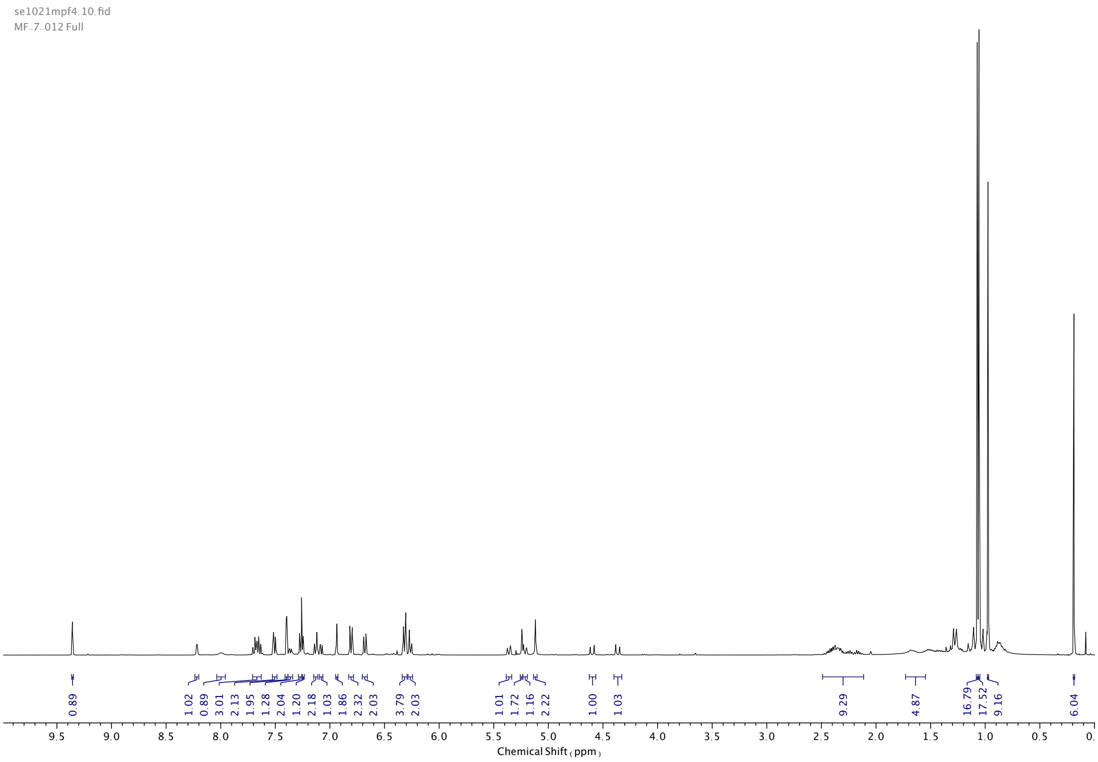

Figure **357**. ^{1}H NMR (CDCl$_3$, 400 MHz) of **75**.

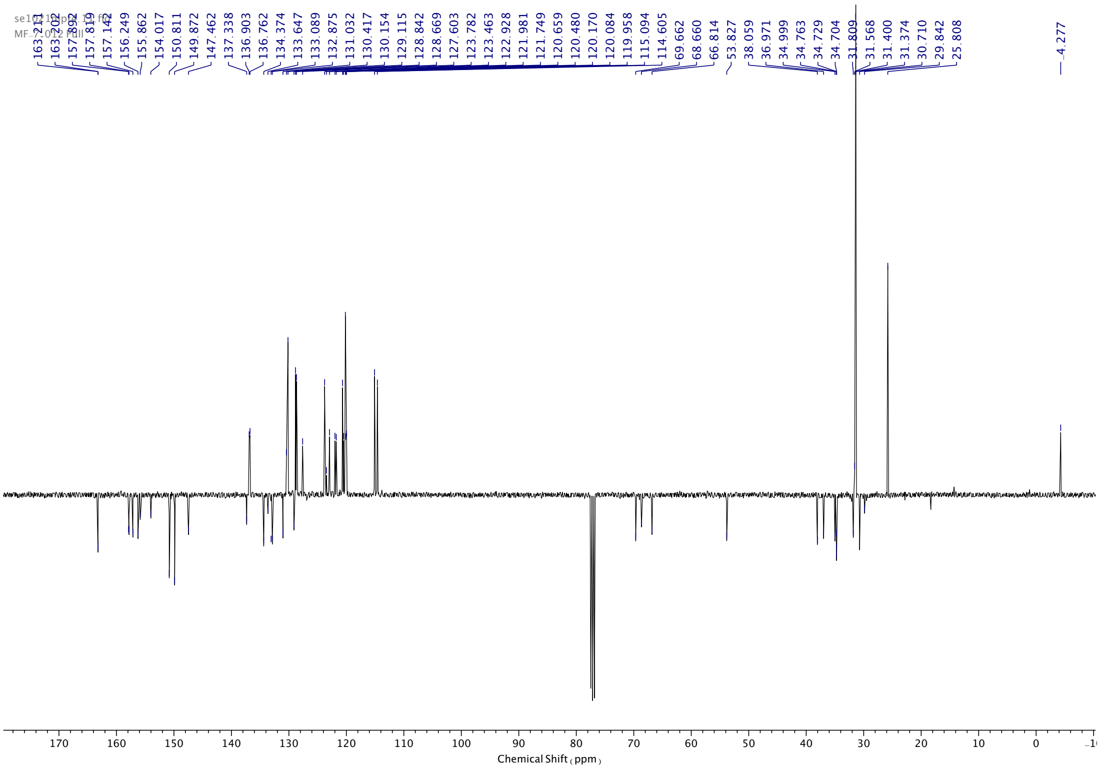

Figure **358**. ^{13}C NMR (CDCl$_3$, 101 MHz) of **75**.

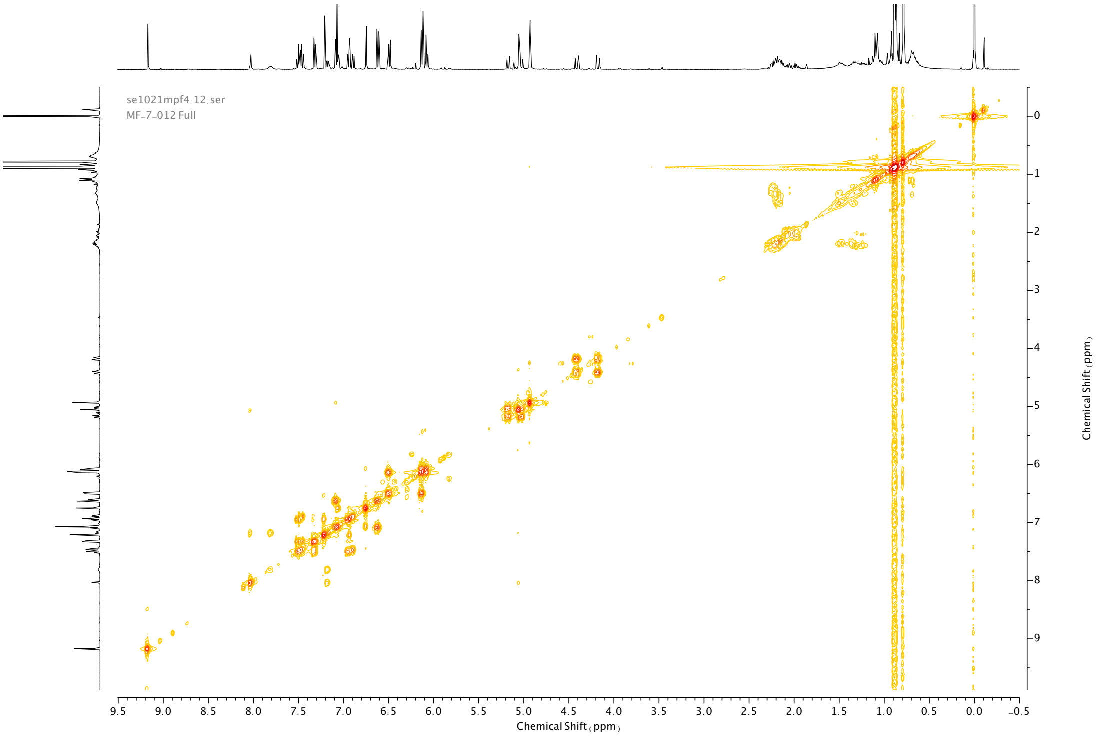

Figure **359**. COSY NMR ($CDCl_3$) of **75**.

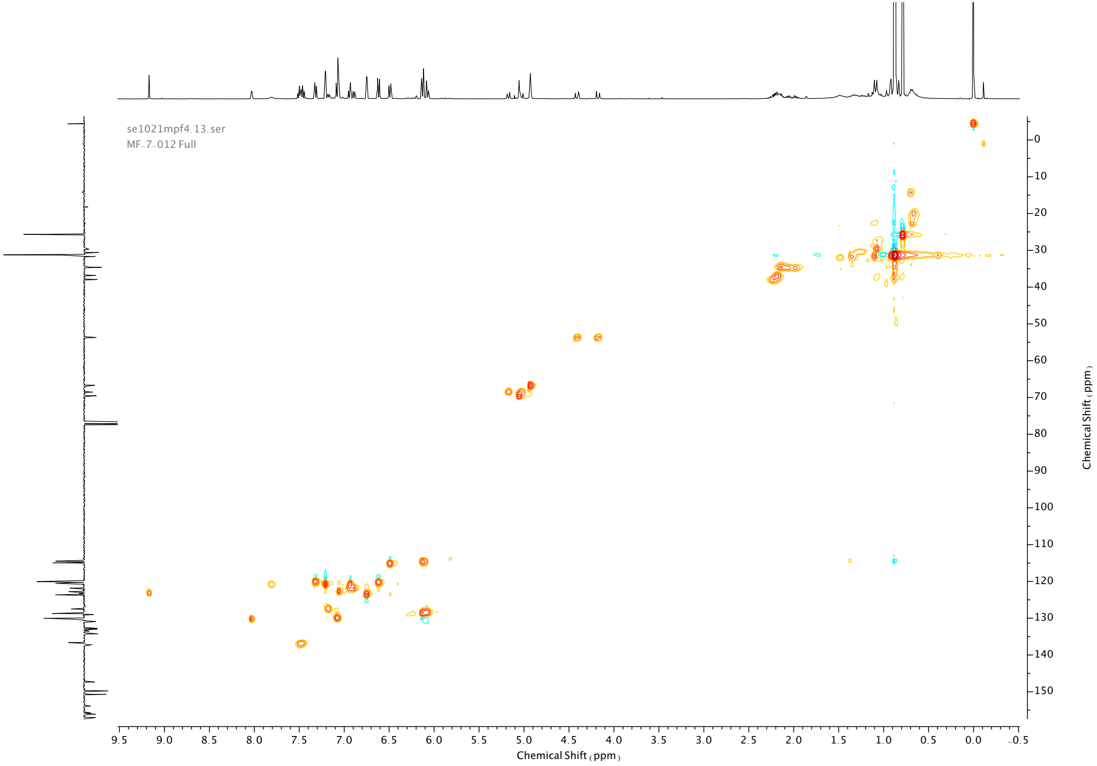

Figure **360**. HSQC NMR ($CDCl_3$) of **75**.

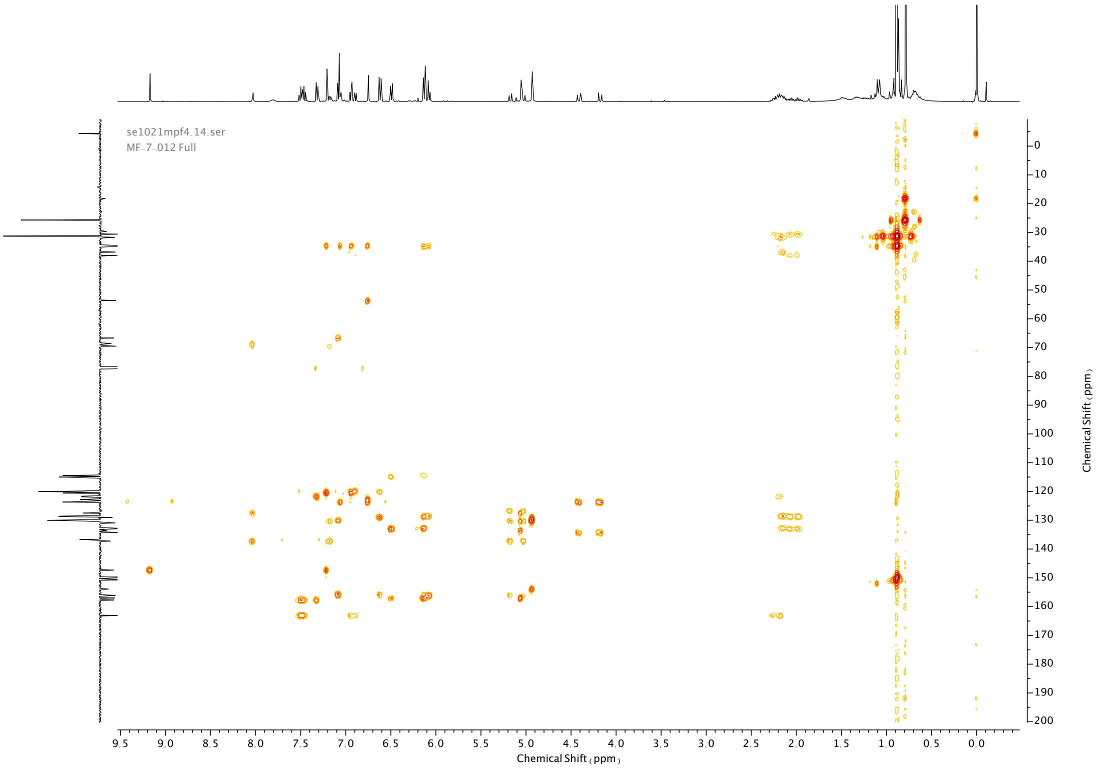

Figure **361**. HMBC NMR ($CDCl_3$) of **75**.

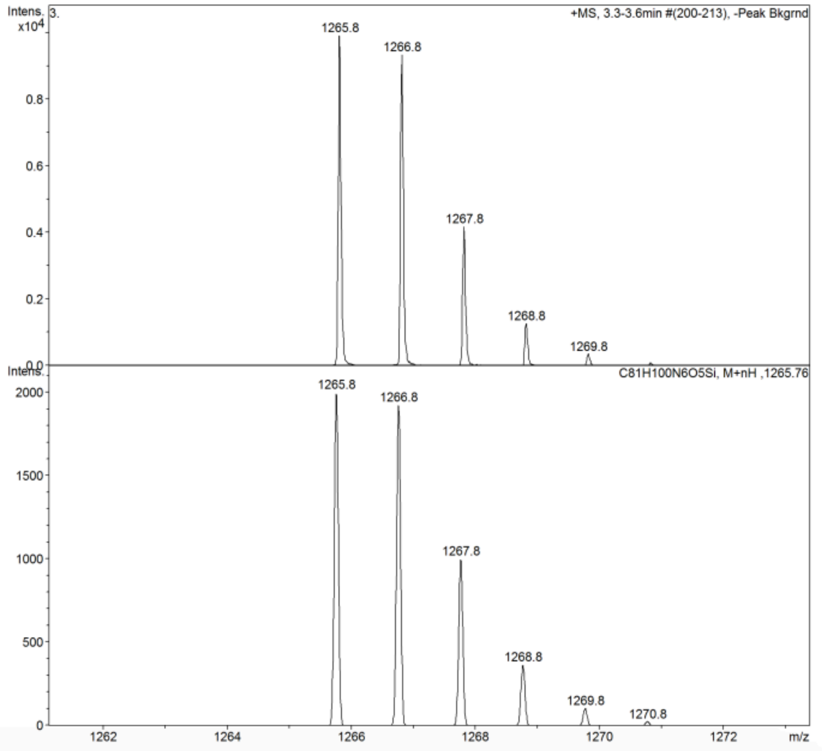

Figure **362**. Isotope pattern of **75**.

Compound **89**

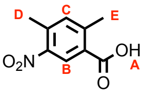

NH_4NO_3 (4.1 g, 51.7 mmol, 1.2 eq.) was added to a solution of **87** (6.5 g, 43.1 mmol, 1.0 eq.) in CH_2Cl_2 (50 mL) and stirred for 10 min at room temperature. Conc. H_2SO_4 (8.1 mL, 150.9 mmol, 3.5 eq.) was added dropwise over 15 min at 0 °C. The mixture was stirred for 30 min at 0 °C then at room temperature for a further 3 h. The mixture was dropped onto ice water and extracted with EtOAc (3 x 100 mL). Organic extracts were washed with water (100 mL) and brine (100 mL). Aqueous washings were extracted with EtOAc (2 x 100 mL). Combined organic extracts were dried over anhydrous $MgSO_4$, filtered and concentrated *in vacuo* to afford a regioisomeric mixture of **88** and **89** (2.5:7.5) as a white solid (8.1 g, 41.5 mmol, 96%) that was carried forward to the next step without further purification. ^1H NMR (400 MHz, $CDCl_3$, 298 K) δ_H 8.73 (1H, s, H_B), 7.28 (1H, s, H_C), 2.70 (3H, s, H_D), 2.66 (3H, s, H_E).

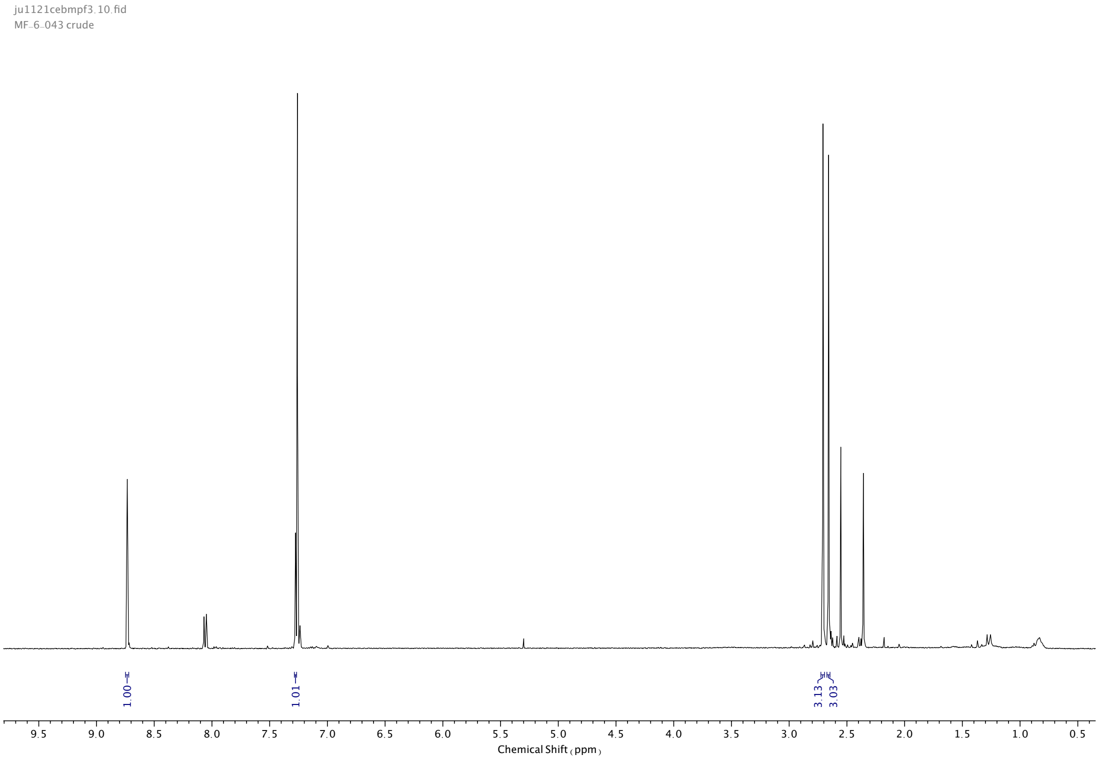

Figure **363**. ^1H NMR ($CDCl_3$, 400 MHz) of **89**.

Compound **91**

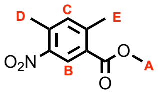

A mixture of **88** and **89** (2.5:7.5) (8.1 g, 41.6 mmol, 1.0 eq.) and conc. H_2SO_4 (0.2 mL, 4.2 mmol, 0.1 eq.) in MeOH (150 mL) was refluxed at 75 °C overnight. Once cooled to room temperature, the mixture was diluted with CH_2Cl_2 (200 mL) and washed with $NaHCO_3$ (2 x 100 mL) and brine (100 mL). Aqueous washings were extracted with CH_2Cl_2 (2 x 100 mL). Combined organic extracts were dried over anhydrous $MgSO_4$, filtered and concentrated *in vacuo* to afford regioisomeric mixture of **90** and **91** (2.5:7.5) as a colourless oil (8.3 g, 39.70 mmol, 95%) that was carried forward to the next step without further purification. ^{1}H NMR (400 MHz, $CDCl_3$, 298 K) δ_H 8.61 (1H, s, H_B), 7.23 (1H, s, H_C), 3.92 (3H, s, H_A), 2.66 (3H, s, H_D), 2.63 (3H, s, H_E).

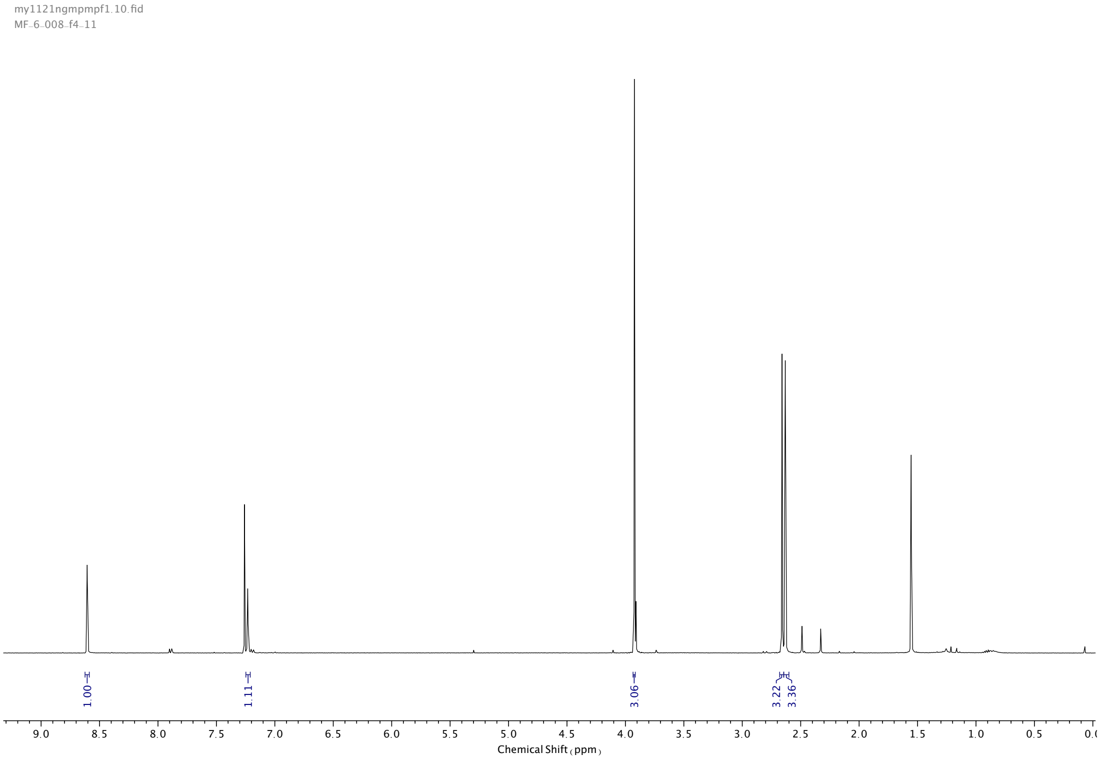

Figure **364**. ^{1}H NMR ($CDCl_3$, 400 MHz) of **91**.

Compound **92**

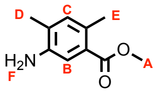

Pd/C (10 % wt.) (630 mg, 7.0 eq.) was added to a mixture of **90** and **91** (2.5:7.5) (3.2 g, 15.5 mmol) in EtOH (120 mL). The mixture was degassed under N_2 then cyclohexene (12 mL) was added and the mixture stirred at 85 °C overnight. Once cooled to room temperature, the mixture was filtered over Celite, dried over anhydrous $MgSO_4$, filtered and concentrated *in vacuo.* The crude regioisomeric mixture was purified *via* silica-gel chromatography using a Biotage Isolute SPE column (eluent 9:1 → 4.1 PE: EtOAc) to afford regioisomer **92** as an off-white solid (1.5 g, 8.37 mmol, 54 %). ^{1}H NMR (400 MHz, $CDCl_3$, 298 K) δ_H 7.29 (1H, d, *J* = 3.8 Hz, H_B), 6.93 (1H, s, H_C), 3.85 (3H, s, H_A), 2.46 (3H, s, H_E), 2.18 (3H, d, *J* = 1.8 Hz, H_D). ^{13}C NMR (101 MHz, $CDCl_{3,}$ 298 K) δ_C 168.2 (HMBC), 142.0, 130.6 (x2), 127,7, 127.5, 117.3, 51.7, 20.9, 17.5.

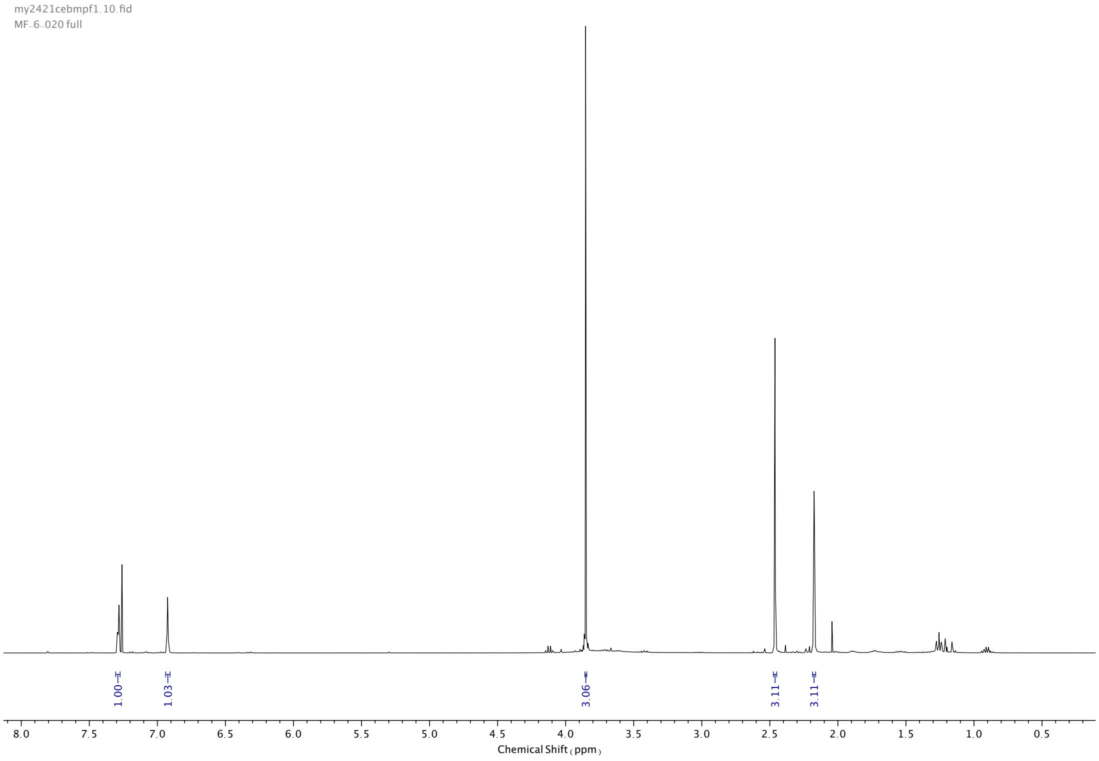

Figure **365**. ^{1}H NMR ($CDCl_3$, 400 MHz) of **92**.

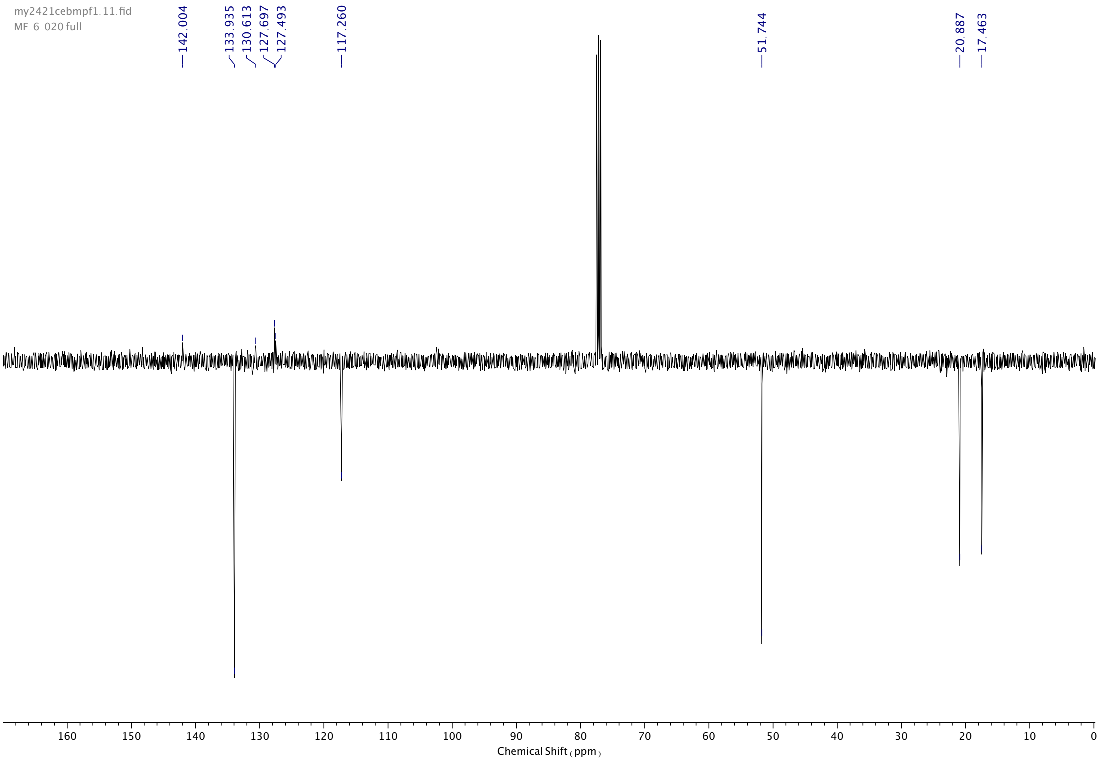

Figure **366**. ^{13}C NMR (CDCl$_3$, 101 MHz) of **92**.

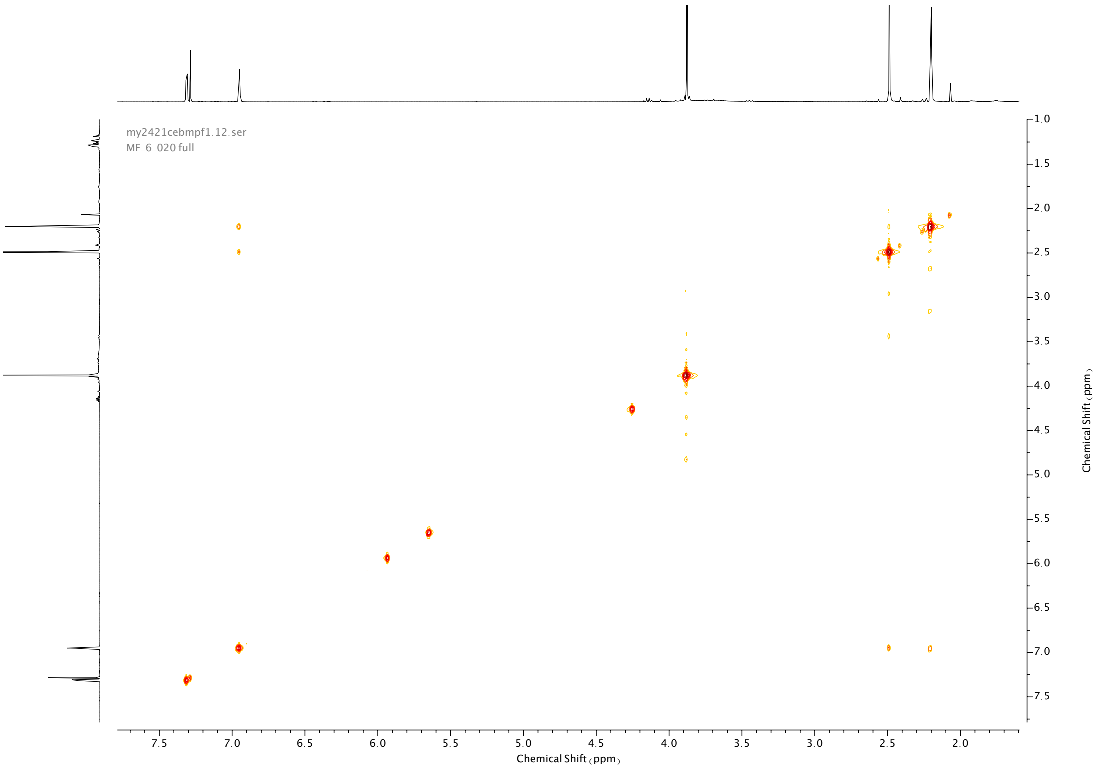

Figure **367**. COSY NMR (CDCl$_3$) of **92**.

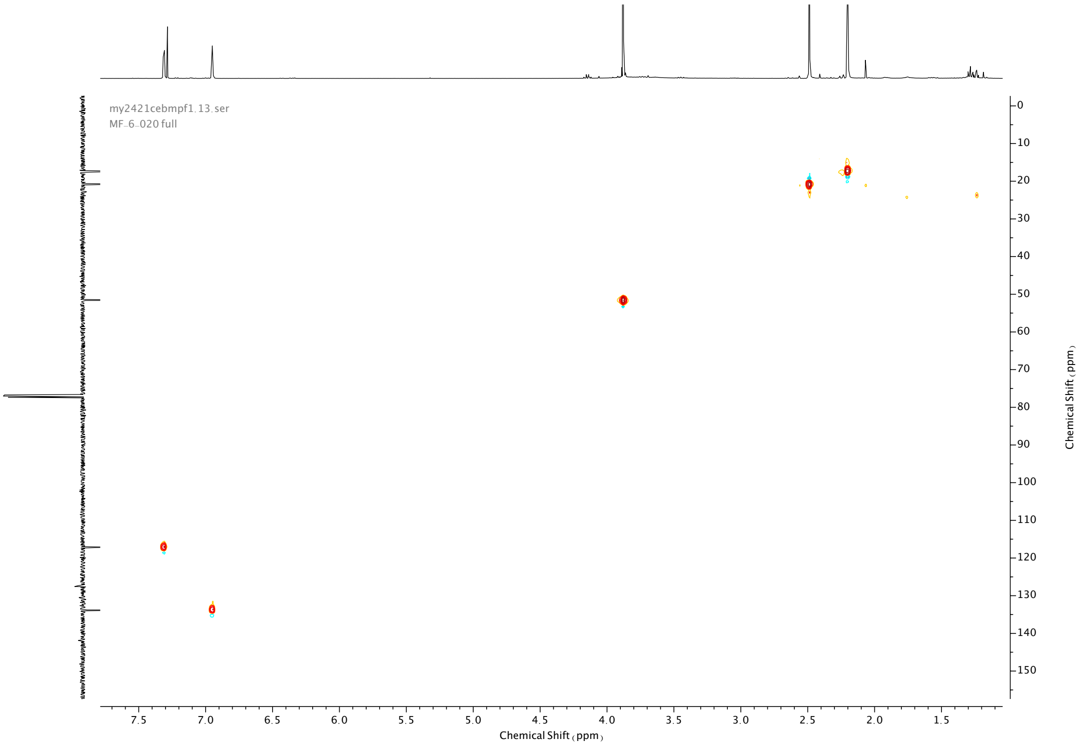

Figure **368**. HSQC NMR ($CDCl_3$) of **92**.

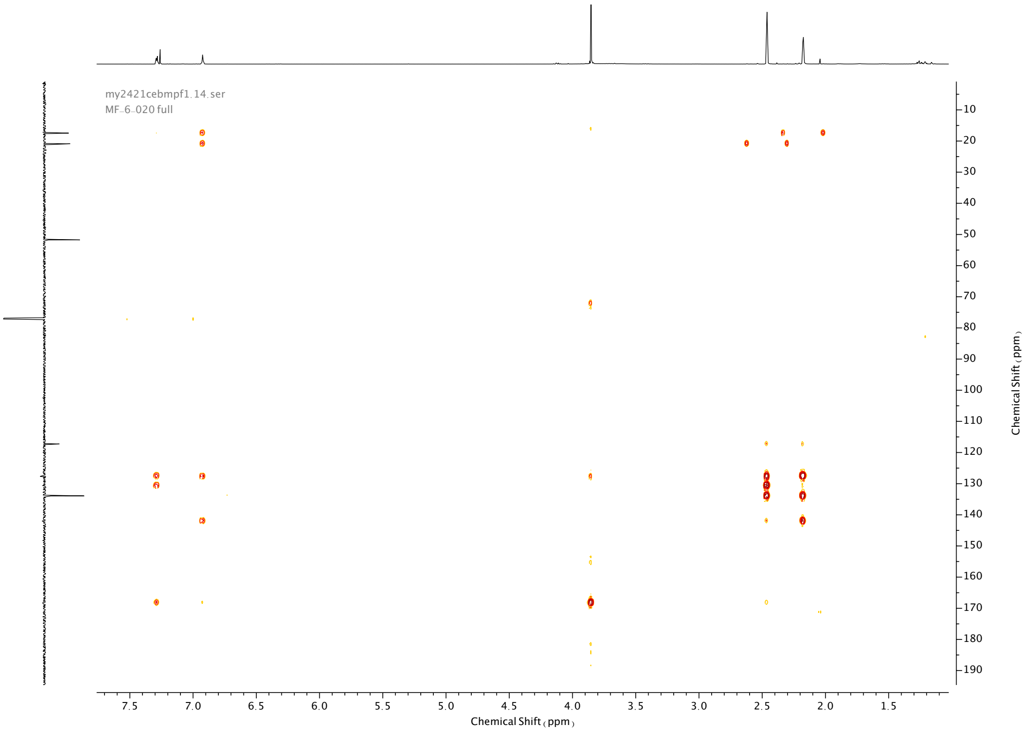

Figure **369**. HMBC NMR ($CDCl_3$) of **92**.

Compounds **93** and **94**

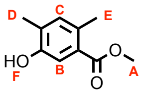

+

93

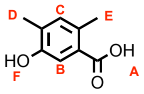

94

$NaNO_2$ (1.5 g, 22.1 mmol, 1.2 eq.) in H_2O (60 mL) was added dropwise to a solution of **92** (3.3 g, 18.4 mmol, 1.0 eq.) in aqueous H_2SO_4 (20% v/v) (115 mL) over 20 min at -10 °C, then stirred for a further 30 min at -10 °C. To the resulting diazonium salt was added conc. H_2SO_4 (115 mL) at -5 °C. The mixture was allowed to reach room temperature then added to aqueous H_2SO_4 (50% v/v) (250 mL) and heated at 100 °C for 5 min. After cooling to room temperature, the mixture was poured onto ice and extracted with EtOAc (3 x 200 mL). Organic extracts were washed with brine (200 mL), dried over anhydrous $MgSO_4$, filtered and concentrated *in vacuo* to afford a mixture of **93** and **94** (3:2) as an off-white solid (2.7 g) that was carried forward to the next step without further purification. ^{1}H NMR (400 MHz, $CDCl_3$, 298 K) δ_H **93**: 7.46 (1H, s, H_B), 7.02 (1H, s, H_C), 2.53 (3H, s, H_E), 2.27 (3H, s, H_D). **94**: 7.36 (1H, s, H_B), 6.99 (1H, s, H_C), 3.86 (3H, s, H_A), 2.49 (3H, s, H_E), 2.25 (3H, s, H_D).

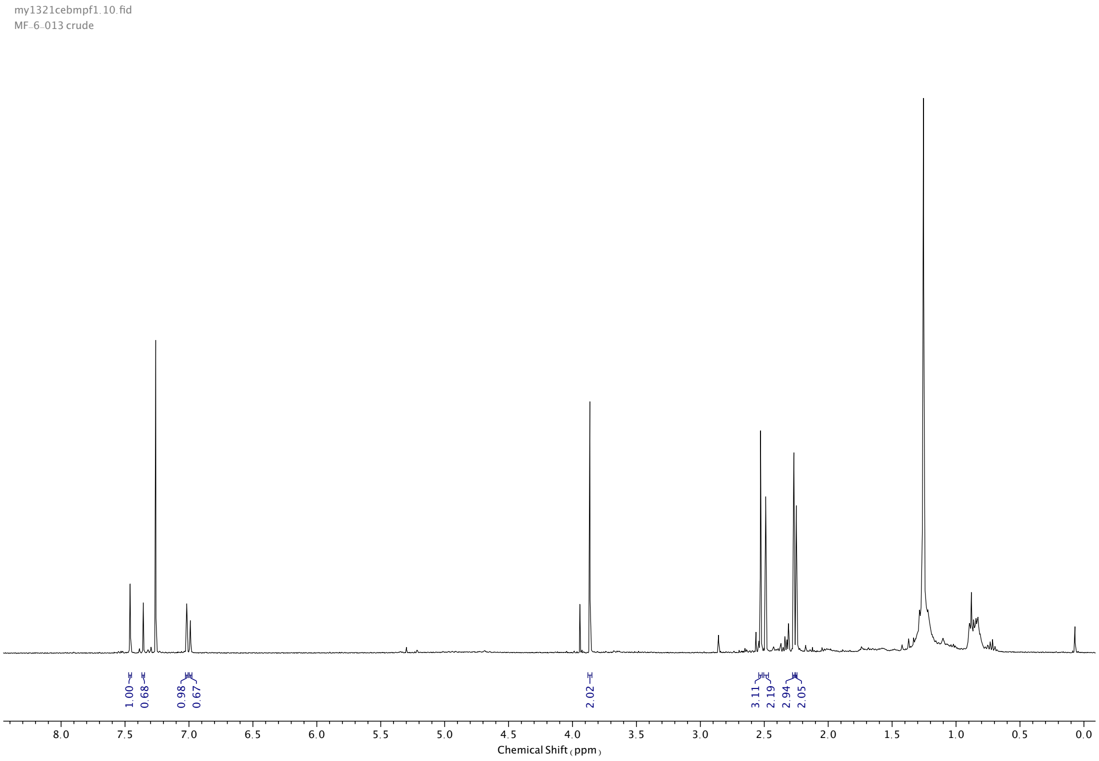

Figure **370**. ^{1}H NMR ($CDCl_3$, 400 MHz) of **93** and **94** (3:2).

Compound **95**

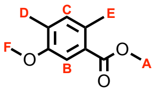

CH_3I (10.1 mL, 162.6 mL, 10 eq.) and K_2CO_3 (9.0 g, 65.1 mmol, 4.0 eq.) were added to a solution of product mixture **93** and **94** (3:2) (2.7 g, 1.0 eq.) from previous reaction in acetone (150 mL) and stirred overnight at 65 °C. After cooling to room temperature, the mixture was diluted with CH_2Cl_2 (200 mL) and washed with water (2 x 200 mL) and brine (200 mL). Combined aqueous washings were extracted with CH_2Cl_2 (2 x 100 mL). Combined organic extracts were dried over anhydrous $MgSO_4$, filtered and concentrated *in vacuo*. The crude product was purified *via* silica-gel chromatography using a Biotage Isolute SPE column (eluent 1:0 → 1.1 PE: CH_2Cl_2) to afford **95** as a pale-yellow oil (3.4 g, 17.5 mmol, 95% over 2 steps). ^{1}H NMR (400 MHz, $CDCl_3$, 298 K) δ_H 7.38 (1H, s, H_B), 7.00 (1H, s, H_C), 3.88 (3H, s, H_A), 3.85 (3H, s, H_F), 2.50 (3H, s, H_E), 2.22 (3H, s, H_D). ^{13}C NMR (101 MHz, $CDCl_3$, 298 K) δ_C 168.2, 155.6, 134.2, 132.5, 131.6, 127.3, 111.8, 55.6, 51.9, 21.0, 16.3.

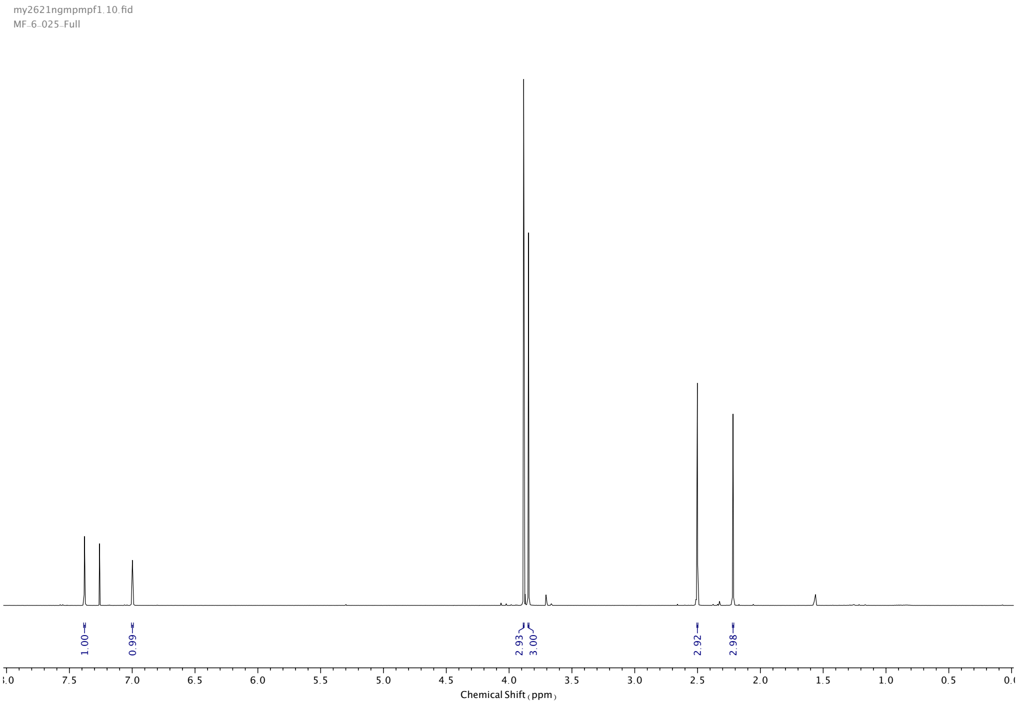

Figure **371**. ^{1}H NMR ($CDCl_3$, 400 MHz) of **95**.

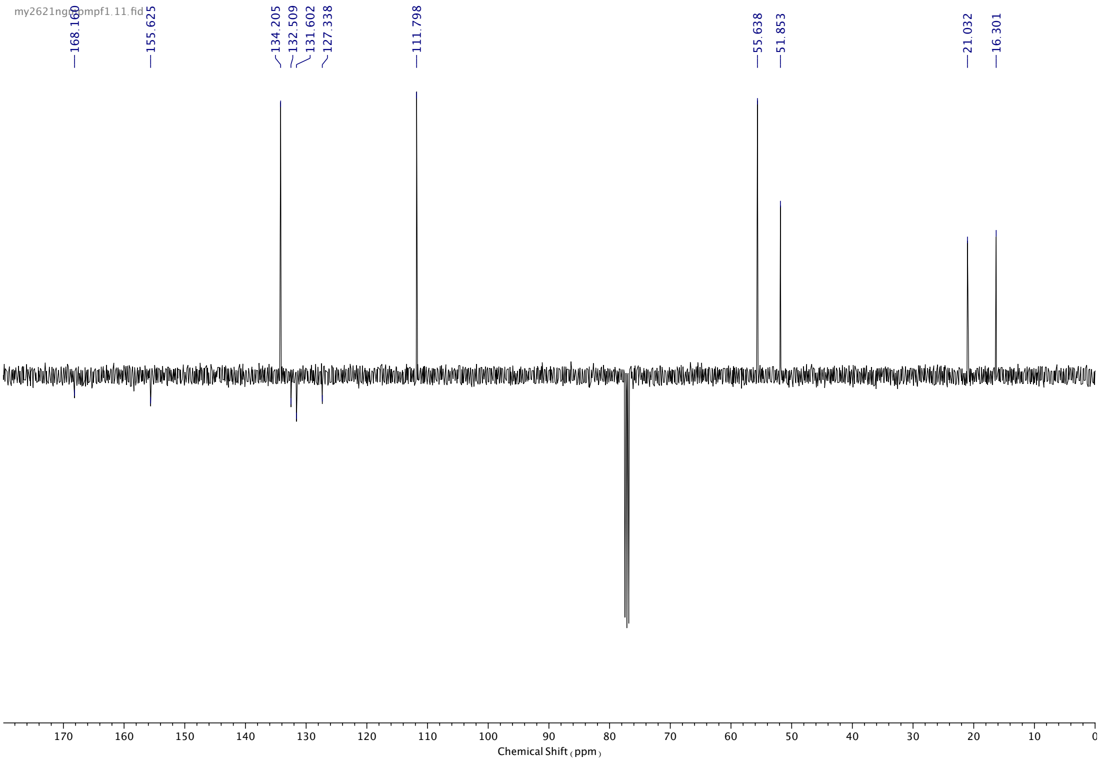

Figure **372**. ^{13}C NMR ($CDCl_3$, 101 MHz) of **95**.

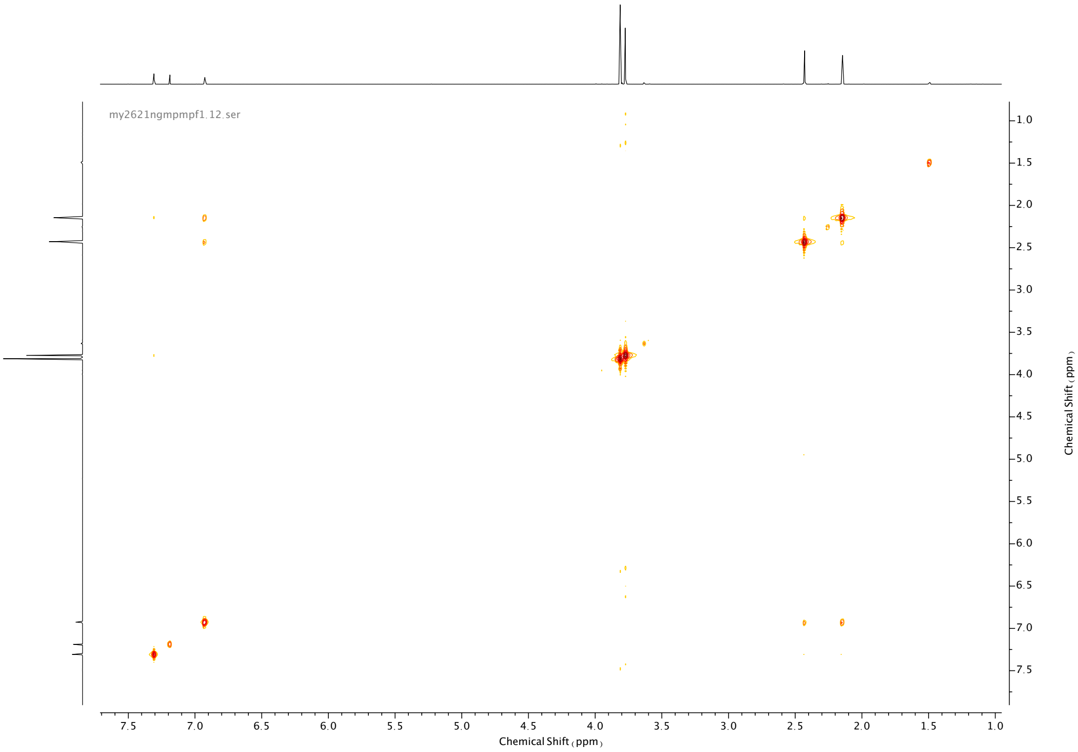

Figure **373**. COSY NMR ($CDCl_3$) of **95**.

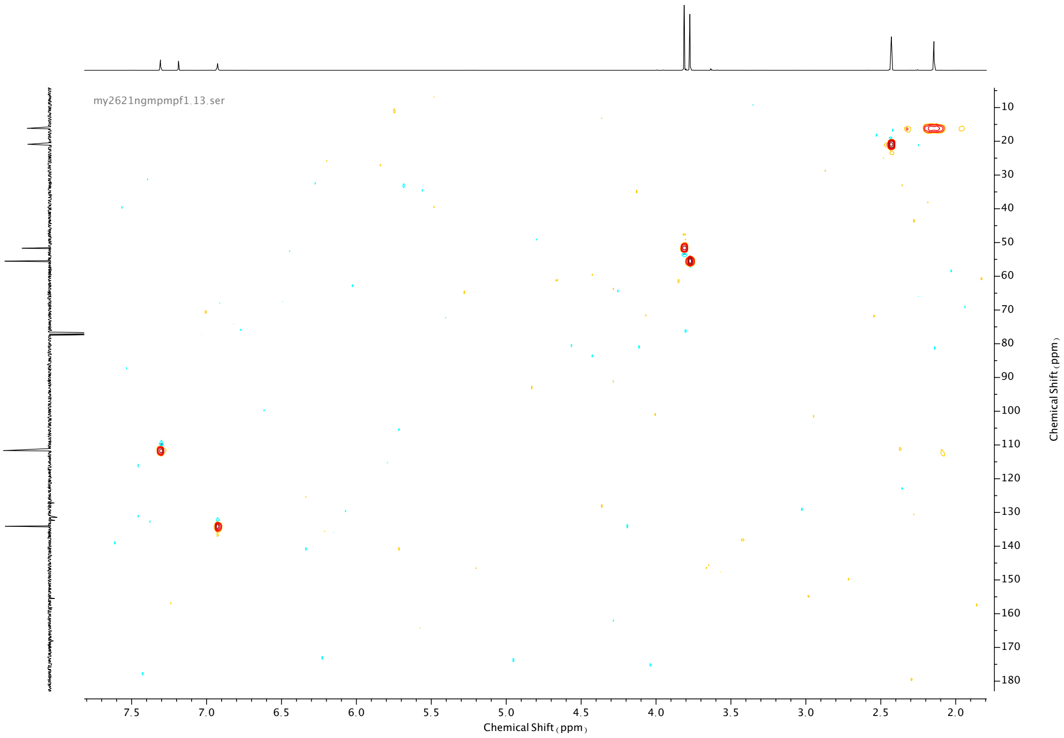

Figure **374**. HSQC NMR (CDCl$_3$) of **95**.

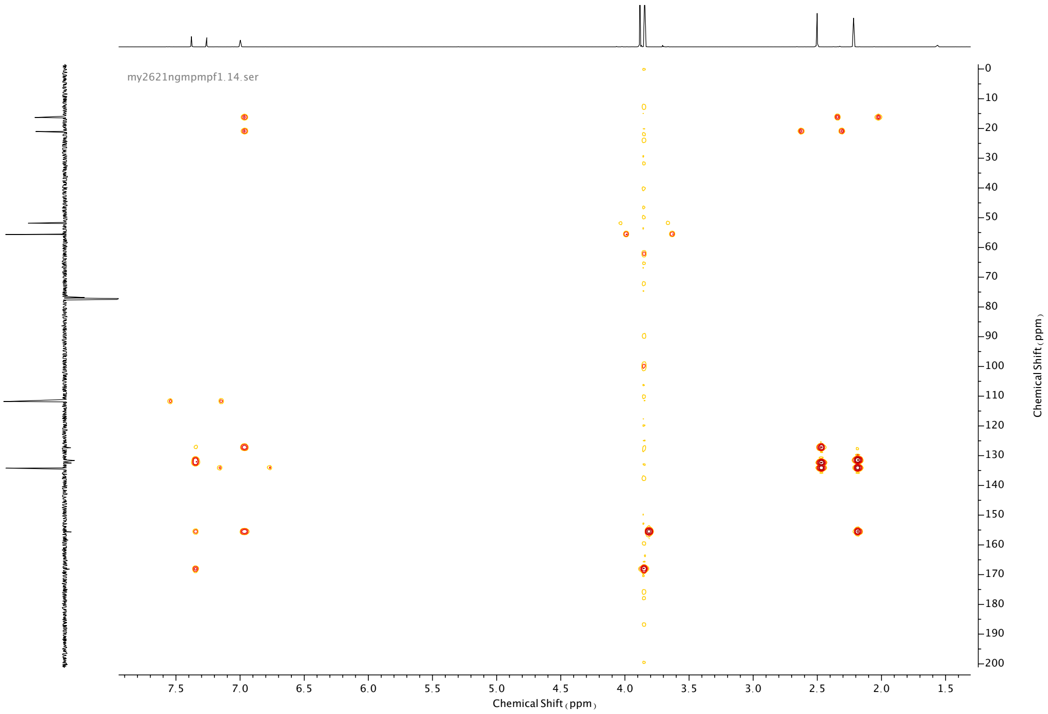

Figure **375**. HMBC NMR (CDCl$_3$) of **95**.

Compound **96**

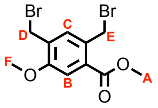

A mixture of **95** (1.1 g, 5.5 mmol, 1.0 eq.), NBS (2.2 g, 12.1 mmol, 2.2 eq.) and benzoyl peroxide (80 mg, 0.3 mmol, 0.06 eq.) in chlorobenzene (15 mL) was heated at 80 °C for 2 h. Once cooled to room temperature, the mixture was diluted with EtOAc (100 mL), washed with water (100 mL), $NaHCO_3$ (100 mL) and brine (100 mL). Combined aqueous phases were extracted with EtOAc (2 x 50 mL). The combined organic extracts were then dried over anhydrous $MgSO_4$, filtered and concentrated *in vacuo*. The crude product was purified *via* silica-gel chromatography using a Biotage Isolute SPE column (eluent 1:0 → 19.1 PE: Et_2O) to afford **96** as a white solid (1.33 g, 3.8 mmol, 68%). ^{1}H NMR (400 MHz, $CDCl_3$, 298 K) δ_H 7.46 (1H, s, H_B), 7.42 (1H, s, H_C), 4.91 (2H, s, H_E), 4.50 (2H, s, H_D), 3.96 (3H, s, H_A), 3.95 (3H, s, H_F). ^{13}C NMR (101 MHz, $CDCl_3$, 298 K) δ_C 166.6, 157.1, 134.3, 131.7, 130.7, 130.5, 113.6, 56.2, 52.6, 31.5, 27.0.

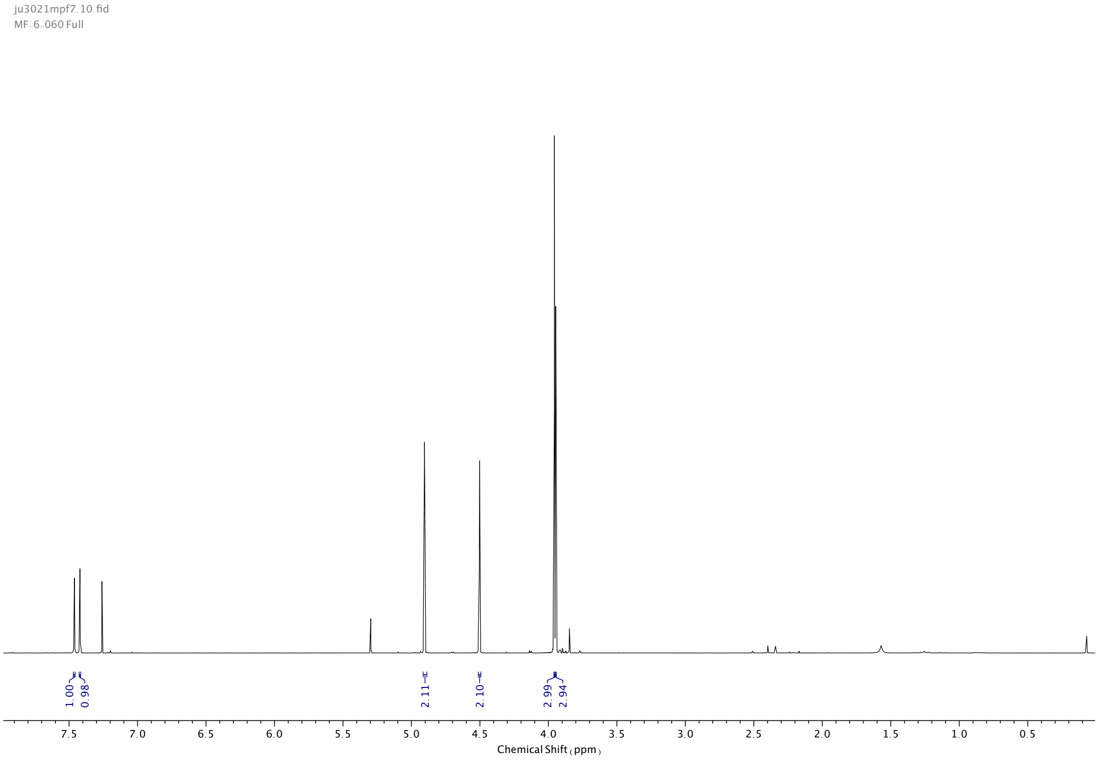

Figure **376**. ^{1}H NMR ($CDCl_3$, 400 MHz) of **96**.

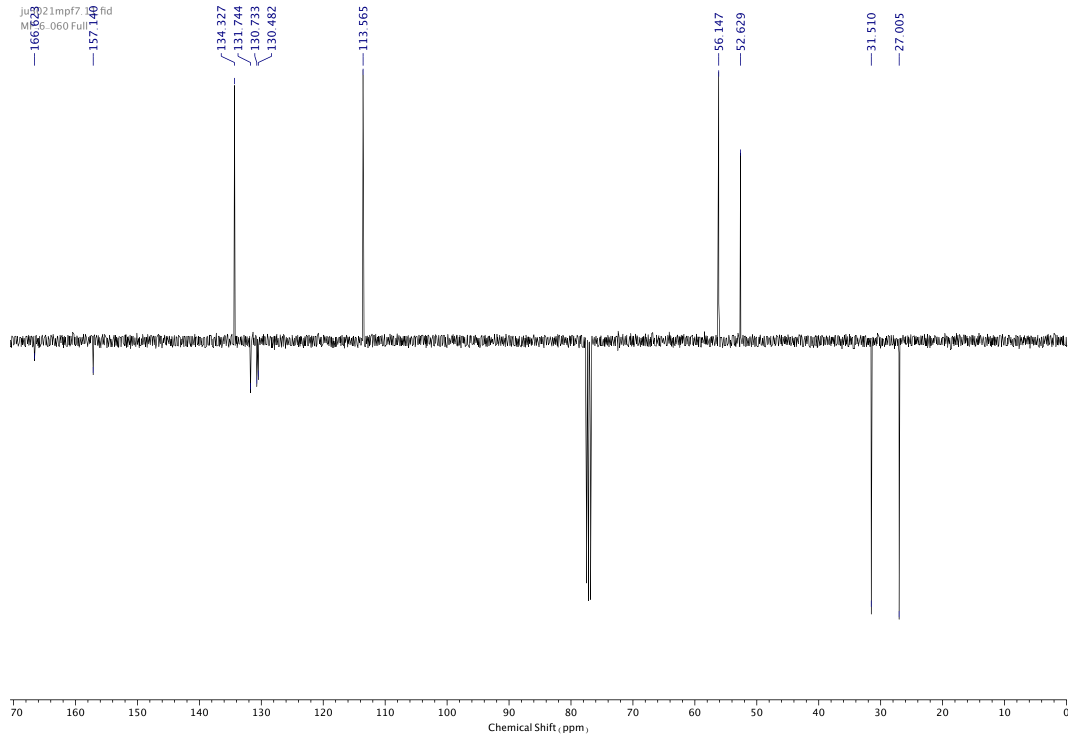

Figure **377**. ^{13}C NMR (CDCl$_3$, 101 MHz) of **96**.

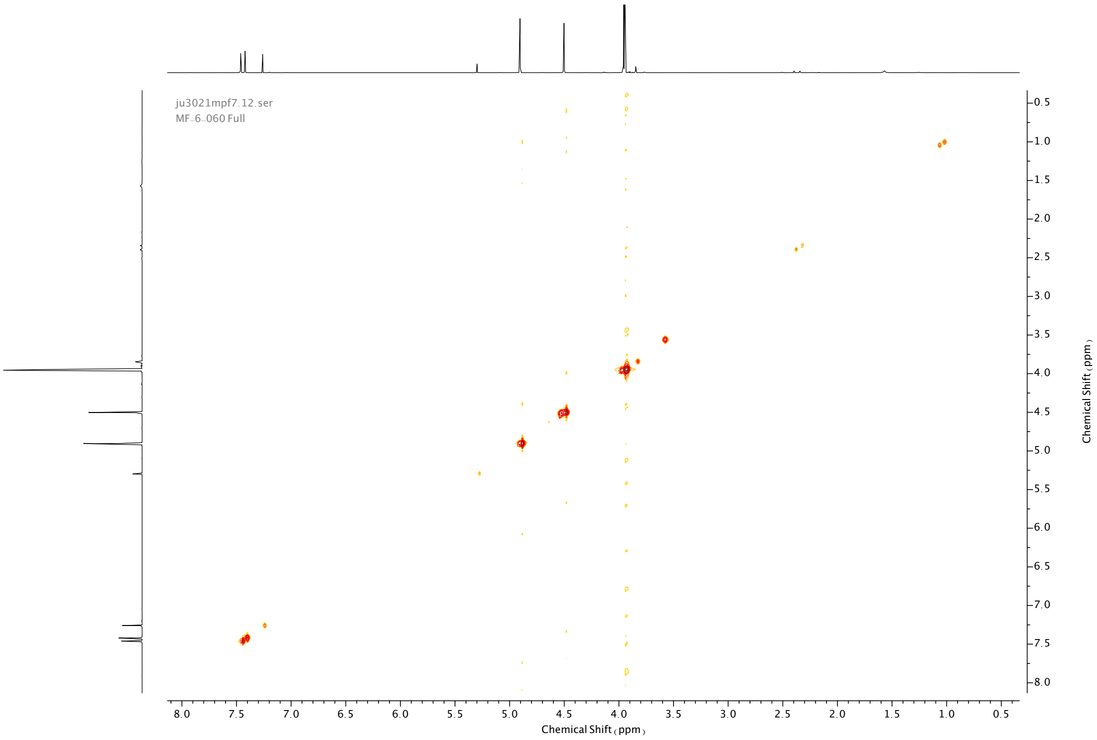

Figure **378**. COSY NMR (CDCl$_3$) of **96**.

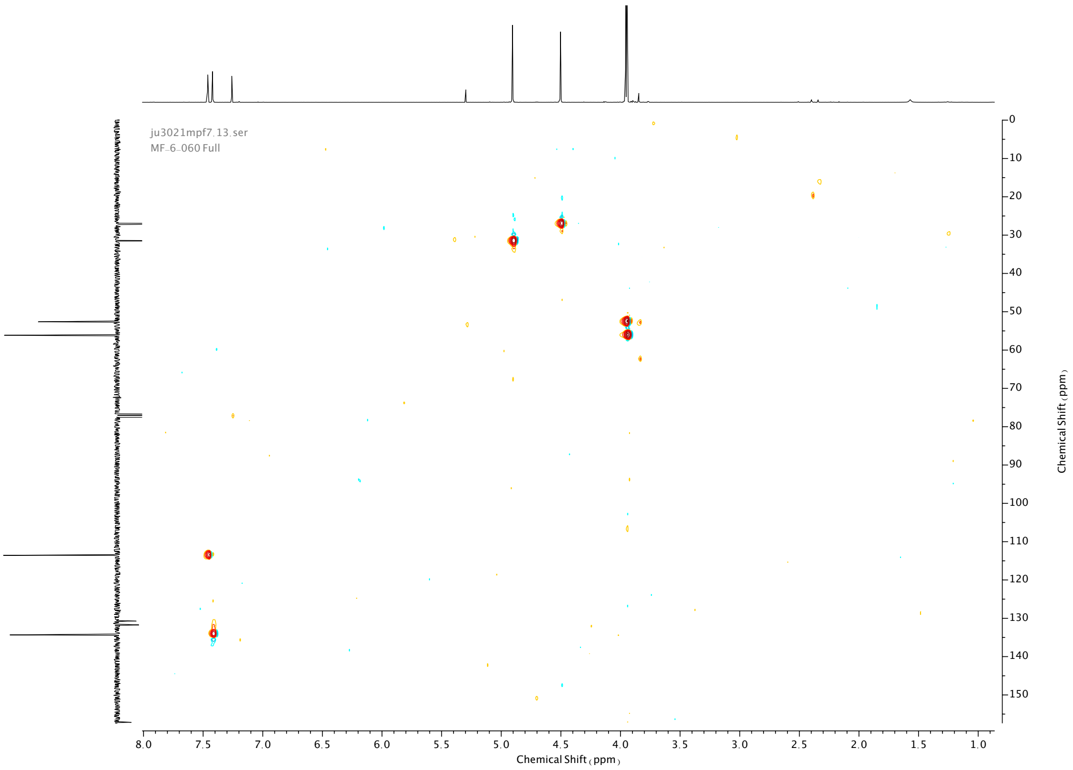

Figure **379**. HSQC NMR ($CDCl_3$) of **96**.

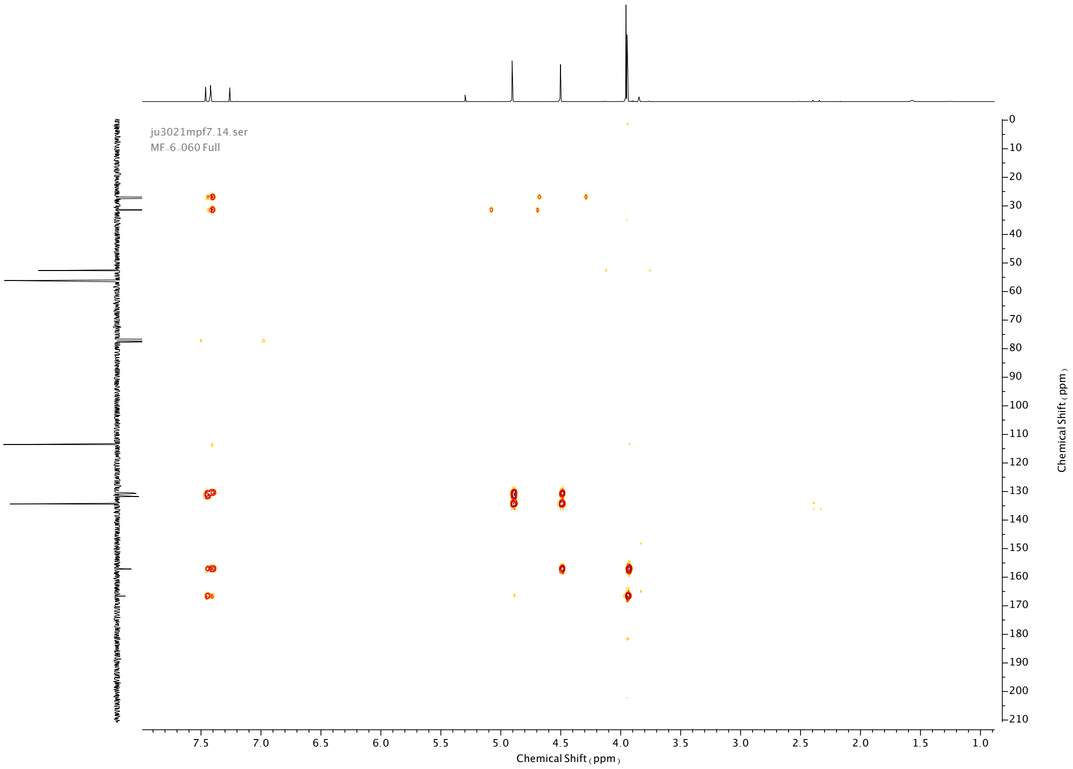

Figure **380**. HMBC NMR ($CDCl_3$) of **96**.

Compound **97**

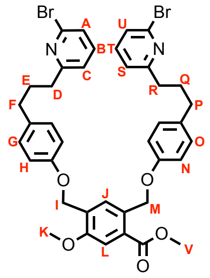

97 was prepared according to general procedure **(1)** from phenol **45** (2.2 g, 7.6 mmol) and linker **96** (1.3 g, 3.8 mmol). Purification by column chromatography (eluent 9:1 → 7.3 PE: EA) afforded **97** as a yellow oil (2.4 g, 3.1 mmol, 82%). ^{1}H NMR (400 MHz, CDCl$_3$, 298 K) δ_H 7.83 (1H, s, H$_J$), 7.51 (1H, s, H$_L$), 7.44-7.40 (2H, m, H$_B$ & H$_T$), 7.28 (2H, dd, *J* = 7.8, 0.6 Hz, H$_A$ & H$_U$), 7.10-7.04 (6H, m, H$_C$, H$_S$, H$_G$ & H$_O$), 6.88 (2H, d, *J* = 8.7 Hz, H$_H$ or H$_N$), 6.86 (2H, d, *J* = 8.7 Hz, H$_H$ or H$_N$), 5.36 (2H, s, H$_M$), 5.10 (2H, s, H$_I$), 3.92 (3H, s, H$_K$), 3.88 (3H, s, H$_V$), 2.80-2.75 (4H, m, H$_D$ & H$_R$), 2.64-2.58 (4H, m, H$_F$ & H$_P$), 2.04-1.96 (4H, m, H$_E$ & H$_Q$). ^{13}C NMR (101 MHz, CDCl$_3$, 298 K) δ_C 167.4, 164.0 (x2), 157.2, 157.1, 155.8, 141.7 (x2), 141.6, 138.7 (x2), 134.4, 134.2, 131.9, 130.5, 129.5 (x2), 128.6, 128.5, 125.4 (x2), 121.7, 115.0, 114.9, 112.2, 68.2, 64.8, 55.8, 52.3, 37.6 (x2), 34.7 (x2), 31.6 (x2). HR-ESI-MS (CH$_3$CN): *m/z* = 773.1211 [M+H]$^+$ calc. 773.1220.

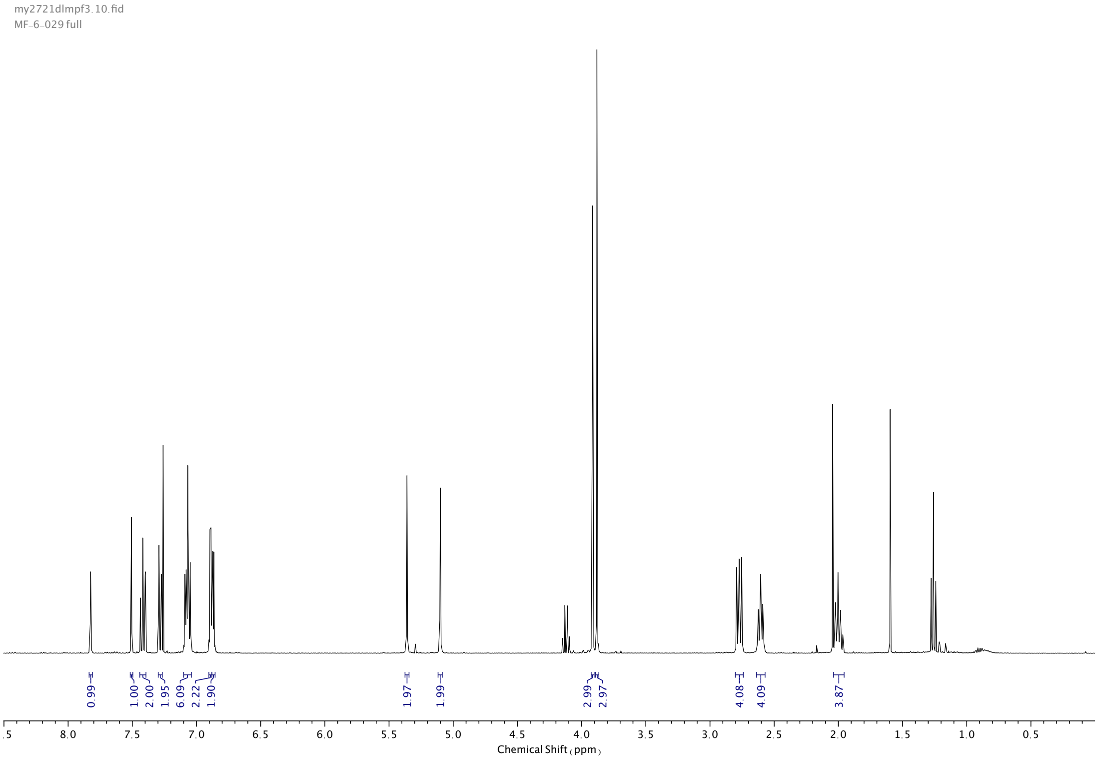

Figure **381**. ^{1}H NMR (CDCl$_3$, 400 MHz) of **97**.

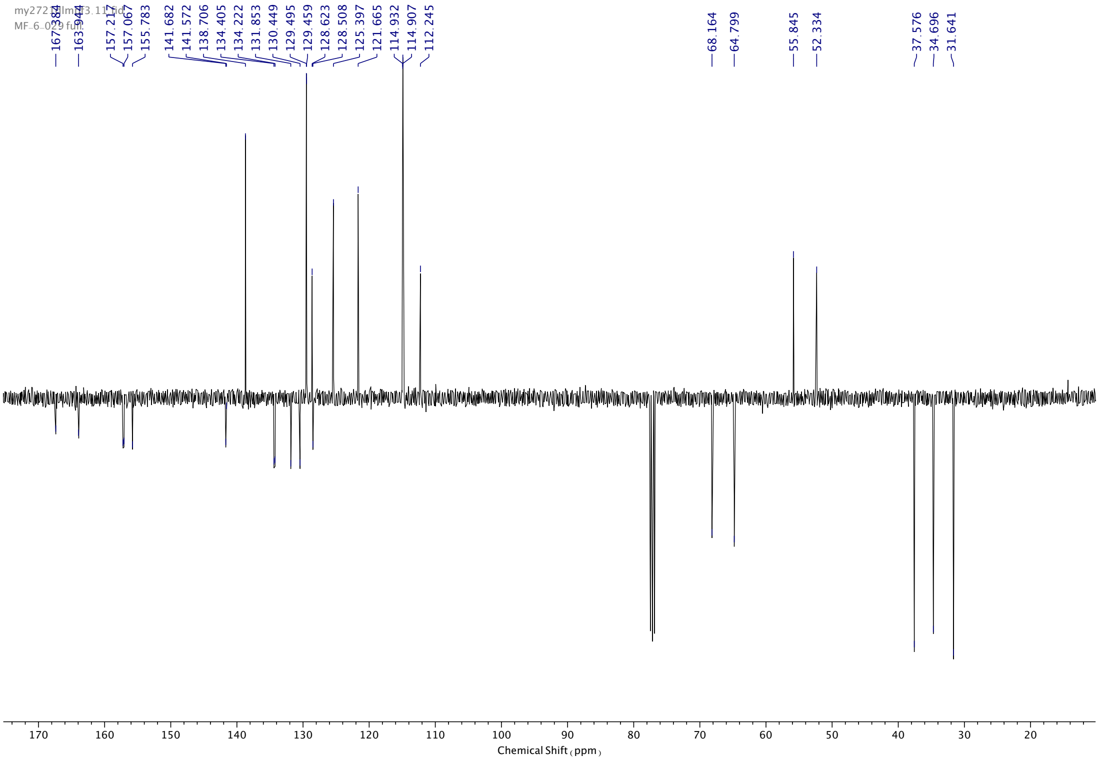

Figure **382**. ^{13}C NMR (CDCl$_3$, 101 MHz) of **97**.

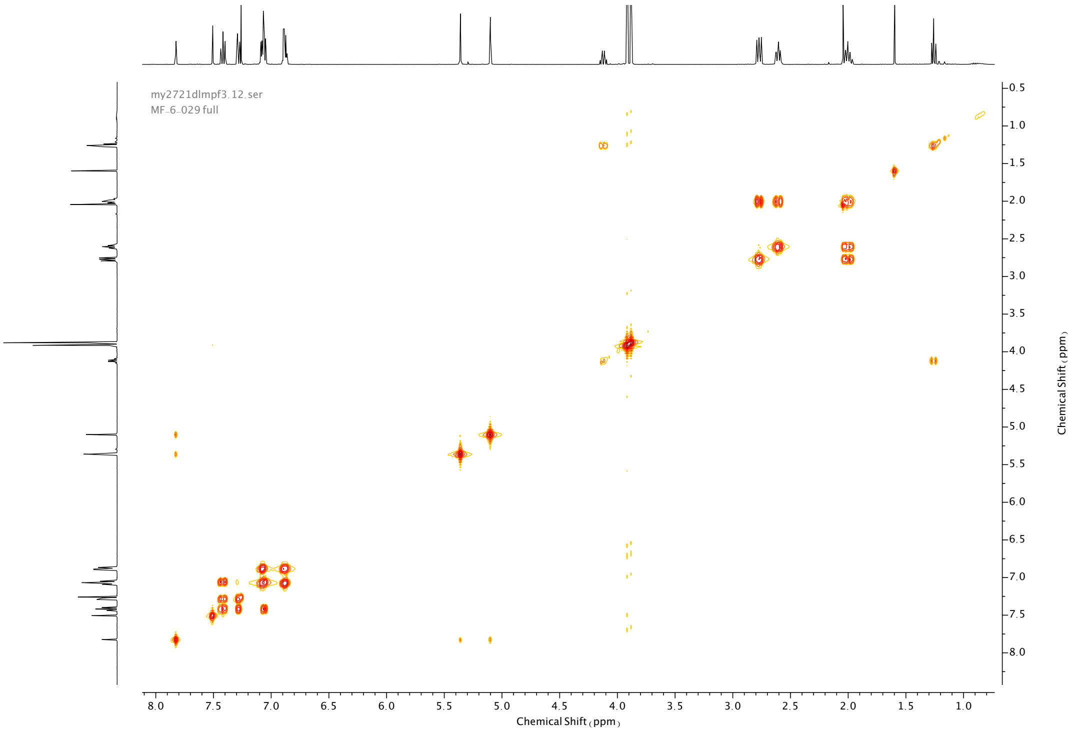

Figure **383**. COSY NMR ($CDCl_3$) of **97**.

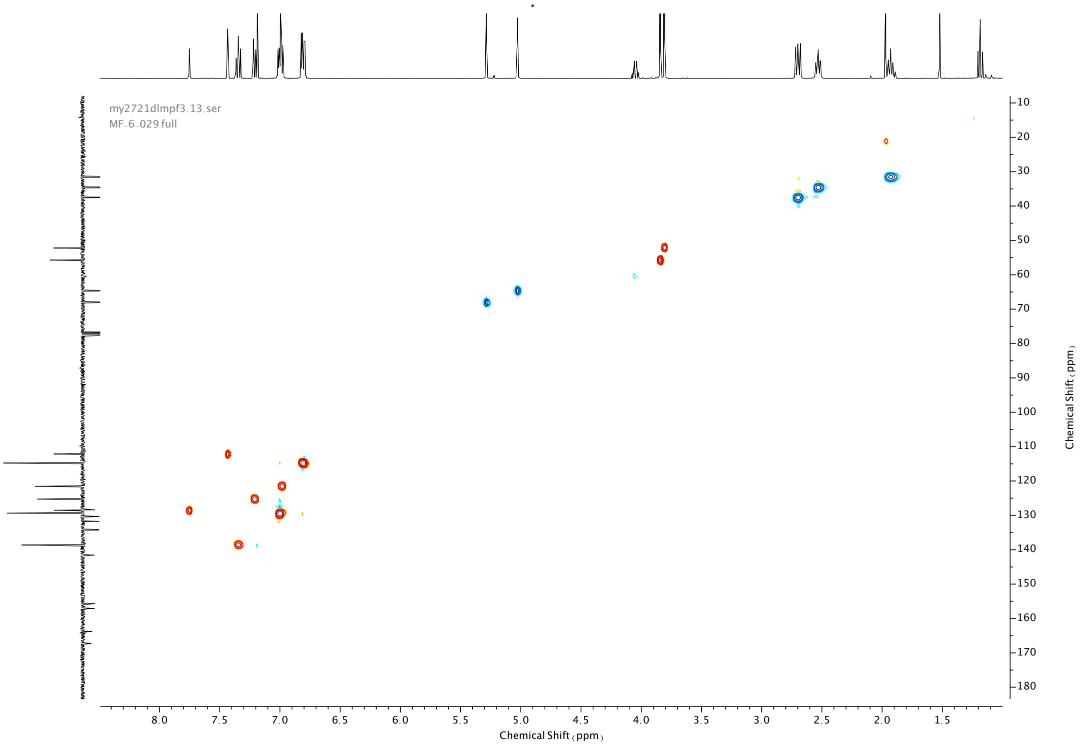

Figure **384**. HSQC NMR ($CDCl_3$) of **97**..

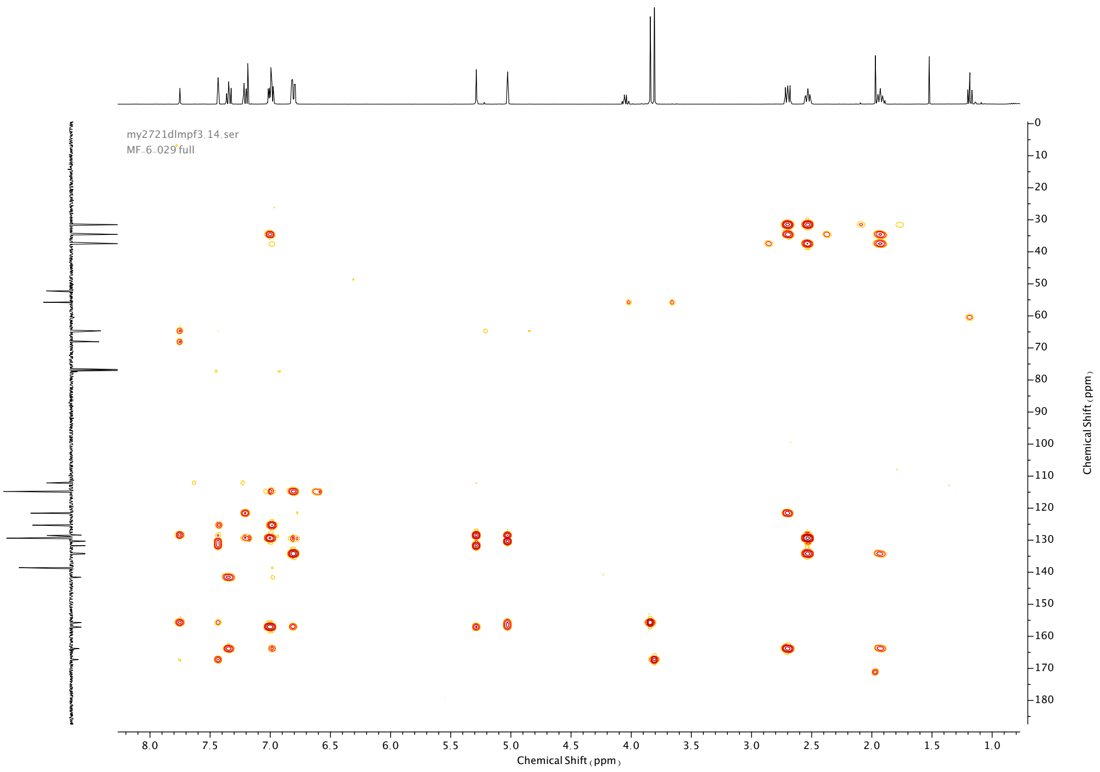

Figure **385**. HMBC NMR ($CDCl_3$) of **97**.

Compound **98**

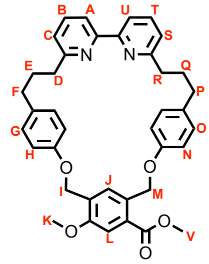

98 was prepared according to general procedure **(2)** from macrocycle precursor **97** (2.2 g, 2.9 mmol). Purification by column chromatography (eluent 1:0 → 9.1 PE: Acetone) afforded **98** as a white foam (850 mg, 1.38 mmol, 48%). ^{1}H NMR (400 MHz, $CDCl_3$, 298 K) δ_H 7.68-7.64 (3H, m, H_J, H_A & H_U), 7.64-7.58 (2H, m H_B & H_T), 7.48 (1H, s, H_L), 7.10 (1H, dd, *J* = 7.6, 1.2 Hz, H_C or H_S), 7.09 (1H, dd, *J* = 7.6, 1.2 Hz, H_C or H_S), 7.01-6.95 (4H, m, H_G & H_O), 6.67-6.62 (4H, m, H_H & H_N), 5.39 (2H, s, H_M), 5.12 (2H, s, H_I), 3.91 (3H, s, H_V), 3.90 (3H, s, H_K), 2.92 (4H, t, *J* = 7.3 Hz, H_D & H_R), 2.66-2.61 (4H, m, H_F & H_P), 2.18-2.10 (4H, m, H_E & H_Q). ^{13}C NMR (101 MHz, $CDCl_3$, 298 K) δ_C 167.3, 162.3 (x2), 157.0 (x2), 156.7, 156.6, 155.2, 136.8, 136.7, 135.0, 134.8, 132.8, 131.1, 129.6, 129.5, 127.3 (x2), 122.5 (x2), 119.4 (x2), 115.0 (x2), 112.0, 68.1, 64.9, 55.7, 52.2, 37.9, 37.8, 34.4 (x2), 31.33 (x2). HR-ESI-MS (CH_3CN): *m/z* = 615.2855 [M+H]$^+$ calc. 615.2853.

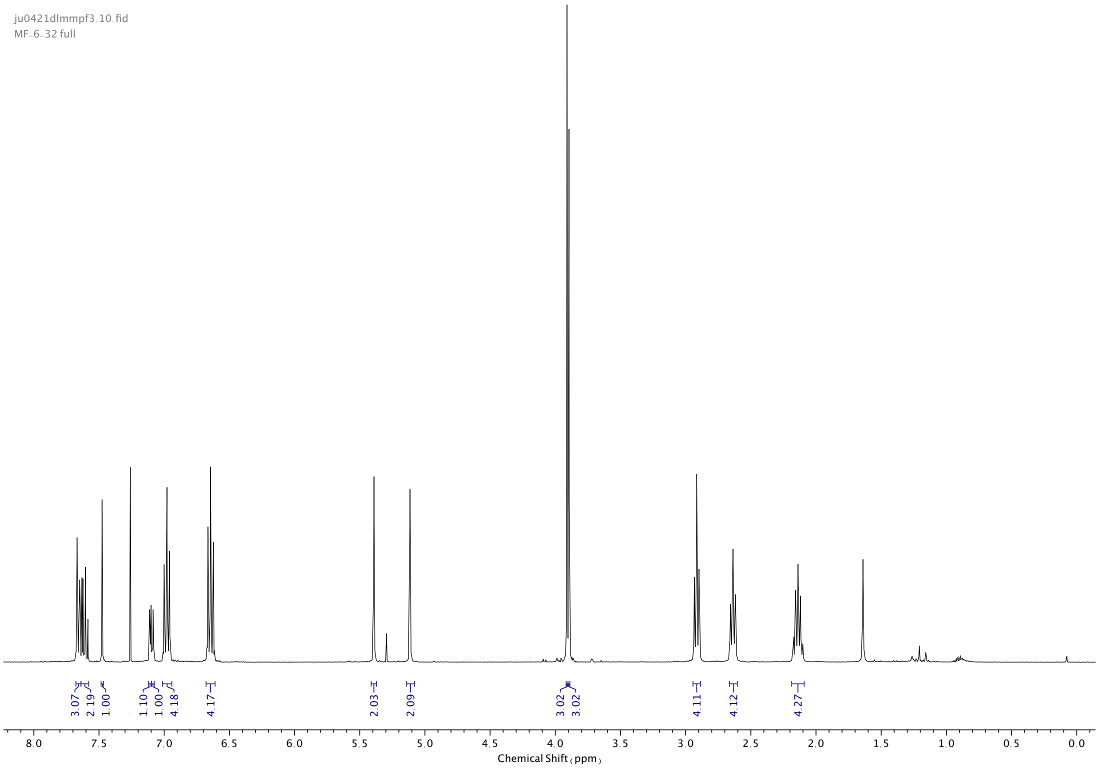

Figure **386**. ^{1}H NMR ($CDCl_3$, 400 MHz) of **98**.

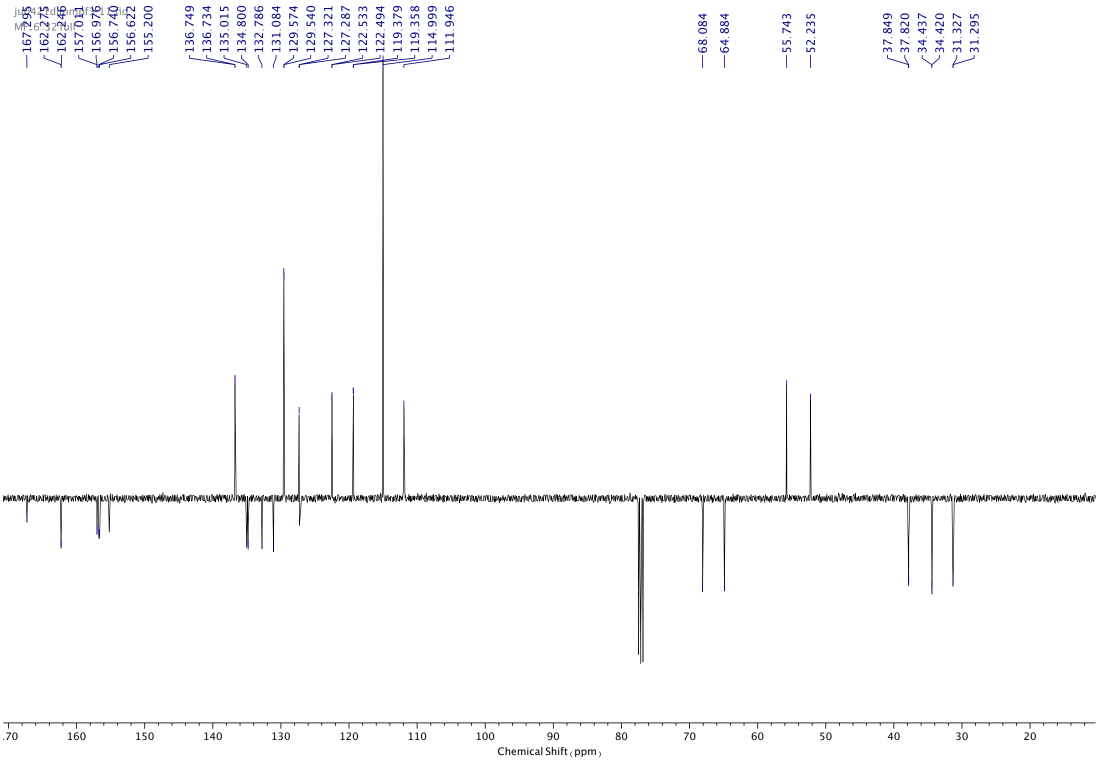

Figure **387**. ^{13}C NMR ($CDCl_3$, 101 MHz) of **98**.

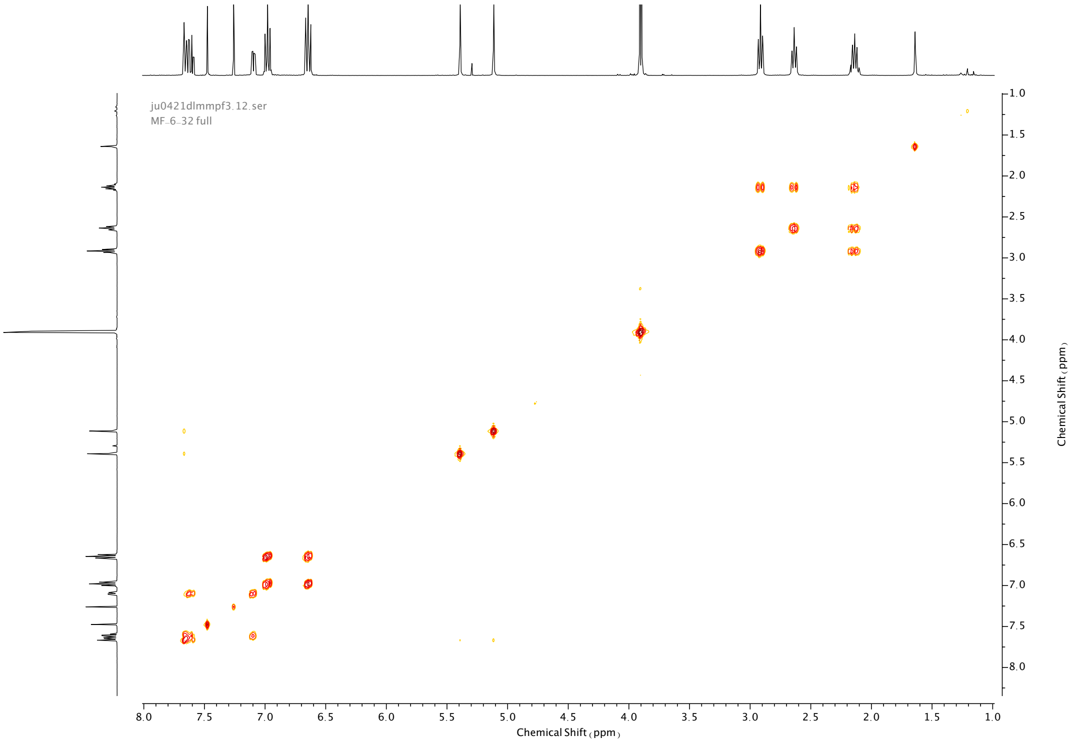

Figure **388**. COSY NMR ($CDCl_3$) of **98**.

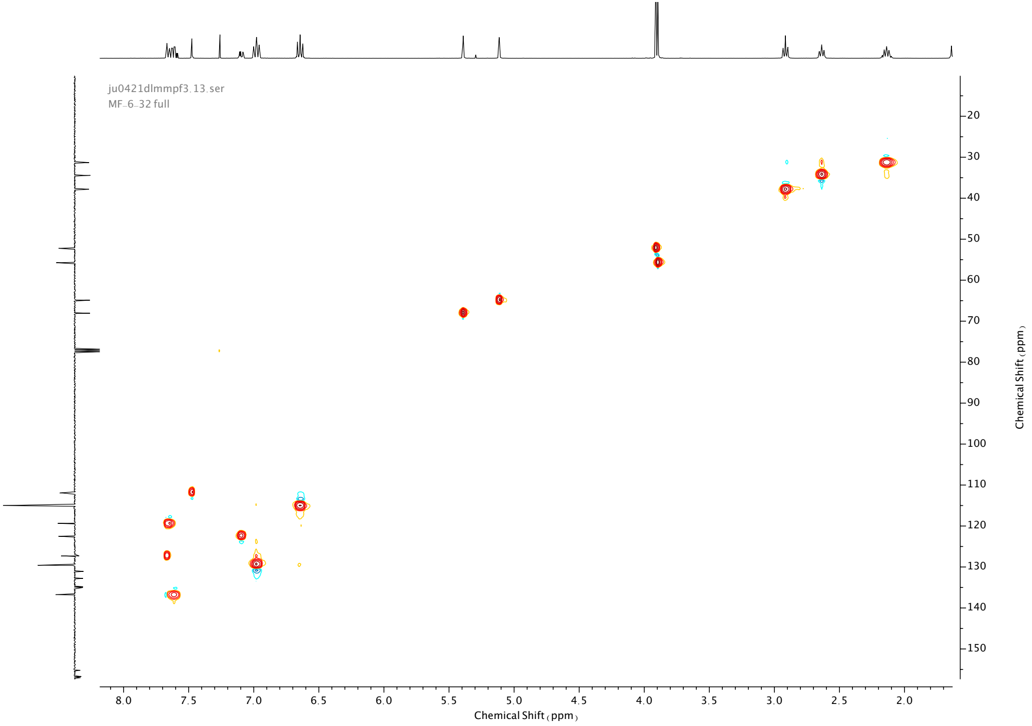

Figure **389**. HSQC NMR ($CDCl_3$) of **98**.

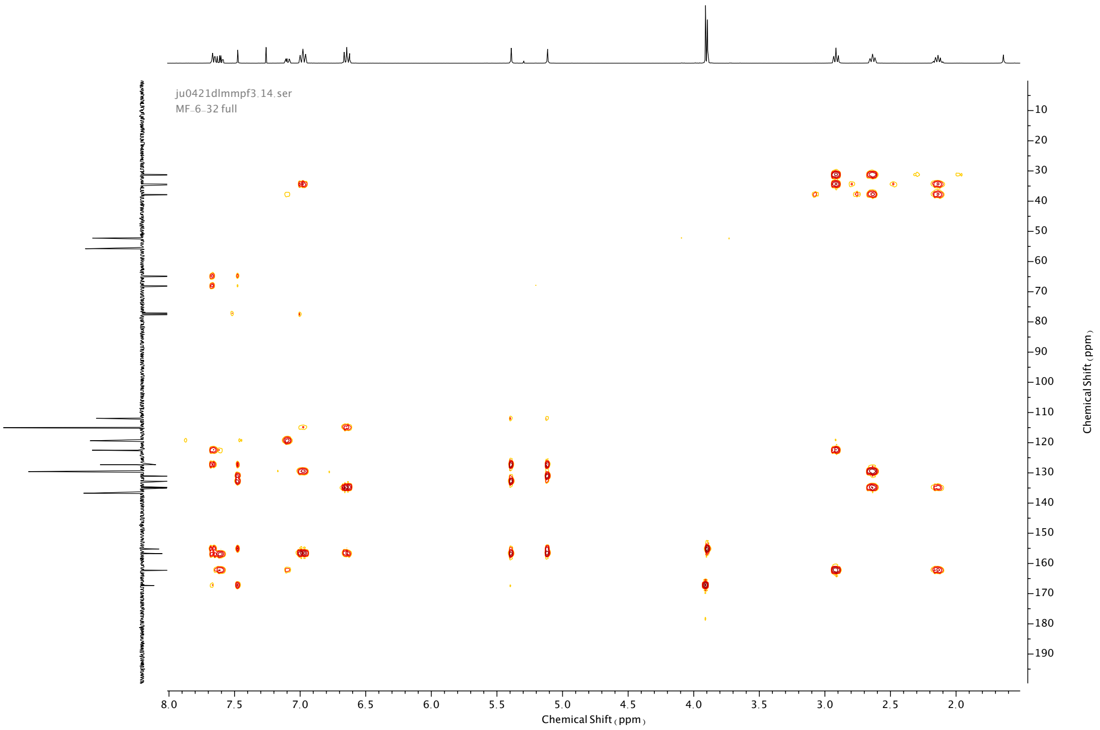

Figure **390**. HMBC NMR ($CDCl_3$) of **98**.

Compound **99**

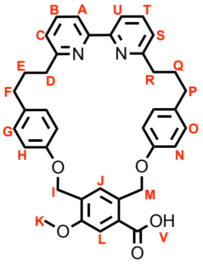

99 was prepared according to general procedure **(3)** from macrocycle **98** (560 mg, 0.91 mmol). **99** was achieved as a white solid (520 mg, 0.86 mmol, 95%) and used in the next step without further purification. M.p. 193-195 °C. ^{1}H NMR (400 MHz, DMSO-d_6, 298 K) δ_H 13.18 (1H, br. s, O-H_V), 7.80-7.76 (2H, m, H_A & H_U), 7.76-7.70 (2H, m, H_B & H_T), 7.50 (1H, s, H_J), 7.48 (1H, s, H_L), 7.25 (1H, t, *J* = 1.5 Hz, H_C or H_S), 7.21 (1H, t, *J* = 1.5 Hz, H_C or H_S), 6.98-6.94 (4H, m, H_G & H_O), 6.65 (2H, d, *J* = 8.6 Hz, H_H or H_N), 6.60 (2H, d, *J* = 8.6 Hz, H_H or H_N), 5.34 (2H, s, H_M), 5.08 (2H, s, H_I), 3.87 (3H, s, H_K), 2.80 (4H, t, *J* = 7.1 Hz, H_D & H_R), 2.57 (4H, t, *J* = 7.1 Hz, H_F & H_P), 2.07-1.99 (4H, m, H_E & H_Q).^{13}C NMR (101 MHz, DMSO-d_6, 298 K) δ_C 168.3, 161.7 (x2), 156.6, 156.5 (x2), 156.4, 155.4, 137.41 (x2), 134.8, 134.6, 131.5, 129.9, 129.8 (x2), 129.5, 127.5, 123.1 (x2), 119.4 (x2), 115.0, 114.9, 112.6, 67.5, 64.3, 56.1, 37.2 (x2), 33.9 (x2), 31.1 (x2). HR-ESI-MS (CH_3CN): *m/z* = 601.2698 [M+H]$^+$ calc. 601.2702.

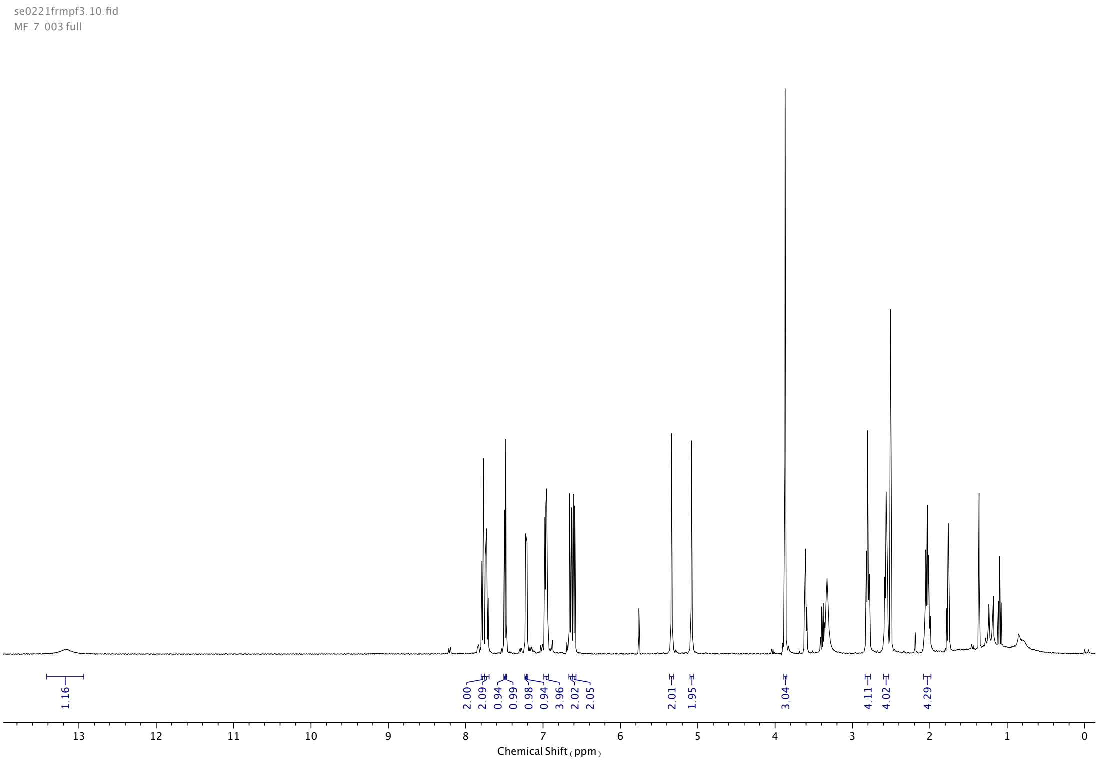

Figure **391**. ^{1}H NMR (DMSO-d$_6$, 400 MHz) of **99**.

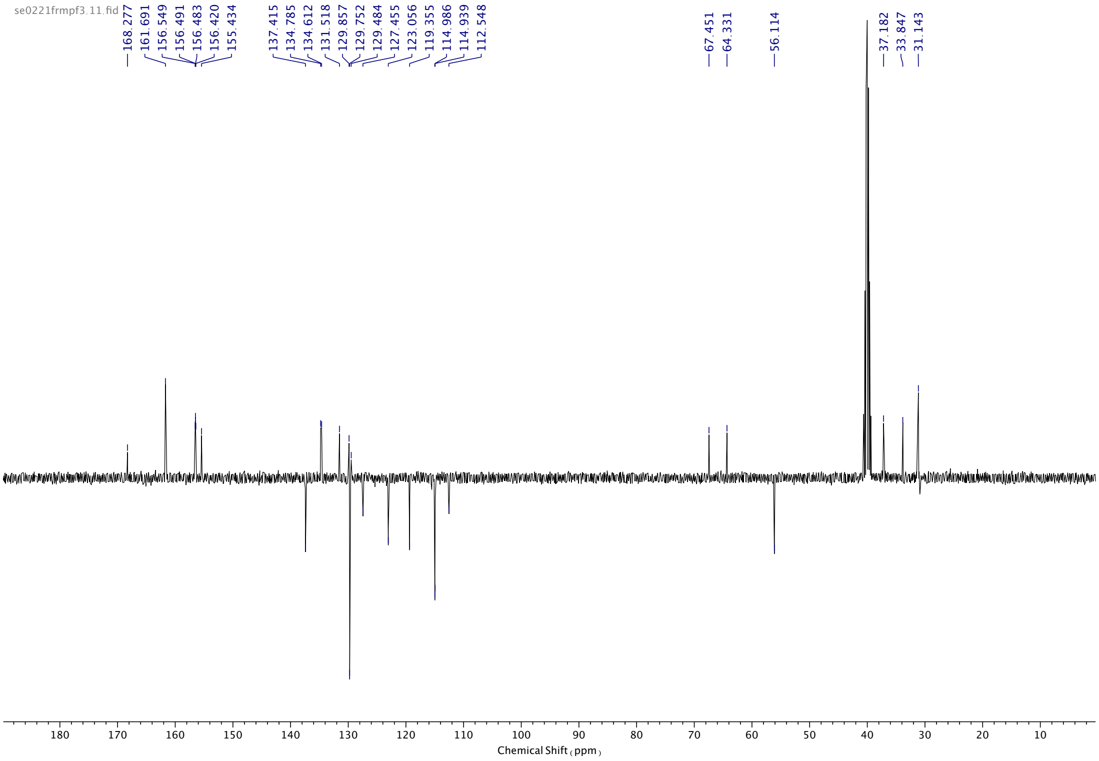

Figure **392**. ^{13}C NMR (DMSO-d$_6$, 101 MHz) of **99**.

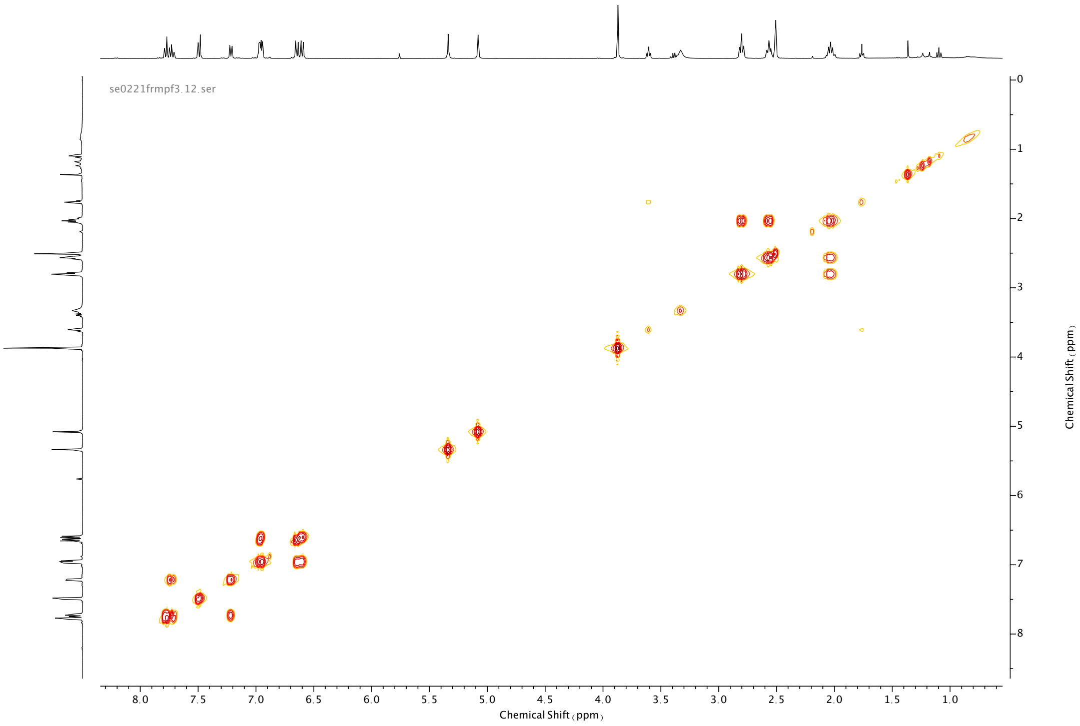

Figure **393**. COSY NMR (DMSO-d$_6$) of **99**.

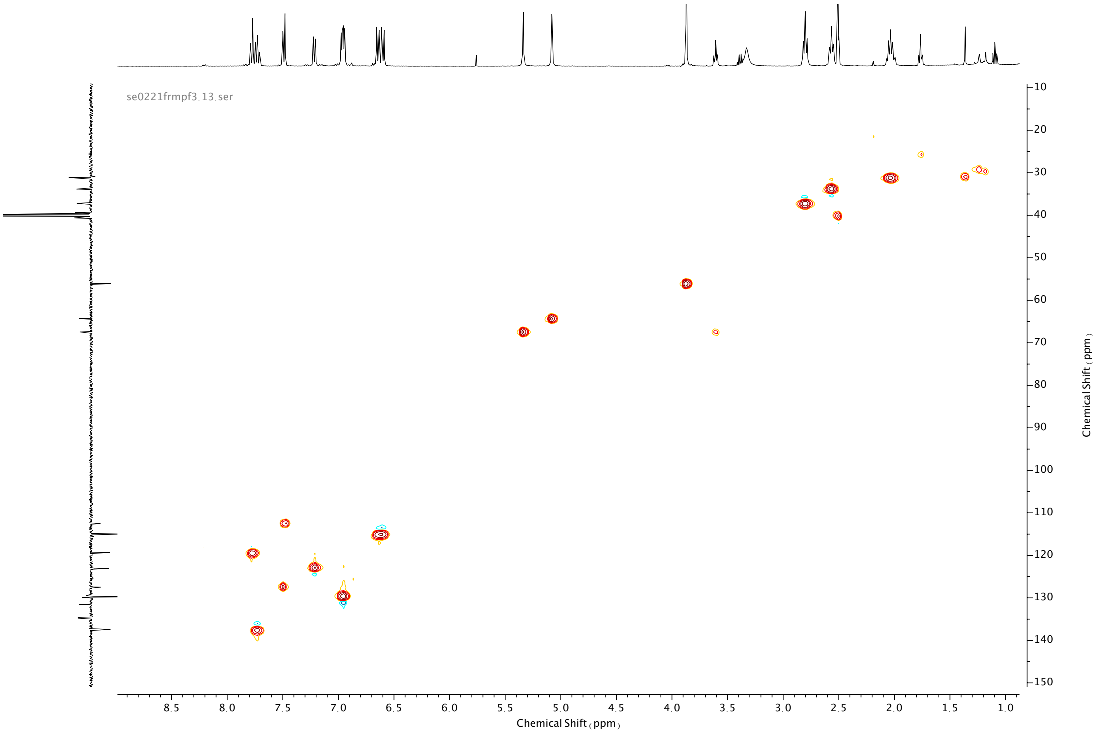

Figure **394**. HSQC NMR (DMSO-d$_6$) of **99**.

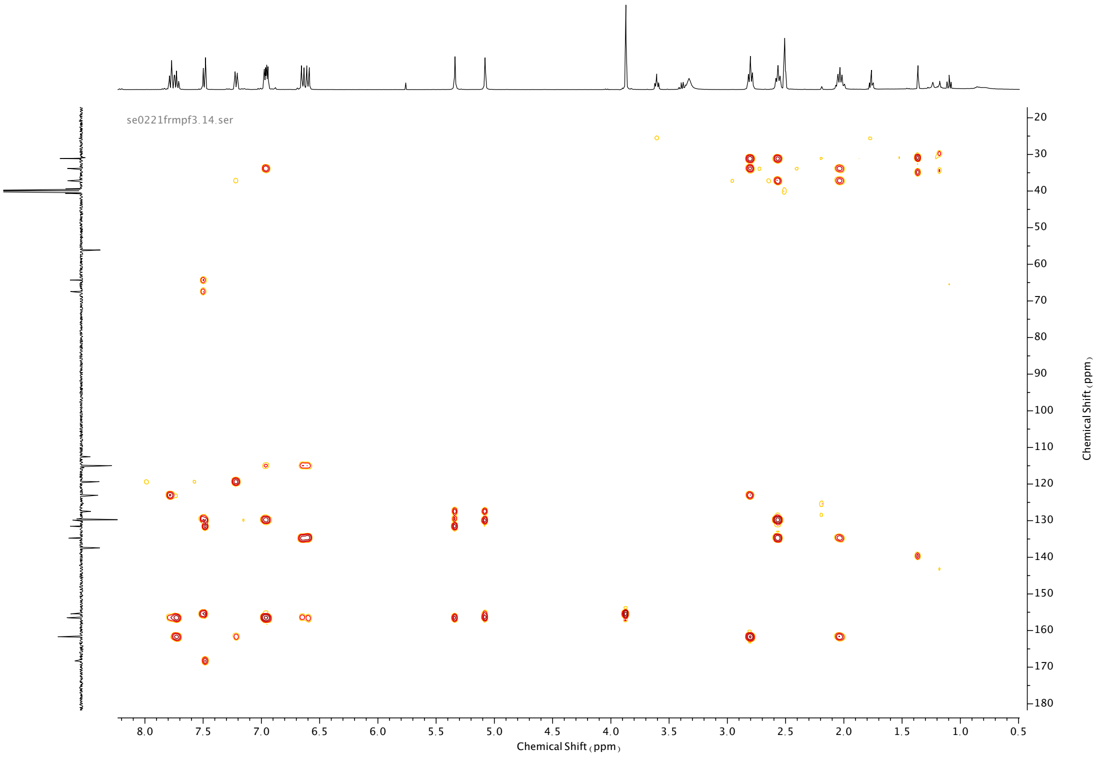

Figure **395**. HMBC NMR (DMSO-d$_6$) of **99**.

Compound **100**

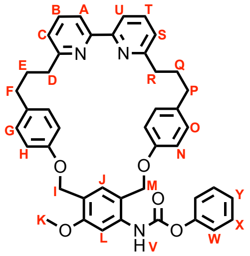

100 was prepared according to general procedure **(5)** from macrocycle **99** (123 mg, 0.21 mmol). Purification by column chromatography (eluent 1:0 → 19:1 CH_2Cl_2: Et_2O) afforded **100** as a colourless oil (88 mg, 0.13 mmol, 62%). ^{1}H NMR (400 MHz, $CDCl_3$, 298 K) δ_H 8.23 (1H, br. s, N-H_V), 7.81-7.74 (3H, m, H_A, H_U & H_L), 7.61 (1H, t, *J* = 7.8 Hz, H_B or H_T), 7.58 (1H, t, *J* = 7.8 Hz, H_B or H_T), 7.44-7.38 (2H, m, H_X), 7.27-7.19 (3H, m, H_W & H_Y), 7.11 (1H, s, H_J), 7.07 (1H, dd, *J* = 7.7, 1.0 Hz, H_C or H_S), 7.03 (1H, dd, *J* = 7.7, 1.0 Hz, H_C or H_S), 7.00 (2H, d, *J* = 8.7 Hz, H_G or H_O), 6.91 (2H, d, *J* = 8.7 Hz, H_G or H_O), 6.74 (2H, d, *J* = 8.7 Hz, H_H or H_N), 6.68 (2H, d, *J* = 8.7 Hz, H_H or H_N), 5.11 (2H, s, H_I or H_M), 5.01 (2H, s, H_I or H_M), 3.83 (3H, s, H_K), 2.93-2.87 (4H, m, H_D & H_R), 2.68 (2H, t, *J* = 7.3 Hz, H_F or H_P), 2.62 (2H, t, *J* = 7.3 Hz, H_F or H_P), 2.18-2.10 (4H, m, H_E & H_Q). ^{13}C NMR (101 MHz, $CDCl_3$, 298 K) δ_C 161.9, 161.7, 157.1, 156.7 (x2), 156.6, 155.3, 152.0, 150.6, 137.7, 136.6 (x2), 135.7, 134.9, 129.5 (x2), 129.4, 128.9, 125.8, 122.5, 122.4, 121.8, 118.9 (x2), 115.5 (x2), 102.9, 69.6, 65.4, 55.6, 37.8 (x2), 34.6, 34.4, 31.3, 30.7. HR-ESI-MS (CH_3CN): *m/z* = 692.3124 $[M+H]^+$ calc. 692.3119.

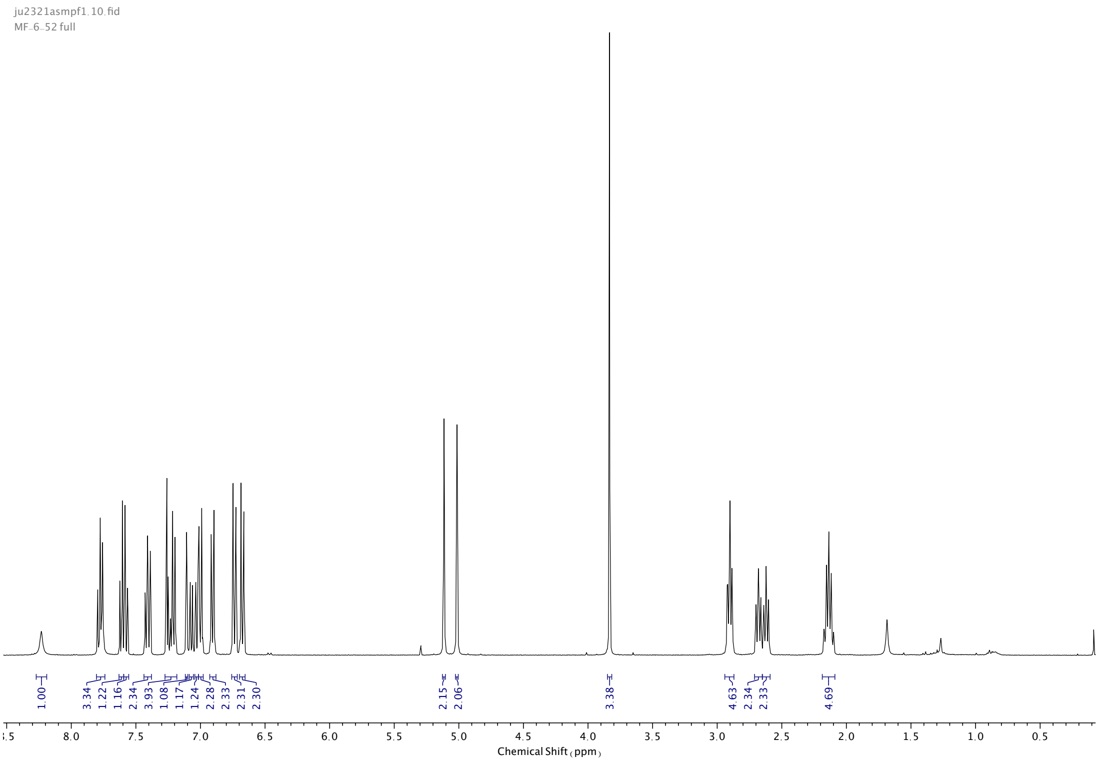

Figure **396**. ^{1}H NMR ($CDCl_3$, 400 MHz) of **100**.

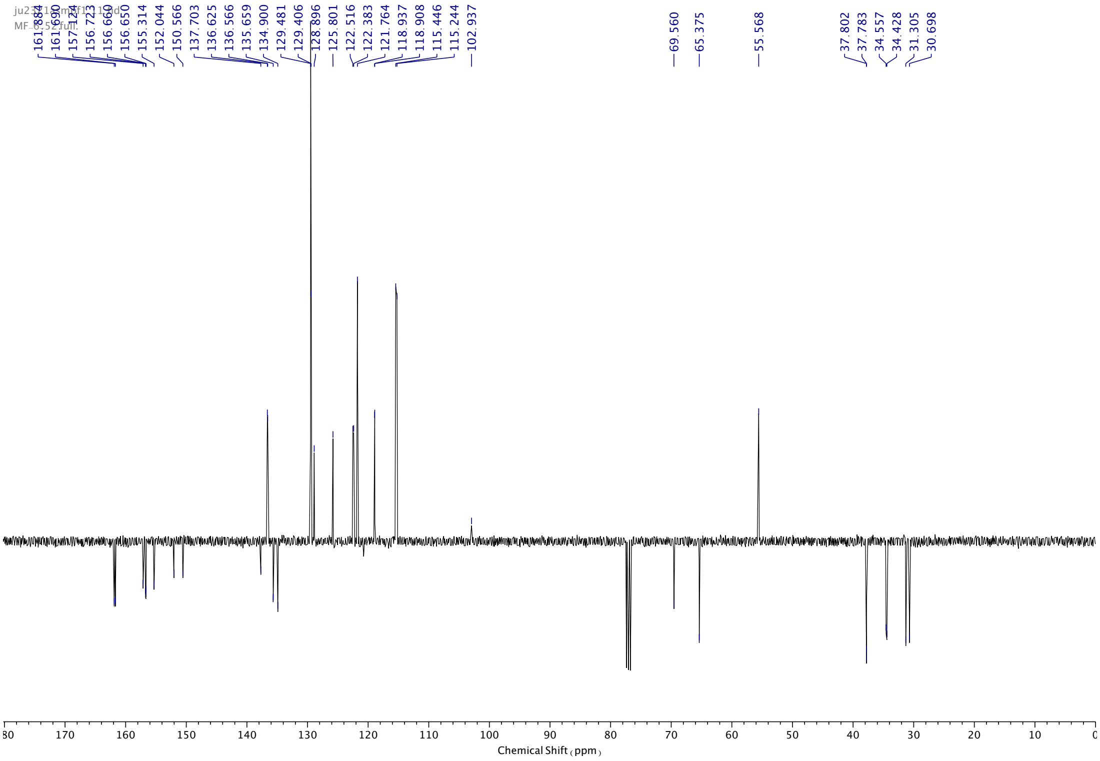

Figure **397**. ^{13}C NMR ($CDCl_3$, 101 MHz) of **100**.

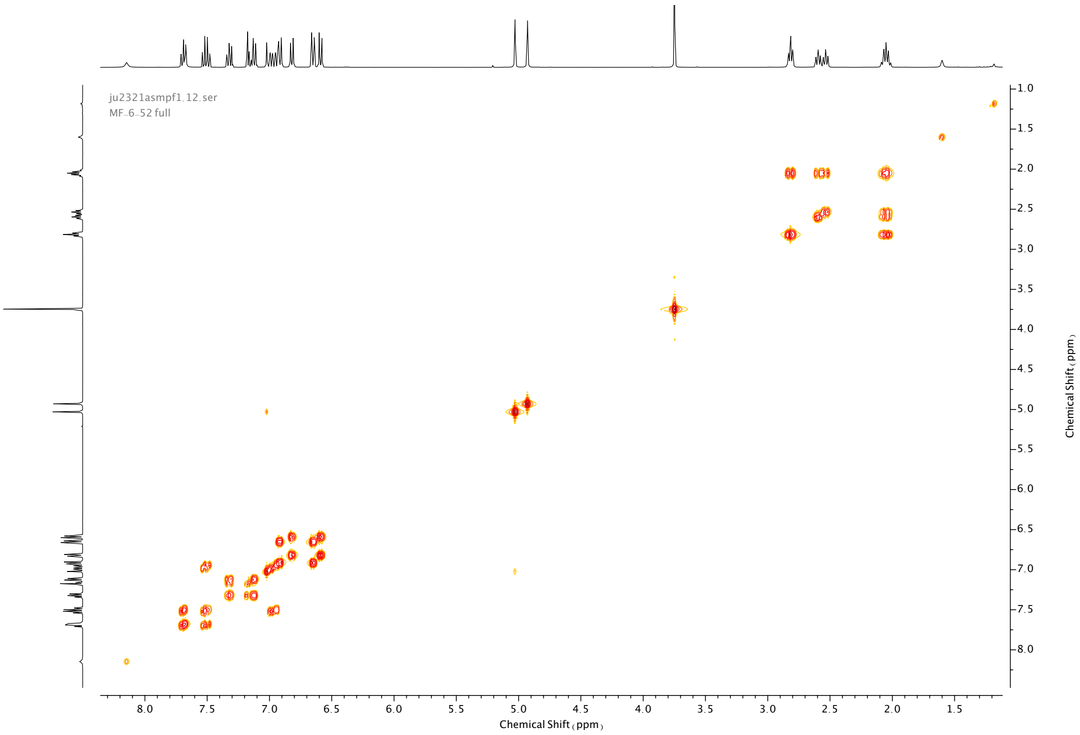

Figure **398**. COSY NMR ($CDCl_3$) of **100**.

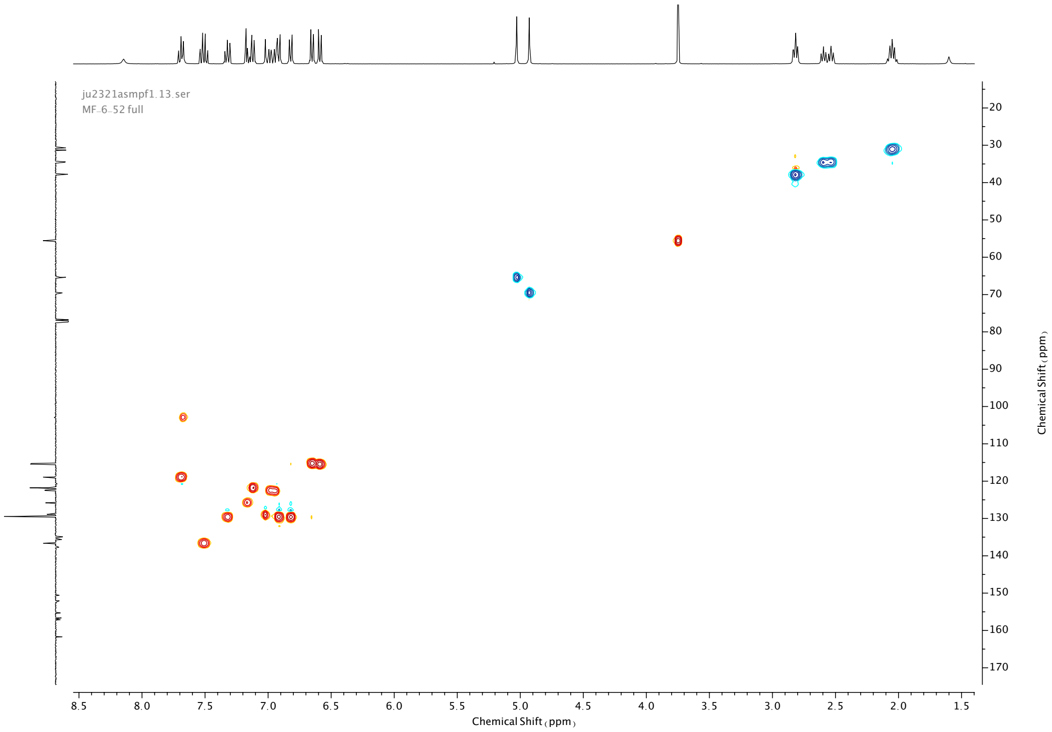

Figure **399**. HSQC NMR ($CDCl_3$) of **100**.

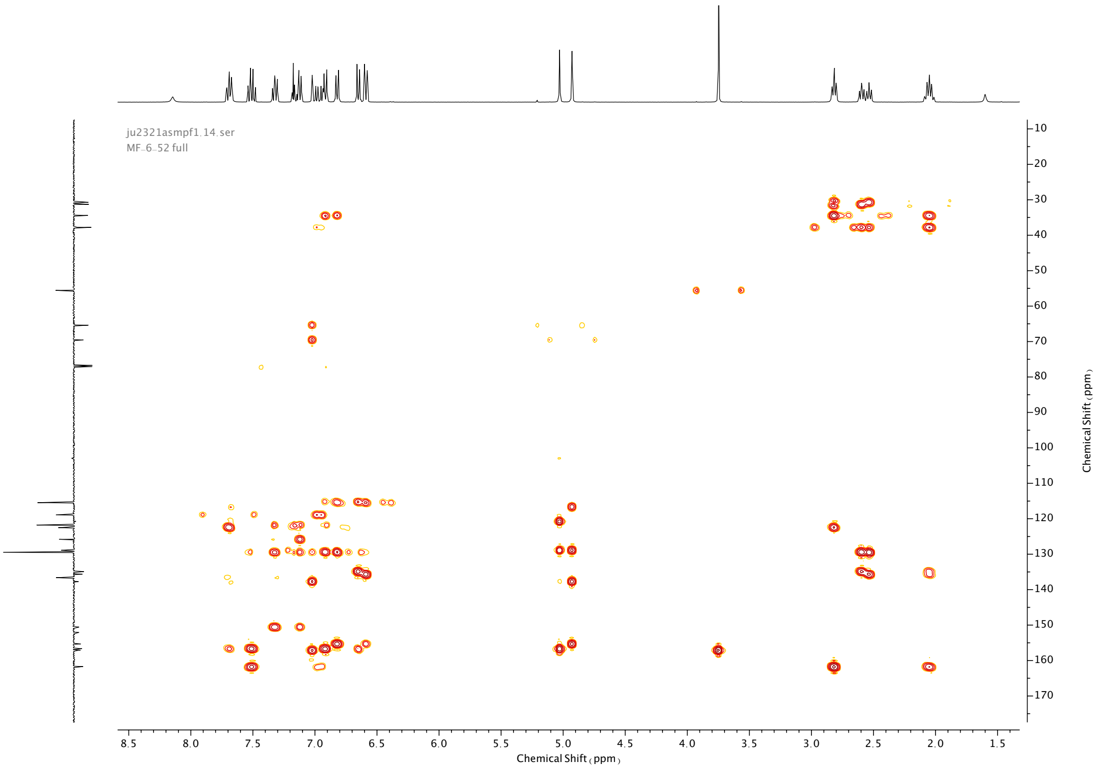

Figure **400**. HMBC NMR ($CDCl_3$) of **100**.

Compound **117**

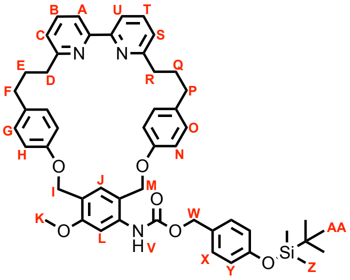

117 was synthesised according to general procedure **(6)** from macrocycle **100** (68 mg, 0.098 mmol) and trigger alcohol **51** (70 mg, 0.30 mmol). Purification by column chromatography (eluent 1:0 → 19:1 CH_2Cl_2: Et_2O) afforded **117** as a white foam (70 mg, 0.084 mmol, 85%). ^1H NMR (400 MHz, $CDCl_3$, 298 K) δ_H 7.82-7.74 (3H, m, H_A, H_U & N-H_V), 7.72-7.64 (1H, m, H_L), 7.59 (1H, t, *J* = 7.7 Hz, H_B or H_T), 7.55 (1H, t, *J* = 7.7 Hz, H_B or H_T), 7.28 (2H, d, *J* = 8.7 Hz, H_X), 7.06-7.04 (2H, m, H_J & H_C or H_S), 7.00-6.95 (3H, m, H_G or H_O & H_C or H_S), 6.88-6.82 (4H, m, H_G or H_O & H_Y), 6.70 (2H, d, *J* = 8.7 Hz, H_H or H_N), 6.60 (2H, d, *J* = 8.7 Hz, H_H or H_N), 5.14 (2H, s, H_W), 5.08 (2H, s, H_I or H_M), 4.90 (2H, s, H_I or H_M), 3.85 (3H, s, H_K), 2.94-2.86 (4H, m, H_D & H_R), 2.67 (2H, t, *J* = 7.6 Hz, H_F or H_P), 2.60 (2H, t, *J* = 7.6 Hz, H_F or H_P), 2.17-2.08 (4H, m, H_E & H_Q), 0.99 (9H, s, H_{AA}), 0.20 (6H, s, H_Z). ^{13}C NMR (101 MHz, $CDCl_3$, 298 K) δ_C 162.0, 161.8, 157.2, 156.9 (x2), 156.0, 155.5, 153.8, 138.3, 136.7 (x2), 135.6, 134.9, 130.1, 129.5 (x2), 129.2, 128.9, 122.7, 122.5, 121.9, 120.4, 120.3 (x2), 119.0 (x2), 115.6, 115.4, 103.2 (HSQC), 69.6, 67.0, 65.5, 55.7, 37.9 (x2), 34.7, 34.5, 31.3, 30.8, 25.8, 18.3 (HMBC), -4.3. HR-ESI-MS (CH_3CN): *m/z* = 836.4107 $[M+H]^+$ calc. 836.4089.

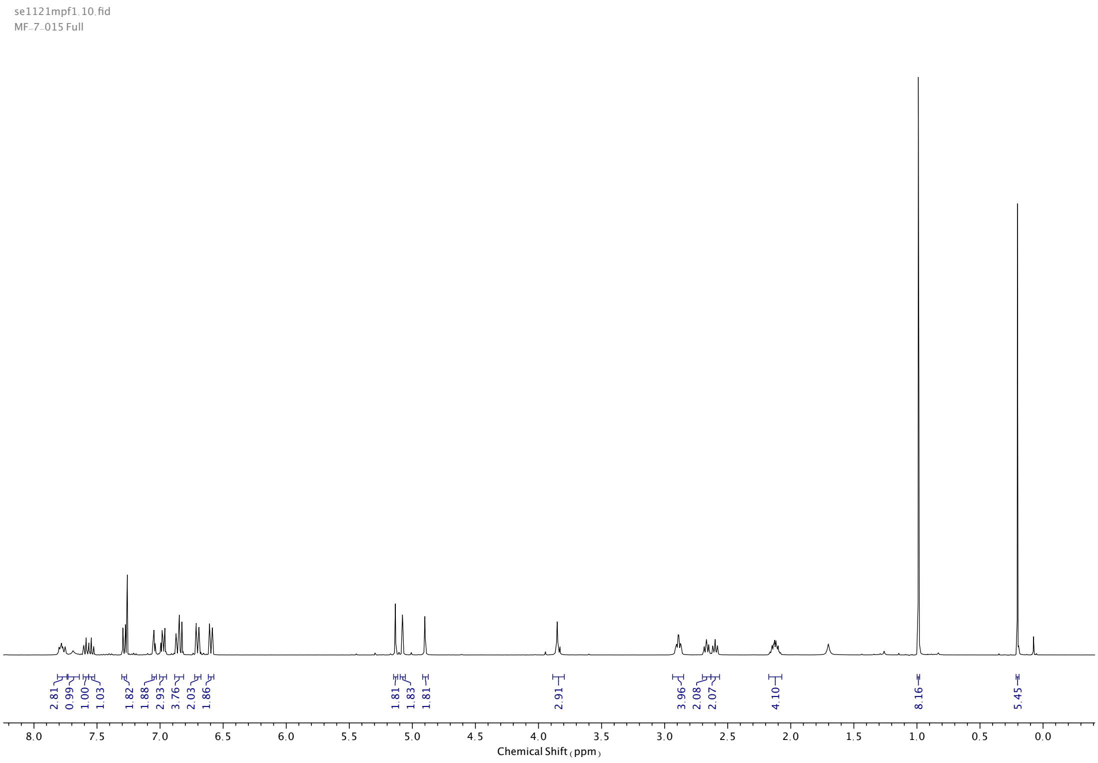

Figure **401**. ^1H NMR ($CDCl_3$, 400 MHz) of **117**.

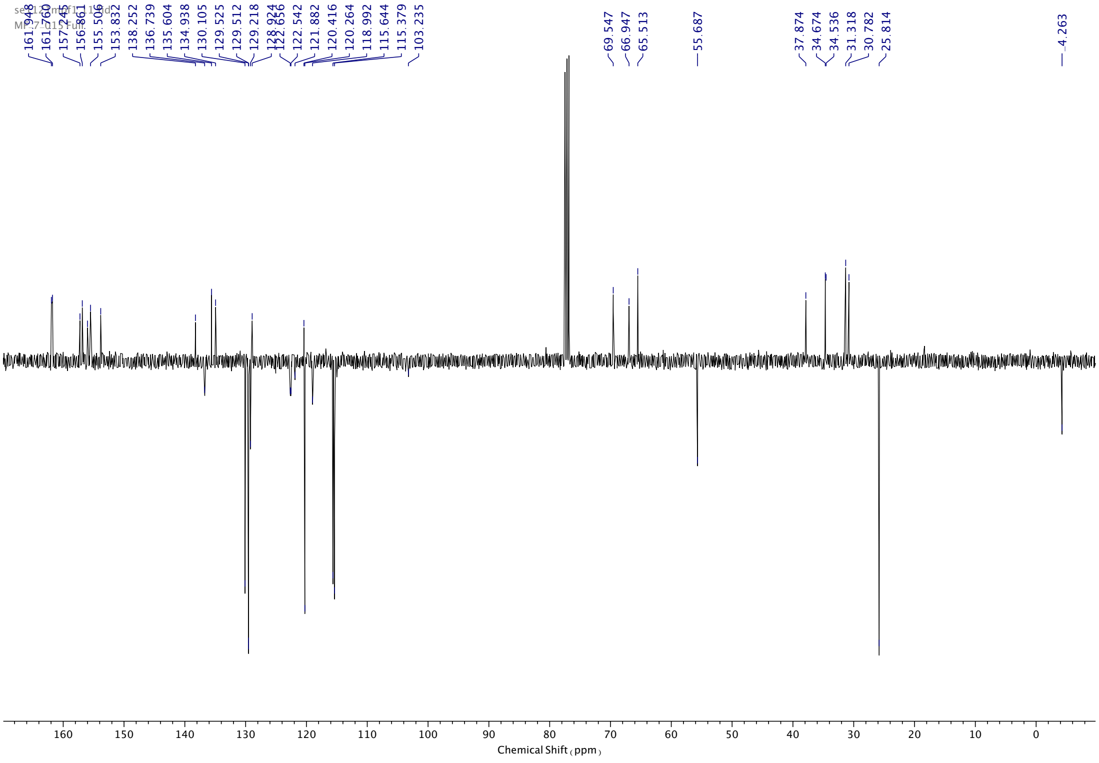

Figure **402**. ^{13}C NMR ($CDCl_3$, 101 MHz) of **117**.

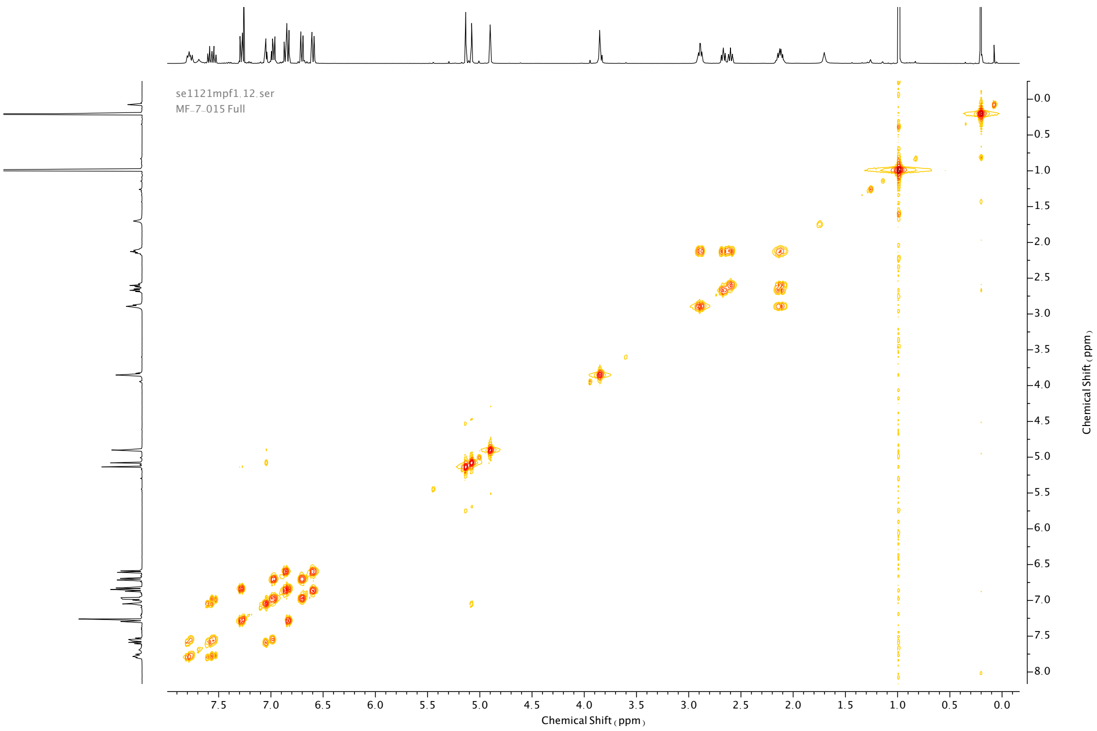

Figure **403**. COSY NMR ($CDCl_3$) of **117**.

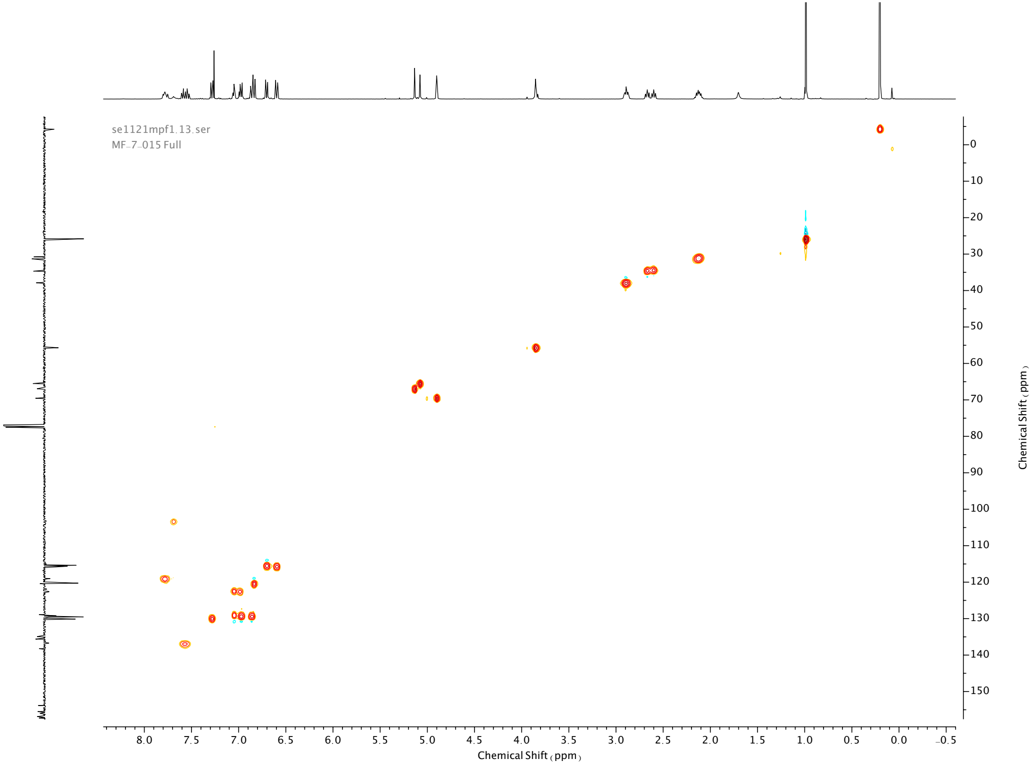

Figure **404**. HSQC NMR ($CDCl_3$) of **117**.

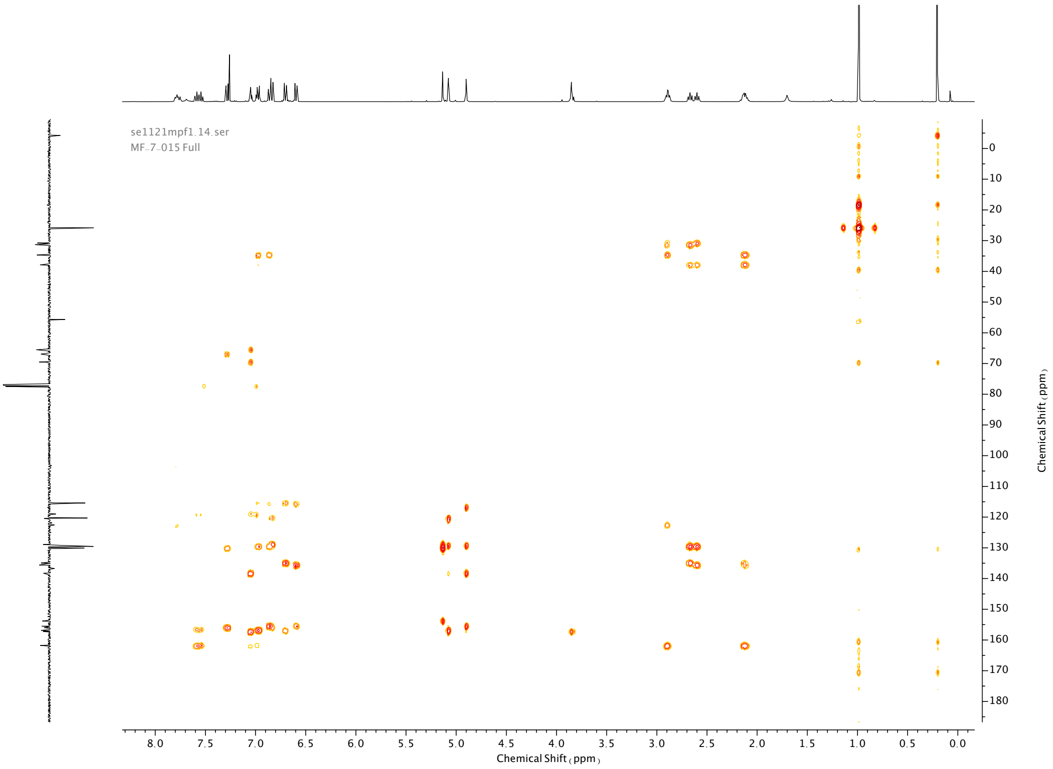

Figure **405**. HMBC NMR ($CDCl_3$) of **117**.

Compound **120**

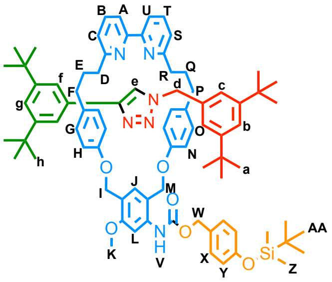

120 was synthesised according to general procedure **(7)** from macrocycle **117** (48 mg, 0.057 mmol), azide stopper **72** (21 mg, 0.086 mmol) and alkyne stopper **71** (18 mg, 0.086 mmol). Purification by column chromatography (eluent 1:0 → 19:1 CH$_2$Cl$_2$: Et$_2$O) afforded **120** as a white foam (37 mg, 0.029 mmol, 49%). ^{1}H NMR (400 MHz, CDCl$_3$, 298 K) δ_H 9.25 (1H, s, H$_e$), 8.10 (1H, s, H$_J$), 7.83-7.75 (1H, m, H$_L$), 7.74-7.69 (2H, m, N-H$_V$, H$_B$ or H$_T$), 7.66 (1H, t, *J* = 7.7 Hz, H$_B$ or H$_T$), 7.53-7.50 (2H, m, H$_A$ & H$_U$), 7.34 (2H, d, *J* = 1.8 Hz, H$_f$), 7.31 (1H, t, *J* = 1.8 Hz, H$_b$), 7.26 (2H, d, *J* = 8.6 Hz, H$_X$), 7.17 (1H, dd, *J* = 7.8, 0.8 Hz, H$_C$ or H$_S$), 7.12 (1H, t, *J* = 1.8 Hz, H$_g$), 7.08 (1H, dd, *J* = 7.8, 0.8 Hz, H$_C$ or H$_S$), 7.05 (2H, d, *J* = 1.8 Hz, H$_c$), 6.80 (2H, d, *J* = 8.6 Hz, H$_Y$), 6.66 (2H, d, *J* = 8.7 Hz, H$_G$), 6.26-6.21 (4H, m, H$_H$ & H$_O$), 6.18 (2H, d, *J* = 8.7 Hz, H$_N$), 5.33 (1H, d, *J* = 10.2 Hz, H$_M$ or H$_{M'}$), 5.23 (2H, d, *J* = 1.8 Hz, H$_I$), 5.19-5.09 (3H, m, H$_W$ & H$_M$ or H$_{M'}$), 4.75 (1H, d, *J* = 14.1 Hz, H$_d$ or H$_{d'}$), 4.44 (1H, d, *J* = 14.1 Hz, H$_d$ or H$_{d'}$), 3.95 (3H, s, H$_K$), 2.50-2.32 (6H, m, H$_D$, H$_R$ & H$_F$ or H$_P$), 2.22-2.04 (2H, m, H$_F$ or H$_P$), 1.76-1.49 (4H, m, H$_E$ & H$_Q$), 1.13 (18H, s, H$_h$), 1.08 (18H, s, H$_a$), 0.97 (9H, s, H$_{AA}$), 0.19 (6H, s, H$_Z$). ^{13}C NMR (101 MHz, CDCl$_3$, 298 K) δ_C 163.3 (x2), 158.1, 158.0, 157.3, 157.2, 156.4, 155.9, 154.0, 150.9, 149.7, 147.3, 138.4, 137.0, 136.7, 134.7, 132.9, 132.3, 131.0, 130.9, 130.1, 129.1, 128.7, 128.5, 123.8, 123.1, 123.0, 122.1, 121.8, 121.3 (x2), 120.7, 120.3 (x2), 120.2, 120.0, 115.0, 114.3, 103.0 (HMBC), 68.0, 66.8, 65.8, 55.8, 53.8, 38.3, 36.8, 35.0, 34.8, 34.7, 32.1, 31.4 (x2), 30.6, 29.8, 25.8, 18.3, -4.3. HR-ESI-MS (CH$_3$CN): *m/z* = 1295.8 [M+H]$^+$ calc. 1295.7708.

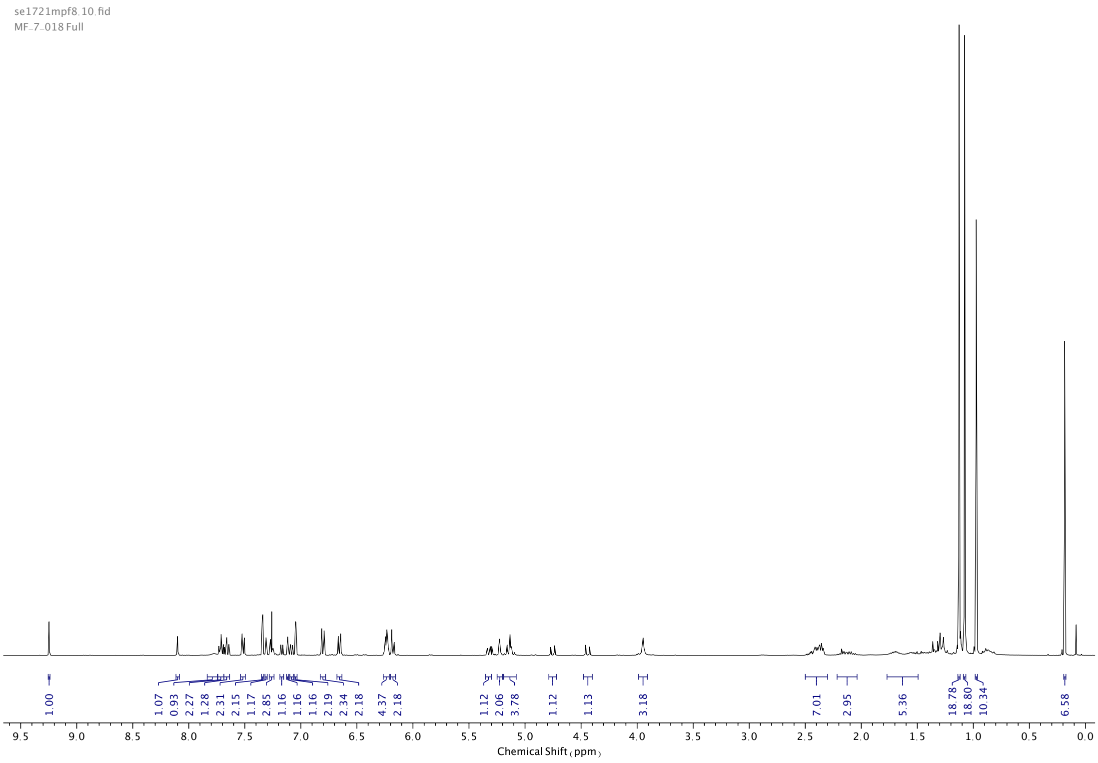

Figure **406**. ^{1}H NMR ($CDCl_3$, 400 MHz) of **120**.

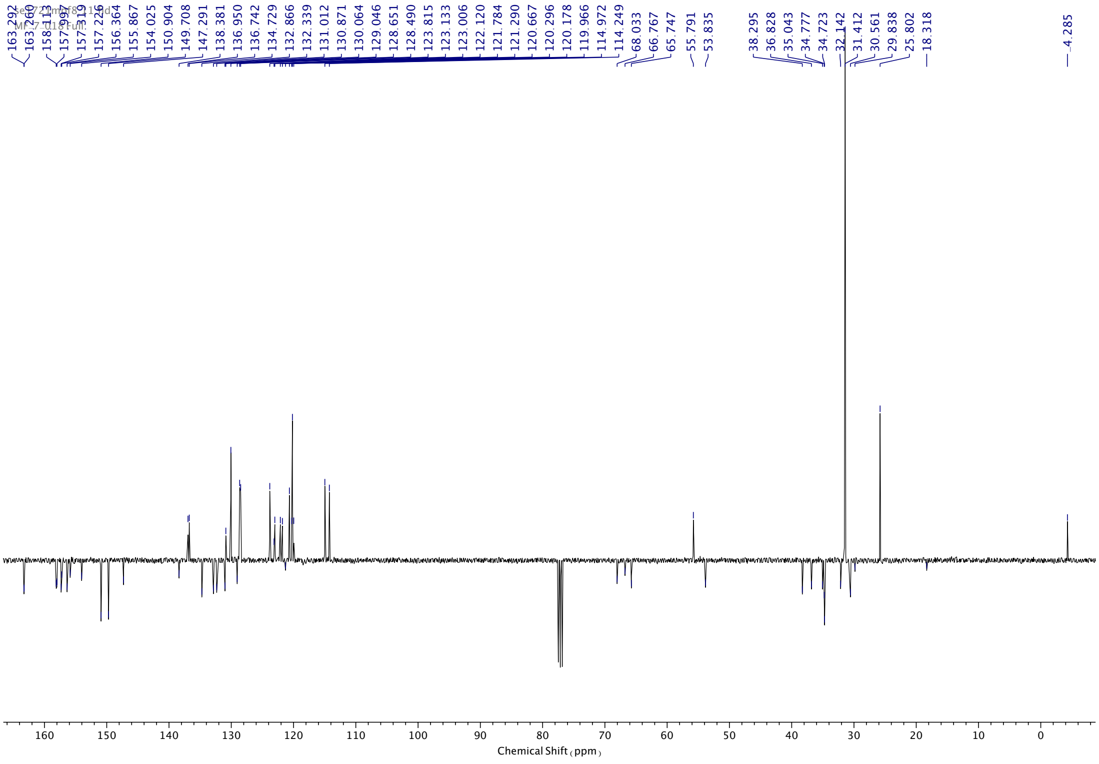

Figure **407**. ^{13}C NMR ($CDCl_3$, 101 MHz) of **120**.

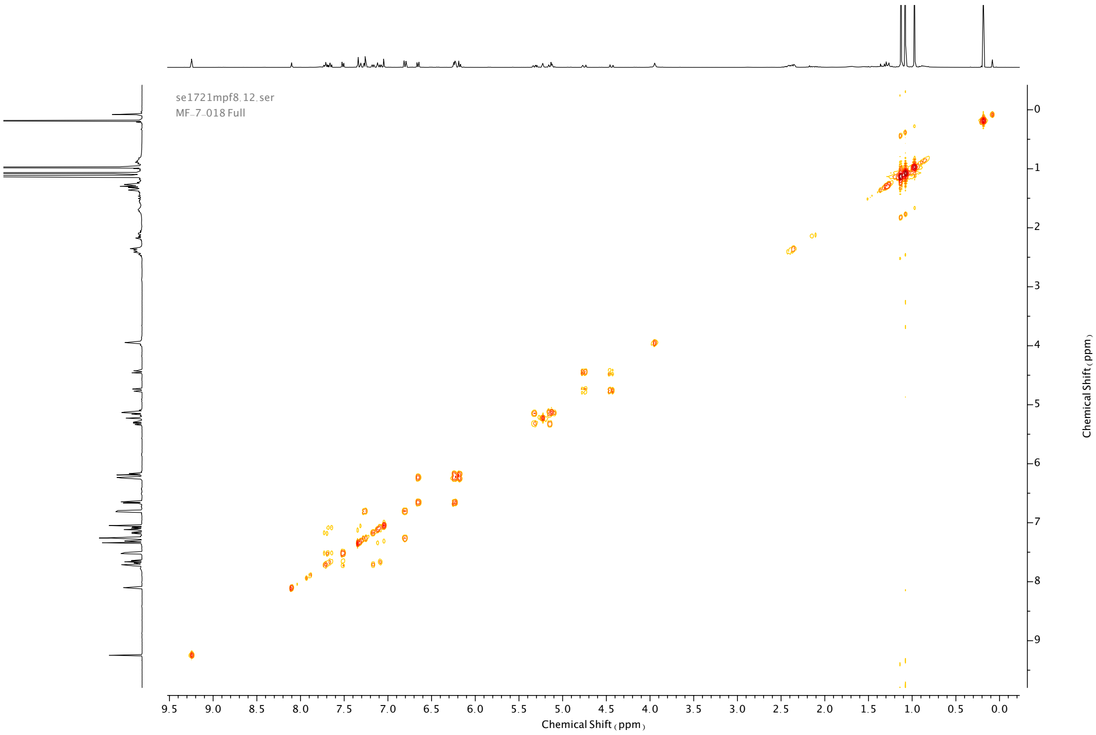

Figure **408**. COSY NMR ($CDCl_3$) of **120**.

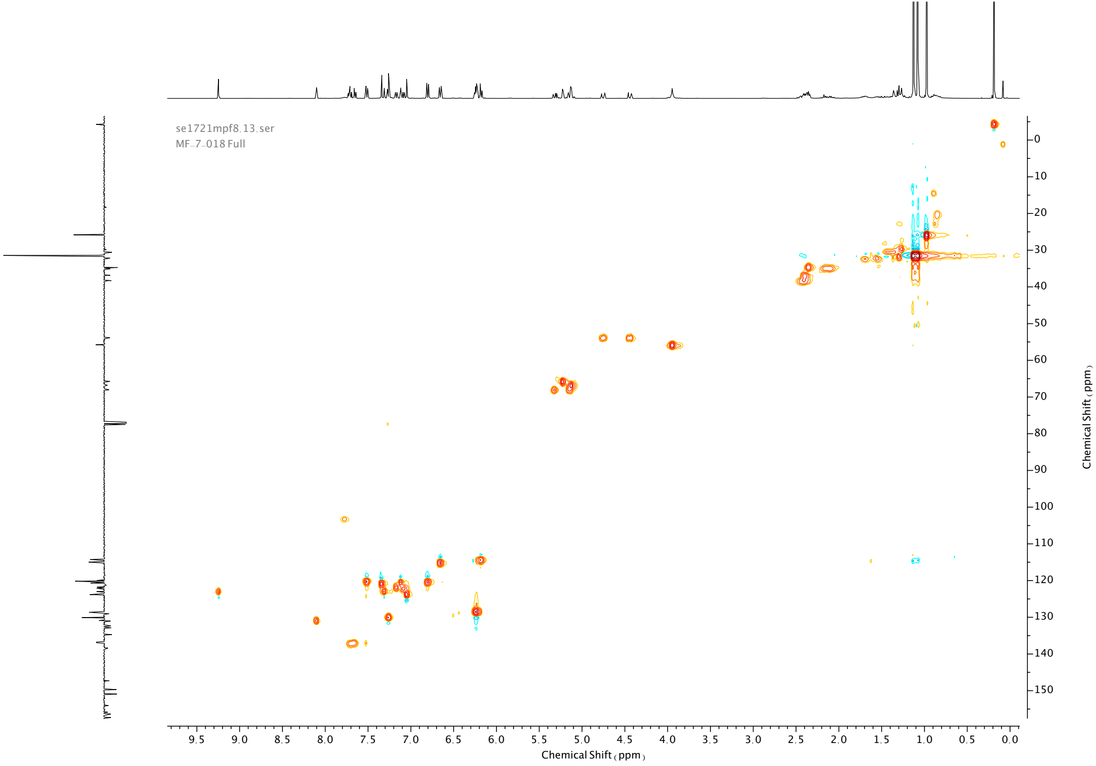

Figure **409**. HSQC NMR ($CDCl_3$) of **120**.

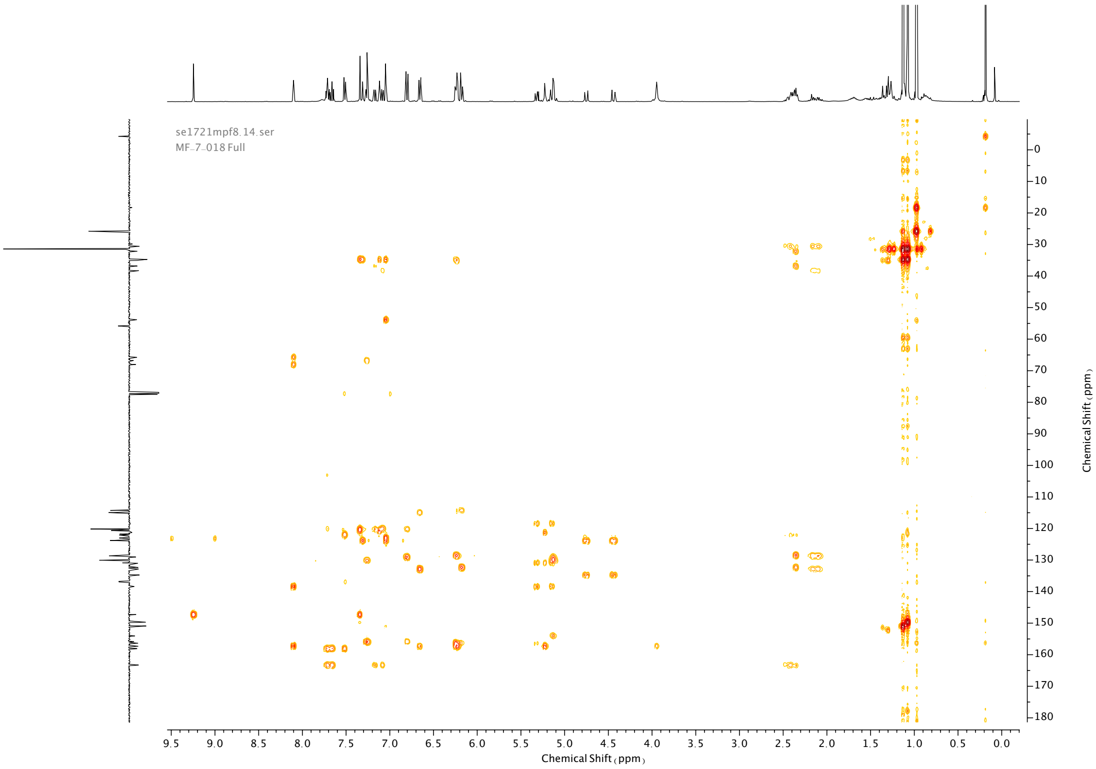

Figure **410**. HMBC NMR (CDCl$_3$) of **120**.

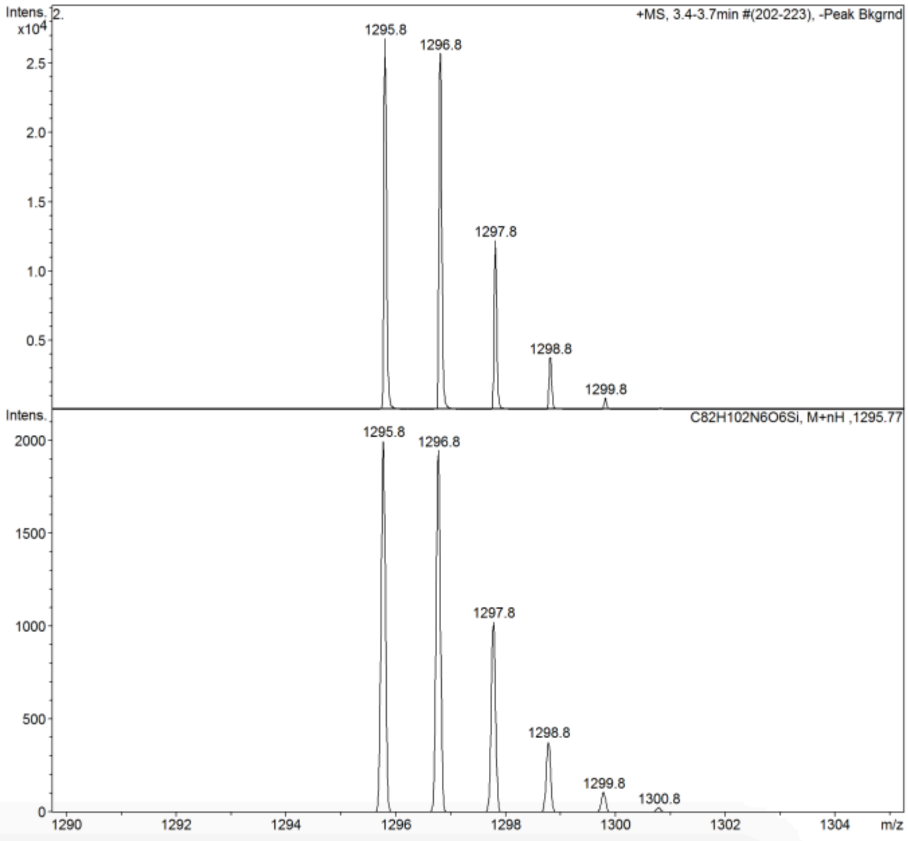

Figure **411**. Isotope pattern of **120**.

Compound **104**

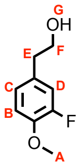

A solution of **103** (5.0 g, 27.2 mmol, 1.0 eq.) in anhydrous THF (50 mL) was degassed under N_2. $LiAlH_4$ (1 M in THF) (32.5 mL, 32.5 mmol, 1.2 eq.) was added dropwise over 10 min at 0 °C. The mixture was slowly allowed to reach room temperature and stirred for a further 4 h. The mixture was quenched at -10 °C *via* slow addition of EtOAc (100 mL), followed by H_2O (1.5 mL), NaOH (15% w/v) (1.5 mL) then H_2O (5 mL) again. The resulting mixture was stirred at room temperature for 2 h, diluted with EtOAc (250 mL), dried over anhydrous $MgSO_4$, filtered over Celite and concentrated *in vacuo*. The crude product was purified *via* silica-gel chromatography using a Biotage Isolute SPE column (eluent 1:0 → 9:1 CH_2Cl_2: MeOH) to afford **104** as a colourless oil (3.0 g, 17.7 mmol, 65%). ^{1}H NMR (400 MHz, $CDCl_3$, 298 K) δ_H 6.98-6.86 (3H, m, H_B, H_C & H_D), 3.86 (3H, s, H_A), 3.81 (2H, t, *J* = 6.6 Hz, H_F), 2.78 (2H, t, *J* = 6.6 Hz, H_E). ^{13}C NMR (101 MHz, $CDCl_3$, 298 K) δ_C 152.4 (d, *J* = 245.9 Hz, $J^1_{C\text{-}F}$), 146.3 (d, *J* = 10.7 Hz, $J^2_{C\text{-}F}$), 131.7 (d, *J* = 6.1 Hz, $J^3_{C\text{-}F}$), 124.7 (d, *J* = 3.5 Hz, $J^3_{C\text{-}F}$), 116.7 (d, *J* = 18.0 Hz, $J^2_{C\text{-}F}$), 113.7 (d, *J* = 2.2 Hz, $J^4_{C\text{-}F}$), 63.6, 56.5, 38.3.^{19}F NMR (376 MHz, $CDCl_3$, 298 K) δ_F -135.5.

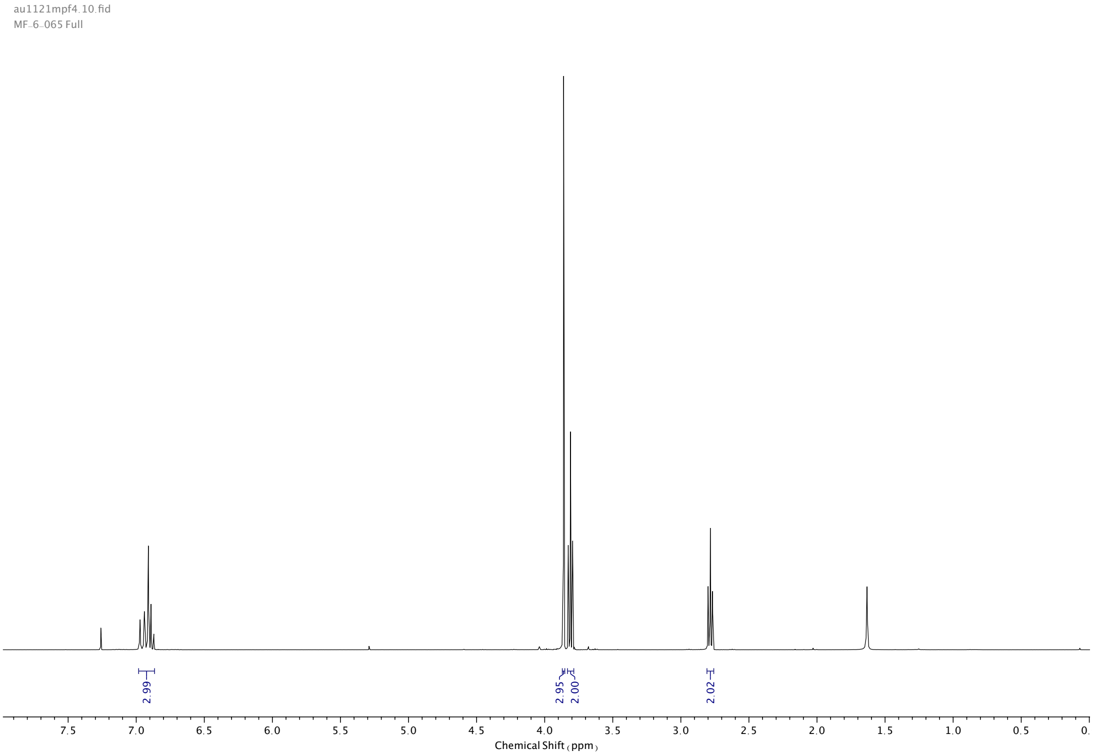

Figure **412**. ^{1}H NMR ($CDCl_3$, 400 MHz) of **104**.

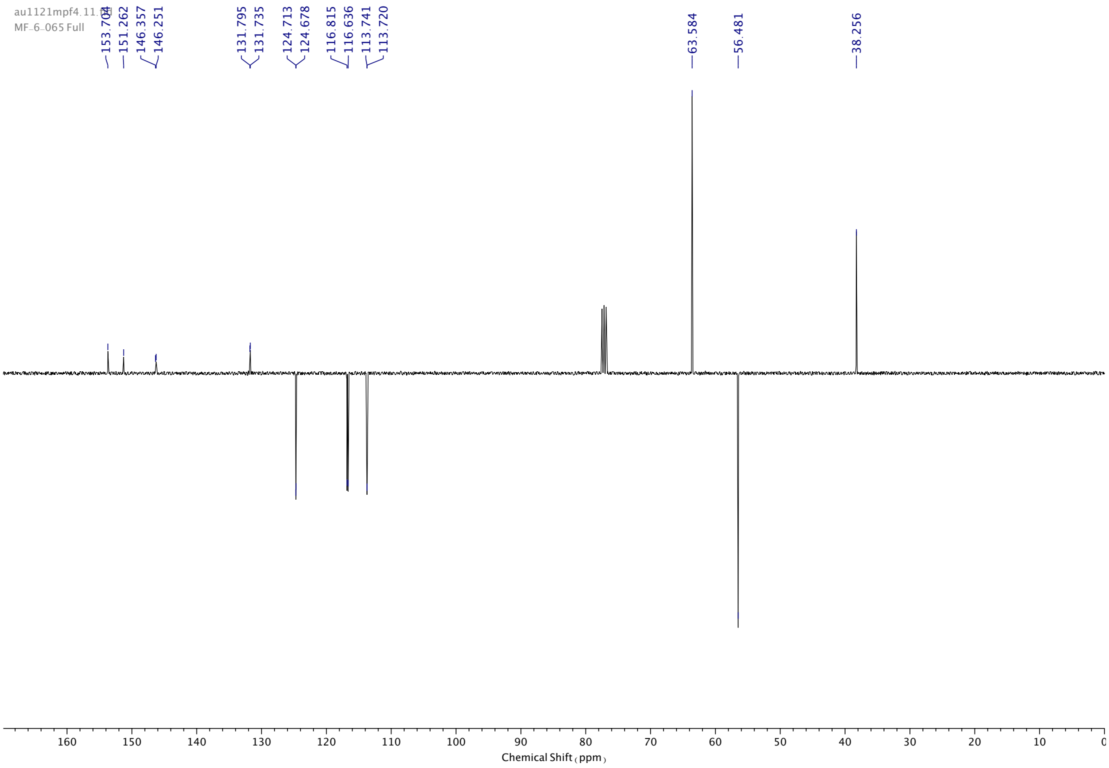

Figure **413**. ^{13}C NMR (CDCl$_3$, 101 MHz) of **104**.

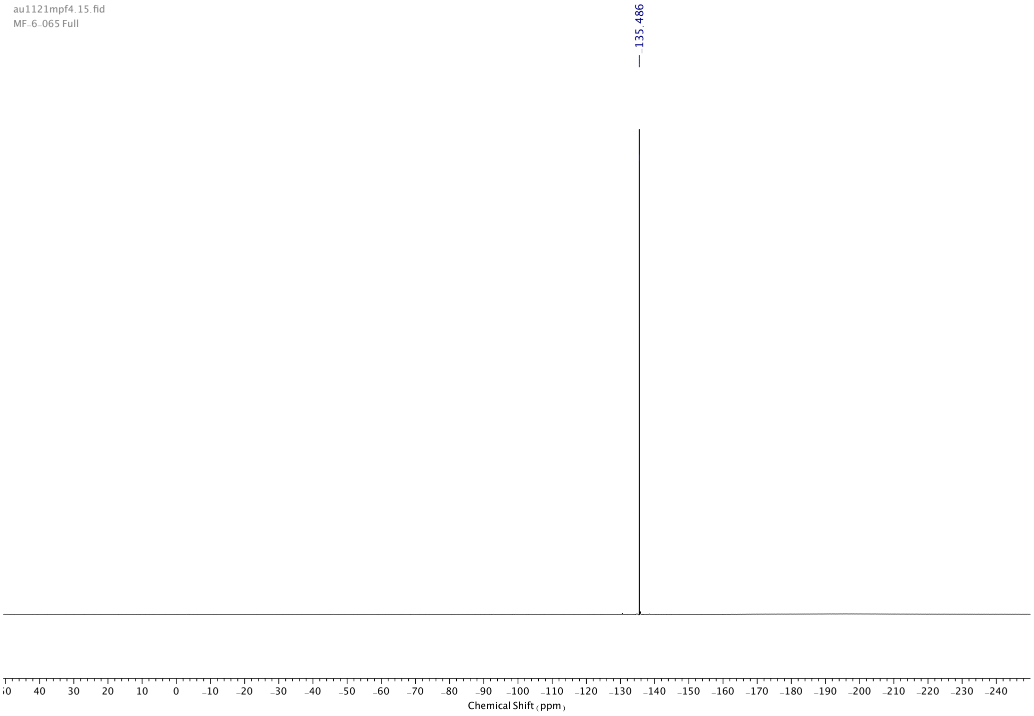

Figure **414**. ^{19}F NMR (CDCl$_3$, 376 MHz) of **104**.

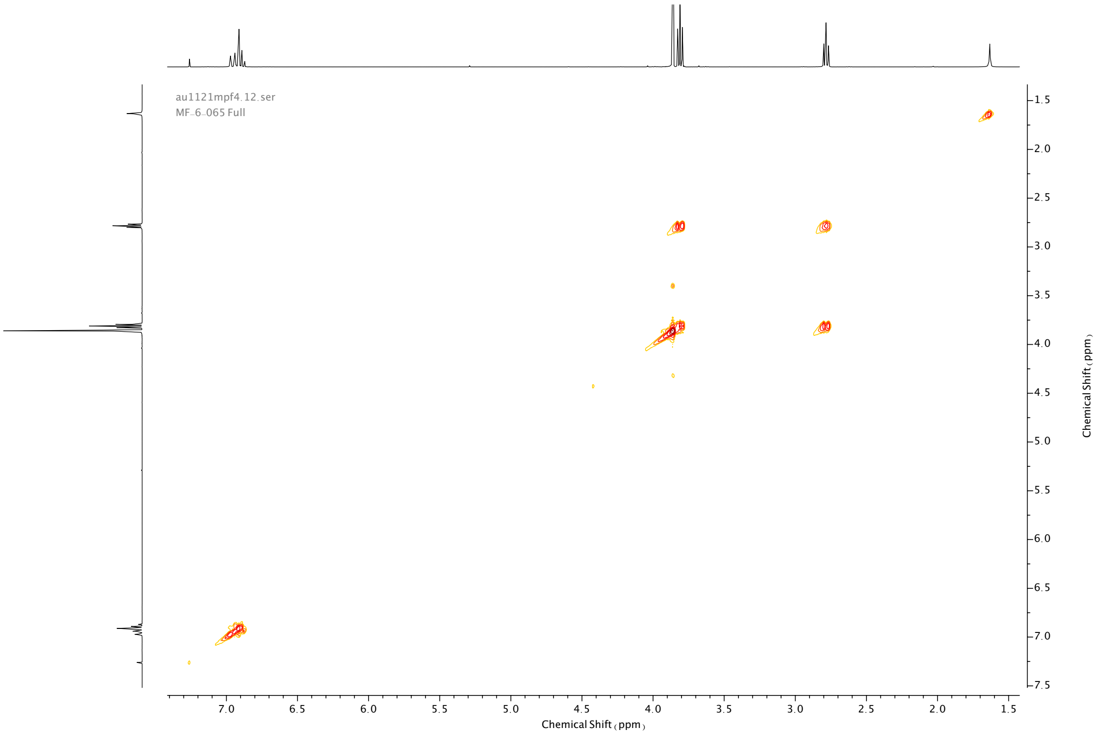

Figure **415**. COSY NMR ($CDCl_3$) of **104**.

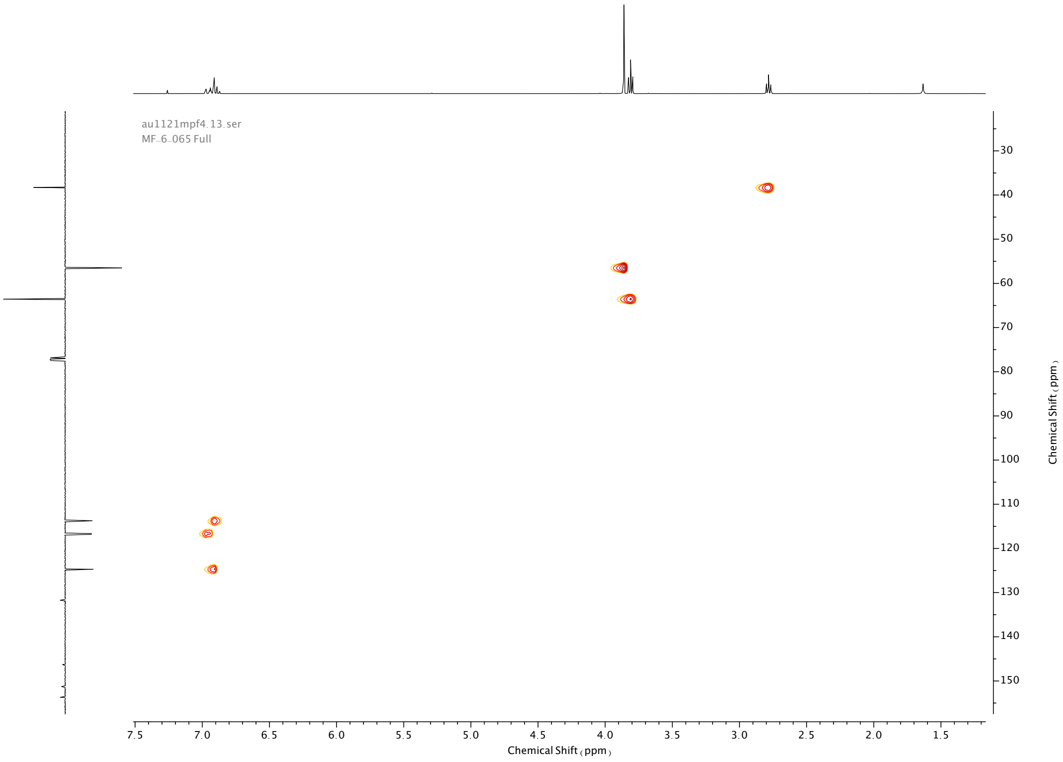

Figure **416**. HSQC NMR ($CDCl_3$) of **104**.

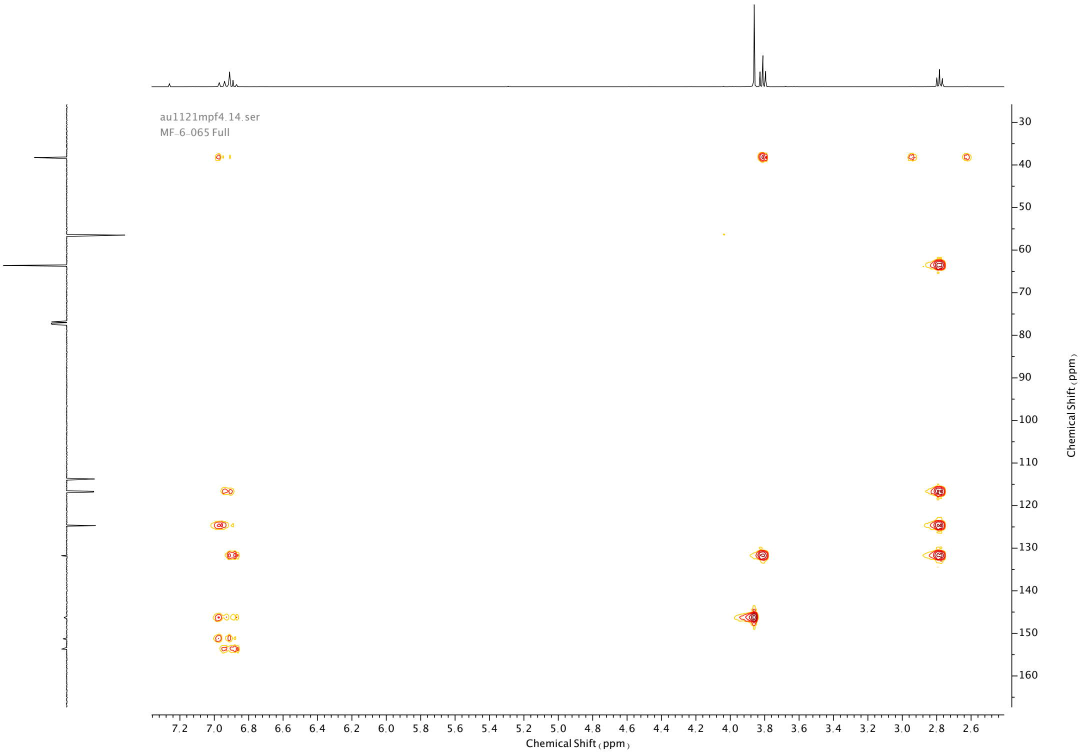

Figure **417**. HMBC NMR ($CDCl_3$) of **104**.

Compound **105**

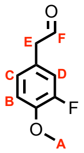

DMP (8.82 g, 20.8 mmol, 1.3 eq.) was added to a degassed solution of **104** (2.72 g, 16.0 mmol, 1.0 eq.) in CH_2Cl_2 (50 mL) in one portion at 0 °C, then allowed to reach room temperature and stirred for a further 2 h. The mixture was diluted with CH_2Cl_2 (50 mL) then washed with water (50 mL) and brine (50 mL). Combined aqueous phases were extracted with CH_2Cl_2 (2 x 25 mL). The combined organic extracts were then dried over anhydrous $MgSO_4$, filtered and concentrated *in vacuo*. The crude product was purified *via* silica-gel chromatography using a Biotage Isolute SPE column (eluent 19:1 → 9:1 PE: EA) to afford **105** as a colourless oil (1.93 g, 11.5 mmol, 72%). ^{1}H NMR (400 MHz, $CDCl_3$, 298 K) δ_H 9.72 (1H, t, *J* = 2.2 Hz, H_F), 6.98- 6.89 (3H, m, H_B, H_C & H_D), 3.88 (3H, s, H_A), 3.62 (2H, d, *J* = 2.2 Hz, H_E). ^{13}C NMR (101 MHz, $CDCl_3$, 298 K) δ_C 190.0, 152.6 (d, *J* = 247.1 Hz, J^1_{C-F}), 147.2 (d, *J* = 10.6 Hz, J^2_{C-F}), 125.5 (d, *J* = 3.7 Hz, J^3_{C-F}), 124.7 (d, *J* = 6.5 Hz, J^3_{C-F}), 117.4 (d, *J* = 18.6 Hz, J^2_{C-F}), 114.0 (d, *J* = 2.2 Hz, J^4_{C-F}), 56.4, 49.6. ^{19}F NMR (376 MHz, $CDCl_3$, 298 K) δ_F -134.6.

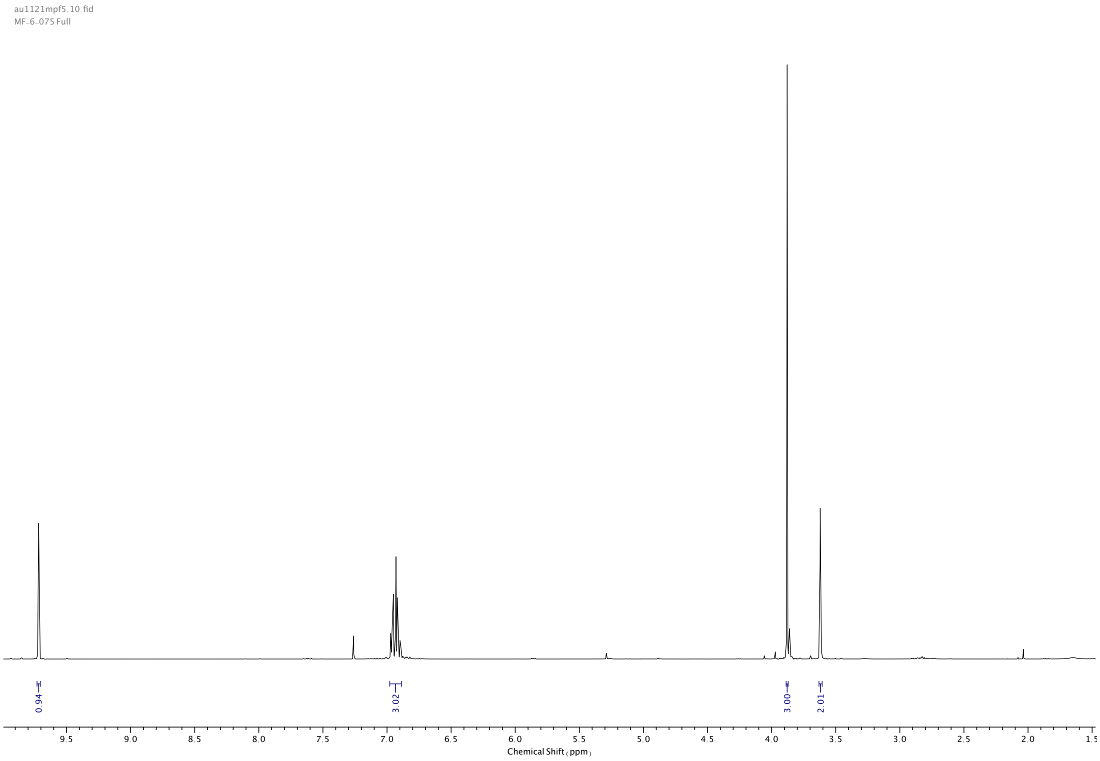

Figure **418**. ^{1}H NMR ($CDCl_3$, 400 MHz) of **105**.

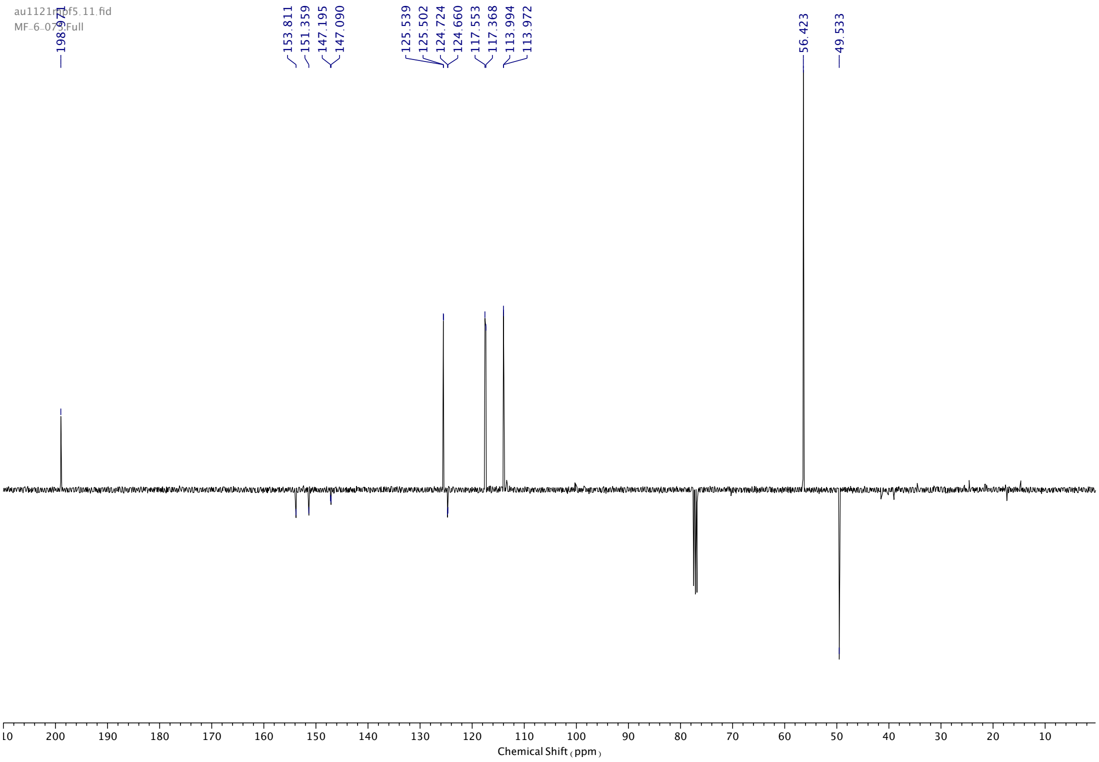

Figure **419**. ^{13}C NMR (CDCl$_3$, 101 MHz) of **105**.

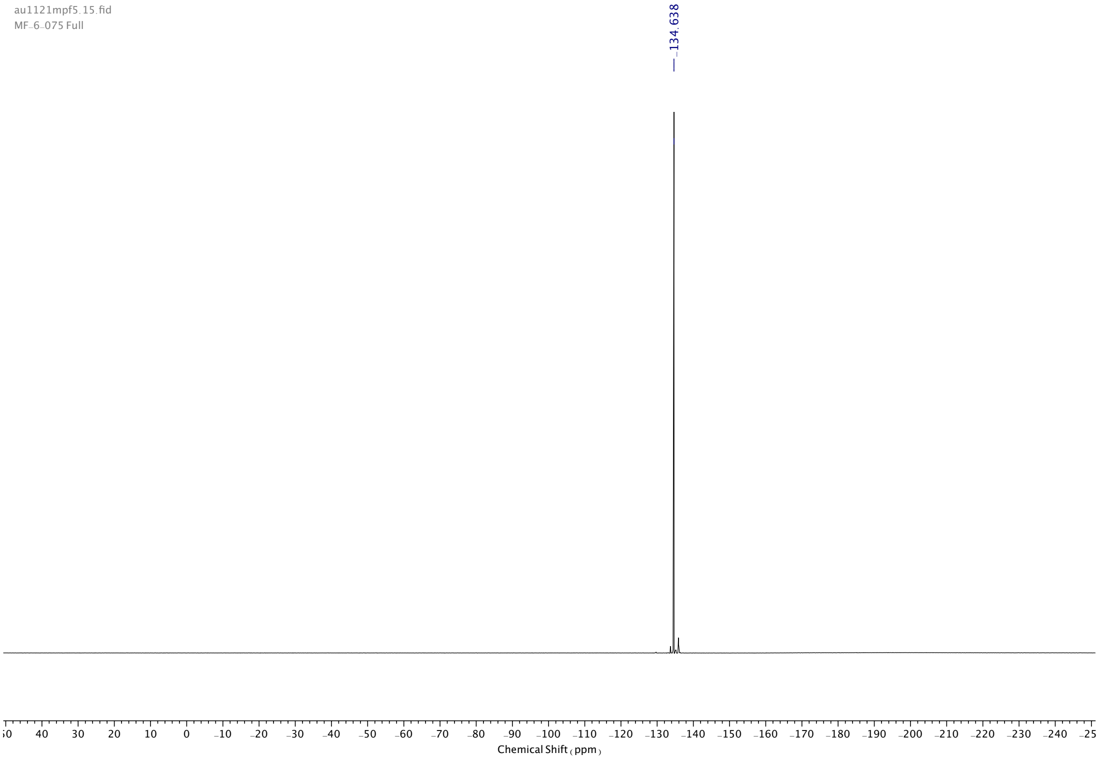

Figure **420**. ^{19}F NMR (CDCl$_3$, 376 MHz) of **105**.

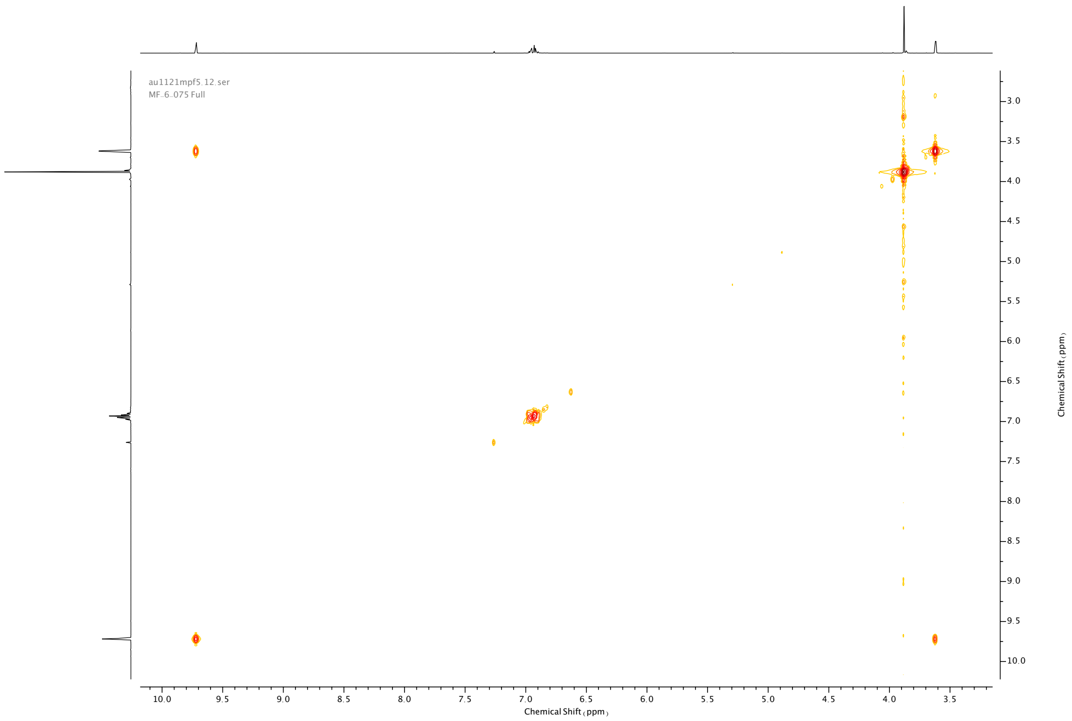

Figure **421**. COSY NMR (CDCl$_3$) of **105**.

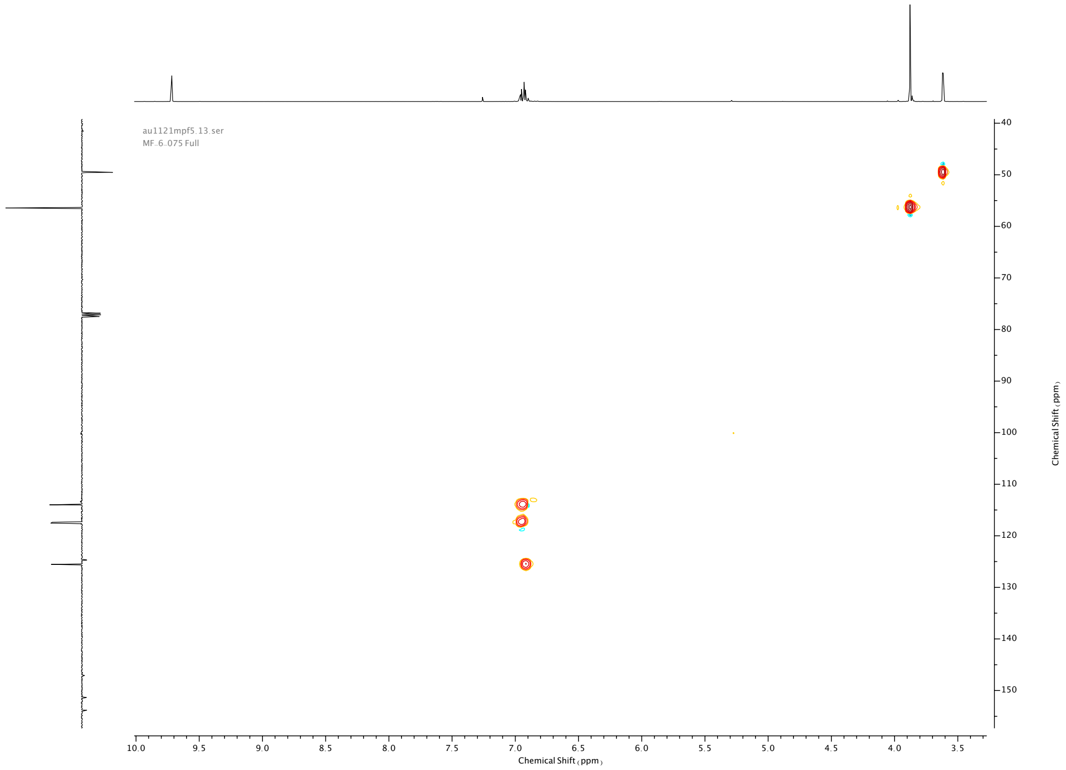

Figure **422**. HSQC NMR (CDCl$_3$) of **105**.

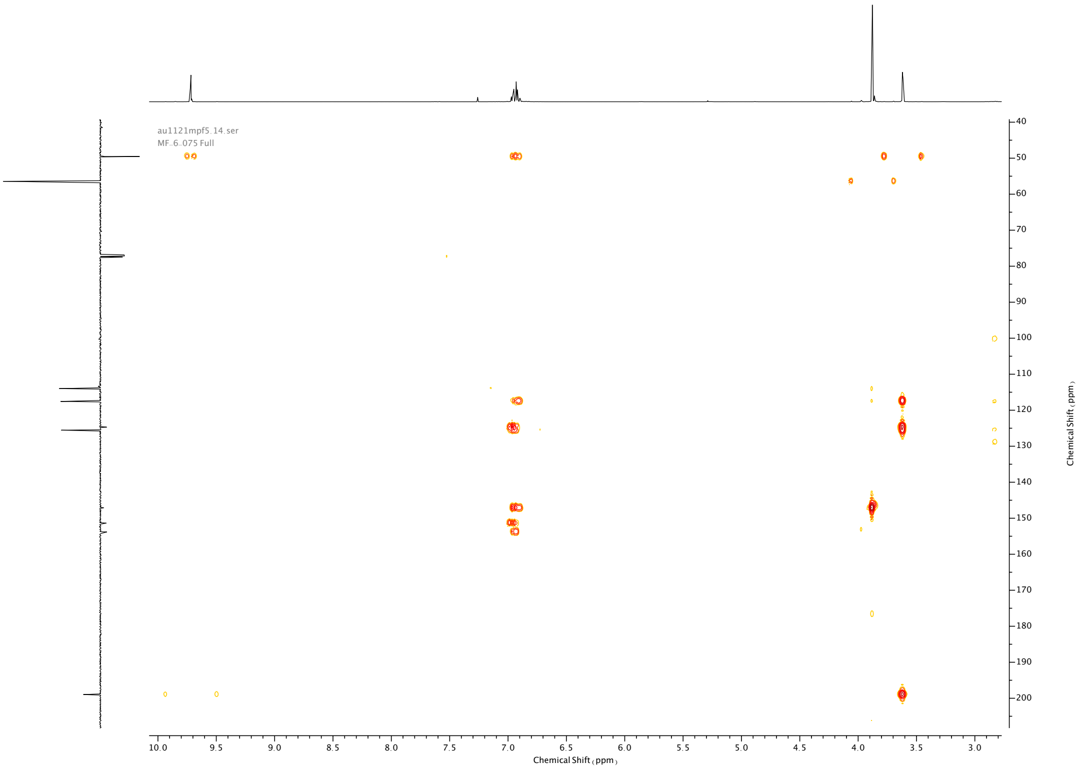

Figure **423**. HMBC NMR ($CDCl_3$) of **105**.

Compound **106**

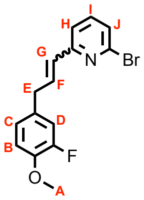

101 (1.7 g, 6.9 mmol, 1.1 eq.) was added to solution of PPh_3 (1.8 g, 6.9 mmol, 1.1 eq.) in anhydrous THF (18 mL), which was then degassed under N_2 and stirred overnight at 80 °C. The mixture was cooled to 0 °C and KO^tBu (1 M in THF) (6.9 mL, 6.9 mmol, 1.1 eq.) was added dropwise over 10 min, then stirred for a further 10 min at 0 °C. **105** (1.1 g, 6.2 mmol, 1.0 eq.) in anhydrous THF (16 mL) was added dropwise at 0 °C then stirred for a further 4 h at 50 °C. Once cooled to room temperature, the mixture was diluted with Et_2O (100 mL), washed with $NaHCO_3$ (100 mL), water (100 mL) and brine (100 mL). Combined aqueous phases were extracted with Et_2O (2 x 50 mL). The combined organic extracts were then dried over anhydrous Na_2SO_4, filtered and concentrated *in vacuo*. The crude product was purified *via* silica-gel chromatography using a Biotage Isolute SPE column (eluent 9:1 → 2:1 PE: CH_2Cl_2) to afford **106** as a colourless oil (1.32 g, 4.1 mmol, 66%).[8] ^1H NMR (400 MHz, $CDCl_3$, 298 K) δ_H 7.44 (1H, t, *J* = 7.7 Hz, H_I), 7.28 (1H, dd, *J* = 7.8, 0.8 Hz, H_J), 7.16 (1H, dd, *J* = 7.8, 0.7 Hz, H_H),6.97-6.84 (4H, m, H_B, H_C, H_D & H_F), 6.39 (1H, dt, *J* = 15.5, 1.6 Hz, H_G), 3.87 (3H, s, H_A), 3.50 (2H, dd, *J* = 6.9, 1.6 Hz, H_E). ^{13}C NMR (101 MHz, $CDCl_3$, 298 K) δ_C 157.0, 152.6 (d, *J* = 245.8 Hz, $J^1_{C\text{-}F}$), 146.3 (d, *J* = 10.6 Hz, $J^2_{C\text{-}F}$), 142.1, 138.8, 135.8, 132.2 (d, *J* = 10.6 Hz, $J^3_{C\text{-}F}$), 129.7, 126.1, 124.5 (d, *J* = 3.7 Hz, $J^3_{C\text{-}F}$), 120.0, 116.8 (d, *J* = 18.3 Hz, $J^2_{C\text{-}F}$), 113.8 (d, *J* = 2.2 Hz, $J^4_{C\text{-}F}$), 56.5, 38.1. ^{19}F NMR (376 MHz, $CDCl_3$, 298 K) δ_F -135.4. HR-ESI-MS (CH_3CN): *m/z* = 322.0240 $[M+H]^+$ calc. 322.0237.

---

[8] Reaction was highly selective, leading to the formation of only one geometric isomer.

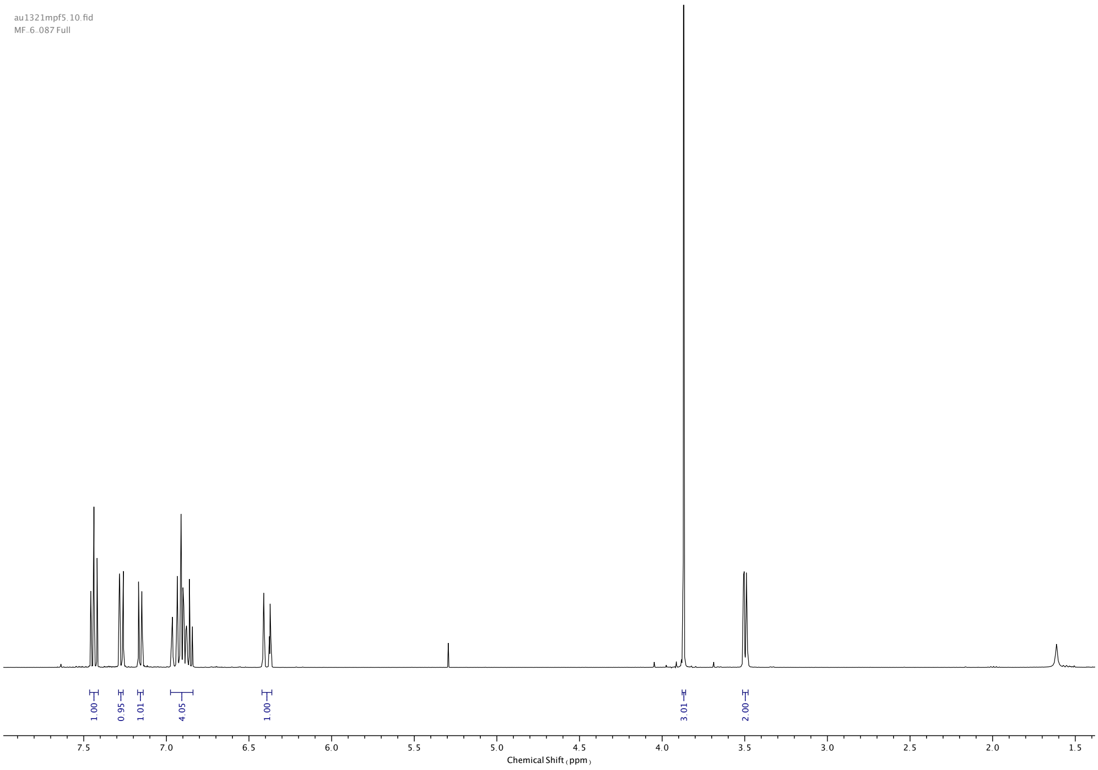

Figure **424**. ^{1}H NMR ($CDCl_3$, 400 MHz) of **106**.

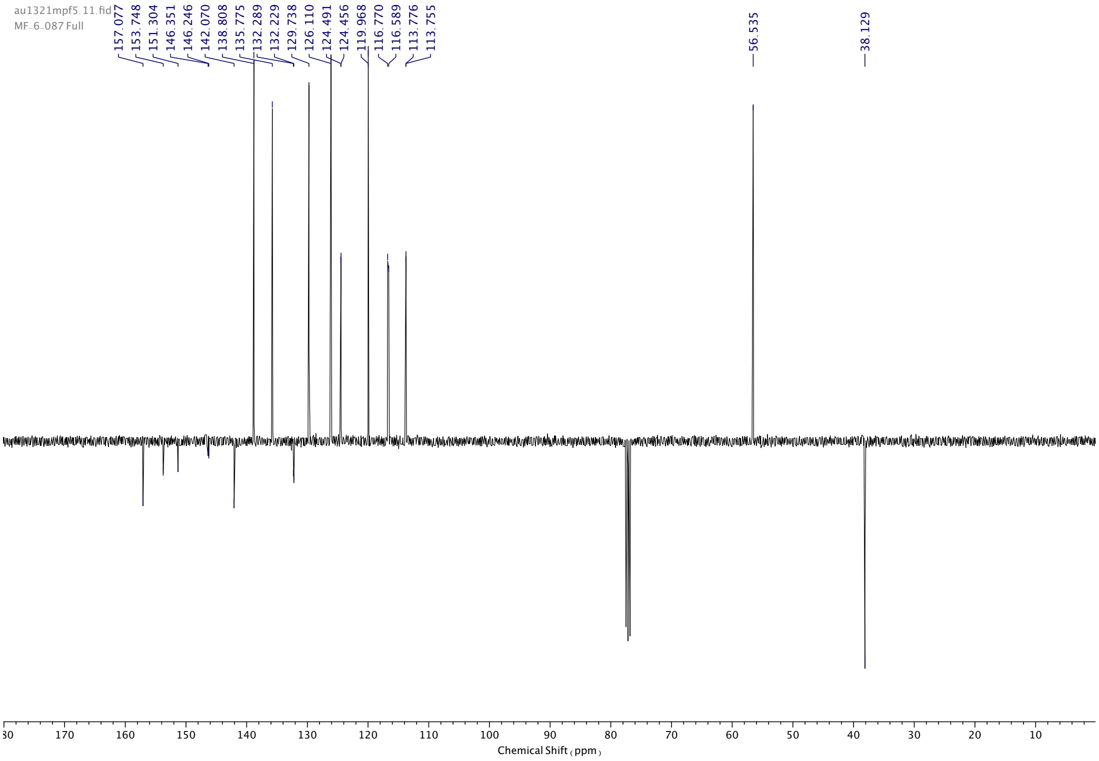

Figure **425**. ^{13}C NMR ($CDCl_3$, 101 MHz) of **106**.

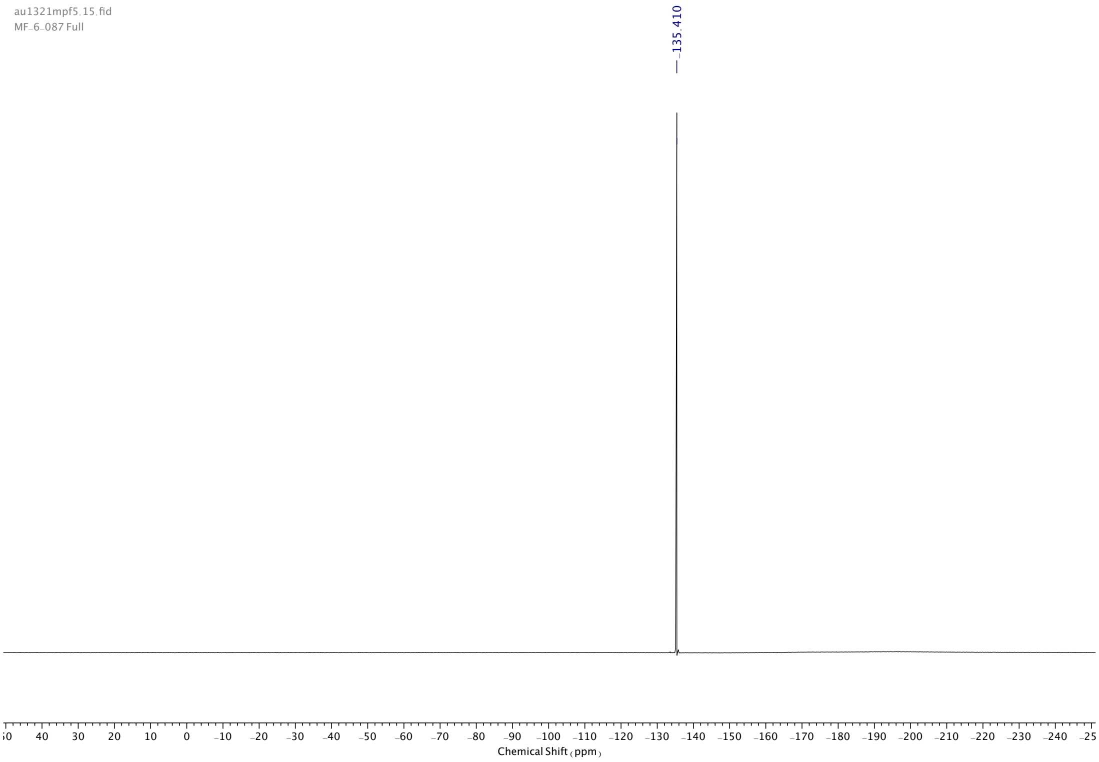

Figure **426**. ^{19}F NMR (CDCl$_3$, 376 MHz) of **106**.

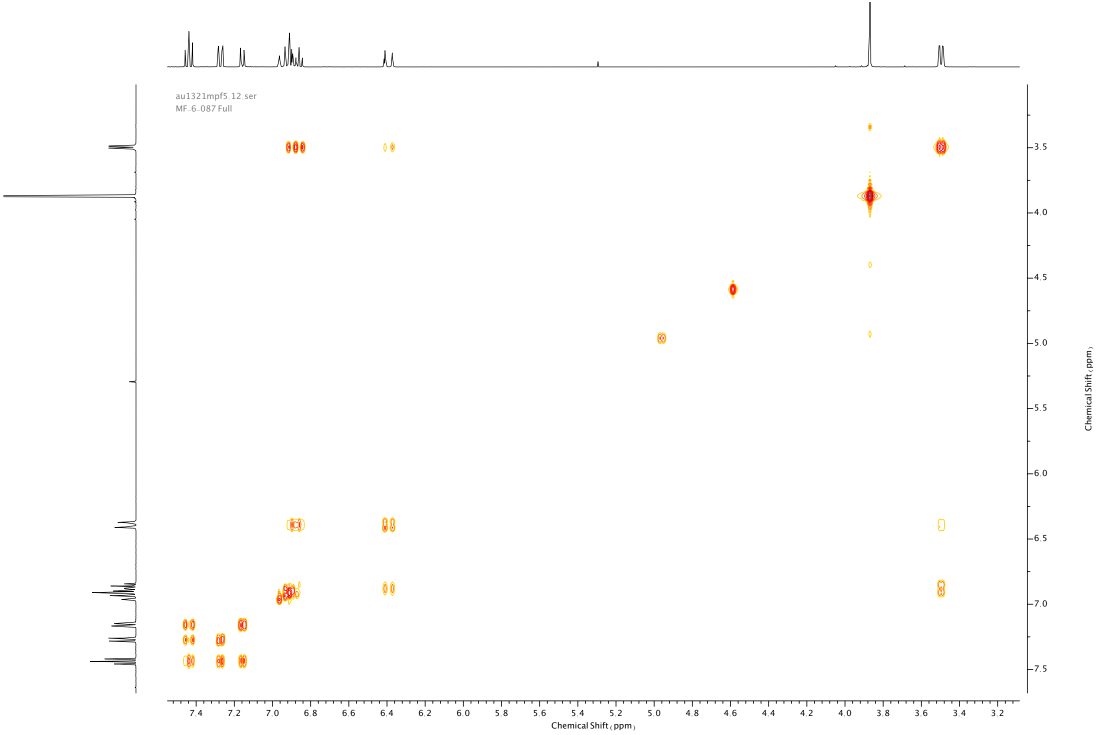

Figure **427**. COSY NMR (CDCl$_3$) of **106**.

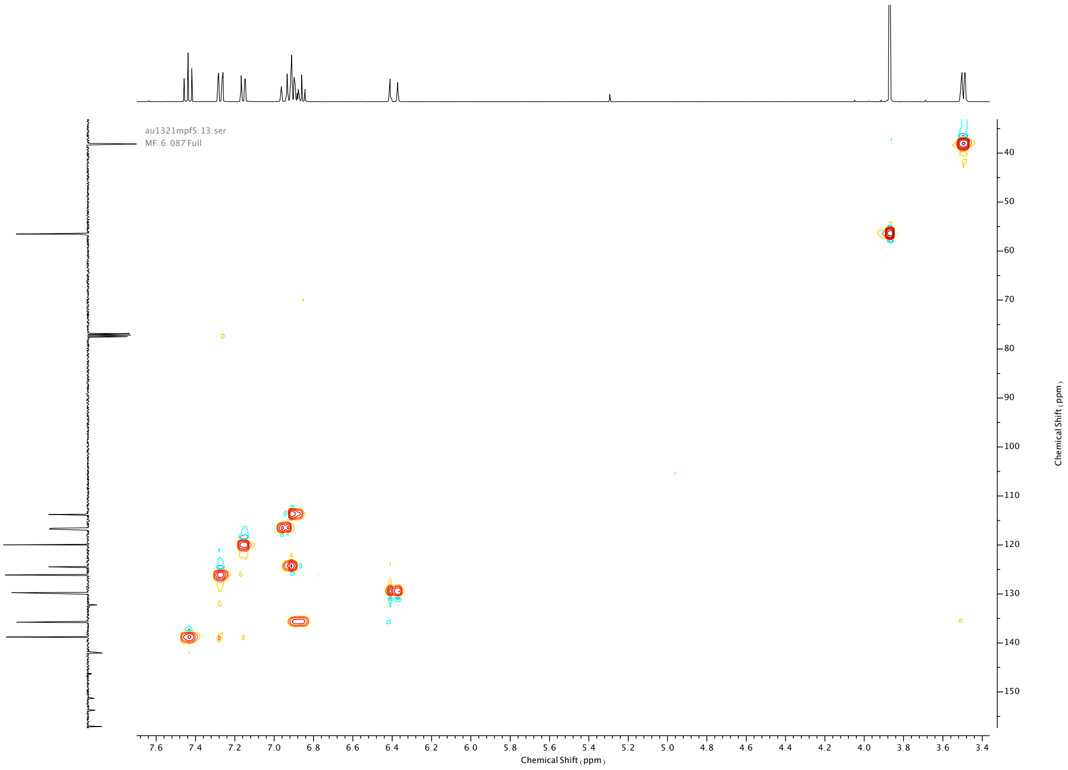

Figure **428**. HSQC NMR (CDCl$_3$) of **106**.

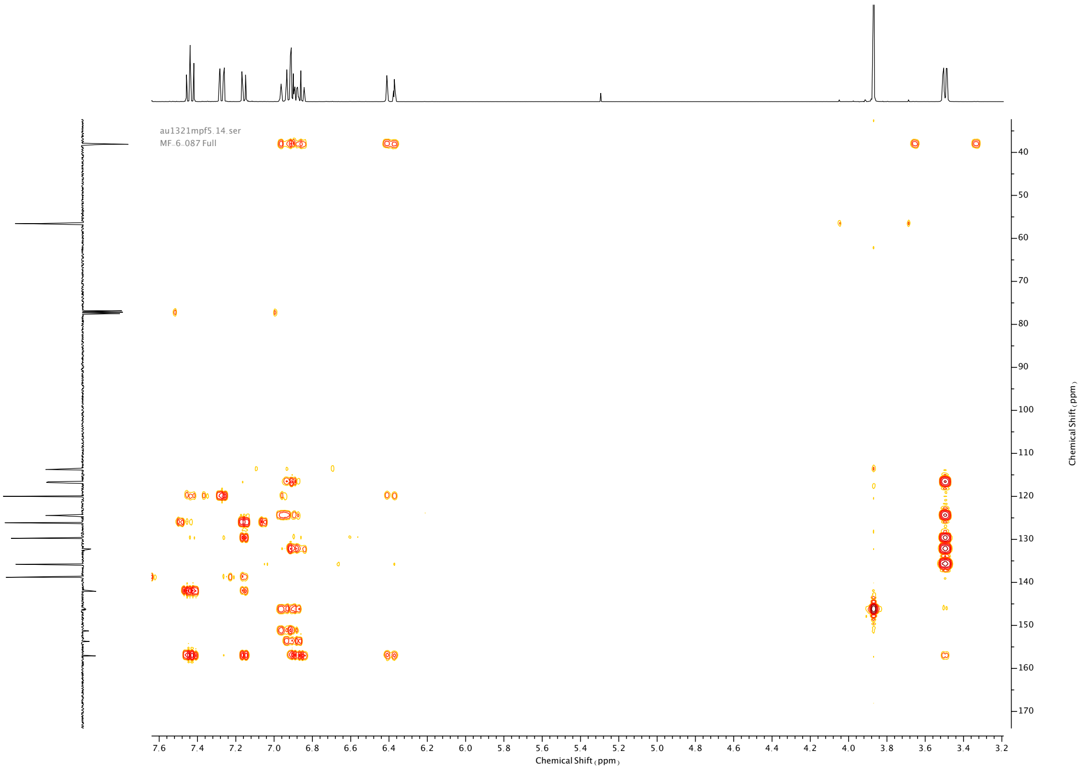

Figure **429**. HMBC NMR (CDCl$_3$) of **106**.

Compound **107**

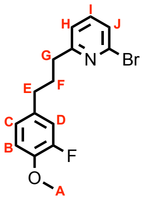

NaOAc (662 mg, 8.1 mmol, 2.0 eq.) and TsNHNH$_2$ (3.0 g, 16.2 mmol, 4.0 eq.) were added to a solution of **106** (1.3 g, 4.0 mmol, 1.0 eq.) in anhydrous EtOH (30 mL), degassed under N$_2$ and stirred overnight at 80 °C. Once cooled to room temperature, the mixture was diluted with EtOAc (100 mL), washed with sat. NH$_4$Cl (100 mL), water (100 mL) and brine (100 mL). Combined aqueous phases were extracted with EtOAc (2 x 50 mL). The combined organic extracts were then dried over anhydrous MgSO$_4$, filtered and concentrated *in vacuo*. The crude product was purified *via* silica-gel chromatography using a Biotage Isolute SPE column (eluent 9:1 → 1:1 PE: CH$_2$Cl$_2$) to afford **107** as a colourless oil (1.2 g, 3.7 mmol, 88%). ^{1}H NMR (400 MHz, CDCl$_3$, 298 K) δ_H 7.44 (1H, t, *J* = 7.6 Hz, H$_I$), 7.30 (1H, d, *J* = 7.9 Hz, H$_J$), 7.07 (1H, d, *J* = 7.9 Hz, H$_H$), 6.93-6.88 (1H, m, H$_D$), 6.88-6.84 (2H, m, H$_B$ & H$_C$), 3.86 (3H, s, H$_A$), 2.77 (2H, app. t, *J* = 7.8 Hz, H$_G$), 2.60 (2H, app. t, *J* = 7.7 Hz, H$_E$), 2.05-1.96 (2H, m, H$_F$). ^{13}C NMR (101 MHz, CDCl$_{3,}$ 298 K) δ_C 163.6, 152.4 (d, *J* = 245.2 Hz, $J^1_{C\text{-}F}$), 145.8 (d, *J* = 10.7 Hz, $J^2_{C\text{-}F}$), 141.7, 138.8, 135.2 (d, *J* = 5.9 Hz, $J^3_{C\text{-}F}$), 125.5, 124.1 (d, *J* = 3.5 Hz, $J^3_{C\text{-}F}$), 121.7, 116.2 (d, *J* = 17.8 Hz, $J^2_{C\text{-}F}$), 113.6 (d, *J* = 2.1 Hz, $J^4_{C\text{-}F}$), 56.5, 37.39, 34.6, 31.3. ^{19}F NMR (376 MHz, CDCl$_3$, 298 K) δ_F -135.9. HR-ESI-MS (CH$_3$CN): *m/z* = 324.0397 [M+H]$^+$ calc. 324.0394.

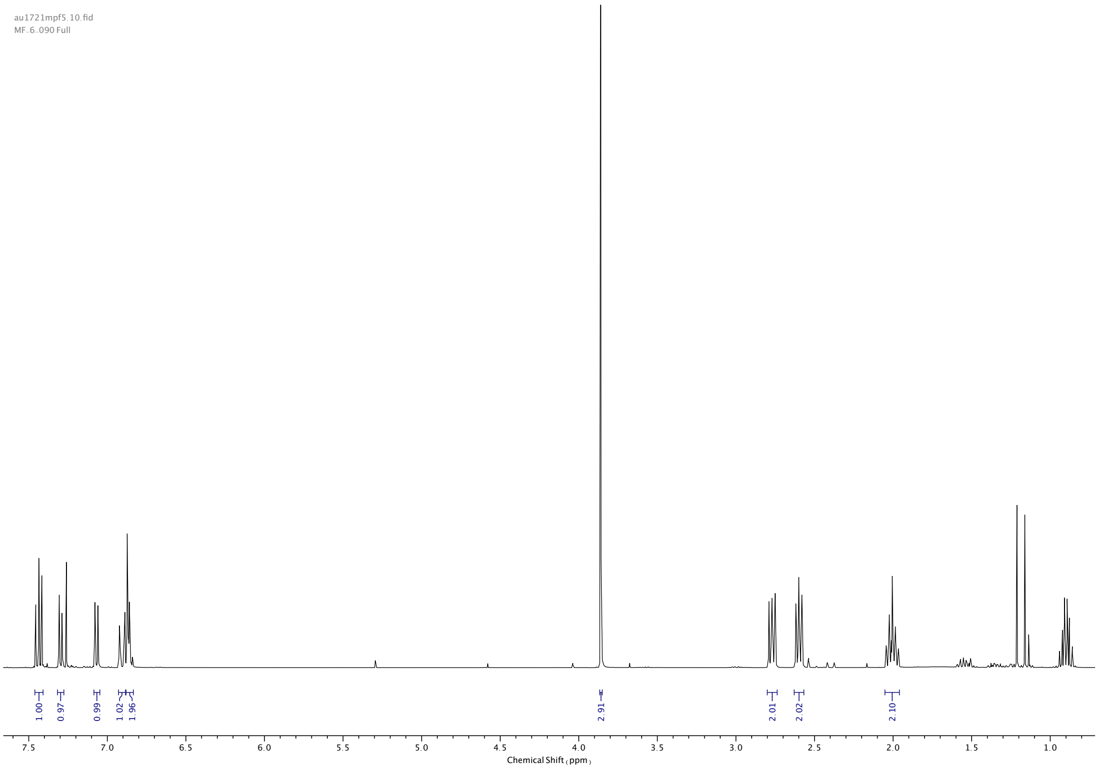

Figure **430**. ^{1}H NMR (CDCl$_3$, 400 MHz) of **107**.

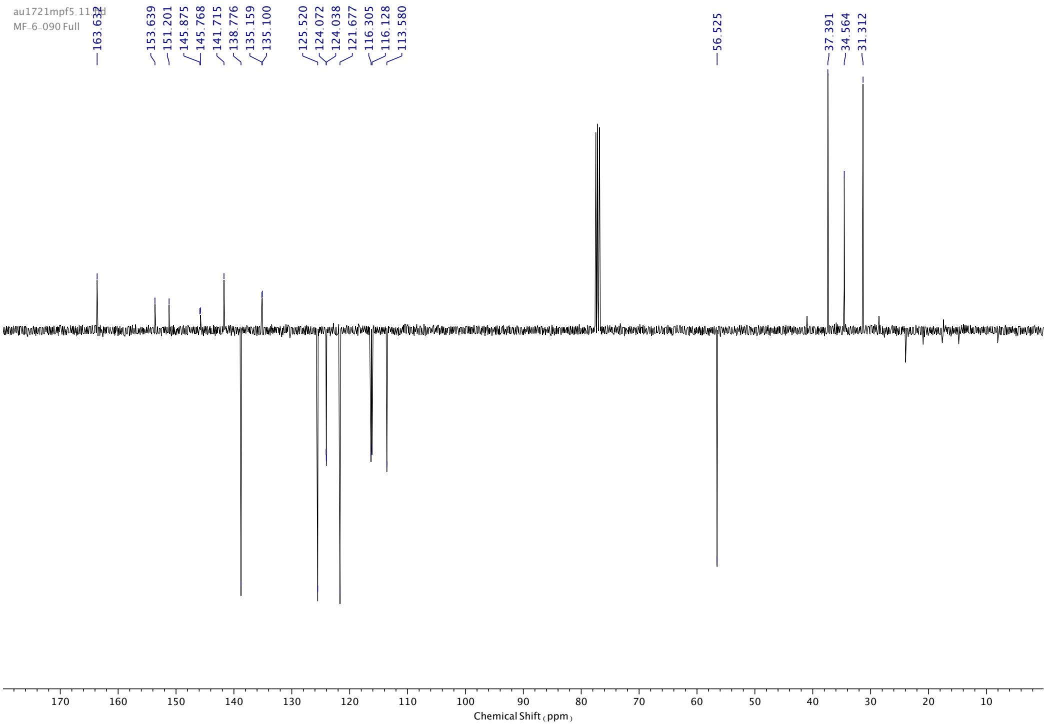

Figure **431**. ^{13}C NMR (CDCl$_3$, 101 MHz) of **107**.

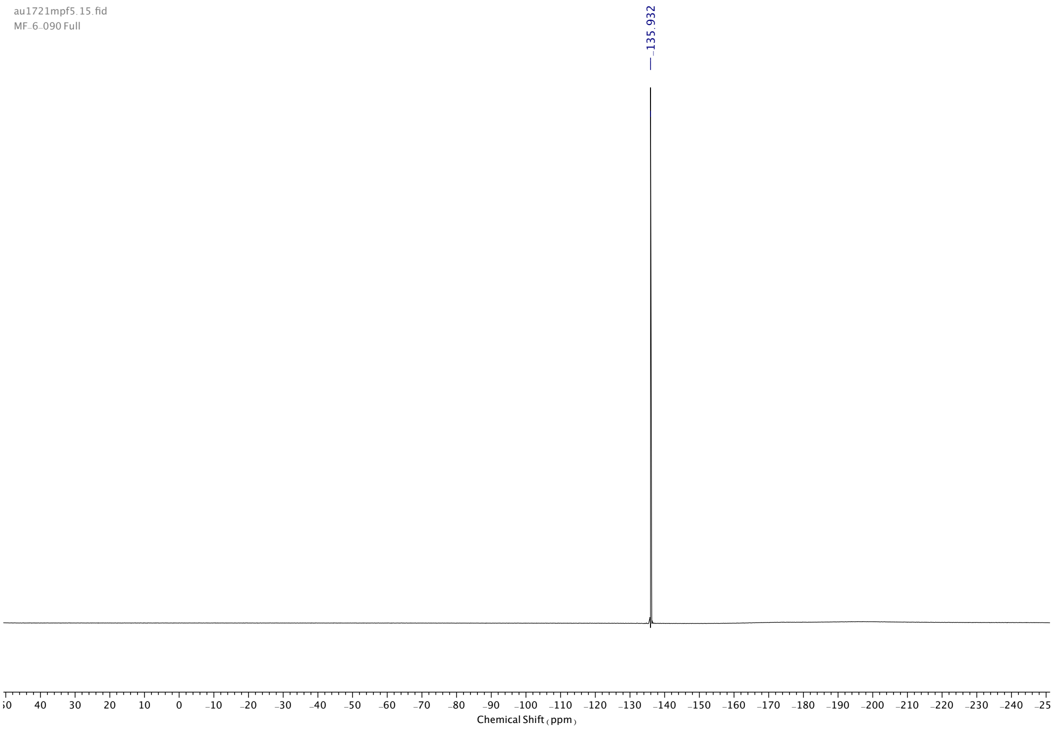

Figure **432**. ^{19}F NMR ($CDCl_3$, 376 MHz) of **107**.

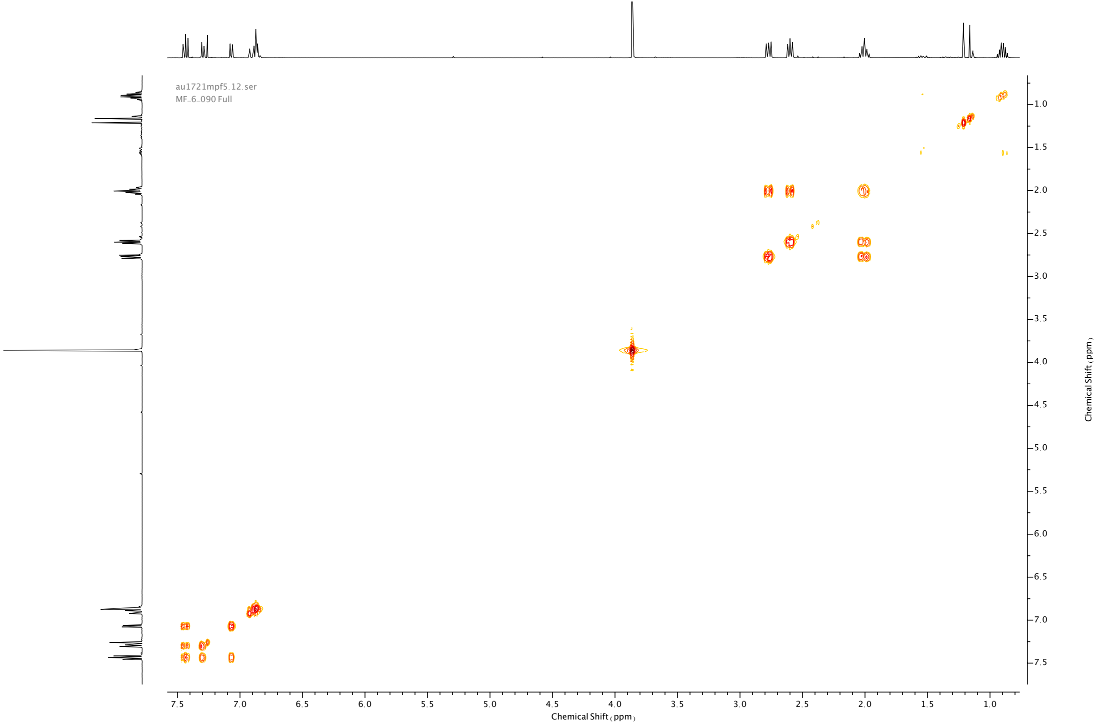

Figure **433**. COSY NMR ($CDCl_3$) of **107**.

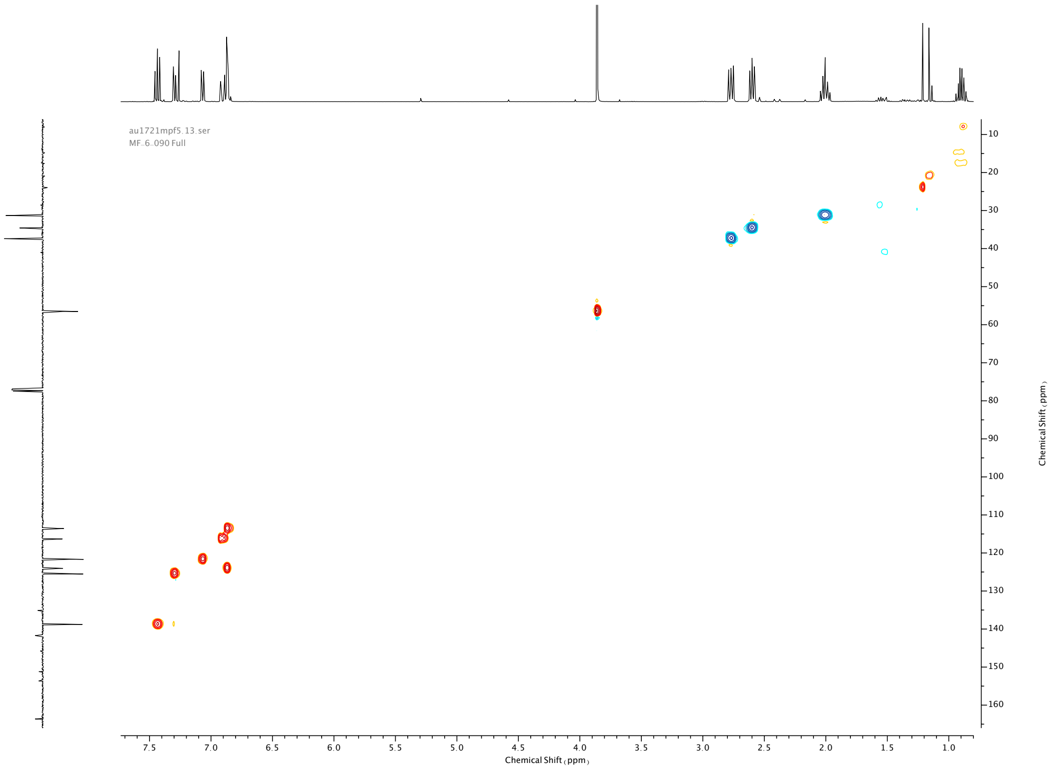

Figure **434**. HSQC NMR ($CDCl_3$) of **107**.

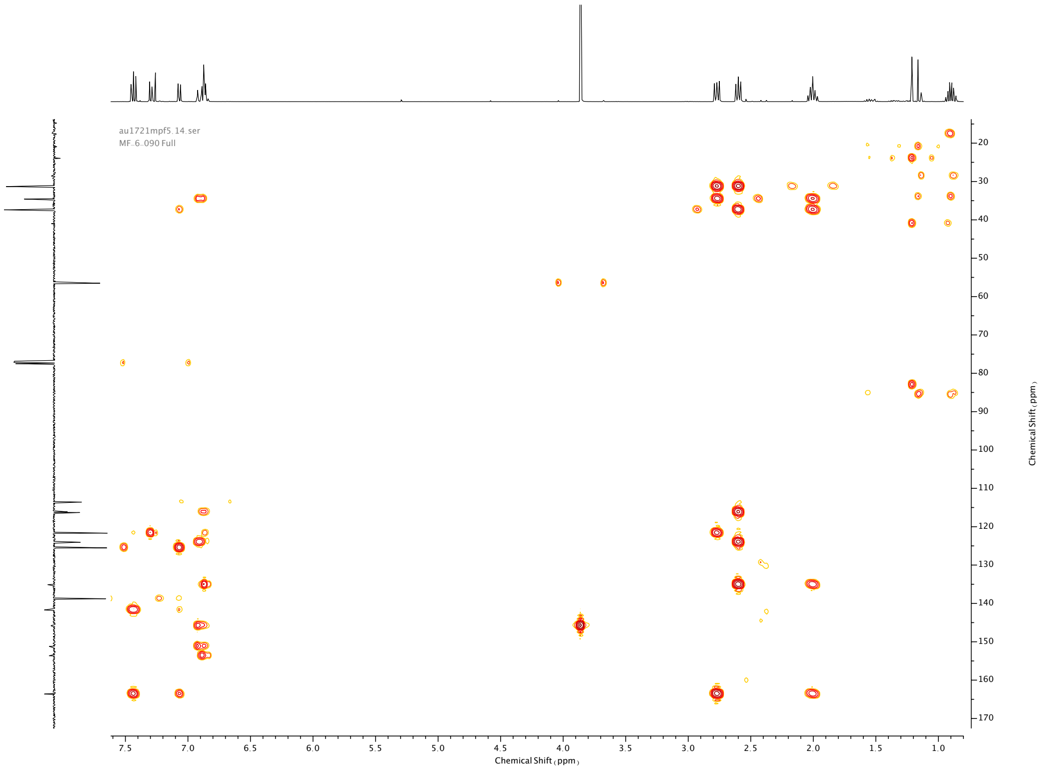

Figure **435**. HMBC NMR ($CDCl_3$) of **107**.

Compound **108**

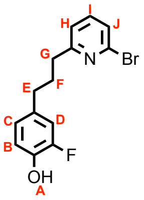

BBr_3 (1M in CH_2Cl_2) (6.9 mL, 6.9 mmol, 2.0 eq.) was added dropwise to a degassed solution of **107** (1.1 g, 3.4 mmol, 1.0 eq.) in anhydrous CH_2Cl_2 (30 mL) at 0 °C, then stirred at room temperature for a further 2 h. The mixture was diluted with CH_2Cl_2 (100 mL) and quenched *via* dropwise addition of sat. $NaHCO_3$ (50 mL) at 0 °C. The solution was neutralized with HCl (1M) and the organic phase separated. The aqueous phase was extracted with CH_2Cl_2 (2 x 50 mL). The combined organic extracts were then dried over anhydrous $MgSO_4$, filtered and concentrated *in vacuo*. The crude product was purified *via* silica-gel chromatography using a Biotage Isolute SPE column (eluent 1:0 → 4:1 PE: EtOAc) to afford **108** as an orange solid (970 mg, 3.1 mmol, 92%). ^{1}H NMR (400 MHz, $CDCl_3$, 298 K) δ_H 7.44 (1H, t, *J* = 7.6 Hz, H_I), 7.30 (1H, d, *J* = 7.6 Hz, H_J) 7.07 (1H, d, *J* = 7.6 Hz, H_H), 6.92-6.86 (2H, m, H_B & H_D), 6.83-6.80 (1H, m, H_C), 2.77 (2H, app. t, *J* = 8.0 Hz, H_G), 2.58 (2H, app. t, *J* = 8.0 Hz, H_E), 2.04-1.95 (2H, m, H_F). ^{13}C NMR (101 MHz, $CDCl_3$, 298 K) δ_C 163.7, 151.1 (d, *J* = 237.3 Hz, J^{1}_{C-F}) 141.7, 141.6 (d, *J* = 14.3 Hz, J^{2}_{C-F}), 138.8, 134.9 (d, *J* = 5.9 Hz, J^{3}_{C-F}), 125.6, 124.7 (d, *J* = 3.3 Hz, J^{4}_{C-F}), 121.7, 117.2 (d, *J* = 2.2 Hz, J^{3}_{C-F}), 115.5 (d, *J* = 17.8 Hz, J^{2}_{C-F}), 37.4, 34.6, 31.4. ^{19}F NMR (376 MHz, $CDCl_3$, 298 K) δ_F -141.1. HR-ESI-MS (CH_3CN): *m/z* = 310.0236 $[M+H]^+$ calc. 310.0237

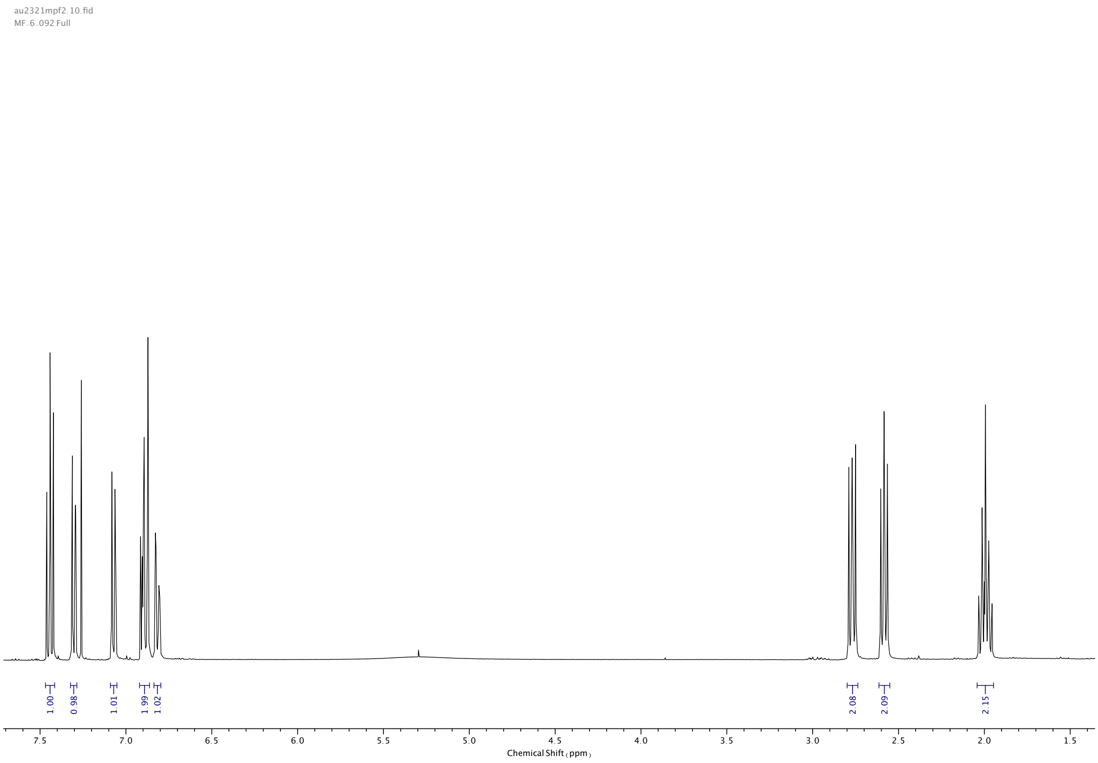

Figure **436**. ^{1}H NMR (CDCl$_3$, 400 MHz) of **108**.

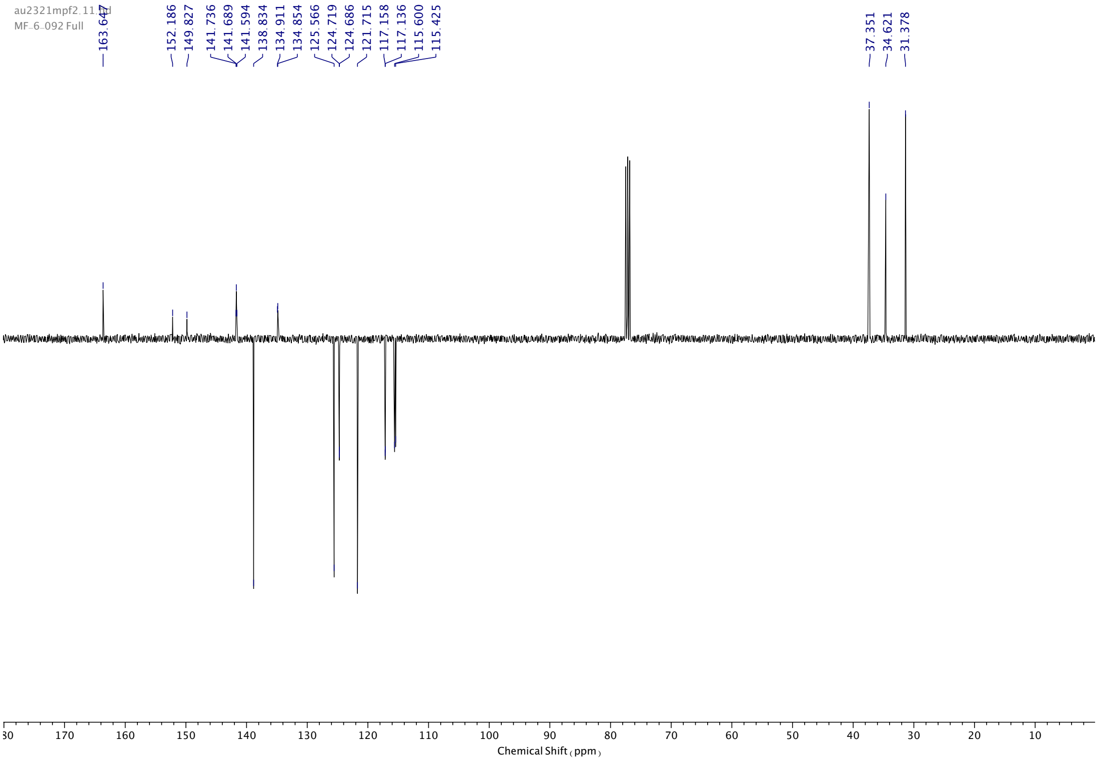

Figure **437**. ^{13}C NMR (CDCl$_3$, 101 MHz) of **108**.

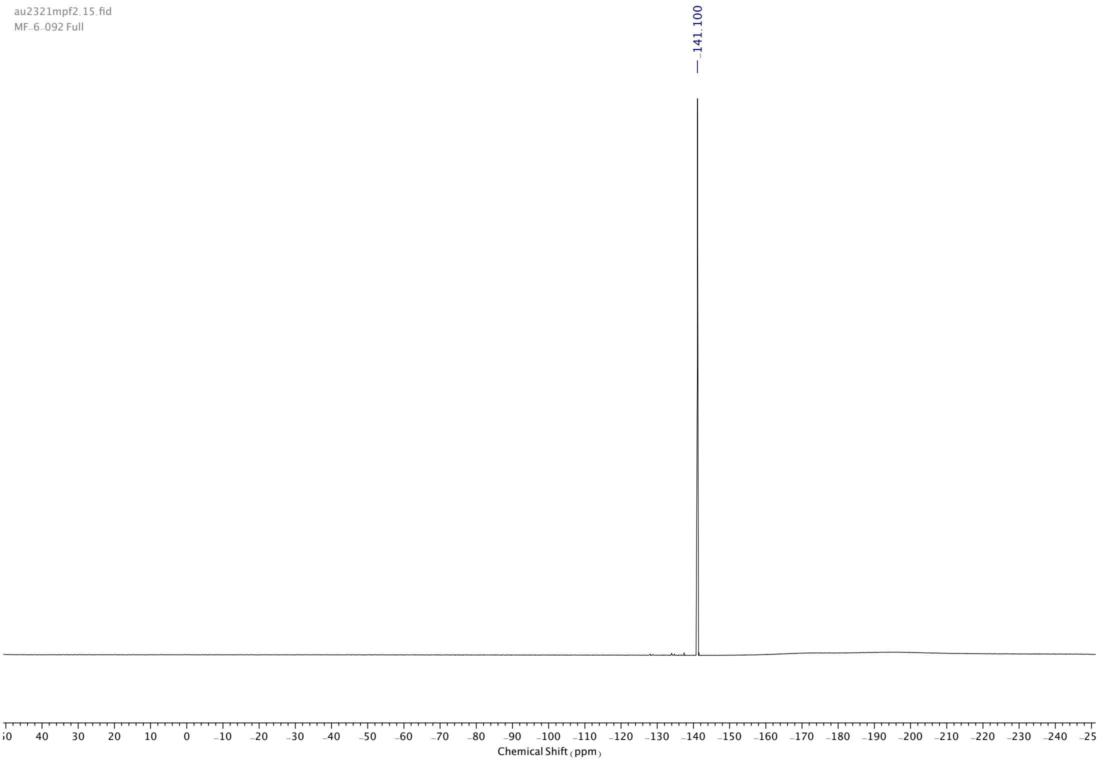

Figure **438**. ^{19}F NMR (CDCl$_3$, 376 MHz) of **108**.

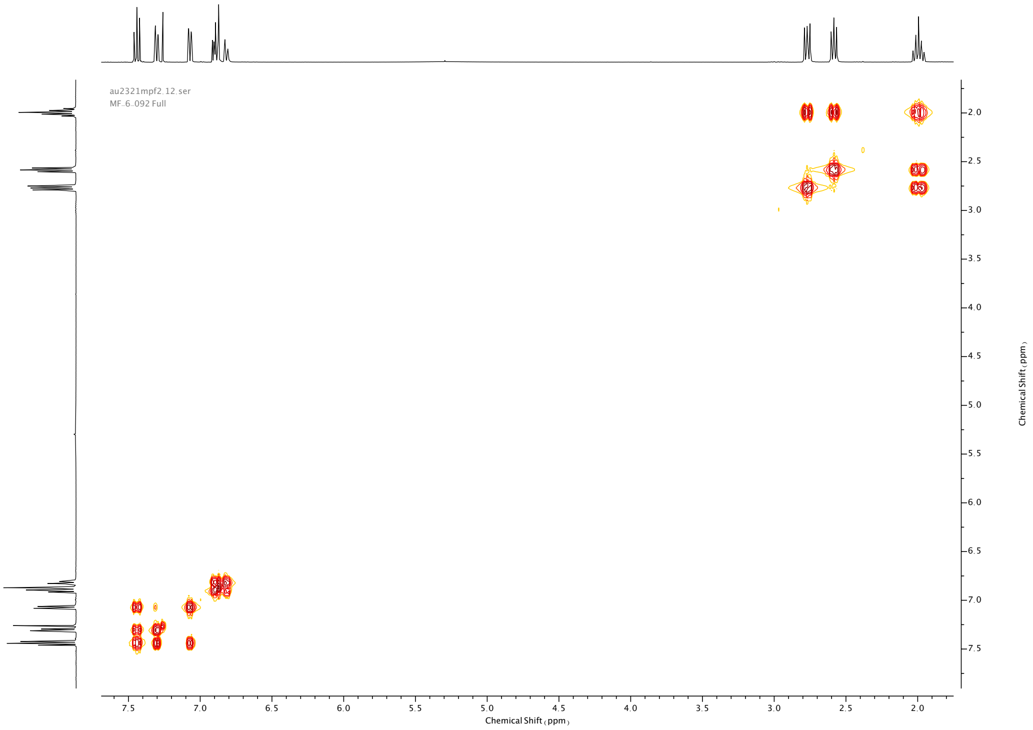

Figure **439**. COSY NMR (CDCl$_3$) of **108**.

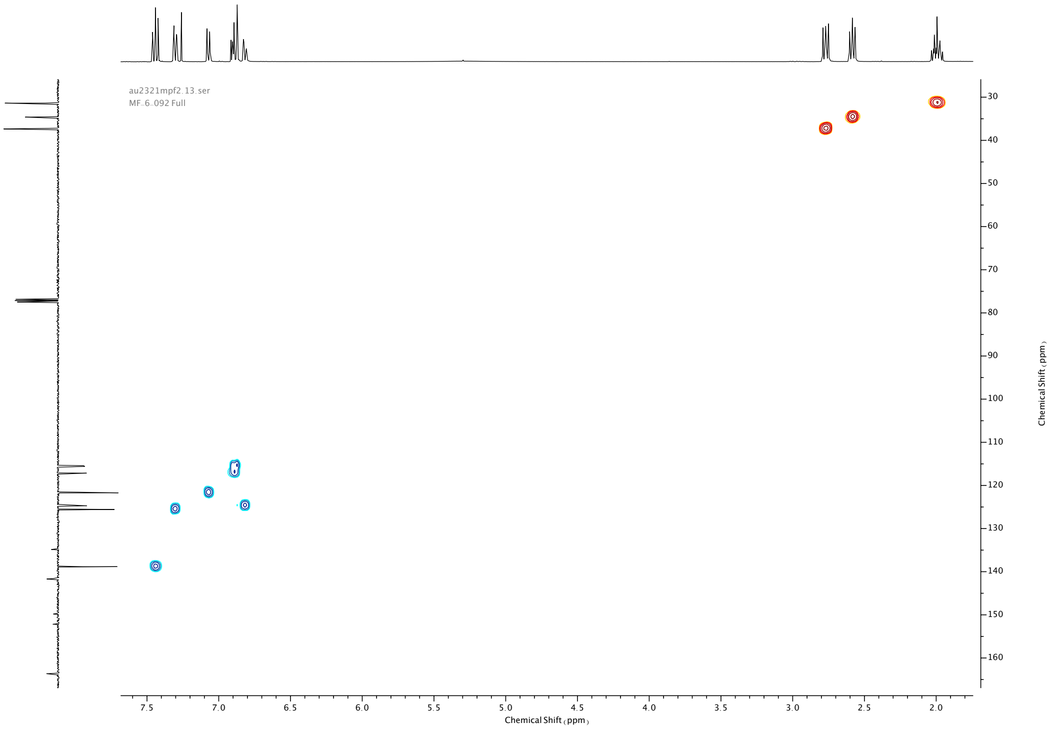

Figure **440**. HSQC NMR ($CDCl_3$) of **108**.

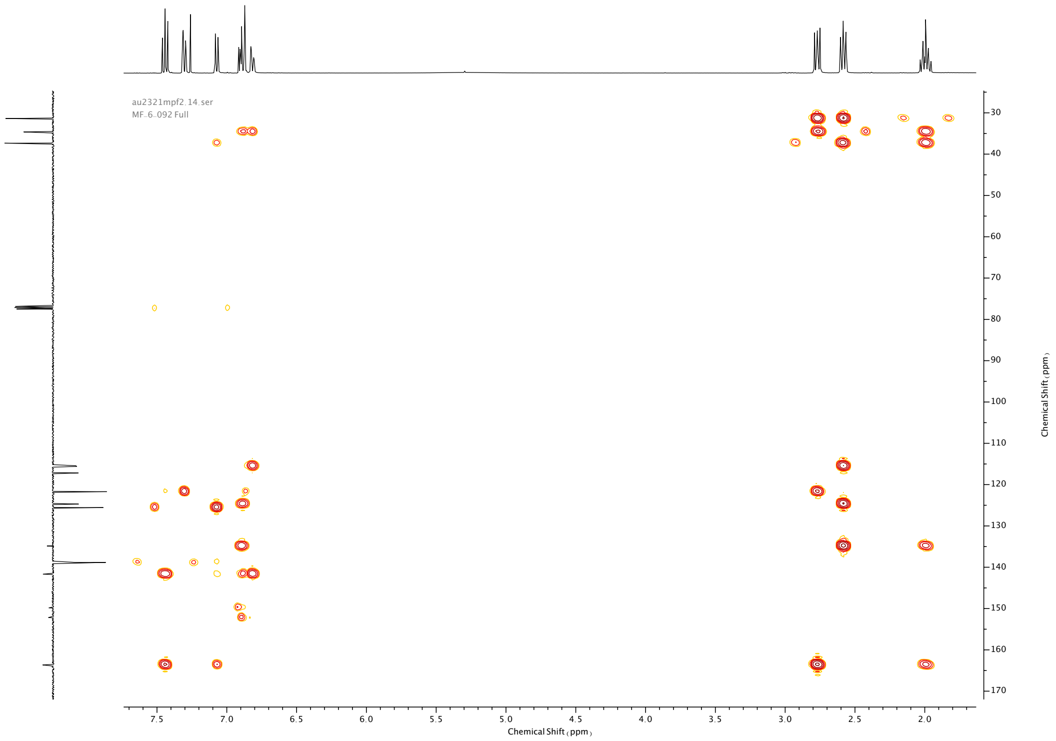

Figure **441**. HMBC NMR ($CDCl_3$) of **108**.

Compound **109**

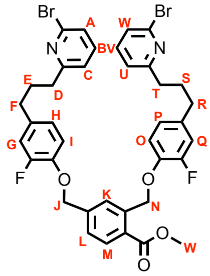

109 was prepared according to general procedure **(1)** from phenol **108** (300 mg, 0.97 mmol) and linker **44** (155 mg, 0.49 mmol). Purification by column chromatography (eluent 49:1 → 19:1 (1:1 PE:CH_2Cl_2): EtOAc) afforded **109** as a colourless oil (320 mg, 0.41 mmol, 84%). ^{1}H NMR (400 MHz, $CDCl_3$, 298 K) δ_H 8.04 (1H, d, *J* = 8.1 Hz, H_M), 7.85 (1H, s, H_K), 7.49 (1H, dd, *J* = 8.0, 1.8 Hz, H_L), 7.43 (1H, t, *J* = 7.7 Hz, H_B or H_V), 7.42 (1H, t, *J* = 7.7 Hz, H_B or H_V), 7.31-7.27 (2H, m, H_A & H_W), 7.07 (1H, dd, *J* = 7.5, 0.9 Hz, H_C or H_U), 7.06 (1H, dd, *J* = 7.6, 0.9 Hz, H_C or H_U), 6.96-6.89 (3H, m, H_G, H_Q & H_I or H_O), 6.88-6.78 (3H, m, H_P, H_H & H_I or H_O), 5.53 (2H, s, H_N), 5.17 (2H, s, H_J), 3.89 (3H, s, H_W), 2.80-2.73 (4H, m, H_D & H_T), 2.62-2.56 (4H, m, H_F & H_R), 2.05-1.95 (4H, m, H_E & H_S). ^{13}C NMR (101 MHz, $CDCl_3$, 298 K) δ_C 167.2, 163.6 (x2), 152.9 (d, *J* = 246.1 Hz, $J^1_{C\text{-}F}$), 152.8 (d, *J* = 246.0 Hz, $J^1_{C\text{-}F}$), 144.9 (d, *J* = 10.9 Hz, $J^2_{C\text{-}F}$), 144.6 (d, *J* = 10.8 Hz, $J^2_{C\text{-}F}$), 142.0, 141.7 (x2), 140.0, 138.8 (x2), 136.1 (d, *J* = 6.0 Hz, $J^3_{C\text{-}F}$), 135.7 (d, *J* = 6.1 Hz, $J^3_{C\text{-}F}$), 131.4, 127.1, 126.0 (x2), 125.5 (x2), 124.2 (d, *J* = 3.4 Hz, $J^3_{C\text{-}F}$), 124.1 (d, *J* = 3.4 Hz, $J^3_{C\text{-}F}$), 121.7 (x2), 116.5 (d, *J* = 18.1 Hz, $J^2_{C\text{-}F}$), 116.4 (d, *J* = 17.9 Hz, $J^2_{C\text{-}F}$), 116.1 (d, *J* = 1.9 Hz, $J^4_{C\text{-}F}$), 115.7 (d, *J* = 2.0 Hz, $J^4_{C\text{-}F}$), 71.1, 69.6, 52.2, 37.4 (x2), 34.6 (x2), 31.3, 31.2. ^{19}F NMR (376 MHz, $CDCl_3$, 298 K) δ_F -134.2, -134.6. HR-ESI-MS (CH_3CN): *m/z* = 779.0924 $[M+H]^+$ calc. 779.0926.

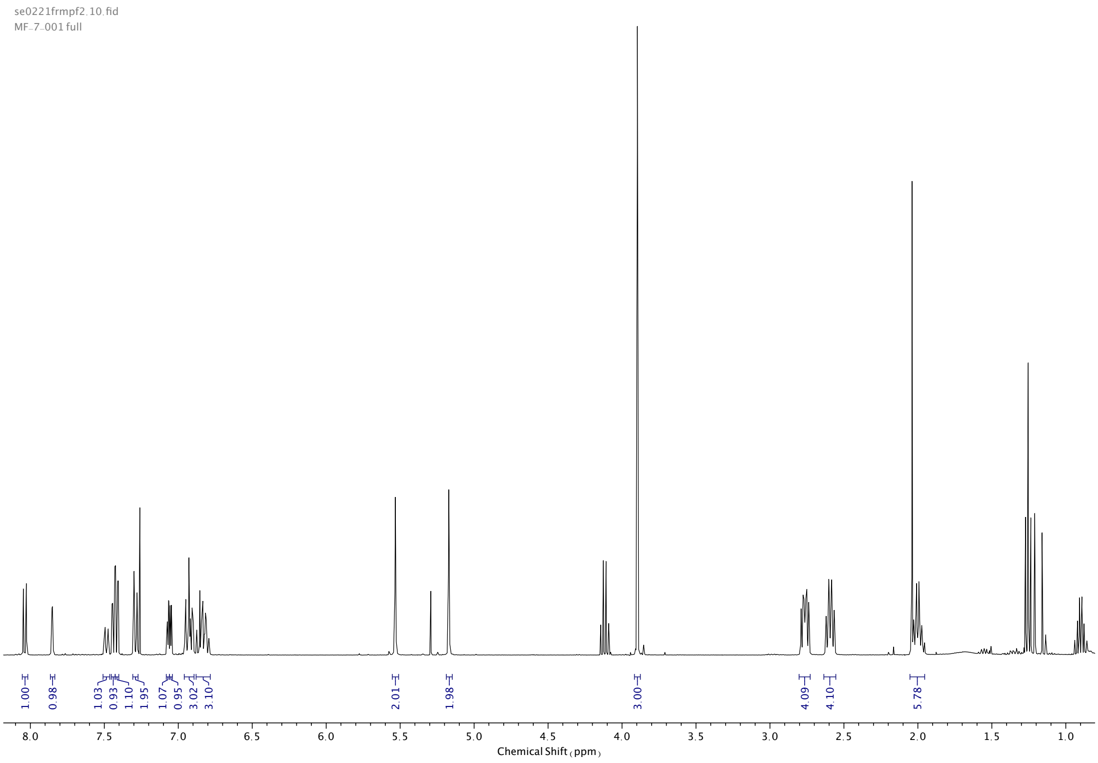

Figure **442**. ^{1}H NMR ($CDCl_3$, 400 MHz) of **109**.

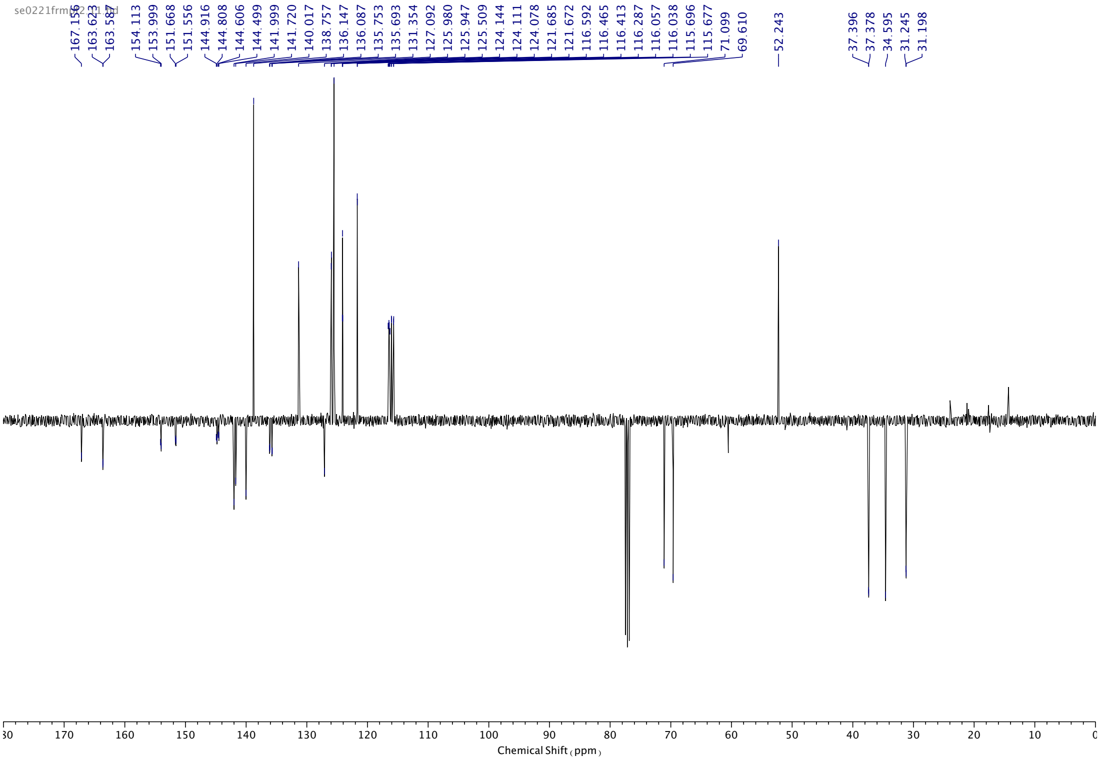

Figure **443**. ^{13}C NMR ($CDCl_3$, 101 MHz) of **109**.

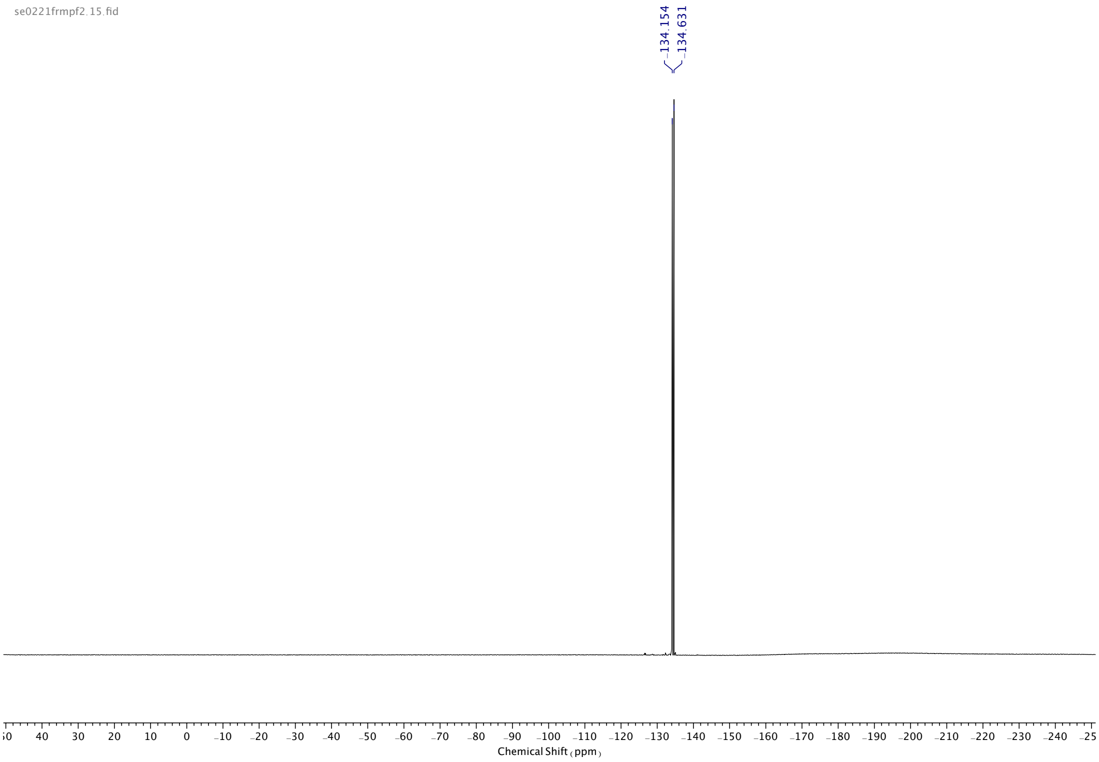

Figure **444**. ^{19}F NMR ($CDCl_3$, 376 MHz) of **109**.

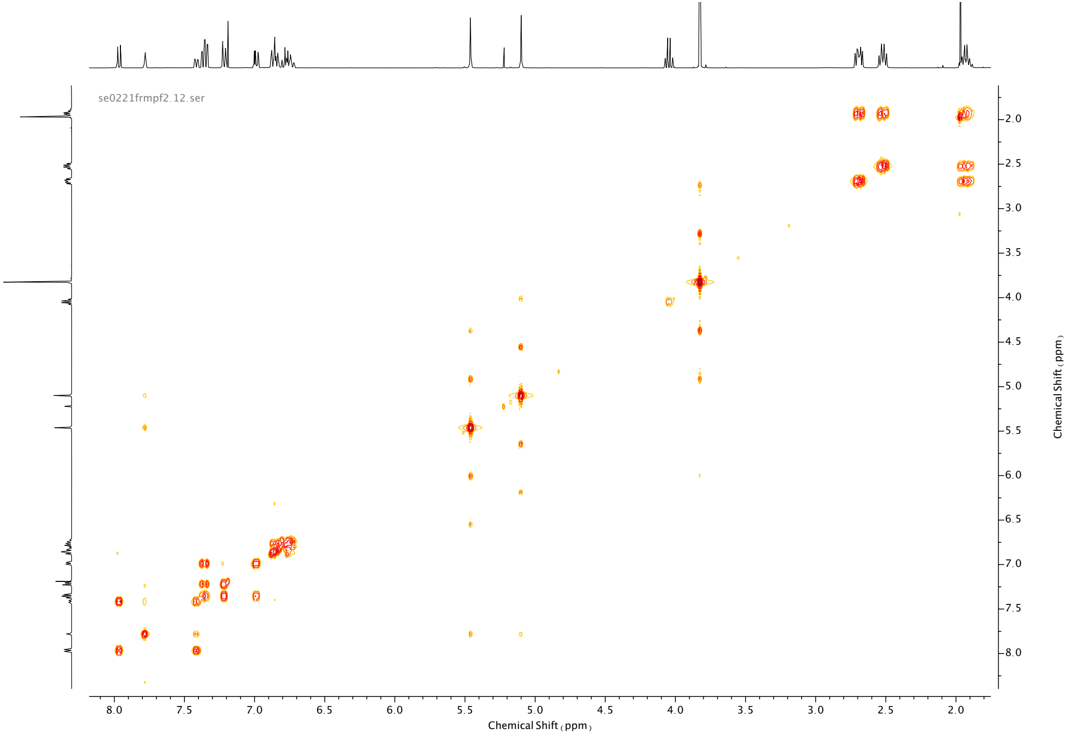

Figure **445**. COSY NMR ($CDCl_3$) of **109**.

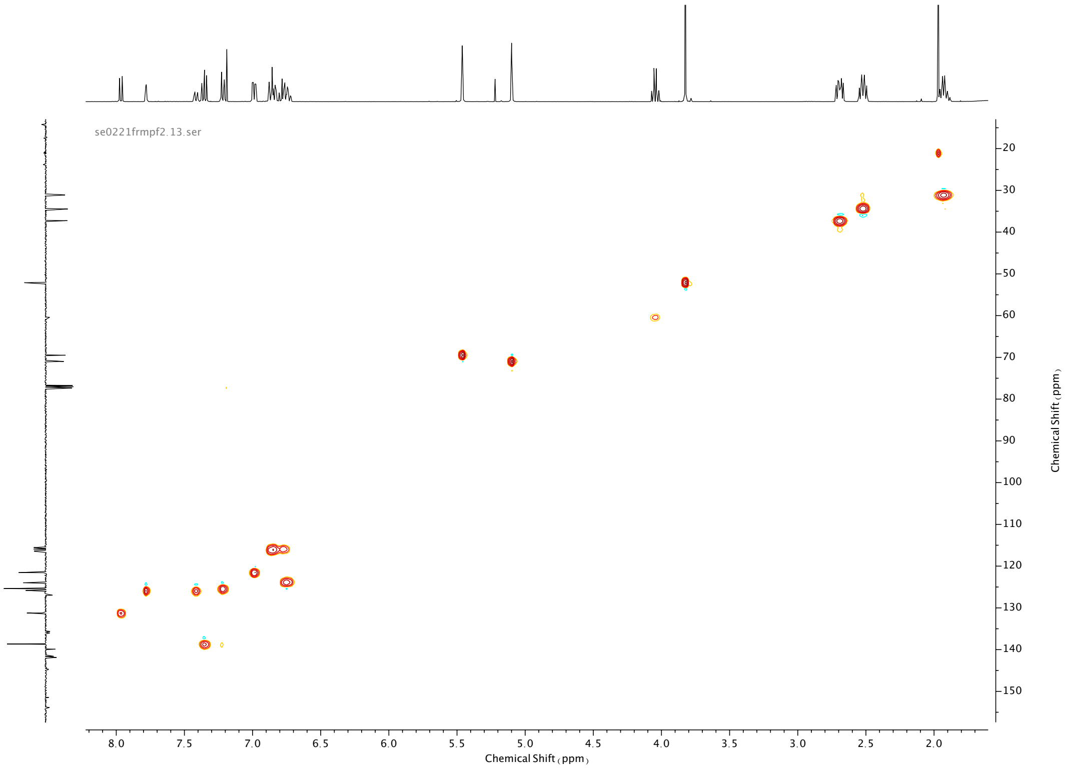

Figure **446**. HSQC NMR (CDCl$_3$) of **109**.

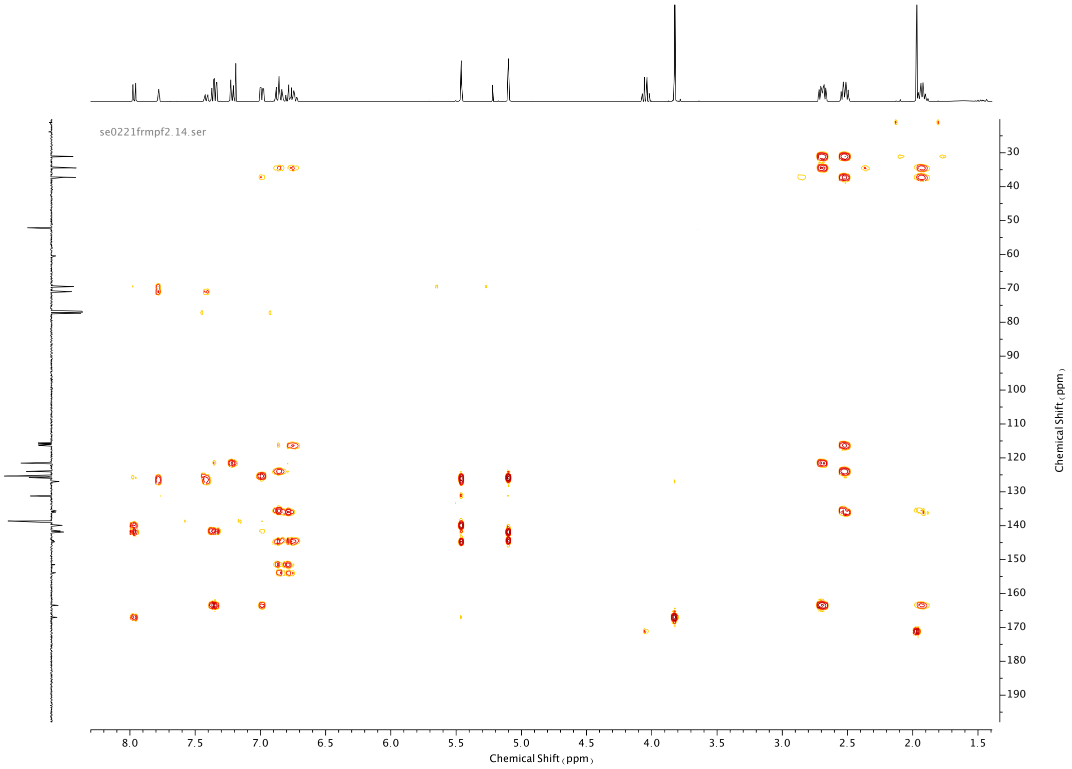

Figure **447**. HMBC NMR (CDCl$_3$) of **109**.

Compound **110**

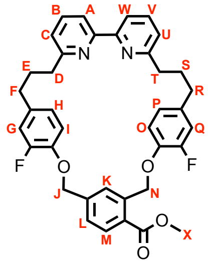

110 was prepared according to general procedure **(2)** from macrocycle precursor **109** (330 mg, 0.42 mmol). Purification by column chromatography (eluent 1:0 → 9:1 CH_2Cl_2: Et_2O) afforded **110** as a white foam (87 mg, 0.14 mmol, 34%). ^1H NMR (400 MHz, $CDCl_3$, 298 K) δ_H 8.00 (1H, d, *J* = 8.0 Hz, H_M), 7.78 (1H, d, *J* = 7.7 Hz, H_A or H_W), 7.75 (1H, d, *J* = 7.7 Hz, H_A or H_W), 7.65-7.60 (2H, m, H_K & H_B or H_V), 7.60-7.55 (1H, m, H_B or H_V), 7.36 (1H, dd, *J* = 8.0, 1.7 Hz, H_L), 7.08 (1H, dd, *J* = 7.7, 0.8 Hz, H_C or H_U), 7.04 (1H, dd, *J* = 7.7, 0.8 Hz, H_C or H_U), 6.87 (1H, dd, *J* = 12.3 Hz, 2.1 Hz, H_Q), 6.80 (1H, dd, *J* = 12.3 Hz, 2.1 Hz, H_G), 6.71-6.66 (1H, m, H_P), 6.60 (1H, t, *J* = 8.5 Hz, H_O), 6.57-6.48 (2H, m, H_H & H_I), 5.58 (2H, s, H_N), 5.07 (2H, s, H_J), 3.90 (3H, s, H_X), 2.93-2.86 (4H, m, H_D & H_T), 2.66-2.56 (4H, m, H_F & H_R), 2.17-2.08 (4H, m, H_E & H_S). ^{13}C NMR (101 MHz, $CDCl_3$, 298 K) δ_C 167.1, 161.8, 161.7, 156.5 (x2), 152.8 (d, *J* = 245.3 Hz, $J^1_{C\text{-}F}$), 152.6 (d, *J* = 245.0 Hz, $J^1_{C\text{-}F}$), 144.2 (d, *J* = 10.8 Hz, $J^2_{C\text{-}F}$), 143.8 (d, *J* = 10.8 Hz, $J^2_{C\text{-}F}$), 142.2, 140.4, 136.9, 136.8 (d, *J* = 6.0 Hz, $J^3_{C\text{-}F}$), 136.4 (d, *J* = 6.0 Hz, $J^3_{C\text{-}F}$), 131.4, 126.9 (x2), 126.0, 125.9, 124.1 (d, *J* = 3.4 Hz, $J^4_{C\text{-}F}$), 124.0 (d, *J* = 3.4 Hz, $J^4_{C\text{-}F}$), 122.7, 122.6, 119.2 (x2), 116.7 (d, *J* = 18.1 Hz, $J^2_{C\text{-}F}$), 116.6 (d, *J* = 1.7 Hz, $J^3_{C\text{-}F}$), 116.5 (d, *J* = 18.0 Hz, $J^2_{C\text{-}F}$), 115.7 (d, *J* = 1.7 Hz, $J^3_{C\text{-}F}$), 71.2, 69.7, 52.2, 37.7 (x2), 34.4, 34.3, 31.1, 30.6. ^{19}F NMR (376 MHz, $CDCl_3$, 298 K) δ_F -134.5, -134.9. HR-ESI-MS (CH_3CN): *m/z* = 621.2561 $[M+H]^+$ calc. 621.2559.

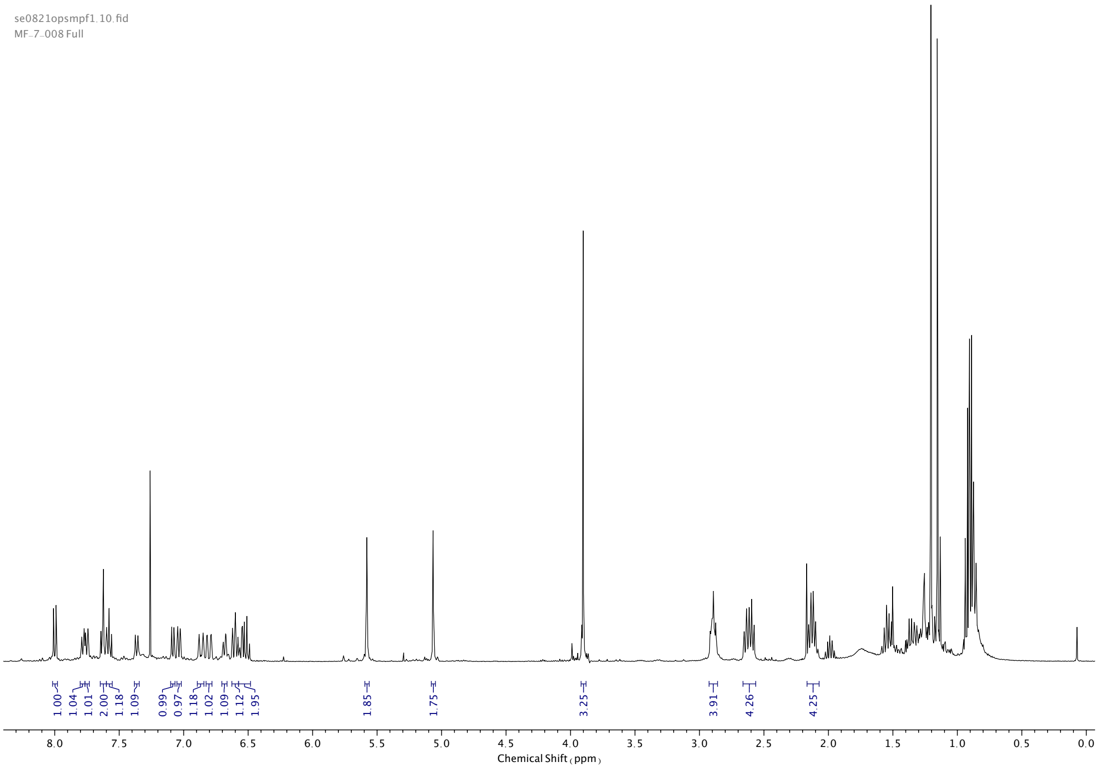

Figure **448**. ^{1}H NMR ($CDCl_3$, 400 MHz) of **110**.

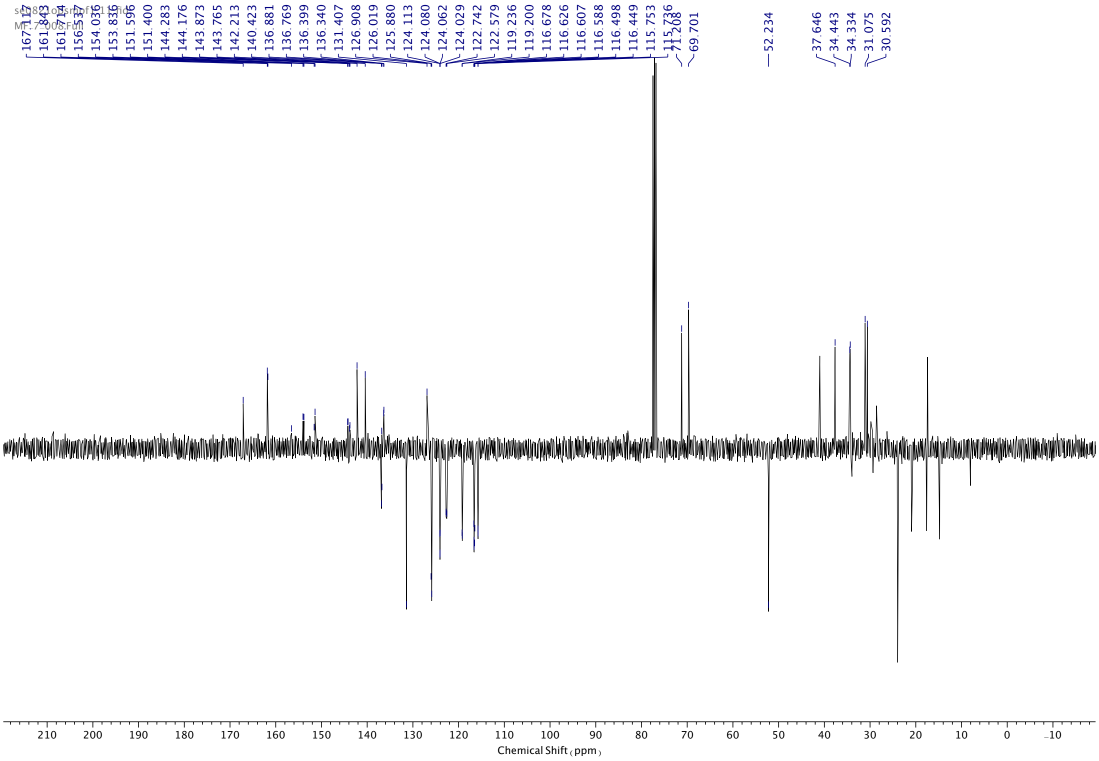

Figure **449**. ^{13}C NMR ($CDCl_3$, 101 MHz) of **110**.

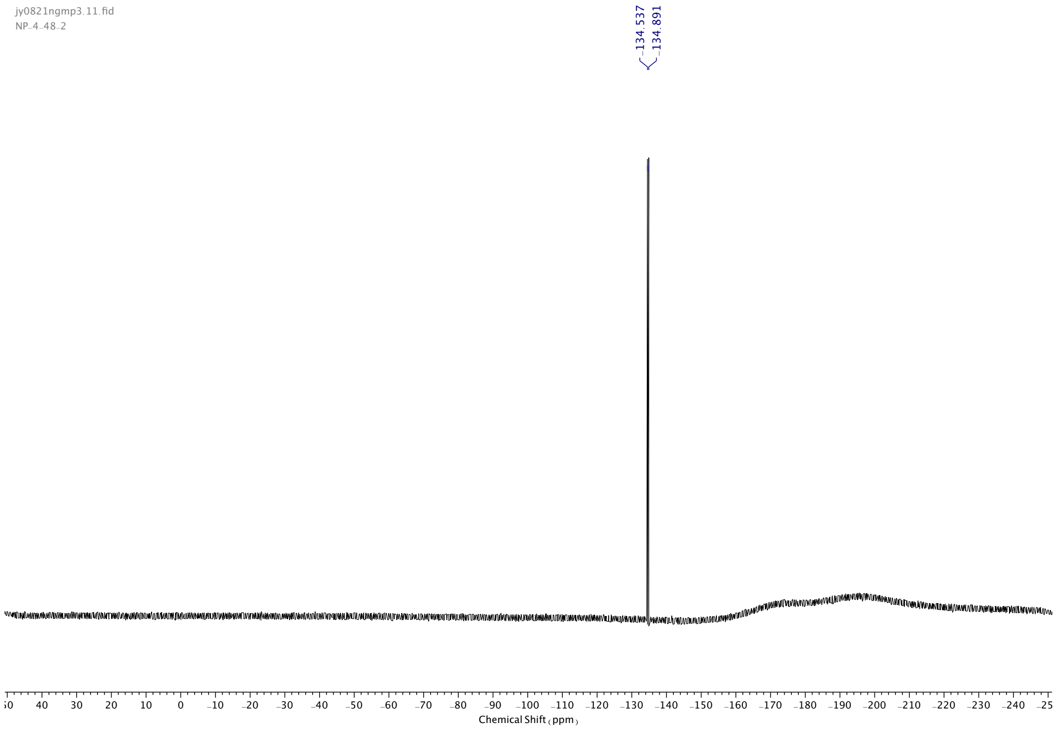

Figure **450**. ^{19}F NMR (CDCl$_3$, 376 MHz) of **110**.

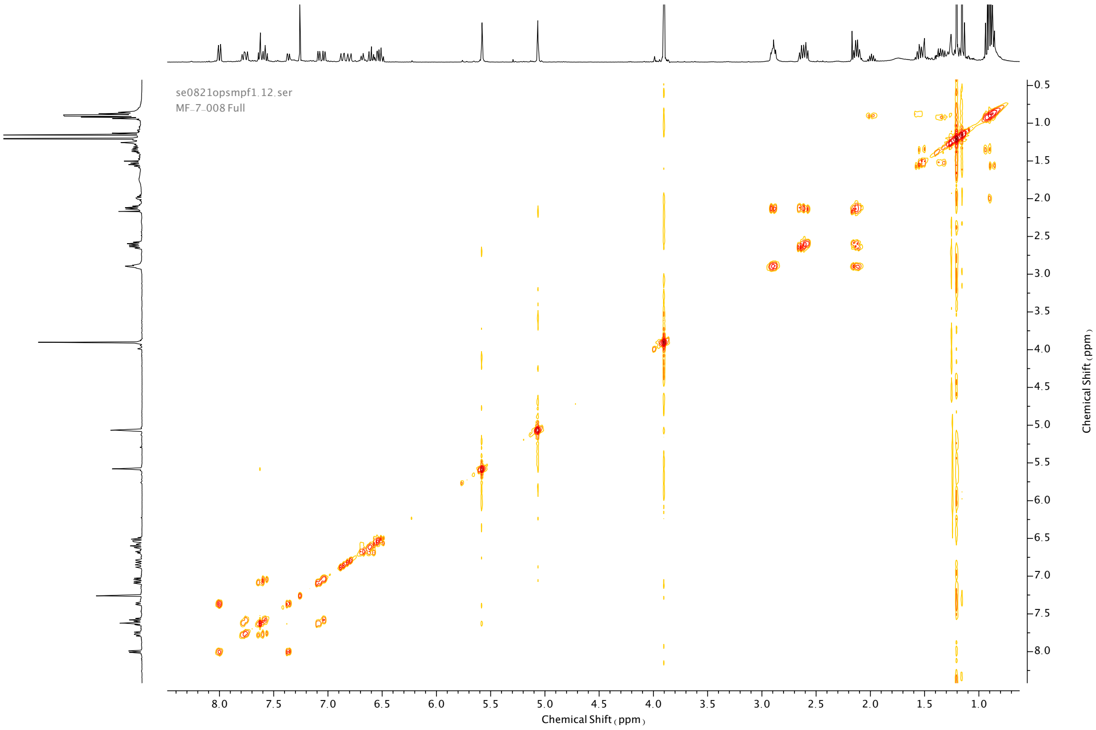

Figure **451**. COSY NMR (CDCl$_3$) of **110**.

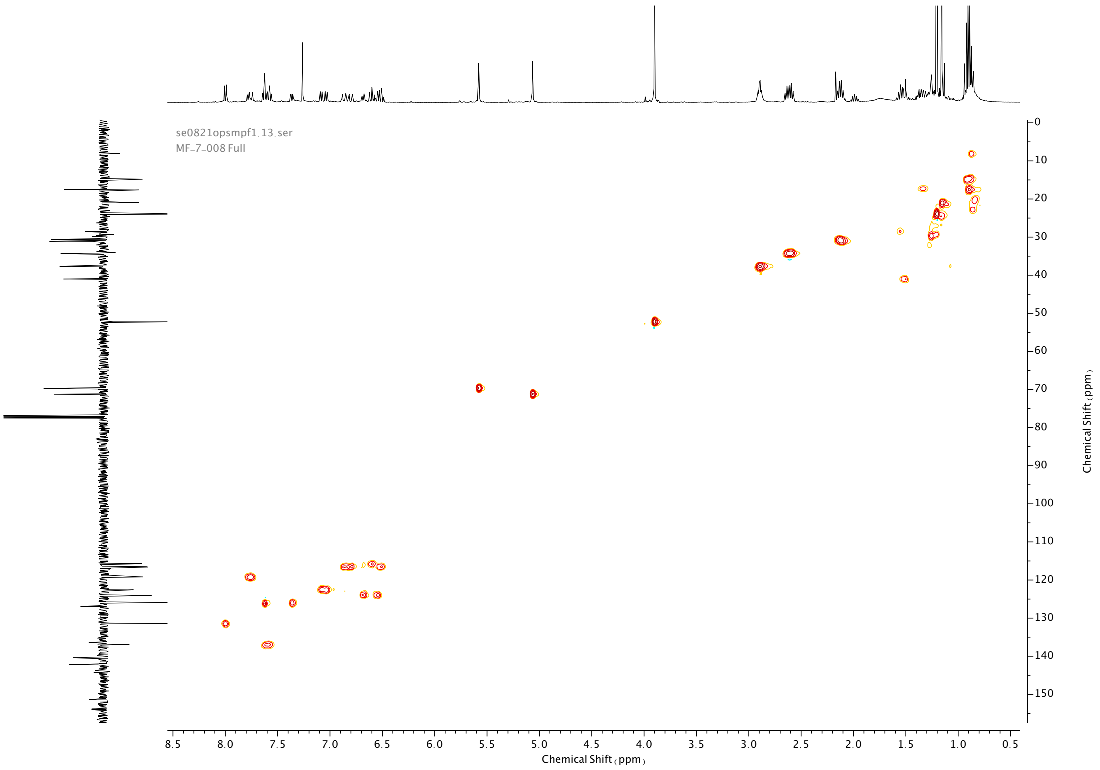

Figure **452**. HSQC NMR ($CDCl_3$) of **110**.

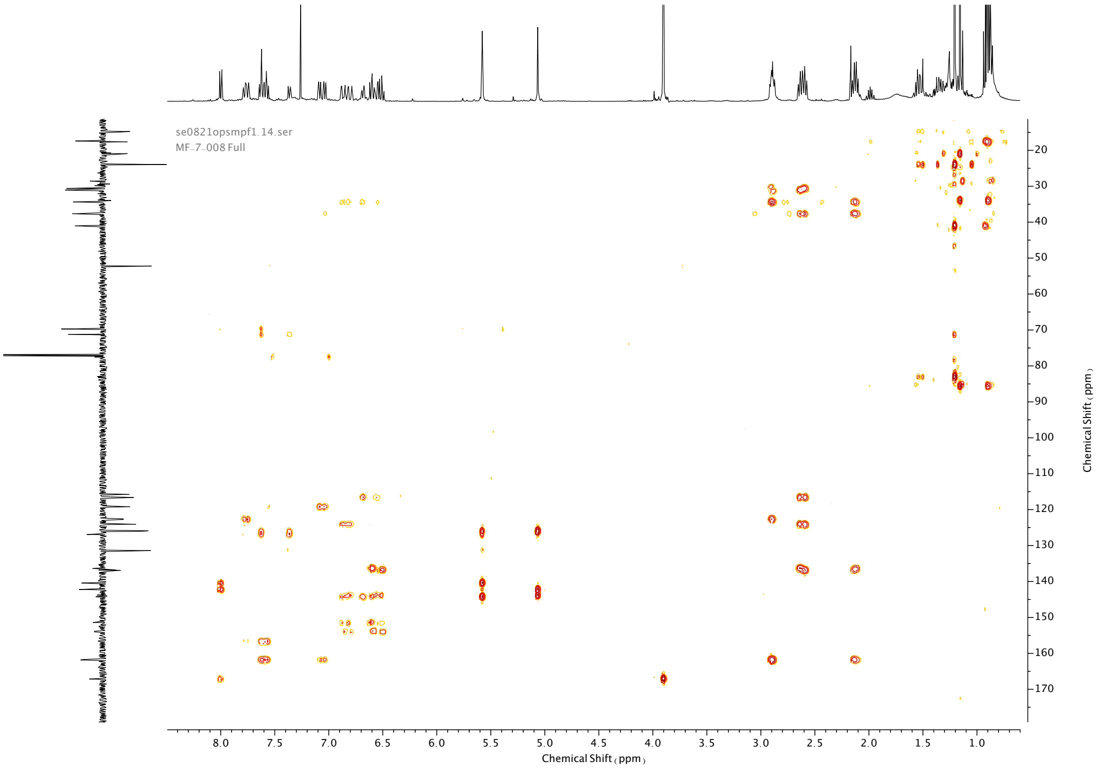

Figure **453**. HMBC NMR ($CDCl_3$) of **110**.

Compound **111**

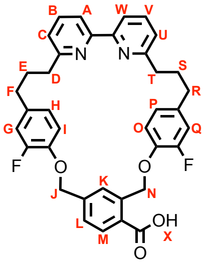

111 was prepared according to general procedure **(3)** from macrocycle **110** (75 mg, 0.12 mmol). **111** was achieved as a yellow solid (67 mg, 0.11 mmol, 92%) and used in the next step without further purification. M.p. 204-206 °C. ^{1}H NMR (400 MHz, DMSO-d$_6$, 298 K) δ_H 7.90-7.81 (3H, m, H_M, H_A & H_W), 7.74-7.64 (2H, m, H_B & H_V), 7.45 (1H, s, H_K), 7.33 (1H, d, *J* = 7.6 Hz, H_L), 7.20-7.12 (2H, m, H_C & H_U), 6.92-6.61 (6H, m, H_G & H_Q, H_H & H_P, H_I & H_O), 5.55 (2H, s, H_J or H_N), 5.07 (2H, s, H_J or H_N), 2.83-2.74 (4H, m, H_D & H_T), 2.61-2.53 (4H, m, H_F & H_R), 2.10-2.00 (4H, m, H_E & H_S). ^{13}C NMR (400 MHz, DMSO-d$_6$, 298 K) δ_C 161.0, 160.9, 155.7 (x2), 155.6 (x2), 151.6 ((d, *J* = 243.7 Hz, J^1_{C-F}) x 2), 143.7 (d, *J* = 10.3 Hz, J^2_{C-F}), 143.3 (d, *J* = 10.5 Hz, J^2_{C-F}), 136.9, 136.8, 135.6 (d, *J* = 6.2 Hz, J^3_{C-F}), 135.4 (d, *J* = 6.0 Hz, J^3_{C-F}), 130.5 (x2), 126.0, 124.2 (d, *J* = 3.1 Hz, J^4_{C-F}), 124.1 (d, *J* = 3.1 Hz, J^4_{C-F}), 122.8, 122.6, 118.4 ((d, *J* = 2.9 Hz, J^3_{C-F}) x 2), 115.6 ((d, *J* = 17.3 Hz, J^2_{C-F}) x 2), 115.5 (x2), 115.1, 69.8, 68.7, 36.6 (x2), 33.3 (x2), 30.4, 30.2.[9] ^{19}F NMR (376 MHz, CDCl$_3$, 298 K) δ_F -134.0 (x2). HR-ESI-MS (CH$_3$CN): *m/z* = 607.2400 [M+H]$^+$ calc. 607.2403.

---

[9] ^{13}C signal for carboxylate position not observed

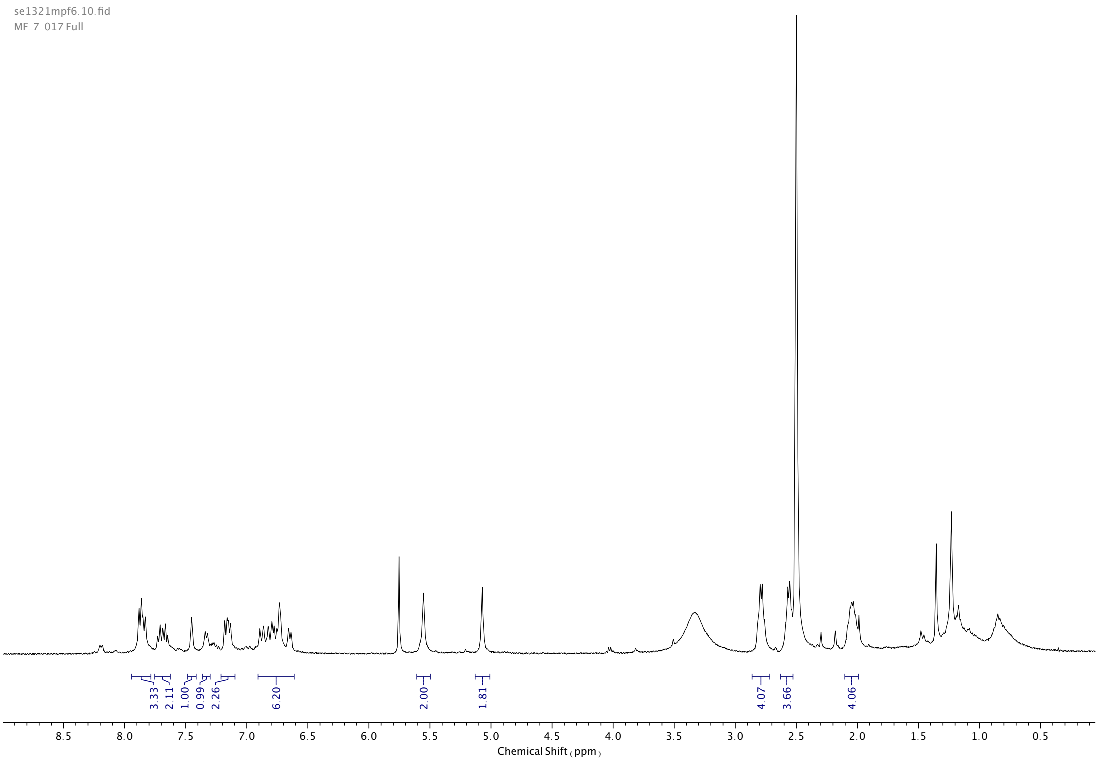

Figure **454**. ^{1}H NMR (DMSO-d$_6$, 400 MHz) of **111**.

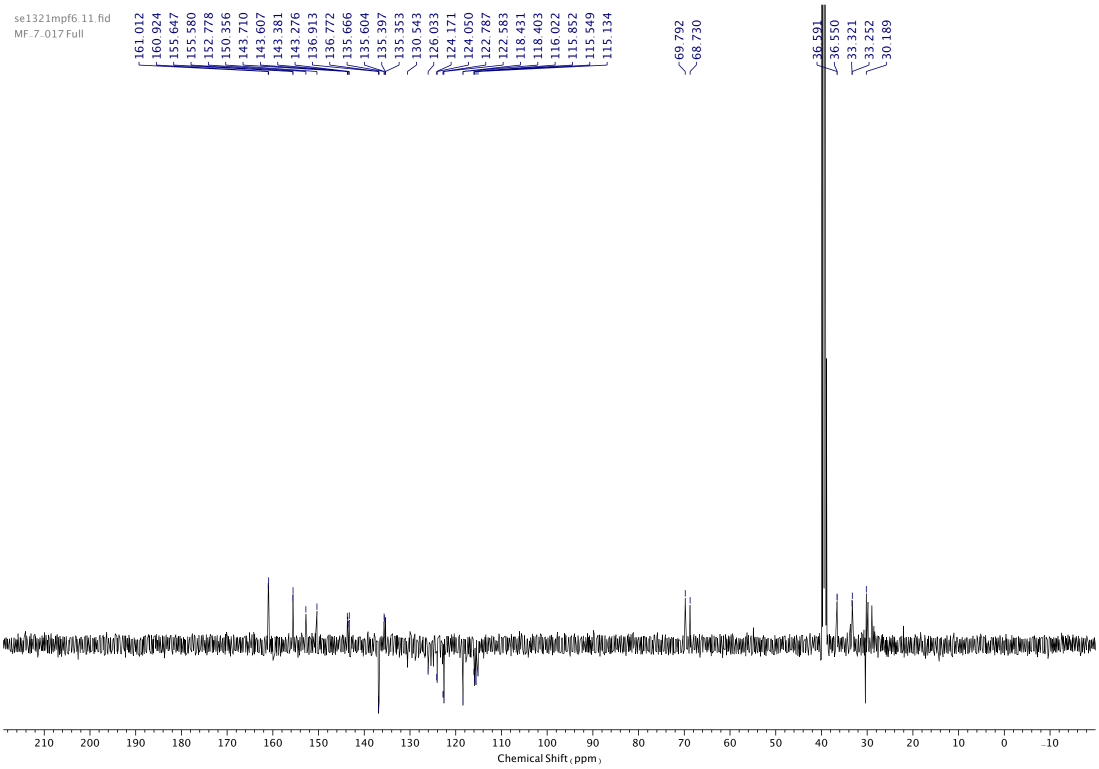

Figure **455**. ^{13}C NMR (DMSO-d$_6$, 101 MHz) of **111**.

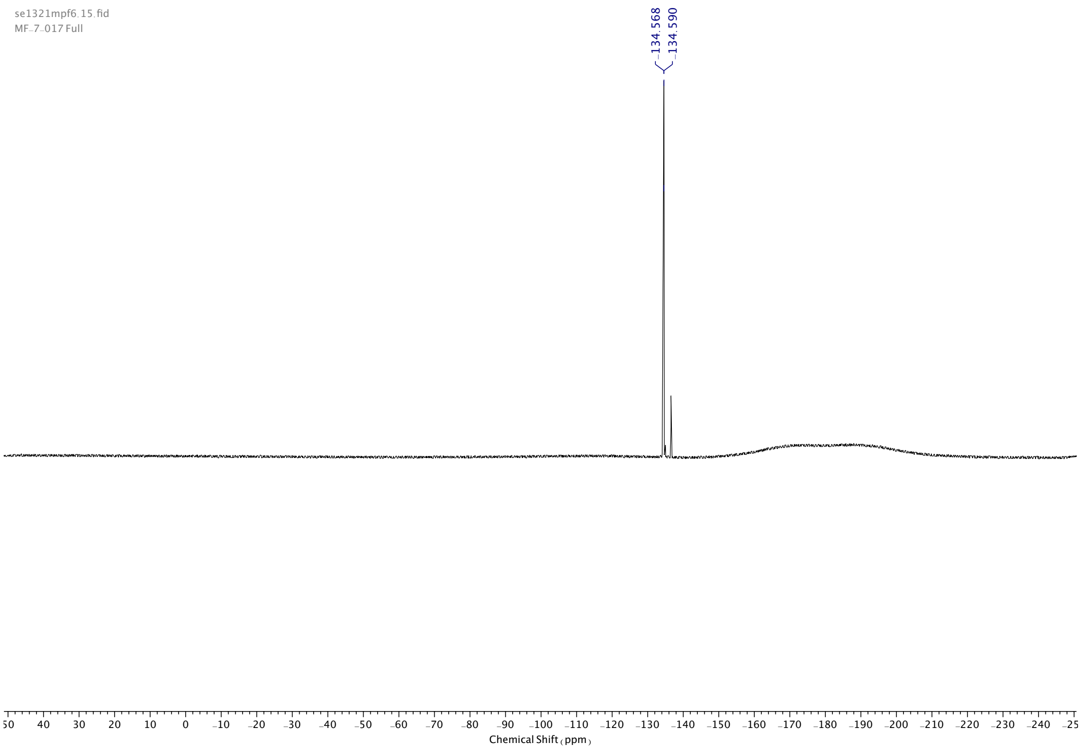

Figure **456**. ^{19}F NMR (DMSO-d$_6$, 376 MHz) of **111**.

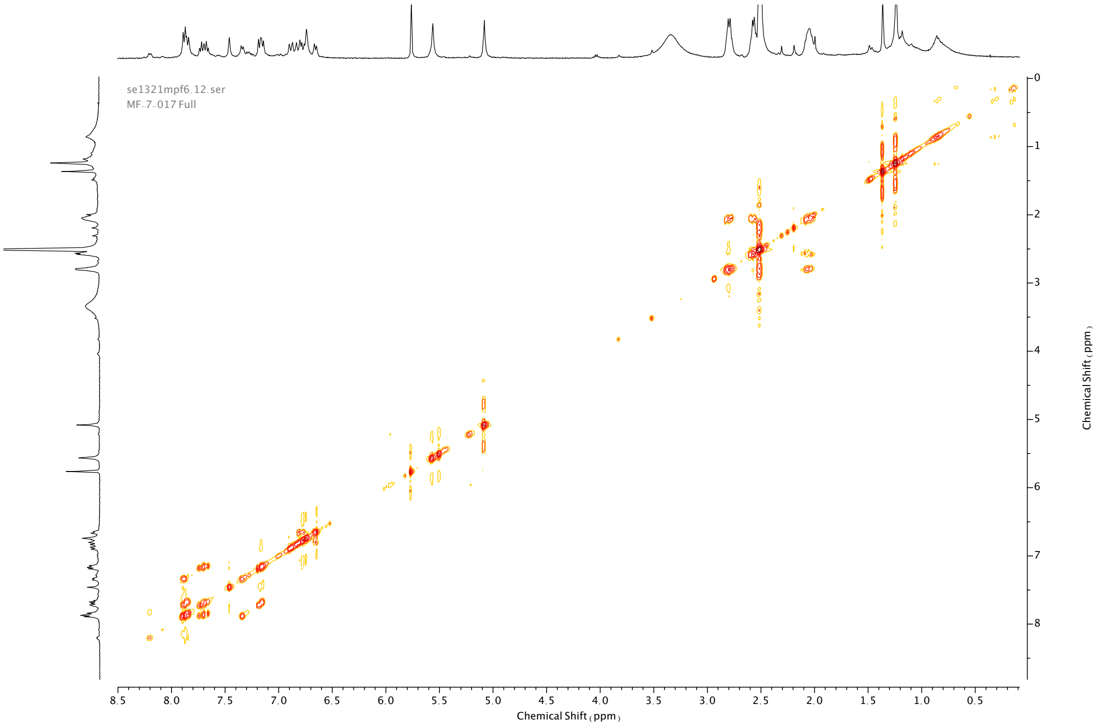

Figure **457**. COSY NMR (DMSO-d$_6$) of **111**.

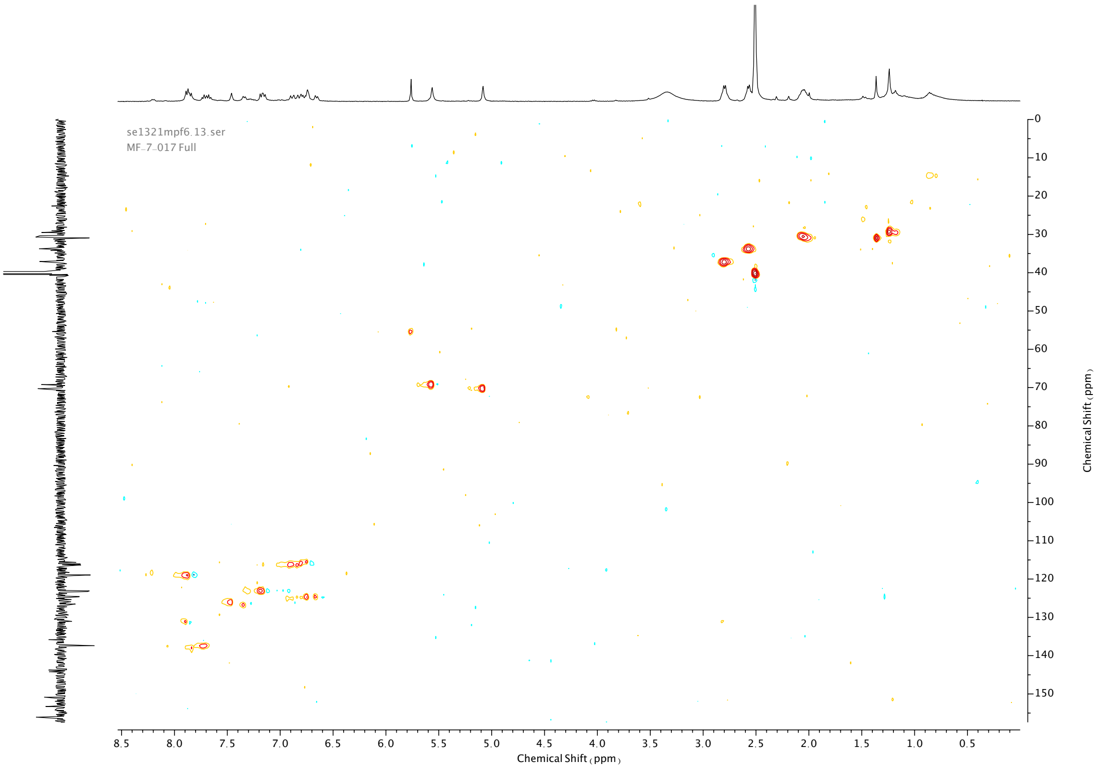

Figure **458**. HSQC NMR (DMSO-d$_6$) of **111**.

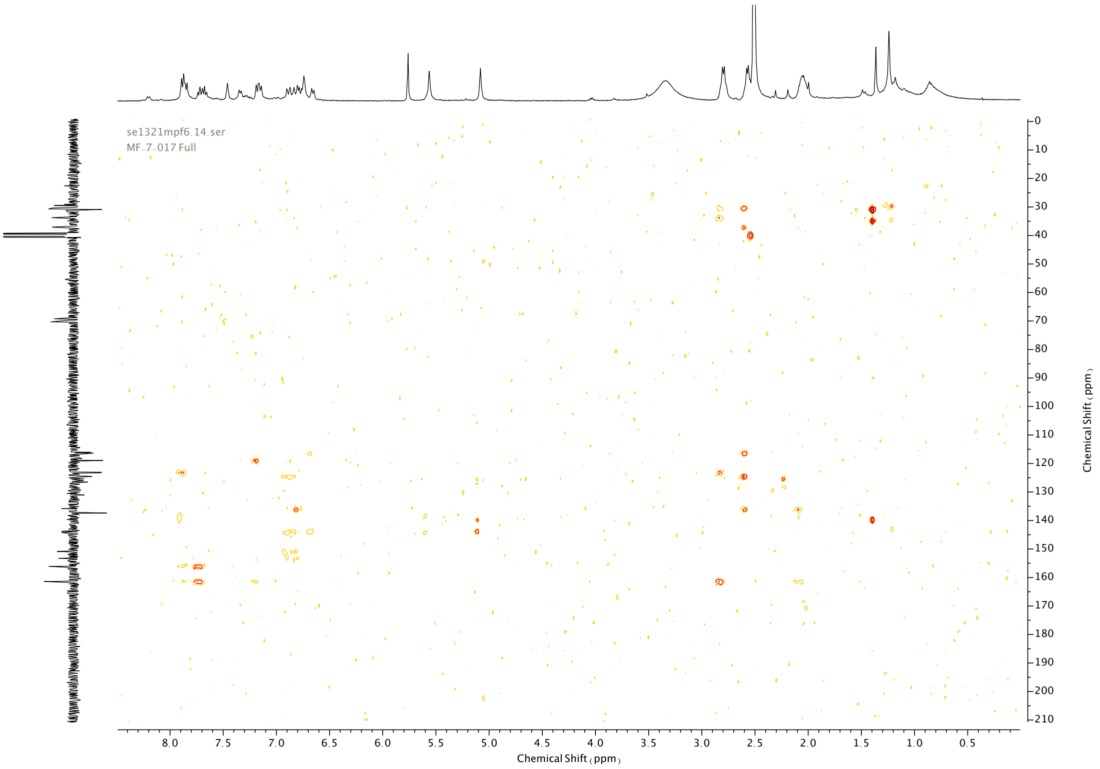

Figure **459**. HMBC NMR (DMSO-d$_6$) of **111**.

Compound **112**

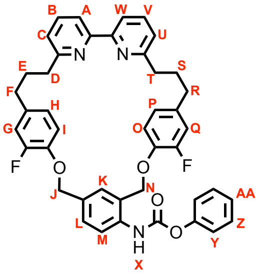

112 was prepared according to general procedure **(5)** from macrocycle **111** (44 mg, 0.073 mmol). Purification by column chromatography (eluent 1:0 → 19:1 CH_2Cl_2: Et_2O) afforded **112** as a white foam (20 mg, 0.029 mmol, 42%). ^{1}H NMR (400 MHz, $CDCl_3$, 298 K) δ_H 8.11 (1H, br. s, N-H$_X$), 7.99 (1H, d, *J* = 8.1 Hz, H$_M$), 7.89 (2H, app. t, *J* = 7.5 Hz, H$_A$ & H$_W$), 7.62 (1H, t, *J* = 7.7 Hz, H$_B$ or H$_V$), 7.59 (1H, t, *J* = 7.7 Hz, H$_B$ or H$_V$), 7.43-7.37 (2H, m, H$_Z$), 7.31 (1H, dd, *J* = 8.5, 1.9 Hz, H$_L$), 7.26-7.20 (3H, m, H$_Y$ & H$_{AA}$), 7.09 (1H, d, *J* = 1.9 Hz, H$_K$), 7.04 (2H, app. t, *J* = 7.7 Hz, H$_C$ & H$_U$), 6.84 (1H, dd, *J* = 12.1, 2.0 Hz, H$_G$ or H$_Q$), 6.77 (1H, dd, *J* = 12.2, 2.0 Hz, H$_G$ or H$_Q$), 6.67 (1H, t, *J* = 8.3 Hz, H$_I$ or H$_O$), 6.65-6.59 (2H, m, H$_H$ & H$_P$), 6.55 (1H, t, *J* = 8.4 Hz, H$_I$ or H$_O$), 5.07 (2H, s, H$_J$ or H$_N$), 4.98 (2H, s, H$_J$ or H$_N$), 2.92-2.82 (4H, m, H$_D$ & H$_T$), 2.66-2.59 (4H, m, H$_F$ & H$_R$), 2.18-2.09 (4H, m, H$_E$ & H$_S$). ^{13}C NMR (101 MHz, $CDCl_3$, 298 K) δ_C 161.4 (x2), 156.4 (x2), 154.7, 154.4, 153.5 (d, *J* = 245.5 Hz, $J^1_{C\text{-}F}$), 153.4 (d, *J* = 245.3 Hz, $J^1_{C\text{-}F}$), 152.1, 143.6 (d, *J* = 10.8 Hz, $J^2_{C\text{-}F}$), 142.6 (d, *J* = 10.8 Hz, $J^2_{C\text{-}F}$), 138.2 (d, *J* = 6.2 Hz, $J^3_{C\text{-}F}$), 137.2 (x2), 137.0 (d, *J* = 6.1 Hz, $J^3_{C\text{-}F}$), 136.9 (x2), 132.3, 129.5, 129.4, 129.2, 125.8, 124.4 (d, *J* = 3.3 Hz, $J^4_{C\text{-}F}$), 124.2 (d, *J* = 3.3 Hz, $J^4_{C\text{-}F}$), 122.8 (x2), 121.8, 119.0 (x2), 118.4 (s, $J^3_{C\text{-}F}$), 117.8 (s, $J^3_{C\text{-}F}$), 116.6 (d, *J* = 18.1 Hz, $J^2_{C\text{-}F}$), 116.5 (d, *J* = 18.1 Hz, $J^2_{C\text{-}F}$), 71.8, 71.7, 37.7, 37.6, 34.6 (x2), 30.60 (x2). ^{19}F NMR (376 MHz, $CDCl_3$, 298 K) δ_F -134.0 (x2). HR-ESI-MS (CH_3CN): *m/z* = 698.2823 [M+H]$^+$ calc. 698.2825.

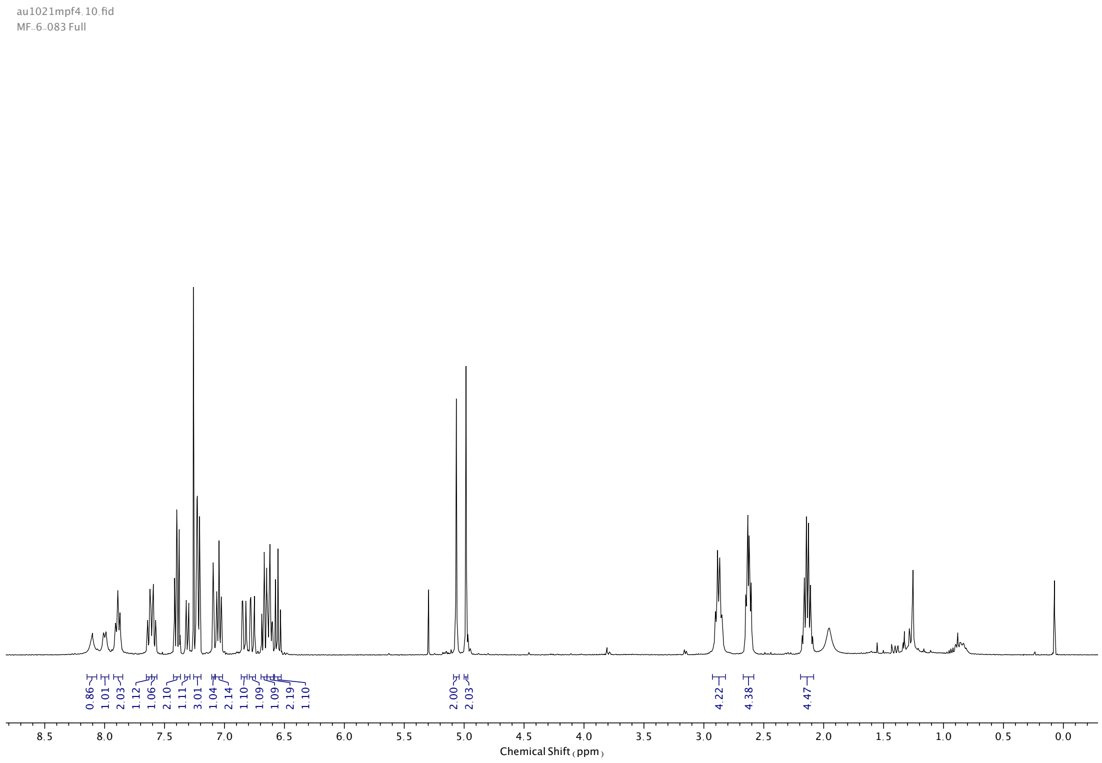

Figure **460**. ^{1}H NMR (CDCl$_3$, 400 MHz) of **112**.

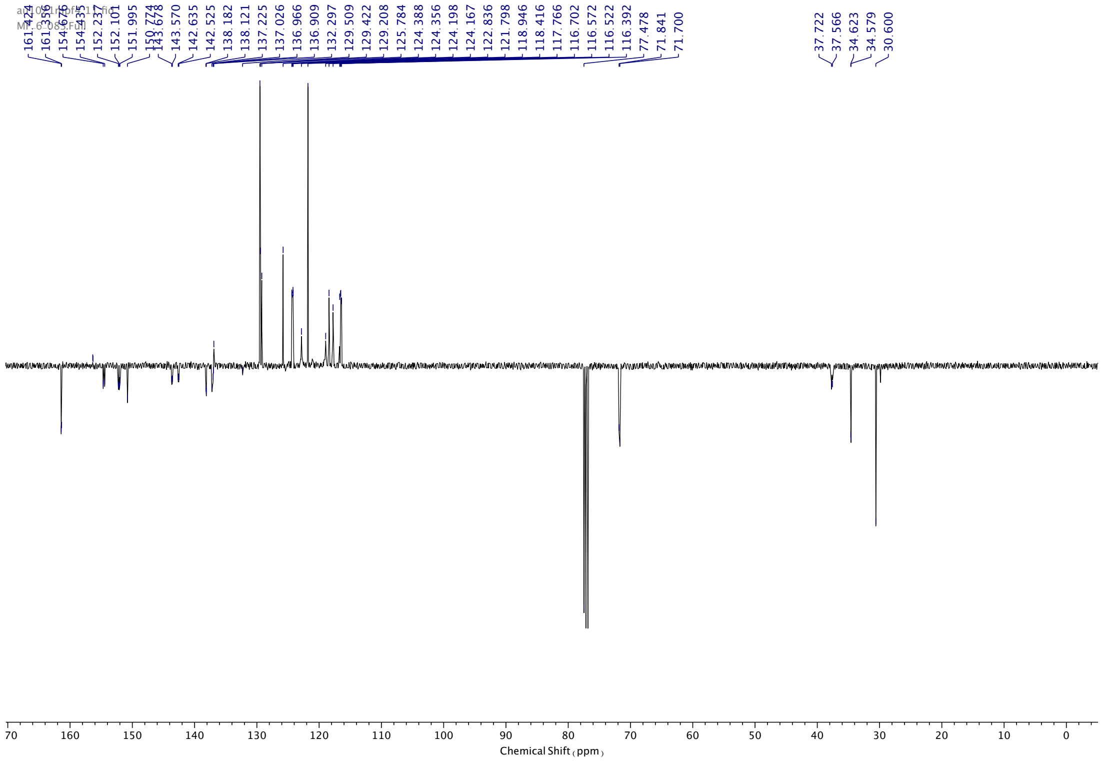

Figure **461**. ^{13}C NMR (CDCl$_3$, 101 MHz) of **112**.

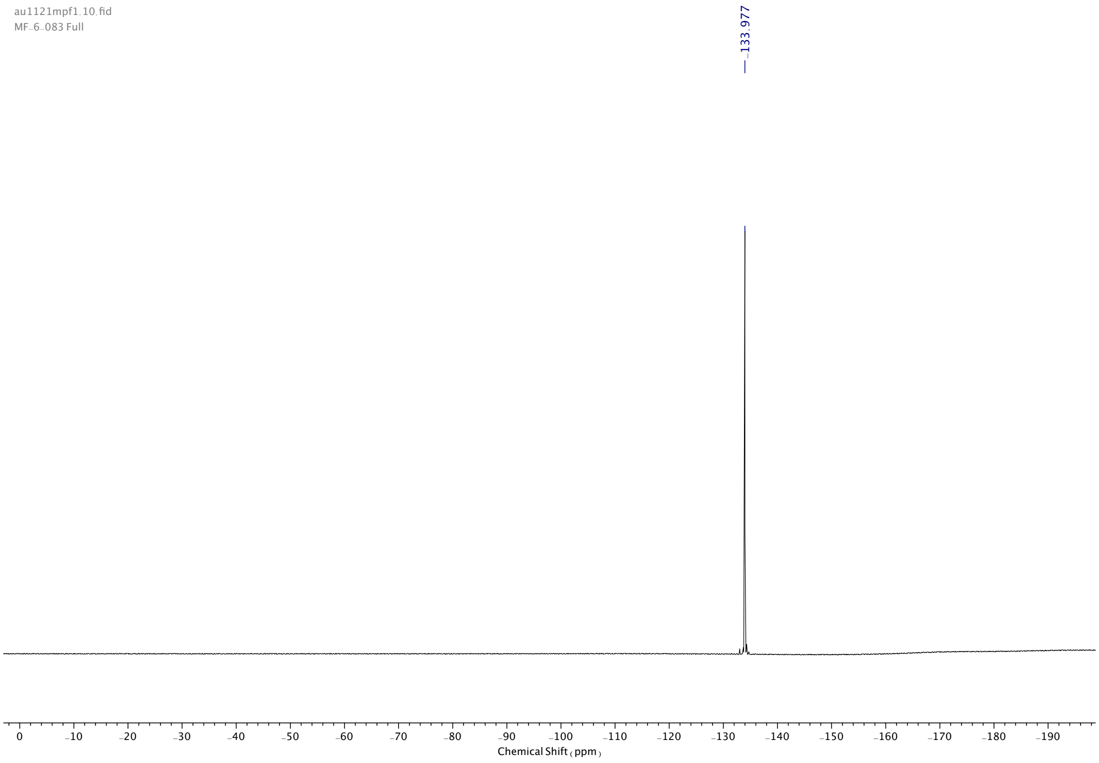

Figure **462**. ^{19}F NMR (CDCl$_3$, 376 MHz) of **112**.

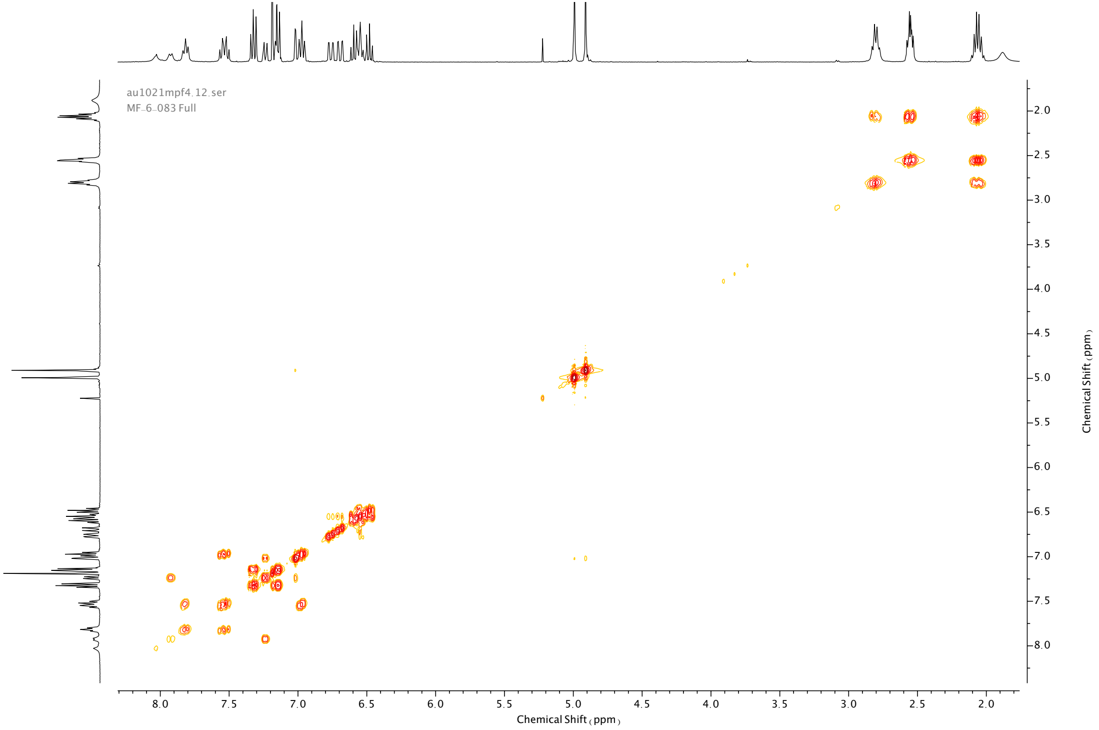

Figure **463**. COSY NMR (CDCl$_3$) of **112**.

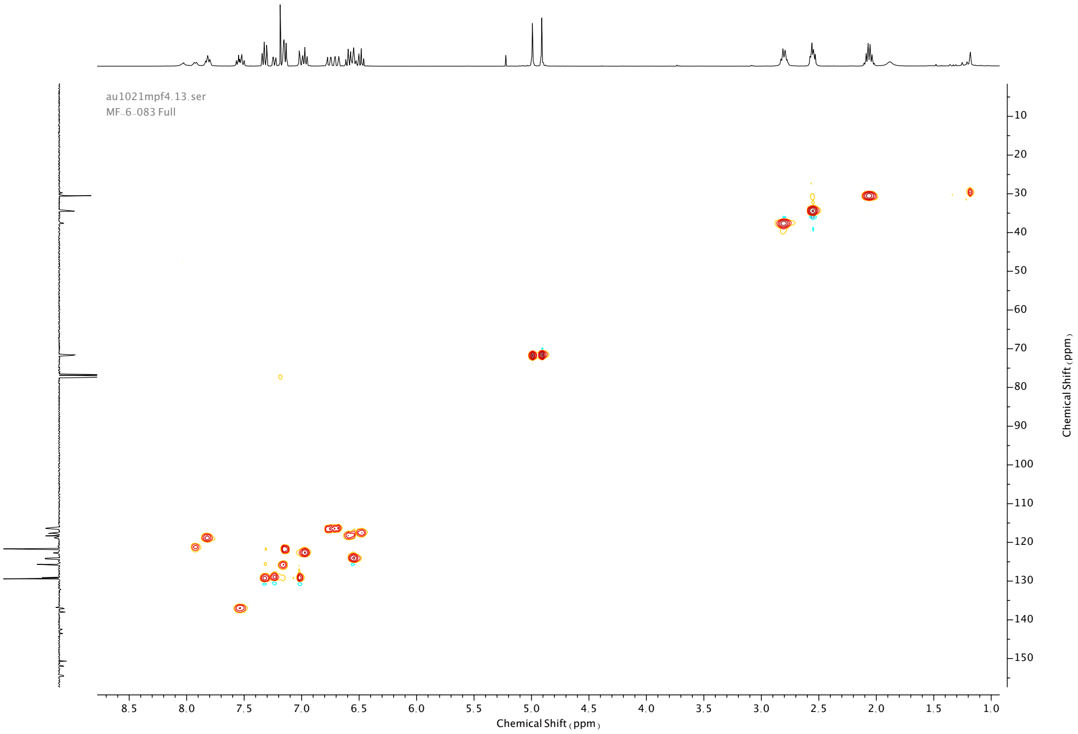

Figure **464**. HSQC NMR ($CDCl_3$) of **112**.

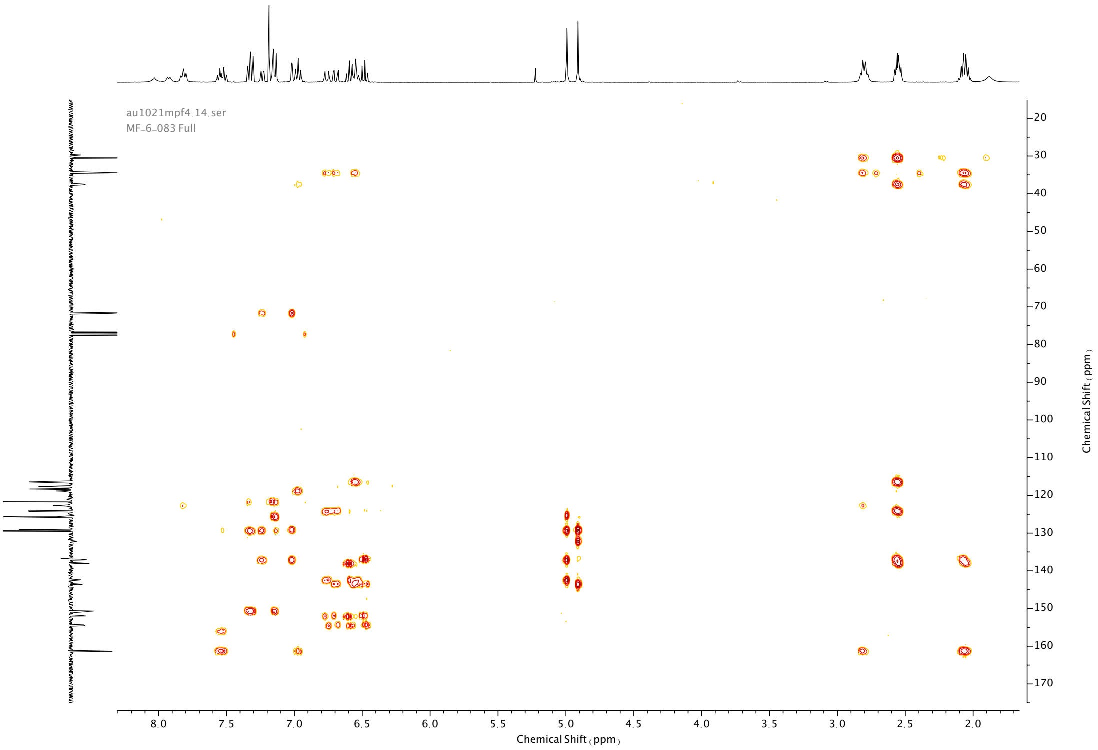

Figure **465**. HMBC NMR ($CDCl_3$) of **112**.

Compound **118**

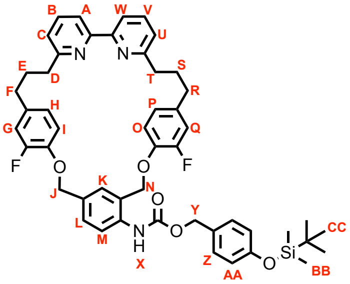

118 was synthesised according to general procedure **(6)** from macrocycle **112** (18 mg, 0.026 mmol) and trigger alcohol **51** (19 mg, 0.078 mmol). Purification by column chromatography (eluent 49:1 → 19:1 PE: Acetone) afforded **118** as a white foam (15 mg, 0.018 mmol, 69%). ^{1}H NMR (400 MHz, $CDCl_3$, 298 K) δ_H 7.99-7.85 (3H, m, H_M, H_A & H_W), 7.67 (1H, br. s, N-H_X), 7.64-7.54 (2H, m, H_B & H_V), 7.32-7.27 (3H, m, H_Z & H_L), 7.05-6.99 (3H, m, H_K, H_C & H_U), 6.84 (2H, d, *J* = 8.7 Hz, H_{AA}), 6.81-6.77 (1H, m, H_G or H_Q), 6.74 (1H, dd, *J* = 12.3, 2.0 Hz, H_G or H_Q), 6.62-6.56 (3H, m, H_H, H_P & H_I or H_O), 6.52 (1H, t, *J* = 8.4 Hz, H_I or H_O), 5.14 (2H, s, H_Y), 4.97 (2H, s, H_J or H_N), 4.94 (2H, s, H_J or H_N), 2.95-2.83 (4H, m, H_D & H_T), 2.66-2.57 (4H, m, H_F & H_R), 2.19-2.07 (4H, m, H_E & H_S), 0.99 (9H, s, H_{CC}), 0.20 (6H, s, H_{BB}). ^{13}C NMR (101 MHz, $CDCl_3$, 298 K) δ_C 161.4, 159.8, 156.0, 153.9 (x2), 153.7 (d, *J* = 245.4 Hz, J^1_{C-F}), 153.0, 152.4 (d, *J* = 245.8 Hz, J^1_{C-F}), 143.7 (d, *J* = 11.0 Hz, J^2_{C-F}), 142.7 (d, *J* = 11.1 Hz, J^2_{C-F}), 138.1 (d, *J* = 6.5 Hz, J^3_{C-F}), 137.6 (x2), 136.9 (d, *J* = 6.8 Hz, J^3_{C-F}), 133.9 (x2), 131.9, 130.1, 129.5, 129.2, 129.0, 124.3 (d, *J* = 3.3 Hz, J^4_{C-F}), 124.2 (d, *J* = 3.3 Hz, J^4_{C-F}), 122.9 (x2), 121.9, 121.8 (x2), 120.2, 118.7 (d, *J* = 1.7 Hz, J^3_{C-F}), 117.8 (d, *J* = 1.6 Hz, J^3_{C-F}), 116.5 (d, *J* = 18.2 Hz, J^2_{C-F}), 116.4 (d, *J* = 18.2 Hz, J^2_{C-F}), 71.8 (x2), 67.0, 37.6 (HSQC(x2)), 34.6 (x2), 30.6, 30.5, 25.8, 18.4 (HMBC), -4.3. ^{19}F NMR (376 MHz, $CDCl_3$, 298 K) δ_F -133.8, -134.1. HR-ESI-MS (CH_3CN): *m/z* = 842.3788 $[M+H]^+$ calc. 842.3795.

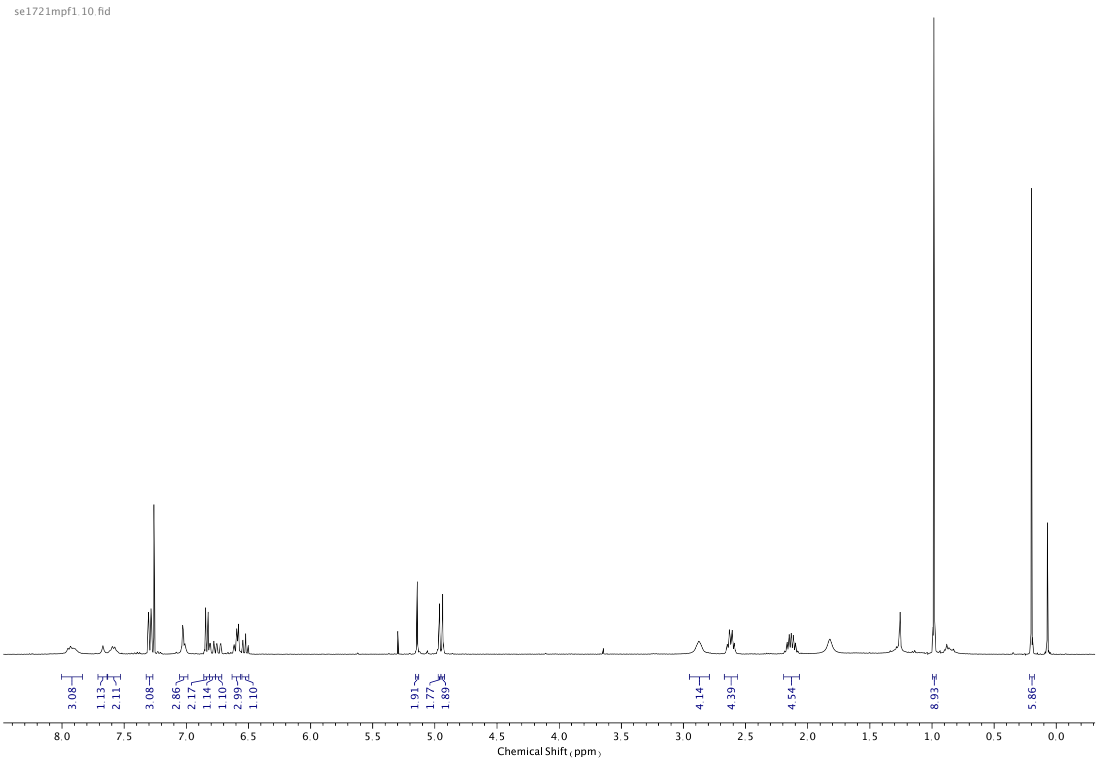

Figure **466**. ^{1}H NMR ($CDCl_3$, 400 MHz) of **118**.

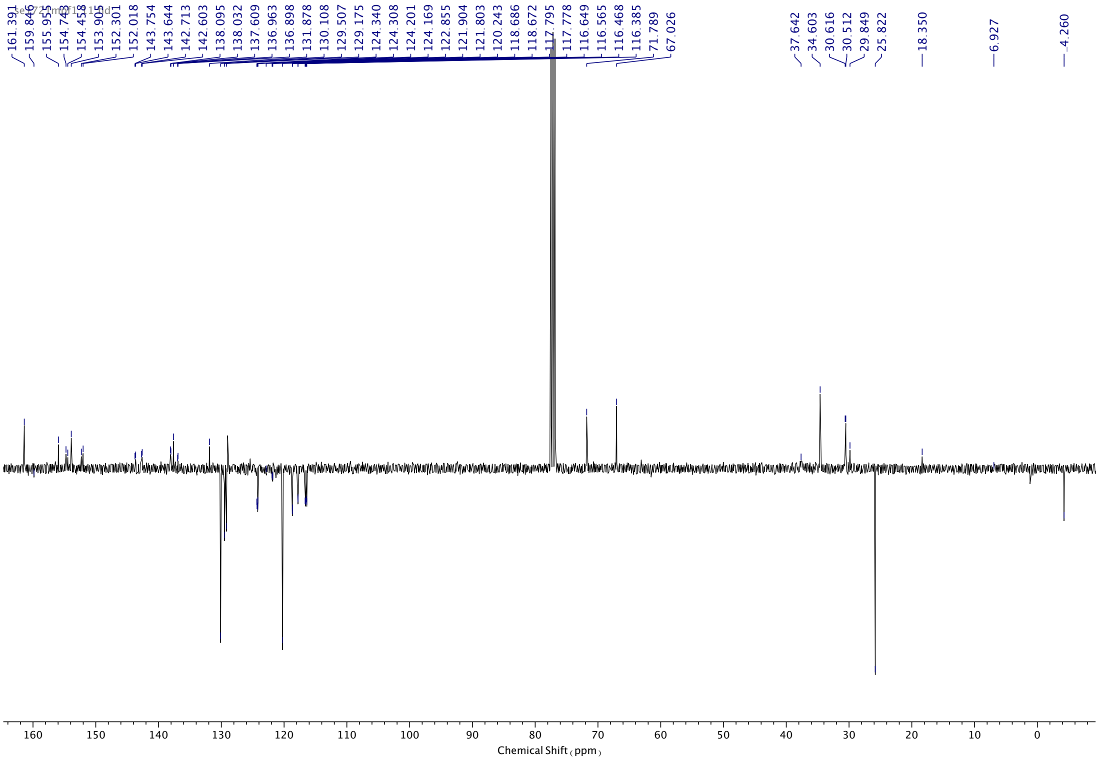

Figure **467**. ^{13}C NMR ($CDCl_3$, 101 MHz) of **118**.

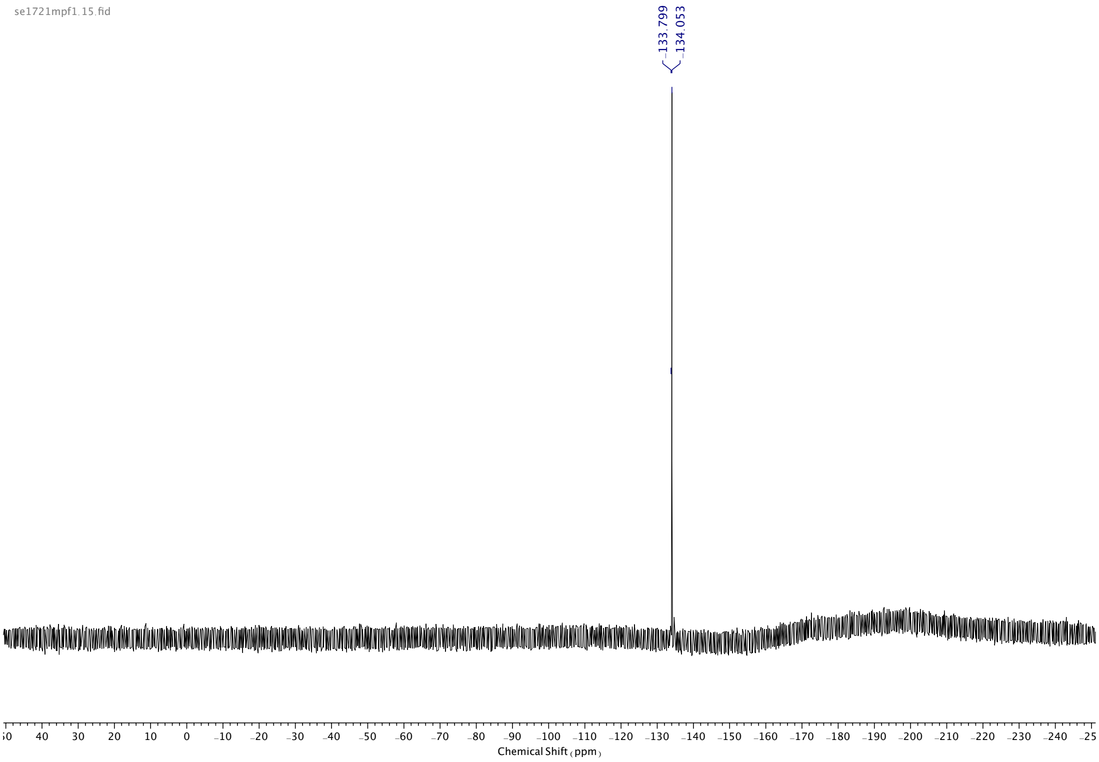

Figure **468**. ^{19}F NMR ($CDCl_3$, 376 MHz) of **118**.

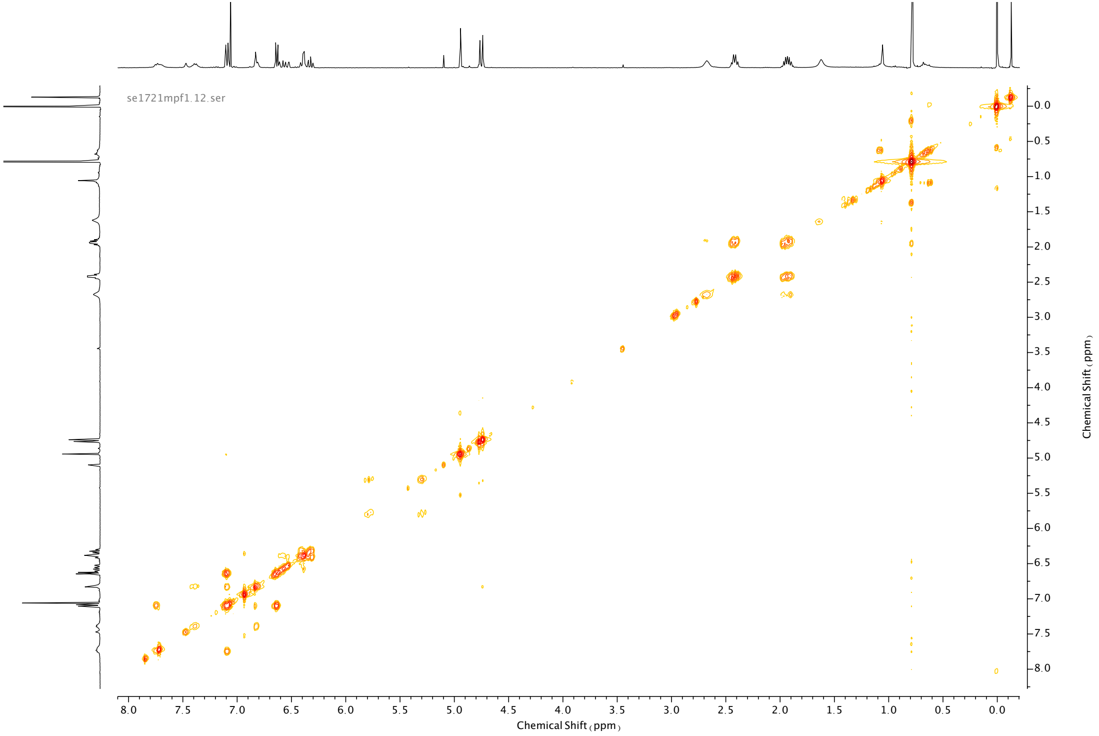

Figure **469**. COSY NMR ($CDCl_3$) of **118**.

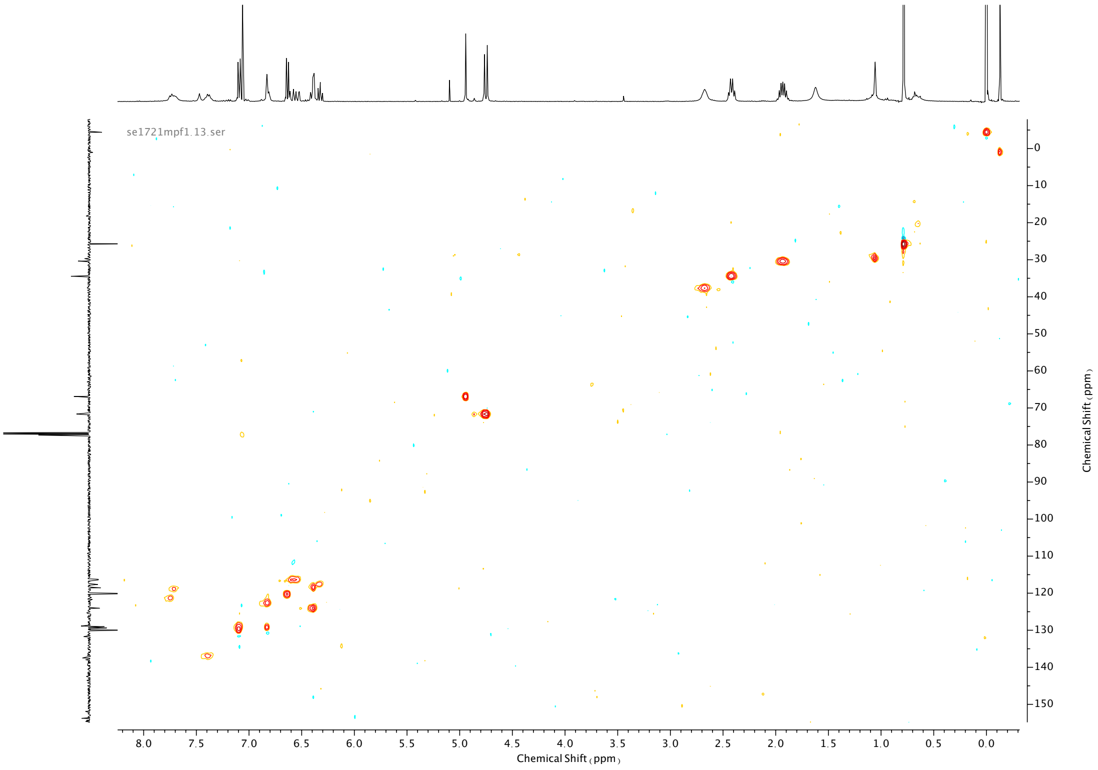

Figure **470**. HSQC NMR (CDCl$_3$) of **118**.

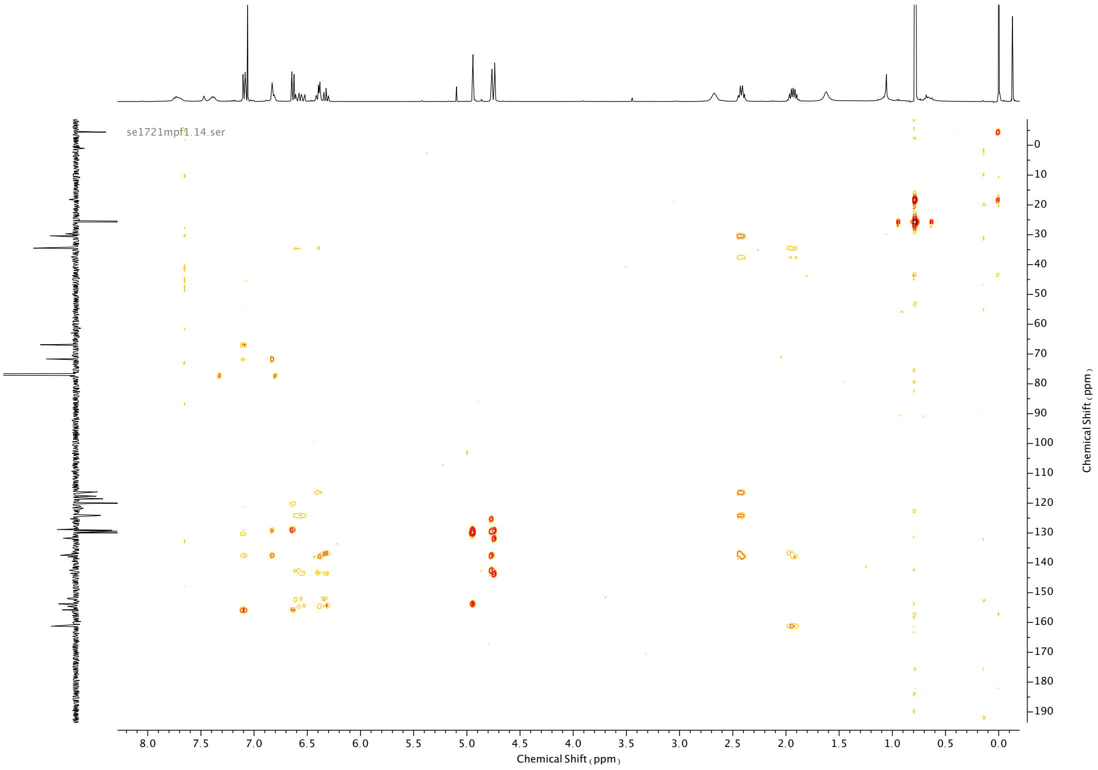

Figure **471**. HMBC NMR (CDCl$_3$) of **118**.

Compound **121**

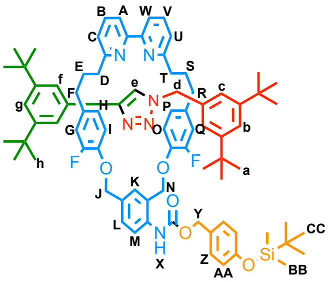

121 was synthesised according to general procedure **(7)** from macrocycle **118** (10 mg, 0.012 mmol), azide stopper **72** (4 mg, 0.018 mmol) and alkyne stopper **71** (4 mg, 0.018 mmol). Purification by column chromatography (eluent 1:0 → 9:1 CH_2Cl_2: Et_2O) afforded **121** as a white foam (10 mg, 0.0077 mmol, 64%).^1H NMR (400 MHz, $CDCl_3$, 298 K) δ_H 9.30 (1H, s, H_e), 8.24 (1H, d, *J* = 1.9 Hz, H_K), 8.06-7.97 (1H, m, H_M), 7.77 (1H, br. s, N-H_X), 7.70 (1H, t, *J* = 7.7 Hz, H_B or H_V), 7.67 (1H, t, *J* = 7.7 Hz, H_B or H_V), 7.56-7.52 (2H, m, H_A & H_W), 7.40 (1H, dd, *J* = 8.4, 2.2 Hz, H_L), 7.37 (2H, d, *J* = 1.8 Hz, H_f), 7.29-7.26 (3H, m, H_Z & H_b), 7.15-7.11 (2H, m, H_g & H_C or H_U), 7.10-7.07 (1H, dd, *J* = 7.6, 0.8 Hz, H_C or H_U), 6.98 (2H, d, *J* = 1.8 Hz, H_c), 6.80 (2H, d, *J* = 8.6 Hz, H_{AA}), 6.69 (1H, t, *J* = 8.7 Hz, H_I or H_O), 6.44-6.37 (2H, m, H_G or H_Q & H_I or H_O), 6.34 (1H, dd, *J* = 11.9, 2.1 Hz, H_G or H_Q), 5.74 (1H, d, *J* = 8.3 Hz, H_H or H_P), 5.67 (1H, d, *J* = 8.3 Hz, H_H or H_P), 5.44 (1H, d, *J* = 11.3 Hz, H_N or $H_{N'}$), 5.28-5.23 (3H, m, H_J & H_N or $H_{N'}$), 5.13 (2H, s, H_Y), 4.69 (1H, d, *J* = 14.0 Hz, H_d or $H_{d'}$), 4.42 (1H, d, *J* = 14.0 Hz, H_d or $H_{d'}$), 2.50-2.10 (8H, m, H_D, H_T, H_F & H_R), 1.65-1.35 (4H, m, H_E & H_S), 1.09 (18H, s, H_a), 1.05 (18H, s, H_h), 0.97 (9H, s, H_{CC}), 0.18 (6H, s, H_{BB}).^{13}C NMR (101 MHz, $CDCl_3$, 298 K) δ_C 159.3, 158.7, 154.2, 151.6, 151.0 150.8, 149.7, 149.2, 147.6, 145.7, 139.6, 136.8 ((HSQC) x 2), 130.1, 130.0, 126.9, 123.0, 122.7 ((HSQC) x 2), 122.5, 120.1, 120.0 ((HSQC) x 2), 119.8, 117.5, 115.5, 70.9 (x2), 70.1, 54.5 (HSQC), 37.5, 34.9 (x2), 33.9, 31.6, 31.4, 29.9 (x2), 25.9, -4.2.[10] ^{19}F NMR (376 MHz, $CDCl_3$, 298 K) δ_F -132.7, -134.7. HR-ESI-MS (CH_3CN): *m/z* = 1301.7 $[M+H]^+$ calc. 1301.7414.

---

[10] Compound **121** was left in $CDCl_3$ solution for several weeks before ^{19}F, ^{13}C and 2D experiments could be performed, resulting in protonation and peak shifting — reported ^1H peaks are prior to protonation. Reported ^{13}C and ^{19}F peaks are from the mixture of protonated and non-protonated sample — assigned through HMBC and HSQC. Several ^{13}C are absent due to weak concentration.

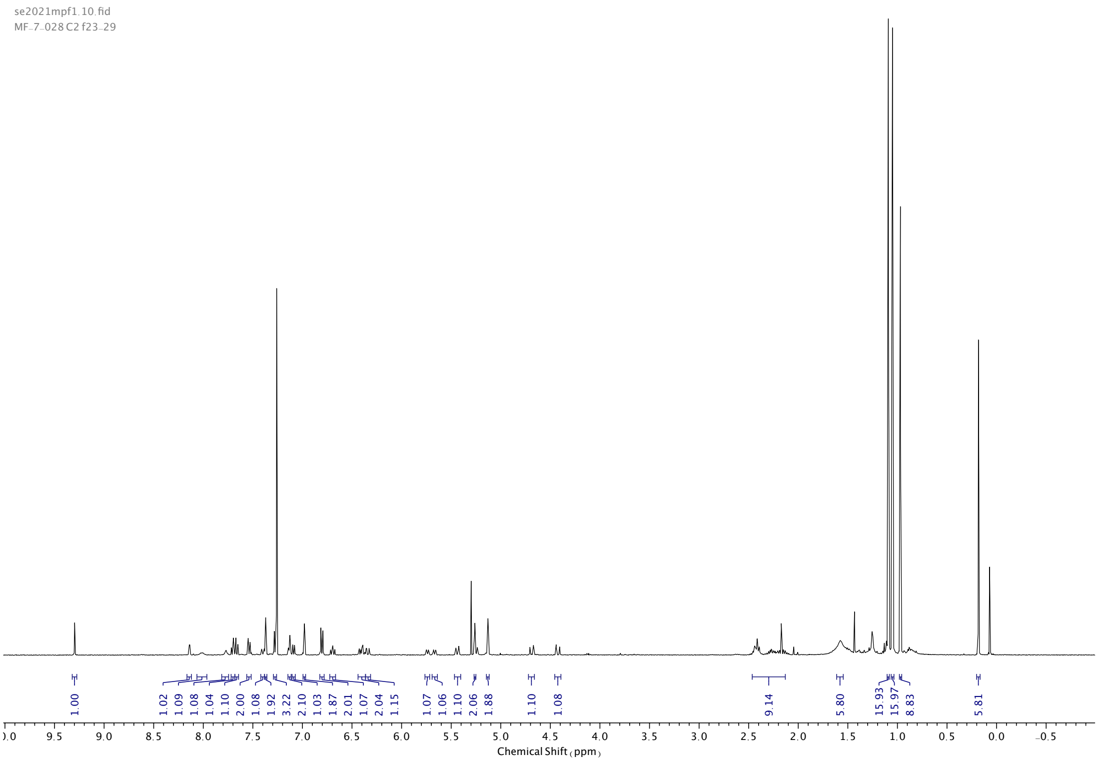

Figure **472**. ^{1}H NMR (CDCl$_3$, 400 MHz) of **121**.

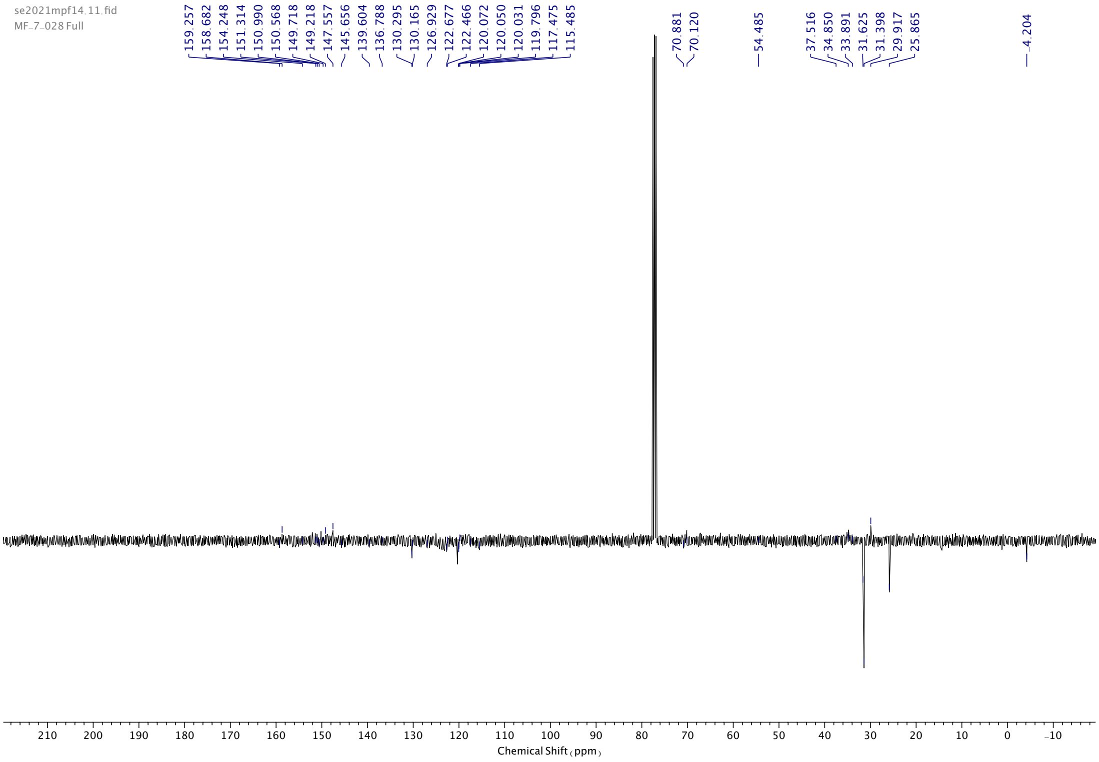

Figure **473**. ^{13}C NMR (CDCl$_3$, 101 MHz) of **121**.

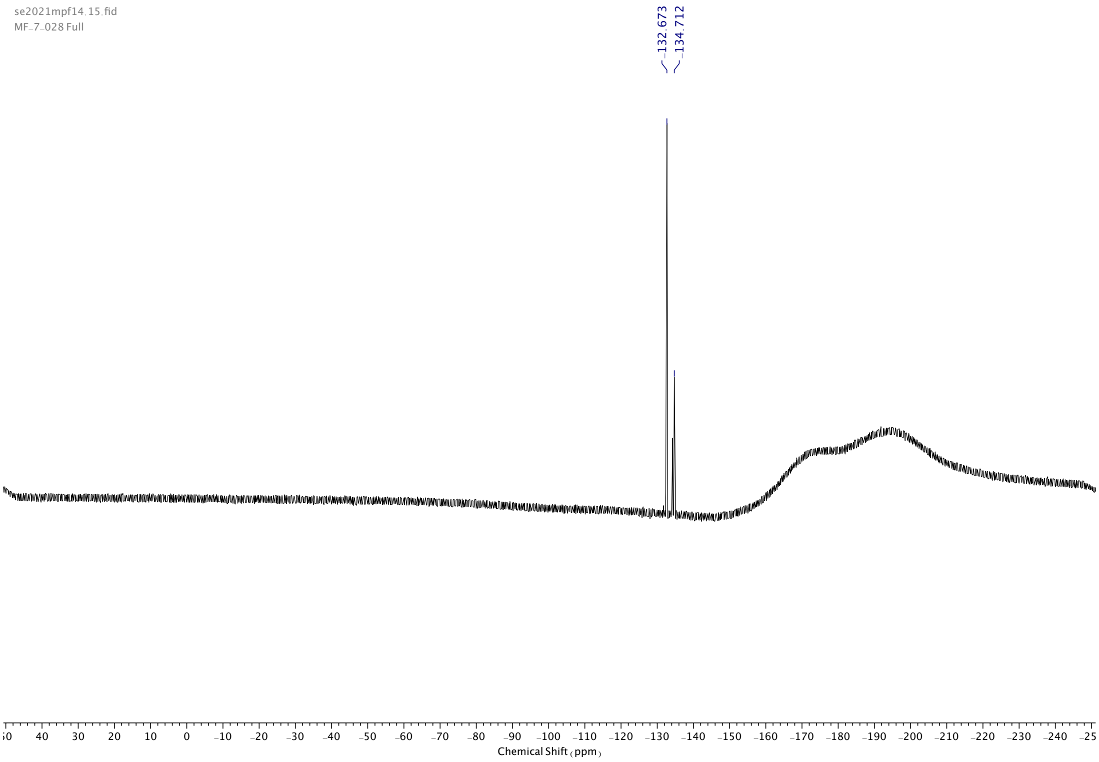

Figure **474**. ^{19}F NMR ($CDCl_3$, 376 MHz) of **121**.

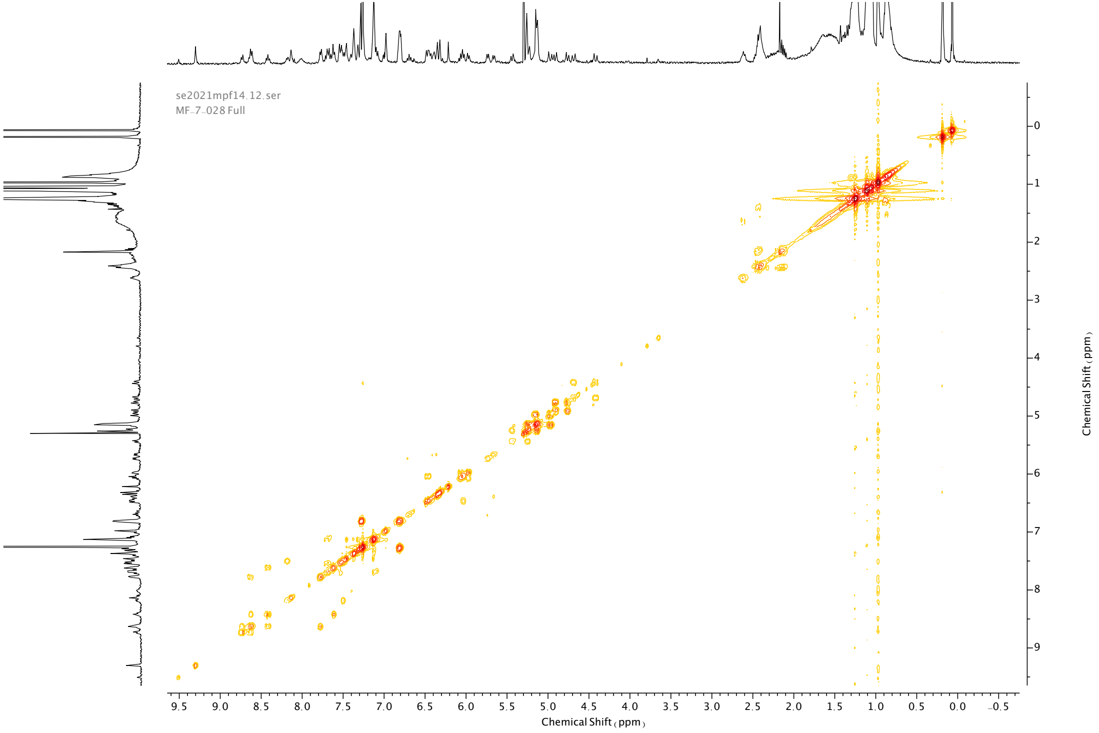

Figure **475**. COSY NMR ($CDCl_3$) of **121**.

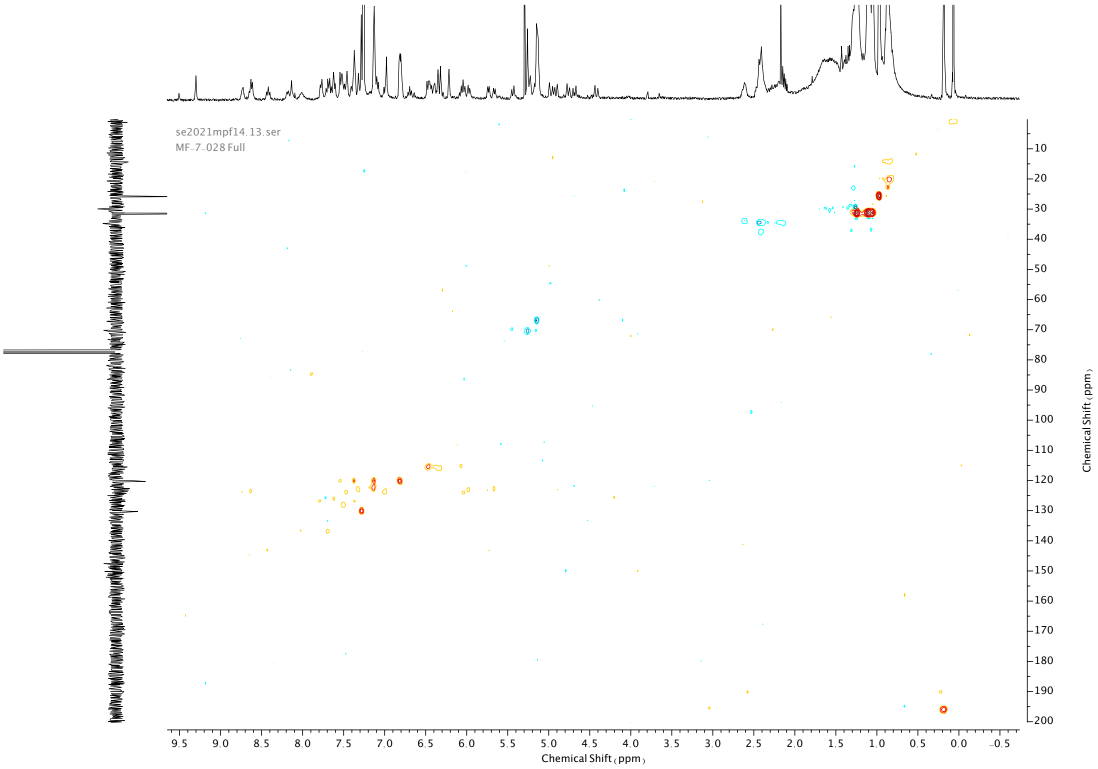

Figure **476**. HSQC NMR ($CDCl_3$) of **121**.

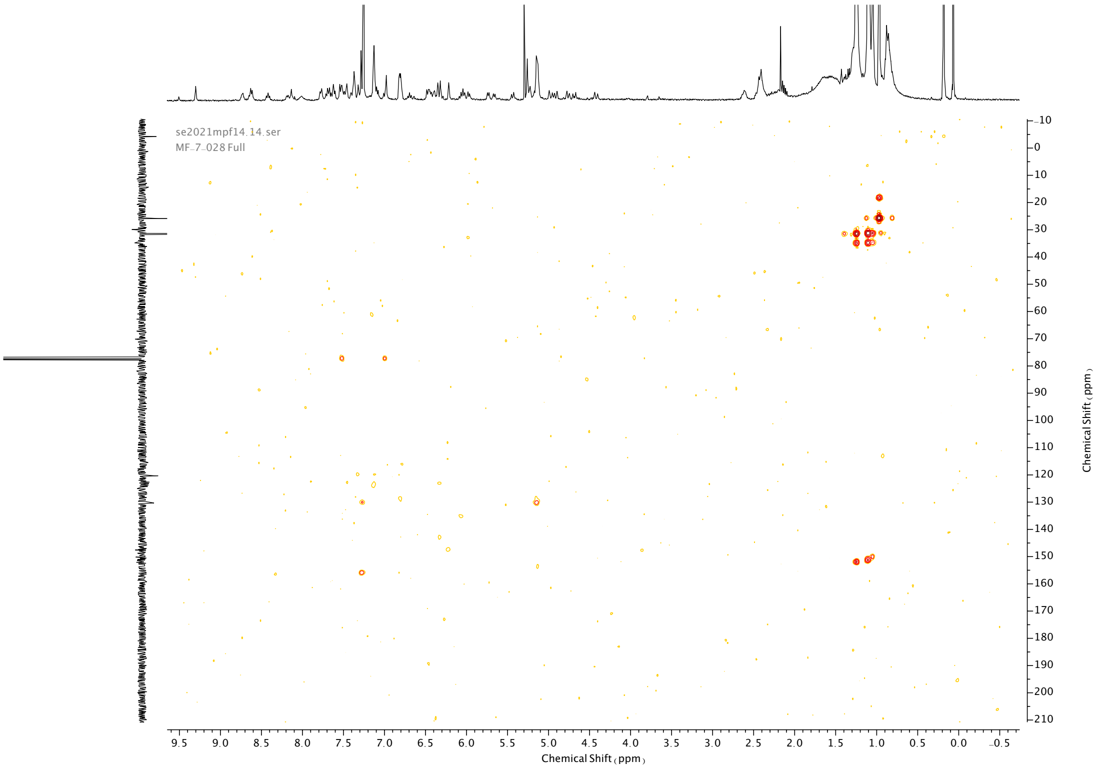

Figure **477**. HMBC NMR ($CDCl_3$) of **121**.

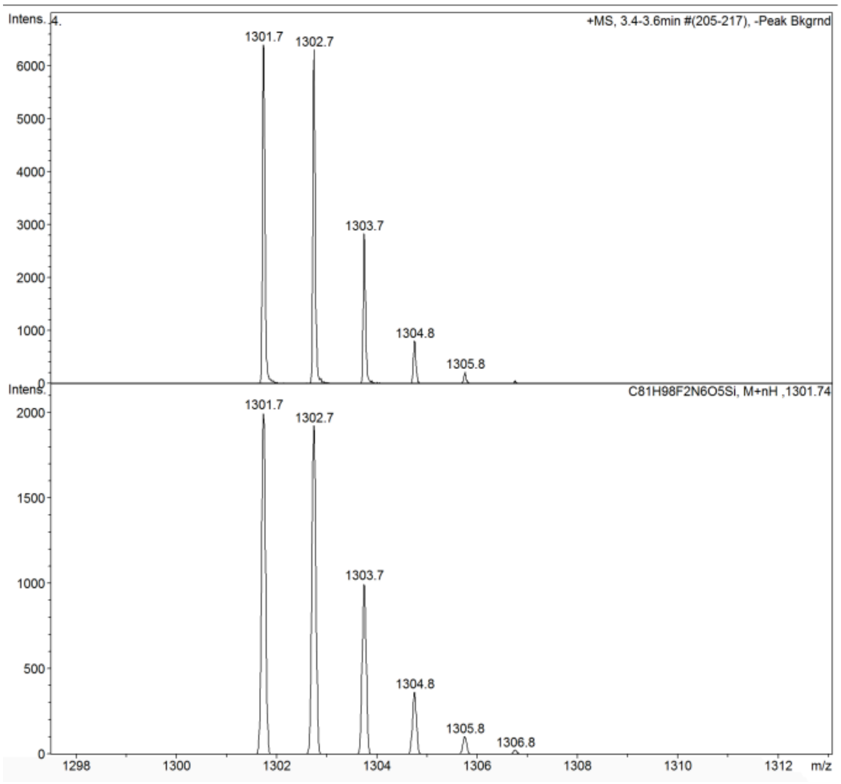

Figure **478**. Isotope pattern of **121**.

Compound **113**

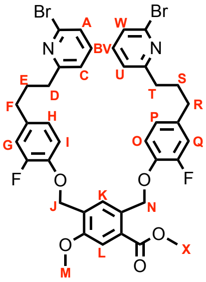

113 was prepared according to general procedure **(1)** from phenol **108** (273 mg, 0.88 mmol) and linker **96** (155 mg, 0.44 mmol). Purification by column chromatography (eluent 49:1 → 19:1 (1:1 PE: CH_2Cl_2): EtOAc) afforded **113** as a colourless oil (344 mg, 0.43 mmol, 97%). ^{1}H NMR (400 MHz, $CDCl_3$, 298 K) δ_H 7.86 (1H, s, H_K), 7.50 (1H, s, H_L), 7.45-7.40 (2H, m, H_B & H_V), 7.29 (2H, d, *J* = 7.8 Hz, H_A & H_W), 7.06 (2H, d, *J* = 7.6 Hz, H_C & H_U), 6.94-6.86 (4H, m, H_I, H_O, H_G & H_Q), 6.83-6.78 (2H, m, H_H & H_P), 5.42 (2H, s, H_N), 5.16 (2H, s, H_J), 3.91 (3H, s, H_M), 3.89 (3H, s, H_X), 2.79-2.73 (4H, m, H_D & H_T), 2.58 (4H, t, *J* = 7.8 Hz, H_F & H_R), 2.05-1.95 (4H, m, H_E & H_S). ^{13}C NMR (101 MHz, $CDCl_3$, 298 K) δ_C 167.3, 163.7, 163.6 (x2), 155.9, 152.8 (d, *J* = 246.0 Hz, $J^1_{C\text{-}F}$), 152.7 (d, *J* = 246.2 Hz, $J^1_{C\text{-}F}$), 144.9 (d, *J* = 16.9 Hz, $J^2_{C\text{-}F}$), 144.8 (d, *J* = 17.0 Hz, $J^2_{C\text{-}F}$), 141.7 (x2), 138.8 (x2), 135.8 (d, *J* = 6.0 Hz, $J^3_{C\text{-}F}$), 135.5 (d, *J* = 6.0 Hz, $J^3_{C\text{-}F}$), 130.0, 128.7 (x2), 125.5 (x2), 124.1 (d, *J* = 3.4 Hz, $J^4_{C\text{-}F}$), 124.0 (d, *J* = 3.4 Hz, $J^4_{C\text{-}F}$), 121.7 (x2), 116.4 (d, *J* = 18.0 Hz, $J^2_{C\text{-}F}$), 116.3 (d, *J* = 18.0 Hz, $J^2_{C\text{-}F}$), 115.8 (d, *J* = 2.0 Hz, $J^3_{C\text{-}F}$), 115.7 (d, *J* = 2.1 Hz, $J^3_{C\text{-}F}$), 112.3, 69.5, 66.4, 55.9, 52.4, 37.4 (x2), 34.6 (x2), 31.3 (x2). ^{19}F NMR (376 MHz, $CDCl_3$, 298 K) δ_F -134.2, -134.5. HR-ESI-MS (CH_3CN): *m/z* = 809.1029 $[M+H]^+$ calc. 809.1032.

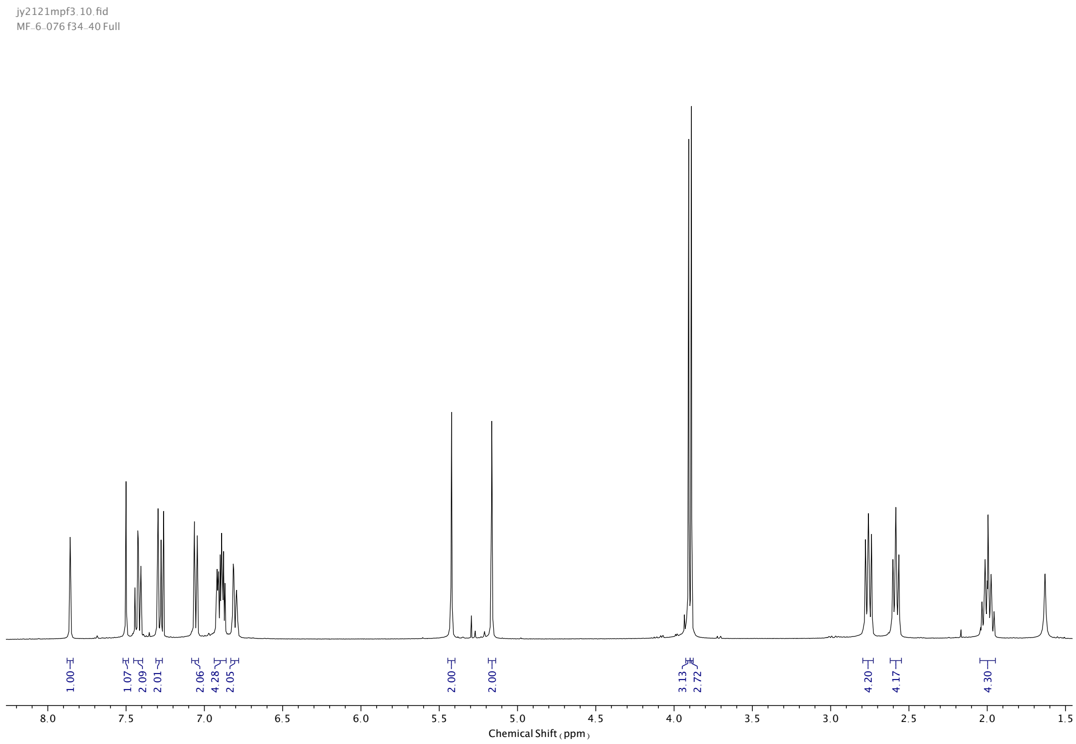

Figure **479**. ^{1}H NMR (CDCl$_3$, 400 MHz) of **113**.

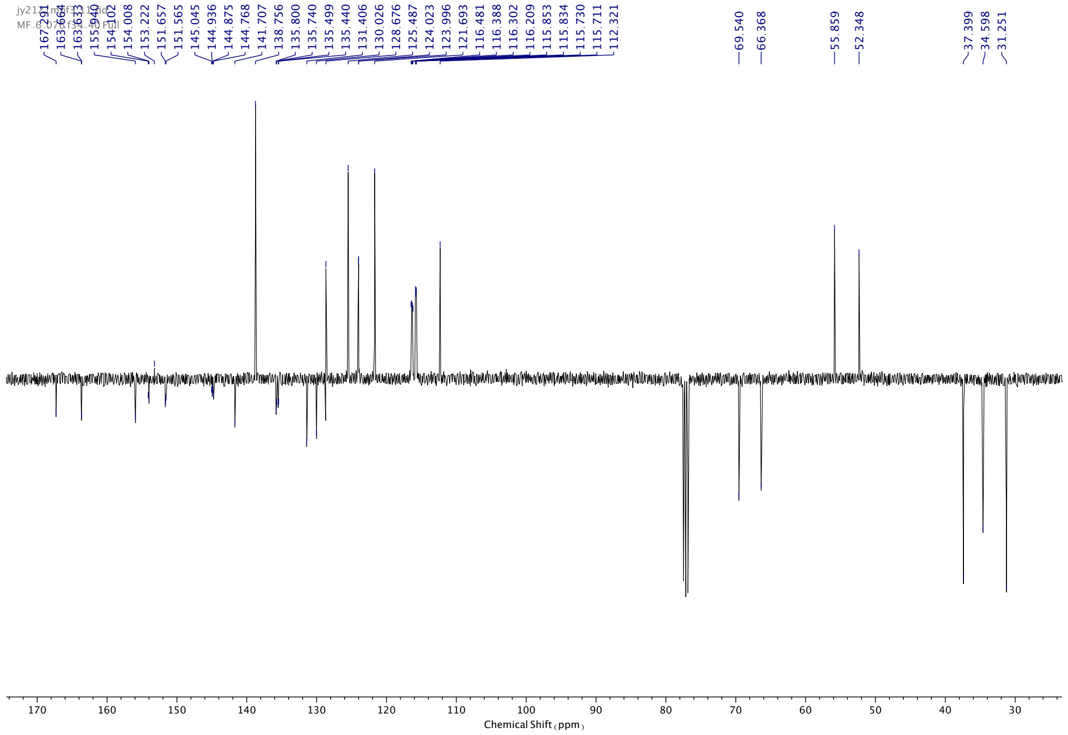

Figure **480**. ^{13}C NMR (CDCl$_3$, 101 MHz) of **113**.

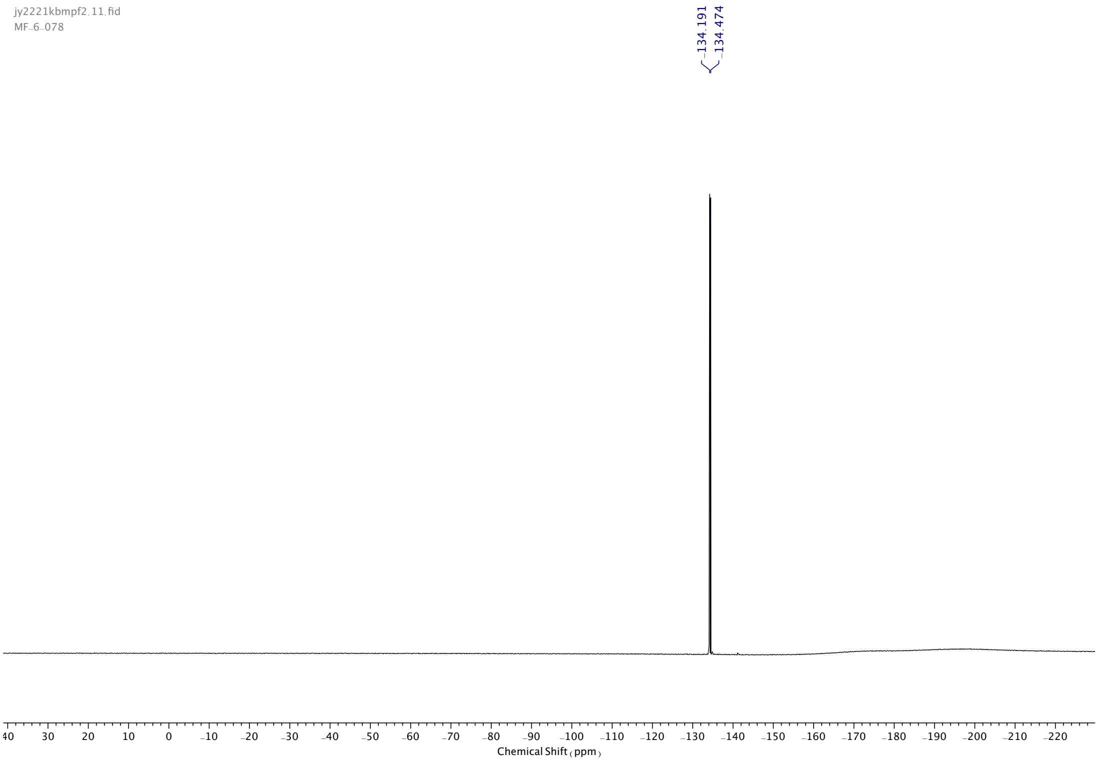

Figure **481**. ^{19}F NMR (CDCl$_3$, 376 MHz) of **113**.

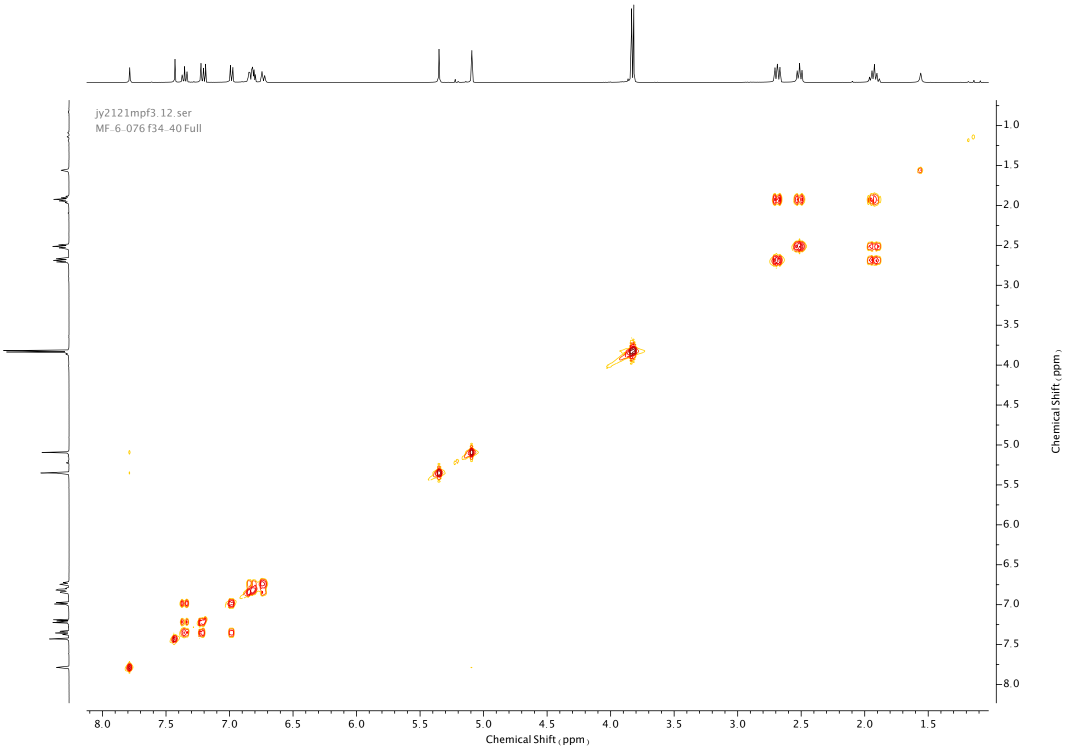

Figure **482**. COSY NMR (CDCl$_3$) of **113**.

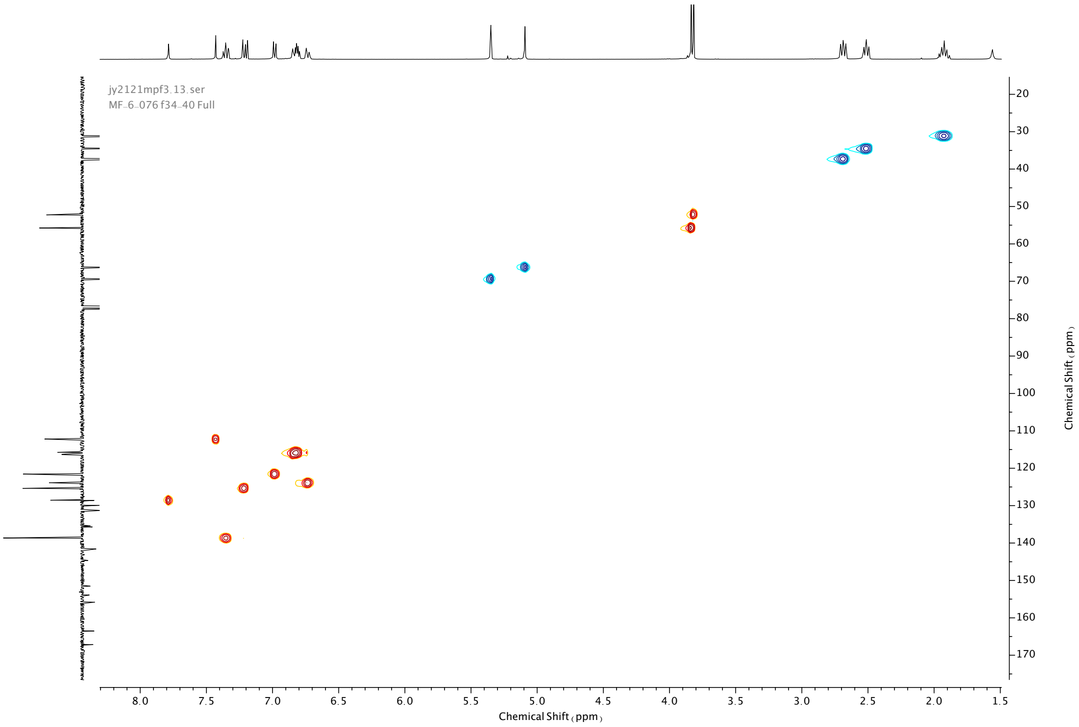

Figure **483**. HSQC NMR ($CDCl_3$) of **113**.

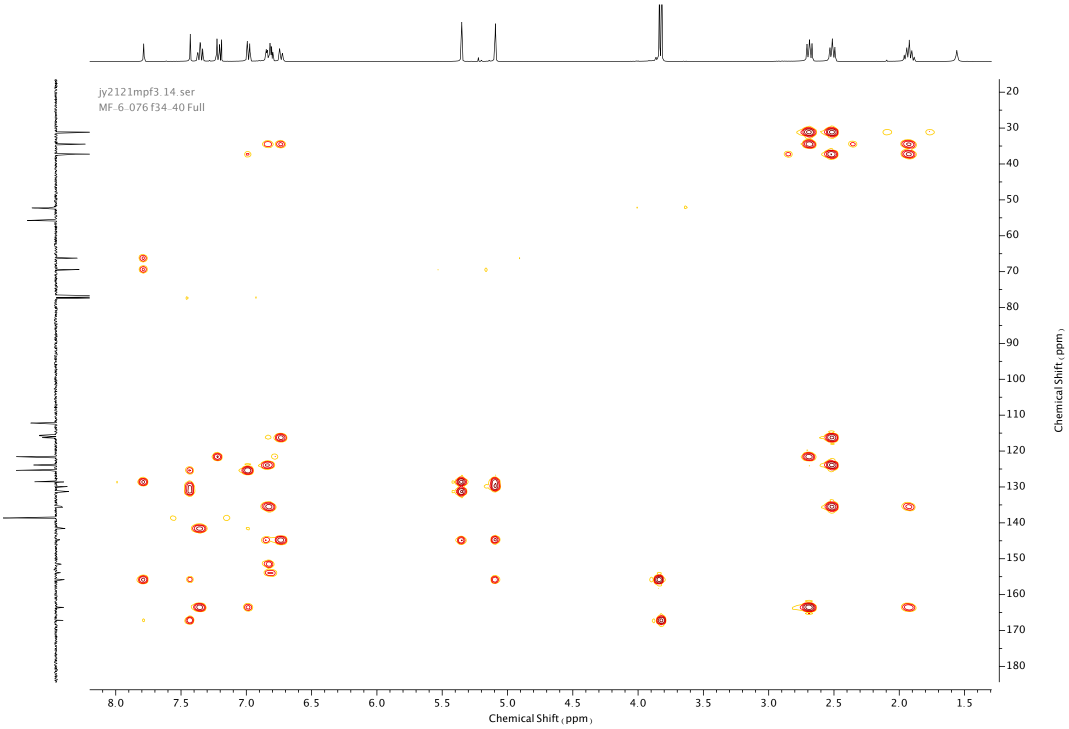

Figure **484**. HMBC NMR ($CDCl_3$) of **113**.

Compound **114**

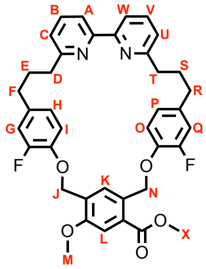

114 was prepared according to general procedure **(2)** from macrocycle precursor **113** (306 mg, 0.38 mmol). Purification by column chromatography (eluent 1:0 → 9:1 CH_2Cl_2:Et_2O) afforded **114** as a yellow oil (147 mg, 0.23 mmol, 63%). ^{1}H NMR (400 MHz, $CDCl_3$, 298 K) δ_H 7.78-7.73 (2H, m, H_A & H_W), 7.67 (1H, s, H_K), 7.62 (1H, t, *J* = 7.7 Hz, H_B or H_V), 7.61 (1H, t, *J* = 7.7 Hz, H_B or H_V), 7.47 (1H, s, H_L), 7.10-7.05 (2H, m, H_C or H_U), 6.86-6.79 (2H, m, H_G & H_Q), 6.69-6.58 (4H, m, H_I, H_O, H_H & H_P), 5.43 (2H, s, H_N), 5.16 (2H, s, H_J), 3.91 (3H, s, H_X), 3.89 (3H, s, H_M), 2.94-2.88 (4H, m, H_D & H_T), 2.63 (4H, t, *J* = 7.6 Hz, H_F & H_R), 2.19-2.10 (4H, m, H_E & H_S). ^{13}C NMR (101 MHz, $CDCl_3$, 298 K) δ_C 167.2, 161.9 (x2), 156.6 (x2), 155.6, 153.0 (d, *J* = 245.7 Hz, $J^1_{C\text{-}F}$), 152.9 (d, *J* = 245.5 Hz, $J^1_{C\text{-}F}$), 144.3 (d, *J* = 16.7 Hz, $J^2_{C\text{-}F}$), 144.2 (d, *J* = 16.7 Hz, $J^2_{C\text{-}F}$), 136.8 (x2), 136.6 (d, *J* = 6.2 Hz, $J^3_{C\text{-}F}$), 136.2 (d, *J* = 6.1 Hz, $J^3_{C\text{-}F}$), 132.0, 130.4, 127.9, 127.8, 124.0 (d, *J* = 3.5 Hz, $J^4_{C\text{-}F}$), 123.9 (d, *J* = 3.6 Hz, $J^4_{C\text{-}F}$), 122.7, 122.6, 119.3 (x2), 116.6 (d, *J* = 18.1 Hz, $J^2_{C\text{-}F}$), 116.5 (d, *J* = 18.1 Hz, $J^2_{C\text{-}F}$), 116.2 (d, *J* = 1.7 Hz, $J^3_{C\text{-}F}$), 115.8 (d, *J* = 1.7 Hz, $J^3_{C\text{-}F}$), 112.1, 69.4, 66.5, 55.8, 52.8, 37.6 (x2), 34.3 (x2), 30.9, 30.8. ^{19}F NMR (376 MHz, $CDCl_3$, 298 K) δ_F -134.3, -134.6. HR-ESI-MS (CH_3CN): *m/z* = 651.2667 $[M+H]^+$ calc. 651.2665.

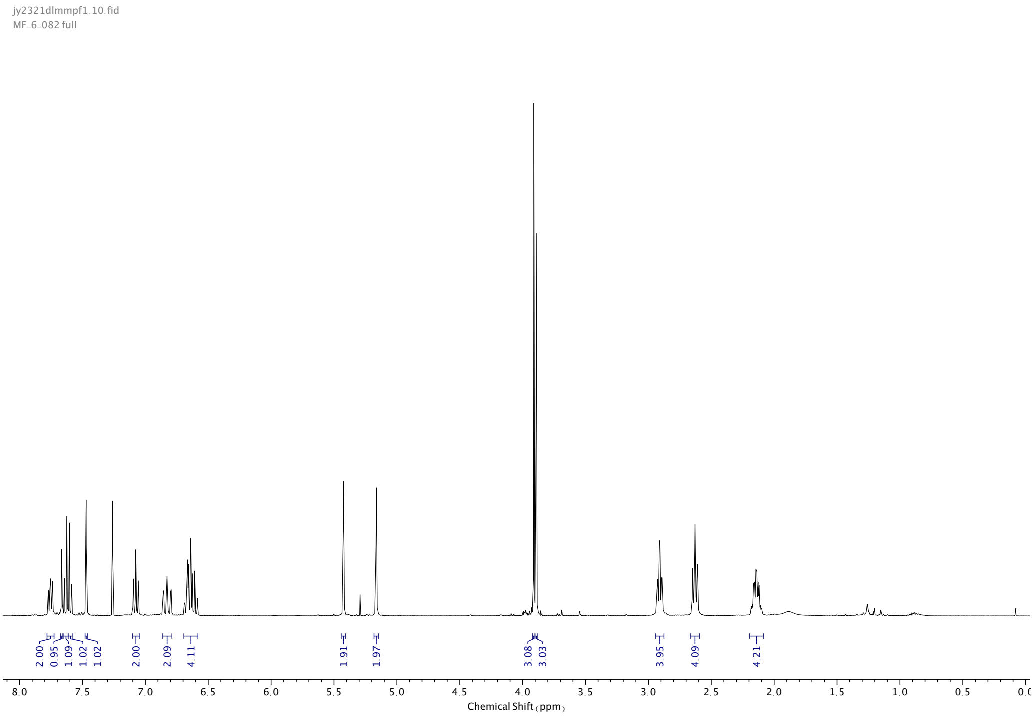

Figure **485**. ^{1}H NMR ($CDCl_3$, 400 MHz) of **114**.

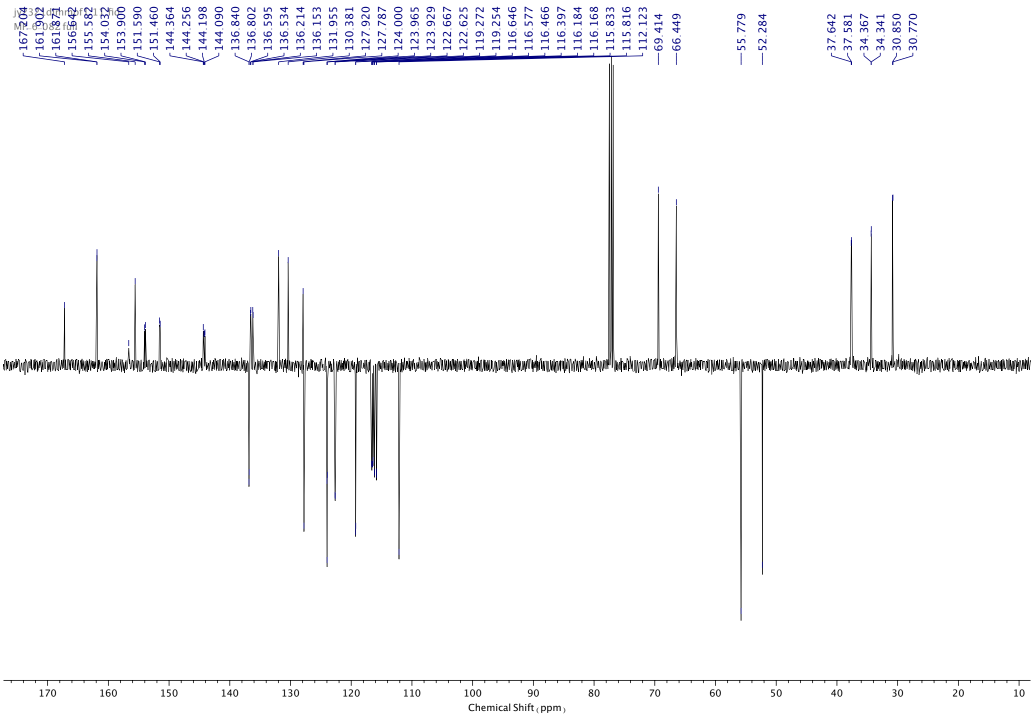

Figure **486**. ^{13}C NMR ($CDCl_3$, 101 MHz) of **114**.

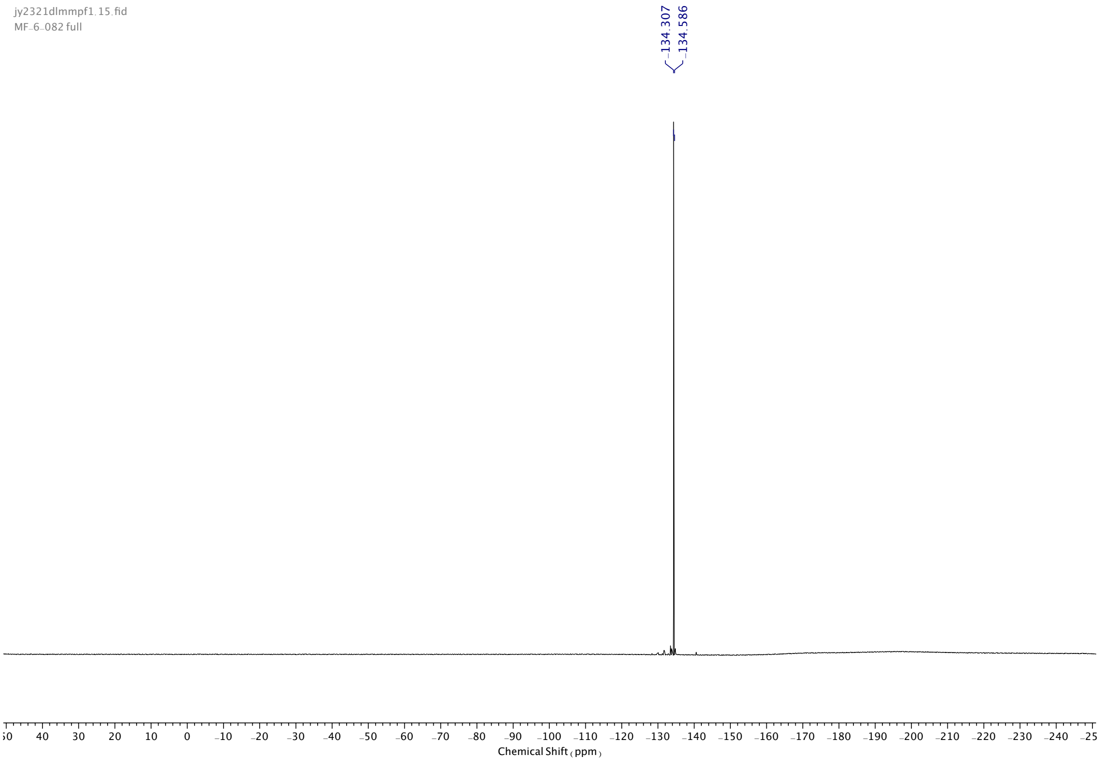

Figure **487**. ^{19}F NMR (CDCl$_3$, 376 MHz) of **114**.

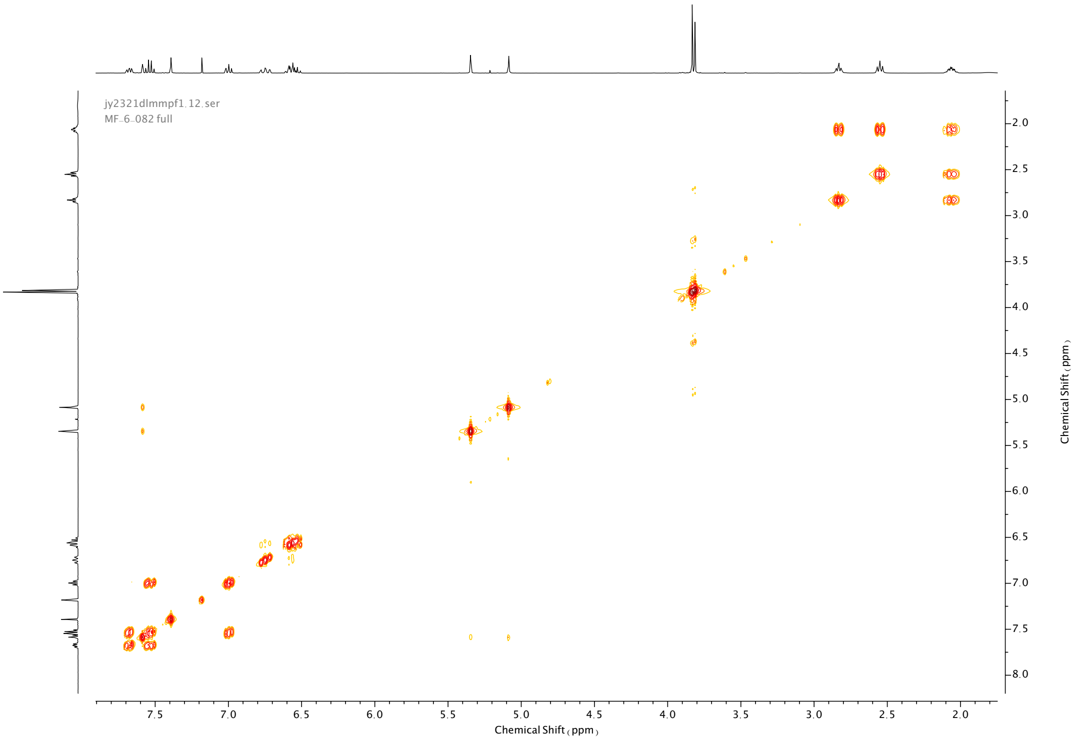

Figure **488**. COSY NMR (CDCl$_3$) of **114**.

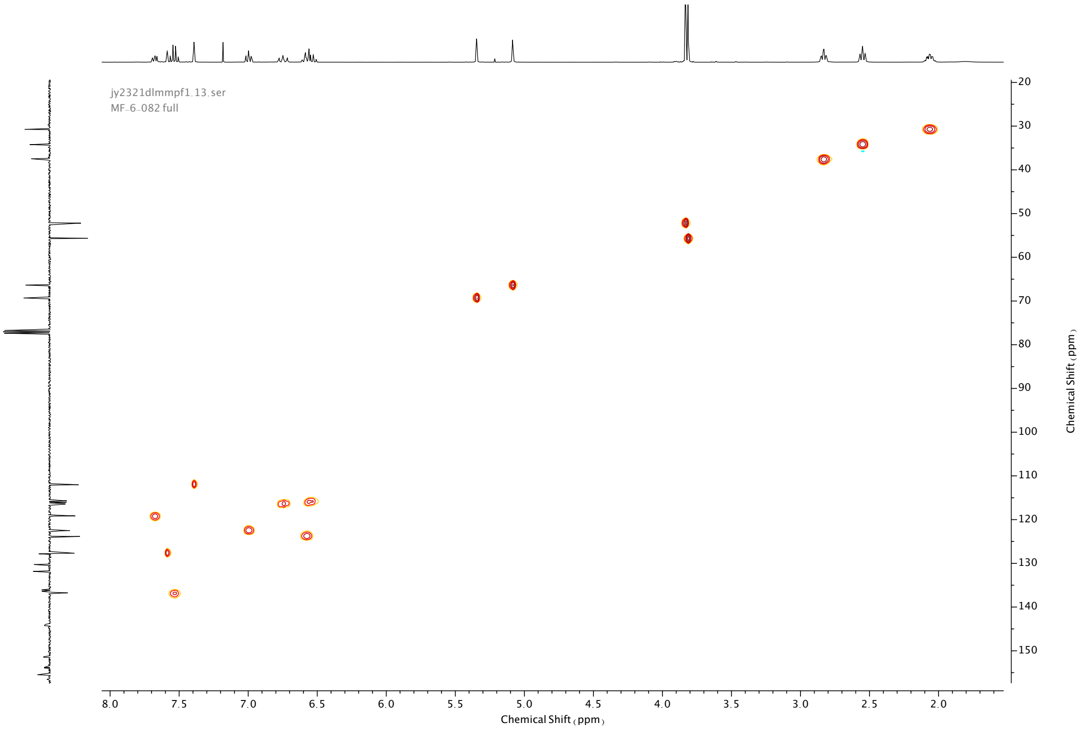

Figure **489**. HSQC NMR ($CDCl_3$) of **114**.

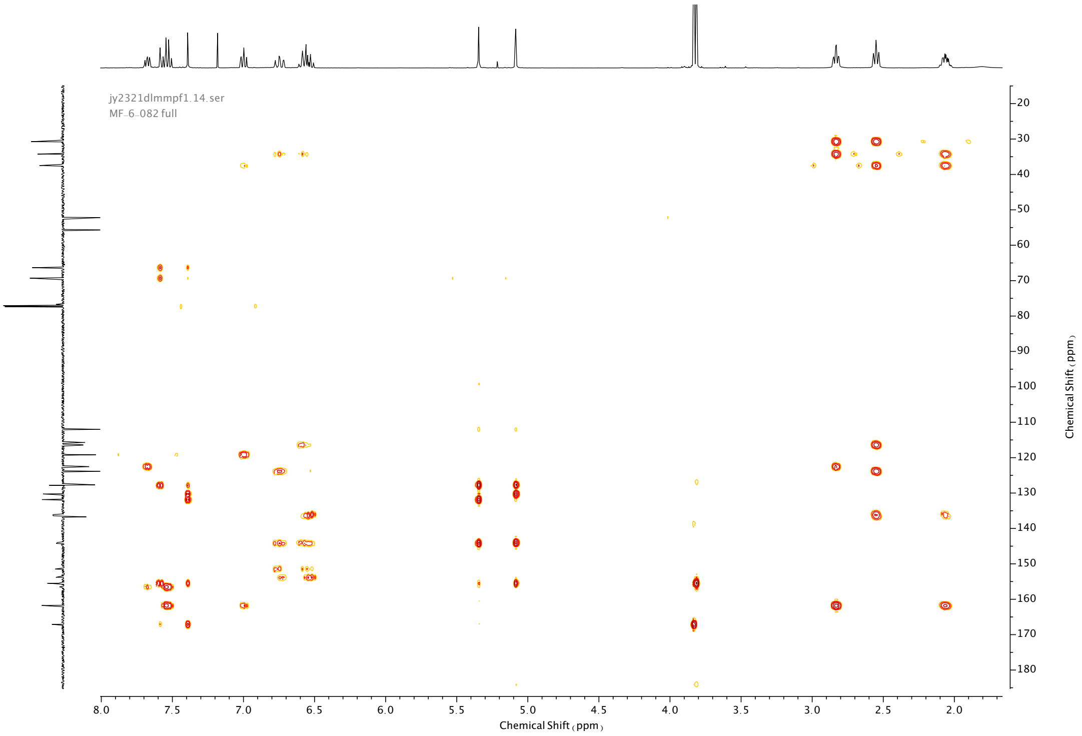

Figure **490**. HMBC NMR ($CDCl_3$) of **114**.

Compound **115**

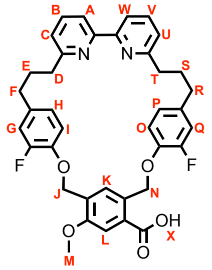

115 was prepared according to general procedure **(3)** from macrocycle **114** (145 mg, 0.22 mmol). **115** was achieved as white solid (140 mg, 0.22 mmol, quant.) and used in the next step without further purification. M.p. 202-204 °C. ^{1}H NMR (400 MHz, DMSO-d_6, 298 K) δ_H 7.84 (2H, d, *J* = 7.8 Hz, H_A & H_W), 7.73-7.65 (2H, m, H_B & H_V), 7.49 (1H, s, H_L), 7.36 (1H, s, H_K), 7.18 (1H, d, *J* = 7.6 Hz, H_C or H_U), 7.13 (1H, d, *J* = 7.5 Hz, H_C or H_U), 6.88-6.65 (6H, m, H_G & H_Q, H_H & H_P, H_I & H_O), 5.51 (2H, s, H_N), 5.06 (2H, s, H_J), 3.79 (3H, s, H_M), 2.82-2.73 (4H, m, H_D & H_T), 2.59-2.51 (4H, m, H_F & H_R), 2.09-1.97 (4H, m, H_E & H_S). ^{13}C NMR (101 MHz, DMSO-d_6, 298 K) δ_C 161.1, 155.7 (x2), 155.1, 151.7 (d, *J* = 243.9 Hz, $J^1_{C\text{-}F}$), 151.6 (d, *J* = 243.2 Hz, $J^1_{C\text{-}F}$), 150.4, 150.3, 143.9 (d, *J* = 10.5 Hz, $J^2_{C\text{-}F}$), 143.6 (d, *J* = 10.6 Hz, $J^2_{C\text{-}F}$), 136.9 (x2), 135.5 (d, *J* = 6.3 Hz, $J^3_{C\text{-}F}$) 134.9 (d, *J* = 5.7 Hz, $J^3_{C\text{-}F}$), 128.8 (HMBC), 126.8 (HSQC), 125.6 (HMBC), 124.2 ((s, $J^3_{C\text{-}F}$) x 2), 122.8, 122.7, 118.6 (x2), 115.9 (d, *J* = 18.0 Hz, $J^2_{C\text{-}F}$), 115.8 (d, *J* = 17.8 Hz, $J^2_{C\text{-}F}$), 115.3 (d, *J* = 2.4 Hz, $J^3_{C\text{-}F}$), 114.8 (s, *J* = 2.4 Hz, $J^3_{C\text{-}F}$), 112.2 (HSQC), 68.4, 65.3, 55.4, 36.6 (x2), 33.3 (x2), 30.1 (x2).[11] ^{19}F NMR (376 MHz, DMSO-d_6, 298 K) δ_F -134.5, -134.8. HR-ESI-MS (CH_3CN): *m/z* = 637.2510 $[M+H]^+$ calc. 637.2509.

---

[11] ^{13}C signal of carboxylate position not observed

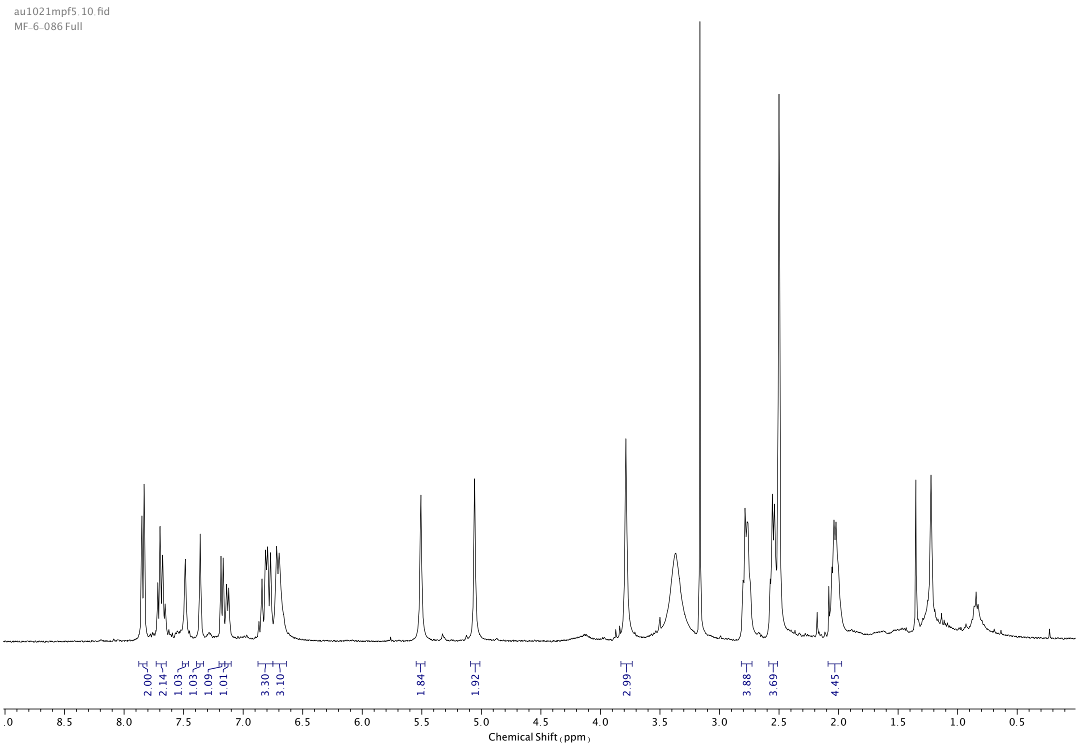

Figure **491**. ^{1}H NMR (DMSO-d$_6$, 400 MHz) of **115**.

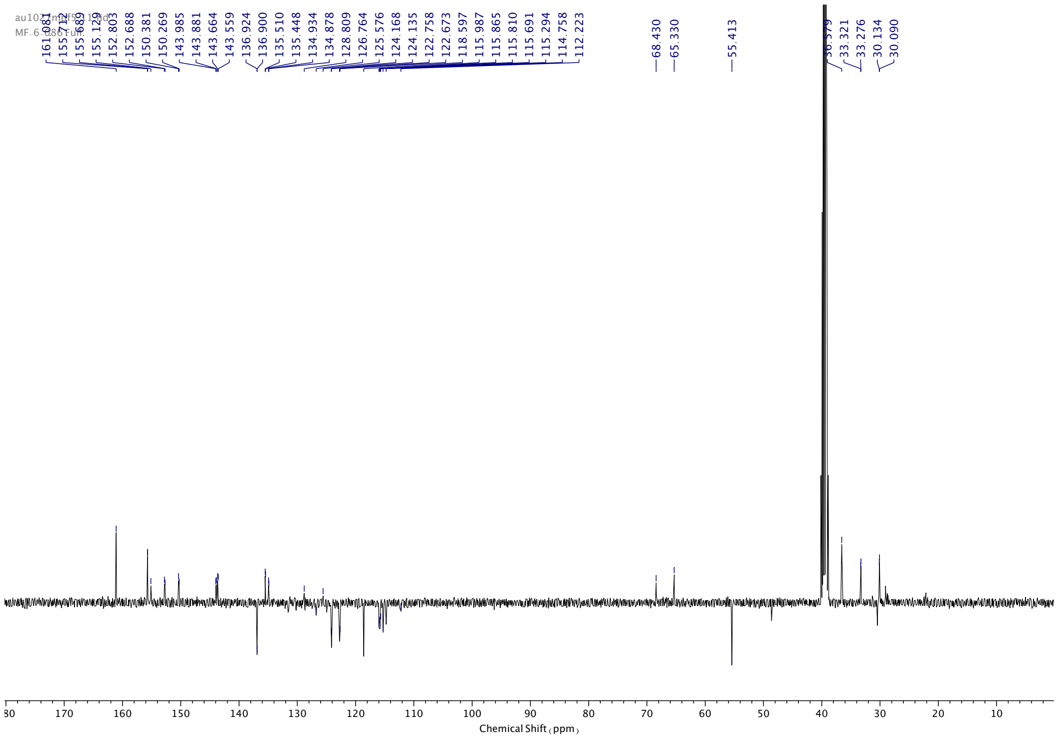

Figure **492**. ^{13}C NMR (DMSO-d$_6$, 101 MHz) of **115**.

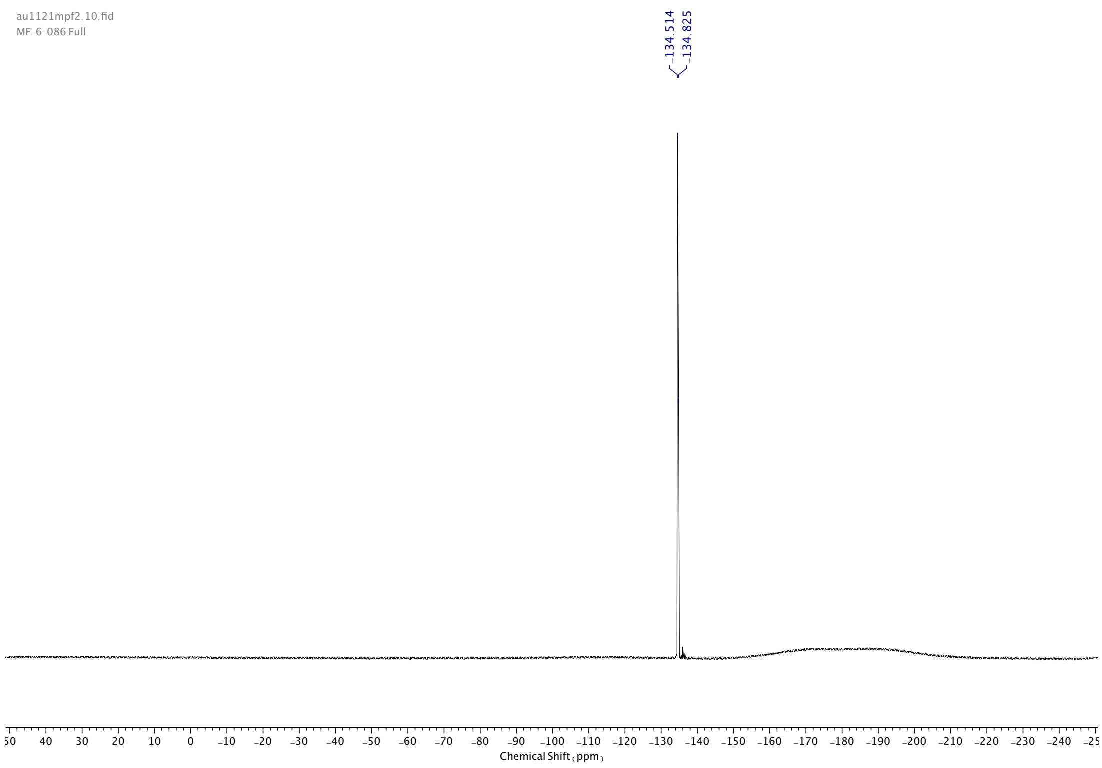

Figure **493**. ^{19}F NMR (DMSO-d$_6$, 376 MHz) of **115**.

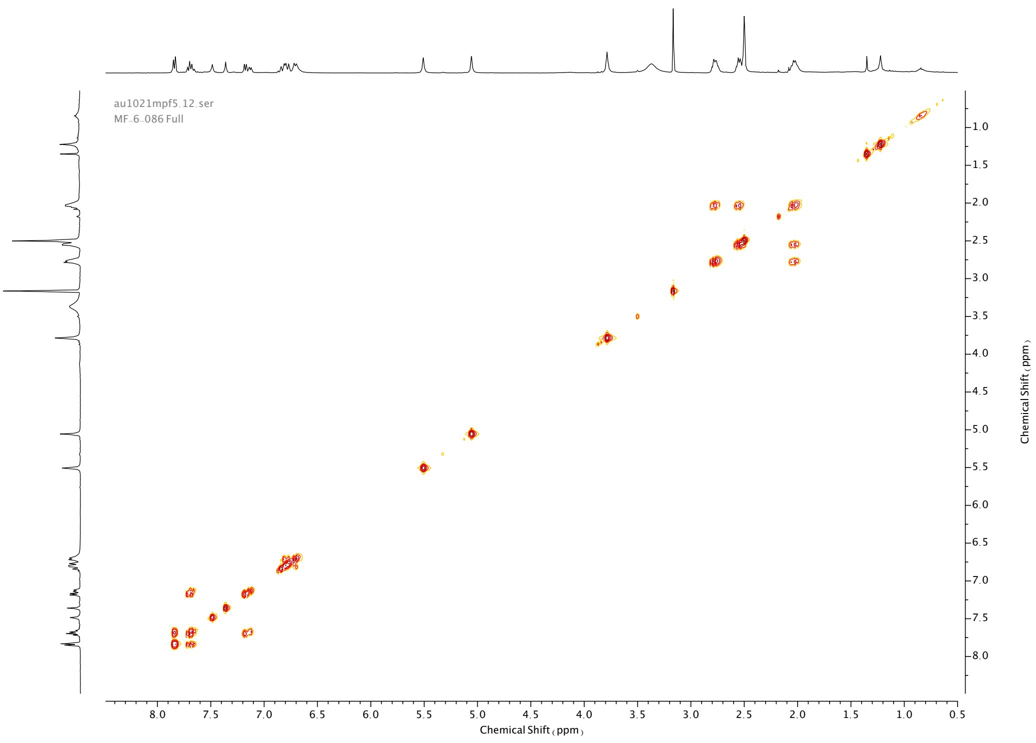

Figure **494**. COSY NMR (DMSO-d$_6$) of **115**.

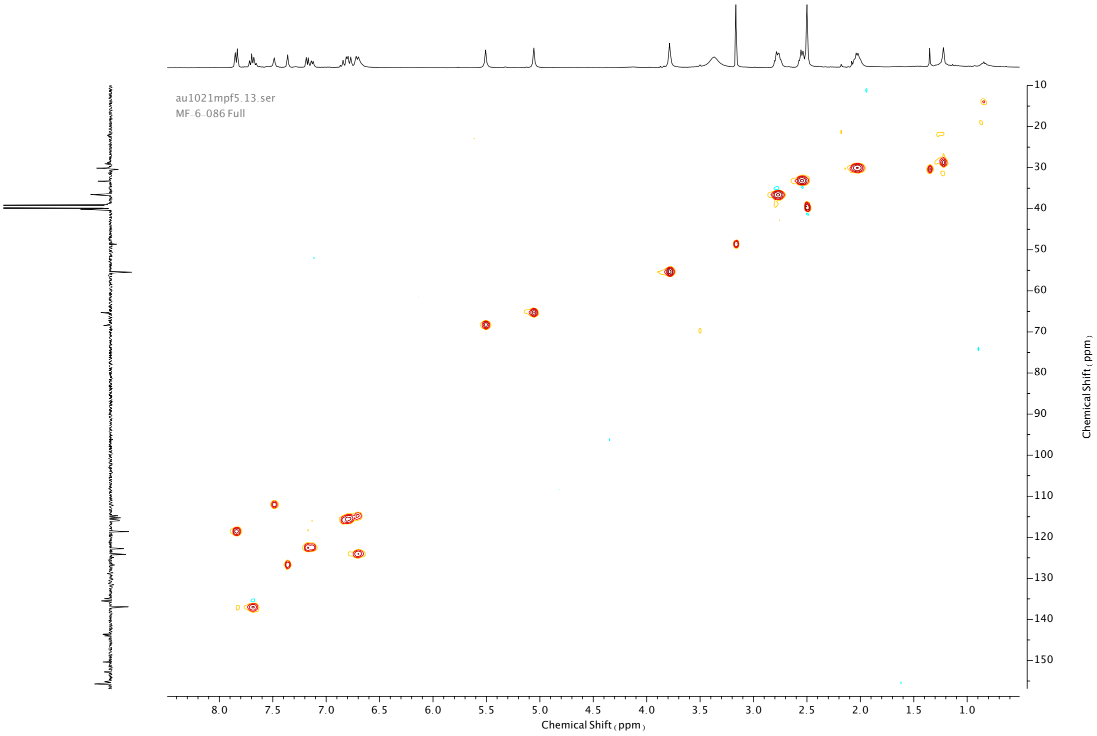

Figure **495**. HSQC NMR (DMSO-d_6) of **115**.

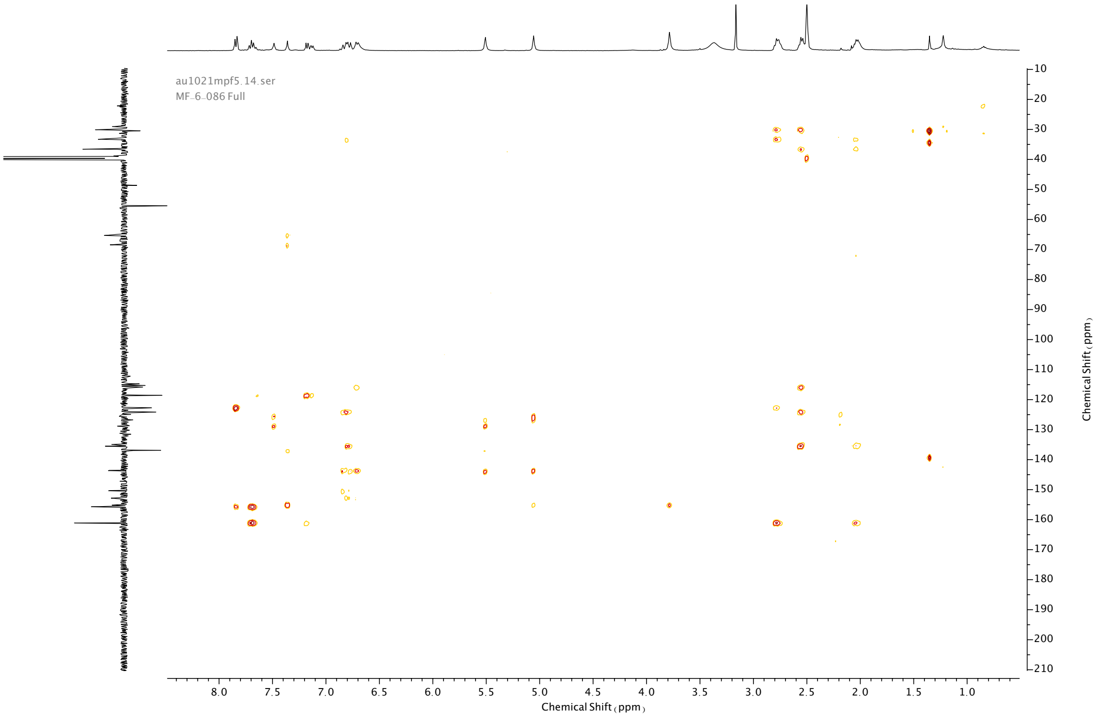

Figure **496**. HMBC NMR (DMSO-d_6) of **115**.

Compound **116**

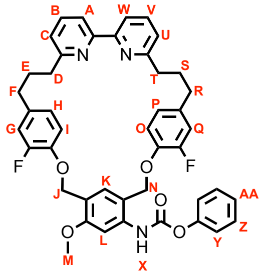

116 was prepared according to general procedure **(5)** from macrocycle **115** (140 mg, 0.22 mmol). Purification by column chromatography (eluent 1:0 → 19:1 CH_2Cl_2: Et_2O) afforded **116** as a white foam (93 mg, 0.13 mmol, 58%). ^{1}H NMR (400 MHz, $CDCl_3$, 298 K) δ_H 8.19 (1H, br. s, N-H_X), 7.93-7.89 (2H, t, H_B & H_V), 7.76 (1H, s, H_L), 7.64-7.55 (2H, m, H_A & H_W), 7.44-7.38 (2H, m, H_Z), 7.27-7.20 (3H, m, H_Y & H_{AA}), 7.07-6.99 (3H, H_C, H_U & H_K), 6.83-6.77 (2H, m, H_G & H_Q), 6.72-6.68 (1H, m, H_P or H_H), 6.64 (1H, t, *J* = 8.4 Hz, H_I or H_O), 6.61 (1H, t, *J* = 8.4 Hz, H_I or H_O), 6.57-6.52 (1H, m, H_P or H_H), 5.08 (2H, s, H_J or H_N), 4.95 (2H, s, H_J or H_N), 3.83 (3H, s, H_M), 2.94-2.88 (2H, m, H_D or H_T), 2.87-2.81 (2H, m, H_D or H_T), 2.69-2.60 (4H, m, H_F & H_R), 2.21-2.09 (4H, m, H_E & H_S). ^{13}C NMR (101 MHz, $CDCl_3$, 298 K) δ_C 161.5, 161.3, 153.5 (d, *J* = 245.3 Hz, J^1_{C-F}), 153.4 (d, *J* = 245.4 Hz, J^1_{C-F}), 150.8, 144.1 (d, *J* = 10.9 Hz, J^2_{C-F}), 142.6 (d, *J* = 11.1 Hz, J^2_{C-F}), 137.9, 137.8, 136.9 (x2), 136.8 (d, *J* = 5.9 Hz, J^3_{C-F}), 136.7 (d, *J* = 5.9 Hz, J^3_{C-F}), 130.3, 130.1, 129.6, 125.9, 124.4 (d, *J* = 3.3Hz, J^4_{C-F}), 124.2 (d, *J* = 3.2 Hz, J^4_{C-F}),122.9, 122.6 (x2), 121.9, 120.0, 118.9 (x2), 118.1 (d, *J* = 2.1 Hz, J^3_{C-F}), 117.6 (d, *J* = 2.1 Hz, J^3_{C-F}), 116.5 (d, *J* = 18.3 Hz, J^2_{C-F}), 116.4 (d, *J* = 18.4 Hz, J^2_{C-F}), 103.1, 71.4, 67.1, 55.8, 37.6, 37.5, 34.7 (x2), 30.8, 30.3. ^{19}F NMR (376 MHz, $CDCl_3$, 298 K) δ_F -134.3 (x2). HR-ESI-MS (CH_3CN): *m/z* = 728.2947 $[M+H]^+$ calc. 728.2931.

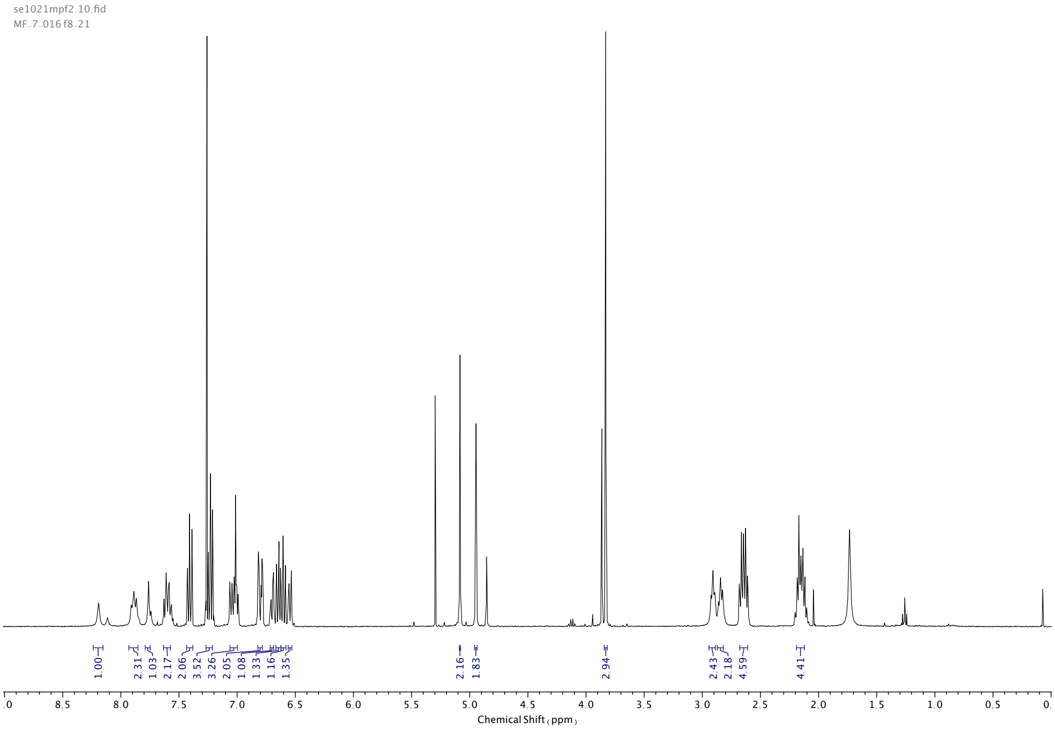

Figure **497**. ^{1}H NMR (CDCl$_3$, 400 MHz) of **116**.

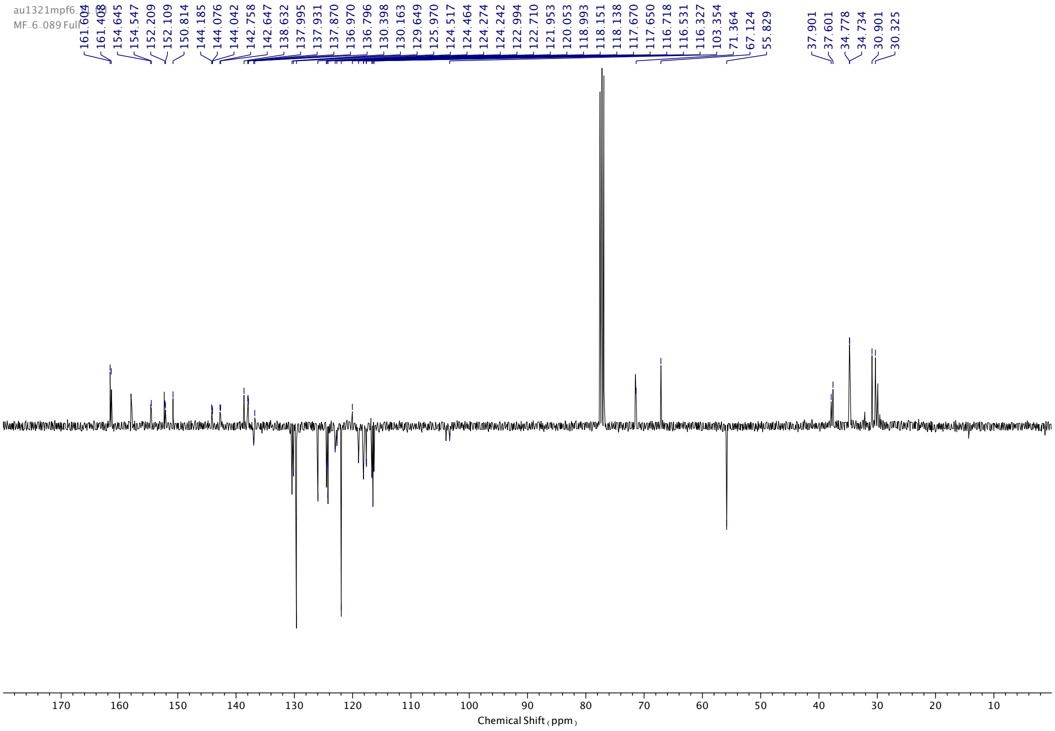

Figure **498**. ^{13}C NMR (CDCl$_3$, 101 MHz) of **116**.

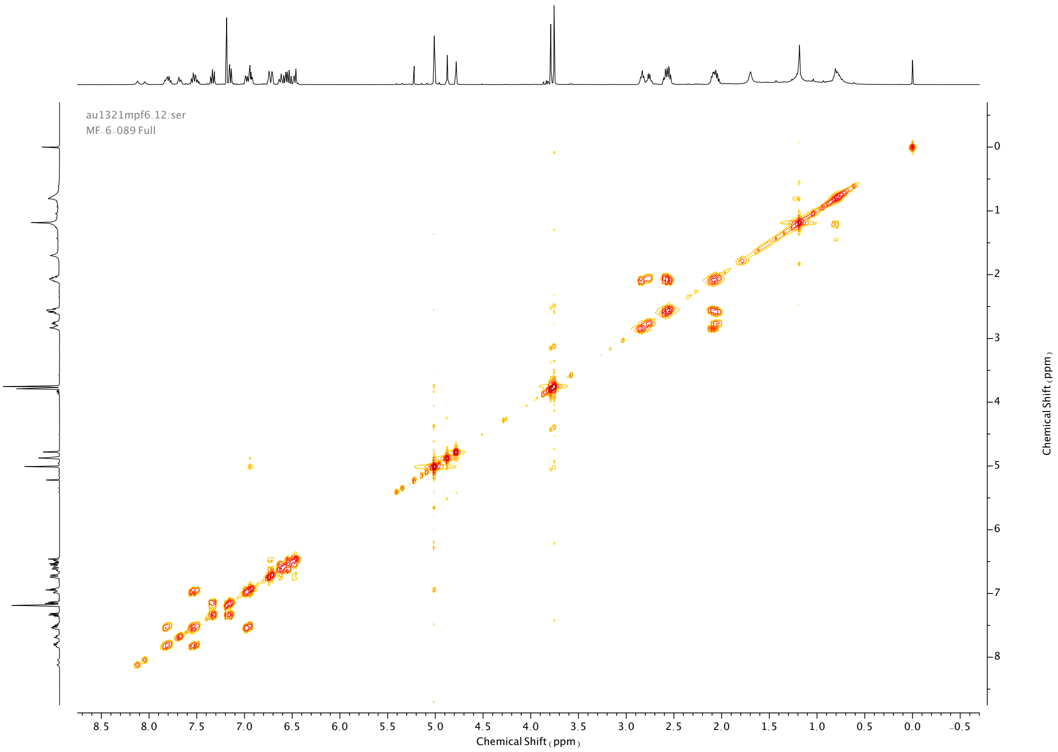

Figure **499**. COSY NMR ($CDCl_3$) of **116**.

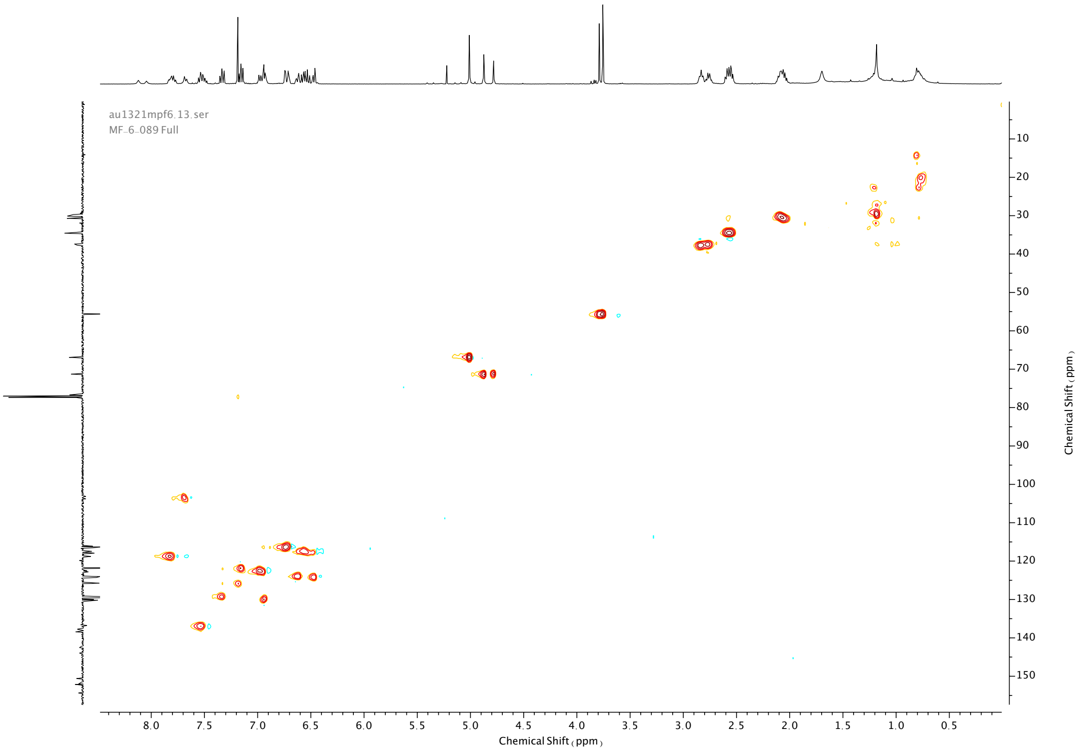

Figure **500**. HSQC NMR ($CDCl_3$) of **116**.

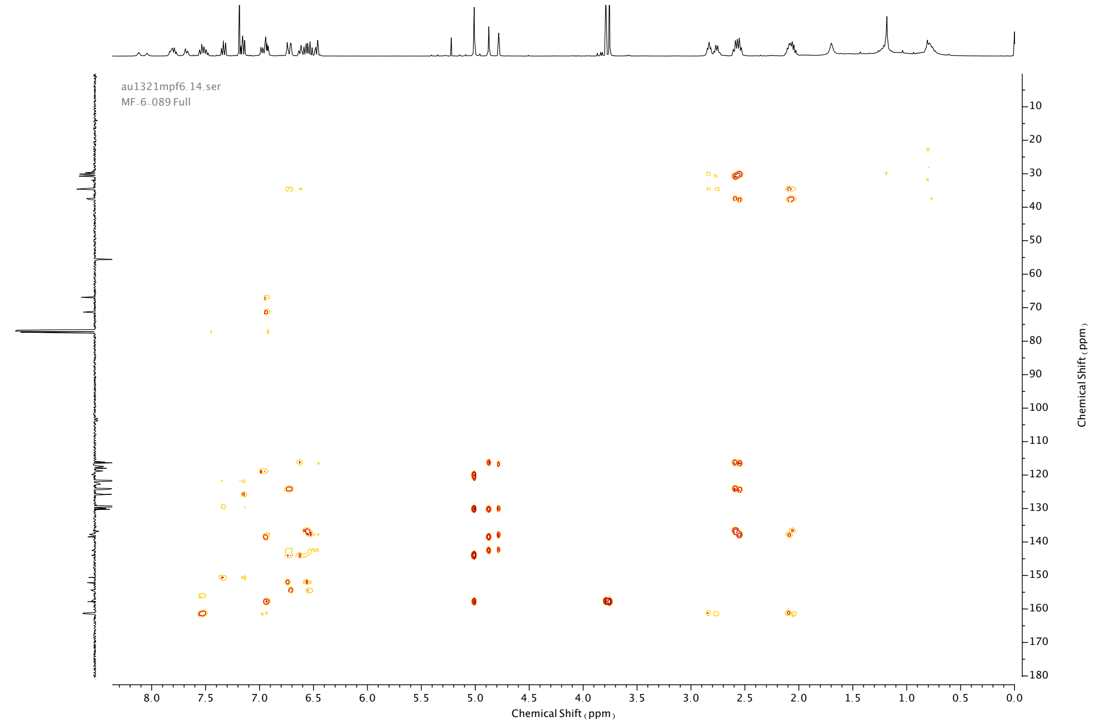

Figure **501**. HMBC NMR (CDCl$_3$) of **116**.

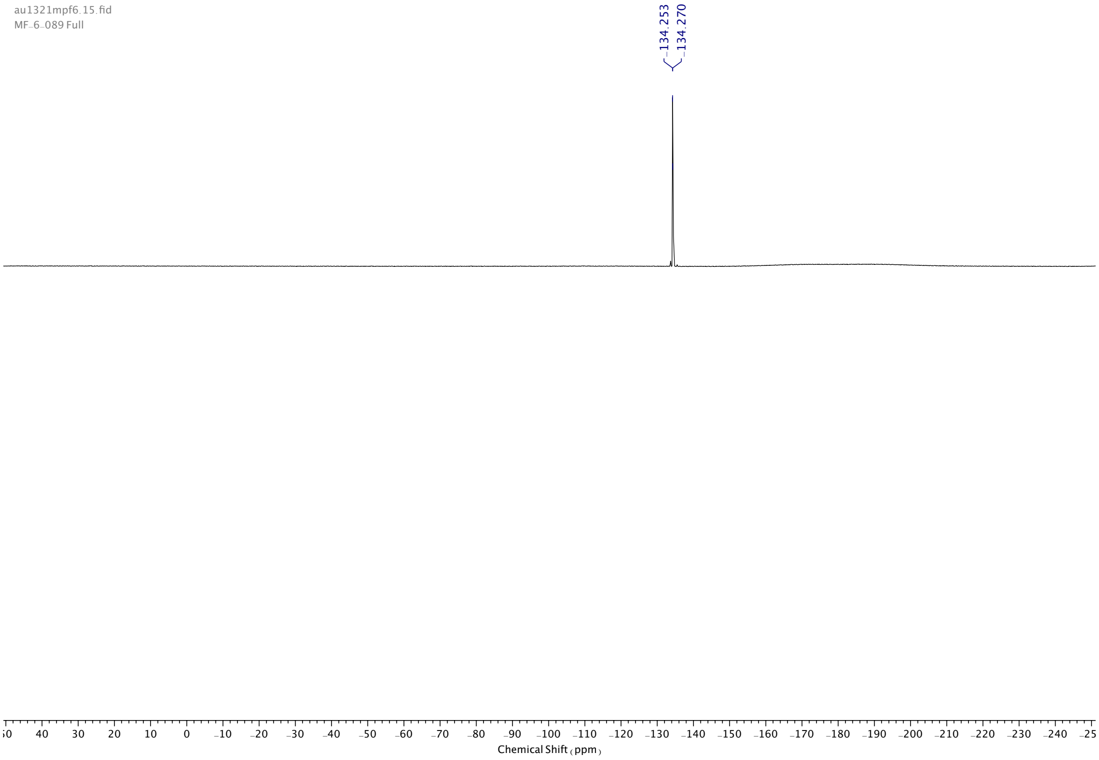

Figure **502**. ^{19}F NMR (CDCl$_3$, 376 MHz) of **116**.

Compound **119**

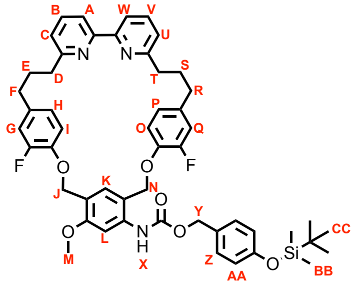

119 was synthesised according to general procedure **(6)** from macrocycle **116** (78 mg, 0.11 mmol) and trigger alcohol **51** (81 mg, 0.34 mmol). Purification by column chromatography (eluent 1:0 → 19:1 CH_2Cl_2: Et_2O) afforded **119** as a white foam (75 mg, 0.086 mmol, 76%). ^1H NMR (400 MHz, $CDCl_3$, 298 K) δ_H 7.88 (1H, d, J = 7.7 Hz, H_A or H_W), 7.85 (1H, d, J = 7.7 Hz, H_A or H_W), 7.78 (1H, br. s, N-H_X), 7.70 (1H, s, H_L), 7.58 (1H, t, J = 7.7 Hz, H_B or H_V), 7.53 (1H, t, J = 7.7 Hz, H_B or H_V), 7.30 (2H, d, J = 8.6 Hz, H_Z), 7.02 (1H, d, J = 7.6 Hz, H_C or H_U), 6.98-6.94 (2H, m, H_K & H_C or H_U), 6.84 (2H, d, J = 8.6 Hz, H_{AA}), 6.78 (1H, t, J = 2.1 Hz, H_G), 6.76-6.74 (1H, m, H_Q), 6.70-6.66 (1H, m, H_H), 6.62 (1H, t, J = 8.4 Hz, H_I), 6.57-6.49 (2H, m, H_P & H_O), 5.15 (2H, s, H_Y), 5.05 (2H, s, H_J), 4.85 (2H, s, H_N), 3.86 (3H, s, H_M), 2.88 (2H, t, J = 6.8 Hz, H_D or H_T), 2.82 (2H, t, J = 6.8 Hz, H_D or H_T), 2.65 (2H, t, J = 7.2 Hz, H_F or H_R), 2.61 (2H, t, J = 7.2 Hz, H_F or H_R), 2.20-2.08 (4H, m, H_E & H_S), 0.99 (9H, s, H_{CC}), 0.20 (6H, s, H_{BB}). ^{13}C NMR (101 MHz, $CDCl_3$, 298 K) δ_C 161.5, 161.3, 157.9, 156.2 (HMBC (x2)), 156.0, 153.9, 153.4 (d, J = 245.4 Hz, $J^1_{C\text{-}F}$), 153.3 (d, J = 245.4 Hz, $J^1_{C\text{-}F}$), 144.1 (d, J = 10.9 Hz, $J^2_{C\text{-}F}$), 142.7 (d, J = 11.1 Hz, $J^2_{C\text{-}F}$), 139.0, 137.7 (d, J = 6.2 Hz, $J^3_{C\text{-}F}$), 136.8 (x2), 136.7 (d, J = 6.1 Hz, $J^3_{C\text{-}F}$), 130.5, 130.0, 129.0, 124.3 (d, J = 3.3 Hz, $J^4_{C\text{-}F}$), 124.2 (d, J = 3.2 Hz, $J^4_{C\text{-}F}$), 122.8, 122.6, 120.3, 119.6, 118.8 (x2), 118.2 (d, J = 1.8 Hz, $J^3_{C\text{-}F}$), 117.6 (d, J = 1.8 Hz, $J^3_{C\text{-}F}$), 116.5 (d, J = 17.7 Hz, $J^2_{C\text{-}F}$), 116.4, 116.3 (, J = 17.7 Hz, $J^2_{C\text{-}F}$), 103.4, 71.3, 67.1, 67.0, 55.8, 37.9, 37.6, 34.7 (x2), 30.7, 30.3, 25.8, 18.4, -4.3. ^{19}F NMR (376 MHz, $CDCl_3$, 298 K) δ_F -134.3 (x2). HR-ESI-MS (CH_3CN): m/z = 872.3896 $[M+H]^+$ calc. 872.3901.

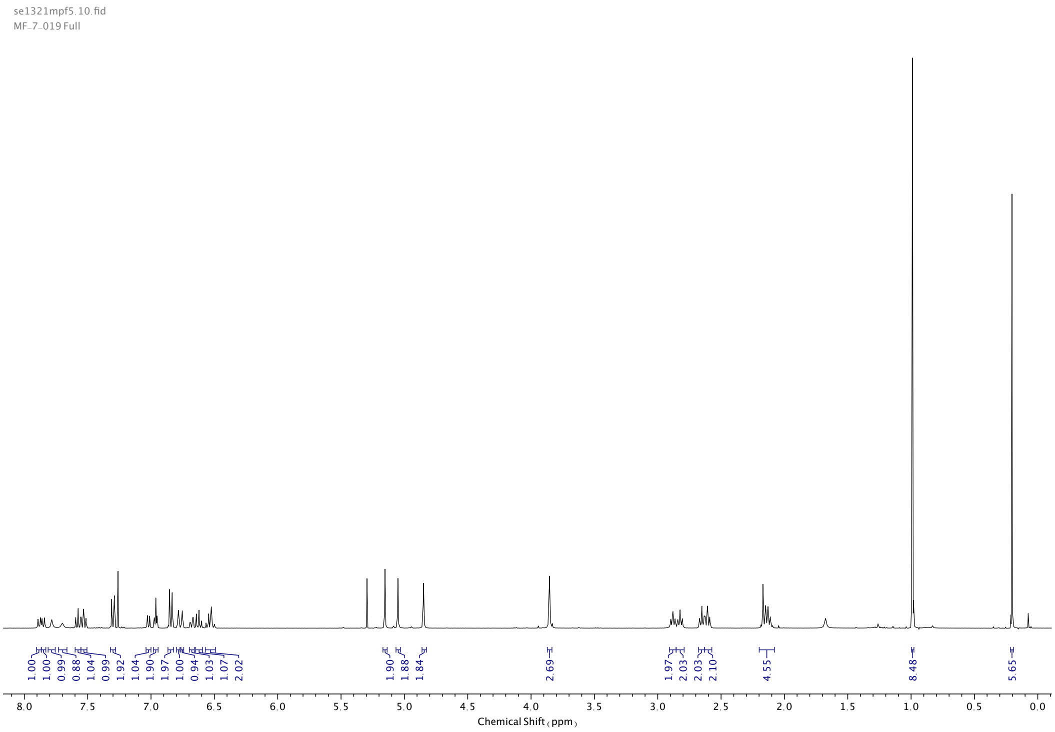

Figure **503**. ^{1}H NMR ($CDCl_3$, 400 MHz) of **119**.

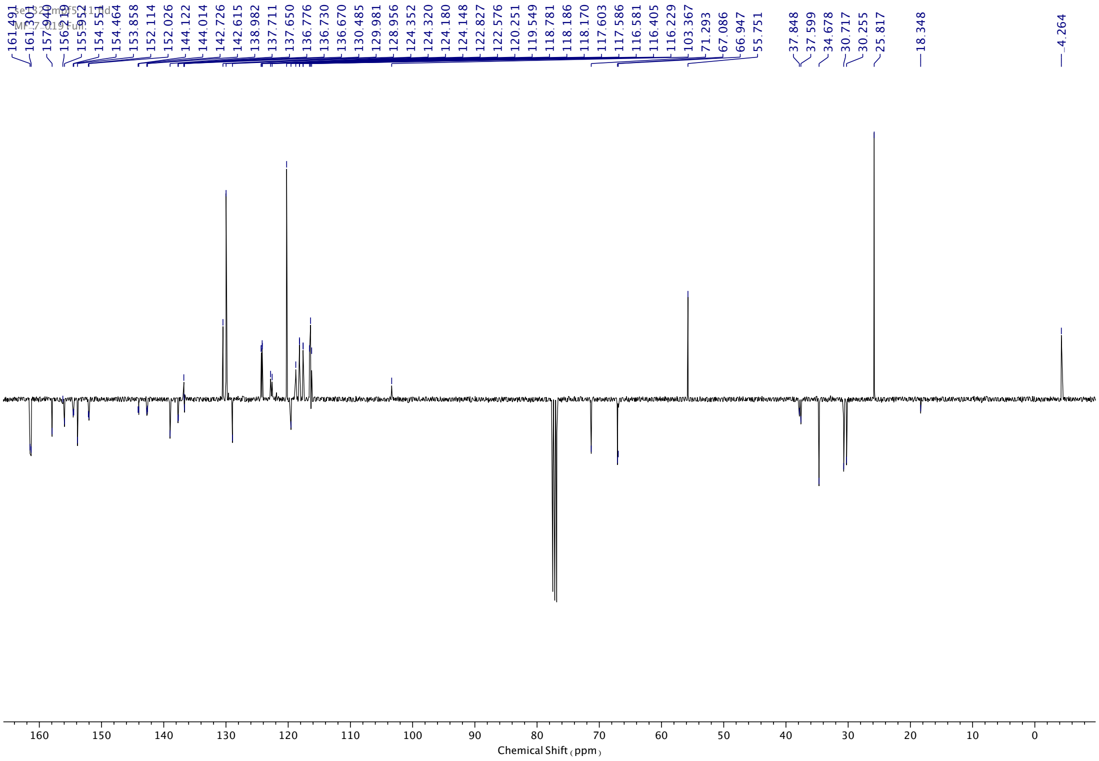

Figure **504**. ^{13}C NMR ($CDCl_3$, 101 MHz) of **119**.

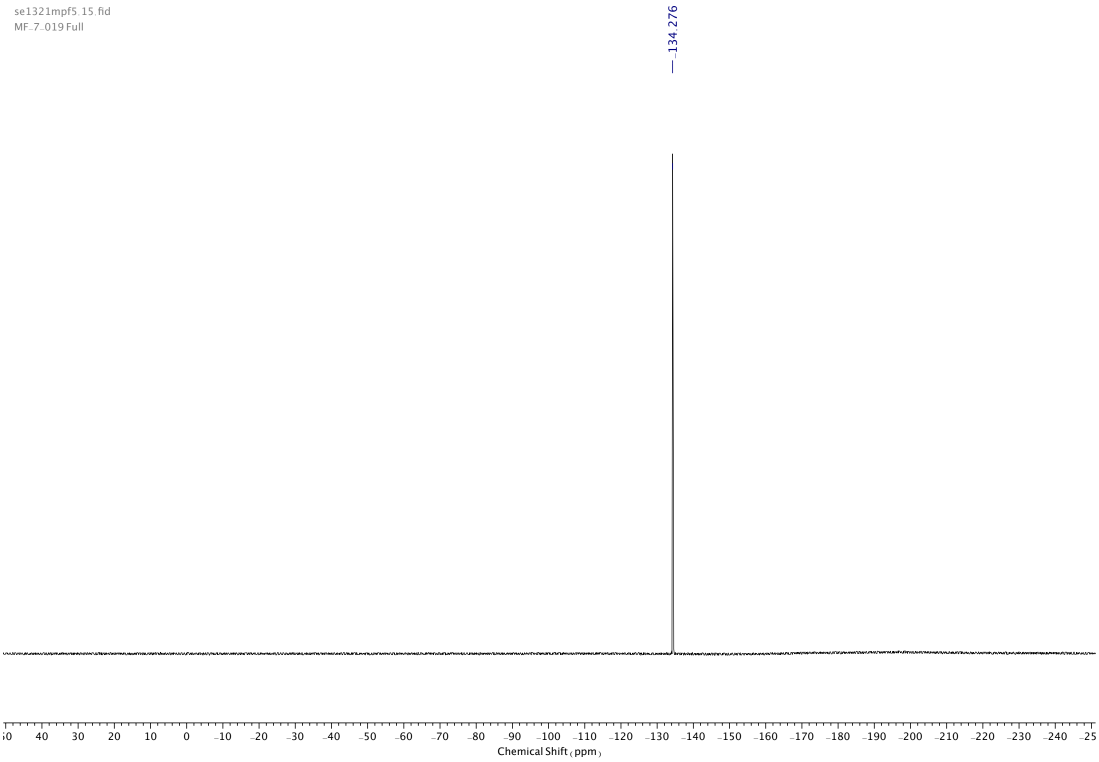

Figure **505**. ^{19}F NMR (CDCl$_3$, 376 MHz) of **119**.

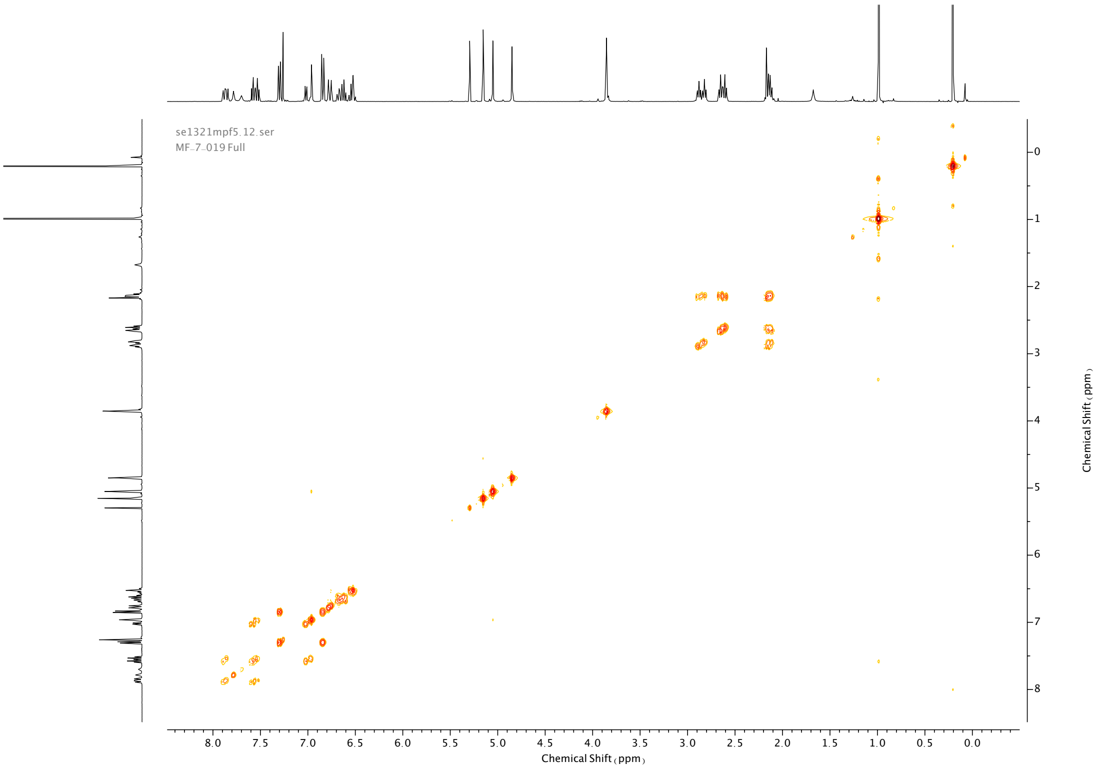

Figure **506**. COSY NMR (CDCl$_3$) of **119**.

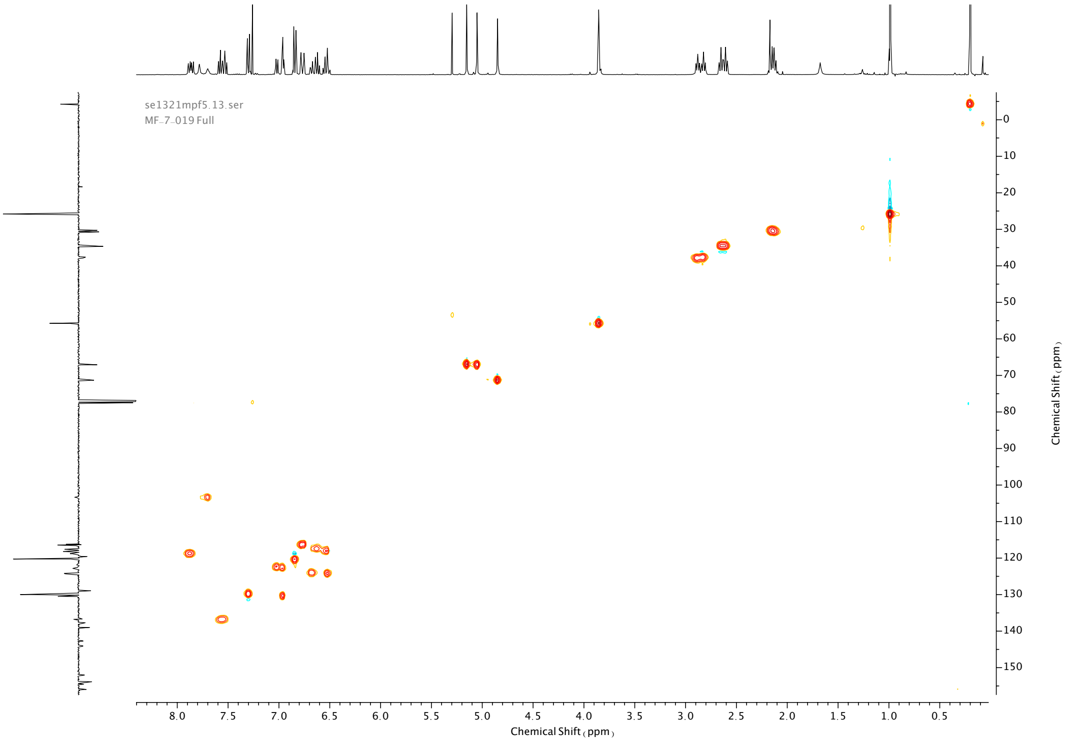

Figure **507**. HSQC NMR ($CDCl_3$) of **119**.

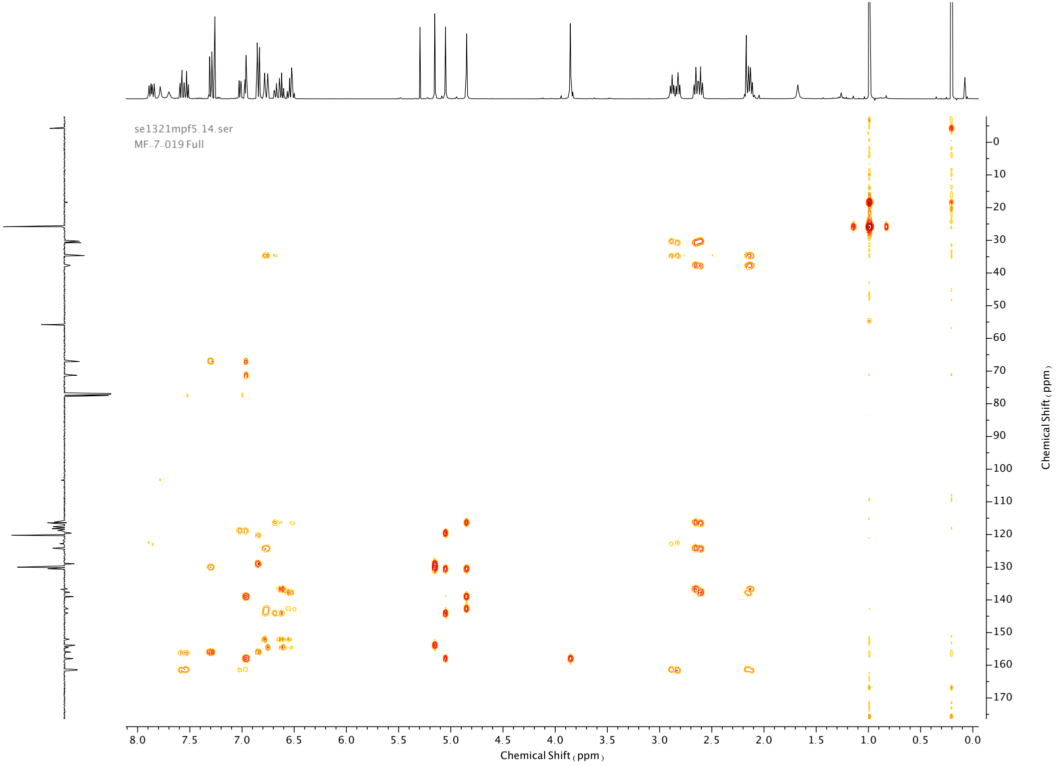

Figure **508**. HMBC NMR ($CDCl_3$) of **119**.

Compound **122**

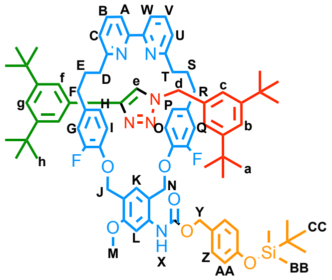

122 was synthesised according to general procedure **(7)** from macrocycle **119** (57 mg, 0.065 mmol), azide stopper **72** (24 mg, 0.098 mmol) and alkyne stopper **71** (21 mg, 0.098 mmol). Purification by column chromatography (eluent 1:0 → 19:1 CH_2Cl_2: Et_2O) afforded **122** as a white foam (42 mg, 0.032 mmol, 49%). ^{1}H NMR (400 MHz, $CDCl_3$, 298 K) δ_H 9.20 (1H, s, H_e), 8.03 (1H, s, H_K), 7.86 (1H, br. s, N-H_X), 7.78 (1H, br. s, H_L), 7.72 (1H, t, *J* = 7.8 Hz, H_B or H_V), 7.68 (1H, t, *J* = 7.8 Hz, H_B or H_V), 7.57-7.52 (2H, m, H_A & H_W), 7.34-7.31 (3H, m, H_f & H_b), 7.29-7.25 (2H, m, H_Z), 7.17 (1H, dd, *J* = 7.8, 0.8 Hz, H_C or H_U), 7.13 (1H, t, *J* = 1.8 Hz, H_g), 7.11-7.08 (3H, m, H_c & H_C or H_U), 6.80 (2H, d, *J* = 8.6 Hz, H_{AA}), 6.61 (1H, t, *J* = 8.7 Hz, H_H or H_P), 6.37-6.29 (2H, m, H_G & H_Q), 6.24 (1H, t, *J* = 8.6 Hz, H_H or H_P), 5.68-5.62 (2H, m, H_I & H_O), 5.41 (1H, d, *J* = 10.5 Hz, H_N or H_N’), 5.32-5.10 (5H, m, $H_{Y,}$ H_N or H_N’, H_J & H_J’), 4.86 (1H, d, *J* = 14.1 Hz, H_d or H_d’), 4.44 (1H, d, *J* = 14.1 Hz, H_d or H_d’), 3.94 (3H, s, H_M), 2.50-2.35 (4H, m, H_D & H_T), 2.33-2.28 (2H, m, H_F or H_R), 2.16-2.02 (2H, m, H_F or H_R), 1.72-1.40 (4H, m, H_E & H_S), 1.13 (18H, s, H_h or H_a), 1.07 (18H, s, H_h or H_a), 0.97 (9H, s, H_{CC}), 0.18 (6H, s, H_{BB}). ^{13}C NMR (101 MHz, $CDCl_{3,}$ 298 K) δ_C 163.1, 163.0, 158.2, 158.1, 157.4, 155.9, 154.2, 154.1, 152.1 (d, *J* = 243.9 Hz, J^1_{C-F}), 151.9 (d, *J* = 246.1 Hz, J^1_{C-F}), 151.1, 147.4, 145.3 (d, *J* = 10.6 Hz, J^2_{C-F}), 144.1 (d, *J* = 10.9 Hz, J^2_{C-F}), 138.9, 137.1, 136.9, 134.7, 134.0 (d, *J* = 6.0 Hz, J^3_{C-F}), 133.5 (d, *J* = 5.6 Hz, J^3_{C-F}), 130.9, 130.7, 130.0, 129.2, 123.9, 123.8 (d, *J* = 3.0 Hz, J^3_{C-F}), 123.2, 123.0, 122.9 (d, *J* = 3.1 Hz, J^3_{C-F}), 122.4, 122.3, 122.0, 120.9 (x2), 120.7, 120.3 (x2), 120.2, 120.1, 115.9 (s, J^4_{C-F}), 115.7 (d, *J* = 17.9 Hz, J^2_{C-F}), 115.2 (d, *J* = 17.8 Hz, J^2_{C-F}), 114.6 (s, J^4_{C-F}), 69.2, 67.2, 66.8, 55.9, 54.0, 38.3, 37.0, 35.0, 34.9, 34.8, 34.6, 31.7, 31.6, 31.5, 31.4, 25.9, 18.4, -4.2. ^{19}F NMR (376 MHz, $CDCl_3$, 298 K) δ_F -134.3, -135.0. HR-ESI-MS (CH_3CN): *m/z* = 1331.8 $[M+H]^+$ calc. 1331.7520

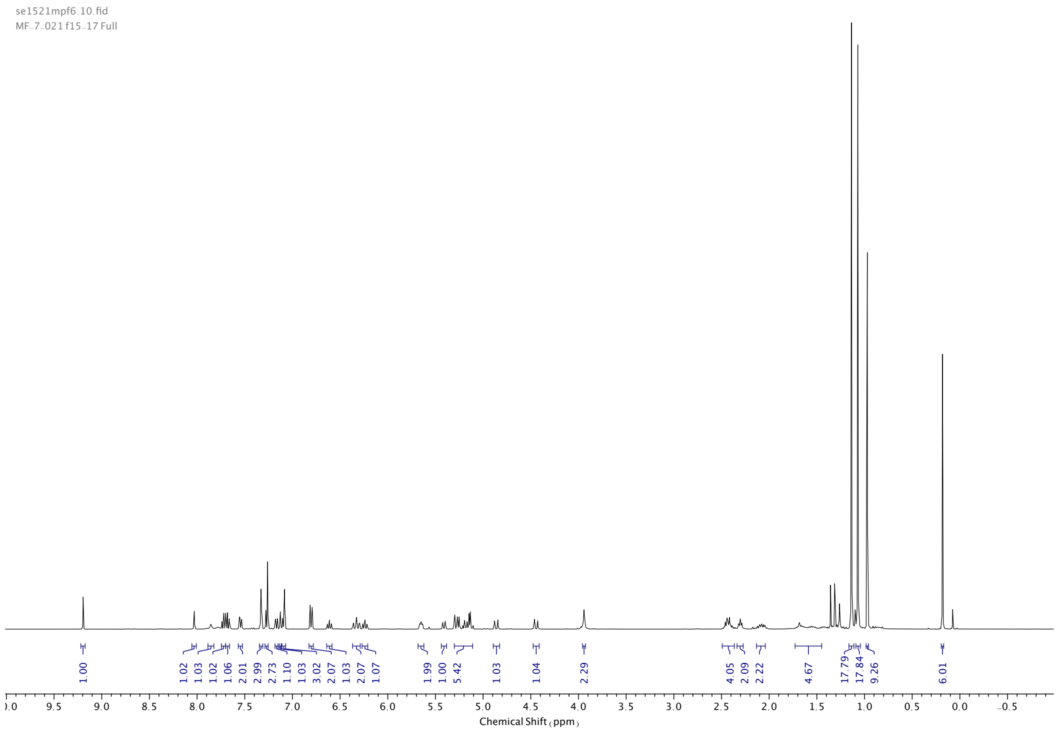

Figure **509**. ^{1}H NMR (CDCl$_3$, 400 MHz) of **122**.

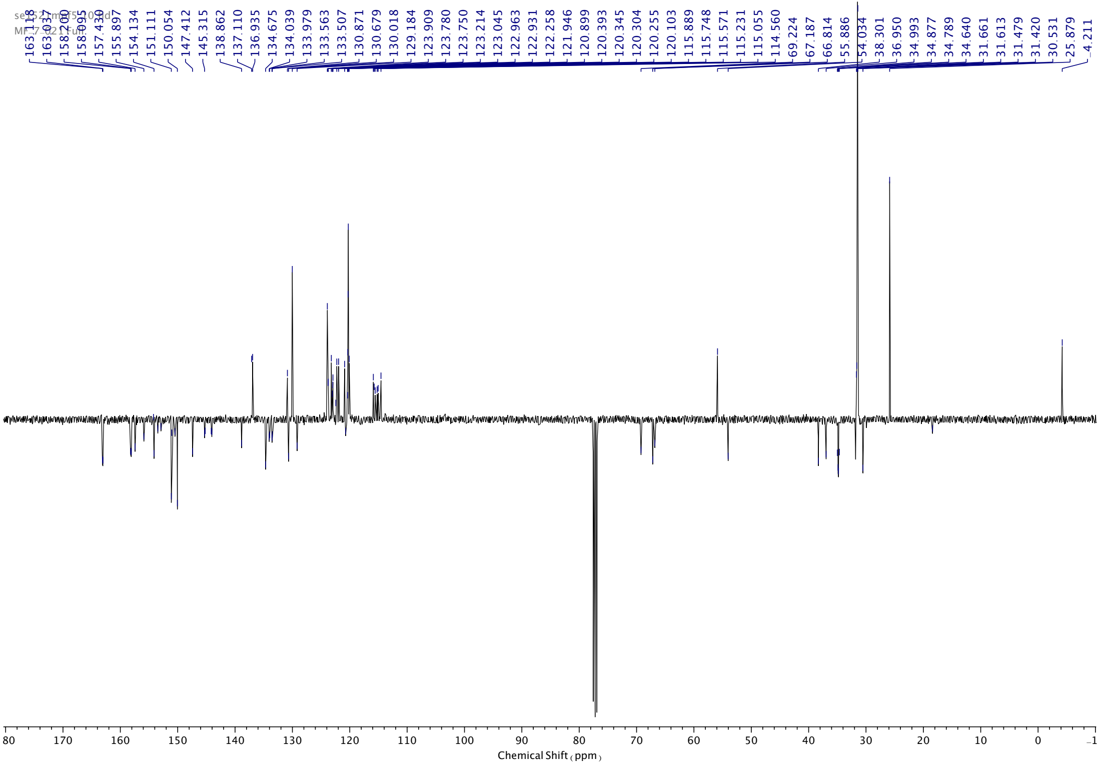

Figure **510**. ^{13}C NMR (CDCl$_3$, 101 MHz) of **122**.

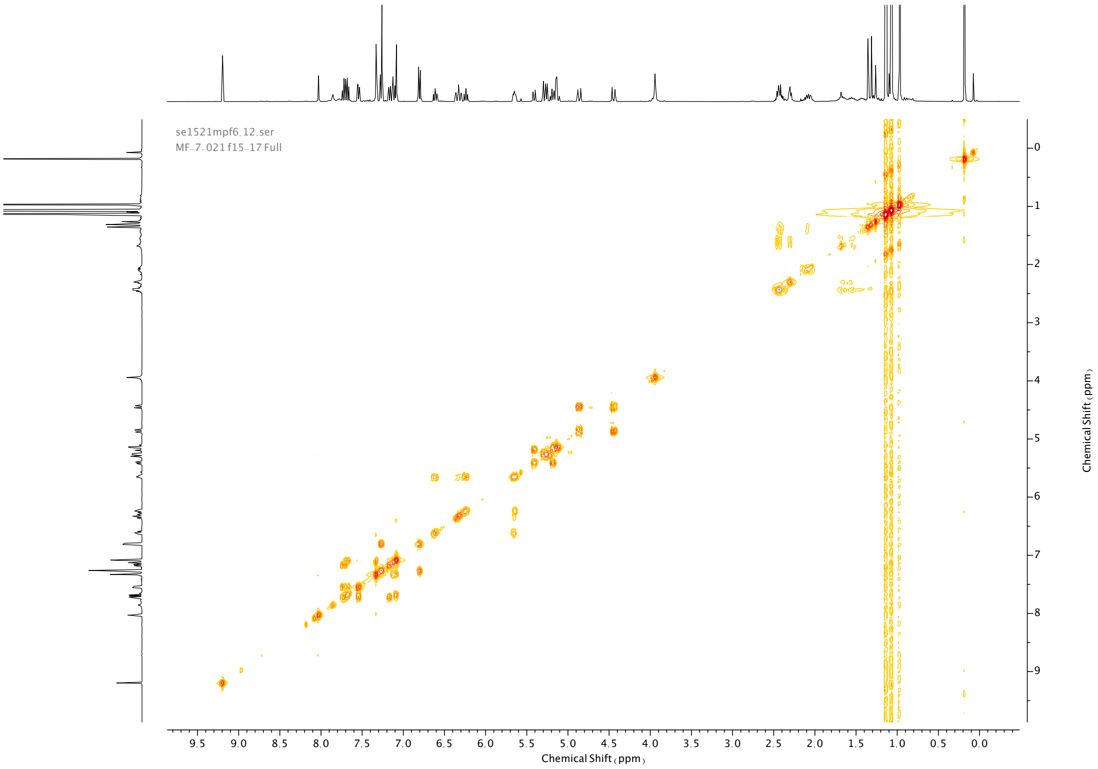

Figure **511**. COSY NMR ($CDCl_3$) of **122**.

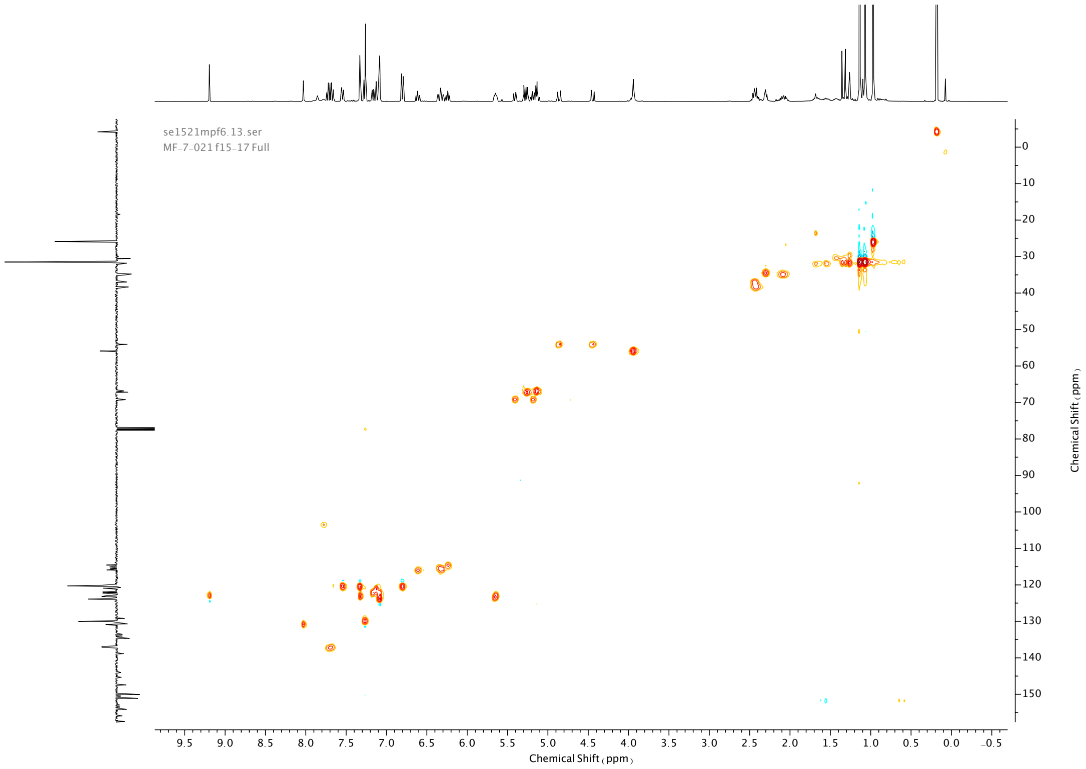

Figure **512**. HSQC NMR ($CDCl_3$) of **122**.

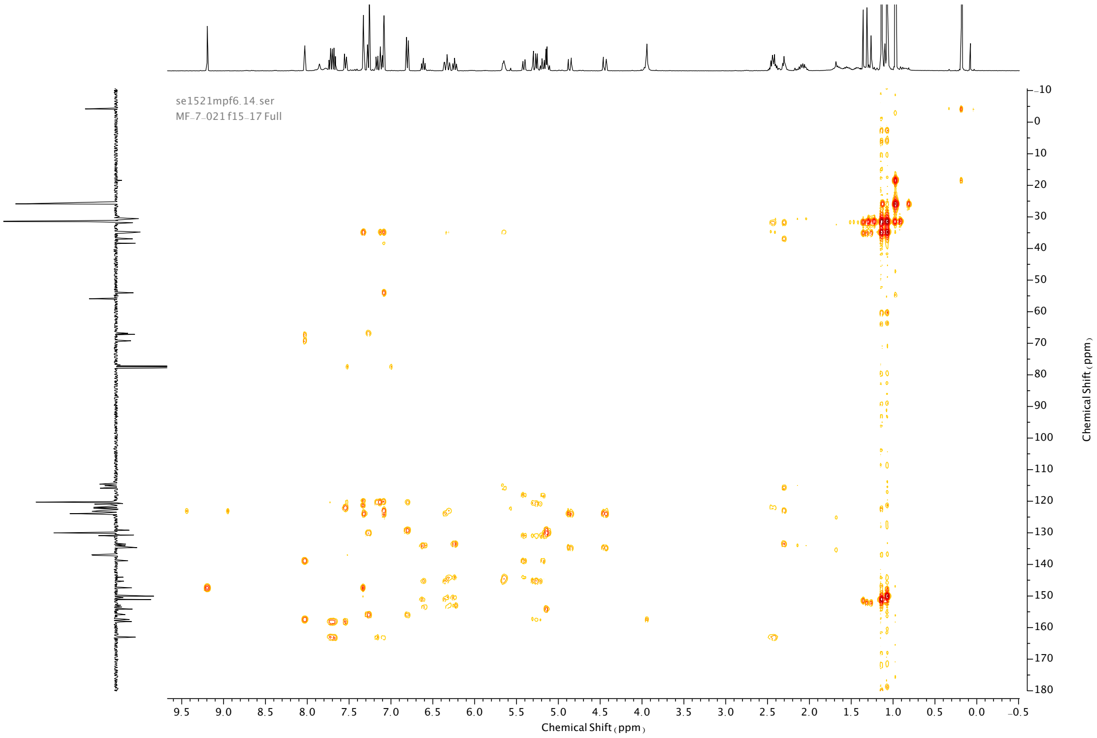

Figure **513**. HMBC NMR (CDCl$_3$) of **122**.

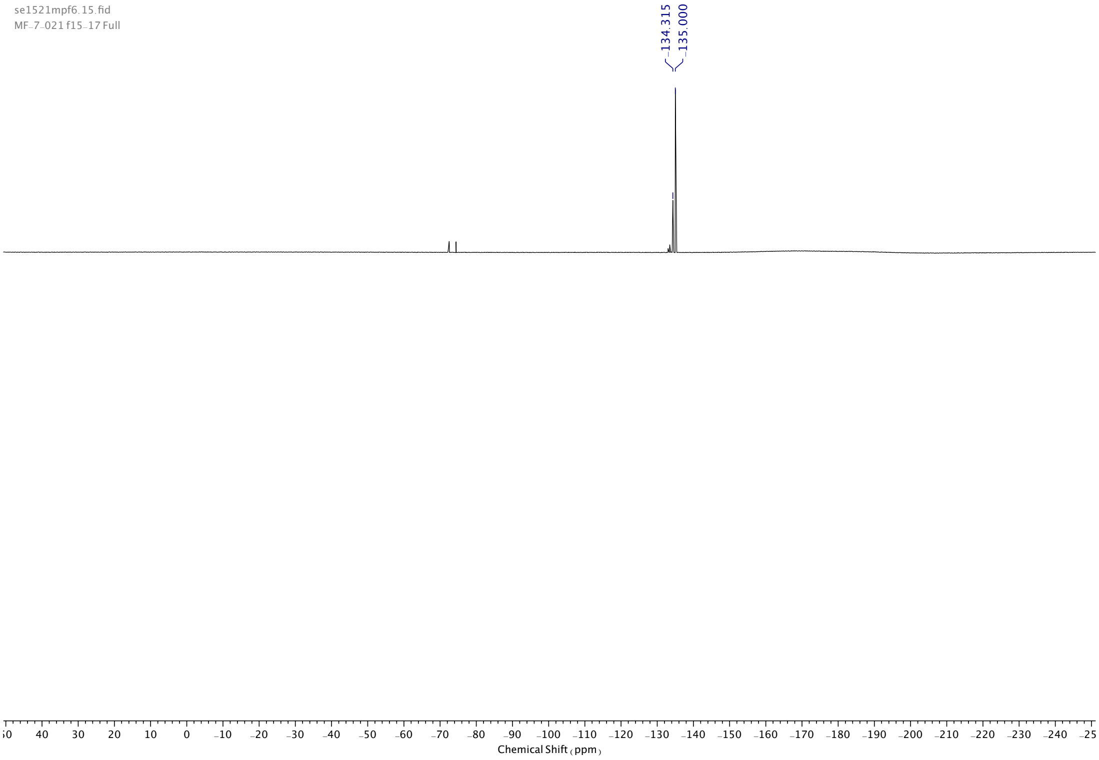

Figure **514**. ^{19}F NMR (CDCl$_3$, 376 MHz) of **122**.

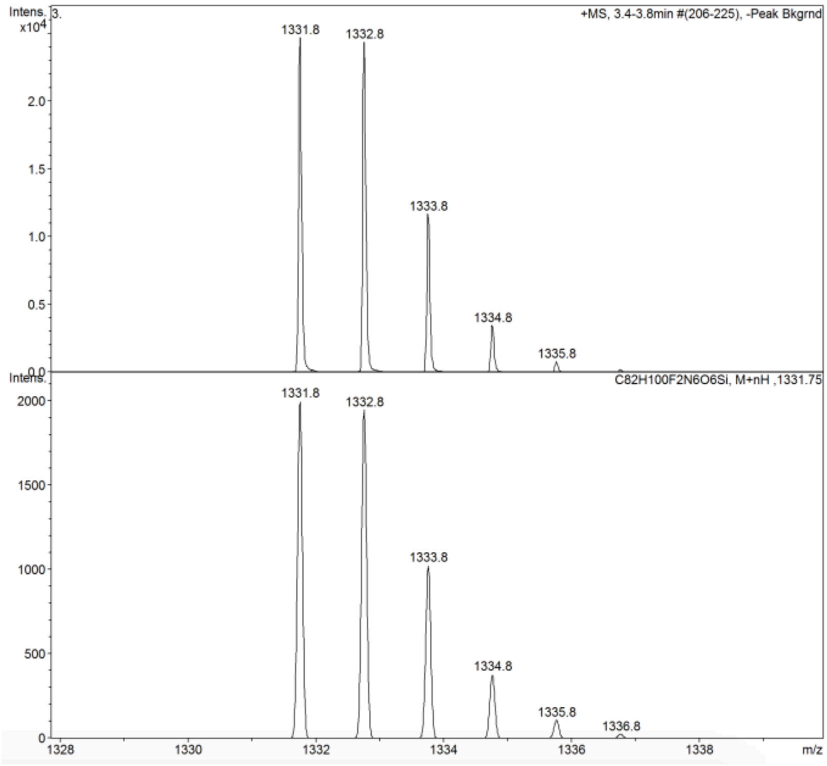

Figure **515**. Isotope pattern of **122**.

3.5. Bibliography

[1] P. K. Chakravarty, P. L. Carl, M. J. Weber, J. A. Katzenellenbogen, *J. Med. Chem.* **1983**, 26, 638–644.

[2] P. L. Carl, P. K. Chakravarty, J. A. Katzenellenbogen, *J. Med. Chem.* **1981**, 24, 479–480.

[3] C. A. Blencowe, A. T. Russell, F. Greco, W. Hayes, D. W. Thornthwaite, *Polym. Chem.* **2011**, 2, 773–790.

[4] M. E. Roth, O. Green, S. Gnaim, D. Shabat, *Chem. Rev.* **2016**, 116, 1309–1352.

[5] S. T. Phillips, A. M. Dilauro, *ACS Macro Lett.* **2014**, 3, 298–304.

[6] J. Yan, S. Lee, A. Zhang, J. Yoon, *Chem. Soc. Rev.* **2018**, 47, 6900–6916.

[7] E. Sella, D. Shabat, *Chem. Commun.* **2008**, 5701–5703.

[8] K. Haba, M. Popkov, M. Shamis, R. A. Lerner, C. F. Barbas, D. Shabat, *Angew. Chemie Int. Ed*. **2005**, 44, 716–720.

[9] A. Alouane, R. Labruère, T. Le Saux, F. Schmidt, L. Jullien, *Angew. Chemie Int. Ed.* **2015**, 54, 7492–7509.

[10] E. Sella, D. Shabat, *J. Am. Chem. Soc.* **2009**, 131, 9934–9936.

[11] J. L. M. Jourden, K. B. Daniel, S. M. Cohen, *Chem. Commun*. **2011**, 47, 7968–7970.

[12] A. K. Ghosh, M. Brindisi, *J. Med. Chem*. **2015**, 58, 2895–2940.

[13] P. D. Senter, W. E. Pearce, R. S. Greenfield, *J. Org. Chem.* **1990**, 55, 2975–2978.

[14] R. Perry-Feigenbaum, P. S. Baran, D. Shabat, *Org. Biomol. Chem.* **2009**, 7, 4825–4828.

[15] L. D. Taylor, J. M. Grasshoff, M. Pluhar, *J. Org. Chem.* **1978**, 43, 1197–1200.

[16] G. Le Corre, E. Guibé-Jampel, M. Wakselman, *Tetrahedron* **1978**, 34, 3105–3112.

[17] S. Zalipsky, M. Qazen, J. A. Walker, N. Mullah, Y. P. Quinn, S. K. Huang, *Bioconjug. Chem.* **1999**, 10, 703–707.

[18] F. M. H. De Groot, C. Albrecht, R. Koekkoek, P. H. Beusker, H. W. Scheeren, *Angew. Chemie Int. Ed.* **2003**, 42, 4490–4494.

[19] M. Shamis, D. Shabat, *Chem. - A Eur. J.* **2007**, 13, 4523–4528.

[20] R. Weinstain, E. Segal, R. Satchi-Fainaro, D. Shabat, *Chem. Commun.* **2010**, 46, 553–555.

[21] J. L. Bolton, T. Dunlap, *Chem. Res. Toxicol.* **2017**, 30, 13–37.

[22] J. C. Briggs, A. H. Haines, R. J. K. Taylor, *J. Chem. Soc. Chem. Commun*. **1993**, 1410–1411.

[23] J. C. Briggs, A. H. Haines, R. J. K. Taylor, *J. Chem. Soc.* **1995**, 27–32.

[24] B. M. Sykes, M. P. Hay, D. Bohinc-Herceg, N. A. Helsby, C. J. O'Connor, W. A. Denny, *J. Chem. Soc.* **2000**, 1601–1608.

[25] M. P. Hay, B. M. Sykes, W. A. Denny, C. J. O'Connor, *J. Chem. Soc.* **1999**, 2759–2770.

[26] K. M. Schmid, L. Jensen, S. T. Phillips, *J. Org. Chem.* **2012**, 77, 4363–4374.

[27] A. Zheng, D. Shan, B. Wang, *J. Org. Chem*. **1999**, 64, 156–161.

[28] U. Grether, H. Waldmann, *Angew. Chemie Int. Ed.* **2000**, 39, 1629–1632.

[29] R. J. Amir, D. Shabat, *Chem. Commun.* **2004**, 4, 1614–1615.

[30] N. Nakamura, S. Uchinomiya, K. Inoue, A. Ojida, *Molecules* **2020**, 25, 2153.

[31] Z. Deng, J. Hu, S. Liu, *Macromol. Rapid Commun.* **2020**, 41, 1099531.

[32] A. Sagi, E. Segal, R. Satchi-Fainaro, D. Shabat, *Bioorganic Med. Chem.* **2007**, 15, 3720–3727.

[33] M. A. DeWit, E. R. Gillies, *J. Am. Chem. Soc.* **2009**, 131, 18327–18334.

[34] E. K. Y. Chen, R. A. McBride, E. R. Gillies, *Macromolecules* **2012**, 45, 7364–7374.

[35] R. V. Gonzaga, L. A. do Nascimento, S. S. Santos, B. A. Machado Sanches, J. Giarolla, E. I. Ferreira, *J. Pharm. Sci.* **2020**, 109, 3262–3281.

[36] J. Anderski, L. Mahlert, J. Sun, W. Birnbaum, D. Mulac, S. Schreiber, F. Herrmann, D. Kuckling, K. Langer, *Int. J. Pharm.* **2019**, 557, 182–191.

[37] M. L. Szalai, R. M. Kevwitch, D. V. McGrath, *J. Am. Chem. Soc.* **2003**, 125, 15688–15689.

[38] A. Ortiz, C. S. Shanahan, D. T. Sisk, S. C. Perera, P. Rao, D. V. McGrath, *J. Org. Chem.* **2010**, 75, 6154–6162.

[39] N. W. Polaske, M. L. Szalai, C. S. Shanahan, D. V. McGrath, *Org. Lett.* **2010**, 12, 4944-4947.

[40] A. Warnecke, F. Kratz, *J. Org. Chem.* **2008**, 73, 1546–1552.

[41] W. Seo, S. T. Phillips, *J. Am. Chem. Soc.* **2010**, 132, 9234–9235.

[42] R. Perry-Feigenbaum, E. Sella, D. Shabat, *Chem. - A Eur. J.* **2011**, 17, 12123–12128.

[43] P. Swietach, R. D. Vaughan-Jones, A. L. Harris, A. Hulikova, *Philos. Trans. R. Soc. B Biol. Sci.* **2014**, 369, 1638.

[44] A. Ghaffar, B. Yameen, M. Latif, M. I. Malik in *Metal Nanoparticles for Drug Delivery and Diagnostic Applications* (Eds.: M. R. Shah, M. Imran, S. Ullah), Elsevier, **2019**, pp. 259–278.

[45] M. A. Dewit, E. R. Gillies, *Org. Biomol. Chem*. **2011**, 9, 1846–1854.

[46] A. P. Esser-Kahn, N. R. Sottos, S. R. White, J. S. Moore, *J. Am. Chem. Soc.* **2010**, 132, 10266–10268.

[47] M. Gisbert-Garzaran, D. Lozano, M. Vallet-Regí, M. Manzano, *RSC Adv.* **2017**, 7, 132–136.

[48] T. Eom, W. Yoo, Y. D. Lee, J. H. Park, Y. Choe, J. Bang, S. Kim, A. Khan, *J. Mater. Chem. B* **2017**, 5, 4574–4578.

[49] W. A. Henne, D. D. Doorneweerd, A. R. Hilgenbrink, S. A. Kularatne, P. S. Low, *Bioorganic Med. Chem. Lett.* **2006**, 16, 5350–5355.

[50] A. El Alaoui, F. Schmidt, M. Amessou, M. Sarr, D. Decaudin, J. C. Florent, L. Johannes, *Angew. Chemie Int. Ed.* **2007**, 46, 6469–6472.

[51] E. Aoyama, H. Fuchida, Y. Oshikawa, S. Uchinomiya, A. Ojida, *Chem. Commun.* **2016**, 52, 7715–7718.

[52] E. K. Lei, S. O. Kelley, *J. Am. Chem. Soc.* **2017**, 139, 9455–9458.

[53] G. Liu, X. Wang, J. Hu, G. Zhang, S. Liu, *J. Am. Chem. Soc.* **2014**, 136, 7492–7497.

[54] F. Zhang, Q. Ni, O. Jacobson, S. Cheng, A. Liao, Z. Wang, Z. He, G. Yu, J. Song, Y. Ma, G. Niu, L. Zhang, G. Zhu, X. Chen, *Angew. Chemie Int. Ed.* **2018**, 57, 7066–7070.

[55] S. S. Dunn, S. Tian, S. Blake, J. Wang, A. L. Galloway, A. Murphy, P. D. Pohlhaus, J. P. Rolland, M. E. Napier, J. M. DeSimone, *J. Am. Chem. Soc.* **2012**, 134, 7423–7430.

[56] K. Dutta, D. Hu, B. Zhao, A. E. Ribbe, J. Zhuang, S. Thayumanavan, *J. Am. Chem. Soc.* **2017**, 139, 5676–5679.

[57] D. W. Norbeck, P. A. Lartey, W. Rosenbrook, J. B. Kramer, D. J. Graepovnik, *J. Med. Chem.* **1989**, 32, 625–629.

[58] H. J. Forman, H. Zhang, *Nat. Rev. Drug Discov.* **2021**, 20, 689–709.

[59] J. L. Major Jourden, S. M. Cohen, *Angew. Chemie Int. Ed.* **2010**, 49, 6795–6797.

[60] Y. Zhang, Q. Yin, L. Yin, L. Ma, L. Tang, J. Cheng, *Angew. Chemie Int. Ed.* **2013**, 52, 6435-6438.

[61] C. De Gracia Lux, S. Joshi-Barr, T. Nguyen, E. Mahmoud, E. Schopf, N. Fomina, A. Almutairi, *J. Am. Chem. Soc.* **2012**, 134, 15758–15764.

[62] K. E. Broaders, S. Grandhe, J. M. J. Fréchet, *J. Am. Chem. Soc.* **2011**, 133, 756–758.

[63] L. C. Lo, C. Y. Chu, *Chem. Commun.* **2003**, 2728–2729.

[64] C. Sandford, V. K. Aggarwal, *Chem. Commun.* **2017**, 53, 5481–5494.

[65] Y. Hu, X. Li, Y. Fang, W. Shi, X. Li, W. Chen, M. Xian, H. Ma, *Chem. Sci.* **2019**, 10, 7690–7694.

[66] W. Tao, Z. He, *Asian J. Pharm. Sci.* **2018**, 13, 101–112.

[67] A. Höcherl, E. Jäger, A. Jäger, M. Hrubý, R. Konefał, O. Janoušková, J. Spěváček, Y. Jiang, P. W. Schmidt, T. P. Lodge, P. Štěpánek, *Polym. Chem.* **2017**, 8, 1999–2004.

[68] A. Sagi, R. Weinstain, N. Karton, D. Shabat, *J. Am. Chem. Soc.* **2008**, 130, 5434–5435.

[69] A. Raposo Moreira Dias, A. Pina, A. Dean, H. G. Lerchen, M. Caruso, F. Gasparri, I. Fraietta, S. Troiani, D. Arosio, L. Belvisi, L. Pignataro, A. Dal Corso, C. Gennari, *Chem. - A Eur. J.* **2019**, 25, 1696–1700.

[70] E. L. Sievers, P. D. Senter, *Annu. Rev. Med.* **2013**, 64, 15–29.

[71] Y. Anami, C. M. Yamazaki, W. Xiong, X. Gui, N. Zhang, Z. An, K. Tsuchikama, *Nat. Commun.* **2018**, 9, 2512.

[72] S. O. Doronina, B. E. Toki, M. Y. Torgov, B. A. Mendelsohn, C. G. Cerveny, D. F. Chace, R. L. DeBlanc, R. P. Gearing, T. D. Bovee, C. B. Siegall, J. A. Francisco, A. F. Wahl, D. L. Meyer, P. D. Senter, *Nat. Biotechnol.* **2003**, 21, 778–784.

[73] A. Younes, U. Yasothan, P. Kirkpatrick, *Nat. Rev. Drug Discov.* **2012**, 11, 19–20.

[74] E. Bakina, D. Farquhar, *Anticancer. Drug Des.* **1999**, 14, 507–515.

[75] M. Thomas, F. Rivault, I. Tranoy-Opalinski, J. Roche, J. P. Gesson, S. Papot, *Bioorganic Med. Chem. Lett.* **2007**, 17, 983–986.

[76] M. Thomas, J. Clarhaut, P. O. Strale, I. Tranoy-Opalinski, J. Roche, S. Papot, *ChemMedChem* **2011**, 6, 1006–1010.

[77] M. Grinda, J. Clarhaut, B. Renoux, I. Tranoy-Opalinski, S. Papot, in *Med. Chem. Comm,* **2012**, 3, 68–70.

[78] F. Hamon, B. Renoux, C. Chadéneau, J. M. Muller, S. Papot, *Eur. J. Med. Chem.* **2010**, 45, 1678–1682.

[79] B. Renoux, T. Legigan, S. Bensalma, C. Chadéneau, J. M. Muller, S. Papot, *Org. Biomol. Chem.* **2011**, 9, 8459–8465.

[80] J. P. Gesson, J. C. Jacquesy, M. Mondon, P. Petit, B. Renoux, S. Andrianomenjanahary, H. Van Dufat-Trinh, M. Koch, S. Michel, F. Tillequin, J. C. Florent, C. Monneret, K. Bosslet, J. Czech, D. Hoffmann, *Anticancer. Drug Des*. **1994**, 9, 409–423.

[81] K. Bosslet, J. Czech, D. Hoffmann, *Cancer Res*. **1994**, 54, 2151-2159.

[82] T. Legigan, J. Clarhaut, I. Tranoy-Opalinski, A. Monvoisin, B. Renoux, M. Thomas, A. Le-Pape, S. Lerondel, S. Papot, *Angew. Chemie Int. Ed.* **2012**, 51, 11606–11610.

[83] N. Pairault, R. Barat, I. Tranoy-Opalinski, B. Renoux, M. Thomas, S. Papot, *Comptes Rendus Chim.* **2016**, 19, 103-112.

[84] J. Riebe, J. Niemeyer, *European J. Org. Chem.* **2021**, 2021, 5106–5116.

[85] M. W. Ambrogio, T. A. Pecorelli, K. Patel, N. M. Khashab, A. Trabolsi, H. A. Khatib, Y. Y. Botros, J. I. Zink, J. F. Stoddart, *Org. Lett.* **2010**, 12, 3304–3307.

[86] H. Meng, M. Xue, T. Xia, Y.-L. Zhao, F. Tamanoi, J. F. Stoddart, J. I. Zink, A. E. Nel, *J. Am. Chem. Soc.* **2010**, 132, 12690–12697.

[87] K. Patel, S. Angelos, W. R. Dichtel, A. Coskun, Y.-W. Yang, J. I. Zink, J. F. Stoddart, *J. Am. Chem. Soc.* **2008**, 130, 2382–2383.

[88] J. Lu, E. Choi, F. Tamanoi, J. I. Zink, *Small* **2008**, 4, 421–426.

[89] Y. Yamada, S. Daikuhara, A. Tamura, K. Nishida, N. Yui, H. Harashima, R. Li, *Chem. Commun.* **2019**, 55, 7203.

[90] T. Ooya, H. S. Choi, A. Yamashita, N. Yui, Y. Sugaya, A. Kano, A. Maruyama, H. Akita, R. Ito, K. Kogure, H. Harashima*, J. Am. Chem. Soc.* **2006**, 128, 3852-3853.

[91] A. Fernandes, A. Viterisi, F. Coutrot, S. Potok, D. A. Leigh, V. Aucagne, S. Papot, *Angew. Chemie Int. Ed.* **2009**, 48, 6443–6447.

[92] A. Fernandes, A. Viterisi, V. Aucagne, D. A. Leigh, S. Papot, *Chem. Commun.* **2012**, 48, 2083.

[93] R. Barat, T. Legigan, I. Tranoy-Opalinski, B. Renoux, E. Péraudeau, J. Clarhaut, P. Poinot, A. E. Fernandes, V. Aucagne, D. A. Leigh, S. Papot, *Chem. Sci.* **2015**, 6, 2608–2613.

[94] J. Maynard, PhD Thesis, University of Southampton (UK), **2019**.

[95] J. E. M. Lewis, R. J. Bordoli, M. Denis, C. J. Fletcher, M. Galli, E. A. Neal, E. M. Rochette, S. M. Goldup, *Chem. Sci.* **2016**, 7, 3154–3161.

[96] P. Wang, Y. Ma, S. Liu, F. Zhou, B. Yang, Y. Deng, *Green Chem.* **2015**, 17, 3964–3971.

[97] A. W. Hofmann, *Berichte der Dtsch. Chem. Gesellschaft* **1881**, 14, 2725–2736.

[98] P. Debnath, *Curr. Org. Chem.* **2019**, 23, 2402–2435.

[99] A. A. Zagulyaeva, C. T. Banek, M. S. Yusubov, V. V. Zhdankin, *Org. Lett.* **2010**, 12, 4644–4647.

[100] A. Yoshimura, M. W. Luedtke, V. V. Zhdankin, *J. Org. Chem.* **2012**, 77, 2087–2091.

[101] P. Liu, Z. Wang, X. Hu, *European J. Org. Chem.* **2012**, 2012, 1994–2000.

[102] M. Uyanik, K. Ishihara, *Chem. Commun.* **2009**, 2086–2099.

[103] B. Sammet, *Synlett* **2009**, 18, 3050–3051.

[104] T. Curtius, *Berichte der Dtsch. Chem. Gesellschaft* **1890**, 23, 3023–3033.

[105] T. Shioiri, S. ichi Yamada, *Chem. Pharm. Bull.* **1974**, 22, 849–854.

[106] J. A. Barltrop, P. J. Plant, P. Schofield, *Chem. Commun.* **1966**, 822–823.

[107] W. A. Velema, J. P. Van Der Berg, W. Szymanski, A. J. M. Driessen, B. L. Feringa, *ACS Chem. Biol.* **2014**, 9, 1969–1974.

[108] A. Patchornik, B. Amit, R. B. Woodward, *J. Am. Chem. Soc.* **1970**, 92, 6333–6335.

[109] P. Klán, T. Šolomek, C. G. Bochet, A. Blanc, R. Givens, M. Rubina, V. Popik, A. Kostikov, J. Wirz, *Chem. Rev.* **2013**, 113, 119–191.

[110] A. M. Piloto, S. P. G. Costa, M. S. T. Gonçalves, *Tetrahedron* **2014**, 70, 650–657.

[111] C. G. Bochet, *Tetrahedron Lett.* **2000**, 41, 6341–6346.

[112] E. Modica, R. Zanaletti, M. Freccero, M. Mella, *J. Org. Chem.* **2001**, 66, 41–52.

[113] R. Schmidt, D. Geissler, V. Hagen, J. Bendig, *J. Phys. Chem. A* **2007**, 111, 5768–5774.

[114] E. J. Corey, A. Venkateswarlu, *J. Am. Chem. Soc.* **1972**, 94, 6190–6191.

[115] A. M. Dilauro, W. Seo, S. T. Phillips, *J. Org. Chem.* **2011**, 76, 7352–7358.

[116] M. M. Toteva, J. P. Richard, *Adv. Phys. Org. Chem.* **2011**, 45, 39-91.

[117] M. M. Toteva, M. Moran, T. L. Amyes, J. P. Richard, *J. Am. Chem. Soc.* **2003**, 125, 8814–8819.

[118] C. Huang, Y. Liu, S. E. Rokita, *Signal Transduct. Target. Ther.* **2016**, 1, 16009.

[119] K. M. Schmid, L. Jensen, S. T. Phillips, *J. Org. Chem.* **2012**, 77, 4363–4374.

[120] M. Azoulay, F. Chalard, J. P. Gesson, J. C. Florent, C. Monneret, *Carbohydr. Res.* **2001**, 332, 151–156.

[121] A. Pigorsch, M. Köckerling, *Cryst. Growth Des.* **2016**, 16, 4240–4246.

[122] P. Wei, F. Xue, Y. Shi, R. Strand, H. Chen, T. Yi, *Chem. Commun.* **2018**, 54, 13115–13118.

[123] S. A. Nuñez, K. Yeung, N. S. Fox, S. T. Phillips, *J. Org. Chem.* **2011**, 76, 10099–10113.

[124] S. Davies, B. L. Oliveira, G. J. L. Bernardes, *Org. Biomol. Chem.* **2019**, 17, 5725–5730.

[125] M. A. Jinks, A. de Juan, M. Denis, C. J. Fletcher, M. Galli, E. M. G. Jamieson, F. Modicom, Z. Zhang, S. M. Goldup, *Angew. Chemie Int. Ed.* **2018**, 57, 14806–14810.

[126] F. Modicom, E. M. G. Jamieson, E. Rochette, S. M. Goldup, *Angew. Chemie Int. Ed.* **2019**, 58, 3875–3879.

[127] E. Martinand-Lurin, R. Gruber, P. Retailleau, P. Fleurat-Lessard, P. Dauban, *J. Org. Chem.* **2015**, 80, 1414–1426.

Thesis Conclusion

This thesis outlines the development and proof-of-concept application of a stimuli-responsive interlocked molecular caging platform. The approach utilises mechanical bond formation, *via* AT-CuAAC rotaxination, to encircle the axle component with a ring-opening 2,2'-bipyridine macrocycle. In doing so, the chemical and biological activity of the axle is silenced. In response to an appropriate stimulus, key chemical bonds in the macrocyclic component are cleaved, causing the macrocycle to ring-open and disassemble the mechanical bond – liberating the de-caged axle component and restoring its activity. Two successful methods, differing in they way in which they incorporate the stimuli-responsive trigger unit, have been outlined in chapters **2** and **3**, respectively.

The first approach involved the direct incorporation of the trigger motif within the backbone of the 2,2'-bipyridine macrocycle – a photocleavable DEABn protecting group was chosen to validate this approach (Chapter **2**). Upon exposure to the appropriate wavelength of UV light, photo-heterolytic C-O bond cleavage resulted in an effective ring-opening mechanism, which was shown to proceed efficiently in several model rotaxanes to release the corresponding axle. Despite the success observed with this approach, there were numerous limitations. The choice of protecting group was limited to those that possessed suitable structural connectivity and a chemical tolerance to the numerous synthetic steps required to attain the final macrocycle. If the trigger choice were to be altered, this would also require an entirely new synthetic route to be explored, which is costly, time-consuming, and often challenging.

Overcoming the limitations of this first approach led to the concepts developed in Chapter **3** – a universal platform approach for the synthesis of cleavable 2,2'-bipyridine macrocycles. Rather than placing the stimuli-responsive unit directly within the macrocyclic framework, this approach employed a self-immolative spacer conjugated to the trigger motif on the periphery of the macrocycle. A robust displacement reaction allowed the trigger motif to be installed as the final synthetic step under mild conditions, granting rapid access to a host of 2,2'-bipyridine macrocycle designed to ring-open in response to various stimuli (pH, chemical, UV light). All macrocycles developed through the platform approach mediated the AT-CuAAC reaction with high efficiency. Upon deprotection of the trigger motif, the ring-opening of the macrocycle proceeded through cascade elimination of the incorporated amino-benzyl-based self-immolative linker. Although effective axle release was observed under highly acidic conditions, or when being actively irradiated with UV light, the rate of ring-opening in the deprotected macrocycle component was slow under mild conditions (neutral pH, no irradiation). The sub-optimal rate of ring-opening was significantly later improved by altering the electronic properties of the macrocycle-bound self-immolative spacer, facilitating ring-opening and axle release, even under mild (neutral pH, non-radiative) conditions.

With the utility of the two interlocked caging approaches successfully demonstrated in simple rotaxane models, the next logical step is to apply these materials to develop synthetic stimuli-responsive for biological applications. Efforts toward this goal were shown in Chapter **2**, with the successful incorporation of a DEABn-based 2,2'-bipyridine macrocycle into an oligonucleotide rotaxane sequence. However, proof-of-concept release is yet to be attempted. With the ever-increasing use of triazoles as biocompatible links and bioisosteric motifs in biology and medicine, the potential to install macrocyclic cages in a range biologically functional molecules *via* AT-CuAAC coupling is vast – suggesting the application of the interlocked caging approach is far from limited to just oligonucleotide-based applications.